The India-Asia collision from the perspective of Myanmar : insights from paleomagnetism and paleogeographic reconstructions

Jan Westerweel

UNIVERSITÉ DE RENNES 1

THESE DE DOCTORAT

L'UNIVERSITE DE RENNES 1

ECOLE DOCTORALE N° 600
Ecole doctorale Ecologie, Géosciences, Agronomie et Alimentation
Spécialité : Sciences de la terre et de l'environnement

Par
Jan WESTERWEEL

The India-Asia collision from the perspective of Myanmar: Insights from paleomagnetism and paleogeographic reconstructions

Thèse présentée et soutenue à Géosciences Rennes (CNRS, Univ. Rennes), le 04/12/2020
Unité de recherche : UMR 6118

Rapporteurs avant soutenance :

Douwe van Hinsbergen	Professeur, Utrecht University
Frédéric Fluteau	Professeur, IPGP Paris

Composition du Jury :

Présidente du jury Annick Chauvin	Professeur, Université de Rennes 1
Douwe van Hinsbergen	Professeur, Utrecht University
Frédéric Fluteau	Professeur, IPGP
Yani Najman	Maitre de conférence, Lancaster University
Chris Morley	Professeur, Chian Mai University
Alexis Licht	Chargé de recherche, CEREGE
Directeur de thèse Pierrick Roperch	Directeur de recherche, Université de Rennes 1
Co-directeur de thèse Guillaume Dupont-Nivet	Chargé de recherche, Potsdam University

The India-Asia collision from the perspective of Myanmar: Insights from paleomagnetism and paleogeographic reconstructions

Ph.D. thesis Jan Westerweel

Department: Geosciences Rennes (UMR 6118), Université de Rennes 1, CNRS

Doctorate: Doctorat de l'Université de Rennes 1, Sciences de la Terre et de l'Environnement

Doctoral school: Ecole Doctorale N°600 Ecologie Géosciences Agronomie Alimentation (ED EGAAL), Université Bretagne Loire

Funded by: ERC consolidator grant MAGIC 649081

Thesis presented and defended in Rennes on 04-12-2020

Jury:

Dr. Pierrick Roperch, University of Rennes 1 (FR)	Thesis supervisor
Dr. Guillaume Dupont-Nivet, University of Potsdam (GE)	Thesis co-supervisor
Prof. dr. Frédéric Fluteau, IPGP Paris (FR)	Rapporteur
Prof. dr. Douwe van Hinsbergen, Utrecht University (NL)	Rapporteur
Prof. dr. Annick Chauvin, University of Rennes 1 (FR)	President of jury
Dr. Yani Najman, Lancaster University (UK)	Jury member
Prof. dr. Chris Morley, Chiang Mai University (TH)	Jury member
Dr. Alexis Licht, CEREGE Aix-en-Provence (FR)	Invited member

Acknowledgements

My PhD adventure in Rennes started 3 years, 4 fieldworks, 1740 rock samples and 0 cups of coffee before writing this, and what an adventure it has been. Perhaps it was always my destiny to become a geologist in France. Every summer when I was a child, my parents, my sister and I stereotypically went on holidays to southern France. One of the towns, Espéraza, which we visited for four consecutive years, had a tiny dinosaur museum. I think I visited this museum every year. I owned plenty of dinosaur books and I knew the names of countless prehistoric species and all the geological time periods by heart. And although I know less dinosaur names fifteen years later, but more about Myanmar, plate tectonics and paleomagnetism, it makes me happy that during the last three years, I was able to turn my childhood hobby into my actual work. That passion has definitely not waned since, and for a huge part that is thanks to many great people that I have met during this adventure.

The first person I wish to thank is my thesis director and daily supervisor Pierrick Roperch. Thank you for sharing your enormous scientific knowledge with me, and for always trying to take this project to the next level. On a personal level, you sometimes acted as a father figure to me in Rennes. Much like my father, you have the habit to be always right. Also much like my father, you never hesitated to help me out with a lot of personal stuff. Helping me with French insurances and calling the police when I was recovering from a bike accident are just some examples of this.

Next, I would like to thank my other thesis director Guillaume Dupont-Nivet. I am indebted to you for seeing a chance in me for your ERC project MAGIC. I really admire your style of leadership, characterized by a lot of patience, friendliness and mediating. I have not been able to find a monkey in amber for you, but at least we have gained a better understanding of Asian tectonics and paleogeography.

Despite not being an official supervisor, I have worked a lot with Alexis Licht as well. Thank you so much for enthusiastically sharing your knowledge about Myanmar and for organizing all the fieldworks. During these trips, we shared many good adventures, ideas, beers and jokes. I hope we can finish the pitch for our television series about timetravelling settlers in the Cretaceous someday.

I am grateful to my two rapporteurs Frédéric Fluteau and Douwe van Hinsbergen for carefully reviewing my thesis before submission. Besides them, I am also grateful to Annick Chauvin, Chris Morley and Yani Najman for fruitful discussions as members of my PhD defense committee.

Fieldwork in Myanmar was easily the most exciting part of my thesis. It was very interesting to work with our Burmese collaborators. ‘Chay-tzoo-beh’ to Zaw Win, Hnin Hnin Swe, Myat Kai Thi, Day Wa Aung and Kyi Kyi Thein for all your help in your amazing country. Lots of thanks as well for the good

times to the remaining people from the Myanmar Paleoclimate and Geodynamics Research Group: Amy Gough, Carina Hoorn, Huasheng Huang, Virginia Littell, Willem Renema and Sarawute Chantraprasert.

Furthermore, I thank all the great colleagues from ERC project MAGIC for all their positive feedback and enjoyable company during meetings. I would like to mention all welcoming people from Geosciences Rennes as well. With the other PhD students / Post-docs I enjoyed a lot of fun trips and evenings, and of course there are the thousands of games of Tarot during lunchbreaks. In addition, I would like to thank the following scientists not mentioned before: Eldert Advokaat, Sietske Batenburg, Nathan Cogné, Pauline Coster, Philippe Cullerier, Olivier Dauteuil, François Guillocheau, Erwan Hallot, Gwenaël Hervé, Oliver Jagoutz, Marc Jolivet, Catherine Kissel, France Lagroix, Andrew Mitchell, Julien Morin, Pavel Pitra, Jean-Noël Proust, Claude Rangin, Anne Replumaz, Gilles Ruffet, Mike Searle and Camille Wandres. I think it is also safe to say that I would not be here without Cor Langereis, Bora Uzel and Nuretdin Kaymakci.

Finally, I think I am blessed with great family and friends in life and I would like to take this opportunity to thank them. My parents and sister for always being there for me, the many old friends for visiting me in Rennes and making time for me when I was back in the Netherlands, the many new friends in Rennes for discovering ‘la Bretagne’ together, and lastly Laurel who made everything extra worthwhile and special.

Abstract

The Himalayan-Tibetan orogen, formed primarily due to the India-Asia collision, represents a complex interplay of collisional tectonics, climate and environmental processes. However, its paleogeographic evolution, as well as the timing of the collision itself, remain the subject of intense debate. This controversy is partly the result of understudying major components of the Himalayan orogen. At the eastern edge of the orogen, the paleogeography of the Burma Terrane (Myanmar) is particularly uncertain but key for solving the India-Asia collision puzzle. Therefore, this thesis presents a complete set of Late Cretaceous to Miocene paleomagnetic data from the Burma Terrane. With sedimentology and geochronology data, these results were incorporated into plate tectonic reconstructions to elucidate the paleogeographic history of the India-Asia collision from the perspective of the Burma Terrane. The three key implications are: (1) the Burma Terrane was in an equatorial position distant from Asia from the Cretaceous until the Paleogene, (2) it was incorporated onto the Indian Plate in the latest Paleocene – middle Eocene, and (3) it subsequently moved northward with India. This latitudinal displacement explains why the Burma Terrane does not record major compressional deformation before the late Oligocene – early Miocene. Yet, the sedimentary basins of Myanmar received erosional products from the collision zone already in the Eocene. By the Miocene, they record rapid exhumation of the Eastern Himalayan Syntaxis. The complete dataset is used to infer an India-Asia collision model with a Trans-Tethyan Arc, which comprises the Burma Terrane formed from Gondwanan crustal fragments. This model invites a critical re-evaluation of many aspects of the regional tectonic history, and has additional implications for Asian biotic and climatic evolution.

Résumé détaillé en français

L'orogène Himalayen-Tibétain, formé principalement à la suite de la collision entre l'Inde et l'Asie, est largement reconnu comme l'archétype de l'orogène pour l'étude des systèmes de collision entre continents. Il représente une interaction complexe de processus géodynamiques et environnementaux qui ont une profonde influence sur le climat régional et mondial. La surrection de la chaîne de montagne Himalaya-Tibet est une des causes possibles du début des moussons Asiatiques et du refroidissement global à la transition Éocène-Oligocène. Par conséquent, il est essentiel de déchiffrer l'évolution paléogéographique de l'orogène pendant la convergence de l'Inde et de l'Asie pour comprendre pleinement ces interactions. Cependant, cette évolution paléogéographique, ainsi que le moment de la collision elle-même, font toujours l'objet d'un débat intense dans la communauté des géosciences, ce qui se traduit par des modèles concurrents très différents.

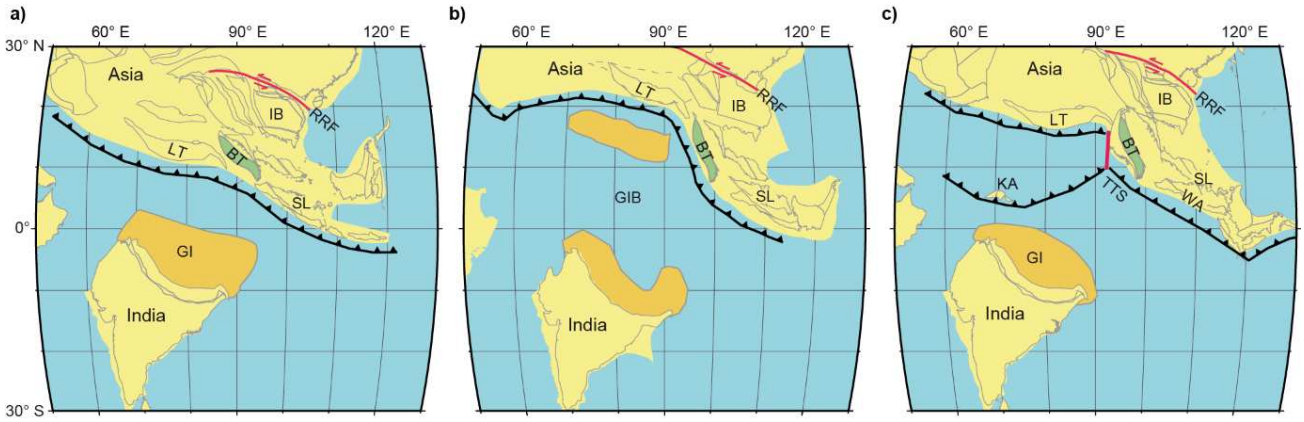

Figure 1 : *Reconstructions des plaques tectoniques alternatives de la paléogéographie Inde-Asie à 60 Ma avec le logiciel GPlates : a) Reconstruction avec une zone de subduction presque linéaire et une extrusion importante de blocs d'Indochine; b) Reconstruction avec un Bassin de la Grande Inde; c) Reconstruction avec un système de subduction Trans-Téthysien. Abréviations, références, et plus de détails : Chapitre 4.*

Les modèles traditionnels proposaient un scénario simple dans lequel la Plaque Indienne se déplaçait vers le nord jusqu'à la collision Éocène de la Grande Inde, la partie de la Plaque Indienne qui s'est subduite depuis la collision initiale, avec la marge de l'Asie du Sud (Fig. 1a). Cependant, des informations actualisées basées sur la première arrivée de sédiments ayant une affinité avec l'Asie sur la Plaque Indienne confirment une collision plus précoce au Paléocène (~58 Ma). Avec les contraintes tectoniques, cela place le continent Indien à une latitude quasi-équatoriale à cette époque, à des milliers de kilomètres de la marge de l'Asie du Sud. Une collision au Paléocène pourrait encore être compatible avec ce modèle en plaçant la marge Asiatique à de basses latitudes

(~10°N), mais cette position est invalidée par les données paléomagnétiques. Par ailleurs, une Grande Inde continentale extra-large pourrait expliquer l'âge d'une collision au Paléocène. Cependant, ce scénario nécessiterait une subduction continentale de l'Inde d'une taille irréaliste et un raccourcissement important de la marge Asiatique, ce qui ne peut être résolu qu'en partie par l'extrusion latérale des blocs d'Indochine loin de la zone de collision, mais cette extrusion reste beaucoup plus élevée que ne le laissent supposer les donnéesde géologie structurale. Pour tenter de résoudre ces divergences, deux nouveaux modèles ont été proposés : (1) les modèles du Bassin de la Grande Inde qui proposent l'existence d'un bassin océanique entre l'Inde et la Grande Inde qui aurait pu facilement se subducter après une première collision de fragments de la Grande Inde du nord avec l'Asie à 58 Ma jusqu'à une seconde collision de l'Inde avec l'Asie au Miocène (Fig. 1b), et (2) les modèles de collision de l'Arc Trans-Téthysien qui proposent que l'Inde a d'abord heurté un système de subduction Trans-Téthysien à ~60 à 50 Ma avant qu'ils n'entrent conjointement en collision avec l'Asie plus tard à la fin de l'Eocène (Fig. 1c). Une telle double zone de subduction rendrait également mieux compte des taux de convergence rapide inféré entre l'Inde et l'Asie avant la collision finale.

Ces vues contrastées sont en partie le résultat de la sous-étude des composantes occidentale et orientale de la zone de collision Himalayenne, longue de ~2700 km, par rapport à l'orogène central, long de ~2600 km. Le Terrane de Birmanie, la principale microplaque située à l'extrémité orientale de la zone de collision Himalayenne et qui comprend la majeure partie du Birmanie, en est un bon exemple (Fig. 2).

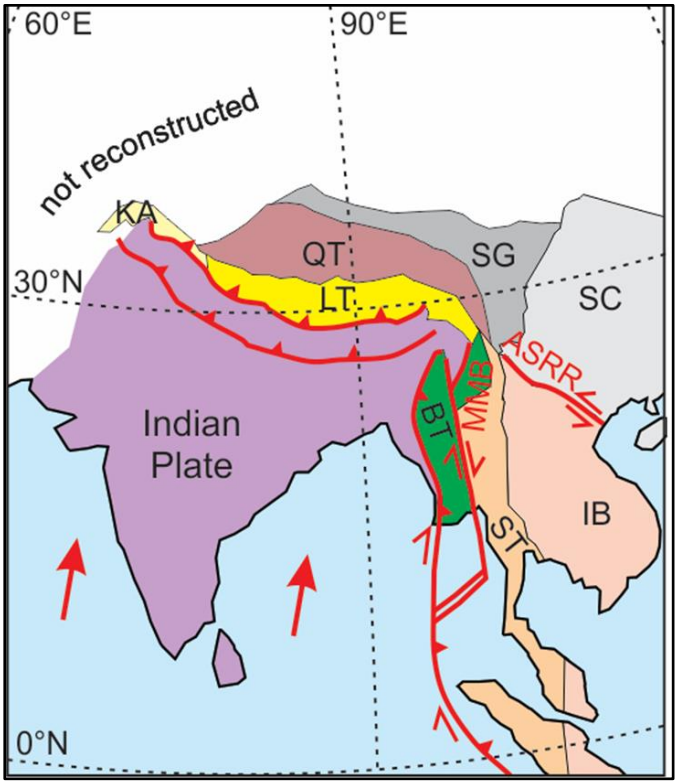

Figure 2 : *Cadre tectonique général de la collision entre l'Inde et l'Asie, et la Terrane de Birmanie. Abréviations, références, et plus de détails : Chapitre 1.*

La recherche géologique en Birmanie présente des défis fondamentaux, notamment son isolement politique et scientifique au cours des 70 dernières années, son accès routier limité et la jungle qui couvre une grande partie de la l'exposition. Heureusement, le pays s'ouvre à la recherche scientifique depuis peu, ce qui permet de mieux comprendre son histoire géologique unique. Le cadre tectonique actuel du Terrane de Birmanie (Fig. 3) est caractérisé par une subduction hyper-oblique de la Plaque Indienne sous la marge active Birmane à l'ouest, provoquant un volcanisme sporadique dans l'Arc Wuntho-Popa qui affleurant au centre de cette microplaque à tendance N-S. À l'est, la Faille de Sagaing, une faille dextre très active, forme la limite du Terrane de Birmanie avec le Terrane de Sibumasu (Indochine) et se transforme par une ouverture océanique de la Mer d'Andaman au sud. Ces caractéristiques tectoniques permettent un mouvement décrochant vers le nord du Terrane de Birmanie, qui fait partie de la ceinture mobile Birmane proprement dite, ce qui entraîne une indentation continue avec l'Himalaya oriental au nord. La géologie du Terrane de Birmanie lui-même est traditionnellement divisée en plusieurs ceintures orientées approximativement vers le nord-sud. Les Bassins du Centre de la Birmanie couvrent la majeure partie du Terrane de Birmanie, constitué de sédiments Albien à Quaternaire. Pour cette raison, le socle du Terrane de Birmanie est mal exposé et mal compris, avec les seuls affleurements sporadiques trouvés dans l'Arc Wuntho-Popa dans la partie centrale du Terrane de Birmanie et aux Chaînes Indo-Birmanes, une chaîne de montagnes formant la limite occidentale du Terrane de Birmanie. Ces roches du socle contiennent des preuves apparemment contrastées de l'origine du Terrane de Birmanie, avec des âges de zircons détritiques et des assemblages de fossiles suggérant une origine du Gondwana, Sibumasu ou Cathaysia. En plus, une partie des Chaînes Indo-Birmanes constitue potentiellement un bloc tectonique distinct dérivé du Gondwana, appelé le Bloc du Mont Victoria. Ce Bloc du Mont Victoria est séparé du Terrane de Birmanie par l'Ophiolite de la Ceinture Occidentale des Chaînes Indo-Birmanes, qui, selon une autre interprétation, consiste en des nappes de matériau d'accrétion. L'Arc Wuntho-Popa lui-même est le principal arc volcanique du Terrane de Birmanie, divisant les Bassins du Centre de la Birmanie en bassins orientés N-S en position d'avant-arc et d'arrière-arc. Il s'est développé au Crétacé Supérieur (~110-90 Ma) sous la forme d'un arc de type Andin suite à la mise en place de l'Ophiolite de la Ceinture Occidentale. De l'autre côté de cette ceinture ophiolitique, la majorité des Chaînes Indo-Birmanes constituent un prisme d'accrétion qui s'est développé en raison de la subduction de la Plaque Indienne. Les Bassins du Centre de la Birmanie sont coupés à l'est par la Faille de Sagaing, qui forme la limite complexe avec les roches plus anciennes du Paléozoïque-Mésozoïque du Terrane de Sibumasu, à côté de l'Ophiolite de la

Ceinture de Jade et de la Ceinture de Mogok-Mandalay-Mergui, une ceinture avec un haut degré de métamorphisme.

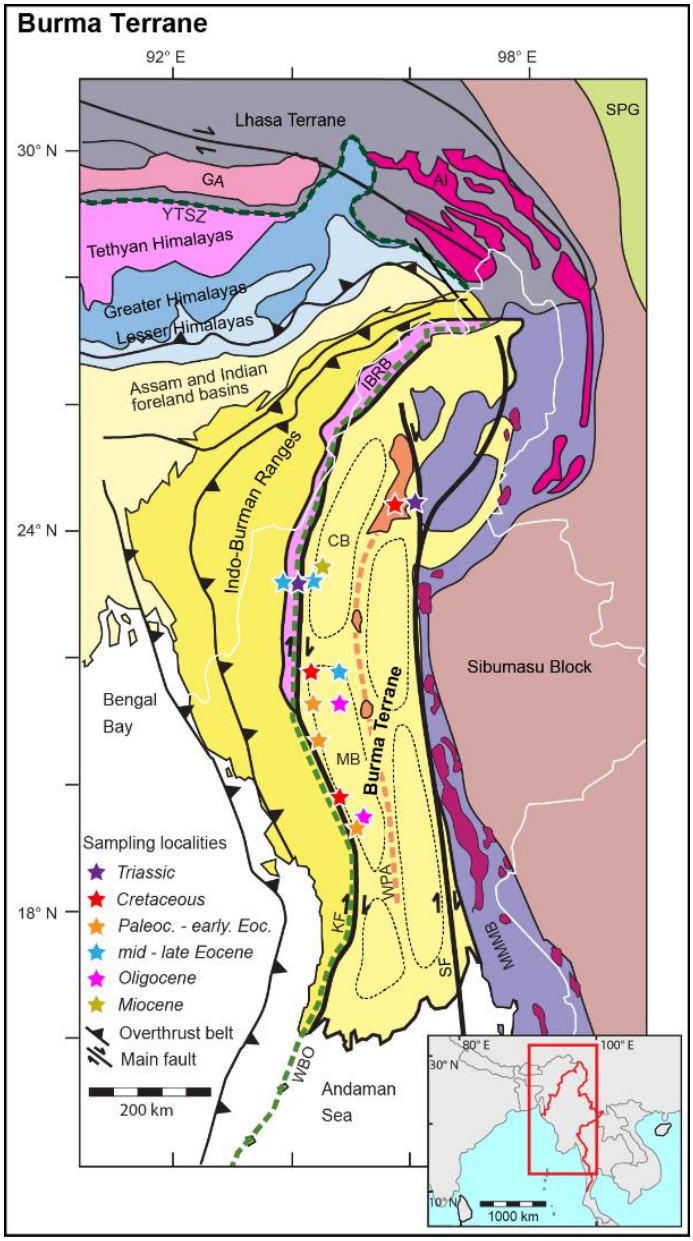

Figure 3 : *Carte géologique généralisée de la Birmanie avec les localités échantillonnées dans le cadre de ce projet (Étoiles). Abréviations, références, et plus de détails : Chapitres 2 et 3.*

Ce cadre géologique unique, mais mal compris, a donné lieu à un rôle fondamentalement différent pour le Terrane de Birmanie dans les trois modèles de collision Inde-Asie mentionnés ci-dessus (Fig. 1). Dans les modèles continentaux traditionnels de la Grande Inde à forte extrusion, le Terrane de Birmanie est initialement situé à une latitude relativement élevée au Paléogène, à côté du Terrane de Lhassa, dans le cadre d'une marge Asiatique linéaire et approximativement orientée E-O. De cette position, le Terrane de Birmanie a été extrudé vers son emplacement actuel. Il est important de

noter que l'Arc volcanique Wuntho-Popa du Terrane de Birmanie est interprété dans ce contexte comme la continuation vers l'est de l'Arc de Gangdese du Terrane de Lhassa, ce qui a été la raison principale de nombreuses études visant à reconstruire le Terrane de Birmanie près de sa latitude actuelle. Cependant, l'Arc Wuntho-Popa est actuellement orienté approximativement N-S et ces modèles nécessitent donc une rotation post-collision importante du Terrane de Birmanie dans le sens horaire. En revanche, la marge de l'Asie du Sud-Est est plus conservatrice dans les modèles océaniques de la Grande Inde pendant la collision, et le Terrane de Birmanie subit donc peu de rotation post-collision, mais subit plutôt une convergence hyper-oblique avec l'Inde déjà au début du Paléogène. Enfin, la position du Terrane de Birmanie est moins contrainte dans les modèles de subduction Trans-Téthysien, car plusieurs études ont proposé qu'il pourrait avoir fait partie de l'Arc Incertus, l'arc insulaire intra-océanique du système de subduction Trans-Téthysien. Cela permettrait potentiellement d'obtenir une latitude plus méridionale pour le Terrane de Birmanie au cours des premières périodes de collision. Ceci illustre comment le Terrane de Birmanie offre une excellente opportunité de déterminer l'évolution de l'orogène (oriental) de l'Himalaya et la collision entre l'Inde et l'Asie.

À cette fin, l'objectif de cette thèse était de déchiffrer l'évolution paléogéographique du Terrane de Birmanie afin d'apporter de nouveaux éclairages dans cet important débat sur la collision entre l'Inde et l'Asie. Les données paléomagnétiques fournissent des contraintes sur le mouvement rotationnel et latitudinal des terranes tectoniques et constituent donc la majeure partie des données présentées dans cette étude (Figs. 3 et 4). Le travail sur le champ paléomagnétique au cours de cette thèse a consisté en trois saisons d'échantillonage paléomagnétique en Birmanie : Quatre semaines en novembre 2017, cinq semaines en janvier 2019 et deux semaines en janvier 2020. Ces travaux de terrain ont été entrepris après l'obtention de données préliminaires suite à un premier échantillonage en décembre 2016 par l'équipe encadrante et dont les résultats sont aussi inclus dans cette thèse. Le travail sur le terrain a été dirigé par Alexis Licht pour la sédimentaologie et l'échantillonnage paléomagnétique a été encadré par Pierrick Roperch et Guillaume Dupont-Nivet. Parallèlement à l'échantillonnage paléomagnétique, des échantillons ont été prélevés pour des datations U-Pb sur zircons détritiques (A. Licht), de la thermochronologie sur apatite (N. Cogné), des datations $^{40}Ar/^{39}Ar$ (G. Ruffet) et un échantillonnage pour des études palynologiques (H. Huang et C. Hoorn). Les deux principales zones d'étude étaient l'avant-arc Birman, composé du Bassin de Chindwin au nord et du Bassin Minbu au sud, ainsi que les Montagnes Wuntho, le segment nord de l'Arc Wuntho-Popa à prédominance Crétacée. La prospection et l'échantillonnage paléomagnétiques ont été difficiles en Birmanie, en raison de la végétation qui recouvre de nombreux affleurements, de la forte altération des affleurements due au climat tropical et de la faible disponibilité de cartes

géologiques détaillées. Par conséquent, la prospection a généralement consisté à explorer la campagne tout en recherchant sur des images satellites des affleurements potentiels dans les rivières, les bords de routes et les carrières utilisées pour la construction de routes. Les lieux d'échantillonnage lors des premiers travaux sur le terrain en 2017 étaient les sédiments de l'Éocène supérieur au Miocène moyen exposés dans une section sédimentaire homocline autour du village de Kalewa (Bassin de Chindwin), et le complexe volcanique du Crétacé Supérieur des Montagnes Wuntho. Au cours des travaux de terrain suivants, en 2019, l'échantillonnage a été étendu aux sédiments du Paléocène à l'Oligocène tardif du Bassin de Minbu, au sud. Ici, la Formation Paunggyi du Paléocène et la Formation Laungshe de l'Éocène inférieur ont été échantillonnées près des villages de Sidoktaya et Datkon. De plus, une section magnétostratigraphique a été échantillonnée près de la ville de Minbu dans la Formation Yaw de l'Éocène supérieur et la Formation Shwezetaw de l'Oligocène inférieur pour delimiter la Transition Éocène-Oligocène. Des sites paléomagnétiques ont également été obtenus dans la Formation Padaung de l'Oligocène moyenne, dans l'anticlinal de la pagode de Tantkyitaung à l'ouest de Bagan et dans la Formation Pondaung de l'Éocène supérieur, exposée dans l'anticlinal des Montagnes Pondaung qui forme la limite entre les Bassins de Chindwin et de Minbu. Enfin, des sites d'exploration ont également été forés dans les Chaînes Indo-Birmane au cours du deuxième travail de terrain, consistant en turbidites et en unités de mélange ophiolitique du Trias au Paléogène à l'ouest de la ville de Kalay, et en roches péridotites ophiolitiques à l'ouest de Datkon dans le Bassin de Minbu. Les résultats préliminaires de la Formation Laungshe à Sidoktaya étant prometteurs, le but du troisième et dernier travail de terrain en 2020 était d'échantillonner davantage de sites paléomagnétiques plus au nord dans le bassin du Minbu, près du village de Saw. Les sites autour de Saw comprennent les Formations Laungshe, Tilin et Tabyin du début de l'Éocène, ainsi que la dernière Formation Kabaw du Crétacé.

Figure 4 : *Echantillonnage paléomagnétique des roches volcaniques (à gauche) et des sédiments (à droite) du Terrane de Birmanie. Plus de détails : Chapitre 3.*

Au total, 1740 échantillons paléomagnétiques orientés ont été forés dans le cadre de cette thèse, en utilisant des équipements et des procédures standard du paléomagnétisme. Les échantillons paléomagnétiques ont été mesurés dans le laboratoire de paléomagnétisme de Géosciences Rennes (Université de Rennes 1), en particulier sur un magnétomètre cryogénique 2G installé dans une salle blindée magnétiquement. Les procédures de mesure standard ont été suivies, y compris la désaimantation thermique ou par champs alternatifs à 3 axes. En outre, des mesures de l'Anisotropie de la Susceptibilité Magnétique (AMS), de la susceptibilité magnétique, de l'Aimantation Rémanente Isotherme (IRM) et des cycles d'hystérésis magnétique ont également été effectués. Les ensembles de données paléomagnétiques obtenus ont été complétés par les résultats de la sédimentologie, de la géochronologie (âge du zircon détritique U/Pb, de l'apatite U/Pb et des traces de fission de l'apatite) et de la minéralogie (observations au microscope optique et au Microscope Électronique à Balayage), puis intégrés dans des modèles paléogéographiques et tectoniques robustes à l'aide du logiciel GPlates.

Le premier ensemble de résultats acquis fournit le cadre de cette étude, en utilisant des données paléomagnétiques du Crétacé Supérieur et de l'Éocène supérieur, ainsi que des datations Ar/Ar et des observations minéralogiques, pour donner les premières contraintes sur la paléoposition du Terrane de Birmanie. Les résultats du Crétacé Supérieur ont été obtenus dans la région de Wuntho, le segment nord de l'Arc Wuntho-Popa, qui est principalement caractérisé par le Batholite Kanza Chaung (~110-90 Ma), mais qui contient également des dépôts volcaniques et sédimentaires d'âge similaire. Les données paléomagnétiques provenant de 21 sites forés dans les roches intrusives du Batholite de Kanza Chaung ont permis d'obtenir des directions caractéristiques avec des aimantations primaires portées par la magnétite. Aucune preuve d'un basculement significatif de ce batholite n'a été trouvée. Les 23 autres sites acquis de l'Andésite de Mawgyi et du Groupe de Kondan Chaung, composés de roches volcaniques, volcanoclastiques et de sédiments, ont probablement été réaimantés par la mise en place du Batholite de Kanza Chaung. Ceci est démontré par l'observation de réaimantations liées à l'altération hydrothermale mise en évidence par des observations minéralogiques, et les âges similaires en Ar/Ar de ~97-87 Ma à ceux obtenus pour le Batholite de Kanza Chaung.

Les directions moyennes du Batholite de Kanza Chaung et les directions réaimantées de façon homogène du Groupe de Kondan Chaung donnent un pôle du Crétacé Supérieur avec une grande rotation dans le sens horaire de 60.4±8.7° par rapport à une Eurasie Stable et une latitude de l'hémisphère sud proche de l'équateur de 5.0±4.7°S (Fig. 5a). Les résultats de la fin de l'Éocène ont été obtenus dans le Bassin de Chindwin, le bassin de l'avant-arc nord du Terrane de Birmanie, où a été échantillonnée une section sédimentaire homocline comprenant les grès, siltstones, mudstones

et sidérites marins peu profonds de la Formation Yaw. Une couche de tuf datée dans la Formation Yaw donne une contrainte d'âge de ~38 Ma. Les aimantations primaires provenant de 168 échantillons dans cette section donnent une rotation dans le sens horaire négligeable de 4.6±3.5° par rapport à l'Eurasie Stable, indiquant une rotation majeure dans le sens horaire entre le début du Crétacé Supérieur et la fin de l'Éocène (Fig. 5b,c). En outre, la direction moyenne de la fin de l'Éocène donne une latitude de l'hémisphère nord proche de l'équateur de 2.4±1.5°N, qui ne devient que légèrement plus élevée (4.1±2.3°N) après correction pour une éventuelle compaction. Les paléolatitudes de l'hémisphère sud – quasi-équatoriale du Crétacé Supérieur à l'Éocène supérieur que ces données impliquent, contrastent fortement avec les études précédentes, qui plaçaient généralement le Terrane de Birmanie près de son emplacement actuel (Fig. 5c).

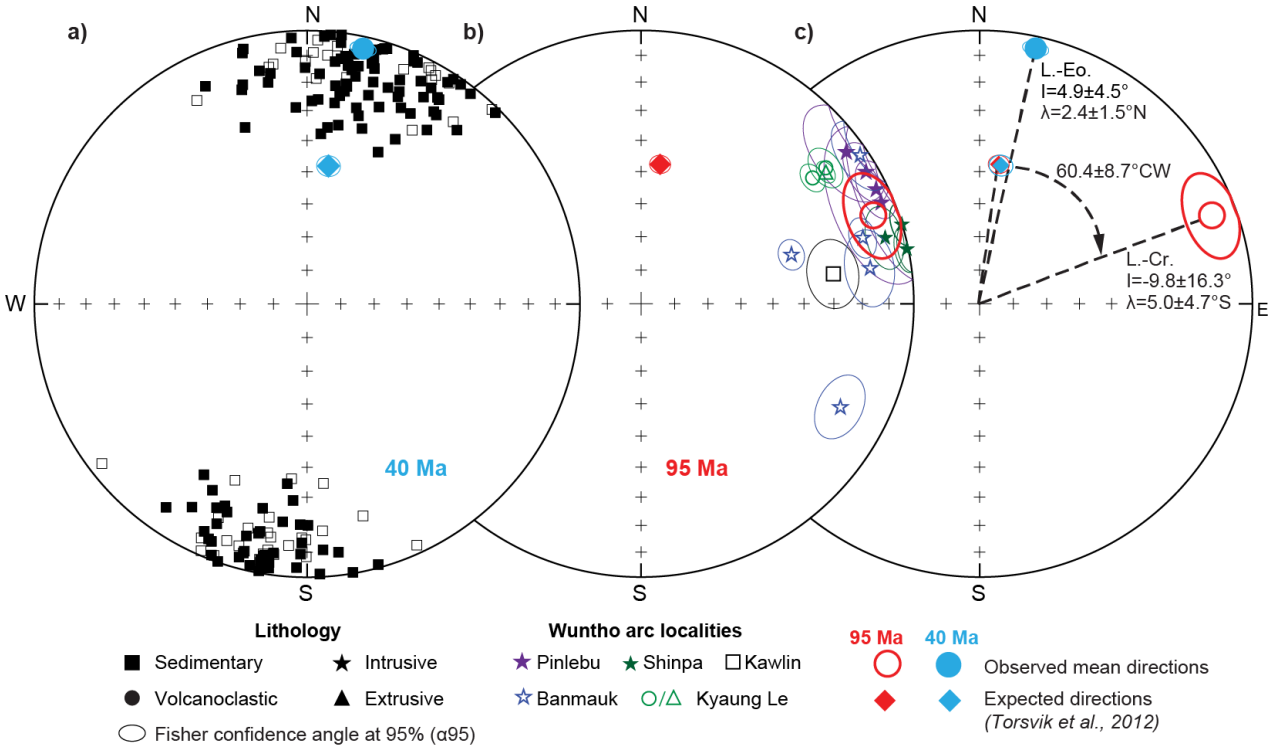

Figure 5 : *Projections stéréonet du premier ensemble de résultats paléomagnétiques du Crétacé Supérieur et de la fin de l'Éocène. Abréviations, références, et plus de détails : Chapitre 4.*

La latitude du Terrane de Birmanie du Crétacé Supérieur est éloignée de celle attendue pour la marge de l'Asie du Sud et correspond donc le mieux aux modèles de subduction Trans-Téthysien, où le Terrane de Birmanie représente un segment de l'Arc Incertus intra-océanique. Au début du Paléogène, l'Inde est entrée en collision avec ce système de subduction Trans-Téthysien lors de sa convergence vers le nord avec l'Asie et le Terrane de Birmanie s'est déplacé vers le nord à ses côtés (Fig. 6). À la fin de l'Éocène, la rotation dans le sens horaire du Terrane de Birmanie s'est achevée et la convergence entre l'Inde et le Terrane de Birmanie avec la marge du sud-est Asiatique est

devenue hyper-oblique (Fig. 6). Cependant, le pôle de la fin de l'Éocène indique que le Terrane de Birmanie était encore situé à des latitudes quasi-équatoriales à cette époque, ce qui suggère un mouvement de glissement vers le nord d'environ 2000 km le long d'une "Faille de Proto Sagaing" depuis cette époque. Au-delà de la géodynamique, ces résultats suggèrent un endémisme insulaire pour les ambres Crétacé du Terrane de Birmanie, très riches en biodiversité et qui font l'objet de plus d'une centaine de publications chaque année, et un climat de mousson fortement équatorial en Birmanie pendant l'Éocène. La principale conclusion de ce premier ensemble de contraintes sur la position du Terrane de Birmanie est que son histoire tectonique est incompatible avec les modèles continentaux et océaniques de la Grande Inde et qu'elle est mieux interprétée dans un cadre géodynamique impliquant une double collision de l'Inde avec un système de subduction Trans-Téthysien et l'Asie.

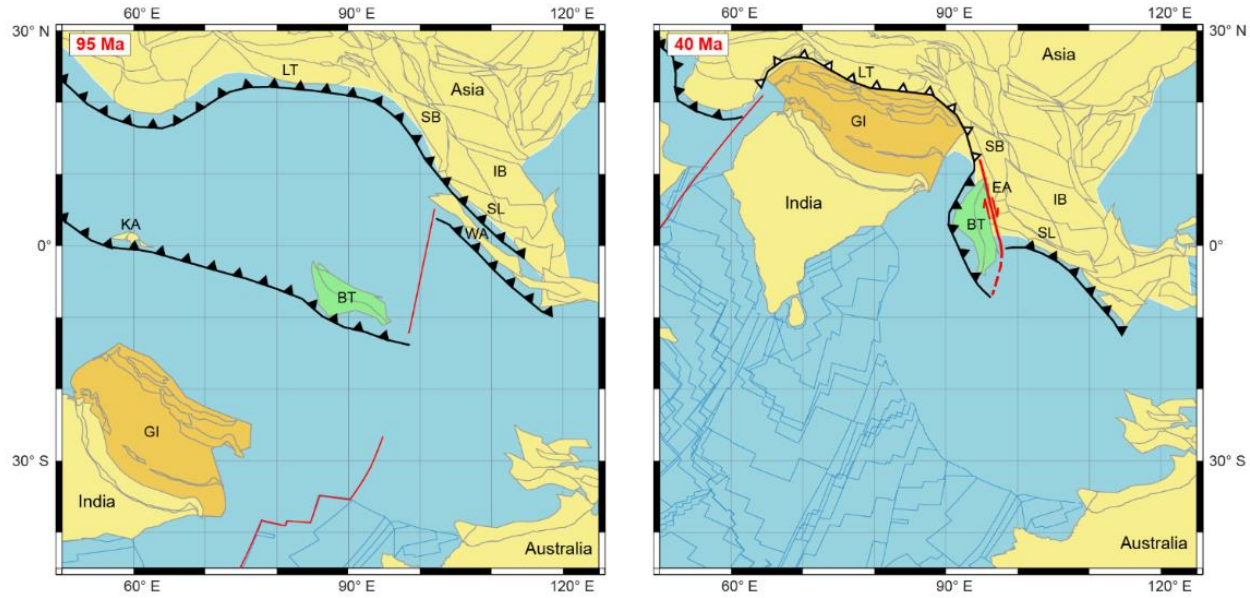

Figure 6 : *Reconstructions initiales de ce projet du Terrane de Birmanie et de l'Asie à 95 Ma (à gauche) et 40 Ma (à droite) avec le logiciel GPlates. Abréviations, références, et plus de détails : Chapitre 4.*

Afin de vérifier plus avant ce cadre tectonique actualisé pour le Terrane de Birmanie, les archives sédimentaires du Cénozoïque de l'avant-arc Birman ont été étudiées, car elles auraient dû enregistrer les changements du cadre tectonique, de la provenance et des paléoenvironnements au cours du long voyage de ~2000 km vers le nord, de l'équateur vers la zone de collision Himalayenne. À cette fin, les résultats de la sédimentologie, de la magnétostratigraphie, de la géochronologie (les âges zircon détritique U/Pb, apatite U/Pb et les traces de fission sur apatite) et les propriétés magnétiques ont été obtenues dans les échantillons de la Formation Yaw de l'Éocène supérieur, la Formation Tonhe de l'Oligocène supérieur et la Formation Letkat du Miocène inférieur du Bassin de

Chindwin. Parallèlement au contexte tectonique des plaques mis à jour, ces données permettent d'élucider l'évolution paléogéographique du Terrane de Birmanie et de l'Himalaya oriental. La section sédimentaire étudiée est caractérisée par deux changements significatifs dans les faciès sédimentaires, les propriétés magnétiques, la minéralogie et la provenance. Ces changements ont été interprétés comme deux hiatus sédimentaires de la fin de l'Éocène - Oligocène moyen et Oligocène le plus récent - début du Miocène, tous deux étant la conséquence d'une importante translation vers le nord du Terrane de Birmanie (Fig. 7).

Figure 7 : *Aperçu des résultats de la stratigraphie (a), géochronologiques (a), de la susceptibilité magnétique (b) et de la magnétostratigraphie (c) du Bassin de Chindwin, comparé avec l'échelle de temps de la polarité géomagnétique (GTS16) et contraintes d'âge. Les lignes rouges mettent en évidence les deux hiatus sédimentaires de la fin de l'Éocène - Oligocène moyen et Oligocène le plus récent - début du Miocène. Abréviations, références, et plus de détails : Chapitre 5.*

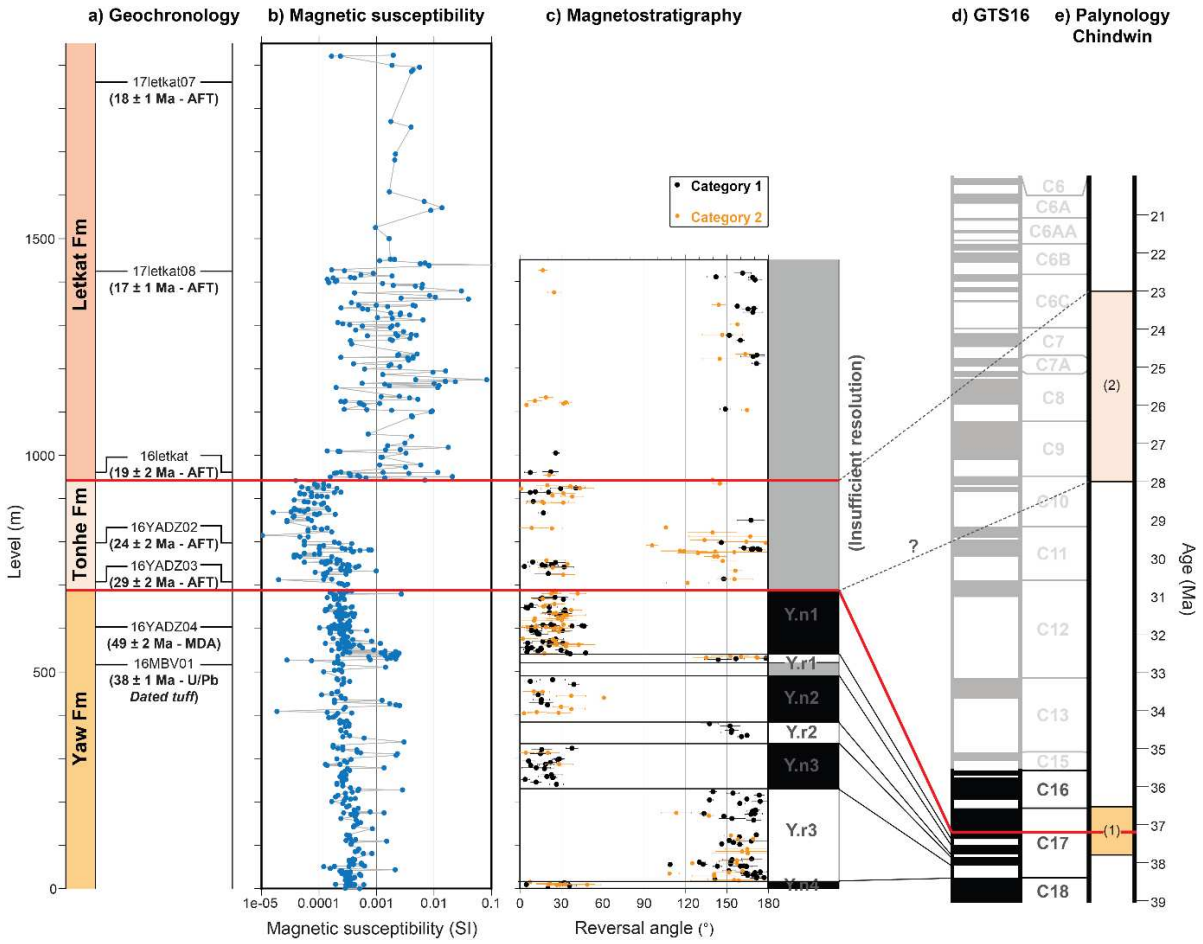

La Formation Yaw présente une variété de faciès sédimentaires comprenant des grès deltaïques et fluviaux, des couches de charbon et des couches de sidérite anoxique. Ensemble, ces faciès sédimentaires correspondent à un paléoenvironnement estuarien quasi-fermé. Pendant le dépôt de la Formation Yaw, l'Arc Wuntho-Popa et sa continuation au nord comme partie de l'Arc Trans-

Téthysien (Batholite de Lohit) ont été les sources sédimentaires probables, comme le montrent les données géochronologiques. Les conditions anoxiques et l'altération chimique étaient importantes dans ce paléoenvironnement estuarien quasi-fermé, entraînant la disparition de la magnétite et la formation de couches de sidérite riches en fer. Heureusement, un enregistrement magnétostratigraphique fiable de 298 échantillons a pu être obtenu, montrant un intervalle d'âge de ~38.4-37.2 Ma et des taux de subsidence rapide de type pull-apart liés à la déformation strike-slip (Fig. 8). La dernière discordance entre l'Éocène et l'Oligocène moyen marque la transition vers des conditions purement fluviales dans la Formation Tonhe caractérisée par des grès, des siltstones et des paléosols. Ce changement correspond au débordement du Bassin de Chindwin suite à la subsidence rapide antérieure. En outre, la Formation Tonhe enregistre une phase d'exhumation de la fin de l'Oligocène dans la région source des sédiments, qui était probablement constituée de sédiments recyclés. Le début de la collision de l'Arc Trans-Téthysien avec l'Asie explique probablement ce premier soulèvement et débordement de l'Éocène tardif - Oligocène moyen, ainsi que la provenance des sédiments du Bassin de Chindwin. Cette collision s'est propagée vers le sud, car on n'observe pas de discordance mais une sédimentation marine continue dans le Bassin de Minbu au sud au cours du dernier Eocène - Oligocène moyen. La deuxième discordance entre les Formations de Tonhe et de Letkat de l'Oligocène tardif - début du Miocène est caractérisée par un brusque déplacement vers des sédiments fluviaux en tresse constitués de grès à gros grains et un apport accru de grains métamorphiques tels que le quartz, la biotite, le muscovite, l'épidote et l’amphibole. De plus, les âges U-Pb sur apatite et les traces de fission apatite montrent une phase majeure d'exhumation au Miocène inférieur. Cette phase est possiblement associée à de l'extrusion dans l'orogène de l'Himalaya Oriental (Fig. 8). Cette deuxième discordance Oligocène tardive - Miocène précoce peut être tracée comme une discordance angulaire à travers tous les bassins sédimentaires du Terrane de Birmanie. Ainsi, la deuxième discordance représente une phase de déformation régionale qui correspond à l'entrée du Terrane de Birmanie dans la zone de collision de l'Himalaya Oriental, suite à la propagation vers le sud de la collision entre l'Inde et l'Asie. Cela a conduit à l'extrusion vers le sud-est de certaines parties de la zone de collision de l'Himalaya Oriental (Ceinture Mogok-Mandalay-Mergui), à la mise en place de la ceinture mobile de Birmanie avec des failles dextres plus prononcées dans les Chaînes Indo-Birmanes, et au développement du système de drainage moderne de l'Himalaya.

Afin de répondre aux questions restantes dans le nouveau modèle de collision Inde-Asie proposé avec le Terrane de Birmanie dans le cadre du système de subduction Trans-Téthysienne, l'ensemble de données paléomagnétiques suivant a été utilisé pour fournir des reconstructions continues des plaques de 95 à 23 Ma dans le logiciel GPlates. Les questions restantes portent sur l'origine pré-

Crétacée du Terrane de Birmanie, le moment de la rotation majeure dans le sens horaire, le moment de son incorporation dans la Plaque Indienne et l'âge de la collision entre le Terrane de Birmanie et Sibumasu. Les données finales comprennent une série de résultats paléomagnétiques provenant des Bassins de Minbu et de Chindwin. Les lithologies échantillonnées comprennent les sédiments du Paléocène supérieur et de l'Éocène moyen des Formations de Paunggyi, Laungshe, Tilin et Tabyin près des villages de Sidoktaya et Saw, les sédiments de l'Éocène supérieur de la Formation Pondaung dans les Montagnes Pondaung, les sédiments de l'Oligocène moyen de la Formation Padaung à l'ouest de Bagan et les sédiments du Miocène moyen de la Formation Natma au nord de Kalewa.

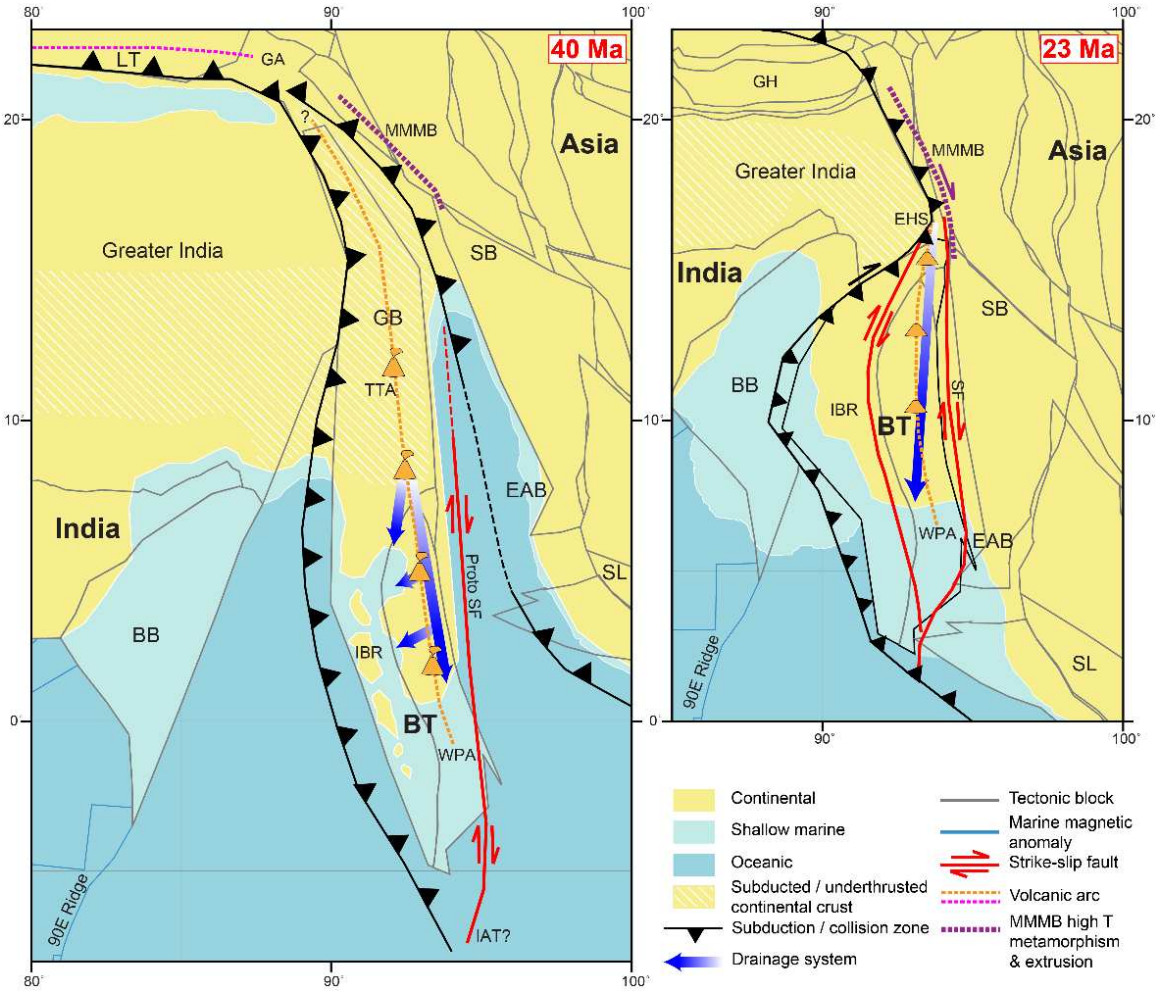

Figure 8 : *Paléogéographie régionale du Terrane de Birmanie à 40 Ma (à gauche) et 23 Ma (à droite). Abréviations, références, et plus de détails : Chapitre 5.*

Le premier groupe de sédiments du Paléocène supérieur et de l'Éocène moyen a donné d'excellents résultats de désaimantation sur sept sites, principalement à partir des marnes argileuses ou les silts très fins de couleur gri-bleue, tandis que les directions paléomagnetiques obtenues à partir des tufs étaient généralement plus dispersées. Les directions moyennes de la fin du Paléocène - Éocène moyen présentent des déclinaisons généralement orientées vers l'est et des paléolatitudes de

l'hémisphère sud à des paléolatitudes proches de zéro, similaires à la position de l'Inde à cette époque, malgré la présence de rotations locales dues aux complexités tectoniques locales autour de Sidoktaya et de Saw. La Formation Pondaung de l'Éocène supérieur a fourni des résultats paléomagnétiques sur des échantillons dans les paléosols, qui ont été affectés par une altération chimique sévère et une réaimantation importante dans le champ actuel. Heureusement, pour des échantillons suffisants, les aimantations caractéristiques portées par la magnétite et l'hématite présentent des changements de polarité magnétique entre différentes couches ou sites différents qui confirment une acquisition pendant le dépôt ou au cours d'une diagénèse précoce dans les paléosols. La direction moyenne résultante, avec une rotation négligeable et une paléolatitude quasi-équatoriale, est indissociable de la Formation Yaw de la fin de l'Éocène et d'un âge similaire, ce qui indique qu'elles peuvent être regroupées. Leur paléolatitude combinée est cohérente avec la position de l'Inde à la fin de l'Éocène. Les résultats paléomagnétiques de 29 échantillons de silts fins dans la Formation Padaung de l'Oligocène moyen donnent à nouveau des latitudes proches de l'équateur qui sont similaires à la position de l'Inde. Les aimantations dans les échantillons de la Formation Padaung sont portées par la magnétite. Cependant, la dispersion augmente après correction de pendage. Ce test de pli négatif ne permet pas d'assurer que ces sites enregistrent bien une aimantation caractéristique primaire. Ce résultat pourrait aussi s'expliquer par une petite rotation tectonique relative entre les sites de part et d'autres de l'anticlinal el la présence d'une faille. La Formation Natma du Miocène moyen est constituée de grès fluviatiles et de nombreux paléosols qui ont été échantillonnés pour l'étude paléomagnétique. Malgré la présence d'une intense altération chimique et d'une surimpression du champ actuel dans ces paléosols, une moyenne direction paléomagnétique a pu être acquise à partir des directions caractéristiques portées par la magnétite et l'hématite. Cette direction moyenne montre encore une rotation négligeable et une paléolatitude plus au nord que celles observées dans les sédiments plus anciens. Ce résultat montre que les données dans les sédiments Paléogène sont effectivement anormales et ne peuvent pas être expliquées par le phénomène d' »inclination shallowing ». Trois implications clés peuvent être tirées de l'ensemble des résultats paléomagnétiques, à savoir 1) le Terrane de Birmanie se trouvait proche de l'équateur dans l'hémisphère sud éloigné de la marge de l'Asie du Sud du début du Crétacé Supérieur jusqu'au début du Paléogène, 2) le Terrane de Birmanie a subi une rotation majeure dans le sens horaire et a été incorporé à la Plaque Indienne au Paléocène tardif - Éocène moyen, et 3) il s'est ensuite déplacé vers le nord avec l'Inde le long d'un système dextral de glissement vers l'est formant la limite de la Plaque Indienne (Fig. 9).

La position initiale éloignée de la marge de l'Asie du Sud au début du Crétacé Supérieur, parallèlement à l'activité volcanique intense et à la subduction à cette époque, correspond le mieux

au système de subduction Trans-Téthysienne intra-océanique précédemment proposé pour le Terrane de Birmanie (Fig. 10). Ceci est en outre corroboré par des tendances similaires d'activité volcanique et de mise en place d'ophiolite le long d'autres segments proposés du système de subduction Trans-Téthysienne, tels que l'Arc du Kohistan intra-océanique et l'Ophiolite du Spontang dans l'Himalaya Occidental. Ce cadre tectonique nouveau explique les différentes origines pré-Cretacé proposées du Terrane de Birmanie, à savoir le Gondwana, Sibumasu ou Cathaysien, car des fragments crustraux d'origines diverses ont pu être incorporés dans le système de subduction Trans-Téthysien lors de la formation du Terrane de Birmanie. Par ailleurs, le système de subduction Trans-Téthysien s'est initialement développé sur l'Archipel de l'Argoland, un système d'arcs insulaires supposé composé de fragments crustaux séparés du Gondwana à ~160 Ma. Les résultats paléomagnétiques présentés dans cette étude ne permettent pas encore de distinguer ces origines Argoland ou composite.

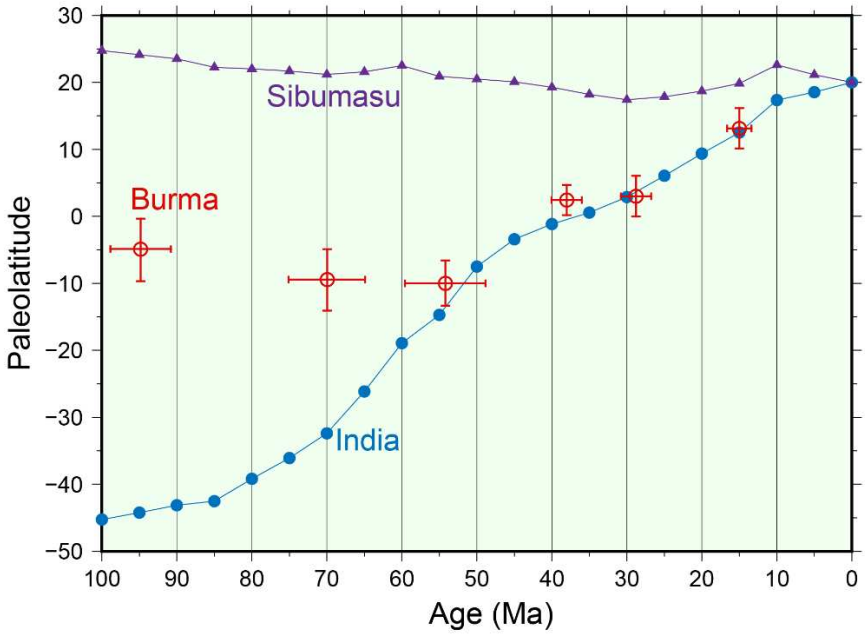

Figure 9 : *Mouvement latitudinal du Terrane de Birmanie de 100-0 Ma, en utilisant les résultats paléomagnétiques de cette étude, comparé aux mouvements latitudinaux de l'Inde et de Sibumasu. Abréviations, références, et plus de détails : Chapitre 6.*

En tout cas, l'Inde est entrée en collision avec le système de subduction Trans-Téthysien au cours du Paléocène tardif - Éocène moyen, ce qui a provoqué une rotation majeure dans le sens horaire du Terrane de Birmanie et peut-être un rollback asymétrique le long de sa marge de subduction (Fig. 10). Il a ensuite été incorporé à la Plaque Indienne et a commencé son mouvement coévalant vers le nord avec l'Inde le long d'une faille de transform dextrale à son est. Cependant, il n'y a pas de preuve d'une collision directe entre le Terrane de Birmanie et l'Inde, donc probalement l'Inde a plutôt

heurté une région de la Grande Birmanie qui forme la continuation vers le nord de l'Arc Wuntho-Popa en tant que partie de l'Arc Trans-Téthysien. Cette région de la Grande Birmanie a aujourd'hui presque complètement disparu par subduction ou par chevauchement sous la marge Asiatique, mais un vestige possible est le Batholite de Lohit dans la Syntaxe de l'Himalaya Oriental. En raison de la position relative du Terrane de Birmanie par rapport à l'Inde depuis la fin du Paléocène - Éocène moyen jusqu'à l'Oligocène, il est probable que ce système de faille transformante dextre a duré jusqu'à cette époque (Fig. 10). À la fin de l'Oligocène - milieu du Miocène, le Terrane de Birmanie est entré en collision avec le nord de Sibumasu, en accord avec les observations susmentionnées des Bassins du Centre de la Birmanie, l'ouverture de la Mer d'Andaman au sud, l'extrusion dans la zone de collision de l'Himalaya Oriental et la mise en place de la ceinture mobile Birmane (Figs. 8 et 10). Depuis lors, la Faille de Sagaing au Néogène a permis au Terrane Birman de se déplacer plus au nord.

Les autres sites d'échantillonnage paléomagnétique n'ont pas fourni de résultats publiables. L'altération intense des roches qui se traduit par une surimcomposante secondaire d'aimantation rémanente dans le champ actuel, les incertitudes dans l'estimation de l'âge, les déformations locales et les réaimantations sont malheureusement des problèmes récurrents lors des recherches paléomagnétiques en Birmanie. La plupart des localités d'échantillonnage paléomagnétique ont toutes été plus ou moins affectées par un ou plusieurs de ces problèmes. Les sites préliminaires du socle présumé du Terrane de Birmanie du Trias, que ce soit au niveau de Wuntho et de la Chaîne Indo-Birmane (Formations de Shwedaung et Pane Chaung), soit n'ont pas d'aimantations stables ou ont été réaimantées. Malheureusement, ces deux formations représentent probablement le meilleur moyen de déchiffrer l'origine du Terrane de Birmanie antérieure au Crétacé moyen. Huit sites dans les turbidites du Paléogène et le mélange ophiolitique des Chaînes Indo-Birmanes à l'ouest de Kalay montrent également des indications de réaimantation. Il en va de même pour les quatre sites d'ophiolites serpentinisées à l'ouest de Datkon, qui enregistrent d'excellentes aimantations rémanentes très stables portées par de la magnétite mais pour lesquelles nous n'avons aucune contrainte de pendage tectonique. Six sites de la Formation Paunggyi, dans le sud du Bassin de Minbu, près de Datkon et de Ngape, présentent de aimantations rémanentes de faible intensité et une forte composante dans le champ actuel. Le dernier site d'échantillonnage était une section sédimentaire composée de la Formation Yaw de l'Éocène supérieur et de la Formation Shwezetaw de l'Oligocène inférieur dans le Bassin de Minbu, près de la Pagode de Shwezetaw.

Figure 10 : *Reconstructions finales de ce projet du Terrane de Birmanie et de l'Asie à 95 Ma, 80 Ma, 58 Ma, 50 Ma, 40 Ma et 23 Ma avec le logiciel GPlates. Abréviations, références, et plus de détails : Chapitre 6.*

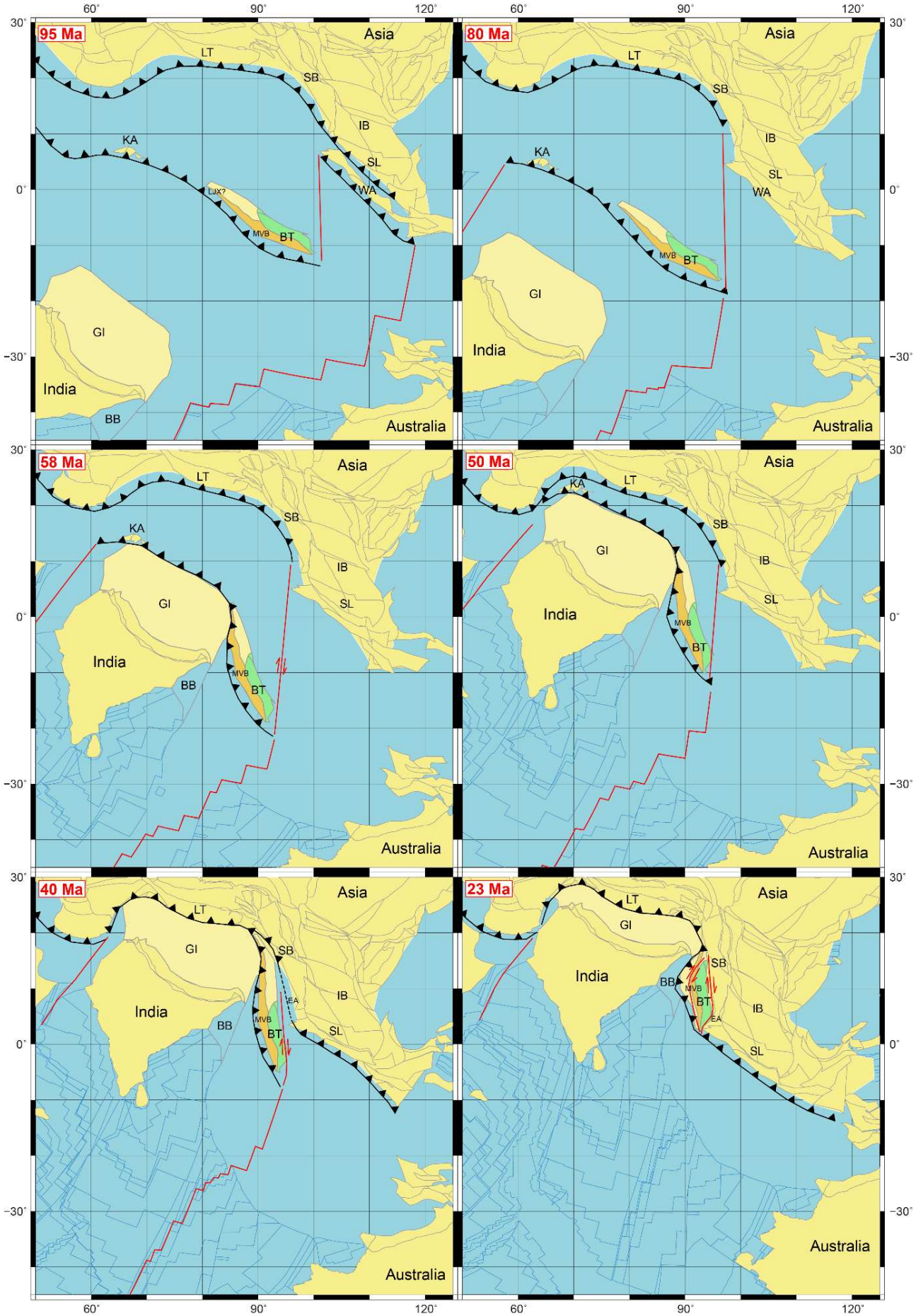
95 Ma
Asia
LT
SB
IB
SL
WA
KA
LJX?
MVB
BT
GI
India
BB
Australia
80 Ma
58 Ma
50 Ma
40 Ma
EA
23 Ma
60°
90°
120°
30°
0°
−30°

Elle contenait potentiellement la première identification de la Transition Éocène-Oligocène en Birmanie, mais malheureusement içi aussi on peut mettre en évidence une aimantation acquise au cours des derniers siècles certainement lors d'une altération météorique. Tous ces échantillons inédits constituent des frontières pour la poursuite des recherches paléomagnétiques et géologiques en Birmanie. En outre, le nouveau contexte tectonique du Terrane de Birmanie présenté dans cette étude laisse de nombreuses questions scientifiques en suspens. Les perspectives les plus importantes pour la poursuite des recherches concernent l'origine pré-Crétacé du Terrane de Birmanie, l'âge de la collision du Bloc du Mont Victoria (Chaînes Indo-Birmanes) avec le Terrane de Birmanie, la transition au nord et à l'est du Terrane de Birmanie avec la zone de collision de l'Himalaya Oriental/Sibumasu, la provenance des sédiments dans les bassins de l'arrière-arc Birman (Bassins de Shwebo et de Pegu) et la conciliation du mouvement vers le nord du Terrane de Birmanie avec l'histoire tectonique de l'ouverture océanique de la Mer d'Andaman.

En conclusion, les résultats paléomagnétiques de cette étude ont fourni une histoire tectonique passionnante et inattendue pour le Terrane de Birmanie, avec les nouvelles connaissances nécessaires sur la collision entre l'Inde et l'Asie. En outre, elles ont des implications cruciales pour les études de la biodiversité, du paléoclimat et des paléoenvironnements. Plus important encore, les contraintes paléomagnétiques de cette étude ont montré que le Terrane de Birmanie faisait initialement partie d'un système de subduction Trans-Téthysien intra-océanique éloigné de la marge de l'Asie du Sud au début du Crétacé Supérieur. L'Inde est entrée en collision avec ce système au cours du dernier Paléocène – Éocène moyen et le Terrane de Birmanie s'est déplacé vers le nord en tant que partie de la Plaque Indienne. Il est ensuite entré en collision avec le nord de Sibumasu à la fin de l'Oligocène - début du Miocène et se déplace finalement vers le nord, vers sa position actuelle dans la zone de collision de l'Himalaya Oriental. Ces contraintes invitent à réévaluer de nombreux aspects de la géologie de la Birmanie, et à poursuivre les recherches sur l'orogène de l'Himalaya Oriental et la collision entre l'Inde et l'Asie.

Table of contents

Chapter 1: Introduction

The Minbu Basin, view on the Irrawaddy River.
(Tant Kyi Taung Pagoda, Myanmar, Fieldwork November 2017)

At present, Asian monsoons control weather conditions over mainland Asia and are an important component of global atmospheric circulation (Xu et al., 2006). During summer monsoons, the Inter Tropical Convergence Zone (ITCZ) moves over the Asian continent, producing landward directed oceanic winds that carry abundant moisture, often causing excessive rainfall in East and South Asia. During winter monsoons, the ITCZ moves southward and the wind directions reverses, bringing dry continent-derived winds (Fig. 1.1). Traditionally, the onset of this monsoonal system was linked to the formation of high topographic relief due to the uplift of the Himalayan-Tibetan orogen in the late Oligocene – early Miocene (Clift et al., 2008; Guo et al., 2002; Prell & Kutzbach, 1992; Rowley & Currie, 2006). However, more recent studies have pushed the onset of intense Asian monsoons back to the late Eocene (Evans et al., 2013; Licht et al., 2014; Quan et al., 2012; Wang et al., 2013), arguing that the warmer global climatic conditions of the Eocene greenhouse world enhanced Asian monsoons (Huber & Goldner, 2012; Pagani et al., 2005). As intense monsoonal weather conditions are often associated with increased weathering rates and hence a decrease in pCO_2 (Clift et al., 2008), there is a fascinating possibility that late Paleogene monsoons in Asia triggered global cooling from greenhouse to icehouse conditions around the Eocene – Oligocene transition (EOT) at ~34 Ma.

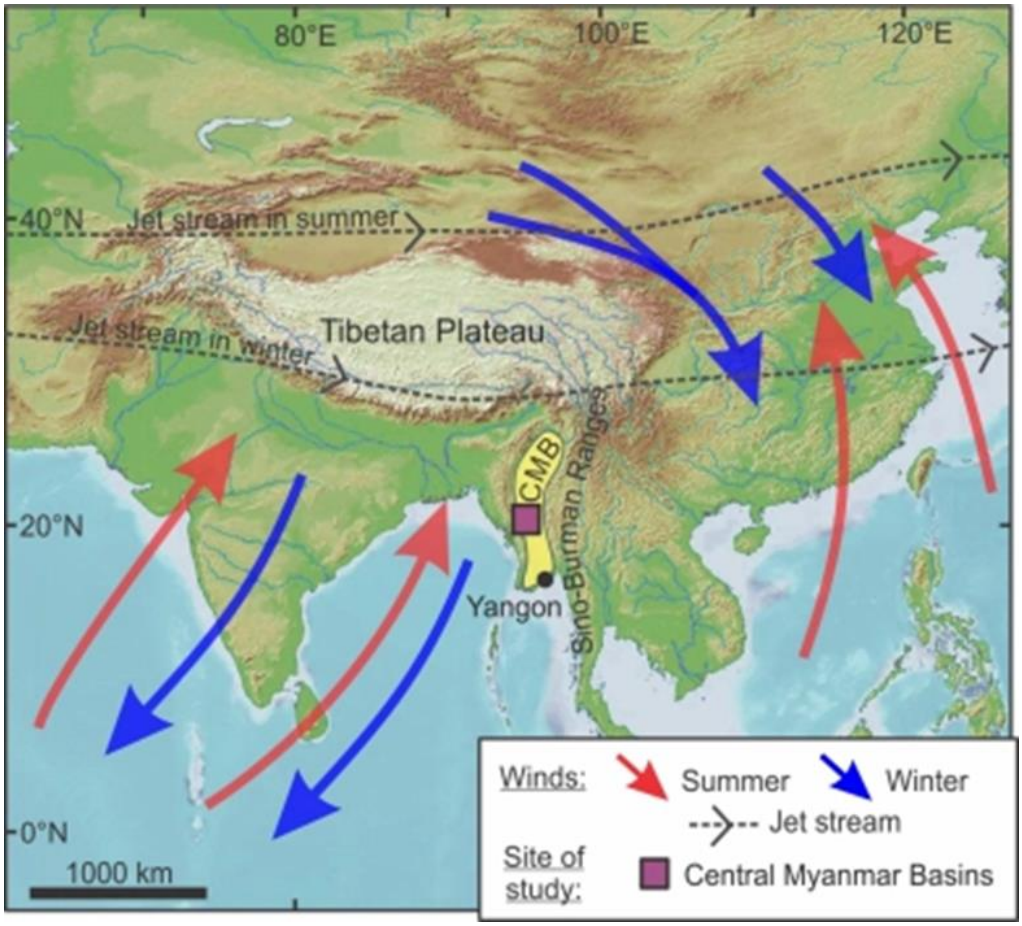

Figure 1.1: *Prevailing summer (red arrows) and winter (blue) wind directions corresponding to the present-day Asian monsoons (Licht et al., 2014).*

To fully understand this complex interplay between Asian monsoons, the formation of the Himalayan-Tibetan orogen and global climate, detailed reconstructions of the Cenozoic paleogeography of Asia are required. The record of this paleogeographic evolution is exposed throughout the Himalayan-Tibetan orogen, the most dramatic mountain range on Earth. This orogen is characterized by its immense size and elevation, numerous intracontinental and continental margin basins, plate-boundaries, regional thrust and strike-slip systems, widespread volcanism and metamorphism. Because of these characteristics, it is commonly considered as the type orogen to study continent-continent collisional systems (Yin & Harrison, 2000). The primary driver behind the Himalayan-Tibetan collisional system is the convergence of India and Asia since the Cenozoic, which is continuing nowadays by a ~N20°E motion of India relative to Asia of ~36 mm/yr (Avouac, 2003; Bilham et al., 1997; Jouanne et al., 2004), but various earlier ocean closure and intercontinental suturing events have played a role as well (Kapp & DeCelles, 2019).

Numerous studies have already investigated the Himalayan-Tibetan orogen along its central part, which is approximately ~E-W striking and covers a distance of ~2600 km throughout India, Nepal, Bhutan and Tibet. Yet, outstanding questions remain regarding the paleogeographic evolution of this mountain range. In particular, there is an intense debate on the timing of the India-Asia collision as well as the amount and manner of post-collisional convergence (Jagoutz et al., 2015; Replumaz et al., 2010, 2013; Royden et al., 2008; Shen et al., 2001; van Hinsbergen et al., 2011). A possible reason for this is that the vast ~1500 km of the eastern orogen are underrepresented in comprehending paleogeographic evolution of the entire orogen, even though these regions have the potential to provide crucial new insights in this debate.

The Burma Terrane (BT), Myanmar, is a tectonic terrane or microplate that forms the principal eastward continuation of the Himalayan-Tibetan orogen (Fig. 1.2). Currently, its geodynamic setting is characterized in the west by hyper-oblique subduction of the Indian Plate beneath the Burmese active margin, causing the formation of the Indo-Burman Ranges accretionary prism and volcanism in the Wuntho-Popa Arc, and in the east by the large-scale active dextral strike-slip Sagaing Fault (Fig. 1.3) accommodating northward indentation of the BT into the Eastern Himalayan syntaxis (e.g. Maung, 1987; Rangin et al., 2013; Socquet et al., 2006). To the south, the Sagaing Fault transitions in the oceanic spreading centre of the Andaman Sea. This unique geodynamic setting makes the BT an ideal region for studying the paleogeographic evolution of the Himalayan-Tibetan orogen from a different perspective. However, there are fundamental challenges for conducting geological research in Myanmar, including its political and scientific isolation over the past 70 years, limited road access and jungle covering much of the exposure. This caused many uncertainties regarding the geological history of this region to persist, such as origin of the BT and its paleolatitudal motion (Barber &

Crow, 2009; Hall, 2012; Sevastjanova et al., 2016; Yao et al., 2017), the amount of dextral displacement along the eastern margin of the BT (Maung, 1987; Mitchell, 1993; Morley & Arboit, 2019), the possible existence of multiple Burmese tectonic blocks (Acharyya, 2015; Morley et al., 2019; Rangin et al., 2013; Searle et al., 2017), and the interaction or suturing of the BT with neighbouring tectonic entities (e.g. India, Indochina, Lhasa and the Eastern Himalayan Syntaxis; Lin et al., 2019; Liu et al., 2016; Mitchell et al., 2012; Searle et al., 2017; Sevastjanova et al., 2016). Fortunately, the country has welcomed international scientific research since the last few years, generating new prospects for understanding this pivotal eastern edge of the Himalayan-Tibetan orogen.

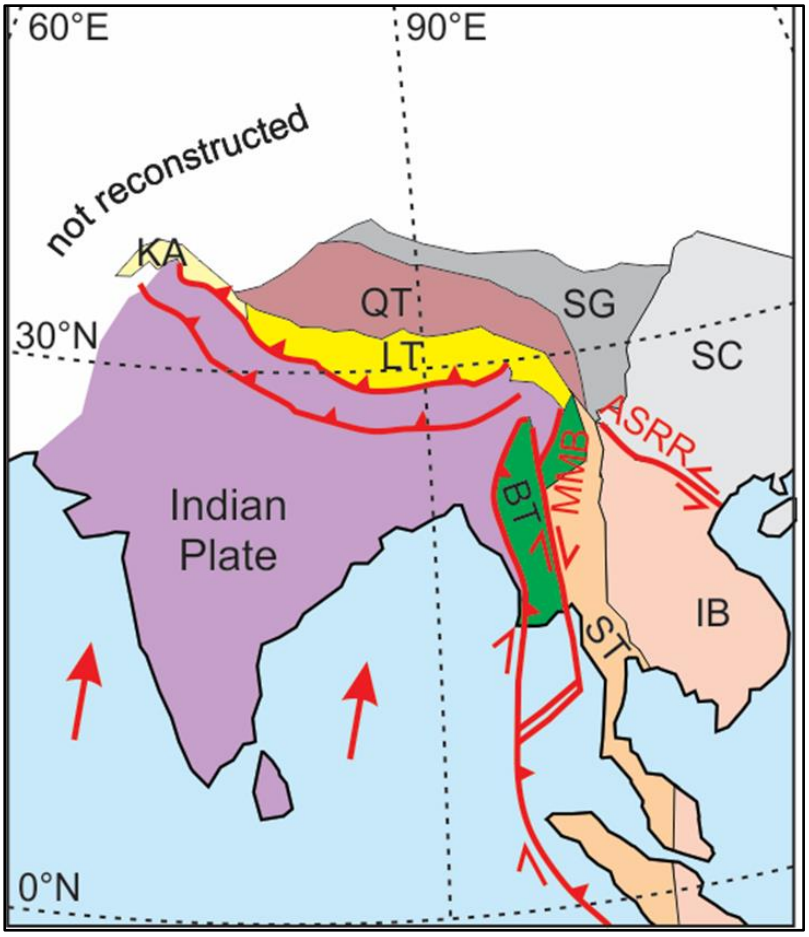

Figure 1.2: *General tectonic setting of the India-Asia collision. Abbreviations: ASRR = Ailao Shan – Red River shear zone, BT = Burma Terrane, IB = Indochina block, KA = Kohistan Arc, LT = Lhasa Terrane, MMB = Mogok-Mandalay-Mergui Belt, QT = Qiantang Terrane, SC = South China Craton, SG = Songpan Ganzi complex, ST = Sibumasu Terrane (after Hall, 2012; Licht et al., 2019; Royden et al., 2008; van Hinsbergen et al., 2011).*

Paleomagnetic research on the BT is one these prospects, as the only previous paleomagnetic study in Myanmar was conducted on the neighbouring Sibumasu Block (Fig. 1.4; Richter & Fuller, 1996).

Paleomagnetism provides constraints on the rotational and latitudinal motion of tectonic terranes, making it a powerful tool for constraining the paleogeographic and plate tectonic evolution of the BT. This study reports the first paleomagnetic data for BT and combines that with additional results from sedimentology, mineralogy and geochronology to make advanced plate tectonic and paleogeographic reconstructions using GPlates software (Müller et al., 2018). This thesis will first provide a detailed overview of the geology of the Himalayan-Tibetan orogen, from Pakistan to Sumatra, and uncertainties therein, using existing literature (Chapter 2). This is followed by the benchmark results of this study, which yield the first paleomagnetic constraints on the BT from Late Cretaceous and late Eocene sampling (Chapter 4). These constraints provide surprising new insights into the India- Asia collision by showing near-equatorial low latitudes for the BT in stark contrast with previous ideas. Furthermore, they entail a major reexamation of regional geological interpretations including the magmatic history, degree of active subduction, deformation phases and sedimentary source regions of the BT. Many of these required reexaminations were only identified after publishing Chapter 4. Therefore, Chapter 5 will correlate the updated geodynamic framework with the paleogeographic evolution of the Burmese forearc basin, using new sedimentological, magnetostratigraphic, mineralogic and geochronological data. Finally, a complete tectonic history for the BT is proposed in Chapter 6 by incorporating Campanian - Maastrichtian, latest Paleocene – early Eocene, late Eocene, middle Oligocene and middle Miocene paleomagnetic data in an integrated plate model.

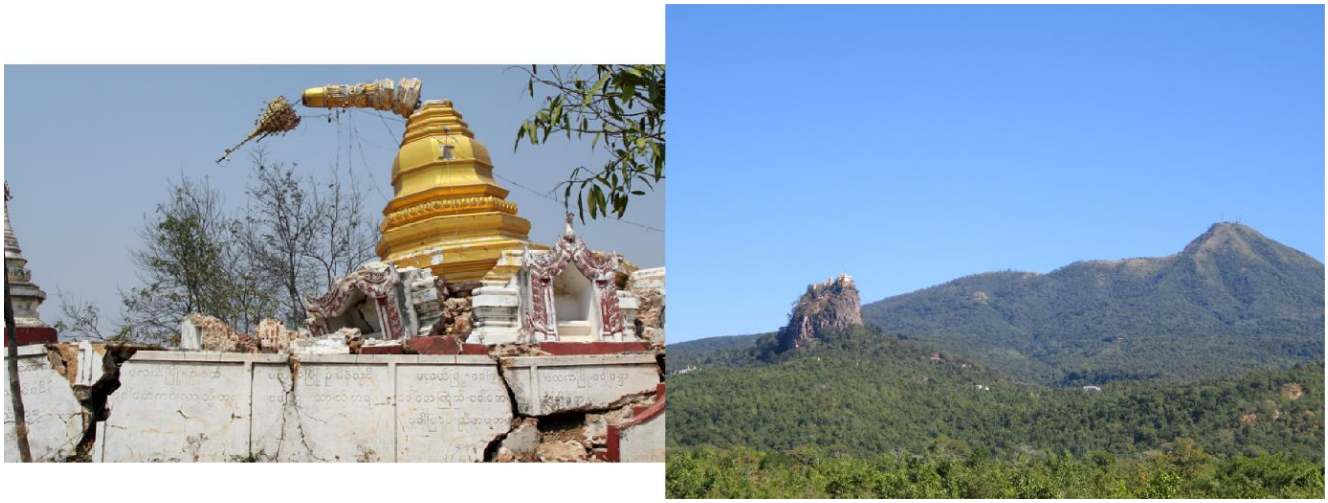

Figure 1.3: *Active geology in Myanmar: Left) Earthquake damage along the active Sagaing Fault; Right) The Quaternary volcanism of Mount Popa.*

Figure 1.4: *Overview of paleomagnetic data in the Himalayas and Indochina during the crucial time periods of 65-130 Ma (a) and 20-65 Ma (b), highlighting the lack of data from Myanmar. Apparent Polar Wander Path (APWP) from Torsvik et al. (2012).*

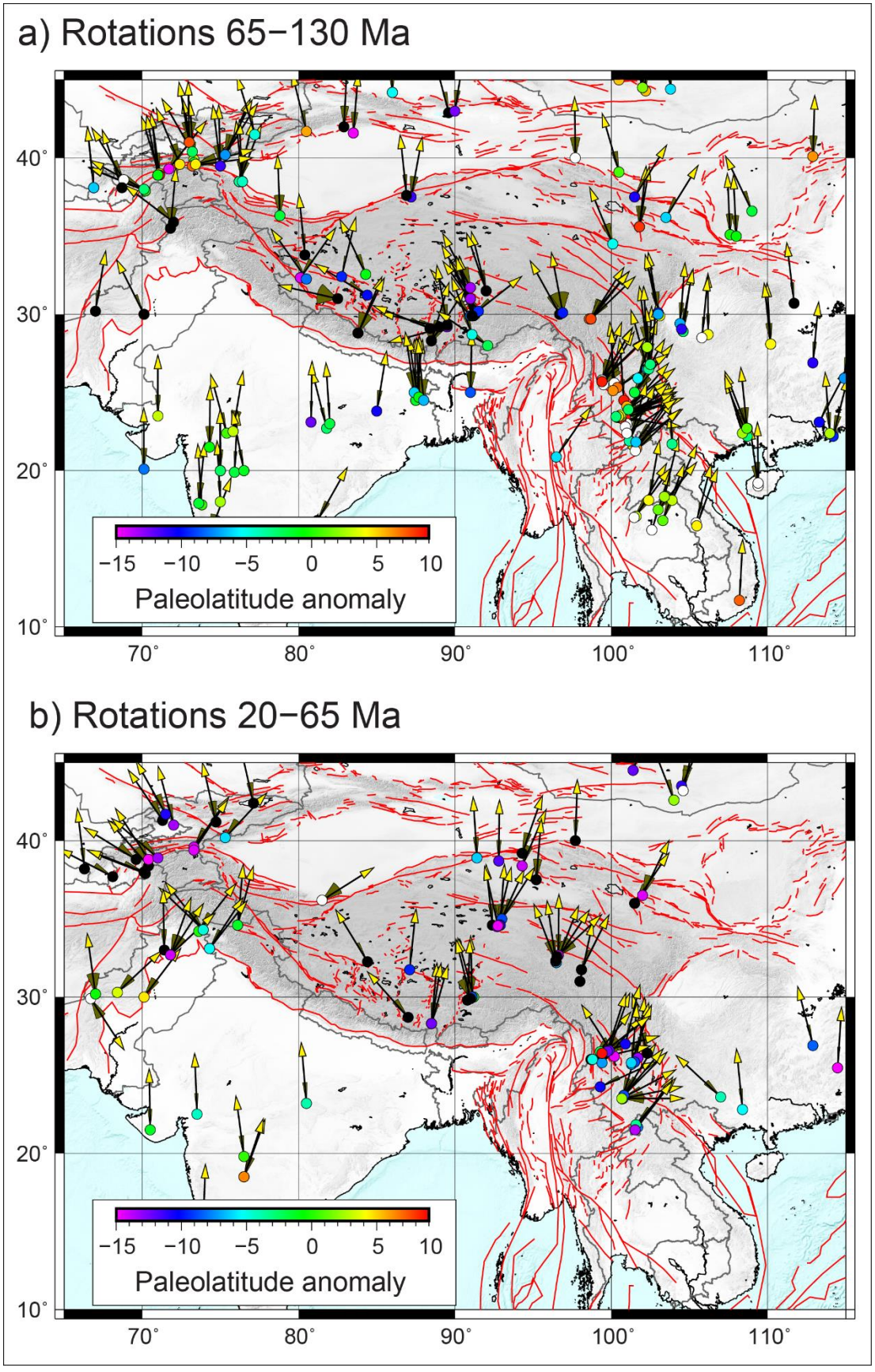

References Chapter 1

Included in reference list of Chapter 2: Geological Setting.

Chapter 2: Geological setting

The Indo-Burman Ranges, western extend of the Burma Terrane.
(Falam, Myanmar, Fieldwork January 2019)

1. Himalayan-Tibetan orogen

This first section will focus on the general geology of the central India-Asia collision zone, covering ~2600 km along an approximately west-east trend across India, Nepal, Bhutan and Tibet, followed by a description of relevant areas on the western and eastern edges of the main orogen. Finally, an overview of different models for the collision and uncertainties therein will be given.

1.1. Central Himalayan-Tibetan orogen

1.1.1. The Yarlung-Tsangpo Suture Zone

Perhaps the one of the most crucial geological features of the central Himalayan-Tibetan orogen (Fig. 2.1) is the Yarlung-Tsangpo Suture Zone (YTSZ), representing a tectonic suture resulting from the collision of the Indian and Eurasian Plates (Aitchison et al., 2011; Allegre et al., 1984; Gansser, 1980; van Hinsbergen et al., 2019). The YTSZ is comprised of a complex assemblage of ophiolitic complexes and ophiolitic mélange, including sedimentary, metamorphic and igneous rocks. Although it is acknowledged that this ophiolitic assemblage was formed in supra-subduction zone setting (Chan et al., 2015; Hébert et al., 2012; Maffione et al., 2015; van Hinsbergen et al., 2019), its tectonic history and role in the India-Asia collision have long been debated. The earliest paleomagnetic data from Lower Cretaceous radiolarian cherts that are interpreted as being part of the ophiolitic assemblage reported paleolatitudes close to the Lhasa Terrane (Pozzi et al., 1984). A subsequent study suggested that these rocks were formed near the equator, but their conclusions were based only on a few sites (Abrajevitch et al., 2005). By contrast, turbidites with Lower Cretaceous maximum depositional ages from detrital zircons that unconformably overlie the YTSZ ophiolites yield paleolatitudes close to the Lhasa Terrane after correcting for inclination shallowing (Huang et al., 2015).

Apart from these discrepancies between paleomagnetic results, there are further conflicting interpretations regarding the characteristics and provenance of the sediments in the YTSZ. Initially, uppermost Cretaceous sandstones of the Tethyan Himalaya on the Indian Plate (Section 1.1.2) were assumed to be olistostromes formed due to obducting YTSZ ophiolites (Searle, 1986; Searle & Treloar, 2010). However, subsequent data showed that mafic minerals in these sediments were sourced by uplifting plume or rift Deccan Traps volcanics (Garzanti & Hu, 2015). Detrital zircon age spectra from other sedimentary rocks corresponding to the YTSZ have been denoted as having an Asian-derived provenance (Huang et al., 2015; Najman et al., 2010) or a provenance and detritus assemblage corresponding to intra-oceanic island arc assemblages (Aitchison et al., 2011).

Figure 2.1: *Geological map of the Central Himalayan-Tibetan orogen (Kapp & DeCelles, 2019).*

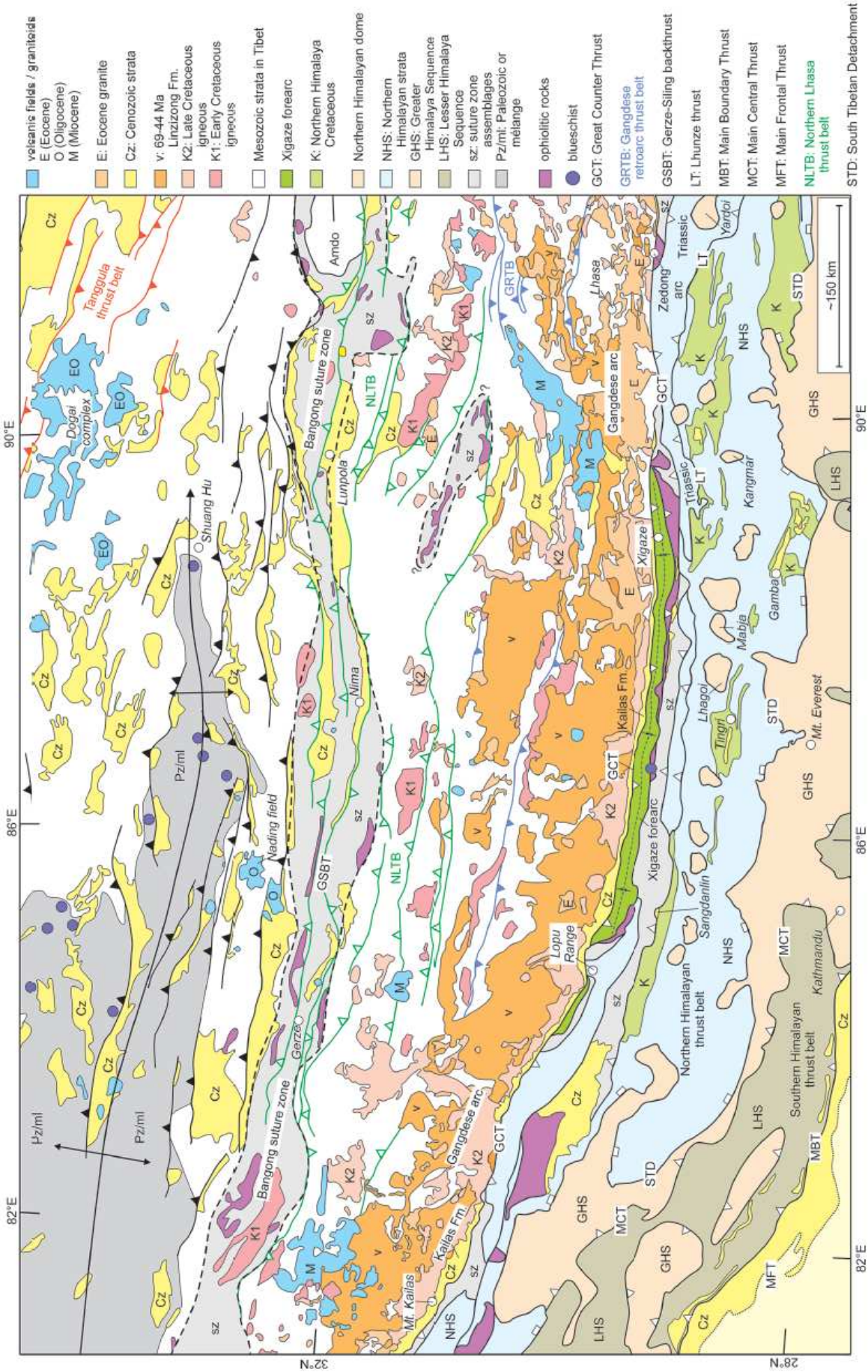
volcanic fields / granitoids
E (Eocene)
O (Oligocene)
M (Miocene)
E: Eocene granite
Cz: Cenozoic strata
v: 69-44 Ma Linzizong Fm.
K2: Late Cretaceous igneous
K1: Early Cretaceous igneous
Mesozoic strata in Tibet
Xigaze forearc
K: Northern Himalaya Cretaceous
Northern Himalayan dome
NHS: Northern Himalayan strata
GHS: Greater Himalaya Sequence
LHS: Lesser Himalaya Sequence
sz: suture zone assemblages
Pz/ml: Paleozoic or mélange
ophiolitic rocks
blueschist
GCT: Great Counter Thrust
GRTB: Gangdese retroarc thrust belt
GSBT: Gerze-Siling backthrust
LT: Lhunze thrust
MBT: Main Boundary Thrust
MCT: Main Central Thrust
MFT: Main Frontal Thrust
NLTB: Northern Lhasa thrust belt
STD: South Tibetan Detachment
82°E
86°E
90°E
32°N
28°N
~150 km
Tanggula thrust belt
Dogai complex
Shuang Hu
Nading field
Amdo
Gerze
Lunpola
Nima
Bangong suture zone
Gangdese arc
Kailas Fm.
Mt. Kailas
Lopu Range
Xigaze forearc
Sangdanlin
Northern Himalayan thrust belt
Southern Himalayan thrust belt
Kathmandu
Lhagoi Kangri
Mabja
Gamba
Kangmar
Mt. Everest
Zedong arc
Lhasa
Yardoi
Triassic

Hence, it is no surprise that these conflicting interpretations have resulted in numerous contrasting tectonic histories for the YTSZ ophiolites (e.g. Aitchison et al., 2011; Hébert et al., 2012; Huang et al., 2015; Jagoutz et al., 2015; Maffione et al., 2015; Metcalfe, 2013; van Hinsbergen et al., 2019). This debate is at the core of the debate on the widely different models for the evolution of the India-Asia collision that have been put forward. These models will be further discussed in Section 1.4.

1.1.2. The Himalayan thrust belt

South of the YTSZ on the Indian Plate, the Himalayan thrust belt is located, which terminates at the Main Frontal Thrust that forms the present-day boundary between India and Asia (Fig. 2.2). From north to south, the Himalayan thrust belt is commonly subdivided into three extremely deformed units called the Tethyan, Greater, and Lesser Himalayas (Gansser, 1964; Hodges, 2000). Collectively these three units represent fragments of Greater India, the portion of the Indian continent that subducted underneath Asia since the initial collision. All three units shared a common history in the Late Paleozoic, receiving sediments from cratonic India as part of Gondwana (Cawood et al., 2007; DeCelles et al., 2000; McKenzie et al., 2011; McQuarrie et al., 2013; Myrow et al., 2003; Parrish & Hodges, 1996). Hence, their subdivision is based on their observed metamorphic grade, major fault bounding systems and stratigraphy.

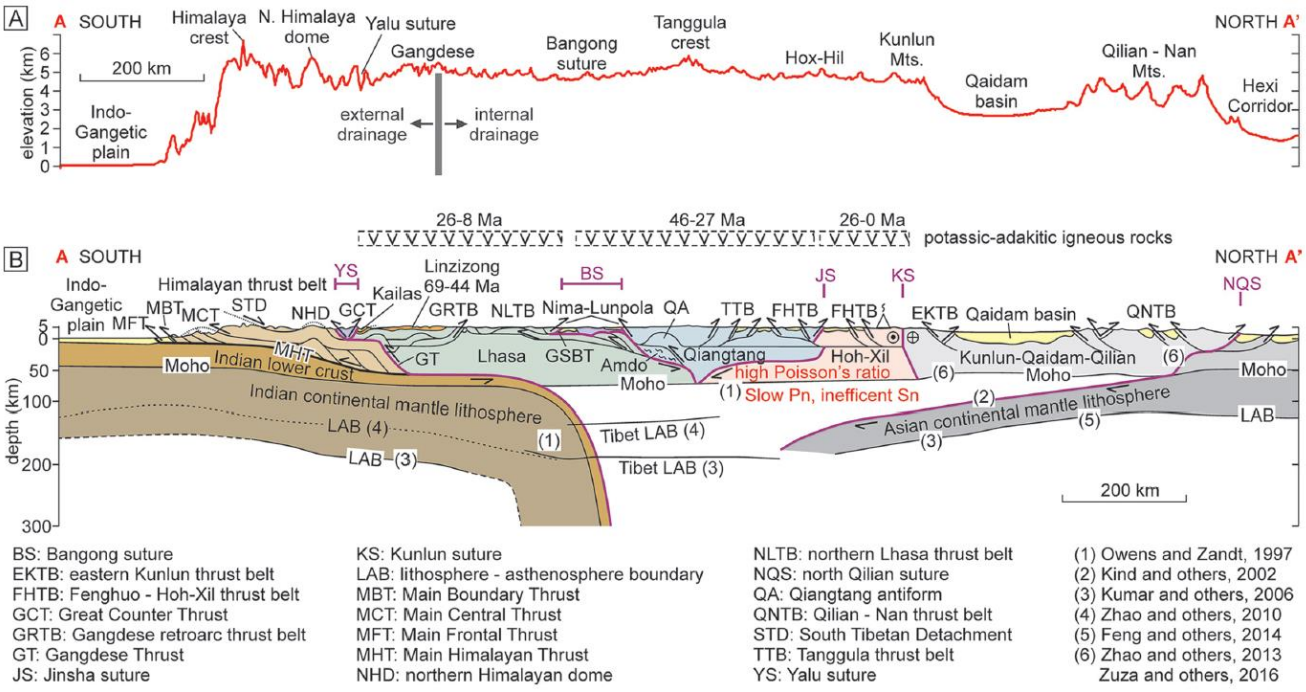

BS: Bangong suture
EKTB: eastern Kunlun thrust belt
FHTB: Fenghuo - Hoh-Xil thrust belt
GCT: Great Counter Thrust
GRTB: Gangdese retroarc thrust belt
GT: Gangdese Thrust
JS: Jinsha suture

KS: Kunlun suture
LAB: lithosphere - asthenosphere boundary
MBT: Main Boundary Thrust
MCT: Main Central Thrust
MFT: Main Frontal Thrust
MHT: Main Himalayan Thrust
NHD: northern Himalayan dome

NLTB: northern Lhasa thrust belt
NQS: north Qilian suture
QA: Qiangtang antiform
QNTB: Qilian - Nan thrust belt
STD: South Tibetan Detachment
TTB: Tanggula thrust belt
YS: Yalu suture

(1) Owens and Zandt, 1997
(2) Kind and others, 2002
(3) Kumar and others, 2006
(4) Zhao and others, 2010
(5) Feng and others, 2014
(6) Zhao and others, 2013
Zuza and others, 2016

Figure 2.2: *Topographic (above) and lithospheric (below) cross-sections across the Himalayan-Tibetan orogen (Kapp & DeCelles, 2019).*

The Tethyan Himalayas, directly south of the YTSZ, are characterized by Neoproterozoic to Paleogene active margin deposits, mainly comprising carbonates with subordinate volcanics and clastic sediments (Garzanti et al., 1987; Garzanti & Hu, 2015; Jadoul et al., 1998; McQuarrie et al., 2013). Neo-Tethyan oceanic crust formation is represented along the northern margin of the Tethyan Himalayas by Carboniferous syn-rift deposits, Lower Permian tholeiitic basalts and a Permian to Paleocene passive margin sequence (Garzanti et al., 1999; Garzanti & Sciunnach, 1997). In addition, there is evidence for Cretaceous rifting in the Tethyan Himalaya represented by mafic lavas and volcanic sandstones (Ma et al., 2016; Yang et al., 2015). Geochemical signatures of Upper Cretaceous sediments show that these deposits are similar in composition to both the Deccan Traps volcanics and Lower Cretaceous Tethyan Himalayan volcanics (Garzanti & Hu, 2015). The oldest input of foreland sediments with a postulated Asian affinity are near-uniformly dated across the Tethyan Himalaya at ~59-54 Ma by provenance studies (Hu et al., 2015; Najman et al., 2005; Orme et al., 2015). In addition, U/Pb dating of eclogite-facies rocks within the Tethyan Himalayas (Tso Morari complex)exhibit metamorphic ages of ~54 Ma (Guillot et al., 2008; Leech et al., 2005) or 47-43 Ma (Donaldson et al., 2013), yielding a minimum onset of Indian continental subduction. Importantly in the context of this study, reliable paleomagnetic data from the Tethyan Himalayas for the Cretaceous to Paleogene, the crucial period of India-Asia convergence, are ambiguous. Several Late Cretaceous and Paleocene paleomagnetic studies on the Tethyan Himalayas placed it at the Asian margin already around ~65-55 Ma, requiring 1500-2500 km of subduction of Greater Indian lithosphere (Meng et al., 2020; Patzelt et al., 1996; Yi et al., 2011). By contrast, recent Paleocene constraints have put the Tethyan Himalayas at southern hemisphere to near-equatorial latitudes during the latest Cretaceous to Paleocene (Yuan et al., 2020). Yet, several studies have interpreted various paleomagnetic data from the Tethyan Himalays to be affected by either insufficient averaging of paleosecular variation of the geomagnetic field (Lippert et al., 2014), inclination shallowing (Dupont-Nivet, van Hinsbergen, et al., 2010) and remagnetization (Huang et al., 2017a,b). The only reliable paleomagnetic data from the Tethyan Himalayas of Ordovician, Triassic and Lower Cretaceous ages consistently demonstrate a coeval position with India during these times (van Hinsbergen et al., 2012). When these positions would be extrapolated, it would yield a very young, Miocene India-Asia collision age (van Hinsbergen et al., 2019). However, paleolatitude data of Lower Cretaceous age specifically can be deceiving for determining the position of the Tethyan Himalayas and hence the size of Greater India, because India was still attached to Gondwana at this time along its present-day eastern margin. Thus paleolatitude variations from the Lower Cretaceous represent present-day longitude variations (Fig. 2.3).

Figure 2.3: *GPlates reconstruction (Matthews et al., 2016) of India and three different sizes for Greater India at 130 Ma, showing that paleomagnetic data from the Early Cretaceous specifically obtained in the Tethyan Himalayas (green square) do not provide consequential constraints on the size of Greater India as longitudinal differences cannot be deduced with paleomagnetism.*

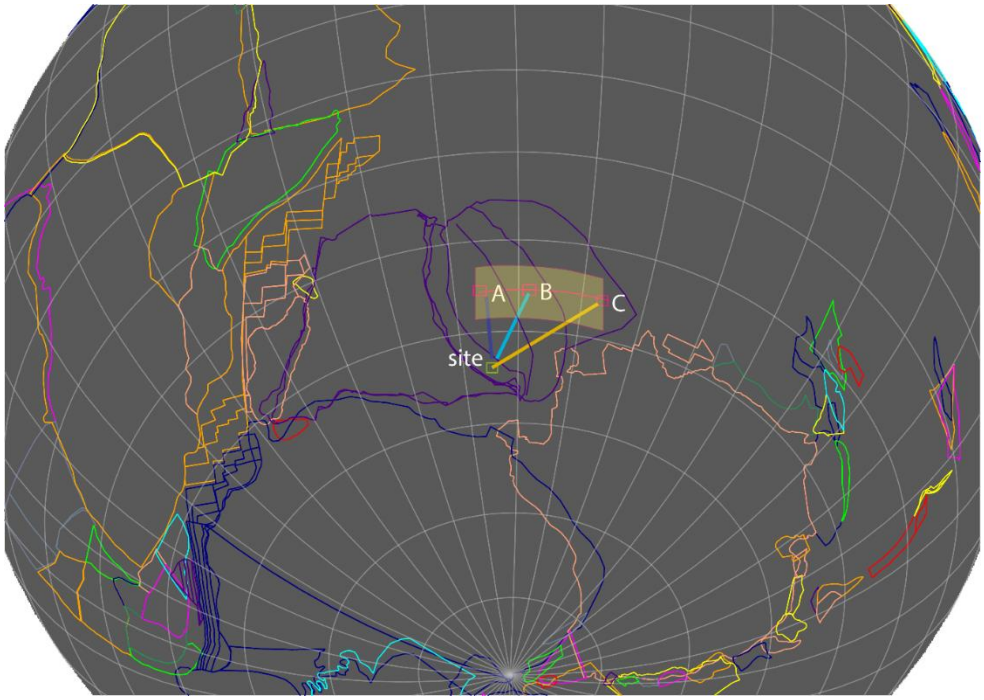

The apparent discrepancies between paleomagnetic and geochronological data gave rise to the contrasting collision models discussed in Section 1.4.

The South Tibetan Detachment fault separates the Tethyan Himalayas at its southern margin from the high-grade metamorphic Greater Himalayas (Hodges et al., 1992). The Greater Himalayas are comprised of metasedimentary and metavolcanic rocks of probable Paleozoic age, and it has been suggested that they represent the metamorphosed part of a stratigraphic sequence similar to the Tethyan Himalayas (Martin, 2017; Searle et al., 1992). These rocks have undergone metamorphism up to amphibolite-facies and partial melting conditions, with prograde metamorphic ages of ~55 Ma and peak metamorphic ages of ~45 Ma showing that metamorphism in the Greater Himalayas started in the Eocene (Lee & Whitehouse, 2007; Pullen et al., 2011; Smit et al., 2014). The metamorphic rocks were subsequently intruded by ~32-14 Ma leucogranites (Hodges, 2000; Wang et al., 2015). A major phase of exhumation and thrusting in the Greater Himalayas has occurred in the early Miocene (Garzanti, 2019; Vannay et al., 2004).

In between the Main Central Thrust and Main Frontal Thrust, south of the Greater Himalayas, the low-grade metamorphic Lesser Himalayas are located. They contain Paleo-Mesoproterozoic to sporadically Eocene – Oligocene metasedimentary and metaigneous rocks (DeCelles et al., 2004;

Hodges, 2000; Kapp & DeCelles, 2019; Long et al., 2011). Oligocene to Neogene metamorphism is thought to have been caused by underthrusting of the Lesser Himalayas underneath the Greater Himalayas along the Main Central Thrust (DeCelles et al., 2002; Robinson & Martin, 2014). The latter thus represented the India-Asia plate boundary, until it ceased to be active in the Miocene when the Main Frontal Thrust took over this role. Subsequently, the Lesser Himalayas deformed into a foreland propagating fold-thrust belt (DeCelles et al., 2004; Najman et al., 2009).

1.1.3. The Lhasa Terrane

North of the YTSZ on the Eurasian Plate, numerous terranes are located that have been accreted to each other before the arrival of the Indian continent. In the context of this study, the most important of these terranes is the Lhasa Terrane, directly north of the YTSZ. It collided with the Qiantang Terrane in the Early Cretaceous, an event preserved by the Bangong-Nujiang suture (Kapp et al., 2007a; Li et al., 2016; Yin & Harrison, 2000; Zhu et al., 2011). During the Early Cretaceous to Eocene, the Lhasa Terrane was an Andean-type convergent margin with northward subduction of Neo-Tethyan oceanic lithosphere during the northward motion of India towards Asia (Fig. 2.4). The geology of the Lhasa Terrane is dominated by two magmatic arcs: The I-type Cretaceous to Eocene Gangdese Arc along the ancient Neo-Tethyan margin and the S-type Jurassic to Cretaceous Central Lhasa Belt towards the north (Kapp & DeCelles, 2019; Lin et al., 2019 and references therein). The northern Lhasa Terrane experienced thrusting and intermontane basin development in the latest Cretaceous and Oligocene – early Miocene (DeCelles et al., 2007; Kapp et al., 2007b; Volkmer et al., 2007, 2014), while the southern Lhasa Terrane was uplifted above sea level by ~100 Ma along the mid-Cretaceous - Eocene Gangdese retroarc thrust belt (Kapp et al., 2007b; Leier et al., 2007; Pullen et al., 2008). Younger tectonic events on the Lhasa Terrane are represented by post-collisional or syn-collisional emplacement of late Oligocene - Miocene igneous rocks found across the Tibetan Plateau (Chen et al., 2013; Ding & Lai, 2003; Turner et al., 1996).

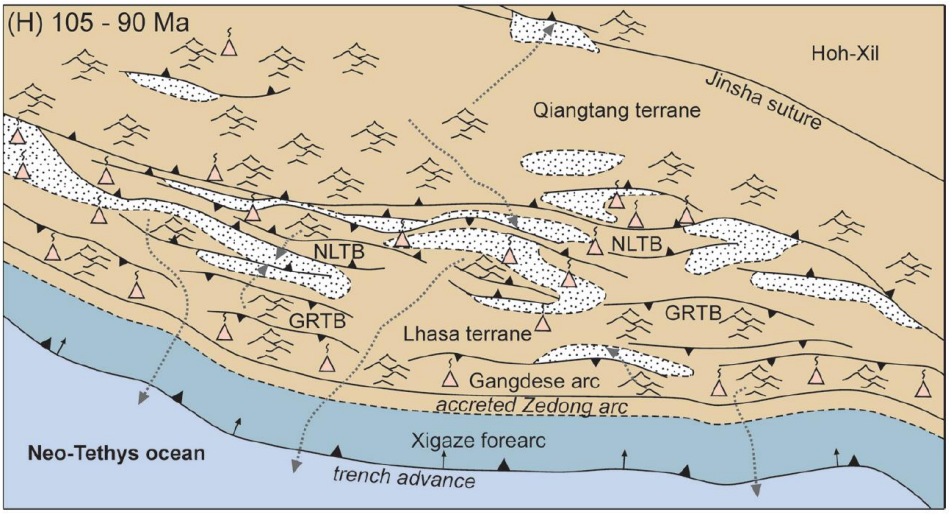

Figure 2.4: *Early Late Cretaceous tectonic setting of the Lhasa Terrane (after Kapp & DeCelles, 2019).*

Paleomagnetic results from the Linzizong volcanics, consisting of clastic and volcanic units as part of the Gangdese Arc, place the Lhasa Terrane, and hence the southern Asian margin during Neo-Tethyan subduction, at a latitude of ~15°N in the Cretaceous shifting to ~20°N in the Paleogene. The Lhasa Terrane drifted northward towards its present-day latitude of 29°N since the early Eocene (Dupont-Nivet, Lippert, et al., 2010; Lippert et al., 2014).

1.2. Kohistan Arc

At the Western Himalayan Syntaxis, the Lhasa Terrane disappears and the intra-oceanic Kohistan Arc is found in between the Tethyan Himalayas and the Qiangtang Terrane. The Kohistan Arc is a mid-Cretaceous to lower Eocene volcanic arc built on top of oceanic crust (Bouilhol et al., 2011; Heuberger et al., 2007; Yamamoto et al., 2005). The volcanic arc is unusually thick, with crustal thickness and batholith thickness estimates of ~50 km and ~30 km respectively (Jagoutz & Schmidt, 2012; Petterson, 2010, 2019). The collision of the Kohistan Arc with the Asian margin, represented by the Shyok suture, was initially estimated at ~70 Ma (Burtman & Molnar, 1993; Schwab et al., 2004). More recent constraints yield a ~40 Ma cessation of magmatism, used to infer a collision with Asia at that time preceded by a ~60-50 Ma collision with India (Bouilhol et al., 2013; Jagoutz et al., 2015; Petterson, 2019). The first paleomagnetic constraints on the Kohistan Arc, coming from Cretaceous red beds, yielded near-equatorial paleolatitudes (Zaman & Torii, 1999). However, the same study also reports near-equatorial paleolatitudes north of the Shyok suture, which is inconsistent with other paleomagnetic constraints from Tibet. A more robust recent paleomagnetic dataset from Kohistan volcano-sedimentary sequence confirms near-equatorial paleolatitudes at ~65 Ma (Martin et al., 2020), and uses this to support models placing the Kohistan Arc in a Trans-Tethyan subduction system during the mid-Cretaceous that collides with India in the Paleocene and then with Asia in the late Eocene (Jagoutz et al., 2015; Petterson, 2019; Zahirovic et al., 2014). However, additional geological knowledge from the western Himalayas is undoubtedly required to reconcile this late Eocene collision of Kohistan/India with Asia with the Paleocene arrival of Asian-derived detritus across the Indian continent (Hu et al., 2015, 2016; Najman et al., 2005; Orme et al., 2015).

1.3. The eastern Himalayan orogen

The Eastern Himalayan Syntaxis (Fig. 2.5) represents the eastern extend of the Himalayan Orogen. It is a ~E-W towards ~NW-SE trending oroclinal bend which is extremely deformed and shortened with major thrusts and strike-slip faults subdividing the different geological units. The aforementioned early Miocene phase of thrusting and exhumation of the Greater Himalayas was especially rapid in

the Eastern Himalayan Syntaxis (Godin et al., 2006; Kellett et al., 2013; Najman et al., 2019), with an even greater magnitude of shortening compared to the Central Himalayan Orogen (Haproff et al., 2019).

Notably, the Greater Himalayas, as well as the Tethyan and Lesser Himalayas disappear farther towards the east (Haproff et al., 2018, 2019; Yin, 2006; Yin et al., 2010). Important units within the eastern Himalayan orogen in the context of this study include: (1) the Late Jurassic – Cretaceous I-type Lohit Batholith, which has been correlated with the Gangdese Arc of the Lhasa Terrane (Lin et al., 2019); (2) the Tidding mélange complex consisting of garnet / amphibolite / chlorite-muscovite schists, (serpentinized) ultramafics and cherts; (3) the high-grade Mayodia (augen) gneiss: (4) metasedimentary rocks of the Lapani schist comprised of schists, paragneiss, quartzite, carbonates and mafics; (5) siliciclastic sandstones and conglomerates of the Tezu unit and (6) metasedimentary quartzites, marbles, cherts, slates and schists of the Sewak unit. These units form the complex transition of the eastern Himalayan orogen with the Indo-Burman Ranges (IBR) and Burma Terrane (BT). Further to the (north)-east within the Eastern Himalayan orogen, the Jurassic – Cretaceous S-type Bomi-Chayu Batholith is located, which has been interpreted as an extension of the similar Central Lhasa Belt to the west (Lin et al., 2019). Based on composition and volcanic ages, many of the intrusives in the eastern Himalayan orogen have also been correlated with similar lithologies in Myanmar to the (south-)east, such as the Bomi-Chayu Batholith with the Dianxi Batholith in the metamorphic Mogok-Mandalay-Mergui Belt (MMMB) and the Lohit Batholith with the Wuntho-Popa Arc and Sodon Batholith (Lin et al., 2019; Mitchell et al., 2012).

Structural geology shows that the onset of high temperature metamorphism (Searle et al., 2007, 2017, 2020) and major thrusting (Haproff et al., 2020) in the Eastern Himalayan orogen including the MMMB (see also Section 4.2) both initiated during the late Eocene, and these studies related this to the India-Asia collision although it remains possible that the collision started before this time.

Figure 2.5: *General geological maps of (a) the Himalayan-Tibetan orogen; (b) the easternmost Himalayan orogen and south-eastern Tibetan Plateau; and (c) the Eastern Himalayan syntaxis, directly north of the Burma Terrane. Abbreviations: EHS = Eastern Himalayan Syntaxis, GHC = Greater Himalayan Crystalline Complex (Greater Himalayas), IYSZ = Indus-Yarlung suture zone (YTSZ), JF = Jiali Fault, LHS = Lesser Himalayan Sequence (Lesser Himalayas), LPC = Lohit Plutonic Complex (Lohit Batholith), MBT = Main Boundary Thrust, MCT = Main Central Thrust, MFT = Main Frontal Thrust, STD = South Tibetan Detachment, THS = Tethyan Himalayan Sequence (Tethyan Himalayas) (Haproff et al., 2019).*

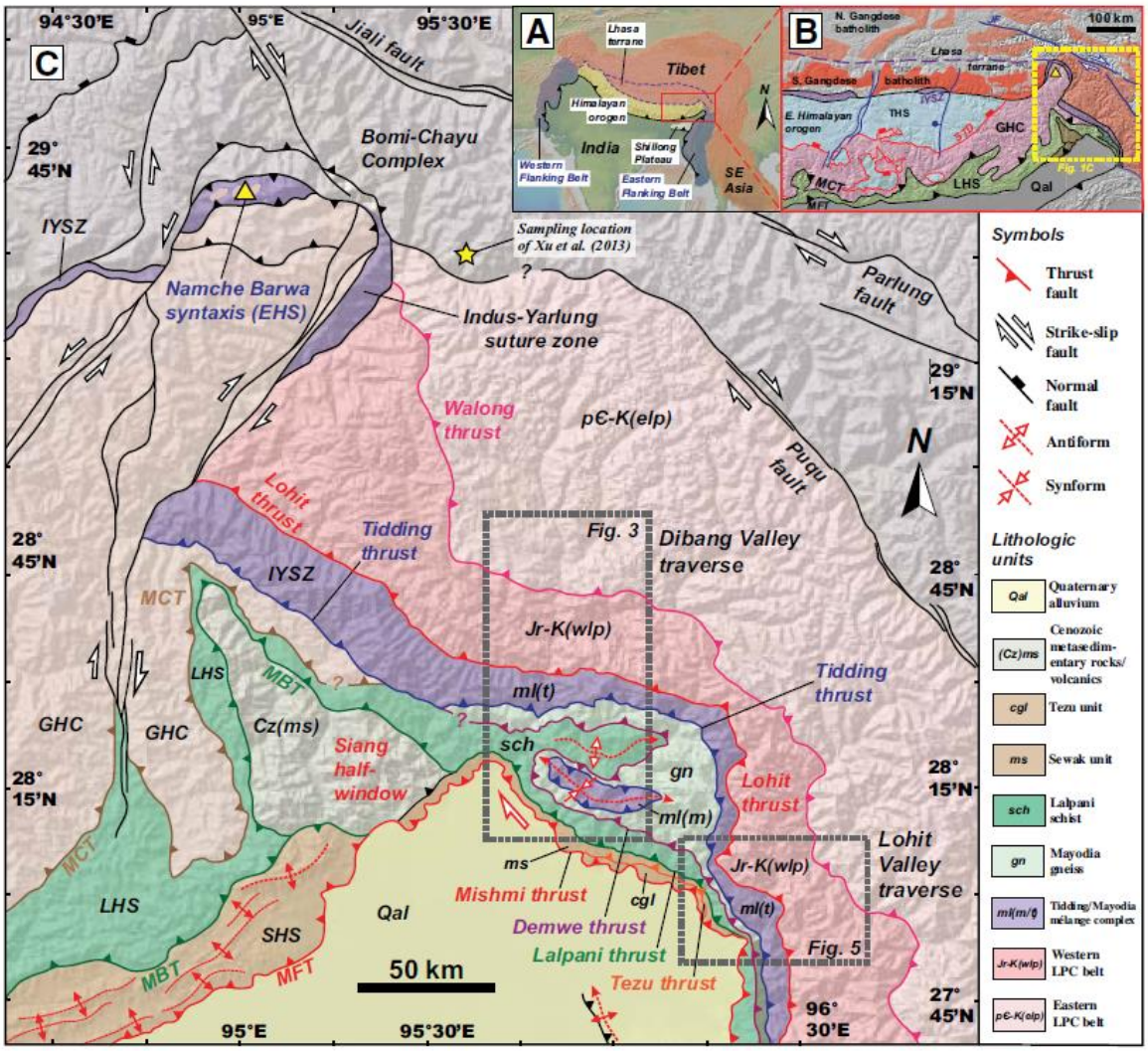

1.4. Evolution of the India-Asia collision

With the complicated geology of the Himalayan Orogen described in the previous sections, it is no surprise that there is a lot of ongoing debate regarding the geodynamic history and paleogeography of the India-Asia collision, especially regarding the timing of collision and the amount of post-collisional convergence (e.g. Replumaz et al., 2010, 2013; Royden et al., 2008; Shen et al., 2001; van Hinsbergen et al., 2011). Traditional models (Fig. 2.6a) proposed that the Indian plate moved northward resulting in an Eocene collision of Greater India with the southern Asian margin (Cogne et al., 2013; Molnar & Tapponnier, 1975). However, new information supports a Paleocene collision age, primarily based on the first arrival of sediments with Asian affinity on the Indian Plate (Tethyan Himalayas; Hu et al., 2015, 2016; Najman et al., 2005; Orme et al., 2015). At the same time, paleomagnetic and tectonic constraints put the Indian continent at a near-equatorial latitude at that time, thousands of kilometres away from the southern Asian margin (Cogne et al., 2013; Ingalls et al., 2016; Jagoutz et al., 2015; Replumaz et al., 2010, 2013; Royden et al., 2008; Tapponnier et al., 1982; Van Hinsbergen et al., 2012; van Hinsbergen et al., 2019; Zahirovic et al., 2014). A Paleocene

collision could be compatible with the traditional model by assuming a southern Asian margin at low latitudes (Cogne et al., 2013), but available paleomagnetic data contradict this (Dupont-Nivet, Lippert, et al., 2010; Huang et al., 2015). Alternatively, an extra-large continental Greater India (Ingalls et al., 2016; Meng et al., 2020) could explain a Paleocene collision age (Fig. 2.6b). However, this scenario would require wholesale continental subduction of India (Ingalls et al., 2016), but from a geodynamic perspective the unusually high speed of the Indian Plate recorded by marine magnetic anomalies is difficult to reconcile with a slab consisting entirely of buoyant continental crust (van Hinsbergen et al., 2019). This can only be partly solved by lateral extrusion of the Indochina Blocks away from the collision zone towards the south-east (Cogne et al., 2013; Replumaz et al., 2010, 2013; Royden et al., 2008; Tapponnier et al., 1982; Fig. 2.6a), but remains much higher than accounted for by structural data (van Hinsbergen et al., 2011). Furthermore, these models cannot account for the apparent discrepancy between paleomagnetic and geochronological data from the Tethyan Himalaya, as described in Section 1.1.2 (van Hinsbergen et al., 2019).

Recently, two new models have been proposed that try to tackle these problems. The first group of models (Fig. 2.6c) postulates the existence of an opening oceanic basin between India and Greater India (Tethyan and Greater Himalayas) that could have subducted more easily after an initial collision of Greater India with Asia at 58 Ma until a second collision of India with Asia in the Miocene (van Hinsbergen et al., 2012, 2019). However, the remnants of the opening and closure of this oceanic basin are not clearly observed in the Himalayan geological record at its proposed location within the Greater Himalayas or along the Main Central Thrust (Kapp & DeCelles, 2019).

The other group of models (Fig. 2.6d) envisions the existence of a Trans-Tethyan subduction system, including an intra-oceanic arc, with which the Indian continent would initially collide at ~60 to 50 Ma before jointly colliding with Asia later in the Paleogene (Aitchison et al., 2007a; Gibbons et al., 2015; Hall, 2012; Jagoutz et al., 2015; Martin et al., 2020; Zahirovic et al., 2014). Most studies assume that a Trans-Tethyan subduction system developed in the mid-Cretaceous, possibly by southward back-arc extension at the southern Asian margin (Aitchison et al., 2007a; Aitchison et al., 2007b; Gibbons et al., 2015; Kapp & DeCelles, 2019; Zahirovic et al., 2014), while others propose a comparable system developed on Gondwanan crustal fragments as part of 'Greater Argoland' (Section 3.3; Hall, 2012). A double subduction zone could potentially account for the rapid India–Asia convergence between 80 to 65 Ma (Fig. 2.7; Jagoutz et al., 2015; Martin et al., 2020). Several Trans-Tethyan collision models include the Kohistan Arc as a western compartment of its intra-oceanic arc (Gibbons et al., 2015; Jagoutz et al., 2015; Zahirovic et al., 2014). In the Central Himalayan Orogen the evidence for Trans-Tethyan Arc remnants are scarce, but parts of the YTSZ (e.g. Xigaze Arc, Spontang Arc, Dras island arc terrane) represent proposed fragments (Aitchison et al., 2007a; Aitchison et al.,

2011; Buckman et al., 2018; Jagoutz et al., 2015; Kapp & DeCelles, 2019). Complete subduction of intra-oceanic arc fragments with generally thinner crust is another speculated mechanism by several modelling studies (e.g. Boutelier et al., 2003; Yamamoto et al., 2009), but not all intra-oceanic arcs have necessarily a thin crust as shown by the Kohistan Arc (Section 1.2). However, the largest problem with Trans-Tethyan Arc collision models is that they have difficulty explaining the Paleocene arrival of Asian-derived detritus in the Tethyan Himalayas (Garzanti & Hu, 2015; Hu et al., 2015; Najman et al., 2005; Orme et al., 2015). It has been speculated that either the Trans-Tethyan Arc itself or the Greater Indian landmass could have been the source of this detritus (Martin et al., 2020), but these speculations are not clearly supported by available geological data.

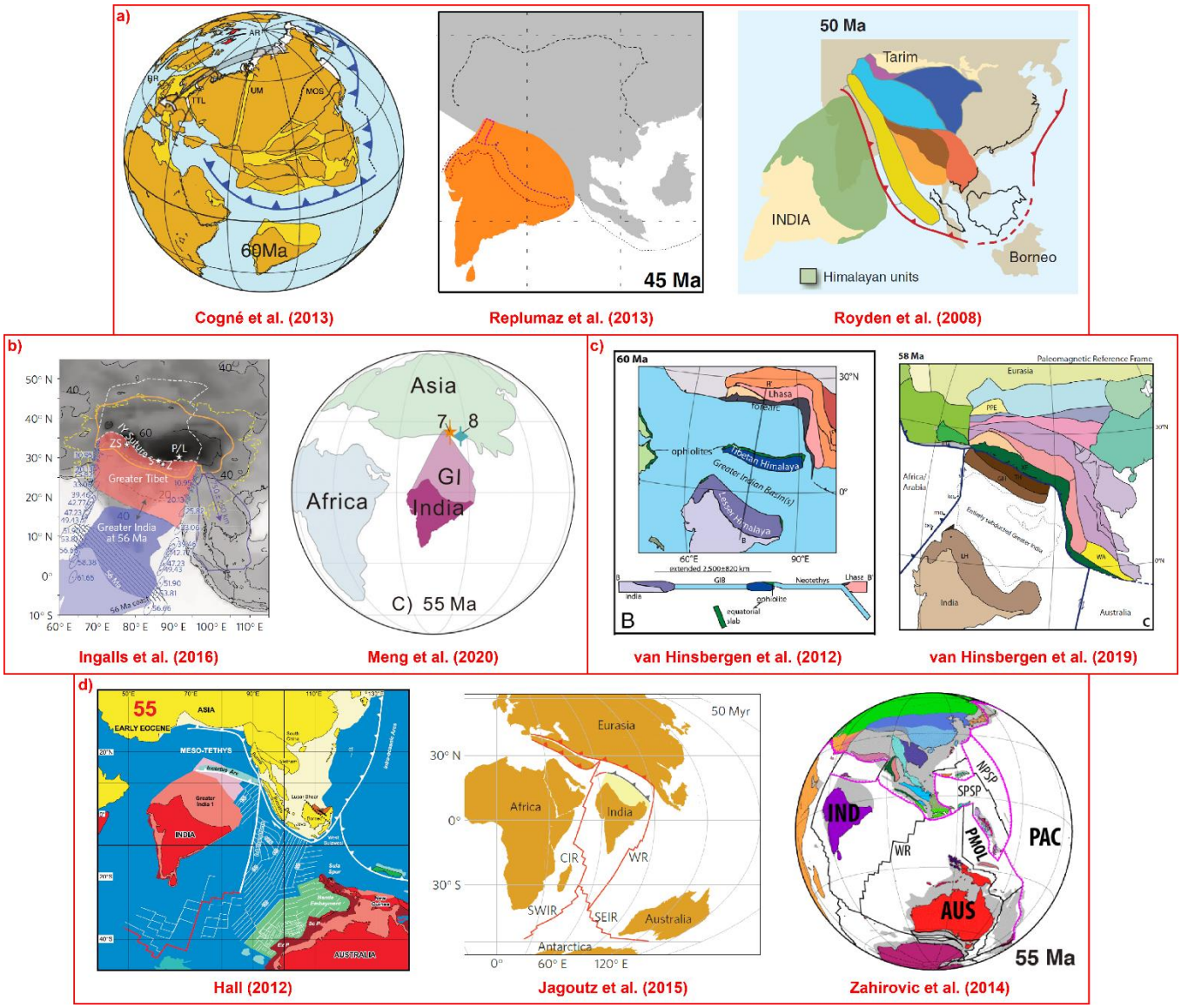

Figure 2.6: *Alternative plate reconstructions of the India-Asia collision at 60-45 Ma: a) Reconstructions with a nearly linear subduction zone and significant extrusion of Indochina blocks (Cogne et al., 2013; Replumaz et al., 2013; Royden et al., 2008); b) Reconstructions with a large*

continental Greater India (Ingalls et al., 2016; Meng et al., 2020); c) Reconstructions with a Greater India Basin (van Hinsbergen et al., 2012, 2019)*; d) Reconstructions with a second Trans-Tethyan subduction zone (Hall, 2012; Jagoutz et al., 2015; Zahirovic et al., 2014).*

Because of the complexity in finding the correct model for the India-Asia collision outlined above, a good alternative approach could be to look at this event from the perspective of neighbouring regions, representing the continuation of the Himalayan Orogen to the west and east. To the east, the BT is an ideal candidate for this, as will be outlined in the following sections.

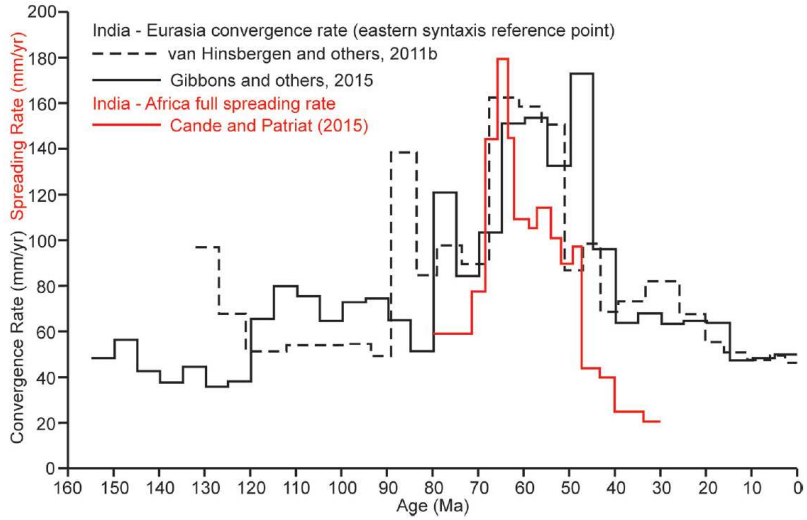

Figure 2.7: *Reconstructions of India-Asia convergence rates (Kapp & DeCelles, 2019).*

2. The Burma Terrane

2.1. General overview

At the eastern edge of the India-Asia collision zone, Myanmar (Figs. 2.8, 2.9 and 2.10) represents a large spatial gap in understanding the India-Asia collision, because the country only recently opened up to international geological research. Most of the country is situated on a microplate called the Burma Terrane (BT). Since the Neogene, the tectonic regime of the BT is characterized in the west by hyper-oblique subduction of the Indian Plate beneath the Burmese active margin, causing sporadic volcanism in the Wuntho-Popa Arc, and a sequence of faults called the Kabaw, Churachandpur Mao and Kaladan Faults. Tomography reveals a discontinuous presence of subducted slab material underneath the BT, IBR and Andaman Sea (Fig. 2.11; Hall & Spakman, 2015; Rangin, 2018; Replumaz et al., 2010). In the east, the tectonic regime of the BT is dominated by a more large-scale active dextral strike-slip fault called the Sagaing Fault, which transitions into the Andaman Sea spreading centre to the south. The Sagaing Fault and the other dextral strike-slip faults in the IBR have have

accommodated northward transcurrent motion of the BT, as part of the so-called Burma mobile belt (Bertrand & Rangin, 2003; Rangin, 2018; Rangin et al., 2013; Socquet et al., 2006).

This unique geodynamic setting within the framework of the bigger Himalayan region, resulted in fundamentally different tectonic histories for the BT in the various geodynamic models for the India-Asia collision published before this study (See Section 1.4). In the continental Greater India models (Cogne et al., 2013; Replumaz et al., 2010, 2013; Royden et al., 2008), the BT was reconstructed at a relatively high latitude during the Paleogene, next to the Lhasa Terrane as part of a linear and ~E-W oriented Asian margin. From this position, the BT is extruded towards its present-day location. These models require that the Western Belt Ophiolite, representing the western delineation of the BT, is the eastward continuation of the YTSZ, while the Wuntho-Popa Arc, the volcanic arc of the BT, has a similar relationship with the Gangdese Arc (Lhasa Terrane). However, the Wuntho-Popa Arc is currently oriented ~N-S. Therefore, these models induce major post-collisional clockwise rotation for the BT. In previous models with a Greater India Basin (van Hinsbergen et al., 2012, 2019), the Asian margin was less deformed during the collision and therefore the BT experiences only little post-collisional rotation. Finally, the position of the BT is less constrained in the Trans-Tethyan subduction models (Aitchison et al., 2007a; Gibbons et al., 2015; Hall, 2012; Jagoutz et al., 2015; Zahirovic et al., 2014). Most of these models show the BT at a similar position as the other groups of models (Hall, 2012; Zahirovic et al., 2014), but (part of) the Wuntho-Popa Arc could have also been part of the Incertus Arc, the proposed name for the island arc of the Trans-Tethyan subduction system, also including the Sumatran Woyla Arc (Barber & Crow, 2009; Hall, 2012). This would potentially allow initially more southern latitudes for the BT isolated from Asia.

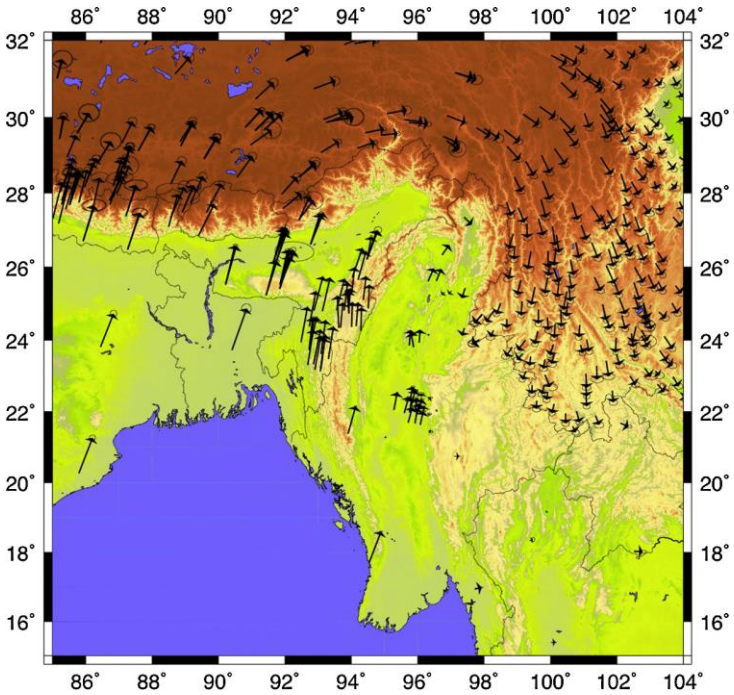

Figure 2.8: *Topography and GPS velocity field map of the Burma Terrane and the Eastern Himalayan Syntaxis in an Eurasian fixed reference frame (after Rangin et al., 2013).*

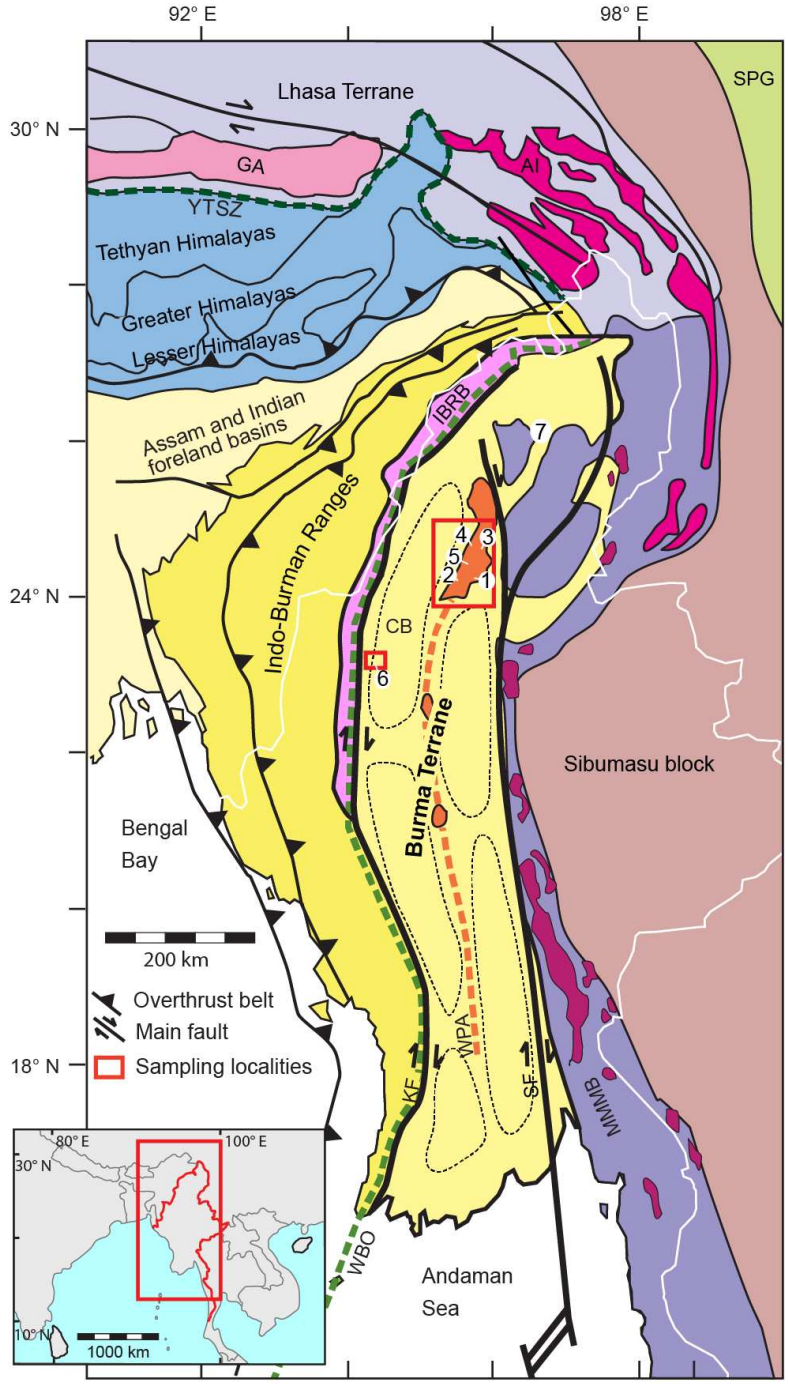

Figure 2.9: *Generalized Myanmar geologic map (after Licht et al., 2019). Localities: 1 = Kawlin, 2 = Pinlebu, 3 = Banmauk, 4 = Kyaung Le, 5 = Shinpa, 6 = Kalewa, 7 = Burmese ambers (Grimaldi et al., 2002; Poinar, 2018). Abbreviations: AI = Cretaceous-Paleogene Asian intrusives, CB = Chindwin Basin, GA = Cretaceous Gangdese Arc, IBRB: Indo-Burman Ranges basement, KF = Kabaw Fault, MMMB = Mogok–Mandalay–Mergui Belt (including Jurassic Eastern Belt Ophiolites & Jade Belt Ophiolite), SF =*

Sagaing Fault, SPG = Songpan Ganze & Yangtze complexes, WBO = Cretaceous Western Belt Ophiolite, WPA = Wuntho-Popa Arc, YTSZ = Yarlung-Tsangpo Suture Zone. Dashed black lines: Central Myanmar Basins.

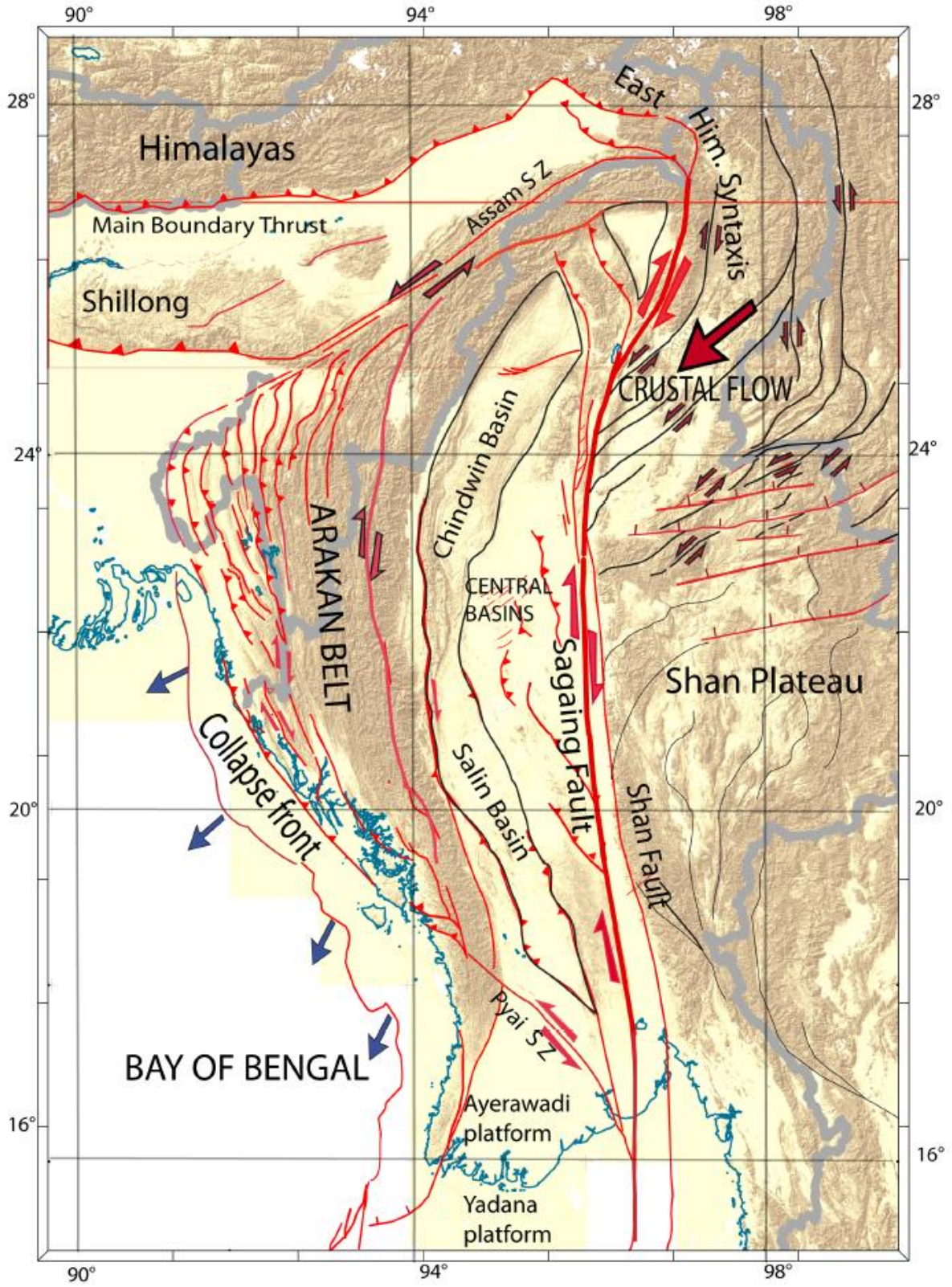

Figure 2.10: *Topographic map showing the main structures of Myanmar and surrounding regions (Rangin, 2018).*

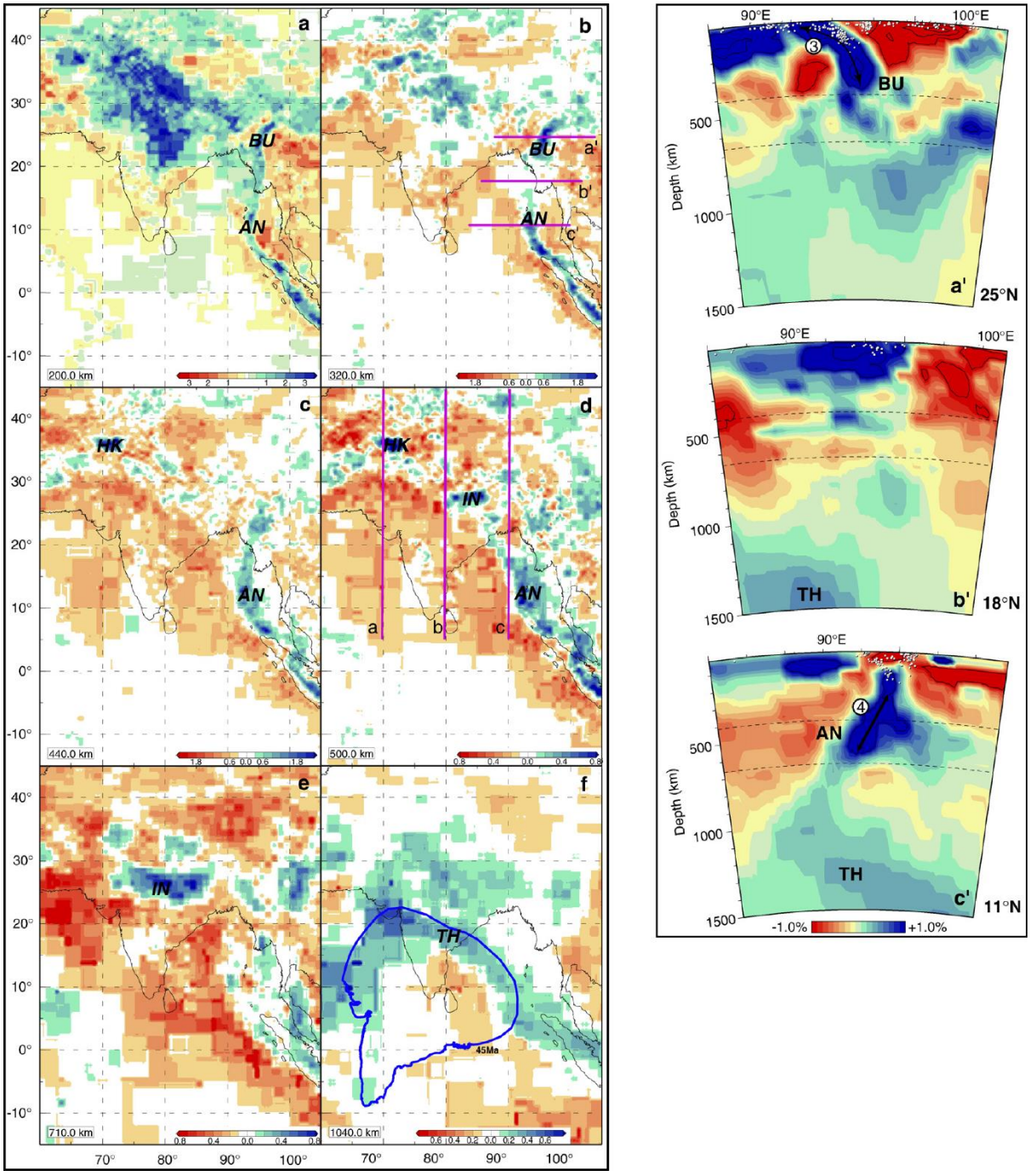

Figure 2.11: *Tomography images of India, Asia and the Burma Terrane: Left) Overview maps showing distinct high wavespeed anomalies associated with slab fragments of subducted Indian/Neo-Tethyan lithosphere; Right) Tomographic cross-sections perpendicular to the Burma/Andaman trench, as indicated on overview map b. Abbreviations: AN = Andaman slab, BU = Burma slab, TH = proposed Neo-Tethyan slab fragments (after Replumaz et al., 2010).*

2.2. The Wuntho-Popa Arc

The Wuntho-Popa Arc is the volcanic arc of the BT, initially formed due to Tethyan subduction. It is ~N-S trending across the middle of the BT, although it is covered by a thick Eocene-Quaternary sedimentary cover of the Central Myanmar Basins (See Section 2.3) in many places (Mitchell, 2017; Zhang et al., 2017). Its main phase of magmatism occurred from 110-90 Ma, followed by a 70-40 Ma subordinate stage (Barley & Zaw, 2009; Gardiner et al., 2015, 2017; Mitchell et al., 2012; Wang et al., 2014; Zhang et al., 2017). More recent volcanism is discontinuously present in the form of Miocene igneous rocks near Monywa and Salingyi and three Quaternary stratovolcanoes: Mount Loimye, Mount Popa and Taungthonlon (Mitchell, 2017; United Nations, 1978a).

The Wuntho Ranges (Fig. 2.12), the northern segment of the larger Wuntho-Popa Arc, were a primary objective in this study. They represent the largest exposure of the arc, consisting primarily of Cretaceous igneous rocks. Fresh outcrops in this area are limited, occurring mainly in rivers and quarries used for road construction. Apart from observations during this study, information on lithologies in the Wuntho Ranges, which will be described below, originate only from United Nation geological reports that have been recently updated in a special volume on Myanmar geology (Mitchell, 2017; United Nations, 1978a). The Hpyu Taung Metamorphics, the Ubye Serpentinite Complex and the Shwedaung Formation constitute the basement rocks of the Wuntho Range. They represent the only exposure of basement rocks on the BT, apart from lithologies in the IBR (See Section 3.3) and scattered undated xenoliths in volcanic deposits (Mitchell, 2017). The Hpyu Taung Metamorphics consists of high-grade metamorphic rocks and granites, while the Shwedaung Formation is a low-grade metamorphic sequence of sediments, extrusives and volcaniclastics. The contact with younger lithologies in the area is uncertain, but the age of the Shwedaung Formation is believed to be Late Triassic based on tentative similarities with the Pane Chaung Formation in the IBR, although the latter is predominantly comprised of metasandstone (See Section 3.3).

A sequence of Cretaceous volcanics and sediments lies unconformably on top of these basement rocks. The Mawgyi Andesite is poorly dated, but has been interpreted as the oldest formation of this Cretaceous sequence. These volcanics are the most extensive extrusives in the area. They are typically massive, with a grey to green or black colour, alternating with finer brecciated flows and agglomerates, as well as occasionally volcanogenic sediments. Sills and dikes can be found intruding the other lithologies. Previous studies have suggested that the Mawgyi Andesites are a remnant of an oceanic arc (Incertus Arc) thrusted on the BT prior to the establishment of the Wuntho-Popa Arc (Barber & Crow, 2009; Hall, 2012; Mitchell, 1993). However, there is no field evidence for a major thrusting event in the Wuntho Ranges, raising the possibility that they were emplaced

contemporaneously with the Kanza Chaung Batholith or during a precursory extrusive phase. This would imply a similar history for both volcanic units and hence the whole Wuntho-Popa Arc could have been part of the Incertus Arc.

The Kondan Chaung Group comes after the Mawgyi Andesite in the Wuntho Ranges stratigraphy. This sequence has a diverse composition, consisting of sandstones, limestones, volcaniclastics and (rhyo-)dacites. It is predominantly exposed in the northern part of the Wuntho Ranges. The Maingthon Dacites are the minor volcanic part of the Kondan Chaung Group. These dacites are generally porphyritic with a bleached white to dark grey-green colour. It also contains massive rhyodacite flows with a grey-purple colour with few phenocrysts. The presence of pyrite, sulphide and chlorite suggests hydrothermal alteration. The sandstones and siltstones of the Mawlin Formation are also part of the Kondan Chaung Group. They typically have a grey-brown to greenish colour. Fining-upwards sequences and cross-bedding are common sedimentary structures in this formation, corresponding to a turbiditic facies. Locally, tuffaceous deposits and breccia layers are mixed or interbedded with these sediments. The overlying limestones of the Namakauk Formation contain shell debris and abundant algae together with volcanic fragments, but lack age-diagnostic fossils.

The Kondan Chaung Group underwent a significant amount of folding. On the other hand, structural observations from the Kanza Chaung Batholith show no signs of significant tilting. This NE-SW trending batholith constitutes the main component of the Wuntho Range, exposed in a large part of the area. The batholith primarily consists of medium to coarse I-type (grano)diorites with several mafic inclusions, as well as smaller diorite plutons and an area consisting of 2-mica granite in the north. U-Pb dating of these intrusions yielded ages of ~108–90 Ma Ma (Gardiner et al., 2017; Licht et al., 2020; Mitchell, 2017). A second phase of I-type magmatism of late Eocene age is found at the Shangalon copper district (Gardiner et al., 2017).

A Late Cretaceous – Paleogene sequence of sediments, postdating the main Kanza Chaung Batholith, surround the Wuntho Ranges, resulting in a NE-SW trending anticline. In the west, the thick stratigraphic succession of predominantly sedimentary rocks dip to the northwest to form the eastern limb of the Chindwin Basin. There is no major known thrust between the Chindwin Basin and the Wuntho Ranges. To the east of the Wuntho Ranges, the sedimentary basins are disrupted by major faults (e.g. Taung Chaung Fault) and deformation related to displacements along the Sagaing Fault system.

Figure 2.12: *General geological map of the Wuntho Ranges (Mitchell, 2017).*

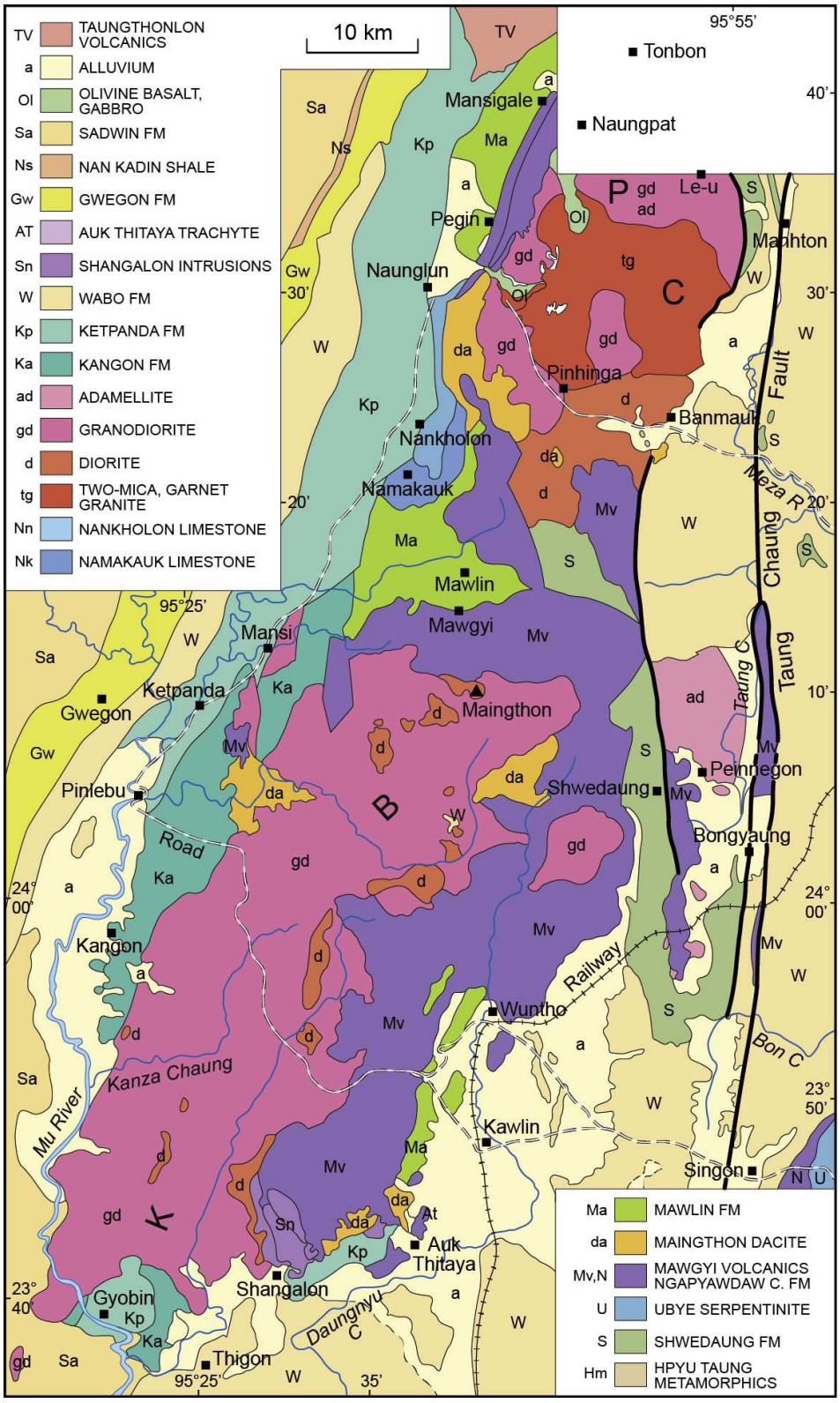

2.3. Central Myanmar Basins

The Wuntho-Popa Arc subdivides the BT into a series of ~N-S trending forearc and back-arc basins, which started to develop contemporaneously with the main phase of magmatism in the Late

Cretaceous. Collectively these basins are called the Central Myanmar Basins (Fig. 2.13; Bender, 1983; Licht et al., 2019; Pivnik et al., 1998; Zhang et al., 2017). The back-arc consists of the Shwebo Basin in the north and the Pegu Basin in the south. The Paleogene deposits in the Shwebo Basin are exclusively continental (Thein & Maung, 2017), while those in the Pegu Basin remain poorly described. In the Neogene, both basins were characterized by southward prograding tidal-influenced estuarian sequences, before being overlain by the Quaternary fluviatile Irrawaddy Formation (Bender, 1983; Khin, 1999; Pivnik et al., 1998; Thein & Maung, 2017). The Burmese forearc is commonly subdivided into the Minbu (or Salin) Basin in the south and the Chindwin Basin in the north. The Burmese forearc is the subject of this study and hence the geology of the Chindwin and Minbu Basins will be described in greater detail in Sections 2.3.1 to 2.3.3. Interpreted seismic sections across the Central Myanmar Basins have distinguished three phases of uplift in the Central Myanmar Basins in the Late Cretaceous, Eocene and Late Oligocene. The Paleogene sedimentary sequence is immediately followed by a basin-wide unconformity of late Oligocene age (Rangin, 2018; Zhang et al., 2017). In the Neogene, basin-wide inversion took place (Bertrand & Rangin, 2003; Pivnik et al., 1998; Rangin, 2018; Zhang et al., 2017).

2.3.1. The Chindwin Basin

The Chindwin Basin constitutes the northern basin of the Burmese forearc. It is separated from the Minbu Basin in the south by a small topographic high called the Pondaung Ranges (Bender, 1983; Licht et al., 2019; Pivnik et al., 1998; Zhang et al., 2017). The oldest sediments in the Chindwin Basin are the poorly-exposed marine limestones and mudstones of the Kabaw Formation of presumed Albian to Maastrichtian age (Bender, 1983), presumably directly overlying the Western Belt Ophiolite (Licht et al., 2019; Liu et al., 2016). This is followed by a Paleocene to middle Eocene sequence of shallow-marine siliciclastics, alternating with sporadic continental episodes, consisting of the Paunggyi, Laungshe, Tilin and Tabyin Formations with poorly defined lithostratigraphic boundaries based only on grain size (Bender, 1983; Licht et al., 2019). Afterwards, the westward directed, fossil-rich, fluvio-deltaic sediments of the upper Eocene Pondaung Formation were deposited. This thick and prominent formation has received significantly more attention compared to the other Paleogene units, because of its prolific mammalian faunal and paleobotanical fossils. The Pondaung Formation was dated at ~40 Ma with a combination of biostratigraphy and geochronology (Jaeger et al., 1999; Zaw et al., 2014; Licht et al., 2014, 2015).

Figure 2.13: *Synthetic logs for the three main basins constituting the Central Myanmar Basins: (1) the Shwebo Basin in the backarc (after Thein & Maung, 2017), (2) the Minbu Basin, (southern forearc;*

after Pivnik et al., 1998), and (3) the Chindwin Basin (northern forearc; after Bender, 1983; Licht et al., 2019). vfs—very fine sand; fs—fine sand; ms—medium sand; cs—coarse sand.

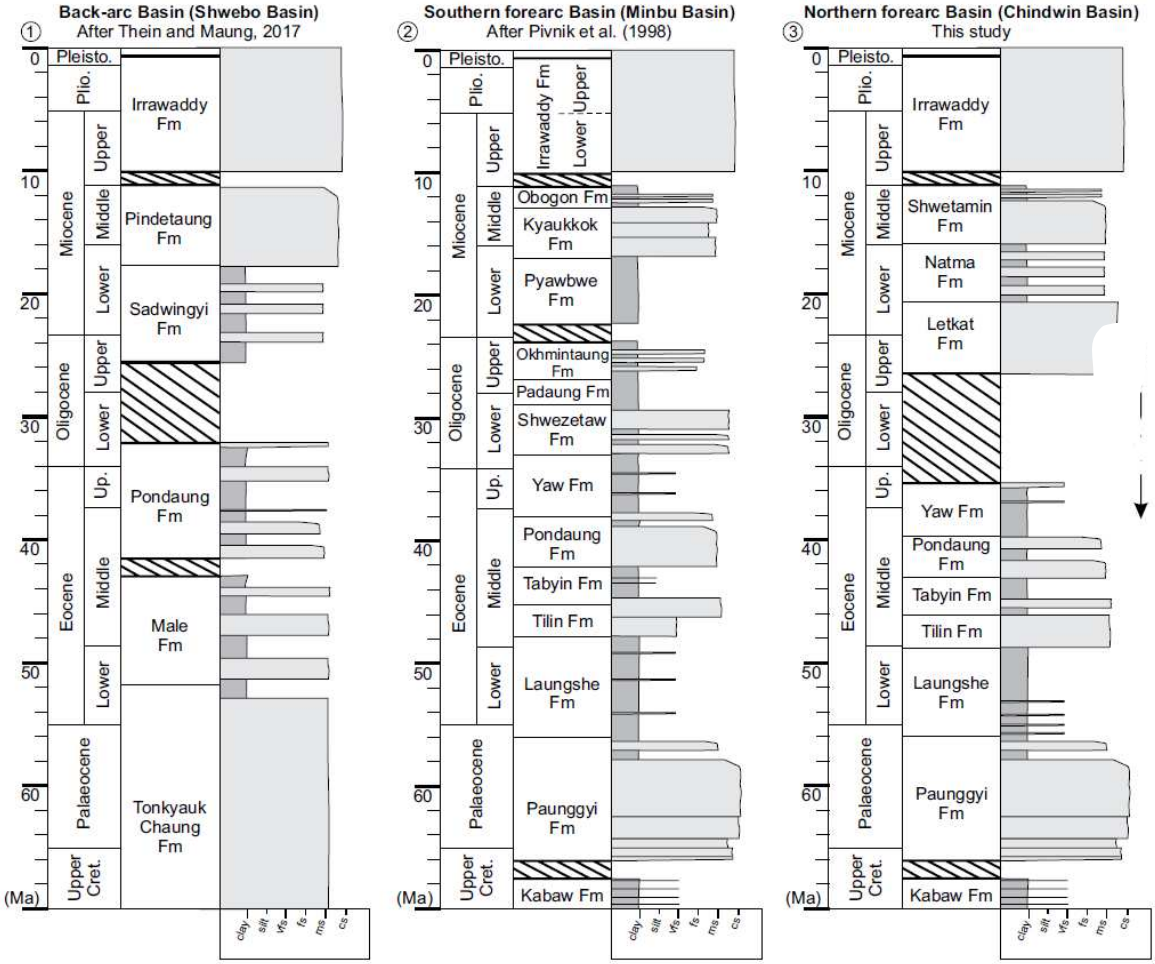

Further upward in the sequence, the late Eocene Yaw Formation has a variation of sedimentary facies, comprised of deltaic tidal sand flat sediments, anoxic sediments containing organic-rich dark mudstones and siderite-rich carbonate layers, and finally continental episodes with thick fluvial sandstone bodies and thick lignite layers containing vertebrate fossils (Fig. 2.14). This combination of sedimentary facies was interpreted as a quasi-closed estuary system, sustained primarily by tectonic uplift (Bender, 1983; Licht et al., 2019). A single tuff layer is also present in the Yaw Formation, yielding a U-Pb age constraint of 38.0 ± 1.1 Ma (Licht et al., 2019). The Yaw Formation is overlain by the ~1.5-km-thick Letkat Formation, comprised exclusively of thick afossiliferous fluviatile sandstones that are capped by pedogenised, finer-grained sands (Fig. 2.14). Hence, the depositional environment of the Letkat Formation likely represents a braided river system (Licht et al., 2019). The base of the Letkat has yielded ~35 Ma detrital zircons, while the upper part has yielded detrital zircons as young as 26-23 Ma, suggesting an upper Oligocene or even early Miocene age for this formation (Licht et al., 2019). Moreover, the sharp contact between the Letkat Formation and the

Yaw Formation, defined by the occurrence of several sandstone bodies with thick basal lags and a shift from SWW to SSW oriented paleocurrents, is likely unconformable (Licht et al., 2019; United Nations, 1978a; Wang et al., 2014), although some studies have argued for a conformable contact (Bender, 1983). The Neogene part of the sedimentary infill of the Chindwin Basin consists of the fluviatile Natma, Shwethamin and Irrawaddy Formations. The Natma and Shwethamin Formations are of probable Miocene age. They are unconformably overlain by the fluviatile late middle Miocene - Pliocene Irrawaddy Formation, deposited by the modern Irrawaddy river system that originates in the Eastern Himalayan Syntaxis (Bender, 1983; Licht et al., 2019; United Nations, 1978a).

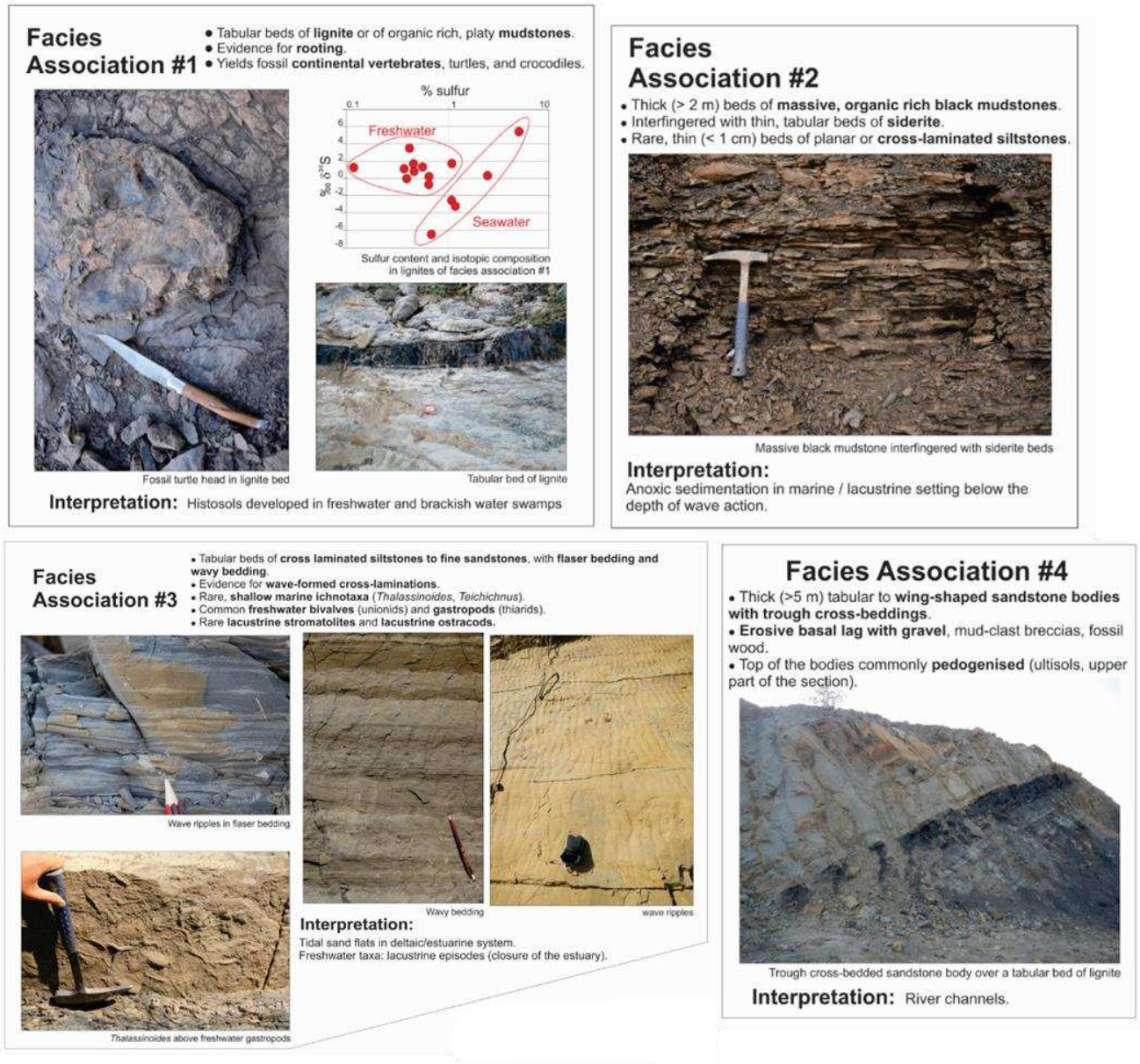

Figure 2.14: *Sedimentary facies associations for the Yaw and Letkat Formations in the Chindwin Basin (after Licht et al., 2019).*

2.3.2. The Minbu Basin

The Minbu Basin is the southern basin of the Burmese forearc. Its stratigraphic history is roughly similar to the Chindwin Basin up until the late Eocene Yaw Formation, which exclusively consists of shallow-marine, fine-grained sediments containing nummulites in the Minbu Basin, compared to the estuarian paleoenvironment in the Chindwin Basin, which has a degree of continental input. In contrast to the Chindwin Basin, all subsequent Oligocene formations in the Minbu Basin, the Shwezetaw, Padaung and Okhmintaung Formations, are continuous and remain shallow-marine with deposits containing gastropods, bivalves and foraminifera (Bender, 1983; Licht et al., 2019). This shallow-marine sequence is covered by the Neogene fluvio-deltaic deposits of the Pyawbwe, Kyaukkok, Obogon and Irrawaddy Formations, becoming once more similar to the Chindwin Basin.

2.3.3. Partitioning in the Burmese forearc

Recent research has showed a diverging stratigraphic record between the Chindwin and Minbu Basins since the late Eocene, and suggested that this was caused by an onset of hyper-oblique subduction at ~39-37 Ma. This resulted into partitioning of the Burmese forearc into en echelon pull-apart basins (Licht et al., 2019; Rangin, 2018). Pull-apart deformation is further supported by rapid subsidence of the Chindwin Basin (~ 1.0 m/ky) during deposition of the Yaw Formation (Licht et al., 2019), although this is might not be restricted only to the Yaw Formation based on the large thickness of the upper Eocene Pondaung Formation (Section 2.3.1). Around this time, there was also a change of sedimentary provenance from a proximal Andean-type volcanic arc in the Pondaung and Yaw Formations, supposedly the Wuntho-Popa Arc, to increasingly more input of high-grade metamorphic basement rocks in the Letkat Formation, supposedly from the MMMB to the east (Licht et al., 2013, 2019; Wang et al., 2014). This previously proposed Paleogene evolution of the Burmese forearc is shown in figure 2.15 (Licht et al., 2019). However, recent seismic studies along the Wuntho-Popa Arc showed that a considerable part of the arc was buried by the late Paleogene (Zhang et al., 2017), which is seemingly difficult to reconcile with active (hyper-oblique) subduction and a predominant Wuntho-Popa Arc source for the late Eocene Yaw Formation. Therefore, one of the topics in Chapters 5 and 6 of this thesis will be to further investigate and evualuate the previously proposed evolution and sedimentary sourcing of the Burmese forearc, using the new paleomagnetic constraints on the position of the BT presented in Chapter 4.

Figure 2.15: *Proposed evolution of the Burmese subduction margin and forearc basin during the Paleocene-middle Eocene (a), the late middle Eocene (b), and the upper Eocene–Oligocene (c). Numbers: 1 = Shwebo Basin, 2 = Minbu Basin, 3 = Chindwin Basin. Abbreviations: AT = Arakan*

Trench, AP = accretionary prism, FB = forearc basin, WPA = Wuntho-Popa Arc, BB = back-arc basin, MB = metamorphic belts (Licht et al., 2019).

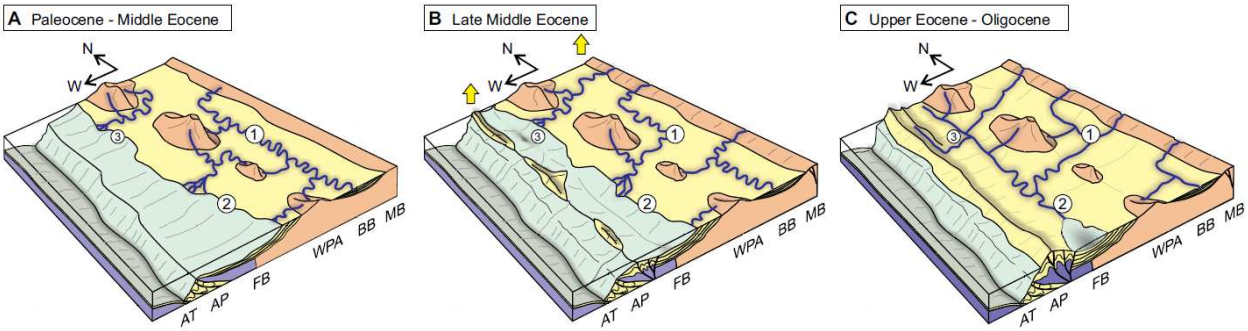

3. The Indo-Burman Ranges

3.1. General overview

The IBR separates the BT from the Indian Foreland Basin and Bay of Bengal. Traditionally, it was seen as an accretionary complex due to subduction of Neo-Tethyan and Indian lithosphere beneath the Burmese subduction margin. However, the Burmese slab is poorly imaged or missing on tomography images except close to the collision zone in the north (Fig. 2.11). Therefore, there is debate whether subduction of Indian oceanic lithosphere continues in the Neogene (Lee et al., 2016; Rangin, 2018; Steckler et al., 2016) or was replaced by continent collision/coupling in the Eocene (Rangin, 2017; Morley, 2009; Morley et al., 2020). This also in agreement with structural observations showing predominantly dextral strike-slip faulting between the BT and India within the IBR (Fig. 2.10).

The Western Belt Ophiolite, alongside the Neogene Kabaw Fault, forms the western boundary of the BT in the IBR (Barber & Crow, 2009; Liu et al., 2016; Mitchell et al., 2012; Searle et al., 2017). The Western Belt Ophiolite was presumably formed and emplaced during the Cretaceous following the onset of Neo-Tethyan subduction (Aitchison et al., 2019; Fareeduddin & Dilek, 2015; Licht et al., 2019; Pivnik et al., 1998; Singh et al., 2016; Zhang et al., 2018a). Therefore, it was often correlated with the YTSZ (Liu et al., 2016), although rocks within the latter have been dated to be slightly older (Aitchison et al., 2019).

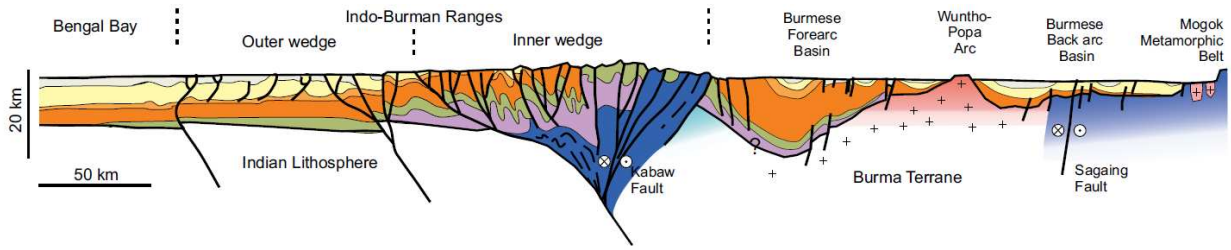

Figure 2.16: *Schematic present-day W-E cross-section of the Bay of Bengal, Indo-Burman Ranges (Outer and Inner Wedge), Burma Terrane and Mogok-Mandalay-Mergui Belt. The question mark indicates that the presence of Triassic rocks thrusted on the ophiolitic basement of the forearc is still unclear (after Licht et al., 2019).*

3.2. The Outer Wedge & Bay of Bengal

Traditionally, the IBR are divided into an Outer Wedge and an Inner Wedge (Fig. 2.16; Bannert et al., 2012; Brunnschweiler, 1966; Maurin & Rangin, 2009; Mitchell, 2017; Zhang et al., 2017). The Outer Wedge is a fold and thrust belt, forming the deformed continuation of Bay of Bengal sediments in the India-Burma collision zone (Fig. 2.17). Significant uplift in the Outer Wedge started during the late Miocene (Maurin & Rangin, 2009; Rangin et al., 2013).

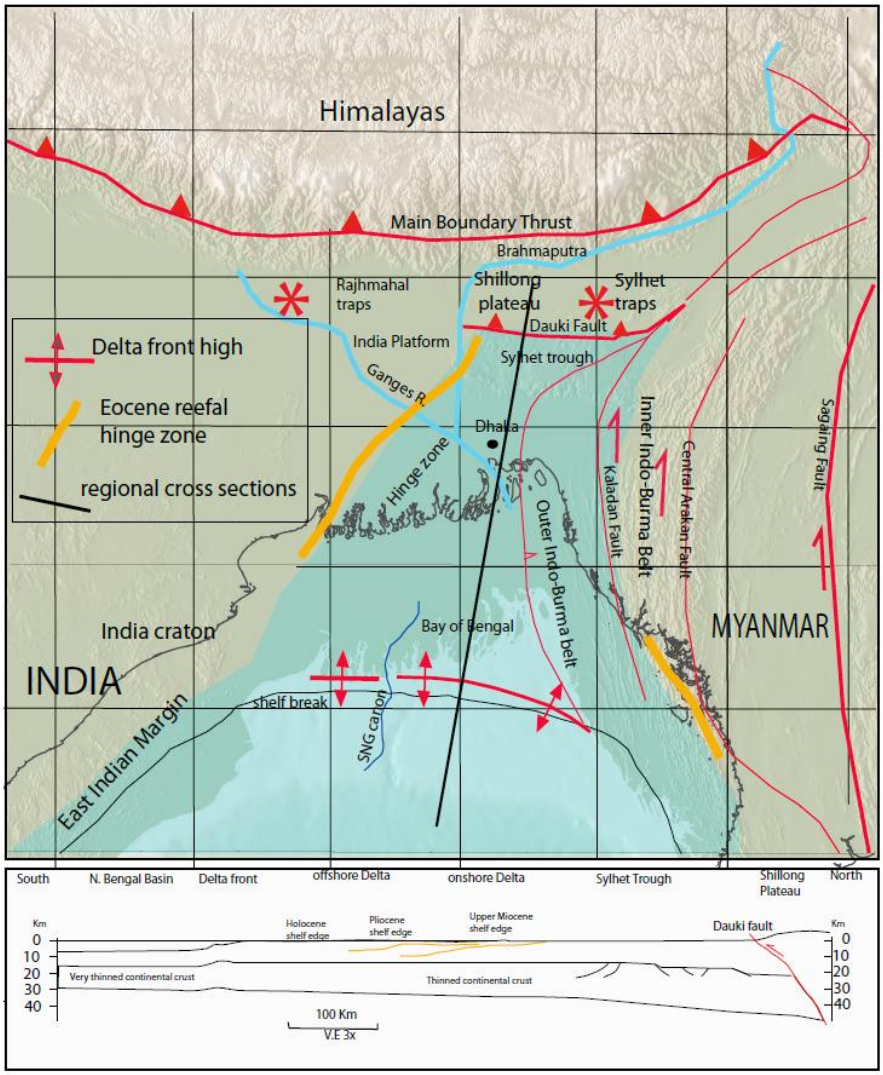

Figure 2.17: *Topographic map of the Bay of Bengal, Indo-Burman Ranges, Himalayas, Indian Craton and Myanmar. Main geological structures are indicated, as well as a schematic N-S cross-section (Rangin, 2018).*

The general consensus on the Bay of Bengal basement is that it consists of hyper-extended continental crust that formed the passive margin of India during the fragmentation of Gondwana, potentially transitioning into oceanic crust at the slab underlying the BT (Rangin, 2018; Sloan et al., 2017; Steckler et al., 2016). Others have argued that this slab consists of continental lithosphere (Zheng et al., 2020), but this is difficult to reconcile with the known fit of Gondwana and the subsequent rifting of (Greater) India during the Early Cretaceous (Fig. 2.18; I'Anson et al., 2019; Seton et al., 2012; Thompson et al., 2019).

Paleogene sediments in the Bay of Bengal region were primarily sourced by the Indian craton (e.g. the Eocene Disang Formation in NE Assam - Aitchison et al., 2019). Subsequent Oligocene to recent infill of the Assam Basin and Bay of Bengal is dominated by Himalayan-derived sediments, in particular from the Eastern Himalayan Syntaxis by the Brahmaputra River (Najman et al., 2019). In the Outer Wedge, these Neogene sediments were often scraped off from the Bay of Bengal and recycled during thrusting (Allen et al., 2008).

3.3. The Inner Wedge

The geology of the Inner Wedge and its relationship with the BT is more complex and its deformation and uplift history are less understood compared to the Outer Wedge. The oldest exposed units in the Inner Wedge are the low-grade metamorphic Pane Chaung Formation and the high-grade metamorphic Kanpetlet Schist. They were presumably deposited in the Triassic (Mitchell, 2017; United Nations, 1978a). The origin of this basement is unclear. It has been interpreted as either (1) a separate tectonic block accreted to the BT either in the Early Cretaceous to Mid-Cretaceous (Mitchell, 2017; Morley et al., 2020; Rangin, 2018) or in the Late Cretaceous to Paleogene (Gibbons et al., 2015; Searle et al., 2017), or (2) an accretionary-type setting without block collision (Fareeduddin & Dilek, 2015; Morley et al., 2019; Zhang et al., 2018a).

Almost coevally conducted studies on U-Pb detrital zircon age distributions have not been able to provide a clear answer on this matter as well, suggesting that the Pane Chaung Formation is of either Gondwana/India (Wang et al., 2016; Yao et al., 2017) or Sibumasu (Sevastjanova et al., 2016) affinity, which has implications for possible origin of the BT. In addition, the Pane Chaung Formation has been correlated with the Langjiexue Formation as part of Greater Argoland forming the margin of NW Australia (Fig. 2.18), which would correspond to a Gondwanan origin (Cai et al., 2016; Meng et al., 2019; Morley et al., 2020; Yao et al., 2017). In this context, the name Argoland itself is specifically referring to Gondwana-derived rocks in East Java and Sulawesi (Hall, 2009; Sikumbang, 1990; Wakita et al., 1998), while fragments of the larger Greater Argoland rifted from NW Australia at ~155 Ma (Fig. 2.18; Hall, 2012; I'Anson et al., 2019; Morley et al., 2020; Seton et al., 2012). Geochronology

studies on the basement of the Wuntho-Popa Arc (e.g. Shwedaung Formation – Section 2.2) are absent, making the origin of the BT and a potential separate IBR block very uncertain. Adding confusion to these discrepancies, the postulated separate IBR block has erroneously been named Mawgyi Nappe (Barber & Crow, 2009; Zhang et al., 2017), after the emplaced oceanic arc interpretation of Mitchell (1993) for the Mawgyi Andesites that are not located in the IBR but much farther east in the Wuntho Ranges (See Section 2.2). Therefore, a better proposed name for the IBR terrane is Mount Victoria Block (Morley et al., 2020; Rangin et al., 2013; Rangin, 2018), named after the main exposure of the Kanpetlet Schist near around Mount Victoria, the highest peak of the IBR in Central Myanmar. The possible existence of this IBR terrane has implications for the manner of emplacement of the Western Belt Ophiolite as well, as it could either represent the suture between a Gondwana derived Mount Victoria Block and the BT or exhumed slices of accretionary prism material (review in: Morley et al., 2020).

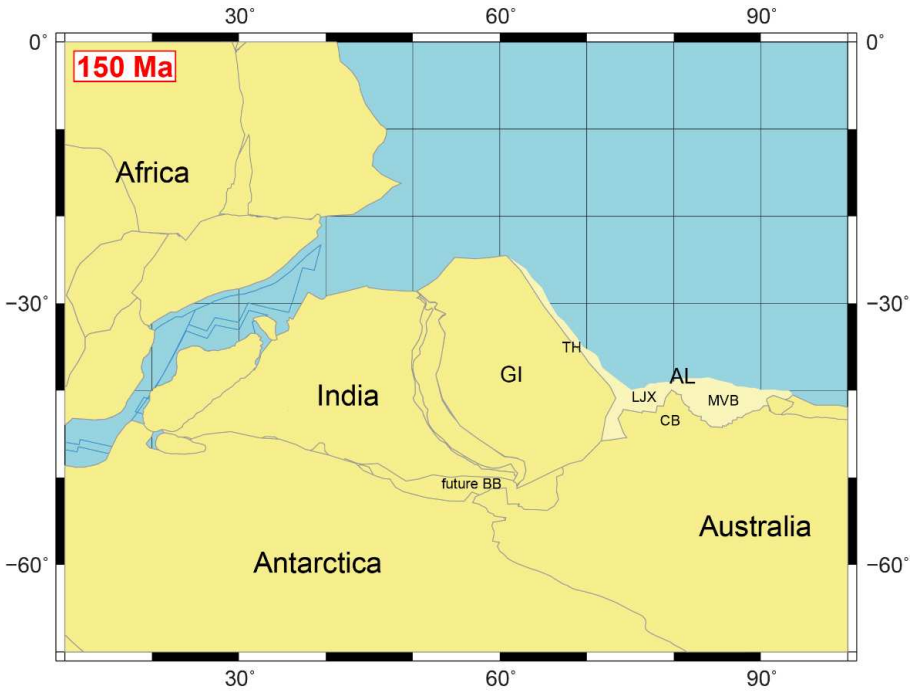

Figure 2.18: *Schematic reconstruction of Gondwana at 155 Ma using the GPlates model of Matthews et al. (2016). Size of Greater India based on geological constraints from NW Australia (e.g. Carnarvon Basin; I'Anson et al., 2019). Abbreviations: AL = Argoland, BB = Bay of Bengal, CB = Carnarvon Basin, LJX = Langjiexue Formation, MVB = Mount Victoria Block (Pane Chaung Formation), TH = Tethyan Himalayas.*

In any case, these older units are overlain by a sequence of Upper Cretaceous – Eocene marine turbiditic sediments, in the Eocene occasionally laterally alternating with littoral sediments (Bannert et al., 2012; Maurin & Rangin, 2009; Myint, 2019; United Nations, 1978a). Petrographic, heavy

mineral and isotopic data from these deposits in the Arakan Yoma, southern IBR, show that they were probably sourced by the Wuntho-Popa Arc (Allen et al., 2008). The lateral variation of sedimentary environment could perhaps indicate incipient uplift of the IBR, which is further corroborated by a late Eocene unconformity in the IBR marking the onset of molasse deposition (Bannert et al., 2012; Ghose et al., 2014; Morley et al., 2020). Evidence from late Eocene deposits from the Chindwin Basin also suggest basin overfilling due to the emergence of the IBR during this time (Licht et al., 2019). Additionally, a recent low temperature thermochronological age elevation profile documented a major uplift phase within the IBR during the latest Oligocene – earliest Miocene, and a possible earlier event in the middle Eocene (Najman et al., 2018). However, there are different ideas on the cause for these phases of uplift. One group of studies has proposed that late Paleogene uplift of the IBR was the result of accretion of thin Indian continental crust (Morley, 2002, 2009; Rangin et al., 2013; Vérard et al., 2017) or an allochthonous terrane (Acharyya, 2007, 2015). Others have argued that the geology of the Inner Wedge accretionary prism is more complex, because it formed along a hyper-oblique margin with a rapidly uplifting retro-wedge. Such retro-wedges undergo a phase of rapid uplift due to the transition of localized to full strain partitioning. Eventually, full strain partitioning causes the motion to become accommodated by one or only a few strike-slip faults, as is the case for the IBR since the Neogene , illustrated by the dextral South Kabaw, Churachandpur Mao and Kaladan Faults who together accommodate ~1.8 cm/yr northward motion of the BT, as part of the Burma mobile belt (Licht et al., 2019; Maurin & Rangin, 2009; Morley et al., 2020; Nielsen et al., 2004; Rangin, 2018).

4. Sibumasu

4.1. The Shan Plateau

East of the BT, the Shan Plateau is characterized by a Cambrian to Triassic stratigraphic sequence, similar to western Thailand and the Malay Peninsula. Together they form the Sibumasu Block, interpreted to have rifted from Gondwana in the Permian and accreted to Eurasia in the Triassic (Metcalfe, 2013; Sevastjanova et al., 2016). A potential collision age of the BT with Sibumasu is poorly constrained and even the existence of a suture between both blocks has been challenged (Metcalfe, 2013; Mitchell, 1993; Searle et al., 2017; Sevastjanova et al., 2016).

4.2. The Mogok-Mandalay-Mergui Belt

The Sibumasu Terrane is separated from the BT by the dextral Sagaing Fault, the Jade Belt Ophiolite, which is only exposed at the northern edge of the Sagaing Fault and has unclear constraints for its emplacement age and correlation with other nearby sutures (Morley, 2017b; Ridd et al., 2019;

Searle et al., 2017; Yui et al., 2013), and finally the MMMB, a complex N-S trending belt of metamorphic rocks.

4.2.1. The Mogok-Mandalay-Mergui Belt

The most prominent rocks of the MMMB include Cretaceous – Cenozoic I-type intrusives (e.g. the Sodon Batholith) and S-type intrusives (e.g. the Dianxi Batholith), the Jurassic - Cretaceous Tagaung-Myitkyina Ophiolite Belt, or Eastern Belt Ophiolite, and regionally metamorphosed sedimentary rocks (Lin et al., 2019; Mitchell, 2017; Mitchell et al., 2012; Searle et al., 2017). Many of these units are correlated with similar units in the Himalayas (Section 1), for example the Sodon Batholith with the Lohit and Gangdese intrusives, the Dianxi with the Bomi Chayu and Central Lhasa intrusives and the Eastern Belt Ophiolite with the Bangong-Nujiang suture (Fig. 2.19; Lin et al., 2019; Liu et al., 2016).

The metamorphic rocks of the MMMB include phlogopite + diopside + spinel ± forsterite olivine ± ruby corundum marbles, scapolite + garnet + biotite calc-silicate rocks, K-feldspar augen gneisses, clinopyroxene-bearing quartzites and sillimanite ± andalusite mica schists and gneisses. In-situ crustal melting has resulted in tourmaline ± garnet leucogranitic pods and dykes. The MMMB records two main metamorphic events: A latest Cretaceous – early Paleocene phase of metamorphism and partial melting, followed by a phase of high temperature metamorphism during the late Eocene – Oligocene (Searle et al., 2007, 2017, 2020) and finally a phase of rapid uplift during the late Oligocene – early Miocene (Bertrand et al., 2001; Bertrand & Rangin, 2003; Searle et al., 2017). This last phase has been related to both the strike-slip deformation and extrusion of the MMMB (Bertrand et al., 2001; Bertrand & Rangin, 2003). Plate tectonic studies suggest that the majority of the MMMB, including the Tenchong and Baoshan blocks, was extruded from the Eastern Himalayan Syntaxis towards the south-east since approximately the late Paleogene (Li et al., 2018; Matthews et al., 2016; Tong et al., 2013).

4.2.2. The Jade Belt Ophiolite

The Jade Belt Ophiolite, consisting of high pressure metamorphic jadeite, has uncertain constraints for its emplacement age, with estimates varying from the Early to Late Cretaceous, although these constraints might not be reliable (Searle et al., 2017; Shi et al., 2008; Yui et al., 2013). As a consequence, the Jade Belt has been correlated with different other regional ophiolites, including the Western and Eastern Belt Ophiolites, dismembered ophiolitic fragments along the trace of the Sagaing Fault (Central Belt Ophiolite), or as a separate structure entirely (Htay et al., 2017; Morley, 2017b; Searle et al., 2017). It is clear that its proximity to northern splays of the Sagaing Fault make

it difficult to interpret. In turn, this has resulted in the uncertainties regarding the suturing of the BT with Sibumasu (Metcalfe, 2013; Mitchell, 1993; Searle et al., 2017; Sevastjanova et al., 2016).

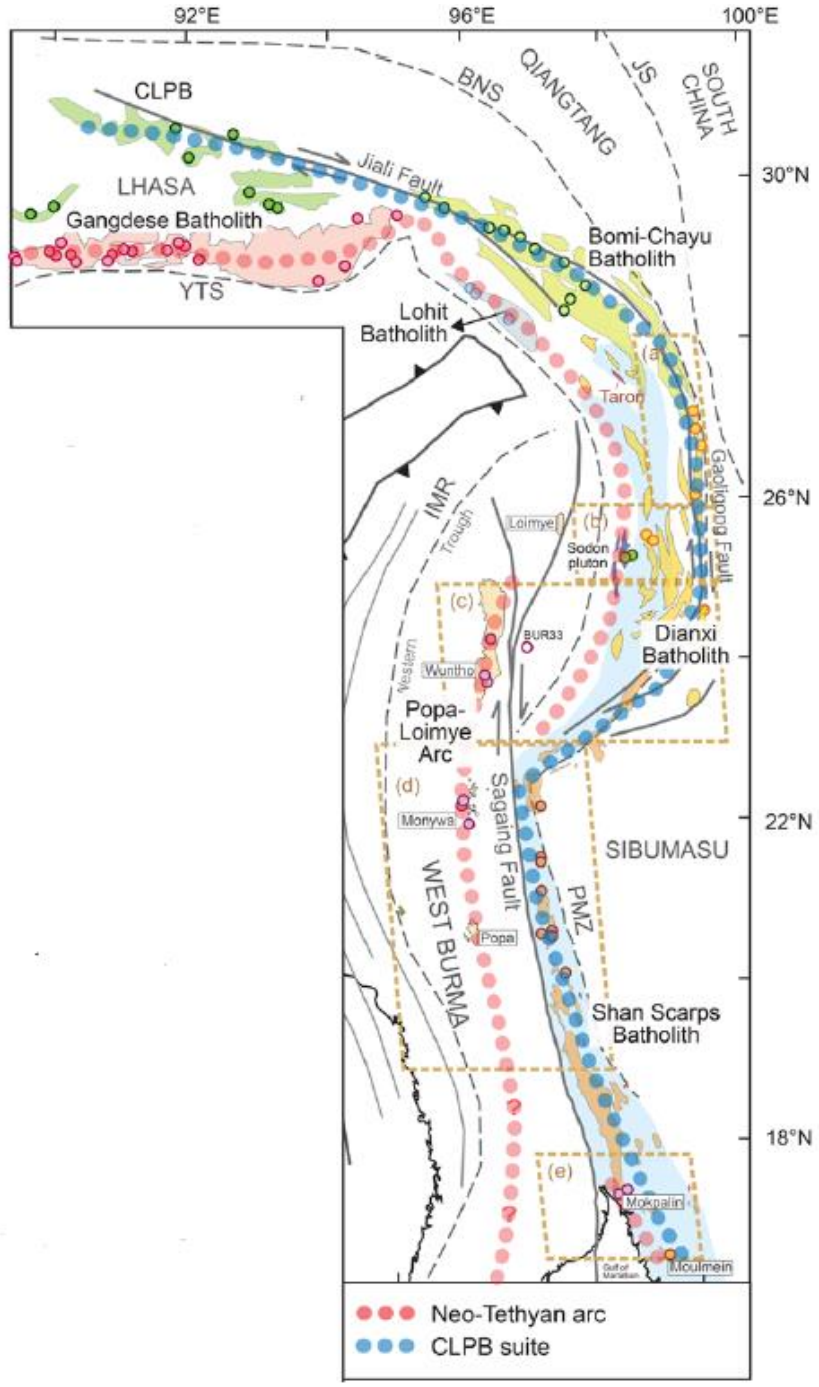

Figure 2.19: *Previously proposed correlations of magmatic arcs in the BT, Lhasa Terrane and Eastern Himalayan Syntaxis by Lin et al. (2019).*

4.2.3. The Sagaing Fault

The dextral strike-slip Sagaing Fault is of suggested Neogene age, with a current motion of 1.8 cm/yr and a total displacement of around ~400 km since that time (Maung, 1987; Morley, 2017b; Rangin et

al., 2013; Socquet et al., 2006), although earlier estimations proposed around ~1100 km of offset (Mitchell, 1993). In most of onshore Myanmar, the Sagaing Fault is a single brittle ~N-S trending fault, but it splays into different segments north of the city of Mandalay (Morley, 2017b; Sloan et al., 2017; Socquet et al., 2006). Farther south in the offshore, the Sagaing Fault transitions in the South Sagaing Fault (Morley, 2017a). Earlier dextral motions east of the Sagaing Fault are recorded by the Oligocene Shan Fault or Mergui Fault (Bertrand et al., 2001; Morley, 2017a; Rangin, 2018), the Oligocene West Sagaing Fault (Morley & Arboit, 2019) and the hypothesized Cretaceous – Paleogene Medial-Myanmar Shear Zone, which includes the Panlaung Fault (Morley & Arboit, 2019; Ridd et al., 2019; Ridd & Watkinson, 2013). However, the latter links up with the predominantly sinistral regime of the Mae Ping and Three Pagodas faults on Sibumasu in the Eocene-Oligocene (Morley, 2004).

4.3. Extrusion of Sibumasu/Indochina

The lateral south-eastward extrusion of Sibumasu from the Asian margin, alongside Indochina as a whole, played a role in accommodating the convergence of India and Asia, although the importance of this remains intensely debated in the different collision models (Section 1.4). In Indochina itself, constraining the exact amount of latitudinal and rotational motion with paleomagnetic data is complicated by two well-recognized problems common in Tibet and SE Asia: (1) Inclination shallowing of clastic sediments (e.g. Dupont-Nivet et al., 2010; Li et al., 2017; Tan et al., 2010; Zhang et al., 2018b), and (2) distinguishing between wholesale tectonic rotations and local rotations along the extremely deformed strike-slip fault systems of the extrusion system (Pellegrino et al., 2018; Speranza et al., 2019). This has motivated a wealth of paleomagnetic studies in Indochina, which often contradict each other (Fig. 1.4), resulting in three end-member models for the mechanism of extrusion (Fig. 2.20). The first mechanism advocates continuous deformation and rotation of the whole Indochina during its extrusion (Fig. 2.20a; Kornfeld et al., 2014; Otofuji et al., 2010; Sato et al., 2007); this was often used to infer an initial E-W orientation of the subcontinent as part of the Asian margin (e.g. Replumaz et al., 2010, 2013; Royden et al., 2008). By contrast, the second mechanism states that the rotation of rigid blocks accommodated the extrustion (Fig. 2.20b; Gao et al., 2015; Li et al., 2017; Tong et al., 2013), while the final group of models emphasises the role of local rotations along strike-slip fault systems (Fig. 2.20c; Pellegrino et al., 2018; Speranza et al., 2019). Both the second and third group of models can account for the large variation in rotations observed in the paleomagnetic data from Indochina (Fig. 1.4), and the initial NW-SE orientation of the subcontinent in more recent collision models (e.g. Hall, 2012; van Hinsbergen et al., 2019; Zahirovic et al., 2016). As will further be illustrated in Chapters 4-6, the BT was part of a system separate from Sibumasu, but the orientation of Indochina is nonetheless important for understanding the collision history of the BT.

5. The Andaman Sea

The Andaman Sea represents a complex and partitioned back-arc extensional basin that developed mostly in the Neogene along the oblique convergent margin of India/Australia and Eurasia as the BT moved northward. Its tectonic setting is characterized by complex interplay of extensional and dextral strike-slip fault systems, resulting in a large-scale pull-apart structural style (Curray, 2005). The tectonic regimes of the BT and Andaman Sea are mainly connected by the (South) Sagaing Fault and Shan/Mergui Fault horsetail structures, splaying into the East Andaman Fault farther south, connecting it with the Andaman spreading centre (Rangin, 2018). The East Andaman Fault marks the boundary between the Andaman Sea spreading centre and the rifted continental margin of Sundaland (Eastern Andaman Basins). In this context, the Neogene tectonic setting of the Andaman Sea can be interpreted as a southern continuation of the Burma mobile belt as the Andaman mobile belt (Fig. 2.21; Rangin, 2018).

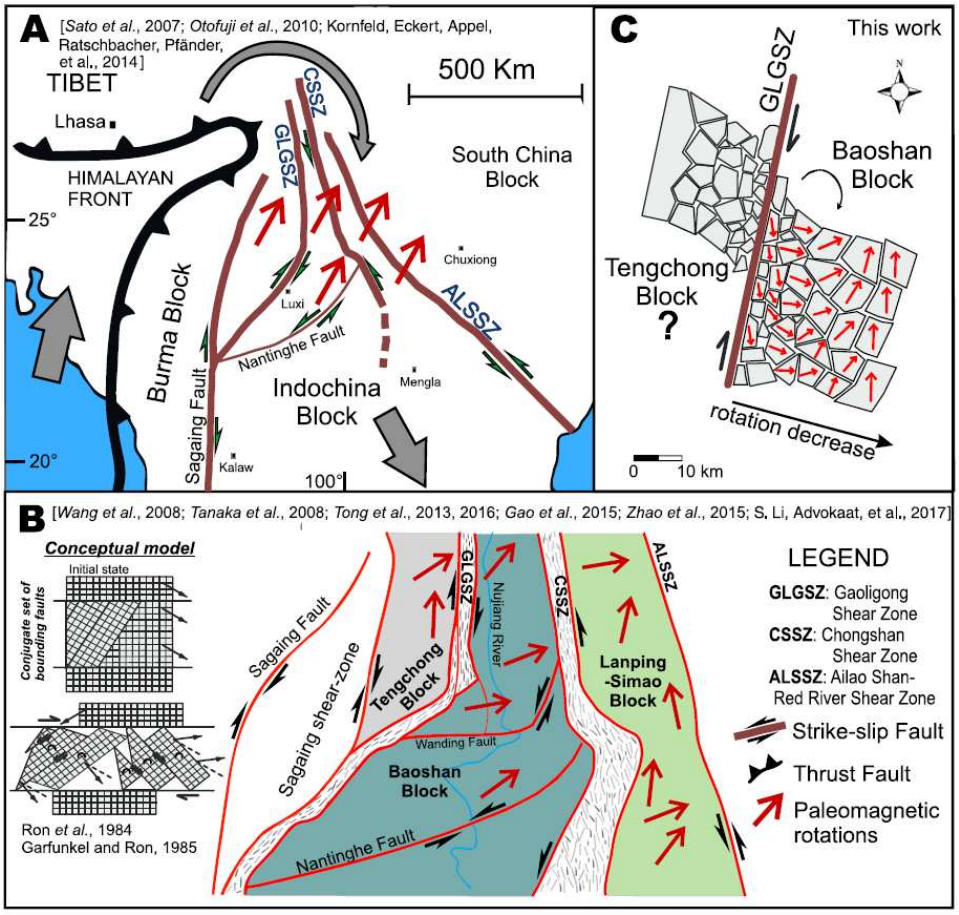

Figure 2.20: *Proposed extrusion mechanisms of Indochina (after Pellegrino et al., 2018).*

5.1. Eastern Andaman Basins

The Eastern Andaman Basins, including the Mergui and North Sumatra Basins, represent the rifted and sheared margin of Sundaland, underlain by extended continental crust, and developed in a back-

arc setting (Morley, 2017a). In this context, the main transtensional development phase of these basins occurred in the late Oligocene – early Miocene with NNW-SSE oriented extension, although basin formation initiated already in the late Eocene – early Oligocene with a WNW-ESE oriented direction of oblique extension. This age is based on unpublished strontium ages of ~32-34 Ma from carbonates on a basement high in the Mergui Basin (Srisuriyon & Morley, 2014). The change in the extensional direction could reflect the coupling of India with the BT and hence a switch from slab rollback-driven extension to India motion driving extension (Bertrand & Rangin, 2003; Morley, 2017a). In the late Miocene, extension became less focused in the Eastern Andaman Basins and was concentrated in the Alcock and Sewell rise areas as part of the Andaman spreading centre instead, although minor extensional reactivation occurred (Morley, 2017a).

5.2. Andaman spreading centre

The ENE-WSW oriented Andaman spreading centre or Central Andaman Basin separates two rises with rugged topography in shallow water depth named the Alcock and Sewell rises. The shallow water depths of these rises has been interpreted by either abnormally thick and buoyant oceanic crust due to magmatic underplating, island-arc crust, crustal fragments or extended continental crust (Morley, 2017a). Most earlier studies favoured the oceanic crust interpretation, formed by back-arc seafloor spreading and justified by the occurrence of early Miocene basalts (Curray, 2005; Raju et al., 2004). However, their rugged topography and crustal thickness of ~15 km thick from gravity modelling suggest that they are rather comprised of hyper-thinned continental crust (Morley & Alvey, 2015; Radhakrishna et al., 2008). In this interpretation, the basalts would represent synrift volcanic extrusions over older crust (Morley, 2017a). In any case, the Alcock-Sewell rises probably represent exotic terranes that accreted to Sundaland (Rangin, 2018).

As described in the previous section, extension became concentrated in the Central Andaman Basin since the late Miocene following prolonged transtension. The present-day pull-apart geometry of the Andaman Sea likely developed during this time. Furthermore, oceanic spreading likely initiated at this time as well (Curray et al., 1979; Morley & Alvey, 2015), although younger ages of oceanic spreading (~4-5 Ma) have also been proposed (Curray, 2005; Raju et al., 2004). This discrepancy is the result of sediment blanketing in large parts of the spreading centre such that only the marine magnetic anomaly data is only good in a narrow section of the Central Andaman Basin (Morley, 2017a). The geometry of these sediments, suggestive of a considerable period of deposition, was the main observation for Morley & Alvey (2015) to argue for an earlier onset of oceanic spreading in the Andaman Sea.

Figure 2.21: *Structural geological map showing the Burma and Andaman mobile belts in green, transitioning in the Sumatra trench (Rangin, 2018).*

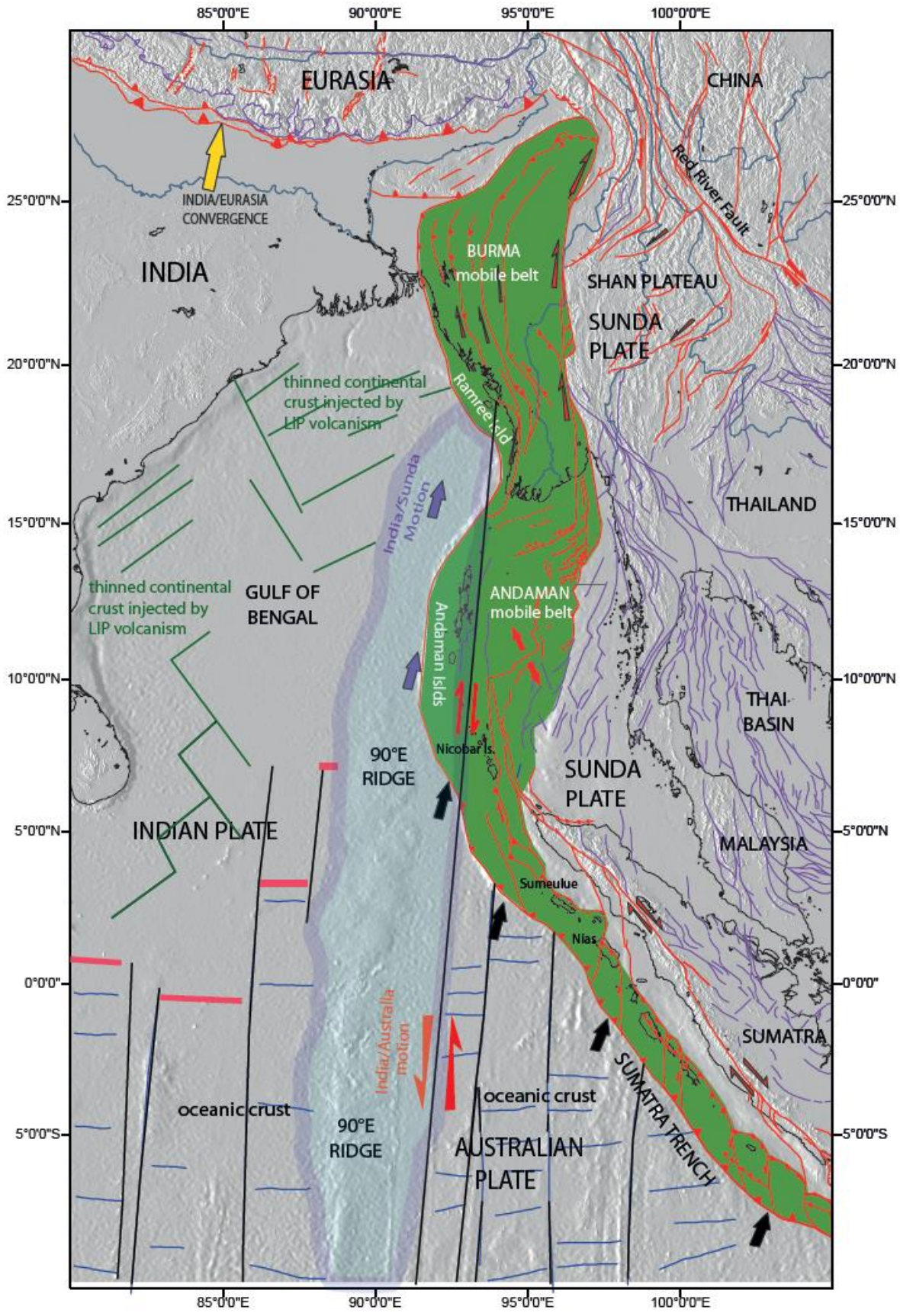

5.3. Andaman-Nicobar ridge

The geology of the western Andaman Sea is characterized by an accretionary prism and an ophiolitic belt found on the Andaman-Nicobar ridge, forming the northern continuation of the Sumatra active margin and separated from the Andaman spreading centre by the Oligocene dextral strike-slip West Andaman Fault (Curray, 2005; Morley, 2017a). Dextral wrenching also takes place along the Andaman trench as a result of oblique subduction (Rangin, 2018). The Andaman-Nicobar Ophiolites were likely developed in the latest Cretaceous to early Paleogene (Morley & Searle, 2017; Pedersen et al., 2010) in a supra-subduction spreading setting (Curray, 2005; Ghosh et al., 2017) and subsequently emplaced as imbricate slices in an accretionary prism before the Eocene (Morley & Searle, 2017) without interference of Indian continental crust, although obduction onto a buoyant (thinned continental) block may have triggered the emplacement. Similarities in timing and tectonic setting led many studies to identify the Andaman-Nicobar Ophiolites as the southern extend of the Western Belt Ophiolite in the IBR as part of a Neo-Tethyan suture (Ghosh et al., 2017; Morley & Searle, 2017; Pedersen et al., 2010; Sengupta et al., 1990), although paleomagnetic and sedimentary provenance data are required to confirm a similar origin for Andaman-Nicobar ridge as the BT. Moreover, the Andaman-Nicobar ridge and the western Andaman Sea as a whole are often considered as an exotic terrane accreted to Sundaland (Rangin, 2018). Sedimentary deposits in the accretionary prism of the western Andaman Sea were primarily sourced by the Andaman-Nicobar Ophiolites until ~30 Ma, afterwards a northward source, similar to the Bay of Bengal became prominent (Garzanti et al., 2013; Morley & Searle, 2017).

6. Sumatra

The Andaman spreading centre and the West Andaman Fault connect with the Sumatra Fault Zone to south, a dextral strike slip fault that parallels the Sumatra active margin (Curray, 2005; Morley, 2017a; Rangin, 2018). At this margin, active and oblique subduction of Australian oceanic lithosphere underneath Indonesia takes place since ~45 Ma, as India passed towards Asia and the Australian continent started to move northward (Hall, 2009, 2012; Royer & Sandwell, 1989). The Sumatra Fault Zone is the result of partitioning due to his oblique subduction. It transects West Sumatra and the Woyla Arc on the island of Sumatra (Fig. 2.22).

6.1. West Sumatra Block

West Sumatra is a tectonic block that constitutes a part of Sundaland or Cathaysia forming the core of SE Asia (Indochina) since the Triassic, similar to Sibumasu (Hall, 2012; Metcalfe, 2013). Of particular interest in West Sumatra for this study is the Medial Sumatra Tectonic Zone, a highly deformed dextral shear zone consisting of metamorphic rocks such as schists and gneisses (Barber et

al., 2005). The Medial Sumatra Tectonic Zone has been interpreted as a continuation of the MMMB, and consequentially the West Sumatra Block was correlated with the BT (West Burma Block), making both of them a dextrally transported continental sliver with Cathaysian affinity (Fig. 2.23; Barber & Crow, 2009; Metcalfe, 2013). These studies mainly based this correlation on the occurrence of Cathaysian fauna in a sample from Permian limestones near Karmine, northern BT (Oo et al., 2002). However, this correlation is tentative at best, as it is only one sample from a locality that is in close proximity to the strands of the Sagaing Fault (Oo et al., 2002), making it potentially allochthonous from the BT.

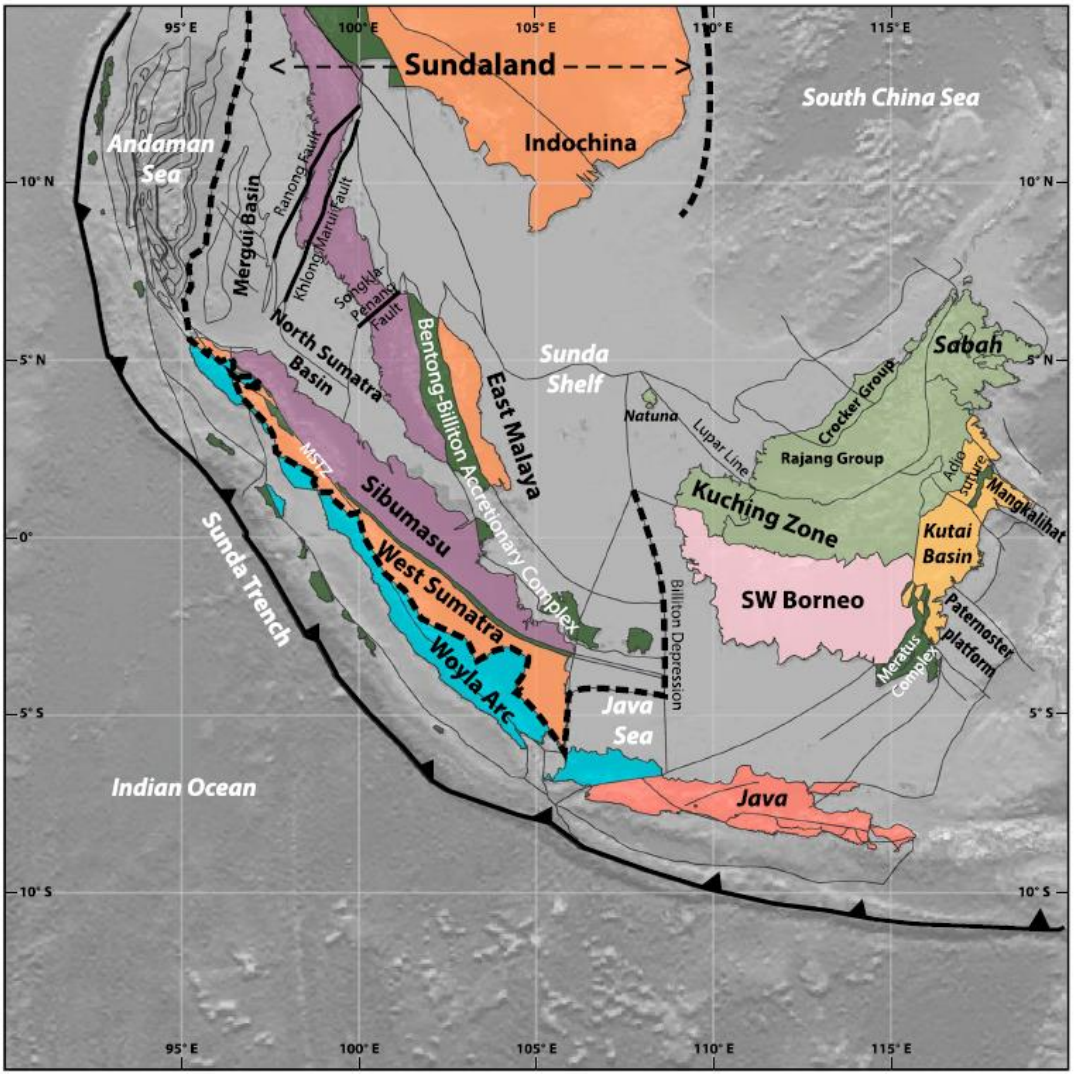

Figure 2.22: *General tectonic map of SE Asia. Abbreviations: MSTZ = Medial Sumatra Tectonic Zone (Advokaat et al., 2018).*

6.2. Woyla Arc

The Woyla Arc volcanic assemblage consists of basaltic to andesitic volcanics rocks. Sparse radiometric dates indicate that Woyla Arc volcanism supposedly took place from the Late Jurassic

until Late Cretaceous (Advokaat et al., 2018; Hall, 2012). Usually, the arc is interpreted to be an intra-oceanic island arc that was accreted to the southern margin of West Sumatra around ~90 Ma, evidenced by the cessation of magmatism on Sumatra around that time (Barber & Crow, 2009; Hall, 2009, 2012).Based on the occurrence of similar andesites in the Woyla Arc volcanic assemblage as the Mawgyi Andesites on the BT, Mitchell (1993) correlated both a single intra-oceanic arc that was thrusted on the margin of Sundaland in the Late Cretaceous. This intra-oceanic arc was named Incertus Arc (Barber & Crow, 2009; Hall, 2012), although it should be stressed that these later studies following the correlation of Mitchell (1993) erroneously did not include the Mawgyi Andesites in their postulated Mawgyi Nappe (See Section 3.3). A recent paleomagnetic study on the Woyla Arc reconstructed it as part of the Australian Plate since the Early Cretaceous (Advokaat et al., 2018). However, the paleomagnetic site means from this study show significant differences in rotation and degree of remagnetization with only few sites supporting the proposed tectonic model.

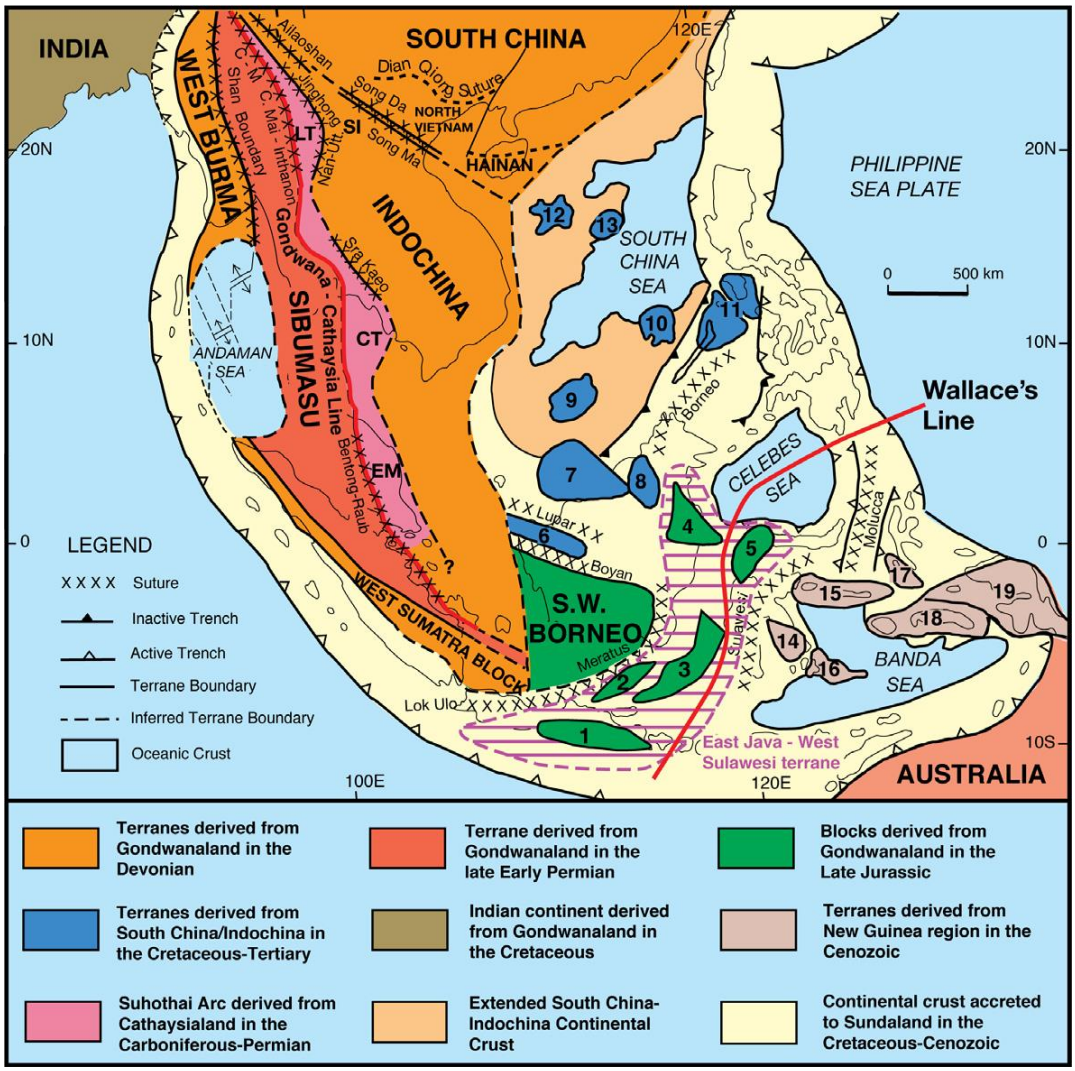

Figure 2.23: *Proposed Cathaysian tectonic correlation between the BT (West Burma) and the West Sumatra Block (Metcalfe, 2013).*

References Chapters 1 and 2

Abrajevitch, A. V., Ali, J. R., Aitchison, J. C., Davis, A. M., Liu, J., & Ziabrev, S. V. (2005). Neotethys and the India–Asia collision: insights from a palaeomagnetic study of the Dazhuqu ophiolite, southern Tibet. *Earth and Planetary Science Letters*, *233*(1–2), 87–102.

Acharyya, S. K. (2007). Collisional emplacement history of the Naga-Andaman ophiolites and the position of the eastern Indian suture. *Journal of Asian Earth Sciences*, *29*(2–3), 229–242.

Acharyya, S. K. (2015). Indo-Burma Range: a belt of accreted microcontinents, ophiolites and Mesozoic–Paleogene flyschoid sediments. *International Journal of Earth Sciences*, *104*(5), 1235–1251.

Advokaat, E. L., Bongers, M. L. M., Rudyawan, A., BouDagher-Fadel, M. K., Langereis, C. G., & van Hinsbergen, D. J. J. (2018). Early Cretaceous origin of the Woyla Arc (Sumatra, Indonesia) on the Australian plate. *Earth and Planetary Science Letters*, *498*, 348–361. https://doi.org/10.1016/j.epsl.2018.07.001

Aitchison, J. C., Ali, J. R., & Davis, A. M. (2007). When and where did India and Asia collide? *Journal of Geophysical Research*, *112*(B5). https://doi.org/10.1029/2006JB004706

Aitchison, J. C., Ao, A., Bhowmik, S., Clarke, G. L., Ireland, T. R., Kachovich, S., … Zhou, R. (2019). Tectonic Evolution of the Western Margin of the Burma Microplate Based on New Fossil and Radiometric Age Constraints. *Tectonics*, 2018TC005049. https://doi.org/10.1029/2018TC005049

Aitchison, J. C., McDermid, I. R. C., Ali, J. R., Davis, A. M., & Zyabrev, S. V. (2007). Shoshonites in southern Tibet record Late Jurassic rifting of a Tethyan intraoceanic island arc. *The Journal of Geology*, *115*(2), 197–213.

Aitchison, J. C., Xia, X., Baxter, A. T., & Ali, J. R. (2011). Detrital zircon U–Pb ages along the Yarlung-Tsangpo suture zone, Tibet: Implications for oblique convergence and collision between India and Asia. *Gondwana Research*, *20*(4), 691–709. https://doi.org/10.1016/j.gr.2011.04.002

Allegre, C. o, Courtillot, V., Tapponnier, P., Hirn, A., Mattauer, M., Coulon, C., … Marcoux, J. (1984). Structure and evolution of the Himalaya–Tibet orogenic belt. *Nature*, *307*(5946), 17.

Allen, R., Najman, Y., Carter, A., Barfod, D., Bickle, M. J., Chapman, H. J., … Parrish, R. R. (2008). Provenance of the Tertiary sedimentary rocks of the Indo-Burman Ranges, Burma (Myanmar): Burman arc or Himalayan-derived? *Journal of the Geological Society*, *165*(6), 1045–1057.

Avouac, J.-P. (2003). Mountain building, erosion, and the seismic cycle in the Nepal Himalaya. *Advances in Geophysics*, *46*, 1–80.

Bannert, D., Sang Lyen, A., & Htay, T. (2012). The geology of the Indoburman Ranges in Myanmar.

Barber, A. J., & Crow, M. J. (2009). Structure of Sumatra and its implications for the tectonic assembly of Southeast Asia and the destruction of Paleotethys. *Island Arc*, *18*(1), 3–20. https://doi.org/10.1111/j.1440-1738.2008.00631.x

Barber, A. J., Crow, M. J., & Milsom, J. (2005). *Sumatra: geology, resources and tectonic evolution*. (Geological Society of London, Ed.). London: The Geological Society.

Barley, M. E., & Zaw, K. (2009). SHRIMP U-Pb in zircon geochronology of granitoids from Myanmar: temporal constraints on the tectonic evolution of Southeast Asia. In *EGU General Assembly Conference Abstracts* (Vol. 11, p. 3842).

Bender, F. (1983). *Geology of Burma*. Berlin: Gebrüder Borntraeger.

Bertrand, G., & Rangin, C. (2003). Tectonics of the western margin of the Shan plateau (central Myanmar): implication for the India–Indochina oblique convergence since the Oligocene. *Journal of Asian Earth Sciences*, *21*(10), 1139–1157.

Bertrand, G., Rangin, C., Maluski, H., & Bellon, H. (2001). Diachronous cooling along the Mogok Metamorphic Belt (Shan scarp, Myanmar): the trace of the northward migration of the Indian syntaxis. *Journal of Asian Earth Sciences*, *19*(5), 649–659. https://doi.org/10.1016/S1367-9120(00)00061-4

Bilham, R., Larson, K., & Freymueller, J. (1997). GPS measurements of present-day convergence across the Nepal Himalaya. *Nature*, *386*(6620), 61.

Bouilhol, P., Jagoutz, O., Hanchar, J. M., & Dudas, F. O. (2013). Dating the India–Eurasia collision through arc magmatic records. *Earth and Planetary Science Letters*, *366*, 163–175. https://doi.org/10.1016/j.epsl.2013.01.023

Bouilhol, P., Schaltegger, U., Chiaradia, M., Ovtcharova, M., Stracke, A., Burg, J.-P., & Dawood, H. (2011). Timing of juvenile arc crust formation and evolution in the Sapat Complex (Kohistan–Pakistan). *Chemical Geology*, *280*(3–4), 243–256.

Brunnschweiler, R. O. (1966). On the geology of the Indoburman ranges: (Arakan Coast and Yoma, Chin Hills, Naga Hills). *Journal of the Geological Society of Australia*, *13*(1), 137–194.

Buckman, S., Aitchison, J. C., Nutman, A. P., Bennett, V. C., Saktura, W. M., Walsh, J. M., … Hidaka, H. (2018). The Spongtang Massif in Ladakh, NW Himalaya: an Early Cretaceous record of spontaneous, intra-oceanic subduction initiation in the Neotethys. *Gondwana Research*, *63*, 226–249.

Burtman, V. S., & Molnar, P. H. (1993). *Geological and geophysical evidence for deep subduction of continental crust beneath the Pamir* (Vol. 281). Geological Society of America.

Cai, F., Ding, L., Laskowski, A. K., Kapp, P., Wang, H., Xu, Q., & Zhang, L. (2016). Late Triassic paleogeographic reconstruction along the Neo–Tethyan Ocean margins, southern Tibet. *Earth and Planetary Science Letters*, *435*, 105–114. https://doi.org/10.1016/j.epsl.2015.12.027

Cawood, P. A., Johnson, M. R., & Nemchin, A. A. (2007). Early Palaeozoic orogenesis along the Indian margin of Gondwana: Tectonic response to Gondwana assembly. *Earth and Planetary Science Letters*, *255*(1–2), 70–84.

Chan, G. H. N., Aitchison, J. C., Crowley, Q. G., Horstwood, M. S., Searle, M. P., Parrish, R. R., & Chan, J. S.-L. (2015). U–Pb zircon ages for Yarlung Tsangpo suture zone ophiolites, southwestern Tibet and their tectonic implications. *Gondwana Research*, *27*(2), 719–732.

Chen, J., Wu, J., Xu, J., Dong, Y., Wang, B., & Kang, Z. (2013). Geochemistry of Eocene high-Mg# adakitic rocks in the northern Qiangtang terrane, central Tibet: Implications for early uplift of the plateau. *Bulletin*, *125*(11–12), 1800–1819.

Claude Rangin. (2017). Chapter 3 Active and recent tectonics of the Burma Platelet in Myanmar. *Geological Society, London, Memoirs*, *48*(1), 53–64. https://doi.org/10.1144/M48.3

Clift, P. D., Hodges, K. V., Heslop, D., Hannigan, R., Van Long, H., & Calves, G. (2008). Correlation of Himalayan exhumation rates and Asian monsoon intensity. *Nature Geoscience*, *1*(12), 875.

Cogne, J.-P., Besse, J., Chen, Y., & Hankard, F. (2013). A new Late Cretaceous to Present APWP for Asia and its implications for paleomagnetic shallow inclinations in Central Asia and Cenozoic Eurasian plate deformation. *Geophysical Journal International*, *192*(3), 1000–1024. https://doi.org/10.1093/gji/ggs104

Curray, J. R. (2005). Tectonics and history of the Andaman Sea region. *Journal of Asian Earth Sciences*, *25*(1), 187–232. https://doi.org/10.1016/j.jseaes.2004.09.001

Curray, J. R., Moore, D. G., Lawver, L. A., Emmel, F. J., Raitt, R. W., Henry, M., & Kieckhefer, R. (1979). Tectonics of the Andaman Sea and Burma: convergent margins.

DeCelles, P. G., Gehrels, G. E., Najman, Y., Martin, A. J., Carter, A., & Garzanti, E. (2004). Detrital geochronology and geochemistry of Cretaceous–Early Miocene strata of Nepal: implications for timing and diachroneity of initial Himalayan orogenesis. *Earth and Planetary Science Letters*, *227*(3–4), 313–330.

DeCelles, P. G., Gehrels, G. E., Quade, J., LaReau, B., & Spurlin, M. (2000). Tectonic implications of U-Pb zircon ages of the Himalayan orogenic belt in Nepal. *Science*, *288*(5465), 497–499.

DeCelles, P. G., Kapp, P., Ding, L., & Gehrels, G. E. (2007). Late Cretaceous to middle Tertiary basin evolution in the central Tibetan Plateau: Changing environments in response to tectonic

partitioning, aridification, and regional elevation gain. *Geological Society of America Bulletin*, *119*(5–6), 654–680.

DeCelles, P. G., Robinson, D. M., & Zandt, G. (2002). Implications of shortening in the Himalayan fold-thrust belt for uplift of the Tibetan Plateau. *Tectonics*, *21*(6), 12–1.

Ding, L., & Lai, Q. (2003). New geological evidence of crustal thickening in the Gangdese block prior to the Indo-Asian collision. *Chinese Science Bulletin*, *48*(15), 1604–1610.

Donaldson, D. G., Webb, A. A. G., Menold, C. A., Kylander-Clark, A. R., & Hacker, B. R. (2013). Petrochronology of Himalayan ultrahigh-pressure eclogite. *Geology*, *41*(8), 835–838.

Dupont-Nivet, G., Lippert, P. C., Van Hinsbergen, D. J. J., Meijers, M. J. M., & Kapp, P. (2010). Palaeolatitude and age of the Indo-Asia collision: palaeomagnetic constraints: Palaeolatitude and age of the Indo-Asia collision. *Geophysical Journal International*, *182*(3), 1189–1198. https://doi.org/10.1111/j.1365-246X.2010.04697.x

Dupont-Nivet, G., van Hinsbergen, D. J. J., & Torsvik, T. H. (2010). Persistently low Asian paleolatitudes: Implications for the India-Asia collision history: PERSISTENTLY LOW ASIAN PALEOLATITUDES. *Tectonics*, *29*(5), n/a-n/a. https://doi.org/10.1029/2008TC002437

Evans, D., Müller, W., Oron, S., & Renema, W. (2013). Eocene seasonality and seawater alkaline earth reconstruction using shallow-dwelling large benthic foraminifera. *Earth and Planetary Science Letters*, *381*, 104–115.

Fareeduddin, A., & Dilek, Y. (2015). Structure and petrology of the Nagaland-Manipur Hill ophiolitic mélange zone. *NE India: A Fossil Tethyan Subduction Channel at the India-Burma Plate Boundary: Episodes*, *38*, 298–314.

Gansser, A. (1964). Geology of the Himalayas.

Gansser, A. (1980). The significance of the Himalayan suture zone. *Tectonophysics*, *62*(1–2), 37–52.

Gao, L., Yang, Z., Tong, Y., Wang, H., & An, C. (2015). New paleomagnetic studies of Cretaceous and Miocene rocks from Jinggu, western Yunnan, China: Evidence for internal deformation of the Lanping–Simao Terrane. *Journal of Geodynamics*, *89*, 39–59. https://doi.org/10.1016/j.jog.2015.06.004

Gardiner, N. J., Hawkesworth, C. J., Robb, L. J., Whitehouse, M. J., Roberts, N. M. W., Kirkland, C. L., & Evans, N. J. (2017). Contrasting Granite Metallogeny through the Zircon Record: A Case Study from Myanmar. *Scientific Reports*, *7*(1). https://doi.org/10.1038/s41598-017-00832-2

Gardiner, N. J., Searle, M. P., Robb, L. J., & Morley, C. K. (2015). Neo-Tethyan magmatism and metallogeny in Myanmar – An Andean analogue? *Journal of Asian Earth Sciences*, *106*, 197–215. https://doi.org/10.1016/j.jseaes.2015.03.015

Garzanti, E. (2019). The Himalayan Foreland Basin from collision onset to the present: a sedimentary–petrology perspective. *Geological Society, London, Special Publications*, SP483.17. https://doi.org/10.1144/SP483.17

Garzanti, E., Baud, A., & Mascle, G. (1987). Sedimentary record of the northward flight of India and its collision with Eurasia (Ladakh Himalaya, India). *Geodinamica Acta*, *1*(4–5), 297–312.

Garzanti, E., & Hu, X. (2015). Latest Cretaceous Himalayan tectonics: Obduction, collision or Deccan-related uplift? *Gondwana Research*, *28*(1), 165–178.

Garzanti, E., Le Fort, P., & Sciunnach, D. (1999). First report of Lower Permian basalts in South Tibet: tholeiitic magmatism during break-up and incipient opening of Neotethys. *Journal of Asian Earth Sciences*, *17*(4), 533–546.

Garzanti, E., Limonta, M., Resentini, A., Bandopadhyay, P. C., Najman, Y., Andò, S., & Vezzoli, G. (2013). Sediment recycling at convergent plate margins (Indo-Burman Ranges and Andaman–Nicobar Ridge). *Earth-Science Reviews*, *123*, 113–132. https://doi.org/10.1016/j.earscirev.2013.04.008

Garzanti, E., & Sciunnach, D. (1997). Early Carboniferous onset of Gondwanian glaciation and Neo-tethyan rifting in South Tibet. *Earth and Planetary Science Letters*, *148*(1–2), 359–365.

Ghose, N. C., Chatterjee, N., & Fareeduddin. (2014). *A Petrographic Atlas of Ophiolite: An example from the eastern India-Asia collision zone*. New Delhi: Springer 234 pp.

Ghosh, B., Bandyopadhyay, D., & Morishita, T. (2017). Chapter 7 Andaman–Nicobar Ophiolites, India: origin, evolution and emplacement. *Geological Society, London, Memoirs*, *47*(1), 95–110. https://doi.org/10.1144/M47.7

Gibbons, A. D., Zahirovic, S., Müller, R. D., Whittaker, J. M., & Yatheesh, V. (2015). A tectonic model reconciling evidence for the collisions between India, Eurasia and intra-oceanic arcs of the central-eastern Tethys. *Gondwana Research*, *28*(2), 451–492. https://doi.org/10.1016/j.gr.2015.01.001

Godin, L., Grujic, D., Law, R. D., & Searle, M. P. (2006). Channel flow, ductile extrusion and exhumation in continental collision zones: an introduction. *Geological Society, London, Special Publications*, *268*(1), 1–23.

Grimaldi, D. A., Engel, M. S., & Nascimbene, P. C. (2002). Fossiliferous Cretaceous Amber from Myanmar (Burma): Its Rediscovery, Biotic Diversity, and Paleontological Significance. *American Museum Novitates*, *3361*, 1–71. https://doi.org/10.1206/0003-0082(2002)361<0001:FCAFMB>2.0.CO;2

Guillot, S., Mahéo, G., De Sigoyer, J., Hattori, K. H., & Pecher, A. (2008). Tethyan and Indian subduction viewed from the Himalayan high-to ultrahigh-pressure metamorphic rocks. *Tectonophysics*, *451*(1–4), 225–241.

Guo, Z. T., Ruddiman, W. F., Hao, Q. Z., Wu, H. B., Qiao, Y. S., Zhu, R. X., … Liu, T. S. (2002). Onset of Asian desertification by 22 Myr ago inferred from loess deposits in China. *Nature*, *416*(6877), 159.

Hall, R. (2009). Hydrocarbon basins in SE Asia: understanding why they are there. *Petroleum Geoscience*, *15*(2), 131–146.

Hall, R. (2012). Late Jurassic–Cenozoic reconstructions of the Indonesian region and the Indian Ocean. *Tectonophysics*, *570–571*, 1–41. https://doi.org/10.1016/j.tecto.2012.04.021

Hall, R., & Spakman, W. (2015). Mantle structure and tectonic history of SE Asia. *Tectonophysics*, *658*, 14–45.

Haproff, P. J., Odlum, M. L., Zuza, A. V., Yin, A., & Stockli, D. F. (2020). Structural and Thermochronologic Constraints on the Cenozoic Tectonic Development of the Northern Indo-Burma Ranges. *Tectonics*. https://doi.org/10.1029/2020TC006231

Haproff, P. J., Zuza, A. V., & Yin, A. (2018). West-directed thrusting south of the eastern Himalayan syntaxis indicates clockwise crustal flow at the indenter corner during the India-Asia collision. *Tectonophysics*, *722*, 277–285.

Haproff, P. J., Zuza, A. V., Yin, A., Harrison, T. M., Manning, C. E., Dubey, C. S., … Chen, J. (2019). Geologic framework of the northern Indo-Burma Ranges and lateral correlation of Himalayan-Tibetan lithologic units across the eastern Himalayan syntaxis. *Geosphere*. https://doi.org/10.1130/GES02054.1

Hébert, R., Bezard, R., Guilmette, C., Dostal, J., Wang, C. S., & Liu, Z. F. (2012). The Indus–Yarlung Zangbo ophiolites from Nanga Parbat to Namche Barwa syntaxes, southern Tibet: First synthesis of petrology, geochemistry, and geochronology with incidences on geodynamic reconstructions of Neo-Tethys. *Gondwana Research*, *22*(2), 377–397.

Heuberger, S., Schaltegger, U., Burg, J.-P., Villa, I. M., Frank, M., Dawood, H., … Zanchi, A. (2007). Age and isotopic constraints on magmatism along the Karakoram-Kohistan Suture Zone, NW Pakistan: Evidence for subduction and continued convergence after India-Asia collision. *Swiss Journal of Geosciences*, *100*(1), 85–107.

Hla Htay, Khin Zaw, & Than Than Oo. (2017). Chapter 6 The mafic–ultramafic (ophiolitic) rocks of Myanmar. *Geological Society, London, Memoirs*, *48*(1), 117–141. https://doi.org/10.1144/M48.6

Hodges, K. V. (2000). Tectonics of the Himalaya and southern Tibet from two perspectives. *Geological Society of America Bulletin*, *112*(3), 324–350.

Hodges, K. V., Parrish, R. R., Housh, T. B., Lux, D. R., Burchfiel, B. C., Royden, L. H., & Chen, Z. (1992). Simultaneous Miocene extension and shortening in the Himalayan orogen. *Science*, *258*(5087), 1466–1470.

Hu, X., Garzanti, E., Moore, T., & Raffi, I. (2015). Direct stratigraphic dating of India-Asia collision onset at the Selandian (middle Paleocene, 59$\pm$1 Ma). *Geology*, *43*(10), 859–862.

Hu, X., Garzanti, E., Wang, J., Huang, W., An, W., & Webb, A. (2016). The timing of India-Asia collision onset–Facts, theories, controversies. *Earth-Science Reviews*, *160*, 264–299.

Huang, W., Lippert, P. C., Jackson, M. J., Dekkers, M. J., Zhang, Y., Li, J., … van Hinsbergen, D. J. J. (2017). Remagnetization of the Paleogene Tibetan Himalayan carbonate rocks in the Gamba area: Implications for reconstructing the lower plate in the India-Asia collision: Carbonates Were Remagnetized in Gamba. *Journal of Geophysical Research: Solid Earth*, *122*(2), 808–825. https://doi.org/10.1002/2016JB013662

Huang, W., Lippert, P. C., Zhang, Y., Jackson, M. J., Dekkers, M. J., Li, J., … van Hinsbergen, D. J. J. (2017). Remagnetization of carbonate rocks in southern Tibet: Perspectives from rock magnetic and petrographic investigations: Carbonates in Himalayas Are Remagnetized. *Journal of Geophysical Research: Solid Earth*, *122*(4), 2434–2456. https://doi.org/10.1002/2017JB013987

Huang, W., Van Hinsbergen, D. J., Maffione, M., Orme, D. A., Dupont-Nivet, G., Guilmette, C., … Kapp, P. (2015). Lower Cretaceous Xigaze ophiolites formed in the Gangdese forearc: Evidence from paleomagnetism, sediment provenance, and stratigraphy. *Earth and Planetary Science Letters*, *415*, 142–153.

Huber, M., & Goldner, A. (2012). Eocene monsoons. *Journal of Asian Earth Sciences*, *44*, 3–23.

l'Anson, A., Elders, C., & McHarg, S. (2019). Marginal fault systems of the Northern Carnarvon Basin: Evidence for multiple Palaeozoic extension events, North-West Shelf, Australia. *Marine and Petroleum Geology*, *101*, 211–229. https://doi.org/10.1016/j.marpetgeo.2018.11.040

Ingalls, M., Rowley, D. B., Currie, B., & Colman, A. S. (2016). Large-scale subduction of continental crust implied by India–Asia mass-balance calculation. *Nature Geoscience*, *9*(11), 848–853. https://doi.org/10.1038/ngeo2806

Jadoul, F., Berra, F., & Garzanti, E. (1998). The Tethys Himalayan passive margin from Late Triassic to Early Cretaceous (South Tibet). *Journal of Asian Earth Sciences*, *16*(2–3), 173–194.

Jaeger, J.-J., Thein, T., Benammi, M., Chaimanee, Y., Soe, A. N., Lwin, T., … Ducrocq, S. (1999). A new primate from the middle Eocene of Myanmar and the Asian early origin of anthropoids. *Science*, *286*(5439), 528–530.

Jagoutz, O., Royden, L., Holt, A. F., & Becker, T. W. (2015). Anomalously fast convergence of India and Eurasia caused by double subduction. *Nature Geoscience*, *8*(6), 475–478. https://doi.org/10.1038/ngeo2418

Jagoutz, O., & Schmidt, M. W. (2012). The formation and bulk composition of modern juvenile continental crust: The Kohistan arc. *Chemical Geology*, *298*, 79–96.

Jouanne, F., Mugnier, J.-L., Gamond, J. F., Le Fort, P., Pandey, M. R., Bollinger, L., … Avouac, J. P. (2004). Current shortening across the Himalayas of Nepal. *Geophysical Journal International*, *157*(1), 1–14.

Kapp, P., & DeCelles, P. G. (2019). Mesozoic–Cenozoic geological evolution of the Himalayan-Tibetan orogen and working tectonic hypotheses. *American Journal of Science*, *319*(3), 159–254.

Kapp, P., DeCelles, P. G., Gehrels, G. E., Heizler, M., & Ding, L. (2007). Geological records of the Lhasa-Qiangtang and Indo-Asian collisions in the Nima area of central Tibet. *Geological Society of America Bulletin*, *119*(7–8), 917–933.

Kapp, P., DeCelles, P. G., Leier, A. L., Fabijanic, J. M., He, S., Pullen, A., … Ding, L. (2007). The Gangdese retroarc thrust belt revealed. *GSA Today*, *17*(7), 4.

Kellett, D. A., Grujic, D., Coutand, I., Cottle, J., & Mukul, M. (2013). The South Tibetan detachment system facilitates ultra rapid cooling of granulite-facies rocks in Sikkim Himalaya. *Tectonics*, *32*(2), 252–270.

Khin, K. (1999). Marine transgression and regression in Miocene sequences of northern Pegu (Bago) Yoma, central Myanmar. *Journal of Asian Earth Sciences*, *17*(3), 369–393.

Khin Zaw, Meffre, S., Takai, M., Suzuki, H., Burrett, C., Thaung Htike, … Maung Maung. (2014). The oldest anthropoid primates in SE Asia: Evidence from LA-ICP-MS U–Pb zircon age in the Late Middle Eocene Pondaung Formation, Myanmar. *Gondwana Research*, *26*(1), 122–131. https://doi.org/10.1016/j.gr.2013.04.007

Kornfeld, D., Eckert, S., Appel, E., Ratschbacher, L., Sonntag, B.-L., Pfänder, J. A., … Liu, D. (2014). Cenozoic clockwise rotation of the Tengchong block, southeastern Tibetan Plateau: A paleomagnetic and geochronologic study. *Tectonophysics*, *628*, 105–122. https://doi.org/10.1016/j.tecto.2014.04.032

Lee, H.-Y., Chung, S.-L., & Yang, H.-M. (2016). Late Cenozoic volcanism in central Myanmar: Geochemical characteristics and geodynamic significance. *Lithos*, *245*, 174–190. https://doi.org/10.1016/j.lithos.2015.09.018

Lee, J., & Whitehouse, M. J. (2007). Onset of mid-crustal extensional flow in southern Tibet: Evidence from U/Pb zircon ages. *Geology*, *35*(1), 45–48.

Leech, M. L., Singh, S., Jain, A. K., Klemperer, S. L., & Manickavasagam, R. M. (2005). The onset of India–Asia continental collision: early, steep subduction required by the timing of UHP metamorphism in the western Himalaya. *Earth and Planetary Science Letters*, *234*(1–2), 83–97.

Leier, A. L., DeCelles, P. G., Kapp, P., & Gehrels, G. E. (2007). Lower Cretaceous strata in the Lhasa Terrane, Tibet, with implications for understanding the early tectonic history of the Tibetan Plateau. *Journal of Sedimentary Research*, *77*(10), 809–825.

Li, S., Advokaat, E. L., van Hinsbergen, D. J. J., Koymans, M., Deng, C., & Zhu, R. (2017). Paleomagnetic constraints on the Mesozoic-Cenozoic paleolatitudinal and rotational history of Indochina and South China: Review and updated kinematic reconstruction. *Earth-Science Reviews*, *171*, 58–77. https://doi.org/10.1016/j.earscirev.2017.05.007

Li, S., van Hinsbergen, D. J. J., Deng, C., Advokaat, E. L., & Zhu, R. (2018). Paleomagnetic Constraints From the Baoshan Area on the Deformation of the Qiangtang-Sibumasu Terrane Around the Eastern Himalayan Syntaxis. *Journal of Geophysical Research: Solid Earth*. https://doi.org/10.1002/2017JB015112

Li, Z., Ding, L., Lippert, P. C., Song, P., Yue, Y., & van Hinsbergen, D. J. J. (2016). Paleomagnetic constraints on the Mesozoic drift of the Lhasa terrane (Tibet) from Gondwana to Eurasia. *Geology*, *44*(9), 727–730. https://doi.org/10.1130/G38030.1

Licht, A., Boura, A., De Franceschi, D., Ducrocq, S., Aung Naing Soe, & Jaeger, J.-J. (2014). Fossil woods from the late middle Eocene Pondaung Formation, Myanmar. *Review of Palaeobotany and Palynology*, *202*, 29–46. https://doi.org/10.1016/j.revpalbo.2013.12.002

Licht, A., Boura, A., De Franceschi, D., Utescher, T., Sein, C., & Jaeger, J.-J. (2015). Late middle Eocene fossil wood of Myanmar: Implications for the landscape and the climate of the Eocene Bengal Bay. *Review of Palaeobotany and Palynology*, *216*, 44–54. https://doi.org/10.1016/j.revpalbo.2015.01.010

Licht, A., Dupont-Nivet, G., Win, Z., Swe, H. H., Kaythi, M., Roperch, P., … Sein, K. (2019). Paleogene evolution of the Burmese forearc basin and implications for the history of India-Asia convergence. *Geological Society of America Bulletin*, *1*(130), 20.

Licht, A., France-Lanord, C., Reisberg, L., Fontaine, C., Soe, A. N., & Jaeger, J.-J. (2013). A palaeo Tibet–Myanmar connection? Reconstructing the Late Eocene drainage system of central Myanmar using a multi-proxy approach. *Journal of the Geological Society*, *170*(6), 929–939.

Licht, A., van Cappelle, M., Abels, H. A., Ladant, J.-B., Trabucho-Alexandre, J., France-Lanord, C., … Jaeger, J.-J. (2014). Asian monsoons in a late Eocene greenhouse world. *Nature*, *513*(7519), 501–506. https://doi.org/10.1038/nature13704

Licht, A., Win, Z., Westerweel, J., Cogné, N., Morley, C., Chantraprasert, S., … Dupont-Nivet, G. (2020). Magmatic history of central Myanmar and implications for the evolution of the Burma Terrane. *Gondwana Research*. https://doi.org/10.1016/j.gr.2020.06.016

Lin, T.-H., Mitchell, A. H. G., Chung, S.-L., Tan, X.-B., Tang, J.-T., Oo, T., & Wu, F.-Y. (2019). Two parallel magmatic belts with contrasting isotopic characteristics from southern Tibet to Myanmar: zircon U–Pb and Hf isotopic constraints. *Journal of the Geological Society*, *176*(3), 574–587. https://doi.org/10.1144/jgs2018-072

Lippert, P. C., Van Hinsbergen, D. J., & Dupont-Nivet, G. (2014). Early Cretaceous to present latitude of the central proto-Tibetan Plateau: A paleomagnetic synthesis with implications for Cenozoic tectonics, paleogeography, and climate of Asia. *Geological Society of America Special Papers*, *507*, 1–21.

Liu, C.-Z., Chung, S.-L., Wu, F.-Y., Zhang, C., Xu, Y., Wang, J.-G., … Guo, S. (2016). Tethyan suturing in Southeast Asia: Zircon U-Pb and Hf-O isotopic constraints from Myanmar ophiolites. *Geology*, *44*(4), 311–314. https://doi.org/10.1130/G37342.1

Long, S., McQuarrie, N., Tobgay, T., Rose, C., Gehrels, G., & Grujic, D. (2011). Tectonostratigraphy of the Lesser Himalaya of Bhutan: Implications for the along-strike stratigraphic continuity of the northern Indian margin. *Bulletin*, *123*(7–8), 1406–1426.

Ma, Y., Yang, T., Bian, W., Jin, J., Zhang, S., Wu, H., & Li, H. (2016). Early Cretaceous paleomagnetic and geochronologic results from the Tethyan Himalaya: Insights into the Neotethyan paleogeography and the India–Asia collision. *Scientific Reports*, *6*, 21605.

Maffione, M., van Hinsbergen, D. J. J., Koornneef, L. M. T., Guilmette, C., Hodges, K., Borneman, N., … Kapp, P. (2015). Forearc hyperextension dismembered the south Tibetan ophiolites. *Geology*, *43*(6), 475–478. https://doi.org/10.1130/G36472.1

Martin, A. J. (2017). A review of Himalayan stratigraphy, magmatism, and structure. *Gondwana Research*, *49*, 42–80.

Martin, C. R., Jagoutz, O., Upadhyay, R., Royden, L. H., Eddy, M. P., Bailey, E., … Weiss, B. P. (2020). Paleocene latitude of the Kohistan–Ladakh arc indicates multistage India–Eurasia collision. *Proceedings of the National Academy of Sciences*, 202009039. https://doi.org/10.1073/pnas.2009039117

Matthews, K. J., Maloney, K. T., Zahirovic, S., Williams, S. E., Seton, M., & Müller, R. D. (2016). Global plate boundary evolution and kinematics since the late Paleozoic. *Global and Planetary Change*, *146*, 226–250. https://doi.org/10.1016/j.gloplacha.2016.10.002

Maung, H. (1987). Transcurrent movements in the Burma–Andaman Sea region. *Geology*, *15*(10), 911. https://doi.org/10.1130/0091-7613(1987)15<911:TMITBS>2.0.CO;2

Maurin, T., & Rangin, C. (2009). Structure and kinematics of the Indo-Burmese Wedge: Recent and fast growth of the outer wedge: GROWTH OF THE OUTER INDO-BURMESE WEDGE. *Tectonics*, *28*(2), n/a-n/a. https://doi.org/10.1029/2008TC002276

McKenzie, N. R., Hughes, N. C., Myrow, P. M., Xiao, S., & Sharma, M. (2011). Correlation of Precambrian–Cambrian sedimentary successions across northern India and the utility of isotopic signatures of Himalayan lithotectonic zones. *Earth and Planetary Science Letters*, *312*(3–4), 471–483.

McQuarrie, N., Long, S. P., Tobgay, T., Nesbit, J. N., Gehrels, G., & Ducea, M. N. (2013). Documenting basin scale, geometry and provenance through detrital geochemical data: Lessons from the Neoproterozoic to Ordovician Lesser, Greater, and Tethyan Himalayan strata of Bhutan. *Gondwana Research*, *23*(4), 1491–1510.

Meng, J., Gilder, S. A., Li, Y., Wang, C., & Liu, T. (2020). Expanse of Greater India in the late Cretaceous. *Earth and Planetary Science Letters*, *542*, 116330. https://doi.org/10.1016/j.epsl.2020.116330

Meng, Z., Wang, J., Ji, W., Zhang, H., Wu, F., & Garzanti, E. (2019). The Langjiexue Group is an in situ sedimentary sequence rather than an exotic block: Constraints from coeval Upper Triassic strata of the Tethys Himalaya (Qulonggongba Formation). *Science China Earth Sciences*, *62*(5), 783–797. https://doi.org/10.1007/s11430-018-9314-9

Metcalfe, I. (2013). Gondwana dispersion and Asian accretion: Tectonic and palaeogeographic evolution of eastern Tethys. *Journal of Asian Earth Sciences*, *66*, 1–33. https://doi.org/10.1016/j.jseaes.2012.12.020

Mitchell, A. (2017). *Geological Belts, Plate Boundaries, and Mineral Deposits in Myanmar*. Elsevier.

Mitchell, A., Chung, S.-L., Oo, T., Lin, T.-H., & Hung, C.-H. (2012). Zircon U–Pb ages in Myanmar: Magmatic–metamorphic events and the closure of a neo-Tethys ocean? *Journal of Asian Earth Sciences*, *56*, 1–23. https://doi.org/10.1016/j.jseaes.2012.04.019

Mitchell, A. H. G. (1993). Cretaceous–Cenozoic tectonic events in the western Myanmar (Burma)–Assam region. *Journal of the Geological Society*, *150*(6), 1089–1102.

Molnar, P., & Tapponnier, P. (1975). Cenozoic tectonics of Asia: effects of a continental collision. *Science*, *189*(4201), 419–426.

Morley, C. K. (2002). A tectonic model for the Tertiary evolution of strike–slip faults and rift basins in SE Asia. *Tectonophysics*, *347*(4), 189–215.

Morley, C. K. (2004). Nested strike-slip duplexes, and other evidence for Late Cretaceous–Palaeogene transpressional tectonics before and during India–Eurasia collision, in Thailand, Myanmar and Malaysia. *Journal of the Geological Society*, *161*(5), 799–812.

Morley, C. K. (2009). Evolution from an oblique subduction back-arc mobile belt to a highly oblique collisional margin: the Cenozoic tectonic development of Thailand and eastern Myanmar. *Geological Society, London, Special Publications*, *318*(1), 373–403. https://doi.org/10.1144/SP318.14

Morley, C. K. (2017a). Chapter 4 Cenozoic rifting, passive margin development and strike-slip faulting in the Andaman Sea: a discussion of established v. new tectonic models. *Geological Society, London, Memoirs*, *47*(1), 27–50. https://doi.org/10.1144/M47.4

Morley, C. K. (2017b). Syn-kinematic sedimentation at a releasing splay in the northern Minwun Ranges, Sagaing Fault zone, Myanmar: significance for fault timing and displacement. *Basin Research*, *29*, 684–700. https://doi.org/10.1111/bre.12201

Morley, C. K., & Alvey, A. (2015). Is spreading prolonged, episodic or incipient in the Andaman Sea? Evidence from deepwater sedimentation. *Journal of Asian Earth Sciences*, *98*, 446–456. https://doi.org/10.1016/j.jseaes.2014.11.033

Morley, C. K., & Arboit, F. (2019). Dating the onset of motion on the Sagaing fault: Evidence fromdetrital zircon and titanite U-Pb geochronology from the NorthMinwun Basin, Myanmar. *Geology*. https://doi.org/10.1130/G46321.1

Morley, C. K., Naing, T. T., Searle, M., & Robinson, S. A. (2019). Structural and tectonic development of the Indo-Burma Ranges. *Earth-Science Reviews*, 102992. https://doi.org/10.1016/j.earscirev.2019.102992

Morley, C. K., & Searle, M. (2017). Chapter 5 Regional tectonics, structure and evolution of the Andaman–Nicobar Islands from ophiolite formation and obduction to collision and back-arc spreading. *Geological Society, London, Memoirs*, *47*(1), 51–74. https://doi.org/10.1144/M47.5

Morley, C. K., Tin Tin Naing, Searle, M., & Robinson, S. A. (2020). Structural and tectonic development of the Indo-Burma ranges. *Earth-Science Reviews*, *200*, 102992. https://doi.org/10.1016/j.earscirev.2019.102992

Müller, R. D., Cannon, J., Qin, X., Watson, R. J., Gurnis, M., Williams, S., … Zahirovic, S. (2018). GPlates: Building a virtual Earth through deep time. *Geochemistry, Geophysics, Geosystems*, *19*(7), 2243–2261.

Myint, T. S. (2019). Paleontological Evidences from the Chunsung Formation Exposed in Northern Chin Hill, Myanmar, 12.

Myrow, P. M., Hughes, N. C., Paulsen, T. S., Williams, I. S., Parcha, S. K., Thompson, K. R., … Ahluwalia, A. D. (2003). Integrated tectonostratigraphic analysis of the Himalaya and implications for its tectonic reconstruction. *Earth and Planetary Science Letters*, *212*(3–4), 433–441.

Najman, Y., Appel, E., Boudagher-Fadel, M., Bown, P., Carter, A., Garzanti, E., … Oliver, G. (2010). Timing of India-Asia collision: Geological, biostratigraphic, and palaeomagnetic constraints. *Journal of Geophysical Research: Solid Earth*, *115*(B12).

Najman, Y., Bickle, M., Garzanti, E., Pringle, M., Barfod, D., Brozovic, N., … Ando, S. (2009). Reconstructing the exhumation history of the Lesser Himalaya, NW India, from a multitechnique provenance study of the foreland basin Siwalik Group. *Tectonics*, *28*(5).

Najman, Y., Carter, A., Oliver, G., & Garzanti, E. (2005). Provenance of Eocene foreland basin sediments, Nepal: Constraints to the timing and diachroneity of early Himalayan orogenesis. *Geology*, *33*(4), 309–312.

Najman, Y., Mark, C., Barfod, D. N., Carter, A., Parrish, R., Chew, D., & Gemignani, L. (2019). Spatial and temporal trends in exhumation of the Eastern Himalaya and syntaxis as determined from a multitechnique detrital thermochronological study of the Bengal Fan. *GSA Bulletin*, *131*(9–10), 1607–1622. https://doi.org/10.1130/B35031.1

Najman, Y., Sobel, E. R., Millar, I., Stockli, D. F., Govin, G., Garzanti, E., … Szymanski, E. (2018). The exhumation of the Indo-Burman Ranges, Myanmar. In *AGU Fall Meeting Abstracts*.

Nielsen, C., Chamot-Rooke, N., & Rangin, C. (2004). From partial to full strain partitioning along the Indo-Burmese hyper-oblique subduction. *Marine Geology*, *209*(1–4), 303–327.

Oo, T., Hlaing, T., & Htay, N. (2002). Permian of Myanmar. *Journal of Asian Earth Sciences*, *20*(6), 683–689. https://doi.org/10.1016/S1367-9120(01)00074-8

Orme, D. A., Carrapa, B., & Kapp, P. (2015). Sedimentology, provenance and geochronology of the upper Cretaceous–lower Eocene western Xigaze forearc basin, southernTibet. *Basin Research*, *27*(4), 387–411.

Otofuji, Y., Yokoyama, M., Kitada, K., & Zaman, H. (2010). Paleomagnetic versus GPS determined tectonic rotation around eastern Himalayan syntaxis in East Asia. *Journal of Asian Earth Sciences*, *37*(5–6), 438–451. https://doi.org/10.1016/j.jseaes.2009.11.003

Pagani, M., Zachos, J. C., Freeman, K. H., Tipple, B., & Bohaty, S. (2005). Marked decline in atmospheric carbon dioxide concentrations during the Paleogene. *Science*, *309*(5734), 600–603.

Parrish, R. R., & Hodges, V. (1996). Isotopic constraints on the age and provenance of the Lesser and Greater Himalayan sequences, Nepalese Himalaya. *Geological Society of America Bulletin*, *108*(7), 904–911.

Patzelt, A., Li, H., Wang, J., & Appel, E. (1996). Palaeomagnetism of Cretaceous to Tertiary sediments from southern Tibet: evidence for the extent of the northern margin of India prior to the collision with Eurasia. *Tectonophysics*, *259*(4), 259–284.

Pedersen, R. B., Searle, M. P., Carter, A., & Bandopadhyay, P. C. (2010). U–Pb zircon age of the Andaman ophiolite: implications for the beginning of subduction beneath the Andaman–Sumatra arc. *Journal of the Geological Society*, *167*(6), 1105–1112.

Pellegrino, A. G., Zhang, B., Speranza, F., Maniscalco, R., Yin, C., Hernandez-Moreno, C., & Winkler, A. (2018). Tectonics and Paleomagnetic Rotation Pattern of Yunnan (24°N-25°N, China): Gaoligong Fault Shear Versus Megablock Drift. *Tectonics*, *37*(5), 1524–1551. https://doi.org/10.1029/2017TC004899

Petterson, M. G. (2010). A Review of the geology and tectonics of the Kohistan island arc, north Pakistan. *Geological Society, London, Special Publications*, *338*(1), 287–327. https://doi.org/10.1144/SP338.14

Petterson, M. G. (2019). The plutonic crust of Kohistan and volcanic crust of Kohistan–Ladakh, north Pakistan/India: lessons learned for deep and shallow arc processes. *Geological Society, London, Special Publications*, *483*(1), 123–164. https://doi.org/10.1144/SP483.4

Pivnik, D. A., Nahm, J., Tucker, R. S., Smith, G. O., Nyein, K., Nyunt, M., & Maung, P. H. (1998). Polyphase Deformation in a Fore-Arc/Back-Arc Basin, Salin Subbasin, Myanmar (Burma). *AAPG Bulletin*, *82(10)*, 1837–1856.

Poinar, G. (2018). Burmese amber: evidence of Gondwanan origin and Cretaceous dispersion. *Historical Biology*, 1–6. https://doi.org/10.1080/08912963.2018.1446531

Pozzi, J. P., Westphal, M., Girardeau, J., Besse, J., Zhou, Y. X., Chen, X. Y., & Xing, L. S. (1984). Paleomagnetism of the Xigaze ophiolite and flysch (Yarlung Zangbo suture zone, southern Tibet): latitude and direction of spreading. *Earth and Planetary Science Letters*, *70*(2), 383–394.

Prell, W. L., & Kutzbach, J. E. (1992). Sensitivity of the Indian monsoon to forcing parameters and implications for its evolution. *Nature*, *360*(6405), 647.

Pullen, A., Kapp, P., DeCelles, P. G., Gehrels, G. E., & Ding, L. (2011). Cenozoic anatexis and exhumation of Tethyan sequence rocks in the Xiao Gurla Range, southwest Tibet. *Tectonophysics*, *501*(1–4), 28–40.

Pullen, A., Kapp, P., Gehrels, G. E., DeCelles, P. G., Brown, E. H., Fabijanic, J. M., & Ding, L. (2008). Gangdese retroarc thrust belt and foreland basin deposits in the Damxung area, southern Tibet. *Journal of Asian Earth Sciences*, *33*(5–6), 323–336.

Quan, C., Liu, Y.-S. C., & Utescher, T. (2012). Eocene monsoon prevalence over China: a paleobotanical perspective. *Palaeogeography, Palaeoclimatology, Palaeoecology*, *365*, 302–311.

Radhakrishna, M., Lasitha, S., & Mukhopadhyay, M. (2008). Seismicity, gravity anomalies and lithospheric structure of the Andaman arc, NE Indian Ocean. *Tectonophysics*, *460*(1–4), 248–262.

Raju, K. K., Ramprasad, T., Rao, P. S., Rao, B. R., & Varghese, J. (2004). New insights into the tectonic evolution of the Andaman basin, northeast Indian Ocean. *Earth and Planetary Science Letters*, *221*(1–4), 145–162.

Rangin, C. (2018). *The western Sunda basins and the India/Asia collision: an atlas.* Geotecto, Paris, France.

Rangin, C., Maurin, T., & Masson, F. (2013). Combined effects of Eurasia/Sunda oblique convergence and East-Tibetan crustal flow on the active tectonics of Burma. *Journal of Asian Earth Sciences*, *76*, 185–194. https://doi.org/10.1016/j.jseaes.2013.05.018

Replumaz, A., Guillot, S., Villaseñor, A., & Negredo, A. M. (2013). Amount of Asian lithospheric mantle subducted during the India/Asia collision. *Gondwana Research*, *24*(3–4), 936–945. https://doi.org/10.1016/j.gr.2012.07.019

Replumaz, A., Negredo, A. M., Guillot, S., & Villaseñor, A. (2010). Multiple episodes of continental subduction during India/Asia convergence: Insight from seismic tomography and tectonic reconstruction. *Tectonophysics*, *483*(1–2), 125–134. https://doi.org/10.1016/j.tecto.2009.10.007

Richter, B., & Fuller, M. (1996). Palaeomagnetism of the Sibumasu and Indochina blocks: Implications for the extrusion tectonic model. *Geological Society, London, Special Publications*, *106*(1), 203–224.

Ridd, M. F., Crow, M. J., & Morley, C. K. (2019). The role of strike-slip faulting in the history of the Hukawng Block and the Jade Mines Uplift, Myanmar. *Proceedings of the Geologists' Association*, *130*(2), 126–141. https://doi.org/10.1016/j.pgeola.2019.01.002

Ridd, M. F., & Watkinson, I. (2013). The Phuket-Slate Belt terrane: tectonic evolution and strike-slip emplacement of a major terrane on the Sundaland margin of Thailand and Myanmar. *Proceedings of the Geologists' Association*, *124*(6), 994–1010. https://doi.org/10.1016/j.pgeola.2013.01.007

Robinson, D. M., & Martin, A. J. (2014). Reconstructing the Greater Indian margin: A balanced cross section in central Nepal focusing on the Lesser Himalayan duplex. *Tectonics*, *33*(11), 2143–2168.

Rowley, D. B., & Currie, B. S. (2006). Palaeo-altimetry of the late Eocene to Miocene Lunpola basin, central Tibet. *Nature*, *439*(7077), 677.

Royden, L. H., Burchfiel, B. C., & van der Hilst, R. D. (2008). The Geological Evolution of the Tibetan Plateau. *Science*, *321*(5892), 1054–1058. https://doi.org/10.1126/science.1155371

Royer, J.-Y., & Sandwell, D. T. (1989). Evolution of the eastern Indian Ocean since the Late Cretaceous: Constraints from Geosat altimetry. *Journal of Geophysical Research: Solid Earth*, *94*(B10), 13755–13782.

Sato, K., Liu, Y., Wang, Y., Yokoyama, M., Yoshioka, S., Yang, Z., & Otofuji, Y. (2007). Paleomagnetic study of Cretaceous rocks from Pu'er, western Yunnan, China: evidence of internal deformation of the Indochina block. *Earth and Planetary Science Letters*, *258*(1–2), 1–15.

Schwab, M., Ratschbacher, L., Siebel, W., McWilliams, M., Minaev, V., Lutkov, V., … Frisch, W. (2004). Assembly of the Pamirs: Age and origin of magmatic belts from the southern Tien Shan to the southern Pamirs and their relation to Tibet. *Tectonics*, *23*(4).

Searle, M. P., Garber, J. M., Hacker, B. R., Htun, K., Gardiner, N. J., Waters, D. J., & Robb, L. J. (2020). Timing of syenite-charnockite magmatism and ruby-and sapphire metamorphism in the Mogok valley region, Myanmar. *Tectonics*, e2019TC005998.

Searle, M. P., Morley, C. K., Waters, D. J., Gardiner, N. J., Htun, U. K., Than Than Nu, & Robb, L. J. (2017). Chapter 12 Tectonic and metamorphic evolution of the Mogok Metamorphic and Jade Mines belts and ophiolitic terranes of Burma (Myanmar). *Geological Society, London, Memoirs*, *48*(1), 261–293. https://doi.org/10.1144/M48.12

Searle, M. P., Noble, S. R., Cottle, J. M., Waters, D. J., Mitchell, A. H. G., Hlaing, T., & Horstwood, M. S. A. (2007). Tectonic evolution of the Mogok metamorphic belt, Burma (Myanmar) constrained by U-Th-Pb dating of metamorphic and magmatic rocks: U-TH-PB AGES OF MOGOK BELT. *Tectonics*, *26*(3), n/a-n/a. https://doi.org/10.1029/2006TC002083

Searle, M. P., Waters, D. J., Rex, D. C., & Wilson, R. N. (1992). Pressure, temperature and time constraints on Himalayan metamorphism from eastern Kashmir and western Zanskar. *Journal of the Geological Society*, *149*(5), 753–773.

Sengupta, S., Ray, K. K., Acharyya, S. K., & De Smeth, J. B. (1990). Nature of ophiolite occurrences along the eastern margin of the Indian plate and their tectonic significance. *Geology*, *18*(5), 439–442.

Seton, M., Müller, R. D., Zahirovic, S., Gaina, C., Torsvik, T., Shephard, G., … Maus, S. (2012). Global continental and ocean basin reconstructions since 200 Ma. *Earth-Science Reviews*, *113*(3–4), 212–270.

Sevastjanova, I., Hall, R., Rittner, M., Paw, S. M. T. L., Naing, T. T., Alderton, D. H., & Comfort, G. (2016). Myanmar and Asia united, Australia left behind long ago. *Gondwana Research*, *32*, 24–40. https://doi.org/10.1016/j.gr.2015.02.001

Shen, F., Royden, L. H., & Burchfiel, B. C. (2001). Large-scale crustal deformation of the Tibetan Plateau. *Journal of Geophysical Research: Solid Earth*, *106*(B4), 6793–6816. https://doi.org/10.1029/2000JB900389

Shi, G., Cui, W., Cao, S., Jiang, N., Jian, P., Liu, D., … Chu, B. (2008). Ion microprobe zircon U–Pb age and geochemistry of the Myanmar jadeitite. *Journal of the Geological Society*, *165*(1), 221–234. https://doi.org/10.1144/0016-76492006-119

Sikumbang, N. (1990). The geology and tectonics of the Meratus mountains, south Kalimantan, Indonesia. *Geologi Indonesia*, *13*(2), 1–31.

Singh, A. K., Khogenkumar, S., Singh, L. R., Bikramaditya, R. K., Khuman, Ch. M., & Thakur, S. S. (2016). Evidence of Mid-ocean ridge and shallow subduction forearc magmatism in the Nagaland-Manipur ophiolites, northeast India: constraints from mineralogy and geochemistry of gabbros and associated mafic dykes. *Geochemistry*, *76*(4), 605–620. https://doi.org/10.1016/j.chemer.2016.09.002

Sloan, R. A., Elliott, J. R., Searle, M. P., & Morley, C. K. (2017). Active tectonics of Myanmar and the Andaman Sea. *Geological Society, London, Memoirs*, *48*(1), 19–52.

Smit, M. A., Hacker, B. R., & Lee, J. (2014). Tibetan garnet records early Eocene initiation of thickening in the Himalaya. *Geology*, *42*(7), 591–594.

Socquet, A., Vigny, C., Chamot-Rooke, N., Simons, W., Rangin, C., & Ambrosius, B. (2006). India and Sunda plates motion and deformation along their boundary in Myanmar determined by GPS: GPS INDIA-SUNDA MOTION, MYANMAR STRAIN. *Journal of Geophysical Research: Solid Earth*, *111*(B5), n/a-n/a. https://doi.org/10.1029/2005JB003877

Speranza, F., Pellegrino, A. G., Zhang, B., Maniscalco, R., Chen, S., & Hernandez-Moreno, C. (2019). Paleomagnetic Evidence for 25–15 Ma Crust Fragmentation of North Indochina (23–26°N): Consequence of Collision With Greater India NE Corner? *Geochemistry, Geophysics, Geosystems*, *20*(11), 5425–5448. https://doi.org/10.1029/2019GC008308

Srisuriyon, K., & Morley, C. K. (2014). Pull-apart development at overlapping fault tips: Oblique rifting of a Cenozoic continental margin, northern Mergui Basin, Andaman Sea. *Geosphere*, *10*(1), 80–106. https://doi.org/10.1130/GES00926.1

Steckler, M. S., Mondal, D. R., Akhter, S. H., Seeber, L., Feng, L., Gale, J., … Howe, M. (2016). Locked and loading megathrust linked to active subduction beneath the Indo-Burman Ranges. *Nature Geoscience*, *9*(8), 615–618. https://doi.org/10.1038/ngeo2760

Tan, X., Gilder, S., Kodama, K. P., Jiang, W., Han, Y., Zhang, H., … Zhou, D. (2010). New paleomagnetic results from the Lhasa block: Revised estimation of latitudinal shortening across Tibet and implications for dating the India–Asia collision. *Earth and Planetary Science Letters*, *293*(3–4), 396–404. https://doi.org/10.1016/j.epsl.2010.03.013

Tapponnier, P., Peltzer, G., Le Dain, A. Y., Armijo, R., & Cobbold, P. (1982). Propagating extrusion tectonics in Asia: New insights from simple experiments with plasticine. *Geology*, *10*(12), 611–616.

Thein, M., & Maung, M. (2017). The Eastern (Back-arc) Basin of Central Myanmar: Basement rocks, lithostratigraphic units, palaeocurrents, provenance and developmental history. *Geological Society, London, Memoirs*, *48*(1), 169–183.

Thompson, J. O., Moulin, M., Aslanian, D., de Clarens, P., & Guillocheau, F. (2019). New starting point for the Indian Ocean: Second phase of breakup for Gondwana. *Earth-Science Reviews*, *191*, 26–56. https://doi.org/10.1016/j.earscirev.2019.01.018

Tong, Y.-B., Yang, Z., Zheng, L.-D., Xu, Y.-L., Wang, H., Gao, L., & Hu, X.-Z. (2013). Internal crustal deformation in the northern part of Shan-Thai Block: New evidence from paleomagnetic results of Cretaceous and Paleogene redbeds. *Tectonophysics*, *608*, 1138–1158. https://doi.org/10.1016/j.tecto.2013.06.031

Torsvik, T. H., Van der Voo, R., Preeden, U., Mac Niocaill, C., Steinberger, B., Doubrovine, P. V., … Cocks, L. R. M. (2012). Phanerozoic polar wander, palaeogeography and dynamics. *Earth-Science Reviews*, *114*(3–4), 325–368. https://doi.org/10.1016/j.earscirev.2012.06.007

Turner, S., Arnaud, N., LIU, J., Rogers, N., Hawkesworth, C., Harris, N., … Deng, W. (1996). Post-collision, shoshonitic volcanism on the Tibetan Plateau: implications for convective thinning of the lithosphere and the source of ocean island basalts. *Journal of Petrology*, *37*(1), 45–71.

United Nations. (1978a). Geology and exploration geochemistry of the Pinlebu-Banmauk area, Sagaing Division, northern Burma. Technical Report No. 2. DP/UN/BUR-72-002. *Geological Survey and Exploration Project, United Nations Development Programme, New York*, 66.

van Hinsbergen, D. J. J., Kapp, P., Dupont-Nivet, G., Lippert, P. C., DeCelles, P. G., & Torsvik, T. H. (2011). Restoration of Cenozoic deformation in Asia and the size of Greater India: RESTORING CENOZOIC ASIAN DEFORMATION. *Tectonics*, *30*(5), n/a-n/a. https://doi.org/10.1029/2011TC002908

van Hinsbergen, D. J. J., Lippert, P. C., Li, S., Huang, W., Advokaat, E. L., & Spakman, W. (2019). Reconstructing Greater India: Paleogeographic, kinematic, and geodynamic perspectives. *Tectonophysics*. https://doi.org/10.1016/j.tecto.2018.04.006

van Hinsbergen, D. J., Lippert, P. C., Dupont-Nivet, G., McQuarrie, N., Doubrovine, P. V., Spakman, W., & Torsvik, T. H. (2012). Greater India Basin hypothesis and a two-stage Cenozoic collision between India and Asia. *Proceedings of the National Academy of Sciences*, *109*(20), 7659–7664.

Vannay, J.-C., Grasemann, B., Rahn, M., Frank, W., Carter, A., Baudraz, V., & Cosca, M. (2004). Miocene to Holocene exhumation of metamorphic crustal wedges in the NW Himalaya: Evidence for tectonic extrusion coupled to fluvial erosion. *Tectonics*, *23*(1).

Vérard, C., Stampfli, G., Borel, G., & Hochard, C. (2017). The Indian promontory: A bridge between plate tectonics and life evolution models. *Universal Journal of Geoscience*, *5*(2), 25–32.

Volkmer, J. E., Kapp, P., Guynn, J. H., & Lai, Q. (2007). Cretaceous-Tertiary structural evolution of the north central Lhasa terrane, Tibet. *Tectonics*, *26*(6).

Volkmer, J. E., Kapp, P., Horton, B. K., Gehrels, G. E., Minervini, J. M., & Ding, L. (2014). Northern Lhasa thrust belt of central Tibet: evidence of Cretaceous–early Cenozoic shortening within a passive roof thrust system. *Geological Society of America Special Papers*, *507*, 59–70.

Wakita, K., Miyazaki, K., Zulkarnain, I., Sopaheluwakan, J., & Sanyoto, P. (1998). Tectonic implications of new age data for the Meratus Complex of south Kalimantan, Indonesia. *Island Arc*, *7*(1–2), 202–222.

Wang, D., Lu, S., Han, S., Sun, X., & Quan, C. (2013). Eocene prevalence of monsoon-like climate over eastern China reflected by hydrological dynamics. *Journal of Asian Earth Sciences*, *62*, 776–787.

Wang, J.-G., Wu, F.-Y., Garzanti, E., Hu, X., Ji, W.-Q., Liu, Z.-C., & Liu, X.-C. (2016). Upper Triassic turbidites of the northern Tethyan Himalaya (Langjiexue Group): The terminal of a sediment-routing system sourced in the Gondwanide Orogen. *Gondwana Research*, *34*, 84–98. https://doi.org/10.1016/j.gr.2016.03.005

Wang, J.-G., Wu, F.-Y., Tan, X.-C., & Liu, C.-Z. (2014). Magmatic evolution of the Western Myanmar Arc documented by U–Pb and Hf isotopes in detrital zircon. *Tectonophysics*, *612–613*, 97–105. https://doi.org/10.1016/j.tecto.2013.11.039

Wang, J.-M., Rubatto, D., & Zhang, J.-J. (2015). Timing of partial melting and cooling across the Greater Himalayan Crystalline Complex (Nyalam, Central Himalaya): In-sequence thrusting and its implications. *Journal of Petrology*, *56*(9), 1677–1702.

Xu, M., Chang, C.-P., Fu, C., Qi, Y., Robock, A., Robinson, D., & Zhang, H. (2006). Steady decline of east Asian monsoon winds, 1969–2000: Evidence from direct ground measurements of wind speed. *Journal of Geophysical Research: Atmospheres*, *111*(D24).

Yamamoto, H., Kobayashi, K., Nakamura, E., Kaneko, Y., & Kausar, A. B. (2005). U-Pb zircon dating of regional deformation in the lower crust of the Kohistan Arc. *International Geology Review*, *47*(10), 1035–1047.

Yang, T., Ma, Y., Bian, W., Jin, J., Zhang, S., Wu, H., … Ding, J. (2015). Paleomagnetic results from the Early Cretaceous Lakang Formation lavas: Constraints on the paleolatitude of the Tethyan Himalaya and the India–Asia collision. *Earth and Planetary Science Letters*, *428*, 120–133.

Yao, W., Ding, L., Cai, F., Wang, H., Xu, Q., & Zaw, T. (2017). Origin and tectonic evolution of upper Triassic Turbidites in the Indo-Burman ranges, West Myanmar. *Tectonophysics*, *721*, 90–105. https://doi.org/10.1016/j.tecto.2017.09.016

Yi, Z., Huang, B., Chen, J., Chen, L., & Wang, H. (2011). Paleomagnetism of early Paleogene marine sediments in southern Tibet, China: Implications to onset of the India–Asia collision and size of Greater India. *Earth and Planetary Science Letters*. https://doi.org/10.1016/j.epsl.2011.07.001

Yin, A. (2006). Cenozoic tectonic evolution of the Himalayan orogen as constrained by along-strike variation of structural geometry, exhumation history, and foreland sedimentation. *Earth-Science Reviews*, *76*(1–2), 1–131.

Yin, A., Dubey, C. S., Kelty, T. K., Webb, A. A. G., Harrison, T. M., Chou, C. Y., & Célérier, J. (2010). Geologic correlation of the Himalayan orogen and Indian craton: Part 2. Structural geology, geochronology, and tectonic evolution of the Eastern Himalaya. *Bulletin*, *122*(3–4), 360–395.

Yin, A., & Harrison, T. M. (2000). Geologic Evolution of the Himalayan-Tibetan Orogen. *Annual Review of Earth and Planetary Sciences*, *28*(1), 211–280. https://doi.org/10.1146/annurev.earth.28.1.211

Yuan, J., Yang, Z., Deng, C., Krijgsman, W., Hu, X., Li, S., … Zhu, R. (2020). Rapid drift of the Tethyan Himalaya terrane before two-stage India-Asia collision. *National Science Review*, nwaa173. https://doi.org/10.1093/nsr/nwaa173

Yui, T.-F., Fukoyama, M., Iizuka, Y., Wu, C.-M., Wu, T.-W., Liou, J. G., & Grove, M. (2013). Is Myanmar jadeitite of Jurassic age? A result from incompletely recrystallized inherited zircon. *Lithos*, *160–161*, 268–282. https://doi.org/10.1016/j.lithos.2012.12.011

Zahirovic, S., Matthews, K. J., Flament, N., Müller, R. D., Hill, K. C., Seton, M., & Gurnis, M. (2016). Tectonic evolution and deep mantle structure of the eastern Tethys since the latest Jurassic. *Earth-Science Reviews*, *162*, 293–337. https://doi.org/10.1016/j.earscirev.2016.09.005

Zahirovic, S., Seton, M., & Müller, R. D. (2014). The Cretaceous and Cenozoic tectonic evolution of Southeast Asia. *Solid Earth*, *5*(1), 227–273. https://doi.org/10.5194/se-5-227-2014

Zaman, H., & Torii, M. (1999). Palaeomagnetic study of Cretaceous red beds from the eastern Hindukush ranges, northern Pakistan: palaeoreconstruction of the Kohistan-Karakoram composite unit before the India-Asia collision. *Geophysical Journal International*, *136*(3), 719–738. https://doi.org/10.1046/j.1365-246x.1999.00757.x

Zhang, J., Xiao, W., Windley, B. F., Wakabayashi, J., Cai, F., Sein, K., … Naing, S. (2018). Multiple alternating forearc- and backarc-ward migration of magmatism in the Indo-Myanmar Orogenic Belt since the Jurassic: Documentation of the orogenic architecture of eastern Neotethys in SE Asia. *Earth-Science Reviews*, *185*, 704–731. https://doi.org/10.1016/j.earscirev.2018.07.009

Zhang, P., Mei, L., Hu, X., Li, R., Wu, L., Zhou, Z., & Qiu, H. (2017). Structures, uplift, and magmatism of the Western Myanmar Arc: Constraints to mid-Cretaceous-Paleogene tectonic evolution of the western Myanmar continental margin. *Gondwana Research*, *52*, 18–38. https://doi.org/10.1016/j.gr.2017.09.002

Zhang, Y., Huang, W., Huang, B., Hinsbergen, D. J. J., Yang, T., Dupont-Nivet, G., & Guo, Z. (2018). 53–43 Ma Deformation of Eastern Tibet Revealed by Three Stages of Tectonic Rotation in the Gongjue Basin. *Journal of Geophysical Research: Solid Earth*, *123*(5), 3320–3338. https://doi.org/10.1002/2018JB015443

Zheng, T., He, Y., Ding, L., Jiang, M., Ai, Y., Mon, C. T., … Thant, M. (2020). Direct structural evidence of Indian continental subduction beneath Myanmar. *Nature Communications*, *11*(1), 1944. https://doi.org/10.1038/s41467-020-15746-3

Zhu, D.-C., Zhao, Z.-D., Niu, Y., Mo, X.-X., Chung, S.-L., Hou, Z.-Q., … Wu, F.-Y. (2011). The Lhasa Terrane: record of a microcontinent and its histories of drift and growth. *Earth and Planetary Science Letters*, *301*(1–2), 241–255.

Chapter 3: Methodology

Paleomagnetic sampling of the Kanza Chaung Batholith.
(Wuntho Ranges, Myanmar, Fieldwork November 2017)

1. Fieldwork & sampling

The fieldwork during this PhD thesis consisted of three field seasons in Myanmar: Four weeks in November 2017, five weeks in January 2019 and two weeks in January 2020. The main goal during these three fieldworks was to prospect and obtain paleomagnetic samples from different ages, localities and lithologies to constrain the tectonic evolution of the BT. Another important part of these fieldworks was collaborating with a multidisciplinary team consisting of sedimentologists, petrologists, palynologists and structural geologists as part of the Myanmar Paleoclimate and Geodynamics Research Group (MyaPGR) and ERC project MAGIC. The results from the paleomagnetic sampling will be presented in detail in Chapters 4-7, while the co-authored work with MyaPGR is listed in Appendix 5.

In total, we drilled 1740 oriented paleomagnetic cores as part of this PhD project, using standard paleomagnetic field equipment and procedures with both magnetic and sun compasses. Both prospecting and sampling was challenging in Myanmar, because of limited road access, jungle covering much of the exposure, strong weathering of outcrops due to the tropical climate, and scientific isolation of the country. Access to detailed geological maps was difficult, and hence prospecting usually involved driving around the countryside while searching on Google Earth for potential outcrops in rivers, road cuts and quarry's used for road construction (Figs. 3.1 and 3.2).

***Figure 3.1**: Paleomagnetic sampling in a typical quarry in the Wuntho Ranges.*

***Figure 3.2**: Paleomagnetic sampling of the Natma Formation along the Chindwin River.*

The initial sampling localities (Fig. 3.3) during the first fieldwork were the late Eocene to middle Miocene sediments exposed in a homoclinal sedimentary section around the township of Kalewa (Chindwin Basin), and the early Late Cretaceous volcanic complex of the Wuntho Ranges (See Chapter 2 for details on the geology of the BT). During the following fieldwork, the sampling was expanded to the Cretaceous to upper Oligocene sediments of the Minbu Basin. Here we sampled the Paleocene Paunggyi Formation and lower Eocene Laungshe Formation near the townships of Sidoktaya and Datkon. A magnetostratigraphic section was sampled near the town of Minbu in the upper Eocene Yaw Formation and lower Oligocene Shwezetaw Formation. Three sites were obtained in the middle Oligocene Padaung Formation in the Tantkyitaung Pagoda anticline to the west of Bagan. We took nine sites in the upper Eocene Pondaung Formation, exposed in the Pondaung Ranges forming the boundary between the Chindwin and Minbu Basins. Finally, multiple sites were drilled in the Indo-Burman Ranges during the second fieldwork as well, consisting of the Triassic to Eocene turbidites west of the Kalay Township, and the mafic rocks of the Western Belt Ophiolite west of Datkon in the Minbu Basin (Fig. 3.3). Because the preliminary results from the Laungshe Formation near Sidoktaya were interesting, the focus of the third and final fieldwork was to obtain more sites near the township of Saw in the early Eocene Laungeshe, Tilin and Tabyin Formations, as well as the Campanian - Maastrichtian Kabaw Formation.

The paleomagnetic results from the the early Late Cretaceous Wuntho volcanics and the upper Eocene Yaw Formation near Kalewa localities will be discussed in Chapter 4. The magnetostratigraphy and magnetic properties from the Kalewa sedimentary sequence (upper

Eocene Yaw Formation, upper Oligocene Tonhe Formation and lower Miocene Letkat Formation) are presented in Chapter 5.

The results used for the final publication of this PhD project are described in Chapter 6, which consists of the early Eocene sites around Sidoktaya and Saw, the middle Oligocene Padaung Formation near Bagan, the middle to upper Eocene Pondaung Formation in the Pondaung Ranges and the middle Miocene Natma Formation north of Kalewa. The goal of Chapter 6 is to provide a complete paleomagnetic record for the BT. Chapter 7 lists the paleomagnetic analysis of the remaining localities that were of insufficient quality for paleomagnetism.

Figure 3.3: *Generalized Myanmar geologic map with sampling localities from this PhD project (after Licht et al., 2019). Abbreviations: AI = Cretaceous-Paleogene Asian intrusives, CB = Chindwin Basin, GA = Cretaceous Gangdese Arc, IBRB: Indo-Burman Ranges basement, KF = Kabaw Fault, MMMB = Mogok–Mandalay–Mergui Belt (including Jurassic Eastern Belt Ophiolites & Jade Belt Ophiolite), SF = Sagaing Fault, SPG = Songpan Ganze & Yangtze complexes, WBO = Cretaceous Western Belt Ophiolite, WPA = Wuntho-Popa Arc, YTSZ = Yarlung-Tsangpo Suture Zone. Dashed black lines: Central Myanmar Basins.*

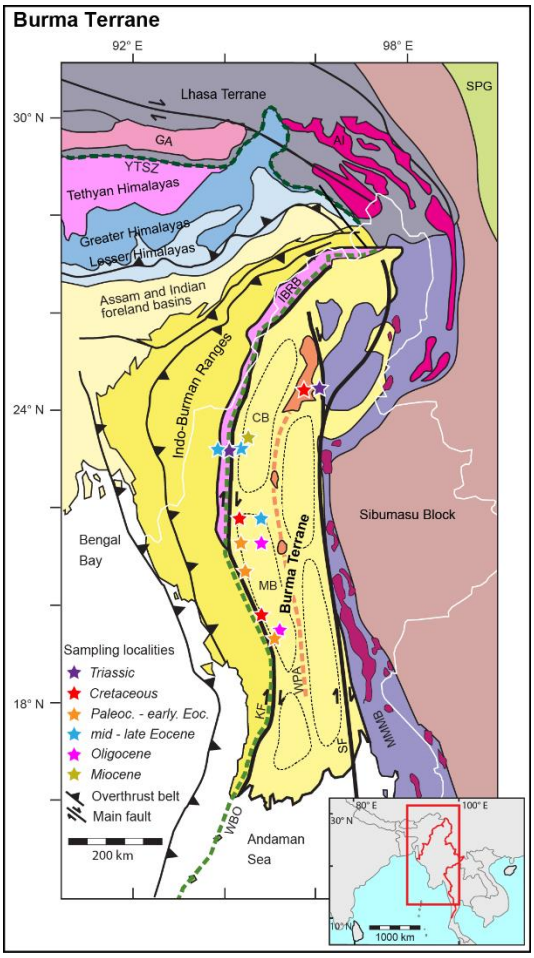

2. Paleomagnetic analysis

Paleomagnetism is the study of the record of the Earth's magnetic field in rocks (Tauxe, 2010). The Earth's magnetic field is predominantly dipolar with a magnetic north pole and south pole. In addition, the geomagnetic north pole and south pole describe the poles generated by only a geocentric axial dipole (GAD) field. Relative to the Earth's surface it has a horizontal component called the declination, and a vertical component called the inclination. The inclination varies with latitude following the simple equation tan (I) = 2 tan (λ), where I is the inclination and λ the latitude. The inclination is around zero near the equator and becomes perpendicular to the Earth's surface close to the poles (Fig. 3.4). The declination points towards the magnetic north pole. Magnetic minerals (e.g. magnetite, hematite, greigite) in rocks retain a record of the Earth's magnetic field direction during diagenesis, which is called Natural Remanent Magnetization (NRM). Upon rotation of tectonic plates, terranes and blocks, the retained directions in rocks will rotate as well with respect to the current magnetic north pole. Hence, paleomagnetic analysis provides information about the paleolatitude (inclination) and paleo-rotation (declination) of these tectonic entities through time. Using this information, paleomagnetists have been at the forefront of validating the scientific theory of plate tectonics throughout the 20th century.

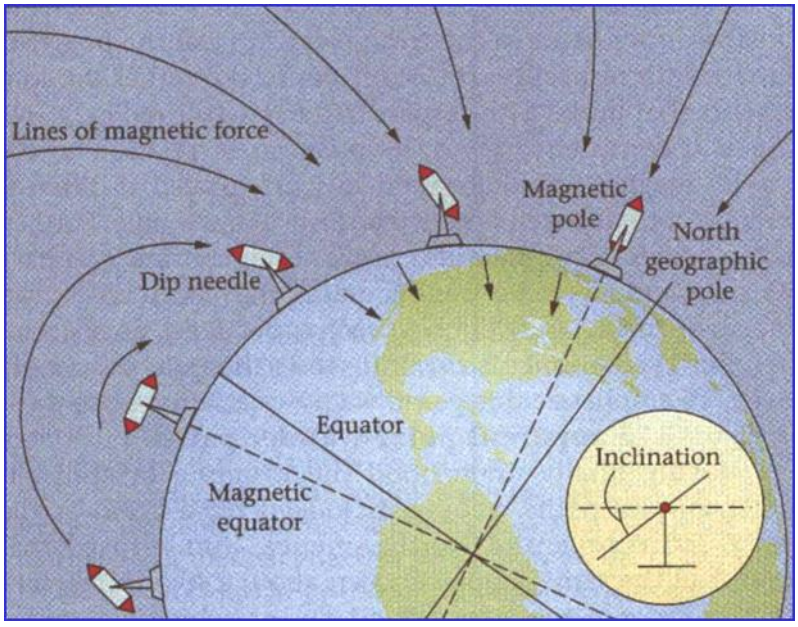

Figure 3.4*: The variation of inclination with respect to the Earth's surface (after De Groot & Krijgsman, 2015).*

However, a major challenge regarding plate reconstructions using paleomagnetic data is that the Earth's magnetic field is not constant in direction and intensity through time. Paleosecular variation (PSV) describes field fluctuations and magnetic excursions around the GAD on the scale of ~10^2-10^4

years (Fig. 3.5). Furthermore, the Earth's magnetic field can completely reverse on the scale of ~10^5-10^7 years. The resulting chrons and subchrons of normal and reverse polarity are used in magnetostratigraphy, a method to date a stratigraphic record using the unique pattern fit provided by these reversals (Fig. 3.6). Because of these variations, as well as uncertainties in orienting paleomagnetic cores, paleomagnetists rely on Fisher vector statistics (Fisher, 1953) to determine paleomagnetic mean directions. The distribution of individual samples must average out PSV to approximate the GAD at a certain time. Volcanic rocks cool relatively fast and hence retain spot readings of the geomagnetic field, while sedimentary rocks average out PSV because of relatively slower sedimentation rates. The magnetic signal of sedimentary rocks is overall weaker compared to volcanic rocks. Therefore, paleomagnetic sampling is preferably distributed over different lithologies, stratigraphic levels, or numerous volcanic flows.

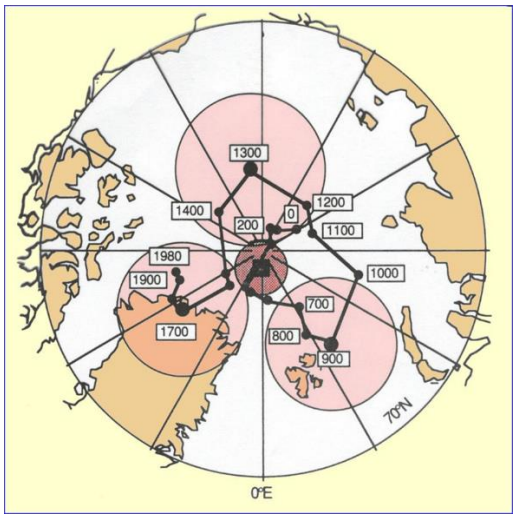

Figure 3.5: *Paleosecular variation of the Earth's magnetic field with respect to an average geomagnetic north pole. Numbers indicate years (after De Groot & Krijgsman, 2015).*

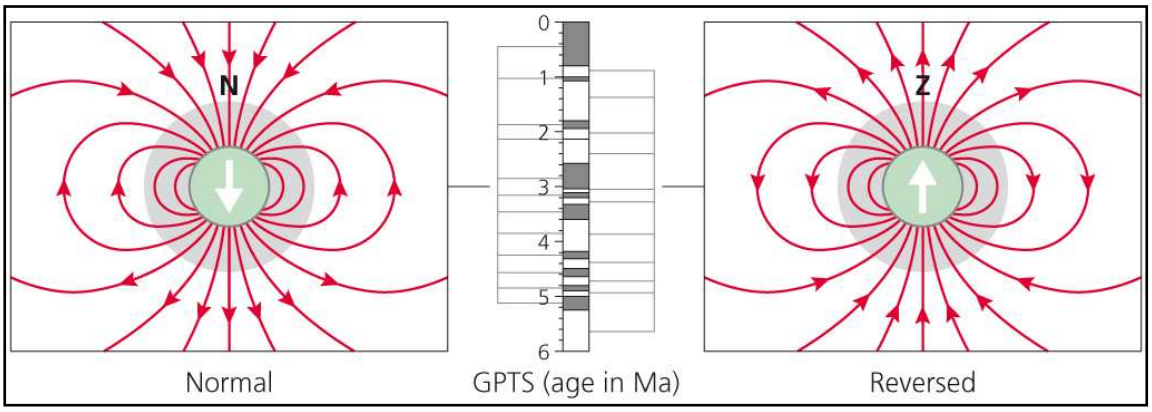

Figure 3.6: *The Earth's magnetic field in normal (black) and reverse polarity (white), as recorded in the Geomagnetic Polarity Time Scale (GPTS) (after De Groot & Krijgsman, 2015).*

Polar wander due to PSV is also of major importance in plate reconstructions. The Apparent Polar Wander Path (APWP) of a continent describes the perceived movement of the magnetic poles relative to a continent while assuming the continent to be fixed in position. In reality however, the APWP is a combination of real polar wander and the motion of the continent. Therefore, the paleomagnetic record from a certain terrane can only describe its relative plate motion with respect to another terrane (Fig. 3.7). In the case of the BT, this reference will be the relatively stable Eurasian continent (Torsvik et al., 2012).

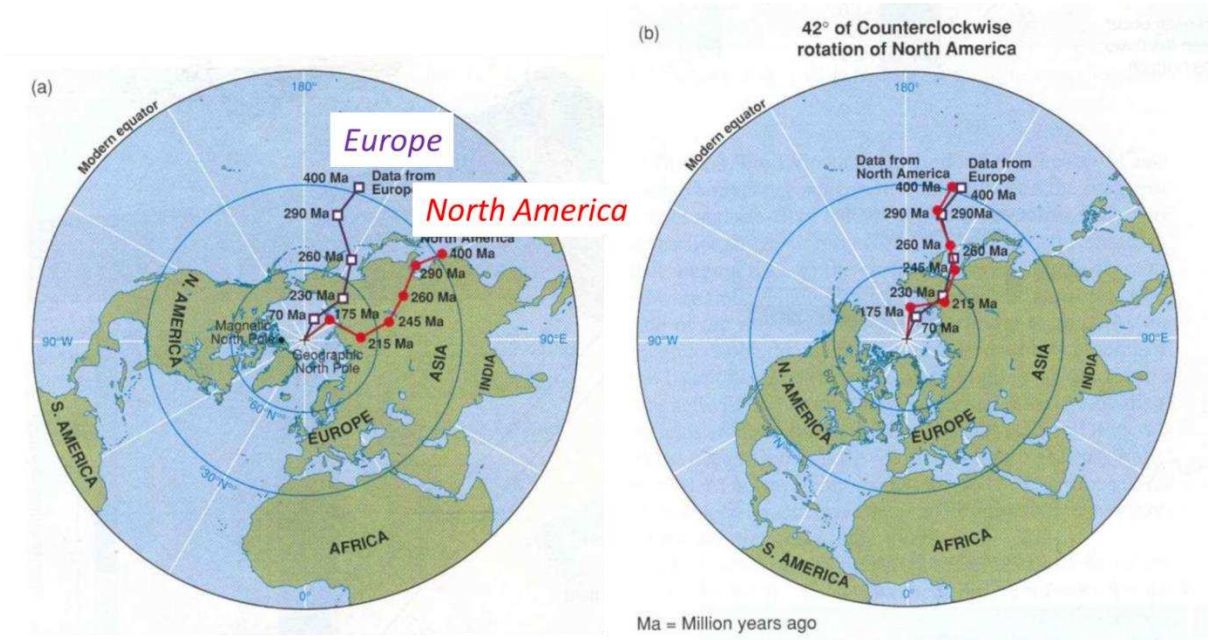

Figure 3.7*: Correlating the APWPs from North America and Europe to determine their relative plate motions (after Irving, 1958).*

Another major challenge in paleomagnetism is the partial or complete overprint of the primary magnetic direction, which is called the Characteristic Remanent Magnetization (ChRM), in a certain rock. Common causes for overprint are chemical weathering and alteration, (re-)heating of the rock (e.g. due to baked contact with igneous rocks) and contact with a stronger magnetic field. Due to the tropical climate in Myanmar, chemical weathering and alteration were an important problem during fieldwork with a scarcity of fresh unaltered outcrops, resulting in severe overprint of the primary magnetic signal by the present-day field.

Hence, the total NRM is the sum of the original magnetization and subsequent overprints. The main goal during paleomagnetic labwork is therefore to isolate the ChRM from the NRM by stepwise demagnetization of the samples (Fig. 3.8). To this end, samples were measured on a 2G cryogenic magnetometer hosted in a magnetically shielded room at Geosciences Rennes (University of Rennes 1). Demagnetization was done using both thermally, with increments of 20° to 50 °C up to 680 °C,

and with 3-axis alternating fields (AF) demagnetization, with increments of 2.5 to 10 mT up to 120 mT. During AF demagnetization, the Gyro Remanent Magnetizations (GRMs) were cancelled by measuring their magnetization after each axis of AF demagnetization (x,y,z) (Roperch & Taylor, 1986). Afterwards, demagnetizations of each sample was plotted on orthogonal demagnetization plots (Zijderveld, 1967), which allowed for interpretation of the ChRMs with principal component analysis (Kirschvink, 1980), or, when necessary, a great-circle approach (McFadden & McElhinny, 1988). Samples with interpretable ChRMs from the same locality and age were grouped, after which mean directions and corresponding statistical parameters (Fisher cone of confidence α95 and dispersion k) could be calculated (Butler, 1992; Fisher, 1953). Because of compaction during sedimentary burial, the effect of inclination shallowing on sedimentary rocks was tested with the following generalized formula:

$$\tan(I_1) = 0.6 \tan(I_0)$$

where I1 is the measured inclination, I0 is the unflattened inclination (King, 1955; Tauxe & Kent, 1984).

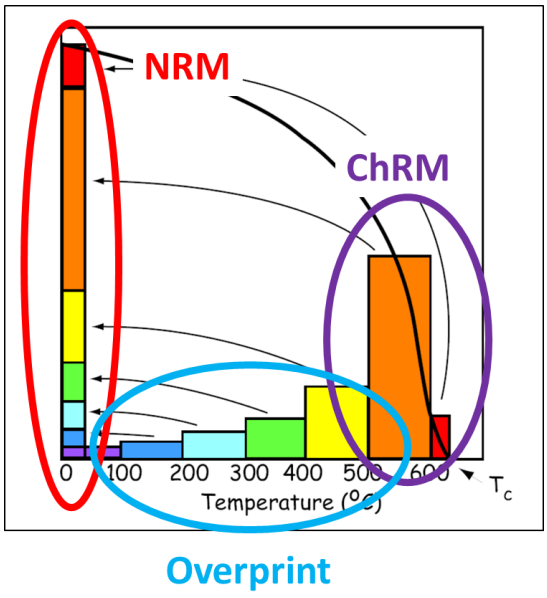

Figure 3.8: *Total magnetization (NRM) of a sample versus its primary magnetization (ChRM) and overprint that are isolated during stepwise demagnetization at increasing temperature steps (after Tauxe, 2010).*

There are different paleomagnetic tests to verify whether an obtained ChRM represents the primary magnetization of a sample. The fold test can be used in sampled sites with different bedding to determine whether the magnetization acquired before or after tilting (Fig. 3.9; Tauxe & Watson,

1994). The classic coordinate bootstrap reversal test can verify whether normal and reverse polarities from a locality are antiparallel (Tauxe, 2010).

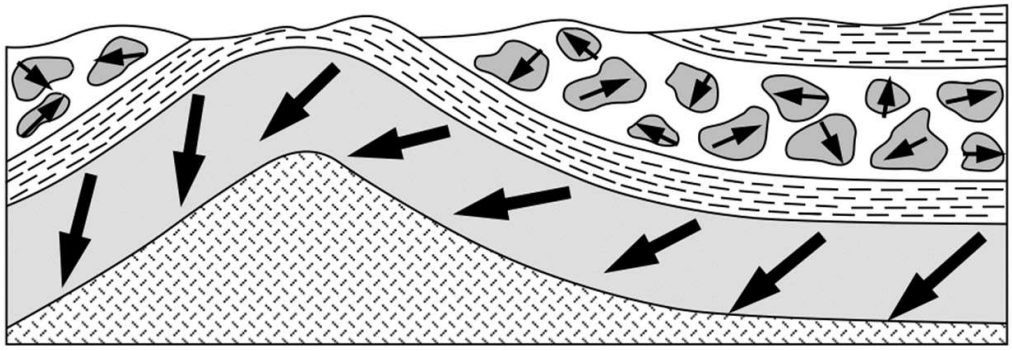

Figure 3.9*: A positive fold test: All magnetic directions in the fold become parallel upon restoring the bedding to its original horizontal position (after Butler, 1992).*

3. Rock magnetism

In addition, the magnetic properties of samples was investigated to constrain their origin of magnetization. Before demagnetization, the anisotropy of magnetic susceptibility (AMS) of each sample was measured on a KLY3S AGICO kappabridge to acquire the magnetic fabric in every locality. In compressive regimes, the maximum axis K_{max} of the AMS tensor in sedimentary samples will gradually be aligned perpendicular to the direction of maximum compression, while the minimum axis K_{min} will be vertical after bedding correction (Hrouda, 1982; Kissel et al., 1986). Similarly, the magnetic foliation from AMS in intrusive rocks, perpendicular to a near-vertical foliation, tend to follow the trend of the larger volcanic complex. The AMS can thus provide first order constraints on the origin of magnetization and tilting in different types of lithologies. Magnetic mineralogy and chemical alteration were investigated by conducting several experiments. Bulk magnetic susceptibility, a measure of how much a material will become magnetized in an applied magnetic field, of certain samples was measured at increasing temperature steps on a KLY3S AGICO kappabridge. Furthermore, magnetic hysteresis loops are plots representing the ease of magnetic particles in a sample flipping their direction when applying an external magnetic field. These plots have different shapes for different magnetic properties (diamagnetism, paramagnetism and ferromagnetism) from different magnetic carriers (magnetite, hematite). Hysteresis plots were obtained on an alternating gradient magnetometer (AGM 2900) were obtained at LSCE (Gif-sur-Yvette). Finally, during acquisition of isothermal remanent magnetization (IRM), a large external field of constant direction is applied to constrain differences in mineralogy and magnetic carriers. Magnetite usually saturates at 300 mT during IRM acquisition, while hematite saturates above 2400

mT. Thermal demagnetization of the acquired IRM can be used to further characterize the present magnetic components.

These rock magnetic experiments were then compared with observations from thin sections under both an optical microscope in transmitted and reflected light, as well as a Scanning Electron Microscope (SEM - JEOL JSM 7100F with Oxford energy dispersive X-ray spectroscopy and electron backscatter diffraction) at the Centre de Microscopie Électronique à Balayage et Microanalyse– ScanMAT platform (University of Rennes 1).

4. Choice for reference frame

As described in the previous section, plate reconstructions should be done using relative plate motions of one plate with respect to the other. However, this means that the absolute position of the benchmark plates are required as well. In paleomagnetic reference frames, high quality paleomagnetic data from preferably tectonically stable continents are used for this, while hotspot reference frames use the record of stable hotspots as plates move over them.

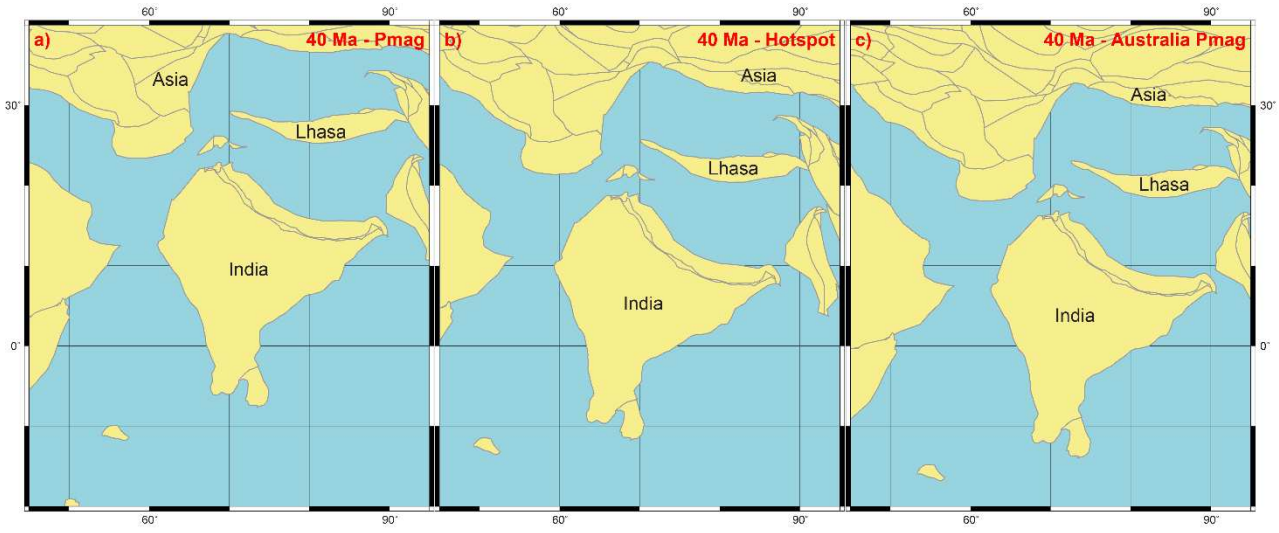

Figure 3.10: *GPlates reconstruction showing the difference in position of India relative to Asia at 40 Ma in (a) paleomagnetic and (b) hotspot reference frames, as well as a (c) paleomagnetic reference frame incorporating data from Australia (Hansma & Tohver, 2019). Continental polygons are from Matthews et al. (2016). Old position of the Burma Terrane is used (For updated position, see Chapters 4-6).*

Customarily, paleomagnetic studies should use a paleomagnetic reference frame. In order to validate this for reconstructing the BT, we investigated differences in our plate tectonic reconstructions of the India-Asia collision between a paleomagnetic and hotspot reference frame. At most ages there are no significant latitudinal differences between both reference frames (Torsvik et

al., 2008). Around 40 Ma however, India and Eurasia are about 5° farther north in the paleomagnetic reference frame compared to the hotspot reference frame (Fig. 3.10a,b; fig. 6.S3). Indeed, low inclinations in Asia around 40 Ma have been a long-standing concern (Cogné et al., 2013; Dupont-Nivet et al., 2010), and the global APWP (Torsvik et al., 2012) is mainly based on poles from North America, whose north-western margin is characterized by a long and complicated tectonic history of active subduction, as well as from north-east Africa. No nearer pole from Siberia has been included in the calculation of the global APWP at 40 Ma. Moreover, the selection of several poles used in this global APWP is questionable. In particular, two poles from late Eocene sediments and volcanics from north-east Africa are used, while they likely underwent local clockwise rotation according to the original publication (Lofty & Van der Voo, 2007). Furthermore, inclination shallowing corrections were applied on results that were partly derived from volcanic rocks (Lofty & Van der Voo, 2007). Interestingly, when incorporating recent paleomagnetic results from Cenozoic hotspot volcanics in the tectonically stable eastern Australian continent (Hansma & Tohver, 2019), the paleomagnetic reference frame becomes once more similar to the hotspot reference frame with a more southern position of India relative to Asia (Fig. 3.10c; fig. 6.S3). Therefore, we chose to make all our plate reconstructions in the combined hotspot (0-70 Ma) and paleomagnetic (70-250 Ma) reference frame from the Matthews 2016 GPlates model (Torsvik et al., 2008; Matthews et al., 2016) instead of the outdated paleomagnetic reference frame. This puts India and Eurasia slightly more to the south at that time, providing a more logical comparison with our obtained 40 Ma position for the BT (Chapters 4 and 6).

References Chapter 3

Butler, R. F. (1992). Paleomagnetism: magnetic domains to geologic terranes (Vol. 319). Blackwell Scientific Publications Boston.

Cogne, J.-P., Besse, J., Chen, Y., & Hankard, F. (2013). A new Late Cretaceous to Present APWP for Asia and its implications for paleomagnetic shallow inclinations in Central Asia and Cenozoic Eurasian plate deformation. Geophysical Journal International, 192(3), 1000–1024. https://doi.org/10.1093/gji/ggs104

De Groot, L.V.; Krijgsman, W. (2015). Course: Paleomagnetism. Utrecht University

Dupont-Nivet, G., van Hinsbergen, D. J. J., & Torsvik, T. H. (2010). Persistently low Asian paleolatitudes: Implications for the India-Asia collision history: PERSISTENTLY LOW ASIAN PALEOLATITUDES. Tectonics, 29(5), n/a-n/a. https://doi.org/10.1029/2008TC002437

Fisher, R. (1953). Dispersion on a sphere. Proceedings of the Royal Society of London. Series A. Mathematical and Physical Sciences, 217(1130), 295–305.

Hansma, J., & Tohver, E. (2019). Paleomagnetism of Oligocene Hot Spot Volcanics in Central Queensland, Australia. Journal of Geophysical Research: Solid Earth, 124(7), 6280–6296. https://doi.org/10.1029/2019JB017639

Hrouda, F. (1982). Magnetic anisotropy of rocks and its application in geology and geophysics. Geophysical Surveys, 5(1), 37–82. https://doi.org/10.1007/BF01450244

Irving, E. (1958). Rock magnetism: a new approach to the problems of polar wandering and continental drift. In Continental Drift: a symposium on the present status of the continental drift hypothesis (held March 1956, proceedings reprinted 1963) (pp. 24-61).

King, R. F. (1955). The remanent magnetism of artificially deposited sediments. Geophysical Journal International, 7(s3), 115–134.

Kirschvink, J. L. (1980). The least-squares line and plane and the analysis of palaeomagnetic data. Geophysical Journal International, 62(3), 699–718.

Kissel, C., Barrier, E., Laj, C., & Lee, T.-Q. (1986). Magnetic fabric in “undeformed” marine clays from compressional zones. Tectonics, 5(5), 769–781.

Licht, A., Dupont-Nivet, G., Win, Z., Swe, H. H., Kaythi, M., Roperch, P., … Sein, K. (2019). Paleogene evolution of the Burmese forearc basin and implications for the history of India-Asia convergence. Geological Society of America Bulletin, 1(130), 20.

Lofty, H., & Van der Voo, R. (2007). Tropical northeast Africa in the middle-late Eocene: Paleomagnetism of the marine-mammals site and basalts in the Fayoum province. Egypt. J. Afr. Earth Sci, 47, 135–152.

Matthews, K. J., Maloney, K. T., Zahirovic, S., Williams, S. E., Seton, M., & Müller, R. D. (2016). Global plate boundary evolution and kinematics since the late Paleozoic. Global and Planetary Change, 146, 226–250. https://doi.org/10.1016/j.gloplacha.2016.10.002

McFadden, P. L., & McElhinny, M. (1988). The combined analysis of remagnetisation circles and direct observation in palaeomagnetism. Earth and Planetary Science Letters, 87, 161–172.

Roperch, P., & Taylor, G. K. (1986). The importance of gyromagnetic remanence in alternating field demagnetization. Some new data and experiments on GRM and RRM. Geophysical Journal International, 87(3), 949–965.

Tauxe, L., & Kent, D. V. (1984). Properties of a detrital remanence carried by haematite from study of modern river deposits and laboratory redeposition experiments. Geophysical Journal of the Royal Astronomical Society, 76(3), 543–561.

Tauxe, L., & Watson, G. S. (1994). The fold test: an eigen analysis approach. Earth and Planetary Science Letters, 122(3–4), 331–341.

Tauxe, L. (2010). Essentials of paleomagnetism. Univ of California Press.

Torsvik, T. H., Müller, R. D., Van der Voo, R., Steinberger, B., & Gaina, C. (2008). Global plate motion frames: Toward a unified model. Reviews of Geophysics, 46(3). https://doi.org/10.1029/2007RG000227

Torsvik, T. H., Van der Voo, R., Preeden, U., Mac Niocaill, C., Steinberger, B., Doubrovine, P. V., … Cocks, L. R. M. (2012). Phanerozoic polar wander, palaeogeography and dynamics. Earth-Science Reviews, 114(3–4), 325–368. https://doi.org/10.1016/j.earscirev.2012.06.007

Zijderveld, J. D. A. (1967). AC demagnetization of rocks: Analysis of results, Methods in Paleomagnetism DW Collinson, KM Creer, SK Runcorn, 254–286. Elsevier, New York.

Chapter 4: Burma Terrane part of the Trans-Tethyan arc during collision with India according to paleomagnetic data

The Wuntho Ranges, northern segment of the Wuntho-Popa Arc.
(Kawlin, Myanmar, Fieldwork November 2017)

Reference: Westerweel, J., Roperch, P., Licht, A., Dupont-Nivet, G., Win, Z., Poblete, F., … Aung, D. W. (2019). Burma Terrane part of the Trans-Tethyan arc during collision with India according to palaeomagnetic data. Nature Geoscience. https://doi.org/10.1038/s41561-019-0443-2

nature geoscience

ARTICLES

https://doi.org/10.1038/s41561-019-0443-2

Burma Terrane part of the Trans-Tethyan arc during collision with India according to palaeomagnetic data

Jan Westerweel[1*], Pierrick Roperch[1], Alexis Licht[2], Guillaume Dupont-Nivet[1,3], Zaw Win[4], Fernando Poblete[1,5], Gilles Ruffet[1], Hnin Hnin Swe[6], Myat Kai Thi[6] and Day Wa Aung[6]

[1] Geosciences Rennes, CNRS, University of Rennes 1, Rennes, France. [2] Dept. Earth and Space Sciences, University of Washington, Seattle, United States. [3] Department of Earth Sciences, Potsdam University, Potsdam, Germany. [4] Department of Geology, University of Shwebo, Shwebo, Myanmar. [5] Instituto de Ciencias de la Ingeniería, Universidad de O'Higgins, Rancagua, Chile. [6] Department of Geology, University of Yangon, Yangon, Myanmar.

[*] Corresponding author (e-mail: jan.westerweel@univ-rennes1.fr)

Abstract

Convergence between the Indian and Asian plates has reshaped large parts of Asia, changing regional climate and biodiversity. Yet geodynamic models fundamentally diverge on how convergence was accommodated since the India-Asia collision. Here we report paleomagnetic data from the Burma Terrane, at the eastern edge of the collision zone and famous for its Cretaceous amber biota, to better determine the evolution of the India-Asia collision. The Burma Terrane was part of a Trans-Tethyan island arc and stood at a near-equatorial southern latitude at ~95 Ma, suggesting island endemism for the Burmese amber biota. The Burma Terrane underwent significant clockwise rotation between ~80-50 Ma, causing its subduction margin to become hyper-oblique. Subsequently, it was translated northward on the Indian Plate, by an exceptional distance of at least 2000 km, along a dextral strike-slip fault system in the east. Our reconstructions are only compatible with geodynamic models involving a first collision of India with a near-equatorial Trans-Tethyan subduction system at ~60 Ma, followed by a later collision with the Asian margin.

Introduction

The Himalayan-Tibetan orogen, resulting from terrane amalgamation including the India-Asia collision, is commonly considered as a natural laboratory for continent-continent collisional systems. Yet the paleogeography of the India-Asia collision remains a controversial issue [1–5] with widely different competing geodynamic models. For decades, a simple model prevailed proposing that the Indian plate moved northward until collision of Greater India with the Asian margin in the Eocene [1,6]. However, updated information supporting a Paleocene (~58 Ma [7]) collision age, alongside tectonic constraints, put the Indian continent at near-equatorial latitude at that time, thousands of kilometers away from the southern Asian margin [3–6,8–13]. A Paleocene collision could still be compatible with this first model by assuming an Asian margin at low latitude (~10°N [6]), but this is invalidated by paleomagnetic data [14]. Alternatively, an extra-large continental Greater India [4] could explain a Paleocene collision age. However, this would require unrealistic continental subduction of India [4] and major shortening of the Asian margin, which can only be partly solved by lateral extrusion of Indochina blocks away from the collision zone [3,6,9–11], but remains much higher than accounted for by structural data [15]. Two new models have recently been proposed assuming: (1) the existence of an oceanic basin between India and Greater India that could have easily subducted after a first collision of Greater India with Asia at 58 Ma until a second collision of India with Asia in the Miocene [5,12], or (2) the existence of a Trans-Tethyan subduction system with which the Indian continent would firstly collide at ~60-50 Ma, before jointly colliding with Asia later in the Paleogene [2,16,17,8,13]. Such a double subduction zone may also better account for the rapid India-Asia convergence prior to the final collision [8].

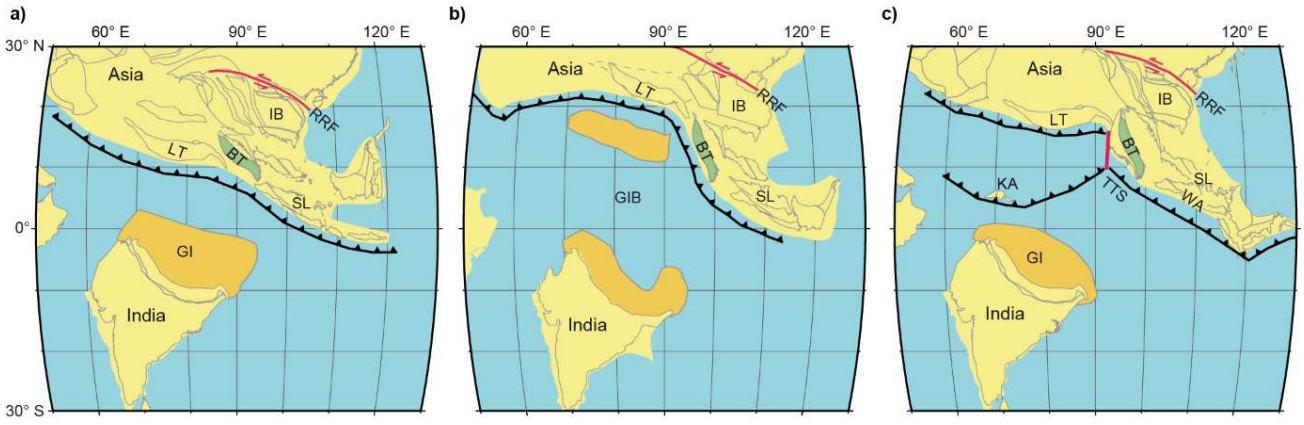

Figure 4.1: *Alternative plate reconstructions of India-Asia paleogeography at 60 Ma with GPlates (See also Methods): a) Reconstruction with a nearly linear subduction zone and significant extrusion of Indochina blocks [6,9]; b) Reconstruction with a Greater India Basin [5]; c) Reconstruction with a second Trans-Tethyan subduction zone [13]. Abbreviations: BT = Burma Terrane, GI(B) = Greater India (Basin),*

IB = Indochina Blocks, KA = Kohistan Arc, LT = Lhasa Terrane, RRF = Red River Fault (accommodating Indochina extrusion), SL = Sundaland, TTS = Trans-Tethyan subduction system, WA = Woyla Arc.

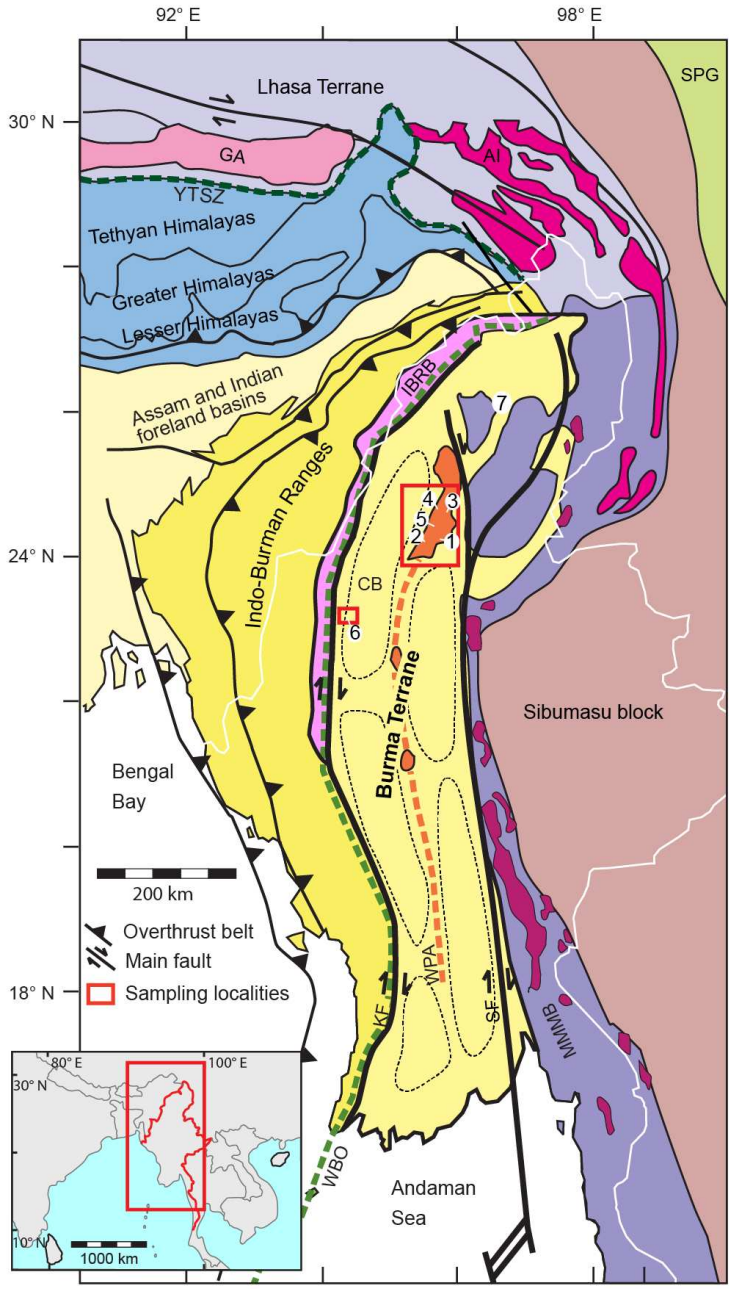

Figure 4.2: *Generalized Myanmar geologic map [21]. Localities: 1 = Kawlin, 2 = Pinlebu, 3 = Banmauk, 4 = Kyaung Le, 5 = Shinpa, 6 = Kalewa, 7 = Burmese ambers [18,19]. Abbreviations: AI = Cretaceous-Paleogene Asian intrusives, CB = Chindwin Basin, GA = Cretaceous Gangdese Arc, IBRB: Indo-Burman Ranges basement, KF = Kabaw Fault, MMMB = Mogok–Mandalay–Mergui Belt (including Jurassic Eastern Belt Ophiolites & Jade Belt Ophiolite), SF = Sagaing Fault, SPG = Songpan Ganze & Yangtze complexes, WBO = Cretaceous Western Belt Ophiolite, WPA = Wuntho-Popa Arc, YTSZ = Yarlung-Tsangpo Suture Zone. Dashed black lines: Central Myanmar Basins.*

The paleogeographic evolution of the Burma Terrane (BT, also named West Burma Block), at the eastern edge of the collision zone, is different in these geodynamic scenarios and therefore offers a way to determine the most realistic model (Fig. 4.1). For continental Greater India models [3,6,9,10], the BT is located at a relatively high latitude during the Paleogene, next to the Lhasa Terrane as part of a linear ~E-W oriented Asian margin. From this position, the BT is extruded towards its present-day location. Because the volcanic arc of the BT, the Wuntho-Popa Arc, was interpreted as the eastward continuation of the Gangdese magmatic arc required in these models, but is nowadays ~N-S oriented (Fig. 4.2), these models necessitate significant post-collisional clockwise rotation for the BT. In the oceanic Greater India models [12,5], the Asian margin is less deformed during the collision and the BT experienced little post-collisional rotation. Finally, the position of the BT is less constrained in Trans-Tethyan subduction models. Most reconstructions involving double subduction show the BT north of Sumatra [13,17], but it could have also been part of the Incertus Arc, the island arc of the Trans-Tethyan subduction system [17]. This would potentially allow a more southern latitude for the BT during early collisional times [2,8,13,16,17].

Presently, the paleogeographic evolution of the BT is virtually undocumented, despite being of critical importance for biodiversity studies, as the fossil amber from the BT harbours one of the most diverse and largest known records of Cretaceous biota [18,19]. Furthermore, the paleogeography of the BT is important for paleoenvironmental studies investigating Asian monsoonal history [20,21]. This study aims to fill this gap and solve these controversies by providing necessary constraints on the motion of the BT using new paleomagnetic and $^{40}Ar/^{39}Ar$ age data.

Geology of the Burma Terrane

The present-day BT geodynamic setting is characterized by hyper-oblique subduction of the Indian plate below the Burmese margin in the west and by the large-scale active dextral strike-slip Sagaing Fault in the east, resulting in a northward transcurrent motion of the terrane [22]. The western boundary of the BT is delineated by either another strike-slip fault, the Kabaw Fault, or the Naga Hills–Kaleymyo–Andaman Ophiolite (herein called the Western Belt Ophiolite) in the Indo-Burman Ranges (IBR) [23–26]. The IBR basement has been interpreted as a separate tectonic block, accreted to the BT in the Early Cretaceous [27] or Late Cretaceous - Paleogene [16,26], or an accretionary-type setting without block collision [21,28,29]. East of the BT, there is a complex succession of metamorphic rocks called the Mogok-Mandalay-Mergui Belt (MMMB), forming the boundary of the BT with the Shan Plateau (Sibumasu Block), alongside the Sagaing Fault and the Jade Belt ophiolite [26]. Total dextral displacement along this fault system has been estimated to be between 400 and 1100 km [30–32]. Prior to the development of the Sagaing Fault, there is evidence for dextral deformation along the Shan Scarp, directly east of the Sagaing fault [33,34], although the tectonic regime of Sibumasu was

predominantly sinistral [35]. Another example of earlier dextral deformation is the late Oligocene West Andaman Fault to the south [34].

The oldest exposed rocks of the BT are the low-grade metamorphic Triassic Shwedaung and Pane Chaung Formations, as well as the higher-grade Kanpetlet Schist. Both a late Mesozoic Gondwanan [36] or Cathaysian [37] origin has been suggested for the Pane Chaung Formation, based on detrital zircon U-Pb age data. The Burmese margin formed as an Andean-type setting during the Cretaceous, evidenced by Andean-type magmatic activity in the Wuntho-Popa Arc that today crops out in the middle of a wide belt of forearc/back-arc basins which developed contemporaneously: The Central Myanmar Basins (Fig. 4.2) [21,27,38]. Published U-Pb data indicate an early Late Cretaceous main phase of magmatism from 110-85 Ma, followed by a 70-40 Ma subordinate stage [39,24,27,40]. Our new 97-87 Ma $^{40}Ar/^{39}Ar$ dates in the Kanza Chaung Batholith, the main unit of the northern Wuntho-Popa Arc (Fig. 2, Supplementary Data 1), confirm this major magmatic phase. The Western Belt Ophiolite was likely emplaced during that time as well [21,27,28,38,41]. The Wuntho-Popa Arc has been correlated with the similar Gangdese Arc (Lhasa Terrane) [24,27]. The correlation of the Gangdese arc with the Wuntho-Popa arc, and the correlation of the Western Belt Ophiolite with the Tibetan Yarlung-Tsangpo Suture Zone [24,25], are key arguments for a similar to present-day latitude of the BT and a position next to the Lhasa Terrane prior to the India-Asia collision. However, the Mawgyi Andesite, which is most likely part of the Wuntho-Popa Arc (See Supplementary Information), has been correlated with the intra-oceanic mid-Cretaceous Woyla Arc (Sumatra) [17,23,30] as part of the Incertus Arc (Fig. 4.1) [17] with subsequent studies continuing this arc farther west by incorporating the Kohistan Arc (Pakistan) [8,13].

Paleomagnetic study

A paleomagnetic pole was obtained from a homoclinal sedimentary sequence in the upper Eocene (~38 Ma – from a dated tuff layer [21]) shallow-marine Yaw Formation in the Chindwin Basin, the northernmost forearc basin of Myanmar (Fig. 4.2). Furthermore, an early Late Cretaceous pole was obtained from five localities (Pinlebu, Shinpa, Banmauk, Kawlin and Kyaung Le) in the Wuntho Range, the predominantly Cretaceous (~110-85 Ma [24,40]) northern segment of the Wuntho-Popa Arc, where the volcano-sedimentary rocks of the Kondan Chaung Group are intruded by I-type intrusions (Kanza Chaung Batholith) and andesitic stocks (Mawgyi Andesite). Detailed information on the geology, paleomagnetic analysis and $^{40}Ar/^{39}Ar$ dating is provided in the Methods, Supplementary Information and Supplementary Data tables.

The upper Eocene samples are from mudstones and siderite beds with primary detrital or early-diagenetic magnetizations, mostly carried by magnetite. They yield well-defined antipodal normal and reverse polarity directions in coherent magnetozones, resulting in a mean with a north oriented

declination and shallow positive inclination in tectonic coordinates (Fig. 4.3a, Supplementary Data 1). This corresponds to a negligible rotation (4.6±3.5°) compared to stable Eurasia [42] and a near-equatorial latitude of 2.4±1.5°N. A slightly higher, but not significantly different 4.1±2.3°N paleolatitude is obtained after inclination shallowing corrections (See Supplementary Information). This result is corroborated by similarly low inclinations obtained from the siderite beds devoid of shallowing, and in general agreement with the low impact of inclination shallowing in sedimentary rocks at low latitudes, compared to mid to high latitudes [43].

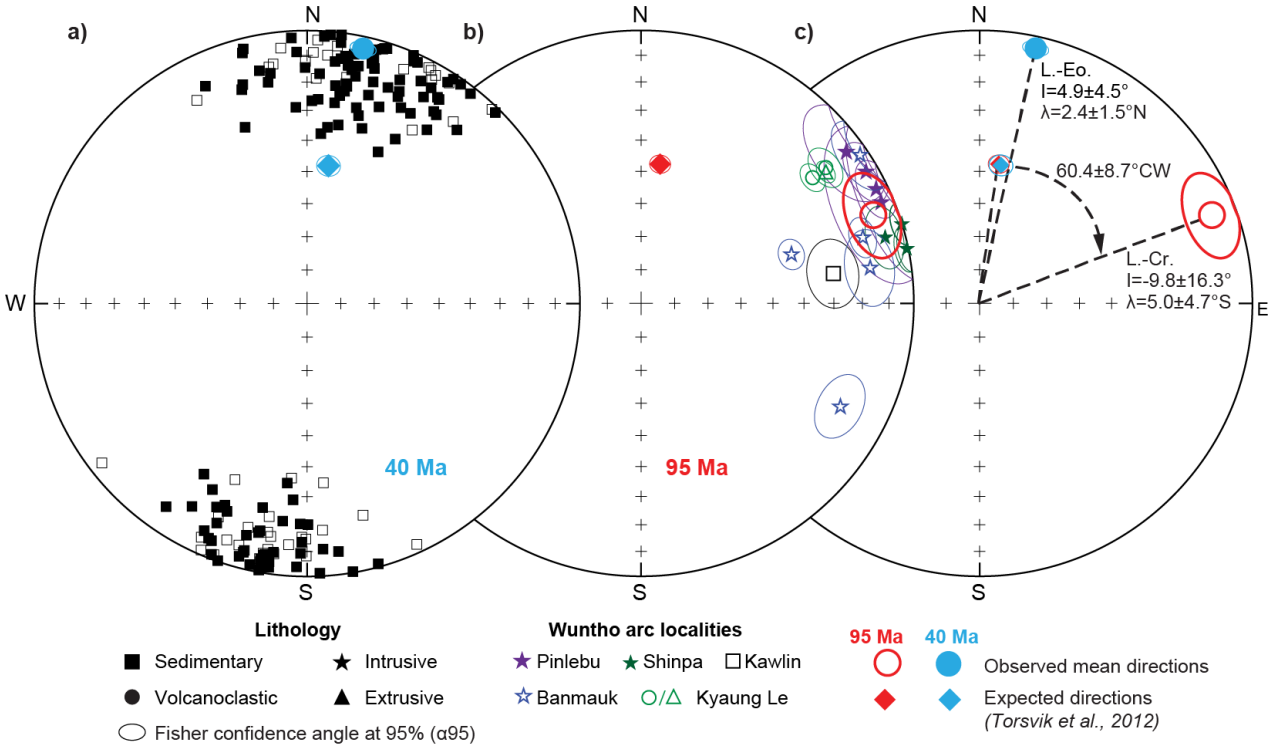

Figure 4.3: *Equal-area projections of interpretable paleomagnetic results: a) Tilt-corrected characteristic directions (squares) of samples from upper Eocene sediments from Kalewa and mean direction (blue); b) Early Late Cretaceous Wuntho Range site means with 95% confidence angles in in-situ coordinates, coloured by locality: Pinlebu (purple), Shinpa (dark green), Banmauk (blue), Kawlin (black) and Kyaung Le (green) and mean direction (red); c) Early Late Cretaceous/late Eocene (red/blue circles) final mean directions compared with the stable Eurasia APWP in the early Late Cretaceous/late Eocene (red/blue diamonds) [42]. Corresponding paleolatitudes and rotation magnitudes are indicated with 95% confidence angles. Open/closed symbols denote negative/positive inclinations.*

In early Late Cretaceous rocks from the Wuntho Range, reliable directions were obtained from sites of the Kanza Chaung Batholith (Pinlebu, Shinpa and Banmauk) with characteristic remanent magnetizations (ChRMs) carried by magnetite, as well as sites from the Kondan Chaung Group

(Kawlin, Kyaung Le), which were homogeneously magnetized during emplacement of the batholith, as shown by our petrologic observations and $^{40}Ar/^{39}Ar$ dates (See Supplementary Information). Blocking temperatures of the ChRMs are similar to the closure temperatures in $^{40}Ar/^{39}Ar$ dating, suggesting the age of magnetization of the Wuntho rocks to be around ~97-87 Ma, in accordance with existing Wuntho-Popa Arc U-Pb data [24,40]. A systematic trend to east-directed declinations and horizontal to slightly negative inclinations can be inferred from our data (Supplementary Data 1), despite significant differences in rock types and magnetic properties. Tilting is recorded by rocks of the Kondan Chaung Group, but occurred prior to the intrusion of the batholith in most cases. No field evidence for significant tilting of the Kanza Chaung Batholith was observed, in agreement with our anisotropy of magnetic susceptibility (AMS) data (See Supplementary Information). If we omit data from brecciated and non-homogeneously hydrothermally altered sites from the Mawgyi Andesite (Kawlin), and the westernmost sites from the Kondan Chaung Group (Kyaung Le), which were slightly tilted after acquiring their magnetization, we obtain a similar, but better defined overall final mean direction for the Wuntho Range from 16 sites (Fig. 4.3b, Supplementary Data 1). The mean corresponds to a slightly southern hemisphere paleolatitude of 5.0±4.7°S for the BT in the early Late Cretaceous and a significant clockwise rotation (60.4±8.7°) with respect to the expected direction from stable Eurasia [42]. This implies that most rotation of the BT occurred between the early Late Cretaceous and late Eocene with ~800 km of northward motion (Fig. 4.3c). Although we cannot discard a component of local rotation associated with dextral shear, the systematic rotation values and the regionally-coherent N-S trends of the batholith and main tectonic structures, suggest that the mean declination better reflects a wholesale rotation of the Wuntho rocks. The near-equatorial early Late Cretaceous – late Eocene paleolatitudes implied by our data are in stark contrast with previous studies, usually placing the BT close to its present-day location since the early Cenozoic, [17,24,34,26,27] and these data therefore have major tectonic implications.

Tectonic implications

The southern hemisphere shallow latitude at ~95 Ma for the Wuntho Arc is distant from the southern Asian margin and Indochina and is therefore best explained as having been formed above a near-equatorial Trans-Tethyan subduction system, as part of the Incertus Arc, with northward subducting Neo-Tethyan oceanic lithosphere (Fig. 4.4) [8]. This is further supported by the development of the Burmese margin as an Andean-type setting around that time (Late Cretaceous) and coeval emplacement of the Western Belt Ophiolite [21,24,27,28,38,40,41]. The Trans-Tethyan subduction system could have been partly intra-oceanic, possibly incorporating the Kohistan Arc which also formed at near-equatorial latitude [8,44]. Because the Indonesian Woyla Arc is interpreted as being

already accreted at ~90 Ma [17,23], we reconstructed a transform fault east of the BT, accommodating an earlier Woyla Arc - Sundaland collision.

The major clockwise rotation of the BT between 95 and 40 Ma (Fig. 4.4) may be either linked to the accretion of the BT to the margin of southern Sibumasu/northern Sundaland or the collision of India with the Trans-Tethyan subduction system. In support of the latter possibility is that in most models with Trans-Tethyan subduction [8,13,16], decreasing convergence rates between India and Asia at ~60-50 Ma are associated with collision of the (Greater) Indian continent with the arc. At the eastern end of this collision, thin Indian continental crust may thus have interacted with the BT, causing its clockwise rotation [45]. However, the exact timing and mechanism of this rotation needs to be refined with future research.

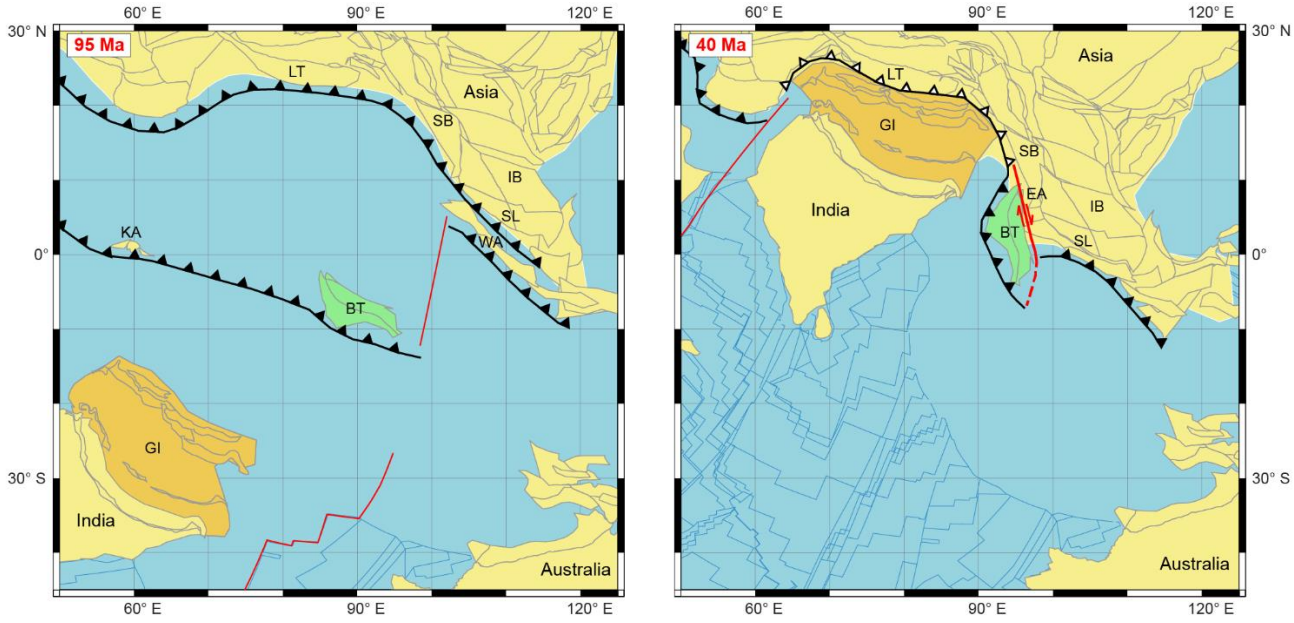

Figure 4.4: *Reconstructions of the Burma Terrane and Asia at 95 Ma (left) and 40 Ma (right) with GPlates (See also Methods). Abbreviations: BT = Burma Terrane, EA = Eastern Andaman Basins, IB = Indochina Blocks, GI = Greater India, KA = Kohistan Arc, LT = Lhasa Terrane, SB = Sibumasu Block, SL = Sundaland, WA = Woyla Arc.*

Since the late Eocene (~38 Ma [21]), our results indicate a significant ~2000 km northward motion, coeval with the motion of India (Fig. 4.4), during a period when Indochina is extruded towards the south-east [46–49]. This suggests that the northward motion of the BT was coupled with the Indian Plate. Our paleomagnetic data indicate that the Burmese subduction margin was already oriented approximately N-S in the late Eocene, such that subduction of the Indian Plate beneath the BT was already hyper-oblique. This hyper-obliquity provides a mechanism for the full-partitioning of the Burmese subduction margin relative to Indochina and its coupling with the Indian motion; it is also

consistent with the inferred onset of pull-apart subsidence in the Chindwin Basin [21] and a significant decrease in Wuntho-Popa Arc magmatism at ~38 Ma [27,40]. Furthermore, the coeval motion of the BT and India suggests that dextral wrenching within the IBR has not been important until the Neogene.

Hence, the northward motion of the BT since the late Eocene requires a major dextral strike-slip system east of the BT. However, the ~2000 km northward motion indicated by our paleomagnetic data is much more than the ~400 km of motion estimated along the active dextral Sagaing Fault at the eastern margin of the BT [31]. Furthermore, the age of the Sagaing Fault - Quaternary, Neogene, or older - remains debated [30–32]. A precursor dextral strike-slip system is thus required by our data, pathway and location of which remains enigmatic and has probably been obscured by posterior activity of the Sagaing Fault and opening of the Andaman Sea. Potential remnants of this precursor strike-slip system are an early segment of the Sagaing Fault [33,34] or the Oligocene West Andaman Fault [34]. The latter could have effectively separated the BT to its west from the developing Eastern Andaman Basins and the predominantly sinistral tectonic regime of Sibumasu to its east, as the BT moved northward and passed west of these features (Fig. 4.4) [32,34,35]. This separation potentially explains why late Eocene sedimentary infill of the Central Myanmar Basins was predominantly derived from an Andean-type arc, likely the Wuntho-Popa Arc, with an increasing contribution of older metamorphic detritus in the Oligocene – Miocene [21] as the BT moved closer to Sibumasu and the eastern Himalayan syntaxis.

Additionally, the late Eocene low paleolatitude for the BT demonstrates that an India-BT collision next to the Lhasa Terrane [2] is impossible. Instead, the near-equatorial latitude of the BT provides the space and free border for the lateral extrusion of the Tengshong and Baoshan Blocks which rotated clockwise by ~40-70° [47,48] and, to a minor extent, the Indochina Block that rotated ~15-20°, all of which occurred mainly during the Oligocene – Miocene. This is the period of major sinistral deformation along the main shear zones separating these blocks [46,49]. The northward motion and later emplacement without rotation of the BT also accounts for the striking difference between the linear N-S orientation of the Sagaing Fault and - directly to the west- the curvilinear sinistral faults (Gaoligong, Wanding, Nanting) associated with the clockwise rotations in the Tengshong and Baoshan Blocks.

Beyond geodynamics, our results suggest that the BT was isolated as part of the Incertus Arc at the time of deposition of the prolific Cretaceous Burmese fossil ambers, which raises questions about the potential endemic character of the amber biota and their connection with species from India, Gondwana and SE Asia [18,19]. From a paleoenvironmental perspective, our near-equatorial paleolatitudes for the BT are surprising, considering the evidence for strongly seasonal climate in

Myanmar in the Eocene [20]. Strong seasonality at Eocene equatorial latitudes in SE Asia is corroborated by independent evidence from paleoclimatic data from Java [50]. Paleomagnetic and paleoenvironmental data can only be reconciled with a massive seasonal migration of the Intertropical Convergence Zone over SE Asia, confirming well-marked South Asian monsoons during the Eocene [20], although future climate models incorporating our new reconstructions need to verify this.

The foremost conclusion from our paleomagnetic results is that they are incompatible with both continental and oceanic Greater India models and are best interpreted in a geodynamic framework with a Trans-Tethyan subduction system accommodating India-Asia convergence. As part of this system, the BT was a segment of the Incertus Arc, when Neo-Tethyan subduction started in the Late Cretaceous. In the period including the early Paleogene collision of India with the Trans-Tethyan subduction system, the BT rotated ~60° clockwise, and then moved northward at least 2000 km since ~38 Ma, as part of the Indian Plate, along a dextral strike-slip system until it reached its present-day position. Hence, our findings provide much needed evidence to settle a longstanding geodynamic debate on the India-Asia collision and the existence of a Trans-Tethyan subduction system. Furthermore, they pave the way to reinterpreting regional structural and paleogeographic data by taking into account the near-equatorial position for the BT during the Late Cretaceous to Eocene as part of this system.

References Chapter 4

1. Molnar, P. & Tapponnier, P. Cenozoic Tectonics of Asia: Effects of a Continental Collision: Features of recent continental tectonics in Asia can be interpreted as results of the India-Eurasia collision. *Science* **189**, 419–426 (1975).

2. Aitchison, J. C., Ali, J. R. & Davis, A. M. When and where did India and Asia collide? *J. Geophys. Res.* **112**, (2007).

3. Replumaz, A., Negredo, A. M., Guillot, S. & Villaseñor, A. Multiple episodes of continental subduction during India/Asia convergence: Insight from seismic tomography and tectonic reconstruction. *Tectonophysics* **483**, 125–134 (2010).

4. Ingalls, M., Rowley, D. B., Currie, B. & Colman, A. S. Large-scale subduction of continental crust implied by India–Asia mass-balance calculation. *Nat. Geosci.* **9**, 848–853 (2016).

5. van Hinsbergen, D. J. J. *et al.* Reconstructing Greater India: Paleogeographic, kinematic, and geodynamic perspectives. *Tectonophysics* (2018). doi:10.1016/j.tecto.2018.04.006

6. Cogne, J.-P., Besse, J., Chen, Y. & Hankard, F. A new Late Cretaceous to Present APWP for Asia and its implications for paleomagnetic shallow inclinations in Central Asia and Cenozoic Eurasian plate deformation. *Geophys. J. Int.* **192**, 1000–1024 (2013).

7. Hu, X. *et al.* The timing of India-Asia collision onset – Facts, theories, controversies. *Earth-Sci. Rev.* **160**, 264–299 (2016).

8. Jagoutz, O., Royden, L., Holt, A. F. & Becker, T. W. Anomalously fast convergence of India and Eurasia caused by double subduction. *Nat. Geosci.* **8**, 475–478 (2015).

9. Replumaz, A., Guillot, S., Villaseñor, A. & Negredo, A. M. Amount of Asian lithospheric mantle subducted during the India/Asia collision. *Gondwana Res.* **24**, 936–945 (2013).

10. Royden, L. H., Burchfiel, B. C. & van der Hilst, R. D. The Geological Evolution of the Tibetan Plateau. *Science* **321**, 1054–1058 (2008).

11. Tapponnier, P., Peltzer, G., Le Dain, A. Y., Armijo, R. & Cobbold, P. Propagating extrusion tectonics in Asia: New insights from simple experiments with plasticine. *Geology* **10**, 611–616 (1982).

12. Van Hinsbergen, D. J. *et al.* Greater India Basin hypothesis and a two-stage Cenozoic collision between India and Asia. *Proc. Natl. Acad. Sci.* **109**, 7659–7664 (2012).

13. Zahirovic, S., Seton, M. & Müller, R. D. The Cretaceous and Cenozoic tectonic evolution of Southeast Asia. *Solid Earth* **5**, 227–273 (2014).

14. Dupont-Nivet, G., Lippert, P. C., Van Hinsbergen, D. J. J., Meijers, M. J. M. & Kapp, P. Palaeolatitude and age of the Indo-Asia collision: palaeomagnetic constraints: Palaeolatitude and age of the Indo-Asia collision. *Geophys. J. Int.* **182**, 1189–1198 (2010).

15. van Hinsbergen, D. J. J. *et al.* Restoration of Cenozoic deformation in Asia and the size of Greater India. *Tectonics* **30**, n/a-n/a (2011).

16. Gibbons, A. D., Zahirovic, S., Müller, R. D., Whittaker, J. M. & Yatheesh, V. A tectonic model reconciling evidence for the collisions between India, Eurasia and intra-oceanic arcs of the central-eastern Tethys. *Gondwana Res.* **28**, 451–492 (2015).

17. Hall, R. Late Jurassic–Cenozoic reconstructions of the Indonesian region and the Indian Ocean. *Tectonophysics* **570–571**, 1–41 (2012).

18. Poinar, G. Burmese amber: evidence of Gondwanan origin and Cretaceous dispersion. *Hist. Biol.* 1–6 (2018). doi:10.1080/08912963.2018.1446531

19. Grimaldi, D. A., Engel, M. S. & Nascimbene, P. C. Fossiliferous Cretaceous Amber from Myanmar (Burma): Its Rediscovery, Biotic Diversity, and Paleontological Significance. *Am. Mus. Novit.* **3361**, 1–71 (2002).

20. Licht, A. *et al.* Asian monsoons in a late Eocene greenhouse world. *Nature* **513**, 501–506 (2014).

21. Licht, A. *et al.* Paleogene evolution of the Burmese forearc basin and implications for the history of India-Asia convergence. *Geol. Soc. Am. Bull.* **1**, 20 (2018).

22. Socquet, A. *et al.* India and Sunda plates motion and deformation along their boundary in Myanmar determined by GPS. *J. Geophys. Res. Solid Earth* **111**, B05406 (2006).

23. Barber, A. J. & Crow, M. J. Structure of Sumatra and its implications for the tectonic assembly of Southeast Asia and the destruction of Paleotethys. *Isl. Arc* **18**, 3–20 (2009).

24. Mitchell, A., Chung, S.-L., Oo, T., Lin, T.-H. & Hung, C.-H. Zircon U–Pb ages in Myanmar: Magmatic–metamorphic events and the closure of a neo-Tethys ocean? *J. Asian Earth Sci.* **56**, 1–23 (2012).

25. Liu, C.-Z. *et al.* Tethyan suturing in Southeast Asia: Zircon U-Pb and Hf-O isotopic constraints from Myanmar ophiolites. *Geology* **44**, 311–314 (2016).

26. Searle, M. P. *et al.* Chapter 12 Tectonic and metamorphic evolution of the Mogok Metamorphic and Jade Mines belts and ophiolitic terranes of Burma (Myanmar). *Geol. Soc. Lond. Mem.* **48**, 261–293 (2017).

27. Zhang, P. *et al.* Structures, uplift, and magmatism of the Western Myanmar Arc: Constraints to mid-Cretaceous-Paleogene tectonic evolution of the western Myanmar continental margin. *Gondwana Res.* **52**, 18–38 (2017).

28. Fareeduddin, A. & Dilek, Y. Structure and petrology of the Nagaland-Manipur Hill ophiolitic mélange zone. *NE India Foss. Tethyan Subduction Channel India-Burma Plate Bound. Episodes* **38**, 298–314 (2015).

29. Zhang, J. *et al.* Multiple alternating forearc- and backarc-ward migration of magmatism in the Indo-Myanmar Orogenic Belt since the Jurassic: Documentation of the orogenic architecture of eastern Neotethys in SE Asia. *Earth-Sci. Rev.* **185**, 704–731 (2018).

30. Mitchell, A. H. G. Cretaceous–Cenozoic tectonic events in the western Myanmar (Burma)–Assam region. *J. Geol. Soc.* **150**, 1089–1102 (1993).

31. Morley, C. K. Syn-kinematic sedimentation at a releasing splay in the northern Minwun Ranges, Sagaing Fault zone, Myanmar: significance for fault timing and displacement. *Basin Res.* **29**, 684–700 (2017).

32. Morley, C. K. & Arboit, F. Dating the onset of motion on the Sagaing fault: Evidence fromdetrital zircon and titanite U-Pb geochronology from the NorthMinwun Basin, Myanmar. *Geology* (2019). doi:10.1130/G46321.1

33. Bertrand, G. & Rangin, C. Tectonics of the western margin of the Shan plateau (central Myanmar): implication for the India–Indochina oblique convergence since the Oligocene. *J. Asian Earth Sci.* **21**, 1139–1157 (2003).

34. Morley, C. K. Chapter 4 Cenozoic rifting, passive margin development and strike-slip faulting in the Andaman Sea: a discussion of established v. new tectonic models. *Geol. Soc. Lond. Mem.* **47**, 27–50 (2017).

35. Morley, C. K. Nested strike-slip duplexes, and other evidence for Late Cretaceous–Palaeogene transpressional tectonics before and during India–Eurasia collision, in Thailand, Myanmar and Malaysia. *J. Geol. Soc.* **161**, 799–812 (2004).

36. Yao, W. *et al.* Origin and tectonic evolution of upper Triassic Turbidites in the Indo-Burman ranges, West Myanmar. *Tectonophysics* **721**, 90–105 (2017).

37. Sevastjanova, I. *et al.* Myanmar and Asia united, Australia left behind long ago. *Gondwana Res.* **32**, 24–40 (2016).

38. Pivnik, D. A. *et al.* Polyphase Deformation in a Fore-Arc/Back-Arc Basin, Salin Subbasin, Myanmar (Burma). *AAPG Bull.* **82(10)**, 1837–1856 (1998).

39. Gardiner, N. J. *et al.* Contrasting Granite Metallogeny through the Zircon Record: A Case Study from Myanmar. *Sci. Rep.* **7**, (2017).

40. Wang, J.-G., Wu, F.-Y., Tan, X.-C. & Liu, C.-Z. Magmatic evolution of the Western Myanmar Arc documented by U–Pb and Hf isotopes in detrital zircon. *Tectonophysics* **612–613**, 97–105 (2014).

41. Singh, A. K. *et al.* Evidence of Mid-ocean ridge and shallow subduction forearc magmatism in the Nagaland-Manipur ophiolites, northeast India: constraints from mineralogy and geochemistry of gabbros and associated mafic dykes. *Geochemistry* **76**, 605–620 (2016).

42. Torsvik, T. H. *et al.* Phanerozoic polar wander, palaeogeography and dynamics. *Earth-Sci. Rev.* **114**, 325–368 (2012).

43. Arason, P. & Levi, S. Models of inclination shallowing during sediment compaction. *J. Geophys. Res.* **95**, 4481 (1990).

44. Zaman, H. & Torii, M. Palaeomagnetic study of Cretaceous red beds from the eastern Hindukush ranges, northern Pakistan: palaeoreconstruction of the Kohistan-Karakoram composite unit before the India-Asia collision. *Geophys. J. Int.* **136**, 719–738 (1999).

45. Rangin, C., Maurin, T. & Masson, F. Combined effects of Eurasia/Sunda oblique convergence and East-Tibetan crustal flow on the active tectonics of Burma. *J. Asian Earth Sci.* **76**, 185–194 (2013).

46. Leloup, P. H., Tapponnier, P., Lacassin, R. & Searle, M. P. Discussion on the role of the Red River shear zone, Yunnan and Vietnam, in the continental extrusion of SE Asia Journal, Vol. 163, 2006, 1025–1036. *J. Geol. Soc.* **164**, 1253–1260 (2007).

47. Li, S., van Hinsbergen, D. J. J., Deng, C., Advokaat, E. L. & Zhu, R. Paleomagnetic Constraints From the Baoshan Area on the Deformation of the Qiangtang-Sibumasu Terrane Around the Eastern Himalayan Syntaxis. *J. Geophys. Res. Solid Earth* **123**, 977–997 (2018).

48. Tong, Y.-B. *et al.* Internal crustal deformation in the northern part of Shan-Thai Block: New evidence from paleomagnetic results of Cretaceous and Paleogene redbeds. *Tectonophysics* **608**, 1138–1158 (2013).

49. Wang, Y. *et al.* Kinematics and 40Ar/39Ar geochronology of the Gaoligong and Chongshan shear systems, western Yunnan, China: Implications for early Oligocene tectonic extrusion of SE Asia. *Tectonophysics* **418**, 235–254 (2006).

50. Evans, D., Müller, W., Oron, S. & Renema, W. Eocene seasonality and seawater alkaline earth reconstruction using shallow-dwelling large benthic foraminifera. *Earth Planet. Sci. Lett.* **381**, 104–115 (2013).

Acknowledgements

This research was primarily funded by the ERC consolidator grant MAGIC 649081 to G.D.-N.. We thank Catherine Kissel for the use of the AGM vibrating magnetometer at the LSCE paleomagnetic laboratory, France. Furthermore, we thank Loic Joanny and Francis Gouttefangeas for their help with SEM data acquisition. We are grateful to P. Cullerier and A. Bernard for their help in the laboratory. We thank Eldert Advokaat, Frédéric Fluteau, Stéphane Guillot, Erwan Hallot, Claude Rangin, Anne Replumaz, Mike Searle and Douwe van Hinsbergen for prolific discussions in the course of this study.

Finally, we are grateful to Chris Morley, Robert Hall and John Geissman for their constructive reviews, which helped to clarify our data presentation and model.

Author contributions

P.R., A.L. and G.D.-N conceived the project. J.W., P.R., A.L., G.D.-N., Z.W., F.P., H.H.S., M.K.T. and D.W.A. participated in the sampling. J.W. and P.R. performed the paleomagnetic analysis. G.R. performed the radiometric analysis. J.W., P.R. and F.B. built the GPlates model. J.W., P.R, A.L. and G.D.-N. wrote the manuscript with contributions from other authors.

Competing interests

The authors declare no competing financial interests.

Methods

Paleomagnetic sampling

Conventional paleomagnetic core plug samples were obtained from two localities in northern Myanmar, both part of the Burma Terrane (BT). Sampling and orientation of the samples were done using standard paleomagnetic field equipment and procedures with both magnetic and sun compasses. The first locality consists of the early Late Cretaceous intrusive, extrusive, volcaniclastic and sedimentary rocks of the Wuntho Range, near the towns of Kawlin, Pinlebu, Shinpa, Banmauk and Kyaung Le, and the second locality of upper Eocene sedimentary rocks in the Chindwin forearc basin, near the town of Kalewa. A detailed geologic setting, including regional maps, is provided in the Supplementary Information.

We sampled 19 sites in intrusive rocks, 13 sites in extrusive rocks and 9 sites in sedimentary rocks of early Late Cretaceous age in the Wuntho Range, mostly drilled in recently exposed quarries or rivers, providing fresh samples with almost no weathering. Most sites in intrusive rocks were drilled around Pinlebu, Shinpa and Banmauk in the western and northern part of the study area. These sites belong to the regional I-type Kanza Chaung Batholith, which constitutes the main component of the Wuntho Range. Near Kawlin in the southern part of the study area, 11 sites in extrusive rocks of the Mawgyi Andesite Formation were established. The volcanic rocks are often massive or brecciated; hence they did not yield clear bedding orientations. Apart from these sites in andesites, two sites in sandstones from the volcano-sedimentary Kondan Chaung Group with a clearly observable bedding and one undefined stock were sampled near Kawlin. At Kyaung Le in the northernmost part of the study area, all sampled rocks belong to the Kondan Chaung Group, and consist of nine sites in

sedimentary and volcaniclastic rocks, as well as one rhyodacitic unit and finally one site in undefined extrusive rocks.

In the Chindwin basin, 520 samples were collected from the upper Eocene shallow-marine Yaw Formation in a continuous homoclinal Cenozoic sedimentary section near Kalewa, as well as two additional sites. Most of these samples are mudstones and sandstones, and we also collected several samples in siderite-rich carbonate beds intercalated in the mudstones.

Paleomagnetic analysis

Natural Remanent Magnetizations (NRMs) were measured on a 2G cryogenic magnetometer hosted in a magnetically shielded room at the University of Rennes 1. Stepwise demagnetization was used to isolate their Characteristic Remanent Magnetization (ChRM) components, using either thermal demagnetization, with increments of 20-50°C up to 680°C, or 3-axis Alternating Field (AF) demagnetization, with increments of 2.5-10 mT up to 120 mT. During the AF demagnetization, Gyro Remanent Magnetizations (GRMs) were cancelled by measuring the magnetization after each axis of AF demagnetization [51]. Samples with interpretable components were grouped per site after isolating their ChRM using principal component analysis [52], and when necessary a great-circle approach [53]. Subsequently, mean directions and corresponding statistical parameters were calculated per site and finally per locality using Fisher statistics [54,55]. Whenever possible, the fold test [56] was utilized to investigate whether the magnetization was pre- or post-tectonic in origin. To check whether normal and reverse polarities from the same locality are antiparallel, the classic coordinate bootstrap reversal test was used [57]. Finally, due to the lack of volcanic rocks in the upper Eocene sedimentary section, we checked for inclination shallowing in the results from this area, using several approaches including the classic Elongation versus Inclination (E/I) method [58–60], and by assuming that the sedimentary package consists of uniform rigid particles, which rotate during burial and attending compaction [61].

In addition to obtaining mean directions, the magnetic properties of the samples were investigated using several methods. After each thermal demagnetization step, the bulk magnetic susceptibility of the samples was measured. To investigate the mineralogy and magnetic properties for a selection of samples, we measured mass-normalized bulk magnetic susceptibility curves with increasing temperature steps up to 580 °C on a KLY3-CS3 AGICO kappabridge, as well as magnetic hysteresis loops on a MicroMag vibrating sample magnetometer. To further identify the possible effect of a magnetic fabric on the remanent magnetization for the different rocks, anisotropy of magnetic susceptibility (AMS) was determined for most samples on a KLY3S AGICO kappabridge. In highly anisotropic intrusive igneous rocks, Thermal Remanent Magnetization (TRM) vectors may be

deflected from the direction of the field upon cooling below the Curie point of magnetite, which is the main magnetic carrier in those rocks. However, most of the AMS is likely dictated by multidomain magnetite, yet the magnetic carriers of the remanent magnetization (finest grained magnetite) may have a different magnetic fabric. For this reason, we investigated the anisotropy of remanent magnetization (ARM) in selected samples of intrusive rocks. TRM anisotropy correction is common in archeomagnetism, but we did not attempt this, because it requires heating of the samples above 580°C (general NRM unblocking temperature), and alteration is likely to occur after heating to higher temperatures. Anisotropy of isothermal remanent magnetization (IRM) was performed on selected samples instead. IRM acquisition was done on x,-x,y,-y,z,-z at 600 mT, well above the saturation field of magnetite (250 mT). After each measurement, the sample was AF demagnetized at 20 mT to remove the lowest magnetic coercivity fraction. In most cases, 90% of the full IRM was randomized at 20 mT.

A detailed description of the various ChRM characteristics, mean calculations, tests and magnetic properties is given per locality in the Supplementary Information. The paleomagnetic results per site and per locality is given in Supplementary Data 1, while the results all used samples are listed in Supplementary Data 2.

Petrology

Polished thin sections were made on selected samples from different lithologies for observation under an optical microscope in transmitted light and reflected light. The samples were then analysed with a scanning electron microscope (SEM - JEOL JSM 7100F with energy dispersive X-ray spectroscopy - Oxford EDS/EBSD) at the CMEBA - ScanMAT platform (University of Rennes 1). Our petrologic observations are described in the Supplementary Information.

$^{40}Ar/^{39}Ar$ dating

There are only a few available U-Pb age data available for the Wuntho Range volcanic complex [24,39]. Therefore, we carried out $^{40}Ar/^{39}Ar$ dating on 14 samples from our paleomagnetic sites in order to better understand the ages of these rocks and their resulting ChRMs.

Samples were analysed with an $^{40}Ar/^{39}Ar$ laser probe and a Map 215 mass spectrometer. Analyses were performed on mm-sized grains of single biotite or amphibole crystals, carefully handpicked under a binocular microscope from crushed rocks. For samples with fine-grained matrix from which it was not possible to extract biotites or amphiboles, experiments were performed on whole-rock samples.

Irradiation of samples was performed at McMaster Nuclear Reactor (Hamilton, Ontario, Canada) in the 8F facility and lasted 66.667 h with a global efficiency (J/h) of 9.767 x 10^{-5} h^{-1}. The irradiation standard was sanidine TCRs (28.608 ± 0.033 Ma [62–64]).

Apparent age errors are plotted at the 1σ level and do not include the errors on the $^{40}Ar^{*}/^{39}Ar_{K}$ ratio and age of the monitor and decay constant. Plateau ages were calculated if 70% or more of the $^{39}Ar_{K}$ was released in at least three or more contiguous steps, the apparent ages of which agreeing to within 1σ of the integrated age of the plateau segment. Pseudo-plateau ages can be defined with less than 70% of the $^{39}Ar_{K}$ released and possibly less than three contiguous steps. The errors on the $^{40}Ar^{*}/^{39}Ar_{K}$ ratio and age of the monitor and decay constant are included in the final calculation of the error margins on the (pseudo-)plateau ages.

Analytical data and parameters used for calculations (e.g. isotopic ratios measured on K, Ca and Cl pure salts; mass discrimination; atmospheric argon ratios; J parameter; decay constants) and reference sources are available in Supplementary Data 3.

Plate model

For our final geodynamic model, we used the global rotations and continental polygons from the Matthews 2016 GPlates model [65,66] as a template. From this template, we modified the tectonic history of the BT to reflect our paleomagnetic results. Furthermore, the positions and paleogeography of Greater India, Indochina, Kohistan, Lhasa, Sumatra and Woyla were configured to better reflect more recent studies [8,67,68]. In Figure 4.1b, the global reconstruction with the Greater India basin hypothesis is based on a different set of poles of rotations [5]. All plate tectonic reconstructions were made in the combined hotspot (0-70 Ma) and paleomagnetic (70-250 Ma) reference frame that is also used in the Matthews 2016 GPlates model [66,69]. See Supplementary Information for a detailed discussion on the choice for this reference frame.

Data availability

The authors declare that all data supporting the findings of this study are available within the main article, its Supplementary Information, Supplementary Data 1 (paleomagnetic mean directions), Supplementary Data 2 (paleomagnetic data per sample) and Supplementary Data 3 ($^{40}Ar/^{39}Ar$ data and parameters).

References Chapter 4 - Methods

51. Roperch, P. & Taylor, G. K. The importance of gyromagnetic remanence in alternating field demagnetization. Some new data and experiments on GRM and RRM. *Geophys. J. Int.* **87**, 949–965 (1986).

52. Kirschvink, J. L. The least-squares line and plane and the analysis of palaeomagnetic data. *Geophys. J. Int.* **62**, 699–718 (1980).

53. McFadden, P. L. & McElhinny, M. The combined analysis of remagnetisation circles and direct observation in palaeomagnetism. *Earth Planet. Sci. Lett.* **87**, 161–172 (1988).

54. Butler, R. F. *Paleomagnetism: magnetic domains to geologic terranes*. **319**, (Blackwell Scientific Publications Boston, 1992).

55. Fisher, R. Dispersion on a sphere. *Proc. R. Soc. Lond. Ser. Math. Phys. Sci.* **217**, 295–305 (1953).

56. Tauxe, L. & Watson, G. S. The fold test: an eigen analysis approach. *Earth Planet. Sci. Lett.* **122**, 331–341 (1994).

57. Tauxe, L. *Essentials of paleomagnetism*. (Univ of California Press, 2010).

58. King, R. F. The remanent magnetism of artificially deposited sediments. *Geophys. J. Int.* **7**, 115–134 (1955).

59. Tauxe, L. & Kent, D. V. A simplified statistical model for the geomagnetic field and the detection of shallow bias in paleomagnetic inclinations: was the ancient magnetic field dipolar. *Timescales Paleomagn. Field* **145**, 101–116 (2004).

60. Tauxe, L., Kodama, K. P. & Kent, D. V. Testing corrections for paleomagnetic inclination error in sedimentary rocks: a comparative approach. *Phys. Earth Planet. Inter.* **169**, 152–165 (2008).

61. Cogné, J.-P. Contribution a l'étude paléomagnétique des roches déformées. (Université Rennes 1, 1987).

62. Renne, P. R. *et al.* Intercalibration of standards, absolute ages and uncertainties in 40Ar/39Ar dating. *Chem. Geol.* **145**, 117–152 (1998).

63. Renne, P. R., Mundil, R., Balco, G., Min, K. & Ludwig, K. R. Joint determination of 40K decay constants and 40Ar∗/40K for the Fish Canyon sanidine standard, and improved accuracy for 40Ar/39Ar geochronology. *Geochim. Cosmochim. Acta* **74**, 5349–5367 (2010).

64. Renne, P. R., Balco, G., Ludwig, K. R., Mundil, R. & Min, K. Response to the comment by W.H. Schwarz et al. on "Joint determination of 40K decay constants and 40Ar∗/40K for the Fish Canyon sanidine standard, and improved accuracy for 40Ar/39Ar geochronology" by P.R. Renne et al. (2010). *Geochim. Cosmochim. Acta* **75**, 5097–5100 (2011).

65. Müller, R. D. *et al.* GPlates: Building a virtual Earth through deep time. *Geochem. Geophys. Geosystems* **19**, 2243–2261 (2018).

66. Matthews, K. J. *et al.* Global plate boundary evolution and kinematics since the late Paleozoic. *Glob. Planet. Change* **146**, 226–250 (2016).

67. Advokaat, E. L. *et al.* Cenozoic Rotation History of Borneo and Sundaland, SE Asia Revealed by Paleomagnetism, Seismic Tomography, and Kinematic Reconstruction. *Tectonics* (2018). doi:10.1029/2018TC005010

68. Li, S. *et al.* Paleomagnetic constraints on the Mesozoic-Cenozoic paleolatitudinal and rotational history of Indochina and South China: Review and updated kinematic reconstruction. *Earth-Sci. Rev.* **171**, 58–77 (2017).

69. Torsvik, T. H., Müller, R. D., Van der Voo, R., Steinberger, B. & Gaina, C. Global plate motion frames: Toward a unified model. *Rev. Geophys.* **46**, (2008).

Supplementary Information

1. Geological summary

1.1. Myanmar

The present-day tectonic setting of Myanmar is characterized by active hyper-oblique subduction of Indian crust beneath the Burmese margin [1–3]. Within this setting, two broadly north–south oriented major blocks are often distinguished: The Burma Terrane (BT), and the Shan Plateau on the Sibumasu Block (Fig. 4.2). The BT has been called West Burma Block before, but we prefer the name Burma Terrane, because its tectonic history is significantly different from surrounding features as explained below. The collision age of the BT with the Sibumasu Block is not well constrained and even the existence of a suture between both blocks is challenged [4,5]. The western border of the Sibumasu Block presents a complex belt of metamorphic rocks, called the Mogok–Mandalay–Mergui Belt (MMMB) which records two main metamorphic events: A late Cretaceous – early Paleocene phase of metamorphism and partial melting, followed by a phase of late Eocene - Oligocene high-temperature metamorphism [6]. Certain areas of Shan Scarps in the MMMB have been interpreted as

a shear zone, either as part of a dextral or sinistral tectonic regime [7–9]. In any case, major dextral displacements between the BT and the Sibumasu Block have occurred since the late Miocene along the active Sagaing Fault, which forms the present-day tectonic boundary between the two blocks. These displacements have been estimated up to 400 km [1,2,10–12]. Other examples of dextral strike-slip faults in eastern Myanmar are the Neogene South Sagaing Fault and the late Oligocene West Andaman Fault to the south [13]. The Jade Belt ophiolite [6,14,15] is found at the northern end of the Sagaing fault and is part of the BT. Oceanic crust of ~163 Ma is incorporated in this ophiolite, while the jadeite itself has varying age constraints [6,16].

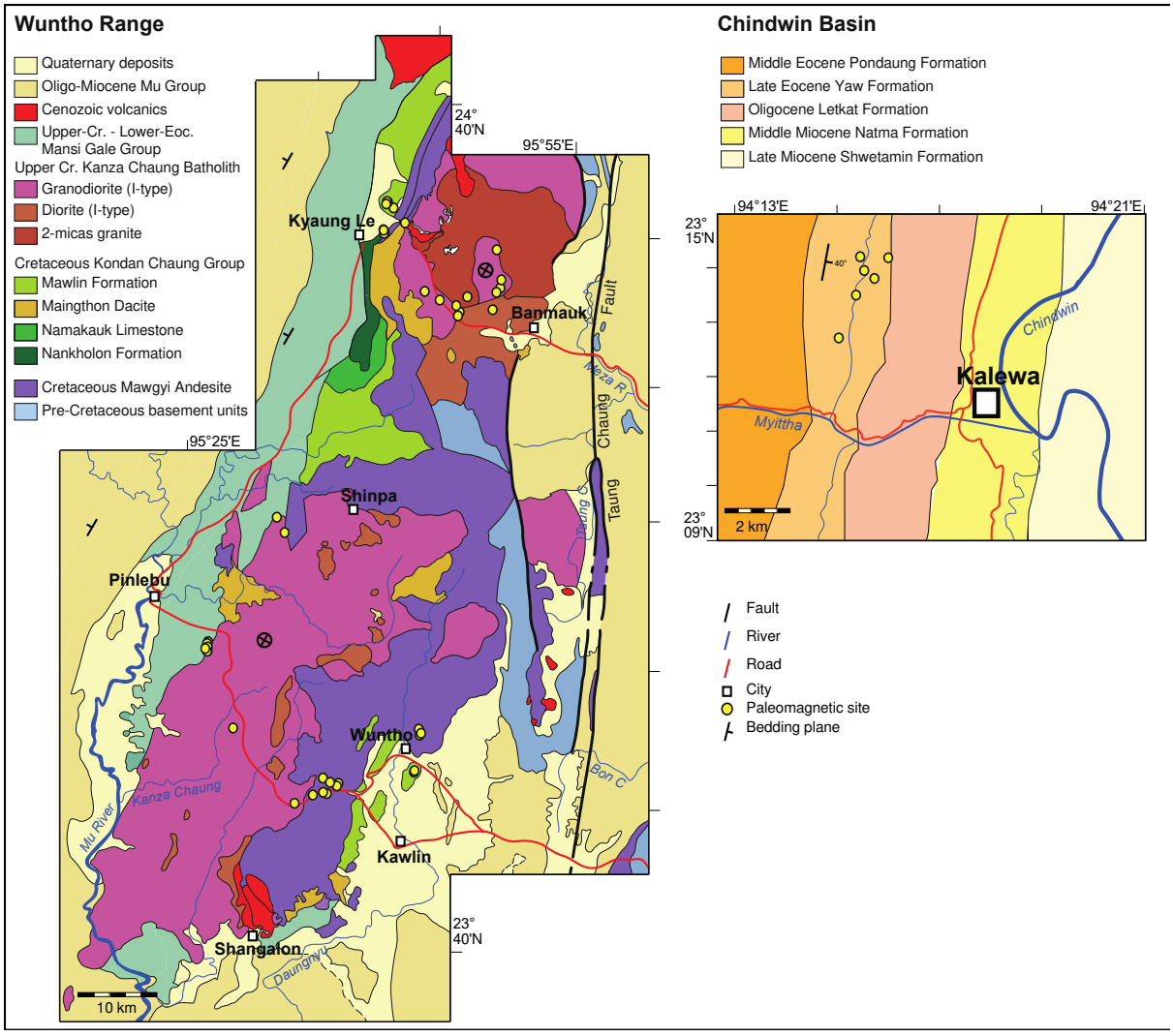

Figure 4.S1: *Geological maps of study areas: Wuntho Range (Left), Kalewa, Chindwin Basin (Right)* [19,30].

The western boundary of the BT is delineated by the Kabaw Fault or the ~127 Ma Western Belt Ophiolite in the Indo-Burman Ranges (IBR) [6,14,17,18]. The most recent detrital zircon studies of the Late Triassic Pane Chaung Formation, a key turbiditic sedimentary sequence directly flanking the Western

Belt ophiolites in the IBR [19–21], indicate either a late Mesozoic Gondwana or Cathaysian origin for this formation [20,21]. The subduction of Neo-Tethyan oceanic crust marked the beginning of the development of the present-day Andean-type Burmese subduction margin, leading to the development of multiple N-S trending Cretaceous-Neogene forearc and back-arc basins on the BT which are collectively called the Central Myanmar Basins. The forearc and back-arc are separated by the N-S trending Cretaceous-Neogene Wuntho-Popa Arc, an Andean-type volcanic arc, as evidenced by the occurrence of I-type batholiths and andesitic bodies [22–24]. Published U-Pb data suggest a main magmatic event from 110-90 Ma, followed by subordinate stage from 70-30 Ma [14,24–26]. The Western Belt Ophiolite was likely emplaced during the Late Cretaceous as well [23,24,27–29].

The focus of this study is on two areas on the BT: The Wuntho Range and the Chindwin Forearc Basin (Fig. 4.S1) [19,30].

1.2. Chindwin Basin

The paleomagnetic sampling in the Chindwin Basin was made near the town of Kalewa, western Myanmar (Fig. 4.S1). Below is a brief summary of the geology of the Chindwin basin described by a previous study [28]. The Chindwin Basin is the northernmost forearc sub-basin of the Central Myanmar Basins, situated on the BT. On its western side, the basin infill is deposited on top of the Western Belt ophiolites. To the east, the basin is delineated by the Wuntho-Popa Arc. The sedimentary sequence is homoclinal around Kalewa, and starts with Albian-Eocene marine deposits, followed by the westward-directed fossil-rich fluvio-deltaic sediments of the late middle Eocene Pondaung Formation. The overlying upper Eocene Yaw Formation is characterized by both shallow marine and lacustrine continental intervals, indicating a quasi-closed estuarian depositional environment. Sandstones and mudstones are the dominant sediments in the Yaw Formation (Fig. 4.S2e). They are intercalated with coal- or gastropod- bearing layers, as well as early-diagenetic siderite-rich carbonate layers (Fig. 4.S2f). Siderite is often one of the earliest minerals to precipitate in sediments and is formed during shallow burial as a result of bacterial reduction in anoxic or suboxic conditions [31]. A single tuff layer is also present in the Yaw Formation, yielding an age constraint of ~38 Ma [28]. The Yaw Formation is overlain by an Oligocene - Pliocene continental fluvial sequence consisting of the Letkat, Natma, Shwethamin and Irrawaddy Formations, marking the uplift of the IBR in the west. The Paleocene – Eocene sediments are mostly derived from the Wuntho-Popa Arc, while erosion of metamorphic rocks, from the MMMB and the IBR, also contributed to the Oligocene - Miocene basin fill [28].

1.3. Wuntho Arc

The Wuntho Range is located in the northern BT (Fig. 4.S1). It is the northern segment of the Upper Cretaceous to Eocene Wuntho-Popa Arc that subdivides the Central Myanmar Basins into forearc and back-arc basins. Its main component is the early Late Cretaceous Kanza Chaung Batholith. The arc has been correlated either with the Gangdese Arc or with the Indonesian Woyla Arc, based on similarities in age and lithology [4,17]. Despite limited outcrops exposure in the Wuntho Range, fresh outcrops were found in rivers as well as quarries used for road construction.

Figure 4.S2: *Representative outcrops and lithologies from this study. Site name, lithology and locality are indicated per image.*

Apart from our own observations, the descriptions of Wuntho Range lithologies are mostly taken from detailed United Nations geological reports [19] that have been recently updated in a special volume on Myanmar geology [30]. The Hpyu Taung Metamorphics, the Ubye Serpentinite Complex and the Shwedaung Formation constitute the basement rocks of the Wuntho Range and are part of the BT. The Hpyu Taung Metamorphics consists of high-grade metamorphic rocks and granites, while the Shwedaung Formation is a low-grade metamorphic sequence of sediments, extrusives and volcaniclastics. The contact with younger lithologies in the area is uncertain, but the age of the Shwedaung Formation is believed to be Late Triassic based on similarities with the Pane Chaung Formation in the IBR, western Myanmar. A sequence of Cretaceous volcanics and sediments lies unconformably on top of these basement rocks (Fig. 4.S2a,c,d). The Mawgyi Andesite is poorly dated, but has been interpreted as the oldest formation of this Cretaceous sequence. These volcanics are the most extensive extrusives in the area. They are typically massive, with a grey to green or black colour, alternating with finer brecciated flows and agglomerates, as well as occasionally volcanogenic sediments. Sills and dikes can be found intruding the other lithologies. Previous studies have suggested that the Mawgyi Andesites are a remnant of an oceanic arc thrusted on the BT prior to the establishment of the Wuntho-Popa Arc [4,17]. However, we do not observe field evidence for a major thrusting event in the Wuntho Range. Moreover, our $^{40}Ar/^{39}Ar$ dating of the Mawgyi Andesite yields an age contemporaneous with the Kanza Chaung batholith (Supplementary section 3), suggesting that they were emplaced contemporaneously or during a precursory extrusive phase. The Kondan Chaung Group comes after the Mawgyi Andesite in the Wuntho Range stratigraphy. This sequence has a diverse composition, consisting of sandstones, limestones, volcaniclastics and (rhyo-)dacites. It is predominantly exposed in the northern part of the Wuntho Range. The Maingthon Dacites are the minor volcanic part of the Kondan Chaung Group. These dacites are generally porphyritic with a bleached white to dark grey-green colour. It also contains massive rhyodacite flows with a grey-purple colour with few phenocrysts. The presence of pyrite, sulphide and chlorite suggests hydrothermal alteration. The sandstones and siltstones of the Mawlin Formation are also part of the Kondan Chaung Group. They typically have a grey-brown to greenish colour. Fining-upwards sequences and cross-bedding are common sedimentary structures in this formation, corresponding to a turbiditic facies. Locally, tuffaceous deposits and breccia layers are mixed or interbedded with these sediments. The overlying limestones of the Namakauk Formation contain shell debris and abundant algae together with volcanic fragments, but lack age-diagnostic fossils. The Kondan Chaung Group underwent a significant amount of folding. On the other hand, the Kanza Chaung Batholith (Fig. 4.S2b) shows no signs of significant tilting. This NE-SW trending batholith constitutes the main component of the Wuntho Range, exposed in a large part of the area.

The batholith primarily consists of medium to coarse I-type (grano)diorites with several mafic inclusions, as well as smaller diorite plutons and an area consisting of 2-mica granite in the north. U-Pb dating of these intrusions yielded ages of ~100 Ma [25,30]. A second phase of I-type magmatism of late Eocene age is found at the Shangalon copper district[30]. A Late Cretaceous – Paleogene sequence of sediments, postdating the main Kanza Chaung Batholith, surrounds the Wuntho Range, resulting in an apparent regional NE-SW trending anticline. In the west, the thick stratigraphic succession of predominantly sedimentary rocks dip to the northwest to form the eastern limb of the Chindwin Basin. There is no major known thrust between the Chindwin Basin and the Wuntho Range. To the east of the Wuntho Range, the sedimentary basins are disrupted by major faults (Taung Chaung Fault) and deformation related to displacements along the Sagaing Fault system.

2. Petrology

Because of the complex character of Wuntho Range geology and for a better understanding of the paleomagnetic record, petrological analysis was conducted on several samples with both an optical microscope and a Scanning Electron Microscope (SEM). Relevant observations resulting from this analysis are shown below per locality.

2.1. Kanza Chaung Batholith

The majority of samples from the Kanza Chaung Batholith are (grano)diorites. This is clearly confirmed by microscope observations under both transmitted and cross-polarized light, in a sample from site MY04, Pinlebu. We observe no alteration in accordance with previous studies [19,25,30].

2.2. Mawgyi Andesite

Optical microscope images of andesitic samples from sites MY08, MY10 and MY11 all exhibit signs of alteration (Fig. 4.S3a-d). In MY08, larger plagioclase grains exhibit altered rims under the optical microscope, which could correspond to either low-grade metamorphism or hydrothermal alteration (Fig. 4.S3a). In MY10, brecciation is suggested by the juxtaposition of crystal-rich parts and aphanitic ones (Fig. 4.S3b-c), with the latter parts containing large vacuoles and chlorite-epidote metamorphism (Fig. 4.S3b). Both MY08 and MY10 contain large calcite veins, as evidenced by SEM analysis (Fig. 4.S3c-e). In fact, calcite is not only observed in veins, but is also partly penetrating the sample matrices. On the other hand, in site MY11, quartz alteration is observed instead of calcite alteration. Chalcopyrite was only observed in some samples (MY10, Fig. 4.S3h). A large amount of magnetite is observed in most samples with various grain size (Fig. 4.S3e-h). The largest magnetite grains often contain titanite inclusions. The micron-size magnetite grains are found in close association with calcite alteration (Fig. 4.S3e). All these observations point towards the presence of

either calcite or quartz hydrothermal alteration due to local mineralizing events, as well as low-grade chlorite-epidote metamorphism in the Mawgyi Andesite.

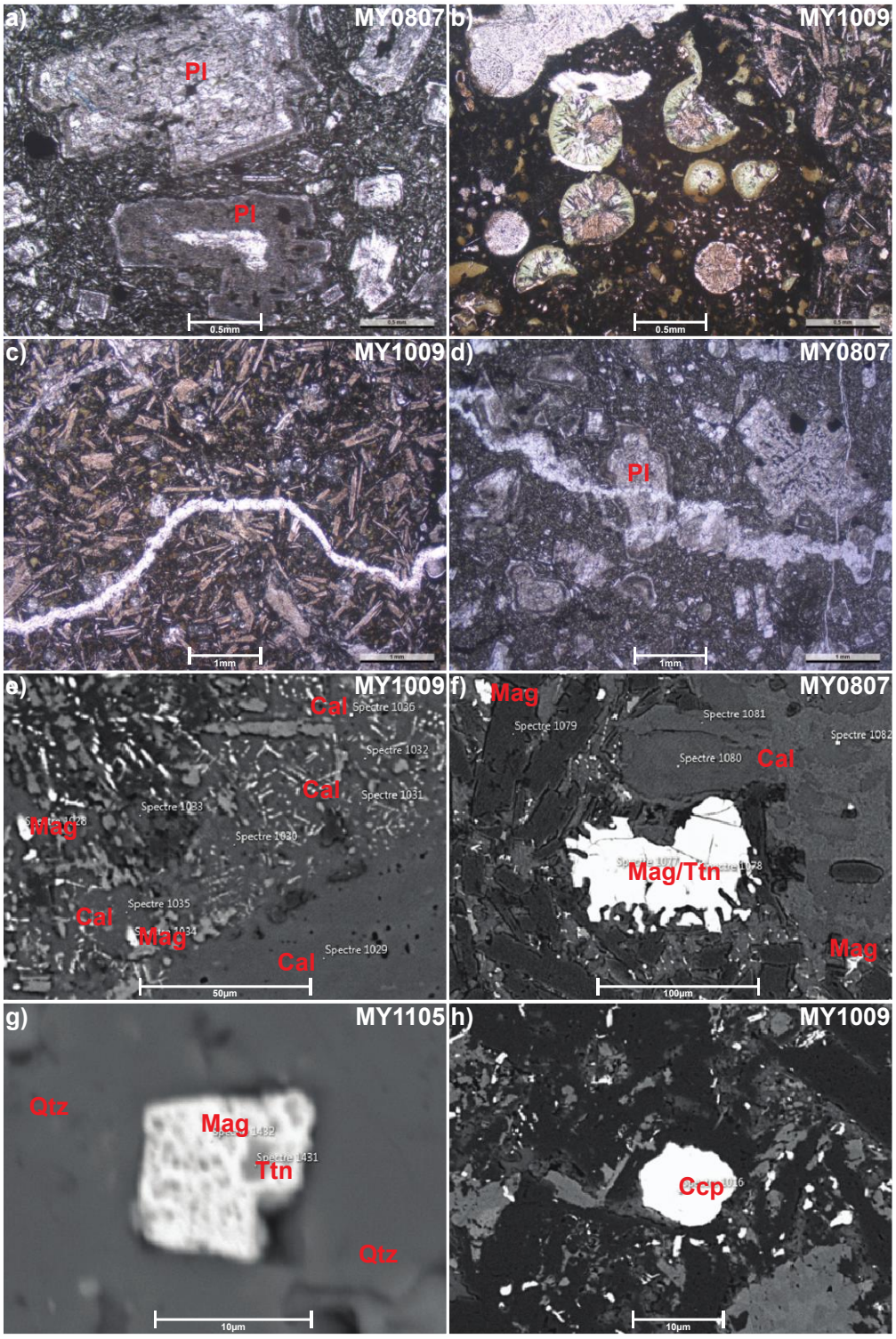

Figure 4.S3: *Representative microscope images from the Mawgyi Andesite, Wuntho Range. Sample name and scale are indicated per image. Mineral abbreviations (red): Cal = calcite, Ccp = chalcopyrite, Mag = magnetite, Pl = plagioclase, Qtz = quartz, Ttn = Titanite.*

2.3. Kondan Chaung Group

The Kondan Chaung Group is the most variable in lithology, containing sandstones, limestones, volcanic and volcaniclastic lithologies. They all display various types of alteration according to the lithology (Fig. 4.S4). Site MY22, a very fine-grained volcanic sill or dike, contains large iron-oxide grains (Fig. 4.S4a) with pervasive titanite alteration. Titanite is found especially replacing previous lamellae formed by primary exsolution of titanomagnetite to ilmenite or ulvöspinel. This process is indicative of posterior hydrothermal alteration [32].

MY45 is a mixture of siltstone and pyroclastic material, containing large unaltered quartz grains. However, the glass and silicate matrix have been replaced with secondary quartz and calcite (Fig. 4.S4d). Site MY25 is another volcanic sandstone and fine breccia. Quartz recrystallization is important in this site and secondary crystallization of Ti-oxides indicates dissolution of previous detrital Ti-Fe oxides. The same observation is made for the sandstones from site MY24 and MY41. The most striking feature in these sedimentary rocks is the widespread authigenic formation of small TiO_2 oxides with in some cases sub-micron zircons in close association with the titanium oxides (Fig. 4.S4c). Iron-oxides in the form of magnetite or hematite were not recognized in SEM.

The fossil-rich limestone at site MY23 contains framboidal pyrite (Fig. 4.S4b). SEM data shows altered silicate clast assemblages (Fig. 4.S4e,f) with likely relict lattice of micron-size Ti-oxide and apatite rods after dissolution of magnetite.

Kondaung Chaung sandstones were also drilled at site MY34, near Kawlin. The lithology is different from the sandstones at sites MY24 and MY41. At Kawlin, volcanic clasts and silicate minerals are less pervasively replaced. This is the single site where we identify detrital chalcopyrite grains (Fig. 4.S4g), suggesting that the sandstones are derived from the nearby mineralized Mawgyi Andesite. Secondary iron-sulphurs, mainly pyrite, are found in veins and fractures (Fig. 4.S4h). In contrast with the sites near Kyaung Le, titanite is present instead of secondary TiO_2 minerals.

Figure 4.S4: *Representative microscope images from the Kondan Chaung sediments, Wuntho Range. Sample name and scale are indicated per image. Mineral abbreviations (red): Ap = apatite, Cal = calcite, Ccp = chalcopyrite, LREE = Light Rare Earth Elements, Mag = magnetite, Py = pyrite, Qtz =*

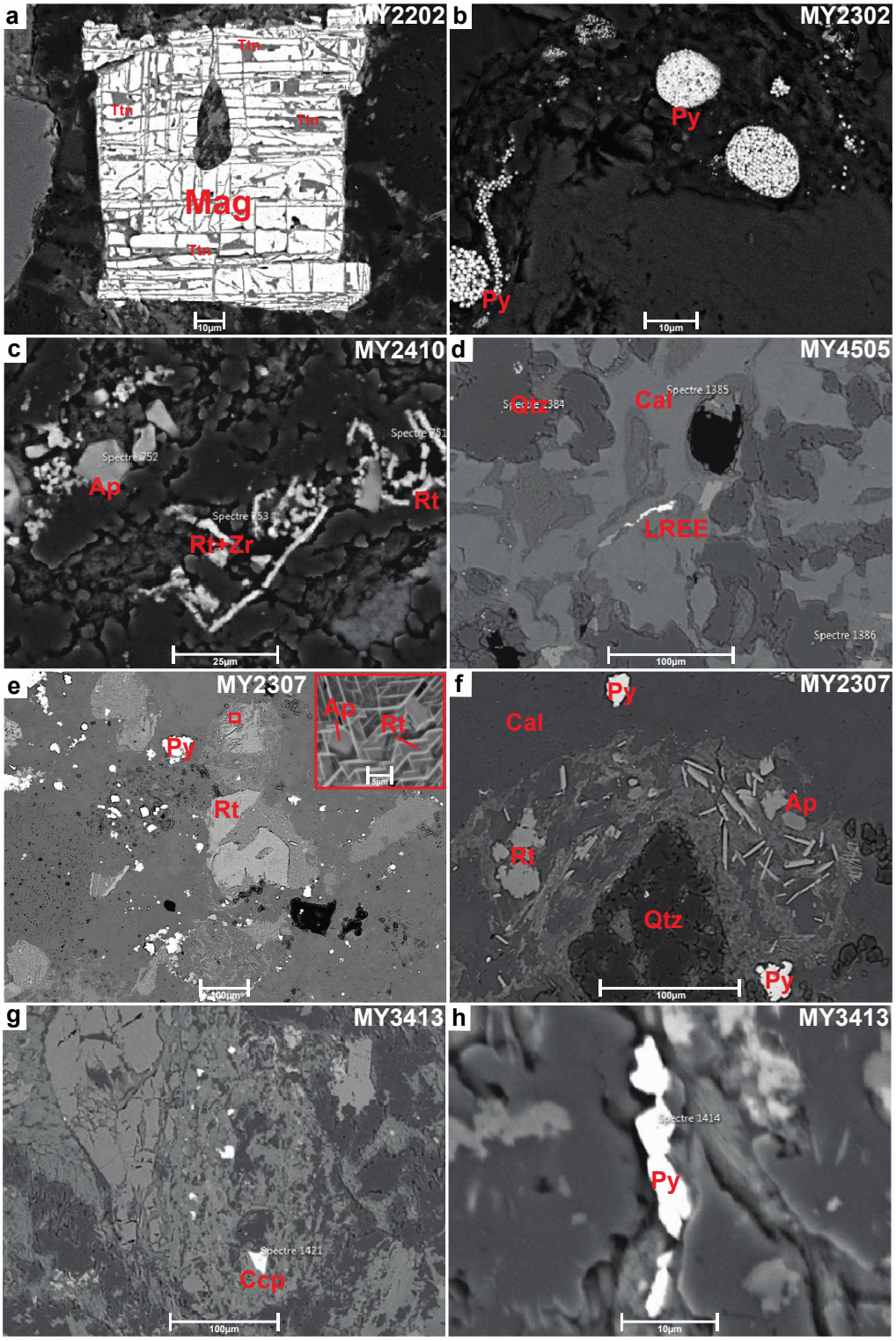

3. $^{40}Ar/^{39}Ar$ dating

From the total of 14 measured samples, nine yielded interpretable $^{40}Ar/^{39}Ar$ plateau dates on whole rock samples, as well as amphiboles and biotites (Fig. 4.S5, Supplementary Data 3). $^{40}Ar/^{39}Ar$ dates from the batholith range from ~97 to ~87 Ma and are only slightly younger than reported U-Pb dates (~103-97 Ma) [14,25,26].

Age determination of the Mawgyi Andesite was no possible due to the low potassium content. A minimum date of 100.9±0.2 was obtained in site MY07, indicating that at least part of the Mawgyi Andesite is younger than the previously interpreted Early Cretaceous age, although it could also be reset by low-grade metamorphism during batholith emplacement.

At Kyaung Le, the two plateau dates obtained at site MY22 and MY43 confirm that these rocks are contemporaneous with the batholith emplacement.

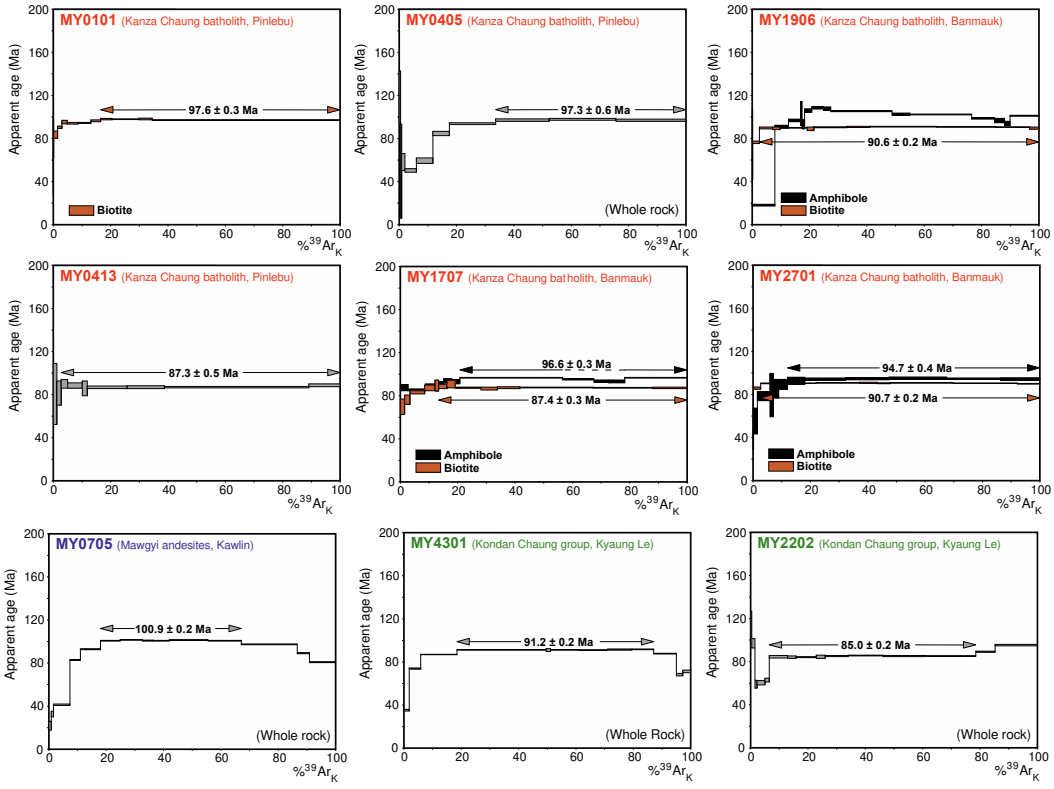

Figure 4.S5: *$^{40}Ar/^{39}Ar$ dates for representative sampled sites in the Wuntho arc.*

4. Paleomagnetic results

The results are presented according to the location and the distinct sampled rock types, which control the magnetic behaviour in demagnetization. Both progressive thermal demagnetization with steps of 30 to 50°C and AF demagnetization were used to identify the characteristic remanent magnetization (ChRM). The resulting mean directions are given per site and locality in Supplementary Data 1, while all resulting directions from each paleomagnetic sample are listed in Supplementary Data 2.

4.1. Pinlebu, Shinpa & Banmauk (Kanza Chaung Batholith)

The whole rock magnetic properties (magnetic susceptibility, coercive fields, Curie points) are mainly controlled by multidomain magnetite. For six out of eleven sampled sites near Banmauk, the intensity of the natural remanent magnetization (NRM) is usually very low (< 2 10^{-2} Am^{-1}) after 10 mT and no well-defined ChRM was recovered. At the other sites however, a small amount of fine-grained magnetite was sufficient to record interpretable ChRMs, which were recovered by AF above 15-20 mT or thermal demagnetization above 400°C (Fig. 4.S6a). Reliable paleomagnetic results were obtained at four sites around Pinlebu area, at three sites around Shinpa and at five sites around Banmauk (Fig. 4.S6c, Supplementary Data 1). The Pinlebu and Shinpa sites give well-determined paleomagnetic means with an east oriented declination and nearly horizontal inclination. The ChRM directions from Banmauk yield east-oriented declinations as in Pinlebu, but with a slightly negative inclination and a larger scatter in declination. Unrecognized small tilts or local-block rotations may contribute to this scatter. There is no field evidence for significant wholesale tilting of the complete batholith.

The anisotropy of magnetic susceptibility (AMS) results from the Wuntho intrusions have a generally sub-vertical NE-SW trending magnetic foliation with a near vertical lineation (Fig. 4.S6b). This means that AMS foliations of the Kanza Chaung Batholith are roughly parallel to the general trend of the Wuntho Arc, further indicating that the batholith was not tilted. The degree of AMS P' is high (~1.1-1.4 for most samples, Fig. 4.S6b), but mainly controlled by multidomain magnetite. In order to test the effect of anisotropy on the ChRM, we obtained anisotropy of remanent magnetization data. Full anisotropy of isothermal remanent magnetization (AIRM) tensors have similar fabrics than the AMS but the shape and anisotropy degree is usually higher. Because the ChRM is carried by magnetite with coercivities above 20 mT, tensors of AIRM left above 20 mT AF demagnetization (AIRM@20mT) were also calculated. The orientation of AIRM@20mT tensors is often different from the AIRM and AMS tensors, with greater scatter and an anisotropy degree below 1.5. Applying the inverse tensor to correct the ChRMs indicates that the ChRMs were not deflected by anisotropy from the original field. Therefore, anisotropy cannot account for the large tectonic rotation or latitudinal translation recorded by the intrusions.

Figure 4.S6: *Paleomagnetic results from the Kanza Chaung Batholith, Pinlebu, Shinpa and Banmauk, Wuntho Ranges: a) Representative orthogonal demagnetization plots. Open/closed dots denote projections on the vertical/horizontal plane. Reference frame, locality and lithology are indicated per plot; b) left) Equal-area projection of mean-site anisotropy of magnetic susceptibility (AMS) results with ellipse of confidence at 95%; right) Plot of the shape of the anisotropy ellipsoid (T) versus the*

corrected anisotropy degree; c) Equal-area projection of the mean-site characteristic directions of all reliable paleomagnetic data in in-situ coordinates.

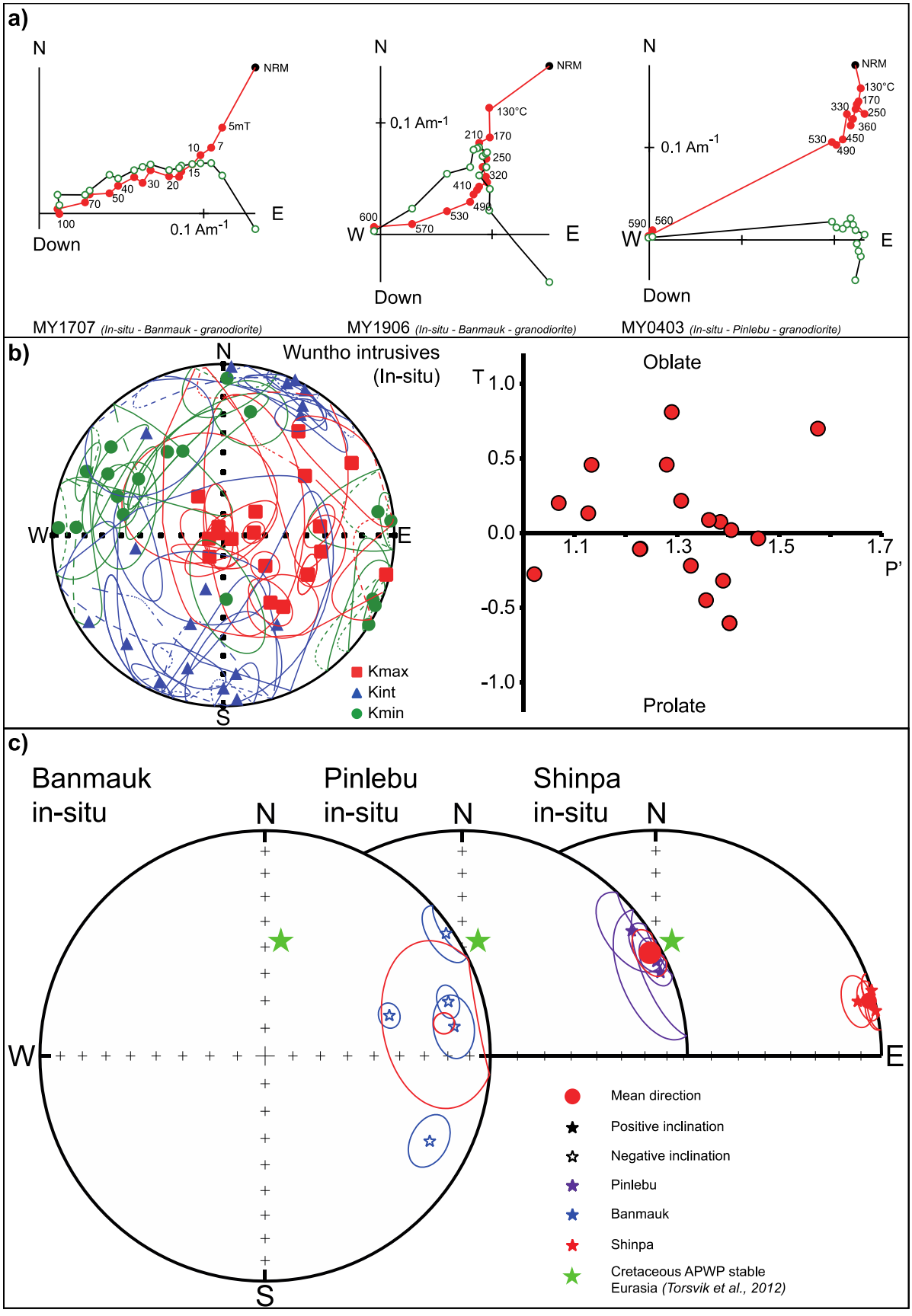

4.2. Kawlin (Mawgyi Andesite)

High magnetic susceptibilities (> 0.01 SI in most samples) and bulk magnetic susceptibility versus temperature (K-T) experiments confirm that magnetite is the main magnetic mineral in the Mawgyi Andesite (Fig. 4.S7c). K-T curves show slight maghemitization in some samples. The same ChRM was recovered after thermal demagnetization above 400-500°C and after AF demagnetization above 20 to 30 mT, in agreement with magnetite being the main magnetic carrier (Fig. 4.S7a). The low temperature and low coercivity secondary magnetizations are often parallel to the present-day field. When the overprint is large, great circles were determined and combined with best-fit line vectors to determine the mean-site direction. Paleomagnetic results were obtained at six sites out of nine sampled sites (Fig. 4.S7d). Two sites (MY06 and MY35) are in brecciated rocks that yield scattered paleomagnetic data despite similar magnetic properties. This observation indicates that there is no homogeneous widespread remagnetization in these rocks, despite petrologic evidence for local mineralizing events causing hydrothermal alteration at several sites. Moreover, an estimate of age (Supplementary section 3) as well as bedding from paleohorizontals flow contacts in the Mawgyi Andesites is not straightforward. The AMS degree is low (P' = ~1.0-1.1) and the magnetic fabric is either coherent or scattered at the site level. There is no clear trend in the AMS ellipsoids between sites. These complications make it difficult to provide a reliable mean direction from the andesitic sites around Kawlin, although the east oriented declination of the ChRM is similar to Pinlebu, Shinpa and Banmauk.

In addition to the andesites, two sites were drilled in the sandstones from the Mawlin Formation (MY09, MY34) south of the town of Wuntho. At site MY34, the ChRM is especially well-defined over a very limited temperature range (290-350°C) (Fig. 4.S7a,b). Magnetite is the main magnetic remanence carrier seen in high-field experiments, but an inflection is also seen at ~300°C upon thermal demagnetization of the highest coercivity part of the IRM. Hence, we associate the sharp laboratory unblocking temperature range of the NRM with pyrrhotite and interpret the ChRM to be secondary. The sandstones are intruded by thin sills or dykes, likely related to the Kanza Chaung Batholith, suggesting that pyrrhotite was likely formed by metamorphism related to volcanic intrusion. Indeed, the application of a tilt correction results in an unrealistic, steep negative inclination for MY34. Therefore, the in-situ mean direction obtained at MY34 probably best represents the expected field direction at ~100 Ma around Kawlin (Fig. 4.S7d, Supplementary Data 1).

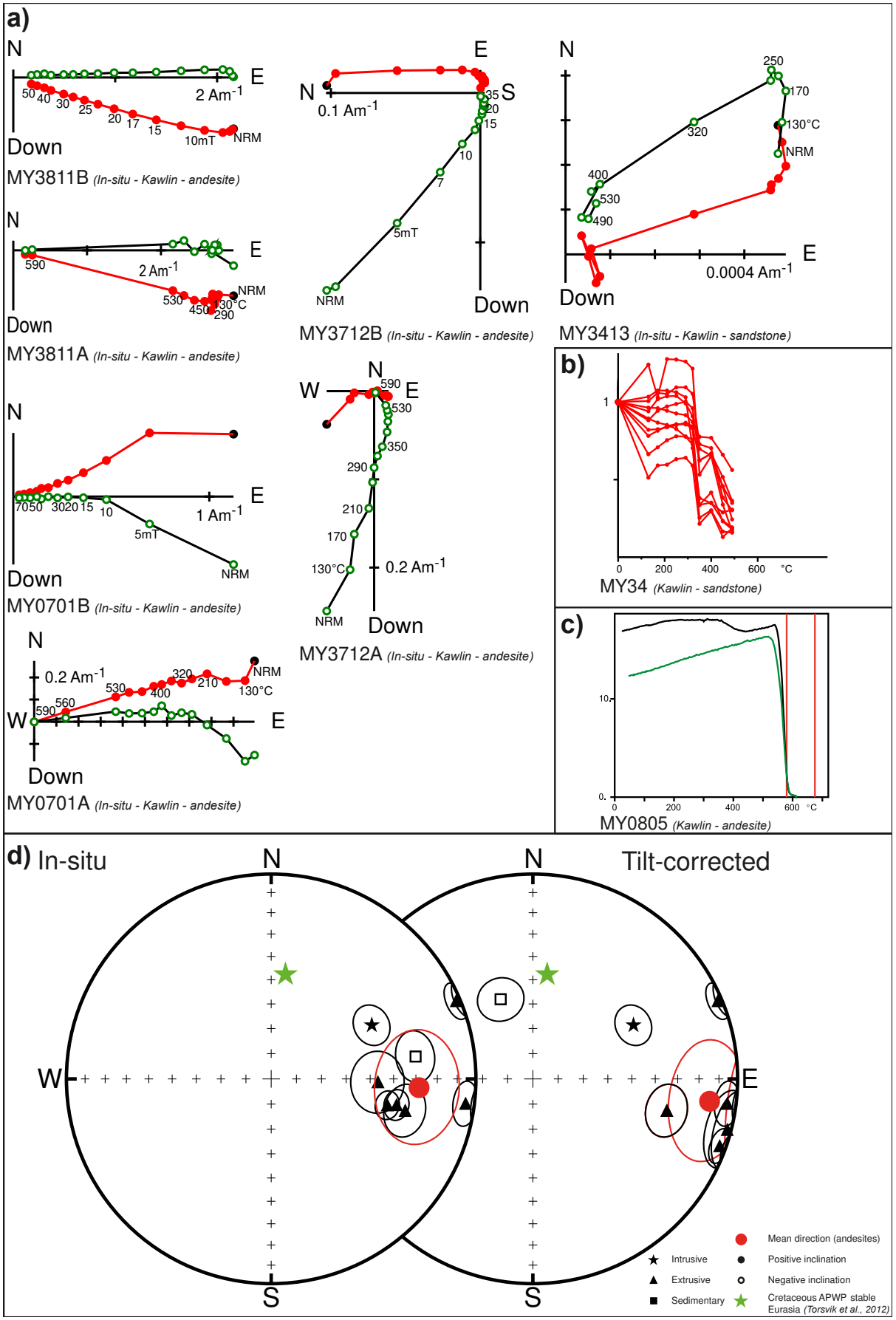
a)
N
E
2 Am-1
50 40 30 25 20 17 15 10mT NRM
Down
MY3811B (In-situ - Kawlin - andesite)
N
E
590
2 Am-1
NRM
530 450 130°C 290
Down
MY3811A (In-situ - Kawlin - andesite)
N
E
7050 3020 15 10
1 Am-1
5mT
NRM
Down
MY0701B (In-situ - Kawlin - andesite)
N
0.2 Am-1
320
NRM
530
210
130°C
400
590 560
W
E
Down
MY0701A (In-situ - Kawlin - andesite)
E
N
S
0.1 Am-1
35 20 15 10 7 5mT
NRM
Down
MY3712B (In-situ - Kawlin - andesite)
N
W
590
E
530
350
290
210
170
130°C
0.2 Am-1
NRM
Down
MY3712A (In-situ - Kawlin - andesite)
N
E
250
170
320
130°C
NRM
400
530
490
0.0004 Am-1
Down
MY3413 (In-situ - Kawlin - sandstone)
b)
1
0 200 400 600 °C
MY34 (Kawlin - sandstone)
c)
10
0
0 200 400 600 °C
MY0805 (Kawlin - andesite)
d) In-situ
N
W
E
S
Tilt-corrected
N
E
S
Mean direction (andesites)
Intrusive
Positive inclination
Extrusive
Negative inclination
Sedimentary
Cretaceous APWP stable Eurasia (Torsvik et al., 2012)

Figure 4.S7: *Paleomagnetic results from the Mawgyi Andesite, Kawlin, Wuntho Range: a) Representative orthogonal demagnetization plots from the different sampled lithologies. Open/closed dots denote projections on the vertical/horizontal plane. Reference frame, locality and lithology are indicated per plot; b) Normalized intensity of the remanent magnetization versus temperature during thermal demagnetization for all samples from sandstone site MY34; c) Variation of the bulk magnetic susceptibility (10^{-6} m^3/kg) versus temperature (°C) (K-T plot) for a representative sample of the Mawgyi Andesite showing magnetite as the main magnetic mineral. Black/ green curves are respectively the heating/ cooling curves; d) Equal-area projections of the site-mean directions of all reliable paleomagnetic data in both in-situ and tilt-corrected.*

A few kilometres farther west of the andesite exposures, we sampled one site in an igneous stock (MY12). This is the only site in igneous rocks where hematite is the main carrier of the ChRM. This observation might be an indication that this stock is related to the Mawgyi volcanic rocks and not to the magnetite-rich rocks of the Kanza Chaung Batholith.

4.3. Kyaung Le (Kondan Chaung Group)

4.3.1 Volcanic and volcaniclastic rocks

Samples from site MY22 have the highest intensity of magnetization (0.2-0.4 Am^{-1}) and discrete laboratory unblocking temperatures (530-580°C). The titanite replacement of titanomagnetite observed in SEM inspection (Supplementary section 2.3) demonstrates major mineralogic alteration after emplacement. The ChRM was likely acquired during this phase of alteration.

Samples from rhyodacite site MY43 have NRM intensities in the range (0.01-0.04 Am^{-1}) and magnetic susceptibilities ~0.0002 SI. Magnetite and hematite carry the same ChRM vector with respectively ~90% and ~10% of the magnetization, mostly determined above 400°C (Fig. 4.S8a). Hematite is well-defined in IRM acquisition curves.

Site MY45 is in a fine-grained sedimentary rock with lenses of coarse-grained volcaniclastic rocks. Both the NRM intensity and magnetic susceptibility are low in these rocks. Site MY25 is another coarse volcaniclastic sandstone with clasts up to a few millimeters in some samples. Samples with or without clasts both have a ChRM defined in the laboratory unblocking temperature range 400-590°C, with magnetite as the magnetization carrier (Fig. 4.S8a). There is no evidence of hematite at these volcaniclastic sites. All three sites (MY25, MY43 and MY45) record a very similar ChRM direction despite the differences in magnetic properties.

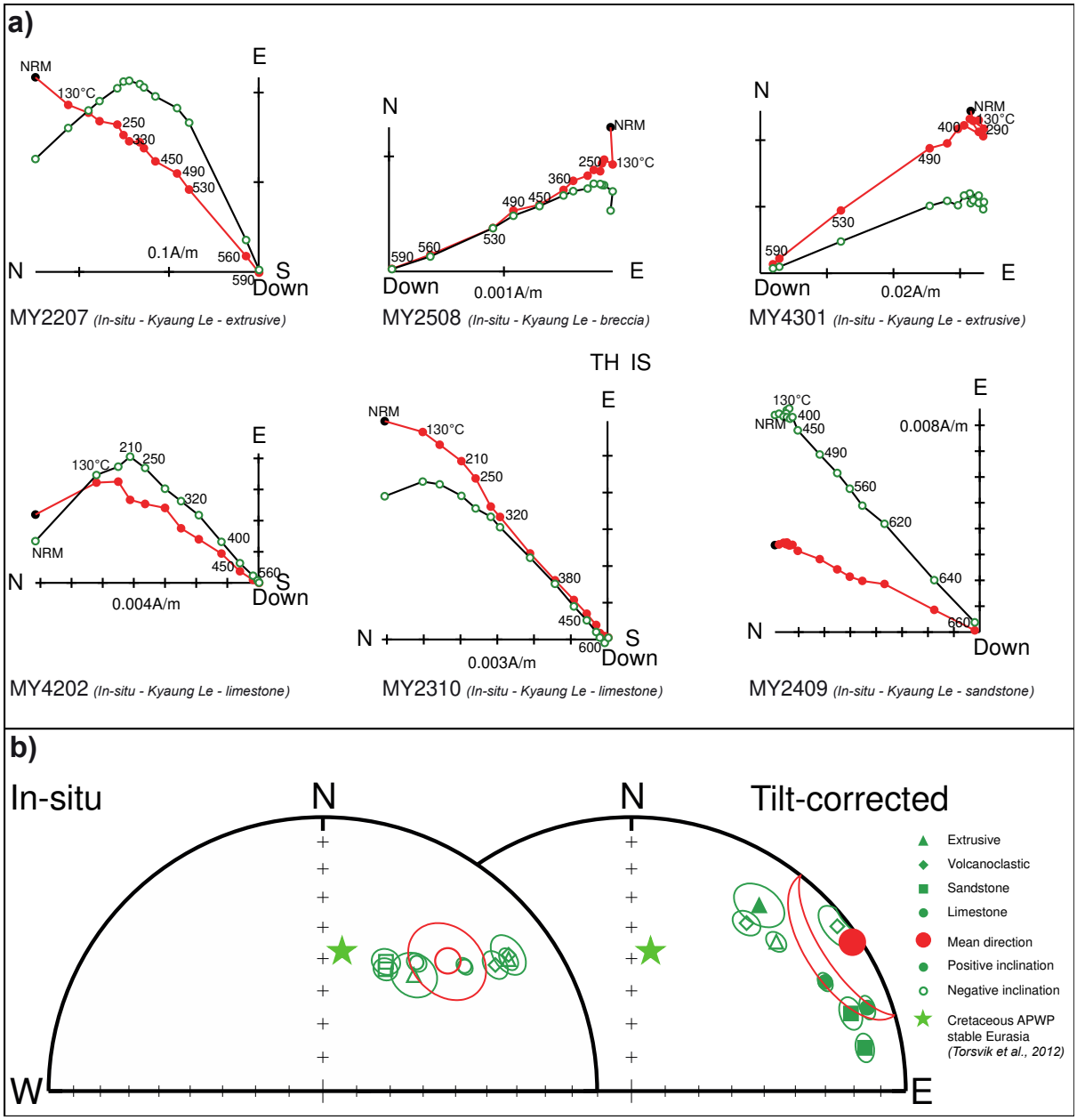

Figure 4.S8: *Paleomagnetic results from the Kondan Chaung Group, Kyaung Le, Wuntho Range: a) Representative orthogonal demagnetization plots from the different sampled lithologies. Open/closed dots denote projections on the vertical/horizontal plane. Reference frame, locality and lithology are indicated per plot; b) Equal-area projection of the site-mean directions of all reliable paleomagnetic data in both in-situ and tilt-corrected.*

4.3.2 Sedimentary rocks

Two sites (MY24 and MY41) were established in sandstones, while two other sites (MY23 and MY42) are in limestones. In the sandstones, there is almost no unblocking of the NRM prior to 360-380°C (Fig. 4.S8a). Above 530°C, a spurious magnetization associated with susceptibility enhancement impedes a well-defined linear demagnetization in several samples. The ChRM directions were

therefore determined from data obtained over the temperature interval 320-490°C, with the best-defined lines anchored to the origin. This approach is supported by the very well-defined behaviour of some samples (sample MY2409, Fig. 4.S8a), showing that magnetite and hematite carry the same ChRM vector.

The limestones also have a well-defined magnetization, determined mainly in the temperature range 290-530°C (Fig. 4.S8a). The magnetization carrier is generally magnetite, but IRM acquisition data shows that 10-20% of the IRM is acquired above 250 mT. Thermal demagnetization of IRM demonstrates however that the high coercivity fraction has unblocking temperatures also between 250-330°C, while the low coercivity fraction has a more linear distribution of unblocking temperatures between 150 and 500°C.

4.3.3 Remagnetization at Kyaung Le

Despite the large differences in magnetic properties and rock types among sites, means are well-determined at eight sites and are better grouped in in-situ coordinates than after tilt correction (Fig. 4.S8b, Supplementary Data 1), suggesting a secondary origin for the ChRM that is consistent with our petrologic observations (Supplementary section 2.3). Moreover, the volcanic sandstones and fine breccias at site MY25 record a well-defined uniform magnetization, similar to MY43 and MY45, that is unlikely to be acquired during the formation of these rocks. $^{40}Ar/^{39}Ar$ plateau dates from MY22 and MY43 are in good agreement with those obtained for the Kanza Chaung Batholith intrusive rocks (Fig. 4.S5). Therefore, remagnetization is likely contemporaneous with batholith emplacement.

The overall Kyaung Le in-situ mean direction shows a large clockwise rotation and a negative inclination (Supplementary Data 1). However, the in-situ means are distributed over a small circle. Sites with the steepest inclination ChRM are found in sandstones, where bedding is slightly overturned (MY24 and MY41), suggesting that some additional tilting may have occurred after remagnetization. For this reason, we consider that sites MY25, MY43 and MY45, where tilting was not large, provide the best estimate of the mean direction at Kyaung Le. The ChRM directions for these sites have shallow negative in-situ inclinations.

4.4. Kalewa (Yaw Formation)

4.4.1 Paleomagnetic directions

A total of 520 samples were collected for a magnetostratigraphic study of a ~700m thick section of the upper Eocene shallow-marine Yaw Formation in the Chindwin Basin, near Kalewa. The main magnetic mineral observed in K-T experiments (Fig. 4.S9b) is magnetite, as shown in sandstone sample MA0275. Magnetite formation takes place in heating above 400°C in many samples containing framboidal pyrite, typically in finer-grained rocks. Greater amounts of magnetite are

formed in siderite-rich samples above 450°C, hindering the identification of magnetic phases. However, IRM experiments show magnetite as the main magnetization carrier. Spurious magnetization related to magnetite formation above 400-450°C was observed in several samples, especially samples with siderite (Fig. 4.S9a). GRM acquisition prevented further demagnetization above 400°C by AF methods. Therefore, ChRMs were mostly determined in the temperature interval ~220°C-460°C, with best-fitted lines anchored to the origin (Fig. 4.S9a).

The most stable samples are from mudstone rocks and siderite-rich carbonate layers. In many cases, siltstones and sandstones record a significant overprint in the present-day field. These samples could be used for magnetostratigraphy, the initial goal of sampling this section, because they still yielded an indication for polarity. Unfortunately, their quality was not sufficient for calculating a mean direction. In any case, normal and reverse polarity magnetizations are present in all rock types, with well-defined polarity magnetozones. Rocks of both polarities exhibit similar magnetic behaviour during demagnetization, suggesting a detrital or early diagenetic primary origin for their remanent magnetizations. However, the resulting mean directions of the in-situ normal (N=99) and reverse (N=69) polarity groups are not perfectly antipodal: D=6.6°, I=9.1° and D = 192.2°, I=1.3°. The reversal test is negative (Fig. 4.S10a), because the two polarity mean directions have an angular difference of 13.8°. The most likely cause is a certain degree of overprint by the present-day geomagnetic field. By iteratively subtracting an increasing percentage of this overprint direction simultaneously from both the normal and reverse mean direction, we calculated the minimum angle between the normal and reverse polarities and the possible degree of overprint. This indicates a residual overprint of about 17%. Subtracting it reduced the angular difference between the normal and reverse directions to 3.2°. Fortunately, because we have a significant number of samples of both polarities, the magnetization overprint is cancelled out and the combined mean direction is not affected by the residual overprint.

Figure 4.S9: *Paleomagnetic results from the Late Eocene Yaw Formation, Kalewa, Chindwin Basin: a) Representative orthogonal demagnetization plots from the different sampled lithologies. Open/closed dots denote projections on the vertical/horizontal plane. Reference frame, locality and lithology are indicated per plot; b) Representative bulk magnetic susceptibility (10^{-6} m^3/kg) versus temperature (°C) plots (K-T plots) up to a maximum of 590°C; c) left) Equal-area plots of the anisotropy of magnetic susceptibility (AMS) of all samples in in-situ and after bedding correction; right) plot of the shape (T) of the anisotropy ellipsoid versus the corrected degree of anisotropy (P'); d) Equal-area plots of the ChRMs of samples of the Yaw formation in both in-situ and after bedding correction.*

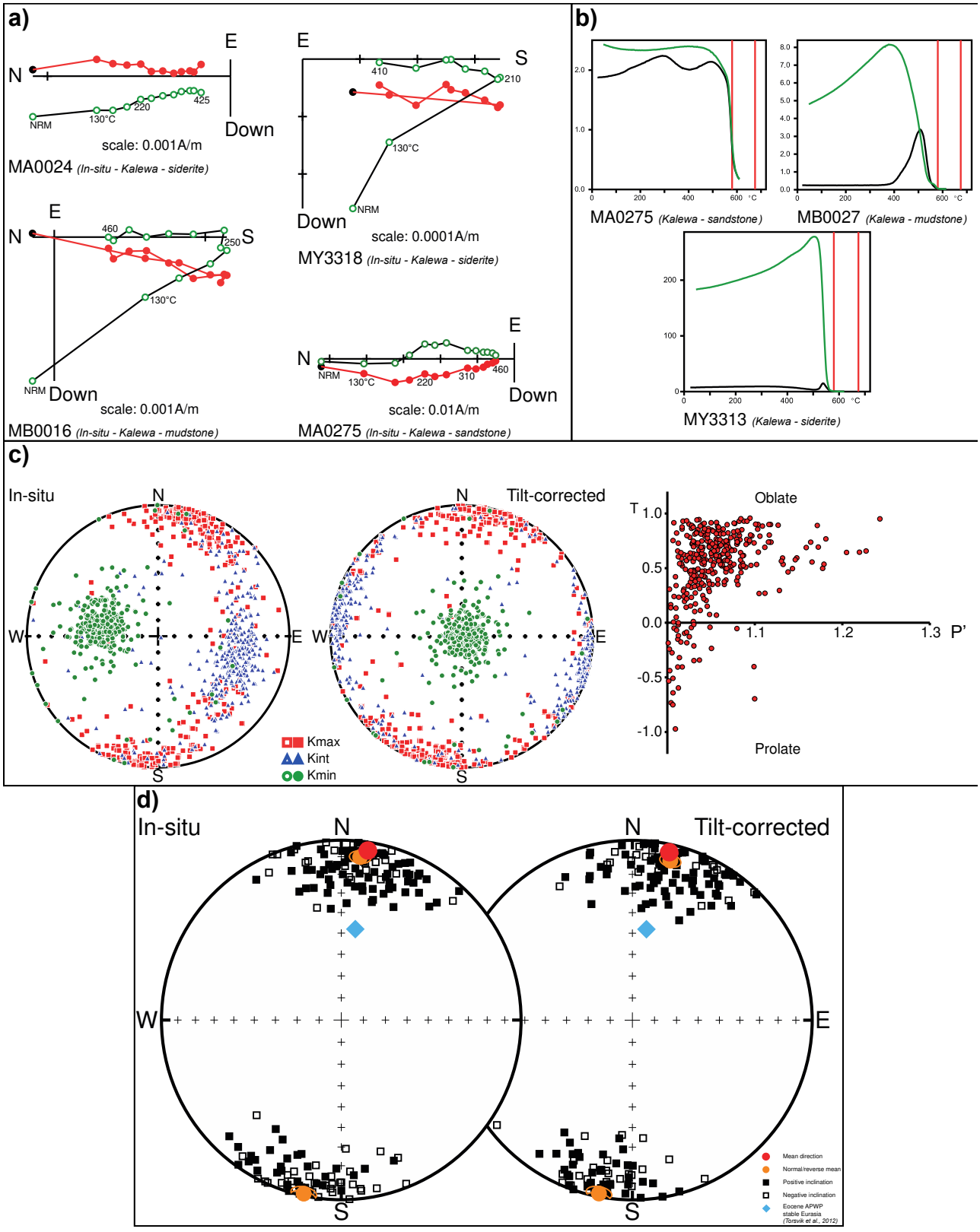

The resulting mean is calculated with the 168 most well-defined ChRMs (99 of normal polarity and 69 of reverse polarity), showing a coherent direction with a north oriented declination and shallow inclination in tectonic coordinates (Supplementary Data 1).

4.4.2 Magnetic fabric

As defined by AMS data, the magnetic fabric of the Yaw sediments is mainly oblate and the minimum axis of the AMS fabric (Fig. 4.S9c) is orthogonal to bedding and controlled by sedimentary processes and compaction. The exceptions to this trend are several siderite samples, which exhibit a typical inverse AMS fabric. The maximum axis is parallel to the fold axis in agreement with a tectonic imprint, typically observed in studies of rocks in orogenic belts [33]. The horizontal magnetic lineations are parallel to the axis of the Chindwin Basin. There is no local complex folding. The tectonic rotation that can be determined from our Kalewa mean direction is thus an estimate of the rotation of the whole Chindwin Basin since the late Eocene.

4.4.3. Inclination shallowing

We used two separate methods to test for inclination shallowing in the Kalewa sedimentary sequence. Our results yielded an Eocene mean inclination of 4.9±2.9° for these Eocene rocks, corresponding to a latitude of 2.4±1.5°N.

The elongation-inclination (E/I) method [34–37] gives an unflattened inclination of 7.9±4.2°, which is equivalent to a latitude of 4.0±2.1°N (Fig. 4.S10b). The E/I method is straightforward to use, but it also has notable limitations when dealing with sedimentary sequences, because it assumes that the principal scatter in direction is caused by paleosecular variation (PSV). This is unlikely the case in slowly accumulating sedimentary deposits or when diagenetic processes average the secular variation [38]. Moreover, measurement errors, as well as the fact that normal and reverse directions are not perfectly antipodal, can cause the data distribution to become more elongated in the horizontal plane when using the complete dataset for the E/I method. For these reasons, we opted to use a second method, with a more physical basis to test for inclination shallowing. In this second method, we assume that the sedimentary rocks consist of uniform rigid particles that rotate during coaxial shortening caused by compaction of the sediments in burial due to the overburden. Furthermore, we assume that this causes the inclination to change as a rotating passive line, resulting in the following equation [39]:

$$\tan(I_1) = \frac{\lambda_1}{\lambda_0}\tan(I_0) \qquad (1)$$

where I_1 is the measured inclination, I_0 is the unflattened inclination and $\frac{\lambda_1}{\lambda_2}$ is the strain ratio. The strain ratio is assumed to be equivalent to the ratio of initial and compacted thickness $\frac{L_1}{L_0}$ of the sedimentary package, giving:

$$\tan(I_1) = \frac{L_1}{L_0}\tan(I_0) \qquad (2)$$

The amount of shortening due to compaction is dependent on the porosity of the sediments. The relationship between change in thickness and change in porosity is given by the following relationship [40,41]:

$$\frac{L_1}{L_0} = \frac{(1-\varphi_0)}{(1-\varphi_1)} \qquad (3)$$

where ϕ_0 is the initial porosity and ϕ_1 is the final porosity. This results in the following equation:

$$\tan(I_1) = \frac{(1-\varphi_0)}{(1-\varphi_1)}\tan(I_0) \qquad (4)$$

If we now assume a total overburden of the Yaw Formation of about 2 km [28], the porosity change in an average clastic sedimentary basin should be ϕ_0=40% to a final porosity ϕ_1=27% [42]. This results in an unflattened inclination of 6.0±2.9°, equivalent to a latitude of 3.0±1.5°N.

It is possible to take into account additional physical parameters. The relationship between porosity change and compaction ΔV is given by the following equation [43]:

$$\Delta V = -\frac{(1-\varphi_0)}{(1-\varphi_1)} - 1 \qquad (5)$$

This allows us to rewrite equation (4) with ΔV = 0.18 based on our estimate of porosity change:

$$\tan(I_1) = (1 - \Delta V)\tan(I_0) \qquad (5)$$

Past laboratory compaction experiments have shown that this equation often overestimates inclination shallowing [44]. To this end, these studies added a constant factor a to equation (5), which is dependent on the shape of the magnetic particles:

$$\tan(I_1) = (1 - a\Delta V)\tan(I_0) \qquad (6)$$

If we consider the most simple assumption where the magnetizations in our sedimentary sequence are carried by equidimensional magnetite, then a = 0.54 [44]. Together with the previously determined value for ΔV = 0.18, this gives an unflattened inclination of 5.4±2.9°, equivalent to a latitude of 2.7±1.5°N. Subsequent studies [43] have determined that equation (6) approximates derivations based on different physical parameters, such as change of randomness of grain rotations and differences in initial dispersion of magnetic moments.

A final, more conservative, generalized approach is to use a ratio f=0.6 in equation (2) [45]. The corrected inclination is then 8.1±4.5° with a paleolatitude of 4.1±2.3°N.

In all cases, the influence of inclination shallowing on our results is not significant, because the initial inclination is low [34,45]. Moreover, the early-diagenetic siderite precipitated during shallow burial [31]

and therefore devoid of clast reorientation during deposition and further compaction effects (See previous sections), yield inclination values equivalent to the other rock types, is another indication of negligible influence of inclination shallowing on our results.

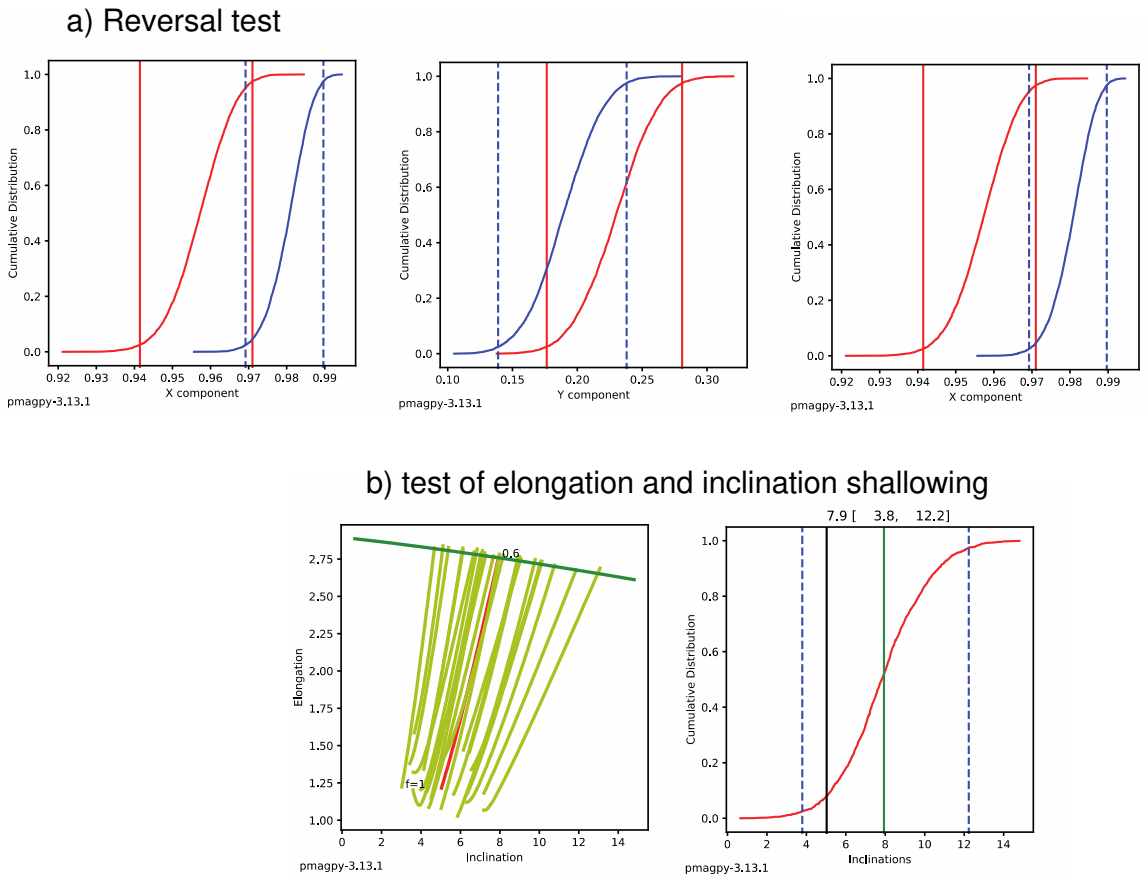

Figure 4.S10: *a) Negative reversal test from the Kalewa sediments (Chindwin Basin) using the Cartesian coordinate bootstrap method [54]; b) Classic Elongation-Inclination (E-I) test to investigate the effect of inclination shallowing on the Kalewa sediments (Chindwin Basin) [34–37].*

5. Reference frame for plate reconstructions

We investigated differences in our plate tectonic reconstructions (Fig. 4) between a paleomagnetic and hotspot reference frame. At 60Ma and 95Ma there are no significant latitudinal differences between both reference frames [46]. At 40 Ma however, India and Eurasia are about 5° farther north in the paleomagnetic reference frame than in the hotspot reference frame. Indeed, low inclinations in Asia around 40 Ma have been a long-standing concern [47,48], and the global apparent polar wander path (APWP) [49] is mainly based on poles from North America (even its north-western margin with a complicated tectonic history) and north-east Africa. No pole from Siberia has been included in the calculation of the global APWP. We have recalculated the expected latitude for India using each

individual pole used in the global APWP after rotation to India, using the current plate rotations from GPlates. The resulting scatter is significant and moreover the selection of several poles used in the global APWP is questionable. In particular, two poles from late Eocene sediments and volcanics from north-east Africa are used, while they likely underwent local clockwise rotation according to the original publication [50]. Furthermore, inclination shallowing corrections were applied on results partly based on volcanic rocks [50]. Therefore, we opted to make all our plate reconstructions in the combined hotspot (0-70 Ma) and paleomagnetic (70-250 Ma) reference frame from the Matthews 2016 GPlates model [46,51], instead of a full paleomagnetic reference frame. This puts India and Eurasia slightly more to the south at that time, which also provides a better match with our 40 Ma position for the BT.

References Chapter 4 – Supplementary information

1. Morley, C. K. Evolution from an oblique subduction back-arc mobile belt to a highly oblique collisional margin: the Cenozoic tectonic development of Thailand and eastern Myanmar. *Geol. Soc. Lond. Spec. Publ.* **318**, 373–403 (2009).

2. Socquet, A. *et al.* India and Sunda plates motion and deformation along their boundary in Myanmar determined by GPS: GPS INDIA-SUNDA MOTION, MYANMAR STRAIN. *J. Geophys. Res. Solid Earth* **111**, n/a-n/a (2006).

3. Rangin, C., Maurin, T. & Masson, F. Combined effects of Eurasia/Sunda oblique convergence and East-Tibetan crustal flow on the active tectonics of Burma. *J. Asian Earth Sci.* **76**, 185–194 (2013).

4. Mitchell, A. H. G. Cretaceous–Cenozoic tectonic events in the western Myanmar (Burma)–Assam region. *J. Geol. Soc.* **150**, 1089–1102 (1993).

5. Metcalfe, I. Gondwana dispersion and Asian accretion: Tectonic and palaeogeographic evolution of eastern Tethys. *J. Asian Earth Sci.* **66**, 1–33 (2013).

6. Searle, M. P. *et al.* Chapter 12 Tectonic and metamorphic evolution of the Mogok Metamorphic and Jade Mines belts and ophiolitic terranes of Burma (Myanmar). *Geol. Soc. Lond. Mem.* **48**, 261–293 (2017).

7. Bertrand, G. & Rangin, C. Tectonics of the western margin of the Shan plateau (central Myanmar): implication for the India–Indochina oblique convergence since the Oligocene. *J. Asian Earth Sci.* **21**, 1139–1157 (2003).

8. Morley, C. K. Nested strike-slip duplexes, and other evidence for Late Cretaceous–Palaeogene transpressional tectonics before and during India–Eurasia collision, in Thailand, Myanmar and Malaysia. *J. Geol. Soc.* **161**, 799–812 (2004).

9. Ridd, M. F. & Watkinson, I. The Phuket-Slate Belt terrane: tectonic evolution and strike-slip emplacement of a major terrane on the Sundaland margin of Thailand and Myanmar. *Proc. Geol. Assoc.* **124**, 994–1010 (2013).

10. Rangin, C., Maurin, T. & Masson, F. Combined effects of Eurasia/Sunda oblique convergence and East-Tibetan crustal flow on the active tectonics of Burma. *J. Asian Earth Sci.* **76**, 185–194 (2013).

11. Maung, H. Transcurrent movements in the Burma–Andaman Sea region. *Geology* **15**, 911 (1987).

12. Morley, C. K. Syn-kinematic sedimentation at a releasing splay in the northern Minwun Ranges, Sagaing Fault zone, Myanmar: significance for fault timing and displacement. *Basin Res.* **29**, 684–700 (2017).

13. Morley, C. K. Chapter 4 Cenozoic rifting, passive margin development and strike-slip faulting in the Andaman Sea: a discussion of established v. new tectonic models. *Geol. Soc. Lond. Mem.* **47**, 27–50 (2017).

14. Mitchell, A., Chung, S.-L., Oo, T., Lin, T.-H. & Hung, C.-H. Zircon U–Pb ages in Myanmar: Magmatic–metamorphic events and the closure of a neo-Tethys ocean? *J. Asian Earth Sci.* **56**, 1–23 (2012).

15. Shi, G. *et al.* Ion microprobe zircon U–Pb age and geochemistry of the Myanmar jadeitite. *J. Geol. Soc.* **165**, 221–234 (2008).

16. Yui, T.-F. *et al.* Is Myanmar jadeitite of Jurassic age? A result from incompletely recrystallized inherited zircon. *Lithos* **160–161**, 268–282 (2013).

17. Barber, A. J. & Crow, M. J. Structure of Sumatra and its implications for the tectonic assembly of Southeast Asia and the destruction of Paleotethys. *Isl. Arc* **18**, 3–20 (2009).

18. Liu, C.-Z. *et al.* Tethyan suturing in Southeast Asia: Zircon U-Pb and Hf-O isotopic constraints from Myanmar ophiolites. *Geology* **44**, 311–314 (2016).

19. United Nations. Geology and exploration geochemistry of the Pinlebu-Banmauk area, Sagaing Division, northern Burma. Technical Report No. 2. DP/UN/BUR-72-002. *Geol. Surv. Explor. Proj. U. N. Dev. Programme N. Y.* 66 (1978a).

20. Sevastjanova, I. *et al.* Myanmar and Asia united, Australia left behind long ago. *Gondwana Res.* **32**, 24–40 (2016).

21. Yao, W. *et al.* Origin and tectonic evolution of upper Triassic Turbidites in the Indo-Burman ranges, West Myanmar. *Tectonophysics* **721**, 90–105 (2017).

22. Bender, F. *Geology of Burma*. (1983).

23. Pivnik, D. A. *et al.* Polyphase Deformation in a Fore-Arc/Back-Arc Basin, Salin Subbasin, Myanmar (Burma). *AAPG Bull.* **82(10)**, 1837–1856 (1998).

24. Zhang, P. *et al.* Structures, uplift, and magmatism of the Western Myanmar Arc: Constraints to mid-Cretaceous-Paleogene tectonic evolution of the western Myanmar continental margin. *Gondwana Res.* **52**, 18–38 (2017).

25. Gardiner, N. J. *et al.* Contrasting Granite Metallogeny through the Zircon Record: A Case Study from Myanmar. *Sci. Rep.* **7**, (2017).

26. Wang, J.-G., Wu, F.-Y., Tan, X.-C. & Liu, C.-Z. Magmatic evolution of the Western Myanmar Arc documented by U–Pb and Hf isotopes in detrital zircon. *Tectonophysics* **612–613**, 97–105 (2014).

27. Fareeduddin, A. & Dilek, Y. Structure and petrology of the Nagaland-Manipur Hill ophiolitic mélange zone. *NE India Foss. Tethyan Subduction Channel India-Burma Plate Bound. Episodes* **38**, 298–314 (2015).

28. Licht, A. *et al.* Paleogene evolution of the Burmese forearc basin and implications for the history of India-Asia convergence. *Geol. Soc. Am. Bull.* **1**, 20 (2018).

29. Singh, A. K. *et al.* Evidence of Mid-ocean ridge and shallow subduction forearc magmatism in the Nagaland-Manipur ophiolites, northeast India: constraints from mineralogy and geochemistry of gabbros and associated mafic dykes. *Geochemistry* **76**, 605–620 (2016).

30. Mitchell, A. *Geological Belts, Plate Boundaries, and Mineral Deposits in Myanmar*. (Elsevier, 2017).

31. Mozley, P. S. & Wersin, P. Isotopic composition of siderite as an indicator of depositional environment. *Geology* **20(9)**, 817–820 (1992).

32. Shau, Y.-H., Torii, M., Horng, C.-S. & Peacor, D. R. Subsolidus evolution and alteration of titanomagnetite in ocean ridge basalts from Deep Sea Drilling Project/Ocean Drilling Program Hole 504B9 Leg 83: Implications for the timing of magnetization. *J. Geophys. Res. Solid Earth* **105**, 23635–23649 (2000).

33. Borradaile, G. J. & Henry, B. Tectonic applications of magnetic susceptibility and its anisotropy. *Earth-Sci. Rev.* **42**, 49–93 (1997).

34. King, R. F. The remanent magnetism of artificially deposited sediments. *Geophys. J. Int.* **7**, 115–134 (1955).

35. Tauxe, L. & Kent, D. V. A simplified statistical model for the geomagnetic field and the detection of shallow bias in paleomagnetic inclinations: was the ancient magnetic field dipolar. *Timescales Paleomagn. Field* **145**, 101–116 (2004).

36. Tauxe, L., Kodama, K. P. & Kent, D. V. Testing corrections for paleomagnetic inclination error in sedimentary rocks: a comparative approach. *Phys. Earth Planet. Inter.* **169**, 152–165 (2008).

37. Koymans, M. R., Langereis, C. G., Pastor-Galán, D. & van Hinsbergen, D. J. *Paleomagnetism. org: An online multi-platform open source environment for paleomagnetic data analysis*. (Elsevier, 2016).

38. Li, Y.-X. & Kodama, K. P. Detecting and correcting for paleomagnetic inclination shallowing of sedimentary rocks: A review. *Front. Earth Sci.* **4**, 7 (2016).

39. Cogné, J.-P. Contribution a l'étude paléomagnétique des roches déformées. (Université Rennes 1, 1987).

40. Addis, M. A. & Jones, M. E. Volume changes during diagenesis. *Mar. Pet. Geol.* **2**, 241–246 (1985).

41. Brewster Baldwin. Ways of Deciphering Compacted Sediments. *SEPM J. Sediment. Res.* **Vol. 41**, (1971).

42. Ehrenberg, S. N. & Nadeau, P. H. Sandstone vs. carbonate petroleum reservoirs: A global perspective on porosity-depth and porosity-permeability relationships. *AAPG Bull.* **89**, 435–445 (2005).

43. Arason, P. & Levi, S. Models of inclination shallowing during sediment compaction. *J. Geophys. Res.* **95**, 4481 (1990).

44. Anson, G. L. & Kodama, K. P. Compaction-induced inclination shallowing of the post-depositional remanent magnetization in a synthetic sediment. *Geophys. J. R. Astron. Soc.* **88**, 673–692 (1987).

45. Tauxe, L. & Kent, D. V. Properties of a detrital remanence carried by haematite from study of modern river deposits and laboratory redeposition experiments. *Geophys. J. R. Astron. Soc.* **76**, 543–561 (1984).

46. Torsvik, T. H., Müller, R. D., Van der Voo, R., Steinberger, B. & Gaina, C. Global plate motion frames: Toward a unified model. *Rev. Geophys.* **46**, (2008).

47. Cogne, J.-P., Besse, J., Chen, Y. & Hankard, F. A new Late Cretaceous to Present APWP for Asia and its implications for paleomagnetic shallow inclinations in Central Asia and Cenozoic Eurasian plate deformation. *Geophys. J. Int.* **192**, 1000–1024 (2013).

48. Dupont-Nivet, G., van Hinsbergen, D. J. J. & Torsvik, T. H. Persistently low Asian paleolatitudes: Implications for the India-Asia collision history: PERSISTENTLY LOW ASIAN PALEOLATITUDES. *Tectonics* **29**, n/a-n/a (2010).

49. Torsvik, T. H. *et al.* Phanerozoic polar wander, palaeogeography and dynamics. *Earth-Sci. Rev.* **114**, 325–368 (2012).

50. Lofty, H. & Van der Voo, R. Tropical northeast Africa in the middle-late Eocene: Paleomagnetism of the marine-mammals site and basalts in the Fayoum province. *Egypt J Afr Earth Sci* **47**, 135–152 (2007).

51. Matthews, K. J. *et al.* Global plate boundary evolution and kinematics since the late Paleozoic. *Glob. Planet. Change* **146**, 226–250 (2016).

52. Poinar, G. Burmese amber: evidence of Gondwanan origin and Cretaceous dispersion. *Hist. Biol.* 1–6 (2018). doi:10.1080/08912963.2018.1446531

53. Grimaldi, D. A., Engel, M. S. & Nascimbene, P. C. Fossiliferous Cretaceous Amber from Myanmar (Burma): Its Rediscovery, Biotic Diversity, and Paleontological Significance. *Am. Mus. Novit.* **3361**, 1–71 (2002).

54. Tauxe, L. *Essentials of paleomagnetism*. (Univ of California Press, 2010).

Press release: The India-Asia collision as seen from Myanmar

Researchers from the University of Rennes 1 / CNRS (France), the University of Washington (USA) and the Universities of Yangon and Shwebo (Myanmar) have obtained new paleomagnetic evidence that the Burma Microplate was located close to the equator between 95 and 40 million years ago. These results, published in Nature Geoscience, support a double collision of India, first with an isolated volcanic arc between India and Asia, followed by a final collision with Asia. These results shed new light on the paleogeography of this region, and suggest island endemism for the flora and fauna trapped in the famous fossil ambers from Myanmar.

The collision of the Indian continent with Asia is the most dramatic geological event on Earth since the extinction of the dinosaurs 66 million years ago (Ma). It is responsible for the formation of the highest mountains in the world – the Himalayas and the Tibetan Plateau. The formation of these mountains led to the onset of Asian monsoons and probably a global climatic cooling, changing the Earth from an icecap-free world to a planet with icecaps at its two poles. Despite its importance, the India-Asia collision remains poorly understood and therefore it is currently one of the most intensely debated subjects among earth scientists. They argue over two main collision models: (1) A simple collision between India and Asia around 60-50 Ma, or (2) a two-stage collision with firstly a collision of India with a small volcanic chain in the ancient Tethys Ocean between India and Asia, before the final India-Asia collision. Adopting one of these models has major implications for understanding mountain formation processes and their impact on both regional and global climate change.

As not many rocks have been preserved in the collision zone between India and Asia, scientists have turned their attention to the sides of this zone, notably to Myanmar, a country only recently opened to international geological research. The sedimentary basins and magmatic rocks of Myanmar represent valuable archives of the collision. Therefore, they are investigated as part of ERC project MAGIC ('Monsoons of Asia caused Greenhouse to Icehouse Cooling') with the primary objective of constraining the role of monsoons in the evolution of global climate during the India-Asia collision. The investigated rocks are mainly situated on a tectonic microplate (Burma Microplate), bounded to the north by the eastern syntaxis of the Himalaya mountain range, to the west by the Indian Plate, to the south by the oceanic spreading ridge of the Andaman Sea and to the east by the Sagaing Fault, a large-scale active fault which moves around 2 cm/year. Despite the complex geological history and significant tectonic displacements that these characteristics suggest, most previous geological studies suggested that the Burma Microplate did not move much, being part of Asia for more than 200 Ma. No paleogeographic data was available to confirm this hypothesis.

Hence, a paleomagnetic study was conducted to put constraints on the paleogeography of the Burma Microplate. Using the ancient magnetic field of the Earth recorded in a given rock, paleomagnetism can determine determine the latitude at which this rock was formed and whether it has undergone a rotation around its vertical axis. Paleomagnetic results from a volcanic arc in Myanmar (Wuntho-Popa Arc) put the Burma Microplate at a latitude close to the equator (~5 degrees south) at 95 Ma and show that it underwent around 60 degrees of clockwise rotation since this time. Paleomagnetic data from sedimentary rocks formed at 40 Ma also show near-equatorial latitudes, but record no significant rotation of the Burma Microplate.

These results have multiple major implications. First of all, the near-equatorial position of the Burmese volcanic arc at 95 Ma is almost 3000 km away from the Asian margin. Therefore, it was rather part of a Trans-Tethyan volcanic arc in the middle of the ocean. This reinforces the hypothesis of a first collision of India with a volcanic chain in the Tethys Ocean at ~60 Ma before a final collision with Asia at a later point in time.

Beyond plate tectonics, proof for the existence of an isolated volcanic arc in the Tethys Ocean also has implications for paleoclimatology and paleontology. As part of ERC project MAGIC, paleoclimatic simulations can now take into account the updated paleogeography of Myanmar and Asia. It is now evident that sedimentary rocks of Myanmar between 100 and 40 Ma old, which also contain the oldest discovered primate fossils, were formed in an equatorial climate. Moreover, fossil ambers from Myanmar harbour one of the most diverse and well-known records of biodiversity with more than 870 reported species, including plants, insects and vertebrates. This biodiversity is the subject of more than a hundred scientific articles each year. The new paleomagnetic data from Myanmar can therefore provide insight into the importance of volcanic chains forming land bridges for the dispersion of species, a possible Gondwanan affinity and island endemism.

This study highlights the importance of paleomagnetic data to constrain tectonic displacements and understand the formation of mountain ranges and associated changes in climatic and biologic conditions.

Reference: https://sciglow.com/the-india-asia-collision-as-seen-from-myanmar/

Chapter 5: Eocene to Miocene northward motion of the Burma Terrane and its indentation in the Eastern Himalayas.

Vertebrate fossil in the Letkat Formation, Chindwin Basin.
(Kalewa, Myanmar, Fieldwork November 2017)

Reference: Westerweel, J., Licht, A., Cogné, N., Roperch, P., Dupont-Nivet, G., Kai, M. T., … Aung, D. W (2020). Eocene to Miocene northward motion of the Burma Terrane and its indentation in the Eastern Himalayas. Tectonics. https://doi.org/10.1029/2020TC006413

Jan Westerweel[1,*], Alexis Licht[2], Nathan Cogné[1], Pierrick Roperch[1], Guillaume Dupont-Nivet[1,3], Myat Kay Thi[4], Hnin Hnin Swe[4], Huasheng Huang[5], Zaw Win[6], Day Wa Aung[4]

[1] Geosciences Rennes, CNRS, Univ. Rennes, Rennes, France. [2] Dept. Earth and Space Sciences, University of Washington, Seattle, United States. [3] Department of Geociences, Potsdam University, Potsdam, Germany. [4] Department of Geology, University of Yangon, Yangon, Myanmar. [5] Institute for Biodiversity and Ecosystem Dynamics, University of Amsterdam, Amsterdam, The Netherlands. [6] Department of Geology, University of Shwebo, Shwebo, Myanmar.

* Corresponding author (e-mail: jan.westerweel@univ-rennes1.fr)

Abstract

The Burma Terrane (Myanmar) played an important role in the India-Asia collision and moved over 2000 km northward on the Indian Plate during the Cenozoic, before colliding with the Asian margin. However, the timing of this collision and its correlation to regional uplift phases, sedimentary provenance and basin development, remain poorly constrained. We report sedimentological, paleomagnetic and geochronological data from the late Eocene to early Miocene strata of the Chindwin Basin in the Burmese forearc, constraining the paleogeographic evolution of the Burma Terrane and the Eastern Himalayan orogen. Our results highlight two unconformities of late Eocene – middle Oligocene and latest Oligocene – early Miocene age, revealing a two stage interaction of the Burma Terrane with the Asian margin during its northward translation. The first unconformity follows rapid ~0.6 m/k.y. subsidence in the Burmese forearc, as shown by magnetostratigraphy. The transition to a fluvial depositional environment and the occurrence of reworked sediments at this first unconformity likely records the commencing collision of India and the northern extent of the Burma Terrane with the Asian margin. The second unconformity shows drastic changes in magnetic properties, mineralogy and provenance, with high-grade metamorphic grains and early Miocene apatite U-Pb and fission track ages indicating that it is coeval to a major deformation phase in Myanmar and the Eastern Himalayan orogen. It likely records the indentation of the Burma Terrane into the Eastern Himalayan collision zone, forming the modern Eastern Himalayan Syntaxis.

Plain language summary

The evolution of the India-Asia collision and the resulting formation of the dramatic Himalayan mountain chain are highly debated among geologists. One of the reasons is that the easternmost extent of this mountain range is understudied compared to its central part. In Myanmar, at the eastern end of the Himalayas, this is partly caused by political and scientific isolation over the past 70 years, limited road access, and jungle covering much of the exposure. This study helps to

constrain the paleogeographic evolution of the Burma Terrane, the microplate including most of Myanmar. To this end, we used a variety of methods including describing sedimentary deposits of the Burma Terrane, dating these deposits and determining their corresponding source regions. With this new information, we were able to determine that the deposition of these sediments occurred from ~40 to 23 million years ago but was discontinuous with two large hiatuses of millions of years long. Our results show that these two hiatuses are a consequence of a two-stage process during the large northward motion of the Burma Terrane involving (1) the first collision of India and the northern Burma Terrane with Asia and (2) the indentation of Burma into the Himalayan collision zone.

Key Points:

The Eocene to Lower Miocene sedimentary infill of the Chindwin forearc basin of the Burma Terrane is punctuated by two major unconformities.

The first late Eocene - middle Oligocene unconformity records the initial collision of India and the northern Burma Terrane with Asia.

The second late Oligocene - early Miocene unconformity marks major deformation in the Eastern Himalayas due to Burma Terrane northward motion.

1. Introduction

The Himalayan-Tibetan orogen, formed primarily as a result of the India-Asia collision, is widely recognized as the archetype orogen for studying the evolution of continent-continent collision systems. Its complex geodynamic history and profound influence on Asian paleoenvironments and climate have been described by a diversity of studies (Dupont-Nivet et al., 2007; Kapp & DeCelles, 2019; Licht et al., 2014a; Royden et al., 2008; Yin & Harrison, 2000). Yet, the paleogeographic evolution of the Asian margin during the convergence of India and Asia, as well as the timing of the collision itself, remain subject to debate (e.g. Hu et al., 2015; Jagoutz et al., 2015; Replumaz et al., 2010, 2013; Royden et al., 2008; Shen et al., 2001; van Hinsbergen et al., 2011, 2018; Westerweel et al., 2019). An important reason behind this ongoing debate is that the ~1500 km long eastern extent of the Himalayas in Myanmar remains understudied compared to the central orogen in terms of timing of tectonic events, sedimentary sourcing and roles of different tectonic terranes, resulting in a substantial spatial gap in our understanding of the India-Asia collision.

This is best illustrated by the Burma Terrane (BT, also called West Burma Block), a major tectonic terrane comprising most of Myanmar. Fundamental aspects of the geological history of the BT remain debated, despite it being key to the geodynamic evolution of the India-Asia collision (Licht et al., 2019; Westerweel et al., 2019). Since the Neogene, its unique tectonic regime (Fig. 5.1a) is characterized by hyper-oblique subduction of the Indian Plate beneath the Burmese active margin to the west, causing sporadic volcanism along the Wuntho-Popa Arc (WPA; (Lin et al., 2019; Mitchell et al., 2012). In addition, it induced large-scale dextral strike-slip displacements along the Sagaing Fault bounding the BT to the east, resulting in a northward transcurrent motion of the BT (Bertrand & Rangin, 2003; Mitchell et al., 2012; Morley, 2017; Morley et al., 2020; Morley & Arboit, 2019; Rangin, 2018; Rangin et al., 2013; Socquet et al., 2006).

Recent paleo-rotation and paleolatitude data from paleomagnetism indicate that the BT was part of a near-equatorial, isolated Trans-Tethyan Arc from the Late Cretaceous to the early Paleogene when India collided with this Trans-Tethyan Arc (Westerweel et al., 2019). The paleomagnetic data also show that since the late Eocene, the BT underwent over 2000 km of northward translation alongside India from a near-equatorial position (Westerweel et al., 2019). To the east, strike-slip motion along the Sagaing Fault, a precursor thereof, or an India-Australia Transform separated the BT from the Indochina margin (Morley et al., 2020; Morley & Arboit, 2019). This significant northward translation moved the BT from near-equatorial latitudes towards the Eastern Himalayan collision zone. However, crucial questions such as the location and timing of indentation of the BT into the collision zone and subsequent underthrusting, its interaction with India, as well as the relation of these events to regional phases of uplift and exhumation remain unanswered within this new tectonic

context. Furthermore, the new tectonic context requires a re-evaluation of the provenance of the Cenozoic sedimentary basins within the BT, because it shows that the BT was potentially isolated from sedimentary sources in Asia and Indochina until the Eocene to Oligocene (Morley et al., 2020; Westerweel et al., 2019).

In this paper, we study the Cenozoic sedimentary record of the Burmese forearc to constrain changes in tectonic setting, sedimentary provenance and paleoenvironment during the ~2000 km northward journey from the equator towards the collision zone. To constrain the interaction of the BT with Asia and India, we investigated a ~2 km thick Eocene to Oligocene sedimentary section in the Chindwin Basin, north-western Myanmar, using results from sedimentology, magnetostratigraphy, magnetic properties and zircon U-Pb, apatite U-Pb and apatite fission track (AFT) dating. Our results enable us to evaluate the plate tectonic and paleogeographic evolution of the Eastern Himalayan collision zone.

2. Geological setting

Traditionally, the geology of Myanmar is subdivided into three broad N-S trending regions: The Indo-Burman Ranges (IBR), the Burma Terrane (BT) and the Shan Plateau on the Sibumasu Block. In northern Myanmar, these regions extend into the Eastern Himalayan orogen.

2.1. The Burma Terrane

The BT forms the bulk of western and central Myanmar. Known basement units of the BT only crop out in the IBR and in the Wuntho Ranges, the predominantly Mesozoic volcanic complex forming the northern segment of the WPA (Mitchell, 2017; United Nations, 1978a). Northeast of the Wuntho Ranges, the serpentinites and jadeites of the Jade Belt are only exposed at the northern edge of the Sagaing Fault (Fig. 5.1a) and have a poorly constrained emplacement age (Searle et al., 2017; Yui et al., 2013). East of the Jade Belt, the Tagaung-Myitkyina Belt comprises Triassic to Jurassic metasedimentary rocks and Jurassic to Cretaceous volcanics (Mitchell, 2017), notably the ~50 Ma Sodon Batholith that has been correlated with the WPA (Lin et al., 2019).

The Sagaing Fault and Mogok-Mandalay-Mergui Belt (MMMB) form the boundary of the BT with the Shan Plateau, Sibumasu (Fig. 5.1a). The MMMB is a metamorphic belt forming the southeast continuation of the pre-collision Asian margin. The most prominent rocks of the MMMB include Cretaceous – Cenozoic intrusives with generally negative εHf(t) values, as well as regionally metamorphosed ophiolitic and sedimentary rocks (Gardiner et al., 2018; Lin et al., 2019; Mitchell, 2017; Mitchell et al., 2012; Searle et al., 2017). The MMMB records two main metamorphic events: A latest Cretaceous – early Paleocene phase of metamorphism and partial melting, followed by a phase of high temperature metamorphism during the late Eocene – Oligocene, suggested to be

related to the India-Asia collision (Searle et al., 2007, 2017, 2020). Low temperature thermochronometers show a late Eocene - Miocene phase of rapid exhumation related to the strike-slip deformation and extrusion of the MMMB (Bertrand et al., 2001; Bertrand & Rangin, 2003). Plate reconstructions suggest that the MMMB, including the Tengchong and Baoshan blocks, was extruded from the Eastern Himalayan Syntaxis towards the southeast since approximately the late Paleogene (Li et al., 2018; Tong et al., 2013; Westerweel et al., 2019).

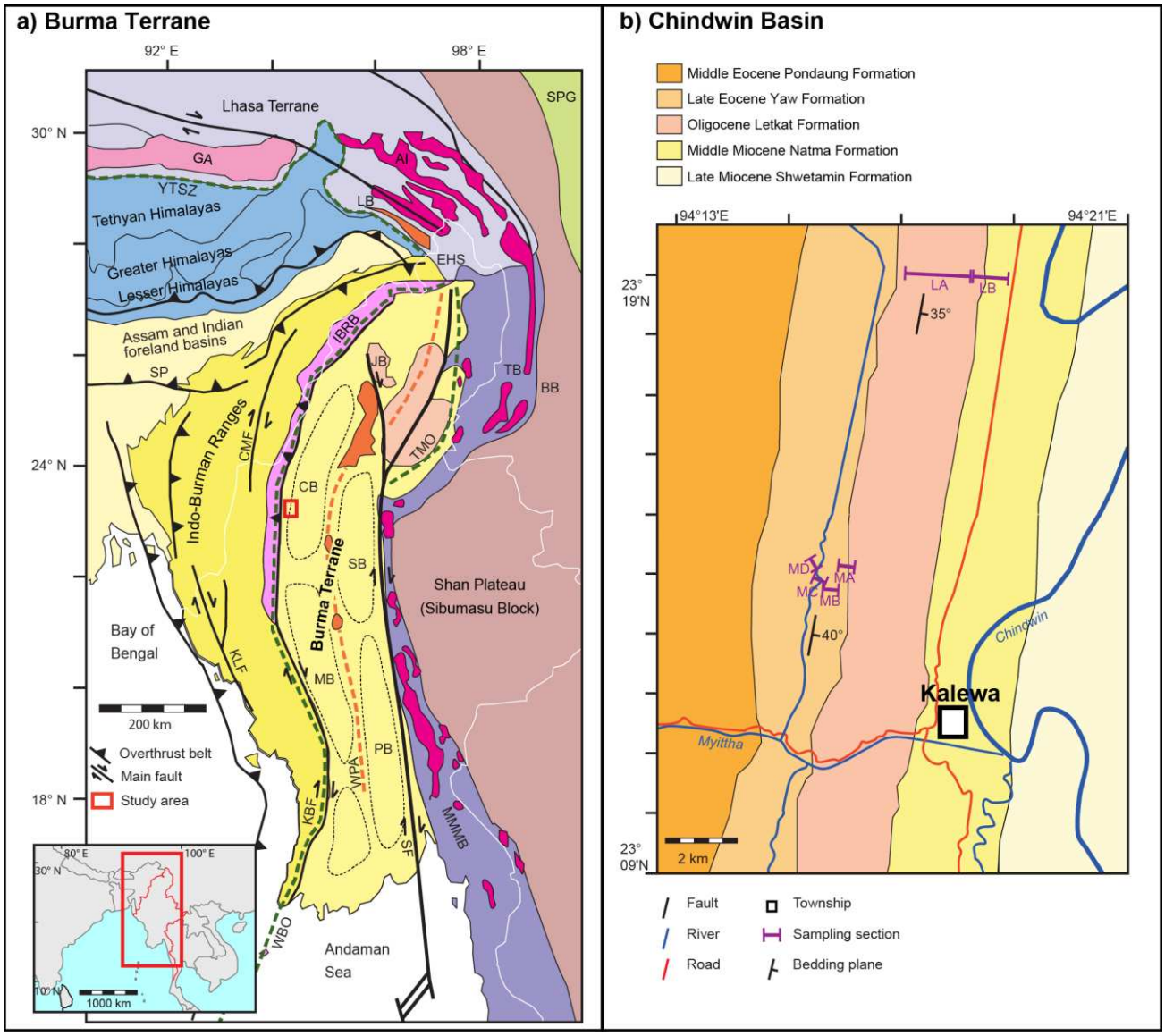

Figure 5.1: *a) Geological map of Myanmar and surrounding regions. Abbreviations: AI = Cretaceous-Paleogene Asian intrusives, BB = Baoshan Block, CB = Chindwin Basin, CMF = Churachandpur Mao Fault, EHS = Eastern Himalayan Syntaxis, GA = Cretaceous Gangdese Arc, IBRB: Indo-Burman Ranges basement, JB = Jade Belt, KBF = Kabaw Fault, KLF = Kaladan Fault, LB = Lohit Batholith, MB = Minbu Basin, MMMB = Mogok–Mandalay–Mergui Belt, PB = Pegu Basin, SB = Shwebo Basin, SF = Sagaing Fault, SP = Shilong Plateau, SPG = Songpan Ganze & Yangtze complexes, TB = Tengchong Block, TMO*

= Tagaung-Myitkyina Ophiolite, WBO = Cretaceous Western Belt Ophiolite, WPA = Wuntho-Popa Arc, YTSZ = Yarlung-Tsangpo Suture Zone. Dashed black lines: Central Myanmar Basins; b) Geological map of the study area around Kalewa in the Chindwin Basin (after Westerweel et al., 2019).

The Burmese subduction margin, located west of the BT, formed during the mid-Cretaceous as evidenced by emplacement of the Naga Hills-Kaleymyo-Andaman Ophiolitic belt (also called the Western Belt Ophiolite; Fig. 1a; Fareeduddin & Dilek, 2015; Licht et al., 2019; Morley et al., 2020; Pivnik et al., 1998; Singh et al., 2016). This was followed by early Late Cretaceous Andean-type magmatism in the WPA. The near-equatorial latitudes from paleomagnetic data from the early Late Cretaceous WPA rocks imply that the BT was part of a Trans-Tethyan Arc at that time (Westerweel et al., 2019). Magmatic activity in the WPA peaked at ~110-90 Ma, followed by a ~70-40 Ma subordinate stage indicating a decrease in activity (Barley & Zaw, 2009; Gardiner et al., 2017; Mitchell et al., 2012; Wang et al., 2014; Zhang et al., 2017). The WPA rocks are today exposed in the Wuntho Ranges, where only the ~110-90 Ma stage and a minor peak in volcanic activity at ~42-36 Ma are present (Barley & Zaw, 2009; Gardiner et al., 2017; Licht et al., 2020; Lin et al., 2019). The remaining part of the WPA is covered by Cenozoic sediments. The Paleogene sequence of this sedimentary cover was partially eroded during a subsequent Oligocene phase of exhumation, as shown by a large angular unconformity in seismic lines across the WPA (Zhang et al., 2017).

2.2. Indo-Burman Ranges

The Western Belt Ophiolite and the Kabaw Fault form the western boundary separating the BT from the IBR (Fig. 5.1a; Liu et al., 2016; Mitchell et al., 2012; Morley et al., 2020; Searle et al., 2017). The IBR constitute an accretionary complex formed by subduction of the Indian Plate, separating the BT from the Indian Foreland Basins and Bay of Bengal (Rangin, 2018). The IBR are divided into an Outer Wedge and an Inner Wedge (Bannert et al., 2012; Brunnschweiler, 1966; Maurin & Rangin, 2009; Mitchell, 2017). The Outer Wedge consists of a predominantly Neogene fold and thrust belt deforming the sediments of the Bengal fan with Himalayan affinity (Betka et al., 2018; Najman et al., 2012; Rangin, 2018; Steckler et al., 2008).

The geology and deformation history of the Inner Wedge are more complex compared to the Outer Wedge. The oldest basement units in the Inner Wedge (Triassic Pane Chaung Formation and Kanpetlet Schists) are covered by a sequence of Upper Cretaceous – Eocene marine turbiditic rocks (Bannert et al., 2012; Maurin & Rangin, 2009; Mitchell, 2017). These turbiditic rocks are unconformably overlain by late Eocene - early Oligocene molasse deposits, indicating an initial uplift phase within the IBR at that time (Bannert et al., 2012; Ghose et al., 2014; Morley et al., 2020). The IBR turbiditic rocks share the same petrography and zircon U-Pb age distributions as coeval

sediments in the Burmese forearc basin, indicating both have similar source regions, likely including the WPA (Licht et al., 2019; Naing et al., 2014; Najman et al., 2020; Wang et al., 2014). By contrast, more recent Neogene sediments in the IBR were likely supplied by Himalayan sources or uplifting IBR basement (Naing et al., 2014; Najman et al., 2020). Recent low temperature thermochronological data documented a major exhumation phase within the IBR during the latest Oligocene – earliest Miocene, and a possible earlier event in the late middle Eocene (Najman et al., 2020). Changes of sedimentary facies in the late middle Eocene in the forearc basin, indicating the onset of wide barrier-bound estuaries, were interpreted as reflecting incipient IBR uplift (Licht et al., 2019).

There are differing interpretations on the cause for these uplift phases. It has been proposed that late middle Eocene uplift of the IBR was the result of coupling with India (Aitchison et al., 2007; Morley, 2009; Morley et al., 2020; Vérard et al., 2017) or an allochthonous terrane (Acharyya, 2007, 2015). Other studies have argued that the uplift of the Inner Wedge was induced by the rapidly uplifting retro-wedge region of the IBR formed due to hyper-oblique subduction (Licht et al., 2019; Maurin & Rangin, 2009; Nielsen et al., 2004). Major strike-slip deformation in the IBR occurred since the Neogene, illustrated by the initiation of major dextral faults such as the (South) Kabaw, Kaladan and Churachandpur Mao Faults (Maurin & Rangin, 2009; Morley et al., 2020; Rangin, 2018).

2.3. Eastern Himalayan orogen

To the north, the transition from the BT to the Eastern Himalayan orogen is defined by the intersection of the Sagaing Fault and the IBR (Lin et al., 2019; Mitchell, 2017; Mitchell et al., 2012). However, it is unclear how much of the northern extension of the BT (i.e. Greater Burma) was shortened, subducted and underthrust in the Eastern Himalayan syntaxis during its northward motion (Haproff et al., 2019, 2020; Morley et al., 2020; Westerweel et al., 2019). At present, the orogen bends from ~E-W to ~NW-SE at the Eastern Himalayan Syntaxis (Fig. 5.1a). Prominent lithologies in the Eastern Himalayan Syntaxis directly north of the BT include deformed metamorphosed rocks such as gneiss and schist, ophiolitic mélange and (meta)sediments, but also volcanic complexes such as the Late Jurassic - Cretaceous I-type Lohit Batholith and the Jurassic – Cretaceous S-type Bomi-Chayu Batholith (Haproff et al., 2019; Lin et al., 2019). Many of the intrusive units in the Eastern Himalayan orogen have also been correlated with similar lithologies in Myanmar to the (south-)east based on age and εHf(t) values, notably the Bomi-Chayu Batholith with the Dianxi Batholith in the MMMB or the Lohit Batholith with the WPA (Lin et al., 2019; Mitchell et al., 2012).Important deformation phases in the Eastern Himalayan orogen include an early Miocene phase of uplift and exhumation, as recorded by ~20-15 Ma activity along the Lohit thrust (Haproff et

al., 2019). This corresponds to a ~23-16 Ma phase of uplift and exhumation of the Greater Himalayas across the entire Himalayan orogen (Garzanti, 2019; Vannay et al., 2004). Additional rapid exhumation at ~14-17 Ma is reported from the Greater Himalayas along the Main Central Thrust in the Eastern Himalayan Syntaxis (Godin et al., 2006; Kellett et al., 2013; Najman et al., 2019). This early Miocene deformation phase led to the set-up of the modern Eastern Himalayan Syntaxis, which sources the Yarlung Tsangpo Brahmaputra River flowing towards the Bay of Bengal (Bracciali et al., 2015). Finally, this was followed by the intense late Miocene - Pliocene exhumation phases in the Eastern Himalayan Syntaxis core (Bracciali et al., 2016; Lang et al., 2016; Najman et al., 2019; van der Beek et al., 2019; Zeitler et al., 2014).

2.4. Central Myanmar Basins

The Central Myanmar Basins (CMB) on the BT developed as early as the Albian in forearc and back-arc positions, subdivided by the WPA (Fig. 5.1a; Bender, 1983; Cai et al., 2019; Licht et al., 2019; Pivnik et al., 1998; Zhang et al., 2017). Seismic lines across the CMB show four regional unconformities, interpreted to reflect deformation phases attributed to the Late Cretaceous, late Eocene, Oligocene, and late Miocene (Pivnik et al., 1998; Zhang et al., 2017). The Oligocene unconformity is particularly well expressed (Rangin, 2018; Zhang et al., 2017). Most basins experienced tectonic inversion starting in the late Miocene (Bertrand & Rangin, 2003; Pivnik et al., 1998; Rangin, 2018; Zhang et al., 2017).

The Burmese back-arc consists of the Shwebo Basin in the north and the Pegu Basin in the south (Fig. 5.1a). The Paleogene deposits in the Shwebo Basin are exclusively continental with southward prograding fluvio-deltaic sequences (Thein & Maung, 2017), while those in the Pegu Basin have not been described. Since the Neogene, both basins were characterized by southward prograding tidal-influenced estuarian sequences, before being overlain by fluvial deposits of the Quaternary Irrawaddy Formation (Bender, 1983; Khin, 1999; Pivnik et al., 1998; Thein & Maung, 2017). The Burmese forearc basins are commonly subdivided into the Minbu (or Salin) Basin in the south, which has been relatively well documented due to its hydrocarbon potential (Pivnik et al., 1998), and the less well documented Chindwin Basin in the north (Fig. 5.1a). The Burmese forearc basins are subject of this study and their geology will be described in further detail below.

2.4.1. The Minbu Basin

East of the IBR and west of the WPA, the Minbu Basin (Fig. 5.1) constitutes the southern Burmese forearc basin separated from the Chindwin Basin by a small topographic high called the Pondaung Ranges (Bender, 1983; Licht et al., 2019; Pivnik et al., 1998; Zhang et al., 2017). The sedimentary

sequence of the Minbu Basin (Fig. 5.2) begins with the poorly-exposed marine sediments of the Albian to Maastrichtian Kabaw Formation (Bender, 1983; Cai et al., 2019).

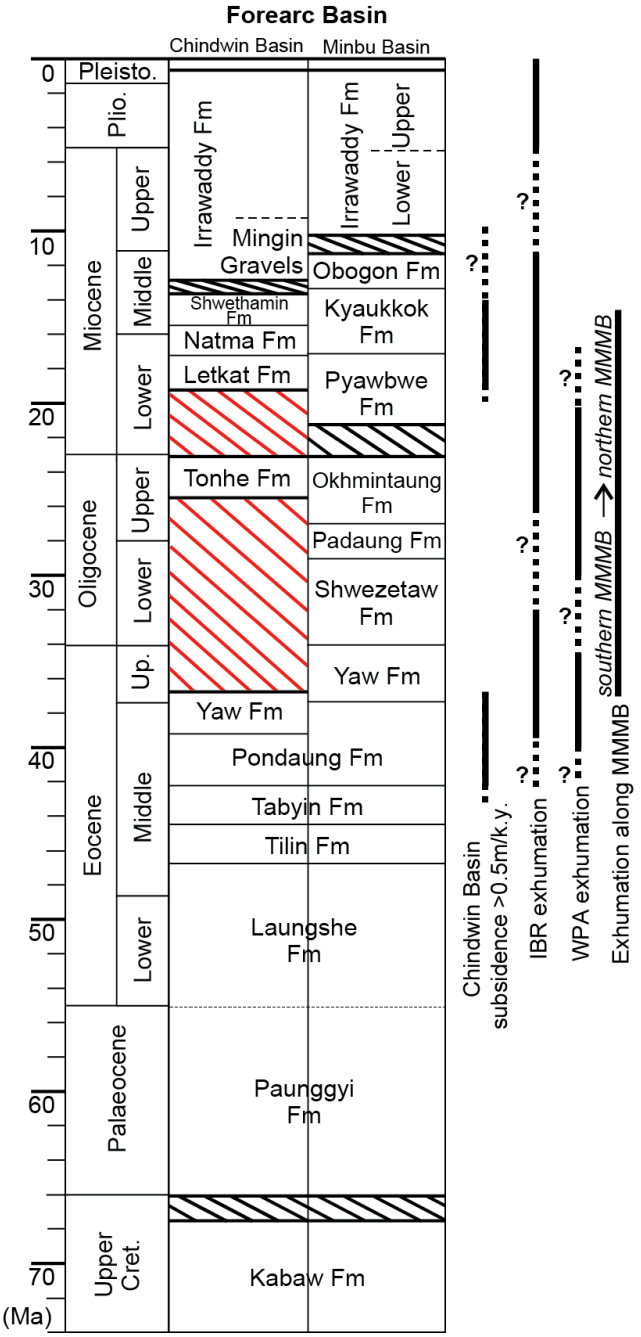

Figure 5.2: *Synthetic log of the Chindwin Basin (modified from Licht et al., 2019 based on our new magnetostratigraphic and geochronological constraints) and Minbu Basin (after Cai et al., 2019; Zhang et al., 2019), compared to periods of rapid subsidence in the Chindwin Basin (>0.5 m/k.y.; after Licht et al., 2019; this study), the timing of uplift in the Indo-Burman Ranges (IBR; after Licht et al., 2019; Morley et al., 2020; Najman et al., 2020), WPA (Wuntho-Popa Arc; after Zhang et al., 2017) and Mogok–Mandalay–Mergui Belt (MMMB; after Bertrand et al., 2001). Unconformities constrained by this study are highlighted in red.*

This is followed by a Paleocene to middle Eocene sequence of shallow-marine siliciclastics alternating with sporadic continental deposits, consisting of the Paunggyi, Laungshe, Tilin and Tabyin Formations with poorly defined lithostratigraphic boundaries (Bender, 1983; Licht et al., 2019). This sequence is followed by the middle to upper Eocene Pondaung Formation, which is made of fluvio-deltaic sediments and has been dated at ~40 Ma (Jaeger et al., 1999; Zaw et al., 2014; Licht et al., 2014b; Licht et al., 2015). It is overlain by the upper Eocene Yaw Formation consisting of shallow-marine sediments. All subsequent Oligocene formations in the Minbu Basin, the Shwezetaw, Padaung and Okhmintaung Formations, are continuous and consist of fluvio-deltaic to predominantly marine facies towards the south (Bender, 1983; Gough et al., 2020). This sequence is covered by the lower and middle Miocene fluvio-deltaic deposits of the Pyawbwe, Kyaukkok and Obogon Formations; the sequence is finally capped by the middle Miocene - Pliocene Irrawaddy Formation, which covers most lowlands of the CMB.

2.4.2. The Chindwin Basin

The depositional history of the Chindwin Basin is similar to that of the Minbu Basin up until the upper Eocene Yaw Formation. By contrast to the Minbu Basin, the Yaw Formation in the Chindwin Basin comprises four distinct sedimentary facies (Fig. 5.3; Licht et al., 2019). These are anoxic sediments containing organic-rich dark mudstones and siderite-rich carbonate layers (FA1), deltaic tidal sand flat sediments (FA2), and finally continental deposits with thick fluvial sandstone bodies (FA3) and thick lignite layers containing vertebrate fossils (FA4). Paleocurrents measured in FA3 have an average direction towards the WSW. The combination of these four sedimentary facies was interpreted as a quasi-closed estuarian system, sustained primarily by tectonic uplift of the IBR (Licht et al., 2019). A single tuff layer is also present in the Yaw Formation, yielding a U-Pb age constraint of 38.3 ± 1.1 Ma (Licht et al., 2019), consistent with palynological results (Huang et al., 2020).

The Yaw Formation is overlain by 6 km of coarse fluviatile facies, divided into the Tonhe, Letkat, Natma, Shwethamin, and Irrawaddy Formations (Bender, 1983). The Tonhe Formation consists of thick packages of particularly coarse gravel and sand beds with thick sets of planar bedding and trough cross-bedding, alternating with paleosols (Figs. 5.3 and 5.4). It has yielded an abundant Oligocene pollen assemblage (Lwin et al., 2017), including Florschuetzia semilobata that suggests an upper Oligocene age (R. Morley, pers. com.). The subsequent Letkat, Natma and Shwethamin Formations consist of afossiliferous fluviatile sandstones and pedogenised finer-grained sands and mudstones (Licht et al., 2019). Paleocurrents in the sandstones of the Letkat Formation cover a broad range of directions with an average SSW direction (Licht et al., 2019). The upper part of the Letkat Formation has yielded detrital zircons as young as 23-17 Ma, indicating a lower Miocene age

or younger (Licht et al., 2019; Wang et al., 2014). The base of the Irrawaddy Formation, also named Mingin Gravels in the southern Chindwin Basin, has yielded fossil mammals indicating a middle Miocene (14-11 Ma) age, coeval to the Chinji fauna of Pakistan (Bender, 1983).

Recent studies have suggested that the diverging stratigraphic record between both forearc basins was caused by the onset of hyper-oblique convergence at ~39-37 Ma, which resulted in the development of en echelon pull-apart basins (Licht et al., 2019). The coeval motion of India and the BT from paleomagnetic data suggest that most strike-slip displacements were concentrated east of the BT at that time (Westerweel et al., 2019). The Chindwin Basin is interpreted as a pull-apart basin partly due to rapid subsidence (~1.0 m/ky) during deposition of the Yaw Formation (Licht et al., 2019). Around this time, there was also a change from primarily volcanic arc provenance in the Pondaung and Yaw Formations to increasingly more input of metamorphic grains, possibly derived from MMMB basement rocks (Licht et al., 2013, 2019; Wang et al., 2014).

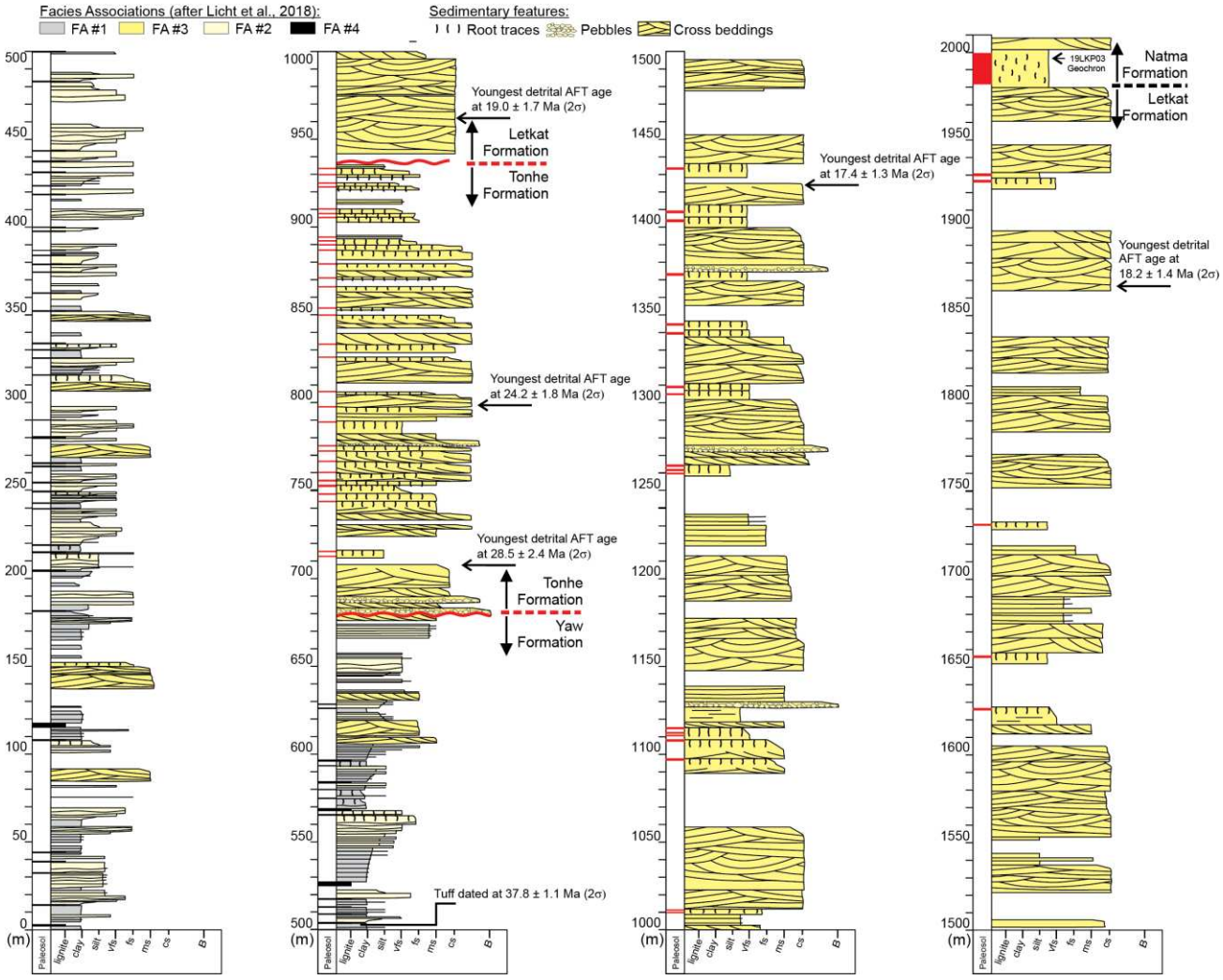

Figure 5.3: *Composite log of the investigated section in this study, including the upper part of the Yaw Formation, the Tonhe Formation and the Letkat Formation. The first ~1450 m of this section was*

already logged by Licht et al. (2019); during this study it was extended upward for ~535 m and reinterpreted to include the Tonhe Formation and two major unconformities (highlighted in red). Relevant maximum depositional ages from sandstone samples and age of the tuff layer redated in this study are also shown (cf Table 1). In the Paleosol column, black lines indicate histosols whereas red lines indicate ultisols and vertisols. vfs—very fine sand; fs—fine sand; ms—medium sand; cs—coarse sand; B—Boulder.

3. Methods

3.1. Sedimentology

During five consecutive field seasons between 2015 and 2019, we described deposits along a north–south trending portion of the Chindwin Basin north of the Kalewa Township (Fig. 5.1b). Additionally, we used a composite section spanning the Yaw, Tonhe, and Letkat Formations, composed of six stratigraphic sections (Fig. 5.1b; from bottom to top: MD, MC, MB, MA, LA, and LB sections). The five stratigraphic sections spanning ~1450 m of the Yaw Formation, the Tonhe Formation, and the base of the Letkat Formation (sections MD, MC, MB, MA, LA) have already been published, together with details on sedimentary facies (Licht et al., 2019). Here we extend our log by an additional 535 m covering the entire Letkat Formation up to the base of the Natma Formation (section LB), measured at ~1m resolution. We also distinguish between the Tonhe and Letkat Formations, which were treated as a single unit in Licht et al. (2019). Detailed logs are available in figure 5.S1, and are combined into a composite log in figure 5.3.

3.2. Rock magnetism

Paleomagnetic sampling was conducted in the lower ~1450 m of the composite stratigraphic section, yielding 582 conventional paleomagnetic core plug samples for magnetostratigraphy. In addition, 63 hand samples were obtained from the Letkat Formation (LA-section) up until the top of the section (~940-1925 m) (Appendix 2, Supplementary Table 1). The magnetic properties of the different lithologies within the logged sequence were investigated and compared with petrologic and mineralogic observations from thin sections.

Before demagnetization, the volume-corrected bulk magnetic susceptibility of every sample was measured and plotted alongside the (magneto)stratigraphic results to constrain differences in magnetic properties and mineralogy. Their anisotropy of magnetic susceptibility (AMS) was determined on a KLY3S AGICO kappabridge to investigate the magnetic fabric. The AMS tensor could potentially be used to determine a paleocurrent, if samples have strong anisotropy controlled by sedimentary deposition under high current flow (Tauxe, 2010). However, in compressive regimes, the maximum axis K_{max} of the AMS tensor will gradually be aligned perpendicular to the direction of

maximum compression (Kissel et al., 1986). Even an incipient tectonic shortening creates a magnetic lineation parallel to fold axes (layer parallel shortening) that usually fully overprints paleocurrent information.

To gain more insight into magnetic properties and mineralogy of the different units, additional types of experiments were conducted for a selection of samples. Firstly, mass-corrected bulk magnetic susceptibility versus temperature (K-T) plots were obtained by measuring the mass-corrected bulk magnetic at increasing temperature steps up to 580°C on a KLY3-CS3 AGICO kappabridge for different lithologies. Isothermal remanent magnetization (IRM) acquisition was done up until 2400 mT for different samples to constrain differences in grain size and content. Finally, we measured several magnetic hysteresis loops on an AGM magnetometer.

To further investigate magnetic properties of the various lithologies by identifying their (magnetic) mineralogy, polished thin sections were made from selected samples for observation under an optical microscope in both transmitted light and reflected light. Samples were also analyzed with a scanning electron microscope (SEM - JEOL JSM 7100F with energy dispersive X-ray spectroscopy - Oxford EDS/EBSD) at Geosciences Rennes. Additional petrology (e.g. grain counting) was already done in the preceding study from the same stratigraphic section (Licht et al., 2019).

3.3. Paleomagnetic analysis

Orientation of 582 conventional paleomagnetic core plug samples in the first ~1450 m of the composite stratigraphic section was done using standard paleomagnetic field equipment and procedures, with both magnetic and sun compasses (Appendix 2, Supplementary Table 1). Most of the collected samples are mudstones, siltstones and sandstones with preference for the finest grained layers whenever possible. In addition, a portion of samples was acquired in the siderite-rich carbonate layers of the Yaw Formation. The paleomagnetic results of the Yaw Formation are already published in preceding research for calculating a mean direction (Westerweel et al., 2019), and are herein interpreted for magnetostratigraphy.

On a 2G cryogenic magnetometer hosted in a magnetically shielded room at Geosciences Rennes, stepwise demagnetization was conducted on these samples in order to isolate their characteristic remanent magnetizations (ChRMs) from their total natural remanent magnetizations (NRMs). Both thermal demagnetization, with increments of 20-50°C up to 680°C, and 3-axis alternating field (AF) demagnetization, with increments of 2.5-10 mT up to 120 mT, were used for this. During AF demagnetization, Gyro Remanent Magnetizations (GRMs) were cancelled by measuring the magnetization after each axis of AF demagnetization (Roperch & Taylor, 1986). The demagnetization of individual samples was plotted on orthogonal demagnetization plots (Zijderveld, 1967) and their

ChRM directions were isolated using principal component analysis (Kirschvink, 1980) or in some cases a Fisher mean on the demagnetization results (Fisher, 1953). Subsequently, these ChRM directions were corrected for the tilt of the sedimentary bedding and then grouped based on polarity (normal or reverse) and data quality (Category 1 or 2). Samples are denoted as Category 1 when both the polarity and ChRM direction are well-constrained, while demagnetization is less stable in Category 2 samples but the polarity can still be inferred. Afterwards, the reversal angle of each sample, defined as the angular distance between the observed direction in an individual sample and the mean paleomagnetic direction in normal polarity, was plotted versus sampling level for constructing the magnetostratigraphic log. Subsequently, antipodal normal (black) and reverse (white) polarity magnetozones could be distinguished by sequences of samples exhibiting the same polarity. Finally, these magnetozones could be compared with the latest Geomagnetic Polarity Timescale (GTS16) (Ogg et al., 2016).

3.4. Zircon U-Pb dating

To constrain the age and sedimentary provenance of the Chindwin Basin, one sandstone from the top of the Letkat Formation was sampled for zircon U-Pb dating during this study (17letkat07). Detailed analytical protocols and information about the data reduction schemes are provided in the Supplementary Information (Appendix 3) and in Licht et al. (2020). Briefly, zircon crystals were extracted by traditional methods of heavy mineral separation. U-Pb ages were generated using laser-ablation inductively-coupled-plasma mass-spectrometry (LA-ICP-MS), using an iCAP RQ Quadrupole ICP-MS coupled to an Analyte G2 excimer laser at the University of Washington, using a spot diameter of 25 microns. Data reduction was first conducted with Iolite, using their U_Pb_Geochron4 Data Reduction Scheme to calculate U-Pb ages uncorrected for common lead (Paton et al., 2010). In addition, age uncertainties for all samples were calculated with Matlab using a modified version of the method of Matthew and Guest (2017) that takes into account the impact of 207Pb beam intensity on age uncertainties. The ten secondary zircon reference materials during these sessions yielded offset around TIMS ages <1% in most cases, <2% otherwise.

Maximum depositional age for the detrital sample was calculated with multiple zircon ages using Tuffzirc (Ludwig, 2003). We also recalculated the crystallization age of a tuff layer and seven maximum depositional ages from the Yaw, Tonhe and Letkat Formations in the same sedimentary section, already published in Licht et al. (2019; Appendix 2, Supplementary Table 2) based on recalculated age uncertainties. To this we added additional maximum depositional ages from Wang et al. (2014) and Cai et al. (2019) obtained elsewhere in the Yaw, Tonhe and Letkat Formations (Table 5.1). The final age error calculated for each sample is the quadratic sum of the uncertainty of

Tuffzirc age calculation and of the systematic uncertainty (∼2.67% for the 238U/206Pb ratios; same value used for the samples of Wang et al, 2014, and Cai et al., 2019). Age distributions of all selected samples were compared on a multidimensional scaling (MDS) map, which is a visual way to assess the misfit between age distributions using the Kolmogorov-Smirnov (KS) statistic as the dissimilarity measure (Vermeesch, 2013).

3.5. Apatite U-Pb and fission-track dating

To further constrain the age, sedimentary sourcing and tectonic context of the Chindwin Basin, detrital apatites were extracted from the same eight sandstones for apatite U-Pb and AFT dating during this study (Appendix 2, Supplementary Table 3). Both types of ages were acquired simultaneously at the GeOHeLiS Analytical Platform (Geosciences Rennes), using an ESI NWR193UC Excimer laser coupled to a quadrupole Agilent 7700x ICP-MS. Detailed analytical conditions can be found in the Supplementary Information (Appendix 3). A total of 120 grains were analysed whenever possible.

Data reduction for U-Pb ages was conducted with Iolite, using the VisualAgeUcomPbine Data Reduction Scheme of Chew et al. (2014) to calculate U-Pb ages corrected for common lead. Single grain ages and subsequent population mean ages were obtained following two different methods. Single grain ages were determined following the iterative approach for 207Pb correction of Chew et al. (2011), using a terrestrial Pb evolution model for the determination of common lead isotopic composition (Stacey & Kramers, 1975). Population ages were calculated independently of single grain age calculation, using data uncorrected for common lead. Age populations were first defined by identifying linear arrays of data in Tera-Wasserburg (TW) plots using IsoplotR (Vermeesch, 2018). Per age population, 207Pb/206Pb ratio of each array was either anchored at a value given by the single stage Pb evolution model of Stacey and Kramers (1975), or unanchored. Anchored and unanchored ages are coherent for all populations. The final age error is the quadratic sum of the uncertainty of IsoplotR age calculation and of the systematic uncertainty (using the same values as for zircon U-Pb ages, i.e. ∼2.67% for the 238U/206Pb ratios).

AFT data were obtained on the same spot as the U-Pb measurements using the protocol of Cogné et al. (2020). Spontaneous tracks were acquired by acid etching with 5.5 M HNO3 at 21°C for 20 s. Grain mounting and etching procedure is analogous to the protocol described by Donelick et al. (2005). Fission-track counting was done using a Zeiss AxioImager Z1m microscope equipped with an Autoscan automated stage system. Data reduction was conducted with Iolite with a modified version of the Trace_Elements DRS (Woodhead et al., 2007) and an in-house spreadsheet. The different populations were then untangled using U-Pb data. AFT data were plotted in a radial plot to get the

AFT age of the population, using IsoplotR (Vermeesch, 2018). All populations identified show a low degree of AFT single grain age dispersion.

4. Results

4.1. Sedimentology

Our 2010 m composite sedimentary log of the Yaw, Tonhe and Letkat Formations is displayed in figure 5.3. Deposits and associated lithofacies of these formations have already been extensively described and illustrated in Licht et al. (2019) (Section 2.4.2), only our new sedimentological observations are presented here. In particular, previous studies near Kalewa have grouped both the Tonhe and Letkat Formations into a larger Letkat Formation (Licht et al., 2019; United Nations, 1978a; Zat & Aung, 2018; Zhang et al., 2019). However, our observations show that the Yaw, Tonhe and Letkat Formations all have distinctive features, and are separated by abrupt changes in sedimentary facies. The contact between the Yaw Formation and Tonhe Formation is sharp, marked by the occurrence of two consecutive sandstone bodies with thick (> 2m) basal lags including blocks of reworked sediment, altered siderite, and lignified fossil trunks. The shallow marine to continental sedimentary facies of the estuarian Yaw Formation are replaced by solely continental fluvial deposits in the Tonhe Formation and the subsequent Letkat Formation. The Tonhe Formation is ~250 m thick and is particularly coarse, with gravel beds made of rounded quartz being common forming stacked beds of trough cross-bedding. Gravel and sand beds are organized in 5-15 m thick packages, each overlain by a 1-4 m thick paleosol profile resembling modern ultisols (Fig. 5.4a, b). Paleosols are red to brown, with grey, green, red, orange, and purple mottles, occasionally following root traces; parent sediment is highly mixed, peds are blocky; they sometimes display a high density of red adhesive meniscate burrows, similar to ichnogenus Naktodemasis sp. (Fig. 5.4c; Smith et al., 2008). Carbonated pedogenic nodules are particularly small and have only been found in two beds at the top of the unit (<2 mm in diameter). Sparse silicified and lignified fossil trunks can be found within gravel beds (Fig. 5.4d).

The contact between the Tonhe and Letkat Formations is marked by the abrupt disappearance of gravel beds. Gravels are sporadically present in the Letkat Formation but only reappear much later, ~500 m higher in the section, in isolated channel lags or as small lenses in bigger sand beds together with mud breccias. The sandstone beds of the Letkat Formation are stacked sometimes over more than 60 m of thickness without any change in facies or grain-size (Fig. 5.4e). Sands are rich in plant debris (Fig. 5.4f), include rare rounded vertebrate bones and lignified wood pieces. Paleosols occur at a much lower frequency than in the Tonhe Formation, every 50 to 200 m in the section, isolated or in packages of 2-4 profiles. These paleosols are 0.5 to 1.5 m thick and resemble modern vertisols

with brown to grey with purple, red, and green mottles; parent sediment is finer (silt to very fine sand), highly mixed, peds are blocky or rounded. They include 0.5 to 1.5 cm thick carbonated pedogenic nodules. The transition to the overlying Natma Formation is marked by a sudden decrease in grain-size, with pedogenised brown to red clay and silt becoming the dominant facies; sandstone bodies in the Natma Formation are commonly thinner (1-5 m thick), embedded into finer-grained material, and display inclined heterolithic stratifications.

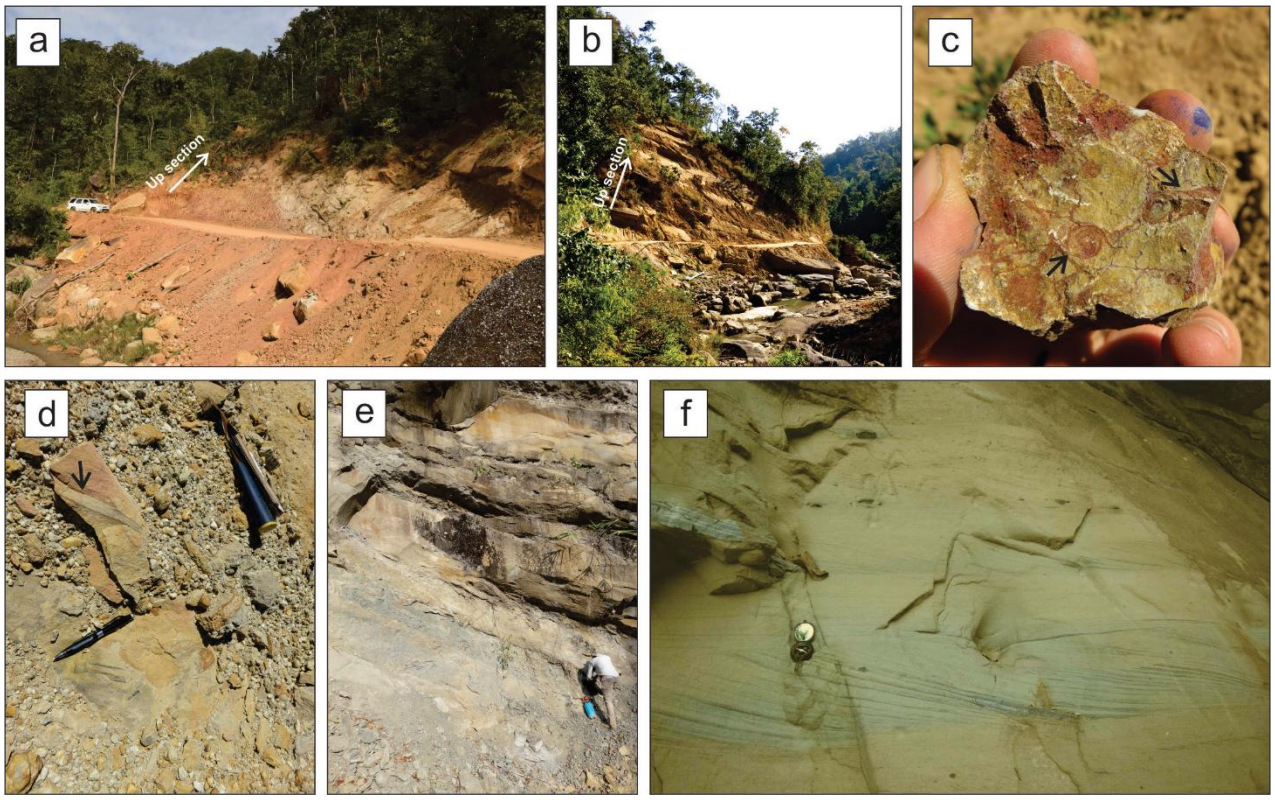

Figure 5.4: *Relevant sedimentological observations from this study: a) and b) alternation of reds beds and gravel beds in the Tonhe Formation; c) Red mottles and trace fossils Naktodemasis sp. (black arrows) in red beds of the Tonhe Formation; d) Quartz gravels and tree stem print (black arrow) in sandstones of the Tonhe Formation; e) and f) coarse sandstones of the Letkat Formation, with organic matter in the foresets. When the scale is not displayed, rock hammers, pencils, compass, cars and humans can be used for scale.*

4.2. Rock magnetism

4.2.1. Magnetic properties

We measured the volume-corrected bulk magnetic susceptibility (SI) of our core plug samples before demagnetization, as well as the 63 additional hand samples from the Letkat Formation (Appendix 2, Supplementary Table 1). The obtained values were plotted against the (magneto)stratigraphic results, showing that the Yaw, Tonhe and Letkat Formations have distinct magnetic properties (Figs.

5.5-5.7). Bulk magnetic susceptibilities of samples from the Yaw Formation are of low magnitude in general, averaging around ~0.0002-0.0003 SI. Exceptions to this are the siderite-rich rocks, which are easily recognized by much higher magnetic susceptibilities of around ~0.0015-0.0025 SI. K-T, hysteresis, and IRM plots (Fig. 5.5) confirm these results, showing that the magnetic properties of most rocks in the Yaw Formation, especially the finer grained and siderite-rich rocks, are dominated by paramagnetic components with only a minor contribution of magnetite, which is the magnetic carrier based on stable demagnetizations above 400°C (Fig. 5.S2). Upon heating, the magnetic susceptibility increases at ~370°C in many samples with paramagnetic characteristics, likely due to the transformation of iron sulphide minerals, such as pyrite, to magnetite. An even larger increase in magnetic susceptibility occurs in siderite-rich rocks above 400°C.

Measured bulk magnetic susceptibilities from the Tonhe Formation, mostly from siltstones and sandstones, are distinct from those of the underlying Yaw Formation. In general, they are of an even lower magnitude than in the Yaw Formation, averaging around ~4*10-5-1.5*10-4 SI. These low values suggest only a minor presence of magnetite. Nonetheless, IRM acquisition shows that magnetic remanence is still carried by magnetite, although several finer-grained, pedogenised sandstone samples exhibit high coercivity phases as well (Fig. 5.5d).

The transition to the Letkat Formation is even more abrupt compared to the Yaw – Tonhe boundary with a sharp and significant increase in overall magnitudes of bulk magnetic susceptibility, averaging around ~0.001-0.003 SI. K-T. Magnetic hysteresis and IRM acquisition experiments on the predominantly sandstone lithologies of the Letkat Formation show that magnetic properties and remanence in this formation are dominated by pseudo-single domain or multidomain magnetite, although IRM acquisition shows the occurrence of high coercivity phases related to hematite in several samples, especially in finer grained sands where pedogenesis is observed (Fig. 5.5d).

Before demagnetization (Fig. 5.S2), the AMS of all paleomagnetic samples was measured (Fig. 5.S3). In both the Yaw, Tonhe and Letkat Formations, the obtained magnetic fabric is mainly oblate with the minimum axis K_{min} of the AMS fabric oriented orthogonal to the bedding. In addition, the maximum axes K_{max} are oriented ~NNE-SSW, parallel to the fold axis of the stratigraphic section. These properties are typical for a sedimentary AMS fabric with ESE-WNW tectonic shortening. Only the siderite-rich rocks in the Yaw Formation depart from these trends, sometimes exhibiting an inverse AMS fabric which is often observed for this lithology (Rochette, 1988). The AMS in the Letkat Formation is on average much higher compared to the underlying formations, with a few coarse grained sandstone samples having P' anisotropy values up to 1.6-1.8 (Fig. 5.5b). This is probably related to an increase in magnetite content.

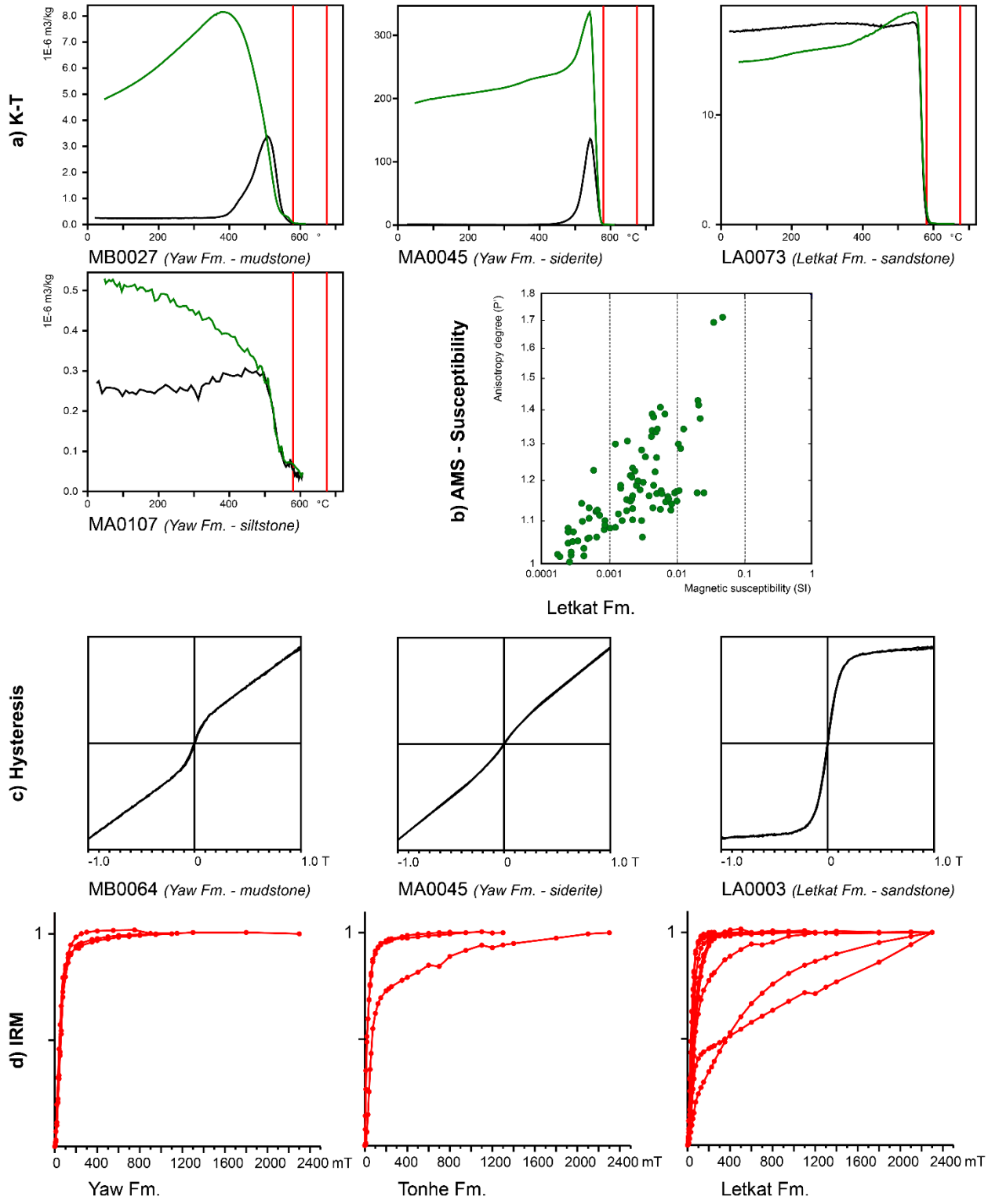

Figure 5.5: *Rock magnetic experiments showing differences in magnetic properties between the Yaw, Tonhe and Letkat Formations. Representative bulk magnetic susceptibility (10-6 m3/kg) versus temperature (°C) plots (K-T plots) up to a maximum of 590°C (a), plot of degree of anisotropy (P') versus bulk magnetic susceptibility (SI) (b), hysteresis loops (c) and plots of Isothermal Remanent Magnetization (IRM) acquisition (d).*

4.2.2. Petrologic and mineralogic observations

Optical microscope and SEM observations were made during this study to further investigate the inferred (magnetic) mineralogy from the measured magnetic properties. Observations from sandstones, mudstones and siderites in the Yaw Formation largely confirm the inferred (magnetic) mineralogy. Yaw Formation lithologies typically contain large concentrations of siderite and organic material (Fig. 5.6a-c), and an abundance of framboidal pyrite grains is often observed in and around these organic-rich parts (Fig. 5.6a). Furthermore, the fine to coarse grained sandstone parts consist of subangular and poorly-sorted clasts, mostly (polycrystalline) quartz, but also a contribution of feldspars and micas, as well as several zircons, apatites and volcanic rock fragments. Quartz minerals often look recrystallized, exhibiting dissolution features at their edges (Fig. 5.6c). These observations corroborate the strong paramagnetic behaviour of the Yaw Formation lithologies with only minor evidence for magnetite.

Like the Yaw Formation, sandstones from the overlying Tonhe Formation are comprised almost exclusively of (polycrystalline) quartz minerals (Fig. 5.6d). They are usually subrounded and poorly sorted. The biggest grains are cemented by a finer-grained matrix, consisting of quartz or phyllosilicates. Especially in this finer-grained matrix, oxidation features are present as well. However, in contrast to the Yaw Formation, organic and sideritic material is lacking in the Tonhe Formation. Optical microscope observations show that there is a near absence of opaque minerals such as magnetite. This is all in agreement with the low magnetic susceptibilities, induced by only a minor presence of magnetite in the Tonhe Formation.

Sandstones from the Letkat Formation are composed of much coarser, less sorted and more angular clasts compared to the underlying formations (Fig. 5.6e-h). In addition to the minerals common in the underlying formations, the sedimentary composition of the Letkat Formation includes a significant amount of high-grade metamorphic and ultramafic minerals, such as quartz, (perthitic) feldspar, biotite, muscovite, epidote and amphibole (Fig. 5.6e,f). Fragments of high-grade metamorphic rocks such as schist and quartzite can be identified as well. In contrast to Yaw sandstones, little to no organic and siderite material is present. Large grains and concentrations of (occasionally oxidised) magnetite, sometimes alongside titanite, rutile, ilmenite and titanomagnetite, are easily observed in coarse-grained sandstones, often occurring as thin bedded layers (Fig. 5.6g,h). From this it can be inferred that the highly degree of AMS in the Letkat rocks are related to a highly anisotropic distribution of magnetite due to concentration of heavy minerals by gravity separation during sedimentary transport instead of paleocurrents (Fig. 5.5b), illustrating the difficulty in using AMS for reliable paleocurrent determinations. Our mineralogic observations are in

good agreement with the obtained magnetic properties of Letkat rocks, confirming that they are dominated by large grains of magnetite.

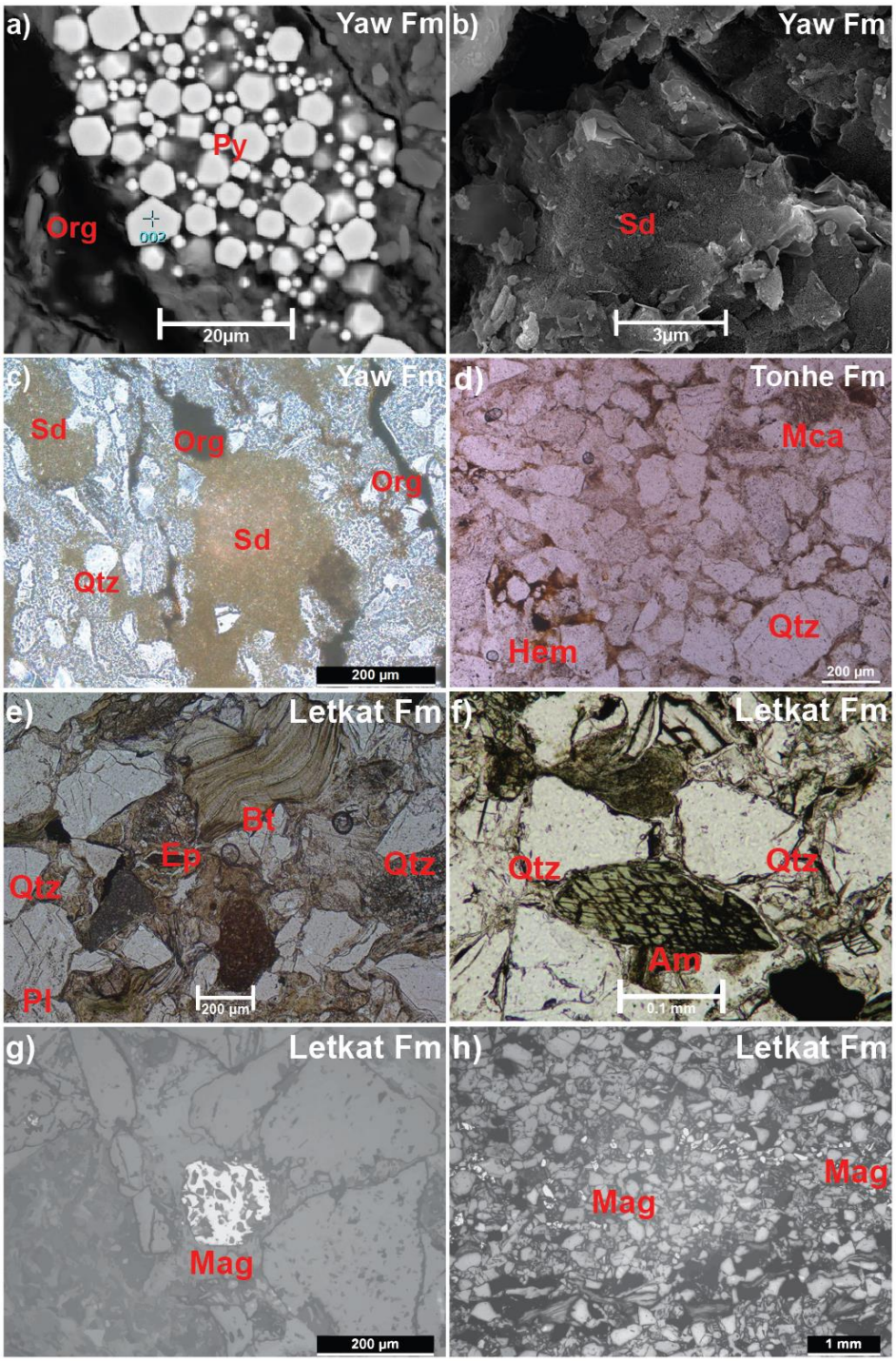

Figure 5.6: *Representative microscope images showing differences in mineralogy between the Yaw (a-c), Tonhe (d) and Letkat Formations (e-h). Sample name and scale are indicated per image. Mineral abbreviations (red): Am = amphibole, Bt = biotite, Ep = epidote, Hem = hematite, Mag = magnetite, Mca = mica, Org = organic material, Pl = plagioclase, Py = pyrite, Qtz = quartz, Sd = siderite.*

4.3. Magnetostratigraphy

In total, 298 demagnetized samples were sorted according to depth and data quality, and subsequently used to construct a magnetostratigraphic section (Fig. 5.7, Appendix 2, Supplementary Table 1). Rocks from the late Eocene Yaw Formation (0-680 m) often yield stable demagnetizations with ChRMs that were mostly determined in the temperature interval ~220°C-460°C, with best-fitted lines anchored to the origin. The most stable samples are from fine-grained mudstone rocks and a few siderite-rich carbonate layers, whose ChRM directions are in good correspondence with each other. Stable samples with coherent polarities and ChRM directions were denoted as Category 1 in figure 5.7, while samples with distinguishable polarities but less constrained ChRM directions were denoted as Category 2. The remaining samples, often coarse-grained siltstones and sandstones with persistent overprint of the magnetic signal in the present-day field, were not used for magnetostratigraphy. Despite these occurrences, the Yaw Formation exhibits well-defined antipodal normal and reverse magnetozones. Rocks of both polarities exhibit similar magnetic behaviour during demagnetization, suggesting a detrital or early diagenetic primary origin for the ChRMs. Hence, the ChRMs were corrected for the general tilt of our homoclinal sedimentary section (Azimuth/Dip = ~010/40E). This resulted in seven distinct magnetozones for the Yaw Formation, which were labelled Y.n1-Y.n4 (normal) and Y.r1-Y.r3 (reverse).

The majority of samples in the overlying Tonhe Formation and especially in the Letkat Formation are characterized by significant overprint of the magnetic signal (often by the present-day field), likely related to the presence of multidomain magnetite in the coarse sandstones comprising the majority of lithologies in both formations (Section 4.2, figs. 5.5 and 5.6). AF demagnetization was completely ineffective in removing these overprints. Thermal demagnetization yielded a few stable samples, with roughly similar demagnetizations as those from the Yaw Formation (Fig. 5.7, Fig. 5.S2). The resulting stratigraphic resolution was insufficient to build a magnetostratigraphic correlation for the Tonhe and Letkat Formations, but fortunately their ages could be reliably determined using other geochronological constraints (Section 5.1).

Figure 5.7: *Overview of stratigraphy, magnetic properties and magnetostratigraphy of this study: a) Formation depths and geochronology results (Table 1); b) Bulk magnetic susceptibility (SI) log; c) Magnetostratigraphic results (left) and interpretation (right); d) Comparison with Geomagnetic Polarity Timescale (GTS16) (Ogg et al., 2016); e) Palynological age constraints from the Chindwin Basin: (1) = Meyeripollis naharkotensis, Cicatricosisporites dorogensis, Proxapertites operculatus (Huang et al., 2020), (2) = Florschuetzia semilobata (Lwin et al., 2017). Formation colors are identical*

to figure 1b. Red lines highlight the two unconformities constrained by this study of latest Eocene - middle Oligocene and late Oligocene - early Miocene age.

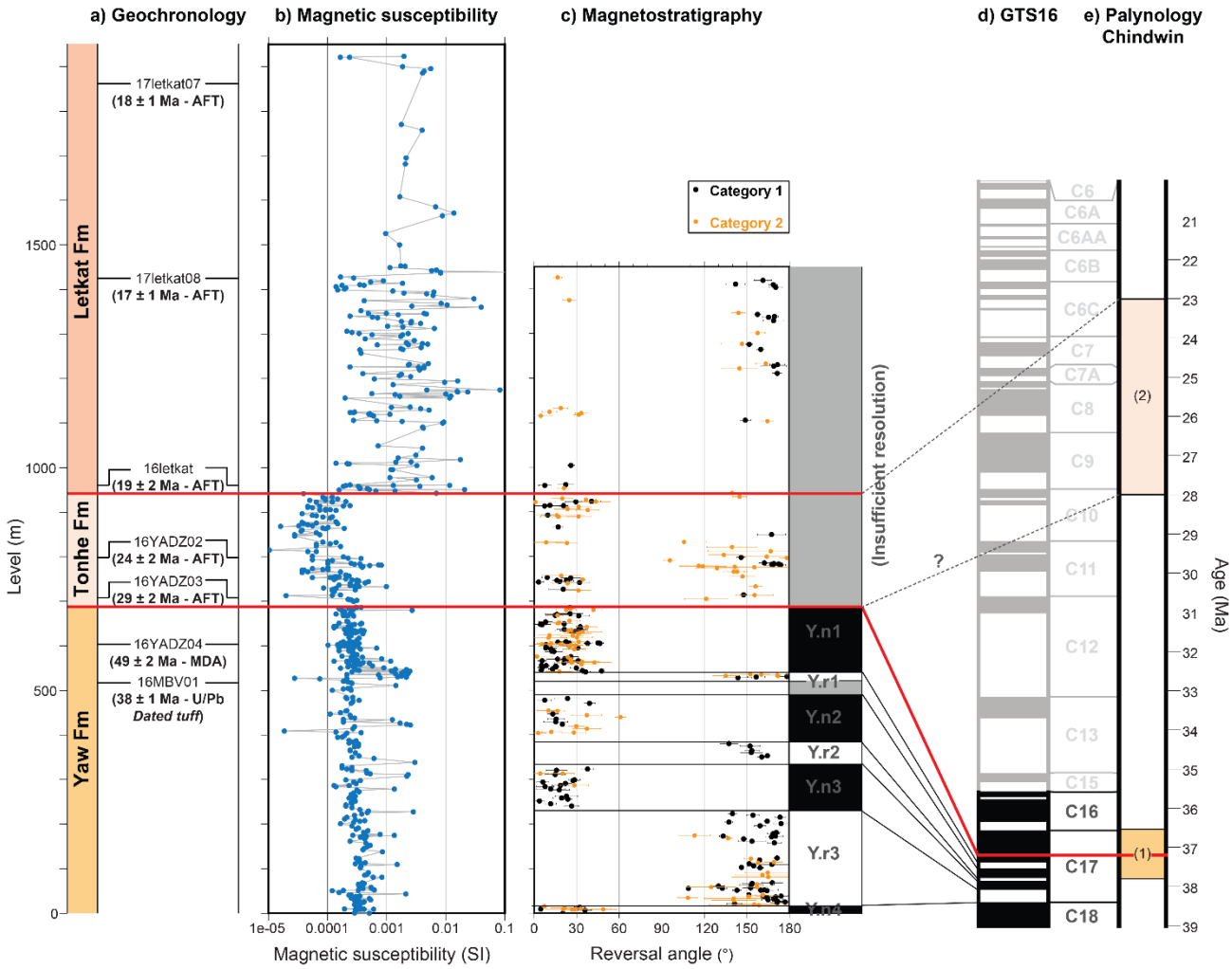

4.4. Zircon U-Pb dating

Youngest U-Pb age populations of detrital zircons from the Yaw, Tonhe, and Letkat Formation are displayed in Table 5.1, alongside the recalculated volcanic tuff age in the Yaw Formation (Licht et al., 2019), which now yields an age of 37.8 ± 1.1 Ma (2σ; n = 14 zircons)(Licht et al., 2019). Kernel density estimates (KDE) and age histograms of U-Pb age distributions of new sandstone sample 17letkat07 as well as published sandstones from Licht et al. (2019) of the Yaw, Tonhe and Letkat Formations are shown in figure 5.8. These samples, as well as additional samples from the Chindwin Basin (Cai et al., 2019; Wang et al., 2014; Zhang et al., 2019) and modern river sediments in Myanmar (Garzanti et al., 2016) are compared on a MDS map to show changes in provenance (Fig. 5.9).

Figure 5.8: *Kernel density estimators (KDE) and histograms (5 Myr bins) for individual sandstone samples of this study for zircon U-Pb ages from this study (17letkat07) and Licht et al. (2019), as well as and apatite U-Pb ages from this study. The kernel density bandwidth of each plot was determined*

with the plug-in bandwidth selection method of Botev et al. (2010). Apatite U-Pb ages are 207-corrected ages for common lead; we excluded apatite ages with high age uncertainties (2s > 50%) usually reflecting low U content.

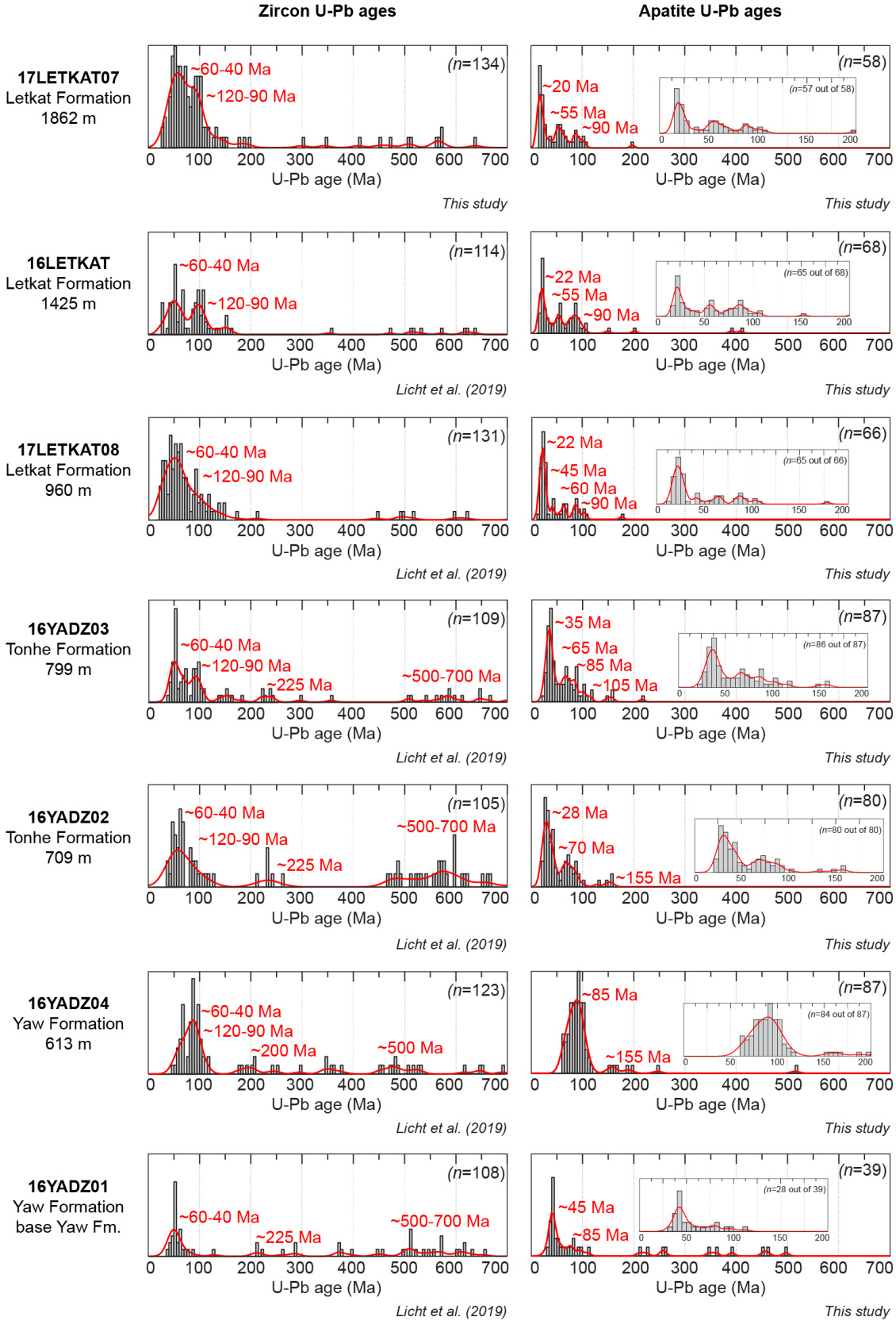

Yaw Formation and Tonhe Formation sandstones from the Chindwin Basin are dominated by Late Cretaceous (~120-90 Ma), Paleogene (~60-40 Ma) and pre-Cretaceous zircon populations (Fig. 5.8; Appendix 2, Supplementary Table 2). Samples from the Yaw and Tonhe Formations also yield a significant proportion of older zircons, with two notable peaks at 500 and 1200 Ma. Sandstones from the Letkat Formation appear statistically different from other sandstones on the MDS plot (Fig. 5.9), with a prominent age population of Paleogene grains but a smaller population of pre-Cretaceous grains compared to Yaw and Tonhe samples.

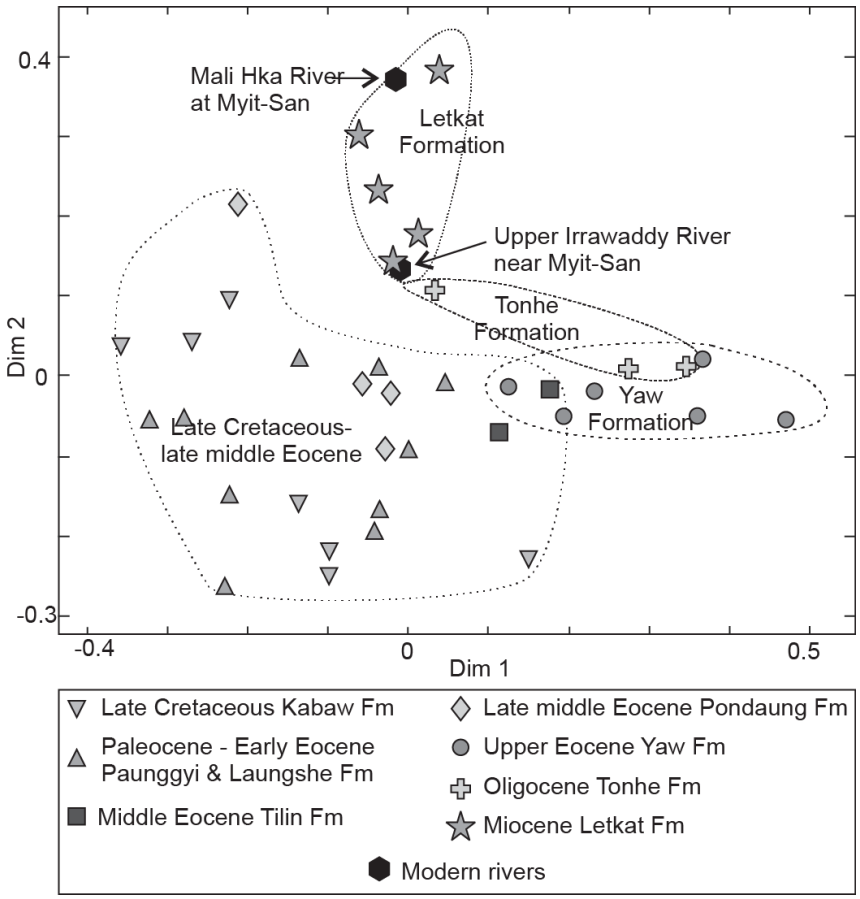

Figure 5.9: *Multidimensional scaling map showing the dissimilarities between individual samples of this study and previously published samples (Cai et al., 2019; Garzanti et al., 2016; Licht et al., 2019; Wang et al., 2014; Zhang et al., 2019). Axes are in dimensionless 'KeS units' (-1 < KS < 1) of dissimilarity between samples. Final 'stress' value is 0.11, indicating a 'fair' fit (Vermeesch, 2013). Ranges of variation for different units are highlighted by dashed lines.*

4.5 Apatite dating

Kernel density estimates (KDE) and age histograms of apatite U-Pb age distributions of sandstones of the Yaw, Tonhe and Letkat Formations are shown in figure 5.8. Determinations of U-Pb age population averages and uncertainties on Tera-Wassenburg diagrams are displayed on figure 5.S4.

AFT radial plots are displayed on figure 5.10. In all cases, apatites yielding the youngest U-Pb ages also yielded the youngest AFT ages (Table 5.1).

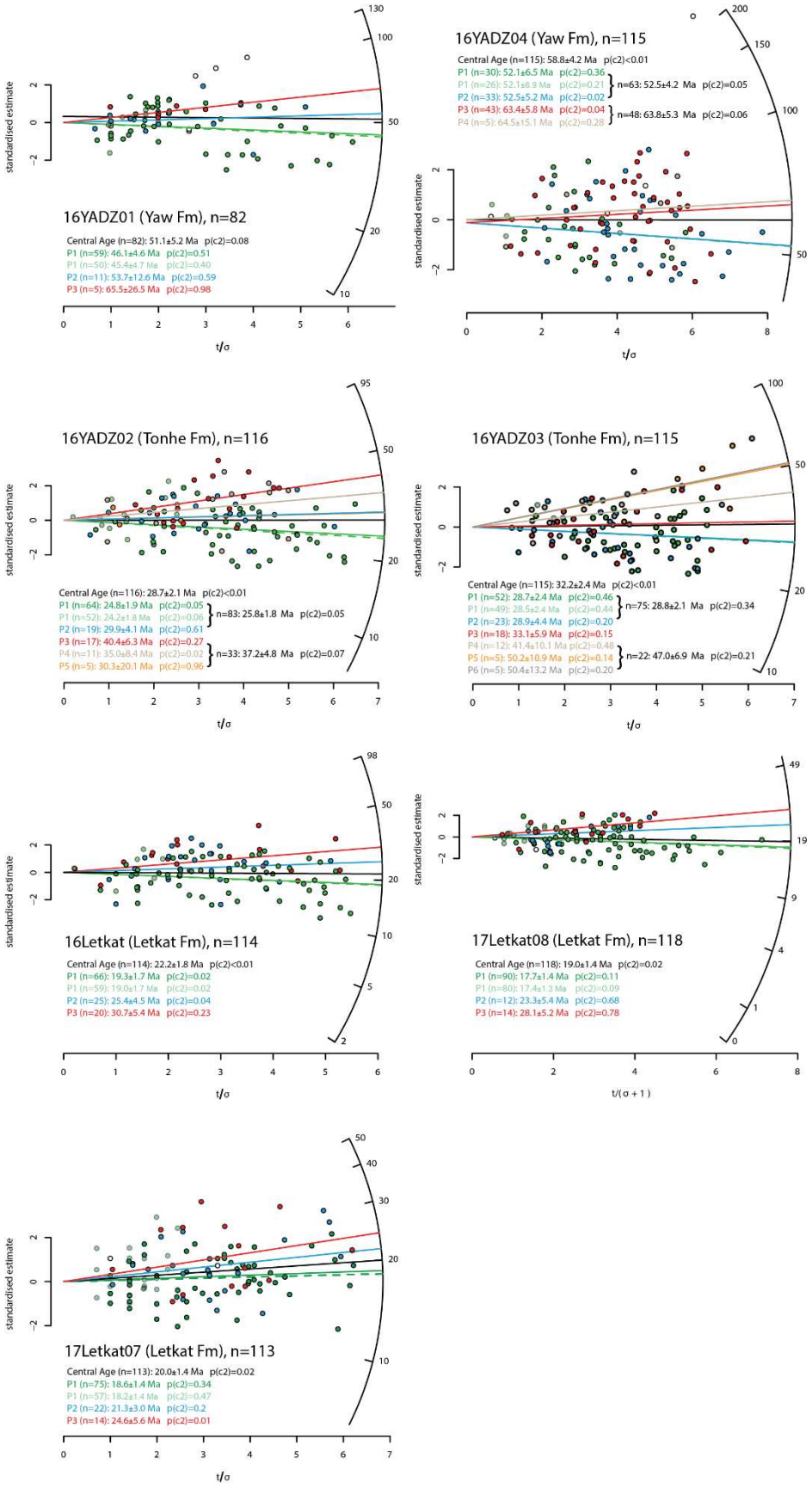

Figure 5.10: *AFT radial plots for every sample analyzed in this study, showing the abrupt changes in youngest age population between the Yaw, Tonhe and Letkat Formations. P1 to P6 indicate the different age populations (youngest to oldest) of each sample.*

Apatite U-Pb and AFT ages of sandstones from the Yaw Formation are all older than the youngest zircon ages and older than the age of the dated tuff. Given the thickness of the sedimentary sequence, post-depositional annealing of tracks cannot be excluded for these two samples. However, the youngest population in 16YADZ01 shows similar apatite U-Pb and AFT ages. Therefore, it is likely that annealing is minor if present. Most apatite U-Pb and AFT ages for sandstones of the Tonhe Formation are younger than the ~35-30 Ma zircon ages of the same sandstones, with the youngest population at ~30-25 Ma. These ages remain in the proposed age range for the deposition of the Tonhe Formation based on pollen assemblages (upper Oligocene; Lwin et al., 2017; R. Morley, pers. com.). Similarly, apatite U-Pb and AFT ages of sandstones from the Letkat Formation are commonly younger than their youngest zircon U-Pb age population (~27-17 Ma) with the youngest population showing a U-Pb age of ~22-20 Ma and an AFT age of ~18 Ma. They are in the range of what has been proposed for the deposition age of the Lektat Formation: older than 14-11 Ma based on biostratigraphic data in the Mingin Gravels above, and older than one zircon U-Pb age dated 16.8 ± 1.3 Ma (2s) at the top of the unit by Wang et al. (2014). For both the Tonhe and Letkat Formations, the AFT and U-Pb youngest populations are close in time. We thus interpret these AFT ages to be detrital ages, exempt of resetting due to burial or annealing. Moreover, youngest AFT ages of Tonhe and Letkat sandstones never overlap with and are always much younger than zircon U-Pb ages from the same samples. Therefore, we interpret AFT ages of these two formations to be non-volcanic, i.e. to be a product of exhumation of older rocks, and to provide a limit on the maximum depositional ages of these sandstones.

5. Interpretations

5.1. Age model for the Chindwin Basin

An overview of the different age constraints from magnetostratigraphy, U-Pb and AFT dating, and palynology is presented in figure 5.7. In the Yaw Formation, magnetozone Y.r1 was anchored to the GTS16 (Ogg et al., 2016) using the 37.8 ± 1.1 Ma U-Pb age from the dated tuff layer, correlating it with chron C17r.1r, which lies within the error range of the age of the tuff layer (Fig. 5.7). From this, the other magnetozones of the Yaw Formation could be straightforwardly correlated with the GTS16, with the base of the section corresponding to chron C18n.1n and the top to chron C17n.1n, constraining the age of the section to ~38.4-37.2 Ma. The very base of the Yaw Formation is located at ~500 m below our composite log; a sandstone near the base of the formation yielded a youngest

zircon dated at 36.3 ± 1.9 Ma by Cai et al. (2019), which is within error range of our magnetostratigraphic age interval.

Sample name	Origin, location in composite log	age + 2s (Ma)	n	U-Pb ages + 2s (unanchored; Ma)	Fission track ages + 2s (Ma)
Yaw Formation					
16MBV01	Tuff layer, level 508 m	37.8 ± 1.1 (*n*=14, MSWD=1.9) *(2)*		N/A	
16YADZ01	sandstone, base of formation, outside log	39± 1.3 (n=1) *(2)*	50	43.7 ± 2 (MSWD=1.4) ***(1)***	45.4 ± 4.7 (p(χ2)=0.4) ***(1)***
16YADZ04	sandstone, level 613 m	48.5 ± 1.5 (n=1) *(2)*	26	69.1 ± 3.2 (MSWD=0.6) ***(1)***	52.1 ± 6.9 (p(c2)=0.21) ***(1)***
2013m287	base Yaw Fm.	48.5 ± 1.6 (n=1) *(3)*		N/A	
2013m286	base Yaw Fm.	36.3 ± 1.9 (n=1) *(3)*		N/A	
2013m288	base Yaw Fm.	50 ± 1.5 (n=1) *(3)*		N/A	
2013m281	middle Yaw Fm.	37.9 ± 1.4 (n=1) *(3)*		N/A	
Tonhe Formation					
16YADZ03	sandstone, level 709 m	35.3 ± 1.7 (n=1) *(2)*	49	35.4 ± 1.8 (MSWD=1.8) ***(1)***	28.5 ± 2.4 (p(c2)=0.44) ***(1)***
16YADZ02	sandstone, Level 799 m	35.8 ± 1.2 (n=1) *(2)*	52	28.3 ± 1.7 (MSWD=2.2) ***(1)***	24.2 ± 1.8 (p(c2)=0.06) ***(1)***
2013m289	top Tonhe Fm.	33.2 ± 1.1 (n=1) *(3)*		N/A	
Letkat Formation					
16letkat	sandstone, level 960 m	26.7 ± 1 (n=3, MSWD=0.8) *(2)*	59	21.7 ± 1.2 (MSWD=1.9) ***(1)***	19 ± 1.7 (p(c2)=0.02) ***(1)***
17letkat08	sandstone, level 1425 m	20.2 ± 1.2 (n=1) *(2)*	80	19.8 ± 1.5 (MSWD=2.7) ***(1)***	17.4 ± 1.3 (p(c2)=0.09) ***(1)***
17letkat07	sandstone, level 1862 m	27 ± 0.8 (n=1) ***(1)***	57	20.4 ± 1.4 (MSWD=2.1) ***(1)***	18.2 ± 1.4 (p(c2)=0.47) ***(1)***
25-3-1	sandstone, middle Letkat Fm.	28.5 ± 1.8 (n=1) *(4)*		N/A	
25-4-2	sandstone, top Letkat Fm.	16.8 ± 1.3 (n=1) *(4)*		N/A	

Table 5.1: *Youngest age populations for various geochronometers (Zircon U-Pb, apatite U-Pb and AFT) per sample, both from this study and previous studies: (1, in bold) = This study, (2) = Licht et al. (2019), (3) = Cai et al. (2019), (4) = Wang et al. (2014). Depths on the composite log are indicated as well. Best maximum age estimate for each formation (Yaw, Tonhe and Letkat) is highlighted per sample. U-Pb Age uncertainties for zircons and apatites include systematic uncertainty.*

The Pondaung Formation, just below the Yaw Formation, has been dated at ~40-39 Ma using a combination of geochronology and biostratigraphy in the Minbu Basin (Jaeger et al., 1999; Zaw et al., 2014; Licht et al., 2014b, 2015); this age is in agreement with the youngest zircon of another sample dated at 39.0 ± 1.3 Ma near the base of the Yaw Formation (Table 5.1). We thus assign an upper Bartonian age to the Yaw Formation by combining our constraints from magnetostratigraphy, the dated tuff and detrital zircon U-Pb dating. The magnetostratigraphic correlation confirms that the Yaw Formation was deposited under rapid sedimentation and subsidence rates (~0.6 m/k.y.), similar to previous estimations (Licht et al., 2019).

Above the Yaw Formation, our observations show sharp transitions in sedimentary facies, magnetic properties, mineralogy and maximum depositional ages at both the Yaw – Tonhe and Tonhe – Letkat

boundaries (Figs. 5.4-5.10, Table 5.1). These are interpreted as two depositional unconformities occurring in the Chindwin Basin, separating the Tonhe Formation from the underlying Yaw Formation and overlying Letkat Formation. Unfortunately, these unconformable contacts, alongside the large effect of overprint of the magnetic signal in the Tonhe and Letkat lithologies, make it difficult to extend our magnetostratigraphic correlation from the Yaw Formation upward. Yet, we can observe a distinct change in maximum depositional ages given by zircon U-Pb, apatite U-Pb and AFT dating results between the three formations (Figs. 5.3, 5.7, 5.8 and 5.10, Table 5.1). The youngest age at the base of the Tonhe Formation is 28.5 ± 2.4 Ma (AFT), while the youngest age higher in the section is 24.2 ± 1.8 Ma (AFT), both in agreement with the upper Oligocene age for the Tonhe Formation from palynology (Lwin et al., 2017; R. Morley, pers. com.).

The youngest AFT ages in the Letkat Formation are 19.0 ± 1.7 Ma, 18.2 ± 1.4Ma and 17.4 ± 1.3 Ma; these ages are in agreement with a zircon dated at 16.8 ± 1.3 Ma at the top of the unit by Wang et al (2014). The Letkat Formation cannot be younger than 14-11 Ma, based on the mammalian fauna age of the Mingin Gravels (Bender, 1983). This would thus indicate an upper lower Miocene (19-16 Ma) up to a lower middle Miocene age (up to 16-14 Ma) for the Letkat Formation. Two points suggest that the Letkat Formation does not extend up to the middle Miocene and is upper lower Miocene only: (1) the Natma and Shwethamin Formations form an additional 3 km thick sequence of fluviatile deposits between the Letkat Formation and the base of the Mingin Gravels (United Nations, 1978a); if the Letkat extended up to the upper lower Miocene, both units would require extremely high depositional and subsidence rates (>1.5 m/k.y.) to be deposited before 14-11 Ma; (2) the very short time lag between apatite youngest U-Pb and AFT age populations (~2 Myr for the three samples) indicates high exhumation rates in the source areas, and thus a short delay between the youngest AFT age and the actual depositional age of the unit. In summary, these constraints suggest significant depositional hiatuses before deposition of both the Tonhe and Letkat Formations. The first unconformity should be of latest Eocene to middle Oligocene age, while the second unconformity is likely of latest Oligocene to early Miocene age.

5.2. Changes in depositional environment

The combination and alternation of facies associations FA1 to FA4 in the Yaw Formation have previously been interpreted as reflecting a barrier-bound, quasi-closed estuary (Licht et al., 2019) and our interpretations here are in line with this previous work. Facies association FA1 with black mudstones and siderite beds reflects the sub-tidal, anoxic central basin depositional environment of the estuary (Anthony et al., 1996). FA2 reflects near-shore environments, tidal flat and intertidal marsh or freshwater lakeshore deposits during periods of estuary closure (Licht et al., 2019). FA3

and FA4 are attributed to respectively bay-head deltaic river distributaries and coastal swamps (paleo-histosols).

By contrast, the Tonhe and Letkat Formations are characterized by pure fluviatile deposition, suggesting complete overfilling of the Chindwin Basin. Thick, wide bodies made of trough cross-beddings lacking any clear inclined heterolithic stratification, and sometimes capped by finer grained sets of pedogenised sands, suggest fluvial channel bodies typical of braided river systems (Leeder, 2009). Yet both fluviatile units display clear differences. The Tonhe Formation, with its coarse channel bodies (commonly gravelly) regularly alternating with thick ultisols, recalls braided channels in distal alluvial fans where channel avulsion is common and can create such regular packages (Leeder, 2009). The Letkat Formation is more monotonous and recalls long-term aggradation of a wide braided river and its floodplain; the replacement of ultisols by vertisols in the rare pedogenised fine-grained deposits suggest a shift to a more seasonal or drier climate at the time of deposition (Retallack, 2008).

Magnetic properties of these three geological units are also very different (Figs. 5.5-5.7). The magnetic properties of the Yaw Formation samples do not evidence a significant contribution of magnetite to the magnetic susceptibility, as it is mainly controlled by paramagnetic minerals. Framboidal pyrites are observed in SEM, and magnetic susceptibility changes around 370°C suggests that pyrite transformed to magnetite upon heating. The main susceptibility peaks in the Yaw Formation (up to 0.002 SI) are however associated with siderite layers. Siderite also transforms to magnetite upon heating and therefore we cannot discard a siderite presence in most samples. In addition, SEM images show dissolution features in quartz grains (Figs. 5.5 and 5.6). There are three potential causes to explain the lack of magnetite in the Yaw Formation sediments. The first one is a source poor in detrital magnetite. The second is the almost complete dissolution of iron-bearing minerals, such as magnetite, resulting in the formation of pyrite. This is a common process in anoxic depositional environments that are rich in organic material and sulphides (Roberts, 2015). Finally, chemical weathering in the upstream areas could have supplied enough iron to the basin for the formation of siderite-rich carbonate layers, possibly by dissimilatory iron reduction occurring in anoxic conditions (Tang et al., 2018). Chemical weathering of magnetite was potentially prolonged by sediment recycling. The magnetic properties of the Yaw Formation show that magnetite grains were not completely dissolved or otherwise were formed anew by early diagenesis, as they preserve a primary paleomagnetic record, evidenced by well-defined normal and reverse magnetozones with similar demagnetizations and no outliers (Section 4.3, fig. 5.7).

The magnetic and mineralogical properties of the Tonhe Formation indicate a clear disappearance of pyrite and siderite (Figs. 5.5 and 5.6), likely representing the shift from estuarian to a purely fluviatile environment lacking anoxic conditions. This is even more apparent in the braided river depositional environment of the overlying Letkat Formation, where magnetic properties are dominated by layers of large detrital magnetite grains and occasionally the occurrence of hematite in finer-grained, pedogenised overbank deposits (Figs. 5.5-5.7). These changes in magnetic properties suggest a lack of anoxic conditions in contrast to the Yaw Formation, implying that chemical alteration of (magnetic) minerals during diagenesis and recycling played a much less significant role here (Roberts, 2015). This is further evidenced by the occurrence of larger and more angular sedimentary clasts, also comprising less stable minerals, such as serpentinized olivine and epidote (Fig. 5.6).

Hence, the first unconformity between the Yaw Formation and Tonhe Formation shows an abrupt change from an anoxic estuarian to a purely fluvial depositional environment. This change in sedimentation conditions becomes even more pronounced in the braided river depositional environment of the Letkat Formation.

5.3. Sedimentary provenance

5.3.1. Yaw Formation

The bulk of detrital zircon and apatite U-Pb ages in the Yaw Formation, dated between 40 and 120 Ma (Fig. 5.8), correspond to the age span of volcanic activity in the proximal WPA (Zhang et al., 2017), suggesting this arc was a dominant source for sediments in the Chindwin Basin until at least the late Eocene, as already proposed in previous studies (Cai et al., 2019; Licht et al., 2019; Wang et al., 2014). However, the Wuntho Ranges (northern segment WPA) directly east of the Chindwin Basin has a more limited volcanic age range compared to the Yaw Formation, only yielding two age groups of ~110-90 Ma and ~42-36 Ma (Barley & Zaw, 2009; Gardiner et al., 2017; Licht et al., 2020; Lin et al., 2019). Furthermore, seismic interpretations show large parts of the WPA were buried by Eocene sediments within the CMB (Zhang et al., 2017). These observations suggest that the Yaw Formation, including its significant population of ~80-50 Ma zircons (Fig. 5.8; Appendix 2, Supplementary Table 2), was not solely sourced by the WPA intersecting the CMB.

North of the BT, ~80-50 Ma volcanic ages are present in the Sodon Batholith and in the Lohit Batholith, which are correlated with the WPA (Haproff et al., 2019; Lin et al., 2019) and could potentially be located in the reconstructed Greater Burma region as part of the Trans-Tethyan Arc (Fig. 5.11a; Westerweel et al., 2019). For these reasons, we propose that the exhuming northernmost perpetuation of the WPA, forming a segment of the Trans-Tethyan Arc in the Greater Burma region, should have significantly contributed to the late Eocene sediment supply of central

Myanmar alongside the Wuntho Ranges (Fig. 5.11a). Similarly, pre-Cretaceous zircons in the Yaw Formation could have been supplied by exhuming basement rocks in the Greater Burma region to the north, because the Eocene Phokphur conglomerates in the northern IBR (Aitchison et al., 2019; Cai et al., 2019) and Eocene sediments in the northernmost Chindwin Basin (Arboit et al., 2020) have comparable pre-Cretaceous age peaks as the Yaw Formation suggesting similar sourcing (Fig. 8). Yaw Formation sourcing from north of the BT could have occurred in the Burmese back-arc where sparse paleocurrent measurements suggest southward directed drainage systems since the late Eocene (Fig. 5.11a; Thein & Maung, 2017). In any case, apatite U-Pb and AFT ages for the Yaw Formation are up to ~30 Ma older than the depositional age of the unit, suggesting that the Yaw Formation sources were just starting to get exhumed and that deeply buried rocks had not been exposed yet.

5.3.2. Tonhe Formation

The zircon U-Pb age distributions from two sandstones of the Tonhe Formation are almost indistinguishable from those of the Yaw Formation (Fig. 5.8). However, the third uppermost sandstone displays an age distribution that is statistically more similar to the Letkat sandstones. An increase in petrographic maturity is shown by the presence of large quartz gravels and illustrated in sandstone grain-counting results (Licht et al., 2019). Apatite U-Pb and AFT ages from the Tonhe Formation are also much younger compared to those in the Yaw Formation, as well as volcanic ages in the WPA (Section 5.3.1). They are also much younger than zircon U-Pb ages in the Tonhe Formation itself, with AFT ages being almost coeval to the proposed upper Oligocene age of deposition of the unit based on palynological evidence. Finally, the sedimentary facies of the Tonhe Formation, corresponding to an alluvial fan setting, suggest a relatively proximal source.

Together this suggests the source remained the WPA and Greater Burma basement similar to the Yaw Formation. Prolonged exhumation in the Greater Burma region exposed more deeply buried rocks by this time, explaining the late Oligocene AFT ages that are close to the depositional age of the Tonhe Formation (Fig. 5.10; Table 5.1). Furthermore, the transitional provenance of the Tonhe Formation in between the Yaw and Letkat Formations and the observed increase in petrographic maturity could be explained by reworking of sedimentary rocks from the exhuming margins of the Chindwin Basin (Fig. 5.9).

5.3.3. Letkat Formation

The zircon U-Pb age distributions of the Letkat sandstones are significantly different from the underlying formations, characterized by (1) a decreased contribution of older, pre-Cretaceous zircons, (2) an increase of the Paleogene zircon age population and (3) the presence of 27 to 17 Ma zircon U-Pb ages, younger than the late Eocene magmatic event in the WPA (Mitchell et al., 2012;

Wang et al., 2014; Zhang et al., 2017). This is accompanied by an increased occurrence of high-grade metamorphic grains (Section 4.2, fig. 5.6) and negative εHf(t) values (Wang et al., 2014; Zhang et al., 2019). Apatite U-Pb and AFT ages from Letkat sandstones provide the most interesting constraints on the age and source of these sediments, indicating rapid exhumation during the early Miocene, with only ~2 Ma lag between these ages (Table 5.1).

The presence of young Oligo-Miocene zircon ages indicates a contribution of the MMMB where these ages are present (Mitchell et al., 2012). The MMMB was located in the Eastern Himalayan Syntaxis north(-east) of the BT during deposition of the Letkat Formation (Fig. 5.11b). Modern river sands from the Upper Irrawaddy River draining the MMMB in northern Myanmar and in the Eastern Himalayan Syntaxis are dominated by Paleogene grains (Garzanti et al., 2016), display young grains (30-17 Ma) and are notably poor in pre-Cretaceous zircons despite draining pre-Cretaceous metamorphics, further suggesting that this area could be an important source. The occurrence of ultramafic and high-grade metamorphic minerals, including the abundance of large detrital magnetite grains, in the Letkat deposits (Section 4.2.2) and the appearance of Cenozoic zircons with negative εHf(t) values also support input from the MMMB (Gardiner et al., 2018). Finally, Ar-Ar ages on MMMB rocks in northern Myanmar and in the Eastern Himalayan Syntaxis indicate early Miocene exhumation, coeval to AFT ages of Letkat sandstones (Bertrand et al., 2001; Haproff et al., 2019). This is coeval with a major phase of shortening, thrusting and exhumation that has been documented for the Himalayan orogen during the early Miocene (e.g. Garzanti, 2019; Vannay et al., 2004). In the Eastern Himalayan Syntaxis directly north of the BT, this phase was even more rapid and intense with similar short lag times as recorded by our apatite U-Pb and AFT ages in the Letkat Formation (Table 5.1; Godin et al., 2006; Haproff et al., 2019; Kellett et al., 2013; Najman et al., 2019).

However, the MMMB largely lacks the ~100 Ma magmatic rocks that are prominent in the WPA . Because this age is still significant in Letkat sandstone age distributions, the WPA probably remained a substantial source in addition to the MMMB signal. This dual sourcing suggests the development of an integrated fluvial system in the CMB in the early Miocene, draining north to south. This is in agreement with SSW paleocurrent measurements in the Letkat Formation (Licht et al., 2019), coeval provenance data in the Minbu Basin showing a similar northern MMMB input (Zhang et al., 2019) and the sedimentary facies of the Letkat Formation that recall the set-up of a wide braided river and its floodplain.

Figure 5.11: *Paleogeography of the Burma Terrane at 40 Ma (left) and 23 Ma (right). Reconstructions were made with GPlates software (Müller et al., 2018), adapted from Westerweel et al. (2019) and*

modified using new tectonic constraints from Morley et al. (2020) as well as deforming plate plate margins (Müller et al., 2019) for the Burma Terrane, Greater India and Bay of Bengal. Abbreviations: BB = Bay of Bengal, BT = Burma Terrane, CB = Chindwin Basin, EAB = Eastern Andaman Basins, EHS = Eastern Himalayan Syntaxis, GA = Gangdese Arc, GB = Greater Burma, GH = Greater Himalayas, IAT = India-Australia Transform, IBR = Indo-Burman Ranges, LT = Lhasa Terrane, MB = Minbu Basin, MMMB = Mogok-Mandalay-Mergui Belt, SB = Sibumasu, SF = Sagaing Fault, SL = Sundaland, TH = Tethyan Himalayas, TTA = Trans-Tethyan Arc, WPA = Wuntho-Popa Arc.

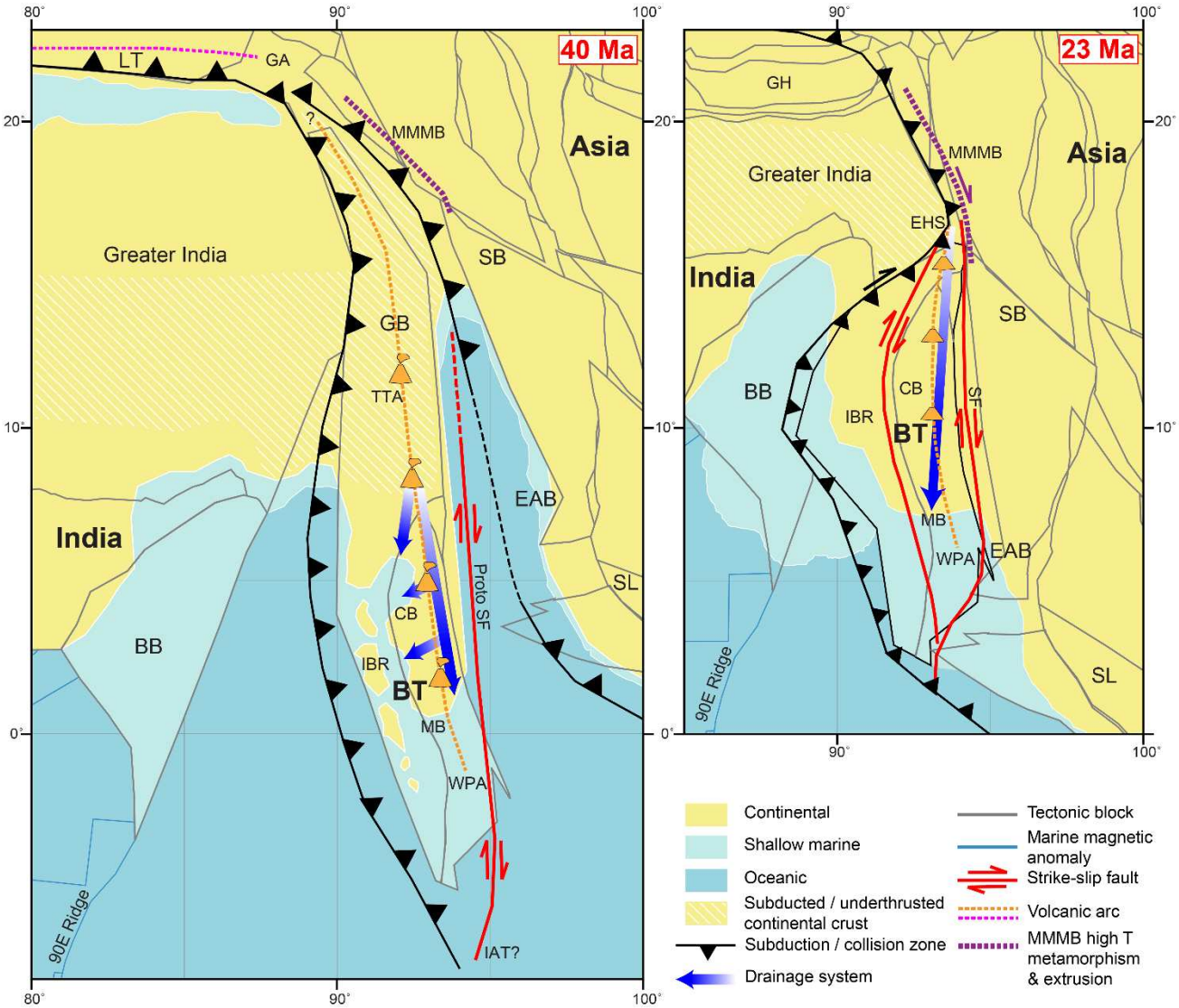

6. Implications for regional tectonic evolution

We explore here potential tectonic control on sedimentation in the Chindwin Basin that may explain the abrupt changes in sedimentary facies, magnetic properties, mineralogy and provenance.

6.1. Late Eocene – middle Oligocene unconformity

The sedimentary facies, magnetostratigraphy and provenance of the Yaw Formation record rapid subsidence (~0.6 m/k.y.) in the Chindwin Basin during the late Eocene. Moreover, there is evidence for coeval uplift in the WPA (Zhang et al., 2017), and incipient emergence of the IBR that sustained the quasi-closed estuarine system of the Chindwin Basin (Licht et al., 2019; Najman et al., 2020). The rapid subsidence has been related to pull-apart deformation of the Burmese forearc (Licht et al., 2019; Rangin, 2018). This is interpreted to relate to major dextral strike-slip displacement east of the BT, along a Proto-Sagaing Fault or India-Australia Transform (Fig. 5.11a; Morley et al., 2020; Westerweel et al., 2019).

The rapid subsidence is interrupted by the latest Eocene - middle Oligocene unconformity constrained by this study. It marks the onset of an uplift phase in the northern BT sometime in this period, evidenced by the occurrence of reworked sediments in the Tonhe Formation that were likely exhumed before (Section 5.3.2; figs. 5.3 and 5.7), and a late Eocene - Oligocene depositional hiatus observed within sedimentary sequences along the WPA (Zhang et al., 2017). The unconformity is also coeval with a proposed uplift event in the IBR (Licht et al., 2019; Morley et al., 2020; Najman et al., 2020), while continuous sedimentation prevailed in the Minbu Basin to the south (Bender, 1983; Licht et al., 2019).

This uplift phase in the northern BT could be explained by the collision of India and the BT along the northern segment of the IBR, recorded by Eocene emplacement of the Western Belt Ophiolite onto the Indian passive margin in the Naga Hills (Aitchison et al., 2019). However, the timing of this emplacement as suggested by Aitchison et al. (2019) is likely earlier in the Eocene, which is more in agreement with an initial early Paleogene (Paleocene - early Eocene) collision of India with the Trans-Tethyan Arc shown by plate reconstructions (Westerweel et al., 2019). According to these reconstructions, this first collision is followed by the collision of India, including the Greater Burma region, with the Asian margin during the late Eocene (Fig. 5.11a; Haproff et al., 2020; Morley et al., 2020; Westerweel et al., 2019). This is supported by the coeval late Eocene onset of high temperature metamorphism along the MMMB (Searle et al., 2007, 2017, 2020) and late Eocene thrusting in the Eastern Himalayan collision zone north of the IBR (Haproff et al., 2020), which these studies also attributed to the India-Asia collision. This together leads us to propose that the latest Eocene - middle Oligocene unconformity from this study was induced by the onset of the collision of India and Greater Burma with Asia in the Eastern Himalayas.

Furthermore, plate reconstructions suggest that deformation associated with this collision would have propagated from north to south starting in the late Eocene (Fig. 5.11a; Morley et al., 2020;

Westerweel et al., 2019). This fits with the late Eocene setting of the IBR with ongoing continental collision in the northern IBR (Aitchison et al., 2019), incipient emergence of the central IBR (Licht et al., 2019; This study), and no or only localized uplift in the southern IBR (Gough et al., 2020). It also fits with the prevailing marine conditions and ongoing subsidence in the Minbu Basin (Gough et al., 2020; Zhang et al., 2019), in contrast to the latest Eocene - middle Oligocene unconformity to the north (This study). This southward propagating collision event in the BT and Eastern Himalayas is consistent with our proposition that the source for the Yaw Formation includes WPA rocks that were presumably exhuming farther north in the Greater Burma region that has now disappeared in the collision zone (Section 5.3.1). This northern extent of the BT would have entered the collision zone in the late Eocene as part of the Trans-Tethyan Arc, while the majority of the BT comprising the CMB farther south was still separated from the Asian margin (Fig. 5.11a; Morley et al., 2020).

6.2. Late Oligocene – early Miocene unconformity

The latest Oligocene - early Miocene unconformity is characterized by significant changes in sedimentary facies, provenance, magnetic properties and mineralogy. Notably, there are abrupt shifts towards late Oligocene - early Miocene zircon U-Pb and apatite U-Pb maximum depositional ages (Table 5.1), early Miocene AFT ages (Fig. 5.10), and braided river sandstones containing an abundance of metamorphic grains and detrital magnetite (Figs. 5.3, 5.6 and 5.7). Furthermore, it corresponds to a basin-wide late Oligocene angular unconformity on seismic lines (Zhang et al., 2017). The unconformity is coeval with pronounced exhumation in the IBR (Najman et al., 2020) as well as in the northern segment of the WPA (Li et al., 2013; Zhang et al., 2017, 2019), indicative of a major deformation event. This period is a time of important regional deformation and drainage reorganisation across the entire Himalayan orogen, particularly around the Eastern Himalayan Syntaxis (Garzanti, 2019; Godin et al., 2006; Haproff et al., 2019; Kellett et al., 2013; Najman et al., 2019; Vannay et al., 2004), leading to the development of the modern Himalayan drainage systems (Bracciali et al., 2015). In the Chindwin Basin, the early Miocene Letkat Formation records the first clear sediment input from rapidly exhuming, deeply buried metamorphosed rocks of the Eastern Himalayan Syntaxis, evidenced by the appearance of early Miocene apatite U-Pb and AFT ages recording short lag times (Section 5.3.3), as well as sandstones rich in high-grade metamorphic grains.

Plate tectonic reconstructions (Fig. 5.11b; Morley et al., 2020; Rangin, 2018; Westerweel et al., 2019) show that the entire BT is indenting the Eastern Himalayan collision zone at the onset of the Miocene, squeezed in between India and the Asian margin during its ongoing northward motion. Therefore, we propose that the latest Oligocene to early Miocene unconformity constrained by this

study is the result of this indentation, enhancing orogenic build-up at the collision front, with shortening within the BT and potential underthrusting of the Greater Burma region. This caused major uplift and exhumation in the Eastern Himalayan orogen and the BT, notably the MMMB and the WPA (Godin et al., 2006; Kellett et al., 2013; Li et al., 2013; Najman et al., 2019; Zhang et al., 2017), providing the dual sourcing of the Letkat Formation. Interestingly, plate reconstructions show a similar timing of southeast directed extrusion of tectonic blocks away from the Eastern Himalayan Syntaxis, such as the Tengchong and Baoshan blocks (Li et al., 2018; Tong et al., 2013; Westerweel et al., 2019). This is also coeval with phases of extrusion-related exhumation and shearing in the northern MMMB (Bertrand et al., 2001; Bertrand & Rangin, 2003). We suggest that these events could be a consequence of ongoing indentation of the BT (Fig. 5.11b). These events would have slowed down the motion of the BT relative to India, leading to more pronounced dextral strike-slip faulting in the IBR during the Neogene (Rangin, 2018; Rangin et al., 2013).

7. Conclusions

Our new results from the late Eocene to early Miocene sedimentary infill of the Chindwin Basin in the Burmese forearc constrain two unconformities that reveal a two-stage interaction of the BT with the Asian margin during its northward motion alongside India. Observations from sedimentary facies and magnetic mineralogy show that the first unconformity between the late Eocene Yaw Formation and late Oligocene Tonhe Formation marks the transition of an anoxic estuarian to a purely fluvial depositional environment, alongside a larger contribution of reworked grains in the sediments. This first unconformity was determined to be of latest Eocene – middle Oligocene age, using a combination of magnetostratigraphy and the appearance of ~29-24 Ma AFT maximum depositional ages in the Tonhe Formation. Furthermore, our magnetostratigraphic results infer rapid ~0.6 m/k.y. subsidence of the Chindwin Basin during deposition of the Yaw Formation. Cessation of subsidence recorded by the first unconformity was likely induced by the initial collision of India, including the Greater Burma region (the northern extension of the BT) and the northern IBR, with the Asia margin. Both the Yaw and Tonhe Formations have a differing zircon age record compared to the WPA directly east of the Chindwin Basin, suggesting that the exhuming northern extension of the WPA in the Greater Burma region was an additional source region throughout the Eocene and Oligocene.

The second unconformity of late Oligocene – early Miocene age is characterized by an abrupt shift towards braided river sandstones rich in high-grade metamorphic grains and detrital magnetite, as well as the appearance of early Miocene (~20-17 Ma) zircon U-Pb, apatite U-Pb and AFT ages. Short lag times of ~2 Ma between the apatite U-Pb and AFT ages record rapid exhumation identical to major phases of thrusting, exhumation and extrusion in the Eastern Himalayan orogen and MMMB north of the BT. Furthermore, this unconformity can be traced across the BT and corresponds to a

phase of uplift and exhumation of the WPA. Hence, this regional deformation phase is interpreted to result from the entire BT indenting the Eastern Himalayan collision zone. Our findings support recent plate reconstructions showing that the BT was part of a Trans-Tethyan Arc, and moved at least 2000 km northward alongside India since the late Eocene.

Acknowledgements

This research was primarily funded by the ERC consolidator grant MAGIC 649081 to Guillaume Dupont-Nivet. Raw data and additional files supporting our analyses and conclusions are in Appendix 2 and Appendix 3 and will be stored in a Mendeley Data repository. We would like to thank Catherine Kissel for the use of the AGM magnetometer at the LSCE paleomagnetic laboratory, France. Furthermore, we thank Loic Joanny and Francis Gouttefangeas for their help with SEM data. We thank P. Cullerier and A. Bernard for helping with the paleomagnetic experiments. We are grateful to François Guillocheau, Amy Gough, Erwan Hallot, France Lagroix, Andrew Mitchell, Chris Morley, Robert Morley, Pavel Pitra, Claude Rangin and Anne Replumaz for helpful discussions during this study. Finally, we would like to thank Rishav Mallick and Paul Betka for constructive reviewing of this manuscript.

References Chapter 5

Acharyya, S. K. (2007). Collisional emplacement history of the Naga-Andaman ophiolites and the position of the eastern Indian suture. Journal of Asian Earth Sciences, 29(2–3), 229–242.

Acharyya, S. K. (2015). Indo-Burma Range: a belt of accreted microcontinents, ophiolites and Mesozoic–Paleogene flyschoid sediments. International Journal of Earth Sciences, 104(5), 1235–1251.

Aitchison, J. C., Ali, J. R., & Davis, A. M. (2007). When and where did India and Asia collide? Journal of Geophysical Research, 112(B5). https://doi.org/10.1029/2006JB004706

Aitchison, J. C., Ao, A., Bhowmik, S., Clarke, G. L., Ireland, T. R., Kachovich, S., … Zhou, R. (2019). Tectonic Evolution of the Western Margin of the Burma Microplate Based on New Fossil and Radiometric Age Constraints. Tectonics, 2018TC005049. https://doi.org/10.1029/2018TC005049

Anthony, E. J., Lang, J., & Oyédé, L. M. (1996). Sedimentation in a tropical, microtidal, wave-dominated coastal-plain estuary. Sedimentology, 43(4), 665–675.

Arboit, F., Min, M., Chew, D., Mitchell, A., Drost, K., Badenszki, E., & Daly, J. S. (2020). Constraining the links between the Himalayan belt and the Central Myanmar Basins during the Cenozoic: An

integrated multi-proxy detrital geochronology and trace-element geochemistry study. Geoscience Frontiers, S1674987120301705. https://doi.org/10.1016/j.gsf.2020.05.024

Bannert, D., Sang Lyen, A., & Htay, T. (2012). The geology of the Indoburman Ranges in Myanmar.

Barley, M. E., & Zaw, K. (2009). SHRIMP U-Pb in zircon geochronology of granitoids from Myanmar: temporal constraints on the tectonic evolution of Southeast Asia. In EGU General Assembly Conference Abstracts (Vol. 11, p. 3842).

Bender, F. (1983). Geology of Burma. Berlin.

Bertrand, G., & Rangin, C. (2003). Tectonics of the western margin of the Shan plateau (central Myanmar): implication for the India–Indochina oblique convergence since the Oligocene. Journal of Asian Earth Sciences, 21(10), 1139–1157.

Bertrand, G., Rangin, C., Maluski, H., & Bellon, H. (2001). Diachronous cooling along the Mogok Metamorphic Belt (Shan scarp, Myanmar): the trace of the northward migration of the Indian syntaxis. Journal of Asian Earth Sciences, 19(5), 649–659. https://doi.org/10.1016/S1367-9120(00)00061-4

Betka, P. M., Seeber, L., Thomson, S. N., Steckler, M. S., Sincavage, R., & Zoramthara, C. (2018). Slip-partitioning above a shallow, weak décollement beneath the Indo-Burman accretionary prism. Earth and Planetary Science Letters, 503, 17–28.

Bracciali, L., Najman, Y., Parrish, R. R., Akhter, S. H., & Millar, I. (2015). The Brahmaputra tale of tectonics and erosion: Early Miocene river capture in the Eastern Himalaya. Earth and Planetary Science Letters, 415, 25–37.

Bracciali, L., Parrish, R. R., Najman, Y., Smye, A., Carter, A., & Wijbrans, J. R. (2016). Plio-Pleistocene exhumation of the eastern Himalayan syntaxis and its domal 'pop-up.' Earth-Science Reviews, 160, 350–385.

Brunnschweiler, R. O. (1966). On the geology of the Indoburman ranges: (Arakan Coast and Yoma, Chin Hills, Naga Hills). Journal of the Geological Society of Australia, 13(1), 137–194.

Cai, F., Ding, L., Zhang, Q., Orme, D. A., Wei, H., Li, J., … Sein, K. (2019). Initiation and evolution of forearc basins in the Central Myanmar Depression. GSA Bulletin. https://doi.org/10.1130/B35301.1

Chew, D. M., Petrus, J. A., & Kamber, B. S. (2014). U–Pb LA–ICPMS dating using accessory mineral standards with variable common Pb. Chemical Geology, 363, 185–199.

Chew, D. M., Sylvester, P. J., & Tubrett, M. N. (2011). U–Pb and Th–Pb dating of apatite by LA-ICPMS. Chemical Geology, 280(1–2), 200–216.

Cogné, N., Chew, D. M., Donelick, R. A., & Ansberque, C. (2020). LA-ICP-MS apatite fission track dating: A practical zeta-based approach. Chemical Geology, 531, 119302.

Donelick, R. A., O'Sullivan, P. B., & Ketcham, R. A. (2005). Apatite fission-track analysis. Reviews in Mineralogy and Geochemistry, 58(1), 49–94.

Dupont-Nivet, G., Krijgsman, W., Langereis, C. G., Abels, H. A., Dai, S., & Fang, X. (2007). Tibetan plateau aridification linked to global cooling at the Eocene–Oligocene transition. Nature, 445(7128), 635–638. https://doi.org/10.1038/nature05516

Fareeduddin, A., & Dilek, Y. (2015). Structure and petrology of the Nagaland-Manipur Hill ophiolitic mélange zone. NE India: A Fossil Tethyan Subduction Channel at the India-Burma Plate Boundary: Episodes, 38, 298–314.

Fisher, R. (1953). Dispersion on a sphere. Proceedings of the Royal Society of London. Series A. Mathematical and Physical Sciences, 217(1130), 295–305.

Gardiner, N. J., Hawkesworth, C. J., Robb, L. J., Whitehouse, M. J., Roberts, N. M. W., Kirkland, C. L., & Evans, N. J. (2017). Contrasting Granite Metallogeny through the Zircon Record: A Case Study from Myanmar. Scientific Reports, 7(1). https://doi.org/10.1038/s41598-017-00832-2

Gardiner, N. J., Searle, M. P., Morley, C. K., Robb, L. J., Whitehouse, M. J., Roberts, N. M. W., … Spencer, C. J. (2018). The crustal architecture of Myanmar imaged through zircon U-Pb, Lu-Hf and O isotopes: Tectonic and metallogenic implications. Gondwana Research. https://doi.org/10.1016/j.gr.2018.02.008

Garzanti, E. (2019). The Himalayan Foreland Basin from collision onset to the present: a sedimentary–petrology perspective. Geological Society, London, Special Publications, SP483.17. https://doi.org/10.1144/SP483.17

Garzanti, E., Wang, J.-G., Vezzoli, G., & Limonta, M. (2016). Tracing provenance and sediment fluxes in the Irrawaddy River basin (Myanmar). Chemical Geology, 440, 73–90. https://doi.org/10.1016/j.chemgeo.2016.06.010

Ghose, N. C., Chatterjee, N., & Fareeduddin. (2014). A Petrographic Atlas of Ophiolite: An example from the eastern India-Asia collision zone. Springer 234 pp.

Godin, L., Grujic, D., Law, R. D., & Searle, M. P. (2006). Channel flow, ductile extrusion and exhumation in continental collision zones: an introduction. Geological Society, London, Special Publications, 268(1), 1–23.

Gough, A., Hall, R., & BouDagher-Fadel, M. K. (2020). Mid-Cenozoic fluvio-deltaic to marine environments of the Salin Sub-basin, Central Myanmar. Journal of Asian Earth Sciences, 104143. https://doi.org/10.1016/j.jseaes.2019.104143

Haproff, P. J., Odlum, M. L., Zuza, A. V., Yin, A., & Stockli, D. F. (2020). Structural and Thermochronologic Constraints on the Cenozoic Tectonic Development of the Northern Indo-Burma Ranges. Tectonics. https://doi.org/10.1029/2020TC006231

Haproff, P. J., Zuza, A. V., Yin, A., Harrison, T. M., Manning, C. E., Dubey, C. S., … Chen, J. (2019). Geologic framework of the northern Indo-Burma Ranges and lateral correlation of Himalayan-Tibetan lithologic units across the eastern Himalayan syntaxis. Geosphere. https://doi.org/10.1130/GES02054.1

Hu, X., Garzanti, E., Moore, T., & Raffi, I. (2015). Direct stratigraphic dating of India-Asia collision onset at the Selandian (middle Paleocene, 59$\pm$1 Ma). Geology, 43(10), 859–862.

Huang, H., Morley, R., Licht, A., Dupont-Nivet, G., Grímsson, F., Zetter, R., … Hoorn, C. (2020). Eocene palms from central Myanmar in a South-East Asian and global perspective: evidence from the palynological record. Botanical Journal of the Linnean Society. https://doi.org/10.1093/botlinnean/boaa038

Jaeger, J.-J., Thein, T., Benammi, M., Chaimanee, Y., Soe, A. N., Lwin, T., … Ducrocq, S. (1999). A new primate from the middle Eocene of Myanmar and the Asian early origin of anthropoids. Science, 286(5439), 528–530.

Jagoutz, O., Royden, L., Holt, A. F., & Becker, T. W. (2015). Anomalously fast convergence of India and Eurasia caused by double subduction. Nature Geoscience, 8(6), 475–478. https://doi.org/10.1038/ngeo2418

Kapp, P., & DeCelles, P. G. (2019). Mesozoic–Cenozoic geological evolution of the Himalayan-Tibetan orogen and working tectonic hypotheses. American Journal of Science, 319(3), 159–254.

Kellett, D. A., Grujic, D., Coutand, I., Cottle, J., & Mukul, M. (2013). The South Tibetan detachment system facilitates ultra rapid cooling of granulite-facies rocks in Sikkim Himalaya. Tectonics, 32(2), 252–270.

Khin, K. (1999). Marine transgression and regression in Miocene sequences of northern Pegu (Bago) Yoma, central Myanmar. Journal of Asian Earth Sciences, 17(3), 369–393.

Khin Zaw, Meffre, S., Takai, M., Suzuki, H., Burrett, C., Thaung Htike, … Maung Maung. (2014). The oldest anthropoid primates in SE Asia: Evidence from LA-ICP-MS U–Pb zircon age in the Late Middle Eocene Pondaung Formation, Myanmar. Gondwana Research, 26(1), 122–131. https://doi.org/10.1016/j.gr.2013.04.007

Kirschvink, J. L. (1980). The least-squares line and plane and the analysis of palaeomagnetic data. Geophysical Journal International, 62(3), 699–718.

Kissel, C., Barrier, E., Laj, C., & Lee, T.-Q. (1986). Magnetic fabric in "undeformed" marine clays from compressional zones. Tectonics, 5(5), 769–781.

Lang, K. A., Huntington, K. W., Burmester, R., & Housen, B. (2016). Rapid exhumation of the eastern Himalayan syntaxis since the late Miocene. Bulletin, 128(9–10), 1403–1422.

Leeder, M. R. (2009). Sedimentology and sedimentary basins: from turbulence to tectonics. John Wiley & Sons.

Li, R., Mei, L., Zhu, G., Zhao, R., Xu, X., Zhao, H., … Ma, Y. (2013). Late mesozoic to cenozoic tectonic events in volcanic arc, West Burma Block: Evidences from U-Pb zircon dating and apatite fission track data of granitoids. Journal of Earth Science, 24(4), 553–568. https://doi.org/10.1007/s12583-013-0349-7

Li, S., van Hinsbergen, D. J. J., Deng, C., Advokaat, E. L., & Zhu, R. (2018). Paleomagnetic Constraints From the Baoshan Area on the Deformation of the Qiangtang-Sibumasu Terrane Around the Eastern Himalayan Syntaxis. Journal of Geophysical Research: Solid Earth. https://doi.org/10.1002/2017JB015112

Licht, A., Boura, A., De Franceschi, D., Utescher, T., Sein, C., & Jaeger, J.-J. (2015). Late middle Eocene fossil wood of Myanmar: Implications for the landscape and the climate of the Eocene Bengal Bay. Review of Palaeobotany and Palynology, 216, 44–54. https://doi.org/10.1016/j.revpalbo.2015.01.010

Licht, A., Cojan, I., Caner, L., Soe, A. N., Jaeger, J.-J., & France-Lanord, C. (2014). Role of permeability barriers in alluvial hydromorphic palaeosols: The Eocene Pondaung Formation, Myanmar. Sedimentology, 61(2), 362–382. https://doi.org/10.1111/sed.12059

Licht, A., Dupont-Nivet, G., Win, Z., Swe, H. H., Kaythi, M., Roperch, P., … Sein, K. (2019). Paleogene evolution of the Burmese forearc basin and implications for the history of India-Asia convergence. Geological Society of America Bulletin, 1(130), 20.

Licht, A., France-Lanord, C., Reisberg, L., Fontaine, C., Soe, A. N., & Jaeger, J.-J. (2013). A palaeo Tibet–Myanmar connection? Reconstructing the Late Eocene drainage system of central Myanmar using a multi-proxy approach. Journal of the Geological Society, 170(6), 929–939.

Licht, A., van Cappelle, M., Abels, H. A., Ladant, J.-B., Trabucho-Alexandre, J., France-Lanord, C., … Jaeger, J.-J. (2014). Asian monsoons in a late Eocene greenhouse world. Nature, 513(7519), 501–506. https://doi.org/10.1038/nature13704

Licht, A., Win, Z., Westerweel, J., Cogné, N., Morley, C., Chantraprasert, S., … Dupont-Nivet, G. (2020). Magmatic history of central Myanmar and implications for the evolution of the Burma Terrane. Gondwana Research. https://doi.org/10.1016/j.gr.2020.06.016

Lin, T.-H., Mitchell, A. H. G., Chung, S.-L., Tan, X.-B., Tang, J.-T., Oo, T., & Wu, F.-Y. (2019). Two parallel magmatic belts with contrasting isotopic characteristics from southern Tibet to Myanmar: zircon U–Pb and Hf isotopic constraints. Journal of the Geological Society, 176(3), 574–587. https://doi.org/10.1144/jgs2018-072

Liu, C.-Z., Chung, S.-L., Wu, F.-Y., Zhang, C., Xu, Y., Wang, J.-G., … Guo, S. (2016). Tethyan suturing in Southeast Asia: Zircon U-Pb and Hf-O isotopic constraints from Myanmar ophiolites. Geology, 44(4), 311–314. https://doi.org/10.1130/G37342.1

Ludwig, K. R. (2003). User's manual for isoplot 3.00, a geochronlogical toolkit for microsoft excel. Berkeley Geochronl. Cent. Spec. Publ., 4, 25–32.

Lwin, S. M., Thu, S. S., Aung, M. M., Khine, K. K., Aung, H., Thidar, M., & Pau, S. K. (2017). Paleo-environment of the Miocene Sediments, Central Belt, Myanmar.

Matthews, W. A., & Guest, B. (2017). A practical approach for collecting large-n detrital zircon U-Pb data sets by quadrupole LA-ICP-MS. Geostandards and Geoanalytical Research, 41(2), 161–180.

Maurin, T., & Rangin, C. (2009). Structure and kinematics of the Indo-Burmese Wedge: Recent and fast growth of the outer wedge: GROWTH OF THE OUTER INDO-BURMESE WEDGE. Tectonics, 28(2), n/a-n/a. https://doi.org/10.1029/2008TC002276

Mitchell, A. (2017). Geological Belts, Plate Boundaries, and Mineral Deposits in Myanmar. Elsevier.

Mitchell, A., Chung, S.-L., Oo, T., Lin, T.-H., & Hung, C.-H. (2012). Zircon U–Pb ages in Myanmar: Magmatic–metamorphic events and the closure of a neo-Tethys ocean? Journal of Asian Earth Sciences, 56, 1–23. https://doi.org/10.1016/j.jseaes.2012.04.019

Morley, C. K. (2009). Evolution from an oblique subduction back-arc mobile belt to a highly oblique collisional margin: the Cenozoic tectonic development of Thailand and eastern Myanmar. Geological Society, London, Special Publications, 318(1), 373–403. https://doi.org/10.1144/SP318.14

Morley, C. K. (2017). Syn-kinematic sedimentation at a releasing splay in the northern Minwun Ranges, Sagaing Fault zone, Myanmar: significance for fault timing and displacement. Basin Research, 29, 684–700. https://doi.org/10.1111/bre.12201

Morley, C. K., & Arboit, F. (2019). Dating the onset of motion on the Sagaing fault: Evidence fromdetrital zircon and titanite U-Pb geochronology from the NorthMinwun Basin, Myanmar. Geology. https://doi.org/10.1130/G46321.1

Morley, C. K., Tin Tin Naing, Searle, M., & Robinson, S. A. (2020). Structural and tectonic development of the Indo-Burma ranges. Earth-Science Reviews, 200, 102992. https://doi.org/10.1016/j.earscirev.2019.102992

Müller, R. D., Cannon, J., Qin, X., Watson, R. J., Gurnis, M., Williams, S., … Zahirovic, S. (2018). GPlates: Building a virtual Earth through deep time. Geochemistry, Geophysics, Geosystems, 19(7), 2243–2261.

Müller, R. D., Zahirovic, S., Williams, S. E., Cannon, J., Seton, M., Bower, D. J., … Gurnis, M. (2019). A global plate model including lithospheric deformation along major rifts and orogens since the Triassic. Tectonics, 2018TC005462. https://doi.org/10.1029/2018TC005462

Naing, T. T., Bussien, D. A., Winkler, W. H., Nold, M., & Von Quadt, A. (2014). Provenance study on Eocene–Miocene sandstones of the Rakhine Coastal Belt, Indo-Burman Ranges of Myanmar: geodynamic implications. Geological Society, London, Special Publications, 386(1), 195–216. https://doi.org/10.1144/SP386.10

Najman, Y., Allen, R., Willett, E. A. F., Carter, A., Barfod, D., Garzanti, E., … Ando, S. (2012). The record of Himalayan erosion preserved in the sedimentary rocks of the Hatia Trough of the Bengal Basin and the Chittagong Hill Tracts, Bangladesh. Basin Research, 24(5), 499–519.

Najman, Y., Mark, C., Barfod, D. N., Carter, A., Parrish, R., Chew, D., & Gemignani, L. (2019). Spatial and temporal trends in exhumation of the Eastern Himalaya and syntaxis as determined from a

multitechnique detrital thermochronological study of the Bengal Fan. GSA Bulletin, 131(9–10), 1607–1622. https://doi.org/10.1130/B35031.1

Najman, Y., Sobel, E. R., Millar, I., Stockli, D. F., Govin, G., Lisker, F., … Kahn, A. (2020). The exhumation of the Indo-Burman Ranges, Myanmar. Earth and Planetary Science Letters, 530, 115948. https://doi.org/10.1016/j.epsl.2019.115948

Nielsen, C., Chamot-Rooke, N., & Rangin, C. (2004). From partial to full strain partitioning along the Indo-Burmese hyper-oblique subduction. Marine Geology, 209(1–4), 303–327.

Ogg, J. G., Ogg, G., & Gradstein, F. M. (2016). A concise geologic time scale.

Paton, C., Woodhead, J. D., Hellstrom, J. C., Hergt, J. M., Greig, A., & Maas, R. (2010). Improved laser ablation U-Pb zircon geochronology through robust downhole fractionation correction. Geochemistry, Geophysics, Geosystems, 11(3).

Pivnik, D. A., Nahm, J., Tucker, R. S., Smith, G. O., Nyein, K., Nyunt, M., & Maung, P. H. (1998). Polyphase Deformation in a Fore-Arc/Back-Arc Basin, Salin Subbasin, Myanmar (Burma). AAPG Bulletin, 82(10), 1837–1856.

Rangin, C. (2018). The western Sunda basins and the India/Asia collision: an atlas. Geotecto, Paris, France.

Rangin, C., Maurin, T., & Masson, F. (2013). Combined effects of Eurasia/Sunda oblique convergence and East-Tibetan crustal flow on the active tectonics of Burma. Journal of Asian Earth Sciences, 76, 185–194. https://doi.org/10.1016/j.jseaes.2013.05.018

Replumaz, A., Guillot, S., Villaseñor, A., & Negredo, A. M. (2013). Amount of Asian lithospheric mantle subducted during the India/Asia collision. Gondwana Research, 24(3–4), 936–945. https://doi.org/10.1016/j.gr.2012.07.019

Replumaz, A., Negredo, A. M., Guillot, S., & Villaseñor, A. (2010). Multiple episodes of continental subduction during India/Asia convergence: Insight from seismic tomography and tectonic reconstruction. Tectonophysics, 483(1–2), 125–134. https://doi.org/10.1016/j.tecto.2009.10.007

Retallack, G. J. (2008). Soils of the past: an introduction to paleopedology. John Wiley & Sons.

Roberts, A. P. (2015). Magnetic mineral diagenesis. Earth-Science Reviews, 151, 1–47. https://doi.org/10.1016/j.earscirev.2015.09.010

Rochette, P. (1988). Inverse magnetic fabric in carbonate-bearing rocks. Earth and Planetary Science Letters, 90(2), 229–237.

Roperch, P., & Taylor, G. K. (1986). The importance of gyromagnetic remanence in alternating field demagnetization. Some new data and experiments on GRM and RRM. Geophysical Journal International, 87(3), 949–965.

Royden, L. H., Burchfiel, B. C., & van der Hilst, R. D. (2008). The Geological Evolution of the Tibetan Plateau. Science, 321(5892), 1054–1058. https://doi.org/10.1126/science.1155371

Searle, M. P., Garber, J. M., Hacker, B. R., Htun, K., Gardiner, N. J., Waters, D. J., & Robb, L. J. (2020). Timing of syenite-charnockite magmatism and ruby-and sapphire metamorphism in the Mogok valley region, Myanmar. Tectonics, e2019TC005998.

Searle, M. P., Morley, C. K., Waters, D. J., Gardiner, N. J., Htun, U. K., Than Than Nu, & Robb, L. J. (2017). Chapter 12 Tectonic and metamorphic evolution of the Mogok Metamorphic and Jade Mines belts and ophiolitic terranes of Burma (Myanmar). Geological Society, London, Memoirs, 48(1), 261–293. https://doi.org/10.1144/M48.12

Searle, M. P., Noble, S. R., Cottle, J. M., Waters, D. J., Mitchell, A. H. G., Hlaing, T., & Horstwood, M. S. A. (2007). Tectonic evolution of the Mogok metamorphic belt, Burma (Myanmar) constrained by U-Th-Pb dating of metamorphic and magmatic rocks: U-TH-PB AGES OF MOGOK BELT. Tectonics, 26(3), n/a-n/a. https://doi.org/10.1029/2006TC002083

Shen, F., Royden, L. H., & Burchfiel, B. C. (2001). Large-scale crustal deformation of the Tibetan Plateau. Journal of Geophysical Research: Solid Earth, 106(B4), 6793–6816. https://doi.org/10.1029/2000JB900389

Singh, A. K., Khogenkumar, S., Singh, L. R., Bikramaditya, R. K., Khuman, Ch. M., & Thakur, S. S. (2016). Evidence of Mid-ocean ridge and shallow subduction forearc magmatism in the Nagaland-Manipur ophiolites, northeast India: constraints from mineralogy and geochemistry of gabbros and associated mafic dykes. Geochemistry, 76(4), 605–620. https://doi.org/10.1016/j.chemer.2016.09.002

Smith, J. J., Hasiotis, S. T., Kraus, M. J., & Woody, D. T. (2008). Naktodemasis bowni: new ichnogenus and ichnospecies for adhesive meniscate burrows (AMB), and paleoenvironmental implications, Paleogene Willwood Formation, Bighorn Basin, Wyoming. Journal of Paleontology, 82(2), 267–278.

Socquet, A., Vigny, C., Chamot-Rooke, N., Simons, W., Rangin, C., & Ambrosius, B. (2006). India and Sunda plates motion and deformation along their boundary in Myanmar determined by GPS: GPS INDIA-SUNDA MOTION, MYANMAR STRAIN. Journal of Geophysical Research: Solid Earth, 111(B5), n/a-n/a. https://doi.org/10.1029/2005JB003877

Stacey, J. t, & Kramers, 1JD. (1975). Approximation of terrestrial lead isotope evolution by a two-stage model. Earth and Planetary Science Letters, 26(2), 207–221.

Steckler, M. S., Akhter, S. H., & Seeber, L. (2008). Collision of the Ganges–Brahmaputra Delta with the Burma Arc: implications for earthquake hazard. Earth and Planetary Science Letters, 273(3–4), 367–378.

Tang, D., Shi, X., Jiang, G., Wu, T., Ma, J., & Zhou, X. (2018). Stratiform siderites from the Mesoproterozoic Xiamaling Formation in North China: Genesis and environmental implications. Gondwana Research, 58, 1–15. https://doi.org/10.1016/j.gr.2018.01.013

Tauxe, L. (2010). Essentials of paleomagnetism. Univ of California Press.

Thein, M., & Maung, M. (2017). The Eastern (Back-arc) Basin of Central Myanmar: Basement rocks, lithostratigraphic units, palaeocurrents, provenance and developmental history. Geological Society, London, Memoirs, 48(1), 169–183.

Tong, Y.-B., Yang, Z., Zheng, L.-D., Xu, Y.-L., Wang, H., Gao, L., & Hu, X.-Z. (2013). Internal crustal deformation in the northern part of Shan-Thai Block: New evidence from paleomagnetic results of Cretaceous and Paleogene redbeds. Tectonophysics, 608, 1138–1158. https://doi.org/10.1016/j.tecto.2013.06.031

United Nations. (1978a). Geology and exploration geochemistry of the Pinlebu-Banmauk area, Sagaing Division, northern Burma. Technical Report No. 2. DP/UN/BUR-72-002. Geological Survey and Exploration Project, United Nations Development Programme, New York, 66.

van der Beek, P., Govin, G., Najman, Y., Millar, I., Gemignani, L., Huyghe, P., … Wijbrans, J. R. (2019). Early Onset and Late Acceleration of Rapid Exhumation in the Namche Barwa Syntaxis, Eastern Himalaya. AGUFM, 2019, T54A–07.

van Hinsbergen, D. J. J., Kapp, P., Dupont-Nivet, G., Lippert, P. C., DeCelles, P. G., & Torsvik, T. H. (2011). Restoration of Cenozoic deformation in Asia and the size of Greater India: RESTORING CENOZOIC ASIAN DEFORMATION. Tectonics, 30(5), n/a-n/a. https://doi.org/10.1029/2011TC002908

van Hinsbergen, D. J. J., Lippert, P. C., Li, S., Huang, W., Advokaat, E. L., & Spakman, W. (2018). Reconstructing Greater India: Paleogeographic, kinematic, and geodynamic perspectives. Tectonophysics. https://doi.org/10.1016/j.tecto.2018.04.006

Vannay, J.-C., Grasemann, B., Rahn, M., Frank, W., Carter, A., Baudraz, V., & Cosca, M. (2004). Miocene to Holocene exhumation of metamorphic crustal wedges in the NW Himalaya: Evidence for tectonic extrusion coupled to fluvial erosion. Tectonics, 23(1).

Vérard, C., Stampfli, G., Borel, G., & Hochard, C. (2017). The Indian promontory: A bridge between plate tectonics and life evolution models. Universal Journal of Geoscience, 5(2), 25–32.

Vermeesch, P. (2013). Multi-sample comparison of detrital age distributions. Chemical Geology, 341, 140–146.

Vermeesch, P. (2018). IsoplotR: A free and open toolbox for geochronology. Geoscience Frontiers, 9(5), 1479–1493.

Wang, J.-G., Wu, F.-Y., Tan, X.-C., & Liu, C.-Z. (2014). Magmatic evolution of the Western Myanmar Arc documented by U–Pb and Hf isotopes in detrital zircon. Tectonophysics, 612–613, 97–105. https://doi.org/10.1016/j.tecto.2013.11.039

Westerweel, J., Roperch, P., Licht, A., Dupont-Nivet, G., Win, Z., Poblete, F., … Aung, D. W. (2019). Burma Terrane part of the Trans-Tethyan arc during collision with India according to palaeomagnetic data. Nature Geoscience. https://doi.org/10.1038/s41561-019-0443-2

Woodhead, J. D., Hellstrom, J., Hergt, J. M., Greig, A., & Maas, R. (2007). Isotopic and elemental imaging of geological materials by laser ablation inductively coupled plasma-mass spectrometry. Geostandards and Geoanalytical Research, 31(4), 331–343.

Yin, A., & Harrison, T. M. (2000). Geologic Evolution of the Himalayan-Tibetan Orogen. Annual Review of Earth and Planetary Sciences, 28(1), 211–280. https://doi.org/10.1146/annurev.earth.28.1.211

Yui, T.-F., Fukoyama, M., Iizuka, Y., Wu, C.-M., Wu, T.-W., Liou, J. G., & Grove, M. (2013). Is Myanmar jadeitite of Jurassic age? A result from incompletely recrystallized inherited zircon. Lithos, 160–161, 268–282. https://doi.org/10.1016/j.lithos.2012.12.011

Zat, M., & Aung, D. W. (2018). Sedimentology and Sequence Stratigraphy of Letkat Formation in Kalewa-Mawleik Area, Sagaing Region.

Zeitler, P. K., Meltzer, A. S., Brown, L., Kidd, W. S., Lim, C., & Enkelmann, E. (2014). Tectonics and topographic evolution of Namche Barwa and the easternmost Lhasa block, Tibet. In Toward an Improved Understanding of Uplift Mechanisms and the Elevation History of the Tibetan Plateau (Vol. 507, pp. 23–58). Geological Society of America Special Papers Boulder, CO.

Zhang, P., Mei, L., Hu, X., Li, R., Wu, L., Zhou, Z., & Qiu, H. (2017). Structures, uplift, and magmatism of the Western Myanmar Arc: Constraints to mid-Cretaceous-Paleogene tectonic evolution of the western Myanmar continental margin. Gondwana Research, 52, 18–38. https://doi.org/10.1016/j.gr.2017.09.002

Zhang, P., Najman, Y., Mei, L., Millar, I., Sobel, E. R., Carter, A., … Hu, X. (2019). Palaeodrainage evolution of the large rivers of East Asia, and Himalayan-Tibet tectonics. Earth-Science Reviews, 192, 601–630. https://doi.org/10.1016/j.earscirev.2019.02.003

Zijderveld, J. D. A. (1967). AC demagnetization of rocks: Analysis of results, Methods in Paleomagnetism DW Collinson, KM Creer, SK Runcorn, 254–286. Elsevier, New York.

Supplementary figures

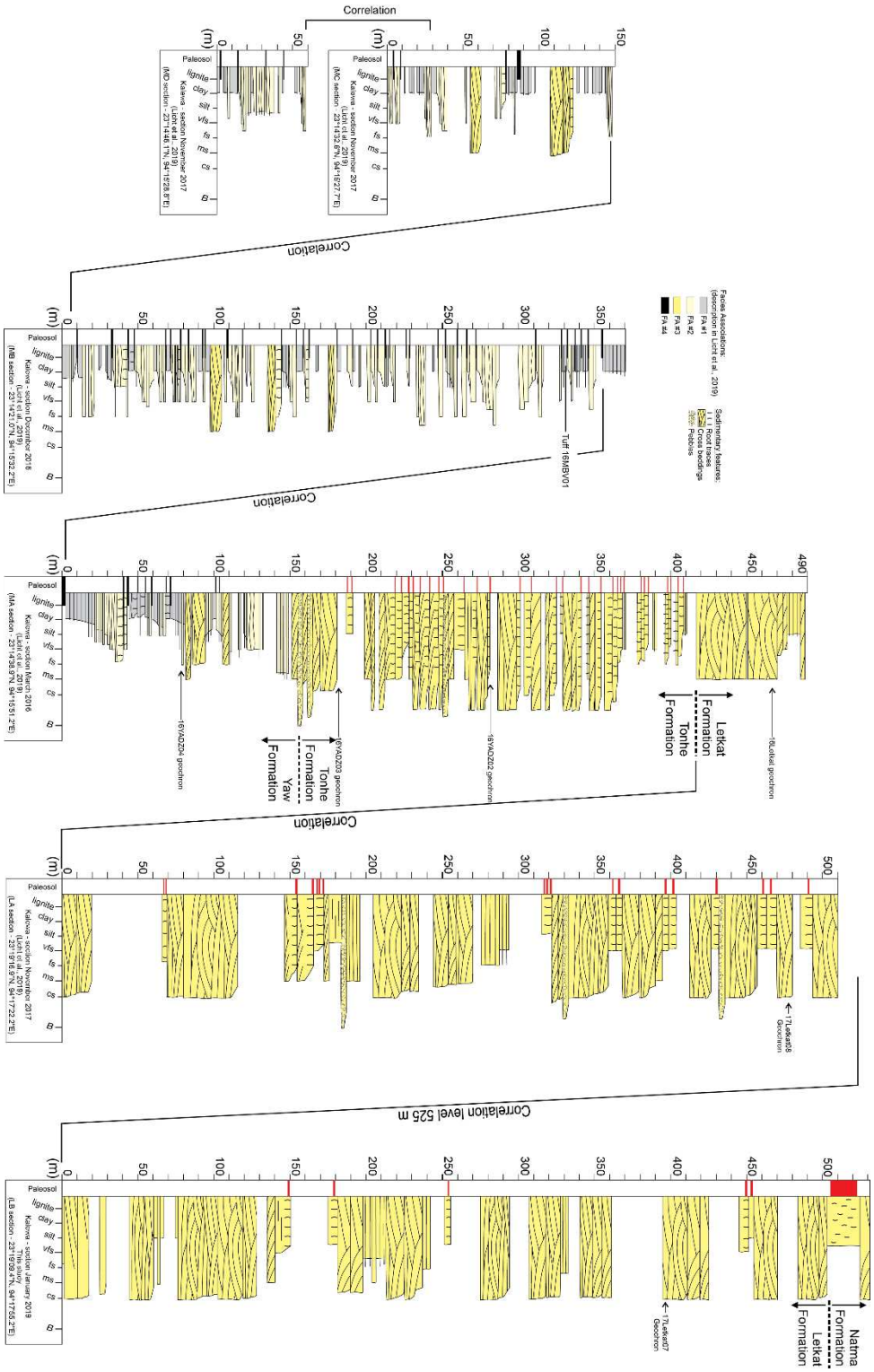

Figure 5.S1: *Detailed logs of the five sections from Licht et al. (2019) (MA, MB, MC, MD, LA) and this study (LB) with level of sandstones for zircon and apatite dating and facies associations from Licht et al. (2019). The locations of these logs are shown on figure 5.1b.*

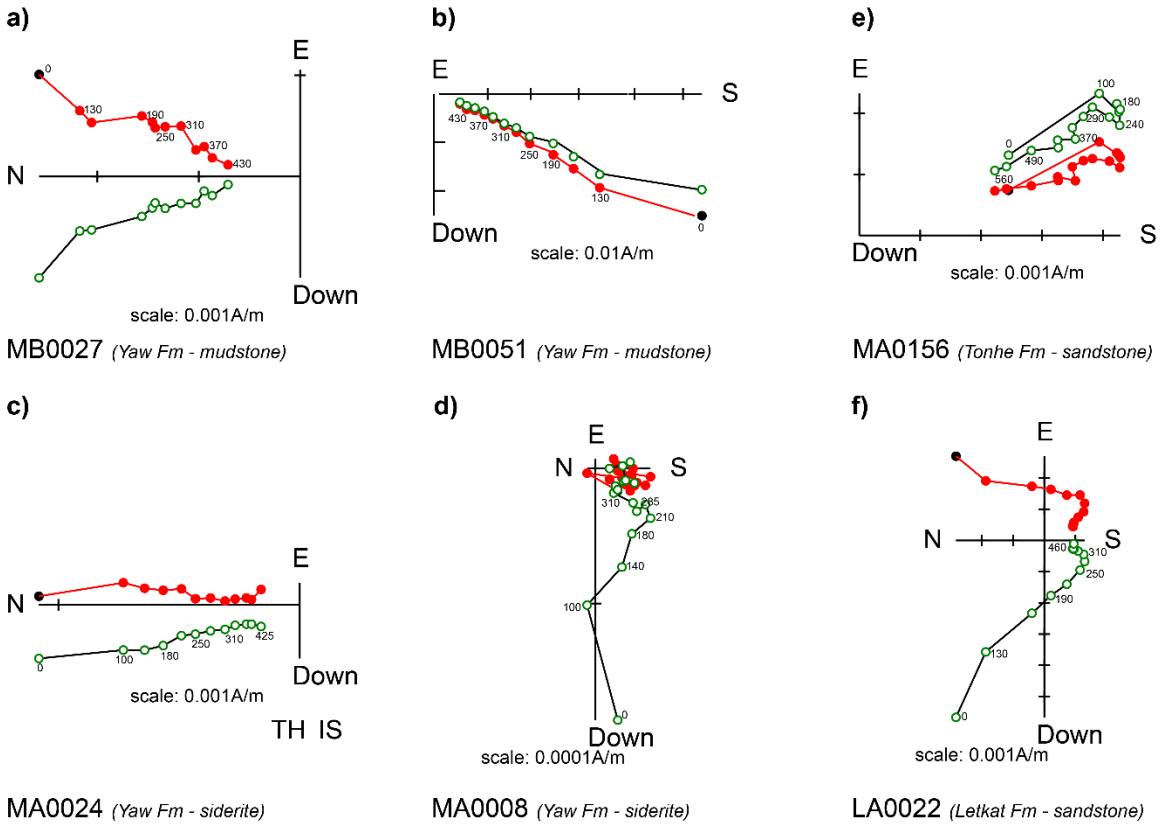

Figure 5.S2: *Representative orthogonal demagnetization plots from the different formations and lithologies in this study. Both samples of reversed and normal polarity are shown.*

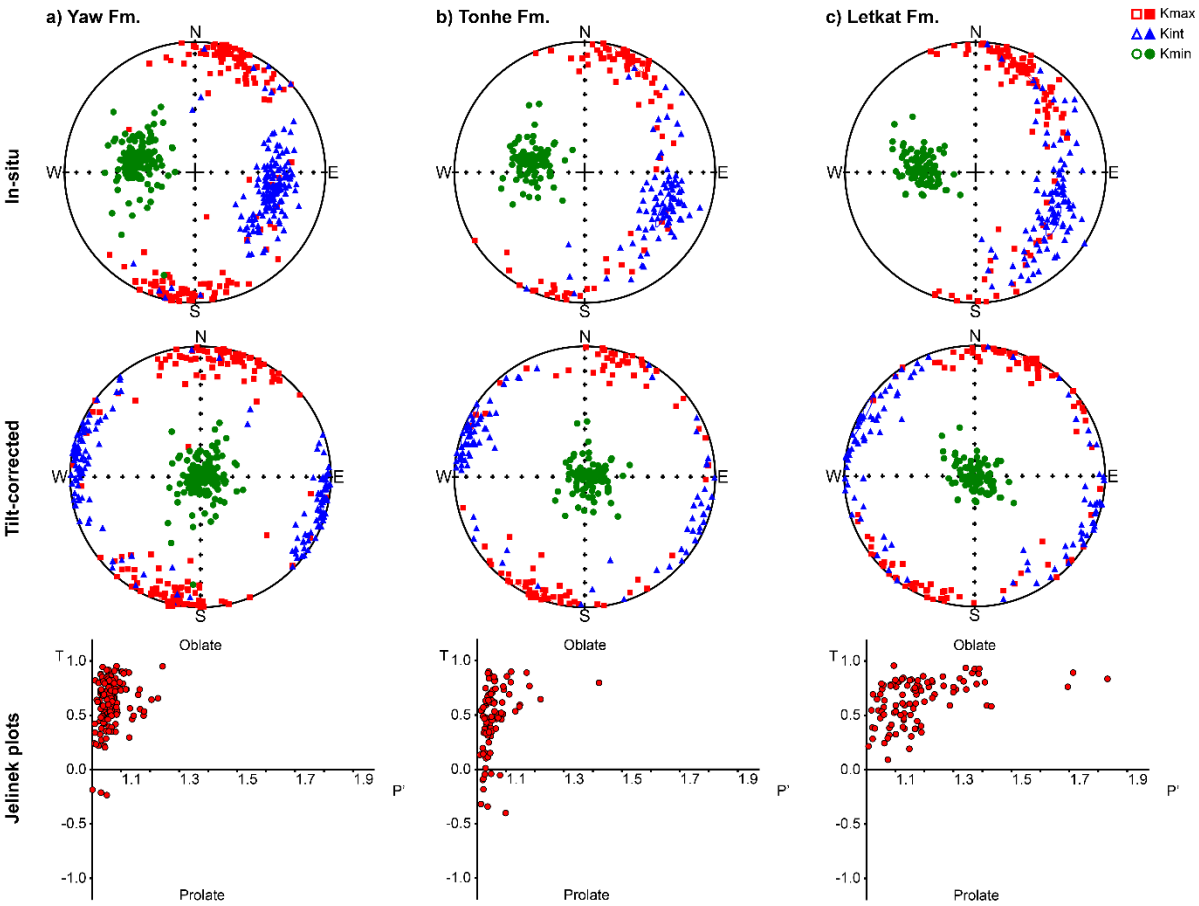

Figure 5.S3: *Equal-area plots of the anisotropy of magnetic susceptibility (AMS) of all samples in in-situ and after bedding correction, as well as Jelinek plots of the shape (T) of the anisotropy ellipsoid versus the corrected degree of anisotropy (P') for the Yaw (a), Tonhe (b) and Letkat (c) Formations.*

Figure 5.S4: *Tera-Wasserburg plots and regressions for U-Pb apatite data of every sample analyzed in this study. P1 to P6 indicate the age population (youngest to oldest). Ages are calculated for every sample, with anchored (@anch) and unanchored 207Pb/206Pb values for common lead. Ellipses are 2s errors.*

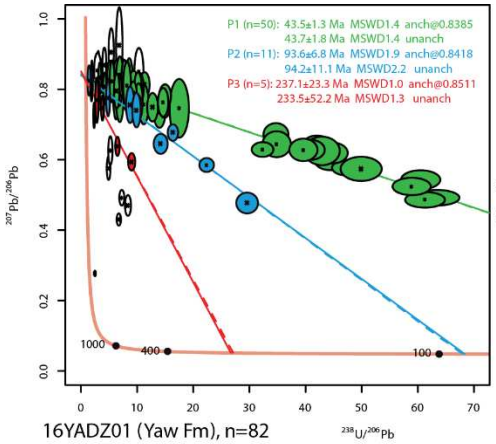

16YADZ01 (Yaw Fm), n=82

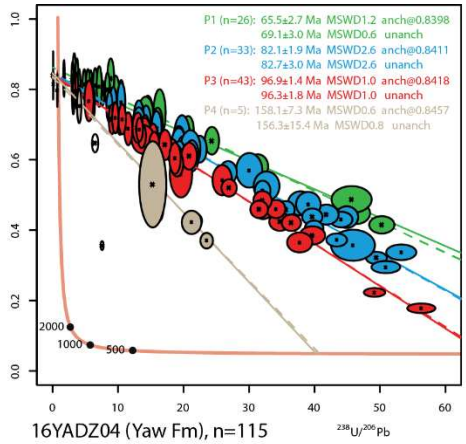

16YADZ04 (Yaw Fm), n=115

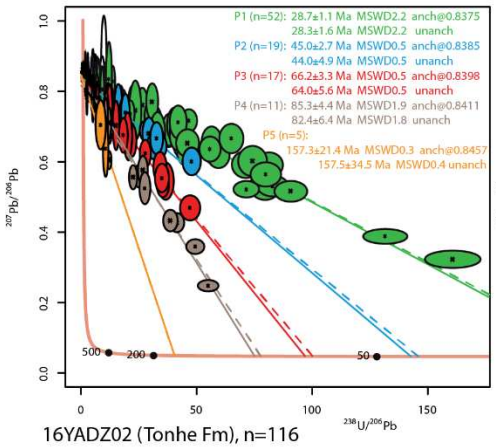

16YADZ02 (Tonhe Fm), n=116

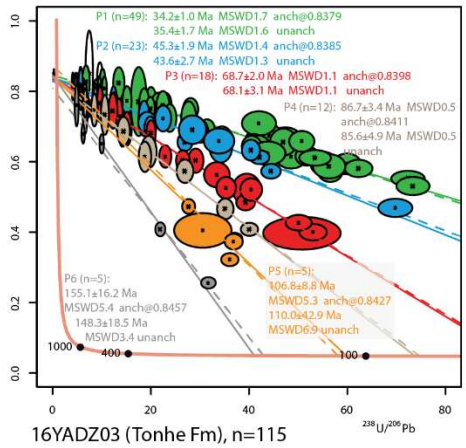

16YADZ03 (Tonhe Fm), n=115

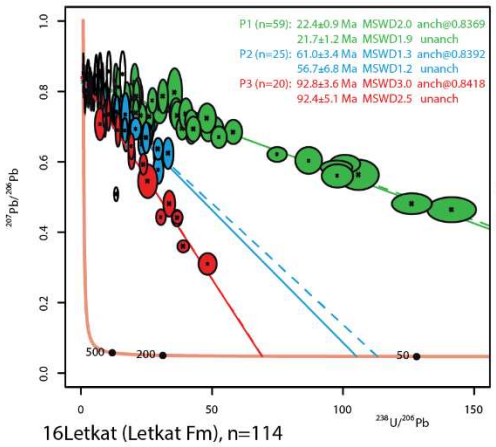

16Letkat (Letkat Fm), n=114

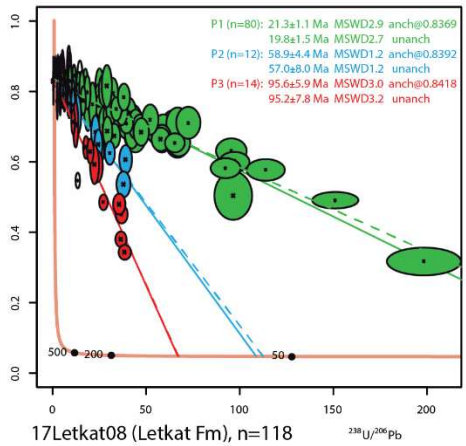

17Letkat08 (Letkat Fm), n=118

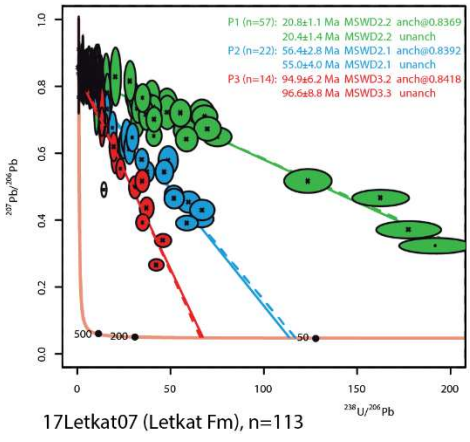

17Letkat07 (Letkat Fm), n=113

Chapter 6: Late Cretaceous to Miocene paleogeography of the India-Asia collision revealed by Burma Terrane (Myanmar) paleomagnetic data

View on the Indo-Burman Ranges from the Minbu Basin.
(Sidoktaya, Myanmar, Fieldwork January 2019)

Reference: *Manuscript in preparation.*

Abstract

The paleogeographic evolution of the India-Asia collision and the resulting formation of the Himalayan orogen remain an intensely debated topic, illustrated by a variety of disputed collision models. The large spatial knowledge gap due to understudying the eastern extension of the collision zone is an important cause for this unsettled debate. Notably, recent plate tectonic reconstructions have shown that the Burma Terrane (Myanmar), a microplate at the eastern edge of the Himalayan orogen, is key for understanding Asian geodynamic, paleoenvironmental and paleoclimatic evolution. Here we present new paleomagnetic data of Campanian - Maastrichtian, latest Paleocene – middle Eocene, late Eocene, middle Oligocene and middle Miocene age from the Burmese Terrane. Alongside previously published early Late Cretaceous and late Eocene results, these paleomagnetic constraints provide the detailed paleolatitudinal motion of the Burma Terrane, which were then incorporated in plate tectonic reconstructions of the India-Asia collision. Our paleomagnetic constraints show that the Burma Terrane remained at a southern hemisphere position distant from the southern Asian margin throughout the Late Cretaceous and early Paleogene, it was subsequently incorporated and moved northward with the Indian Plate in the latest Paleocene – middle Eocene, and it ultimately indented the Eastern Himalayan collision zone in the late Oligocene – early Miocene. Our findings support collision models with an initial latest Paleocene – middle Eocene collision of India with a Trans-Tethyan subduction system incorporating the Burmese volcanic arc and continental fragments of differing origin, before they conjointly moved northward towards Asia.

1. Introduction

The Himalayan-Tibetan orogen is the most dramatic mountain range on Earth with an impressive tectonic history involving the amalgamation of numerous terranes, in particular during the India-Asia collision. Therefore, it is often regarded as the archetype orogen for studying continental collision systems. However, the paleogeography and chronology of the India-Asia collision are still intensely debated (Hu et al., 2015; Jagoutz et al., 2015; Replumaz et al., 2010, 2013; Royden et al., 2008; Shen et al., 2001; van Hinsbergen et al., 2011, 2018; Westerweel et al., 2019). This debate is further complicated by an enormous spatial gap in investigating the paleogeographic evolution of the India-Asia collision, because the ~1500 km eastern extend of the collision zone remains understudied compared to the central orogen. The Burma Terrane (BT, also named West Burma Block) of Myanmar constitutes the major microplate at the eastern edge of the Himalayan collision zone. This unique position makes the BT not only a crucial component in understanding Himalayan tectonics, but its paleogeographic evolution is also of considerable interest for Asian biodiversity and paleoclimate studies, because it harbours important records of fossil amber biota (Grimaldi et al.,

2002; Liu et al., 2020a; Poinar, 2018; Rasnitsyn & Öhm-Kühnle, 2018; Zheng et al., 2018) and monsoonal history (Licht et al., 2014a).

Due to a lack of paleogeographic constraints, the BT was usually placed close to its present-day location (~20°N) throughout the India-Asia collision (Replumaz et al., 2013; Replumaz & Tapponnier, 2003; Royden et al., 2008; van Hinsbergen et al., 2019), with the notable exception of Rangin (2017) who suggested a very different plate configuration with the BT attached to India during the Paleogene. Subduction along the BT constituted an essential part of the Asian active margin in these traditional collision models, mainly because the Wuntho-Popa Arc (WPA) of the BT was usually seen as the eastward continuation of the Gangdese Arc on the Lhasa Terrane (Lin et al., 2019; Mitchell et al., 2012; Zhang et al., 2019a), while the Western Belt Ophiolite of the BT has been correlated with the Yarlung-Tsangpo Suture Zone (YTSZ; Liu et al., 2016; Mitchell, 1993). However, recent paleogeographic constraints from paleomagnetism, providing the first paleo-rotation and paleolatitude data from the BT, strongly question this proposed tectonic context. They yielded southern hemisphere to near-equatorial latitudes for the BT from the early Late Cretaceous (~95 Ma) up until the late Eocene (~40 Ma) with a major rotation of ~60° clockwise (CW) somewhere in between (Westerweel et al., 2019). This showed that the BT was initially thousands of kilometers away from the Asian margin, implying that it was rather part of an isolated near-equatorial Trans-Tethyan subduction system before it moved northward as part of the Indian Plate. These constraints inferred a two-stage India-Asia collision, where India first collided with this Trans-Tethyan Arc somewhere in the early Paleogene, after which they conjointly collided with Asia (Hall, 2012; Jagoutz et al., 2015; Westerweel et al., 2019; Zahirovic et al., 2016).

However, there are still significant unknowns in this new paleogeographic context, because it necessitates a fundamental revision of many aspects of the BT tectonic history. Most importantly, there is uncertainty regarding the chronology and locations of the collision of India with the Trans-Tethyan Arc, the coupling of the BT with the northward moving Indian Plate and the either separate or conjoint collision of the BT and (Greater) India with Sibumasu. The inferred timing and location of the (Greater) India – Sibumasu collision ranges from the Eocene at southern Sibumasu/Sundaland (Haproff et al., 2020; Sautter et al., 2019) to the late Oligocene – early Miocene at northern Sibumasu (Morley et al., 2020). A prolonged separation of the BT from Indochina would have important implications for determining the sourcing of the thick Cenozoic sedimentary basins characterizing the geology of the BT, as proposed major source regions include the Eastern Himalayan collision zone (Métivier et al., 1999; Robinson et al., 2014) and Sibumasu (Licht et al., 2013, 2019; Zhang et al., 2019b). A final significant unknown in the BT tectonic history is its origin, because contrasting Gondwanan, Cathaysian, intra-oceanic or composite origins have been

postulated (Licht et al., 2020; Metcalfe, 2013; Morley et al., 2020; Sevastjanova et al., 2016; Yao et al., 2017).

This study aims to resolve and reconcile these discrepancies regarding the tectonic history of the BT. To this end, we obtained new Campanian - Maastrichtian, latest Paleocene – middle Eocene, late Eocene, middle Oligocene and middle Miocene paleomagnetic data from the BT in addition to our previously published early Late Cretaceous and late Eocene data (Westerweel et al., 2019). This extensive dataset provides detailed constraints on the latitudinal motion of the BT. These constraints were then integrated into a complete plate tectonic model for the India-Asia collision, taking into account geodynamic, paleoenvironmental and sedimentary provenance data from the BT and eastern Himalayan orogen.

2. Geological setting

2.1. The Burma Terrane

2.1.1. Tectonic regime

The BT (Fig. 6.1) is the principal microplate at the eastern edge of the Himalayan orogen, constituting much of western and central Myanmar. Its Neogene tectonic regime is unique in this orogenic system, as it is controlled by hyper-oblique convergence between India and Indochina, resulting in a northward transcurrent motion of the BT. This northward motion was mostly accommodated by large-scale dextral strike-slip displacements along the Sagaing Fault that separates the BT from the Shan Plateau (Sibumasu) in the east. Dextral displacements along the Sagaing Fault have been estimated around 400 km since the Neogene by observations from structural geology (Maung, 1987; Maurin & Rangin, 2009; Morley, 2017b; Rangin et al., 2013; Socquet et al., 2006). Late Eocene paleomagnetic constraints from the BT show that it moved northward from a near-equatorial position with little rotation, suggesting that dextral displacement of the BT could have been over 2000 km since that time (Westerweel et al., 2019). The BT underwent contemporaneous pull-apart deformation (Licht et al., 2019; Rangin, 2018). The late Eocene paleomagnetic data further imply that there was virtually no relative motion between the BT and India throughout the Eocene - Oligocene, suggesting that strike-slip displacements were almost exclusively concentrated on the eastern margin of the BT (Westerweel et al., 2019), either along the Sagaing Fault, its precursor, or the India-Australia Transform (Morley et al., 2020; Morley & Arboit, 2019). By the late Oligocene – early Miocene, the BT entered the Eastern Himalayan collision zone, causing the dextral motion between the BT and Indochina to become more resisted. This decreased the relative motion of the BT with respect to India, leading to pronounced dextral strike-slip faulting (South Kabaw, Churachandpur Mao and Kaladan Faults) in the Indo-Burman Ranges (IBR) to the west

of the BT (Rangin, 2018; Rangin et al., 2013; Westerweel et al., 2020). This Neogene tectonic regime, characterized by dextral strike-slip faults east and west of the BT and ongoing indentation into the Eastern Himalayan Syntaxis to the north, has been named the Burma mobile belt (Rangin, 2018; Rangin et al., 2013).

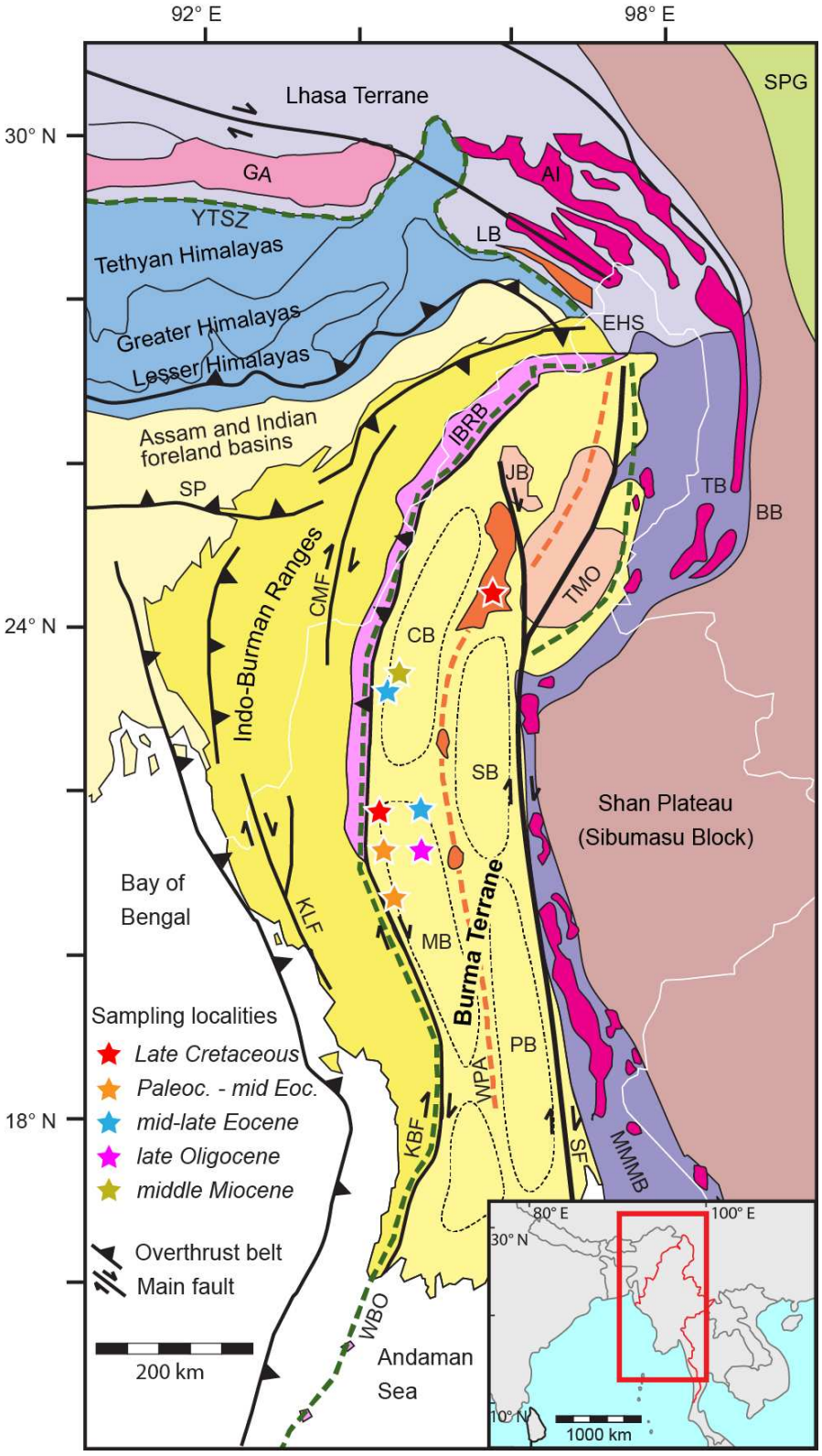

Figure 6.1: *a) Generalized Myanmar geological map showing sampling paleomagnetic sampling localities of this study and Westerweel et al. (2019). Abbreviations: AI = Cretaceous-Paleogene Asian intrusives, BB = Baoshan Block, CB = Chindwin Basin, CMF = Churachandpur Mao Fault, EHS = Eastern Himalayan Syntaxis, GA = Cretaceous Gangdese Arc, IBRB: Indo-Burman Ranges basement, JB = Jade Belt Ophiolite, KBF = Kabaw Fault, KLF = Kaladan Fault, LB = Lohit Batholith, MB = Minbu Basin, MMMB = Mogok–Mandalay–Mergui Belt, PB = Pegu Basin, SB = Shwebo Basin, SF = Sagaing Fault, SPG = Songpan Ganze & Yangtze complexes, Tengchong Block, TMO = Tagaung-Myitkyina Ophiolite, WBO = Cretaceous Western Belt Ophiolite, WPA = Wuntho-Popa Arc, YTSZ = Yarlung-Tsangpo Suture Zone. Dashed black lines: Central Myanmar Basins (after Westerweel et al., 2019).*

2.1.2. Burma Terrane basement

Further back in time, many aspects of the complicated geological history of the BT remain subject to debate. Exposures of the oldest known units of the BT are limited, but include the Triassic Pane Chaung Formation, Kanpetlet Schists and Shwedaung Formation. The first two crop out along the western margin of the BT in the IBR, while the latter is located in the northern WPA. The Pane Chaung and Shwedaung Formations have been tentatively correlated, based solely on their similar ages and turbiditic sedimentary facies (Mitchell, 2017; United Nations, 1978a). The Kanpetlet Schists likely represents the metamorphosed equivalent of the Pane Chaung Formation (Bannert et al., 2012; Maurin & Rangin, 2009; Morley et al., 2020; United Nations, 1978a), evidenced by similar U-Pb age distributions (Najman et al., 2020). Previously, the U-Pb age distributions of the Pane Chaung Formation were correlated to Sibumasu, suggesting that the BT was part of Indochina before the Mesozoic (Sevastjanova et al., 2016; Zhang et al., 2019a). More detailed results from recent studies show that the main age peaks and εHf(t) values from detrital zircons in the Pane Chaung Formation closely resemble the Langjiexue Formation of the NE Himalayan collision zone, suggesting that it was deposited adjacent to the Indian area of northern Gondwana (NW Australia) during the Triassic (Cai et al., 2016, 2019; Wang et al., 2016; Yao et al., 2017). This would suggest that the BT separated from Gondwana after the Triassic.

However, several studies have proposed that the Pane Chaung Formation and Kanpetlet Schists constitute a separate tectonic block named Mount Victoria Block, which was accreted to the BT in the Cretaceous or early Paleogene (Acharyya, 2007; Barber & Crow, 2009; Metcalfe, 2013; Rangin et al., 2013; Searle et al., 2017; Zhang et al., 2017a). The Aptian-Cenomanian Paung Chaung limestones of the BT contains clasts of the Kanpetlet Schists and Pane Chaung Block, and unconformably overlies them, indicating that the Mount Victoria Block should have been accreted to the BT by the mid-Cretaceous, if they were separated before at all (Mitchell, 2017; Morley et al., 2020).

In addition to Shwedaung Formation, Pane Chaung Formation and Kanpetlet Schists, there are descriptions of Permo-Triassic carbonates with a supposed Cathaysian affinity in the eastern BT (Barber & Crow, 2009; Oo et al., 2002; Ueno et al., 2016), which would suggest that at least part of the BT is Cathaysian in origin (Licht et al., 2020). However, the relationship of these carbonates with the BT remains equivocal (Metcalfe, 2017), because they are located in strands of the Sagaing Fault and could thus simply represent displaced slices of Sundaland where these Cathaysian affinities are present.

2.1.3. The Wuntho-Popa Arc

During the early Late Cretaceous, subduction initiated along the southern margin of the BT (the present-day western margin, after ~60° CW rotation; Westerweel et al., 2019), evidenced by similar timing of ophiolite formation and emplacement of the Naga Hills-Kaleymyo-Andaman Ophiolitic belt or simply Western Belt Ophiolite (Fareeduddin & Dilek, 2015; Htay et al., 2017; Liu et al., 2016; Singh et al., 2017; Zhang et al., 2017b). This led to volcanic activity along the WPA, with paleomagnetic data implying that this arc was a segment of a near-equatorial Trans-Tethyan Arc (Westerweel et al., 2019). The main phase of magmatic activity in the WPA was from 110-90 Ma, followed by a much less intense phase from 70-40 Ma, and finally only sporadic activity in the Neogene (Barley & Zaw, 2009; Gardiner et al., 2015, 2017; Licht et al., 2020; Lin et al., 2019; Mitchell et al., 2012; Wang et al., 2014; Zhang et al., 2017a). This magmatic history appears similar to other postulated Trans-Tethyan Arc segments, such as the intra-oceanic Kohistan Arc and Spontang Ophiolite in the Western Himalayas (Buckman et al., 2018; Jagoutz et al., 2019; Petterson, 2019), which could suggest a linkage (Licht et al., 2020).

A decrease in activity of the WPA since the Cenozoic is additionally evidenced seismic lines and drill cores along the WPA (Zhang et al., 2017a), which show that WPA batholiths are largely covered by Paleogene to Neogene sediments of the Central Myanmar Basins (CMB; Section 2.5). The Wuntho Ranges, the predominantly Mesozoic volcanic complex constituting a major segment of the WPA in the northern BT, is a likely exception to this. Overall, these observations suggest that the intensity of subduction of the Indian Plate beneath the Burmese margin decreased since the early Paleogene. The same seismic lines additionally show that the WPA underwent at least two phases of uplift during the late Eocene and late Oligocene – early Miocene (Zhang et al., 2017a).

2.2. The Indo-Burman Ranges

The IBR mainly consist of thick Mesozoic to Cenozoic flysch deposits and associated ophiolitic material that are displaced by multiple major dextral strike-slip faults (South Kabaw, Churachandpur Mao/Lelon and Kaladan Faults), together forming the western boundary of the BT with the Indian

continent. They initially developed in an accretionary prism setting related to subduction of the Tethyan and Indian oceanic lithosphere, and evolved into a fold-and-thrust belt by the late Eocene – early Oligocene after the onset of hyper-oblique convergence between India, the BT and Indochina (Bannert et al., 2012; Maurin & Rangin, 2009; Morley et al., 2020; Rangin, 2018; Rangin et al., 2013). Transpressional deformation has affected the IBR since the late Oligocene - early Miocene, as the western boundary of the Burma mobile belt (Rangin, 2018).

Traditionally, the IBR are divided into an Inner and Outer Wedge (Maurin & Rangin, 2009; United Nations, 1978a). The Outer Wedge consists of a fold and thrust belt deforming the Neogene clastic sediments of the Bengal fan with Himalayan affinity (Allen et al., 2008; Najman et al., 2020; Rangin, 2018). By contrast, the geology of the Inner Wedge is more complex, mainly because it comprises the Pane Chaung Formation and Kanpetlet Schists with a potentially separate history from the BT as part of the Mount Victoria Block (Section 2.1). Moreover, it contains the Western Belt Ophiolite, where there is uncertainty regarding the type of ophiolite, emplacement direction, and role as the potential suture of the BT with the Mount Victoria Block (Reviews in: Morley et al., 2020; Searle et al., 2017).

Geochronological data from the central IBR has constrained a major exhumation phase of the mountain range during the latest Oligocene – Miocene, and a possible precursory event in the late Eocene (Najman et al., 2020). This is in agreement by the late Eocene onset of molasse deposition in the IBR (Bannert et al., 2012; Ghose et al., 2014; Morley et al., 2020) and contemporaneous changes in sedimentary facies within the BT, interpreted as reflecting progressive emergence of the IBR (Licht et al., 2019). In the northern IBR (Naga Hills), an early Paleogene collision event has been postulated, recorded by the Eocene Phokphor conglomerate that is derived from the Western Belt Ophiolite but also exhibits age peaks identical to the older Pane Chaung Formation (Aitchison et al., 2019).

2.3. The Eastern Himalayan orogen

To the north and east of the BT and the Sagaing Fault, the Mogok-Mandalay-Mergui Belt (MMMB) and the Jade Belt or Central Belt Ophiolite form the complex transition of the BT with the Asian margin, particularly the Shan Plateau that represents the western edge of Sibumasu. The MMMB consist of high-grade metamorphics and Jurassic to Cretaceous S-type intrusives with generally negative εHf(t) values, although I-type intrusives similar to the WPA are occasionally present as well (Lohit and Sodon Batholiths; Lin et al., 2019).

Plate tectonic studies have shown that the majority of the MMMB, including the Tengchong and Baoshan blocks, was extruded from the Eastern Himalayan Syntaxis towards the southeast since approximately the late Paleogene (Li et al., 2018; Tong et al., 2013; Westerweel et al., 2019). The

MMMB records several important metamorphic events, starting with a latest Cretaceous to early Paleocene phase of metamorphism and partial melting. This was followed by a phase of high temperature metamorphism during the late Eocene – Oligocene, interpreted as reflecting the collision of India with the Asian margin (Searle et al., 2007, 2017, 2020). Finally, there was an Oligocene to early Miocene phase of rapid exhumation and uplift related to strike-slip deformation and extrusion of the MMMB (Bertrand et al., 2001; Bertrand & Rangin, 2003). The latter metamorphic event fits with the timing of south-eastward extrusion of the MMMB from the Eastern Himalayan Syntaxis inferred by plate tectonic studies, as well as a significant phase of uplift and exhumation across the Eastern Himalayan orogen in the early Miocene (Garzanti, 2019; Godin et al., 2006; Haproff et al., 2019; Kellett et al., 2013; Najman et al., 2019; Vannay et al., 2004).

The Jade Belt is exposed at the northern edge of the Sagaing Fault and has an unclear emplacement age (Searle et al., 2017; Yui et al., 2013). A correlation of the Jade Belt with sporadic dismembered ophiolitic fragments on the trace of the Sagaing Fault has been proposed, together forming the Central Belt Ophiolite (Htay et al., 2017). However, the fragmentary descriptions of these ophiolitic fragments, aforementioned age uncertainties and intense deformation along the Sagaing Fault make regional tectonic relationships difficult to determine.

2.4. The Andaman Sea

The Andaman Sea represents a complex and partitioned back-arc extensional basin, which developed mostly in the Neogene along the oblique convergent margin formed due to the northward motion of the Indian and Australian Plates towards Asia. The tectonic setting of the Andaman Sea is characterized by complex interplay of extensional and dextral strike-slip fault systems, resulting in an overall pull-apart structural style (Curray, 2005). The tectonic regimes of the BT and Andaman Sea are mainly connected by the (South) Sagaing Fault and Shan/Mergui Fault horsetail structures, splaying into the East Andaman Fault farther south, where it transitions into the Andaman spreading centre (Rangin, 2018).

In this context, the Eastern Andaman Basins, which include the Mergui and North Sumatra Basins, represent the rifted and sheared margin of Sundaland, developed in a back-arc setting (Morley, 2017a). The main transtensional development phase of these basins occurred in the late Oligocene – early Miocene with NNW-SSE oriented extension, although basin development initiated already in the late Eocene – early Oligocene (Srisuriyon & Morley, 2014). Basin development has been related to N-S extension caused by crustal scale detachment and exhumation following an enormous underthrusting event with India (Sautter et al., 2019), while others argue that extension was initially oriented E-W and there is no evidence for such an underthrusting event (Morley, 2017a). The latter

arguments led to models where the Indian Plate was separated from the Indochina margin by an India-Australia Transform until the late Oligocene – early Miocene (Morley et al., 2020).

The Western Andaman Sea is characterized by an accretionary prism and an ophiolitic belt comprising the Andaman-Nicobar ridge. The Andaman-Nicobar Ophiolites were likely developed in the latest Cretaceous to early Paleogene (Morley & Searle, 2017; Pedersen et al., 2010) following supra-subduction spreading (Curray, 2005; Ghosh et al., 2017), and subsequently emplaced as slices in an accretionary prism setting before the Eocene (Morley & Searle, 2017). This timing and manner of ophiolite formation are similar to the Western Belt Ophiolite that are located to the north along the same ~N-S trend (Morley & Searle, 2017; Sengupta et al., 1990), resulting in tectonic models where the Andaman-Nicobar Ophiolites are linked with the northward moving BT (Morley et al., 2020). Others have proposed instead that the Andaman-Nicobar Ophiolites represent partitioned remnants of oceanic lithosphere that were originally juxtaposed with the Sumatran Woyla Arc (Advokaat et al., 2018; Plunder et al., 2020).

2.5. Central Myanmar Basins

The WPA subdivides the BT into a series of basins in forearc and a back-arc position, which are collectively called the Central Myanmar Basins (CMB). The Burmese back-arc consists of the northern Shwebo Basin and the southern Pegu Basin. Throughout the Cenozoic, both basins were characterized by southward prograding fluviatile and tidal-influenced estuarian sequences, although the Paleogene deposits of the Pegu Basin remain poorly described (Bender, 1983; Khin, 1999; Pivnik et al., 1998; Thein & Maung, 2017). In the Quaternary, the Shwebo and Pegu Basins were unconformably overlain by the fluviatile Irrawaddy Formation, similar to the rest of the CMB (Bender, 1983).

The Burmese forearc is usually divided into the southern Minbu (or Salin) Basin and northern Chindwin Basin, separated by a topographic high called the Pondaung Ranges (Bender, 1983; Licht et al., 2019). Recent studies have shown a differing stratigraphic record between both forearc basins since the late Eocene, related to pull-apart deformation (Licht et al., 2019; Rangin, 2018; Westerweel et al., 2020). The sediments of the Burmese forearc were sampled for this study and hence their stratigraphy will be described below in more detail.

2.5.1. The Minbu Basin

The oldest sediments of the forearc sequence are the poorly exposed Paung Chaung limestones, which is Aptian-Cenomanian in age based on biostratigraphic constraints from orbitolinas, planktonic foraminiferas and ammonites (Mitchell, 2017). It contains clasts of the BT basement

(Pane Chaung Formation, Western Belt ophiolite and Kanpetlet Schist) and unconformably overlies these units. The Albian-Maastrichtian Kabaw Formation is the second Cretaceous unit of the Burmese forearc, consisting of marine limestones, mudstones and sandstones (Bender, 1983; Cai et al., 2019; Mitchell, 2017). A recent stratigraphic study on the Kabaw Formation yielded maximum depositional ages of ~82-70 Ma from detrital zircons in the Chindwin Basin and ~73-70 Ma in the Minbu Basin (Cai et al., 2019). Moreover, tuff layers overlying amber-bearing sediments of the Kabaw Formation near the village of Tillin have provided an age of 72.1±0.3 Ma (Zheng et al., 2018).

The Cretaceous sequence is unconformably overlain by a Paleocene to middle Eocene sedimentary sequence (Cai et al., 2019; United Nations, 1978a) that is comprised of four sedimentary formations, despite its relatively short age span. Unfortunately, these formations have poorly-defined stratigraphic boundaries and only sporadic geochronological constraints. The first formation within this sequence is the Paunggyi Formation (or Paunggyi conglomerates), which consists of turbiditic deposits including conglomerates, tuffs, volcaniclastics, sandstones, mudstones and limestones (Cai et al., 2019; United Nations, 1978a). The age of the Paunggyi Formation spans the entire Paleocene, based on foraminifera (United Nations, 1978a), ~65 Ma dated tuffs and ~70-62 Ma maximum depositional ages from detrital zircons (Cai et al., 2019). The Paunggyi Formation is followed by the Laungshe Formation, composed of marine mudstones and sandstones (Cai et al., 2019). This formation is poorly dated; foraminifera fossils yielded an lower to middle Eocene age at one locality north of the Kyauktu township, but occasional Paleocene components were suspected to be present elsewhere as well (Bender, 1983). The middle Eocene Tilin and Tabyin Formation have similar sedimentary facies as the Laungshe Formation (Bender, 1983), and there only one published geochronological constraint that yielded a maximum depositional age from detrital zircons of ~47 Ma (Cai et al., 2019). This age is close to the proposed ages for the Laungshe Formation. Because of their proximity to the IBR, this Cretaceous to middle Eocene sedimentary sequence is relatively more deformed than younger deposits. Locally, there is complex folding and numerous faults, although continuous sequences following the general ~N-S trend of the Burmese forearc occur as well (Fig. 6.S1; Pivnik et al., 1998). The sedimentary provenance of the Cretaceous to middle Eocene formations was interpreted to be derived from both volcanic arc and recycled uplifted sedimentary sources (Cai et al., 2019), indicated by U-Pb age distributions with ~100-60 Ma peaks and positive εHf(t) values similar to the WPA (Gardiner et al., 2015, 2017; Lin et al., 2019; Zhang et al., 2017a), as well as significant populations of pre-Cretaceous zircons with similar age spectra as the BT basement (Allen et al., 2008; Naing et al., 2014; Najman et al., 2020).

On top of the Cretaceous to middle Eocene units lies the upper Eocene Pondaung Formation, dated at ~40 Ma (Jaeger et al., 2019; Zaw et al., 2014; Licht, et al., 2014b; Licht et al., 2015). The Pondaung

Formation is composed of westward directed, fluvio-deltaic sediments with a continental upper member containing carbonate-bearing paleosols, stacked channels, fossil vertebrates, and freshwater gastropods. The upper Eocene Yaw Formation overlies the Pondaung Formation and consists of shallow-marine, fine-grained sediments containing nummulites. All subsequent formations, the lower Oligocene Shwezetaw, middle Oligocene Padaung and upper Oligocene Okhmintaung Formations, conformably overlie the Yaw Formation (Gough et al., 2020; Pivnik et al., 1998). They are comprised of fluvio-deltaic to increasingly marine deposits towards the south (Bender, 1983; Gough et al., 2020). These units are followed by the lower to middle Miocene fluvio-deltaic sediments of the Pyawbwe, Kyaukkok and Obogon Formations. Finally, the middle Miocene - Pliocene Irrawaddy Formation unconformably covers the sequence in most of the CMB lowlands.

2.5.2. The Chindwin Basin

The sedimentary sequence of the Chindwin Basin is similar to the Minbu Basin up until the upper Eocene Yaw Formation, which is shallow-marine in the Minbu Basin, but is characterized by shallow marine to estuarian/fluvio-deltaic sediments in the Chindwin Basin (Licht et al., 2019).

The Yaw Formation is overlain by the exclusively fluviatile deposits of the upper Oligocene Tonhe Formation and lower Miocene Letkat Formation (Bender, 1983; Licht et al., 2019; Westerweel et al., 2020). In contrast to continuous deposition in the Minbu Basin, the late Eocene to early Miocene of the Chindwin Basin is characterized by large depositional hiatuses, which are contemporaneous with basin-wide unconformities. These were linked to major uplift and exhumation phases in the northernmost BT, which eventually entered the Eastern Himalayan collision zone during the late Oligocene – early Miocene (Westerweel et al., 2020).

On top of the Letkat Formation, the thick Natma and Shwethamin Formations consist of afossiliferous fluviatile sandstones interlayered with abundant paleosols (Bender, 1983; United Nations, 1978a). These formations should be of middle Miocene age, younger than the Letkat Formation, which has yielded 17 Ma maximum depositional ages, and older than the overlying Mingin Gravels, which has yielded 14-11 Ma fossil mammals (Tetralophodon cf. Falconeri, Bunolophodon cf pandionis, Bunolophodon angust. palaeoindicus, Listriodon pentapotamiae) coeval to the Chinji fauna of Pakistan (Bender, 1983). Similar to the Minbu Basin, the Irrawaddy Formation covers the Chindwin Basin sedimentary sequence.

3. Methods

3.1. Paleomagnetic sampling

Conventional paleomagnetic core plug samples were obtained from several Cenozoic localities with differing lithologies across the Burmese forearc in western Myanmar, in both the Minbu and Chindwin Basins (Figs. 6.1 and 6.2, Table 6.1, Table 6.S1). Sampling and orientation of the samples were done using standard paleomagnetic field equipment and procedures with both magnetic and sun compasses.

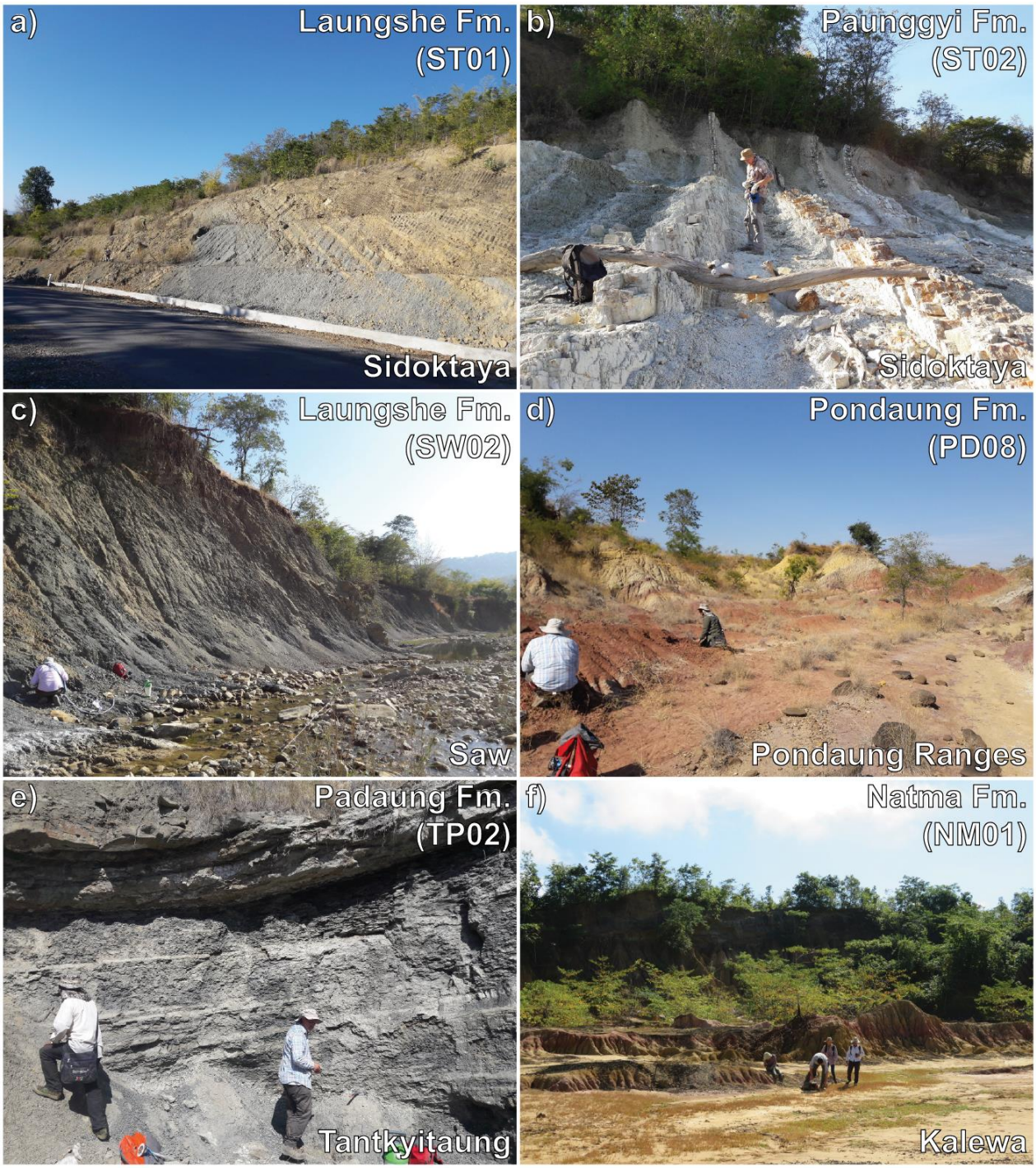

Figure 6.2: *Representative outcrops and lithologies from this study. Site name, lithology and locality are indicated per image.*

3.1.1. The Minbu Basin

The first two sites from this study were located around the Sidoktaya Township (ST), in the south-western Minbu Basin in proximity to the IBR. Local faulting is present in this area due to this proximity to the IBR (Fig. 6.S1). Site ST01 is a ~65 m thick section comprised of sandstones and mudstones of the uppermost Paleocene to late lower Eocene Laungshe Formation, exposed in a recent ~200 m long roadcut to the south-east of Sidoktaya. The sedimentary bedding is largely continuous, following the general ~N-S trend and eastward dip of the basin with no deformation, and the section is not overturned based on observations from sedimentary structures such as cross-bedding. However, small-scale thrusts are present at the bottom of the section. Site ST01 yielded 53 samples from grey-brown to blue-grey mudstones mudstones (Fig. 6.2a). Eleven samples were drilled at site ST02 in grey and white tuffs of the Paunggyi Formation, near the dam north of Sidoktaya (Fig. 6.2b). In contrast to ST01, the bedding of this site is not parallel to the general trend of the basin, and it is internally deformed with local folding and faulting.

In addition, six sites were obtained around the Saw Township (SW) farther to the north in the Minbu Basin. Similarly to the Sidoktaya sites, local faulting is present here due to proximity to the IBR (Fig. 6.S1). All sampled lithologies here consist of fresh grey mudstones and siltstones. Two of these sites (SW02 and SW04) are from the Laungshe Formation, similar to site ST01. SW02 is a long continuous type section of the Laungshe Formation, which yielded 31 samples (Fig. 6.2c). It follows the general ~N-S trend of the and eastward dip of the Minbu Basin, although there are occasional small-scale faults and slumps that were avoided during sampling. SW04 is a smaller site of 10 samples. It does not follow the general basin trend and is located on the strike of a major strike-slip fault (Fig. 6.S1). Two other sites near Saw are from the Tilin Formation (SW03 and SW07). SW03 is located on the same strike-slip fault as SW04, and provided 8 samples. By contrast, site SW07 again follows the general ~N-S trend of the basin with a steep eastward dip and yielded 14 samples. Site SW08, comprised of 16 samples, was obtained in the younger Tabyin Formation. It also follows the general ~N-S trend of the basin, but here local deformation is absent likely due to the larger distance from the IBR.

The final 20 samples near the Saw Township were acquired in site SW09, which is the only site obtained in the uppermost Cretaceous Kabaw Formation that is exposed farther north near the town of Tilin close to the Kabaw Fault. Amber mines proximal to Tilin have yielded geochronological constraints from dated tuff layers that provided Campanian - Maastrichtian ages for the Kabaw

Formation in this area (Zheng et al., 2018), in agreement with maximum depositional ages from Cai et al. (2019). Site SW09 is thus of probable Campanian – Maastrichtian age, although it should be noted that the exact coordinates of these Tilin amber mines are not published.

Our samples from the upper Eocene Pondaung Formation (PD) were collected in nine sites with variable bedding around the townships of Bahin and Pangan. These are part of the Pondaung Ranges, an anticlinal topographic high at the northern edge of the Minbu Basin that separates it from the Chindwin Basin. The 89 samples from these nine sites consisted of fine-grained red to brown and purple paleosols (Fig. 6.2d).

The final locality of the Minbu Basin is the ~N-S trending rollover anticline of the Yenangyat-Chauk thrust (Pivnik et al., 1998) at the Tantkyitaung Pagoda, west of Bagan (Fig. 6.S1). Here we sampled three sites (TP) in the middle Oligocene Padaung Formation, two on the western limb of the anticline near the fold axis (TP01 and TP02) and the third on the eastern limb (TP03). The grey to beige fine-grained sandstones and siltstones of these sites yielded 31 samples (Fig. 6.2e).

3.1.2. The Chindwin Basin

In the Chindwin Basin, we sampled 27 sites in the middle Miocene Natma Formation (NM), which were located in small valleys around the road north of the Kalewa Township in the western Chindwin Basin. In this area, the Natma Formation is part of a large scale monoclinal sedimentary section with a ~N-S trend and ~35° eastward dip, containing the majority of the Cretaceous to Quaternary sedimentary succession of the Chindwin Basin. The 27 sites provided 219 samples in fine-grained red to brown and purple paleosols (Fig. 6.2f).

3.2. Paleomagnetic analysis

Natural remanent Magnetizations (NRMs) from the collected samples were measured on a 2G cryogenic magnetometer hosted in a magnetically shielded room at Geosciences Rennes. Stepwise thermal demagnetization with increments of 20-50 °C up to 680 °C, and 3-axis alternating field (AF) demagnetization with increments of 2.5-10 mT up to 120 mT were used to isolate the characteristic remanent magnetization (ChRM) of each sample. During AF demagnetization, gyroremanent magnetizations (GRMs) were cancelled by measuring their NRM after each axis of AF demagnetization (x,y,z) (Roperch & Taylor, 1986). Subsequently, the demagnetizations of individual samples were displayed on orthogonal demagnetization plots (Zijderveld, 1967), and the ChRM directions of interpretable samples were obtained using principal component analysis (Kirschvink, 1980), and, if necessary, a great-circle approach (McFadden & McElhinny, 1988). Samples with well-determined ChRM directions from the same locality and age were grouped, after which mean

directions and corresponding statistical parameters could be calculated (Butler, 1992; Fisher, 1953). If applicable, we used the fold test to determine whether the magnetization acquired before or after tilting (Tauxe & Watson, 1994), and the reversal test to verify if normal and reverse polarities from a locality were antiparallel (Tauxe, 2010).

The paleomagnetic records of sedimentary packages are prone to inclination shallowing due to compaction, although previous paleomagnetic research of the Burmese forearc sediments showed that the effect of shallowing in these usually fine-grained sediments was negligible (Westerweel et al., 2019). We determined the effect of inclination shallowing with the following generalized formula:

$$\tan(I_1) = 0.6 \tan(I_0)$$

where I_1 is the measured inclination, I_0 is the unflattened inclination (King, 1955; Tauxe & Kent, 1984).

To better constrain the origin of magnetization, we investigated the magnetic properties of our samples using several methods. Before demagnetization, the anisotropy of magnetic susceptibility (AMS) of each sample was measured on a KLY3S AGICO kappabridge to acquire the magnetic fabric in every locality. In compressive regimes, the maximum axis K_{max} of the AMS tensor will gradually be aligned perpendicular to the direction of maximum compression (Hrouda, 1982). After each thermal demagnetization step, the bulk magnetic susceptibility of each sample was measured to monitor chemical changes during heating. Furthermore, magnetic hysteresis loops on an alternating gradient magnetometer (AGM 2900) were obtained for various samples from different localities and lithologies. Finally, acquisition of isothermal remanent magnetization (IRM) was done up until 2400 mT for selected samples to constrain differences in mineralogy. For several samples, the acquired IRM was then thermally demagnetized with increments of 20-50 °C up to 680 °C to further characterize the present magnetic components.

3.3. Plate model

For our plate tectonic reconstructions, we improved the earlier GPlates model (Müller et al., 2018) from the predecessor of this study (Westerweel et al., 2019), which only contained two reconstructions for the early Late Cretaceous and late Eocene. This model used the global rotations, continental polygons and combined hotspot (0-70 Ma) and paleomagnetic (70-250 Ma) reference frame from the Matthews 2016 GPlates model as a template (Matthews et al., 2016). Here we present a continuous 95-23 Ma reconstruction of the India-Asia collision, using our new paleomagnetic constraints on the BT as well as regional tectonic data (e.g. Bouilhol et al., 2013; Hall,

2012; Jagoutz et al., 2015; Mitchell, 2017; Morley et al., 2020; Rangin, 2018). Furthermore, we included deforming plate margins (Müller et al., 2019) for the BT, Bay of Bengal and Greater India, in addition to their rigid templates to better visualize the regional tectonic evolution. The final GPlates input is provided in the Supplementary Information.

4. Results

4.1. Rock magnetism

The bulk magnetic susceptibility provides first-order information about the basic magnetic properties of the sediments sampled during this study, especially when compared with values observed in the magmatic rocks of the Wuntho Ranges (Westerweel et al., 2019) as well as those of the Yaw and Letkat sediments from the Chindwin basin (Westerweel et al., 2020). Most sediments from the CMB exhibit bulk magnetic susceptibility values of around 10-3 up to 10-5 SI, which is on average two orders of magnitude lower than the observed values of around 10-1 to 10-2 SI in the Wuntho Ranges magmatic rocks (See Chapter 7 for further comparison). This indicates an overall low concentration of detrital magnetite in the CMB sediments, with the notable exceptions of the Letkat Formation with a significant amount of detrital magnetite (Westerweel et al., 2020) and some red paleosols of the Pondaung Formation. Hysteresis plots show that there are large presences of paramagnetic components in most sampled lithologies, which would also suggest overall low concentrations of detrital magnetite (Fig. 6.3c). The low concentrations of detrital magnetite could be related to initial low magnetite content of the source lithologies or intense chemical weathering of the sedimentary source, potentially enhanced by sediment reworking or prolonged sediment transport (Roberts, 2015).

Despite its low concentration, IRM acquisition (Fig. 6.3a) shows that magnetite is the main magnetic carrier in the majority of samples. This is further supported by thermal demagnetizations of IRM up to 580 °C (Fig. 6.3b). In the paleosol lithologies of the Pondaung (PD) and Natma (NM) Formations, many samples are not yet fully saturated at 2300 mT, suggesting that high coercivity phases such as hematite play an important role alongside magnetite. This is further illustrated by the fact that the most stable samples from these localities have demagnetizations up to 680 °C (Figs. 6.3b). Layers with relatively higher bulk magnetic susceptibilities of up to 0.003 SI in the Pondaung Formation likely represent relatively higher magnetite content. Natma Formation samples have overall lower bulk magnetic susceptibilities despite their similar lithology to the Pondaung Formation, which could represent differences in sedimentary sourcing. Chemical alteration played an important role in both the Pondaung and Natma Formations, oxidizing magnetite and destroying the primary paleomagnetic record in many of the pedogenized lithologies. This resulted in a reduced proportion

of selected samples to determine mean directions (Table 1). Fortunately, sufficient samples still preserve a primary paleomagnetic record, evidenced by well-defined normal and reverse magnetozones with similar demagnetizations and no outliers (Section 4.2). The influence of chemical alteration on the paleomagnetic record of the Kabaw, Laungshe, Tilin, Tabyin and Padaung (ST, SW, TP) mudstones and siltstones was much less significant, demonstrated by stable demagnetizations and excellent grouping of ChRM directions (Table 1; Section 4.2). Yet, overprint of the present-day field is present in these localities as well, especially in coarser grained sandstones and siltstones and exposures affected by recent weathering. Recent weathering occasionally results in an increase in NRM intensity, but no clear evidence was found for major changes in magnetic properties when applying high fields.

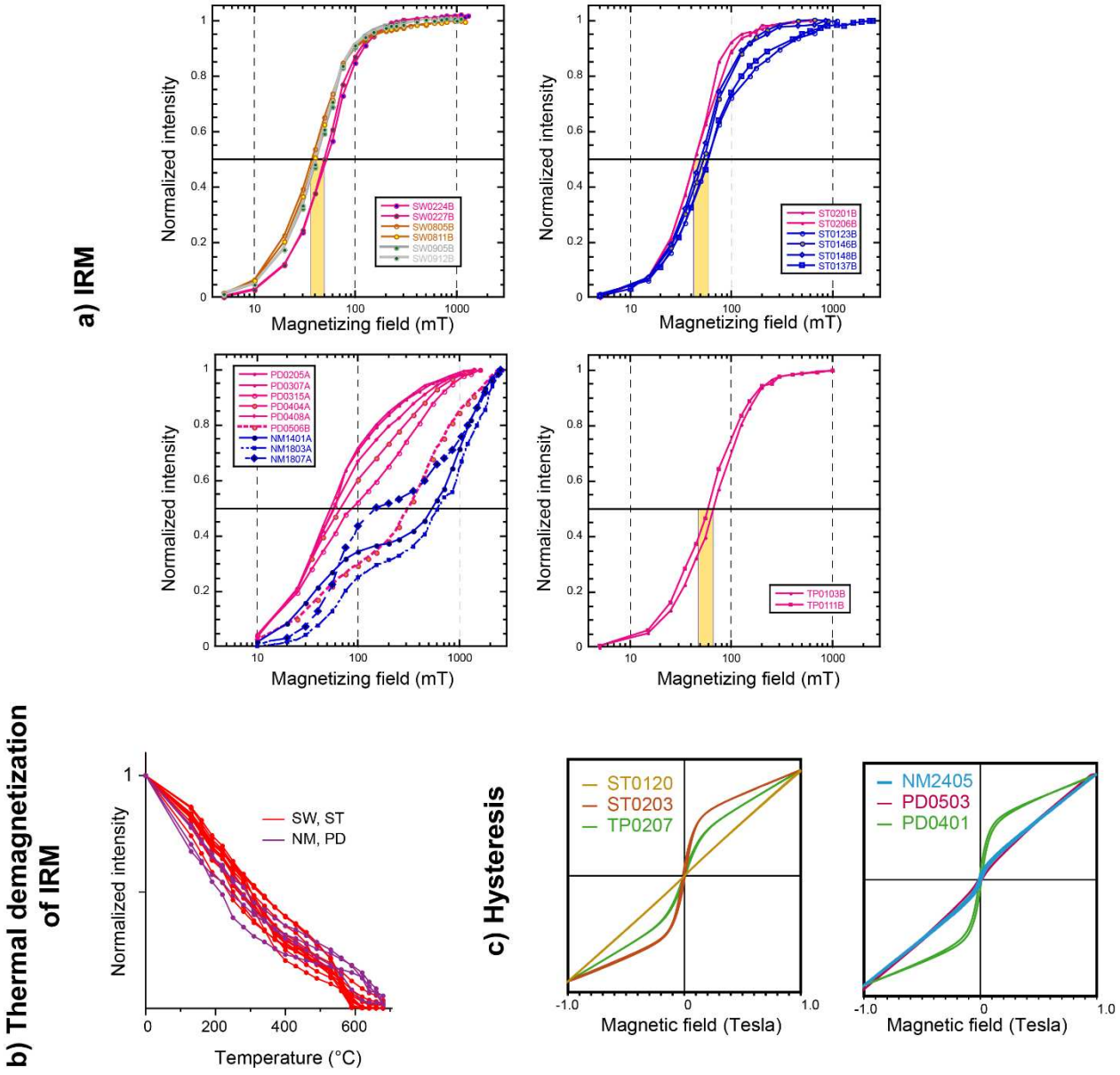

Figure 6.3: *a) Plots of Isothermal Remanent Magnetization (IRM); b) Thermal demagnetization of IRM up until 680 °C. Hematite-bearing samples from the Pondaung (PD) and Natma (NM) Formations are coloured in purple; c) Hysteresis loops from representative samples across all localities.*

In all localities from this study, the AMS results are typical for sediments (Fig. 6.4). They exhibit oblate magnetic fabrics with the minimum axis K_{min} oriented orthogonal to the bedding despite the degree of anisotropy (P') being generally low, especially in localities PD and NM mainly comprised of fine-grained paleosols with both hematite and magnetite as magnetic carriers (Fig. 6.4b,d). The highest degree of anisotropy values (P') are found in site SW08 from the Tabyin Formation (Fig. 6.4a), comprised of fresh grey mudstones and siltstones with excellent quality ChRM directions (Section 4.2.2; Fig. 6.5). Because of the typically sedimentary magnetic fabrics, all AMS tensors from this study are likely controlled by sedimentary processes and compaction. Moreover, the maximum axis K_{max} is parallel to the main trend of the fold axis within the sampling region, in agreement with a slight tectonic imprint typical for tilted sedimentary sequences in orogenic belts (Borradaile & Henry, 1997).

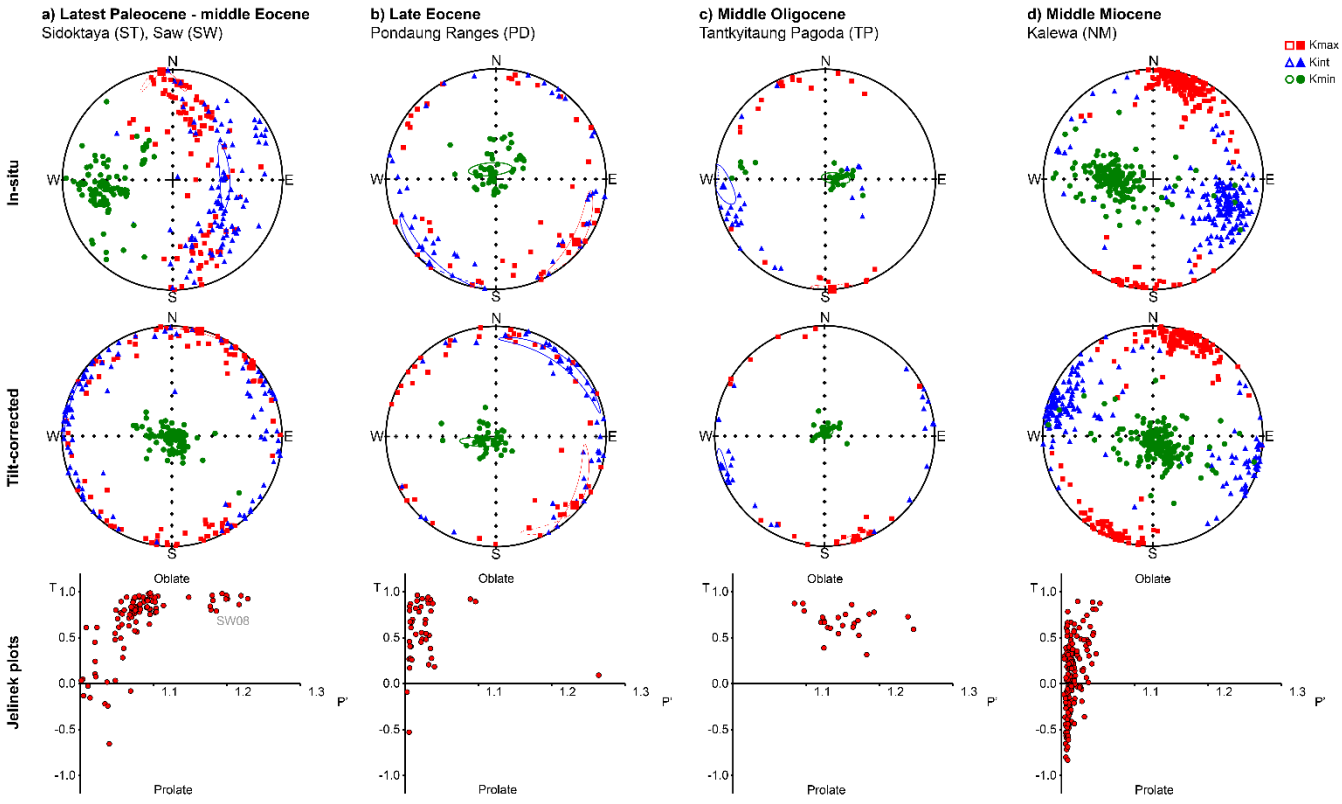

Figure 6.4: *Equal-area plots of the anisotropy of magnetic susceptibility (AMS) of all samples in in-situ and after bedding correction, as well as Jelinek plots of the shape (T) of the anisotropy ellipsoid versus the corrected degree of anisotropy (P') sorted per locality and age.*

Finally, severe alteration of the magnetic properties due to deep burial is rejected particularly for the results from the Kabaw Formation (SW09) due to the abundance of preserved pristine amber in the nearby Kabaw Formation amber mine locality (Zheng et al., 2018). Despite the important thickness of the sedimentary sequence, there is no observed evidence for reset of apatite fission track ages in the late Eocene Yaw formation of the Chindwin Basin (Westerweel et al., 2020) and only partial reset is observed in AFT data from older units of the Chindwin Basin (Ed Sobel, personal communication). This is all in agreement with the low temperature gradient measured in boreholes from oil companies (Racey, 2018). In general, the magnetic properties across our sampled lithologies seem to be affected by a degree of alteration usually increasing with grain size, but they retain a primary or early diagenetic magnetic signal.

4.2. Paleomagnetic results

4.2.1. Campanian - Maastrichtian (Saw)

From the 20 mudstone samples obtained in site SW09 from the Kabaw Formation, 17 samples yielded stable demagnetizations up to 430°C with magnetite as most likely carrier (Fig. 6.5e; Section 4.1). The bedding follows the overall N-S trend of the Minbu Basin with no evidence for overturning. Using this bedding correction, the SW09 mean direction becomes declination (D) = 149.7° / inclination (I) = 17.9°, α95 = 8.3° (Fig. 6.6; Table 6.1).

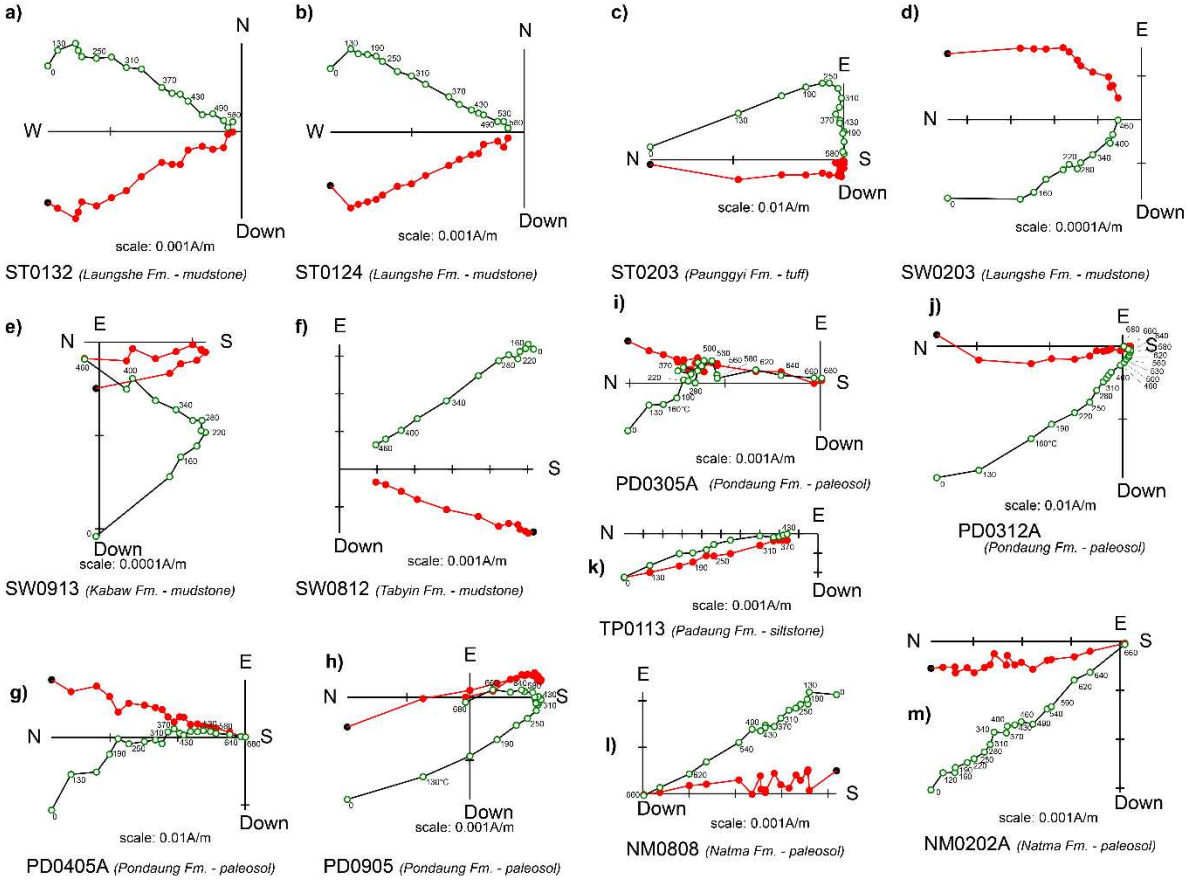

Figure 6.5: *Representative orthogonal demagnetization plots from the different localities in this study.*

4.2.2. Late Paleocene to middle Eocene (Sidoktaya and Saw)

South-east of the Sidoktaya Township, we obtained 26 blue-grey mudstone samples of good quality in the Laungshe Formation along the roadcut section of site ST01. The thickness of the section with paleomagnetic results is about 50 m. The stable samples are characterized by demagnetizations up to 580 °C (Fig. 6.5a,b; Section 4.1), providing a excellently grouped mean direction of D = 253.6° / I = 35.0°, α95 = 4.3° after bedding correction (Fig. 6.6; fig. 6.S2; Table 6.1). The age of the Laungshe Formation should be latest Paleocene to late early Eocene (Bender, 1983). As the Earth's magnetic field was almost exclusively reversed during this time period, the ST01 mean direction is likely reversed as well and the ST01 mean inclination is hence negative.

The 9 results from site ST02, sampled in the grey and white tuffs of the Paunggyi Formation, present a larger overprint and more scatter at the site level than ST01 (Fig. 6.5a-c; Fig. 6.6). Individual ChRMs evidence stable reverse directions up to 580° C, after removal of an overprint in the present-day field (Fig. 6.5c).). The difference between the mean directions at site ST02 and site ST01 suggest there was a component of local rotation. Indeed, the layers of ST02 are folded and the overall bedding is rotated ~45° counter-clockwise (CCW) with respect to the general ~N-S trend of the Minbu Basin, in contrast to the ST01 section that is parallel to this trend. The mean inclination of ST02 is I = -5.2° / α95 = 11.1°.

The other early Paleogene sites from the Saw Township (SW) provide stable ChRMs up to 460°C far from the present-day field direction, although with generally more scatter compared to site ST01 (Fig. 6.6; fig. 6.S2; Table 6.1). Site SW02 is the largest of these sites, sampled along a ~200 m long continuous Laungshe Formation section with occasional deformation. Deformation is not visible in the AMS results (Fig. 6.4), but the magnetic fabric may be controlled by compaction. The majority of samples in site SW02 are of normal polarity, suggesting a latest early Eocene age where normal polarity chrons become more common. Fourteen reliable samples with stable demagnetizations and coherent ChRM directions away from the present-day field (Fig. 6.5d) yield a mean direction of D = 55.0° / I = 3.1° / α95 = 10.7° after bedding correction, which is similar to ST01 albeit with a near-zero positive inclination.

Site SW07 in the Tilin Formation gives reliable results from 8 samples, providing a mean direction of D = 25.1° / I = -21.7° / α95 = 7.8° after tilt correction. Similar to sites ST01 and SW02, the declination is directed eastward, but it is of a lower magnitude. The SW07 negative mean inclination is placed in between the two other sites. Sites SW03 (Tilin Formation, 7 samples) and SW04 (Laungshe

Formation, 8 samples) exhibited mean directions of respectively D = 179.7° / I = 18.8° / α95 = 12.1° and D = 0.7° / I = -0.4° / α95 = 11.8°, again showing near-zero to negative mean inclinations. However, their mean declinations show negligible rotations compared to the other sites. As they were both obtained along a major fault (Fig. 6.S1), the SW03 and SW04 mean directions may be affected by local rotations. The last site of the early Paleogene sequence is site SW08 in the Tabyin Formation, the youngest formation in this sequence with a middle Eocene age. All 16 samples in this site provided excellently stable ChRMs of reverse polarity (Fig. 6.5f), resulting in a well-determined mean direction of D = 201.7° / I = 0.7° / α95 = 4.9°.

4.2.3. Late Eocene (Pondaung Ranges)

Chemical weathering played an important role in the Pondaung Formation and the normal overprint was not ways fully removed in many samples, neither by thermal (Fig. 6.5j) or AF demagnetization. From the 9 sites in the upper Eocene Pondaung Formation (PD), 29 samples yielded reliable results carried by both magnetite and hematite (Section 4.1). These samples exhibit stable demagnetizations up to 680 °C of both normal and reverse polarity (Fig. 6.5g,h,i). These normal and reversed polarities were identified stratigraphically at different locations and not within the same beds. This observation indicates that the obtained ChRMs at high temperatures were acquired during sedimentation or early diagenesis in the paleosols. This clearly demonstrates that previous magnetostratigraphic results in the Pondaung Formation of only normal polarity (Benammi et al., 2002) are the consequence of poorly identified normal overprint with wide unblocking temperatures. Therefore, the close to present-day paleolatitude of Benammi et al. (2002) is not correct.

Our new mean direction for the Pondaung Formation, with D = 10.0°/ I = 3.7° / α95 = 6.1° after bedding correction, is analogous to preceding published results from the upper Eocene Yaw Formation in the Chindwin Basin (Fig. 6.6; Table 6.1; Westerweel et al., 2019). As the sampled sites of the Pondaung and Yaw Formations were dated at ~40 and ~38 Ma respectively (Section 2.5), we combined both mean directions. This yielded D = 11.8° / I = 5.0° / α95 = 2.6° (Table 1), corresponding to a near-equatorial paleolatitude of 2.5±1.3°N and a negligible CW rotation of 3.0±4.4° compared to stable Eurasia (Torsvik et al., 2012), which indistinguishable from the findings of (Westerweel et al., 2019). Moreover, inclination shallowing has little effect on low inclinations (King, 1955; Tauxe & Kent, 1984), as our combined late Eocene mean direction provides an unflattened I of 8.3° (α95 = 4.3°), corresponding to paleolatitude of 4.2±2.2°N.

Name	Locality	Formation	Lithology	Sites	N/n	In-situ (IS)				Tectonic (TC)			
						D	I	α95	k	D	I	α95	k
Late Cretaceous													
MY*	Wuntho Ranges	Wuntho volcanic complex	intrusives, extrusives, volcaniclastics, clastics	16	151/194	69.2	-9.8	10.1	14.2	-	-	-	-
SW09	Saw Township	Kabaw Formation	mudstones, siltstones	1	17/20	185	40.1	8.3	19.3	149.7	17.9	8.3	19.3
late Paleocene - early Eocene													
ST01	Sidoktaya Township	Laungshe Formation	mudstones, siltstones	1	26/53	253.7	-23.0	4.3	44.2	253.6	35.0	4.3	44.2
ST02	Sidoktaya Township	Paunggyi Formation	tuffs	1	9/11	164.8	-66.4	11.6	20.6	190.3	3.2	11.6	20.6
SW02	Saw Township	Laungshe Formation	mudstones, siltstones	1	14/31	37.3	36.6	10.7	14.7	55	3.1	10.7	14.7
SW03	Saw Township	Tilin Formation	mudstones, sandstones	1	7/8	200.1	43.0	12.1	25.9	179.7	18.8	12.1	25.9
SW04	Saw Township	Laung She Formation	mudstones	1	8/10	3.6	-10.9	11.8	22.9	0.7	-0.4	11.8	22.9
SW07	Saw Township	Tilin Formation	mudstones, siltstones	1	8/14	29.2	15.2	7.8	51.4	25.1	-21.7	7.8	51.4
SW08	Saw Township	Tabyin Formation	mudstones, siltstones	1	16/16	193.8	-23.2	4.9	57.8	201.7	0.7	4.9	57.8
ST01, SW02, SW07	Burmese forearc	Laungshe & Tilin Fms.	mudstones, siltstones	3	49/49	-	-	-	-	-	-21.4	7.0	-
late Eocene													
PD	Pondaung Ranges	Pondaung Formation	paleosols	9	29/89	190.1	5.0	5.9	21.9	10.0	3.7	6.1	20.3
MA-MD*	Kalewa Township	Yaw Formation	mudstones, siltstones, sandstones, siderites	6	168/520	8.9	5.1	2.9	15.1	12.4	4.9	2.9	15.2
MA-MD, PD	Burmese forearc	Pondaung & Yaw Fms.	mudstones, siltstones, sandstones, siderites, paleosols	15	196/197	8.8	3.7	2.6	15.9	11.8	5.0	2.6	16.3
late Oligocene													
TP	Tantkyitaung Pagoda	Padaung Formation	mudstones, siltstones, sandstones	3	29/31	355.3	14.6	4.0	46.4	357.7	6.2	5.9	21.3
middle Miocene													
NM	Kalewa Township	Natma Formation	paleosols	27	98/219	357.5	19.9	4.8	9.7	12.3	25.0	4.9	9.3

* Previously published in Westerweel et al. (2019)

Table 6.1: *Paleomagnetic mean directions from this study and Westerweel et al. (2019), with the latter indicated with an asterisk (*). Combined mean directions are also shown. The results are displayed in both in-situ (IS) and tectonic corrected (TC) coordinates (Applied bedding corrections and site coordinates are listed in Supplementary Table 1). Notes: N/n = number of samples used for mean direction/total samples; D = mean declination; I = mean inclination; α95 = Fisher cone of 95% confidence; k = dispersion parameter.*

4.2.4. Middle Oligocene (Tantkyitaung Pagoda)

From the middle Oligocene Padaung Formation exposed within the large Tantkyitaung Pagoda anticline (TP), 30 fine-grained siltstone samples were progressively demagnetized thermally or by AF, providing univectorial demagnetizations (Fig. 6.5k). Bulk magnetic susceptibilities of on average ~0.0006SI but up to ~0.002 SI indicate that these fine-grained mudstone contain a degree of detrital magnetite. The NRM is similarly high with a mean value of around 8 mAm-1. Medium demagnetization temperatures are within the range ~200-250°C, but demagnetization plots do not permit to clearly separate two magnetization components. ChRMs were determined in the high coercivity range or above 200°C with vectors anchored to the origin. The mean directions in in situ coordinates are different from the dipole field and with lower inclination than the present-day field. After bedding correction, all three sampled sites exhibit low inclinations. Unfortunately, the tilt-corrected mean declinations are different between the three sites providing a negative fold test. Sites TP01 and TP02 from western limb of the anticline near the fold axis yield a mean declination of ~350°, while the declination of the ChRM at site TP03 on the eastern limb is ~25° (Fig. 6.6).

As the Tantkyitaung Pagoda anticline was formed due to a large thrust fault to its east (Fig. 6.S1), we suspect that these differing declinations are the result of local deformation. This interpretation is supported by the observation of a similar relative difference between the AMS lineations of site TP01 and TP02 from the western limb and TP03 from the eastern limb. Therefore, only the near-zero mean inclination I = 5.7° (α95 = 5.8°) may be useable. It provides a paleolatitude of 2.9±2.9°N, which becomes 4.7±4.7°N after correcting for inclination shallowing, confirming that the Eocene low latitudes persisted in the Oligocene. However, this result needs to be confirmed by further studies with more sites and a better fold test.

Figure 6.6: *Equal-area projections of interpretable paleomagnetic results from this study and Westerweel et al. (2019) before and after tilt correction. The site (Early Late Cretaceous and latest Paleocene – middle Eocene) and sample (other localities) results and corresponding mean directions (coloured circles) are sorted by age. Expected directions from stable Eurasia (coloured triangles) are indicated as well (Torsvik et al., 2012).*

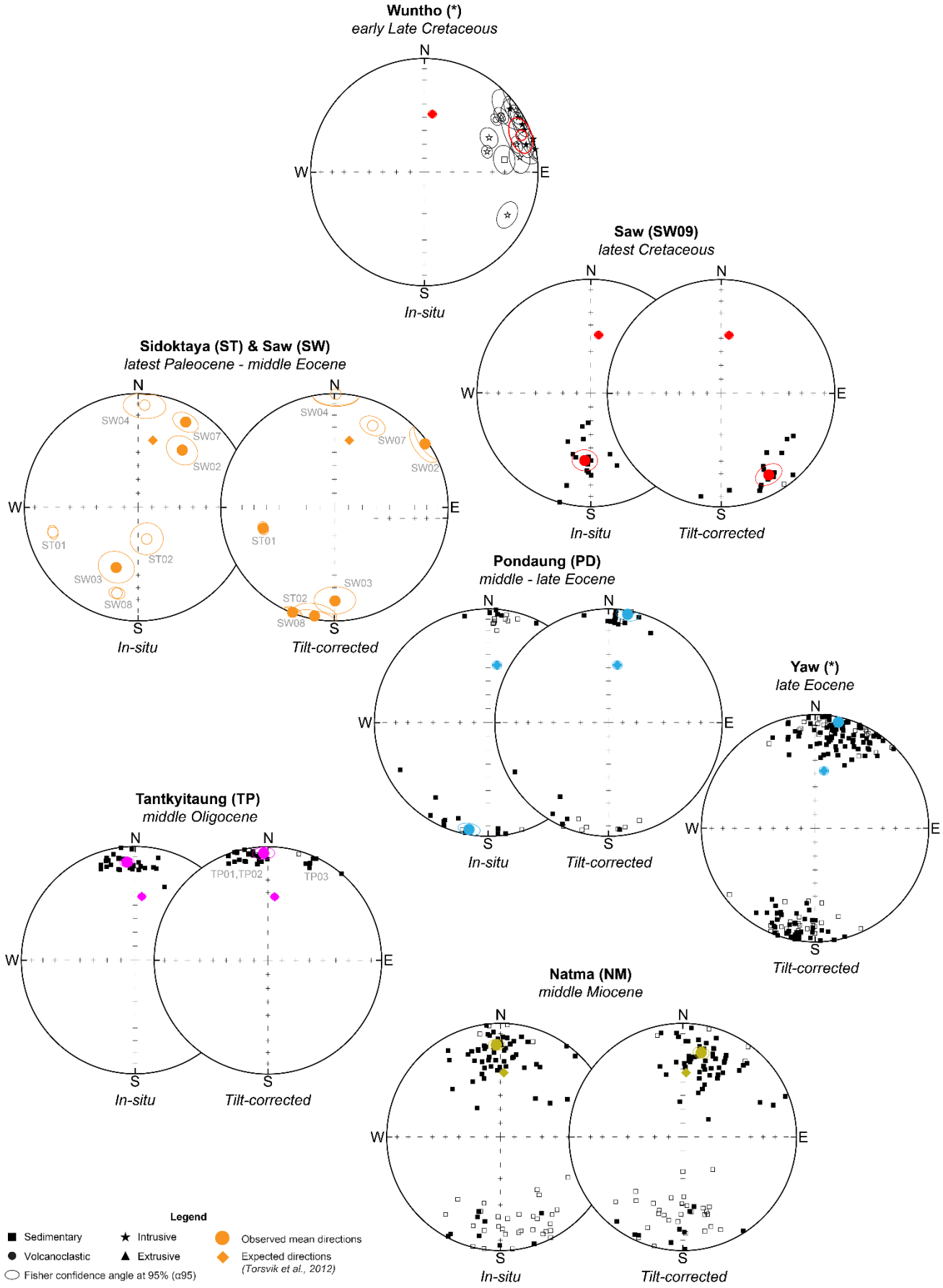
Wuntho (*)
early Late Cretaceous
N
W
E
S
In-situ
Saw (SW09)
latest Cretaceous
In-situ
Tilt-corrected
Sidoktaya (ST) & Saw (SW)
latest Paleocene - middle Eocene
SW04
SW07
SW02
ST01
ST02
SW03
SW08
In-situ
Tilt-corrected
Pondaung (PD)
middle - late Eocene
Yaw (*)
late Eocene
Tantkyitaung (TP)
middle Oligocene
TP01,TP02
TP03
Natma (NM)
middle Miocene
Legend
Sedimentary
Volcanoclastic
Fisher confidence angle at 95% (α95)
Intrusive
Extrusive
Observed mean directions
Expected directions
(Torsvik et al., 2012)

4.2.5. Middle Miocene (Kalewa)

In the 27 sites of the middle Miocene Natma Formation, 98 samples with stable demagnetizations up to 680 °C of both normal and reverse polarity were obtained, with remanence carried by both magnetite and hematite (Fig. 6.5l,m; Section 4.1). Normal and reverse polarity samples from different sites have similar magnetic properties, supporting a likely primary detrital or early diagenetic remanent magnetization during paleosol formation. Furthermore, normal and reverse polarity mean directions are nearly antiparallel with an angular difference of 6.4° compatible with a residual recent field overprint. This is cancelled in the mean combining the normal and reverse polarties yielding D = 12.3° / I = 25.0° / α95 = 4.9°, corresponding to a paleolatitude of 13.1±2.9°N and a negligible CW rotation of 9.3±4.8° compared to stable Eurasia (Torsvik et al., 2012). Hence, this middle Miocene position of the BT was much farther north than before, in agreement with offset estimates along the Neogene Sagaing Fault from structural geology placing the BT at similar latitudes with little rotation during this time (Matthews et al., 2016; Maung, 1987; Maurin & Rangin, 2009; Morley, 2017b; Socquet et al., 2006). This suggests that the effect of inclination shallowing on these deposits was minimal, as the unflattened paleolatitude equals 21.3±5.3°N, which is much farther north than the offset estimates of the Sagaing Fault.

5. Interpretations

Previous early Late Cretaceous and late Eocene paleomagnetic results from the BT showed that it was at near-equatorial to southern hemisphere latitudes during that time period, much more to the south than imagined before (Westerweel et al., 2019). The new paleomagnetic data from this study confirm this, but also present some scatter (Fig. 6.6) that requires further discussion.

Sites with declination to the north or to the south are unambiguously attributed to respectively normal and reverse polarity, because an unlikely near ~180° tectonic rotation would otherwise be necessary. Yet there is scatter in declination for the latest Paleocene to middle Eocene sites that impedes a clear fold test. Fortunately, the scatter in inclination decreases significantly after tilt correction (Fig. 6.7a), showing that magnetizations were probably acquired prior to folding. This scatter is further reduced to about 20° when converting these inclinations to paleolatitudes (Fig. 6.7a). In the time range of ~65-40 Ma, southern paleolatitudes and a latitudinal motion of nearly 30° are expected if the BT is fixed with respect to India (Fig. 6.7a). By contrast, paleolatitudes higher than 20° with little latitudinal changes are expected if the BT is fixed with respect to Sibumasu. Therefore, the scatter in inclination is interpreted to relate to northward motion of the BT alongside India. This interpretation encourages further work on a more comprehensive age control for the

Laungshe Formation, as the southern paleolatitude at site ST01 rather supports an earlier Paleocene age in a context where the BT moves northward with India.

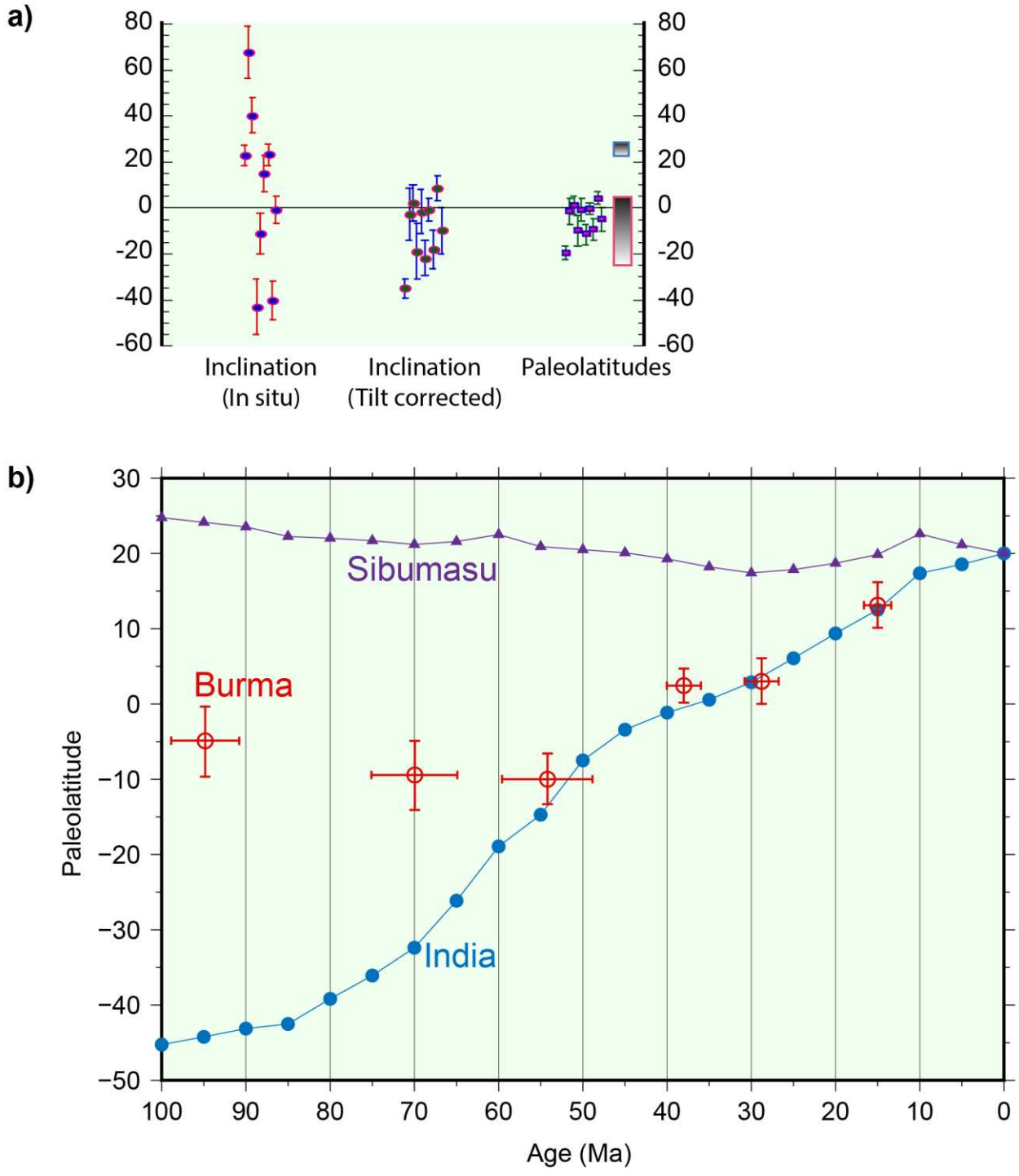

Figure 6.7: *a) Scatter in inclination of latest Paleocene to middle Eocene results before and after tilt correction. Resulting paleolatitudes are similar to the expected paleolatitude if the BT is fixed to the northward moving Indian continent (red grey box) in the time range 65-40Ma, but strongly contrast with the expected constant paleolatitude (blue grey box) if the BT is fixed to Sibumasu in the same*

time frame; b) Latitudinal motion of the Burma Terrane from 100-0 Ma, using the paleomagnetic mean results from this study, compared with the latitudinal motions of India and Sibumasu (after Matthews et al., 2016; Torsvik et al., 2012 and references therein).

In general, our new Campanian - Maastrichtian to middle Eocene paleomagnetic data confirm the southern hemisphere low latitudes of the previously published results in Westerweel et al. (2019), and they together show an impressive ~3000 km northward motion of the BT from the early Late Cretaceous until the present-day (Fig. 6.7b). Moreover, our latest Paleocene to middle Oligocene results all show a coeval northward motion alongside India (Fig. 6.7b; fig. 6.S3), indicating that the BT was part of the Indian Plate for a significant amount of time. The consistency of the near-equatorial to southern hemisphere latitudes and their similarity to the position of India further indicate that the effect of inclination shallowing on our results is negligible (Section 4.2). An inclination shallowing correction for sites with negative inclinations would even provide more southern paleolatitudes for these sites.

A wholesale ~60° CW rotation of the BT was first postulated based on the available early Late Cretaceous and late Eocene mean directions (Westerweel et al., 2019). The general trend in the latest Paleocene to middle Eocene results from the Laungshe and Tilin Formations is also eastward directed declinations of intermediate to similar magnitude as the early Late Cretaceous mean direction (ST01, SW02, SW07), but the scatter in declination provides evidence for local block rotations as well (Fig. 6.6). The mean direction of site SW08 from the middle Eocene Tabyin Formation is clearly transitional between the Laungshe / Tilin Formation results (ST01, SW02, SW07) and the late Eocene Pondaung / Yaw Formation results. However, the hypothesis of a wholesale CW rotation of the BT occurring during the latest Paleocene to middle Eocene time period, as it started to move northward with India is not fully supported by results at sites ST02, SW03, SW04 and SW09. Significant deformation is observed in sampling areas of site ST02, SW03 and SW04, and their differing declinations can potentially be explained by local block rotations. The result at site SW09 in the Kabaw Formation is more puzzling. In contrast to sites SW03 and SW04, it is difficult to attribute its excessive ~137 CW rotation to local deformation only, because the bedding and AMS lineation of site SW09 both follow the general ~N-S trend of the Minbu Basin. It seems likely that significant deformation occurred during the latest Paleocene to middle Eocene as the BT started to move northward with India, and in this context site SW09 could be of that age instead of the postulated Campanian – Maastrichtian age for the Kabaw Formation. In general, it seems difficult to establish a robust evolution of the rotation through time prior to the middle Eocene with the available paleomagnetic results and age uncertainties.

From the middle Eocene to present, the BT did not experience significant tectonic rotations. It underwent ~2000 km northward motion with little rotation to reach its present-day position, as indicated by our late Eocene to middle Miocene paleomagnetic results. This was interpreted before as representing a major strike-slip motion to the east of the BT (Westerweel et al., 2019) and our new results fit with this interpretation.

To summarize, the key implications from this paleomagnetic study are the initial early Late Cretaceous southern hemisphere position of the BT distant from southern Asia, followed in the latest Paleocene - middle Eocene by the onset of a coeval northward motion with India and possibly CW rotation, and finally a major ~2000 km northward strike-slip translation during the late Eocene to present-day. These findings are seemingly contradicted by another paleomagnetic study providing a close to present-day paleolatitude for the BT from the Paleocene Paunggyi Formation in the southern Minbu Basin (Li et al., 2020). However, their results were likely not obtained from stable ChRM vectors as will be further discussed in Chapter 7 by comparing their data with own results from the same location. Based on these arguments, the data and conclusions of Li et al. (2020) are discarded.

6. Discussion

To further discuss our paleomagnetic dataset for the BT showing near-equatorial to southern hemisphere paleolatitudes, it is necessary to check whether available regional geological information from the BT supports our Trans-Tethyan Arc plate model for the India-Asia collision that is based on these paleolatitudes (Figs. 6.8-6.13; Supplementary Information).

6.1. Origin of the Burma Terrane

Our paleomagnetic data showing southern hemisphere latitudes for the BT from at least the early Late Cretaceous until the early Eocene indicate that its tectonic history must have been distinct from southern Asia for a significant amount of time, which strongly opposes many previous models (e.g. Li et al., 2020; Lin et al., 2019; Searle et al., 2017; Sevastjanova et al., 2016; Zhang et al., 2019a). Alongside the evidence for an important subduction phase along the BT starting in the mid-Cretaceous, notably the peak in WPA volcanism (Barley & Zaw, 2009; Licht et al., 2020; Lin et al., 2019; Mitchell et al., 2012; Zhang et al., 2017a) and coeval emplacement of the Western Belt Ophiolite (Fareeduddin & Dilek, 2015; Htay et al., 2017; Liu et al., 2016; Singh et al., 2017; Zhang et al., 2017b), our paleomagnetic constraints agree best with an island arc origin for the BT as part of a near-equatorial Trans-Tethyan subduction system (Figs. 6.8 and 6.9). This is corroborated by similar trends of mid-Cretaceous magmatic activity and ophiolite emplacement along other proposed intra-oceanic arc segments of this Trans-Tethyan subduction system, such as the Kohistan Arc and

Spontang Ophiolite in the Western Himalayas (Buckman et al., 2018; Jagoutz et al., 2019; Petterson, 2019). Furthermore, the Kohistan Arc presumably formed at near-equatorial latitudes as well (Zaman & Torii, 1999). To the east, it less certain whether the intra-oceanic Woyla Arc of Sumatra also fits with this trend, because it was interpreted as having been already accreted to southern Sundaland at ~90 Ma (Figs. 6.8 and 6.9; Advokaat et al., 2018; Barber & Crow, 2009; Hall, 2012).

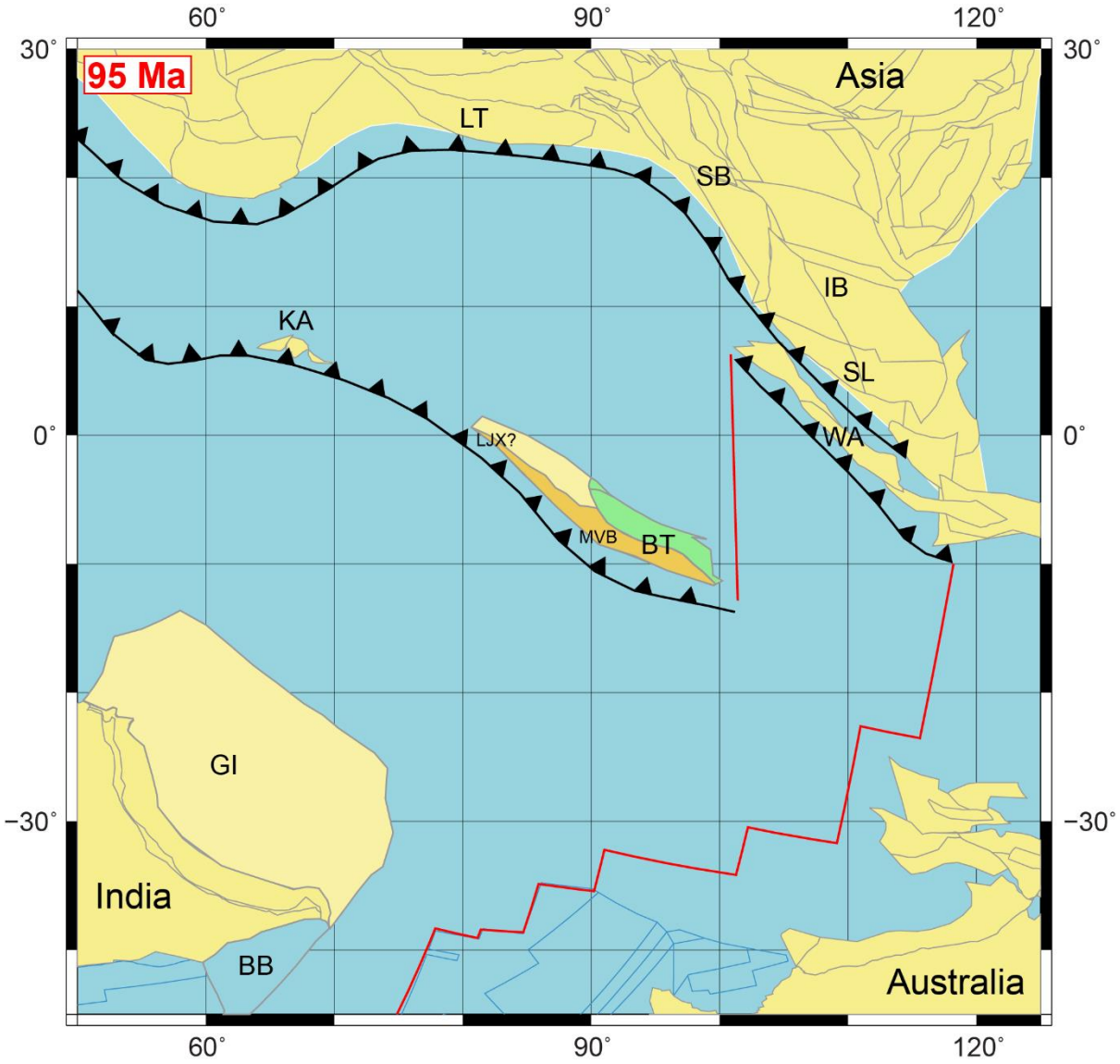

Figure 6.8: *Reconstruction of the Burma Terrane and Asia at 95 Ma. Abbreviations: BB = Bay of Bengal, BT = Burma Terrane EA = Eastern Andaman Basins, GI = Greater India, IB = Indochina Block, KA = Kohistan Arc, LJX = Langjiexue Formation, LT = Lhasa Terrane MVB = Mount Victoria Block, SB = Sibumasu Block, SL = Sundaland, WA = Woyla Arc. Legend: Black lines = subduction/collision zones, thin blue lines = seafloor magnetic isochrons on present-day oceanic crust, red lines = oceanic ridges and transform faults. Figure constructed using GPlates software (Matthews et al., 2016; Müller et al., 2018, 2019).*

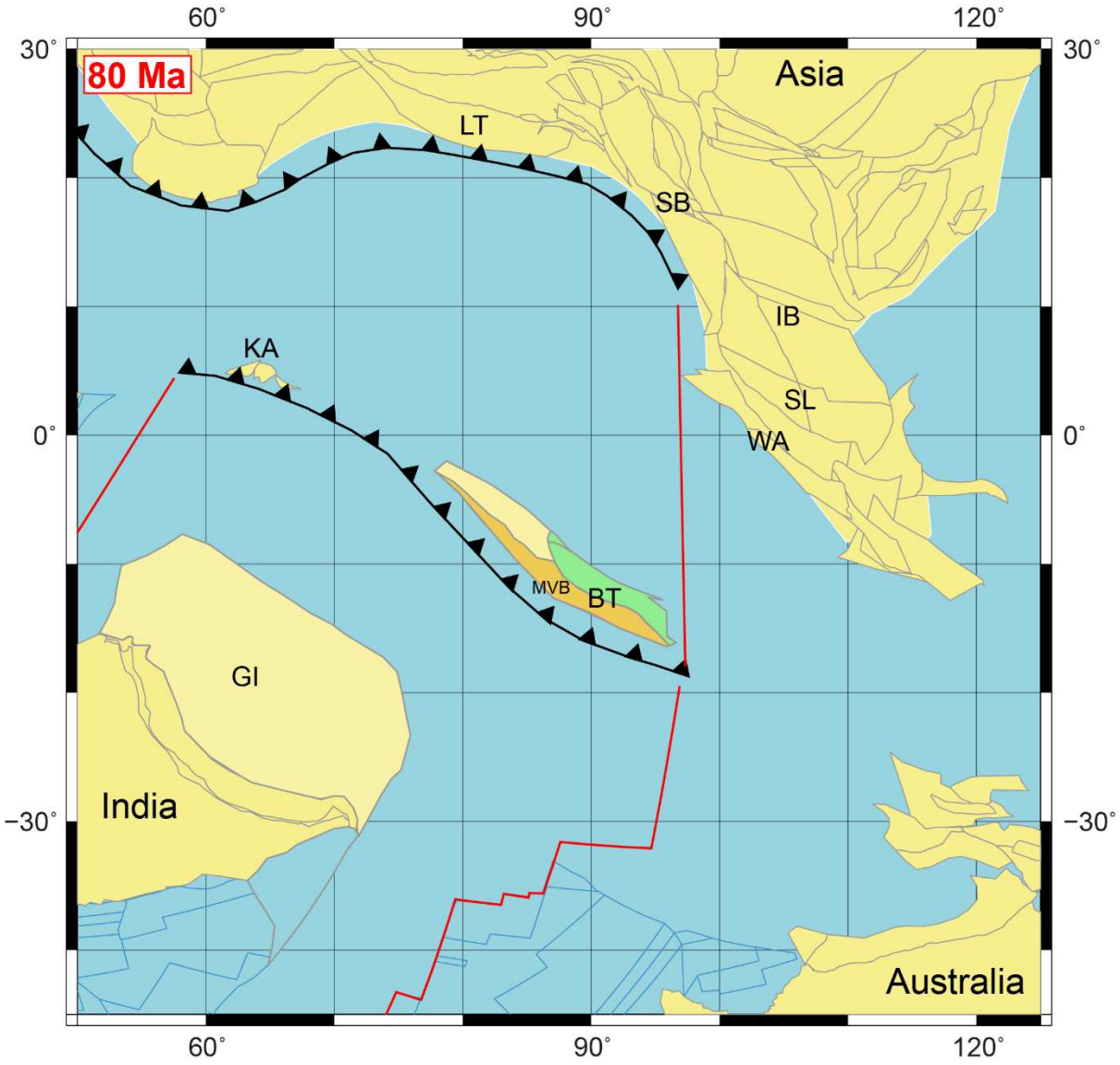

Figure 6.9: *Reconstruction of the Burma Terrane and Asia at 80 Ma. See figure 6.8 caption for abbreviations, legend and references.*

Our proposed Trans-Tethyan subduction system setting for the BT has the advantage to potentially reconcile apparent discrepancies regarding the pre-Cretaceous origin of the BT, where contradicting pieces of evidence indicate either Gondwanan, Sibumasu or Cathaysian origins (Barber & Crow, 2009; Metcalfe, 2013; Sevastjanova et al., 2016; Ueno et al., 2016; Yao et al., 2017). Crustal ribbon fragments could have been amalgamated within the Trans-Tethyan subduction system, comprising either fragments of composite origin or solely of Gondwanan origin (Licht et al., 2020). The clear correlation of the Pane Chaung Formation of the Mount Victoria Block with the Langjiexue Formation of the NE Tethyan Himalayas now provides the best piece of evidence for crustal fragments of Gondwanan origin within the BT (Cai et al., 2016; Liu et al., 2020b; Yao et al., 2017), contradicting preliminary evidence for a correlation with Sibumasu (Sevastjanova et al., 2016). These

Gondwanan crustal fragments have specifically been referred to as the 'Greater Argoland' archipelago (Argoland itself referring to Gondwana-derived rocks in East Java and Sulawesi; Hall et al., 2009; Sikumbang, 1990; Wakita et al., 1998), which would have rifted at ~155 Ma from NW Australia (Hall, 2012; I'Anson et al., 2019; Morley et al., 2020; Seton et al., 2012). The Pane Chaung and Langjiexue Formations can then be interpreted as representing Greater Argoland crustal fragments incorporated along the Trans-Tethyan subduction system. A Greater Argoland origin for the entire BT would mean that the sporadic Cathaysian fragments along the Sagaing Fault were not originally part of the BT, but represent displaced slices of Sundaland instead (Metcalfe, 2017). Both the Greater Argoland and composite origins for the BT can explain the potential collision of the Gondwana-derived Mount Victoria Block with the BT, which should have occurred by the mid-Cretaceous (Mitchell, 2017; Morley et al., 2020).

Beyond geodynamics, the rich Burmese record of Cretaceous fossil amber biota contains indications for both Gondwanan and endemic traits within the wide range of available species (e.g. Grimaldi et al., 2002; Liu et al., 2020a; Poinar, 2018; Rasnitsyn & Öhm-Kühnle, 2018). For these reasons, an isolated island arc origin for the BT as part of a Trans-Tethyan subduction system, which incorporated crustal fragments from Gondwana and possibly elsewhere, seems the best way to reconcile the available paleomagnetic, geological and paleontological information from the BT. This proposed origin for the BT shows that the India-Asia collision was more complex than the simple continent-continent collision proposed in traditional models.

6.2. India – Trans-Tethyan Arc collision

The latest Paleocene – middle Eocene appears to be a crucial time period for the BT, as our paleomagnetic results indicate that the coeval northward motion with India initiated at that time, potentially accompanied by a degree of CW rotation. These events could represent further proof for a Trans-Tethyan Arc setting for the BT, because convergence rates between India and Asia decreased during the same time interval. Most models with a Trans-Tethyan subduction system interpret this event to reflect the collision of (Greater) India with this system (Jagoutz et al., 2015; Zahirovic et al., 2016). This is also true for the Kohistan Arc, where collision with India is generally estimated between ~60-40 Ma (Catlos et al., 2019; Petterson, 2019). Hence, we propose that a latest Paleocene to middle Eocene collision of India with the Trans-Tethyan subduction system induced its incorporation onto the Indian Plate, impeding active subduction underneath the BT as it moved northward with India (Figs. 6.10 and 6.11).

The onset of the India – Trans-Tethyan Arc collision event within the BT could be represented by the early Paleocene unconformity in the Minbu Basin that separates the Kabaw Formation from the

Paunggyi Formation (Section 2.5.1; Cai et al., 2019; United Nations, 1978a). Another suggestion for this collision event could be the roughly coeval emplacement of the Western Belt Ophiolite onto the Indian passive margin in the northern IBR (Naga Hills; Aitchison et al., 2019). However, an early Paleogene collision event along the BT is seemingly contradicted by ongoing deposition of deep-water turbidites along the central and southern IBR during this time (Allen et al., 2008; Gough et al., 2020; Mitchell, 2017; Najman et al., 2020). Moreover, a younger late Eocene coupling of the BT with India has been inferred based on the onset of molasse deposition and uplift in the IBR (Bannert et al., 2012; Ghose et al., 2014; Morley et al., 2020; Najman et al., 2020). These apparent discrepancies can be reconciled by extending the BT farther northward as part of the Trans-Tethyan Arc, and letting India initially collide only with this Greater Burma region (Fig. 6.10). This is compatible with uplift in the BT recorded by the Paunggyi Formation unconformity and emplacement of the Western Belt Ophiolite in the northern IBR, while no collision was recorded in the central and southern IBR. The subsequent middle to late Eocene collision of the conjoint India/Trans-Tethyan Arc system, including the Greater Burma region, with the Asian margin in the Eastern Himalayas could then represent an alternative explanation for the onset of molasse deposition along the IBR (Fig. 6.12; Westerweel et al., 2020). This is further supported by coeval late Eocene onset of high temperature metamorphism in the northern MMMB (Searle et al., 2007, 2017, 2020) and significant thrusting in the Eastern Himalayan collision zone north of the IBR (Haproff et al., 2020), which have both been attributed to the India-Asia collision.

These collision events could explain the significant populations of ~80-50 Ma and pre-Cretaceous detrital zircon ages in Eocene sediments within the CMB. In past sedimentary provenance studies, these populations were viewed as coming from respectively the WPA and Sibumasu (Licht et al., 2013, 2019; Wang et al., 2014; Zhang et al., 2019b). However, our plate reconstructions show an Eocene position for the BT distant from Sibumasu, and the incorporation of the BT onto the Indian Plate likely impeded significant subduction underneath the Burmese margin that likely largely shut down volcanic activity along the WPA (Figs. 6.10-6.12). Indeed only ~110-90 Ma and sporadic ~42-36 Ma volcanic ages are present in the Wuntho Ranges volcanic complex (Licht et al., 2020; Lin et al., 2019). Furthermore, seismic lines show that the vast areas of the WPA delineating the CMB farther south were already buried by the Eocene (Zhang et al., 2017a), although sporadic volcanic activity at ~65 Ma is suggested by the volcanic rocks, tuffs and volcanic clasts of the Paunggyi Formation in the Minbu Basin (Cai et al., 2019).

To this end, the Gangdese Arc of the Lhasa Terrane and exhumed rocks from the northern extension of the WPA in the Greater Burma region could have been important source regions for the CMB since the Eocene, when the conjoint India/Trans-Tethyan Arc system collided with Asia. They could

contain ~80-50 Ma magmatic rocks and reworked sediments exhumed due to collision. Similarly, the significant population of pre-Cretaceous zircons in the Paleogene sediments in the CMB could have been sourced by exhuming basement rocks in the Greater Burma region during collision. The Eocene Phokphur conglomerates in the northern IBR (Aitchison et al., 2019) and uppermost Cretaceous to Paleogene sediments in the CMB have coinciding pre-Cretaceous age peaks (Arboit et al., 2020; Cai et al., 2019; Westerweel et al., 2020) as Gondwanan basement rocks exposed in the collision zone such as the Triassic Pane Chaung and Langjiexue Formations (Section 6.1; Cai et al., 2016; Wang et al., 2016; Yao et al., 2017).

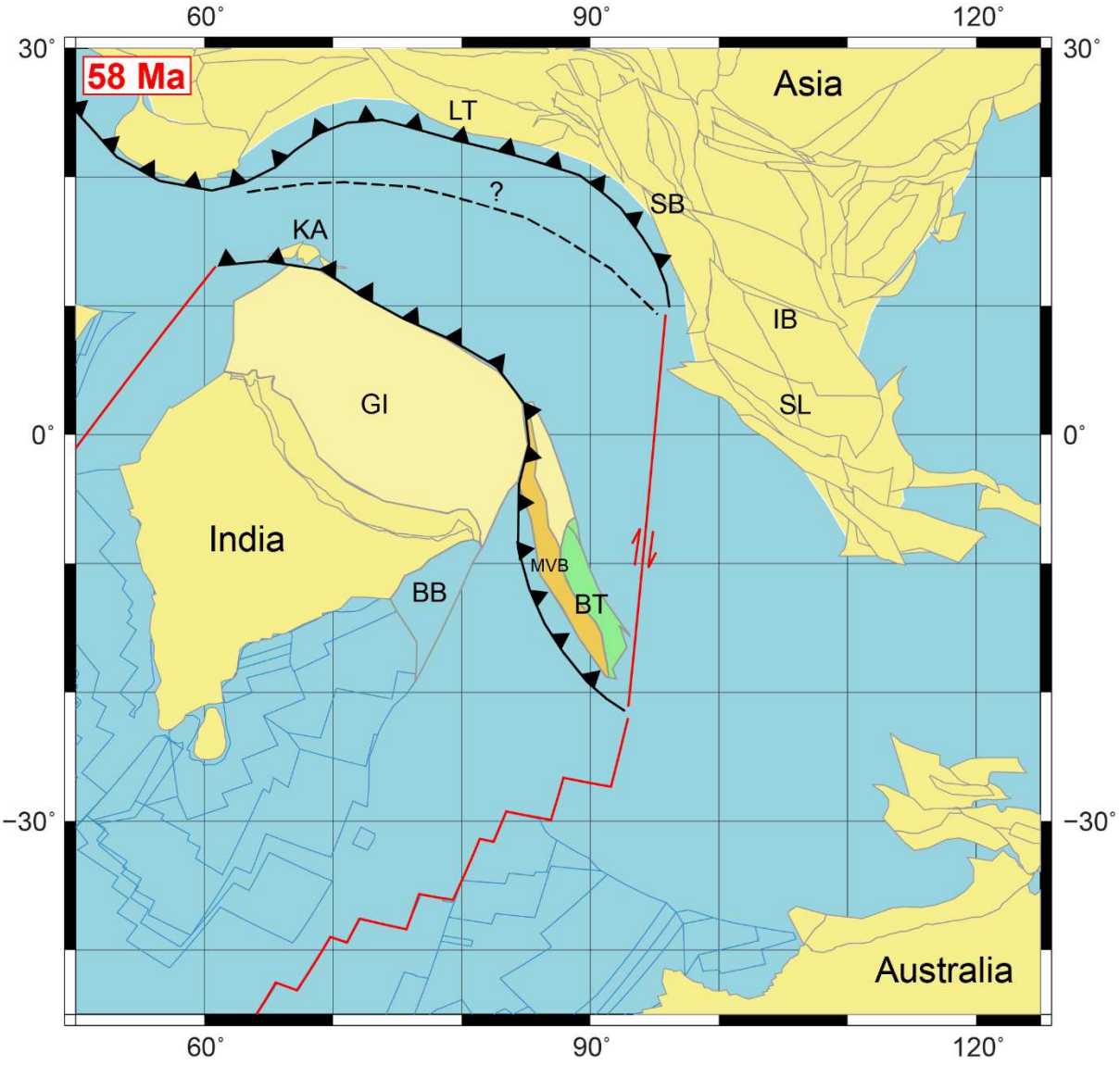

Figure 6.10: *Reconstruction of the Burma Terrane and Asia at 80 Ma. See figure 6.8 caption for abbreviations, legend and references.*

Exhumation and prolonged transport of magmatic rocks, basement rocks and reworked sediments from the collision zone towards the south provides an explanation for the overall low magnetite

content and paramagnetic phases in our sampled lithologies (Section 4.1). Deviations in magnetite content, discerned for example by the low bulk magnetic susceptibilities of the Natma Formation in contrast to the Pondaung Formation of similar lithology and the Letkat Formation of similar age, could then be the result of different exhumation phases, variable importance of source lithologies or sporadic volcanic activity along the WPA.

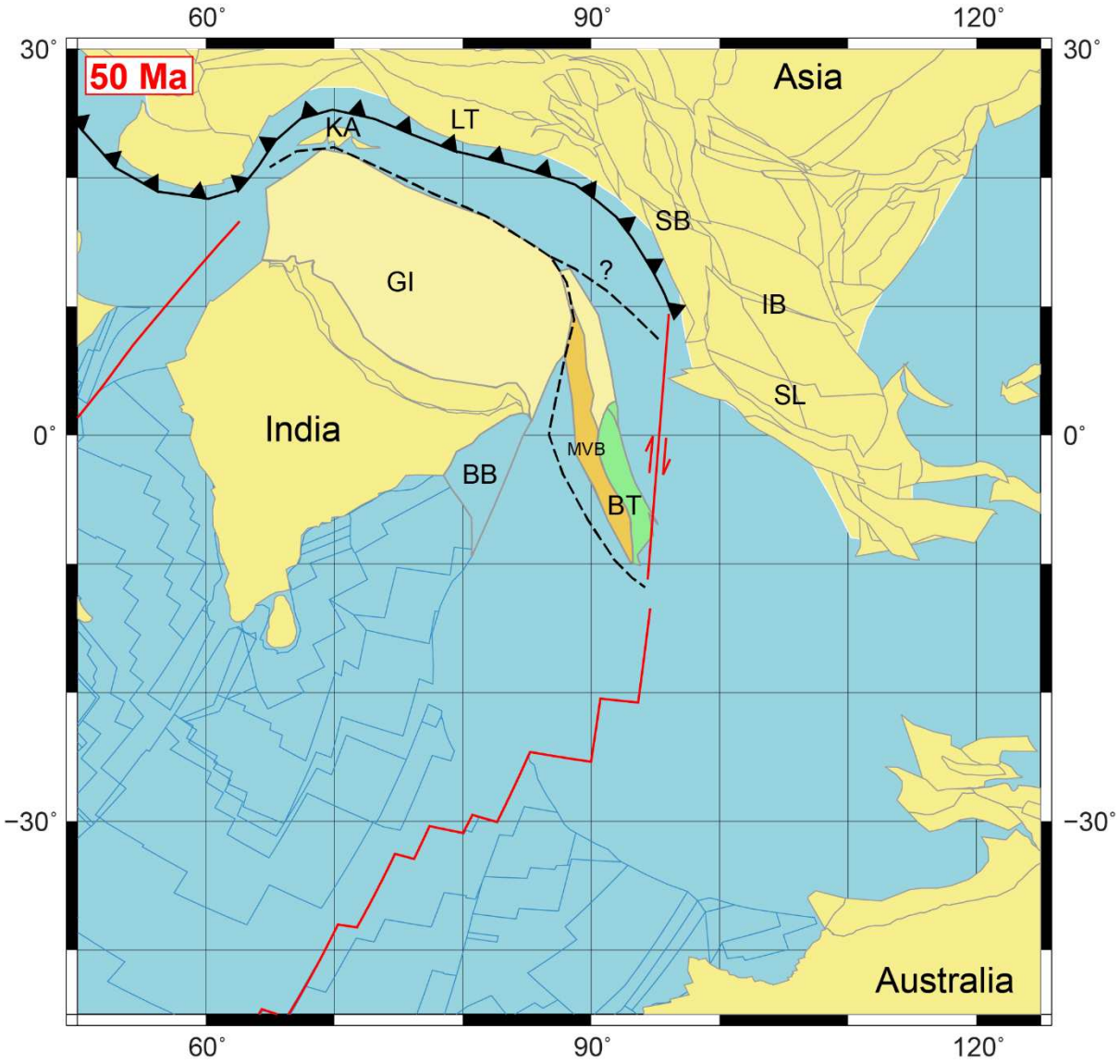

Figure 6.11: *Reconstruction of the Burma Terrane and Asia at 80 Ma. See figure 6.8 caption for abbreviations, legend and references.*

However, much of the Greater Burma region would have been subducted or underthrusted underneath the Asian margin, but potential remainders are the Lohit and Sodon Batholiths that have been correlated to both the WPA and Gangdese Arc (Lin et al., 2019). There are currently no direct paleomagnetic constraints on the Lohit and Sodon Batholiths to distinguish between these two volcanic arcs in the Eastern Himalayan collision zone. Roperch et al. (In prep.) in Appendix 5 further

discusses potential source regions for the CMB in the collision zone, including the Greater Burma region and the Gangdese Arc.

6.3. Burma Terrane – Sibumasu collision

After it was incorporated onto the Indian Plate in the latest Paleocene – middle Eocene, the BT started its rapid northward motion alongside India. Our paleomagnetic results show that the position of the BT with respect to India remained constant from this time onwards (Figs 6.6 and 6.7), indicating little relative motion between them. Therefore, deformation accommodating the northward translation of the BT should have been concentrated to its east, most straightforwardly by the India-Australia Transform that formed the eastern boundary of the Indian Plate (Hall, 2012; Morley et al., 2020; Figs 6.10-6.12).

There are differing constraints on the timing of when the BT/India collided with Sibumasu in the Eastern Himalayan collision zone. Based on our initial early Late Cretaceous and late Eocene paleomagnetic constraints, we first interpreted the BT as being already accreted to Sibumasu by the late Eocene and then forming forearc sliver coupling with the motion of India since that time (Westerweel et al., 2019). Others have similarly argued for a late Eocene collision of (Greater) India with Sibumasu based on metamorphism and deformation along the Eastern Himalayan collision zone, MMMB and Eastern Andaman Basins (Haproff et al., 2020; Sautter et al., 2019). However, there are several important issues with this hypothesis. First of all, there is a lack of evidence for a suture between the BT and Sibumasu, in the form of an ophiolite belt or an accretionary prism (Morley et al., 2020), although it is possible that posterior strike-slip deformation along the Sagaing Fault has obscured this suture. It should be noted that dismembered ophiolite fragments of the Jade Belt and Central Ophiolite Belt lie along the trace of the Sagaing Fault (Htay et al., 2017). The second issue is that geological observations indicate that the Eastern Andaman Basins along the margin of Sibumasu experienced E-W extension instead of shortening during the late Eocene - Oligocene (Morley, 2017a; Morley & Alvey, 2015), such that a major collision and underthrusting event could not take place there. Finally, significant deformation and uplift within the BT is only observed in the late Oligocene – early Miocene on seismic lines and exhumation ages, with only incipient or no uplift before during the late Eocene (Gough et al., 2020; Licht et al., 2019, 2020; Najman et al., 2020; Westerweel et al., 2020; Zhang et al., 2017, 2019b).

By contrast, our updated paleomagnetic dataset shows a prolonged coeval motion of the BT with India long before the late Eocene and continuing afterwards (Figs. 6.7, 6.10-6.12). Based on this, we propose that the BT and Sibumasu were still separated by a transform fault throughout the late Eocene and Oligocene, resulting in a later collision event of the BT with northern Sibumasu in the

late Oligocene – early Miocene similar to the model of Morley et al. (2020). This interpretation fits with an earlier collision between Asia and the Greater Burma region, while there is no record of collision within the BT itself (Figs. 6.11 and 6.12; Westerweel et al., 2020). Furthermore, the late Eocene - Oligocene E-W extension in the Eastern Andaman Basins can then be explained by slab rollback due to ongoing subduction underneath Sibumasu (Fig. 6.12; Morley, 2017a).

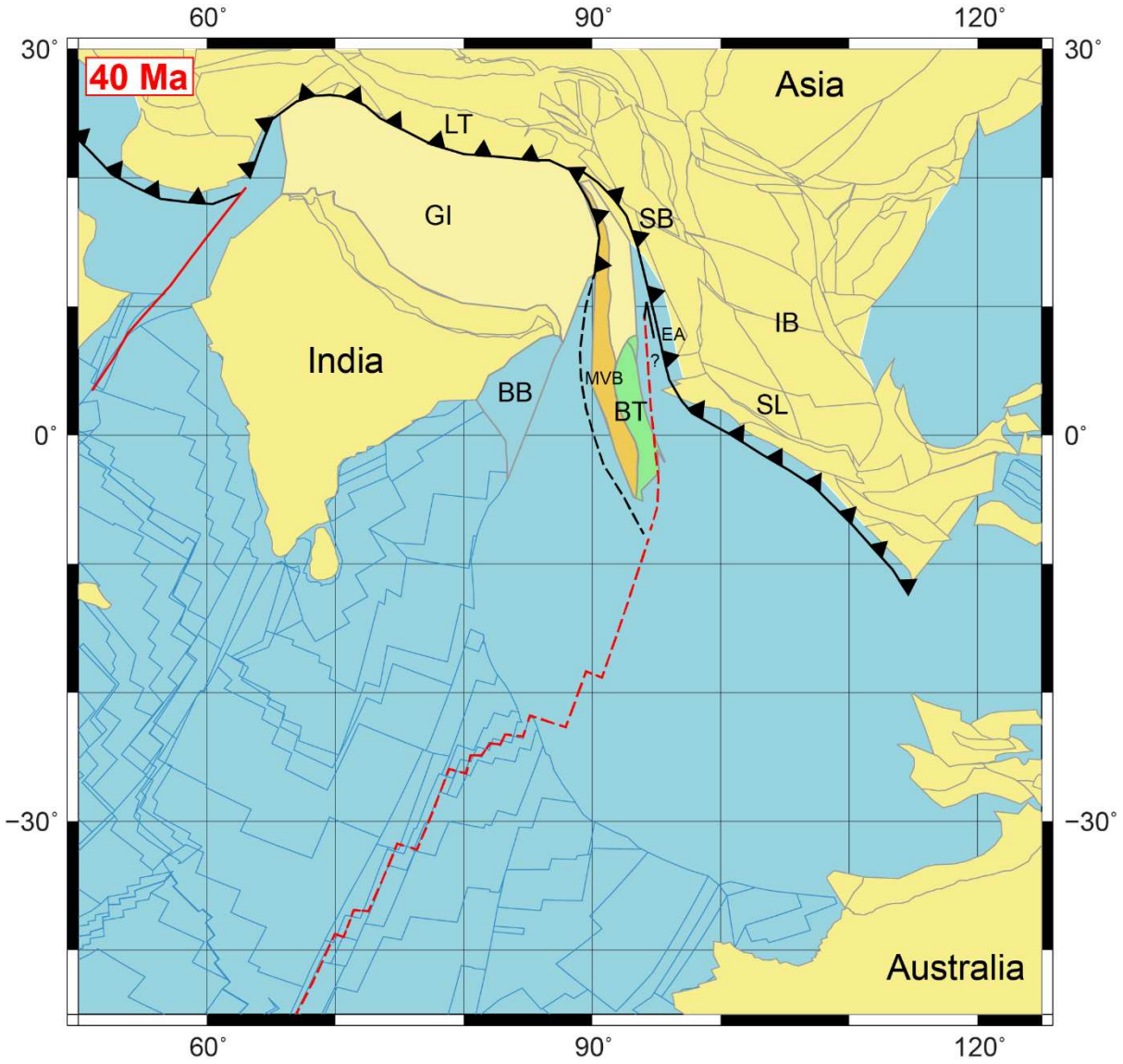

Figure 6.12: *Reconstruction of the Burma Terrane and Asia at 80 Ma. See figure 6.8 caption for abbreviations, legend and references.*

One issue with this later late Oligocene – early Miocene collision event is that the distance between the BT and Sibumasu would require the India-Australia Transform to remain active during the Oligocene (Morley et al., 2020). This is ambiguous, because the motions of the Indian and Australian Plates coupled around 40 Ma such that the India-Australia Transform should have become inactive starting at that time (Hall, 2012; Matthews et al., 2016; Ridd & Watkinson, 2013). Possibly, ongoing

subduction underneath Sibumasu accommodated the BT northward motion instead (Fig. 6.12), until dextral motion resumed after the late Oligocene – early Miocene collision event. The exact nature of the plate margin between the Indian Plate and Sibumasu east of the BT remains a major uncertainty in our model, but it is clear that the western boundary of Sibumasu during the Cenozoic was not a classic Andean-type margin as in most previous models (e.g. Li et al., 2020; Searle et al., 2017; Sevastjanova et al., 2016; Zhang et al., 2019a).

The near-equatorial and isolated position of the BT throughout the Eocene and Oligocene has far-reaching implications for reconstructions of Asian paleoclimate and paleoenvironment. The shared history of India and the BT throughout the Paleogene shown by our updated paleogeography suggests that the Eocene pollen assemblages of Myanmar (Huang et al., 2020) would have more in common with India than with SE Asia. Furthermore, it is necessary to reconcile the geological evidence for a strongly monsoonal climate in Myanmar during the Eocene (Licht et al., 2014a) with the near-equatorial tropical latitudes inferred by our paleomagnetic constraints, which together suggest a massive seasonal migration of the Intertropical Convergence Zone. There are indications for monsoonal conditions at near-equatorial latitudes elsewhere in SE Asia during the Eocene (Evans et al., 2013). Recent climate modelling has shown that a near-equatorial late Eocene position for the BT corresponds to an ever-wet context rather than strong seasonality (Tardif et al., 2020). This study proposed that the region of strong seasonality might have expanded over the BT due to orbital forcing to explain the geological indications for a monsoonal climate in Myanmar (Licht et al., 2014a). More detailed regional climate models incorporating our updated paleogeography and additional paleoclimatic data from Myanmar are required to confirm this.

6.4. Set-up modern of the Eastern Himalayan collision zone

Following its collision with northern Sibumasu, our plate reconstructions show that the BT entered the Eastern Himalayan collision zone in the late Oligocene – early Miocene after the Greater Burma region was largely subducted or underthrusted underneath the Asian margin (Figs. 6.12 and 6.13). This timing is in agreement with our middle Miocene paleolatitude (Figs. 6.6 and 6.7), as well as sedimentological, geochronological and structural observations from the CMB and IBR (Najman et al., 2020; Westerweel et al., 2020; Zhang et al., 2017a) and the onset of major transtension in the Andaman Sea south of the BT (Morley, 2017a; Srisuriyon & Morley, 2014). From the middle Miocene, the collision between the BT and Asia would have slowed down the relative northward motion of the BT with respect to Sibumasu, and further caused a relative dextral motion of the BT with respect to India leading to the development of the Burmese mobile belt with more expressed dextral strike-slip deformation in the IBR (Rangin, 2018; Rangin et al., 2013). It is also a likely cause

for major exhumation and deformation in the Eastern Himalayan Syntaxis (Godin et al., 2006; Kellett et al., 2013; Najman et al., 2019), leading to south-eastward extrusion of the MMMB (Bertrand et al., 2001; Bertrand & Rangin, 2003; Li et al., 2018; Tong et al., 2013) and the set-up of the modern eastern Himalayan drainage system (Bracciali et al., 2015).

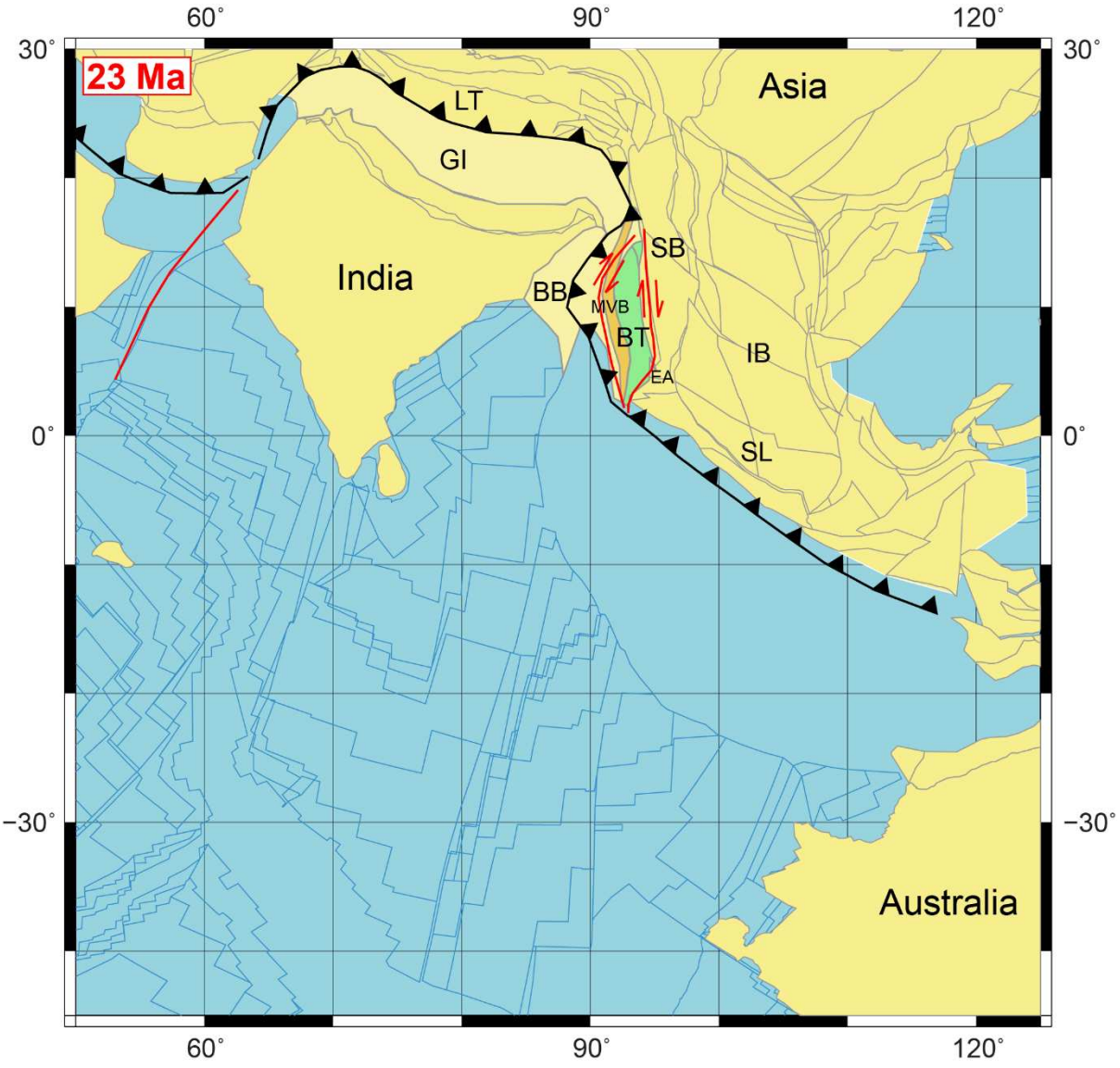

Figure 6.13: *Reconstruction of the Burma Terrane and Asia at 80 Ma. See figure 6.8 caption for abbreviations, legend and references.*

7. Conclusions

This study presents a complete paleomagnetic dataset for the BT of Myanmar to constrain its paleolatitudinal motion, by combining new Campanian - Maastrichtian, latest Paleocene – middle Eocene, late Eocene, middle Oligocene and middle Miocene data from the Burmese forearc (Chindwin and Minbu Basins) with previously published early Late Cretaceous and late Eocene

results. Together they reveal an astonishing tectonic history for the BT. The four key implications from our dataset are that (1) the BT remained in a southern hemisphere position distant from the southern Asian margin throughout the Late Cretaceous and early Paleogene, (2) the BT was incorporated onto the Indian Plate in the latest Paleocene – middle Eocene, and (3) it subsequently moved northward with only minor convergence relative to India along a dextral strike-slip system to its east, until (4) a late Oligocene – early Miocene collision with northern Sibumasu in the Eastern Himalayan collision zone. These constraints on the tectonic history of the BT and Eastern Himalayan orogen provide important new perspectives on the puzzle of the India-Asia collision, because they support collision models involving a Trans-Tethyan subduction colliding with the northward moving Indian continent. This updated paleogeography model of the India-Asia collision has important implications for understanding the interplay between Asian tectonics and climate, as well as the origin and dispersion of the prolific Burmese pollen and fossil record. However, while our collision model is supported by the available geological data, it is also evident that it contains important uncertainties mainly due to the shortage of tectonic constraints from the extremely deformed eastern end of the Himalayan collision zone. Therefore, the collision model presented here opens up new frontiers for further research across the Himalayan orogen to elucidate these uncertainties.

Acknowledgements

This research was primarily funded by the ERC consolidator grant MAGIC 649081 to Guillaume Dupont-Nivet. We would like to thank Catherine Kissel for the use of the AGM magnetometer at the LSCE paleomagnetic laboratory, France. We are grateful to Philippe Cullerier and Kyi Kyi Thein for helping with the paleomagnetic experiments and sampling. We thank Eldert Advokaat, Francesco Arboit, François Guillocheau, Amy Gough, France Lagroix, Andrew Mitchell, Chris Morley, Yani Najman, Anne Replumaz, Ed Sobel and Douwe van Hinsbergen for constructive discussions throughout this study.

References Chapter 6

Acharyya, S. K. (2007). Collisional emplacement history of the Naga-Andaman ophiolites and the position of the eastern Indian suture. Journal of Asian Earth Sciences, 29(2–3), 229–242.

Advokaat, E. L., Bongers, M. L. M., Rudyawan, A., BouDagher-Fadel, M. K., Langereis, C. G., & van Hinsbergen, D. J. J. (2018). Early Cretaceous origin of the Woyla Arc (Sumatra, Indonesia) on the Australian plate. Earth and Planetary Science Letters, 498, 348–361. https://doi.org/10.1016/j.epsl.2018.07.001

Aitchison, J. C., Ao, A., Bhowmik, S., Clarke, G. L., Ireland, T. R., Kachovich, S., … Zhou, R. (2019). Tectonic Evolution of the Western Margin of the Burma Microplate Based on New Fossil and Radiometric Age Constraints. Tectonics, 2018TC005049. https://doi.org/10.1029/2018TC005049

Allen, R., Najman, Y., Carter, A., Barfod, D., Bickle, M. J., Chapman, H. J., … Parrish, R. R. (2008). Provenance of the Tertiary sedimentary rocks of the Indo-Burman Ranges, Burma (Myanmar): Burman arc or Himalayan-derived? Journal of the Geological Society, 165(6), 1045–1057.

Arboit, F., Min, M., Chew, D., Mitchell, A., Drost, K., Badenszki, E., & Daly, J. S. (2020). Constraining the links between the Himalayan belt and the Central Myanmar Basins during the Cenozoic: An integrated multi-proxy detrital geochronology and trace-element geochemistry study. Geoscience Frontiers, S1674987120301705. https://doi.org/10.1016/j.gsf.2020.05.024

Bannert, D., Sang Lyen, A., & Htay, T. (2012). The geology of the Indoburman Ranges in Myanmar.

Barber, A. J., & Crow, M. J. (2009). Structure of Sumatra and its implications for the tectonic assembly of Southeast Asia and the destruction of Paleotethys. Island Arc, 18(1), 3–20. https://doi.org/10.1111/j.1440-1738.2008.00631.x

Barley, M. E., & Zaw, K. (2009). SHRIMP U-Pb in zircon geochronology of granitoids from Myanmar: temporal constraints on the tectonic evolution of Southeast Asia. In EGU General Assembly Conference Abstracts (Vol. 11, p. 3842).

Benammi, M., Naing Soe, A., Tun, T., Bo, B., Chaimanee, Y., Ducrocq, S., … Jaeger, J.-J. (2002). First magnetostratigraphic study of the Pondaung Formation: implications for the age of the Middle Eocene anthropoids of Myanmar. The Journal of Geology, 110(6), 748–756.

Bender, F. (1983). Geology of Burma. Berlin.

Bertrand, G., & Rangin, C. (2003). Tectonics of the western margin of the Shan plateau (central Myanmar): implication for the India–Indochina oblique convergence since the Oligocene. Journal of Asian Earth Sciences, 21(10), 1139–1157.

Bertrand, G., Rangin, C., Maluski, H., & Bellon, H. (2001). Diachronous cooling along the Mogok Metamorphic Belt (Shan scarp, Myanmar): the trace of the northward migration of the Indian syntaxis. Journal of Asian Earth Sciences, 19(5), 649–659. https://doi.org/10.1016/S1367-9120(00)00061-4

Borradaile, G. J., & Henry, B. (1997). Tectonic applications of magnetic susceptibility and its anisotropy. Earth-Science Reviews, 42(1–2), 49–93.

Bouilhol, P., Jagoutz, O., Hanchar, J. M., & Dudas, F. O. (2013). Dating the India–Eurasia collision through arc magmatic records. Earth and Planetary Science Letters, 366, 163–175. https://doi.org/10.1016/j.epsl.2013.01.023

Bracciali, L., Najman, Y., Parrish, R. R., Akhter, S. H., & Millar, I. (2015). The Brahmaputra tale of tectonics and erosion: Early Miocene river capture in the Eastern Himalaya. Earth and Planetary Science Letters, 415, 25–37.

Buckman, S., Aitchison, J. C., Nutman, A. P., Bennett, V. C., Saktura, W. M., Walsh, J. M., … Hidaka, H. (2018). The Spongtang Massif in Ladakh, NW Himalaya: an Early Cretaceous record of spontaneous, intra-oceanic subduction initiation in the Neotethys. Gondwana Research, 63, 226–249.

Butler, R. F. (1992). Paleomagnetic Stability. PALEOMAGNETISM: Magnetic Domains to Geologic Terranes, 5, 81–84.

Cai, F., Ding, L., Laskowski, A. K., Kapp, P., Wang, H., Xu, Q., & Zhang, L. (2016). Late Triassic paleogeographic reconstruction along the Neo–Tethyan Ocean margins, southern Tibet. Earth and Planetary Science Letters, 435, 105–114. https://doi.org/10.1016/j.epsl.2015.12.027

Cai, F., Ding, L., Zhang, Q., Orme, D. A., Wei, H., Li, J., … Sein, K. (2019). Initiation and evolution of forearc basins in the Central Myanmar Depression. GSA Bulletin. https://doi.org/10.1130/B35301.1

Catlos, E. J., Pease, E. C., Dygert, N., Brookfield, M., Schwarz, W. H., Bhutani, R., … Schmitt, A. K. (2019). Nature, age and emplacement of the Spongtang ophiolite, Ladakh, NW India. Journal of the Geological Society, 176(2), 284–305.

Claude Rangin. (2017). Chapter 3 Active and recent tectonics of the Burma Platelet in Myanmar. Geological Society, London, Memoirs, 48(1), 53–64. https://doi.org/10.1144/M48.3

Curray, J. R. (2005). Tectonics and history of the Andaman Sea region. Journal of Asian Earth Sciences, 25(1), 187–232. https://doi.org/10.1016/j.jseaes.2004.09.001

Evans, D., Müller, W., Oron, S., & Renema, W. (2013). Eocene seasonality and seawater alkaline earth reconstruction using shallow-dwelling large benthic foraminifera. Earth and Planetary Science Letters, 381, 104–115.

Fareeduddin, A., & Dilek, Y. (2015). Structure and petrology of the Nagaland-Manipur Hill ophiolitic mélange zone. NE India: A Fossil Tethyan Subduction Channel at the India-Burma Plate Boundary: Episodes, 38, 298–314.

Fisher, R. (1953). Dispersion on a sphere. Proceedings of the Royal Society of London. Series A. Mathematical and Physical Sciences, 217(1130), 295–305.

Gardiner, N. J., Hawkesworth, C. J., Robb, L. J., Whitehouse, M. J., Roberts, N. M. W., Kirkland, C. L., & Evans, N. J. (2017). Contrasting Granite Metallogeny through the Zircon Record: A Case Study from Myanmar. Scientific Reports, 7(1). https://doi.org/10.1038/s41598-017-00832-2

Gardiner, N. J., Searle, M. P., Robb, L. J., & Morley, C. K. (2015). Neo-Tethyan magmatism and metallogeny in Myanmar – An Andean analogue? Journal of Asian Earth Sciences, 106, 197–215. https://doi.org/10.1016/j.jseaes.2015.03.015

Garzanti, E. (2019). The Himalayan Foreland Basin from collision onset to the present: a sedimentary–petrology perspective. Geological Society, London, Special Publications, SP483.17. https://doi.org/10.1144/SP483.17

Ghose, N. C., Chatterjee, N., & Fareeduddin. (2014). A Petrographic Atlas of Ophiolite: An example from the eastern India-Asia collision zone. Springer 234 pp.

Ghosh, B., Bandyopadhyay, D., & Morishita, T. (2017). Chapter 7 Andaman–Nicobar Ophiolites, India: origin, evolution and emplacement. Geological Society, London, Memoirs, 47(1), 95–110. https://doi.org/10.1144/M47.7

Godin, L., Grujic, D., Law, R. D., & Searle, M. P. (2006). Channel flow, ductile extrusion and exhumation in continental collision zones: an introduction. Geological Society, London, Special Publications, 268(1), 1–23.

Gough, A., Hall, R., & BouDagher-Fadel, M. K. (2020). Mid-Cenozoic fluvio-deltaic to marine environments of the Salin Sub-basin, Central Myanmar. Journal of Asian Earth Sciences, 104143. https://doi.org/10.1016/j.jseaes.2019.104143

Grimaldi, D. A., Engel, M. S., & Nascimbene, P. C. (2002). Fossiliferous Cretaceous Amber from Myanmar (Burma): Its Rediscovery, Biotic Diversity, and Paleontological Significance. American Museum Novitates, 3361, 1–71. https://doi.org/10.1206/0003-0082(2002)361<0001:FCAFMB>2.0.CO;2

Hall, R. (2012). Late Jurassic–Cenozoic reconstructions of the Indonesian region and the Indian Ocean. Tectonophysics, 570–571, 1–41. https://doi.org/10.1016/j.tecto.2012.04.021

Hansma, J., & Tohver, E. (2019). Paleomagnetism of Oligocene Hot Spot Volcanics in Central Queensland, Australia. Journal of Geophysical Research: Solid Earth, 124(7), 6280–6296. https://doi.org/10.1029/2019JB017639

Haproff, P. J., Odlum, M. L., Zuza, A. V., Yin, A., & Stockli, D. F. (2020). Structural and Thermochronologic Constraints on the Cenozoic Tectonic Development of the Northern Indo-Burma Ranges. Tectonics. https://doi.org/10.1029/2020TC006231

Haproff, P. J., Zuza, A. V., Yin, A., Harrison, T. M., Manning, C. E., Dubey, C. S., … Chen, J. (2019). Geologic framework of the northern Indo-Burma Ranges and lateral correlation of Himalayan-Tibetan lithologic units across the eastern Himalayan syntaxis. Geosphere. https://doi.org/10.1130/GES02054.1

Hla Htay, Khin Zaw, & Than Than Oo. (2017). Chapter 6 The mafic–ultramafic (ophiolitic) rocks of Myanmar. Geological Society, London, Memoirs, 48(1), 117–141. https://doi.org/10.1144/M48.6

Hrouda, F. (1982). Magnetic anisotropy of rocks and its application in geology and geophysics. Geophysical Surveys, 5(1), 37–82. https://doi.org/10.1007/BF01450244

Hu, X., Garzanti, E., Moore, T., & Raffi, I. (2015). Direct stratigraphic dating of India-Asia collision onset at the Selandian (middle Paleocene, 59$\pm$1 Ma). Geology, 43(10), 859–862.

Huang, H., Morley, R., Licht, A., Dupont-Nivet, G., Grímsson, F., Zetter, R., … Hoorn, C. (2020). Eocene palms from central Myanmar in a South-East Asian and global perspective: evidence from the palynological record. Botanical Journal of the Linnean Society. https://doi.org/10.1093/botlinnean/boaa038

l'Anson, A., Elders, C., & McHarg, S. (2019). Marginal fault systems of the Northern Carnarvon Basin: Evidence for multiple Palaeozoic extension events, North-West Shelf, Australia. Marine and Petroleum Geology, 101, 211–229. https://doi.org/10.1016/j.marpetgeo.2018.11.040

Jaeger, J.-J., Chavasseau, O., Lazzari, V., Soe, A. N., Sein, C., Le Maître, A., … Chaimanee, Y. (2019). New Eocene primate from Myanmar shares dental characters with African Eocene crown anthropoids. Nature Communications, 10(1), 1–10.

Jagoutz, O., Bouilhol, P., Schaltegger, U., & Müntener, O. (2019). The isotopic evolution of the Kohistan Ladakh arc from subduction initiation to continent arc collision. Geological Society, London, Special Publications, 483(1), 165–182.

Jagoutz, O., Royden, L., Holt, A. F., & Becker, T. W. (2015). Anomalously fast convergence of India and Eurasia caused by double subduction. Nature Geoscience, 8(6), 475–478. https://doi.org/10.1038/ngeo2418

Kellett, D. A., Grujic, D., Coutand, I., Cottle, J., & Mukul, M. (2013). The South Tibetan detachment system facilitates ultra rapid cooling of granulite-facies rocks in Sikkim Himalaya. Tectonics, 32(2), 252–270.

Khin, K. (1999). Marine transgression and regression in Miocene sequences of northern Pegu (Bago) Yoma, central Myanmar. Journal of Asian Earth Sciences, 17(3), 369–393.

Khin Zaw, Meffre, S., Takai, M., Suzuki, H., Burrett, C., Thaung Htike, … Maung Maung. (2014). The oldest anthropoid primates in SE Asia: Evidence from LA-ICP-MS U–Pb zircon age in the Late Middle Eocene Pondaung Formation, Myanmar. Gondwana Research, 26(1), 122–131. https://doi.org/10.1016/j.gr.2013.04.007

King, R. F. (1955). The remanent magnetism of artificially deposited sediments. Geophysical Journal International, 7(s3), 115–134.

Kirschvink, J. L. (1980). The least-squares line and plane and the analysis of palaeomagnetic data. Geophysical Journal International, 62(3), 699–718.

Koymans, M. R., Langereis, C. G., Pastor-Galán, D., & van Hinsbergen, D. J. (2016). Paleomagnetism. org: An online multi-platform open source environment for paleomagnetic data analysis. Elsevier.

Li, S., van Hinsbergen, D. J. J., Deng, C., Advokaat, E. L., & Zhu, R. (2018). Paleomagnetic Constraints From the Baoshan Area on the Deformation of the Qiangtang-Sibumasu Terrane Around the Eastern Himalayan Syntaxis. Journal of Geophysical Research: Solid Earth. https://doi.org/10.1002/2017JB015112

Li, Z., Ding, L., Zaw, T., Wang, H., Cai, F., Yao, W., … Yue, Y. (2020). Kinematic evolution of the West Burma block during and after India-Asia collision revealed by paleomagnetism. Journal of Geodynamics, 134, 101690. https://doi.org/10.1016/j.jog.2019.101690

Licht, A., Boura, A., De Franceschi, D., Ducrocq, S., Aung Naing Soe, & Jaeger, J.-J. (2014). Fossil woods from the late middle Eocene Pondaung Formation, Myanmar. Review of Palaeobotany and Palynology, 202, 29–46. https://doi.org/10.1016/j.revpalbo.2013.12.002

Licht, A., Boura, A., De Franceschi, D., Utescher, T., Sein, C., & Jaeger, J.-J. (2015). Late middle Eocene fossil wood of Myanmar: Implications for the landscape and the climate of the Eocene Bengal Bay. Review of Palaeobotany and Palynology, 216, 44–54. https://doi.org/10.1016/j.revpalbo.2015.01.010

Licht, A., Dupont-Nivet, G., Win, Z., Swe, H. H., Kaythi, M., Roperch, P., … Sein, K. (2019). Paleogene evolution of the Burmese forearc basin and implications for the history of India-Asia convergence. Geological Society of America Bulletin, 1(130), 20.

Licht, A., France-Lanord, C., Reisberg, L., Fontaine, C., Soe, A. N., & Jaeger, J.-J. (2013). A palaeo Tibet–Myanmar connection? Reconstructing the Late Eocene drainage system of central Myanmar using a multi-proxy approach. Journal of the Geological Society, 170(6), 929–939.

Licht, A., van Cappelle, M., Abels, H. A., Ladant, J.-B., Trabucho-Alexandre, J., France-Lanord, C., … Jaeger, J.-J. (2014). Asian monsoons in a late Eocene greenhouse world. Nature, 513(7519), 501–506. https://doi.org/10.1038/nature13704

Licht, A., Win, Z., Westerweel, J., Cogné, N., Morley, C., Chantraprasert, S., … Dupont-Nivet, G. (2020). Magmatic history of central Myanmar and implications for the evolution of the Burma Terrane. Gondwana Research. https://doi.org/10.1016/j.gr.2020.06.016

Lin, T.-H., Mitchell, A. H. G., Chung, S.-L., Tan, X.-B., Tang, J.-T., Oo, T., & Wu, F.-Y. (2019). Two parallel magmatic belts with contrasting isotopic characteristics from southern Tibet to Myanmar: zircon U–Pb and Hf isotopic constraints. Journal of the Geological Society, 176(3), 574–587. https://doi.org/10.1144/jgs2018-072

Liu, C.-Z., Chung, S.-L., Wu, F.-Y., Zhang, C., Xu, Y., Wang, J.-G., … Guo, S. (2016). Tethyan suturing in Southeast Asia: Zircon U-Pb and Hf-O isotopic constraints from Myanmar ophiolites. Geology, 44(4), 311–314. https://doi.org/10.1130/G37342.1

Liu, Y. M., Dai, J. G., Wang, C. S., Li, H. A., Wang, Q., & Zhang, L. L. (2020). Provenance and tectonic setting of Upper Triassic turbidites in the eastern Tethyan Himalaya: Implications for early-stage evolution of the Neo–Tethys. Earth-Science Reviews, 200, 103030.

Liu, Y., Tihelka, E., Yamamoto, S., Yin, Z., Huang, D., Tian, L., & Cai, C. (2020). The first fossil record of the rove beetle subfamily Protopselaphinae (Coleoptera: Staphylinidae) from mid-Cretaceous Burmese amber. Cretaceous Research, 110, 104416. https://doi.org/10.1016/j.cretres.2020.104416

Matthews, K. J., Maloney, K. T., Zahirovic, S., Williams, S. E., Seton, M., & Müller, R. D. (2016). Global plate boundary evolution and kinematics since the late Paleozoic. Global and Planetary Change, 146, 226–250. https://doi.org/10.1016/j.gloplacha.2016.10.002

Maung, H. (1987). Transcurrent movements in the Burma–Andaman Sea region. Geology, 15(10), 911. https://doi.org/10.1130/0091-7613(1987)15<911:TMITBS>2.0.CO;2

Maurin, T., & Rangin, C. (2009). Structure and kinematics of the Indo-Burmese Wedge: Recent and fast growth of the outer wedge: GROWTH OF THE OUTER INDO-BURMESE WEDGE. Tectonics, 28(2), n/a-n/a. https://doi.org/10.1029/2008TC002276

McFadden, P. L., & McElhinny, M. (1988). The combined analysis of remagnetisation circles and direct observation in palaeomagnetism. Earth and Planetary Science Letters, 87, 161–172.

Metcalfe, I. (2013). Gondwana dispersion and Asian accretion: Tectonic and palaeogeographic evolution of eastern Tethys. Journal of Asian Earth Sciences, 66, 1–33. https://doi.org/10.1016/j.jseaes.2012.12.020

Metcalfe, I. (2017). Tectonic evolution of Sundaland, 63, 35.

Métivier, F., Gaudemer, Y., Tapponnier, P., & Klein, M. (1999). Mass accumulation rates in Asia during the Cenozoic. Geophysical Journal International, 137(2), 280–318.

Mitchell, A. (2017). Geological Belts, Plate Boundaries, and Mineral Deposits in Myanmar. Elsevier.

Mitchell, A., Chung, S.-L., Oo, T., Lin, T.-H., & Hung, C.-H. (2012). Zircon U–Pb ages in Myanmar: Magmatic–metamorphic events and the closure of a neo-Tethys ocean? Journal of Asian Earth Sciences, 56, 1–23. https://doi.org/10.1016/j.jseaes.2012.04.019

Mitchell, A. H. G. (1993). Cretaceous–Cenozoic tectonic events in the western Myanmar (Burma)–Assam region. Journal of the Geological Society, 150(6), 1089–1102.

Morley, C. K. (2017a). Chapter 4 Cenozoic rifting, passive margin development and strike-slip faulting in the Andaman Sea: a discussion of established v. new tectonic models. Geological Society, London, Memoirs, 47(1), 27–50. https://doi.org/10.1144/M47.4

Morley, C. K. (2017b). Syn-kinematic sedimentation at a releasing splay in the northern Minwun Ranges, Sagaing Fault zone, Myanmar: significance for fault timing and displacement. Basin Research, 29, 684–700. https://doi.org/10.1111/bre.12201

Morley, C. K., & Alvey, A. (2015). Is spreading prolonged, episodic or incipient in the Andaman Sea? Evidence from deepwater sedimentation. Journal of Asian Earth Sciences, 98, 446–456. https://doi.org/10.1016/j.jseaes.2014.11.033

Morley, C. K., & Arboit, F. (2019). Dating the onset of motion on the Sagaing fault: Evidence fromdetrital zircon and titanite U-Pb geochronology from the NorthMinwun Basin, Myanmar. Geology. https://doi.org/10.1130/G46321.1

Morley, C. K., & Searle, M. (2017). Chapter 5 Regional tectonics, structure and evolution of the Andaman–Nicobar Islands from ophiolite formation and obduction to collision and back-arc spreading. Geological Society, London, Memoirs, 47(1), 51–74. https://doi.org/10.1144/M47.5

Morley, C. K., Tin Tin Naing, Searle, M., & Robinson, S. A. (2020). Structural and tectonic development of the Indo-Burma ranges. Earth-Science Reviews, 200, 102992. https://doi.org/10.1016/j.earscirev.2019.102992

Müller, R. D., Cannon, J., Qin, X., Watson, R. J., Gurnis, M., Williams, S., … Zahirovic, S. (2018). GPlates: Building a virtual Earth through deep time. Geochemistry, Geophysics, Geosystems, 19(7), 2243–2261.

Müller, R. D., Zahirovic, S., Williams, S. E., Cannon, J., Seton, M., Bower, D. J., … Gurnis, M. (2019). A global plate model including lithospheric deformation along major rifts and orogens since the Triassic. Tectonics, 2018TC005462. https://doi.org/10.1029/2018TC005462

Naing, T. T., Bussien, D. A., Winkler, W. H., Nold, M., & Von Quadt, A. (2014). Provenance study on Eocene–Miocene sandstones of the Rakhine Coastal Belt, Indo-Burman Ranges of Myanmar: geodynamic implications. Geological Society, London, Special Publications, 386(1), 195–216. https://doi.org/10.1144/SP386.10

Najman, Y., Mark, C., Barfod, D. N., Carter, A., Parrish, R., Chew, D., & Gemignani, L. (2019). Spatial and temporal trends in exhumation of the Eastern Himalaya and syntaxis as determined from a multitechnique detrital thermochronological study of the Bengal Fan. GSA Bulletin, 131(9–10), 1607–1622. https://doi.org/10.1130/B35031.1

Najman, Y., Sobel, E. R., Millar, I., Stockli, D. F., Govin, G., Lisker, F., … Kahn, A. (2020). The exhumation of the Indo-Burman Ranges, Myanmar. Earth and Planetary Science Letters, 530, 115948. https://doi.org/10.1016/j.epsl.2019.115948

Oo, T., Hlaing, T., & Htay, N. (2002). Permian of Myanmar. Journal of Asian Earth Sciences, 20(6), 683–689. https://doi.org/10.1016/S1367-9120(01)00074-8

Pedersen, R. B., Searle, M. P., Carter, A., & Bandopadhyay, P. C. (2010). U–Pb zircon age of the Andaman ophiolite: implications for the beginning of subduction beneath the Andaman–Sumatra arc. Journal of the Geological Society, 167(6), 1105–1112.

Petterson, M. G. (2019). The plutonic crust of Kohistan and volcanic crust of Kohistan–Ladakh, north Pakistan/India: lessons learned for deep and shallow arc processes. Geological Society, London, Special Publications, 483(1), 123–164. https://doi.org/10.1144/SP483.4

Pivnik, D. A., Nahm, J., Tucker, R. S., Smith, G. O., Nyein, K., Nyunt, M., & Maung, P. H. (1998). Polyphase Deformation in a Fore-Arc/Back-Arc Basin, Salin Subbasin, Myanmar (Burma). AAPG Bulletin, 82(10), 1837–1856.

Plunder, A., Bandyopadhyay, D., Ganerød, M., Advokaat, E. L., Ghosh, B., Bandopadhyay, P., & van Hinsbergen, D. J. (2020). History of subduction polarity reversal during arc-continent collision: Constraints from the Andaman ophiolite and its metamorphic sole. Tectonics, 39(6), e2019TC005762.

Poinar, G. (2018). Burmese amber: evidence of Gondwanan origin and Cretaceous dispersion. Historical Biology, 1–6. https://doi.org/10.1080/08912963.2018.1446531

Racey, A. (2018). Exploration in the Central Burma Depression, Onshore Myanmar.

Rangin, C. (2018). The western Sunda basins and the India/Asia collision: an atlas. Geotecto, Paris, France.

Rangin, C., Maurin, T., & Masson, F. (2013). Combined effects of Eurasia/Sunda oblique convergence and East-Tibetan crustal flow on the active tectonics of Burma. Journal of Asian Earth Sciences, 76, 185–194. https://doi.org/10.1016/j.jseaes.2013.05.018

Rasnitsyn, A. P., & Öhm-Kühnle, C. (2018). Three new female Aptenoperissus from mid-Cretaceous Burmese amber (Hymenoptera, Stephanoidea, Aptenoperissidae): Unexpected diversity of paradoxical wasps suggests insular features of source biome. Cretaceous Research, 91, 168–175. https://doi.org/10.1016/j.cretres.2018.06.004

Replumaz, A., Guillot, S., Villaseñor, A., & Negredo, A. M. (2013). Amount of Asian lithospheric mantle subducted during the India/Asia collision. Gondwana Research, 24(3–4), 936–945. https://doi.org/10.1016/j.gr.2012.07.019

Replumaz, A., Negredo, A. M., Guillot, S., & Villaseñor, A. (2010). Multiple episodes of continental subduction during India/Asia convergence: Insight from seismic tomography and tectonic reconstruction. Tectonophysics, 483(1–2), 125–134. https://doi.org/10.1016/j.tecto.2009.10.007

Replumaz, A., & Tapponnier, P. (2003). Reconstruction of the deformed collision zone Between India and Asia by backward motion of lithospheric blocks: BLOCKS RECONSTRUCTION OF ASIA. Journal of Geophysical Research: Solid Earth, 108(B6). https://doi.org/10.1029/2001JB000661

Ridd, M. F., & Watkinson, I. (2013). The Phuket-Slate Belt terrane: tectonic evolution and strike-slip emplacement of a major terrane on the Sundaland margin of Thailand and Myanmar. Proceedings of the Geologists' Association, 124(6), 994–1010. https://doi.org/10.1016/j.pgeola.2013.01.007

Roberts, A. P. (2015). Magnetic mineral diagenesis. Earth-Science Reviews, 151, 1–47. https://doi.org/10.1016/j.earscirev.2015.09.010

Robinson, R. A., Brezina, C. A., Parrish, R. R., Horstwood, M. S., Oo, N. W., Bird, M. I., … Zaw, K. (2014). Large rivers and orogens: The evolution of the Yarlung Tsangpo–Irrawaddy system and the eastern Himalayan syntaxis. Gondwana Research, 26(1), 112–121.

Roperch, P., & Taylor, G. K. (1986). The importance of gyromagnetic remanence in alternating field demagnetization. Some new data and experiments on GRM and RRM. Geophysical Journal International, 87(3), 949–965.

Roperch, P., Westerweel, J., … (In prep.). The Burma terrane related to India: Evidence from the U-Pb zircons in Late Cretaceous-Paleogene sediments from the Central Myanmar Basins. Abstract originally submitted to RST 2020 Lyon (Postponed to 2021).

Royden, L. H., Burchfiel, B. C., & van der Hilst, R. D. (2008). The Geological Evolution of the Tibetan Plateau. Science, 321(5892), 1054–1058. https://doi.org/10.1126/science.1155371

Sautter, B., Pubellier, M., Králiková Schlögl, S., Matenco, L., Andriessen, P., & Mathew, M. (2019). Exhumation of west Sundaland: A record of the path of India? Earth-Science Reviews, 198, 102933. https://doi.org/10.1016/j.earscirev.2019.102933

Searle, M. P., Garber, J. M., Hacker, B. R., Htun, K., Gardiner, N. J., Waters, D. J., & Robb, L. J. (2020). Timing of syenite-charnockite magmatism and ruby-and sapphire metamorphism in the Mogok valley region, Myanmar. Tectonics, e2019TC005998.

Searle, M. P., Morley, C. K., Waters, D. J., Gardiner, N. J., Htun, U. K., Than Than Nu, & Robb, L. J. (2017). Chapter 12 Tectonic and metamorphic evolution of the Mogok Metamorphic and Jade Mines belts and ophiolitic terranes of Burma (Myanmar). Geological Society, London, Memoirs, 48(1), 261–293. https://doi.org/10.1144/M48.12

Searle, M. P., Noble, S. R., Cottle, J. M., Waters, D. J., Mitchell, A. H. G., Hlaing, T., & Horstwood, M. S. A. (2007). Tectonic evolution of the Mogok metamorphic belt, Burma (Myanmar) constrained by U-Th-Pb dating of metamorphic and magmatic rocks: U-TH-PB AGES OF MOGOK BELT. Tectonics, 26(3), n/a-n/a. https://doi.org/10.1029/2006TC002083

Sengupta, S., Ray, K. K., Acharyya, S. K., & De Smeth, J. B. (1990). Nature of ophiolite occurrences along the eastern margin of the Indian plate and their tectonic significance. Geology, 18(5), 439–442.

Seton, M., Müller, R. D., Zahirovic, S., Gaina, C., Torsvik, T., Shephard, G., … Maus, S. (2012). Global continental and ocean basin reconstructions since 200 Ma. Earth-Science Reviews, 113(3–4), 212–270.

Sevastjanova, I., Hall, R., Rittner, M., Paw, S. M. T. L., Naing, T. T., Alderton, D. H., & Comfort, G. (2016). Myanmar and Asia united, Australia left behind long ago. Gondwana Research, 32, 24–40. https://doi.org/10.1016/j.gr.2015.02.001

Shen, F., Royden, L. H., & Burchfiel, B. C. (2001). Large-scale crustal deformation of the Tibetan Plateau. Journal of Geophysical Research: Solid Earth, 106(B4), 6793–6816. https://doi.org/10.1029/2000JB900389

Singh, A. K., Chung, S.-L., Bikramaditya, R. K., & Lee, H. Y. (2017). New U–Pb zircon ages of plagiogranites from the Nagaland–Manipur Ophiolites, Indo-Myanmar Orogenic Belt, NE India. Journal of the Geological Society, 174(1), 170–179.

Socquet, A., Vigny, C., Chamot-Rooke, N., Simons, W., Rangin, C., & Ambrosius, B. (2006). India and Sunda plates motion and deformation along their boundary in Myanmar determined by GPS: GPS INDIA-SUNDA MOTION, MYANMAR STRAIN. Journal of Geophysical Research: Solid Earth, 111(B5), n/a-n/a. https://doi.org/10.1029/2005JB003877

Srisuriyon, K., & Morley, C. K. (2014). Pull-apart development at overlapping fault tips: Oblique rifting of a Cenozoic continental margin, northern Mergui Basin, Andaman Sea. Geosphere, 10(1), 80–106. https://doi.org/10.1130/GES00926.1

Tardif, D., Fluteau, F., Donnadieu, Y., Le Hir, G., Ladant, J.-B., Sepulchre, P., … Dupont-Nivet, G. (2020). The origin of Asian monsoons: a modelling perspective. Climate of the Past, 16(3), 847–865. https://doi.org/10.5194/cp-16-847-2020

Tauxe, L. (2010). Essentials of paleomagnetism. Univ of California Press.

Tauxe, L., & Kent, D. V. (1984). Properties of a detrital remanence carried by haematite from study of modern river deposits and laboratory redeposition experiments. Geophysical Journal of the Royal Astronomical Society, 76(3), 543–561.

Tauxe, L., & Watson, G. S. (1994). The fold test: an eigen analysis approach. Earth and Planetary Science Letters, 122(3–4), 331–341.

Thein, M., & Maung, M. (2017). The Eastern (Back-arc) Basin of Central Myanmar: Basement rocks, lithostratigraphic units, palaeocurrents, provenance and developmental history. Geological Society, London, Memoirs, 48(1), 169–183.

Tong, Y.-B., Yang, Z., Zheng, L.-D., Xu, Y.-L., Wang, H., Gao, L., & Hu, X.-Z. (2013). Internal crustal deformation in the northern part of Shan-Thai Block: New evidence from paleomagnetic results of Cretaceous and Paleogene redbeds. Tectonophysics, 608, 1138–1158. https://doi.org/10.1016/j.tecto.2013.06.031

Torsvik, T. H., Van der Voo, R., Preeden, U., Mac Niocaill, C., Steinberger, B., Doubrovine, P. V., … Cocks, L. R. M. (2012). Phanerozoic polar wander, palaeogeography and dynamics. Earth-Science Reviews, 114(3–4), 325–368. https://doi.org/10.1016/j.earscirev.2012.06.007

Ueno, K., Thein, M., & Barber, A. J. (2016). Permian fusuline fauna from the Minwun Range, Central Myanmar. In 5th Symposium of the International Geosciences Programme (IGCP) (Vol. 589, pp. 27–28).

United Nations. (1978a). Geology and exploration geochemistry of the Pinlebu-Banmauk area, Sagaing Division, northern Burma. Technical Report No. 2. DP/UN/BUR-72-002. Geological Survey and Exploration Project, United Nations Development Programme, New York, 66.

van Hinsbergen, D. J. J., Kapp, P., Dupont-Nivet, G., Lippert, P. C., DeCelles, P. G., & Torsvik, T. H. (2011). Restoration of Cenozoic deformation in Asia and the size of Greater India: RESTORING CENOZOIC ASIAN DEFORMATION. Tectonics, 30(5), n/a-n/a. https://doi.org/10.1029/2011TC002908

van Hinsbergen, D. J. J., Lippert, P. C., Li, S., Huang, W., Advokaat, E. L., & Spakman, W. (2018). Reconstructing Greater India: Paleogeographic, kinematic, and geodynamic perspectives. Tectonophysics. https://doi.org/10.1016/j.tecto.2018.04.006

Vannay, J.-C., Grasemann, B., Rahn, M., Frank, W., Carter, A., Baudraz, V., & Cosca, M. (2004). Miocene to Holocene exhumation of metamorphic crustal wedges in the NW Himalaya: Evidence for tectonic extrusion coupled to fluvial erosion. Tectonics, 23(1).

Wang, J.-G., Wu, F.-Y., Garzanti, E., Hu, X., Ji, W.-Q., Liu, Z.-C., & Liu, X.-C. (2016). Upper Triassic turbidites of the northern Tethyan Himalaya (Langjiexue Group): The terminal of a sediment-routing system sourced in the Gondwanide Orogen. Gondwana Research, 34, 84–98. https://doi.org/10.1016/j.gr.2016.03.005

Wang, J.-G., Wu, F.-Y., Tan, X.-C., & Liu, C.-Z. (2014). Magmatic evolution of the Western Myanmar Arc documented by U–Pb and Hf isotopes in detrital zircon. Tectonophysics, 612–613, 97–105. https://doi.org/10.1016/j.tecto.2013.11.039

Westerweel, J., Licht, A., Cogné, N., Roperch, P., Dupont-Nivet, G., Thi, M. K., … Aung, D. W. (2020). Burma Terrane collision and northward indentation in the Eastern Himalayas recorded in the Eocene - Miocene Chindwin Basin (Myanmar). Tectonics. https://doi.org/10.1029/2020TC006413

Westerweel, J., Roperch, P., Licht, A., Dupont-Nivet, G., Win, Z., Poblete, F., … Aung, D. W. (2019). Burma Terrane part of the Trans-Tethyan arc during collision with India according to palaeomagnetic data. Nature Geoscience. https://doi.org/10.1038/s41561-019-0443-2

Yao, W., Ding, L., Cai, F., Wang, H., Xu, Q., & Zaw, T. (2017). Origin and tectonic evolution of upper Triassic Turbidites in the Indo-Burman ranges, West Myanmar. Tectonophysics, 721, 90–105. https://doi.org/10.1016/j.tecto.2017.09.016

Yui, T.-F., Fukoyama, M., Iizuka, Y., Wu, C.-M., Wu, T.-W., Liou, J. G., & Grove, M. (2013). Is Myanmar jadeitite of Jurassic age? A result from incompletely recrystallized inherited zircon. Lithos, 160–161, 268–282. https://doi.org/10.1016/j.lithos.2012.12.011

Zahirovic, S., Matthews, K. J., Flament, N., Müller, R. D., Hill, K. C., Seton, M., & Gurnis, M. (2016). Tectonic evolution and deep mantle structure of the eastern Tethys since the latest Jurassic. Earth-Science Reviews, 162, 293–337. https://doi.org/10.1016/j.earscirev.2016.09.005

Zaman, H., & Torii, M. (1999). Palaeomagnetic study of Cretaceous red beds from the eastern Hindukush ranges, northern Pakistan: palaeoreconstruction of the Kohistan-Karakoram composite unit before the India-Asia collision. Geophysical Journal International, 136(3), 719–738. https://doi.org/10.1046/j.1365-246x.1999.00757.x

Zhang, J., Xiao, W., Windley, B. F., Cai, F., Sein, K., & Naing, S. (2017). Early Cretaceous wedge extrusion in the Indo-Burma Range accretionary complex: implications for the Mesozoic subduction of Neotethys in SE Asia. International Journal of Earth Sciences, 106(4), 1391–1408.

Zhang, P., Mei, L., Hu, X., Li, R., Wu, L., Zhou, Z., & Qiu, H. (2017). Structures, uplift, and magmatism of the Western Myanmar Arc: Constraints to mid-Cretaceous-Paleogene tectonic evolution of the western Myanmar continental margin. Gondwana Research, 52, 18–38. https://doi.org/10.1016/j.gr.2017.09.002

Zhang, X., Chung, S.-L., Lai, Y.-M., Ghani, A. A., Murtadha, S., Lee, H.-Y., & Hsu, C. (2019). A 6000-km-long Neo-Tethyan arc system with coherent magmatic flare-ups and lulls in South Asia. Geology, 47(6), 4.

Zheng, D., Chang, S.-C., Perrichot, V., Dutta, S., Rudra, A., Mu, L., … Wang, B. (2018). A Late Cretaceous amber biota from central Myanmar. Nature Communications, 9(1), 3170. https://doi.org/10.1038/s41467-018-05650-2

Zijderveld, J. D. A. (1967). AC demagnetization of rocks: Analysis of results, Methods in Paleomagnetism DW Collinson, KM Creer, SK Runcorn, 254–286. Elsevier, New York.

Supplementary figures

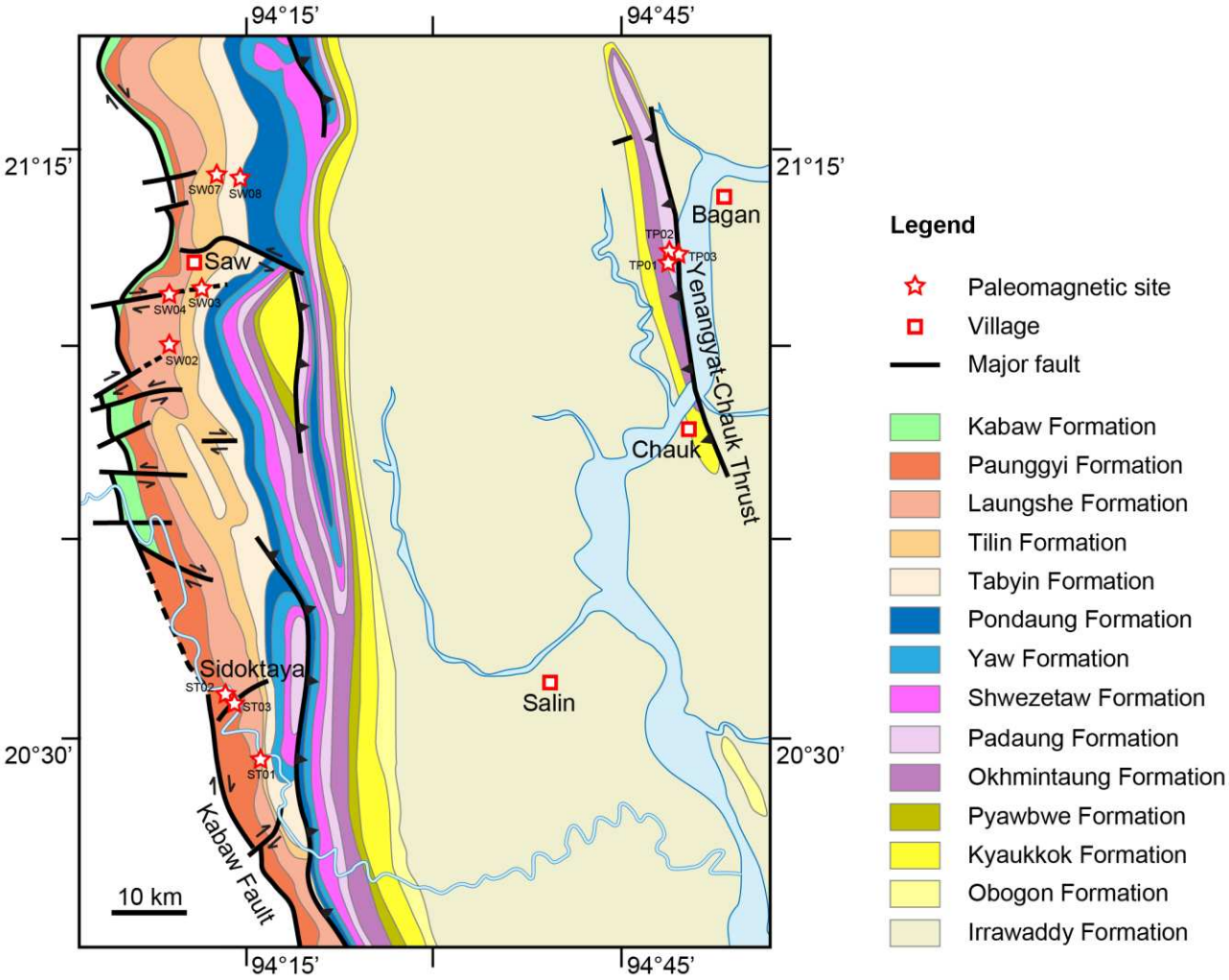

Figure 6.S1: *Geological map of part of the paleomagnetic sampling area from this study in the Minbu Basin that highlights the regional tectonic complexities around Sidoktaya, Saw and the Tantkyitaung Pagoda (after Pivnik et al., 1998).*

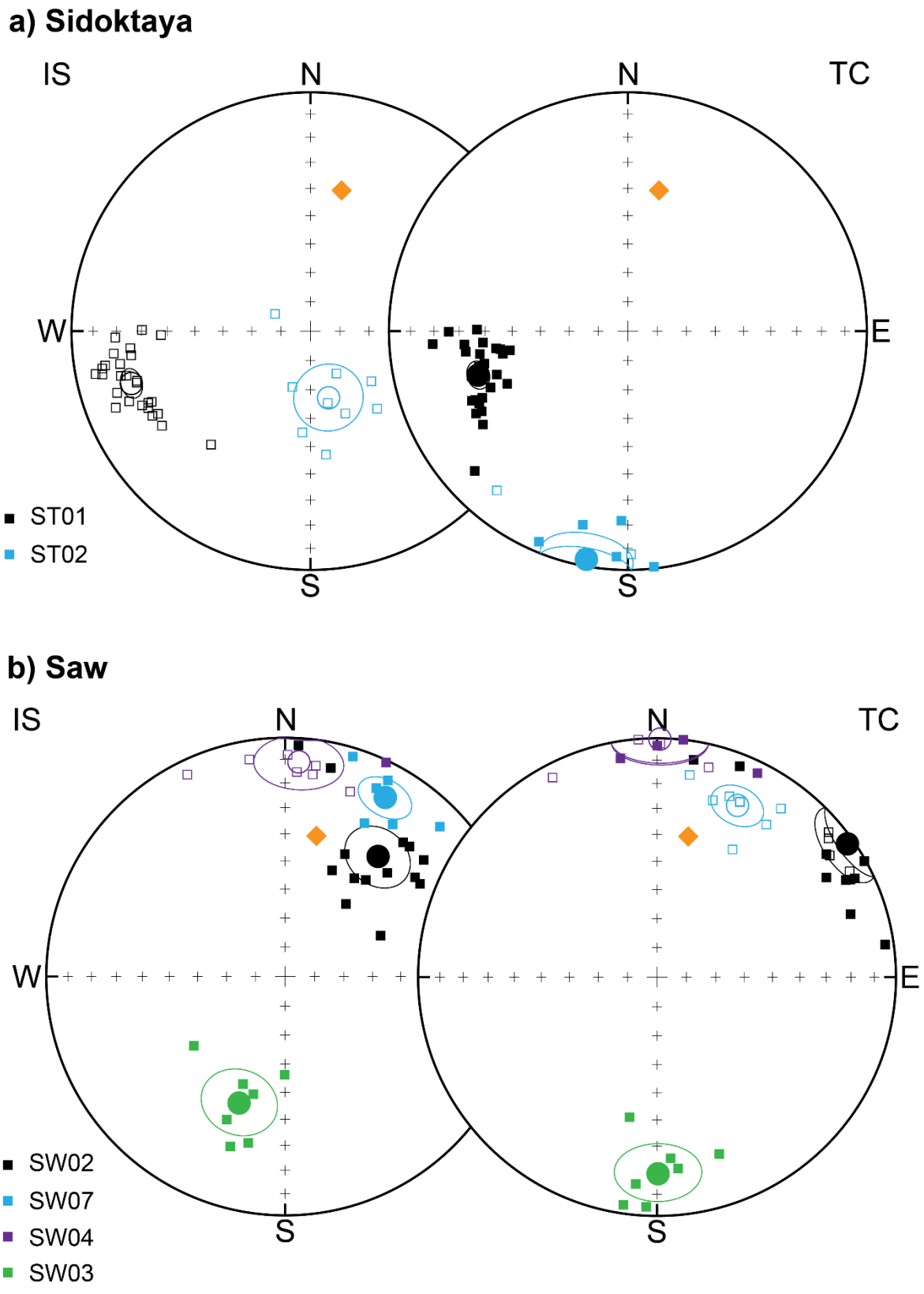

Figure 6.S2: *Equal-area projections of interpreted ChRM directions (squares) from the latest Paleocene – middle Eocene sites around Sidoktaya and Saw. Mean directions are shown as well (circles).*

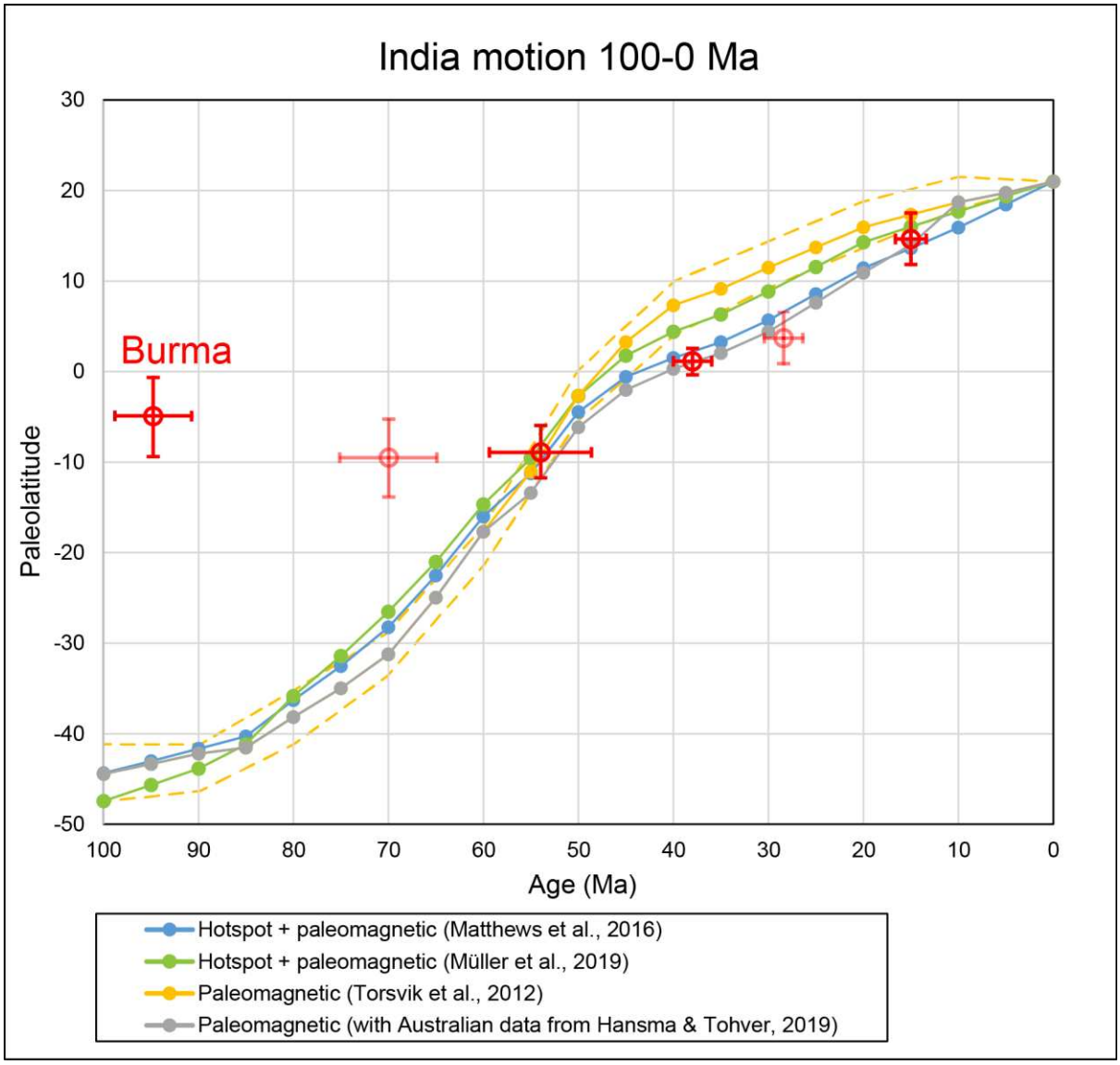

Figure 6.S3: *Absolute plate motion of India from 100-0 Ma using different reference frames, illustrating the large differences in paleolatitudes during the time period of 50-20 Ma crucial for the India-Asia collision (References: Hansma & Tohver, 2019; Matthews et al., 2016; Müller et al., 2019; Torsvik et al., 2012).*

Chapter 7: Other paleomagnetic sampling

Fossil shells in the Shwezetaw Formation, Minbu Basin.
(Salin, Myanmar, Fieldwork January 2019)

1. Introduction

In addition to the paleomagnetic results provided in Chapters 4-6 of this thesis, more sites were sampled in other key locations in Myanmar (Fig. 3.3, Table 7.1). Unfortunately, these remaining sites were unusable for publication due to either bad demagnetization quality, age uncertainties, weathering or deformation. The following sections will describe the importance of sampling each of the unused localities, and then the difficulties in interpreting their results (For paleomagnetic methodology, see Chapter 3).

Name	Coordinates (Lat/Lon)	Formation	Age	Lithology	Bedding (Strike/Dip)	N
Kawlin (Wuntho Ranges)						
MY54	23.05050°/95.83250°	Shwedaung Formation	Triassic?	metasediments, metavolcanics	???/??	11
Kalay (Indo-Burman Ranges)						
PC01	23.19694°/93.93750°	Pane Chaung Formation	Triassic	metasandstones	312/57	3
PC02	23.19870°/93.93512°	Falam Formation	Upper Cretaceous	turbidites	325/35	10
PC03	23.21744°/93.81111°	Falam Formation	Upper Cretaceous	turbidites	336/36	10
PC04	23.22091°/93.81833°	Falam Formation	Upper Cretaceous	turbidites	205/18	10
PC05	23.22850°/93.82176°	Falam Formation	Upper Cretaceous	turbidites	229/39	14
PC06	23.22321°/93.82116°	Falam Formation	Upper Cretaceous	turbidites	158/39	16
PC07	23.19728°/93.80051°	Falam Formation	Upper Cretaceous	turbidites	283/29	12
PC08	23.21754°/93.87026°	Falam Formation	Upper Cretaceous	turbidites	354/34	7
PC09	22.98148°/93.96958°	Falam Formation	Upper Cretaceous	turbidites	320/78	14
PC10	23.05050°/95.83250°	Western Belt Ophiolite	Upper Cretaceous	ophiolitic mafic volcanics	???/??	12
PC11	23.05050°/95.83250°	Western Belt Ophiolite	Upper Cretaceous	ophiolitic mafic volcanics	???/??	3
Ngape (Indo-Burman Ranges)						
OP01	23.19694°/93.93750°	Western Belt Ophiolite	Upper Cretaceous	serpentinized ophiolitic rocks	???/??	9
OP02	23.19694°/93.93750°	Western Belt Ophiolite	Upper Cretaceous	serpentinized ophiolitic rocks	???/??	9
OP03	23.19694°/93.93750°	Western Belt Ophiolite	Upper Cretaceous	serpentinized ophiolitic rocks	???/??	10
OP04	23.19694°/93.93750°	Western Belt Ophiolite	UpperCretaceous	serpentinized ophiolitic rocks	???/??	9
Datkon (Minbu Basin)						
DK01	19.96313°/94.57194°	Yaw Formation	Late Eocene	limestones	353/11	10
DK02	20.10408°/94.41917°	Paunggyi Formation	Paleocene	sandstones	330/60	12
DK03	20.10000°/94.42389°	Paunggyi Formation	Paleocene	tuffs, volcaniclastics, sandstones	332/60	15
DK04	20.09975°/94.42350°	Paunggyi Formation	Paleocene	mudstones	332/60	8
DK05	20.09975°/94.42265°	Paunggyi Formation	Paleocene	sandstones	324/54	9
DK06	20.12387°/94.38710°	Paunggyi Formation	Paleocene	sandstones	353/35	11
DK07	20.26703°/94.32644°	Paunggyi Formation	Paleocene	tuffs	000/40	10
Sidoktaya (Minbu Basin)						
ST03	20.47892°/94.24972°	Paunggyi Formation	Paleocene – lower Eocene	tuffs	252/113	7
Saw (Minbu Basin)						
SW01	21.14497°/94.16137°	Tilin Formation	Middle Eocene	greyish siltstones	005/57	36
SW05	21.14465°/94.16077°	Tilin Formation	Middle Eocene	greyish siltstones	335/40	10
Shwezetaw Pagoda (Minbu Basin)						
SP00	20.04186°/94.58561°	Shwezetaw Formation	lower Oligocene	mudstones, siltstones, sandstones	331/40	63
YP00	20.04186°/94.58561°	Yaw Formation	upper Eocene	mudstones	331/40	19

Table 7.1: *Paleomagnetic sampling of all sites discussed in this chapter. Abbreviations: N = number of samples per site.*

2. Results

2.1. Burma Terrane basement and Indo-Burman Ranges

In previous chapters (Chapter 2: Sections 2.2 and 3.3, Chapter 6), the ongoing debate on the origin of the Burma Terrane (BT) was already described in detail. Briefly, earlier studies advocated a Sibumasu / Cathaysia origin (e.g. Barber & Crow, 2009; Sevastjanova et al., 2016), while more recent studies propose a Gondwana / Argoland origin instead (e.g. Morley et al., 2020; Yao et al., 2017). Both arguments are based mainly on provenance results from detrital U-Pb zircon dating. Moreover, there is a possibility that the Indo-Burman Ranges (IBR) constituted a separate block (Mount Victoria Block or Mawgyi Nappe) that was accreted to the BT either in the Early Cretaceous (Barber & Crow, 2009; Zhang et al., 2017) or in the Late Cretaceous to Paleogene (Acharyya, 2007; Gibbons et al., 2015; Rangin et al., 2013; Searle et al., 2017). Paleomagnetic results will provide first-order constraints on the origin of these blocks and their position with respect to each other, making high quality paleomagnetic results potentially extremely useful in solving this debate.

To this end, one site in the Triassic Shwedaung Formation metavolcaniclastics of the Wuntho Ranges basement (MY54) was acquired near the township of Kawlin. In addition, three oriented hand samples in the Triassic Pane Chaung Formation metasandstones of the IBR (PC01), and eight sites in the Upper Cretaceous Falam Formation turbidites of the IBR were acquired (PC02-PC09), respectively on the road from Kalay to Falam (Table 7.1, Fig. 7.1).

The magnetic properties on hysteresis plots from all samples show strongly paramagnetic behaviour (Fig. 7.2), suggesting a relatively low concentration of ferromagnetic minerals such as magnetite. This could correspond to intense chemical weathering of the sources of these lithologies, potentially enhanced by sediment reworking, or initial low magnetite content of the source units (Roberts, 2015). Yet, individual samples often exhibit stable demagnetizations as visualized in orthogonal demagnetization plots (Fig. 7.3a-c), although occasionally with multiple components. However, there are significant differences in Characteristic Remanent Magnetization (ChRM) directions between different samples or even between two specimens from the same sample, as exemplified by two specimens of sample PC0712 from the Falam Formation (Fig. 7.3b-c). Many samples also show overprint of the present-day field. These characteristics suggest that the magnetic properties of these samples was strongly influenced by (chemical) alteration. In the case of MY54 (Shwedaung Formation), there is no clear bedding constraint either. For these reasons, interpretation of these paleomagnetic directions becomes problematic.

Furthermore, the ages of the all three formations discussed here are not well-determined. The Triassic age of the Pane Chaung Formation is based on the rare occurrence of *Halobia* fossils (United

Nations, 1978a; Bannert et al., 2011; Mitchell, 2017), as well as on Late Triassic to Early Jurassic detrital zircon ages (Sevastjanova et al., 2016; Yao et al., 2017). However, the majority of this formation was identified based on lithological correlation (Morley et al., 2020). The Shwedaung Formation is even more poorly investigated; its Triassic age is based only on a tentative correlation with the distant Pane Chaung Formation (United Nations, 1978a; Mitchell, 2017). Finally, the Upper Cretaceous (Campanian – Maastrichtian; Mitchell, 2017) age of the Falam Formation flysch is also based on rare fossils, but it is entirely possible this formation is as old as the Lower Jurassic without a depositional gap with the underlying Pane Chaung Formation (Morley et al., 2020). Interestingly, several sites of the Falam Formation exhibit similar paleomagnetic directions with low inclinations as the Eocene results from the Central Myanmar Basins (CMB) (Chapters 4 and 6). It is possible that these sites were remagnetized during the postulated early late Eocene uplift event in the IBR (Chapter 5; Licht et al., 2019; Morley et al., 2020; Najman et al., 2020).

Figure 7.1: *Representative field pictures of localities discussed in this chapter.*

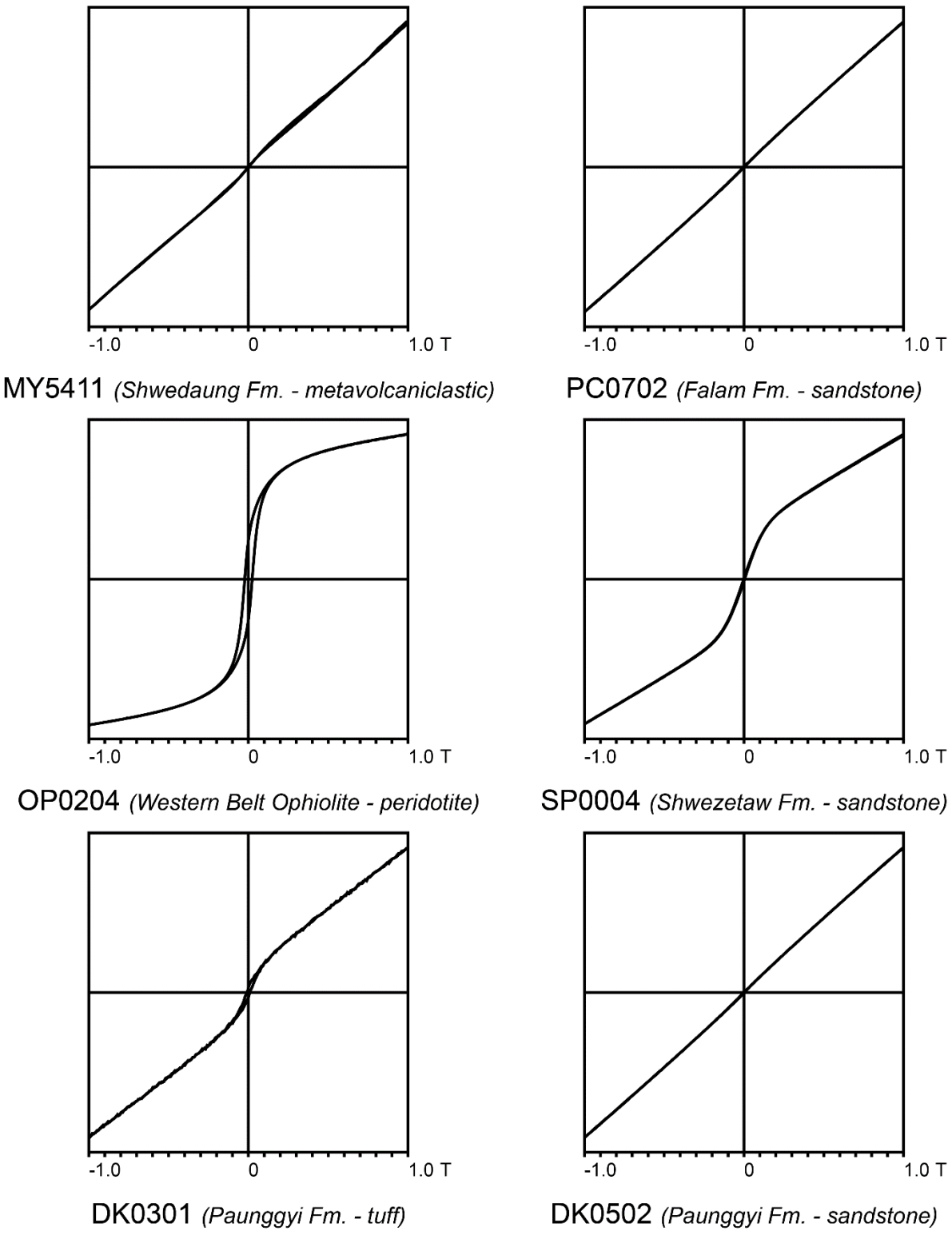

Figure 7.2: *Representative hysteresis plots from sites discussed in this chapter.*

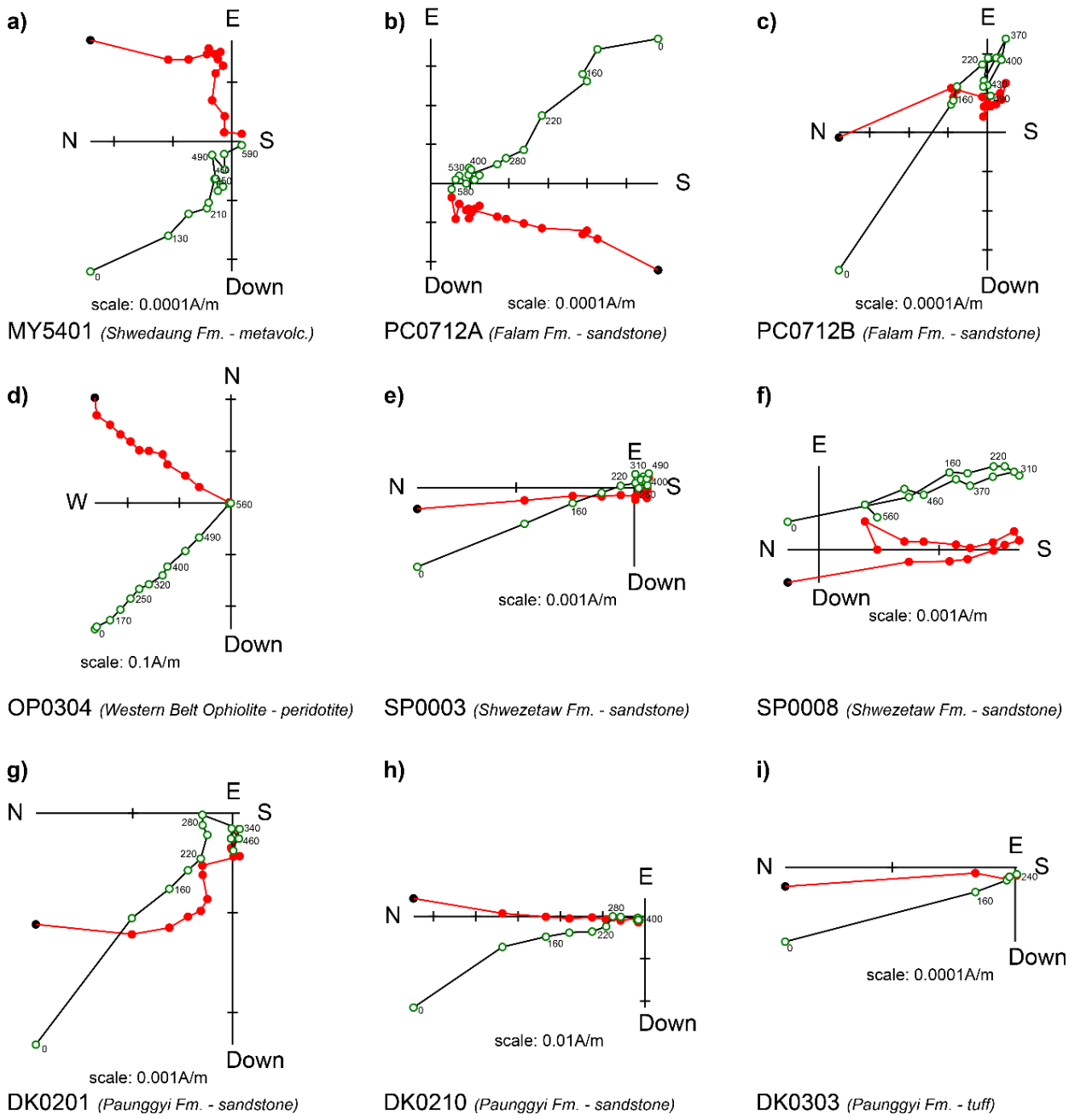

Figure 7.3: *Representative orthogonal demagnetization plots from sites discussed in this chapter.*

2.2. Western Belt Ophiolite

The Western Belt Ophiolite (WBO) forms the western limit of the BT. However, its origin, manner and timing of emplacement are subject to debate, as it either represents slices of accretionary material or a suture with the postulated Mount Victoria Block (see also Chapter 2: Section 3, Chapter 7: Section 2.1; Morley et al., 2020). The best age constraint comes from its metamorphic sole with an early Late Cretaceous age (Liu et al., 2016). Therefore, paleomagnetic constraints on the WBO could provide information on the location of its emplacement, which has important implications for the tectonic history of both the BT and the hypothetical Mount Victoria Block.

We drilled four sites (OP) in a small valley crosscutting the WBO in the IBR near the township of Ngape (Fig. 7.1; Table 7.1). A full ophiolitic sequence was not preserved here, field observations and images from thin sections under an optical microscope show that the sampled lithologies represent emplaced slices of serpentinized ophiolitic rocks (Fig. 7.4). Hysteresis plots, high NRM values of ~0.1-1.0 A/m, and promising stable demagnetizations up to 580°C (Figs. 7.2 and 7.3) show that magnetizations were predominantly carried by pseudo-single domain magnetite (Tauxe, 2010). Unfortunately, there are no constraints on bedding in this highly deformed part of the IBR. It is likely that the ophiolitic slices were tilted during thrusting. The closest bedding constraint comes from sedimentary site DK06 (Table 7.1, Section 2.3), ~500m east of site OP01 at the bottom of the section. The transition between DK06 and OP01 is obscured by soil and Quaternary conglomerates, therefore possibly covering a faulted or folded contact. In addition, thin sections (Fig. 7.4) show an abundance of hydrothermal veining. This can be either related to serpentinization during the formation of oceanic lithosphere or younger chemical alteration due to tectonic deformation. High NRM and susceptibility values as well as pseudo-domain magnetite are indicative of serpentinization (Oufi et al., 2002). However, many ChRM directions are close to the present-day field (Fig. 7.5a) even after correcting with the DK06 sedimentary bedding (Fig. 7.5b), suggesting that the magnetic signal from this lithology might have been overprinted by the intense posterior Oligecene-recent exhumation and deformation events in the IBR (Allen et al., 2008; Najman et al., 2020; Maurin & Rangin, 2009).

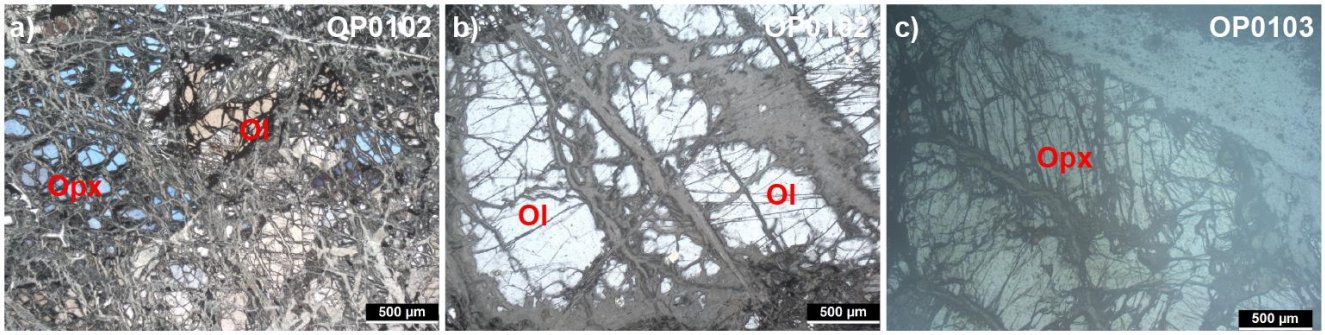

Figure 7.4: *Representative optical microscope images of thin sections from the Western Belt Ophiolite (sites OP).*

In addition, two sites (PC10 and PC11) were obtained in the ophiolitic mélange that is exposed at the spillway area of the Yazagyo Dam (Fig. 7.1, Table 7.1). These sites were extremely altered and deformed. Furthermore, their demagnetizations were generally unstable resulting in scattering ChRM directions, although several plot close to the OP sites.

The Western Belt Ophiolite is an important component for obtaining a clear understanding of the tectonics that governed the BT. More paleomagnetic, structural, petrological and geochronological

research to gain more insight into the origin of the magnetic record presented here is therefore definitely beneficial.

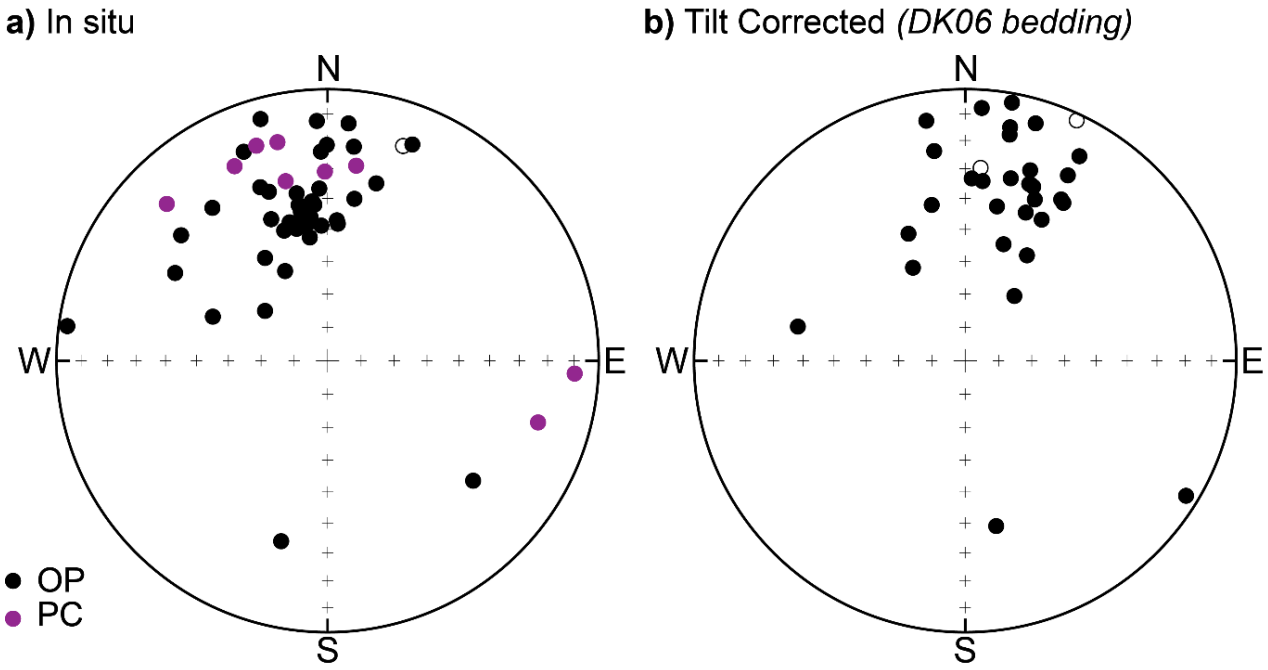

Figure 7.5: *Stable ChRM directions of (a) OP and PC10/PC11 sites at 530-590°C in in-situ coordinates, and (b) OP sites at 530-590°C corrected for the bedding of proximal site DK06 (Table 7.1; Section 2.4).*

2.3. Paunggyi and Tilin Formations

The time period in between the early Late Cretaceous and late Eocene is important for the tectonic history of the BT, because it should provide a record of rotation of the BT, as well as records of potential collisions between India and the Trans-Tethyan Arc and between the BT and the margin of Sibumasu (more details in Chapters 4 and 6). The Paunggyi Formation (or Paunggyi conglomerates) span the Paleocene part of the CMB sedimentary sequence, as constrained by foraminifera (United Nations, 1978a), ~65 Ma dated tuffs and ~70-62 Ma maximum depositional ages from detrital zircons (Cai et al., 2019). The Tilin formation is of probable middle Eocene age (Chapter 6; Cai et al., 2019).

In the Minbu Basin, we obtained six Paunggyi Formation sites near the township of Datkon (DK), two Paunggyi Formation sites near the township of Sidoktaya (ST02 and ST03), and two Tilin Formation sites near the township of Saw (SW01 and SW05; Table 7.1). The Paunggyi Formation sites contained tuffs and sandstones, and were often locally faulted and folded (Fig. 7.1). In addition, two sites were acquired in greyish siltstones of Tilin Formation near the Saw Township (SW01 and SW05). ChRMs in ST02 were well-determined, and these results were hence discussed in Chapter 6. It was impossible to determine stable ChRM vectors in all other Paunggyi Formation sites. Demagnetizations were

often characterized by persistent overprint of the present-day field (Fig. 7.6a), high degree of scatter (Fig. 7.6b), local rotation or low intensity of magnetite (Figs. 7.2 and 7.3g-i). Therefore, these samples were likely affected by strong weathering conditions. The same is true for the siltstones of sites SW01 and SW05 in the Tilin Formation, which were probably affected more by weathering than the finer-grained mudstones of the other sites near the Saw Township (Chapter 6).

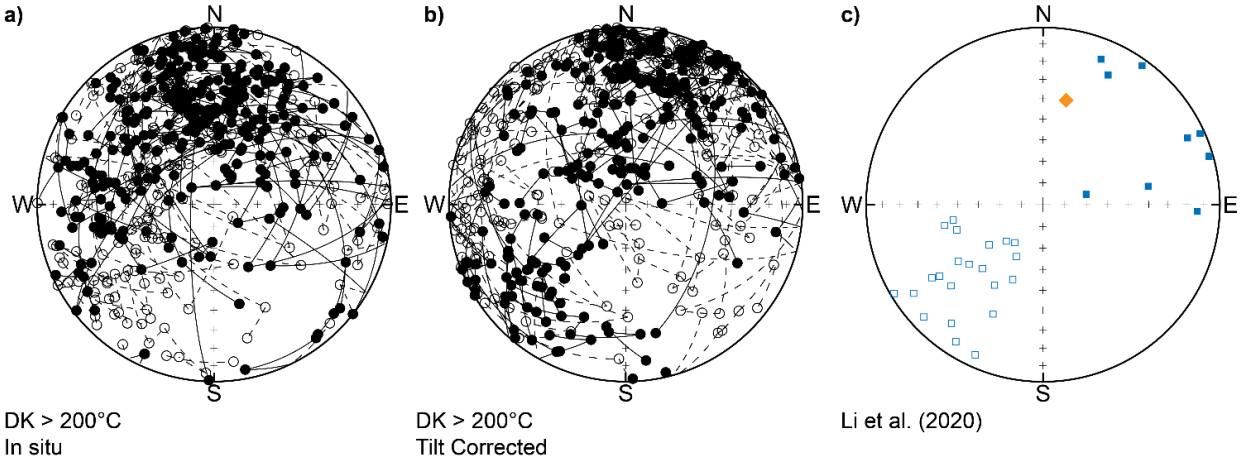

Figure 7.6: *Demagnetizations of sites near Datkon (DK) at temperatures higher than 200°C, showing the persistent overprint of the present-day field in in-situ coordinates (a) and the high degree of scatter after tilt correction (b). The results of Li et al. (2020) are shown for comparison (c).*

Despite the impossibility of determining stable ChRM vectors in sites DK02 and DK03 (Fig. 7.6), there are already published paleomagnetic results from the Paunggyi Formation from the same locations (Li et al., 2020). The mean direction of this study (D = 50.8±11.0°/ I = 33.1±9.2° / α95 = 9.2°) is characterized by a huge degree of scatter (k = 8.9; Fig. 7.6c). This mean direction strongly contradicts our reliable site ST01 from the lower to middle Eocene Laung She Formation, which follows the same trend as the rest of the Minbu Basin and has a low degree of scatter with a k-value of 44.2 (Chapter 6). Moreover, bedding was considered as overturned by Li et al. (2020) contrary to our own observations (Table 7.1) and contrary to the younging direction observed in the radiometric data from Cai et al. (2019) at the same locations. Even if we combine the results of Li et al. (2020) with ST01, both overturned and not overturned, we obtain a mean direction for ST01 similar as before (Fig. 7.7). However, it is more likely that the results of Li et al. (2020) were not obtained from stable ChRM vectors in agreement with our own observations in the Datkon sites (Fig. 7.6), and therefore the data and conclusions of this study are discarded.

Figure 7.7: *Paleomagnetic results from site ST01 in the Laung She Formation (black; Chapter 6) plotted alongside published results (blue) from the same location as sites DK02 and DK03 in the Paunggyi Formation (Li et al., 2020), both overturned and not overturned. The mean direction from*

ST01 (orange) is almost the same as a combined mean from ST01 and Li et al. (2020) (brown) due to the large degree of scatter in the latter.

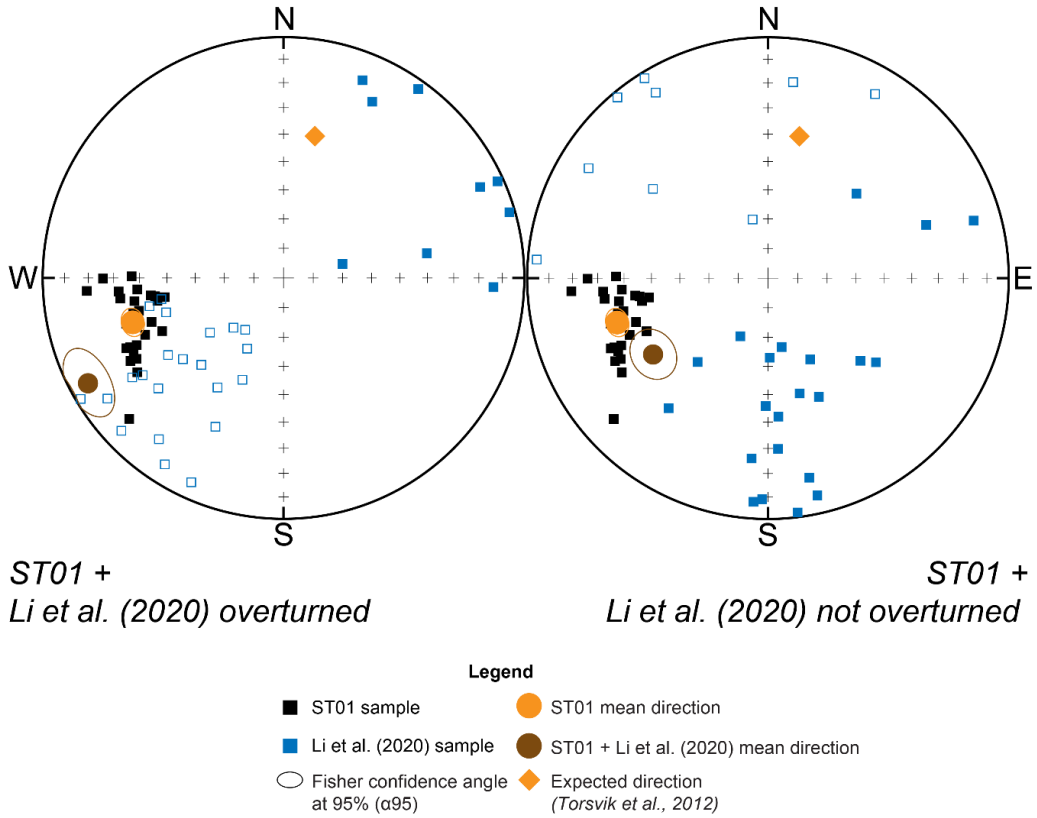

2.4. Shwezetaw and Yaw Formations, Minbu Basin

As discussed in Chapter 1, another goal of this PhD thesis was to investigate paleoclimate conditions in Myanmar and their relationship with the onset of Asian monsoons (Licht et al., 2014). An important component in this regard was to provide magnetostratigraphic dating of the Eocene-Oligocene Transition (EOT) preserved in the thick sedimentary sequence of the CMB. As discussed in Chapter 5, the late Eocene sediments of the Chindwin Basin (Yaw, Tonhe and Letkat Formations) are characterized by two major depositional hiatuses. Hence, the EOT is not preserved there. By contrast, sedimentation in the Minbu Basin to the south was continuous during this time span (Pivnik et al., 1998; Gough et al., 2020; Licht et al. 2019), hence providing a better possibility to sample the EOT.

To this end, we obtained a magnetostratigraphic section consisting of 19 samples in the late Eocene Yaw Formation (YP) and 63 samples in the early Oligocene Shwezetaw Formation (SP) of the Minbu Basin exposed in a stream near the Shwezetaw Pagoda (Table 7.1). Unfortunately, strong weathering of the sediments in this section alongside an abundance of sandy lithologies resulted in a magnetic overprint with low to intermediate unblocking temperatures (Fig. 7.3e). Furthermore, hysteresis

plots showing strong paramagnetism again indicate an overall lack of ferromagnetic magnetite in these lithologies (Fig. 7.2).

Low temperature overprints are generally accepted as being viscous magnetizations acquired acquired in the present-day field or during the normal field of the current normal Brunhes chron. However, our data from the Shwezetaw Formation provide evidence that their overprint was acquired specifically during the last few centuries (Fig. 7.8). Most samples from the SP section have lower inclinations than expected by the present-day field or the normal dipole field. The global secular variation of the earth's magnetic field is well established for the last four centuries (GUFM model; Jackson et al., 2000), showing that the inclination over Myanmar was low during this time. Therefore, the low temperature component of the SP samples is likely the result of a weathering process lasting over four to five centuries. This illustrates the importance of recognizing such secondary magnetizations.

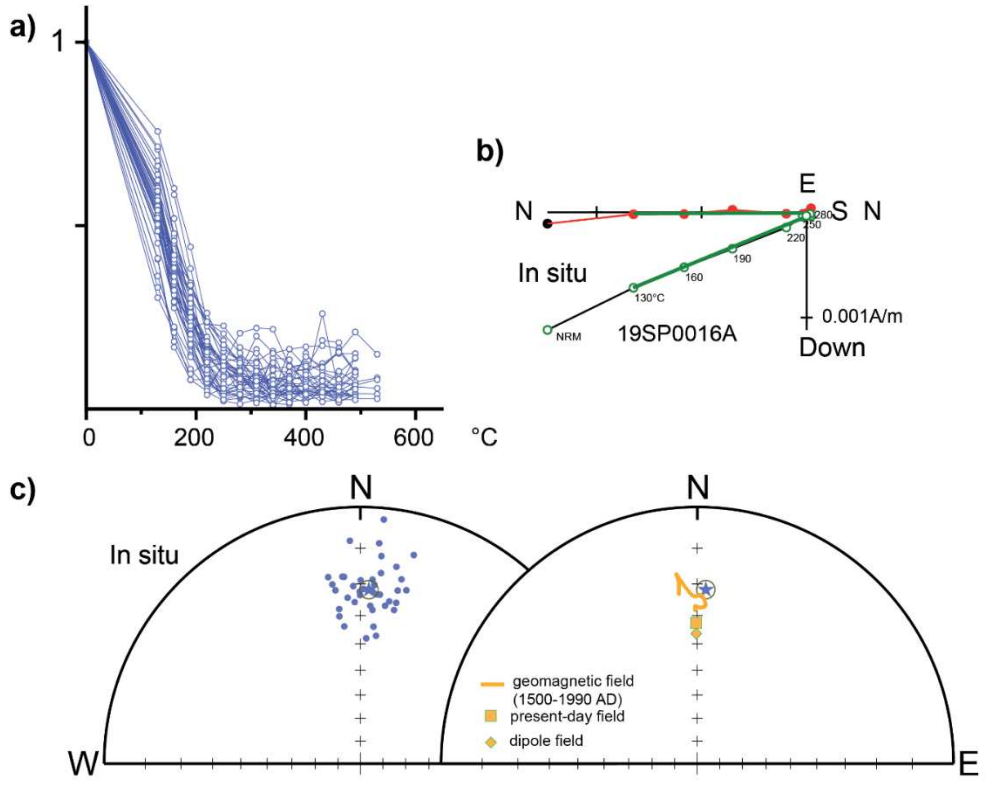

Figure 7.8: *Intensity of the natural remanent magnetization during thermal demagnetization for samples from the SP section carrying large secondary overprint with low unblocking temperatures (a). A representative orthogonal demagnetization plot from the SP section highlights the stability of this overprint in the temperature range 130-250°C (b). Sample directions and resulting mean direction (blue star) at the site level are shown in equal-area stereonets (c). The low temperature*

components in the Shwezetaw Formation compares better with the secular variation during the last four centuries (calculated from model GUFM; Jackson et al., 2000).

A very sporadic amount of samples showed well-determined directions of reverse polarity (Fig. 7.3f), but this was insufficient to construct a reliable magnetostratigraphic correlation for this sedimentary section (Fig. 7.9). Forams at ~150 meter in the section indicate a lower Rupelian age (~33.9-30 Ma) (Licht & Renema, personal communication), tentatively suggesting that the medium quality normal polarity sample in the section could correspond to the Rupelian normal chron amidst the generally reversed polarities around the EOT (Ogg et al., 2016). However, this is a lot of confidence to place in only one medium quality sample. Resampling of this section or sampling a less weathered section is undoubtedly needed to constrain the EOT in the Minbu Basin with magnetostratigraphy.

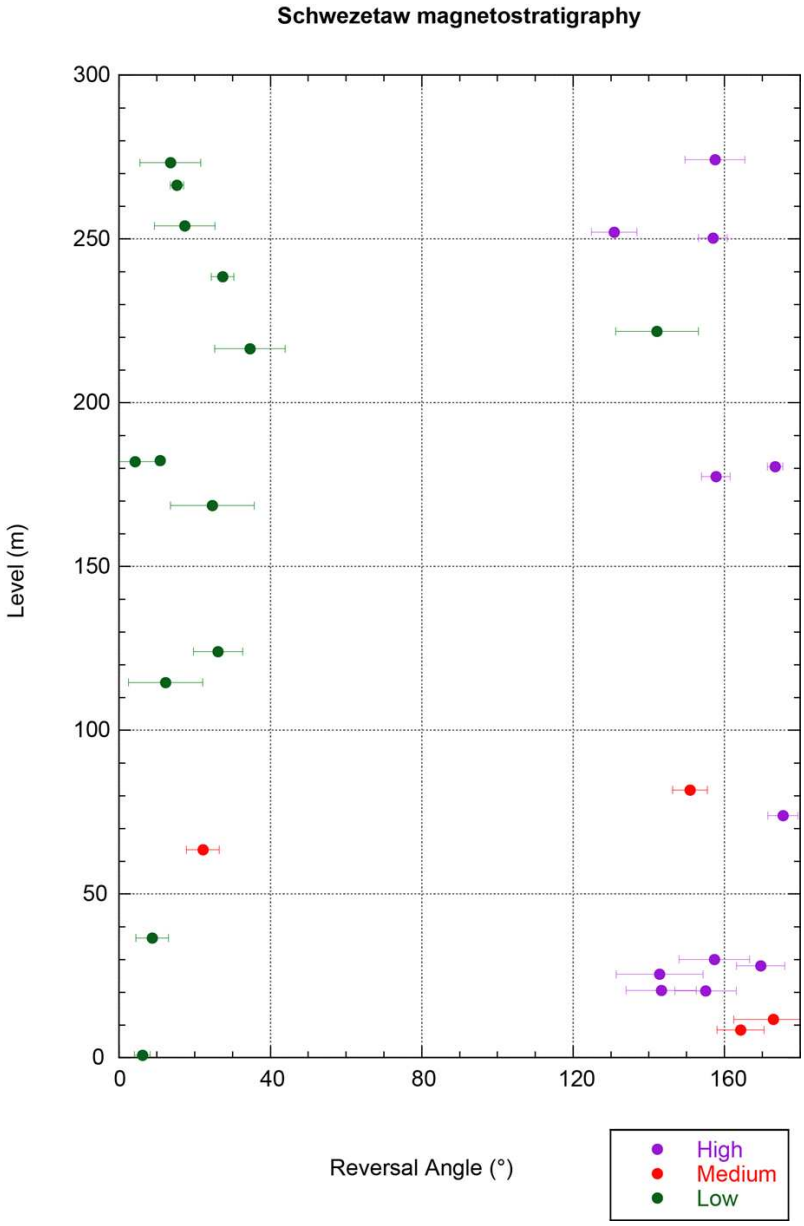

Figure 7.9: *Magnetostratigraphy of the SP and YP sections in the Minbu Basin, plotted as stratigraphic level (m) versus reversal angle (the angular distance between the observed direction in an individual sample and the mean paleomagnetic direction in normal polarity). High confidence results (purple) are of reliable direction and reliable polarity, medium confidence results (red) have reliable polarity but unreliable directions, and low confidence results (green) have neither.*

3. Discussion & Conclusions

It is clear from the difficulties in interpreting the results presented in this chapter that paleomagnetic research in Myanmar is challenging because of a variety of reasons. Overprint of the primary magnetic signal by the present-day field and overall low concentration of magnetite are perhaps the most significant challenges, especially in coarser grained sandstones and siltstones. As a result, paramagnetic minerals contribute significantly to the bulk magnetic properties in many sedimentary samples (Fig. 7.2) and this explains the wider scatter in NRM intensity than in bulk magnetic susceptibility (Fig. 7.10).

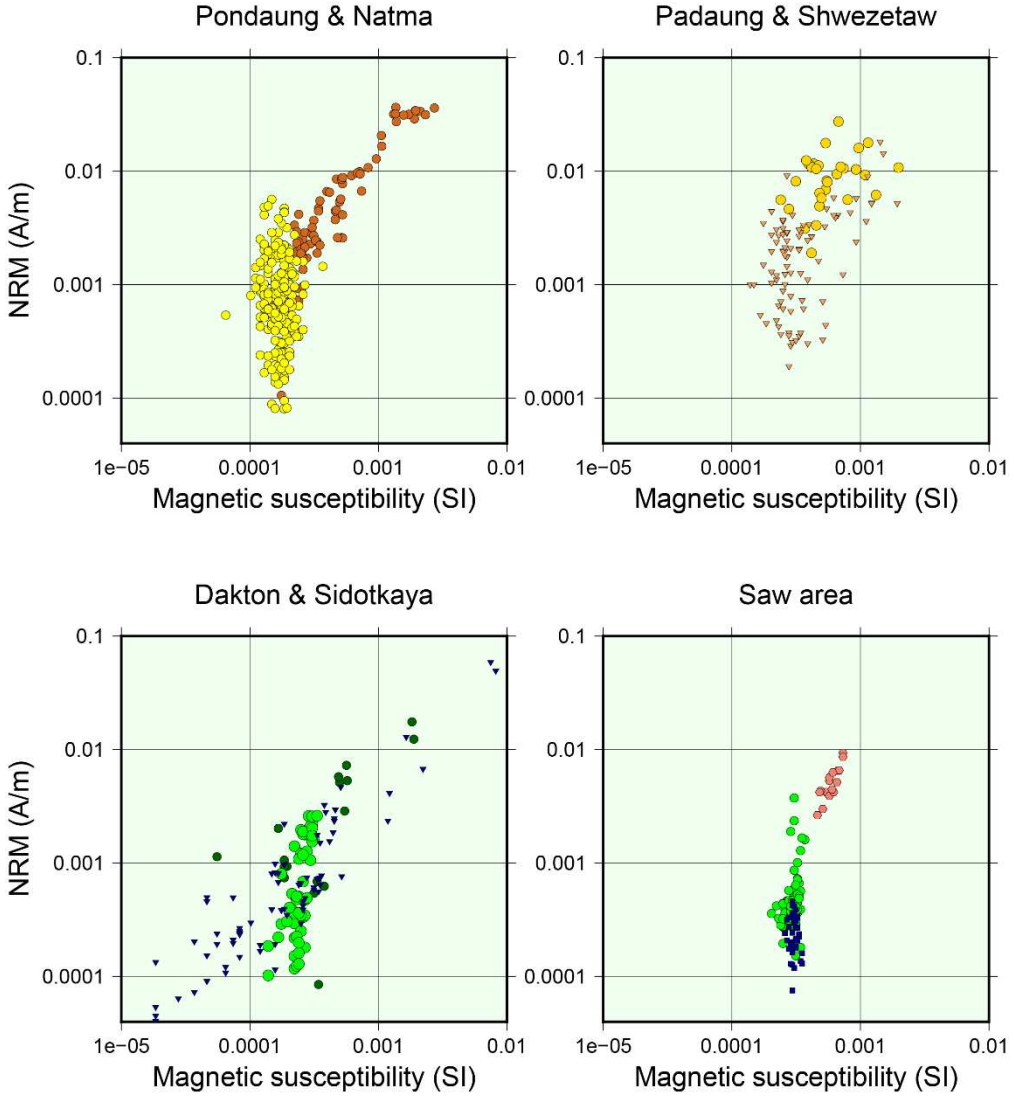

Figure 7.10: *Plots of NRM versus bulk magnetic susceptibility for sediments sampled for paleomagnetism throughout this study (Chapters 4 to 7).*

The aforementioned challenges in obtaining reliable paleomagnetic data in Myanmar could be related to initial low magnetite content of the source lithologies or intense chemical weathering of the sedimentary source, potentially enhanced by sediment reworking, prolonged sediment transport and the tropical climate of Myanmar (Roberts, 2015). A comparison of all bulk magnetic susceptibilities measured during this study (Chapters 4 to 7) further illustrates this, showing that the bulk magnetic susceptibility is on average two orders of magnitude lower in the sediments of the Burmese forearc basins than in the magmatic rocks of the Wuntho Ranges (Fig. 7.11).

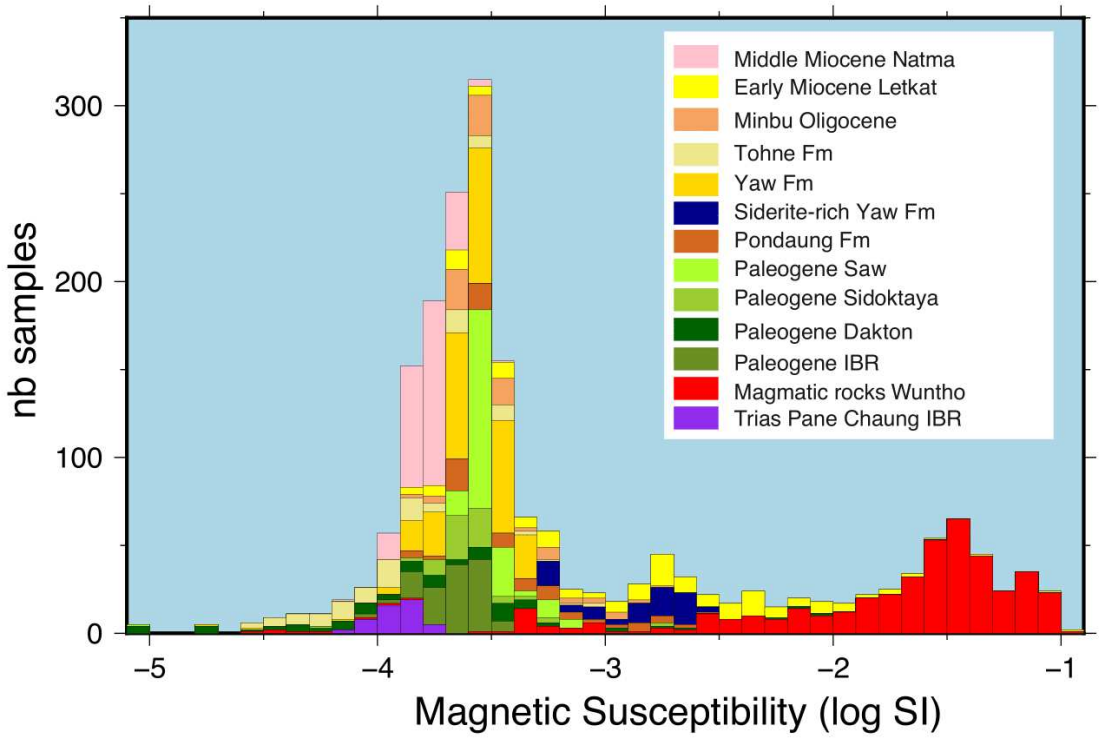

Figure 7.11: *Histograms of volume magnetic susceptibilities (in log and SI unit) observed in the various lithological units investigated during this study (Chapters 4 to 7).*

Even many publishable results are affected by this intense chemical weathering, shown by the low yield of samples with stable ChRM directions in many sedimentary sites (e.g. paleosols of the Natma and Pondaung Formations, sandstones of the Yaw Formation; see Chapters 4-6).

Apart from the low magnetite contents, vegetation covers much of the exposure, making the determination of spatio-temporal relationships and clear bedding constraints difficult during paleomagnetic sampling, especially in igneous lithologies (e.g. site MY54 of the Shwedaung Formation, and sites OP of the WBO). Finally, many regions underwent extreme polyphase deformation, in particular close to the IBR (e.g. Paunggyi, Falam, Pane Chaung Formations, WBO) and older lithologies in the Wuntho Ranges (e.g. Shwedaung Formation), resulting in local rotations and potential secondary magnetizations that are difficult to interpret because of the lack of outcrops. Fortunately, there are also many sampling localities (Chapters 4 to 6) that did provide reliable paleomagnetic constraints for the BT, especially those from fresh exposures along road cuts or in quarries. More detailed mapping, extensive paleomagnetic sampling or even deep drill cores will likely be required to overcome these challenges during future paleomagnetic sampling in Myanmar.

References Chapter 7

Acharyya, S. K. (2007). Collisional emplacement history of the Naga-Andaman ophiolites and the position of the eastern Indian suture. Journal of Asian Earth Sciences, 29(2–3), 229–242.

Allen, R., Najman, Y., Carter, A., Barfod, D., Bickle, M. J., Chapman, H. J., … Parrish, R. R. (2008). Provenance of the Tertiary sedimentary rocks of the Indo-Burman Ranges, Burma (Myanmar): Burman arc or Himalayan-derived? Journal of the Geological Society, 165(6), 1045–1057.

Bannert, D., Sang Lyen, A., & Htay, T. (2012). The geology of the Indoburman Ranges in Myanmar.

Barber, A. J., & Crow, M. J. (2003). An evaluation of plate tectonic models for the development of Sumatra. Gondwana Research, 6(1), 1–28.

Cai, F., Ding, L., Zhang, Q., Orme, D. A., Wei, H., Li, J., … Sein, K. (2019). Initiation and evolution of forearc basins in the Central Myanmar Depression. GSA Bulletin. https://doi.org/10.1130/B35301.1

Gibbons, A. D., Zahirovic, S., Müller, R. D., Whittaker, J. M., & Yatheesh, V. (2015). A tectonic model reconciling evidence for the collisions between India, Eurasia and intra-oceanic arcs of the central-eastern Tethys. Gondwana Research, 28(2), 451–492. https://doi.org/10.1016/j.gr.2015.01.001

Gough, A., Hall, R., & BouDagher-Fadel, M. K. (2020). Mid-Cenozoic fluvio-deltaic to marine environments of the Salin Sub-basin, Central Myanmar. Journal of Asian Earth Sciences, 104143. https://doi.org/10.1016/j.jseaes.2019.104143

Jackson, A., Jonkers, A. R., & Walker, M. R. (2000). Four centuries of geomagnetic secular variation from historical records. Philosophical Transactions of the Royal Society of London. Series A: Mathematical, Physical and Engineering Sciences, 358(1768), 957–990.

Li, Z., Ding, L., Zaw, T., Wang, H., Cai, F., Yao, W., … Yue, Y. (2020). Kinematic evolution of the West Burma block during and after India-Asia collision revealed by paleomagnetism. Journal of Geodynamics, 134, 101690. https://doi.org/10.1016/j.jog.2019.101690

Licht, A., van Cappelle, M., Abels, H. A., Ladant, J.-B., Trabucho-Alexandre, J., France-Lanord, C., … Jaeger, J.-J. (2014). Asian monsoons in a late Eocene greenhouse world. Nature, 513(7519), 501–506. https://doi.org/10.1038/nature13704

Licht, A., Dupont-Nivet, G., Win, Z., Swe, H. H., Kaythi, M., Roperch, P., … Sein, K. (2019). Paleogene evolution of the Burmese forearc basin and implications for the history of India-Asia convergence. Geological Society of America Bulletin, 1(130), 20.

Liu, C.-Z., Chung, S.-L., Wu, F.-Y., Zhang, C., Xu, Y., Wang, J.-G., … Guo, S. (2016). Tethyan suturing in Southeast Asia: Zircon U-Pb and Hf-O isotopic constraints from Myanmar ophiolites. Geology, 44(4), 311–314. https://doi.org/10.1130/G37342.1

Maurin, T., & Rangin, C. (2009). Structure and kinematics of the Indo-Burmese Wedge: Recent and fast growth of the outer wedge: GROWTH OF THE OUTER INDO-BURMESE WEDGE. Tectonics, 28(2), n/a-n/a. https://doi.org/10.1029/2008TC002276

Mitchell, A. (2017). Geological Belts, Plate Boundaries, and Mineral Deposits in Myanmar. Elsevier.

Morley, C. K., Tin Tin Naing, Searle, M., & Robinson, S. A. (2020). Structural and tectonic development of the Indo-Burma ranges. Earth-Science Reviews, 200, 102992. https://doi.org/10.1016/j.earscirev.2019.102992

Najman, Y., Sobel, E. R., Millar, I., Stockli, D. F., Govin, G., Lisker, F., … Kahn, A. (2020). The exhumation of the Indo-Burman Ranges, Myanmar. Earth and Planetary Science Letters, 530, 115948. https://doi.org/10.1016/j.epsl.2019.115948

Ogg, J. G., Ogg, G., & Gradstein, F. M. (2016). A concise geologic time scale.

Oufi, O., Cannat, M., & Horen, H. (2002). Magnetic properties of variably serpentinized abyssal peridotites. Journal of Geophysical Research: Solid Earth, 107(B5), EPM-3.

Pivnik, D. A., Nahm, J., Tucker, R. S., Smith, G. O., Nyein, K., Nyunt, M., & Maung, P. H. (1998). Polyphase Deformation in a Fore-Arc/Back-Arc Basin, Salin Subbasin, Myanmar (Burma). AAPG Bulletin, 82(10), 1837–1856.

Rangin, C., Maurin, T., & Masson, F. (2013). Combined effects of Eurasia/Sunda oblique convergence and East-Tibetan crustal flow on the active tectonics of Burma. Journal of Asian Earth Sciences, 76, 185–194. https://doi.org/10.1016/j.jseaes.2013.05.018

Roberts, A. P. (2015). Magnetic mineral diagenesis. Earth-Science Reviews, 151, 1–47. https://doi.org/10.1016/j.earscirev.2015.09.010

Searle, M. P., Morley, C. K., Waters, D. J., Gardiner, N. J., Htun, U. K., Than Than Nu, & Robb, L. J. (2017). Chapter 12 Tectonic and metamorphic evolution of the Mogok Metamorphic and Jade Mines belts and ophiolitic terranes of Burma (Myanmar). Geological Society, London, Memoirs, 48(1), 261–293. https://doi.org/10.1144/M48.12

Sevastjanova, I., Hall, R., Rittner, M., Paw, S. M. T. L., Naing, T. T., Alderton, D. H., & Comfort, G. (2016). Myanmar and Asia united, Australia left behind long ago. Gondwana Research, 32, 24–40. https://doi.org/10.1016/j.gr.2015.02.001

Tauxe, L. (2010). Essentials of paleomagnetism. Univ of California Press.

United Nations. (1978a). Geology and exploration geochemistry of the Pinlebu-Banmauk area, Sagaing Division, northern Burma. Technical Report No. 2. DP/UN/BUR-72-002. Geological Survey and Exploration Project, United Nations Development Programme, New York, 66.

Yao, W., Ding, L., Cai, F., Wang, H., Xu, Q., & Zaw, T. (2017). Origin and tectonic evolution of upper Triassic Turbidites in the Indo-Burman ranges, West Myanmar. Tectonophysics, 721, 90–105. https://doi.org/10.1016/j.tecto.2017.09.016

Zhang, P., Mei, L., Hu, X., Li, R., Wu, L., Zhou, Z., & Qiu, H. (2017). Structures, uplift, and magmatism of the Western Myanmar Arc: Constraints to mid-Cretaceous-Paleogene tectonic evolution of the western Myanmar continental margin. Gondwana Research, 52, 18–38. https://doi.org/10.1016/j.gr.2017.09.002

Chapter 8: Conclusions and Perspectives

View on the Minbu Basin from the Indo-Burman Ranges.
(Kanpetlet, Myanmar, Fieldwork January 2020)

Conclusions

The findings from this thesis have shown that Myanmar is a crucial yet poorly-investigated region for understanding the complex India-Asia collision, a subject which is still intensely debated in the geoscience community. Beyond tectonics, Myanmar contains important paleoclimate, paleontology and palynology records of unclear affinities. The paleomagnetic constraints from this thesis have provided surprising new insights into these topics alongside the other sedimentological, geochronological and mineralogical results. They invite a critical re-evaluation of many aspects of the regional geological history, including correlations of magmatic and ophiolitic belts, the origin of the Burma Terrane, important sedimentary sources in the Eastern Himalayas, and the chronology of tectonic events in SE Asia and the Himalayas. Furthermore, these constraints can be used for further research into the evolution of the India-Asia collision and Asian paleoclimatic reconstructions.
The key conclusions described in this report are listed below in chronological order:

- The tectonic history of the Burma Terrane was distinct from Asia from at least the early Late Cretaceous until the Eocene, as shown by consistently southern hemisphere to near-equatorial paleolatitudes during throughout that time period. Alongside magmatism and ophiolite emplacement related to Late Cretaceous subduction, this is best explained by an island arc origin for the Burma Terrane as part of a Trans-Tethyan subduction system. Crustal fragments of Gondwanan and possibly Sibumasu and Cathaysian origin could have amalgamated into the Burma Terrane during the development of this subduction system. Furthermore, this tectonic setting suggests that the prolific Burmese fossil amber biota should contain species with Gondwanan and endemic traits.
- Since the latest Paleocene – middle Eocene the Burma Terrane was incorporated onto the Indian Plate due to the collision of India with the Trans-Tethyan subduction system. In addition, this collision event could have induced clockwise rotation of the Burma Terrane, although the exact magnitude of rotation is difficult to estimate from the paleomagnetic dataset due to variations in declinations likely related to local deformation.
- The Burma Terrane subsequently started a ~3000 km northward motion alongside India and with little rotation towards its present-day position. The continuously coeval latitudes with India suggests that little Burmese subduction and corresponding arc volcanism took place throughout this time. Furthermore, it indicates that the northward motion of the Burma Terrane was likely accommodated by dextral strike-slip deformation to its east. This dextral strike-slip system was likely the India-Australia Transform. After the late Oligocene – early Miocene collision of the Burma Terrane with Sibumasu, this strike-slip system transitioned

into the (Proto-) Sagaing Fault that still accommodates the northward transcurrent motion of the Burma Terrane at present.

- The paleomagnetic data from the Burma Terrane show that its position remained coeval with India throughout the late Paleogene until the Neogene. However, the Burmese forearc basins record major changes during this time period. Notably, the late Eocene Yaw Formation, late Oligocene Tonhe Formation and early Miocene Letkat Formation of the Chindwin Basin the northern Burmese forearc show large shifts in sedimentary facies, magnetic properties and provenance with two large depositional hiatuses in between them. When comparing these shifts with regional geological data, they are best explained as representing a two-stage interaction of the Burma Terrane with the Asian margin. The first late Eocene – middle Oligocene unconformity records overfilling of the Chindwin Basin following rapid subsidence, which is interpreted to correspond to incipient uplift of the Burma Terrane due to the onset of the joint India/Trans-Tethyan Arc collision with Asia to the north. This collision event then propagated southward as the Burma Terrane moved northward towards the Eastern Himalayan collision zone. The second late Oligocene – early Miocene uniformity and the overlying Letkat Formation record the ensuing major regional deformation, uplift and exhumation caused by the Burma Terrane finally entering the collision zone, resulting in the set-up of the modern tectonic regime and drainage system of the Burma Terrane and Eastern Himalayas.

Perspectives

As Myanmar only recently opened to international geoscience research, many things remain to be investigated. The most immediate goals in the context of this thesis are listed below.

- The main paleomagnetic results from Myanmar presented in this thesis covered the majority of the Burmese forearc basins (Chindwin and Minbu Basins), the Wuntho Ranges volcanic complex, and part of the IBR. Paleomagnetic sampling in Myanmar is challenging, but there are several key locations left:
    - Perhaps the most important is the region north of the Wuntho Ranges, largely located in the Kachin State which is currently restricted for foreigners. The geology of this region with respect to the rest of the Burma Terrane, its relationship with the nearby Jade Belt Ophiolite and Eastern Belt Ophiolite (Myitkyina), and the transition of the Burma Terrane into the Eastern Himalayan Syntaxis are poorly understood. Moreover, the Cretaceous amber mines are located here as well, whose relationship

with the Burma Terrane has important paleontological, paleoclimatic and tectonic implications (Chapter 4).

- The Jade Belt Ophiolite has been correlated with dismembered ophiolitic fragments on the trace of the Sagaing Fault as part of the Central Belt Ophiolite. The petrological, metamorphic, structural and (paleo)magnetic properties of this proposed Central Belt Ophiolite requires further understanding, as it could potentially represent (fragments of) the Burma Terrane – Sibumasu suture.
- The paleomagnetic and provenance record of the Burmese back-arc (Shwebo and Pegu Basins) should be compared with that of the Burmese forearc and with magmatic ages in the Wuntho Ranges and Eastern Himalayas. Throughout the Cenozoic, there was likely a significant contribution of sediments coming from the India-Asia collision zone to the north (Chapters 5 and 6). The Burmese back-arc is a place where this sedimentary drainage route could have been funnelled.
- Paleomagnetism in combination with structural geology could potentially provide rotational patterns of sediments deposited in the basins and splays surrounding the Sagaing Fault. This information can be used to better determine its deformation phases prior to the Neogene. Hopefully, this will provide constraints on the characteristics of the postulated 'Proto-Sagaing Fault' (Chapters 4 and 6).
- When better age constraints are available, more extensive paleomagnetic sampling of the Indo-Burman Ranges could be attempted to try and answer key questions regarding tectonic history of the Burma Terrane with respect to the hypothetical Mount Victoria Block, as well as the collision history with India.
- Perhaps there are certain outcrops of the Triassic Burma Terrane basement (Pane Chaung or Shwedaung Formations) whose primary magnetic signal has been preserved in contrast to sites discussed in Chapter 7. Paleolatitude constraints from these localities are probably the best way to decisively solve the debate regarding the origin of the Burma Terrane (Cathaysian, Gondwanan, intra-oceanic or composite).

- Between the late Eocene and late Oligocene – early Miocene, the exact nature of the plate margin between the Indian Plate and Sibumasu east of the BT remains perhaps the most critical uncertainty in our model. Northward motion until the late Oligocene – early Miocene collision of the BT with Sibumasu was possibly accommodated by a Proto-Sagaing Fault extending into the Andaman Sea or an India-Australia Transform. Unfortunately, the geological evidence for a Proto-Sagaing Fault is poor and the India-Australia Transform is

believed to be inactive since the coupling of the Indian and Australian Plates at ~40 Ma. Alternatively, the BT northward motion was accommodated by ongoing subduction underneath Sibumasu during this time period (Chapter 6). More evidence from structural geology, placed in the context of our paleomagnetic dataset, is required to further characterize this complex plate boundary.

- More detailed investigation of the mantle structure (e.g. with tomography) beneath Myanmar could be done to check whether the extraordinary tectonic history of the Burma Terrane with ~2000 km northward motion and collision events with India and the Asian margin are preserved there in the form of detached slabs. An interesting possibility is that the Neo-Tethyan slab dangling beneath the Burma Terrane could have been sheared and dragged during the large northward strike-slip translation during the Cenozoic.
- High quality seismic imaging of the Central Myanmar Basins, especially at the contact with the Wuntho-Popa Arc, Eastern Himalayan Syntaxis and Mogok Belt is required to better understand the relationship between the basin infill and regional phases of deformation, uplift and exhumation.

  Notably, it is unclear if the Wuntho Ranges were buried by Paleogene sediments and subsequently exhumed during the regional late Oligocene – early Miocene deformation phase, similar to the southern Wuntho-Popa Arc. This has important implications for the interpretation of provenance in the Central Myanmar Basins, as burial of the Wuntho Ranges necessitates an additional sedimentary source of the same signature as the Wuntho-Popa Arc to the north (e.g. the Trans-Tethyan Arc or Gangdese Arc; Chapters 5 and 6). Further insight on this topic could come from mass-balancing between the Wuntho-Popa Arc and the Central Myanmar Basins using these high quality seismic images. Moreover, the original burial depth of the Wuntho Ranges volcanics could be determined by comparing new geological and petrological results with similar volcanic arcs elsewhere (e.g. the Kohistan Arc).

  Furthermore, the eastward extend of the Central Myanmar Basins and their relationship with the dextral Sagaing and Shan Faults at the eastern edge of the Burma Terrane is poorly imaged on seismics. This is an important issue, because it could provide insight into the age of the dextral strike-slip faulting, basin development, as well as the eastern extend of the Burma Terrane and its collision with Sibumasu.
- Outside of Myanmar, more robust paleomagnetic studies are necessary in the Central Himalayan orogen, as paleomagnetic datasets from the Tethyan Himalaya, YTSZ and Lhasa Terrane currently focus on small areas with contradicting results, mostly due to poorly

constrained remagnetization events. Larger regional datasets from these areas could resolve these contradictions and thus yield further proof for the Trans-Tethyan collision model or other collision models, as well as for the paleolatitude of the Asian margin.

- Furthermore, other paleomagnetic evidence for the Trans-Tethyan Arc collision model (Chapter 4) can be obtained in understudied areas east and west of the Central Himalayan orogen. Immediate targets are Cretaceous I-type volcanics preserved in the Eastern Himalayan Syntaxis (Sodon and Lohit Batholiths) that have no paleomagnetic constraints at present, and the Kohistan Arc in the Western Himalayas with possibly outdated and incomplete paleomagnetic constraints.
- For the Sodon and Lohit Batholiths, additional geochronological, geochemical and structural data is essential as well. These volcanic complexes in the Eastern Himalayan Syntaxis could either correlate to the Gangdese Arc of the Lhasa Terrane, or to the Wuntho-Popa Arc of the Burma Terrane as remnants of the Trans-Tethyan subduction system. Moreover, they could represent source regions for the Central Myanmar Basins, notably providing ~80-50 Ma zircons found in Paleogene sediments (Chapter 5). Putting this together, the margin of Asia was potentially farther south if these batholiths belong to the Gangdese Arc, because an earlier collision with the Burma Terrane is required in that context in order to provide the ~80-50 Ma zircons to early to middle Eocene units in the Central Myanmar Basins exhibiting southern hemisphere paleolatitudes (e.g. certain Tilin Formation sites of Chapter 6). Paradoxically, an earlier collision with the Burma Terrane could mean that Gangdese Arc volcanism ceased earlier as well, as collision would impede active subduction shutting down Andean type volcanism. The same is true for Wuntho-Popa Arc volcanism after the collision of India with the Trans-Tethyan Arc. This shows that integrated regional models incorporating paleolatitudes from paleomagnetic data, magmatic activity, sedimentary provenance and deformation phases are imperative in truly solving the India-Asia collision debate.
- Most findings during this thesis are related to the tectonic history of Myanmar, which is partly due to the unconformable sedimentary record of the Chindwin Basin (Chapter 5) and the profound influence of weathering on the paleomagnetic results (Chapter 7). However, investigating the paleoclimate and monsoonal history of Myanmar was another goal in the context of ERC project MAGIC. Hopefully, the continuous sedimentary records of the Minbu, Shwebo and Pegu Basins of the Burma Terrane will provide more insight into this topic.

Appendices

Fold in the Paunggyi Formation, Minbu Basin.
(Sidoktaya, Myanmar, Fieldwork January 2019)

Appendix 1: Data tables Chapter 4

Reference: *Westerweel, J., Roperch, P., Licht, A., Dupont-Nivet, G., Win, Z., Poblete, F., … Aung, D. W. (2019). Burma Terrane part of the Trans-Tethyan arc during collision with India according to palaeomagnetic data. Nature Geoscience. https://doi.org/10.1038/s41561-019-0443-2*

Supplementary Data 1

Paleomagnetic results per used site and per locality before and after tilt correction (TC).

Name	Information			N/n	In-situ				Tilt (str/dip)				Tectonic (TC)				Age (Ma)
	Formation	Lithology	Coordinates (Lat/Lon)		D	I	α95	k		D	I	α95	k				
Pinlebu (Late Cretaceous)																	
MY01	Kanza Chaung Batholith	Diorite	24.027990°/95.437070°	-/6	-	-	-	-		-	-	-	-				97.6±0.3 (^{40}Ar/^{39}Ar)
MY03	Kanza Chaung Batholith	Diorite	24.030340°/95.438240°	-/6	-	-	-	-		-	-	-	-				
MY04*	Kanza Chaung Batholith	Granodiorite	24.024110°/95.437910°	10/20	64.1	4.7	6.8	52		-	-	-	-				97.3±0.6 (^{40}Ar/^{39}Ar) 87.3±0.5 (^{40}Ar/^{39}Ar)
MY05*	Kanza Chaung Batholith	Granodiorite	24.019300°/95.437490°	6/15	59.7	5.0	7.2	89		-	-	-	-				
MY13	Kanza Chaung Batholith	Granodiorite	23.928920°/95.470440°	-/9	-	-	-	-		-	-	-	-				
MY39*	Kanza Chaung Batholith	Granodiorite	24.019073°/95.436950°	6/12	53.6	7.2	12.4	30		-	-	-	-				
MY40*	Kanza Chaung Batholith	Granodiorite	24.022293°/95.434653°	6/11	67.2	5.1	18.4	14		-	-	-	-				
				4 sites	**61.2**	**5.5**	**6.8**	**183.9**		-	-	-	-				
Shinpa (Late Cretaceous)																	
MY51M*	Kanza Chaung Batholith	Granodiorite (Mafic part)	24.153760°/95.547690°	10/10	78.4	0.6	5.0	94		-	-	-	-				
MY51F*	Kanza Chaung Batholith	Granodiorite (Felsic part)	24.153760°/95.547690°	7/7	73.1	0.1	4.5	183		-	-	-	-				
MY53*	Kanza Chaung Batholith	Granodiorite	24.173940°/95.532670°	7/13	74.9	8.1	7.2	94		-	-	-	-				
				3 sites	**75.5**	**2.9**	**5.3**	**240.3**									
Banmauk (Late Cretaceous)																	
MY16	Kanza Chaung Batholith	Diorite	24.420120°/95.804530°	-/9	-	-	-	-		-	-	-	-				
MY17*	Kanza Chaung Batholith	Diorite	24.412910°/95.759890°	11/11	73.5	-16.3	4.9	89		-	-	-	-				96.6±0.3 (^{40}Ar/^{39}Ar) 102.1±1.0 (U/Pb) (Gardiner et al., 2017)
MY18*	Kanza Chaung Batholith	Diorite	24.417580°/95.761910°	10/10	81.2	-16.1	9.2	29		-	-	-	-				-
MY19*	Kanza Chaung Batholith	Granodiorite	24.431460°/95.736430°	8/8	72	-41.6	4.2	171		-	-	-	-				90.6±0.2 (^{40}Ar/^{39}Ar)
MY20	Kanza Chaung Batholith	Granodiorite	24.441670°/95.717120°	-/9	-	-	-	-		-	-	-	-				
MY26	Kanza Chaung Batholith	Granite	24.445540°/95.814340°	-/8	-	-	-	-		-	-	-	-				
MY27	Kanza Chaung Batholith	Granite	24.455140°/95.815750°	-/8	-	-	-	-		-	-	-	-				94.7±0.4 (^{40}Ar/^{39}Ar)
MY28	Kanza Chaung Batholith	Granite	24.490530°/95.809940°	-/8	-	-	-	-		-	-	-	-				

MY46*	Kanza Chaung Batholith	Granodiorite	24.440472°/95.809454°	13/14	55.9	-3.4	8.5	26	-	-	-	-	-	
MY47	Kanza Chaung Batholith	2-mica granite	24.435280°/95.772020°	-/16	-	-	-	-	-	-	-	-	-	
MY48*	Kanza Chaung Batholith	Diorite	24.424850°/95.757696°	9/10	117.4	-18.8	8.2	43	-	-	-	-	-	
				5 sites	**79.7**	**-20.4**	**25.2**	**10.2**		-	-	-	-	
Kawlin (Late Cretaceous)														
MY06	Mawgyi Andesite	Brecc. andesite	23.920450°/95.710610°	-/8	-	-	-	-	-	-	-	-	-	
MY07	Mawgyi Andesite	Andesite	23.970720°/95.761430°	12/12	67.2	2.2	5.5	65	000/00	67.2	2.2	5.5	65	100.9±0.2 (^{40}Ar/^{39}Ar)
MY08	Mawgyi Andesite	Andesite	23.927640°/95.709470°	7/7	103.4	33.2	9.3	43	000/00	103.4	33.2	9.3	43	
MY09	Kondan Chaung Group	Sandstone	23.877040°/95.703170°	-/10	-	-	-	-	000/00	-	-	-	-	
MY10	Mawgyi Andesite	Andesite	23.860780°/95.603970°	7/9	91.8	46.7	11.4	29	040/51	104.7	2.1	11.4	29	-
MY11	Mawgyi Andesite	Andesite	23.863960°/95.606060°	8/8	102.8	41.4	5.2	115	040/41	109.8	3.4	5.2	115	
MY12	Mawgyi volcanics?	Granodiorite	23.840420°/95.549490°	6/6	61.9	43.6	7.6	78	000/00	61.9	43.6	7.6	78	
MY14	Mawgyi Andesite	Andesite	23.850230°/95.573000°	-/6	-	-	-	-	000/00	-	-	-	-	
MY15	Mawgyi Andesite	Andesite	23.853420°/95.586300°	7/8	97.3	4.8	6.6	29	000/00	97.3	4.8	6.6	29	
MY34*	Kondan Chaung Group	Sandstone	23.878841°/95.703966°	11/13	81.2	-29.4	8.9	27	020/82	337.9	-55.5	8.9	27	
MY35	Mawgyi Andesite	Brecc. andesite	23.922660°/95.712390°	-/11	-	-	-	-	-	-	-	-	-	-
MY36	Mawgyi Andesite	Andesite	23.864950°/95.595260°	-/12	-	-	-	-	-	-	-	-	-	
MY37	Mawgyi Andesite	Andesite	23.851902°/95.590906°	20/20	101.8	37.5	5.5	38	000/00	101.8	37.5	5.5	38	
MY38	Mawgyi Andesite	Andesite	23.853420°/95.586300°	-/11	-	-	-	-	-	-	-	-	-	
				8 sites	**88.3**	**24.1**	**22.1**	**7.2**		-	-	-	-	
Kyaung Le (Late Cretaceous)														
MY22	Kondan Chaung Group	Undef. extrusive	24.522140°/95.691800°	8/8	38.1	-45.2	6.7	71	115/65	34.5	18.7	6.7	71	85.0±0.2 (^{40}Ar/^{39}Ar)
MY23	Kondan Chaung Group	Limestone	24.514070°/95.663900°	10/10	48.6	-31.7	2.4	395	210/97	60.6	20	2.4	395	
MY24	Kondan Chaung Group	Sandstone	24.510480°/95.665540°	12/12	26	-46.4	4	118	207/113	70.5	16.2	4	118	
MY25*	Kondan Chaung Group	Breccia	24.539590°/95.676960°	10/10	53.7	-17.1	5.3	84	098/18	51.3	-4.3	5.3	84	
MY41	Kondan Chaung Group	Sandstone	24.509810°/95.664831°	11/14	27.2	-48.6	3.4	184	213/114	79.5	14.5	3.4	184	
MY42	Kondan Chaung Group	Limestone	24.513537°/95.664268°	10/11	36.1	-41.5	2.8	300	210/97	70.5	9.6	2.8	300	
MY43*	Kondan Chaung Group	Rhyodacite	24.546611°/95.669812°	13/13	54.6	-18.0	2.9	205	035/27	44.1	-25.1	2.9	205	91.2±0.2 (^{40}Ar/^{39}Ar)

MY44	Kondan Chaung Group	Breccia	24.547150°/95.668550°	-/11	-	-	-	-	-	-	-	-	-	
MY45*	Kondan Chaung Group	Sst/Pyroclastic	24.544280°/95.667524°	14/17	53.8	-23.1	3.8	118	040/40	34.4	-26.6	3.8	118	-
				8 sites	**43.8**	**-34.5**	**11.3**	**24.8**		**56.4**	**3.1**	**18.2**	**10.2**	
Wuntho Arc (Late Cretaceous) - all				**28 sites**	**69.0**	**-6.4**	**12.8**	**5.5**		**-**	**-**	**-**	**-**	
Wuntho Arc (Late Cretaceous) - *				**16 sites**	**69.2**	**-9.8**	**10.1**	**14.2**		**-**	**-**	**-**	**-**	
Kalewa (Late Eocene)														
MA	Yaw Formation	Mst/sst/siderite	23.245770°/94.266630°	78/277	2.7	7.3	4.3	15	011/37	8.9	10.9	4.3	15	
MB	Yaw Formation	Mst/sst/siderite	23.239167°/94.262500°	36/116	8.2	6.5	5.9	18	011/40	12.9	6.4	5.9	18	38.0±0.7 (U/Pb) (Licht et al., 2019)
MC	Yaw Formation	Mst/sst/siderite	23.241633°/94.259417°	25/49	199.5	4.4	6.4	22	013/40	195.1	7.8	6.4	22	
MD	Yaw Formation	Mst/sst/siderite	23.245600°/94.258483°	11/35	23.8	0.2	11.3	17	013/38	21.5	-6.8	11.3	17	
MY32	Yaw Formation	Mst/sst/siderite	23.220730°/94.251770°	6/20	21.8	16.0	9.8	48	007/43	28.4	1.6	9.8	48	
MY33	Yaw Formation	Mst/sst/siderite	23.233960°/94.256950°	12/23	8.6	5.0	8	31	005/42	10.9	1	8	31	
				168 samples	**8.9**	**5.1**	**2.9**	**15.1**		**12.4**	**4.9**	**2.9**	**15.2**	

*Notes: N/n = number of samples used for mean direction/total samples; D = mean declination; I = mean inclination; α95 = Fisher cone of 95% confidence; k = dispersion parameter; Age (Ma) = age results from this or previous studies with reference; Wuntho Arc (Late Cretaceous) - all = total Wuntho Range mean calculated from all site mean directions of Pinlebu, Shinpa, Banmauk, Kawlin and Kyaung Le; Wuntho Arc (Late Cretaceous) - * = total Wuntho Range mean calculated only from selected site mean directions indicated by "*", as discussed in the text and Supplementary information; Kalewa (Late Eocene) = total mean calculated from the 168 most stable samples. MA-MD represent successive parts of one composite sedimentary section* (Licht et al., 2019)*, while MY32 and MY33 are two extra sampled sites from the same area.*

Supplementary Data 2

sample	Line or Plane	anchored	Demag type	nb points	step min	step max	Dec IS	inc IS	Dec TC	inc TC	mad value
Site MY03											
16MY0301B	L	y	F	4	18	25	62.4	2.2	62.4	2.2	8.1
16MY0302B	L	y	F	5	13	25	88.8	-10.5	88.8	-10.5	12.5
16MY0303B	L	y	D	5	400	560	62.1	-20.3	62.1	-20.3	7.4
17MY4009A	L	y	D	8	320	590	75.4	17.4	75.4	17.4	1.6
17MY4010A	L	y	D	7	350	590	62.3	19.2	62.3	19.2	1.5
17MY4011A	L	y	D	7	320	560	51.7	21.5	51.7	21.5	2.5
Site MY04											
16MY0406A	L	y	F	4	18	25	57.1	9.2	57.1	9.2	6.9
16MY0403A	L	y	F	12	15	60	62.7	-2.4	62.7	-2.4	4.1
16MY0403B	L	y	D	8	330	590	60.6	-4.1	60.6	-4.1	2.3
16MY0406B	f	n	D	4	380	490	48.5	2.9	48.5	2.9	19.5
17MY0402A	L	y	F	8	35	80	68	14	68	14	2.9
17MY0405A	L	y	F	9	35	100	71	1.9	71	1.9	2.8
17MY0406A	L	y	D	6	400	590	71.2	8.5	71.2	8.5	2.6
17MY0411A	L	n	D	6	450	620	79.4	10	79.4	10	6.9
17MY0403A	P	y	D	10	130	490	327.2	-29.1	327.2	-29.1	8.2
17MY0404A	P	y	D	6	130	320	340.5	-35.8	340.5	-35.8	12.6
Site MY05											
16MY0501B	L	y	D	4	490	600	61.2	4.1	61.2	4.1	3.6
16MY0503A	L	y	D	5	450	590	54.2	12.7	54.2	12.7	6.6
16MY0504B	L	y	F	7	20	45	54.8	5.7	54.8	5.7	4
16MY0506B	L	y	F	6	10	30	70.3	-2.3	70.3	-2.3	1.3
16MY0507A	L	y	D	5	450	590	65.3	6.4	65.3	6.4	12.9
16MY0508B	L	y	F	5	25	45	52.3	3.3	52.3	3.3	6.7
Site MY39											
17MY3903A	L	y	D	8	320	590	34.7	4.4	34.7	4.4	2.2
17MY3904A	L	y	F	10	30	100	62.6	7.2	62.6	7.2	2.4
17MY3901B	f	n	F	8	18	35	61	9.5	61	9.5	5.7
17MY3905B	f	n	F	8	18	35	40.4	-0.2	40.4	-0.2	11
17MY3910A	f	n	F	7	18	35	71.3	15.1	71.3	15.1	8.5
17MY3912B	f	n	F	6	15	28	52.3	6.2	52.3	6.2	16.6
Site MY17											
16MY1701B	L	y	D	10	360	660	75.3	-15.7	75.3	-15.7	2.6
16MY1703B	L	y	D	5	450	590	73.4	-8.9	73.4	-8.9	1.9
16MY1704B	L	y	D	5	450	600	81.3	-25.3	81.3	-25.3	4.1
16MY1706B	L	y	D	8	360	620	66.4	-20.8	66.4	-20.8	4.9
16MY1708B	L	y	D	5	450	600	70.9	-17.5	70.9	-17.5	5.4
16MY1710B	L	y	F	7	18	40	71.8	-21.5	71.8	-21.5	3.3
16MY1711A	L	y	D	5	450	590	80.6	-0.5	80.6	-0.5	3.8
16MY1702A	L	y	F	8	30	100	66.9	-17.1	66.9	-17.1	7.6
16MY1705A	L	y	F	10	20	100	78.6	-18.5	78.6	-18.5	2.6
16MY1707B	L	y	F	10	20	100	71.8	-22.2	71.8	-22.2	4.3
16MY1709A	L	y	F	10	20	100	71.1	-10.5	71.1	-10.5	5.5

Site MY18											
16MY1807A	L	y	F	9	15	60	87.9	-4.4	87.9	-4.4	10.4
16MY1802A	L	y	D	3	400	490	77.8	-22.9	77.8	-22.9	1.1
16MY1803B	L	y	D	5	450	590	62	-38.7	62	-38.7	3.6
16MY1805A	L	y	F	7	40	120	86	-22.3	86	-22.3	3.1
16MY1808B	L	y	D	5	450	590	85.5	0.5	85.5	0.5	5.4
16MY1801A	f	n	F	8	25	60	84.6	-9.8	84.6	-9.8	17
16MY1803A	f	n	F	5	30	50	68.5	-22.3	68.5	-22.3	7.6
16MY1806A	f	n	F	7	20	40	85.1	-4.9	85.1	-4.9	14.2
16MY1809A	f	n	F	7	20	45	92	-12	92	-12	11.8
16MY1802A	P	y	D	9	170	490	134.5	52.8	134.5	52.8	5.8
Site MY19											
16MY1901A	L	y	D	5	450	590	79.2	-41.8	79.2	-41.8	6.6
16MY1903A	L	y	D	4	450	560	69.7	-50	69.7	-50	13.6
16MY1903B	L	y	F	10	28	90	77.4	-35.6	77.4	-35.6	6.7
16MY1904A	L	y	D	5	450	590	78.7	-45.9	78.7	-45.9	11.2
16MY1906A	L	y	D	5	450	600	69	-38.5	69	-38.5	4
16MY1906B	L	y	F	4	18	25	63.4	-40.1	63.4	-40.1	2
16MY1902B	L	y	F	9	25	65	69.5	-40.3	69.5	-40.3	3.3
16MY1905A	L	y	F	11	23	70	69.6	-39.9	69.6	-39.9	4
Site MY46											
16MY2601A	L	y	D	6	560	680	72.6	-0.6	72.6	-0.6	5.7
16MY2602B	f	n	F	6	13	25	66.2	8.1	66.2	8.1	11.3
16MY2702B	P	y	F	9	5	25	140.3	38.7	140.3	38.7	11
16MY2701B	L	y	F	7	40	70	52.1	13.9	52.1	13.9	6.8
16MY2704A	L	y	D	3	360	450	44.8	5.3	44.8	5.3	14.5
16MY2705B	P	y	F	6	8	30	136.9	16.5	136.9	16.5	10.8
16MY2707A	P	y	D	12	130	560	332.8	-29.4	332.8	-29.4	9.9
17MY4606A	L	y	D	7	350	590	54.9	-19.2	54.9	-19.2	8.6
17MY4607A	L	y	D	6	400	590	50.9	8.7	50.9	8.7	6.3
17MY4608A	P	y	D	9	210	490	175.5	-78.4	175.5	-78.4	18.3
17MY4606A	P	y	D	11	130	560	97.9	64.1	97.9	64.1	13.2
17MY4613A	P	y	D	5	130	290	149.7	-15	149.7	-15	13.4
17MY4613B	P	y	F	8	3	20	71.4	67.5	71.4	67.5	22.5
Site MY48											
17MY4801A	L	y	D	7	350	590	115	-32.5	115	-32.5	5.8
17MY4803A	L	y	D	7	320	560	104.8	-9.8	104.8	-9.8	5.3
17MY4805A	L	y	D	4	350	490	120.7	-3.3	120.7	-3.3	14.1
17MY4806A	L	y	F	10	30	100	115.7	-25.4	115.7	-25.4	3.6
17MY4807A	L	y	D	8	320	590	112.4	-21	112.4	-21	4.3
17MY4809A	L	y	D	8	320	590	124.6	-25.8	124.6	-25.8	8.4
17MY4810A	P	y	D	11	130	530	22.5	-9.1	22.5	-9.1	8.4
17MY4802A	P	y	F	11	10	40	204.4	47	204.4	47	13.5
17MY4808A	P	y	F	15	8	60	220.4	-20.4	220.4	-20.4	13.8
Site MY07											
16MY0701A	L	y	D	5	450	600	62.3	-14.4	62.3	-14.4	2.6
16MY0701B	L	y	F	8	20	50	61	-6.4	61	-6.4	2.5
16MY0702A	L	y	D	5	450	590	59.8	-1.3	59.8	-1.3	3.3

16MY0703A	L	y	D	5	450	600	67.3	1.2	67.3	1.2	3
16MY0704A	L	y	D	5	450	590	65.7	8.7	65.7	8.7	5.8
16MY0704B	L	y	F	8	20	55	65.1	16.2	65.1	16.2	9.5
16MY0705A	L	y	D	5	450	600	68.7	12.2	68.7	12.2	0.9
16MY0707A	L	y	D	5	450	590	64.7	2.3	64.7	2.3	1.4
16MY0706A	L	y	F	9	30	70	70.1	2.3	70.1	2.3	1.1
17MY0701A	L	y	D	7	350	590	73.5	-5.4	73.5	-5.4	1.2
17MY0702A	L	y	D	7	350	590	74.9	7.8	74.9	7.8	2.5
17MY0703A	P	y	D	11	130	530	343.3	-6.2	343.3	-6.2	13.9
Site MY08											
16MY0801B	L	y	D	5	450	590	123.1	35.8	123.1	35.8	0.6
16MY0802B	L	y	D	6	410	600	93.9	40.9	93.9	40.9	2.7
16MY0803B	L	y	D	3	530	590	95.8	28.3	95.8	28.3	1.8
16MY0804B	L	y	F	3	18	25	106.5	30.9	106.5	30.9	0.7
16MY0805B	L	y	D	3	530	590	88.4	28.4	88.4	28.4	1.2
16MY0806B	L	y	F	8	20	50	100.8	24.3	100.8	24.3	5.5
16MY0807A	L	y	F	9	20	70	117.6	40.3	117.6	40.3	0.9
Site MY10											
16MY1001B	L	y	F	7	15	45	108.8	56.7	118.2	7.3	6.6
16MY1002B	L	y	F	13	10	70	99.8	62.5	115.8	14.2	1.3
16MY1003B	L	y	D	4	490	590	88.7	20.1	88.9	-19.7	1.7
16MY1004B	L	y	D	4	490	590	83.4	42.9	97.6	1.9	2.3
16MY1005B	L	y	D	4	490	590	81	43.8	96.7	3.7	1.2
16MY1007B	L	y	D	4	490	590	88	47.1	102.6	3.7	4.5
16MY1008B	L	y	F	8	15	70	102.1	50.6	112.5	2.8	1.4
Site MY11											
16MY1101A	L	y	F	4	15	25	98.6	54	111.1	16.3	0.4
16MY1102B	L	y	D	4	450	560	112.6	36.9	116.1	-2.8	1.5
16MY1103B	L	y	D	3	530	600	103.2	38.1	109.1	0.2	0.5
16MY1104B	L	y	F	5	15	30	101.1	38.6	107.6	1.1	0.6
16MY1105B	L	y	D	5	450	600	108.7	44.7	114.8	5.4	1.1
16MY1107A	L	n	F	10	13	40	82.3	40.8	95.3	9	3.8
16MY1107B	L	y	D	5	450	590	94.3	39.7	103.1	4	2.4
16MY1108B	L	y	D	5	450	590	95.3	40.4	104	4.4	1.5
Site MY12											
16MY1201A	L	y	D	11	360	680	64.2	50.3	64.2	50.3	1.8
16MY1202A	L	y	F	3	40	50	53.2	47.7	53.2	47.7	1.5
16MY1203A	L	y	D	11	360	680	73.7	40.7	73.7	40.7	1.7
16MY1204A	L	y	F	3	80	120	70.4	47.2	70.4	47.2	0.3
16MY1205A	L	y	D	11	360	680	59.3	41	59.3	41	1.4
16MY1206A	L	y	F	4	60	120	52	32.7	52	32.7	0.6
Site MY15											
16MY1502B	L	y	F	9	13	45	88.4	28.8	88.4	28.8	1.8
16MY1504B	L	y	D	5	450	590	105	28.8	105	28.8	2.4
16MY1505B	L	y	F	11	15	55	96.6	15.3	96.6	15.3	1.3
16MY1506A	L	y	D	10	360	490	104.8	-7.4	104.8	-7.4	1.3
16MY1506B	L	y	F	6	13	25	108.8	-4.6	108.8	-4.6	0.2

16MY1508B	L	y	D	13	400	590	110	-5.8	110	-5.8	0.5
16MY1503B	P	y	D	12	170	570	355.5	-34.9	355.5	-34.9	8.8
Site MY34											
17MY3401A	L	n	D	5	320	490	98.1	-9.8	9.5	-78.7	8.8
17MY3402A	L	n	D	5	320	490	76.4	-41.7	324.8	-45.4	8.2
17MY3404A	L	n	D	6	290	490	80.5	-23.4	346.9	-58.3	7.2
17MY3406A	L	n	D	3	290	350	79.3	-14.1	5	-59.9	8.7
17MY3407A	L	n	D	6	320	530	62.1	-34.3	341.1	-39.3	10.5
17MY3408A	L	n	D	5	320	490	109.7	-34.1	288.8	-63.9	9.6
17MY3409A	L	n	D	5	320	490	81.3	-44	318.9	-46.5	4
17MY3410A	L	n	D	3	290	350	79.8	-33.7	331.9	-52.5	6.2
17MY3411A	L	n	D	3	290	350	80.1	-32.8	332.9	-53.2	2.6
17MY3412A	L	n	D	3	290	350	73.4	-18.9	358.3	-53.4	11.6
17MY3413A	L	n	D	3	290	350	71.9	-30.6	341.4	-48.4	1.5
Site MY35											
17MY3501A	L	y	F	8	30	80	147.2	37.7	147.2	37.7	0.7
17MY3502A	L	y	F	10	30	100	155.1	11.4	155.1	11.4	7.6
17MY3504A	L	y	D	8	320	590	126.2	-60.5	126.2	-60.5	2.3
17MY3505A	L	y	F	10	30	100	249.9	61.3	249.9	61.3	2.2
17MY3506A	L	y	D	8	320	590	50.2	12.3	50.2	12.3	5.1
17MY3507A	L	y	D	8	320	590	257.8	-20	257.8	-20	3
17MY3508B	L	y	F	10	30	100	118.6	26.6	118.6	26.6	1.6
17MY3509A	L	y	D	8	320	590	67.3	33.1	67.3	33.1	5.9
17MY3510A	L	y	F	10	30	100	342	-13.9	342	-13.9	1.5
17MY3511A	L	y	D	8	320	590	83.2	18.3	83.2	18.3	4.6
Site MY37											
17MY3701A	P	y	D	13	130	590	26.5	-34.3	82.7	-24.5	8
17MY3702A	P	y	D	12	130	560	24.4	-36.3	85.1	-26	12
17MY3704A	P	y	D	12	130	560	208.7	34.5	262.7	22.6	18.4
17MY3705A	P	y	D	12	130	560	212.5	13.3	240.2	18.6	5.2
17MY3706A	P	y	D	12	130	560	206.1	27.5	255.2	25.2	5.2
17MY3708A	L	y	D	6	400	590	100.2	48.1	352.7	39.7	2.8
17MY3709A	L	y	D	6	400	590	108.7	38.9	357.8	50.2	0.8
17MY3713A	L	y	D	6	400	590	118.1	30.2	0.8	61.7	1.3
17MY3703A	L	y	D	5	400	560	90.4	34.6	12.5	39.1	1.6
17MY3707A	P	y	D	12	130	560	258.9	50.5	285.1	-10.1	8.4
17MY3710A	P	y	D	11	130	530	57	-53.3	103	-3.5	8.9
17MY3711A	P	y	D	13	130	590	197	-6	216.2	30.4	13.4
17MY3712A	P	y	D	12	130	560	196.5	-2	220.7	31.9	4.9
17MY3714A	P	y	D	12	130	560	186.4	-16.2	200.5	36.6	8.3
17MY3703B	L	y	F	10	20	50	87.4	32.3	16.2	37.2	0.6
17MY3707B	L	y	F	7	20	40	89.7	44.9	0.7	35	5.6
17MY3710B	P	y	F	11	3	28	46.7	-43.7	92.4	-8.8	6.3
17MY3711B	P	y	F	10	3	25	238.7	15.2	246.1	-6.2	4.8
17MY3712B	P	y	F	10	3	25	230.2	28.5	257.7	4	3.2
17MY3714B	P	y	F	9	3	23	236	37.1	267	0.8	5.1
Site MY38											
17MY3801A	L	y	F	6	20	35	90.2	-0.1	90.2	-0.1	4.9

17MY3804A	P	y	D	9	250	560	355.3	-44.8	355.3	-44.8	6
17MY3805A	P	y	D	11	170	560	6.9	-38.8	6.9	-38.8	7
17MY3808A	L	y	D	8	320	590	97.7	10.3	97.7	10.3	3
17MY3809A	P	y	D	10	210	560	356	-51	356	-51	7.6
17MY3810A	L	y	D	8	320	590	96.6	0.6	96.6	0.6	1.9
17MY3811A	L	y	D	8	320	590	104.6	-1.3	104.6	-1.3	1.4
17MY3802A	P	y	D	12	170	590	23.1	-42.5	23.1	-42.5	5.4
17MY3807A	P	y	D	10	210	560	153.4	-66.1	153.4	-66.1	8.1
17MY3802B	P	y	F	9	3	23	17.4	-42.1	17.4	-42.1	3.9
17MY3807B	P	y	F	9	3	23	358.1	-42.8	358.1	-42.8	9.8
Site MY22											
16MY2201A	L	y	D	5	450	600	32.5	-51.7	29.5	13	2.3
16MY2202A	L	y	D	5	450	590	41.7	-52.8	34.9	10.7	2
16MY2203A	L	y	D	5	450	600	25.2	-33.2	25.2	31.8	5.5
16MY2205B	L	y	D	5	450	600	39.4	-41.3	36.6	22.3	1.9
16MY2206B	L	y	D	5	450	590	38.4	-38.4	36.5	25.2	3.6
16MY2207B	L	y	D	4	490	590	50.1	-53	39.7	8.8	1.3
16MY2204A	P	y	F	9	20	50	120.9	11.1	127.2	-1.2	5.9
16MY2208A	P	y	F	13	10	50	116.6	12.4	126.5	3.2	6.8
Site MY23											
16MY2301B	L	y	D	9	290	570	50.7	-34.3	63.6	21.5	2.5
16MY2303A	L	y	D	10	250	570	53.5	-28.1	57.1	24.5	4.9
16MY2304A	L	y	D	9	250	560	45.7	-37.1	66.2	17.2	2.2
16MY2305A	L	n	D	10	250	590	43	-32.9	61.7	15.2	2.8
16MY2308A	L	y	F	13	30	120	48.6	-31.8	60.8	20	0.5
16MY2309B	L	y	D	9	290	590	50.9	-29.5	58.4	22.2	3.5
16MY2310B	L	y	D	9	290	570	48.6	-34.6	63.7	19.8	1.6
16MY2302A	L	y	F	4	50	80	47.5	-27.3	55.9	19.3	2.1
16MY2306A	L	y	F	10	30	120	49.3	-32.4	61.5	20.5	0.6
16MY2307A	L	y	F	7	35	110	48.1	-28.5	57.3	19.7	1.4
Site MY24											
16MY2405A	L	y	F	5	15	65	22.2	-50.6	75.4	15	0.7
16MY2408A	L	y	F	6	20	90	23.9	-45.4	70	14.5	0.9
16MY2410A	L	y	F	7	15	80	27.1	-47.7	71.6	17.3	0.1
16MY2401A	L	y	D	3	450	530	9.7	-39.7	68.9	2.7	7.7
16MY2402A	L	y	D	4	360	490	18.6	-47.2	72.9	11.7	5.2
16MY2403A	L	y	D	9	250	530	44.9	-52.5	75	29.2	2.7
16MY2403B	L	y	F	5	20	40	42.6	-44.6	66.2	27.2	3.5
16MY2404A	L	y	D	4	400	530	29.3	-43.5	66.9	17.6	3.9
16MY2407A	L	y	D	5	400	560	27.8	-48.5	72.2	17.9	2.8
16MY2409A	L	y	D	10	360	660	24.4	-45.6	70	14.9	0.7
16MY2409B	L	y	F	12	20	140	22.5	-43.7	68.7	13	1.2
16MY2406A	L	y	D	4	410	530	23.2	-42.9	67.7	13.2	2.3
Site MY25											
16MY2502A	L	y	D	6	400	590	49.6	-14.8	47.9	-1.3	2
16MY2503B	L	y	D	5	400	560	56.7	-16.3	54.3	-4.2	3.6
16MY2505A	L	y	D	5	400	560	51.4	-26.1	47.2	-12.7	4
16MY2506A	L	y	N	8	350	650	61.8	-15.8	59.2	-4.9	2

16MY2508A	L	y	D	6	400	590	65.5	-21.5	61	-11.4	1.2
16MY2510A	L	y	D	6	400	590	52.3	-25.1	48.2	-11.8	2.8
16MY2501A	L	y	F	10	15	50	46.7	-12	45.7	2.1	9.8
16MY2504A	L	y	F	10	15	70	52.3	-10.4	51.4	2.5	5
16MY2507A	L	y	F	9	20	80	59.6	-17	56.8	-5.6	1.7
16MY2509B	L	y	F	5	15	30	42	-10.7	41.5	4.2	4.4
Site MY41											
17MY4101A	L	y	D	4	400	530	29.4	-53.9	84.3	17.5	5.9
17MY4103A	L	y	D	5	320	490	28.3	-50.6	81.3	15.8	3.1
17MY4104A	L	y	D	5	320	490	25.6	-52	83.2	14.7	5.5
17MY4105A	L	y	D	5	320	490	25.7	-44.7	76.2	12.2	3.9
17MY4106A	L	y	F	10	30	100	33.2	-44.9	74.6	17.2	4.7
17MY4107A	L	y	D	4	320	450	36.9	-47.8	76.8	20.5	7
17MY4109A	L	y	D	5	320	490	21.7	-42.9	75.7	8.8	5.7
17MY4110A	L	y	D	4	320	450	13.9	-54.2	88.2	9.2	12.9
17MY4111A	L	y	D	3	400	490	18.3	-48.8	82.1	9.2	8.7
17MY4112A	L	y	D	5	320	490	34.6	-46.5	75.9	18.6	8.2
17MY4114A	L	y	D	7	320	560	29.1	-45.6	76.1	14.7	7.4
Site MY42											
17MY4201A	L	n	D	7	290	530	36.2	-38	66.8	9.6	4.7
17MY4202A	L	n	D	7	290	530	37.6	-39	67.8	10.7	3.3
17MY4204A	L	n	D	6	290	490	37.7	-42.7	71.6	10.8	6.7
17MY4205A	L	n	D	6	290	490	31.6	-42.4	71.5	6.3	2.7
17MY4207A	L	n	D	6	290	490	31.4	-43.5	72.6	6.2	4.2
17MY4208A	L	n	D	7	290	530	35.7	-41.9	70.8	9.4	2.6
17MY4209A	L	n	D	6	290	490	31.8	-42.5	71.6	6.5	5
17MY4210A	L	n	D	6	290	490	50.1	-44.9	74.7	19.6	4.6
17MY4211A	L	n	D	6	290	490	31.8	-39	68	6.3	4
17MY4203A	L	n	D	6	290	490	37.7	-40.4	69.3	10.8	3.2
Site MY43											
17MY4301A	L	y	D	7	350	590	54.1	-17	44.1	-24	1.1
17MY4302A	L	y	D	7	350	590	54.6	-14.3	46	-21.8	1.5
17MY4303A	L	y	D	7	350	590	53.8	-15.1	44.8	-22.2	1.1
17MY4304A	L	y	D	7	350	590	58.4	-9.2	52	-18.9	0.8
17MY4305A	L	y	D	7	350	590	51.8	-14.7	43.1	-20.9	1.2
17MY4306A	L	y	D	7	350	590	60.5	-18.7	49.3	-28.4	1.9
17MY4307A	L	y	F	9	35	100	48.4	-18.1	38.4	-22.5	1.1
17MY4308A	L	y	D	7	350	590	51.4	-18.7	40.8	-24.3	1.6
17MY4309A	L	y	F	9	35	100	56.1	-28.6	39.5	-35	1.2
17MY4310A	L	y	D	7	350	590	59.5	-20.1	47.6	-29.1	1
17MY4311A	L	y	D	7	350	590	52.4	-16.7	42.8	-23	2.1
17MY4312A	L	y	D	7	350	590	54.1	-23.4	40.7	-29.6	2.5
17MY4313A	L	y	D	7	350	590	54.4	-18.9	43.4	-25.8	1
Site MY44											
17MY4401A	L	y	F	9	35	100	24.3	-18.7	26.2	-27.7	1.4
17MY4402A	L	n	D	6	400	590	50	-26.7	54.5	-32.8	8.2
17MY4403B	L	y	F	12	35	120	202.9	6.8	203.7	15.9	0.9
17MY4404A	L	n	D	7	400	620	128.7	41.6	120.7	47.4	6.3

17MY4404B	L	n	F	7	35	80	17.5	-6.3	18.1	-15.7	7
17MY4404C	L	n	F	7	35	80	100.5	74.1	66.2	73	7
17MY4405A	L	n	D	5	400	560	57.8	-31.5	63.8	-36.3	7.7
17MY4407A	L	n	D	5	400	560	50.7	-47.2	60.7	-52.8	6
17MY4408A	L	n	D	4	400	530	40	-4.9	41	-12.4	2.1
17MY4409A	L	n	D	5	400	560	75.4	-5	76.5	-7.3	10
17MY4410A	L	n	D	5	400	560	62.6	-5.6	63.8	-10.1	4.2
17MY4411A	L	n	D	6	400	590	33.8	-14.9	35.9	-23.1	3.3
Site MY45											
17MY4501A	P	y	D	10	130	490	128.9	25.8	129	-14.2	7.5
17MY4502A	L	y	D	7	350	590	48.2	-21.3	31.7	-21.7	6.5
17MY4504A	L	y	D	7	350	590	53.4	-22.2	34.9	-25.7	5.1
17MY4505A	P	y	D	8	130	400	128.4	29.8	128.5	-10.2	14.9
17MY4506A	P	y	D	10	130	490	128.5	34.2	128.6	-5.8	8.1
17MY4508A	L	y	D	4	250	350	56.5	-11.5	45	-19.8	3.9
17MY4509A	L	y	D	10	250	590	62.3	-30.9	34	-37.5	9.5
17MY4510A	L	y	D	4	350	490	55.9	-24.6	34.9	-29	5.7
17MY4511A	L	y	D	3	350	450	53.2	-26	31.8	-28.3	2.9
17MY4512A	P	y	D	9	130	450	137	37.2	135.5	-2.5	15
17MY4513A	P	y	D	12	130	560	320.6	8.9	326	47.8	10.8
17MY4514A	L	y	D	4	250	350	59.6	-23.2	38.7	-30.3	5.1
17MY4515A	P	y	D	8	130	400	294.9	-38	298	1.1	8.6
17MY4516A	P	y	D	8	130	400	129.2	17.6	129.2	-22.4	14.9
MY51 Mafic											
19MY5101A	L	y	D	7	400	580	78.9	-3.4	78.9	-3.4	4.7
19MY5102A	L	y	D	6	400	560	69.1	8.6	69.1	8.6	2
19MY5104A	L	y	D	6	400	560	70.6	12.2	70.6	12.2	3.5
19MY5105A	L	y	D	5	400	530	87.3	1.3	87.3	1.3	6.2
19MY5111A	L	y	D	7	400	580	82.2	-0.6	82.2	-0.6	3.1
19MY5113A	L	y	D	7	400	580	81.5	1	81.5	1	2.2
19MY5114A	L	y	D	7	400	580	82.4	-4	82.4	-4	2
19MY5117A	L	y	D	7	400	580	83.5	-5.6	83.5	-5.6	2.9
19MY5107A	L	y	F	4	20	40	72.4	0.6	72.4	0.6	5.9
19MY5109A	L	y	F	5	15	40	76.2	-4	76.2	-4	6.5
Granodiorite											
19MY5103A	L	y	D	7	400	580	74.7	-2.8	74.7	-2.8	2.3
19MY5106A	L	y	D	7	400	580	74.1	-1.1	74.1	-1.1	2.6
19MY5112A	L	y	D	7	400	580	66.9	5	66.9	5	2.1
19MY5108A	L	y	D	7	400	580	75.7	2.9	75.7	2.9	2.2
19MY5110A	L	y	D	7	400	580	76.8	-6	76.8	-6	2.8
19MY5115A	L	y	D	7	400	580	75.9	-2.6	75.9	-2.6	2.8
19MY5116A	L	y	D	7	400	580	67.6	5.6	67.6	5.6	2.4
Site MY53											
19MY5301A	L	y	F	5	30	25	69.4	10.8	69.4	10.8	1.6
19MY5302A	P	y	D	13	190	560	11.9	-50.4	11.9	-50.4	7.1
19MY5304A	L	y	D	4	460	560	76.9	7.7	76.9	7.7	2.3
19MY5305A	P	y	D	13	190	560	193.6	65.2	193.6	65.2	8.4
19MY5308A	P	y	D	13	190	560	172.7	61.9	172.7	61.9	13.2

19MY5310A	P	y	D	11	190	490	186.1	86.6	186.1	86.6	17.3
19MY5313A	P	y	D	11	190	490	351.4	-65.6	351.4	-65.6	10.6
Site MY09											
19MY0901A	L	n	D	9	250	490	40.7	-43.9	332.6	-24.4	13.3
19MY0903A	L	n	D	3	280	370	51.3	-48.1	325.8	-30.4	3.7
19MY0904A	L	n	D	4	250	340	63.1	-31.7	341.4	-44.6	7.3
19MY0905A	L	n	D	5	250	370	73.2	-40.1	325.1	-47.9	9.6
19MY0906A	L	n	D	5	250	370	85.8	-37.2	317.5	-57.1	6.9
19MY0907A	L	n	D	4	250	340	62.2	-28	346.6	-44.9	8.6
19MY0908A	L	n	D	5	250	370	65.1	-30.8	341.8	-46.4	4.2
19MY0910A	L	n	D	5	250	370	61.7	-29.8	344.3	-43.9	3.2
19MY0911A	L	n	D	3	150	370	63.3	-33.2	339.3	-44.2	0.5
19MY0912A	L	n	D	4	280	370	58	-34.6	339.3	-39.5	4.3
16MY0904B	L	n	D	4	250	350	50.8	-18.8	0.4	-35.6	1.9
16MY0909B	L	n	D	6	290	450	69.6	-47.5	319	-41.4	12.4
16MA0004A	L	y	D	4	260	340	159.5	17.6	155.5	-3.4	9.9
16MA0005A	L	y	D	5	210	310	181.9	18.4	172.8	9.3	6.1
16MA0006A	L	y	D	5	220	340	190.6	-2.7	192.4	-2.4	5.1
16MA0009A	L	y	D	5	220	340	191.5	-12.2	198.8	-9.4	11.2
16MA0016A	L	y	D	5	210	310	354.6	37.8	25.1	38.6	3.1
16MA0020A	L	y	D	6	210	340	341.9	25.8	4.6	37.6	4
16MA0021A	L	y	D	4	220	310	9.6	9	15.3	8.1	1.5
16MA0023A	L	y	D	6	210	340	12.6	16.7	22.5	12.3	2.7
16MA0024A	L	y	D	7	220	400	5.3	16.4	16.6	16.4	2.7
16MA0026A	L	y	D	6	210	340	348.2	25.9	9.9	34	4.2
16MA0027A	L	y	D	9	220	440	3.7	6	8.8	9.1	3.3
16MA0028A	L	y	D	7	235	405	357.7	-6.2	356.6	2.9	1.9
16MA0030A	L	y	D	8	220	425	358.4	14.7	10	19.3	2.1
16MA0031A	L	y	D	9	210	440	2.5	9.2	9.8	12.5	2.3
16MA0032A	L	y	D	6	235	370	14.2	5.6	16.9	2.6	4.5
16MA0038A	L	y	D	7	210	370	27.7	14.8	33.1	2.1	6.9
16MA0046A	L	y	D	8	235	500	14.7	5.8	17.4	2.4	3.1
16MA0047A	L	y	D	9	210	475	24.8	31.4	40.8	17.1	3.6
16MA0048A	L	y	D	11	220	500	18.5	26.8	33.4	16.8	5.2
16MA0049A	L	y	D	8	210	410	8.9	25.7	25.6	21.5	3.6
16MA0051A	L	y	D	5	220	340	10.8	20.5	23.5	16.4	7.8
16MA0052A	L	y	D	7	210	370	2.6	24.5	20.1	24.3	4.3
16MA0054A	L	y	D	7	250	425	3.2	-21.4	351.9	-12.4	5.4
16MA0061A	L	y	D	9	210	440	15.4	-8.6	9.3	-9.5	6.1
16MA0062A	L	y	D	4	235	310	6.3	-8.2	2.3	-3.8	3
16MA0069A	L	y	F	7	24	30	20.1	8.3	23.2	1.2	4.3
16MA0070A	L	y	F	5	24	25	2.5	8.9	9.7	12.2	3.5
16MA0072A	L	y	D	5	250	370	338.9	-1.4	343.6	17.5	7.3
16MA0075A	L	y	F	7	24	30	347.1	15.5	1.3	26.6	5.9
16MA0080A	L	y	D	5	250	370	3.9	-2.6	3.7	2.2	9.6

16MA0084A	L	y	D	8	240	440	333.9	-9.5	334.9	13.1	2.3
16MA0086A	L	y	D	7	250	425	347.8	-36.3	331.5	-16.4	3.9
16MA0088A	L	y	D	7	210	370	16.6	-2.1	14.2	-5.1	6.4
16MA0094A	L	y	D	9	210	440	15.7	-19.9	2.3	-18.6	4.1
16MA0095A	L	y	D	8	220	425	8.7	-12.8	1.4	-8.8	5.6
16MA0096A	L	y	D	5	0	210	25	18.1	40.5	15	4.9
16MA0111A	L	y	D	12	235	560	14.5	32.7	34.6	23.7	4.1
16MA0112A	L	y	D	7	260	500	31.4	18.2	37.9	2.9	7.4
16MA0114A	L	y	D	9	235	475	42.4	3.2	38.8	-15.6	4.5
16MA0116A	L	y	D	13	250	560	21.1	22	32.3	11.6	5.1
16MA0117A	L	y	D	9	235	475	2.6	35.2	28.2	32.2	6.3
16MA0120A	L	y	D	12	235	560	37.8	21.2	44.6	2	3
16MA0125A	L	y	D	9	235	475	7.5	-1.5	7.3	0.9	3
16MA0126A	L	y	D	7	220	400	5.6	1.1	7.4	4.1	7
16MA0127A	L	y	D	4	285	370	20.6	-14.1	9.9	-17	5.7
16MA0130A	L	y	D	8	220	425	8.1	12.1	16	11.4	4.8
16MA0132A	L	y	D	7	235	410	345	25.1	6.6	35.3	7.4
16MA0134A	L	y	F	7	24	30	355.1	-1	357.6	8.6	5.1
16MA0136A	L	y	F	8	25	30	353.2	4.9	359.5	14.6	8.1
16MA0138A	L	y	D	12	235	560	355.4	25.6	15.3	29.4	9.1
16MA0148A	L	y	D	12	210	530	344.6	-1.8	348.4	14	5.2
16MA0156A	L	y	D	11	240	560	163.4	-24.7	185.1	-36	2.2
16MA0159A	L	y	D	7	240	440	9.4	-16.7	359.6	-12.3	10.1
16MA0169A	L	y	D	12	235	560	337.5	-0.3	343	19.2	7.2
16MA0170A	L	y	D	13	210	560	11.9	5.8	15.2	4.1	3.8
16MA0171A	L	y	D	12	210	560	356.5	16.9	10	22.1	3
16MA0172A	L	y	D	11	235	560	348.9	16	3.1	26	4.4
16MA0173A	L	y	D	13	210	560	358.1	15.6	10.4	20.2	3.1
16MA0174A	L	y	D	12	210	560	351.8	19.2	7.8	26.7	3.3
16MA0178A	L	y	D	12	235	560	343.3	3	350	18.8	7
16MA0179A	L	y	D	12	235	560	0.4	6.7	6.6	11.7	3.6
16MA0195A	L	y	D	11	240	560	198.1	3.9	194.3	7.4	4.9
16MA0196A	L	y	D	14	235	210	183.6	-6.6	189.1	-9.7	3.5
16MA0197A	L	y	D	13	210	560	177.4	-0.2	180.2	-8.3	1.8
16MA0198A	L	y	D	6	265	410	190.4	3.7	188.3	2.6	2
16MA0199A	L	y	D	12	235	560	180.4	-10.5	188.9	-14.7	3
16MA0200A	L	y	D	13	210	560	176.7	-16.7	190.1	-21.8	3.9
16MA0207A	L	y	D	13	240	560	157.6	-18.2	174.8	-34.4	3.1
16MA0224A	L	y	D	8	235	490	186.4	8.3	182.3	3.9	9.9
16MA0225M	L	y	D	9	235	475	158.4	-2.3	165.2	-20.9	5.5
16MA0229A	L	y	D	13	210	560	355.5	14.3	7.4	20.6	3.5
16MA0240A	L	y	D	8	235	440	2.4	10.9	10.8	13.9	4.5
16MA0250A	L	y	D	7	235	370	5.3	-2.5	5	1.4	10.4
16MA0251A	L	y	D	11	235	560	1.4	-15.4	354.1	-6.6	2.9

16MA0252A	L	y	D	11	235	560	10.9	-7.1	6.7	-5.6	1.9
16MA0254A	L	y	D	10	235	530	353.9	29.6	17.4	33.2	7.5
16MA0257A	L	y	D	11	235	560	328.8	9.6	340.6	32.1	6.7
16MA0275A	L	y	D	9	220	460	348.2	-10.6	346.4	4.7	2.4
16MB0002A	L	y	D	8	220	430	192.1	5.1	188.4	4.9	5.4
16MB0004A	L	y	D	9	220	460	199.1	-9.6	203.3	-1.9	4
16MB0005A	L	y	D	7	220	400	197	0.6	195.1	4.6	2.9
16MB0009A	L	y	D	8	220	430	168.1	-4.8	176.1	-17.9	4
16MB0010A	L	y	D	9	220	460	182.9	-4.5	187.6	-8.3	5.7
16MB0012A	L	y	D	8	220	430	173.3	-4.9	180.3	-14.8	2.1
16MB0016A	L	y	D	9	220	460	193.5	0.7	192.4	2.4	3.8
16MB0018A	L	y	F	4	25	40	201.3	18.4	186.4	20.9	4.5
16MB0019A	L	y	D	9	220	460	221.6	-29.8	232.2	-5.3	2.8
16MB0025A	L	y	D	8	220	430	347.2	-11.1	345.5	5.8	4.9
16MB0027A	L	y	D	8	220	430	18.5	11.1	23.7	3.4	3.9
16MB0029A	L	y	D	8	220	430	5.6	6.1	10.7	7.8	3.4
16MB0030A	L	y	D	9	220	460	9.3	28	28.5	21.8	3.1
16MB0031A	L	y	D	8	220	430	28.1	8.4	29.4	-4.6	6.3
16MB0032A	L	y	D	7	250	430	354.9	22.5	14.1	26.9	7.9
16MB0036A	L	y	D	7	220	400	0.6	20	16.4	21.5	7.1
16MB0037A	L	y	D	6	220	370	1.2	13.2	12	16	10.4
16MB0038A	L	y	D	7	220	400	4.1	10.3	12.2	12	6.1
16MB0040A	L	y	D	8	220	430	19.2	19.8	29.9	9.7	6
16MB0041A	L	y	D	9	220	460	20	23.5	32.9	12	4.4
16MB0042A	L	y	D	8	220	430	7.7	10.3	15.1	9.7	4.4
16MB0044A	L	y	D	9	220	460	4	-22.8	350.8	-13.3	3.9
16MB0045A	L	y	D	8	250	460	341.6	13.6	356.7	28.8	4
16MB0047A	L	y	D	9	220	460	7.1	19	20.5	16.6	7.2
16MB0050A	L	y	D	8	220	430	17.3	17.8	27.1	9.3	7.3
16MB0058A	L	y	F	5	20	40	201.6	10.7	192	15.3	2.9
16MB0059A	L	y	F	6	20	45	173.5	-6.1	181.3	-15.5	1.1
16MB0060A	L	y	F	6	20	45	215.9	-7.1	214.8	10.3	7.7
16MB0061A	L	y	F	5	20	45	213.2	6.6	204	19.5	5
16MB0064A	L	y	F	5	20	40	171	17.3	164.7	1.3	7.1
16MB0082A	L	y	D	10	130	400	353.4	17.1	8.9	23.9	0.9
16MB0085A	L	y	D	7	250	430	354.1	8.1	3.1	16.8	8.5
16MB0088A	L	y	D	7	250	430	12.3	-11.1	4.7	-9.6	5.9
16MB0091A	L	y	D	8	220	430	1.8	6.3	7.9	10.4	4.5
16MB0092A	L	y	D	9	220	460	345.6	0	350.9	15.7	9.1
16MB0098A	L	y	D	8	220	430	22.1	6.4	23.5	-2.5	3.9
17MC0001A	L	y	D	8	220	430	204.3	-0.6	202	7	4.6
17MC0004A	L	y	F	7	34	15	194.3	5.5	190.3	5.4	4.4
17MC0004A	L	y	D	5	310	430	195.2	7.7	189.6	7.6	2.7
17MC0005A	L	y	F	12	22	20	207.7	-0.3	204.4	9.5	5

17MC0006A	L	y	F	20	22	30	189.3	-8.9	195.8	-8.9	4.9
17MC0007A	L	y	F	9	31	15	208.7	18.6	192.3	24.5	4.7
17MC0011A	L	y	D	7	250	430	205.2	-0.8	202.8	7.5	4.2
17MC0012A	L	y	D	5	310	430	202.8	8.7	194.7	13.3	9.8
17MC0013A	L	y	F	10	20	50	202.4	12.8	191.7	16.1	0.9
17MC0015A	L	y	F	9	34	20	213.6	10.2	202.2	21.3	5.5
17MC0018A	L	y	F	11	22	15	196.5	23.3	179.8	20.1	8.5
17MC0020A	L	y	D	6	220	370	215.4	1.4	209.6	15.6	7
17MC0021A	L	y	D	5	340	460	180	-10.6	189.8	-16.1	7.4
17MC0027A	L	y	F	11	25	20	192.9	17.5	181.3	13.6	2.3
17MC0028A	L	y	D	7	250	430	206.1	26.8	184.1	28.7	1.7
17MC0029A	L	y	F	11	22	15	211.6	9.5	201.1	19.5	4.2
17MC0030A	L	y	D	7	220	400	183.6	-13.9	194.8	-16.3	11.8
17MC0031A	L	y	F	9	20	50	178	-29.1	202.3	-30.9	0.6
17MC0032A	L	y	F	7	34	15	175.4	14.4	170.3	0.4	3.8
17MC0034A	L	y	F	9	20	50	209.1	4.6	202.4	14.1	0.8
17MC0036A	L	y	F	13	22	20	197.2	-6.7	200.4	-2.1	2.1
17MC0042A	L	y	F	11	22	15	200.1	-3.9	200.9	1.9	5
17MC0043A	L	y	D	8	220	430	198	22.1	181.8	20.3	9.5
17MC0044A	L	y	F	19	25	30	219.1	9.9	207	24.5	1.9
17MC0046A	L	y	D	7	220	400	197.3	-12.7	204.4	-6.7	4.3
17MD0001A	L	y	D	8	220	430	25.7	15.6	32.4	4.4	4.3
17MD0003A	L	y	F	9	20	50	43.1	-10.1	31.2	-26.6	5.1
17MD0007A	L	y	D	4	340	430	13.8	4.9	16.6	3.1	1.5
17MD0009A	L	y	D	7	130	310	39.1	16.9	43.6	-2	3.8
17MD0014A	L	y	D	6	160	310	211	29.9	186.3	34.2	5.2
17MD0015A	L	y	F	12	22	15	193.4	4.8	190.3	4.4	4.4
17MD0016A	L	y	F	9	28	15	187.4	-0.8	189	-3.7	4
17MD0017A	L	y	D	8	220	430	198	-3.9	199.2	0.3	3.4
17MD0019A	L	y	D	5	280	400	198.1	4	194.4	6.6	6.6
17MD0021A	L	y	F	12	22	20	189.9	-19	202.6	-16.4	3.2
17MD0026A	L	y	F	11	20	70	223.9	11.1	211.2	27.8	3.1
16MY3206A	L	y	D	3	210	290	13.5	25.9	29.5	14.2	2.4
16MY3210A	L	y	D	3	210	290	14.8	31.5	34.4	17.3	2.5
16MY3212A	L	y	D	3	170	250	25.1	11.7	28	-3.7	1.2
16MY3213A	L	y	D	3	170	250	24	11.7	27.3	-3.1	2.1
16MY3214A	L	y	D	3	210	290	23.6	4.9	22.4	-7.9	2.8
16MY3215A	L	y	D	3	170	250	28	10	29.1	-6.8	1.2
16MY3307A	L	y	D	3	170	250	5.8	26.3	23.7	18.4	0.8
16MY3308B	L	y	D	3	210	290	26.6	21.6	35	2.2	1.6
16MY3309B	L	y	D	3	170	250	17.5	15.7	24.6	3.2	1.7
16MY3310A	L	y	D	4	170	290	176	-9.1	184.4	-12.4	0.9
16MY3315A	L	y	D	3	210	250	188.6	8.8	181.5	9.3	1.4
16MY3316A	L	y	D	3	210	290	180	5.7	177.3	1.2	2.2

16MY3318B	L	y	D	3	210	290	192.9	4.5	187.7	8.9	1.4
16MY3319A	L	y	D	3	170	250	185.8	13.4	176.3	10.8	1.7
16MY3320B	L	y	D	3	210	290	183.2	-9.5	190	-7.9	2.3
16MY3321B	L	y	D	3	170	250	185.3	-8.2	190.6	-5.5	1.4
16MY3322A	L	y	D	4	170	290	193.3	1.8	189.8	7.2	2.4
16MY3323A	L	y	D	3	170	250	189.5	-3.2	190.3	0.9	2.7

Supplementary Data 3

			J parameter	error J			Mass Discrimination (1+e)	Err Discrimination							
	MY0705 Whole Rock		6.52E-03	2.21E-05			1.009619	1.32E-03							
laser power	40Ar	Error 40Ar	39Ar	Error 39Ar	38Ar	Error 38Ar	37Ar	Error 37Ar	36Ar	Error 36Ar	40Ar*/39ArK	Error 40Ar*/39ArK	Apparent age (My)	Error Age (My)	Delay to irradiation (day)
300	1061.40231	1.13719	30.173656	0.06303	1E-06	0.018267	11.12973	0.100744	3.511375	0.031846	1.873167	0.356965	21.954071	4.159444	62.163889
360	297.810372	2.35238	26.912735	0.05477	1E-06	0.01919	15.120314	0.077592	0.793901	0.01854	2.797366	0.223967	32.688526	2.5972	62.184028
430	1652.1849	0.88989	209.51469	0.40399	1E-06	0.022403	127.92607	0.217949	3.339972	0.031941	3.536994	0.053099	41.233545	0.635467	62.204167
480	1099.64554	0.87681	128.26012	0.17666	0.01974	0.016004	58.638505	0.179896	0.715575	0.014006	7.191382	0.03812	82.870376	0.54847	62.804167
520	640.117013	0.50837	72.18622	0.09688	1E-06	0.013304	23.810319	0.08921	0.243989	0.008731	8.082605	0.040453	92.880868	0.592536	62.823611
600	1633.80648	1.26429	179.91613	0.27596	1E-06	0.016089	85.823222	0.151341	0.778672	0.027286	8.074338	0.049182	92.788265	0.67009	62.84375
650	2296.32761	0.85947	248.59017	0.21199	1E-06	0.011995	68.206509	0.178787	0.545437	0.008779	8.780981	0.019606	100.68669	0.467608	62.863889
690	2523.58322	1.34276	276.3236	0.25962	0.00353	0.012944	59.482919	0.144595	0.417947	0.020994	8.852346	0.027672	101.48246	0.518331	62.89375
730	1242.61298	1.82788	138.35499	0.30379	0.00049	0.01186	30.611052	0.135541	0.163054	0.018866	8.798552	0.04783	100.88265	0.675276	62.923611
800	1791.55994	2.37089	200.3587	0.24911	1E-06	0.010658	47.212666	0.083569	0.224974	0.017253	8.779823	0.032464	100.67378	0.549446	62.94375
900	4435.40799	5.82703	485.81659	0.7123	1E-06	0.022936	129.54576	0.203231	0.793548	0.014781	8.83249	0.024116	101.26109	0.495035	62.963889
1000	3792.44032	4.61896	418.98565	0.70741	1E-06	0.020664	138.46355	0.277754	0.691119	0.021822	8.771244	0.027524	100.57809	0.514511	63.004167
1200	6109.55906	5.77111	698.37155	2.6681	0.00379	0.036289	264.90587	0.510944	1.154863	0.016134	8.480986	0.036604	97.33775	0.571961	63.023611
1450	1291.74891	0.98393	153.99221	0.27944	1E-06	0.024966	90.587148	0.25908	0.495046	0.021002	7.737286	0.044879	89.008718	0.622781	63.04375
Fusion	3042.77629	3.49165	330.78638	0.54788	0.00793	0.023625	892.92729	1.810377	3.666478	0.029623	7.004583	0.038255	80.765149	0.544792	63.063889
			J parameter	error J			Mass Discrimination (1+e)	Err Discrimination							
	MY0413 Whole Rock		6.51E-03	2.21E-05			1.009619	1.32E-03							
laser power	40Ar	Error 40Ar	39Ar	Error 39Ar	38Ar	Error 38Ar	37Ar	Error 37Ar	36Ar	Error 36Ar	40Ar*/39ArK	Error 40Ar*/39ArK	Apparent age (My)	Error Age (My)	Delay to irradiation (day)
300	2047.60562	1.53763	5.501733	0.03889	1E-06	0.020241	0.378565	0.031059	6.993512	0.029858	7.007316	2.516764	80.708818	28.352037	67.913889
360	243.954688	0.36602	6.845175	0.02348	1E-06	0.019176	0.405742	0.028028	0.682246	0.023007	7.085447	0.989742	81.588712	11.148595	67.94375
440	162.242714	0.19993	10.339587	0.05573	1E-06	0.020583	1.953609	0.037981	0.28775	0.012299	7.83658	0.352153	90.026019	3.963773	67.963889
540	244.476526	0.45157	23.113411	0.12953	1E-06	0.018515	12.184431	0.089701	0.253842	0.017131	7.69095	0.221974	88.393265	2.516239	67.984028
650	76.881444	0.13973	7.962511	0.05777	0.00357	0.017179	3.376835	0.017865	0.067133	0.01683	7.460712	0.616721	85.808898	6.936484	68.023611
900	557.140814	0.41697	63.510411	0.07667	1E-06	0.019527	17.569402	0.060592	0.30571	0.02168	7.56208	0.101127	86.947178	1.190269	68.034028
1150	500.056518	0.37526	59.017129	0.06959	1E-06	0.02348	12.497956	0.055508	0.217596	0.024593	7.561748	0.122365	86.943459	1.419465	68.063889
1500	2692.5756	1.80281	229.39845	0.13637	1E-06	0.023647	69.65546	0.117938	3.475759	0.037099	7.567069	0.057861	87.003187	0.741645	68.084028
Fusion	574.330052	0.47604	49.313446	0.07159	1E-06	0.018674	21.008664	0.073188	0.713624	0.020587	7.719917	0.126139	88.718149	1.460931	68.113889
			J parameter	error J			Mass Discrimination (1+e)	Err Discrimination							
	MY4301 Whole Rock		6.58E-03	2.23E-05			1.009619	1.32E-03							
laser power	40Ar	Error 40Ar	39Ar	Error 39Ar	38Ar	Error 38Ar	37Ar	Error 37Ar	36Ar	Error 36Ar	40Ar*/39ArK	Error 40Ar*/39ArK	Apparent age (My)	Error Age (My)	Delay to irradiation (day)
300	321.303468	0.32944	56.227606	0.093	0.0008	0.021911	0.177671	0.014612	0.540775	0.012762	2.977696	0.068806	35.065357	0.815562	68.154167
360	827.252594	1.02569	119.5413	0.31144	1E-06	0.020381	0.240951	0.019888	0.265315	0.012487	6.339506	0.037441	73.853542	0.524841	68.184028

420	2867.79555	2.88205	374.89763	0.23895	0.01541	0.02561	0.729289	0.028466	0.310698	0.022055	7.478751	0.022283	86.811475	0.437499	68.19375
460	7277.16645	4.98323	923.98213	0.95559	1E-06	0.01994	2.466129	0.044309	0.291449	0.018888	7.856263	0.015719	91.084949	0.414579	68.813889
520	356.861618	0.33182	45.161236	0.03134	1E-06	0.026673	0.663675	0.045307	0.019752	0.017124	7.851923	0.110886	91.035881	1.308481	68.84375
640	2306.25848	1.28199	295.39342	0.26551	1E-06	0.025233	5.715048	0.055846	0.022136	0.016642	7.863445	0.02108	91.166151	0.444225	68.863889
800	2347.27048	2.70413	295.71181	0.23376	0.01015	0.021133	3.970271	0.042027	0.160406	0.017262	7.85704	0.023106	91.093732	0.456691	68.904167
1000	2061.6526	2.23498	256.29498	0.32528	0.00732	0.025877	0.725055	0.025383	0.196657	0.023903	7.895017	0.03228	91.52308	0.524177	68.923611
1300	1828.77672	1.65628	223.35073	0.25842	1E-06	0.023108	0.595739	0.024379	0.281136	0.018384	7.897625	0.029322	91.552557	0.501566	68.94375
1800	1954.98233	2.31562	232.68305	0.29749	0.02324	0.02196	0.951087	0.015519	0.747905	0.022489	7.54708	0.034613	87.58572	0.53257	68.973611
2400	876.916888	0.71244	68.666481	0.13455	0.00097	0.02398	1.256959	0.034357	1.669013	0.018804	5.845232	0.092399	68.202584	1.094868	69.004167
3333	1160.02464	0.56541	80.999243	0.17079	1E-06	0.020862	1.642767	0.041679	2.334907	0.024349	6.100226	0.102466	71.1201	1.207623	69.023611
			J parameter	error J			Mass Discrimination (1+e)	Err Discrimination							
	MY0405 Whole Rock		6.51E-03	2.21E-05			1.009619	1.33E-03							
laser power	40Ar	Error 40Ar	39Ar	Error 39Ar	38Ar	Error 38Ar	37Ar	Error 37Ar	36Ar	Error 36Ar	40Ar*/39ArK	Error 40Ar*/39ArK	Apparent age (My)	Error Age (My)	Delay to irradiation (day)
300	275.19507	0.39638	2.372065	0.02849	1E-06	0.01179	2.107611	0.02578	0.875599	0.017072	10.399325	2.180683	118.45906	24.048845	69.79375
360	86.880858	0.23415	1.520644	0.02415	0.00161	0.018966	1.421921	0.027203	0.281758	0.019869	4.290161	3.81449	49.813301	43.686173	69.804167
450	147.698869	0.14106	5.780395	0.02699	0.00565	0.014278	5.46729	0.073422	0.421182	0.013539	5.025156	0.691899	58.211348	7.890975	69.823611
580	185.755928	0.19355	18.292394	0.06067	0.00869	0.01712	21.4126	0.093842	0.401903	0.008339	4.330378	0.139064	50.273829	1.605793	69.84375
750	191.61473	0.30786	27.220197	0.0595	0.01635	0.022206	71.817468	0.112653	0.281427	0.020022	5.1371	0.216471	59.487002	2.478159	69.873611
1000	222.878485	0.39842	27.477148	0.04621	1E-06	0.022078	112.54651	0.203171	0.232427	0.017227	7.363501	0.185964	84.672696	2.117974	69.904167
1300	649.327986	1.00388	76.595198	0.12787	1E-06	0.025158	351.43316	0.557202	0.585843	0.016713	8.175756	0.069111	93.774512	0.863299	69.913889
1600	790.222685	1.10115	89.194662	0.10882	0.00239	0.034714	439.5163	0.608046	0.751264	0.028052	8.478389	0.095776	97.154017	1.140628	69.934028
2000	991.495952	1.11496	110.75649	0.25701	0.00134	0.032222	579.25201	0.843602	0.994582	0.027859	8.534751	0.079739	97.782707	0.975782	69.984028
Fusion	1090.92861	1.35271	116.88559	0.24264	0.04284	0.0321	797.56138	0.649038	1.492136	0.029517	8.462979	0.081017	96.982083	0.987847	70.004167
			J parameter	error J			Mass Discrimination (1+e)	Err Discrimination							
	MY0101 Biotite		6.51E-03	2.21E-05			1.009619	1.32E-03							
laser power	40Ar	Error 40Ar	39Ar	Error 39Ar	38Ar	Error 38Ar	37Ar	Error 37Ar	36Ar	Error 36Ar	40Ar*/39ArK	Error 40Ar*/39ArK	Apparent age (My)	Error Age (My)	Delay to irradiation (day)
290	7.723008	0.07174	0.099388	0.01917	1E-06	0.01906	0.000001	0.019584	0.000001	0.011267	78.412163	36.18859	745.43895	281.943807	70.034028
360	4.002483	0.06727	0.110476	0.02092	1E-06	0.020206	0.000001	0.02833	0.000001	0.014128	36.556883	37.72785	385.86227	358.599193	70.054167
410	24.463712	0.07905	2.067019	0.01554	1E-06	0.024014	0.000001	0.024468	0.035192	0.01174	7.005305	1.648642	80.601159	18.555195	70.084028
530	354.874747	0.27775	18.851047	0.04564	1E-06	0.019645	0.009777	0.026516	0.762043	0.019023	7.274351	0.301996	83.626212	3.410117	70.104167
600	222.964457	0.19225	22.763929	0.04251	1E-06	0.018998	0.000001	0.029815	0.157215	0.00752	7.880283	0.099491	90.420605	1.173963	70.134028
660	250.259459	0.55328	28.177143	0.06874	0.00015	0.019231	0.010793	0.032212	0.063453	0.014319	8.308736	0.150745	95.209531	1.727564	70.154167
740	471.741641	0.4102	54.442708	0.11885	1E-06	0.014967	0.01799	0.02128	0.09892	0.012616	8.216132	0.071258	94.175553	0.884993	70.173611
790	558.953927	0.66951	65.998122	0.14643	1E-06	0.019257	0.052631	0.023998	0.067223	0.010585	8.250363	0.052493	94.557834	0.703268	70.19375
830	418.776378	0.51185	49.331704	0.07732	1E-06	0.015821	0.049053	0.020136	0.025159	0.011758	8.417701	0.072111	96.425451	0.896644	72.79375
900	494.041104	0.61266	57.924216	0.10179	1E-06	0.011157	0.071377	0.015689	0.007613	0.011775	8.568043	0.062816	98.101727	0.807727	72.823611
1050	1169.27221	1.62732	137.28745	0.23491	1E-06	0.01777	0.112271	0.024759	0.019052	0.013392	8.553494	0.035888	97.93958	0.567273	72.84375
1200	567.120031	0.67304	66.635051	0.18125	1E-06	0.011645	0.088421	0.023517	0.00397	0.014507	8.570491	0.068997	98.129014	0.868147	72.863889

Fusion	8107.42752	6.18553	958.82368	0.92217	0.00075	0.008473	11.645126	0.059764	0.191101	0.015773	8.478842	0.016182	97.10734	0.4378	72.884028
			J parameter	error J			Mass Discrimination (1+e)	Err Discrimination							
	MY1707 Biotite		6.53E-03	2.22E-05			1.009619	1.32E-03							
laser power	40Ar	Error 40Ar	39Ar	Error 39Ar	38Ar	Error 38Ar	37Ar	Error 37Ar	36Ar	Error 36Ar	40Ar*/39ArK	Error 40Ar*/39ArK	Apparent age (My)	Error Age (My)	Delay to irradiation (day)
300	110.649198	0.1436	8.422218	0.0252	0.00943	0.020474	0.009622	0.02503	0.209673	0.018134	6.038122	0.626497	69.909511	7.121	72.923611
380	107.488908	0.24164	10.45886	0.0628	0.01154	0.024201	0.053214	0.0227	0.135865	0.013398	6.605195	0.375367	76.338331	4.259573	72.94375
450	275.858323	0.5083	28.967599	0.06286	1E-06	0.022834	0.047973	0.017751	0.23963	0.012397	7.210593	0.128231	83.176512	1.485701	72.963889
451	182.824896	0.32421	20.983204	0.06991	1E-06	0.020369	0.000001	0.016979	0.08781	0.017352	7.577675	0.242167	87.310262	2.747551	72.984028
452	56.718629	0.17557	6.68887	0.04452	0.00591	0.012919	0.021748	0.021153	0.017841	0.010546	7.783625	0.46108	89.625359	5.192807	73.034028
520	134.901325	0.18854	16.458974	0.04974	1E-06	0.020001	0.000001	0.020359	0.032819	0.009651	7.691511	0.172497	88.59026	1.972868	73.04375
580	128.492449	0.19532	16.037011	0.06779	1E-06	0.019256	0.000001	0.016372	0.010669	0.017037	7.891139	0.310302	90.832753	3.503531	73.063889
670	405.386806	0.44367	50.945104	0.09664	0.02059	0.019493	0.071129	0.016558	0.077765	0.008229	7.586618	0.051271	87.410857	0.679651	73.084028
780	250.317437	0.41579	32.236414	0.0913	1E-06	0.016324	0.051835	0.025467	0.03538	0.012096	7.517036	0.112221	86.628052	1.312122	73.113889
930	349.916074	0.37359	44.952632	0.06962	1E-06	0.017169	0.053999	0.017523	0.040896	0.011012	7.590534	0.073368	87.454898	0.900251	73.14375
1200	1120.68285	0.70462	143.72971	0.17278	1E-06	0.012893	0.185896	0.016399	0.129933	0.014088	7.605407	0.032322	87.622172	0.511976	73.163889
1400	903.870134	0.81768	117.31048	0.18758	0.01262	0.014323	0.120846	0.018785	0.083242	0.00928	7.568617	0.02904	87.208376	0.48527	73.173611
Fusion	521.037691	0.57094	67.777567	0.11694	1E-06	0.018526	0.112202	0.025563	0.042099	0.010277	7.576893	0.047904	87.301462	0.647605	73.19375
			J parameter	error J			Mass Discrimination (1+e)	Err Discrimination							
	MY1906 Biotite		6.54E-03	2.22E-05			1.009619	1.33E-03							
laser power	40Ar	Error 40Ar	39Ar	Error 39Ar	38Ar	Error 38Ar	37Ar	Error 37Ar	36Ar	Error 36Ar	40Ar*/39ArK	Error 40Ar*/39ArK	Apparent age (My)	Error Age (My)	Delay to irradiation (day)
300	31.141484	0.06291	1.240528	0.02723	0.00046	0.017292	0.044382	0.028995	0.080899	0.0122	6.436813	2.858098	74.512483	32.414271	73.79375
400	291.875589	0.46514	29.393752	0.08065	0.02668	0.013726	0.183258	0.023653	0.34583	0.010694	6.610252	0.111445	76.478334	1.301272	73.813889
450	494.366662	0.42025	59.137962	0.1042	0.00413	0.011525	0.108964	0.024953	0.132998	0.014702	7.783157	0.074983	89.716845	0.920441	73.834028
480	263.417194	0.47717	32.657498	0.1243	0.00759	0.017221	0.044092	0.03041	0.041751	0.011544	7.768189	0.108378	89.548515	1.273335	73.84375
550	936.403805	0.74122	117.09283	0.15134	1E-06	0.017517	0.189194	0.02563	0.105844	0.015594	7.807311	0.042062	89.988459	0.600552	73.884028
620	238.991969	0.32383	30.045293	0.06319	1E-06	0.008426	0.027332	0.018678	0.031921	0.013902	7.71794	0.136093	88.983284	1.574233	73.904167
750	1157.68797	1.06064	143.89524	0.09635	1E-06	0.017643	0.374147	0.019469	0.131104	0.016633	7.854342	0.036654	90.517195	0.555274	73.923611
850	792.417623	1.0997	99.658203	0.15125	1E-06	0.026669	0.207228	0.022173	0.047135	0.016446	7.886304	0.051767	90.876444	0.69147	73.94375
1000	2318.06426	2.6152	291.39766	0.43896	1E-06	0.022286	1.040507	0.03938	0.12462	0.013535	7.903752	0.022954	91.072516	0.454733	73.973611
1200	2048.35732	2.43632	258.69092	0.26627	1E-06	0.022563	2.277933	0.046269	0.104007	0.011056	7.876291	0.020726	90.763902	0.439976	73.99375
1500	1173.45678	0.59493	148.66725	0.20033	1E-06	0.024777	4.249001	0.06205	0.053332	0.012358	7.872215	0.028768	90.71809	0.493685	74.013889
Fusion	317.09217	0.35174	40.371974	0.05229	1E-06	0.020607	1.535001	0.041025	0.022036	0.010981	7.782789	0.080757	89.712715	0.980269	74.034028
			J parameter	error J			Mass Discrimination (1+e)	Err Discrimination							
	MY2701 Biotite		6.55E-03	2.22E-05			1.009619	1.32E-03							
laser power	40Ar	Error 40Ar	39Ar	Error 39Ar	38Ar	Error 38Ar	37Ar	Error 37Ar	36Ar	Error 36Ar	40Ar*/39ArK	Error 40Ar*/39ArK	Apparent age (My)	Error Age (My)	Delay to irradiation (day)
300	104.787339	0.1956	3.987123	0.01674	1E-06	0.014088	0.087714	0.024858	0.319567	0.01132	3.288472	0.834479	38.557173	9.681952	74.063889
400	678.967059	0.50339	68.120241	0.10537	0.01675	0.017861	0.258799	0.030952	0.618036	0.020713	7.427648	0.092279	85.948401	1.101181	74.084028

460	1729.03322	1.32915	191.80967	0.13913	1E-06	0.020287	0.322612	0.02421	0.839739	0.013803	7.826469	0.028337	90.449746	0.49031	74.104167
460	1157.06417	1.34806	139.55057	0.16076	1E-06	0.006087	0.21385	0.028623	0.238173	0.005289	7.871425	0.021564	90.956441	0.446041	74.123611
570	1599.95687	1.21479	195.06714	0.22431	1E-06	0.010477	0.491277	0.016837	0.300052	0.01595	7.830623	0.029012	90.496571	0.495442	74.163889
650	3285.92711	2.99156	410.60634	0.26406	1E-06	0.015793	0.582943	0.025608	0.300456	0.013643	7.862708	0.017409	90.858211	0.422016	74.184028
750	1385.64431	1.07259	173.57107	0.12427	1E-06	0.014951	0.224188	0.013747	0.117038	0.02039	7.859661	0.03687	90.823869	0.558721	74.204167
900	1026.01239	1.3286	127.76827	0.20861	0.02532	0.024276	0.325387	0.023567	0.119644	0.021822	7.831726	0.053507	90.509008	0.708755	74.804167
1200	4781.77757	2.23162	597.01242	0.32651	1E-06	0.020561	1.419993	0.021436	0.446496	0.011949	7.865372	0.01406	90.888226	0.405953	74.823611
1600	4837.43791	1.15136	614.81901	0.5206	0.04059	0.02683	1.232196	0.01699	0.203722	0.018743	7.843255	0.015567	90.638956	0.41198	74.84375
Fusion	1682.09276	0.51271	214.78659	0.22171	1E-06	0.021448	0.485629	0.021139	0.077674	0.01946	7.797643	0.029614	90.124773	0.498869	74.863889
			J parameter	error J			Mass Discrimination (1+e)	Err Discrimination							
	MY1707 Amphibole		6.53E-03	2.22E-05			1.009619	1.32E-03							
laser power	40Ar	Error 40Ar	39Ar	Error 39Ar	38Ar	Error 38Ar	37Ar	Error 37Ar	36Ar	Error 36Ar	40Ar*/39ArK	Error 40Ar*/39ArK	Apparent age (My)	Error Age (My)	Delay to irradiation (day)
500	533.21365	0.26573	25.91326	0.05673	1E-06	0.022458	5.360549	0.047879	1.184063	0.021425	7.604891	0.253404	87.616366	2.872578	74.904167
650	454.941361	0.22409	54.853371	0.0279	1E-06	0.013253	3.827733	0.038772	0.185462	0.012333	7.418369	0.067095	85.517457	0.833434	74.923611
780	292.803711	0.43733	36.367782	0.08423	1E-06	0.011962	4.391717	0.026219	0.046846	0.01208	7.80306	0.099512	89.843673	1.177266	74.94375
840	187.703115	0.28255	23.231837	0.05532	1E-06	0.018614	6.909615	0.039119	0.03312	0.015941	7.869975	0.200787	90.595139	2.284978	74.963889
880	221.286359	0.3405	26.754415	0.09976	0.01589	0.037833	15.850329	0.035939	0.041285	0.017389	8.160305	0.192105	93.851981	2.187323	74.99375
950	211.325076	0.31772	25.214753	0.08612	1E-06	0.031718	15.479469	0.044998	0.05716	0.015145	8.070827	0.177645	92.848864	2.028326	75.013889
1050	2875.69918	2.95959	332.97499	0.34705	1E-06	0.034174	505.3655	0.418807	1.129815	0.018517	8.404698	0.024825	96.588977	0.484378	75.04375
1100	869.114431	0.6494	103.21936	0.08488	1E-06	0.030269	145.4638	0.150714	0.30308	0.014962	8.270256	0.045238	95.083858	0.63982	75.063889
1250	390.450216	0.54594	47.868241	0.13939	1E-06	0.016429	48.667767	0.133362	0.091608	0.015624	8.126472	0.099312	93.472755	1.177714	75.104167
1500	414.079195	0.69952	51.379399	0.09611	1E-06	0.020348	45.228797	0.136361	0.072198	0.020446	8.115042	0.118108	93.344624	1.378553	75.123611
Fusion	1756.21689	0.77715	203.34426	0.17826	1E-06	0.024729	321.95541	0.3161	0.704474	0.013019	8.414898	0.024781	96.703113	0.484465	75.14375
			J parameter	error J			Mass Discrimination (1+e)	Err Discrimination							
	MY1906 Amphibole		6.54E-03	2.22E-05			1.009619	1.33E-03							
laser power	40Ar	Error 40Ar	39Ar	Error 39Ar	38Ar	Error 38Ar	37Ar	Error 37Ar	36Ar	Error 36Ar	40Ar*/39ArK	Error 40Ar*/39ArK	Apparent age (My)	Error Age (My)	Delay to irradiation (day)
500	398.848193	0.53963	88.14188	0.13875	1E-06	0.019334	6.921945	0.029683	0.929533	0.022482	1.540634	0.076418	18.115909	0.897272	75.79375
700	543.999266	0.95488	52.436453	0.1672	1E-06	0.027172	2.313966	0.033553	0.469432	0.019836	7.8916	0.116528	90.935955	1.361901	75.813889
850	517.155447	0.87135	48.091031	0.13501	1E-06	0.021946	2.656723	0.026044	0.407127	0.017937	8.420497	0.114732	96.870033	1.34535	75.834028
900	47.042255	0.44667	4.953239	0.03812	0.01809	0.019598	0.482904	0.018262	0.01099	0.017142	8.98349	1.010444	103.16532	11.286907	75.863889
1000	101.283644	0.13595	10.456954	0.027	0.01242	0.017792	1.384088	0.015636	0.063039	0.013513	8.084389	0.3762	93.101248	4.240036	75.89375
1100	290.951918	0.36011	27.937605	0.05477	1E-06	0.019346	6.16245	0.043077	0.131429	0.013486	9.244207	0.143106	106.07321	1.653099	75.923611
1180	478.124221	0.58778	45.956399	0.08321	1E-06	0.016956	21.409549	0.126437	0.197031	0.015662	9.466644	0.102921	108.55044	1.228833	75.934028
1240	273.797113	0.24957	27.121592	0.04906	0.00639	0.017231	17.320916	0.027888	0.101355	0.014194	9.393481	0.154267	107.73602	1.773527	75.954167
1350	2268.49737	1.4095	239.49433	0.25142	1E-06	0.018927	262.34828	0.371502	0.709474	0.035577	9.197276	0.047145	105.55011	0.680902	75.99375
1400	647.036027	0.48577	70.432546	0.11886	1E-06	0.015847	54.376423	0.099675	0.165715	0.018724	8.938043	0.080323	102.65795	0.99086	76.013889
1630	2145.54211	1.48505	240.53957	0.26211	1E-06	0.01419	276.58181	0.447055	0.520642	0.019967	8.895394	0.029897	102.1817	0.536052	76.04375
1630	776.247752	0.76066	89.489361	0.20813	1E-06	0.018664	61.457838	0.181593	0.147621	0.019827	8.585525	0.069168	98.71762	0.873719	76.063889

1800	327.640499	0.19598	38.738854	0.06423	1E-06	0.021363	23.785416	0.069808	0.055817	0.023388	8.394203	0.176489	96.575477	2.016639	76.084028
2050	187.399523	0.29359	21.48086	0.05373	1E-06	0.014435	25.9699	0.06682	0.087384	0.012605	8.170721	0.173316	94.070038	1.982442	76.123611
Fusion	1006.68488	0.85511	113.02271	0.2313	0.00749	0.016208	182.72226	0.358712	0.353463	0.014055	8.816823	0.043579	101.30396	0.64033	76.14375
			J parameter	error J			Mass Discrimination (1+e)	Err Discrimination							
	MY2701 amphibole		6.55E-03	2.22E-05			1.009619	1.32E-03							
laser power	40Ar	Error 40Ar	39Ar	Error 39Ar	38Ar	Error 38Ar	37Ar	Error 37Ar	36Ar	Error 36Ar	40Ar*/39ArK	Error 40Ar*/39ArK	Apparent age (My)	Error Age (My)	Delay to irradiation (day)
500	266.67223	0.26192	4.393762	0.03199	0.02464	0.03819	2.355273	0.041456	0.859777	0.015176	4.74505	1.050638	55.376185	12.07757	76.804167
750	201.933991	0.18244	13.113888	0.04152	1E-06	0.03093	1.881372	0.025802	0.399124	0.016054	6.777592	0.36029	78.58736	4.100938	76.834028
850	43.093289	0.12692	3.507372	0.02956	0.0234	0.031851	0.879461	0.035027	0.068314	0.021563	6.863846	1.785916	79.565807	20.256093	76.854167
950	54.183235	0.10492	5.29029	0.02485	1E-06	0.022272	2.753542	0.024011	0.05843	0.013921	7.369589	0.765876	85.292179	8.665179	76.913889
1050	93.901086	0.13718	9.594016	0.04893	0.03858	0.020749	9.41052	0.034143	0.085598	0.013459	7.738675	0.410971	89.459812	4.649825	76.923611
1120	170.144884	0.21201	18.040452	0.06814	1E-06	0.025174	20.774144	0.05106	0.125867	0.018346	8.02291	0.298501	92.662791	3.382283	76.954167
1200	376.313182	0.38184	42.420803	0.0619	0.00588	0.019456	52.820344	0.192282	0.196227	0.012797	8.183147	0.090564	94.465964	1.090101	76.963889
1250	395.476019	0.57642	45.453142	0.08796	0.02748	0.018863	57.205086	0.12013	0.181879	0.014717	8.199121	0.097648	94.645619	1.165031	77.004167
1330	517.427491	0.66956	60.042206	0.15522	1E-06	0.020221	74.940839	0.141173	0.209066	0.017102	8.261645	0.087591	95.348654	1.059784	77.023611
1450	481.825731	0.6142	56.597175	0.08795	1E-06	0.020783	72.264873	0.22366	0.190281	0.008508	8.204221	0.048975	94.702976	0.674402	77.04375
1650	341.295129	0.28467	40.79451	0.12519	0.00092	0.022551	53.057451	0.20823	0.122443	0.015333	8.171455	0.113377	94.334451	1.33293	77.063889
			J parameter	error J			Mass Discrimination (1+e)	Err Discrimination							
	MY2202 Whole Rock		6.54E-03	2.22E-05			1.009619	1.32E-03							
laser power	40Ar	Error 40Ar	39Ar	Error 39Ar	38Ar	Error 38Ar	37Ar	Error 37Ar	36Ar	Error 36Ar	40Ar*/39ArK	Error 40Ar*/39ArK	Apparent age (My)	Error Age (My)	Delay to irradiation (day)
300	665.430939	0.6189	6.865124	0.01471	0.00587	0.021703	1.526702	0.023139	2.08195	0.023695	9.985567	1.112191	114.37548	12.35343	79.79375
360	1370.37163	1.25587	21.461071	0.0407	1E-06	0.019246	5.344211	0.032056	4.154002	0.017975	8.430801	0.39501	97.035785	4.444492	79.813889
410	168.867756	0.20718	14.339747	0.04117	1E-06	0.018016	4.193895	0.027033	0.343176	0.015493	5.081999	0.317174	59.113278	3.637898	79.834028
480	999.422117	0.74393	53.011596	0.11107	1E-06	0.020211	14.003339	0.064683	2.550365	0.028695	5.19925	0.177026	60.454584	2.039716	79.863889
520	387.23707	0.54014	30.184656	0.07305	1E-06	0.023871	8.824568	0.04892	0.798771	0.014966	5.410889	0.153005	62.873115	1.76654	79.89375
590	1843.87591	1.12959	121.56971	0.22462	0.00897	0.018078	37.171291	0.101646	3.413466	0.032219	7.310664	0.094203	84.439452	1.118437	79.913889
630	520.63935	0.4969	58.372098	0.09872	0.00877	0.019765	15.732053	0.071191	0.370781	0.018868	7.288056	0.096855	84.18431	1.146753	79.94375
700	1204.83827	0.47551	135.11436	0.16256	1E-06	0.015158	68.637782	0.174061	0.910354	0.018314	7.289995	0.044723	84.206194	0.61234	79.963889
750	467.265821	0.48076	58.879898	0.11463	1E-06	0.026944	19.190211	0.091345	0.170136	0.026278	7.327267	0.131304	84.626806	1.521969	79.99375
850	1199.51735	0.51232	155.23039	0.23991	1E-06	0.025316	38.731772	0.114785	0.286533	0.02558	7.382379	0.050739	85.248543	0.671334	80.023611
1000	1797.3333	1.37387	232.50569	0.19785	1E-06	0.026446	23.573983	0.084008	0.34952	0.025774	7.412605	0.035349	85.589454	0.532008	80.04375
1300	2192.40386	2.20856	285.74419	0.2742	1E-06	0.02784	35.196926	0.133298	0.421986	0.028274	7.372709	0.032743	85.139472	0.509162	80.063889
1600	2601.72404	1.7907	336.3724	0.46374	0.01019	0.015293	57.837109	0.109155	0.594653	0.019588	7.37475	0.02374	85.162495	0.441145	80.104167
2000	1301.90009	1.12453	131.10153	0.14658	0.0025	0.015277	112.92462	0.216076	1.22562	0.018041	7.729948	0.047744	89.16473	0.650608	80.134028
Fusion	4013.20463	2.87673	285.182	0.15859	0.01671	0.014364	472.49802	0.51398	6.628085	0.024866	8.273892	0.051716	95.276559	0.699849	80.14375
Parameters	(36Ar/37Ar)Ca	0.00032	3	%											

	(39Ar/37Ar)Ca	0.00079	4	%											
	(38Ar/37Ar)Ca	2.6E-05	100	%											
	(40Ar/37Ar)Ca	0.0006	100	%											
	(40Ar/39Ar)K	0.00085	4	%											
	(38A/39Ar)K	0.011	91	%											
[3]	(36Cli/38Cl)	316	5	%											
[1] and [1']	(40Ar/36Ar)Atm	298.56	0.104	%											
[1] and [1']	(38Ar/36Ar)Atm	0.1885	0.159	%											
[2]	Lambda 40	5.53E-10	1.35E-12	y-1											
	Lambda 39	2.58E-03		y-1											
	Lambda 37	1.98E-02		d-1											
	Lambda 36Cl	2.26E-06		y-1											
References:															
[1]	Lee, JY, Marti, K, Severinghaus, JP, Kawamura, K, Yoo, HS, Lee, JB, Kim, JS (2006). A redetermination of the isotopic abundances of atmospheric Ar. Geochimica Cosmochimica Acta, 70, 4507-4512.														
[1']	Mark, DF, Stuart, FM, De Podesta, M (2011). New high-precision measurements of the isotopic composition of atmospheric argon. Geochimica Cosmochimica Acta, 75, 7494-7501.														
[2]	Renne, PR, Balco, G, Ludwig, RL, Mundil, R, Min, K, . (2011). Response to the comment by W.H. Schwarz et al. on "Joint determination of (40)K decay constants and (40)Ar*/(40)K for the Fish Canyon sanidine standard, and improved accuracy for (40)Ar/(39)Ar geochronology" by PR Renne et al. (2010). Geochimica Cosmochimica Acta, 75, 5097-5100.														
[3]	York, D, Personnal Communication - McMaster reactor														
Regression method	York, D. (1969). Least-squares fitting of a straight line with correlated errors. Earth Planet. Sci. Lett. 5, 320-4.														
Age and error of TCRs monitor refers to:	Rennes, PR, Balco, G, Ludwig, Mundil, R, Min, K, . (2011). Response to the comment by W.H. Schwarz et al. on "Joint determination of (40)K decay constants and (40)Ar*/(40)K for the Fish Canyon sanidine standard, and improved accuracy for (40)Ar/(39)Ar geochronology" by PR Renne et al. (2010). Geochimica Cosmochimica Acta, 75, 5097-5100.														

Appendix 2: Data tables Chapter 5

Reference: *Westerweel, J., Licht, A., Cogné, N., Roperch, P., Dupont-Nivet, G., Kai, M. T., … Aung, D. W (2020). Eocene to Miocene northward motion of the Burma Terrane and its indentation in the Eastern Himalayas. Tectonics. https://doi.org/10.1029/2020TC006413*

Supplementary Table 1

a) All samples used for magnetostratigraphy, sorted by depth; b) All bulk magnetic susceptibility data, sorted by depth.

Depth (m)	Sample	Line, Plane or Fisher	Anchored	Demag type	nb points	step min	step max	Bedding (az./dip)	Dec TC	inc TC	mad value	Category (Quality)	Formation
1426	17LA0099A	L	y	Th	6	280	430	005/35	5.5	35.4	3	2	Letkat Formation
1419.4	17LA0098A	L	y	Th	6	280	430	005/35	157.7	34.1	6.1	1	Letkat Formation
1410.9	17LA0095A	L	y	Th	6	280	430	005/35	215.5	29.5	6.7	1	Letkat Formation
1409.4	17LA0094A	L	y	Th	10	340	660	005/35	161.8	20.9	3	1	Letkat Formation
1403.5	17LA0091A	L	y	Th	7	280	460	005/35	170.7	12.8	4.9	1	Letkat Formation
1375	17LA0077A	L	y	Th	9	220	460	005/35	13	5.3	4.6	2	Letkat Formation
1346.5	17LA0084A	L	y	Th	5	280	400	005/35	183.2	12.8	4.8	2	Letkat Formation
1343	17LA0083A	L	y	Th	7	280	460	005/35	179.6	-0.2	2.1	1	Letkat Formation
1338	17LA0081A	L	y	Th	7	280	460	005/35	184.8	19.1	2.6	1	Letkat Formation
1336.7	17LA0080A	L	y	Th	7	280	460	005/35	172.9	-7.3	4.4	1	Letkat Formation
1329	17LA0079A	L	y	AF	12	175	700	005/35	178.2	11.4	7.1	1	Letkat Formation
1301.4	17LA0063A	f	n	Th	7	220	400	005/35	172	0.3	5.1	2	Letkat Formation
1277.1	17LA0056A	L	y	Th	3	370	430	005/35	185.9	9.3	14.7	2	Letkat Formation
1276	17LA0054A	L	y	Th	7	280	460	005/35	151.6	43.5	2.5	1	Letkat Formation
1264.3	17LA0051A	L	y	Th	8	250	460	005/35	153.5	30.7	2.7	1	Letkat Formation
1232.5	17LA0049A	L	y	AF	5	175	275	005/35	185.1	-35.7	6.9	2	Letkat Formation
1230.3	17LA0048A	L	y	Th	6	250	400	005/35	181.1	27.6	5.3	1	Letkat Formation
1227.1	17LA0047A	L	y	Th	5	250	370	005/35	177.2	11.3	8.9	1	Letkat Formation
1221.6	17LA0045A	L	y	Th	4	370	460	005/35	202.6	-49	12.5	2	Letkat Formation
1211	17LA0043A	L	y	Th	6	250	400	005/35	169.2	29.5	3.3	1	Letkat Formation
1132.6	17LA0029A	L	y	Th	9	220	460	005/35	13.6	28.1	5.1	2	Letkat Formation
1124.5	17LA0027A	L	y	Th	9	220	460	005/35	5.3	19.1	5.2	2	Letkat Formation
1121.2	17LA0026A	L	y	Th	9	220	460	005/35	-3.7	-11.2	4.3	2	Letkat Formation
1117.9	17LA0024A	L	y	Th	5	280	400	005/35	18	0.8	3.6	2	Letkat Formation
1115.6	17LA0023A	L	y	Th	4	340	430	005/35	-10.6	24.2	8.8	2	Letkat Formation
1105.5	17LA0022A	L	y	Th	5	310	430	005/35	145.8	-6.8	3.9	1	Letkat Formation
1103.8	17LA0021A	L	y	Th	3	250	310	005/35	180.1	-7.6	3.9	2	Letkat Formation
1004.5	16MA0275A	L	y	Th	9	220	460	011/37	-14.1	4.3	2.4	1	Letkat Formation
961.2	17LA0008A	L	y	Th	8	220	430	005/35	17.4	29.4	5.8	1	Letkat Formation
959.6	17LA0007A	L	y	Th	9	220	460	005/35	-0.2	27.5	4.3	1	Letkat Formation
953.2	17LA0005A	L	y	Th	6	280	430	005/35	-28	29.3	4.2	2	Letkat Formation
942.6	17LA0001A	L	y	Th	4	370	460	005/35	218.3	-32.3	5.4	2	Letkat Formation
934	16MA0263A	f	n	Th	8	210	410	011/37	165.1	-28.2	4.9	2	Tonhe Formation
930	16MA0259A	f	n	Th	11	235	560	011/37	3.3	22.2	7.6	2	Tonhe Formation
927.5	16MA0258A	L	y	Th	11	235	560	011/37	28.2	37.6	7	2	Tonhe Formation
923.8	16MA0257A	L	y	Th	11	235	560	011/37	-19.4	32.1	6.7	1	Tonhe Formation
923	16MA0255A	L	y	Th	9	235	530	011/37	-18.7	37.6	10	2	Tonhe Formation
922.6	16MA0254A	L	y	Th	10	235	530	011/37	17.4	33.2	7.5	1	Tonhe Formation
922.2	16MA0253A	f	n	Th	9	235	475	011/37	12.1	5.1	14.3	2	Tonhe Formation
914.9	16MA0252A	L	y	Th	11	235	560	011/37	6.7	-5.6	1.9	1	Tonhe Formation
913.7	16MA0251A	L	y	Th	11	235	560	011/37	-5.9	-6.6	2.9	1	Tonhe Formation
913.6	16MA0250A	L	y	Th	7	235	370	011/37	5	1.4	0.4	1	Tonhe Formation
911	16MA0248A	f	n	Th	11	235	560	011/37	-1.6	32.9	8.5	2	Tonhe Formation
906.2	16MA0246A	L	y	Th	12	235	560	011/37	23.7	25	9.2	2	Tonhe Formation
903.9	16MA0243A	f	n	Th	12	210	560	011/37	-10.1	36.2	8.2	2	Tonhe Formation
892.9	16MA0240A	L	y	Th	8	235	440	011/37	10.8	13.9	4.5	1	Tonhe Formation
892.4	16MA0239A	f	n	Th	5	210	310	011/37	-2.8	10.6	19.1	2	Tonhe Formation
890	16MA0238A	L	y	Th	6	210	370	011/37	14.5	35.5	8.5	2	Tonhe Formation
888.9	16MA0237A	L	y	Th	9	235	475	011/37	19.7	19.7	12.7	2	Tonhe Formation
866.3	16MA0229A	L	y	Th	13	210	560	011/37	7.4	20.6	3.5	1	Tonhe Formation
849.3	16MA0224A	L	y	Th	8	235	490	011/37	182.3	3.9	9.9	1	Tonhe Formation
832.6	16MA0221A	f	n	Th	8	210	405	011/37	119.2	-41	15.7	2	Tonhe Formation
831.8	16MA0220A	L	y	Th	5	210	310	011/37	8.8	12.1	12.6	2	Tonhe Formation
830.6	16MA0219A	L	y	Th	8	240	410	011/37	-6.3	-10	7.8	2	Tonhe Formation
821.1	16MA0213A	f	n	Th	6	240	340	011/37	153.9	-20.5	17.6	2	Tonhe Formation
812.2	16MA0212A	f	n	Th	4	235	310	011/37	179.2	-7.8	44.4	2	Tonhe Formation
803.6	16MA0210A	f	n	Th	6	265	370	011/37	154.4	24.2	10.5	2	Tonhe Formation
799.7	16MA0208A	f	n	Th	9	235	475	011/37	176	-4	16	2	Tonhe Formation
798.2	16MA0207A	L	y	Th	13	240	560	011/37	174.8	34.4	3.1	1	Tonhe Formation
797	16MA0206A	f	n	Th	8	340	560	011/37	193.8	-3.5	4.7	2	Tonhe Formation
791.5	16MA0202A	f	n	Th	12	235	560	011/37	211.2	-88.3	4.2	2	Tonhe Formation
785.5	16MA0200A	L	y	Th	13	210	560	011/37	190.1	21.8	3.9	1	Tonhe Formation
784.1	16MA0199A	L	y	Th	12	235	560	011/37	188.9	14.7	3	1	Tonhe Formation
783.5	16MA0198A	L	y	Th	6	265	410	011/37	188.3	2.6	2	1	Tonhe Formation
782	16MA0197A	L	y	Th	13	210	560	011/37	180.2	-8.3	1.8	1	Tonhe Formation
781	16MA0196A	L	y	Th	14	235	210	011/37	189.1	-9.7	3.5	1	Tonhe Formation
780.4	16MA0195A	L	y	Th	11	240	560	011/37	194.3	7.4	4.9	1	Tonhe Formation
779.1	16MA0194A	f	n	Th	9	235	475	011/37	250.1	-42.4	12.7	2	Tonhe Formation
778.1	16MA0193A	f	n	Th	7	285	475	011/37	131.8	-23.9	16.5	2	Tonhe Formation
776.8	16MA0192A	f	n	AF	4	290	300	011/37	190.5	-42.7	24.1	2	Tonhe Formation
775.8	16MA0191A	f	n	Th	6	210	340	011/37	167.3	-2.8	26.3	2	Tonhe Formation
773.7	16MA0190A	f	n	Th	6	210	340	011/37	146.8	21.1	14.8	2	Tonhe Formation
765.8	16MA0186A	f	n	Th	10	240	500	011/37	190.2	-43.5	7.4	2	Tonhe Formation
765.8	16MA0285A	L	y	Th	9	210	410	011/37	192.3	-41	6.5	2	Tonhe Formation
757	16MA0184A	f	n	Th	9	235	470	011/37	-2.9	16.6	13.7	2	Tonhe Formation
755	16MA0182A	f	n	Th	10	210	475	011/37	197.9	-36.9	8.5	2	Tonhe Formation
753	16MA0179A	L	y	Th	12	235	560	011/37	6.6	11.7	3.6	1	Tonhe Formation
751.7	16MA0178A	L	y	Th	12	235	560	011/37	-10	18.8	7	1	Tonhe Formation
748	16MA0175A	L	y	Th	8	100	310	011/37	-2.2	35.9	1.8	2	Tonhe Formation
747.2	16MA0174A	L	y	Th	12	210	560	011/37	7.8	26.7	3.3	1	Tonhe Formation
746.4	16MA0173A	L	y	Th	13	210	560	011/37	10.4	20.2	3.1	1	Tonhe Formation
745	16MA0172A	L	y	Th	11	235	560	011/37	3.1	26	4.4	1	Tonhe Formation
744	16MA0171A	L	y	Th	12	210	560	011/37	10	22.1	3	1	Tonhe Formation
742.9	16MA0170A	L	y	Th	13	210	560	011/37	15.2	4.1	3.8	1	Tonhe Formation
741.4	16MA0169A	L	y	Th	12	235	560	011/37	-17	19.2	7.2	1	Tonhe Formation
740	16MA0168A	L	y	Th	7	240	410	011/37	28	22.1	10.3	2	Tonhe Formation
733.2	16MA0164A	f	n	Th	10	235	500	011/37	214.3	-13.6	4.7	2	Tonhe Formation
726.4	16MA0159A	L	y	Th	7	240	440	011/37	-0.4	12.3	0.1	1	Tonhe Formation
724	16MA0157A	f	n	Th	9	235	500	011/37	33.8	-18.6	8.6	2	Tonhe Formation
714.2	16MA0156A	L	y	Th	11	240	560	011/37	185.1	36	2.2	1	Tonhe Formation
713.3	16MA0155A	f	n	Th	8	235	440	011/37	199.8	-27.7	13.2	2	Tonhe Formation
704.9	16MA0153A	f	n	Th	7	240	410	011/37	135.9	14.6	15.3	2	Tonhe Formation
685.6	16MA0148A	L	y	Th	12	210	530	011/37	-11.6	14	5.2	1	Tonhe Formation
683.3	16MA0146A	L	y	Th	4	235	310	011/37	38	5.5	3	2	Tonhe Formation
680.5	16MA0144A	L	y	AF	6	235	300	011/37	53.9	2.4	6.1	2	Tonhe Formation
680.4	16MA0143A	L	y	Th	4	235	310	011/37	34.6	6.9	7	2	Tonhe Formation
671.7	16MA0138A	L	y	Th	12	235	560	011/37	15.3	29.4	9.1	1	Yaw Formation
670.2	16MA0136A	L	y	AF	8	250	300	011/37	-0.5	14.6	8.1	1	Yaw Formation
668	16MA0134A	L	y	AF	7	235	300	011/37	-2.4	8.6	5.1	1	Yaw Formation
667.8	16MA0133A	L	y	Th	7	250	425	011/37	10.4	20.6	7.9	2	Yaw Formation
667	16MA0132A	L	y	Th	7	235	410	011/37	6.6	35.3	7.4	1	Yaw Formation
656	16MA0131A	L	y	Th	7	235	410	011/37	1.3	27.1	7.6	2	Yaw Formation
653.5	16MA0130A	L	y	Th	8	220	425	011/37	16	11.4	4.8	1	Yaw Formation
651.4	16MA0129A	L	y	Th	5	210	310	011/37	-5.3	8.8	4.4	2	Yaw Formation
650.4	16MA0128A	L	y	Th	5	210	310	011/37	20.4	-10.5	2.5	2	Yaw Formation
649	16MA0127A	L	y	Th	4	285	370	011/37	9.9	17	5.7	1	Yaw Formation
648	16MA0126A	L	y	Th	7	220	400	011/37	7.4	4.1	7	1	Yaw Formation
647	16MA0125A	L	y	Th	9	235	475	011/37	7.3	0.9	3	1	Yaw Formation
642.5	16MA0120A	L	y	Th	12	235	560	011/37	44.6	2	3	1	Yaw Formation
641.9	16MA0119A	L	y	Th	11	250	560	011/37	49	9	7.5	2	Yaw Formation
637.1	16MA0117A	L	y	Th	9	235	475	011/37	28.2	32.2	6.3	1	Yaw Formation
636.5	16MA0116A	L	y	Th	13	250	560	011/37	32.3	11.6	5.1	1	Yaw Formation
635.4	16MA0115A	L	y	Th	7	235	410	011/37	37.2	12	5.6	2	Yaw Formation
634.3	16MA0114A	L	y	Th	9	235	475	011/37	38.8	15.6	4.5	1	Yaw Formation
633.9	16MA0113A	L	y	Th	7	250	425	011/37	35.5	10.6	9.1	2	Yaw Formation
633.5	16MA0112A	L	y	Th	7	260	500	011/37	37.9	2.9	7.4	1	Yaw Formation
631.6	16MA0111A	L	y	Th	12	235	560	011/37	34.6	23.7	4.1	1	Yaw Formation

630.8	16MA0110A	L	y	Th	7	250	425	011/37	28.5	34.8	13.7	2	Yaw Formation
628.3	16MA0108A	L	y	Th	9	235	475	011/37	39.6	22.1	6	2	Yaw Formation
627.2	16MA0107A	L	y	Th	6	250	400	011/37	6	34.7	9.5	2	Yaw Formation
623.2	16MA0103A	L	y	Th	9	240	470	011/37	22.2	8.1	7.8	2	Yaw Formation
622.2	16MA0102A	L	y	Th	7	220	400	011/37	38.1	13.2	7.8	2	Yaw Formation
618.8	16MA0101A	L	y	Th	5	210	310	011/37	19.8	33.5	11	2	Yaw Formation
617.6	16MA0100A	L	y	Th	11	240	530	011/37	17.8	12.6	13.1	2	Yaw Formation
609.1	16MA0087A	L	y	AF	7	240	150	011/37	33.1	28.7	4.8	2	Yaw Formation
608.8	16MA0096A	L	y	Th	7	240	410	011/37	32.8	-4.4	3.8	1	Yaw Formation
608	16MA0095A	L	y	Th	8	220	425	011/37	1.4	-8.8	5.6	1	Yaw Formation
606.2	16MA0094A	L	y	Th	9	210	440	011/37	2.3	18.6	4.1	1	Yaw Formation
606.1	16MA0086A	L	y	Th	7	250	425	011/37	-28.5	16.4	3.9	1	Yaw Formation
605.5	16MA0093A	L	y	Th	3	240	290	011/37	21	12.1	9.9	2	Yaw Formation
605.1	16MA0085A	L	y	Th	8	235	440	011/37	-34.2	13.8	2.2	1	Yaw Formation
605	16MA0084A	L	y	Th	8	240	440	011/37	-25.1	13.1	2.3	1	Yaw Formation
603	16MA0081A	L	y	Th	8	210	410	011/37	10.1	9.4	4.8	2	Yaw Formation
603	16MA0092A	f	n	Th	5	220	340	011/37	7	-13.9	12.1	2	Yaw Formation
602.2	16MA0080A	L	y	Th	5	250	370	011/37	3.7	2.2	9.6	1	Yaw Formation
602.2	16MA0079A	L	y	Th	5	240	340	011/37	1.8	8.7	13.5	2	Yaw Formation
601.1	16MA0077A	L	y	Th	5	210	310	011/37	-12.4	-4.7	8.4	2	Yaw Formation
600.4	16MA0076A	L	y	Th	5	240	340	011/37	-9.2	25.1	8.8	2	Yaw Formation
599.9	16MA0075A	L	y	AF	7	235	300	011/37	1.3	26.6	5.9	1	Yaw Formation
599	16MA0088A	L	y	Th	7	210	370	011/37	14.2	-5.1	6.4	1	Yaw Formation
598.9	16MA0074A	L	y	AF	6	240	300	011/37	19.7	27.6	7.9	2	Yaw Formation
594.8	16MA0070A	L	y	AF	5	240	250	011/37	9.7	12.2	3.5	1	Yaw Formation
594.8	16MA0072A	L	y	Th	5	250	370	011/37	-16.4	17.5	7.3	1	Yaw Formation
594	16MA0069A	L	y	AF	7	235	300	011/37	23.2	1.2	4.3	1	Yaw Formation
592	16MA0067A	L	y	Th	7	210	340	011/37	33.3	23.4	8	2	Yaw Formation
587.5	16MA0062A	L	y	Th	4	235	310	011/37	2.3	-3.8	3	1	Yaw Formation
586.5	16MA0061A	L	y	Th	9	210	440	011/37	9.3	-9.5	6.1	1	Yaw Formation
576	16MA0055A	L	y	Th	8	235	440	011/37	10.9	6	10.5	2	Yaw Formation
575.1	16MA0054A	L	y	Th	7	250	425	011/37	-8.1	12.4	5.4	1	Yaw Formation
574.3	16MA0053A	L	y	Th	8	235	440	011/37	25.9	-15.4	7.4	2	Yaw Formation
570.8	16MA0052A	L	y	Th	7	210	370	011/37	20.1	24.3	4.3	1	Yaw Formation
569.7	16MA0051A	L	y	Th	5	220	340	011/37	23.5	16.4	7.8	1	Yaw Formation
568.9	16MA0050A	L	y	Th	7	235	410	011/37	34.1	18.3	7.3	2	Yaw Formation
567.9	16MA0049A	L	y	Th	8	210	410	011/37	25.6	21.5	3.6	1	Yaw Formation
567	16MA0048A	L	y	Th	11	220	500	011/37	33.4	16.8	5.2	1	Yaw Formation
566	16MA0046A	L	y	Th	8	235	500	011/37	17.4	2.4	3.1	1	Yaw Formation
566	16MA0047A	L	y	Th	9	210	475	011/37	40.8	17.1	3.6	1	Yaw Formation
564	16MA0043A	L	y	Th	8	235	475	011/37	35	30.3	12.3	2	Yaw Formation
562.4	16MA0041A	L	y	Th	5	210	310	011/37	3.7	46.2	11.9	2	Yaw Formation
561.9	16MA0039A	L	y	Th	8	220	425	011/37	18	30.2	10.8	2	Yaw Formation
561.2	16MA0038A	L	y	Th	7	210	370	011/37	33.1	2.1	6.9	1	Yaw Formation
557.9	16MA0033A	L	n	Th	4	100	220	011/37	42.6	19.2	9.3	2	Yaw Formation
556	16MA0032A	L	y	Th	6	235	370	011/37	16.9	2.6	4.5	1	Yaw Formation
555	16MA0031A	L	y	Th	9	210	440	011/37	9.8	12.5	2.3	1	Yaw Formation
554	16MA0030A	L	y	Th	8	220	425	011/37	10	19.3	2.1	1	Yaw Formation
552	16MA0028A	L	y	Th	7	235	405	011/37	-3.4	2.9	1.9	1	Yaw Formation
551	16MA0027A	L	y	Th	9	220	440	011/37	8.8	9.1	3.3	1	Yaw Formation
550	16MA0026A	L	y	Th	6	210	340	011/37	9.9	34	4.2	1	Yaw Formation
547.8	16MA0024A	L	y	Th	7	220	400	011/37	16.6	16.4	2.7	1	Yaw Formation
547.3	16MA0023A	L	y	Th	6	210	340	011/37	22.5	12.3	2.7	1	Yaw Formation
545	16MA0021A	L	y	Th	4	220	310	011/37	15.3	8.1	1.5	1	Yaw Formation
544.1	16MA0020A	L	y	Th	6	210	340	011/37	4.6	37.6	4	1	Yaw Formation
543.3	16MA0018A	L	y	Th	5	220	340	011/37	-35.4	12.7	1.7	1	Yaw Formation
542.1	16MB0116A	f	n	AF	4	250	400	011/37	22.2	-10.5	9.3	2	Yaw Formation
541.1	16MA0016A	L	y	Th	5	210	310	011/37	25.1	38.6	3.1	1	Yaw Formation
535.8	16MA0011A	L	y	Th	3	260	310	011/37	213.7	-22.2	13.5	2	Yaw Formation
535	16MA0010A	f	n	AF	5	210	250	011/37	177.6	9.7	14	2	Yaw Formation
533.6	16MA0009A	L	y	Th	5	220	340	011/37	198.8	-9.4	11.2	2	Yaw Formation
532.7	16MA0008A	f	n	Th	4	210	285	011/37	163.8	32	9.3	2	Yaw Formation
531.8	16MA0007A	L	y	Th	5	210	310	011/37	200	-3.8	9.6	2	Yaw Formation
530.8	16MA0006A	L	y	Th	5	220	340	011/37	192.4	-2.4	5.1	1	Yaw Formation
529.7	16MA0005A	L	y	Th	5	210	310	011/37	172.8	9.3	6.1	1	Yaw Formation
528.3	16MA0004A	L	y	Th	4	260	340	011/37	155.5	-3.4	9.9	1	Yaw Formation
481.5	16MB0092A	L	y	Th	9	220	460	011/40	-9.1	15.7	9.1	1	Yaw Formation
477.6	16MB0091A	L	y	Th	8	220	430	011/40	7.9	10.4	4.5	1	Yaw Formation
471	16MB0089A	L	y	Th	8	220	430	011/40	42.6	20.8	3.9	1	Yaw Formation
454.7	16MB0101A	L	y	Th	8	220	430	011/40	18.1	-3.9	7.9	2	Yaw Formation
453.6	16MB0100A	L	y	Th	7	250	430	011/40	24.5	14.9	5.1	2	Yaw Formation
447	16MB0098A	L	y	Th	8	220	430	011/40	23.5	-2.5	3.9	1	Yaw Formation
444	16MB0097A	L	y	AF	5	200	400	011/40	-18.1	28	10.6	2	Yaw Formation
439.6	16MB0096A	L	y	Th	8	220	430	011/40	72	23	4.1	2	Yaw Formation
435.5	16MB0088A	L	y	Th	7	250	430	011/40	4.7	-9.6	5.9	1	Yaw Formation
429	16MB0085A	L	y	Th	7	250	430	011/40	3.1	16.8	8.5	1	Yaw Formation
423.6	16MB0082A	L	y	Th	10	130	400	011/40	8.9	23.9	0.9	1	Yaw Formation
419	16MB0080A	L	y	Th	7	250	430	011/40	41.1	12.2	5.8	2	Yaw Formation
414	16MB0079A	L	y	Th	8	250	460	011/40	49.4	5.1	9.9	2	Yaw Formation
407	16MB0076A	L	y	Th	8	220	430	011/40	2.8	-3.8	6.5	2	Yaw Formation
405	16MB0075A	f	n	Th	8	220	430	011/40	40	7.2	8.5	2	Yaw Formation
404.3	16MB0074A	L	y	Th	6	250	400	011/40	10.6	6.9	5.8	2	Yaw Formation
380.2	16MB0065A	L	y	Th	7	250	430	011/40	149.5	11.3	6.5	1	Yaw Formation
375	16MB0064A	L	y	AF	5	200	400	011/40	164.7	1.3	7.1	1	Yaw Formation
364.8	16MB0061A	L	y	AF	5	200	450	011/40	204	19.5	5	1	Yaw Formation
360	16MB0060A	L	y	AF	6	200	450	011/40	214.8	10.3	7.7	1	Yaw Formation
352.9	16MB0059A	L	y	AF	6	200	450	011/40	181.3	15.5	1.1	1	Yaw Formation
350.2	16MB0058A	L	y	AF	5	200	400	011/40	192	15.3	2.9	1	Yaw Formation
323.3	16MB0052A	L	y	Th	8	220	430	011/40	16.6	33.2	4.3	1	Yaw Formation
320.4	16MB0050A	L	y	Th	8	220	430	011/40	27.1	9.3	7.3	1	Yaw Formation
313.1	16MB0048A	L	y	Th	8	250	460	011/40	22.6	21.5	8.3	2	Yaw Formation
313.1	16MB0048B	L	y	AF	6	200	450	011/40	15.8	2.2	6	2	Yaw Formation
311.1	16MB0047A	L	y	Th	9	220	460	011/40	20.5	16.6	7.2	1	Yaw Formation
299	16MB0045A	L	y	Th	8	250	460	011/40	-3.3	28.8	4	1	Yaw Formation
297.5	16MB0044A	L	y	Th	9	220	460	011/40	-9.2	13.3	3.9	1	Yaw Formation
294.2	16MB0042A	L	y	Th	8	220	430	011/40	15.1	9.7	4.4	1	Yaw Formation
290.8	16MB0041A	L	y	Th	9	220	460	011/40	32.9	12	4.4	1	Yaw Formation
286.5	16MB0039A	L	y	Th	8	220	430	011/40	39.9	-1.4	10	2	Yaw Formation
286.4	16MB0040A	L	y	Th	8	220	430	011/40	29.9	9.7	6	1	Yaw Formation
283.9	16MB0038A	L	y	Th	7	220	400	011/40	12.2	12	6.1	1	Yaw Formation
278.6	16MB0037A	L	y	Th	6	220	370	011/40	12	16	0.4	1	Yaw Formation
276.4	16MB0036A	L	y	Th	7	220	400	011/40	16.4	21.5	7.1	1	Yaw Formation
262.3	16MB0032A	L	y	Th	7	250	430	011/40	14.1	26.9	7.9	1	Yaw Formation
258.4	16MB0031A	L	y	Th	8	220	430	011/40	29.4	-4.6	6.3	1	Yaw Formation
255.4	16MB0030A	L	y	Th	9	220	460	011/40	28.5	21.8	3.1	1	Yaw Formation
251.5	16MB0029A	L	y	Th	8	220	430	011/40	10.7	7.8	3.4	1	Yaw Formation
245.2	16MB0027A	L	y	Th	8	220	430	011/40	23.7	3.4	3.9	1	Yaw Formation
240.3	16MB0025A	L	y	Th	8	220	430	011/40	-14.5	5.8	4.9	1	Yaw Formation
222.9	16MB0019A	L	y	Th	9	220	460	011/40	232.2	-5.3	2.8	1	Yaw Formation
219.8	16MB0018A	L	y	AF	4	250	400	011/40	186.4	20.9	4.5	1	Yaw Formation
215.2	16MB0016A	L	y	Th	9	220	460	011/40	192.4	2.4	3.8	1	Yaw Formation
206.3	16MB0012A	L	y	Th	8	220	430	011/40	180.3	14.8	2.1	1	Yaw Formation
204.2	16MB0011A	L	y	Th	9	220	460	011/40	188.8	38.4	2.7	1	Yaw Formation
200.8	16MB0010A	L	y	Th	9	220	460	011/40	187.6	-8.3	5.7	1	Yaw Formation
196	16MB0009A	L	y	Th	8	220	430	011/40	176.1	17.9	4	1	Yaw Formation
181.1	16MB0005A	L	y	Th	7	220	400	011/40	195.1	4.6	2.9	1	Yaw Formation
178.3	16MB0004A	L	y	Th	9	220	460	011/40	203.3	-1.9	4	1	Yaw Formation
174.5	17MC0048A	f	n	Th	4	370	460	013/40	195.1	62.5	11	2	Yaw Formation

172.5	16MB0002A	L	y	Th	8	220	430	011/40	188.4	4.9	5.4	1	Yaw Formation
172.5	17MC0047A	L	y	AF	13	220	200	013/40	238.8	-2.9	2.7	1	Yaw Formation
171	17MC0046A	L	y	Th	7	220	400	013/40	204.4	-6.7	4.3	1	Yaw Formation
168	17MC0045A	f	n	AF	8	200	450	013/40	164.5	30.1	3	2	Yaw Formation
166.5	17MC0044A	L	y	AF	19	250	300	013/40	207	24.5	1.9	1	Yaw Formation
161.5	17MC0043A	L	y	Th	8	220	430	013/40	181.8	20.3	9.5	1	Yaw Formation
157.5	17MC0042A	L	y	AF	11	220	150	013/40	200.9	1.9	5	1	Yaw Formation
123.6	17MC0036A	L	y	AF	13	220	200	013/40	200.4	-2.1	2.1	1	Yaw Formation
122.4	17MC0035A	f	n	Th	7	160	340	013/40	192.7	23	4.6	2	Yaw Formation
119	17MC0034A	L	y	AF	9	200	500	013/40	202.4	14.1	0.8	1	Yaw Formation
114.5	17MC0033A	f	n	Th	4	160	250	013/40	201.6	-9.9	6.3	2	Yaw Formation
113	17MC0032A	L	y	AF	7	340	150	013/40	170.3	0.4	3.8	2	Yaw Formation
111	17MC0031A	L	y	AF	9	200	500	013/40	202.3	30.9	0.6	1	Yaw Formation
109.2	17MC0030A	L	y	Th	7	220	400	013/40	194.8	16.3	1.8	1	Yaw Formation
106	17MC0029A	L	y	AF	11	220	150	013/40	201.1	19.5	4.2	1	Yaw Formation
103	17MC0028A	L	y	Th	7	250	430	013/40	184.1	28.7	1.7	1	Yaw Formation
101.6	17MC0027A	L	y	AF	11	250	200	013/40	181.3	13.6	2.3	1	Yaw Formation
91	17MC0026A	f	n	Th	5	310	430	013/40	178.5	-11.5	16.1	2	Yaw Formation
85.5	17MC0024A	f	n	Th	3	370	430	013/40	174.1	2.3	19.4	2	Yaw Formation
81	17MC0022A	f	n	Th	3	250	310	013/40	178.1	1	26	2	Yaw Formation
68	17MC0021A	L	y	Th	5	340	460	013/40	189.8	16.1	7.4	1	Yaw Formation
66.4	17MC0020A	L	y	Th	6	220	370	013/40	209.6	15.6	7	1	Yaw Formation
65	17MC0019A	f	n	Th	7	190	370	013/40	168.9	-3	11.6	2	Yaw Formation
63	17MC0018A	L	y	AF	11	220	150	013/40	179.8	20.1	8.5	1	Yaw Formation
60.8	17MC0017A	L	y	Th	6	280	430	013/40	221	38.1	4.2	1	Yaw Formation
58.5	17MD0029A	f	n	Th	3	370	430	013/40	184	50.5	17.5	2	Yaw Formation
58.2	17MC0016A	f	n	Th	6	190	340	013/40	172.8	-17.2	7.4	2	Yaw Formation
56.7	17MC0015A	L	y	AF	9	340	200	013/40	202.2	21.3	5.5	1	Yaw Formation
55.5	17MC0014A	L	y	AF	11	280	200	013/40	213.3	38.8	3.1	1	Yaw Formation
55.4	17MD0028A	L	y	AF	10	200	600	013/40	257.2	30.8	1.6	1	Yaw Formation
52	17MC0012A	L	y	Th	5	310	430	013/40	194.7	13.3	9.8	1	Yaw Formation
51.2	17MC0013A	L	y	AF	10	200	500	013/40	191.7	16.1	0.9	1	Yaw Formation
51.2	17MD0026A	L	y	AF	11	200	700	013/38	211.2	27.8	3.1	1	Yaw Formation
50.5	17MC0011A	L	y	Th	7	250	430	013/40	202.8	7.5	4.2	1	Yaw Formation
41	17MC0007A	L	y	AF	9	310	150	013/40	192.3	24.5	4.7	1	Yaw Formation
40.5	17MD0024A	f	n	Th	5	280	400	013/38	203.4	10.7	11.4	2	Yaw Formation
38.5	17MC0006A	L	y	AF	20	220	300	013/40	195.8	-8.9	4.9	1	Yaw Formation
37.5	17MC0005A	L	y	AF	12	220	200	013/40	204.4	9.5	5	1	Yaw Formation
37	17MD0022A	f	n	Th	5	280	400	013/38	217.8	8.4	9.4	2	Yaw Formation
36.5	17MC0004A	L	y	AF	7	340	150	013/40	190.3	5.4	4.4	1	Yaw Formation
35.3	17MD0021A	L	y	AF	12	220	200	013/38	202.6	16.4	3.2	1	Yaw Formation
34.5	17MC0003A	f	n	Th	6	250	400	013/40	150.5	59.6	7	2	Yaw Formation
32.8	17MC0002A	f	n	Th	6	280	430	013/40	209.9	31.2	20.5	2	Yaw Formation
31.5	17MD0019A	L	y	Th	5	280	400	013/38	194.4	6.6	6.6	1	Yaw Formation
30	17MC0001A	L	y	Th	8	220	430	013/40	202	7	4.6	1	Yaw Formation
28.7	17MD0018A	f	n	Th	6	280	430	013/38	152.9	0	15.7	2	Yaw Formation
27.1	17MD0017A	L	y	Th	8	220	430	013/38	199.2	0.3	3.4	1	Yaw Formation
25.1	17MD0016A	L	y	AF	9	280	150	013/38	189	-3.7	4	1	Yaw Formation
23.7	17MD0015A	L	y	AF	12	220	150	013/38	190.3	4.4	4.4	1	Yaw Formation
21	17MD0014A	L	y	Th	6	160	310	013/38	186.3	34.2	5.2	1	Yaw Formation
19.5	17MD0013A	f	n	Th	4	280	370	013/38	216.3	-9.8	15.2	2	Yaw Formation
18.3	17MD0012A	f	n	Th	4	310	400	013/38	199.5	16.1	34.9	2	Yaw Formation
15	17MD0010A	L	y	AF	9	25	225	013/38	18.8	1.3	2.5	2	Yaw Formation
13.5	17MD0009A	L	y	Th	7	130	310	013/38	43.6	-2	3.8	1	Yaw Formation
12	17MD0008A	L	y	Th	4	340	430	013/38	26.1	21	9.9	2	Yaw Formation
9.6	17MD0031A	f	n	Th	4	310	400	013/38	10.2	37	21.1	2	Yaw Formation
9	17MD0007A	L	y	Th	4	340	430	013/38	16.6	3.1	1.5	1	Yaw Formation
9	17MD0006A	L	y	Th	5	310	430	013/38	16.4	24.3	12	2	Yaw Formation
8.6	17MD0030A	L	y	Th	8	220	430	013/38	34.6	22.7	9.1	2	Yaw Formation
8.6	17MD0032A	f	n	Th	5	310	430	013/38	55	31.9	9.5	2	Yaw Formation
8	17MD0004A	L	y	AF	16	340	300	013/38	35.8	17.1	4.7	2	Yaw Formation
6.5	17MD0003A	L	y	AF	9	200	500	013/38	31.2	26.6	5.1	1	Yaw Formation
0	17MD0001A	L	y	Th	8	220	430	013/38	32.4	4.4	4.3	1	Yaw Formation

Yaw Formation paleomagnetic data originally published in:

Westerweel, J., Roperch, P., Licht, A., Dupont-Nivet, G., Win, Z., Poblete, F., … Aung, D. W. (2019). Burma Terrane part of the Trans-Tethyan arc during collision with India according to palaeomagnetic data. Nature Geoscience. https://doi.org/10.1038/s41561-019-0443-2

Depth (m)	Sample	Bulk magnetic susceptiblity (SI)	Formation
1923.2	19LAP064	0.001963003	Letkat Formation
1921.2	19LAP063	0.000164431	Letkat Formation
1921.2	19LAP062	0.000237095	Letkat Formation
1899.9	19LAP061	0.001875379	Letkat Formation
1895.7	19LAP060	0.005618839	Letkat Formation
1889.6	19LAP059	0.004335816	Letkat Formation
1885.7	19LAP058	0.004094472	Letkat Formation
1770.1	19LAP057	0.001774959	Letkat Formation
1757.4	19LAP056	0.004005654	Letkat Formation
1695.4	19LAP055	0.002146239	Letkat Formation
1681.9	19LAP054	0.002077094	Letkat Formation
1608	19LAP053	0.001673938	Letkat Formation
1585.4	19LAP052	0.006750805	Letkat Formation
1571.3	19LAP051	0.013730266	Letkat Formation
1565.6	19LAP050	0.008777381	Letkat Formation
1525.9	19LAP049	0.000962906	Letkat Formation
1500	19LAP048	0.001663262	Letkat Formation
1452.5	17LA0105	0.001741	Letkat Formation
1452	19LAP047	0.002056999	Letkat Formation
1449.1	17LA0104	0.001139	Letkat Formation
1444.1	17LA0103	0.006972	Letkat Formation
1442	19LAP046	0.005799574	Letkat Formation
1439	19LAP045	0.11169043	Letkat Formation
1438.8	17LA0102	0.008231	Letkat Formation
1436.7	17LA0101	0.00825	Letkat Formation
1428.1	17LA0100	0.0001667	Letkat Formation
1426	17LA0099	0.0002778	Letkat Formation
1419.4	17LA0098	0.0008796	Letkat Formation
1416.7	17LA0097	0.000537	Letkat Formation
1414	17LA0096	0.00187	Letkat Formation
1410.9	17LA0095	0.0003519	Letkat Formation
1409.4	17LA0094	0.0004167	Letkat Formation
1409	17LA0093	0.0001759	Letkat Formation
1406.2	17LA0092	0.0001389	Letkat Formation
1403.5	17LA0091	0.0002037	Letkat Formation
1400.9	17LA0090	0.0001944	Letkat Formation
1398.4	17LA0089	0.0001481	Letkat Formation
1396.5	17LA0088	0.001278	Letkat Formation
1394.6	17LA0087	0.006343	Letkat Formation
1392	19LAP044	0.001966445	Letkat Formation
1390.8	17LA0086	0.004759	Letkat Formation
1387	17LA0085	0.006111	Letkat Formation
1379.2	17LA0078	0.03007	Letkat Formation
1375	17LA0077	0.0004167	Letkat Formation
1368.8	17LA0076	0.00837	Letkat Formation
1364.8	17LA0075	0.01059	Letkat Formation

1362.5	17LA0074	0.002676	Letkat Formation
1360.5	17LA0073	0.03991	Letkat Formation
1352	19LAP043	0.000367664	Letkat Formation
1346.5	17LA0084	0.0009907	Letkat Formation
1346.5	17LA0084	0.0004907	Letkat Formation
1346.3	17LA0072	0.004333	Letkat Formation
1345	19LAP042	0.004711561	Letkat Formation
1343	17LA0083	0.001574	Letkat Formation
1340	17LA0082	0.0002407	Letkat Formation
1338	17LA0081	0.0005741	Letkat Formation
1336.7	17LA0080	0.0007037	Letkat Formation
1328.1	17LA0071	0.001778	Letkat Formation
1328.1	17LA0071	0.00262	Letkat Formation
1324.6	17LA0070	0.002574	Letkat Formation
1323.4	17LA0069	0.003759	Letkat Formation
1317.5	17LA0068	0.001046	Letkat Formation
1316.5	17LA0067	0.001889	Letkat Formation
1312.1	17LA0066	0.006417	Letkat Formation
1306.3	17LA0065	0.000213	Letkat Formation
1303.2	17LA0064	0.0002593	Letkat Formation
1301.4	17LA0063	0.0003426	Letkat Formation
1301	19LAP041	0.002312945	Letkat Formation
1298.5	17LA0062	0.00187	Letkat Formation
1298	19LAP040	0.000566713	Letkat Formation
1294.2	17LA0061	0.001741	Letkat Formation
1289.4	17LA0060	0.0004352	Letkat Formation
1285.4	17LA0059	0.002954	Letkat Formation
1280.5	17LA0058	0.002167	Letkat Formation
1278.6	17LA0057	0.004056	Letkat Formation
1277.1	17LA0056	0.004972	Letkat Formation
1276	17LA0055	0.0006944	Letkat Formation
1276	17LA0054	0.002333	Letkat Formation
1270	19LAP039	0.00384708	Letkat Formation
1267.2	17LA0052	0.00175	Letkat Formation
1265	19LAP038	0.001880909	Letkat Formation
1264.3	17LA0051	0.0003519	Letkat Formation
1257	19LAP037	0.000370215	Letkat Formation
1233.4	17LA0050	0.005083	Letkat Formation
1232.5	17LA0049	0.002426	Letkat Formation
1230.3	17LA0048	0.002333	Letkat Formation
1227.1	17LA0047	0.004333	Letkat Formation
1226	19LAP036	0.000239704	Letkat Formation
1225.5	19LAP035	0.003495553	Letkat Formation
1224.1	17LA0046	0.004343	Letkat Formation
1221.6	17LA0045	0.003583	Letkat Formation
1219.3	17LA0044	0.00363	Letkat Formation
1211	17LA0043	0.0003981	Letkat Formation

1209.4	17LA0042	0.001778	Letkat Formation
1207	19LAP034	0.001642667	Letkat Formation
1204.6	17LA0041	0.002556	Letkat Formation
1199.2	17LA0040	0.0006204	Letkat Formation
1194.8	17LA0039	0.01596	Letkat Formation
1192	17LA0038	0.009583	Letkat Formation
1186.3	17LA0037	0.001296	Letkat Formation
1174	17LA0036	0.004824	Letkat Formation
1174	17LA0036	0.08296	Letkat Formation
1171.5	17LA0035	0.01562	Letkat Formation
1170	19LAP033	0.023600945	Letkat Formation
1169.9	17LA0034	0.01591	Letkat Formation
1166	19LAP032	0.000563627	Letkat Formation
1165.4	17LA0033	0.01014	Letkat Formation
1163.5	17LA0032	0.001389	Letkat Formation
1161	19LAP031	0.012217458	Letkat Formation
1160.1	17LA0031	0.001685	Letkat Formation
1156.5	19LAP030	0.01173124	Letkat Formation
1156	19LAP029	0.000198636	Letkat Formation
1136.2	17LA0030	0.0025	Letkat Formation
1135	19LAP028	0.001207194	Letkat Formation
1132.6	17LA0029	0.003759	Letkat Formation
1129	17LA0028	0.005259	Letkat Formation
1124.5	17LA0027	0.000287	Letkat Formation
1124	19LAP027	0.000240968	Letkat Formation
1123	19LAP026	0.000274718	Letkat Formation
1121.2	17LA0026	0.0005185	Letkat Formation
1120	19LAP025	0.000499692	Letkat Formation
1119.5	17LA0025	0.001139	Letkat Formation
1117.9	17LA0024	0.0005556	Letkat Formation
1115.6	17LA0023	0.0006019	Letkat Formation
1106	19LAP024	0.0002753	Letkat Formation
1105.5	17LA0022	0.0006759	Letkat Formation
1103.8	17LA0021	0.001833	Letkat Formation
1102.5	17LA0020	0.009296	Letkat Formation
1100.2	17LA0019	0.008861	Letkat Formation
1091	17LA0018	0.004074	Letkat Formation
1088.7	17LA0017	0.004204	Letkat Formation
1048.7	17LA0016	0.0007222	Letkat Formation
1044.1	17LA0015	0.004093	Letkat Formation
1028.4	17LA0014	0.00312	Letkat Formation
1021.8	17LA0013	0.001565	Letkat Formation
1017.9	17LA0012	0.01777	Letkat Formation
1012.7	17LA0011	0.002593	Letkat Formation
1012	19LAP023	0.00143175	Letkat Formation
1009.7	16MA0277	0.0001389	Letkat Formation
1009	19LAP022	0.000215671	Letkat Formation

1008.5	17LA0010	0.0002222	Letkat Formation
1008.5	17LA0009	0.0002315	Letkat Formation
1004.5	16MA0275	0.00325	Letkat Formation
995.7	16MA0274	0.001194	Letkat Formation
995.5	16MA0273	0.001269	Letkat Formation
978	16MA0272	0.005921	Letkat Formation
978	16MA0272	0.001139	Letkat Formation
972.5	16MA0271	0.003185	Letkat Formation
961.2	17LA0008	0.0002407	Letkat Formation
960.5	16MA0270	0.0117	Letkat Formation
960.5	16MA0270	0.001306	Letkat Formation
959.6	17LA0007	0.0002037	Letkat Formation
958.5	17LA0006	0.0003333	Letkat Formation
958.2	16MA0269	0.003653	Letkat Formation
958.2	16MA0269	0.0001852	Letkat Formation
955.3	16MA0268	0.0003519	Letkat Formation
953.2	17LA0005	0.0004722	Letkat Formation
953.2	17LA0004	0.0003519	Letkat Formation
951	16MA0267	0.0005093	Letkat Formation
950.7	17LA0003	0.02107	Letkat Formation
950	16MA0266	0.0001574	Letkat Formation
947.6	17LA0002	0.001398	Letkat Formation
947.6	17LA0002	0.0006574	Letkat Formation
942.6	17LA0001	0.006963	Letkat Formation
942	19LAP021	3.94E-05	Tonhe Formation
934	16MA0263	0.0001204	Tonhe Formation
933.5	16MA0261	0.00008333	Tonhe Formation
930.7	16MA0260	0.00009259	Tonhe Formation
930	16MA0259	0.0001481	Tonhe Formation
927.5	16MA0258	0.00009259	Tonhe Formation
927	19LAP020	5.02E-05	Tonhe Formation
923.8	16MA0257	0.0002037	Tonhe Formation
923.8	16MA0256	0.0001204	Tonhe Formation
923	16MA0255	0.00006481	Tonhe Formation
922.6	16MA0254	0.0001204	Tonhe Formation
922.2	16MA0253	0.00006481	Tonhe Formation
914.9	16MA0252	0.0002407	Tonhe Formation
913.7	16MA0251	0.0001852	Tonhe Formation
913.6	16MA0250	0.00007407	Tonhe Formation
913.3	16MA0249	0.0000463	Tonhe Formation
911	16MA0248	0.0000463	Tonhe Formation
910.2	16MA0247	0.00005556	Tonhe Formation
906.2	16MA0246	0.00009259	Tonhe Formation
905.6	16MA0245	0.0001111	Tonhe Formation
905.2	16MA0244	0.00009259	Tonhe Formation
905	19LAP019	7.41E-05	Tonhe Formation
903.9	16MA0243	0.0001389	Tonhe Formation

897	16MA0241	0.00003704	Tonhe Formation
892.9	16MA0240	0.00005556	Tonhe Formation
892.4	16MA0239	0.00006481	Tonhe Formation
890	16MA0238	0.0001204	Tonhe Formation
888.9	16MA0237	0.00008333	Tonhe Formation
887	16MA0236	0.0001111	Tonhe Formation
878.5	16MA0235	0.0001389	Tonhe Formation
877.4	16MA0234	0.00003704	Tonhe Formation
875.5	16MA0233	0.00006481	Tonhe Formation
875	19LAP018	3.92E-05	Tonhe Formation
874.5	16MA0232	0.0001481	Tonhe Formation
871.7	16MA0231	0.0000463	Tonhe Formation
870	16MA0230	0.00005556	Tonhe Formation
870	19LAP017	3.26E-05	Tonhe Formation
868	19LAP016	1.60E-05	Tonhe Formation
866.3	16MA0229	0.0001019	Tonhe Formation
864.3	16MA0228	0.00008333	Tonhe Formation
864	19LAP015	0.000191924	Tonhe Formation
863	19LAP014	9.18E-05	Tonhe Formation
860.2	16MA0227	0.00003704	Tonhe Formation
858	19LAP013	3.56E-05	Tonhe Formation
854.1	16MA0226	0.00006481	Tonhe Formation
849.7	16MA0225	0.00002778	Tonhe Formation
849.7	16MA0225	0.00002778	Tonhe Formation
849.3	16MA0224	0.00007407	Tonhe Formation
846.4	16MA0223	0.00002778	Tonhe Formation
832.6	16MA0221	0.00008333	Tonhe Formation
831.8	16MA0220	0.0001389	Tonhe Formation
829.5	16MA0218	0.0001111	Tonhe Formation
828.5	16MA0217	0.00006481	Tonhe Formation
825	16MA0215	0.00006481	Tonhe Formation
823	16MA0214	0.0001667	Tonhe Formation
815	19LAP011	1.04E-05	Tonhe Formation
812.2	16MA0212	0.00006481	Tonhe Formation
811.8	16MA0211	0.0000463	Tonhe Formation
801.3	16MA0209	0.00005556	Tonhe Formation
799.7	16MA0208	0.0001852	Tonhe Formation
797	16MA0206	0.0002222	Tonhe Formation
795.8	16MA0205	0.0003704	Tonhe Formation
793.4	16MA0203	0.00005556	Tonhe Formation
791.5	16MA0202	0.0001204	Tonhe Formation
790.5	16MA0201	0.0001019	Tonhe Formation
785.5	16MA0200	0.00025	Tonhe Formation
785	19LAP010	0.000100978	Tonhe Formation
784.1	16MA0199	0.0003519	Tonhe Formation
783.5	16MA0198	0.000287	Tonhe Formation
782	16MA0197	0.0007315	Tonhe Formation

781	16MA0196	0.0008148	Tonhe Formation
780.4	16MA0195	0.0005185	Tonhe Formation
779.1	16MA0194	0.0003704	Tonhe Formation
778.1	16MA0193	0.0003981	Tonhe Formation
776.8	16MA0192	0.0003889	Tonhe Formation
775.8	16MA0191	0.0001019	Tonhe Formation
773.7	16MA0190	0.00005556	Tonhe Formation
771.1	16MA0189	0.0001019	Tonhe Formation
771	16MA0188	0.00008333	Tonhe Formation
770	19LAP009	4.06E-05	Tonhe Formation
769.5	16MA0187	0.00003704	Tonhe Formation
765.8	16MA0186	0.0000463	Tonhe Formation
765.8	16MA0285	0.0001667	Tonhe Formation
764.4	16MA0284	0.00003704	Tonhe Formation
759.5	16MA0185	0.0002037	Tonhe Formation
757	16MA0184	0.0002315	Tonhe Formation
755.8	16MA0183	0.0001389	Tonhe Formation
755	16MA0182	0.0001574	Tonhe Formation
754	16MA0181	0.0001296	Tonhe Formation
753.1	16MA0180	0.00005556	Tonhe Formation
753	16MA0179	0.0001111	Tonhe Formation
751.7	16MA0178	0.0001389	Tonhe Formation
750	16MA0177	0.0002037	Tonhe Formation
749	16MA0176	0.0001296	Tonhe Formation
748	16MA0175	0.0002593	Tonhe Formation
747.2	16MA0174	0.0003148	Tonhe Formation
746.4	16MA0173	0.0003333	Tonhe Formation
745	16MA0172	0.0003333	Tonhe Formation
744	16MA0171	0.0004907	Tonhe Formation
742.9	16MA0170	0.0003148	Tonhe Formation
741.4	16MA0169	0.0004352	Tonhe Formation
740	16MA0168	0.0002407	Tonhe Formation
739	16MA0167	0.0003241	Tonhe Formation
737	16MA0166	0.0001574	Tonhe Formation
735.6	16MA0165	0.0002407	Tonhe Formation
733.2	16MA0164	0.000287	Tonhe Formation
733.2	16MA0163	0.0003426	Tonhe Formation
733	16MA0162	0.0009907	Tonhe Formation
730	19LAP008	8.55E-05	Tonhe Formation
729.4	16MA0161	0.0001389	Tonhe Formation
727.8	16MA0160	0.0001296	Tonhe Formation
726.4	16MA0159	0.0001204	Tonhe Formation
725.4	16MA0158	0.0002963	Tonhe Formation
724	16MA0157	0.0001204	Tonhe Formation
722	19LAP007	0.000128935	Tonhe Formation
714.2	16MA0156	0.0001667	Tonhe Formation
713.3	16MA0155	0.0001204	Tonhe Formation

713	19LAP006	1.99E-05	Tonhe Formation
704.9	16MA0153	0.0002222	Tonhe Formation
704	16MA0152	0.0002407	Tonhe Formation
703.1	16MA0151	0.00025	Tonhe Formation
702	19LAP005	0.00031291	Tonhe Formation
700	19LAP004	0.000275591	Tonhe Formation
686.9	16MA0150	0.0003148	Tonhe Formation
686.3	16MA0149	0.0003704	Tonhe Formation
685.6	16MA0148	0.0002963	Tonhe Formation
684.5	16MA0147	0.0002315	Tonhe Formation
683.3	16MA0146	0.0001574	Tonhe Formation
682.5	16MA0145	0.0002685	Tonhe Formation
680.5	16MA0144	0.00025	Tonhe Formation
680.4	16MA0143	0.0002685	Tonhe Formation
680	19LAP003	0.002717299	Tonhe Formation
679.2	16MA0142	0.0001759	Tonhe Formation
677	19LAP002	0.00019561	Tonhe Formation
672.5	16MA0139	0.0002407	Yaw Formation
671.7	16MA0138	0.0001852	Yaw Formation
671.2	16MA0137	0.0001389	Yaw Formation
670	19LAP001	0.000265342	Yaw Formation
668.9	16MA0135	0.0002037	Yaw Formation
668	16MA0134	0.0001852	Yaw Formation
667.8	16MA0133	0.0002222	Yaw Formation
667	16MA0132	0.0002778	Yaw Formation
656	16MA0131	0.000213	Yaw Formation
653.5	16MA0130	0.0002222	Yaw Formation
651.4	16MA0129	0.0001574	Yaw Formation
650.4	16MA0128	0.0003796	Yaw Formation
649	16MA0127	0.0003611	Yaw Formation
648	16MA0126	0.000287	Yaw Formation
647	16MA0125	0.0002593	Yaw Formation
643.9	16MA0123	0.0001296	Yaw Formation
643.5	16MA0121	0.0001389	Yaw Formation
642.5	16MA0120	0.0002222	Yaw Formation
641.9	16MA0119	0.00025	Yaw Formation
640.9	16MA0118	0.0001296	Yaw Formation
637.1	16MA0117	0.0001944	Yaw Formation
636.5	16MA0116	0.0002037	Yaw Formation
635.4	16MA0115	0.0003704	Yaw Formation
634.3	16MA0114	0.000287	Yaw Formation
633.9	16MA0113	0.0004167	Yaw Formation
633.5	16MA0112	0.00025	Yaw Formation
631.6	16MA0111	0.0003241	Yaw Formation
630.8	16MA0110	0.0002315	Yaw Formation
629.6	16MA0109	0.0002963	Yaw Formation
628.3	16MA0108	0.0002037	Yaw Formation

627.2	16MA0107	0.0003981	Yaw Formation
623.2	16MA0103	0.00025	Yaw Formation
622.2	16MA0102	0.0002407	Yaw Formation
618.8	16MA0101	0.0002315	Yaw Formation
617.6	16MA0100	0.0003426	Yaw Formation
612.6	16MA0099	0.0003148	Yaw Formation
609.6	16MA0098	0.0001852	Yaw Formation
609.1	16MA0087	0.00025	Yaw Formation
608.8	16MA0096	0.0002685	Yaw Formation
608	16MA0095	0.0002315	Yaw Formation
606.2	16MA0094	0.0002222	Yaw Formation
606.1	16MA0086	0.0001667	Yaw Formation
605.5	16MA0093	0.0003426	Yaw Formation
605.1	16MA0085	0.0002222	Yaw Formation
605	16MA0084	0.0003148	Yaw Formation
604	16MA0083	0.0001852	Yaw Formation
603.6	16MA0082	0.0002315	Yaw Formation
603	16MA0092	0.000287	Yaw Formation
603	16MA0081	0.0001852	Yaw Formation
602.2	16MA0079	0.0001574	Yaw Formation
602.2	16MA0091	0.0002037	Yaw Formation
602.2	16MA0080	0.0001481	Yaw Formation
601.8	16MA0078	0.0001019	Yaw Formation
601.1	16MA0077	0.0001759	Yaw Formation
601	16MA0090	0.0002778	Yaw Formation
600.4	16MA0076	0.0001574	Yaw Formation
600	16MA0059	0.0003241	Yaw Formation
599.9	16MA0075	0.0002222	Yaw Formation
599.9	16MA0089	0.0001944	Yaw Formation
599	16MA0088	0.000287	Yaw Formation
598.9	16MA0074	0.0002222	Yaw Formation
594.8	16MA0070	0.0001574	Yaw Formation
594.8	16MA0072	0.0006759	Yaw Formation
594	16MA0069	0.0002407	Yaw Formation
592.7	16MA0068	0.0003611	Yaw Formation
592	16MA0067	0.0002685	Yaw Formation
591	16MA0066	0.0002315	Yaw Formation
590.2	16MA0065	0.0002315	Yaw Formation
589	16MA0064	0.0001574	Yaw Formation
588.2	16MA0063	0.0002315	Yaw Formation
587.5	16MA0062	0.0002407	Yaw Formation
586.5	16MA0061	0.0002685	Yaw Formation
583	16MA0060	0.0002778	Yaw Formation
581	16MA0058	0.0003148	Yaw Formation
577.8	16MA0057	0.0002685	Yaw Formation
576.9	16MA0056	0.0001759	Yaw Formation
576	16MA0055	0.0002593	Yaw Formation

575.1	16MA0054	0.0003889	Yaw Formation
574.3	16MA0053	0.00025	Yaw Formation
570.8	16MA0052	0.0008241	Yaw Formation
569.7	16MA0051	0.0002963	Yaw Formation
568.9	16MA0050	0.0003056	Yaw Formation
567.9	16MA0049	0.00025	Yaw Formation
567	16MA0048	0.0003241	Yaw Formation
566	16MA0047	0.000213	Yaw Formation
566	16MA0046	0.0001296	Yaw Formation
565.8	16MA0045	0.001167	Yaw Formation
564	16MA0043	0.000213	Yaw Formation
563	16MA0042	0.000287	Yaw Formation
562.4	16MA0041	0.0003981	Yaw Formation
561.9	16MA0039	0.0003241	Yaw Formation
561.6	16MA0040	0.0003056	Yaw Formation
561.2	16MA0038	0.0005093	Yaw Formation
560.8	16MA0037	0.0003519	Yaw Formation
559.9	16MA0036	0.0003241	Yaw Formation
558.6	16MA0035	0.0003611	Yaw Formation
558.2	16MA0034	0.0002315	Yaw Formation
557.9	16MA0033	0.0003241	Yaw Formation
556	16MA0032	0.0002778	Yaw Formation
555	16MA0031	0.0005741	Yaw Formation
554	16MA0030	0.0002222	Yaw Formation
553.2	16MA0029	0.0002222	Yaw Formation
552	16MA0028	0.0002778	Yaw Formation
551	16MA0027	0.0008981	Yaw Formation
550	16MA0026	0.0001667	Yaw Formation
547.8	16MA0024	0.001407	Yaw Formation
547.3	16MA0023	0.002167	Yaw Formation
546.1	16MA0022	0.0003056	Yaw Formation
545	16MA0021	0.0003426	Yaw Formation
544.1	16MA0020	0.001204	Yaw Formation
543.3	16MA0018	0.002491	Yaw Formation
542.1	16MB0116	0.001343	Yaw Formation
542	16MA0017	0.0002593	Yaw Formation
541.1	16MA0016	0.001917	Yaw Formation
540	16MA0015	0.002019	Yaw Formation
538.8	16MA0014	0.001806	Yaw Formation
537.8	16MA0013	0.002315	Yaw Formation
537.3	16MA0012	0.001426	Yaw Formation
535.8	16MA0011	0.000213	Yaw Formation
535	16MA0010	0.0007315	Yaw Formation
533.6	16MA0009	0.002102	Yaw Formation
532.7	16MA0008	0.001731	Yaw Formation
531.8	16MA0007	0.001778	Yaw Formation
530.8	16MA0006	0.001537	Yaw Formation

529.7	16MA0005	0.002157	Yaw Formation
528.3	16MA0004	0.0007778	Yaw Formation
527.4	16MA0003	0.000213	Yaw Formation
527.2	16MA0002	0.00002778	Yaw Formation
526.2	16MA0001	0.00007407	Yaw Formation
521.8	16MB0113	0.000213	Yaw Formation
520.7	16MB0112	0.0001852	Yaw Formation
519.1	16MB0111	0.0002222	Yaw Formation
517.5	16MB0109	0.00025	Yaw Formation
516	16MB0108	0.0002593	Yaw Formation
511	16MB0107	0.001435	Yaw Formation
505	16MB0106	0.0002407	Yaw Formation
504.7	16MB0105	0.0002222	Yaw Formation
503.5	16MB0104	0.0001852	Yaw Formation
500.5	16MB0103	0.00025	Yaw Formation
500.5	16MB0102	0.0001204	Yaw Formation
485	16MB0094	0.0002685	Yaw Formation
483.9	16MB0093	0.0002037	Yaw Formation
481.5	16MB0092	0.000213	Yaw Formation
477.6	16MB0091	0.0003426	Yaw Formation
474.9	16MB0090	0.0002685	Yaw Formation
471	16MB0089	0.00025	Yaw Formation
454.7	16MB0101	0.000213	Yaw Formation
453.6	16MB0100	0.0002037	Yaw Formation
450.5	16MB0099	0.0001667	Yaw Formation
447	16MB0098	0.0001111	Yaw Formation
444	16MB0097	0.0002407	Yaw Formation
439.6	16MB0096	0.00025	Yaw Formation
438.5	16MB0095	0.000287	Yaw Formation
435.5	16MB0088	0.0001852	Yaw Formation
434.5	16MB0087	0.001259	Yaw Formation
429	16MB0085	0.0001852	Yaw Formation
427	16MB0083	0.001704	Yaw Formation
423.6	16MB0082	0.002194	Yaw Formation
422.4	16MB0081	0.002519	Yaw Formation
419	16MB0080	0.000287	Yaw Formation
414	16MB0079	0.0002685	Yaw Formation
409	16MB0078	0.00001852	Yaw Formation
407	16MB0076	0.0001389	Yaw Formation
405	16MB0075	0.0003704	Yaw Formation
404.3	16MB0074	0.000213	Yaw Formation
399	16MB0073	0.0001944	Yaw Formation
395.3	16MB0070	0.0001759	Yaw Formation
395	16MB0071	0.0001481	Yaw Formation
388	16MB0069	0.0002315	Yaw Formation
387	16MB0068	0.0003056	Yaw Formation
384	16MB0067	0.0002685	Yaw Formation

382	16MB0066	0.0002315	Yaw Formation
380.2	16MB0065	0.0003333	Yaw Formation
375	16MB0064	0.0003333	Yaw Formation
373.6	16MB0063	0.000287	Yaw Formation
366	16MB0062	0.0002407	Yaw Formation
364.8	16MB0061	0.0002407	Yaw Formation
360	16MB0060	0.0002963	Yaw Formation
352.9	16MB0059	0.0003426	Yaw Formation
350.2	16MB0058	0.0002593	Yaw Formation
347.1	16MB0057	0.0006111	Yaw Formation
338.2	16MB0056	0.003009	Yaw Formation
330.8	16MB0055	0.0001759	Yaw Formation
327	16MB0054	0.0002593	Yaw Formation
326.5	16MB0053	0.0001759	Yaw Formation
323.3	16MB0052	0.000213	Yaw Formation
320.5	16MB0051	0.0004537	Yaw Formation
320.4	16MB0050	0.0002593	Yaw Formation
315.2	16MB0049	0.000463	Yaw Formation
313.1	16MB0048	0.0005278	Yaw Formation
311.1	16MB0047	0.002324	Yaw Formation
307.5	16MB0046	0.002204	Yaw Formation
299	16MB0045	0.0002037	Yaw Formation
297.5	16MB0044	0.0003611	Yaw Formation
294.2	16MB0042	0.0002778	Yaw Formation
290.8	16MB0041	0.0003056	Yaw Formation
286.5	16MB0039	0.0001296	Yaw Formation
286.4	16MB0040	0.0002315	Yaw Formation
283.9	16MB0038	0.0001389	Yaw Formation
278.6	16MB0037	0.001352	Yaw Formation
276.4	16MB0036	0.0003148	Yaw Formation
272.6	16MB0035	0.0003426	Yaw Formation
270.1	16MB0034	0.0002778	Yaw Formation
266.4	16MB0033	0.00025	Yaw Formation
262.3	16MB0032	0.0002963	Yaw Formation
258.4	16MB0031	0.0002315	Yaw Formation
255.4	16MB0030	0.0002685	Yaw Formation
251.5	16MB0029	0.0002963	Yaw Formation
247.9	16MB0028	0.00025	Yaw Formation
245.2	16MB0027	0.0002593	Yaw Formation
243	16MB0026	0.0002037	Yaw Formation
240.3	16MB0025	0.0002037	Yaw Formation
236.7	16MB0024	0.0002593	Yaw Formation
232.4	16MB0023	0.0003519	Yaw Formation
229.2	16MB0022	0.0004907	Yaw Formation
227.5	16MB0021	0.002833	Yaw Formation
225.9	16MB0020	0.0004722	Yaw Formation
222.9	16MB0019	0.0003796	Yaw Formation

219.8	16MB0018	0.000287	Yaw Formation
215.2	16MB0016	0.000213	Yaw Formation
211.6	16MB0015	0.0001944	Yaw Formation
209.7	16MB0014	0.0002963	Yaw Formation
207.8	16MB0013	0.0004259	Yaw Formation
206.3	16MB0012	0.0003519	Yaw Formation
204.2	16MB0011	0.0002778	Yaw Formation
200.8	16MB0010	0.0001667	Yaw Formation
196	16MB0009	0.0002593	Yaw Formation
191	16MB0008	0.0003333	Yaw Formation
188.5	16MB0007	0.0003056	Yaw Formation
184.9	16MB0006	0.0004815	Yaw Formation
181.1	16MB0005	0.0004074	Yaw Formation
178.3	16MB0004	0.0004167	Yaw Formation
177	17MC0049	0.0007778	Yaw Formation
174.9	16MB0003	0.0002685	Yaw Formation
174.5	17MC0048	0.001361	Yaw Formation
172.5	16MB0002	0.0004537	Yaw Formation
172.5	17MC0047	0.0004352	Yaw Formation
171	17MC0046	0.0003611	Yaw Formation
168	17MC0045	0.0004259	Yaw Formation
166.5	17MC0044	0.0004259	Yaw Formation
161.5	17MC0043	0.0002407	Yaw Formation
157.5	17MC0042	0.0004444	Yaw Formation
151.9	17MC0041	0.0005278	Yaw Formation
149.5	17MC0040	0.0004722	Yaw Formation
145.5	17MC0039	0.0004167	Yaw Formation
142.5	17MC0038	0.0003981	Yaw Formation
138	17MC0037	0.0008519	Yaw Formation
123.6	17MC0036	0.0003056	Yaw Formation
122.4	17MC0035	0.0003426	Yaw Formation
119	17MC0034	0.0003333	Yaw Formation
114.5	17MC0033	0.0003519	Yaw Formation
113	17MC0032	0.0004352	Yaw Formation
111	17MC0031	0.0002963	Yaw Formation
109.2	17MC0030	0.001509	Yaw Formation
106	17MC0029	0.0003704	Yaw Formation
103	17MC0028	0.0003611	Yaw Formation
101.6	17MC0027	0.0003611	Yaw Formation
91	17MC0026	0.0004907	Yaw Formation
86.7	17MC0025	0.000463	Yaw Formation
85.5	17MC0024	0.0004259	Yaw Formation
81	17MC0022	0.0008333	Yaw Formation
81	17MC0023	0.0005926	Yaw Formation
68	17MC0021	0.0003889	Yaw Formation
66.4	17MC0020	0.0004167	Yaw Formation
65	17MC0019	0.0003333	Yaw Formation

63	17MC0018	0.0003981	Yaw Formation
60.8	17MC0017	0.0003426	Yaw Formation
58.5	17MD0029	0.0003704	Yaw Formation
58.2	17MC0016	0.0005463	Yaw Formation
56.7	17MC0015	0.0005463	Yaw Formation
55.5	17MC0014	0.0003981	Yaw Formation
55.4	17MD0028	0.0005648	Yaw Formation
52	17MC0012	0.0006204	Yaw Formation
51.2	17MD0026	0.0001852	Yaw Formation
51.2	17MC0013	0.0003333	Yaw Formation
50.5	17MC0011	0.0001204	Yaw Formation
46.5	17MC0010	0.0001574	Yaw Formation
43.3	17MC0009	0.00212	Yaw Formation
41	17MC0007	0.00025	Yaw Formation
40.5	17MD0024	0.0002315	Yaw Formation
38.5	17MC0006	0.0003519	Yaw Formation
37.8	17MD0023	0.0003056	Yaw Formation
37.5	17MC0005	0.0003426	Yaw Formation
37	17MD0022	0.0003333	Yaw Formation
36.5	17MC0004	0.0002963	Yaw Formation
35.3	17MD0021	0.0003241	Yaw Formation
34.5	17MC0003	0.00025	Yaw Formation
33	17MD0020	0.0005093	Yaw Formation
32.8	17MC0002	0.0003333	Yaw Formation
31.5	17MD0019	0.000287	Yaw Formation
30	17MC0001	0.000537	Yaw Formation
28.7	17MD0018	0.000287	Yaw Formation
27.1	17MD0017	0.0003426	Yaw Formation
25.6	17MD0035	0.0003056	Yaw Formation
25.5	17MD0034	0.0004167	Yaw Formation
25.1	17MD0016	0.0003426	Yaw Formation
23.7	17MD0015	0.0003981	Yaw Formation
21	17MD0014	0.0003519	Yaw Formation
19.5	17MD0013	0.000287	Yaw Formation
18.3	17MD0012	0.0003426	Yaw Formation
16.5	17MD0011	0.0003241	Yaw Formation
15	17MD0010	0.0003426	Yaw Formation
13.5	17MD0009	0.0003148	Yaw Formation
12	17MD0008	0.0003611	Yaw Formation
10.8	17MD0033	0.0003148	Yaw Formation
9.6	17MD0031	0.0001944	Yaw Formation
9	17MD0007	0.0004167	Yaw Formation
9	17MD0006	0.0003148	Yaw Formation
9	17MD0005	0.0003426	Yaw Formation
8.6	17MD0032	0.0006019	Yaw Formation
8.6	17MD0030	0.0003704	Yaw Formation
8	17MD0004	0.0002963	Yaw Formation

6.5	17MD0003	0.0003056	Yaw Formation
0.4	17MD0002	0.000287	Yaw Formation
0	17MD0001	0.0005093	Yaw Formation

Supplementary Table 2

All zircon U-Pb data from this study and Licht et al. (2019).

Sample name	Note	lat	long	Source
Yaw Formation				
16MBV01	Tuff layer, level 332 in MB section (508 m composite section)	23°14'23.3''N	94°15'48.3''E	Licht et al., 2019
16YADZ01	Very base Yaw Fm	23°13'06.6''N	94°14'52.2''E	Licht et al., 2019
16YADZ04	very top Yaw Fm, Level 85, MA section (613 m composite section)	23°13'42.6''N	94°15'58.7''E	Licht et al., 2019
Tonhe Formation				
16YADZ02	Base Tonhe Fm, Level 181, MA section (709 m composite section)	23°13'42.6''N	94°15'58.7''E	Licht et al., 2019
16YADZ03	Middle Tonhe Fm, Level 271, MA section (799 m composite section)	23°13'42.6''N	94°15'58.7''E	Licht et al., 2019
Letkat Formation				
17letkat08	Base Letkat Fm (~960 m composite section)	23°19'10.7''N	94°17'54.3''E	Licht et al., 2019
16letkat	Middle Letkat Fm, level 476m LA section (1425 m composite section)	23°11'32.1''N	94°16'07.4''E	Licht et al., 2019
17letkat07	middle top Letkat, Level 386 LB section (1862 m composite section)	23°19'01.1''N	94°18'22.9''E	This study

1. Measured ratios corrected for downhole fraction and instrument bias.

2. All uncertainties include only measurement uncertainties and are given in 2 s.

3. additional systematic uncertainty during the sessions: ~2.67% for 206Pb/238U ratio, ~1.17% for 206Pb/207Pb ratio (2s) over two years (for calculation of igneous ages).

4. Accuracy: observed offset for the ages of our secondary standards (FC1 and GHB) during the sessions is in most of cases < 2%.

5. Ages are given uncorrected for common lead, and corrected following Andersen's method. We recommend the use of uncorrected ages (Andersen's method sometimes fails to accurately reproduce the age of international standards with our set up).

6. Best age for detrital zircon studies is determined from 206Pb/238U age for analyses with 206Pb/238U age <1400 Ma and from 206Pb/207Pb age for analyses with 206Pb/238U age > 1400 Ma.

7. Discordant ages are included but identified as discordant following the procedure below:

7a. Are noted as discordant grains with 206Pb/238U age > 1300 Ma and with >20% discordance (<80% concordance) or with >5% reverse discordance (<105% concordance) following the ratio of 206Pb/238U and 206Pb/207Pb ages

7b. Are noted as discordant grains with 206Pb/238U age between 300 and 1300 Ma and with >20% discordance (<80% concordance) or with >5% reverse discordance (<105% concordance) following the ratio of 207Pb/235U and 206Pb/238U ages

7c. grains with 206Pb/238U age below 300 Ma are not screened for discordance

8. Laser spot diameter 25 microns for all samples

16MBV01 (tuff)					Isotopic Ratios + measurement uncertainty (2s)										Ages uncorrected for common lead + measurement uncertainty (2s)									Ages corrected for common lead (Andersen routine) + measurement uncertainty (2s)							
					Data for Tera-Wasserburg plot					Data for Wetherill plot																				
Sample	U (ppm)	U/Th	U/Th uncertainty 2SE	207Pb (cps)	U238/Pb 206	U238/Pb 206 uncertainty (2s)	Pb207/Pb 206	Pb207/Pb 206 uncertainty (2s)	ρ	Pb207/U 235	Pb207/U 235 uncertainty (2s)	Pb206/U 238	Pb206/U 238 uncertainty (2s)	ρ	Age Pb206/U 238	Age Pb206/U 238 measurement uncertainty (2s)	Age Pb207/U 235	Age Pb207/U 235 measurement uncertainty (2s)	Age Pb207/Pb 206	Age Pb207/Pb 206 measurement uncertainty (2s)	Discordance Pb206/U 238 vs Pb207/U 235 (%)	Discordance Pb206/U 238 vs Pb207/Pb 206 (%)	Best age	Best age measurement uncertainty (2S)	Age Pb206/U 238	Age Pb206/U 238 measurement uncertainty (2s)	Age Pb207/U 235	Age Pb207/U 235 measurement uncertainty (2s)	Age Pb207/Pb 206	Age Pb207/Pb 206 measurement uncertainty (2s)	Common Lead fraction	Common Lead fraction uncertainty (2s)
ZB01	N/A	N/A	N/A	39.3	182.15	5.47	0.0506	0.0074	0.045	0.0387	0.0043	0.0055	0.0002	0.133	35.3	1.1	38.3	4.2	150.0	211.6	8	76	35.3	1.1	35.1	1.1	35.1	1.0	35.3	53.5	0.0	0.0
ZB02	N/A	N/A	N/A	108	170.94	4.92	0.0555	0.0067	0.263	0.0432	0.0040	0.0059	0.0002	-0.036	37.6	1.1	42.8	3.9	290.0	189.6	12	87	37.6	1.1	37.2	1.2	37.2	1.0	37.6	15.9	0.0	0.0
ZB04	N/A	N/A	N/A	118	163.67	4.93	0.0860	0.0106	-0.269	0.0750	0.0095	0.0061	0.0002	0.443	39.2	1.2	73.0	8.7	1050.0	236.3	46	96	39.2	1.2	37.1	1.2	37.1	1.0	39.2	5.2	0.1	0.0
ZB09	N/A	N/A	N/A	169	165.56	5.20	0.0572	0.0058	0.063	0.0477	0.0047	0.0060	0.0002	0.332	38.8	1.2	47.2	4.6	440.0	189.3	18	91	38.8	1.2	38.3	1.2	38.3	1.0	38.8	11.6	0.0	0.0
ZB10	N/A	N/A	N/A	44	171.23	4.76	0.0489	0.0071	0.276	0.0395	0.0045	0.0058	0.0002	-0.064	37.6	1.0	39.2	4.3	70.0	231.7	4	46	37.6	1.0	37.7	1.2	37.7	1.0	37.4	122.1	0.0	0.0
ZB11	N/A	N/A	N/A	44.3	176.68	5.20	0.0533	0.0070	0.355	0.0414	0.0039	0.0057	0.0002	-0.066	36.4	1.1	41.1	3.8	240.0	175.8	11	85	36.4	1.1	36.1	1.1	36.1	1.0	36.4	29.9	0.0	0.0
ZB12	N/A	N/A	N/A	31.2	165.56	5.56	0.0444	0.0084	0.132	0.0369	0.0058	0.0060	0.0002	-0.006	38.8	1.3	36.4	5.7	110.0	265.8	-7	65	38.8	1.3	39.0	1.4	39.0	1.3	38.8	56.2	0.0	0.0
ZB14	N/A	N/A	N/A	37.5	167.79	5.13	0.0457	0.0069	0.344	0.0372	0.0041	0.0060	0.0002	-0.121	38.3	1.2	37.0	4.0	30.0	216.3	-4	-28	38.3	1.2	38.4	1.2	38.4	1.0	38.3	89.5	0.0	0.0
ZB15	N/A	N/A	N/A	175	167.53	3.57	0.0475	0.0036	0.068	0.0394	0.0021	0.0060	0.0001	0.121	38.4	0.8	39.2	2.1	100.0	1051.4	2	62	38.4	0.8	38.3	0.8	38.3	0.5	38.5	1045.6	0.0	0.0
ZB17	N/A	N/A	N/A	252	170.27	3.48	0.0424	0.0026	0.049	0.0350	0.0017	0.0059	0.0001	0.271	37.8	0.8	34.9	1.7	120.0	79.8	-8	69	37.8	0.8	37.9	0.8	37.9	0.4	38.0	13.0	0.0	0.0
ZB19	N/A	N/A	N/A	53.9	174.52	5.29	0.0521	0.0066	0.276	0.0411	0.0040	0.0057	0.0002	-0.060	36.8	1.1	40.8	3.9	220.0	184.3	10	83	36.8	1.1	36.6	1.2	36.6	1.0	36.8	34.4	0.0	0.0
ZB22	N/A	N/A	N/A	47	166.11	5.41	0.0540	0.0105	0.117	0.0443	0.0078	0.0060	0.0002	0.027	38.7	1.3	43.7	7.6	220.0	308.4	11	82	38.7	1.3	38.4	1.4	38.4	1.2	38.7	28.5	0.0	0.0
ZB25	N/A	N/A	N/A	137	173.01	4.48	0.0544	0.0049	0.020	0.0429	0.0032	0.0058	0.0001	0.292	37.1	1.0	42.6	3.1	320.0	142.6	13	88	37.1	1.0	36.7	1.0	36.7	0.7	37.1	16.1	0.0	0.0
ZB27	N/A	N/A	N/A	33.7	171.53	5.52	0.0462	0.0066	0.101	0.0376	0.0039	0.0058	0.0002	0.120	37.5	1.2	37.3	3.9	0.0	222.6	-1	#NAME?	37.5	1.2	37.5	1.2	37.5	1.0	37.3	129.4	0.0	0.0
ZB28	N/A	N/A	N/A	171	169.49	5.22	0.0670	0.0092	-0.429	0.0550	0.0079	0.0059	0.0002	0.620	37.9	1.2	53.8	7.5	700.0	220.6	30	95	37.9	1.2	36.7	1.0	36.7	0.8	37.9	6.5	0.0	0.0
ZB29	N/A	N/A	N/A	222	160.26	3.99	0.0467	0.0027	-0.112	0.0409	0.0019	0.0062	0.0002	0.444	40.1	1.0	40.7	1.9	51.0	116.5	2	21	40.1	1.0	40.0	1.0	40.0	0.7	39.9	86.6	0.0	0.0
ZB30	N/A	N/A	N/A	208	164.74	3.86	0.0647	0.0071	-0.515	0.0573	0.0066	0.0061	0.0001	0.749	39.0	0.9	56.2	6.2	690.0	204.8	31	94	39.0	0.9	38.0	0.9	38.1	0.7	39.3	6.8	0.0	0.0
ZB32	N/A	N/A	N/A	92	158.73	4.22	0.0474	0.0046	-0.009	0.0405	0.0029	0.0063	0.0002	0.287	40.5	1.1	40.3	2.8	100.0	479.8	0	60	40.5	1.1	40.3	1.1	40.3	0.8	40.3	458.3	0.0	0.0

16YADZ01					Isotopic Ratios + measurement uncertainty (2s)										Ages uncorrected for common lead + measurement uncertainty (2s)								Ages corrected for common lead (Andersen routine) + measurement uncertainty (2s)							
					Data for Tera-Wasserburg plot					Data for Wetherill plot																				
Sample	U (ppm)	U/Th	U/Th uncertainty 2SE	207Pb (cps)	U238/Pb 206	U238/Pb 206 uncertainty (2s)	Pb207/Pb 206	Pb207/Pb 206 uncertainty (2s)	ρ	Pb207/U 235	Pb207/U 235 uncertainty (2s)	Pb206/U 238	Pb206/U 238 uncertainty (2s)	ρ	Age Pb206/U 238	Age Pb206/U 238 measurement uncertainty (2s)	Age Pb207/U 235	Age Pb207/U 235 measurement uncertainty (2s)	Age Pb207/Pb 206	Age Pb207/Pb 206 measurement uncertainty (2s)	Discordance Pb206/U 238 vs Pb207/U 235 (%)	Concordance Pb206/U 238 vs Pb207/Pb 206 (%)	Best age	Best age measurement uncertainty (2S)	Age Pb206/U 238	Age Pb206/U 238 measurement uncertainty (2s)	Age Pb207/U 235	Age Pb207/U 235 measurement uncertainty (2s)	Age Pb207/Pb 206	Age Pb207/Pb 206 measurement uncertainty (2s)	Common Lead fraction	Common Lead fraction uncertainty (2s)
Z001	940	6.48	0.48	2360	10.76426	0.167953	0.0591	0.001218	0.36355	0.754	0.014173	0.0929	0.00145	-0.16457	572.7	8.593529	570	7.874008	561	45.85583	-0.47368	-2.08556	572.7	8.593529	571.2	8.77063	552.6	4.803145	488	30.31794	0.0029	0.0013
Z002	439	2.198	0.077	71	128.2051	3.994074	0.0472	0.004453	0.33239	0.057	0.007874	0.0078	0.000243	-0.09876	50.1	1.560765	55.5	7.480307	120	214.9383	9.72973	58.25	50.1	1.560765	49.9	1.632602	50	1.496061	50.1	115.7691	0.0036	0.0085
Z003	383	1.602	0.064	630	16.71682	0.299722	0.0591	0.002391	0.43153	0.484	0.014173	0.05982	0.001073	-0.16457	374.5	6.493317	400	9.448809	539	97.55543	6.375	30.51948	374.5	6.493317	371.9	6.879518	366.5	4.881885	334	63.3361	0.0073	0.003
Z004	841	1.82	0.14	923	21.92982	0.428613	0.0534	0.002315	0.53819	0.34	0.012598	0.0456	0.000891	-0.16097	287.4	5.50713	297	9.448809	320	93.99444	3.232323	10.1875	287.4	5.50713	286.5	5.805814	283.5	4.803145	245	41.8578	0.0036	0.0036
Z005	174	2.929	0.091	905	6.289308	0.113362	0.0754	0.003008	0.2756	1.688	0.055905	0.159	0.002866	0.02059	951	15.99177	1002	20.47242	1063	78.27641	5.08982	10.53622	951	15.99177	944	17.11539	941	11.81101	913	39.42964	0.0085	0.004
Z006	52	0.651	0.013	1191	2.562788	0.049372	0.1312	0.004306	0.24271	7.16	0.220472	0.3902	0.007517	0.27621	2123	34.59339	2127	28.34643	2122	51.58041	0.188058	-0.04713	2122	51.58041	2112	36.95054	2086	26.77163	2054	37.03455	0.0063	0.0041
Z007	790	2.252	0.095	142	125.9446	2.993638	0.0542	0.004407	-0.01793	0.0612	0.005039	0.00794	0.000189	0.23483	51	1.220794	60.1	4.803145	350	158.1284	15.14143	85.42857	51	1.220794	50.4	1.287532	50.5	1.023621	50.9	14.34021	0.0095	0.0065
Z008	329.7	1.876	0.054	2470	4.962779	0.088548	0.0806	0.001438	0.15711	2.229	0.048819	0.2015	0.003595	0.64585	1183	19.48736	1188	15.74802	1206	35.88533	0.420875	1.907131	1183	19.48736	1180	19.48736	1166	14.96061	1139	24.97472	0.0026	0.0013
Z009	121.1	1.66	0.044	379	9.67118	0.178118	0.0661	0.003187	0.30023	0.938	0.040157	0.1034	0.001904	-0.07267	634.3	10.94373	668	20.47242	760	101.0956	5.04491	16.53947	634.3	10.94373	629	11.73226	612	9.448809	566	59.34502	0.0081	0.0038
Z010	840	3.04	0.69	108	153.8462	3.446248	0.0428	0.004642	0.40261	0.0383	0.00378	0.0065	0.000146	-0.24917	41.79	0.92573	38.1	3.700784	100	173.6996	-9.68504	58.21	41.79	0.92573	42	1.023536	42	0.866141	41.79	12.81068	-0.0047	0.0072
Z011	6800	6.56	0.2	1590	82.10181	4.431679	0.0453	0.001494	0.65885	0.0767	0.002598	0.01218	0.000657	0.74644	78	4.142326	75.1	2.440942	15	59.89199	-3.86152	-420	78	4.142326	78.2	4.295167	78.3	4.173224	73.4	11.47566	-0.0019	0.0025
Z012	355	1.906	0.044	156	49.26108	0.863148	0.0477	0.003222	0.2774	0.133	0.007874	0.0203	0.000356	-0.09967	129.5	2.249717	126.1	7.086607	90	128.5724	-2.69627	-43.8889	129.5	2.249717	129.7	2.357378	129.5	1.653542	127.6	50.89034	-0.0013	0.0048
Z014	444	1.062	0.018	75	119.0476	3.19613	0.0451	0.00476	0.41734	0.0526	0.004803	0.0084	0.000226	-0.10161	53.9	1.44293	51.9	4.645665	20	176.2438	-3.85356	-169.5	53.9	1.44293	54.1	1.582292	54	1.338581	53.8	32.49128	-0.0016	0.0074
Z015	43.9	2.246	0.041	46.1	24.03846	0.670099	0.0552	0.00737	0.44105	0.32	0.038583	0.0416	0.00116	-0.22781	262.5	7.214813	274	29.13383	330	325.1671	4.19708	20.45455	262.5	7.214813	261	8.349319	260.6	7.401567	257.7	231.6246	0.007	0.012
Z016	78.7	0.745	0.013	552	5.141388	0.131031	0.0804	0.003786	-0.00344	2.19	0.110236	0.1945	0.004957	0.52587	1145	26.65521	1171	35.43304	1180	93.0116	2.220325	2.966102	1145	26.65521	1138	27.33277	1119	29.13383	1074	56.87564	0.0057	0.0035
Z017	274	1.572	0.097	42.5	126.2626	3.771361	0.0443	0.005667	0.018894	0.0487	0.005748	0.00792	0.000237	0.17686	50.8	1.494031	48.1	5.511806	60	199.3834	-5.61331	15.33333	50.8	1.494031	51	1.564969	50.9	1.417321	50.6	31.71	-0.0029	0.0086
Z018	217.8	1.173	0.028	30.9	138.5042	4.189532	0.0436	0.006364	0.28682	0.0425	0.005433	0.00722	0.000218	-0.07995	46.4	1.397727	42.1	5.354325	100	214.5258	-10.2138	53.6	46.4	1.397727	46.6	1.541182	46.6	1.417321	46.5	28.72155	-0.0044	0.0095
Z019	104	1.002	0.034	870	4.255319	0.091625	0.0815	0.002752	0.26983	2.691	0.07559	0.235	0.00506	0.13848	1361	26.64948	1324	21.25982	1221	66.32087	-2.79456	-11.466	Discordant	Discordant	1357	27.28176	1304	18.11022	1184	54.16085	0.0019	0.0019
Z020	103.7	0.86	0.051	198	76.92308	6.140182	0.328	0.038745	-0.76452	0.64	0.102362	0.013	0.001038	0.89275	83	6.391751	468	62.99206	3300	251.9833	82.26496	97.48485	83	6.391751	51.7	3.108421	57.6	5.039365	270	133.8865	0.342	0.054
Z021	64.7	1.092	0.088	467	4.97265	0.097125	0.0801	0.004188	0.2076	2.26	0.102362	0.2011	0.003928	0.061165	1181	21.164	1194	33.07083	1170	100.9527	1.088777	-0.94017	1181	21.164	1174	21.75626	1144	21.25982	1059	73.01559	0.0052	0.0032
Z022	335	1.307	0.025	4200	3.53857	0.063488	0.0991	0.00157	0.35508	3.917	0.069291	0.2826	0.00507	0.50627	1604	25.42225	1616	14.17321	1605	30.34835	0.742574	0.062305	1605	30.34835	1600	25.96519	1595	16.53542	1573	21.48493	0.0023	0.0016
Z023	545	4.33	0.47	6970	3.570154	0.074671	0.1015	0.001669	-0.30946	3.99	0.11811	0.2801	0.005858	0.80794	1591	29.37452	1629	24.40942	1649	30.17563	2.332719	3.517283	1649	30.17563	1584	29.37452	1588	22.04722	1579	21.54457	0.0056	0.0026
Z024	801	2.92	0.21	1990	11.26126	0.203239	0.0589	0.001165	0.18171	0.732	0.017323	0.0888	0.001603	0.62885	548.4	9.548993	557	10.23621	558	43.25908	1.543986	1.72043	548.4	9.548993	547.1	9.658741	539	7.874008	493	29.35963	0.0025	0.0013
Z025	3340	12.3	1.7	550	146.1988	3.727368	0.0525	0.003649	0.48991	0.0495	0.003071	0.00684	0.000174	-0.16635	43.9	1.10541	49	2.913383	270	126.2718	10.40816	83.74074	43.9	1.10541	43.6	1.173428	43.6	1.023621	43.8	8.579996	0.0078	0.006
Z027	879	4.78	0.1	2608	9.29368	0.14657	0.061	0.001215	0.099703	0.903	0.016535	0.1076	0.001697	0.29948	658.5	9.972176	653	8.661409	629	43.84739	-0.84227	-4.68998	658.5	9.972176	657.4	10.06254	643.4	6.535427	577	33.36905	0.00153	0.00086
Z028	885	3.084	0.099	5830	5.265929	0.127301	0.0779	0.001194	0.3812	2.075	0.047244	0.1899	0.004591	0.82671	1120	24.51038	1139	15.74802	1141	29.29582	1.66813	1.840491	1120	24.51038	1118	25.84025	1120	21.25982	1086	24.36196	0.0026	0.0017
Z029	102	1.42	0.19	1610	3.072197	0.062875	0.1083	0.002976	0.2593	4.89	0.149606	0.3255	0.006662	0.45372	1816	32.6333	1797	25.19683	1760	51.52776	-1.05732	-3.18182	1760	51.52776	1810	33.86403	1769	27.55903	1706	44.2799	0.0032	0.0022
Z030	130	1.281	0.065	554	8.084074	0.200129	0.078	0.003697	0.62689	1.327	0.040945	0.1237	0.003062	-0.03098	751	17.61365	855	18.11022	1130	101.1993	12.16374	33.53982	751	17.61365	739	18.96947	734	14.96061	723	55.38295	0.0178	0.005
Z031	1650	12.8	1.6	23800	3.297066	0.065804	0.1062	0.001153	0.42856	4.51	0.076378	0.3033	0.006053	0.63426	1707	30.12707	1732	14.17321	1734	19.79582	1.443418	1.557093	1734	19.79582	1702	31.33752	1704	21.25982	1683	20.54883	0.0032	0.0019
Z032	153.1	1.611	0.03	45	121.2121	7.34631	0.081	0.023188	-0.37636	0.098	0.031496	0.00825	0.0005	0.49944	52.9	3.224512	91	25.98423	690	409.5055	41.86813	92.33333	52.9	3.224512	49.4	2.994207	49.5	2.913383	52.9	7.52675	0.043	0.036
Z033	314.5	1.97	0.1	338	21.85792	0.469784	0.0542	0.00394	-0.24332	0.35	0.025984	0.04575	0.000983	0.50092	288.4	6.059649	303	19.68502	340	155.5416	4.818482	15.17647	288.4	6.059649	287	5.874176	286.1	4.803145	276	65.29868	0.0045	0.0059
Z034	1130	0.899	0.023	2370	12.43781	0.218893	0.0588	0.001008	0.26189	0.66	0.010236	0.0804	0.001415	0.5458	498.4	8.569969	514.4	6.299206	556	38.65108	3.11042	10.35971	498.4	8.569969	496.8	8.623698	495.3	5.196845	471	25.9905	0.0033	0.0011
Z035	133.1	1.366	0.021	6160	1.956182	0.034167	0.199	0.002697	0.20854	13.99	0.181102	0.5112	0.008929	0.40633	2661	38.09108	2747	12.59841	2816	21.92491	3.130688	5.504261	2816	21.92491	2620	43.70046	2645	26.77163	2671	26.98299	0.0193	0.0061
Z036	575	0.818	0.02	3970	5.154639	0.092191	0.0783	0.001092	0.19297	2.092	0.040945	0.194	0.00347	0.71029	1143	18.62758	1145	13.38581	1152	27.43291	0.174672	0.78125	1143	18.62758	1140	19.1689	1128	12.59841	1107	19.33248	0.00183	0.00099
Z037	318	1.87	0.047	1830	5.910165	0.103548	0.0752	0.00146	0.098397	1.752	0.03937	0.1692	0.002964	0.57788	1007	16.4581	1026	14.17321	1068	41.01701	1.851852	5.71161	1007	16.4581	1003	16.4581	994	12.59841	968	29.08634	0.0042	0.0015
Z038	336	1.181	0.044	876	10.10101	0.154802	0.0589	0.001765	-0.00428	0.805	0.022835	0.099	0.001517	0.27823	608.6	8.954891	598	12.59841	546	65.24288	-1.77258	-11.4652	608.6	8.954891	607.4	8.954891	585	8.661409	490	46.24623	0.0025	0.0013
Z039	770	0.889	0.025	180	104.9318	8.692497	0.0619	0.005912	-0.55302	0.079	0.011024	0.00953	0.000789	0.91043	61.1	5.024273	77	10.23621	580	181.2845	20.64935	89.46552	61.1	5.024273	57.5	3.096501	57.5	2.992123	61.1	9.52259	0.0187	0.009
Z040	153	1.021	0.019	39.7	106.383	3.661845	0.063	0.009273	-0.10623	0.082	0.012598	0.0094	0.000324	0.31432	60.3	2.046865	79	11.81101	540	283.839	23.67089	88.83333	60.3	2.046865	59.1	2.340781	59.1	2.204722	60.1	14.71196	0.02	0.014
Z041	335	1.179	0.02	255	94.16196	4.433742	0.211	0.027993	-0.75981	0.326	0.049606	0.01062	0.0005	0.83961	68.1	3.196514	274	37.79524	2490	299.2204	75.14599	97.26506	68.1	3.196514	52.8	2.016756	53.2	1.811022	68.1	3.775877	0.206	0.043
Z042	458	4.01	0.51	3470	4.796163	0.122409	0.0819	0.002515	0.2334	2.427	0.076378	0.2085	0.005321	0.33262	1220	28.427	1249	22.83462	1235	63.1495	2.321857	1.214575	1220	28.427	1214	29.79017	1207	24.40942	1162	47.97352	0.0055	0.0032
Z043	141.9	1.81	0.15	26.8	125	4.492155	0.052	0.00925	0.19952	0.058	0.009449	0.008	0.000287	0.10046	51.4	1.857417	56	9.448809	160	287.0395	8.214286	67.875	51.4	1.857417	51	2.005093	51	1.889762	51.4	45.19594	0.007	0.014
Z044	334	2.489	0.098	2033	5.440696	0.103164	0.0754	0.001944	0.040825	1.953	0.052756	0.1838	0.003485	0.47326	1088	18.73752	1098	18.11022	1072	51.53382	0.910747	-1.49254	1088	18.73752	1085	19.3079	1075	14.96061	1020	35.9407	0.0024	0.0018
Z045	532	0.763	0.012	1160	11.85536	0.181002	0.0581	0.001509	0.22683	0.675	0.014961	0.08435	0.001288	-0.00567	522	7.65852	523	9.448809	522	54.9433	0.191205	0	522	7.65852	520.5	7.740654	504.2	5.039365	433	35.6335	0.0032	0.0014
Z046	344	1.926	0.032	69.1	105.2632	2.507188	0.0476	0.004329	0.24809	0.0619	0.004961	0.0095	0.000226	0.011199	61	1.423572	60.8	4.724405	80	202.0727	-0.32895	23.75	61	1.423572	61	1.48955	61	1.259841	61	135.8409	0.0005	0.0064
Z047	240	3.16	0.14	38	128.3697	3.653833	0.0458	0.006178	-0.11243	0.0474	0.005433	0.00779	0.000222	0.34433	50	1.418909	46.8	5.275585	30	204.8491	-6.83761	-66.6667	50	1.418909	50.1	1.418909	50.1	1.259841	50	56.69861	-0.0019	0.0089
Z048	100.6	1.351	0.013	712	5.068424	0.092726	0.0799	0.002856	0.27427	2.165	0.064567	0.1973	0.00361	-0.04649	1161	19.30892	1166	21.25982	1171	71.84968	0.428816	0.853971	1161	19.30892	1154	20.43219	1117	14.96061	1047	50.03815	0.0058	0.0025
Z049	394	8.1	1.7	733	13.92758	0.329961	0.057	0.001713	0.11982	0.564	0.018898	0.0718	0.001701	0.60113	447	10.34523	453	12.59841	474	67.43283	1.324503	5.696203	447	10.34523	446	10.34523	435	8.661409	377	43.3369	0.0034	0.002
Z050	1007	3.681	0.06	872	30.07519	0.503417	0.0587	0.005569	-0.66422	0.268	0.025984	0.03325	0.000557	0.76367	210.9	3.499402	238	18.11022	480	175.6536	11.38655	56.0625	210.9	3.499402	208.7	3.355595	206.2	2.125982	182	79.38628	0.0107	0.008
Z051	542	2.87	0.36	3630	5.277045	0.100073	0.0777	0.001101	-0.07219	2.034	0.048031	0.1895	0.003594	0.79307	1118	19.54164	1125	15.74802	1135	28.45633	0.622222	1.497797	1118	19.54164	1116	19.54164	1108	15.74802	1087	22.67207	0.00181	0.00091
Z053	368	2.61	0.52	2145	5.704507	0.107207	0.0741	0.001362	0.025151	1.787	0.032283	0.1753	0.003294	0.53528	1041	18.3802	1040	11.81101	1039	37.19712	-0.09615	-0.19249	1041	18.3802	1039	18.3802	1021	11.02361	992	26.99826	0.0022	0.0011
Z054	436	1.31	0.037	141	87.7193	2.358822	0.0662	0.007363	-0.25698	0.104	0.011811	0.0114	0.000307	0.43646	73.1	1.97657	99	10.23621	670	204.9271	26.16162	89.08955	73.1	1.97657	70.6	1.773198	70.6	1.496061	73.2	9.279045	0.023	0.011
Z055	940	3.76	0.12	22200	2.660282	0.050264	0.1417	0.001492	0.068022	7.34	0.086614	0.3759	0.007102	0.63553	2056	33.58738	2153	10.23621	2247	17.57527	4.505341	8.500223	2247	17.57527	2027	37.16278	2043	26.77163	2073	29.73634	0.0169	0.0045
Z056	374	1.459	0.056	2360	5.157298	0.110912	0.0755	0.001564	0.15208	2.037	0.040945	0.1939	0.00417	0.43467	1142	22.71749	1127	13.38581	1076	41.41631	-1.33097	-6.13383	1142	22.71749	1112	12.59841	1045	12.59841	1045	32.34703	0.0019	0.0014
Z058	580	1.664	0.027	1282	12.03369	0.194556	0.0591	0.001571	0.11342	0.678	0.014961	0.0831	0.001344	0.30368	514.8	8.065379	525	9.448809	558	58.0605	1.942857	7.741935	514.8	8.065379	513.2	8.160144	505.3	5.748026	458	34.21465	0.0034	0.0013
Z059	1120	1.54	0.15	6760	5.411255	0.123761	0.0757	0.001179	0.50265	1.969	0.037008	0.1848	0.004227	0.75374	1093	23.03513	1104	12.59841	1083	31.15298	0.996377	-0.92336	1093	23.03513	1091	23.68538	1086	17.32282	1040	21.88259	0.0018	0.0015
Z060	635	1.469	0.023	6870	3.907776	0.059983	0.0942	0.001218	0.41981	3.317	0.03937	0.2559	0.003928	0.30086	1469	20.02149	1484	9.448809	1509	24.44488	1.010782	2.650762	1509	24.44488	1464	20.43527	1459	9.448809	1447	15.26407	0.0034	0.0015
Z061	1290	3.019	0.09	1031	29.83294	0.506608	0.0538	0.001715	0.12057	0.2477	0.00685	0.03352	0.000569	0.19697	212.5	3.565911	224.4	5.590546	342	99.72539	5.30303	37.8655	212.5	3.565911	211.6	3.616838	210.4	2.283462	201.6	77.02785	0.0046	0.0023
Z063	158.1	1.408	0.059	1931	3.573981	0.077978	0.1004	0.002623	0.30635	3.96	0.110236	0.2798	0.006105	0.37106	1590	30.60541	1624	21.25982	1624	49.11757	2.093596	2.093596	1624	49.11757	1579	32.52063	1566	18.89762	1529	27.90762	0.008	0.0037
Z064	213	2.873	0.068	1860	4.424779	0.105269	0.0872	0.002072	0.23815	2.752	0.076378	0.226	0.005377	0.5943	1313	28.29018	1340	20.47242	1357	45.24053	2.014925	3.242447	1313	28.29018	1307	29.6178	1300	22.83462	1267	31.7034	0.0053	0.0027
Z065	223.8	1.857	0.026	11070	1.964637	0.047153	0.2248	0.004292	0.33434	16.19	0.3937	0.509	0.012216	0.63762	2650	51.17931	2886	22.83462	3013	30.86694	8.177408	12.04779	3013	30.86694	2531	66.98792	2609	58.26766	2662	50.96085	0.055	0.013
Z066	131	2.25	0.11	27.2	126.5823	5.552363	0.062	0.012422	-0.01128	0.074	0.015748	0.0079	0.000347	0.15923	50.7	2.22664	71	14.17321	450	346.7688	28.59155	88.73333	50.7	2.22664	49.3	2.301939	49.3	2.125982	50.4	14.93054	0.02	0.019
Z068	753	1.931	0.024	2030	9.940358	0.169769	0.05955	0.000952	0.29912	0.821	0.012598	0.1006	0.001718	0.63507	618.1	10.06335	610.4	7.716528	583	33.75726	-1.26147	-6.02058	618.1	10.06335	617.6	10.1651	602.9	7.086607	548	26.60888	0.00059	0.00055
Z071	182.7	1.862	0.069	490	9.97009	0.192113	0.0605	0.002165	0.29603	0.833	0.024409	0.1003	0.001933	0.19117	616	11.58791	614	13.38581	598	75.55772	-0.32573	-3.01003	616	11.58791	614	11.58791	593	8.661409	512	48.79353	0.004	0.002
Z072	192	1.293	0.057	2280	3.646973	0.103807	0.1001	0.003349	0.063748	3.89	0.15748	0.2742	0.007805	0.63242	1561	39.82144	1607	33.85823	1617	62.96287	2.862477	3.463203	1617	62.96287	1552	42.64818	1555	39.37004	1521	45.78496	0.0072	0.0053
Z073	221	1.601	0.04	2240	4.051864	0.064983	0.0921	0.001849	0.32388	3.138	0.062992	0.2468	0.003958	0.14191	1422	20.46782	1440	15.74802	1463	38.06955	1.25	2.802461	1463	38.06955	1415	20.93207	1398	11.81101	1378	25.11753	0.0056	0.0021
Z074	1370	2.21	0.25	3310	10.74114	0.202301	0.0591	0.001045	0.053534	0.769	0.01811	0.0931	0.001753	0.59832	573.6	10.32062	579	10.23621	567	39.02637	0.932642	-1.16402	573.6	10.32062	572.4	10.37723	565	8.661409	525	24.99354	0.0023	0.0012
Z075	152.1	0.875	0.018	588	7.680492	0.1279	0.066	0.002307	-0.20935	1.187	0.04252	0.1302	0.002168	0.52064	789	12.51573	791	19.68502	785	71.73691	0.252845	-0.50955	789	12.51573	785.8	12.46634	760	12.59841	697	48.21374	0.0039	0.0018
Z076	423	3.38	0.096	1980	6.839945	0.123319	0.071	0.001498	-0.26715	1.435	0.043307	0.1462	0.002636	0.75626	880	14.85952	901	18.11022	949	43.79478	2.330744	7.270811	880	14.85952	876	14.85952	868	12.59841	856	26.02619	0.0045	0.0017
Z077	538	1.29	0.2	2350	6.839945	0.139434	0.068	0.002057	-0.3893	1.409	0.055905	0.1462	0.00298	0.7686	879	17.18154	890	24.40942	886	51.30197	1.235955	0.790068	879	17.18154	877	16.57544	875	14.96061	831	35.60747	0.0033	0.0019
Z078	1269	5.162	0.068	3250	10.23541	0.166665	0.0594	0.001048	0.20511	0.801	0.013386	0.0977	0.001591	0.13391	601	9.274266	597	7.637788	576	38.92089	-0.67002	-4.34028	601	9.274266	599.8	9.36739	582.8	5.511806	523	28.58908	0.00223	0.00088
Z079	151	1.181	0.014	93	91.74312	8.699034	0.131	0.033409	-0.79446	0.233	0.07559	0.0109	0.001034	0.91112	69.9	6.520576	186	53.54325	1130	409.4711	62.41935	93.81416	69.9	6.520576	59.5	2.827776	60.8	3.700784	70.1	7.82912	0.1	0.048
Z080	879	1.028	0.018	306	108.1081	2.322329	0.0805	0.007754	-0.29821	0.104	0.011024	0.00925	0.000199	0.46118	59.3	1.283298	100	10.23621	1030	181.1338	40.7	94.24272	59.3	1.283298	56.7	1.221414	56.7	0.944881	59.4	3.536705	0.044	0.013
Z082	129.3	0.768	0.021	29.9	124.533	4.23451	0.067	0.010986	0.26565	0.07	0.008661	0.00803	0.000273	0.003577	51.5	1.712468	68	8.661409	540	267.9604	24.26471	90.46296	51.5	1.712468	50.8	2.080276	50.8	1.968502	51.5	11.54296	0.026	0.016
Z083	501	1.12	0.019	261	98.03922	2.741308	0.102

Z084	488	1.242	0.044	16600	2.189621	0.04304	0.1674	0.002367	0.16822	10.53	0.188976	0.4567	0.008977	0.40464	2424	39.95312	2480	16.53542	2529	23.71196	2.258065	4.151839	2529	23.71196	2395	43.60381	2395	25.19683	2411	25.23207	0.0146	0.0049
Z085	773	8.69	0.16	5000	5.109862	0.089642	0.0758	0.001348	0.072873	2.078	0.037008	0.1957	0.003433	0.50971	1152	18.70178	1141	12.59841	1084	35.97691	-0.96407	-6.27306	1152	18.70178	1151	18.70178	1133	11.02361	1066	29.4054	0.00066	0.00067
Z086	158	1.21	0.35	333	12.10654	0.234777	0.0576	0.002369	0.43886	0.653	0.02126	0.0826	0.001602	-0.00304	511.6	9.577829	509	13.38581	490	90.99853	-0.51081	-4.40816	511.6	9.577829	508.5	9.461903	496.9	7.637788	456	51.3686	0.0028	0.0026
Z087	510	1.035	0.067	111	113.3787	2.510787	0.0549	0.005364	0.4005	0.0663	0.005906	0.00882	0.000195	-0.29201	56.6	1.262108	64.9	5.669286	320	181.8748	12.78891	82.3125	56.6	1.262108	56	1.39288	56	1.181101	56.4	16.77779	0.0102	0.0084
Z088	66.2	0.918	0.016	501	4.743833	0.080638	0.0806	0.003019	0.36951	2.337	0.07559	0.2108	0.003583	0.019041	1233	18.85895	1219	23.62202	1185	77.02208	-1.14848	-4.05063	1233	18.85895	1228	19.36182	1185	18.11022	1113	54.83266	0.0045	0.0024
Z090	56.3	15.1	0.43	137	10.79914	0.217564	0.0593	0.00412	0.55831	0.75	0.04252	0.0926	0.001866	-0.35827	571	10.6407	563	25.19683	510	149.6918	-1.42096	-11.9608	571	10.6407	569	11.85346	555	10.23621	501	74.37652	0.0028	0.0059
Z091	110.5	2.146	0.019	17.5	132.9787	4.784075	0.05	0.009444	0.33242	0.05	0.008661	0.00752	0.000271	-0.16894	48.3	1.696258	49	7.874008	30	298.9332	1.428571	-61	48.3	1.696258	48.3	1.992107	48.3	1.889762	48.3	94.92919	0.004	0.014
Z092	346	1.515	0.047	66.1	122.399	2.755817	0.053	0.006092	0.13004	0.0594	0.006378	0.00817	0.000184	0.040793	52.5	1.166676	58.3	6.062986	240	198.4841	9.948542	78.125	52.5	1.166676	52.1	1.297511	52.1	1.102361	52.5	25.433	0.0076	0.0092
Z093	608	1.069	0.03	958	15.70598	0.259008	0.0558	0.001454	0.1241	0.49	0.011024	0.06367	0.00105	0.35773	397.9	6.35915	404.7	7.716528	432	60.45377	1.680257	7.893519	397.9	6.35915	396.8	6.455911	390.2	5.669286	342	39.91439	0.0034	0.0013
Z094	61.2	2.165	0.061	495	4.712535	0.089427	0.0846	0.003194	0.25637	2.47	0.07874	0.2122	0.004027	0.1602	1240	21.03224	1258	22.83462	1283	73.44934	1.430843	3.35152	1240	21.03224	1232	22.18006	1197	13.38581	1168	42.68191	0.0068	0.0031
Z095	412	2.584	0.028	90	96.7118	2.11526	0.048	0.004028	0.19823	0.0665	0.004488	0.01034	0.000226	0.04654	66.3	1.400764	65.2	4.251964	90	210.9113	-1.68712	26.33333	66.3	1.400764	66.3	1.527789	66.2	1.259841	66.4	162.9938	0.0009	0.0059
Z096	302	2.09	0.044	70	105.4852	3.443568	0.0549	0.006467	-0.18303	0.073	0.008661	0.00948	0.000309	0.43763	60.8	1.97705	71	8.661409	310	213.8106	14.3662	80.3871	60.8	1.97705	60.1	1.905184	60.1	1.732282	60.8	22.80923	0.011	0.01
Z097	134	0.919	0.03	316	11.46789	0.188531	0.0625	0.002307	0.22262	0.75	0.020472	0.0872	0.001434	0.093215	539	8.537212	567	11.81101	668	88.30068	4.938272	19.31138	539	8.537212	535.5	8.732514	527.2	5.669286	486	64.01148	0.0068	0.0023
Z098	85.6	1.288	0.05	1060	3.559986	0.072786	0.0992	0.002666	0.33958	3.84	0.102362	0.2809	0.005743	0.44856	1595	28.79317	1596	22.04722	1597	50.58312	0.062657	0.125235	1597	50.58312	1588	30.01611	1560	21.25982	1518	33.76525	0.0044	0.0024
Z099	730	9.72	0.83	990	16.68892	0.26714	0.0519	0.001566	0.13384	0.43	0.011811	0.05992	0.000959	0.18013	375.1	5.852819	363	8.661409	270	63.67994	-3.33333	-38.9259	375.1	5.852819	375.4	5.898719	367.9	3.858264	303	33.55048	-0.0006	0.0022
Z100	63.1	2.03	0.12	11.6	111.6071	9.237858	0.058	0.015848	-0.43043	0.082	0.033071	0.00896	0.000742	0.8852	57.5	4.705805	73	25.98423	150	402.9277	21.23288	61.66667	57.5	4.705805	56.4	3.776003	56.1	3.779524	57.5	33.32168	0.014	0.024
Z102	31.2	0.2326	0.0055	212	5.107252	0.115768	0.0816	0.005957	0.17954	2.19	0.149606	0.1958	0.004438	0.093433	1152	24.05618	1158	48.81885	1130	158.3984	0.518135	-1.9469	1152	24.05618	1142	26.0246	1096	23.62202	1017	71.8945	0.0102	0.0076
Z103	640	1.29	0.044	1200	13.55014	0.402666	0.0607	0.002619	0.49599	0.622	0.023622	0.0738	0.002193	0.4988	459	13.16	489	14.17321	620	101.3024	6.134969	25.96774	459	13.16	455	13.87104	444	8.661409	405	43.93166	0.008	0.003
Z104	1129	2.021	0.035	905	28.74389	0.485054	0.0528	0.001654	0.047187	0.2537	0.007559	0.03479	0.000587	0.29056	220.5	3.643501	229.2	6.141726	303	80.52671	3.795812	27.22772	220.5	3.643501	219.6	3.693359	218	2.283462	188	52.86124	0.0032	0.0021
Z105	620	1.412	0.02	1284	12.34568	0.201393	0.0573	0.001216	0.12281	0.641	0.014173	0.081	0.001321	0.39457	501.8	7.944214	503	8.661409	495	46.75026	0.238569	-1.37374	501.8	7.944214	500.6	8.040406	488.3	6.850387	432	34.54833	0.0025	0.0012
Z106	1558	2.143	0.037	192	164.7446	3.037218	0.0462	0.002728	-0.13434	0.0386	0.002047	0.00607	0.000112	0.37309	39	0.716623	38.5	2.047242	30	100.7137	-1.2987	-30	39	0.716623	39.04	0.716623	39.09	0.527559	38.97	34.86421	-0.001	0.0038
Z107	1350	2.98	0.2	2900	12.09629	0.193906	0.0584	0.000916	0.14997	0.666	0.012598	0.08267	0.001325	0.48499	512	7.856439	517.6	7.637788	539	36.52051	1.081917	5.009276	512	7.856439	510.8	7.947454	504	5.826766	476	24.28472	0.0024	0.0011
Z108	433	1.374	0.023	58.5	141.844	3.272003	0.0437	0.00453	0.21315	0.0424	0.00378	0.00705	0.000163	-0.00265	45.3	1.048669	42	3.700784	80	159.0021	-7.85714	43.375	45.3	1.048669	45.5	1.114588	45.5	0.944881	45.3	21.96385	-0.0042	0.0067
Z109	151	1.072	0.015	52.3	72.15007	2.219751	0.0598	0.007468	0.1647	0.11	0.011024	0.01386	0.000426	0.12547	88.7	2.700176	106	10.23621	470	222.0909	16.32075	81.12766	88.7	2.700176	87.1	2.915468	87.2	2.677163	88.7	26.88335	0.015	0.011
Z110	768	1.083	0.068	20300	2.39521	0.036903	0.1439	0.001575	0.43418	8.32	0.11811	0.4175	0.006432	0.57399	2249	29.43894	2265	13.38581	2273	19.05197	0.706402	1.055873	2273	19.05197	2243	30.31058	2245	17.32282	2234	18.30513	0.0026	0.0017
Z111	212	1.519	0.016	7890	2.067825	0.029958	0.1755	0.002167	0.38351	11.7	0.133858	0.4836	0.007006	0.004237	2543	30.60908	2579	10.23621	2609	20.80848	1.39589	2.529705	2609	20.80848	2530	32.52408	2547	14.17321	2561	18.68938	0.005	0.0033
Z112	392	1.83	0.17	578	16.79825	0.291441	0.0614	0.004061	-0.36912	0.494	0.029921	0.05953	0.001033	0.53296	372.7	6.267163	410	21.25982	570	148.9823	9.097561	34.61404	372.7	6.267163	369.2	6.06608	367.2	4.173224	350	92.16134	0.0095	0.0056
Z113	858	12.12	0.68	133	137.5516	2.988117	0.0488	0.003212	0.21091	0.0484	0.002835	0.00727	0.000158	0.20909	46.7	0.99574	47.9	2.677163	130	138.9794	2.505219	64.07692	46.7	0.99574	46.6	1.059102	46.6	0.866141	46.5	84.64134	0.0024	0.0046
Z114	190	2.705	0.034	441	11.06195	0.179534	0.0584	0.002309	0.22036	0.736	0.027559	0.0904	0.001467	0.007725	558.2	8.672469	558	15.74802	540	87.93678	-0.03584	-3.37037	558.2	8.672469	556	8.910483	534.3	7.086607	437	52.27999	0.0032	0.0024
Z115	146	0.845	0.088	28.7	118.9061	3.584633	0.0521	0.008338	0.17536	0.06	0.008661	0.00841	0.000254	-0.01038	54	1.653547	58	8.661409	150	256.2037	6.896552	64	54	1.653547	53.7	1.79728	53.7	1.653542	54.1	46.4174	0.007	0.013
Z116	331	1.283	0.064	2580	4.599816	0.118148	0.0823	0.001866	0.31448	2.505	0.071653	0.2174	0.005584	0.72102	1268	30.04333	1271	21.25982	1246	43.36147	0.236035	-1.76565	1268	30.04333	1264	30.72689	1246	23.62202	1186	30.70468	0.0033	0.0022
Z117	328	1.093	0.025	64.2	127.8772	3.402453	0.0563	0.005368	0.27407	0.0621	0.005276	0.00782	0.000208	0.023206	50.2	1.350691	60.9	5.039365	420	166.0642	17.56979	88.04762	50.2	1.350691	49.6	1.420058	49.6	1.259841	50.2	15.38557	0.0121	0.0077
Z118	198	0.72	0.062	1380	5.053057	0.089553	0.0787	0.00194	0.28212	2.144	0.047244	0.1979	0.003507	0.084286	1164	18.79784	1166	14.17321	1152	52.10919	0.171527	-1.04167	1164	18.79784	1160	19.33439	1133	11.81101	1096	34.03745	0.0042	0.0016
Z119	308	1.603	0.017	2040	5.175983	0.087211	0.0779	0.001593	0.23106	2.082	0.040945	0.1932	0.003255	0.2234	1138	17.56382	1141	13.38581	1137	40.03552	0.262927	-0.08795	1138	17.56382	1135	17.56382	1113	8.661409	1090	25.98697	0.0028	0.0016
Z120	194	0.55	0.022	404	12.12121	0.203489	0.0574	0.002602	0.34473	0.653	0.025984	0.0825	0.001385	-0.12524	511.1	8.174179	508	15.74802	500	110.4442	-0.61024	-2.22	511.1	8.174179	509.6	8.629125	497.3	7.165347	444	50.68238	0.0022	0.0036

16YADZ04					Isotopic Ratios + measurement uncertainty (2s)										Ages uncorrected for common lead + measurement uncertainty (2s)									Ages corrected for common lead (Andersen routine) + measurement uncertainty (2s)							
					Data for Tera-Wasserburg plot					Data for Wetherill plot																				
Sample	U (ppm)	U/Th	U/Th uncertainty 2SE	207Pb (cps)	U238/Pb 206	U238/Pb 206 uncertainty (2s)	Pb207/Pb 206	Pb207/Pb 206 uncertainty (2s)	ρ	Pb207/U 235	Pb207/U 235 uncertainty (2s)	Pb206/U 238	Pb206/U 238 uncertainty (2s)	ρ	Age Pb206/U 238	Age Pb206/U 238 measurement uncertainty (2s)	Age Pb207/U 235	Age Pb207/U 235 measurement uncertainty (2s)	Age Pb207/Pb 206	Age Pb207/Pb 206 measurement uncertainty (2s)	Discordance Pb206/U 238 vs Pb207/U 235 (%)	Concordance Pb206/U 238 vs Pb207/Pb 206 (%)	Best age	Best age measurement uncertainty (2S)	Age Pb206/U 238	Age Pb206/U 238 measurement uncertainty (2s)	Age Pb207/U 235	Age Pb207/U 235 measurement uncertainty (2s)	Age Pb207/Pb 206	Age Pb207/Pb 206 measurement uncertainty (2s)	Common Lead fraction	Common Lead fraction uncertainty (2s)
Z001	927	1.581	0.093	906	65.18905	0.936921	0.049	0.001634	0.29274	0.1024	0.003071	0.01534	0.00022	0.17733	98.1	1.417321	98.9	2.834643	147	85.64589	0.808898	33.26531	98.1	1.417321	98.1	1.496061	98	1.417321	97.7	59.70886	0.0008	0.0024
Z002	128.8	1.839	0.055	107	72.3589	1.566619	0.0476	0.003898	0.23846	0.0899	0.006378	0.01382	0.000299	0.11851	88.5	1.889762	86.9	5.905506	60	152.4523	-1.8412	-47.5	88.5	1.889762	88.6	2.047242	88.5	2.047242	89.3	72.99463	-0.0006	0.0058
Z003	52.6	1.444	0.067	50.9	63.97953	1.74049	0.0493	0.006791	-0.03322	0.106	0.014173	0.01563	0.000425	0.20022	100	2.677163	100	12.59841	40	339.4741	0	-150	100	2.677163	99.9	2.834643	99.9	2.834643	100	264.6731	0.001	0.01
Z004	159.7	1.039	0.04	151	66.26905	1.314017	0.0482	0.003239	0.28164	0.0988	0.005591	0.01509	0.000299	0.04883	96.6	1.889762	95.3	5.196845	120	141.7506	-1.36411	19.5	96.6	1.889762	96.5	2.047242	96.4	2.047242	96.6	78.40344	0	0.0048
Z005	213.3	2.113	0.097	201	75.70023	1.714643	0.0551	0.003602	0.092743	0.0993	0.005984	0.01321	0.000299	0.27788	84.6	1.889762	95.7	5.511806	350	120.4533	11.59875	75.82857	84.6	1.889762	83.8	1.968502	83.8	1.968502	83.9	23.71848	0.0091	0.0053
Z006	175.2	2.32	0.53	2060	7.911392	0.211919	0.0696	0.002073	-0.53377	1.221	0.054331	0.1264	0.003386	0.86329	767	19.68502	802	26.77163	889	63.93791	4.36409	13.72328	767	19.68502	761	18.89762	752	20.47242	723	38.07829	0.0072	0.0019
Z007	438	4.5	0.36	1770	17.48252	0.288792	0.0545	0.001229	0.25164	0.427	0.009449	0.0572	0.000945	0.49195	358.4	5.826766	360.7	7.007867	378	51.75045	0.637649	5.185185	358.4	5.826766	357.4	5.905506	348.3	5.433065	290	31.30381	0.0028	0.0012
Z008	192	4.34	0.32	5400	4.144219	0.054093	0.0905	0.001522	0.27702	2.996	0.051968	0.2413	0.00315	0.48575	1393	16.53542	1404	13.38581	1428	32.20282	0.783476	2.45098	1393	16.53542	1387	17.32282	1367	13.38581	1343	21.01955	0.0049	0.002
Z009	603	6.65	0.19	127600	1.675042	0.026511	0.2715	0.003021	0.45163	22.25	0.330708	0.597	0.009449	0.75466	3015	38.58264	3192	14.17321	3312	17.50112	5.545113	8.967391	3312	17.50112	2891	54.33065	2956	41.73224	3005	33.9498	0.0527	0.0095
Z010	199.7	1.633	0.038	1184	13.0039	0.173096	0.0586	0.001651	-0.2257	0.619	0.01811	0.0769	0.001024	0.4639	477.7	6.299206	487	11.81101	547	68.30475	1.909651	12.6691	477.7	6.299206	474.2	6.141726	461	6.929127	394	39.09398	0.005	0.0018
Z011	58	1.652	0.039	706	6.973501	0.107215	0.0656	0.002129	0.023223	1.293	0.040945	0.1434	0.002205	0.45544	864	12.59841	839	18.11022	761	68.81046	-2.97974	-13.5348	864	12.59841	861	12.59841	814	14.17321	683	54.3244	0.0026	0.0013
Z012	176.3	1.496	0.057	316	36.12717	0.544678	0.0492	0.00244	0.15709	0.187	0.008661	0.02768	0.000417	0.12375	176	2.677163	173.5	7.165347	150	97.57526	-1.44092	-17.3333	176	2.677163	176.1	2.834643	175.5	2.834643	176.2	45.01695	-0.0003	0.0036
Z013	227.7	1.446	0.052	7580	3.759398	0.044514	0.0959	0.001285	0.25701	3.511	0.053543	0.266	0.00315	0.581	1520	15.74802	1528	11.81101	1541	25.65755	0.52356	1.362751	1541	25.65755	1515	17.32282	1497	14.17321	1478	18.00361	0.0035	0.0015
Z014	385	1.593	0.034	2400	11.99041	0.24905	0.0586	0.001581	0.1885	0.677	0.02126	0.0834	0.001732	0.62819	516	10.23621	523	12.59841	532	57.23441	1.338432	3.007519	516	10.23621	514	10.23621	498	10.23621	423	36.1134	0.0036	0.0016
Z015	793	2.97	0.22	26700	4.025765	0.076567	0.103	0.001222	0.26376	3.526	0.065354	0.2484	0.004724	0.82212	1430	24.40942	1531	14.96061	1676	22.1647	6.596995	14.6778	1676	22.1647	1411	25.98423	1418	25.19683	1430	25.20147	0.0153	0.0028
Z016	262	1.535	0.029	236	71.07321	1.272793	0.0474	0.003057	0.18148	0.0914	0.005433	0.01407	0.000252	0.088371	90	1.574802	88.5	5.039365	90	119.6321	-1.69492	0	90	1.574802	90	1.732282	89.9	1.653542	89.3	46.50939	-0.0005	0.0046
Z017	534	1.656	0.037	508	66.313	0.831006	0.0484	0.001782	0.91958	0.1009	0.003622	0.01508	0.000189	0.19067	96.5	1.181101	97.5	3.307083	122	83.94735	1.025641	20.90164	96.5	1.181101	96.4	1.181101	96.2	1.181101	93.4	51.76088	0.0008	0.0026
Z018	246	1.402	0.029	286	54.40696	0.862396	0.0483	0.002811	0.33015	0.1204	0.005591	0.01838	0.000291	-0.0493	117.4	1.811022	116.6	5.433065	120	114.144	-0.68611	2.166667	117.4	1.811022	117.3	1.968502	117	1.968502	115.7	50.55407	0.0002	0.0042
Z019	1310	1.997	0.039	21750	6.013229	0.07972	0.0762	0.000978	0.52151	1.755	0.024409	0.1663	0.002205	0.62383	991	12.59841	1028	8.661409	1096	26.20826	3.599222	9.580292	991	12.59841	986	13.38581	981	11.81101	959	14.51596	0.006	0.0014
Z020	336	1.907	0.062	465	61.38735	1.483623	0.0628	0.003123	0.018188	0.1393	0.007008	0.01629	0.000394	0.41559	104.1	2.440942	133.5	6.614167	640	102.8993	22.02247	83.73438	104.1	2.440942	102.2	2.519683	102.1	2.519683	103.2	10.91918	0.0191	0.0048
Z022	729	3.579	0.077	9480	7.390983	0.107533	0.0742	0.000864	0.2611	1.381	0.020472	0.1353	0.001969	0.74981	818	11.02361	882	9.448809	1043	24.46539	7.256236	21.57239	818	11.02361	810	11.81101	812	11.81101	818	16.91376	0.0099	0.0015
Z023	726	1.828	0.04	461	92.67841	1.555539	0.0452	0.001773	0.08189	0.0675	0.002598	0.01079	0.000181	0.35641	69.2	1.181101	66.2	2.519683	10	68.11748	-4.53172	-592	69.2	1.181101	69.3	1.181101	69.3	1.181101	69	16.32993	-0.0026	0.0026
Z024	341	2.1	0.14	660	93.02326	2.998	0.138	0.01511	-0.75456	0.215	0.032283	0.01075	0.000346	0.87201	68.9	2.204722	192	24.40942	2020	188.9843	64.11458	96.58911	68.9	2.204722	59.9	1.102361	60.1	1.102361	68.9	2.815519	0.117	0.025
Z025	519	2.026	0.064	526	63.5324	0.889907	0.0481	0.002204	0.044526	0.1053	0.004803	0.01574	0.00022	0.32854	100.6	1.417321	101.4	4.409444	110	95.88648	0.788955	8.545455	100.6	1.417321	100.6	1.496061	100.5	1.496061	99.4	41.20891	0.0004	0.0034
Z027	124.3	1.257	0.028	185	72.04611	2.002687	0.0809	0.007638	-0.45899	0.154	0.015748	0.01388	0.000386	0.68392	88.8	2.440942	143	13.38581	1070	181.2277	37.9021	91.70093	88.8	2.440942	84.7	2.204722	84.9	2.204722	88.8	7.173125	0.043	0.012
Z028	356	1.66	0.14	224	94.16196	3.700179	0.0478	0.00411	0.19674	0.0706	0.005827	0.01062	0.000417	0.21971	68.1	2.677163	68.9	5.511806	80	163.9262	1.161103	14.875	68.1	2.677163	68	2.755903	68	2.755903	67.2	82.41525	0.0009	0.0064
Z029	285.5	0.987	0.043	462	63.13131	1.161147	0.0768	0.005377	0.002985	0.166	0.011024	0.01584	0.000291	0.24525	101.3	1.811022	154	9.448809	980	133.9847	34.22078	89.66327	101.3	1.811022	97.6	1.889762	97.7	1.889762	101.3	6.096539	0.0375	0.0086
Z030	477.1	2.171	0.036	7510	6.281407	0.059029	0.0754	0.000954	0.17543	1.666	0.022047	0.1592	0.001496	0.56144	952	8.661409	995	8.661409	1075	25.68185	4.321608	11.44186	952	8.661409	947	8.661409	947	7.874008	945.1	14.10332	0.0065	0.0014
Z031	171	1.841	0.04	663	18.11594	0.284256	0.0543	0.002065	0.26799	0.415	0.014173	0.0552	0.000866	0.22316	346.2	5.433065	353	9.448809	354	81.81844	1.926346	2.20339	346.2	5.433065	345.2	5.669286	338.9	5.511806	289	42.46995	0.0036	0.0027
Z032	651	1.797	0.044	27500	3.729952	0.048201	0.1204	0.001311	0.39493	4.485	0.059055	0.2681	0.003465	0.67743	1531	17.32282	1727	11.02361	1959	19.18971	11.34916	21.84788	Discordant	Discordant	1488	19.68502	1506	18.89762	1531	18.44844	0.0314	0.0028
Z033	88	1.434	0.035	54.1	121.9512	5.738049	0.0585	0.007951	0.31816	0.0647	0.007717	0.0082	0.000386	0.23251	52.6	2.519683	63	7.322827	360	236.6606	16.50794	85.38889	52.6	2.519683	51.8	2.598423	51.8	2.598423	51.2	14.67706	0.015	0.012
Z034	355	1.63	0.16	11640	4.045307	0.067004	0.1009	0.001409	0.29889	3.467	0.06063	0.2472	0.004094	0.70381	1423	21.25982	1517	14.17321	1635	26.73702	6.19644	12.96636	1635	26.73702	1405	22.83462	1411	22.04722	1415	20.90714	0.0145	0.0029
Z035	164.7	1.633	0.038	5760	3.620565	0.037158	0.0973	0.001245	0.40872	3.74	0.044094	0.2762	0.002835	0.45274	1572	14.17321	1579	9.448809	1574	23.30804	0.443319	0.127065	1574	23.30804	1567	14.96061	1552	11.81101	1523	18.65381	0.0034	0.0014
Z037	762	3.35	0.11	4350	13.58696	0.188966	0.0589	0.001025	0.17225	0.608	0.012598	0.0736	0.001024	0.62657	457.4	6.299206	481	7.874008	553	40.51932	4.906445	17.28752	457.4	6.299206	455.1	6.456686	451.4	5.984246	426	21.66552	0.0052	0.0014
Z038	232	2.016	0.061	248	72.25434	1.397663	0.0589	0.003371	0.22197	0.1133	0.005906	0.01384	0.000268	0.18239	88.6	1.653542	108.6	5.354325	490	111.2053	18.41621	81.91837	88.6	1.653542	87.3	1.732282	87.3	1.732282	87.9	14.74307	0.0153	0.0051
Z039	236	3.046	0.064	2057	9.425071	0.118909	0.0632	0.001391	0.2817	0.937	0.018898	0.1061	0.001339	0.32643	650	7.874008	670	10.23621	711	47.67463	2.985075	8.579466	650	7.874008	647	7.874008	634	7.874008	590	28.67176	0.0056	0.0015
Z040	241.8	1.736	0.065	151	107.0664	2.437058	0.0517	0.004	0.31508	0.0668	0.004567	0.00934	0.000213	-0.0492	60	1.338581	65.4	4.330704	220	137.1696	8.256881	72.72727	60	1.338581	59.6	1.496061	59.6	1.496061	60	29.99167	0.0069	0.0061
Z041	197.5	1.47	0.099	1013	16.50165	0.34306	0.0643	0.002132	0.15279	0.546	0.01811	0.0606	0.00126	0.44444	379.4	7.716528	441	11.81101	723	137.9883	13.96825	47.5242	379.4	7.716528	374	7.874008	373.2	7.559048	368	123.1342	0.0146	0.0031
Z042	1211	3.389	0.089	5030	18.08318	0.437718	0.0576	0.000939	0.38842	0.445	0.010236	0.0553	0.001339	0.79706	347	8.661409	373.3	7.322827	506	41.24724	7.045272	31.42292	347	8.661409	345	8.661409	343	7.874008	330	25.38178	0.007	0.0014
Z043	143.7	2.025	0.089	939	11.64144	0.160067	0.0584	0.001682	0.20574	0.704	0.018898	0.0859	0.001181	0.29229	531.3	7.007867	539	11.02361	522	63.85965	1.428571	-1.78161	531.3	7.007867	529.2	7.244087	515.5	7.480307	432	40.83497	0.0042	0.0018
Z044	130	0.701	0.017	99	110.742	2.993519	0.0658	0.007458	0.47759	0.0805	0.007795	0.00903	0.000244	-0.29627	57.9	1.574802	77.9	7.322827	620	220.6237	25.67394	90.66129	57.9	1.574802	56.5	1.889762	56.5	1.889762	57.7	8.324864	0.025	0.012
Z046	423	2.162	0.064	5870	6.587615	0.082009	0.0693	0.001102	0.3094	1.48	0.023622	0.1518	0.00189	0.50409	911	10.23621	921	9.448809	902	31.55173	1.085776	-0.99778	911	10.23621	908	11.02361	895	9.448809	836	21.13792	0.0036	0.0013
Z047	107.9	2.078	0.056	1442	6.779661	0.083241	0.0698	0.001472	0.12667	1.448	0.029134	0.1475	0.001811	0.45037	887	10.23621	910	11.02361	909	45.66033	2.527473	2.420242	887	10.23621	883	10.23621	875	9.448809	833	31.41411	0.0048	0.0015
Z048	621	2.157	0.084	37500	2.953337	0.041894	0.1359	0.001538	0.47641	6.47	0.086614	0.3386	0.004803	0.67098	1879	22.83462	2040	11.02361	2172	20.302	7.892157	13.48987	2172	20.302	1836	27.55903	1861	26.77163	1884	24.90966	0.027	0.0043
Z049	127.2	3.743	0.091	147	55.21811	1.056359	0.051	0.003566	0.18305	0.129	0.007874	0.01811	0.000346	0.10281	115.7	2.204722	122.8	7.401567	210	27831.96	5.781759	44.90476	115.7	2.204722	115.2	2.362202	115.3	2.362202	114.7	27831.71	0.0048	0.0054
Z050	208	1.68	0.12	175	81.30081	1.665465	0.0509	0.004402	0.20913	0.0863	0.006614	0.0123	0.000252	0.14662	78.8	1.574802	83.6	6.141726	170	160.2592	5.741627	53.64706	78.8	1.574802	78.4	1.732282	78.5	1.732282	78.9	74.82375	0.0057	0.0069
Z051	145.6	1.404	0.048	130	75.87253	1.722458	0.0519	0.004333	0.30883	0.0954	0.007165	0.01318	0.000299	0.017811	84.4	1.889762	93.6	6.929127	250	162.5518	9.82906	66.24	84.4	1.889762	83.8	2.047242	83.8	2.047242	83.9	63.60248	0.0069	0.0067
Z052	413	2.42	0.1	670	66.75567	1.193029	0.0871	0.006207	-0.35083	0.185	0.014173	0.01498	0.000268	0.60344	95.9	1.732282	170	11.81101	1290	141.7824	43.58824	92.56589	95.9	1.732282	90.2	1.574802	90.4	1.574802	95.9	4.152426	0.053	0.01
Z053	221	1.612	0.05	161	101.3171	1.859043	0.0562	0.004766	0.20625	0.078	0.006142	0.00987	0.000181	0.06732	63.3	1.181101	75.8	5.748026	350	150.2827	16.49077	81.91429	63.3	1.181101	62.5	1.259841	62.6	1.259841	63.5	14.29972	0.0131	0.0075
Z054	650	0.982	0.021	2630	17.18213	0.232461	0.0538	0.001047	0.40431	0.4416	0.00748	0.0582	0.000787	0.38253	364.9	4.803145	371	5.275585	353	42.91367	1.644205	-3.3711	364.9	4.803145	363.8	4.960625	356.7	4.566925	283	28.37151	0.0029	0.0011
Z055	221	1.641	0.038	233	64.26735	1.235834	0.0536	0.003849	0.20359	0.1167	0.007717	0.01556	0.000299	0.040464	99.5	1.889762	111.5	7.007867	310	140.4365	10.76233	67.90323	99.5	1.889762	98.6	2.047242	98.6	2.047242	99.4	42.53152	0.0088	0.0061
Z057	699	4.03	0.14	19020	6.915629	0.082848	0.1438	0.001805	0.074193	2.934	0.046457	0.1446	0.001732	0.67689	871	9.448809	1389	11.81101	2269	40.57393	37.29302	61.61305	Discordant	Discordant	791	9.448809	812	10.23621	871	36.28228	0.0978	0.0028
Z058	163	2.564	0.069	20900	1.876173	0.023282	0.1845	0.001915	0.519	13.86	0.15748	0.533	0.006614	0.66007	2753	27.55903	2739	11.02361	2692	16.69116	-0.51114	-2.26597	2692	16.69116	2742	31.49603	2727	14.17321	2656	17.43602	0.003	0.0024
Z059	338	3.52	0.35	2190	12.26994	0.201525	0.0599	0.00123	0.49358	0.69	0.012598	0.0815	0.001339	0.37303	505	7.874008	532	7.795268	597	50.57033	5.075188	15.41039	505	7.874008	502	8.661409	496.6	7.716528	460	29.03546	0.0063	0.0015
Z060	165.3	2.712	0.058	1159	12.70648	0.165268	0.0681	0.002649	0.22231	0.748	0.025197	0.0787	0.001024	0.095831	488.4	5.984246	568	14.96061	829	95.73682	14.01408	41.08565	488.4	5.984246	480.6	6.456686	478.6	5.826766	474	63.42428	0.0159	0.0037
Z061	730	1.068	0.035	1634	31.63556	0.441301	0.0539	0.001378	0.16668	0.2391	0.005906	0.03161	0.000441	0.45746	200.6	2.755903	217.4	4.881885	349	102.8411	7.727691	42.52149	200.6	2.755903	199.4	2.834643	199	2.755903	193.7	88.89186	0.0065	0.0021
Z062	362	1.886	0.042	2370	11.69591	0.129254	0.0585	0.001288	0.30497	0.704	0.013386	0.0855	0.000945	0.26796	529	5.748026	540	7.874008	536	47.6079	2.037037	1.30597	529	5.748026	527.1	5.984246	517.6	5.669286	455	27.90183	0.004	0.0013
Z063	406	2.113	0.047	3190	9.97009	0.109578	0.06	0.001052	0.11429	0.85	0.015748	0.1003	0.001102	0.54595	616.3	6.535427	623	8.661409	602	36.20253	1.075441	-2.37542	616.3	6.535427	614.7	6.692907	605.7	7.637788	544	27.46786	0.0028	0.001
Z064	262.6	0.694	0.023	615	30.47851	0.431554	0.0545	0.002007	0.43436	0.2502	0.007402	0.03281	0.000465	0.011811	208.1	2.913383	226.3	5.984246	361	176.5981	8.042422	42.35457	208.1	2.913383	206.7	3.070863	205.6	3.070863	183	162.1863	0.0072	0.0029
Z065	124.6	1.081	0.023	202	70.57163	1.68626	0.0843	0.006147	0.035079	0.17	0.012598	0.01417	0.000339	0.2648	90.7	2.125982	158	11.02361	1160	134.004	42.59494	92.18103	90.7	2.125982	86.4	2.047242	86.6	2.047242	90.7	6.601704	0.049	0.0095
Z067	57.7	0.766	0.081	1220	4.764173	0.119742	0.0815	0.003367	0.056962	2.39	0.102362	0.2099	0.005276	0.26933	1228	28.34643	1235	30.70863	1200	89.64403	0.566802	-2.33333	1228	28.34643	1216	29.92123	1183	29.13383	1126	57.59541	0.007	0.0033
Z069	1410	1.519	0.075	900	99.8004	2.509634	0.0486	0.001419	0.31347	0.0678	0.002047	0.01002	0.000252	0.53472	64.2	1.574802	66.6	1.968502	125	597.0827	3.603604	48.64	64.2	1.574802	64.1	1.653542	64.1	1.653542	62.3	594.5376	0.0026	0.0022
Z070	127.9	0.551	0.013	1207	14.47178	0.197889	0.1064	0.006115	0.32561	1.023	0.054331	0.0691	0.000945	-0.08157	430.7	5.826766	707	25.98423	1650	105.7696	39.08062	73.89697	Discordant	Discordant	403.3	7.244087	407.3	7.007867	430.7	27.26108	0.0664	0.0098
Z071	515	1.341	0.026	7420	6.480881	0.069452	0.0714	0.001018	0.27239	1.537	0.022047	0.1543	0.001654	0.4641	925	8.661409	944	8.661409	961	29.76931	2.012712	3.746098	925	8.661409	921	9.448809	912	7.874008	878	17.48977	0.0043	0.0013
Z073	243.8	1.294	0.021	4950	5.068424	0.062705	0.0784	0.00121	0.15105	2.157	0.035433	0.1973	0.002441	0.56103	1161	12.59841	1166	11.81101	1150	30.29427	0.428816	-0.95652	1161	12.59841	1157	13.38581	1140	11.02361	1092	20.15547	0.0031	0.0012
Z075	173.6	1.969	0.085	11320	2.680247	0.024888	0.1329	0.001681	0.3266	6.9	0.086614	0.3731	0.003465	0.43513	2043	16.53542	2098	11.02361	2134	21.95395	2.621544	4.264292	2134	21.95395	2028	18.89762	2037	16.53542	2036	18.33783	0.0093	0.0031
Z076	350	1.229	0.022	391	70.72136	1.102694	0.059	0.002413	0.039468	0.1166	0.004567	0.01414	0.00022	0.38624	90.5	1.417321	111.7	4.173224	530	79.6924	18.97941	82.92453	90.5	1.417321	89.2	1.417321	91	12.38378	0.015	0.0035
Z077	114.6	1.835	0.069	124	74.18398	1.689977	0.0602	0.004957	0.08734	0.112	0.008661	0.01348	0.000307	0.16281	86.3	1.968502	107.1	7.637788	490	150.5802	19.4211	82.38776	86.3	1.968502	84.9	2.047242	85	2.047242	85.7	17.23124	0.0166	0.0075
Z078	347	1.014	0.03	319	68.25939	1.137319	0.0476	0.001936	-0.10358	0.0972	0.003858	0.01465	0.000244	0.48849	93.7	1.574802	94	3.622044	106	83.04901	0.319149	11.60377	93.7	1.574802	93.6	1.574802	93.6	1.574802	93.6	43.33751	0.0001	0.0027
Z079	542	4.91	0.3	6940	6.968641	0.084123	0.0684	0.000858	0.14112	1.356	0.02126	0.1435	0.001732	0.64024	864	9.448809	869	9.448809	876	26.27285	0.575374	1.369863	864	9.448809	862	10.23621	850	9.448809	823	17.05821	0.00263	0.0009
Z080	360	1.025	0.034	5300	6.523157	0.077062	0.0736	0.00112	0.39378	1.557	0.02126	0.1533	0.001811	0.42969	919	10.23621	954	8.661409	1025	31.47365	3.668763	10.34146	919	10.23621	914	11.02361	909	9.448809	893	17.08365	0.0062	0.0017
Z081	172	1.649	0.041	184	83.68201	1.599035	0.0686	0.005293	-0.02117	0.113	0.008661	0.01195	0.000228	0.1289	76.6	1.417321	108.3	7.716528	750	141.9488	29.27054	89.78667	76.6	1.417321	74.1	1.653542	74.2	1.653542	76.6	7.967271	0.0273	0.008
Z082	38.3	1.995	0.046	107	30.75031	0.640314	0.064	0.006371	-0.15862	0.284	0.026772	0.03252	0.000677	0.30318	206.3	4.251964	254	22.83462	610	208.0573	18.77953	66.18033	206.3	4.251964	201.7	4.173224	201.9	4.173224	205.6	67.54027	0.0178

Z084	307	1.825	0.08	2800	8.818342	0.128585	0.0614	0.001356	0.33026	0.959	0.020472	0.1134	0.001654	0.35381	692	9.448809	681	10.23621	650	44.95833	-1.61527	-6.46154	692	9.448809	691	10.23621	668	8.661409	588	33.59243	0.00229	0.00094
Z085	149	1.147	0.026	101	97.18173	2.007839	0.0505	0.005341	0.1689	0.0712	0.007087	0.01029	0.000213	0.076361	66	1.338581	69.3	6.692907	150	187.1835	4.761905	56	66	1.338581	65.7	1.496061	65.7	1.496061	65.6	70.93424	0.0041	0.0082
Z086	286	1.904	0.055	2520	9.469697	0.120037	0.0642	0.001374	0.18151	0.926	0.018898	0.1056	0.001339	0.40957	647	7.874008	664	9.448809	733	46.54363	2.560241	11.73261	647	7.874008	644	7.874008	632.1	7.480307	603	25.46663	0.0051	0.0015
Z087	90.8	2.842	0.094	1442	6.146281	0.095185	0.0747	0.003025	-0.0984	1.653	0.066142	0.1627	0.00252	0.46757	972	13.38581	996	27.55903	1031	79.917	2.409639	5.722599	972	13.38581	963	14.17321	933	15.74802	883	36.83297	0.0066	0.0028
Z088	224	1.115	0.064	4880	4.526935	0.08875	0.0786	0.001284	0.048246	2.389	0.059055	0.2209	0.004331	0.77198	1286	22.83462	1236	17.32282	1164	30.73114	-4.04531	-10.4811	1286	22.83462	1285	22.83462	1230	17.32282	1146	26.4364	0.00058	0.00047
Z089	340	1.572	0.033	377	69.01311	1.312584	0.0576	0.002834	0.068808	0.1144	0.005433	0.01449	0.000276	0.32908	92.7	1.732282	109.7	4.881885	460	95.66548	15.49681	79.84783	92.7	1.732282	91.6	1.732282	91.6	1.732282	92.5	15.07198	0.0122	0.0042
Z090	285	2.029	0.042	11820	3.31785	0.041605	0.1045	0.001413	0.61357	4.317	0.048819	0.3014	0.00378	0.42703	1698	18.89762	1696	9.448809	1701	24.19911	-0.11792	0.176367	1701	24.19911	1691	19.68502	1667	13.38581	1634	19.08552	0.004	0.0017
Z091	40.9	0.727	0.024	893	5.181347	0.109922	0.0859	0.002701	-0.02222	2.27	0.07874	0.193	0.004094	0.61086	1137	22.04722	1197	25.19683	1325	60.4327	5.012531	14.18868	1137	22.04722	1125	22.83462	1110	22.04722	1096	39.29519	0.0119	0.0032
Z092	251	1.087	0.041	575	53.10674	0.755047	0.0955	0.007256	0.007279	0.242	0.01811	0.01883	0.000268	0.18775	120.2	1.732282	222	14.96061	1440	126.0739	45.85586	91.65278	120.2	1.732282	113.3	1.889762	113.6	1.889762	120.2	5.062765	0.06	0.011
Z093	315	1.363	0.036	214	92.67841	1.555539	0.0494	0.003241	0.20203	0.073	0.004252	0.01079	0.000181	0.063048	69.2	1.181101	71.3	4.015744	140	210.5295	2.945302	50.57143	69.2	1.181101	69	1.259841	69	1.259841	69.6	179.3669	0.0022	0.0048
Z094	190.4	1.867	0.044	171	72.8863	1.296729	0.0499	0.003732	0.044716	0.0924	0.006457	0.01372	0.000244	0.28621	87.8	1.574802	89.3	5.984246	160	724.9032	1.679731	45.125	87.8	1.574802	88	1.732282	87.9	1.732282	88	713.8739	0.0024	0.0056
Z095	329	1.266	0.036	330	74.46016	1.484304	0.0556	0.002917	-0.09498	0.1024	0.005433	0.01343	0.000268	0.43289	86	1.732282	98.7	4.960625	380	103.9518	12.86727	77.36842	86	1.732282	85.2	1.732282	85.2	1.732282	86	18.19278	0.0097	0.0044
Z096	587	7.24	0.56	489	78.36991	1.209023	0.0491	0.001726	0.2171	0.0855	0.002677	0.01276	0.000197	0.26025	81.7	1.259841	83.2	2.519683	149	232.0152	1.802885	45.16779	81.7	1.259841	81.6	1.259841	81.5	1.259841	81.2	223.3039	0.0015	0.0025
Z097	193	2.024	0.045	1129	13.1406	0.176754	0.0576	0.001796	0.26439	0.599	0.016535	0.0761	0.001024	0.18627	472.4	6.220466	475	10.23621	489	68.56287	0.547368	3.394683	472.4	6.220466	470.9	6.535427	456.3	6.850387	389	39.34676	0.0036	0.0021
Z099	167.5	1.224	0.028	145	75.41478	1.209129	0.0491	0.003333	0.026816	0.089	0.005512	0.01326	0.000213	0.027357	84.9	1.338581	86.2	5.118105	130	300.5964	1.508121	34.69231	84.9	1.338581	84.9	1.417321	84.7	1.417321	83.2	279.6623	0.0013	0.0049
Z100	96	1.514	0.052	104	92.67841	2.434756	0.0729	0.006858	0.26183	0.106	0.008661	0.01079	0.000283	0.030653	69.2	1.811022	101	7.874008	900	173.4014	31.48515	92.31111	69.2	1.811022	66.9	1.968502	67	1.968502	69.2	7.957865	0.032	0.01
Z101	343	1.603	0.054	324	76.98229	1.539896	0.0544	0.003499	0.059405	0.0963	0.00622	0.01299	0.00026	0.19808	83.2	1.653542	92.9	5.669286	340	119.9655	10.44133	75.52941	83.2	1.653542	82.5	1.732282	82.3	1.732282	80.8	21.16745	0.008	0.0053
Z102	440	2.094	0.096	405	72.93946	1.21484	0.051	0.002195	0.15973	0.0951	0.00378	0.01371	0.000228	0.23906	87.8	1.417321	92.1	3.543304	230	106.6491	4.668838	61.82609	87.8	1.417321	87.5	1.496061	87.4	1.496061	87.8	71.94636	0.0035	0.0032
Z103	323	1.604	0.083	259	94.16196	2.722773	0.0532	0.004051	-0.10004	0.0775	0.00622	0.01062	0.000307	0.47336	68.1	1.968502	75.4	5.826766	260	135.4234	9.681698	73.80769	68.1	1.968502	67.6	1.889762	67.5	1.889762	67.2	20.64827	0.0069	0.0063
Z104	290	0.962	0.021	279	66.0066	1.029181	0.0486	0.002745	0.07279	0.1004	0.005354	0.01515	0.000236	0.21781	97	1.496061	96.9	4.960625	130	127.3837	-0.1032	25.38462	97	1.496061	96.9	1.574802	96.8	1.574802	97	75.83435	0.0003	0.0041
Z105	401	1.858	0.056	11480	4.399472	0.05639	0.0947	0.001782	0.27362	2.936	0.054331	0.2273	0.002913	0.39224	1320	14.96061	1389	14.17321	1514	34.32014	4.967603	12.81374	1320	14.96061	1307	16.53542	1305	14.17321	1309	16.88408	0.0113	0.0028
Z106	107.4	2.3	0.094	95.9	70.27407	1.905382	0.0477	0.003863	0.14212	0.093	0.007008	0.01423	0.000386	0.27771	91.1	2.440942	89.8	6.456686	80	155.1855	-1.44766	-13.875	91.1	2.440942	91.2	2.519683	91.1	2.519683	90	78.56291	-0.0007	0.0055
Z109	563	0.996	0.029	345	103.0928	2.343206	0.0492	0.002786	0.15577	0.0638	0.00315	0.0097	0.00022	0.31042	62.2	1.417321	62.7	2.992123	140	148.9497	0.797448	55.57143	62.2	1.417321	62.1	1.496061	62.1	1.496061	62.1	108.2129	0.0019	0.0042
Z110	154	1.389	0.027	408	26.28121	0.46228	0.0527	0.002421	0.24596	0.272	0.011024	0.03805	0.000669	0.14933	240.7	4.094484	244	8.661409	280	105.3646	1.352459	14.03571	240.7	4.094484	240.3	4.330704	237.3	4.015744	233.4	60.30306	0.0021	0.0036
Z111	99.5	3.87	0.11	192	34.84321	0.955943	0.0501	0.003856	0.40256	0.199	0.013386	0.0287	0.000787	0.1172	182.6	5.039365	182	11.02361	190	149.6831	-0.32967	3.894737	182.6	5.039365	182.6	5.354325	183	5.590546	177.2	67.32675	0.0003	0.0058
Z112	172	1.5	0.11	509	62.73526	1.89038	0.143	0.012837	-0.34422	0.317	0.031496	0.01594	0.00048	0.59235	101.9	3.070863	275	24.40942	2110	173.254	62.94545	95.17062	101.9	3.070863	89.4	2.677163	89.9	2.677163	101.9	4.285173	0.121	0.02
Z113	350	2.469	0.097	1185	21.17298	0.264741	0.0546	0.001704	0.062732	0.353	0.010236	0.04723	0.000591	0.31952	297.5	3.622044	305.9	7.795268	372	70.68179	2.745995	20.02688	297.5	3.622044	296.4	3.700784	291.6	3.385823	270	38.98174	0.0036	0.0023
Z114	77.9	3.05	0.12	183	32.72251	0.733514	0.0588	0.004391	0.25538	0.244	0.015748	0.03056	0.000685	0.082345	194	4.251964	219	12.59841	450	173.5329	11.41553	56.88889	194	4.251964	192.1	4.566925	191.4	4.409444	189.6	100.259	0.011	0.0065
Z115	63.8	1.42	0.07	2080	3.94011	0.057453	0.0959	0.002305	0.31483	3.326	0.07559	0.2538	0.003701	0.31472	1457	18.89762	1487	18.89762	1542	48.41573	2.017485	5.512322	1542	48.41573	1446	21.25982	1424	18.89762	1398	31.05773	0.008	0.003
Z116	200	1.344	0.036	167	73.26007	1.563624	0.0465	0.00341	0.26187	0.0867	0.005512	0.01365	0.000291	0.081765	87.4	1.889762	84.1	5.118105	30	124.3265	-3.9239	-191.333	87.4	1.889762	87.6	1.968502	87.5	1.968502	87.5	38.88808	-0.0019	0.0051
Z117	256	1.494	0.065	1810	13.71742	0.237061	0.073	0.001804	0.085776	0.727	0.019685	0.0729	0.00126	0.47574	453.4	7.480307	553	11.02361	996	226.3299	18.01085	54.47791	453.4	7.480307	444	7.559048	445.2	7.480307	452.6	221.6317	0.0209	0.0027
Z118	146.1	1.803	0.06	133	73.36757	1.313911	0.0505	0.004092	0.48743	0.0929	0.006378	0.01363	0.000244	-0.24091	87.3	1.574802	89.8	5.905506	170	226.8344	2.783964	48.64706	87.3	1.574802	87.1	1.811022	87.1	1.811022	87.2	183.1348	0.0032	0.0062
Z119	302	1.681	0.085	1777	12.90323	0.183536	0.0582	0.001605	0.20183	0.615	0.016535	0.0775	0.001102	0.39236	481.2	6.692907	486	10.23621	514	60.17988	0.987654	6.381323	481.2	6.692907	477.6	7.322827	464.1	7.165347	400	33.78784	0.004	0.0019
Z120	143	2.414	0.098	126	70.42254	1.327694	0.0457	0.003757	0.40719	0.0896	0.006772	0.0142	0.000268	-0.16917	90.9	1.653542	86.6	6.299206	30	145.9075	-4.96536	-203	90.9	1.653542	91.1	1.889762	91	1.889762	90.7	34.69867	-0.003	0.0057
Z121	1059	0.93	0.028	2880	25.17623	0.39428	0.0519	0.000962	-0.01588	0.2832	0.006693	0.03972	0.000622	0.6727	251.1	3.858264	252.8	5.275585	272	43.75378	0.672468	7.683824	251.1	3.858264	250.7	3.858264	246.9	3.779524	215	24.1763	0.002	0.0012
Z122	316	1.339	0.052	182	113.8952	2.042852	0.0495	0.003278	0.34903	0.0592	0.003386	0.00878	0.000157	-0.07666	56.4	1.023621	58.2	3.228343	150	136.4557	3.092784	62.4	56.4	1.023621	56.3	1.102361	56.2	1.102361	56	68.34626	0.0028	0.0049
Z123	178.5	1.477	0.036	204	66.5336	1.359385	0.0581	0.00503	0.015071	0.119	0.009449	0.01503	0.000307	0.14319	96.2	1.968502	114	8.661409	400	143.0913	15.61404	75.95	96.2	1.968502	94.7	2.125982	94.6	2.125982	95.5	19.7735	0.0129	0.0079
Z124	78.7	0.806	0.026	1420	5.506608	0.078791	0.0755	0.002064	0.127	1.881	0.050394	0.1816	0.002598	0.32126	1075	14.17321	1071	17.32282	1060	55.0391	-0.37348	-1.41509	1075	14.17321	1069	14.96061	1032	13.38581	957	36.58637	0.0052	0.002
Z125	1939	0.973	0.036	1838	67.06908	1.133419	0.0477	0.001271	0.17093	0.0976	0.002677	0.01491	0.000252	0.45484	95.4	1.574802	94.4	2.440942	88	54.49412	-1.05932	-8.40909	95.4	1.574802	95.4	1.653542	95	1.653542	88.8	21.1238	-0.0002	0.0019
Z126	688	1.059	0.027	438	96.61836	1.690608	0.0467	0.002005	0.27802	0.0662	0.002441	0.01035	0.000181	0.17056	66.3	1.181101	65	2.362202	50	78.17716	-2	-32.6	66.3	1.181101	66.4	1.259841	66.4	1.259841	66.3	29.4174	-0.0014	0.0028
Z127	333	0.574	0.028	2770	12.83697	0.363311	0.0788	0.003061	0.57469	0.828	0.023622	0.0779	0.002205	0.21304	483	13.38581	615	14.17321	1137	3258.891	21.46341	57.51979	Discordant	Discordant	471	14.17321	473	14.17321	483	3258.078	0.0278	0.0052
Z128	249	1.156	0.02	254	64.51613	1.081549	0.0496	0.003063	0.11255	0.1056	0.005906	0.0155	0.00026	0.20835	99.2	1.653542	101.6	5.433065	150	224.9702	2.362205	33.86667	99.2	1.653542	99	1.732282	98.9	1.732282	98.4	200.3419	0.002	0.0046
Z129	132.3	0.989	0.024	146	58.65103	1.002187	0.0497	0.004059	0.17271	0.114	0.007874	0.01705	0.000291	0.099648	109	1.889762	110.8	7.716528	130	225.2358	1.624549	16.15385	109	1.889762	108.8	1.968502	108.6	1.968502	106.7	181.1627	0.0019	0.0062
Z130	148.8	1.364	0.025	133	73.36757	1.568216	0.0494	0.004006	0.3477	0.0925	0.006693	0.01363	0.000291	-0.14555	87.3	1.889762	89.3	6.141726	130	520.9678	2.239642	32.84615	87.3	1.889762	87.9	2.125982	87.9	2.125982	88	503.4815	0.0021	0.006
Z131	144	1.241	0.045	133	73.58352	1.662729	0.0525	0.004334	0.18441	0.1	0.007874	0.01359	0.000307	0.15016	87	1.968502	95.8	7.244087	270	159.2397	9.185804	67.77778	87	1.968502	86.4	2.047242	86.4	2.047242	86.8	54.58154	0.0061	0.0066
Z132	221.6	3.32	0.19	1344	12.90323	0.183536	0.0592	0.001856	0.24653	0.626	0.017323	0.0775	0.001102	0.26217	480.8	6.771647	495	11.81101	544	69.4306	2.868687	11.61765	480.8	6.771647	478.4	7.007867	466.2	7.086607	405	38.56796	0.0049	0.0022
Z133	577	2.002	0.042	444	95.32888	1.431116	0.0545	0.002783	0.1541	0.0775	0.003622	0.01049	0.000157	0.14361	67.3	1.023621	75.6	3.385823	340	103.128	10.97884	80.20588	67.3	1.023621	66.7	1.023621	66.7	1.023621	67	12.58734	0.0092	0.0043
Z134	134	505	81	2850	5.154639	0.066949	0.0804	0.001704	0.34622	2.164	0.044094	0.194	0.00252	0.29875	1143	13.38581	1171	13.38581	1202	44.90839	2.391119	4.908486	1143	13.38581	1140	14.96061	1120	13.38581	1090	25.14565	0.0053	0.0018
Z135	293	1.69	0.052	255	75.58579	1.30459	0.0503	0.002638	0.18419	0.0904	0.004094	0.01323	0.000228	0.20008	84.7	1.417321	87.7	3.779524	180	171.8713	3.420753	52.94444	84.7	1.417321	84.5	1.496061	84.4	1.496061	83.8	148.4631	0.0035	0.0039
Z136	946	1.338	0.036	480	132.2751	2.204308	0.0496	0.002668	0.004765	0.0515	0.002598	0.00756	0.000126	0.25674	48.5	0.787401	50.9	2.519683	200	113.7303	4.715128	75.75	48.5	0.787401	48.3	0.787401	48.3	0.787401	48.5	27.98582	0.0034	0.0041
Z137	73.1	1.265	0.072	85	59.20663	1.656105	0.0512	0.005178	0.25835	0.118	0.011024	0.01689	0.000472	-0.00926	108	2.992123	112	9.448809	210	448.9939	3.571429	48.57143	108	2.992123	107.4	3.307083	107.2	3.228343	107.6	414.2464	0.004	0.0079
Z138	232	1.348	0.027	6610	4.237288	0.05655	0.0893	0.001283	0.21499	2.905	0.048819	0.236	0.00315	0.59751	1365	16.53542	1381	12.59841	1406	28.19755	1.158581	2.916074	1365	16.53542	1359	17.32282	1343	13.38581	1322	19.18129	0.005	0.0015
Z140	1650	3.44	0.18	1060	110.6195	2.40879	0.0512	0.0017	0.2678	0.0635	0.002126	0.00904	0.000197	0.38965	58	1.259841	62.5	2.047242	236	67.6126	7.2	75.42373	58	1.259841	57.7	1.338581	57.7	1.338581	58	14.083	0.0053	0.0026

16YADZ02					Isotopic Ratios + measurement uncertainty (2s)										Ages uncorrected for common lead + measurement uncertainty (2s)									Ages corrected for common lead (Andersen routine) + measurement uncertainty (2s)							
					Data for Tera-Wasserburg plot					Data for Wetherill plot																				
Sample	U (ppm)	U/Th	U/Th uncertainty 2SE	207Pb (cps)	U238/Pb 206	U238/Pb 206 uncertainty (2s)	Pb207/Pb 206	Pb207/Pb 206 uncertainty (2s)	ρ	Pb207/U 235	Pb207/U 235 uncertainty (2s)	Pb206/U 238	Pb206/U 238 uncertainty (2s)	ρ	Age Pb206/U 238	Age Pb206/U 238 measurement uncertainty (2s)	Age Pb207/U 235	Age Pb207/U 235 measurement uncertainty (2s)	Age Pb207/Pb 206	Age Pb207/Pb 206 measurement uncertainty (2s)	Discordance Pb206/U 238 vs Pb207/U 235 (%)	Concordance Pb206/U 238 vs Pb207/Pb 206 (%)	Best age	Best age measurement uncertainty (2S)	Age Pb206/U 238	Age Pb206/U 238 measurement uncertainty (2s)	Age Pb207/U 235	Age Pb207/U 235 measurement uncertainty (2s)	Age Pb207/Pb 206	Age Pb207/Pb 206 measurement uncertainty (2s)	Common Lead fraction	Common Lead fraction uncertainty (2s)
Z001	591	7.1	0.26	1954	10.32418	0.139387	0.0625	0.001998	0.15719	0.832	0.029654	0.09686	0.001308	0.27359	595.9	7.704424	614	16.40003	682	74.78349	2.947883	12.62463	595.9	7.704424	593.4	7.798804	585.6	14.75716	557	65.21787	0.0045	0.0014
Z002	257	6.21	0.16	777	10.30928	0.140109	0.0596	0.002834	0.40559	0.794	0.031529	0.097	0.001318	-0.14687	597.1	7.757904	592	17.48461	569	102.143	-0.86149	-4.93849	597.1	7.757904	595.6	7.950514	576.6	14.76966	512	87.75446	0.0026	0.0014
Z003	682	1.41	0.12	213	78.30854	1.518103	0.0486	0.00441	0.058486	0.085	0.005938	0.01277	0.000248	0.19967	81.8	1.60523	82.7	5.582671	130	366.3726	1.088271	37.07692	81.8	1.60523	81.8	1.60523	81.7	2.750057	81.9	346.8151	0.0009	0.0047
Z004	308	1.342	0.035	858	10.81081	0.167923	0.0601	0.002636	0.26469	0.774	0.030559	0.0925	0.001437	0.23385	570.5	8.438319	581	17.33546	609	100.3771	1.807229	6.321839	570.5	8.438319	568.2	8.664527	556.1	15.36676	498	88.54641	0.0035	0.0016
Z005	349	2.045	0.037	2110	5.980861	0.098045	0.074	0.002279	0.39248	1.699	0.058243	0.1672	0.002741	0.27824	996	15.5182	1007	21.84926	1035	62.90822	1.092354	3.768116	996	15.5182	993	15.5182	978	21.15727	950	54.79073	0.0035	0.0015
Z006	364	1.438	0.052	1770	7.137759	0.136638	0.0729	0.002836	0.27722	1.396	0.056098	0.1401	0.002682	0.30397	845	15.27336	886	23.81609	1001	83.77509	4.62754	15.58442	845	15.27336	839	15.92908	833	21.41742	820	65.87766	0.0066	0.0023
Z007	641	1.237	0.041	10630	3.415301	0.059832	0.1151	0.001791	0.1902	4.635	0.159459	0.2928	0.00513	0.77803	1655	25.31326	1754	28.55465	1880	29.56775	5.644242	11.96809	1880	29.56775	1634	27.19083	1646	33.50027	1661	32.56151	0.015	0.0028
Z008	1013	2.247	0.031	4590	8.510638	0.151492	0.0758	0.002515	0.81791	1.216	0.042433	0.1175	0.002092	-0.442	716	11.99436	807	19.29819	1075	79.18097	11.27633	33.39535	716	11.99436	706	13.27044	708	20.11616	714	57.76164	0.0152	0.0036
Z009	878	5.19	0.35	3320	12.34568	0.328827	0.087	0.002375	0.35132	0.968	0.038594	0.081	0.002157	0.6755	502	12.93139	686	19.65239	1354	288.5686	26.82216	62.92467	Discordant	Discordant	484	12.93139	487	19.15715	502	286.6284	0.0371	0.0027
Z010	589	6.3	1.5	14330	3.388682	0.085271	0.1455	0.002394	0.087418	5.9	0.232659	0.2951	0.007426	0.86159	1665	36.74266	1957	33.75635	2291	31.76977	14.9208	27.32431	Discordant	Discordant	1592	38.88242	1623	43.44918	1665	40.21092	0.0507	0.0042
Z011	126	3.308	0.097	357	11.65501	0.196373	0.0599	0.004213	0.24784	0.704	0.03735	0.0858	0.001446	0.10076	530.8	8.515759	539	22.10162	570	162.1479	1.521336	6.877193	530.8	8.515759	528.3	8.87931	511	15.80449	438	137.7554	0.0049	0.0035
Z012	520	13.4	2.6	1750	10.77586	0.265158	0.0601	0.00201	-0.20946	0.768	0.033105	0.0928	0.002284	0.78995	572	13.2327	577	18.88417	597	74.82794	0.866551	4.187605	572	13.2327	570	13.2327	559	17.80258	525	64.64364	0.0025	0.0011
Z013	68.8	2.247	0.066	558	5.747126	0.096058	0.0818	0.005256	-0.30382	1.95	0.111337	0.174	0.002908	0.49933	1034	15.7466	1090	38.11935	1200	138.6195	5.137615	13.83333	1034	15.7466	1019	15.16494	999	25.66836	968	109.0871	0.0129	0.0045
Z014	167.9	2.068	0.048	42.7	113.7656	2.925483	0.0506	0.009291	0.42192	0.062	0.008094	0.00879	0.000226	-0.3001	56.4	1.400734	60.9	7.691544	200	292.8417	7.389163	71.8	56.4	1.400734	56.1	1.689632	56.1	2.384293	56.4	183.3463	0.004	0.01
Z015	313	0.962	0.028	15150	2.136752	0.032739	0.191	0.002981	0.39826	12.29	0.406325	0.468	0.007171	0.48167	2474	31.43053	2625	31.02986	2748	26.78513	5.752381	9.970888	2748	26.78513	2410	37.37751	2450	39.54279	2485	31.70368	0.0317	0.0059
Z016	129	1.45	0.029	175	24.09058	0.457565	0.0728	0.008122	0.17294	0.414	0.036093	0.04151	0.000788	0.057703	262.1	4.895809	347	26.00822	860	214.6227	24.46686	69.52326	262.1	4.895809	256.6	5.025788	254.7	10.10889	256.2	137.0118	0.0273	0.0099
Z017	1170	2.241	0.065	6570	6.60066	0.086505	0.0712	0.001383	0.001704	1.484	0.048949	0.1515	0.001985	0.48883	909.6	11.05552	923	19.94023	960	40.05637	1.451788	5.25	909.6	11.05552	907.1	11.18681	901.8	19.34701	893	33.93071	0.0029	0.0011
Z019	614	2.11	0.064	4250	5.970149	0.085938	0.0744	0.001754	0.37808	1.718	0.057339	0.1675	0.002411	0.3106	998	13.29083	1014	21.56299	1046	49.69401	1.577909	4.58891	998	13.29083	995	13.81688	987	21.56299	963	42.49087	0.0037	0.0014
Z020	172	1.307	0.039	64	78.61635	2.171516	0.0531	0.008241	0.24356	0.092	0.009096	0.01272	0.000351	-0.02738	81.4	2.229373	89	9.038489	250	245.5965	8.539326	67.44	81.4	2.229373	81	2.374806	80.9	3.396333	81.1	146.8746	0.0069	0.0091
Z021	94.5	0.912	0.032	329	9.891197	0.19441	0.059	0.005091	0.82069	0.812	0.054632	0.1011	0.001987	-0.58265	621	12.09973	613	35.81214	520	181.9532	-1.30506	-19.4231	621	12.09973	621	13.45821	606	19.18357	552	119.0182	0	0.0062
Z022	523	1.221	0.098	136	99.60159	1.967114	0.0464	0.004556	-0.12614	0.0642	0.004039	0.01004	0.000198	0.34937	64.4	1.23921	63.1	3.85823	40	149.143	-2.06022	-61	64.4	1.23921	64.2	1.175007	64.1	2.077242	64.5	115.3979	-0.0012	0.0039
Z023	145.8	1.513	0.067	43.1	91.74312	2.225536	0.0473	0.008465	0.16151	0.0704	0.00808	0.0109	0.000264	0.014617	69.9	1.676967	68.6	7.595478	30	358.2303	-1.89504	-133	69.9	1.676967	70	1.818851	69.9	2.608006	69.9	299.3011	-0.0003	0.0089
Z024	317	1.49	0.1	808	13.29787	0.338888	0.0595	0.002754	0.20869	0.615	0.026497	0.0752	0.001916	0.54222	467	11.35481	485	16.60896	569	119.0946	3.71134	17.92619	467	11.35481	465	11.35481	453	15.02123	401	106.9464	0.0059	0.0019
Z026	149	1.676	0.021	55.3	101.626	2.828244	0.069	0.013913	-0.08047	0.095	0.016782	0.00984	0.000274	0.36358	63.1	1.717203	91	14.42074	620	284.8336	30.65934	89.82258	63.1	1.717203	61.6	2.009972	61.5	3.263267	63.5	27.95976	0.028	0.018
Z027	290	2.692	0.038	905	10.53075	0.138131	0.0597	0.002625	0.10989	0.779	0.031186	0.09496	0.001246	0.18023	584.8	7.341595	584	17.88296	573	97.78369	-0.13699	-2.05934	584.8	7.341595	582.8	7.341595	562.4	15.3706	479	88.36102	0.0034	0.0012
Z028	304	5.203	0.095	899	10.84599	0.150186	0.0586	0.00251	0.12933	0.743	0.028347	0.0922	0.001277	0.27265	568.7	7.682248	563	16.6026	538	92.11432	-1.01243	-5.70632	568.7	7.682248	567.3	7.732525	548.2	14.79457	469	84.21347	0.0022	0.0011
Z029	209	1.203	0.017	52.9	111.9821	2.578256	0.0498	0.008279	0.20092	0.061	0.00679	0.00893	0.000206	-0.04052	57.3	1.334835	59.8	6.465474	120	330.4082	4.180602	52.25	57.3	1.334835	57.1	1.404986	57.1	2.166877	57.3	265.3695	0.0032	0.0089
Z030	394	2.785	0.069	1343	10.30928	0.162339	0.0608	0.002281	0.13301	0.811	0.031422	0.097	0.001527	0.35258	596.8	8.960562	602	17.60945	620	84.29067	0.863787	3.741935	596.8	8.960562	594.8	9.017465	579.7	15.52576	530	73.18823	0.0036	0.0014
Z031	310	2.082	0.098	129	60.90134	1.218798	0.0448	0.004937	0.32057	0.1011	0.0075	0.01642	0.000329	-0.02588	105	2.071066	97.4	6.899801	20	147.8483	-7.80287	-425	105	2.071066	105.4	2.272337	105.3	3.43544	104.3	77.4126	-0.0043	0.0051
Z032	203.1	1.96	0.1	56.8	95.41985	2.518912	0.0458	0.00682	-0.1948	0.0663	0.006535	0.01048	0.000277	0.44464	67.2	1.735245	65	6.130784	0	200.0264	-3.38462	#NAME?	67.2	1.735245	67.4	1.735245	67.3	2.472916	67.3	132.7819	-0.0022	0.0064
Z033	456	1.506	0.039	1166	13.15789	0.217556	0.0576	0.00249	0.34166	0.602	0.024053	0.076	0.001257	0.11163	472.4	7.71405	477	15.41307	496	99.31502	0.964361	4.758065	472.4	7.71405	471.2	8.019449	462.2	13.56926	433	79.07334	0.0029	0.0023
Z035	258	1.426	0.062	66.7	102.6694	2.212839	0.0486	0.007626	0.17293	0.0651	0.007203	0.00974	0.00021	0.045089	62.5	1.294062	63.7	6.874592	90	182207.4	1.88383	30.55556	62.5	1.294062	62.4	1.430593	62.4	2.215358	62.5	182207.3	0.0017	0.0085
Z036	342	0.6651	0.0085	801	12.69036	0.176931	0.057	0.002594	0.15422	0.619	0.024443	0.0788	0.001099	0.19934	488.9	6.565629	489	15.56391	474	101.1485	0.02045	-3.14346	488.9	6.565629	487.8	6.565629	476.8	12.82429	433	87.13023	0.0023	0.0017
Z038	293	1.904	0.075	729	12.06273	0.216389	0.0584	0.002895	0.44059	0.663	0.026476	0.0829	0.001487	0.10129	513.1	9.022842	516	15.94481	524	111.0059	0.562016	2.080153	513.1	9.022842	511.7	9.406364	499	14.54156	440	95.02359	0.0037	0.0021
Z039	194	0.659	0.061	1610	5.213764	0.095745	0.0831	0.003156	0.45158	2.184	0.082529	0.1918	0.003522	0.12957	1131	19.38745	1174	26.27581	1260	78.20019	3.662692	10.2381	1131	19.38745	1122	20.68703	1114	24.51812	1090	63.20498	0.0079	0.0027
Z040	734	0.987	0.063	316	64.55778	1.460538	0.0509	0.004409	0.5374	0.1054	0.006365	0.01549	0.00035	-0.23967	99.1	2.241381	101.5	5.826166	190	486.82	2.364532	47.84211	99.1	2.241381	98.8	2.451447	98.6	3.661941	97.6	472.2822	0.0038	0.0056
Z041	163	2.306	0.024	1138	5.988024	0.084485	0.0748	0.002907	0.47234	1.716	0.060644	0.167	0.002356	-0.02818	995	13.27128	1013	22.69054	1053	81.12531	1.7769	5.508072	995	13.27128	991	13.79807	975	21.22217	941	72.28676	0.0047	0.0017
Z042	55.9	0.99	0.02	801	3.868472	0.092638	0.102	0.004508	-0.20861	3.67	0.179923	0.2585	0.00619	0.76332	1481	31.80923	1557	37.80882	1663	87.57858	4.881182	10.94408	1663	87.57858	1466	32.51288	1470	37.80882	1477	81.50636	0.011	0.0034
Z043	46.4	4.135	0.071	139	11.0742	0.219621	0.0608	0.006263	0.26165	0.752	0.050301	0.0903	0.001791	0.011781	557	10.43488	564	29.83215	560	239.5449	1.241135	0.535714	557	10.43488	554	11.09715	537	16.67385	462	202.2182	0.0054	0.0057
Z044	287	1.82	0.036	2440	5.189414	0.074687	0.0814	0.002522	0.30158	2.156	0.077765	0.1927	0.002773	0.22742	1136	14.77029	1165	24.85983	1221	63.11535	2.48927	6.961507	1136	14.77029	1130	15.28599	1120	23.67173	1102	51.95101	0.0054	0.002
Z045	151	1.918	0.062	52.8	70.17544	1.940801	0.0492	0.008226	0.33574	0.095	0.010631	0.01425	0.000394	-0.08819	91.2	2.487731	91	9.816196	100	941.6049	-0.21978	8.8	91.2	2.487731	91.2	2.779641	91.2	3.718805	91.2	920.8013	0.0016	0.009
Z046	237	4.19	0.29	1255	7.153076	0.150666	0.0707	0.002628	0.075777	1.368	0.055994	0.1398	0.002945	0.59869	843	16.58782	873	24.23306	950	83.6914	3.436426	11.26316	843	16.58782	838	17.26545	830	22.68703	810	73.12311	0.0055	0.002
Z047	641	0.983	0.024	693	27.51789	0.457778	0.0547	0.002968	0.3315	0.273	0.01254	0.03634	0.000605	0.011036	230.1	3.755812	244.5	9.842227	375	271.5796	5.889571	38.64	230.1	3.755812	228.9	3.937147	227.2	7.396582	218	260.5303	0.0055	0.003
Z048	42.7	1.43	0.027	295	5.871991	0.097315	0.0739	0.005039	0.24378	1.729	0.078829	0.1703	0.002822	0.12011	1013	15.6221	1015	29.38584	1010	140.5203	0.197044	-0.29703	1013	15.6221	1008	16.2256	971	24.52076	913	125.7682	0.0054	0.0024
Z049	279	1.367	0.077	82	99.9001	2.668362	0.049	0.006142	0.31535	0.0669	0.00485	0.01001	0.000267	-0.01279	64.2	1.721906	65.6	4.594894	170	1064.236	2.134146	62.23529	64.2	1.721906	64	1.794202	63.9	2.53603	63.7	1054.758	0.0021	0.0057
Z050	126.1	1.237	0.081	46.5	95.41985	3.050483	0.0542	0.010265	0.58251	0.077	0.009731	0.01048	0.000335	-0.42935	67.2	2.17308	75	9.699817	290	276.7953	10.4	76.82759	67.2	2.17308	66.7	2.547406	66.7	3.280951	67.2	95.4035	0.009	0.012
Z051	1003	2.471	0.036	4080	9.920635	0.215139	0.0642	0.002649	-0.66239	0.889	0.050286	0.1008	0.002186	0.80017	619	12.76399	642	25.04763	724	78.74619	3.582555	14.50276	619	12.76399	615	11.43151	612	17.69304	606	50.06378	0.0055	0.0034
Z052	127.1	1.25	0.29	1007	5.938242	0.17099	0.0753	0.003457	0.31208	1.732	0.077136	0.1684	0.004849	0.46156	1003	26.42694	1018	28.80811	1063	95.92263	1.473477	5.644403	1003	26.42694	998	27.88804	974	28.23202	944	78.32785	0.006	0.0026
Z053	145.1	0.584	0.013	91	54.91488	1.183562	0.0464	0.005895	0.25421	0.119	0.010109	0.01821	0.000392	0.047605	116.3	2.469613	113	9.254959	60	197.3392	-2.92035	-93.8333	116.3	2.469613	116.5	2.675666	116.1	4.026694	114.1	128.7418	-0.0024	0.006
Z054	267	146.9	8.7	1060	10.9517	0.146542	0.0585	0.002523	0.32804	0.728	0.027044	0.09131	0.001222	-0.01009	563.2	7.209734	554	16.00554	530	93.06073	-1.66065	-6.26415	563.2	7.209734	561.9	7.348991	542.9	14.47788	461	80.17668	0.0025	0.0012
Z055	313	1.77	0.12	18300	2.183883	0.036591	0.1637	0.002233	0.20742	10.35	0.35	0.4579	0.007672	0.70571	2429	34.09152	2465	31.00162	2493	22.80197	1.460446	2.567188	2493	22.80197	2412	36.54903	2413	35.609	2417	25.08086	0.0089	0.0036
Z056	110.5	1.102	0.035	36	116.144	3.134825	0.0451	0.008775	-0.0938	0.0539	0.007348	0.00861	0.000232	0.33676	55.3	1.46683	52.8	7.104388	40	238.3944	-4.73485	-38.25	55.3	1.46683	55.4	1.46683	55.4	2.061876	55.3	122.1552	-0.0026	0.0092
Z057	57.4	1.719	0.025	35.7	93.63296	3.138948	0.069	0.01451	-0.00366	0.101	0.016041	0.01068	0.000358	0.10746	68.5	2.251915	96	14.44967	630	301.5257	28.64583	89.12698	68.5	2.251915	66.2	2.551376	66.2	3.724408	68.2	37.34447	0.027	0.017
Z058	417	2.222	0.041	186	120.4819	2.159642	0.0652	0.008186	-0.34357	0.075	0.008953	0.0083	0.000149	0.47194	53.32	0.951812	73	8.159472	600	189.6131	26.9589	91.11333	53.32	0.951812	52.03	0.920856	52.06	2.256193	53.32	15.54646	0.023	0.011
Z059	184	1.872	0.032	87	97.84736	2.035652	0.0558	0.007988	-0.10978	0.079	0.008984	0.01022	0.000213	0.30568	65.5	1.378518	76	8.187834	370	196.9508	13.81579	82.2973	65.5	1.378518	64.6	1.378518	64.7	2.536855	65.2	55.49043	0.0108	0.0093
Z060	164.9	2.591	0.068	807	10.66098	0.158229	0.0601	0.002773	0.26854	0.776	0.030606	0.0938	0.001392	0.10837	578.2	8.166359	582	17.35049	591	101.8438	0.652921	2.165821	578.2	8.166359	576.2	8.327618	558.7	14.31484	499	89.49487	0.0041	0.0017
Z061	274	1.442	0.089	119	136.0544	2.763659	0.0717	0.009843	0.18077	0.0699	0.007394	0.00735	0.000149	0.012367	47.2	0.939599	68.2	6.910924	770	205.1423	30.79179	93.87013	47.2	0.939599	45.7	1.07501	45.8	2.215055	47.2	13.11482	0.032	0.012
Z062	603	2.191	0.041	923	26.03489	0.364965	0.0508	0.002213	0.16703	0.2686	0.010516	0.03841	0.000538	0.19499	242.9	3.357832	241.3	8.415614	224	95.87305	-0.66308	-8.4375	242.9	3.357832	242.8	3.40823	240.2	7.022888	215	80.11867	0.0004	0.002
Z064	60.9	1.128	0.016	3390	2.0803	0.032665	0.1668	0.004167	0.54096	11.02	0.361727	0.4807	0.007548	0.23298	2530	32.83838	2524	30.4937	2522	41.82463	-0.23772	-0.31721	2522	41.82463	2519	36.38516	2492	33.87455	2474	40.06819	0.0046	0.0035
Z065	4560	5.41	0.29	1790	100.9082	3.239176	0.0611	0.005901	-0.45971	0.085	0.009791	0.00991	0.000318	0.62574	63.6	2.01162	82	8.988382	480	165.5916	22.43902	86.75	63.6	2.01162	62.3	1.864461	62.3	2.961725	62	9.154276	0.0175	0.0091
Z067	442	1.466	0.025	83.7	131.2336	2.486731	0.0516	0.006504	0.29555	0.0538	0.004114	0.00762	0.000144	-0.13922	48.93	0.91115	53.1	3.945894	220	153.8248	7.853107	77.75909	48.93	0.91115	48.7	1.01615	48.6	1.789156	49.13	75.79307	0.0058	0.0062
Z068	1520	1.234	0.014	210	157.2327	2.742687	0.0488	0.003921	0.22451	0.0427	0.002223	0.00636	0.000111	0.091096	40.84	0.695617	42.4	2.139562	140	154.3137	3.679245	70.82857	40.84	0.695617	40.74	0.720141	40.75	1.3778	40.75	127.7147	0.0025	0.0034
Z069	135.3	1.419	0.072	941	5.035247	0.093633	0.0832	0.003832	0.3601	2.266	0.093546	0.1986	0.003693	0.12944	1167	20.22301	1198	28.98532	1253	95.02325	2.587646	6.863528	1167	20.22301	1158	20.87175	1133	26.46977	1100	79.06844	0.0081	0.0027
Z070	253	1.783	0.021	1140	7.012623	0.13584	0.072	0.002967	0.17767	1.413	0.057529	0.1426	0.002762	0.42988	859	15.35	892	23.8838	973	89.55003	3.699552	11.71634	859	15.35	854	16.00258	842	21.49269	811	76.54089	0.0071	0.0023
Z071	7500	5.54	0.49	2580	57.47126	2.9286	0.0508	0.001712	0.025805	0.1216	0.007156	0.0174	0.000887	0.88966	111.4	5.718245	116.2	6.572169	223	21906.96	4.130809	50.04484	111.4	5.718245	111	5.718245	110.7	6.504369	105.3	21906.89	0.0034	0.002
Z074	247	0.953	0.015	1874	5.67215	0.078354	0.0769	0.002561	0.27294	1.865	0.066964	0.1763	0.002435	0.15183	1047	13.1494	1067	23.60461	1108	68.60809	1.874414	5.505415	1047	13.1494	1042	13.63549	1028	22.08478	1004	58.46443	0.0053	0.0017
Z075	474	1.887	0.068	3020	6.485084	0.210891	0.0717	0.00198	-0.0172	1.522	0.069971	0.1542	0.005014	0.85172	924	27.62796	935	28.18585	969	57.5201	1.176471	4.643963	924	27.62796	920	28.36978	905	29.39188	875	50.3899	0.0042	0.0018
Z076	325	0.959	0.042	336	27.12232	0.438877	0.0504	0.003432	0.048604	0.256	0.012828	0.03687	0.000597	0.17665	233.4	3.719934	231	10.05305	230	147.3406	-1.03896	-1.47826	233.4	3.719934	233.1	3.778639	230.6	6.963763	204	120.1293	0.0002	0.0032
Z078	349	2.35	0.46	1426	9.157509	0.26392	0.0855	0.008121	0.26862	1.27	0.116718	0.1092	0.003147	-0.02207	668	18.65298	814	49.52319	1170	231.4105	17.93612	42.90598	668	18.65298	649	20.86513	644	24.94607	633	171.0914	0.031	0.012
Z079	1680	4.66	0.3	4560	12.57862	0.363246	0.0719	0.003038	-0.04317	0.764	0.034165	0.0795	0.002296	0.5665	493	13.61977	576	20.00514	966	156.7833	14.40972	48.9648	493	13.61977	484	13.61977	486	18.30589	493	138.7855	0.0181	0.0044
Z080	171	0.914	0.033	2900	3.252033	0.050385	0.1101	0.003587	-0.1199	4.68	0.194663	0.3075	0.004764	0.55884	1728	23.37742	1759	34.05561	1789	59.24259	1.762365	3.409726	1789	59.24259	1717	23.94084	1703	30.19577	1692	48.48612	0.006	0.0024
Z081	680	0.573	0.041	88	179.5332	4.056399	0.0489	0.006493	-0.21451	0.038	0.003799	0.00557	0.000126	0.48445	35.78	0.801616	37.8	3.716883	150	215.3684	5.343915	76.14667	35.78	0.801616	35.7	0.787886	35.67	1.311019	36.1	127.9699	0.0026	0.007
Z082	31.4	0.4092	0.0076	259	5.279831	0.099539	0.0828	0.006551	0.019132	2.17	0.128245	0.1894	0.003571	0.30539	1118	19.3183	1160	40.50865	1280	164.0072	3.62069	12.65625	1118	19.3183	1111	21.96171	1087	26.24177	1069	136.7007	0.0099	0.0057
Z083	99.2	1.316	0.026	1513	3.76506

Z084	3830	4.1	0.3	2090	50.83884	1.194562	0.0488	0.001594	0.24184	0.1329	0.005302	0.01967	0.000462	0.58807	125.5	2.930716	126.6	4.729734	152	79.96762	0.868878	17.43421	125.5	2.930716	125.5	3.000749	125.2	4.437565	122.5	64.6087	0.0004	0.0016
Z085	193	1.026	0.014	74	73.80074	1.409929	0.05	0.007134	0.005031	0.093	0.009105	0.01355	0.000259	0.17931	86.8	1.635306	90	8.29504	150	1534.232	3.555556	42.13333	86.8	1.635306	86.5	1.766529	86.4	2.969256	85.8	1525.296	0.003	0.0075
Z086	177	1.053	0.015	624	10	0.134466	0.0608	0.003398	0.14525	0.834	0.039111	0.1	0.001345	0.12092	614.2	7.992141	613	21.63029	600	120.8812	-0.19576	-2.36667	614.2	7.992141	611.5	8.234763	585	16.41553	489	101.3277	0.0052	0.0023
Z087	668	9.83	0.15	28100	2.547771	0.040995	0.1836	0.002272	0.014832	9.93	0.335132	0.3925	0.006316	0.79756	2134	29.05588	2426	31.25709	2684	21.75622	12.03627	20.4918	Discordant	Discordant	2027	31.4338	2080	36.02146	2134	26.02524	0.0588	0.0035
Z088	47.1	1.738	0.034	2570	2.014504	0.02979	0.1871	0.005359	0.29925	12.79	0.444751	0.4964	0.007341	0.25111	2598	31.54841	2662	32.50975	2712	47.78913	2.404207	4.20354	2712	47.78913	2564	36.09463	2575	35.50865	2586	43.58211	0.016	0.0055
Z089	590	1.28	0.1	1830	11.91895	0.249095	0.0623	0.002031	-0.05849	0.726	0.029997	0.0839	0.001753	0.64359	520	10.22754	553	17.48903	674	85.81258	5.96745	22.84866	520	10.22754	516	10.22754	514	15.53661	510	77.04103	0.0061	0.0015
Z090	257	1.132	0.023	272	30.15682	0.52967	0.0555	0.004276	0.41609	0.252	0.013395	0.03316	0.000582	-0.15607	210.3	3.622331	228	10.63555	390	1773.86	7.763158	46.07692	210.3	3.622331	208.9	3.938056	208	6.929274	206.2	1770.911	0.0069	0.0042
Z091	305	1.317	0.031	69.4	125.1564	2.818885	0.0464	0.006593	0.26575	0.0521	0.00498	0.00799	0.00018	-0.06225	51.3	1.165341	51.4	4.738108	50	225.4878	0.194553	-2.6	51.3	1.165341	51.3	1.235079	51.2	1.876452	51.1	161.3866	-0.0009	0.0066
Z093	122.5	1.323	0.03	47.4	75.64297	2.105475	0.0508	0.009079	0.35379	0.091	0.010599	0.01322	0.000368	-0.12385	84.7	2.315235	88	9.788869	140	539.4592	3.75	39.5	84.7	2.315235	84.4	2.607434	84.3	3.481659	83.1	499.111	0.004	0.01
Z094	278	1.54	0.23	712	12.8041	0.328074	0.0582	0.002862	-0.3107	0.629	0.032826	0.0781	0.002001	0.74717	485	12.14209	493	20.33753	515	114.8559	1.622718	5.825243	485	12.14209	483	11.43199	472	16.17761	421	99.78646	0.0037	0.0022
Z095	70.3	1.99	0.35	212	10.91703	0.206624	0.0577	0.004762	0.18407	0.739	0.043893	0.0916	0.001734	0.10696	565	9.836965	558	24.93572	500	173.2585	-1.25448	-13	565	9.836965	563	10.47788	544	16.09627	460	145.0143	0.0017	0.0039
Z096	1190	2.599	0.085	247	132.626	5.058503	0.0527	0.005422	-0.69592	0.0554	0.007128	0.00754	0.000288	0.88042	48.4	1.885818	54.4	6.501611	250	123.5528	11.02941	80.64	48.4	1.885818	47.8	1.585783	47.8	2.197533	47.9	36.3203	0.0073	0.007
Z097	187	1.418	0.064	74	69.06077	1.781665	0.0503	0.007637	0.18532	0.099	0.010664	0.01448	0.000374	0.002285	92.7	2.350673	95	9.844309	140	1515.549	2.421053	33.78571	92.7	2.350673	92.4	2.566294	92.4	3.634615	92.7	1503.723	0.0031	0.0088
Z098	40.2	3.106	0.058	255	5.737235	0.101814	0.0723	0.00549	0.45616	1.728	0.085492	0.1743	0.003093	-0.16378	1036	16.96921	1013	32.44176	950	156.0594	-2.27048	-9.05263	1036	16.96921	1031	17.597	979	26.02629	858	138.2119	0.006	0.0025
Z099	593	5.584	0.066	1420	11.77856	0.168572	0.0578	0.002127	0.3146	0.676	0.024853	0.0849	0.001215	0.13553	525.1	7.353154	523	15.09949	510	81.46961	-0.40153	-2.96078	525.1	7.353154	524	7.512062	510.1	13.73993	458	68.5415	0.0028	0.0013
Z100	959	1.025	0.019	301	74.6826	1.297288	0.0487	0.003753	0.31848	0.0895	0.004972	0.01339	0.000233	-0.0714	85.7	1.441243	86.9	4.673916	130	303.1847	1.380898	34.07692	85.7	1.441243	85.6	1.564986	85.3	2.816504	80.8	288.1059	0.0014	0.004
Z101	1020	8.8	3	195	127.7139	2.809356	0.0475	0.004398	0.18486	0.051	0.003435	0.00783	0.000172	0.096008	50.3	1.091245	50.5	3.3417	80	324.8452	0.39604	37.125	50.3	1.091245	50.2	1.160093	50.2	1.806089	50.3	305.5704	0.0006	0.0046
Z102	243	0.863	0.027	34.3	171.2329	4.980385	0.0498	0.009988	0.21915	0.0394	0.004948	0.00584	0.00017	-0.12103	37.5	1.101926	39	4.8653	100	263.0316	3.846154	62.5	37.5	1.101926	37.4	1.175432	37.4	1.60198	37.4	130.5553	0.004	0.011
Z103	320	1.748	0.064	1120	9.242144	0.129083	0.0638	0.002932	-0.0415	0.952	0.04323	0.1082	0.001511	0.29385	662.4	8.849872	677	22.29529	711	102.0152	2.156573	6.835443	662.4	8.849872	658.6	8.950186	638.2	16.82868	567	83.15803	0.0059	0.0024
Z104	97.4	0.941	0.016	1798	2.994012	0.084222	0.11	0.003822	-0.01364	5.03	0.230398	0.334	0.009395	0.77271	1855	46.74406	1818	38.18137	1792	62.40004	-2.0352	-3.51563	1792	62.40004	1849	47.47449	1790	40.57459	1734	58.09324	0.0033	0.002
Z106	52.5	1.433	0.023	423	5.51572	0.097421	0.0745	0.004523	0.36837	1.856	0.08142	0.1813	0.003202	0.017881	1074	17.80943	1062	29.13919	1027	122.2799	-1.12994	-4.57644	1074	17.80943	1069	18.44223	1023	25.39906	943	107.3778	0.0046	0.0023
Z107	37	1	0.11	117	10.6383	0.2996	0.0581	0.00737	0.2663	0.745	0.071356	0.094	0.002647	0.011076	579	15.40555	557	42.9869	470	267.7763	-3.94973	-23.1915	579	15.40555	580	16.86568	577	21.09061	565	182.7734	-0.0014	0.0086
Z108	189	1.237	0.031	586	11.38952	0.197197	0.0576	0.003196	0.096945	0.697	0.03344	0.0878	0.00152	0.35705	542.7	9.138214	535	19.55624	486	116.965	-1.43925	-11.6667	542.7	9.138214	541	9.138214	515	15.2855	399	100.2285	0.0039	0.002
Z109	158	1.127	0.014	1891	4.340278	0.063941	0.0852	0.002728	0.54887	2.687	0.089517	0.2304	0.003394	0.004428	1336	17.68123	1327	24.91859	1312	61.93947	-0.67822	-1.82927	1336	17.68123	1333	18.21663	1305	24.91859	1260	55.86052	0.0029	0.0017
Z110	147	2.744	0.071	703	8.169935	0.228313	0.0687	0.003542	0.028619	1.16	0.05945	0.1224	0.003421	0.60244	744	19.66459	777	27.51864	865	117.2777	4.247104	13.98844	744	19.66459	739	19.66459	727	25.06622	696	101.0944	0.0069	0.0027
Z111	681	4.211	0.055	2510	9.386146	0.120951	0.0599	0.001675	0.35624	0.882	0.029466	0.10654	0.001373	0.21255	652.6	7.990567	641.5	15.95423	594	57.77059	-1.73032	-9.86532	652.6	7.990567	651.8	8.075467	633.1	15.4488	567	51.74109	0.00086	0.00055
Z113	383	0.915	0.075	73.6	136.0544	3.013705	0.0464	0.006591	0.19395	0.0482	0.004868	0.00735	0.000163	0.1001	47.2	1.07501	47.6	4.704475	60	235.8823	0.840336	21.33333	47.2	1.07501	47.2	1.144835	47.2	1.742438	47.2	160.1042	-0.0007	0.0069
Z114	457	2.02	0.21	98	126.4223	2.759749	0.0492	0.006241	0.34514	0.0531	0.004471	0.00791	0.000173	-0.11882	50.8	1.094024	52.4	4.303126	130	272.9032	3.053435	60.92308	50.8	1.094024	50.7	1.232594	50.7	1.898918	50.8	228.2437	0.0027	0.0066
Z115	427	0.89	0.21	107	106.6098	3.340872	0.0484	0.005598	0.026891	0.0624	0.005086	0.00938	0.000294	0.35355	60.2	1.925141	61.3	4.836083	120	2856.197	1.794454	49.83333	60.2	1.925141	60.1	1.925141	60.1	2.554152	60.3	2853.059	0.0014	0.0056
Z116	479	1.926	0.034	1490	10.29866	0.145053	0.0595	0.002138	0.40764	0.796	0.028738	0.0971	0.001368	0.001721	597.6	8.05422	594	16.1161	574	76.45699	-0.60606	-4.1115	597.6	8.05422	596.2	8.206355	577.3	14.6659	505	66.82942	0.0023	0.0012
Z117	26.6	3.63	0.12	153	6.738544	0.196584	0.0731	0.007156	0.084098	1.49	0.104656	0.1484	0.004329	0.31216	891	24.57369	914	41.30718	940	213.3682	2.516411	5.212766	891	24.57369	883	25.30704	848	29.91159	770	182.8975	0.0104	0.0058
Z118	534	0.788	0.01	1194	12.93661	0.191209	0.0569	0.00226	0.47295	0.605	0.022193	0.0773	0.001143	-0.0806	480	6.855813	480	13.98601	473	88.36576	0	-1.47992	480	6.855813	478.8	7.018032	464.9	12.45756	397	76.59822	0.0028	0.0012
Z119	208	0.774	0.024	35.3	137.5516	4.153519	0.0488	0.009347	0.1062	0.0489	0.005858	0.00727	0.00022	0.10581	46.7	1.431432	48.2	5.694184	100	461.5328	3.112033	53.3	46.7	1.431432	46.6	1.505323	46.6	2.013089	46.7	409.6548	0.0024	0.0095
Z120	577	1.026	0.092	493	27.43484	0.525927	0.0502	0.002933	0.28378	0.251	0.01151	0.03645	0.000699	0.18674	230.8	4.384705	227.3	9.207678	196	121.2392	-1.53982	-17.7551	230.8	4.384705	230.8	4.515666	228.1	7.13952	200	99.3872	0	0.0027

16YADZ03					Isotopic Ratios + measurement uncertainty (2s)										Ages uncorrected for common lead + measurement uncertainty (2s)								Ages corrected for common lead (Andersen routine) + measurement uncertainty (2s)							
					Data for Tera-Wasserburg plot					Data for Wetherill plot																				
Sample	U (ppm)	U/Th	U/Th uncertainty 2SE	207Pb (cps)	U238/Pb 206	U238/Pb 206 uncertainty (2s)	Pb207/Pb 206	Pb207/Pb 206 uncertainty (2s)	ρ	Pb207/U 235	Pb207/U 235 uncertainty (2s)	Pb206/U 238	Pb206/U 238 uncertainty (2s)	ρ	Age Pb206/U 238	Age Pb206/U 238 measurement uncertainty (2s)	Age Pb207/U 235	Age Pb207/U 235 measurement uncertainty (2s)	Age Pb207/Pb 206	Age Pb207/Pb 206 measurement uncertainty (2s)	Discordance Pb206/U 238 vs Pb207/U 235 (%)	Concordance Pb206/U 238 vs Pb207/Pb 206 (%)	Best age	Best age measurement uncertainty (2S)	Age Pb206/U 238	Age Pb206/U 238 measurement uncertainty (2s)	Age Pb207/U 235	Age Pb207/U 235 measurement uncertainty (2s)	Age Pb207/Pb 206	Age Pb207/Pb 206 measurement uncertainty (2s)	Common Lead fraction	Common Lead fraction uncertainty (2s)
Z001	667	2.05	0.068	405	44.5236	0.876217	0.0503	0.002126	0.33044	0.1551	0.00705	0.02246	0.000442	-0.13629	143.2	2.802127	146.2	6.218832	200	86.61409	2.051984	28.4	143.2	2.802127	142.9	2.906392	142.7	3.684599	142.1	1.968502	0.0019	0.0035
Z002	26.2	4.61	0.12	21.6	34.96503	1.270105	0.0542	0.006535	0.48587	0.211	0.024124	0.0286	0.001039	-0.07898	181.5	6.424684	191	20.10837	300	228.3462	4.973822	39.5	181.5	6.424684	180.7	6.928461	180.5	7.518418	179.4	6.614167	0.006	0.01
Z003	356	1.489	0.036	135	120.6273	3.203447	0.079	0.011811	-0.72426	0.091	0.015109	0.00829	0.00022	0.87834	53.2	1.426714	87	13.52925	990	275.5903	38.85057	94.62626	53.2	1.426714	51.2	1.362246	51.2	2.252982	53.2	1.181101	0.04	0.018
Z004	827	1.059	0.061	168	125.6281	2.573992	0.0469	0.002441	0.19058	0.0513	0.002787	0.00796	0.000163	-0.03115	51.12	1.034915	50.8	2.698064	80	102.3621	-0.62992	36.1	51.12	1.034915	51.08	1.083642	51.03	1.36718	51.08	0.645669	-0.0001	0.004
Z005	190	0.835	0.031	61.2	94.87666	2.447669	0.058	0.005591	-0.12052	0.085	0.008883	0.01054	0.000272	0.28573	67.6	1.743438	82	8.087383	460	188.9762	17.56098	85.30435	67.6	1.743438	66.5	1.743438	66.5	2.326921	67.6	1.417321	0.0113	0.008
Z006	1280	1.551	0.034	268	138.1215	3.070346	0.0566	0.007559	-0.18802	0.0552	0.0079	0.00724	0.000161	0.31929	46.53	1.024258	54.3	7.348156	430	244.0942	14.30939	89.17907	46.53	1.024258	45.7	1.113443	45.7	1.506255	46.52	0.748031	0.011	0.012
Z007	183	1.535	0.086	43.1	126.5823	4.35321	0.0621	0.007795	0.18183	0.067	0.0088	0.0079	0.000272	0.029484	50.8	1.74989	68	8.786811	530	244.0942	25.29412	90.41509	50.8	1.74989	49.1	2.111188	49	2.462325	49.6	2.125982	0.02	0.013
Z008	237	0.822	0.026	712	10.77586	0.196251	0.0609	0.002047	0.23391	0.779	0.031651	0.0928	0.00169	0.078219	572.3	9.891773	583	18.17207	609	70.86607	1.835334	6.026273	572.3	9.891773	569.6	10.06821	553.3	12.78841	494	30.70863	0.005	0.0026
Z009	166.6	1.788	0.022	62.2	74.46016	1.897056	0.0521	0.005276	0.39654	0.095	0.008937	0.01343	0.000342	-0.20511	86	2.159816	91	8.134919	200	181.1022	5.494505	57	86	2.159816	85.6	2.353509	85.5	2.837588	85.6	1.732282	0.0054	0.0084
Z010	481	1.495	0.092	190	62.93266	1.906523	0.0493	0.003386	0.072512	0.1075	0.008035	0.01589	0.000481	0.27892	101.6	3.079832	103.3	7.296654	140	125.9841	1.645692	27.42857	101.6	3.079832	101.5	3.148518	101.4	3.520732	101.2	2.519683	0.0016	0.0057
Z011	142	1.296	0.018	29.6	120.1923	3.469956	0.0501	0.007244	0.19241	0.057	0.007984	0.00832	0.00024	-0.03491	53.4	1.494095	55.6	7.665047	80	228.3462	3.956835	33.25	53.4	1.494095	53.2	1.698034	53.2	1.903299	53.4	1.259841	0.001	0.011
Z012	903	5.9	1.2	519	59.52381	1.347796	0.064	0.003543	-0.17158	0.149	0.010061	0.0168	0.00038	0.4469	107.4	2.422076	140	8.445819	680	110.2361	23.28571	84.20588	107.4	2.422076	105.2	2.363779	105.2	3.55129	107.6	1.811022	0.0205	0.006
Z013	1275	2.616	0.085	823	41.8235	0.694619	0.0504	0.001024	0.21175	0.1661	0.00513	0.02391	0.000397	0.11369	152.3	2.49292	156	4.443748	209	43.30704	2.371795	27.12919	152.3	2.49292	152.1	2.526272	151.7	3.557259	149.8	2.677163	0.0019	0.0017
Z014	211	1.092	0.019	53	93.28358	2.43565	0.0437	0.004252	0.18367	0.0663	0.006944	0.01072	0.00028	0.059389	68.7	1.817719	64.8	6.620739	40	173.2282	-6.01852	-71.75	68.7	1.817719	69	1.883057	69	2.150669	68.7	1.496061	-0.0048	0.007
Z015	74.9	1.571	0.057	18.9	103.9501	4.534515	0.049	0.007874	-0.05714	0.066	0.011129	0.00962	0.00042	0.2539	61.7	2.684967	64	10.33959	40	267.7163	3.59375	-54.25	61.7	2.684967	61.5	2.758994	61.5	2.979766	60.7	2.755903	0.003	0.013
Z016	877	1.477	0.034	40400	2.091613	0.03683	0.1808	0.001417	0.20495	11.91	0.307028	0.4781	0.008419	0.6497	2518	36.72131	2600	23.69742	2659	13.38581	3.153846	5.302745	2659	13.38581	2492	39.83911	2524	32.68192	2546	24.40942	0.0128	0.0044
Z017	152	1.585	0.073	383	12.06273	0.266675	0.0579	0.002756	0.083012	0.65	0.03492	0.0829	0.001833	0.19565	514	10.8411	506	21.76277	490	102.3621	-1.58103	-4.89796	514	10.8411	512	11.42582	495	13.81659	433	33.85823	0.0022	0.004
Z018	710	8.84	0.14	2010	10.97574	0.189561	059	0.000866	0.16141	0.741	0.021788	0.09111	0.001574	0.4411	562.1	9.323299	562	12.74853	563	33.07083	-0.01779	0.159858	562.1	9.323299	561	9.362121	550.3	11.84082	521	14.17321	0.00199	0.00095
Z019	396	1.047	0.068	1013	12.22494	0.225459	0.0578	0.00189	-0.3169	0.652	0.02739	0.0818	0.001509	0.52267	506.7	8.920241	508	16.95049	497	66.92907	0.255906	-1.95171	506.7	8.920241	505.1	8.832231	489.6	11.40993	410	27.55903	0.0026	0.0019
Z020	189	1.495	0.081	78.1	65.31679	1.721447	0.0491	0.00378	-0.09063	0.104	0.008991	0.01531	0.000404	0.31109	98	2.583464	100	8.180741	170	157.4802	2	42.35294	98	2.583464	97.6	2.583464	97.7	3.073162	98.3	2.047242	0.0012	0.0061
Z021	120	0.754	0.033	115.9	28.40909	0.68482	0.0514	0.003386	-0.01355	0.249	0.017515	0.0352	0.000849	0.23809	223	5.264995	224	14.18574	210	125.9841	0.446429	-6.19048	223	5.264995	222.6	5.32646	219.6	5.930795	194	14.17321	0.0018	0.0054
Z022	200	1.085	0.035	206	26.08242	0.488655	0.0504	0.002756	0.13511	0.265	0.015449	0.03834	0.000718	0.094262	242.5	4.435132	237	12.07778	200	110.2361	-2.32068	-21.25	242.5	4.435132	242.7	4.577532	240	5.577138	224	10.23621	-0.0001	0.0045
Z024	130	1.275	0.021	51.6	69.58942	2.077515	053	0.006299	0.34549	0.107	0.013614	0.01437	0.000429	-0.23483	91.9	2.735245	102	12.02849	280	220.4722	9.901961	67.17857	91.9	2.735245	90.3	2.872345	90.4	3.33807	91.9	2.362202	0.007	0.011
Z025	186	1.743	0.018	1244	5.773672	0.101768	0.0727	0.001339	0.30454	1.736	0.052113	0.1732	0.003053	0.2858	1029	16.77887	1021	19.0502	999	37.00784	-0.78355	-3.003	1029	16.77887	1027	16.77887	1004	17.68305	957	22.83462	0.0021	0.0011
Z026	301	0.997	0.028	49.8	144.7178	3.820006	0.0454	0.00378	0.42363	0.0439	0.003838	0.00691	0.000182	-0.18291	44.4	1.157167	43.6	3.679185	30	157.4802	-1.83486	-48	44.4	1.157167	44.4	1.288967	44.4	1.482094	43.8	1.181101	-0.0018	0.0063
Z027	118.6	0.9	0.028	1039	4.914005	0.089161	0.0799	0.00189	0.18547	2.241	0.079273	0.2035	0.003692	0.20087	1194	19.80988	1191	24.94864	1181	47.24405	-0.25189	-1.10076	1194	19.80988	1189	20.25861	1157	21.08304	1113	25.98423	0.0046	0.0023
Z028	380	0.755	0.087	129	129.199	8.379297	088	0.022047	-0.63572	0.1	0.032367	0.00774	0.000502	0.83401	49.7	3.237121	94	28.42721	920	425.1964	47.12766	94.59783	49.7	3.237121	46.8	2.105695	46.8	2.90881	49.7	3.149603	0.05	0.035
Z029	568	1.484	0.018	133	118.0638	2.502424	0.0525	0.004016	0.21375	0.0611	0.004857	0.00847	0.00018	-0.05121	54.37	1.129626	60.1	4.613366	260	149.6061	9.53411	79.08846	54.37	1.129626	54	1.191047	53.9	1.609394	54.2	0.866141	0.0072	0.0067
Z030	1640	1.207	0.078	360	103.9501	2.643539	0.0445	0.00189	0.20035	0.0581	0.002997	0.00962	0.000245	0.34038	61.7	1.564433	57.3	2.832305	40	78.74008	-7.67888	-54.25	61.7	1.564433	62	1.628512	61.7	1.918841	60	2.283462	-0.004	0.0031
Z031	151	0.943	0.033	78.6	69.15629	1.926815	072	0.007874	-0.11917	0.145	0.019195	0.01446	0.000403	0.42604	92.6	2.604979	135	16.02808	820	204.7242	31.40741	88.70732	92.6	2.604979	89.8	2.739547	89.8	3.756807	93	2.440942	0.031	0.014
Z032	181	1.552	0.055	529	10.4712	0.227835	0.0575	0.001496	0.10736	0.756	0.026958	0.0955	0.002078	0.34479	588	12.12545	571	15.56779	493	56.69286	-2.97723	-19.2698	588	12.12545	587	12.12545	559	13.86132	448	37.00784	0.0016	0.0014
Z033	290	4.74	0.41	398	21.34472	0.422153	0.0543	0.002205	0.32874	0.35	0.015656	0.04685	0.000927	-0.1005	295.1	5.716062	304	11.91972	360	86.61409	2.927632	18.02778	295.1	5.716062	294.2	5.978492	290.9	7.266334	266	14.17321	0.0036	0.0036
Z034	476	0.729	0.033	82	149.2537	4.02323	0.0488	0.004646	0.31788	0.0446	0.003995	0.0067	0.000181	-0.10638	43.1	1.145644	44.2	3.91106	90	165.3542	2.488688	52.11111	43.1	1.145644	43	1.278632	43	1.492244	43	0.944881	0.0027	0.0077
Z035	125	0.843	0.022	44.3	68.16633	1.78923	0.0465	0.005197	0.33364	0.092	0.010456	0.01467	0.000385	-0.18239	93.9	2.419839	89	9.654989	30	196.8502	-5.50562	-213	93.9	2.419839	94.1	2.682316	94.1	3.025396	93.9	1.968502	-0.0025	0.0084
Z036	1200	1.909	0.038	767	40.60089	0.733323	0.0494	0.001496	0.14983	0.1678	0.006684	0.02463	0.000445	0.2802	156.9	2.820463	157.3	5.811825	163	63.77946	0.254291	3.742331	156.9	2.820463	156.8	2.820463	155.8	3.767162	148.2	6.377946	0.0007	0.0025
Z038	278	0.749	0.024	77.5	90.49774	1.835376	0.0473	0.003386	0.18033	0.0726	0.005613	0.01105	0.000224	0.091657	70.9	1.422884	70.9	5.285597	70	133.8581	0	-1.28571	70.9	1.422884	70.9	1.476347	70.9	1.894766	71.2	1.102361	0	0.0057
Z039	611	1.029	0.057	247	64.10256	1.22095	0.0483	0.00252	0.18535	0.1037	0.005798	0.0156	0.000297	0.071291	99.8	1.905413	99.9	5.360188	110	102.3621	0.1001	9.272727	99.8	1.905413	99.7	1.955198	99.5	2.546766	97.3	3.149603	0.0005	0.0041
Z040	150	0.679	0.049	98	148.368	6.304729	0.164	0.023622	-0.12198	0.152	0.023884	0.00674	0.000286	0.33738	43.3	1.850809	140	20.70703	2070	291.3383	69.07143	97.90821	43.3	1.850809	36.8	1.998973	36.9	3.637597	43.3	1.732282	0.149	0.038
Z041	186	1.814	0.028	78.1	66.97924	1.597337	0.0529	0.004646	0.08844	0.108	0.009775	0.01493	0.000356	0.10113	95.5	2.247487	104	8.9606	260	165.3542	8.173077	63.26923	95.5	2.247487	94.9	2.370991	94.7	2.924405	95.2	1.653542	0.0065	0.0076
Z042	536	1.11	0.13	143	95.2381	3.651806	0.0473	0.00378	-0.01563	0.0665	0.005724	0.0105	0.000403	0.32763	67.3	2.56964	66.8	5.932734	60	141.7321	-0.7485	-12.1667	67.3	2.56964	67.3	2.642205	67.3	2.848812	66.6	2.834643	0	0.0062
Z043	167	1.417	0.026	81.6	66.40106	1.741095	0.0619	0.005276	-0.30633	0.129	0.012949	0.01506	0.000395	0.56432	96.3	2.505379	122	11.34746	600	173.2282	21.06557	83.95	96.3	2.505379	94.2	2.31636	94.3	3.244166	96.3	2.047242	0.0182	0.009
Z044	970	1.094	0.067	284	86.58009	1.80155	0.0477	0.00252	0.32818	0.0771	0.004613	0.01155	0.00024	-0.00966	74	1.565414	75.3	4.355406	110	102.3621	1.726428	32.72727	74	1.565414	74.3	1.680036	74.2	2.104891	73.5	1.811022	0.0001	0.0041
Z045	396	1.224	0.034	78.8	129.3661	2.972264	0.0486	0.004646	0.15287	0.0515	0.00495	0.00773	0.000178	0.079953	49.6	1.143556	50.8	4.786791	100	173.2282	2.362205	50.4	49.6	1.143556	49.6	1.204293	49.5	1.491296	48.9	1.023621	0.002	0.0075
Z046	509	1.706	0.073	189	65.27415	1.408709	0.0455	0.002362	0.16584	0.0958	0.005292	0.01532	0.000331	0.14624	98	2.096535	92.7	4.938132	0	94.48809	-5.71737	#NAME?	98	2.096535	98.3	2.153429	98	2.545496	92.8	3.464563	-0.0031	0.0039
Z047	278	2.41	0.17	71	144.0922	4.630182	062	0.009449	-0.09235	0.063	0.01112	0.00694	0.000223	0.15664	44.6	1.427338	61	10.33098	550	259.8423	26.88525	91.89091	44.6	1.427338	42.8	1.427338	42.8	1.880525	44.6	1.259841	0.02	0.015
Z049	263	2.918	0.046	910	9.442871	0.173185	0.0613	0.001654	0.42813	0.889	0.02906	0.1059	0.001942	-0.07508	648.9	11.25016	645	15.63415	632	58.26766	-0.60465	-2.67405	648.9	11.25016	646.5	11.47524	624.5	12.99084	565	24.40942	0.004	0.002
Z050	337	2.59	0.052	8380	2.724796	0.046759	0.1252	0.000945	0.44768	6.367	0.158504	0.367	0.006298	0.22296	2015	29.72919	2027	21.82887	2031	13.38581	0.592008	0.787789	2031	13.38581	2010	30.51138	2007	23.5372	2005	12.59841	0.0024	0.0019
Z051	1276	0.995	0.023	1452	26.54632	0.472261	0.0574	0.002047	-0.23048	0.299	0.014382	0.03767	0.00067	0.48794	238.4	4.165086	265	10.89407	480	73.22827	10.03774	50.33333	238.4	4.165086	236.3	4.123947	235.3	5.883455	237.5	2.519683	0.0086	0.0034
Z053	202	0.524	0.013	789	8.695652	0.155527	0.0633	0.001496	0.36308	1.003	0.032602	0.115	0.002057	0.23635	701.7	11.81053	704	16.69274	705	49.60625	0.326705	0.468085	701.7	11.81053	699.5	11.97941	682	14.63447	625	24.40942	0.0033	0.0015
Z054	138	1.39	0.041	37	110.6195	3.338466	0.0573	0.006378	0.29896	0.0681	0.006877	0.00904	0.000273	-0.06043	58	1.731681	66.6	6.475788	360	204.7242	12.91291	83.88889	58	1.731681	57.3	1.869417	57.3	2.233837	58.1	1.496061	0.0108	0.0096
Z055	75.4	0.3138	0.0053	229	10.34126	0.217618	0.0597	0.002992	0.35809	0.794	0.044181	0.0967	0.002035	-0.07157	595	11.64758	589	24.38812	540	110.2361	-1.01868	-10.1852	595	11.64758	593	12.76503	578	15.17302	517	34.64563	0.0014	0.0045
Z056	624	7.44	0.25	8230	3.721623	0.062945	0.0922	0.001024	0.54414	3.413	0.089141	0.2687	0.004545	0.15768	1534	23.01735	1507	20.52329	1469	22.04722	-1.79164	-4.42478	1469	22.04722	1532	23.37816	1498	20.52329	1450	17.32282	0.00068	0.0007
Z057	500	0.416	0.031	391	84.74576	13.63217	0.284	0.055118	-0.91309	0.68	0.205331	0.0118	0.001898	0.96455	76	11.86544	420	110.6477	2710	385.8264	81.90476	97.19557	76	11.86544	43.2	3.20024	54	12.88157	400	181.1022	0.28	0.079
Z058	720	1.88	0.51	3820	6.798097	0.137162	0.0693	0.001181	0.26975	1.388	0.040888	0.1471	0.002968	0.37992	884	16.65342	883	17.57829	902	33.85823	-0.11325	1.995565	884	16.65342	882	17.18477	864	18.08248	841	19.68502	0.0027	0.0016
Z059	533	2.25	0.43	4510	4.672897	0.092737	0.0777	0.000945	0.18667	2.282	0.073092	0.214	0.004247	0.69217	1250	22.76508	1205	22.72182	1135	24.40942	-3.73444	-10.1322	1250	22.76508	1249	22.76508	1202	22.18335	1127	22.04722	0.00018	0.00022
Z060	1059	2.11	0.13	225	122.6994	3.008957	0.0487	0.002677	0.04447	0.0547	0.003469	0.00815	0.0002	0.37619	52.3	1.291137	54	3.378259	130	102.3621	3.148148	59.76923	52.3	1.291137	52.2	1.291137	52.2	1.593873	52.4	1.023621	0.0021	0.0045
Z061	369	1.439	0.095	81	113.3787	2.500085	0.053	0.005197	0.059294	0.0638	0.006394	0.00882	0.000194	0.085914	56.6	1.27164	62.5	6.148755	240	181.1022	9.44	76.41667	56.6	1.27164	55.9	1.392648	55.9	1.791978	56	1.102361	0.0074	0.0086
Z062	125.7	1.445	0.024	62.5	59.06675	1.637744	0.0566	0.005748	0.22577	0.131	0.013726	0.01693	0.000469	0.055271	108.2	2.995825	124	12.12208	350	188.9762	12.74194	69.08571	108.2	2.995825	107.9	2.929909	107.8	3.661011	107.7	2.440942	0.011	0.0097
Z064	298.8	2.82	0.13	1118	9.165903	0.20084	0.0634	0.001575	0.56246	0.95	0.030623	0.1091	0.002391	-0.10415	667	14.0166	677	15.91315	704	52.75585	1.477105	5.255682	667	14.0166	664	14.60154	643	13.91792	580	25.19683	0.0048	0.002
Z065	415.9	0.992	0.056	229	46.2963	1.007643	0.0467	0.002441	0.034662	0.1393	0.008293	0.0216	0.00047	0.2308	137.7	2.958987	132	7.358741	50	94.48809	-4.31818	-175.4	137.7	2.958987	138.1	3.016058	137.8	3.579898	136.1	2.677163	-0.0024	0.0041
Z066	209	1.24	0.018	337	17.47641	0.345923	0.0528	0.00252	0.57202	0.415	0.019819	0.05722	0.001133	-0.38032	358.7	6.920961	351	14.36847	290	94.48809	-2.19373	-23.6897	358.7	6.920961	358.7	7.400209	352.4	8.551505	308	22.83462	0.0003	0.0041
Z067	240	1.219	0.053	101	61.95787	1.412266	0.0491	0.002992	-0.09693	0.1086	0.007299	0.01614	0.000368	0.3345	103.2	2.321919	104.4	6.7086	140	118.1101	1.149425	26.28571	103.2	2.321919	103.1	2.381241	103	2.885502	101.5	2.204722	0.0013	0.0048
Z068	518	6.87	0.18	1570	10.60445	0.202505	0.0601	0.00126	0.23448	0.781	0.024006	0.0943	0.001801	0.16109	580.9	10.63364	585	13.48077	597	44.88184	0.700855	2.696817	580.9	10.63364	579.1	10.78043	564.1	12.1404	516	22.04722	0.003	0.0012
Z069	76.2	1.325	0.016	240	10.07049	0.203844	059	0.003071	0.093588	0.807	0.04574	0.0993	0.00201	0.19906	610.4	11.64687	596	25.85883	510	110.2361	-2.41611	-19.6863	610.4	11.64687	609	11.80312	587	15.23809	493	37.79524	0.0021	0.0044
Z070	356	0.944	0.018	62.2	140.2525	3.259849	046	0.00378	0.25013	0.0464	0.004234	0.00713	0.000166	0.022844	45.8	1.10684	45.9	4.073221	50	149.6061	0.217865	8.4	45.8	1.10684	46.1	1.046373	46.1	1.308101	45.8	0.866141	-0.0012	0.0062
Z071	496	1.694	0.048	143	89.6861	1.94307	0.048	0.002756	0.33725	0.0734	0.004289	0.01115	0.000242	0.002238	71.5	1.538619	71.8	4.10848	100	110.2361	0.417827	28.5	71.5	1.538619	71.4	1.595979	71.4	1.99745	71.7	1.102361	0.0007	0.0044
Z072	349	3.62	0.18	1300	9.451796	0.181761	0.0656	0.00189	-0.14829	0.964	0.041237	0.1058	0.002035	0.51499	648	11.75075	683	21.48656	776	65.35427	5.124451	16.49485	648	11.75075	643.3	11.7029	638	14.44688	615	23.62202	0.0076	0.0024
Z073	177	1.619	0.057	55	70.07708	1.71794	0.0424	0.004252	0.046651	0.082	0.008101	0.01427	0.00035	0.1007	91.3	2.208248	79.9	7.690396	130	157.4802	-14.2678	29.76923	91.3	2.208248	91.9	2.398033	91.7	2.65748	90.3	2.204722	-0.0068	0.0069
Z075	623	1.684	0.045	391	41.28819	0.757094	0.0488	0.002126	0.21693	0.1623	0.007748	0.02422	0.000444	0.023394	154.3	2.788994	152.4	6.828721	140	86.61409	-1.24672	-10.2143	154.3	2.788994	154.2	2.8342	152.5	3.717664	130	11.02361	0.0002	0.0034
Z076	2280	0.624	0.022	1103	96.7118	2.236481	0.104	0.011811	-0.68479	0.154	0.020782	0.01034	0.000239	0.74273	66.3	1.545128	143	17.60575	1410	236.2202	53.63636	95.29787	66.3	1.545128	61.1	1.320084	61.2	3.260778	66.5	1.102361	0.075	0.02
Z077	578	2.16	0.45	3980	5.633803	0.143015	0.0738	0.000945	-0.10541	1.797	0.066012	0.1775	0.004506	0.8766	1053	24.5522	1042	24.21113	1033	26.77163	-1.05566	-1.93611	1053	24.5522	1051	24.5522	1031	24.8306	991	21.25982	0.00128	0.00066
Z078	520	1.662	0.077	99	121.5067	2.612654	0.0442	0.003465	0.21817	0.0511	0.004414	0.00823	0.000177	-0.03229	52.8	1.118638	50.4	4.251631	10	141.7321	-4.7619	-428	52.8	1.118638	53	1.175394	52.9	1.435884	52.4	1.023621	-0.0039	0.0057
Z079	266	2.695	0.05	1540	6.618134	0.131987	0.0711	0.001496	0.42086	1.479	0.046576	0.1511	0.003013	0.3148	907	16.87557	920	19.40885	949	43.30704	1.413043	4.425711	907	16.87557	904	17.40014	888	18.87442	845	22.04722	0.004

Z081	429	0.989	0.026	75.3	136.2398	3.225722	0.0453	0.003386	-0.01873	0.0459	0.003775	0.00734	0.000174	0.26469	47.1	1.119496	45.5	3.691038	0	133.8581	-3.51648	#NAME?	47.1	1.119496	47.2	1.119496	47.2	1.348689	47.1	0.866141	-0.0021	0.0057
Z082	328	0.811	0.049	73	125.7862	2.844858	0.0541	0.007244	0.17319	0.0563	0.007593	0.00795	0.00018	0.001017	51.1	1.157432	55.1	7.196975	220	228.3462	7.259528	76.77273	51.1	1.157432	50.6	1.27955	50.7	1.619951	50.9	0.866141	0.009	0.012
Z083	413	1.251	0.021	118	91.65903	2.008397	0.0503	0.003386	0.27164	0.0752	0.005184	0.01091	0.000239	-0.01545	70	1.522763	73.4	4.85503	170	125.9841	4.632153	58.82353	70	1.522763	69.7	1.640368	69.7	2.027195	70	1.102361	0.0036	0.0055
Z086	210.3	0.957	0.023	1562	5.611672	0.119531	0.0787	0.001811	-0.26131	1.912	0.070751	0.1782	0.003796	0.6523	1057	20.4361	1083	24.42043	1154	45.66925	2.400739	8.405546	1057	20.4361	1052	20.98986	1043	21.51877	1039	19.68502	0.0052	0.0019
Z087	383	1.053	0.012	132.3	78.86435	1.707953	0.0522	0.003465	0.12079	0.0913	0.00687	0.01268	0.000275	0.15775	81.2	1.752923	88.4	6.30042	240	125.9841	8.144796	66.16667	81.2	1.752923	80.8	1.810343	80.7	2.382412	81.2	1.338581	0.006	0.006
Z088	552	3.38	0.34	3800	5.640158	0.100101	0.0724	0.000787	0.36203	1.761	0.046056	0.1773	0.003147	0.40424	1052	17.44072	1033	17.34263	993	22.83462	-1.8393	-5.94159	1052	17.44072	1051	17.44072	1026.3	16.9267	975	18.11022	0.00048	0.00044
Z089	95.5	2.145	0.033	26.1	87.10801	2.675727	0.047	0.008661	0.24599	0.073	0.013493	0.01148	0.000353	-0.20277	73.6	2.257335	70	12.69994	60	267.7163	-5.14286	-22.6667	73.6	2.257335	73	2.466042	73.6	2.85456	73	2.362202	0	0.014
Z090	441	1.184	0.038	231	75.87253	4.237327	0.089	0.025984	-0.838	0.152	0.054445	0.01318	0.000736	0.91359	84.4	4.663392	155	50.48941	820	377.9524	45.54839	89.70732	84.4	4.663392	78.9	2.209801	78.7	3.637597	82.2	6.062986	0.051	0.042
Z091	192	0.931	0.016	68.8	75.3012	1.689888	0.0508	0.004331	0.28645	0.0923	0.007932	0.01328	0.000298	-0.10131	85.1	1.906915	89.2	7.360868	180	157.4802	4.596413	52.72222	85.1	1.906915	84.7	2.026703	84.5	2.538183	83	2.519683	0.004	0.0071
Z092	165	1.137	0.025	44.6	92.25092	2.557045	0.0464	0.005591	0.38598	0.0678	0.007721	0.01084	0.0003	-0.13634	69.5	1.955465	66.2	7.319799	10	196.8502	-4.98489	-595	69.5	1.955465	69.6	2.090321	69.6	2.348841	69	1.496061	-0.0014	0.0091
Z093	205	0.85	0.026	90.1	69.30007	1.747182	0.0596	0.005118	0.00414	0.115	0.009818	0.01443	0.000364	0.25668	92.4	2.342744	110	8.995728	470	165.3542	16	80.34043	92.4	2.342744	90.9	2.406709	90.8	3.126999	90.5	2.440942	0.0155	0.0086
Z095	67.2	1.584	0.051	22.7	74.40476	2.37493	0.0464	0.00685	-0.24764	0.087	0.013537	0.01344	0.000429	0.39854	86.1	2.761277	83	12.73871	40	236.2202	-3.73494	-115.25	86.1	2.761277	86.2	2.691923	86.2	3.022383	86.1	2.440942	-0.002	0.011
Z096	630	0.86	0.019	130	126.7427	3.377283	0.0494	0.003071	0.22102	0.0534	0.003458	0.00789	0.00021	0.12754	50.7	1.340095	52.8	3.294881	150	110.2361	3.977273	66.2	50.7	1.340095	50.2	1.340095	50.1	1.625189	50.7	1.181101	0.0031	0.0049
Z097	480	1.009	0.068	214	66.0066	1.780311	0.0618	0.005906	-0.22613	0.131	0.014495	0.01515	0.000409	0.46892	97	2.574908	124	12.89049	510	165.3542	21.77419	80.98039	97	2.574908	95.1	2.510289	95	3.411159	95.4	3.307083	0.018	0.01
Z098	635	1.201	0.092	200	126.2626	3.152467	0.074	0.009449	-0.08911	0.082	0.011187	0.00792	0.000198	0.35526	50.8	1.277828	79	10.39073	760	236.2202	35.6962	93.31579	50.8	1.277828	49.5	1.40714	49.5	2.140607	50.8	1.023621	0.035	0.015
Z099	389	2.845	0.058	1103	11.42857	0.21216	0.0616	0.001732	-0.10356	0.745	0.031208	0.0875	0.001624	0.45684	540.9	9.622618	563	18.02687	639	59.84246	3.9254	15.35211	540.9	9.622618	537.7	9.622618	527	12.77294	503	20.47242	0.0062	0.0025
Z101	820	0.881	0.039	691	114.8106	3.207454	0.205	0.01811	-0.36114	0.248	0.025078	0.00871	0.000243	0.48113	55.9	1.514487	222	21.0008	2740	173.2282	74.81982	97.95985	55.9	1.514487	44.5	1.580592	44.7	4.8688	55.9	1.259841	0.202	0.03
Z103	3850	4.14	0.2	2590	38.77472	0.691007	0.04895	0.000764	0.21208	0.1742	0.005124	0.02579	0.00046	0.3439	164.1	2.910206	163	4.450699	143	34.64563	-0.67485	-14.7552	164.1	2.910206	164.1	2.910206	162.2	3.900579	131	11.81101	0.0007	0.0012
Z104	402	1.257	0.076	89.9	119.0476	2.865771	0.0502	0.004567	0.45831	0.0573	0.004984	0.0084	0.000202	-0.24931	53.9	1.305864	56.4	4.817889	150	165.3542	4.432624	64.06667	53.9	1.305864	53.8	1.432648	53.8	1.739211	53.9	1.023621	0.004	0.0074
Z105	176	1.837	0.089	45.8	100.4016	2.958015	0.0473	0.005433	0.41466	0.0633	0.006775	0.00996	0.000293	-0.24057	63.9	1.844319	62	6.530304	30	196.8502	-3.06452	-113	63.9	1.844319	64	2.04971	63.9	2.290517	63.4	1.574802	-0.0001	0.0089
Z106	1080	0.877	0.022	212	130.3781	3.216059	0.0492	0.002362	-0.04012	0.0522	0.003155	0.00767	0.000189	0.40365	49.3	1.200735	51.6	3.066101	150	94.48809	4.457364	67.13333	49.3	1.200735	49.1	1.200735	49.1	1.502857	49.1	0.944881	0.003	0.004
Z107	175.6	1.363	0.02	1338	5.24109	0.100983	0.0763	0.001654	0.4881	1.977	0.060962	0.1908	0.003676	0.019082	1125	20.04942	1107	20.58913	1095	43.30704	-1.62602	-2.73973	1125	20.04942	1123	20.04942	1090	19.13772	1044	31.49603	0.0021	0.0013
Z108	553	1.42	0.081	4690	4.854369	0.090931	0.0793	0.000945	0.27583	2.24	0.06616	0.206	0.003859	0.58912	1207	20.86094	1192	20.59033	1178	22.83462	-1.25839	-2.4618	1207	20.86094	1206	20.86094	1182	20.59033	1145	17.32282	0.00086	0.00057
Z109	380	0.934	0.036	132.7	73.6377	1.512101	0.0491	0.002598	-0.03702	0.0923	0.005767	0.01358	0.000279	0.29865	86.9	1.759511	89.4	5.345107	150	102.3621	2.796421	42.06667	86.9	1.759511	86.8	1.813306	86.8	2.355753	86.3	1.338581	0.002	0.0045
Z110	311	1.433	0.039	318	26.4131	0.531672	0.0509	0.002441	-0.03501	0.266	0.01474	0.03786	0.000762	0.30161	239.6	4.746452	238	12.08379	210	94.48809	-0.67227	-14.0952	239.6	4.746452	239.5	4.746452	238	5.909336	230	7.716528	0.0003	0.0039
Z111	1198	4.544	0.078	3570	10.5042	0.18518	0.0588	0.000787	0.30473	0.775	0.022895	0.0952	0.001678	0.42601	586	9.888838	582	12.95336	566	32.28343	-0.68729	-3.53357	586	9.888838	585.1	9.92982	571.1	12.02014	518	19.68502	0.00148	0.00077
Z112	240	1.259	0.031	84	70.97232	1.601332	0.0461	0.003307	0.16578	0.0891	0.00663	0.01409	0.000318	0.043202	90.2	2.016778	86.4	6.137208	10	125.9841	-4.39815	-802	90.2	2.016778	90.4	2.13621	90.3	2.539354	89.6	1.732282	-0.0021	0.0054
Z113	263	1.143	0.018	93.1	72.20217	1.614222	0.0485	0.003307	0.33062	0.0918	0.006278	0.01385	0.00031	-0.11385	88.7	1.943462	88.9	5.78285	110	125.9841	0.224972	19.36364	88.7	1.943462	88.6	2.061127	88.4	2.530445	87	2.283462	0.0009	0.0054
Z114	1029	1.301	0.05	260	125.1564	2.915557	0.0604	0.004252	0.10882	0.0663	0.005118	0.00799	0.000186	0.13654	51.3	1.219897	65	4.796059	530	141.7321	21.07692	90.32075	51.3	1.219897	50.4	1.219897	50.4	1.743037	51.2	0.944881	0.0172	0.007
Z115	352	0.99	0.12	65	182.1494	7.328163	0.0608	0.006299	0.14192	0.0442	0.004297	0.00549	0.000221	0.20007	35.3	1.440234	43.7	4.214154	480	196.8502	19.22197	92.64583	35.3	1.440234	34.7	1.440234	34.7	1.669158	35.3	1.338581	0.0162	0.0095
Z116	106.5	0.913	0.023	38.2	117.7856	3.728708	0.081	0.011024	0.31343	0.094	0.012011	0.00849	0.000269	-0.12525	54.5	1.705792	90	11.2079	910	283.4643	39.44444	94.01099	54.5	1.705792	52.2	1.987794	52.2	2.716011	54.5	1.496061	0.045	0.018
Z117	1020	0.695	0.048	180	135.6852	4.037598	0.0466	0.00252	-0.04234	0.0475	0.003263	0.00737	0.000219	0.53258	47.3	1.447191	47.1	3.177086	50	102.3621	-0.42463	5.4	47.3	1.447191	47.3	1.379189	47.3	1.592507	47.4	1.259841	-0.0004	0.0041
Z118	488	2.009	0.039	486	27.83964	0.523056	0.0519	0.001969	0.084568	0.257	0.011846	0.03592	0.000675	0.2526	227.5	4.212016	232	9.230221	270	78.74008	1.939655	15.74074	227.5	4.212016	227	4.259586	225	5.51037	209	11.81101	0.0022	0.0031
Z119	1273	2.43	0.14	1237	28.68617	0.49825	0.052	0.001339	0.29172	0.2487	0.008718	0.03486	0.000605	0.098386	220.9	3.74588	225.3	7.119086	273	57.48026	1.952952	19.08425	220.9	3.74588	220.3	3.824502	217.4	5.183955	196	11.81101	0.0028	0.0024
Z120	78	1.619	0.037	1030	3.725782	0.070585	0.0931	0.002441	0.15839	3.44	0.123682	0.2684	0.005085	0.20431	1532	25.92818	1510	27.4268	1474	51.18105	-1.45695	-3.93487	1474	51.18105	1527	26.41383	1483	22.17722	1412	37.79524	0.0037	0.0019

17letkat08					Isotopic Ratios + measurement uncertainty (2s)										Ages uncorrected for common lead + measurement uncertainty (2s)								Ages corrected for common lead (Andersen routine) + measurement uncertainty (2s)							
					Data for Tera-Wasserburg plot					Data for Wetherill plot																			
Sample	U (ppm)	U/Th	U/Th uncertainty 2SE	207Pb (cps)	U238/Pb 206	U238/Pb 206 uncertainty (2s)	Pb207/Pb 206	Pb207/Pb 206 uncertainty (2s)	ρ	Pb207/U 235	Pb207/U 235 uncertainty (2s)	Pb206/U 238	Pb206/U 238 uncertainty (2s)	ρ	Age Pb206/U 238	Age Pb206/U 238 measurement uncertainty (2s)	Age Pb207/U 235	Age Pb207/U 235 measurement uncertainty (2s)	Age Pb207/Pb 206	Age Pb207/Pb 206 measurement uncertainty (2s)	Discordance Pb206/U 238 vs Pb207/U 235 (%)	Concordance Pb206/U 238 vs Pb207/Pb 206 (%)	Best age	Best age measurement uncertainty (2S)	Age Pb206/U 238	Age Pb206/U 238 measurement uncertainty (2s)	Age Pb207/U 235	Age Pb207/U 235 measurement uncertainty (2s)	Age Pb207/Pb 206	Age Pb207/Pb 206 measurement uncertainty (2s)	Common Lead fraction	Common Lead fraction uncertainty (2s)
Z001	88	47:31.2	0.043	56	64.30868	3.558891	0.0447	0.006496	0.16524	0.096	0.012782	0.01555	0.000861	0.10286	99.5	5.455919	92	11.86228	60	210.5593	-8.2	-65.8	99.5	5.5	100	5.595056	100	6.533408	99.5	74.76919	0.0	0.0
Z002	354	41:45.6	0.031	130	115.3403	6.122597	0.0446	0.003856	0.33841	0.053	0.004815	0.00867	0.00046	-0.04849	55.7	2.937686	52.3	4.667461	30	117.7328	-6.5	-85.7	55.7	2.9	55.9	2.96395	55.8	3.593465	55.4	41.35301	0.0	0.0
Z003	56.2	12:00.0	0.023	30.9	61.01281	3.395426	0.0391	0.006992	0.10003	0.088	0.013925	0.01639	0.000912	0.093818	104.8	5.794902	84	13.04377	280	201.651	-24.8	62.6	104.8	5.8	106.1	5.901448	106	6.148747	104.8	43.81202	0.0	0.0
Z004	281	16:48.0	0.41	55.3	194.9318	15.92707	0.0461	0.005966	-0.0554	0.0331	0.004525	0.00513	0.000419	0.39613	33	2.692162	33	4.369514	0	196.1885	0.0	#NAME?	33.0	2.7	32.9	2.692162	32.9	3.05412	32.8	105.6051	0.0	0.0
Z005	418	25:55.2	0.025	164	147.2754	8.898899	0.063	0.011517	-0.55618	0.059	0.013211	0.00679	0.00041	0.84952	43.6	2.602321	58	11.66437	600	362.3415	24.8	92.7	43.6	2.6	42.8	2.560288	42.9	4.040961	43.6	10.06823	0.0	0.0
Z006	44.9	09:07.2	0.06	63	52.54861	3.013458	0.07	0.012381	-0.1806	0.187	0.035391	0.01903	0.001091	0.39572	121.5	6.888992	166	28.86107	570	302.0274	26.8	78.7	121.5	6.9	118.3	7.045609	118.4	11.37369	121.8	41.35138	0.0	0.0
Z007	136.7	51:50.4	0.091	56.2	110.011	6.133362	0.0485	0.006748	0.12373	0.0604	0.007834	0.00909	0.000507	0.072523	58.4	3.241405	59.1	7.407798	50	3182.525	1.2	-16.8	58.4	3.2	58.3	3.276599	58.3	4.175364	58.3	3177.368	0.0	0.0
Z008	810	12:00.0	0.13	306	115.0748	6.107022	0.0471	0.002734	0.17054	0.0557	0.004354	0.00869	0.000461	0.31186	55.8	2.94371	55	4.190196	60	121.073	-1.5	7.0	55.8	2.9	55.8	2.969921	55.8	3.753097	55.7	91.97675	0.0	0.0
Z009	269	1.758	0.039	3560	5.149331	0.266476	0.0734	0.001494	0.023867	1.964	0.136635	0.1942	0.01005	0.96073	1144	54.30097	1102	46.86036	1019	39.51155	-3.8	-12.3	1143	54.3	1143	54.30097	1096	46.66812	1004	36.62052	0.0	0.0
Z010	84.1	1.323	0.039	50	81.63265	4.703571	0.0538	0.008556	0.20855	0.087	0.011797	0.01225	0.000706	0.03728	78.5	4.494196	84	10.92166	180	238.1183	6.547619	56.38889	78.5	4.494196	77.9	4.614672	77.9	5.996733	77.8	89.98445	0.008	0.012
Z011	99	2.21	0.16	58	83.8223	6.776006	0.067	0.013785	0.36123	0.105	0.019444	0.01193	0.000964	0.15164	76.4	6.13397	99	17.03789	390	308.1705	22.82828	80.41026	76.4	6.13397	74.8	6.320648	74.8	8.227078	75	26.39314	0.025	0.021
Z012	132.8	1.779	0.045	59	102.459	6.347537	0.0489	0.006406	0.14456	0.0656	0.008353	0.00976	0.000605	0.97312	62.6	3.872724	64.1	7.908541	90	923.6845	2.340094	30.44444	62.6	3.872724	62.5	3.919667	62.5	4.830116	62.3	907.2986	0.0013	0.0085
Z013	69	3.612	0.089	122	36.49635	2.165096	0.069	0.010324	-0.16842	0.31	0.081465	0.0274	0.001625	0.55722	173.9	10.28293	251	46.2361	620	212.5898	30.71713	71.95161	173.9	10.28293	193	45.7041	184	33.33252	171.3	57.7389	0.022	0.018
Z014	105	1.356	0.032	54	105.5966	6.407708	0.056	0.009235	0.038386	0.072	0.011328	0.00947	0.000575	0.49449	60.8	3.661626	70	10.50751	280	263.1356	13.14286	78.28571	60.8	3.661626	60.1	3.798751	60.1	5.097905	60.6	41.55578	0.012	0.013
Z015	740	11.1	1.6	455	59.45303	3.774101	0.047	0.002294	0.1022	0.1074	0.009195	0.01682	0.001068	0.62653	107.5	6.787583	103.3	8.429743	60	84.97285	-4.06583	-79.1667	107.5	6.787583	107.7	6.836277	107.5	7.882422	103.4	52.69436	-0.0012	0.0026
Z016	921	2.71	0.17	395	107.5269	5.56791	0.0477	0.002496	0.067749	0.0612	0.004753	0.0093	0.000482	0.28434	59.65	3.08007	60.2	4.520835	93	157.7938	0.913621	35.86022	59.65	3.08007	59.6	3.084053	59.6	4.024568	59.6	139.3599	0.0007	0.0029
Z017	502	2.217	0.026	34300	2.101282	0.109001	0.1543	0.001484	0.17954	10.13	0.697318	0.4759	0.024687	0.82783	2508	107.9251	2445	63.71004	2393	15.83725	-2.57669	-4.80568	2393	15.83725	2506	108.1289	2438	64.24788	2382	16.50813	0.00022	0.00044
Z018	1112	0.728	0.08	260	199.2032	10.57417	0.0494	0.003185	-0.02162	0.0343	0.002889	0.00502	0.000266	0.42274	32.28	1.712945	34.3	2.808024	150	100.5719	5.889213	78.48	32.28	1.712945	32.17	1.718222	32.16	2.343142	32.28	34.45571	0.0035	0.0039
Z019	226	1.038	0.075	880	12.51564	0.66235	0.0544	0.001868	0.201	0.605	0.044304	0.0799	0.004228	0.49448	496	25.20485	479	28.05366	372	69.33175	-3.54906	-33.3333	496	25.20485	495	25.46183	474	27.21228	366	56.23745	0.0005	0.0017
Z020	216	2.219	0.061	131	96.43202	5.774719	0.072	0.011067	-0.61563	0.109	0.020275	0.01037	0.000621	0.73083	66.5	3.986534	102	17.85119	650	244.4305	34.80392	89.76923	66.5	3.986534	63.6	3.642781	63.7	6.890797	66.6	13.00432	0.032	0.017
Z021	4420	6.24	0.26	950	187.9699	10.8158	0.0472	0.00183	0.17871	0.0348	0.002701	0.00532	0.000306	0.58581	34.2	1.955873	34.7	2.662469	67	198.7911	1.440922	48.95522	34.2	1.955873	34.2	1.995104	34.2	2.518877	34.1	189.5728	0.0006	0.0023
Z022	4.1	9.1	4.1	3.5	81.96721	30.43387	0.03	0.189171	0.88859	0.09	0.24417	0.0122	0.00453	0.45574	78	28.61352	-30	259.9037	8200	5511.933	360	99.04878	78	28.61352	59	20.84067	65	21.99798	380	215.8679	-0.13	0.29
Z023	527	1.523	0.063	188	121.5067	6.376927	0.0461	0.003529	0.009287	0.0529	0.00481	0.00823	0.000432	0.31205	52.8	2.756428	52.3	4.662907	20	119.2185	-0.95602	-164	52.8	2.756428	53.2	2.805475	52.9	3.545829	53.4	61.12362	-0.0012	0.0044
Z024	67.8	1.591	0.083	35.1	92.85051	5.171471	0.0464	0.008317	0.077639	0.069	0.011243	0.01077	0.0006	0.13955	69.1	3.82412	67	11.14867	20	283.0608	-3.13433	-245.5	69.1	3.82412	69.2	3.894803	69.2	4.774173	69	143.3323	-0.001	0.011
Z025	69.4	2.279	0.057	25.4	126.4223	7.198769	0.0498	0.008567	-0.03552	0.0546	0.007846	0.00791	0.00045	0.28784	50.8	2.908385	53.5	7.572926	150	289.2189	5.046729	66.13333	50.8	2.908385	50.5	2.908385	50.5	3.816151	50.8	187.194	0.004	0.01
Z026	511	2.688	0.044	149	154.0832	8.053712	0.0485	0.004015	0.20603	0.0432	0.003903	0.00649	0.000339	0.04612	41.7	2.172984	42.9	3.792174	110	190.4013	2.797203	62.09091	41.7	2.172984	41.62	2.189002	41.62	2.910198	41.72	149.342	0.0021	0.0049
Z027	2190	9.6	1.7	470	215.9827	13.52243	0.0474	0.002124	0.2051	0.0302	0.002315	0.00463	0.00029	0.6843	29.8	1.854589	30.2	2.289117	63	302.1055	1.324503	52.69841	29.8	1.854589	29.7	1.854589	29.7	2.289117	29.8	295.1272	0.0011	0.0023
Z028	73	1.686	0.06	930	5.274262	0.28252	0.0733	0.002855	0.000918	1.919	0.147105	0.1896	0.010156	0.59385	1119	54.93038	1083	50.81572	1001	76.74837	-3.3241	-11.7882	1119	54.93038	1116	54.93038	1065	49.10944	987	57.06621	0.0015	0.0013
Z029	330	1.34	0.18	93	162.3377	9.340916	0.0467	0.004638	0.10131	0.0397	0.004014	0.00616	0.000354	0.32393	39.6	2.267264	39.4	3.913643	30	187.6939	-0.50761	-32	39.6	2.267264	39.6	2.267264	39.6	2.836195	39.6	139.1337	-0.0001	0.0055
Z030	282	1.673	0.024	159	83.33333	4.352864	0.0525	0.004527	-0.06952	0.0871	0.008553	0.012	0.000627	0.32832	76.9	3.992476	84.4	7.943921	250	151.5824	8.886256	69.24	76.9	3.992476	76.4	3.992476	76.4	5.592968	76.9	71.13686	0.0064	0.0058
Z033	1160	1.869	0.049	205	243.9024	13.67455	0.0475	0.003888	0.28844	0.026	0.002356	0.0041	0.00023	0.091749	26.35	1.474168	26	2.34258	60	193.837	-1.34615	56.08333	26.35	1.474168	26.33	1.495712	26.33	1.870503	26.16	153.6989	0.0013	0.0052
Z034	1190	0.6304	0.009	565	91.24088	4.729826	0.0466	0.001962	0.29313	0.0704	0.005137	0.01096	0.000568	0.15132	70.3	3.633328	69	4.851751	45	73.07492	-1.88406	-56.2222	70.3	3.633328	70.4	3.633328	70.3	4.599183	69.5	46.12651	-0.0009	0.0022
Z035	395	1.407	0.085	3720	6.489293	0.355599	0.0673	0.00131	0.077657	1.431	0.103306	0.1541	0.008444	0.84446	923	47.16139	899	43.25378	841	39.25398	-2.66963	-9.7503	923	47.16139	922	47.16139	890	43.85168	811	36.42767	0.00084	0.00056
Z036	360	0.92	0.042	114	135.318	7.437196	0.0453	0.003724	0.059232	0.0453	0.00386	0.00739	0.000406	0.31148	47.5	2.58522	44.9	3.791593	10	108.0491	-5.79065	-375	47.5	2.58522	47.3	2.58522	47.3	3.137512	47.6	52.41805	-0.0021	0.004
Z037	388	7.8	1	133	130.8901	7.004993	0.0472	0.003999	0.11598	0.0499	0.004608	0.00764	0.000409	0.18907	49	2.629282	49.4	4.473274	70	206.7519	0.809717	30	49	2.629282	49	2.629282	49	3.387149	49.3	169.6979	0.0004	0.0047
Z038	200	0.956	0.051	60.1	146.4129	8.160024	0.046	0.005749	0.13524	0.0431	0.004956	0.00683	0.000381	0.14936	43.9	2.422185	42.6	4.847285	0	184.0837	-3.05164	#NAME?	43.9	2.422185	43.9	2.456497	43.9	3.035025	43.7	95.33033	-0.0011	0.007
Z039	311	2.426	0.028	106	135.5014	7.5714	0.0512	0.006688	-0.48789	0.0521	0.00735	0.00738	0.000412	0.6987	47.4	2.614505	51.2	6.945867	150	172.7957	7.421875	68.4	47.4	2.614505	46.5	2.524012	46.5	3.497923	47.4	50.17524	0.0054	0.0095
Z040	84.6	1.29	0.082	1161	5.216484	0.27016	0.0759	0.002544	0.32238	2.009	0.143938	0.1917	0.009928	-0.11564	1130	53.75022	1115	48.86624	1075	68.01038	-1.34529	-5.11628	1130	53.75022	1129	53.75022	1090	47.84046	1021	53.55102	0.0035	0.0017
Z041	402	1.327	0.033	240	74.46016	3.881967	0.0464	0.002863	-0.03511	0.0864	0.006986	0.01343	0.0007	0.38736	86	4.44816	84	6.537744	40	98.99805	-2.38095	-115	86	4.44816	86.1	4.44816	85.9	5.5866	85.3	60.04856	-0.0015	0.0032
Z042	117	9.19	0.3	68	71.07321	3.801653	0.0429	0.005532	0.066886	0.084	0.010348	0.01407	0.000753	0.17443	90.1	4.784816	81	9.493375	80	179.5925	-11.2346	-12.625	90.1	4.784816	90.5	4.841494	90.4	5.603924	90.1	47.41529	-0.0063	0.0073
Z043	348	1.645	0.052	73.6	208.3333	11.11346	0.0469	0.004945	0.020124	0.0313	0.003167	0.0048	0.000256	0.22381	30.89	1.649311	31.3	3.145502	40	323.7556	1.309904	22.775	30.89	1.649311	30.87	1.654866	30.87	2.159382	30.89	294.7881	0.0003	0.0056
Z044	175	1.252	0.029	68.4	119.9041	6.55819	0.0496	0.005509	0.26851	0.0571	0.005794	0.00834	0.000456	0.083586	53.6	2.925595	56.2	5.575044	170	216.7045	4.626335	68.47059	53.6	2.925595	53.3	2.958261	53.3	3.905447	53.5	156.7808	0.0033	0.0065
Z047	44	2.53	0.13	52	49.26108	3.372337	0.0536	0.008501	0.040475	0.152	0.022191	0.0203	0.00139	0.32734	129.8	8.843931	140	19.53505	210	425.0306	7.285714	38.19048	129.8	8.843931	130.9	9.344009	130.8	11.28687	131.9	358.544	0.006	0.012
Z048	646	4.1	0.34	139	199.6008	12.91995	0.0457	0.00379	0.31238	0.0311	0.002876	0.00501	0.000324	0.37835	32.2	2.096241	31.1	2.798585	10	122.2336	-3.53698	-222	32.2	2.096241	32.3	2.096241	32.3	2.460219	32.1	52.82847	-0.0011	0.0046
Z049	488	1.918	0.07	335	66.75567	3.534247	0.0485	0.002664	-0.10309	0.1012	0.008209	0.01498	0.000793	0.54967	95.9	5.054268	97.7	7.59176	125	146.7592	1.842375	23.28	95.9	5.054268	95.8	5.054268	95.7	6.503063	96.4	124.8493	0.0009	0.0031
Z050	684	1.599	0.029	285	96.43202	5.175428	0.0439	0.002801	0.071819	0.0627	0.005318	0.01037	0.000557	0.2751	66.5	3.552302	61.7	5.072886	60	90.57768	-7.77958	-10.8333	66.5	3.552302	66.8	3.552302	66.8	4.229795	65.9	26.53913	-0.0044	0.0035
Z051	58.1	2.27	0.065	47	99.30487	5.873525	0.088	0.014955	-0.07697	0.117	0.019033	0.01007	0.000596	0.29974	64.6	3.820992	109	17.30277	960	307.4082	40.73394	93.27083	64.6	3.820992	60.6	3.779389	60.6	7.433776	63.9	14.21156	0.052	0.021
Z052	330	1.811	0.018	226	63.13131	3.257461	0.0476	0.003052	-0.04869	0.1044	0.008564	0.01584	0.000817	0.29237	101.3	5.182437	100.6	7.873812	90	124.5209	-0.69583	-12.5556	101.3	5.182437	101.4	5.200947	101.4	6.590927	101.3	89.46985	-0.0006	0.0035
Z053	136	1.303	0.018	39.1	122.549	7.043235	0.0393	0.006435	0.40971	0.0434	0.006101	0.00816	0.000469	-0.16768	52.4	3.01643	42.9	5.925404	220	198.3313	-22.1445	76.18182	52.4	3.01643	52.8	3.097555	52.8	3.292023	52	24.23962	-0.0099	0.0083
Z054	801	1.752	0.041	143	242.6007	12.96571	0.0474	0.003777	-0.01428	0.027	0.002407	0.004122	0.00022	0.30649	26.52	1.41261	27	2.391062	80	268.8611	1.777778	66.85	26.52	1.41261	26.49	1.418042	26.49	1.866348	26.39	245.2235	0.0012	0.0044
Z055	4890	3.74	0.13	3810	54.49591	2.876394	0.04625	0.000838	0.2661	0.117	0.008188	0.01835	0.000969	0.76508	117.2	6.129809	112.3	7.455013	20	30.25419	-4.36331	-486	117.2	6.129809	116.5	7.433776	95.1	18.47166	-0.0021	0.001
Z056	1180	2.757	0.03	271	182.2822	9.448663	0.0453	0.00281	0.45349	0.0341	0.00266	0.005486	0.000284	-0.21679	35.27	1.823745	34	2.623867	10	92.50232	-3.73529	-252.7	35.27	1.823745	35.34	1.836145	35.34	2.312321	35.27	32.47903	-0.0018	0.0033
Z057	1910	2.091	0.096	1980	46.04052	2.636454	0.04795	0.001149	0.34638	0.1439	0.010409	0.02172	0.001244	0.79167	138.5	7.849254	136.4	9.251056	98	47.39908	-1.53959	-41.3265	138.5	7.849254	138.5	7.88747	136.8	9.370914	107	33.92835	-0.0002	0.0013
Z058	348	1.827	0.02	147	99.50249	5.420406	0.0441	0.003806	-0.19195	0.062	0.006426	0.01005	0.000547	0.57155	64.5	3.487074	60.8	6.127412	20	131.1905	-6.08553	-222.5	64.5	3.487074	64.7	3.487074	64.6	4.213642	63.8	36.62887	-0.004	0.0047
Z059	220	1.27	0.24	89	88.80995	5.692727	0.0418	0.004514	0.089306	0.0644	0.007078	0.01126	0.000722	0.40973	72.2	4.584626	63	6.768601	150	137.3908	-14.6032	51.86667	72.2	4.584626	72.7	4.633724	72.7	5.062901	71.1	31.08465	-0.0072	0.0057
Z060	302	1.95	0.035	100.4	131.2336	6.894812	0.0465	0.004443	0.26469	0.0486	0.004599	0.00762	0.0004	0.018388	48.94	2.561342	48.1	4.469989	40	162.4802	-1.74636	-22.35	48.94	2.561342	49	2.570813	49	3.268149	48.76	102.608	-0.0006	0.0052
Z061	205	6.5	0.94	94	91.74312	8.623035	0.0443	0.004946	-0.08811	0.068	0.009799	0.0109	0.001025	0.79186	70	6.457052	67	9.695718	50	157.2294	-4.47761	-40	70	6.457052	70.2	6.457052	70.1	6.903314	68	48.65956	-0.004	0.0064
Z062	553	7.22	0.23	11300	4.258944	0.222843	0.0968	0.001363	0.25472	3.132	0.217213	0.2348	0.012286	0.8417	1360	64.14481	1440	53.38212	1562	27.29709	5.555556	12.93214	1360	64.14481	1345	64.6071	1352	55.20915	1363	25.50041	0.0112	0.0025
Z063	358	2.05	0.17	84	172.4138	13.09797	0.0436	0.005008	-0.06932	0.0335	0.004202	0.0058	0.000441	0.61772	37.2	2.828813	33.3	4.180424	90	152.6442	-11.7117	58.66667	37.2	2.828813	38.1	2.948997	38.1	3.183574	37.2	30.37716	-0.0041	0.0064
Z064	245	6.62	0.85	143	74.29421	4.044467	0.0443	0.003487	-0.21266	0.0827	0.007621	0.01346	0.000733	0.48118	86.2	4.663914	80.4	7.152531	20	111.2635	-7.21393	-331	86.2	4.663914	86.5	4.633907	86.4	5.506968	85.4	43.65864	-0.0043	0.004
Z065	137	1.596	0.032	88	70.37298	4.054037	0.0499	0.00775	0.1472	0.097	0.014897	0.01421	0.000819	0.039086	90.9	5.225857	93	13.97638	110	7735.909	2.258065	17.36364	90.9	5.225857	90.7	5.34724	90.6	6.682401	89.5	7732.303	0.003	0.011
Z066	3400	17.4	1.8	1199	119.9041	6.430917	0.0458	0.001498	-0.12083	0.0527	0.003952	0.00834	0.000447	0.66894	53.5	2.865642	52.2	3.804226	6	51.40628	-2.49042	-791.667	53.5	2.865642	53.6	2.865642	53.6	3.575714	53.4	23.62501	-0.0016	0.0018
Z067	641	4.75	0.16	92	277.7006	14.53923	0.0434	0.005311	0.15524	0.0214	0.002569	0.003601	0.000189	-0.10418	23.17	1.211724	21.5	2.564325	100	158.698	-7.76744	76.83	23.17	1.211724	23.39	1.247722	23.39	1.504836	23.17	19.62553	-0.0039	0.0073
Z068	109	1.172	0.063	41.2	105.2632	5.976415	0.0421	0.006426	0.19818	0.0567	0.007776	0.0095	0.000539	0.009	61	3.428446	55.6	7.427889	120	193.3653	-9.71223	49.16667	61	3.428446	61.2	3.503576	61.2	4.060238	61	40.99542	-0.0066	0.008
Z069	379	1.65	0.13	142	120.1923	6.489303	0.0484	0.003768	-0.02109	0.0564	0.005091	0.00832	0.000449	0.42741	53.4	2.859697	55.6	4.875674	110	820.0074	3.956835	51.45455	53.4	2.859697	53.3	2.859697	53.3	3.794442	52.6	813.5943	0.0018	0.0043
Z070	191	1.885	0.078	113	69.63788	3.690794	0.0473	0.004257	-0.01265	0.092	0.008563	0.01436	0.000761	0.29348	91.9	4.844365	89	7.97645	60	163.9827	-3.25843	-53.1667	91.9	4.844365	92	4.844365	91.9	5.976935	91.5	113.7664	-0.0006	0.005
Z071	37.6	3.453	0.072	24.6	62.97229	3.582771	0.045	0.008524	0.24804	0.098	0.015637	0.01588	0.000903	0.032808	101.6	5.723338	94	14.00108	40	255.4925	-8.08511	-154	101.6	5.723338	102.5	5.723338	102.3	6.669135	101.5	114.6386	-0.004	0.011
Z072	83	0.822	0.012	1020	5.310674	0.276485	0.0709	0.00236	0.32824	1.837	0.130658	0.1883	0.009803	0.2796	1112	53.2024	1056	46.77113	937	65.65495	-5.30303	-18.6766	Discordant	Discordant	1110	53.2024	1043	46.06993	901	59.49716	0.00147	0.00088
Z073	159	1.391	0.044	73.5	93.54537	5.158946	0.0473	0.005606	-0.00986	0.0698	0.008181	0.01069	0.00059	0.26388	68.6	3.767701	68.1	7.72128	50	229.4031	-0.73421	-37.2	68.6	3.767701	68.6	3.767701	68.6	4.734783	68.6	166.8181	-0.0001	0.007
Z074	209	2.46	0.42	46.6	200	11.53007	0.0499	0.006814	-0.12504	0.0346	0.004508	0.005	0.000288	0.33777	32.1	1.828196	34.4	4.351328	120	183.0473	6.686047	73.25	32.1	1.828196	32	1.828196	32	2.447133	32.1	59.1529	0.0042	0.0082
Z075	28.4	1.293	0.091	11.9	111.7318	7.457681	0.054	0.017474	0.42505	0.059	0.017007	0.00895	0.000597	-0.31938	57.4	3.819587	55	16.20301	50	428.537	-4.36364	-14.8	57.4	3.819587	57	4.320028	57	4.995975	57.4	97.42847	0.009	0.025
Z076	530	1.19	0.11	150	138.3126	7.568711	0.0461	0.003576	-0.137	0.0461	0.004206	0.00723	0.000396	0.46243	46.4	2.538443	45.7	4.085423	20	116.1991	-1.53173	-132	46.4	2.538443	46.5	2.507726	46.5	3.160455	46.3	67.64085	-0.0011	0.0041
Z077	480	2.7	1.1	1830	13.96648	0.92216	0.0545	0.00149	-0.61896	0.542	0.046239	0.0716	0.004728	0.95043	445	28.71663	435	31.58736	383	57.68194	-2.29885	-16.188	445	28

Z079	531	2.037	0.021	440	59.03188	3.671593	0.057	0.00888	-0.85212	0.164	0.050823	0.01694	0.001054	0.97457	108.3	6.675249	126	23.34425	250	161.7816	14.04762	56.68	108.3	6.675249	105.3	5.738811	105.2	9.841187	102.2	37.51332	0.011	0.014
Z080	88	0.857	0.045	477	9.852217	0.517665	0.0584	0.002651	-0.06691	0.818	0.062357	0.1015	0.005333	0.52378	623	31.28091	604	34.58608	517	93.57414	-3.1457	-20.5029	623	31.28091	622	31.28091	595	32.98025	482	75.92918	0.0032	0.0015
Z081	657	1.9	0.11	104	272.5538	14.78966	0.0463	0.004402	0.21365	0.0231	0.002159	0.003669	0.000199	0.16473	23.61	1.276775	23.2	2.150775	50	163.9388	-1.76724	52.78	23.61	1.276775	23.59	1.285848	23.59	1.625295	23.62	104.9007	-0.0002	0.0052
Z082	114	1.501	0.018	39.5	126.7427	7.221096	0.0475	0.007003	0.4037	0.0505	0.006212	0.00789	0.00045	-0.11737	50.7	2.865202	49.8	6.018203	40	458.9769	-1.80723	-26.75	50.7	2.865202	50.7	2.942071	50.7	3.614106	50.7	418.2697	0.0006	0.0085
Z083	850	1.507	0.076	142	274.3484	14.7478	0.0502	0.004177	-0.03058	0.0253	0.002375	0.003645	0.000196	0.32308	23.45	1.258057	25.3	2.309069	180	119.977	7.312253	86.97222	23.45	1.258057	23.34	1.258057	23.34	1.747351	23.45	21.08726	0.0049	0.005
Z084	55.3	2.505	0.041	40.5	62.1504	3.431841	0.048	0.007359	0.30691	0.108	0.01321	0.01609	0.000888	-0.09607	102.9	5.642678	103	12.21797	70	307.001	0.097087	-47	102.9	5.642678	102.9	5.78161	102.9	7.187902	102.9	221.4886	-0.0001	0.0092
Z085	1070	2.53	0.091	484	99.50249	5.583339	0.0453	0.002286	-0.16483	0.0621	0.005238	0.01005	0.000564	0.73704	64.4	3.61968	61.1	5.043977	18	76.30874	-5.40098	-257.778	64.4	3.61968	64.6	3.61968	64.5	4.32963	62.3	30.28561	-0.0025	0.0029
Z086	110.6	1.055	0.015	72.6	68.21282	3.696489	0.0474	0.005563	0.34149	0.095	0.010149	0.01466	0.000794	-0.12043	93.8	5.043038	91.3	9.612097	60	212.2158	-2.73823	-56.3333	93.8	5.043038	94	5.136228	93.9	6.306584	94	142.2643	-0.0005	0.007
Z087	120	1.333	0.024	52.3	100	5.548009	0.0473	0.006517	0.01937	0.069	0.009831	0.01	0.000555	0.22771	64.2	3.536127	67	9.028451	100	284.6035	4.179104	35.8	64.2	3.536127	64	3.570154	63.9	4.689662	64.1	205.552	0.0001	0.0083
Z088	206	3.99	0.22	49.7	192.6782	10.74393	0.0509	0.006847	0.066204	0.0356	0.004279	0.00519	0.000289	0.18804	33.4	1.847102	36.4	4.451912	150	178.8477	8.241758	77.73333	33.4	1.847102	33.2	1.847102	33.2	2.48087	33.4	44.48735	0.0055	0.0084
Z089	355	7.81	0.13	122	117.2333	8.142555	0.0451	0.003871	0.31914	0.052	0.00504	0.00853	0.000592	0.56429	54.7	3.774019	51.3	4.842168	20	120.8114	-6.62768	-173.5	54.7	3.774019	54.9	3.828658	54.9	4.314	53.6	49.51656	-0.0025	0.0046
Z090	640	2.69	0.79	490	43.47826	3.017656	0.0456	0.002471	0.18427	0.143	0.012958	0.023	0.001596	0.65963	146.4	9.939359	135.5	11.3178	0	86.77083	-8.04428	#NAME?	146.4	9.939359	147.1	10.04731	146.5	11.01463	137	37.66241	-0.004	0.0034
Z091	126	1.654	0.044	37.8	140.4494	9.096037	0.0466	0.0073	0.36781	0.0442	0.005922	0.00712	0.000461	0.030407	45.7	2.967371	43.7	5.744531	10	262.4934	-4.57666	-357	45.7	2.967371	45.8	3.070064	45.8	3.547257	45.5	173.6567	-0.0003	0.0092
Z092	2140	1.409	0.042	762	116.144	6.135896	0.045	0.001694	0.26219	0.0533	0.003891	0.00861	0.000455	0.34582	55.2	2.895097	52.7	3.772434	25	55.50762	-4.74383	-120.8	55.2	2.895097	55.4	2.919621	55.3	3.589687	51.4	21.623	-0.0026	0.002
Z093	86	1.29	0.035	32.9	112.8668	6.828704	0.0506	0.00892	0.03838	0.062	0.009617	0.00886	0.000536	0.23409	56.9	3.412944	60	8.829665	90	277.1031	5.166667	36.77778	56.9	3.412944	56.6	3.457165	56.6	4.453985	56.9	144.8782	0.005	0.012
Z094	149	3.163	0.07	990	8.467401	0.464097	0.0614	0.001942	-0.14294	1.002	0.074518	0.1181	0.006473	0.77503	719	37.31213	702	37.69934	641	64.10857	-2.42165	-12.1685	719	37.31213	718	37.31213	690	37.06913	596	56.96497	0.00126	0.00082
Z095	201	2.24	0.45	102	90.09009	5.045421	0.0484	0.004686	0.31633	0.0733	0.007285	0.0111	0.000622	0.26565	71.2	3.987609	71.5	6.931065	110	439.2015	0.41958	35.27273	71.2	3.987609	71.1	3.987609	71	5.012431	69.8	418.3162	0.0014	0.0057
Z096	387	1.13	0.13	154	101.3171	5.566921	0.0427	0.003851	0.18592	0.0578	0.005709	0.00987	0.000542	0.2474	63.3	3.465861	56.9	5.487267	110	128.7013	-11.2478	42.45455	63.3	3.465861	63.7	3.498798	63.6	4.027666	63.2	26.34466	-0.0058	0.0051
Z097	670	15.6	1.7	357	75.58579	4.736001	0.046	0.002341	-0.30805	0.0822	0.006843	0.01323	0.000829	0.78856	84.7	5.270151	80.1	6.426992	22	80.35277	-5.74282	-285	84.7	5.270151	84.8	5.270151	84.7	6.077945	83.7	44.60519	-0.0021	0.0026
Z098	1010	2.17	0.4	541	91.40768	4.792145	0.052	0.003339	-0.47698	0.0789	0.007272	0.01094	0.000574	0.65003	70.2	3.648517	76.9	6.7753	230	109.8257	8.712614	69.47826	70.2	3.648517	69.8	3.648517	69.6	5.093201	67.8	39.86096	0.0061	0.0047
Z099	1230	3.44	0.49	385	145.7726	7.792107	0.052	0.004227	-0.26523	0.0484	0.004933	0.00686	0.000367	0.51697	44.1	2.341221	47.8	4.747312	240	135.4648	7.740586	81.625	44.1	2.341221	44	2.368864	43.9	3.275999	44.1	20.8272	0.0066	0.0062
Z100	45.3	2.012	0.054	27.8	63.0517	3.503732	0.041	0.009183	-0.00034	0.09	0.019099	0.01586	0.000881	0.06567	101.4	5.611077	84	17.47429	260	289.0502	-20.7143	61	101.4	5.611077	102.3	5.717795	102.2	6.25285	101.2	56.60345	-0.009	0.013
Z101	514	1.848	0.025	81.7	252.7167	13.27893	0.0431	0.004474	-0.16773	0.0236	0.00247	0.003957	0.000208	0.33834	25.46	1.334857	23.6	2.461885	100	127.6201	-7.88136	74.54	25.46	1.334857	25.56	1.334857	25.56	1.626246	25.37	20.37318	-0.0045	0.0053
Z102	548	0.39	0.023	237	100.2004	5.464215	0.0454	0.002839	0.048456	0.0625	0.005122	0.00998	0.000544	0.356	64	3.46658	61.5	4.923558	0	89.51916	-4.06504	#NAME?	64	3.46658	64.2	3.497739	64.1	4.267906	63.1	42.62254	-0.0023	0.0032
Z103	118.9	0.7551	0.0085	634	10.26694	0.536617	0.0569	0.002239	0.32292	0.768	0.055959	0.0974	0.005091	0.19515	599	29.99963	577	31.98854	481	82.83592	-3.81282	-24.5322	599	29.99963	598	29.99963	569	30.96428	452	65.49832	0.001	0.0019
Z104	317	1.592	0.03	198	70.12623	3.800714	0.0481	0.003113	-0.03624	0.0948	0.007854	0.01426	0.000773	0.457	91.3	4.896985	91.7	7.248003	110	157.7344	0.436205	17	91.3	4.896985	91.2	4.926648	91.1	6.220044	91.9	131.8398	0.0005	0.0034
Z105	77.5	1.594	0.025	36.3	101.3171	5.534554	0.0514	0.008519	0.19828	0.069	0.009831	0.00987	0.000539	0.005142	63.3	3.465861	67	9.028451	130	254.9286	5.522388	51.30769	63.3	3.465861	63	3.533184	63	4.689662	63.3	127.9945	0.005	0.011
Z106	77	1.53	0.07	800	6.02047	0.308681	0.0704	0.002542	0.035204	1.614	0.116798	0.1661	0.008516	0.39453	991	47.05367	973	45.37603	936	70.88782	-1.84995	-5.87607	991	47.05367	988	47.05367	955	43.67018	874	61.32114	0.0025	0.0013
Z107	3920	1.6	0.35	775	230.9469	13.84037	0.0495	0.002309	0.21858	0.03	0.002563	0.00433	0.000259	0.37693	27.9	1.64218	30	2.492281	158	78.07443	7	82.34177	27.9	1.64218	27.7	1.685039	27.7	2.205916	27.7	16.21071	0.0038	0.0031
Z108	3620	25.2	6.2	850	182.083	9.484844	0.0449	0.001709	0.16146	0.034	0.002479	0.005492	0.000286	0.36944	35.31	1.833737	33.9	2.440662	29	54.51324	-4.15929	-21.7586	35.31	1.833737	35.39	1.837992	35.37	2.307809	34.95	16.47862	-0.0022	0.002
Z109	253	0.6	0.026	207	55.55556	2.937813	0.0479	0.003463	0.26989	0.1178	0.00971	0.018	0.000952	0.20684	115	6.025969	112.8	8.843732	90	134.4478	-1.95035	-27.7778	115	6.025969	115.1	6.077195	114.8	7.476069	110.5	95.70895	-0.0004	0.0042
Z110	3210	186.4	3.8	1506	89.3655	4.916782	0.0448	0.001194	0.020369	0.0692	0.005094	0.01119	0.000616	0.76562	71.7	3.912089	67.9	4.815607	36	39.04227	-5.59647	-99.1667	71.7	3.912089	72	3.912089	71.9	4.700943	70.5	16.48635	-0.0033	0.0014
Z111	1300	51.9	8.2	13200	5.685048	0.331146	0.0668	0.001008	0.36088	1.621	0.118722	0.1759	0.010246	0.90519	1044	56.09685	976	45.73356	829	30.16845	-6.96721	-25.9349	Discordant	Discordant	1044	56.09685	976	45.73356	828	29.47194	0	1
Z112	148	1.1048	0.009	121	112.3596	8.72775	0.098	0.025119	-0.04566	0.129	0.031159	0.0089	0.000691	0.52127	57.1	4.428683	117	25.63136	900	346.5311	51.19658	93.65556	57.1	4.428683	53.9	5.252869	55	8.900878	59.7	8.398016	0.083	0.045
Z113	67	0.5703	0.0065	28.3	148.1481	9.921491	0.065	0.014628	-0.20295	0.063	0.012551	0.00675	0.000452	0.44415	43.4	2.877307	60	11.74611	360	347.0048	27.66667	87.94444	43.4	2.877307	42.2	2.826215	42.3	4.441945	43.4	19.59344	0.024	0.02
Z114	211	3.86	0.12	40.9	225.7336	12.16097	0.0478	0.007642	0.1991	0.0289	0.004043	0.00443	0.000239	-0.04698	28.52	1.535743	28.8	3.962111	30	306.6388	0.972222	4.933333	28.52	1.535743	28.5	1.56652	28.5	2.02781	28.59	220.9743	0.0015	0.0099
Z115	504	0.86	0.13	218	118.0638	10.86806	0.0472	0.00493	0.13514	0.0529	0.006367	0.00847	0.00078	0.74747	54.3	4.980269	52.1	6.16585	40	197.9218	-4.22265	-35.75	54.3	4.980269	54.5	4.980269	54.4	5.407264	50.7	119.9658	0.0003	0.0073
Z116	294	0.767	0.018	88	144.5087	7.61083	0.0484	0.00524	0.56654	0.0452	0.004496	0.00692	0.000364	-0.35729	44.45	2.327104	44.8	4.379642	90	314.7185	0.78125	50.61111	44.45	2.327104	44.4	2.359266	44.4	3.062526	43.9	276.8869	0.002	0.0065
Z117	100.4	2.167	0.055	64.7	68.58711	3.705813	0.0469	0.005147	0.21195	0.094	0.009624	0.01458	0.000788	0.066975	93.3	4.990622	92.6	9.269318	90	188.4862	-0.75594	-3.66667	93.3	4.990622	93.3	5.049901	93.3	6.201053	93.5	124.2671	-0.0012	0.0058
Z118	252	1.169	0.032	135	80.32129	4.448691	0.0471	0.003651	0.22837	0.0805	0.006893	0.01245	0.00069	0.17888	79.8	4.405319	78.4	6.490232	70	140.2556	-1.78571	-14	79.8	4.405319	79.8	4.439666	79.7	5.465521	78.6	103.6784	-0.0005	0.004
Z120	34.2	1.817	0.069	36.2	42.82655	2.41386	0.0525	0.009093	0.14708	0.168	0.026908	0.02335	0.001316	0.092199	148.8	8.294967	153	23.42813	140	6595.648	2.745098	-6.28571	148.8	8.294967	148.2	8.481597	148.2	10.66125	148.8	6591.13	0.004	0.012
Z121	71.8	1.071	0.011	41.1	92.08103	5.149743	0.0571	0.008631	0.14757	0.085	0.01105	0.01086	0.000607	0.14565	69.6	3.849842	82	10.1865	330	210.8139	15.12195	78.90909	69.6	3.849842	68.8	3.920061	68.8	5.659021	69.5	50.33141	0.012	0.011
Z122	108.1	1.763	0.049	35.5	120.3369	7.116958	0.0403	0.007103	0.19149	0.0455	0.006865	0.00831	0.000491	0.022117	53.4	3.138038	46.5	7.039093	200	214.6462	-14.8387	73.3	Discordant	Discordant	53.8	3.223799	53.7	3.485746	53.4	29.62675	-0.0087	0.0094
Z123	1123	0.53	0.074	4680	12.56281	0.654211	0.0539	0.001087	0.3336	0.591	0.041128	0.0796	0.004145	0.52661	493.5	24.73895	471.4	26.22897	359	41.86245	-4.68816	-37.4652	493.5	24.73895	493.3	24.75987	468.3	26.2097	342	36.6844	0.00037	0.00034
Z124	1230	4.72	0.49	467	126.2626	6.64899	0.0516	0.003387	-0.46427	0.0567	0.005265	0.00792	0.000417	0.63655	50.9	2.686316	55.9	5.048557	220	113.3372	8.944544	76.86364	50.9	2.686316	50.6	2.661972	50.6	3.755627	50.7	26.34278	0.006	0.0048
Z125	9990	37.9	4.3	2970	153.1394	9.063659	0.0457	0.00104	-0.04138	0.0411	0.003148	0.00653	0.000386	0.92451	42	2.489889	40.9	3.088277	0	37.58759	-2.68949	#NAME?	42	2.489889	42	2.489889	42	3.015137	41	14.68969	-0.0015	0.0013
Z126	41.3	1.705	0.05	33.3	56.30631	3.234652	0.0477	0.008592	0.28172	0.114	0.018233	0.01776	0.00102	-0.08529	113.5	6.465977	107	17.23507	20	322.149	-6.07477	-467.5	113.5	6.465977	113.7	6.666623	113.7	7.848741	113.5	200.7533	-0.001	0.011
Z127	1390	1.88	0.35	1230	74.51565	5.242185	0.08	0.011162	-0.27626	0.188	0.060399	0.01342	0.000944	0.86324	85.9	6.03683	142	28.87924	990	252.0255	39.50704	91.32323	85.9	6.03683	83.5	6.495915	85	11.97854	86	8.768165	0.042	0.018
Z128	569	10.1	0.12	72	319.081	16.81952	0.0432	0.004772	0.28876	0.0186	0.001892	0.003134	0.000165	-0.12079	20.17	1.061317	18.7	1.889577	100	135.1253	-7.86096	79.83	20.17	1.061317	20.22	1.076629	20.22	1.303327	20.17	18.46516	-0.0041	0.0057
Z129	548	3.01	0.17	8230	5.627462	0.316239	0.0941	0.001545	-0.06308	2.313	0.171575	0.1777	0.009986	0.8984	1054	54.58989	1213	52.62115	1507	35.3282	13.108	30.05972	1054	54.58989	1030	54.94649	1038	54.01653	1054	34.77099	0.0242	0.0023
Z130	739	6.64	0.11	135	244.4988	12.8385	0.0476	0.004002	0.12717	0.0269	0.002454	0.00409	0.000215	0.20144	26.31	1.377985	27	2.438866	110	188.5117	2.555556	76.08182	26.31	1.377985	26.37	1.397642	26.37	1.849982	26.31	146.9245	0.0014	0.0048
Z131	123	0.688	0.056	528	11.99041	0.62858	0.056	0.002426	0.19369	0.643	0.047599	0.0834	0.004372	0.29661	516.4	26.0103	503	29.27187	427	89.9616	-2.66402	-20.9368	516.4	26.0103	516.1	26.10262	499	28.14893	419	70.14663	0.0008	0.0024
Z132	521	3.38	0.14	207	99.9001	5.210649	0.0442	0.003228	-0.10775	0.0611	0.005484	0.01001	0.000522	0.33216	64.2	3.322128	60.1	5.247134	50	107.3107	-6.82196	-28.4	64.2	3.322128	64.5	3.322128	64.5	4.034775	64.2	32.22327	-0.004	0.004
Z133	143.2	1.985	0.064	53.8	145.7726	8.513238	0.0596	0.008441	0.12465	0.0561	0.007482	0.00686	0.000401	0.22204	44.1	2.539393	55	7.136992	400	197.8682	19.81818	88.975	44.1	2.539393	43.4	2.579364	43.4	3.873971	43.9	20.09536	0.016	0.011
Z134	541	10.2	2.2	637	46.72897	4.597951	0.0663	0.002761	-0.09943	0.196	0.023057	0.0214	0.002106	0.94579	136	13.61876	180	19.33352	797	64.20435	24.44444	82.93601	136	13.61876	133	12.94181	133	15.72594	136	24.20162	0.0226	0.0032
Z135	381	0.879	0.024	142	112.3596	6.289827	0.0454	0.003483	0.09929	0.0556	0.004845	0.0089	0.000498	0.35278	57.1	3.187199	54.9	4.684702	0	107.8279	-4.00729	#NAME?	57.1	3.187199	57.2	3.187199	57.2	3.873297	57	51.96981	-0.0021	0.0038
Z136	1043	4.698	0.05	291	152.952	7.871012	0.0455	0.002552	0.02086	0.041	0.003181	0.006538	0.000336	0.26312	42.01	2.154457	40.8	3.121726	2	79.75872	-2.96569	-2000.5	42.01	2.154457	42.08	2.157965	42.06	2.737859	41.52	36.60343	-0.0017	0.0028
Z137	604	0.8576	0.0082	163	147.0588	7.616285	0.0426	0.002947	-0.0675	0.0401	0.003344	0.0068	0.000352	0.33928	43.71	2.254112	39.8	3.24545	119	79.65602	-9.82412	63.26891	43.71	2.254112	43.94	2.254112	43.9	2.695468	43.2	19.7826	-0.0054	0.0032
Z138	19.8	2.881	0.06	17.6	55.46312	3.491804	0.052	0.012587	0.19147	0.133	0.028233	0.01803	0.001135	0.11766	115.2	7.18355	121	24.95073	80	983.5277	4.793388	-44	115.2	7.18355	114.4	7.377709	114.3	9.280158	113.5	926.2708	0.004	0.017
Z139	1450	10.97	0.53	4040	47.16981	5.133806	0.121	0.003591	-0.64297	0.367	0.047837	0.0212	0.002307	0.98778	135	14.97708	308	35.78545	1954	49.73029	56.16883	93.0911	Discordant	Discordant	122	13.58797	123	21.84213	135	13.83841	0.0926	0.0049
Z140	393	2.417	0.034	592	29.6824	1.53475	0.0488	0.002043	-0.15644	0.2272	0.017183	0.03369	0.001742	0.50458	213.6	10.86245	207.5	14.18491	137	80.36037	-2.93976	-55.9124	213.6	10.86245	213.9	10.86245	212	12.96644	193	53.88255	-0.0014	0.0023

16letkat					Isotopic Ratios + measurement uncertainty (2s)										Ages uncorrected for common lead + measurement uncertainty (2s)									Ages corrected for common lead (Andersen routine) + measurement uncertainty (2s)							
					Data for Tera-Wasserburg plot					Data for Wetherill plot																				
Sample	U (ppm)	U/Th	U/Th uncertainty 2SE	207Pb (cps)	U238/Pb 206	U238/Pb 206 uncertainty (2s)	Pb207/Pb 206	Pb207/Pb 206 uncertainty (2s)	ρ	Pb207/U 235	Pb207/U 235 uncertainty (2s)	Pb206/U 238	Pb206/U 238 uncertainty (2s)	ρ	Age Pb206/U 238	Age Pb206/U 238 measurement uncertainty (2s)	Age Pb207/U 235	Age Pb207/U 235 measurement uncertainty (2s)	Age Pb207/Pb 206	Age Pb207/Pb 206 measurement uncertainty (2s)	Discordance Pb206/U 238 vs Pb207/U 235 (%)	Concordance Pb206/U 238 vs Pb207/Pb 206 (%)	Best age	Best age measurement uncertainty (2S)	Age Pb206/U 238	Age Pb206/U 238 measurement uncertainty (2s)	Age Pb207/U 235	Age Pb207/U 235 measurement uncertainty (2s)	Age Pb207/Pb 206	Age Pb207/Pb 206 measurement uncertainty (2s)	Common Lead fraction	Common Lead fraction uncertainty (2s)
Z001	103	2.17	0.32	76	121.8027	8.326335	0.096	0.016786	0.026458	0.132	0.027573	0.00821	0.000561	0.31019	52.7	3.630743	121	22.82821	1320	322.9546	56.44628	96.00758	52.7	3.630743	47.9	3.764876	49.6	6.669147	55.7	9.819781	0.072	0.029
Z002	1240	0.523	0.036	565	122.1001	5.577022	0.0705	0.005405	-0.25497	0.0808	0.00755	0.00819	0.000374	0.50844	52.6	2.39641	78.5	7.086383	820	141.8483	32.99363	93.58537	52.6	2.39641	51	2.306769	51	3.999102	52.6	5.911311	0.0298	0.0078
Z003	1950	0.558	0.053	576	124.6883	5.887006	0.05	0.00268	0.0537	0.0555	0.003967	0.00802	0.000379	0.56917	51.5	2.412465	54.7	3.836846	180	98.61875	5.850091	71.38889	51.5	2.412465	51.3	2.412465	51.3	3.060161	51.9	47.18747	0.0035	0.0035
Z004	180.3	1.91	0.14	68.7	118.0638	7.006825	0.0631	0.008248	-0.0303	0.0706	0.007988	0.00847	0.000503	0.36044	54.4	3.215625	68.9	7.483561	520	190.0472	21.04499	89.53846	54.4	3.215625	52.1	3.03408	52.1	4.052516	54.2	20.30449	0.02	0.01
Z006	283	0.844	0.033	148	66.09385	3.107793	0.0473	0.004274	0.31708	0.0952	0.007403	0.01513	0.000711	0.10363	96.8	4.490508	93.8	7.309352	90	164.1973	-3.19829	-7.55556	96.8	4.490508	96.8	4.588841	95.8	5.161649	95.6	105.3526	-0.0009	0.0052
Z007	1500	7.86	0.29	89100	2.457002	0.107115	0.1961	0.004621	0.52752	10.98	0.610797	0.407	0.017743	0.62146	2196	82.15261	2516	51.83227	2783	39.15183	12.7186	21.09235	Discordant	Discordant	2076	88.65715	2148	70.9369	2206	46.15112	0.065	0.011
Z008	5930	3.07	0.17	1732	127.0648	5.459505	0.0499	0.001868	0.44612	0.0536	0.003069	0.00787	0.000338	0.18881	50.6	2.159927	53	2.946116	181	73.10819	4.528302	72.0442	50.6	2.159927	50.4	2.201155	50.4	2.840035	50.1	29.43982	0.0035	0.0026
Z009	172	2.14	0.086	104	65.74622	3.521632	0.0536	0.005406	-0.05217	0.1089	0.009509	0.01521	0.000815	0.47812	97.3	5.19478	104.4	8.729288	290	182.1842	6.800766	66.44828	97.3	5.19478	94.9	4.808652	94.8	5.939736	96	114.5477	0.007	0.0064
Z010	249	2.13	0.17	97	90.7441	4.441319	0.0466	0.00552	0.20944	0.0716	0.00794	0.01102	0.000539	0.079035	70.6	3.454958	69.8	7.433314	60	196.7367	-1.14613	-17.6667	70.6	3.454958	70.7	3.507496	70.7	4.133637	70.6	106.6235	-0.0012	0.0072
Z011	655	5	0.73	96	239.2344	14.67029	0.0482	0.006704	0.47225	0.0267	0.003133	0.00418	0.000256	0.033765	26.9	1.665003	26.7	3.055839	130	230.1023	-0.74906	79.30769	26.9	1.665003	26.8	1.72894	26.8	1.936996	26.5	88.0389	0.0018	0.0094
Z012	107	1.39	0.11	119	59.70149	3.027591	0.096	0.013365	-0.57974	0.228	0.034237	0.01675	0.000849	0.72268	107.1	5.390013	202	27.64115	1240	244.6405	46.9802	91.3629	107.1	5.390013	99.3	4.790766	99.6	9.820802	106.9	16.75294	0.06	0.019
Z013	488	4.32	0.45	250	65.78947	2.871484	0.0477	0.003146	0.42532	0.0987	0.006514	0.0152	0.000663	0.14082	97.2	4.18871	95.5	6.024998	90	130.784	-1.7801	-8	97.2	4.18871	97.3	4.273698	97.2	5.136205	94.7	98.03309	-0.0005	0.0036
Z015	49.2	1.926	0.068	204	10.74114	0.466105	0.0602	0.004825	0.3072	0.75	0.055522	0.0931	0.00404	0.089023	573	23.85745	569	33.29113	530	172.1378	-0.70299	-8.11321	573	23.85745	572	24.28246	550	25.54603	479	122.7654	0.004	0.0057
Z016	650	1.8	0.15	173	145.5604	8.696973	0.0513	0.004478	-0.12478	0.0489	0.004837	0.00687	0.00041	0.64591	44.1	2.612555	48.3	4.729364	220	139.0154	8.695652	79.95455	44.1	2.612555	43.9	2.612555	43.9	3.129422	44.1	37.56967	0.0055	0.0056
Z017	737	1.446	0.056	654	41.27115	1.840037	0.0497	0.002434	0.40897	0.1647	0.01032	0.02423	0.00108	0.2395	154.3	6.778744	154.5	8.956032	174	115.0645	0.12945	11.32184	154.3	6.778744	154.1	6.913231	153.6	8.187901	149.9	85.48935	0.0007	0.0031
Z018	146	1.415	0.053	71	97.56098	4.544175	0.058	0.00919	-0.03206	0.082	0.011761	0.01025	0.000477	0.065329	65.7	3.065285	79	10.93544	300	246.7012	16.83544	78.1	65.7	3.065285	64.8	3.164803	65.9	4.599195	66.7	35.84744	0.013	0.013
Z019	646	2.384	0.091	200	111.2347	4.676391	0.0476	0.003528	0.29026	0.0585	0.004128	0.00899	0.000378	0.12305	57.7	2.426304	57.6	3.988485	80	215.4428	-0.17361	27.875	57.7	2.426304	57.7	2.465593	57.7	3.075713	57.7	189.5759	0.0004	0.0041
Z020	9500	30.52	0.84	7210	47.75549	1.985952	0.0485	0.001149	0.32592	0.139	0.007697	0.02094	0.000871	0.49084	133.6	5.491117	132.1	6.846503	121	50.67724	-1.1355	-10.4132	133.6	5.491117	133.7	5.527691	133.1	6.718527	127.4	24.05017	-0.0003	0.0017
Z021	79.2	1.502	0.078	41	91.91176	5.237481	0.063	0.017055	-0.13712	0.093	0.023303	0.01088	0.00062	0.13596	69.7	3.937947	87	18.61829	250	285.5702	19.88506	72.12	69.7	3.937947	66.5	4.696235	66.5	5.844706	71	34.91717	0.009	0.014
Z022	150.2	2.05	0.17	102.1	55.24862	2.525221	0.0503	0.004873	0.31205	0.124	0.010022	0.0181	0.000827	0.001955	115.7	5.272953	117.8	9.094609	190	655.3359	1.782683	39.10526	115.7	5.272953	115.5	5.368504	115.4	6.504346	115.6	643.1198	0.0024	0.0055
Z023	437	1.41	0.15	83	220.2643	9.331422	0.0532	0.006594	0.011529	0.0333	0.003844	0.00454	0.000192	0.25789	29.21	1.246016	33.2	3.760415	280	182.2403	12.01807	89.56786	29.21	1.246016	28.87	1.242054	28.87	1.750389	29.5	20.34659	0.0082	0.0084
Z024	263	1.588	0.082	78	122.2494	5.801449	0.0507	0.005763	0.47608	0.0549	0.005127	0.00818	0.000388	-0.09189	52.5	2.490972	54.1	4.939319	180	179.8068	2.957486	70.83333	52.5	2.490972	51.9	2.646647	51.9	3.203259	52.5	86.79261	0.0044	0.0068
Z025	103	1.03	0.05	76	65.83278	3.383136	0.065	0.010763	0.17818	0.137	0.020101	0.01519	0.000781	0.14004	97.1	4.967017	128	17.63069	550	262.4592	24.14063	82.34545	97.1	4.967017	94.3	5.425206	94.3	7.361128	97.1	37.13301	0.021	0.015
Z026	89.8	2.133	0.035	58	59.70149	2.706143	0.066	0.021304	-0.01798	0.149	0.046273	0.01675	0.000759	0.03678	107.1	4.83649	114	16.34516	180	217.3874	6.052632	40.5	107.1	4.83649	105.1	5.444376	106.1	7.298242	107.1	45.4728	0.019	0.028
Z027	99	1.133	0.059	64	60.38647	3.059166	0.053	0.006661	0.033256	0.121	0.01327	0.01656	0.000839	0.16752	105.8	5.304228	115	12.31058	280	281.9127	8	62.21429	105.8	5.304228	104.9	5.412988	104.8	6.656957	107.3	216.0915	0.006	0.0079
Z028	84.8	0.566	0.025	594	7.199424	0.313965	0.0683	0.003114	0.43288	1.294	0.075737	0.1389	0.006057	0.23912	838	34.1996	845	33.06883	870	94.01089	0.828402	3.678161	838	34.1996	834	34.623	801	32.31018	717	77.98812	0.0067	0.0023
Z029	352	0.936	0.058	1285	12.04819	0.522397	0.0578	0.002309	0.17288	0.643	0.037698	0.083	0.003599	0.46007	514	21.30409	507	23.9573	494	86.02364	-1.38067	-4.04858	514	21.30409	512	21.72198	494	23.11433	411	62.0829	0.0032	0.0024
Z030	94.3	1.409	0.065	57.4	68.25939	2.896801	0.0547	0.007799	0.27961	0.109	0.013008	0.01465	0.000622	-0.12258	93.8	3.958651	104	12.10039	270	230.8007	9.807692	65.25926	93.8	3.958651	93	4.081265	93	5.455295	93.6	106.5872	0.0085	0.0099
Z031	1480	2.14	0.25	574	97.46589	4.320192	0.0486	0.002469	0.31408	0.0681	0.004331	0.01026	0.000455	0.22134	65.8	2.927496	66.8	4.102024	150	793.0292	1.497006	56.13333	65.8	2.927496	65.7	2.927496	65.6	3.634832	63.2	788.2893	0.0015	0.0031
Z032	539	0.793	0.062	141	147.929	6.115279	0.0541	0.004999	0.3609	0.0503	0.004218	0.00676	0.000279	-0.08866	43.5	1.780763	49.8	4.041516	310	143.6608	12.6506	85.96774	43.5	1.780763	43.3	1.897082	43.3	2.608535	43.8	23.48689	0.0091	0.0062
Z033	84.1	1.45	0.062	60	61.7284	3.057896	0.0592	0.009114	-0.16392	0.131	0.01852	0.0162	0.000803	0.30145	103.6	5.083686	122	16.07481	370	230.7035	15.08197	72	103.6	5.083686	100.8	5.298666	102.1	6.865448	99.5	68.09538	0.014	0.012
Z034	573	0.769	0.098	7900	5.238345	0.263673	0.0911	0.00269	-0.03322	2.39	0.157348	0.1909	0.009609	0.83475	1124	52.05241	1239	49.81424	1429	58.75426	9.281679	21.3436	1124	52.05241	1107	53.13693	1105	50.36506	1107	42.90318	0.0172	0.004
Z035	1120	15	1.8	9830	6.285355	0.272519	0.073	0.001718	0.11533	1.594	0.09265	0.1591	0.006898	0.70675	951	38.53823	964	36.07294	1003	47.70971	1.348548	5.184447	951	38.53823	947	38.96222	928	36.47461	896	30.3667	0.0051	0.002
Z036	503	1.082	0.017	2230	9.960159	0.388199	0.0593	0.001593	0.41536	0.816	0.043456	0.1004	0.003913	0.23373	616.8	22.85563	605	24.4015	565	57.07575	-1.95041	-9.16814	616.8	22.85563	615.5	22.93078	590.8	23.86469	501	45.3577	0.002	0.0011
Z037	901	1.464	0.028	9290	5.640158	0.223023	0.078	0.001335	0.27139	1.89	0.09961	0.1773	0.007011	0.61651	1052	38.24254	1076	34.98415	1142	34.31954	2.230483	7.880911	1052	38.24254	1047	38.52522	1038	35.51184	1026	25.81338	0.0049	0.0015
Z038	1130	1.01	0.063	790	52.49344	2.252643	0.051	0.002258	0.23867	0.132	0.008026	0.01905	0.000817	0.37906	121.6	5.150292	125.7	7.198064	223	680.6597	3.261734	45.47085	121.6	5.150292	120.4	5.359712	119.7	6.598115	112.9	677.2237	0.0035	0.0028
Z039	81.4	1.579	0.051	652	6.506181	0.274614	0.0704	0.003098	0.27306	1.481	0.087837	0.1537	0.006487	0.41487	921	36.50002	919	36.13796	912	91.10563	-0.21763	-0.98684	921	36.50002	917	36.89704	879	35.71515	786	76.63508	0.0045	0.0019
Z040	73.7	1.626	0.037	36.1	93.19664	4.22944	0.059	0.0102	-0.0771	0.085	0.013296	0.01073	0.000487	0.50113	68.8	3.107544	82	11.71917	330	256.3104	16.09756	79.15152	68.8	3.107544	67.9	3.201879	67.9	4.437789	68.8	47.01362	0.014	0.013
Z041	322	1.48	0.29	133	103.0928	5.412061	0.0589	0.007488	-0.13916	0.077	0.009479	0.0097	0.000509	0.24322	62.2	3.230531	75	8.67035	420	206.054	17.06667	85.19048	62.2	3.230531	60.4	3.401607	60.5	4.418572	62.2	23.48366	0.014	0.011
Z042	92.4	1.384	0.038	64.4	63.13131	2.724171	0.0591	0.008441	0.04143	0.128	0.015551	0.01584	0.000684	-0.03628	101.3	4.314927	120	13.85314	380	214.5288	15.58333	73.34211	101.3	4.314927	99.9	4.528752	101.6	6.933669	100.2	64.29375	0.014	0.011
Z043	790	2.4	0.15	429	68.39945	2.9042	0.0522	0.003056	0.33025	0.1028	0.006523	0.01462	0.000621	0.1229	93.6	3.952639	99.3	6.00774	260	129.8283	5.740181	64	93.6	3.952639	93.1	3.992437	92.9	5.156388	91.3	89.0836	0.0054	0.0039
Z044	736	1.57	0.05	222	126.9036	5.209414	0.051	0.00346	-0.04931	0.0548	0.003722	0.00788	0.000323	0.28371	50.6	2.086046	54.1	3.593769	220	105.1438	6.469501	77	50.6	2.086046	50.2	2.086046	50.2	2.801746	50.2	46.13307	0.0049	0.0038
Z045	216.7	0.86	0.035	185	47.21435	2.215797	0.0527	0.004785	-0.17802	0.152	0.01339	0.02118	0.000994	0.47624	135.1	6.263153	143	11.58243	250	594.0413	5.524476	45.96	135.1	6.263153	133.5	6.074199	133.1	7.578106	129.2	582.2189	0.0051	0.0062
Z046	227	0.3129	0.0051	119	239.2344	12.29814	0.162	0.01584	0.088294	0.0898	0.007672	0.00418	0.000215	0.37603	26.9	1.368662	86.9	7.109194	2390	133.8821	69.04488	98.87448	26.9	1.368662	22.9	1.424161	22.9	4.306813	26.9	2.702779	0.148	0.019
Z048	183	1.442	0.051	114	64.22608	2.872983	0.0523	0.00549	0.23994	0.109	0.009383	0.01557	0.000696	0.024836	99.6	4.432679	104.6	8.538867	260	243.3649	4.780115	61.69231	99.6	4.432679	98.8	4.524052	98.7	5.662742	98.2	185.5666	0.0054	0.007
Z049	536	0.822	0.025	80.1	236.9668	10.71338	0.0466	0.005639	0.16543	0.0271	0.002792	0.00422	0.000191	0.071418	27.15	1.21628	27.1	2.71558	20	246.5062	-0.1845	-35.75	27.15	1.21628	27.15	1.234495	27.15	1.522873	27.15	189.6465	-0.0002	0.007
Z050	724	1.362	0.027	171	156.0062	6.811494	0.0481	0.003567	0.30638	0.0426	0.003009	0.00641	0.00028	0.2449	41.2	1.785549	42.3	2.914502	100	302.3069	2.600473	58.8	41.2	1.785549	41.1	1.785549	41.1	2.279456	40.7	287.1628	0.0014	0.0039
Z052	340	2.24	0.1	58	246.9136	11.91666	0.055	0.008622	-0.13141	0.0304	0.004515	0.00405	0.000195	0.21799	26.1	1.241224	30.2	4.359856	330	236.7999	13.57616	92.09091	26.1	1.241224	25.31	1.221486	25.31	1.677778	26.1	16.57699	0.011	0.012
Z053	1790	0.732	0.063	427	213.2196	9.73177	0.08	0.009159	-0.30758	0.0518	0.006957	0.00469	0.000214	0.42058	30.1	1.361257	50.9	6.631171	930	196.8704	40.86444	96.76344	30.1	1.361257	28.43	1.304722	28.55	2.594562	29.58	2.924725	0.042	0.015
Z054	175	1.94	0.12	123	60.64281	2.649652	0.064	0.010304	-0.05328	0.15	0.027045	0.01649	0.00072	0.099435	105.4	4.566094	137	21.51678	430	215.5499	23.06569	75.48837	105.4	4.566094	105.2	5.031224	105.1	7.367084	104.6	35.77529	0.02	0.015
Z055	94.7	1.11	0.036	57.1	65.27415	2.790495	0.0512	0.007001	0.054786	0.106	0.012946	0.01532	0.000655	0.46221	98	4.171609	102	11.33383	180	519.976	3.921569	45.55556	98	4.171609	97.7	4.254024	97.7	5.374925	97.9	484.4249	0.0038	0.0086
Z056	167	1.115	0.021	90	71.89073	3.155711	0.0521	0.005611	-0.05981	0.0975	0.009194	0.01391	0.000611	0.38417	89	3.894827	96	9.006026	230	218.6483	7.291667	61.30435	89	3.894827	88	3.811152	88.5	4.986191	88.3	159.4699	0.0053	0.0067
Z057	123	1.92	0.35	132	40.68348	1.945907	0.0656	0.007376	0.3133	0.215	0.019723	0.02458	0.001176	-0.09452	156.5	7.408492	201	18.13035	630	175.6721	22.1393	75.15873	156.5	7.408492	152.5	7.771586	152.6	10.37866	154.4	59.56683	0.0207	0.0099
Z058	229	0.775	0.022	1602	7.062147	0.310522	0.0669	0.002163	0.39217	1.279	0.074284	0.1416	0.006226	0.69956	853	35.03795	839	32.18114	818	66.62705	-1.66865	-4.27873	853	35.03795	850	35.46883	812	31.82273	716	53.9754	0.0033	0.0014
Z059	169.6	0.808	0.037	1291	7.230658	0.297561	0.0715	0.002442	0.14468	1.354	0.07678	0.1383	0.005691	0.86569	835	32.18908	867	33.17763	969	70.61895	3.690888	13.82869	835	32.18908	829	32.54346	814	31.80369	798	56.99066	0.0072	0.0022
Z060	53.9	1.91	0.1	41	57.01254	3.007963	0.0544	0.008583	0.12399	0.139	0.019398	0.01754	0.000925	0.46009	112	5.850539	129	16.92297	290	296.2863	13.17829	61.37931	112	5.850539	110.8	5.963892	110.6	7.514387	108.7	198.0079	0.007	0.011
Z061	365	1.24	0.046	222	59.41771	2.421786	0.0481	0.003527	0.2061	0.11	0.00807	0.01683	0.000686	0.23925	107.6	4.367177	105.7	7.347213	100	152.2139	-1.79754	-7.6	107.6	4.367177	107.7	4.367177	107.5	5.374379	105	112.6903	-0.0011	0.0039
Z062	90	0.88	0.062	349	11.60093	0.526961	0.0615	0.003839	0.18258	0.722	0.049493	0.0862	0.003916	0.23104	533	23.14165	548	28.99335	600	143.1313	2.737226	11.16667	533	23.14165	529	23.60585	511	24.73529	455	112.0293	0.0065	0.0043
Z063	6700	0.459	0.033	1700	124.6883	5.737459	0.0453	0.001497	0.32561	0.0502	0.003006	0.00802	0.000369	0.59414	51.5	2.364442	49.7	2.892973	13	52.61985	-3.62173	-296.154	51.5	2.364442	51.6	2.364442	51.6	2.810355	51	17.6224	-0.0025	0.0019
Z064	710	3.64	0.74	231	132.9787	11.53829	0.08	0.014699	0.02112	0.072	0.010111	0.00752	0.000652	0.14615	48.2	4.175767	70	9.308448	730	259.915	31.14286	93.39726	48.2	4.175767	46.1	4.607757	46.3	5.389156	48.3	7.2603	0.041	0.023
Z065	784	1.149	0.021	399	83.33333	3.459796	0.0581	0.003543	-0.13184	0.0957	0.007122	0.012	0.000498	0.4388	76.9	3.192824	92.6	6.537031	480	96.73873	16.95464	83.97917	76.9	3.192824	75.7	3.156695	75.8	4.655252	76.8	20.79954	0.0132	0.0044
Z066	324	1.57	0.072	178	69.01311	2.955567	0.0541	0.004553	0.10438	0.1076	0.008773	0.01449	0.000621	0.24178	92.7	3.926616	103.3	8.062476	320	145.0311	10.26137	71.03125	92.7	3.926616	92	3.966675	92	5.340086	91.8	71.87868	0.0079	0.0057
Z067	200	1.423	0.075	83	100.1001	5.819618	0.0554	0.006946	0.13164	0.0749	0.008436	0.00999	0.000581	0.21316	64.1	3.744819	73.1	7.920537	430	232.3061	12.3119	85.09302	64.1	3.744819	63.1	3.806399	63.1	4.633325	63.2	42.79862	0.01	0.009
Z068	1192	1.529	0.063	335	129.0323	6.01199	0.0492	0.003179	0.099543	0.053	0.004056	0.00775	0.000361	0.35511	49.7	2.314146	52.3	3.934784	170	138.2739	4.971319	70.76471	49.7	2.314146	49.6	2.314146	49.6	2.922075	49.4	92.97263	0.0026	0.0041
Z069	5520	17.11	0.43	1400	141.6431	5.950072	0.0485	0.001971	-0.02567	0.047	0.003016	0.00706	0.000297	0.51069	45.3	1.916694	46.6	2.91098	118	105.5938	2.7897	61.61017	45.3	1.916694	45.2	1.916694	45.2	2.467145	45.2	81.027	0.0017	0.0027
Z070	290	1.303	0.081	107	99.8004	4.64037	0.049	0.004436	0.12544	0.067	0.00523	0.01002	0.000466	0.22636	64.3	2.974666	65.7	5.004914	140	712.0449	2.130898	54.07143	64.3	2.974666	64.2	3.02325	64.1	3.705964	63.3	702.1844	0.002	0.0047
Z071	284	2.48	0.15	274	42.48088	1.903536	0.0519	0.003329	0.38549	0.1716	0.011487	0.02354	0.001055	0.14473	150	6.649347	162.6	10.49175	320	519.7084	7.749077	53.125	150	6.649347	148.9	6.740105	148.5	8.413899	146.3	507.9278	0.0035	0.004
Z072	210	1.608	0.092	113	73.42144	3.110474	0.0541	0.004946	0.14655	0.1009	0.008132	0.01362	0.000577	0.26272	87.2	3.673702	97.2	7.518406	320	147.8346	10.28807	72.75	87.2	3.673702	86.5	3.71315	86.5	5.022213	87	77.37141	0.0079	0.0055
Z073	278	9.88	0.75	969	13.08901	0.513837	0.0591	0.002559	0.25497	0.62	0.03715	0.0764	0.002999	0.12738	474.8	17.93919	489	23.1571	543	101.6897	2.903885	12.55985	474.8	17.93919	472.8	18.07605	464.5	20.70927	441	71.50487	0.0046	0.0028
Z074	157	1.518	0.092	3520	3.480682	0.152918	0.1083	0.002415	0.15702	4.23	0.238504	0.2873	0.012622	0.79873	1626	63.39328	1682	46.984	1764	42.41696	3.32937	7.823129	1764	42.41696	1612	64.71452	1605	52.72339	1599	43.00487	0.0107	0.0034
Z075	93	1.57	0.12	36	147.7105	14.94502	0.068	0.016728	0.17048	0.068	0.012291	0.00677	0.000685	0.29988	43.5	4.395841	65	11.48778	430	425.5271	33.07692	89.88372	43.5	4.395841	42.1	4.469275	42.1	5.278713	43.5	17.26416	0.027	0.025
Z076	420	2.71	0.26	25300	2.739726	0.164704	0.2148	0.004083	-0.84804	10.86	0.790726	0.365	0.021943	0.97964	1990	107.4609	2473	86.07471	2936	33.16866	19.53093	32.22071	Discordant	Discordant	1820	107.4609	1900	98.30145	1990	87.51651	0.1026	0.007
Z077	44.8	1.392	0.058	29.6	63.21113	3.431545	0.059	0.011183	0.31225	0.134	0.023043	0.01582	0.000859	0.018667	101.1	5.463499	125	20.57888	440	312.6995	19.12

Z079	546	2.16	0.28	467	42.37288	2.01585	0.0502	0.002665	-0.01371	0.163	0.011332	0.0236	0.001123	0.56581	150.3	7.086752	152.6	9.931953	190	146.9155	1.507208	20.89474	150.3	7.086752	150.1	7.086752	149.7	8.41277	145.5	124.1888	0.0015	0.0033
Z080	65.8	0.764	0.016	735	5.29661	0.216348	0.0784	0.003027	-0.12543	2.023	0.121288	0.1888	0.007712	0.65974	1114	41.8945	1118	40.93545	1142	77.15361	0.357782	2.451839	1114	41.8945	1109	41.8945	1085	38.13622	1046	65.46847	0.0052	0.0021
Z081	226	1.676	0.051	79.2	104.712	4.749971	0.0499	0.005532	-0.07684	0.065	0.006399	0.00955	0.000433	0.34134	61.2	2.792414	63.7	6.050491	150	238.8624	3.924647	59.2	61.2	2.792414	61	2.792414	61	3.512185	61	186.2148	0.0033	0.0064
Z082	123	1.06	0.11	79	70.52186	3.55901	0.0605	0.007497	0.35148	0.119	0.013933	0.01418	0.000716	0.3462	90.8	4.58055	113	12.27476	500	201.6636	19.64602	81.84	90.8	4.58055	89.4	4.690228	89.4	6.331387	88.4	43.98824	0.016	0.0094
Z083	444	2.17	0.14	11090	3.242542	0.144563	0.1084	0.002053	0.25635	4.58	0.257665	0.3084	0.013749	0.76296	1731	67.61767	1741	47.14372	1776	32.80421	0.574383	2.533784	1776	32.80421	1721	68.96585	1690	51.30039	1661	32.80421	0.0065	0.0027
Z084	309	1.547	0.062	2160	7.651109	0.361554	0.0772	0.005157	-0.14891	1.41	0.137551	0.1307	0.006176	0.46871	791	35.24374	875	51.22358	1100	136.322	9.6	28.09091	791	35.24374	774	34.7566	755	34.78872	726	58.19678	0.0178	0.0071
Z085	114.8	1.216	0.052	60.8	93.72071	4.385807	0.0684	0.008976	0.097815	0.1	0.011392	0.01067	0.000499	0.19323	68.4	3.190871	95	10.51578	690	198.1121	28	90.08696	68.4	3.190871	66.6	3.24004	66.6	5.04905	68.2	22.41138	0.027	0.011
Z086	776	4.04	0.11	7490	6.042296	0.240111	0.0782	0.001317	0.25887	1.776	0.09396	0.1655	0.006577	0.72826	987	36.33338	1035	34.30024	1148	34.68844	4.637681	14.02439	987	36.33338	980	36.63078	982	35.4382	986	27.73604	0.0073	0.0018
Z087	1113	3.96	0.16	272	140.056	7.151051	0.0465	0.003166	0.34748	0.0444	0.003129	0.00714	0.000365	0.45811	45.9	2.307346	44.1	3.029546	40	118.9853	-4.08163	-14.75	45.9	2.307346	46	2.361788	45.9	2.718924	45.8	72.33425	-0.0008	0.0039
Z088	519	1.67	0.17	9440	4.019293	0.177735	0.0985	0.002471	0.2819	3.32	0.187238	0.2488	0.011002	0.57108	1431	56.90317	1483	43.70159	1582	47.38732	3.506406	9.54488	1582	47.38732	1415	57.78971	1395	46.44576	1371	30.46405	0.012	0.003
Z089	134.4	2.201	0.09	71.6	69.8324	3.48228	0.0498	0.006166	0.30164	0.096	0.009903	0.01432	0.000714	0.050257	91.6	4.550607	93	9.042965	170	4647.243	1.505376	46.11765	91.6	4.550607	91.4	4.713239	91.3	5.495217	91.9	4644.014	0.0024	0.0076
Z090	1940	2.413	0.065	1780	38.94081	1.556001	0.0512	0.001501	0.03355	0.1805	0.010261	0.02568	0.001026	0.58104	163.4	6.466709	168.4	8.813333	238	100.9833	2.969121	31.34454	163.4	6.466709	163	6.466709	162	8.186015	151.8	89.11133	0.0026	0.0018
Z091	150	1.154	0.056	31.7	180.1802	10.14968	0.05	0.010434	0.15227	0.0369	0.006262	0.00555	0.000313	0.039554	35.7	1.990458	36.5	6.025281	100	295.926	2.191781	64.3	35.7	1.990458	35.4	2.173597	35.4	2.503001	35.7	84.98495	0.004	0.014
Z093	1900	1.247	0.078	1170	59.4884	2.599946	0.0499	0.002235	0.28743	0.1157	0.007419	0.01681	0.000735	0.28127	107.4	4.670506	111	6.718216	175	212.0528	3.243243	38.62857	107.4	4.670506	107.1	4.713451	106.6	5.836731	103.7	198.1647	0.0023	0.0031
Z094	89.3	1.024	0.045	49.3	66.75567	3.195259	0.055	0.007404	0.05516	0.108	0.010883	0.01498	0.000717	0.25784	95.9	4.562139	104	9.975411	320	213.1903	7.788462	70.03125	95.9	4.562139	95.1	4.61282	95	5.782873	95.8	112.5213	0.0085	0.0084
Z095	51.1	2.39	0.16	37.2	60.24096	3.849801	0.0581	0.008583	0.053571	0.13	0.015593	0.0166	0.001061	0.17057	106.3	6.872254	123	13.88646	430	227.0112	13.57724	75.27907	106.3	6.872254	104.2	7.200478	104.2	8.418644	106.3	98.25585	0.0121	0.0094
Z096	132.1	1.074	0.053	58.1	75.18797	3.501825	0.0467	0.006661	0.31077	0.084	0.01034	0.0133	0.000619	-0.13055	85.2	3.963107	81	9.513016	10	231.0114	-5.18519	-752	85.2	3.963107	85.3	4.112811	85.2	4.758641	84.5	132.8962	-0.0015	0.0085
Z097	390	1.95	0.26	3010	6.161429	0.272084	0.071	0.002266	0.13705	1.58	0.09678	0.1623	0.007167	0.56031	969	39.8669	958	37.66486	937	64.41226	-1.14823	-3.41515	969	39.8669	965	39.8669	925	35.98113	837	48.32639	0.0045	0.0019
Z099	640	3.94	0.24	1350	17.66784	0.879207	0.0522	0.002291	0.43216	0.407	0.026221	0.0566	0.002817	0.52309	355	17.37435	346	18.8461	280	90.32217	-2.60116	-26.7857	355	17.37435	355	17.37435	346	18.36288	301	54.31476	-0.0005	0.0033
Z100	44.2	1.48	0.12	37.4	91.74312	5.85062	0.112	0.030829	0.1447	0.169	0.04567	0.0109	0.000695	-0.03696	69.9	4.438207	152	37.72863	1480	567.1098	54.01316	95.27703	69.9	4.438207	64.6	4.96565	64.7	8.443072	70	14.82622	0.082	0.045
Z101	1392	11.6	3.1	323	149.0313	6.517332	0.0468	0.002955	0.20275	0.0429	0.00302	0.00671	0.000293	0.27336	43.1	1.887212	42.7	2.924488	50	124.9118	-0.93677	13.8	43.1	1.887212	43.1	1.887212	43.1	2.325776	43.1	90.01114	-0.0003	0.0035
Z102	654	5.26	0.19	4300	8.097166	0.366161	0.0721	0.002483	0.33198	1.225	0.073241	0.1235	0.005585	0.4493	750	31.8072	809	33.3057	962	75.27353	7.292954	22.03742	750	31.8072	742	32.26202	733	32.47629	703	44.81188	0.0115	0.0031
Z103	1100	1.67	0.092	385	97.84736	4.954246	0.0477	0.003005	0.18036	0.0664	0.004856	0.01022	0.000517	0.34253	65.5	3.31742	65.2	4.574909	120	162.0862	-0.46012	45.41667	65.5	3.31742	65.5	3.372102	65.4	3.946264	64	125.7059	0.0004	0.0039
Z104	232	2.87	0.11	1067	9.596929	0.391442	0.0598	0.002056	0.23014	0.854	0.048056	0.1042	0.00425	0.46603	639	25.00804	625	26.56323	580	73.41468	-2.24	-10.1724	639	25.00804	637	25.00804	613	25.52773	530	56.93343	0.003	0.0014
Z105	168	1.078	0.028	51.4	119.4743	5.41661	0.0494	0.006573	-0.01156	0.057	0.006275	0.00837	0.000379	0.27318	53.7	2.430499	56	6.013675	160	287.732	4.107143	66.4375	53.7	2.430499	53.5	2.430499	53.5	3.082902	53.7	223.5927	0.0027	0.0076
Z106	51.3	1.514	0.071	30	59.70149	3.247138	0.0463	0.007368	0.37149	0.104	0.011481	0.01675	0.000911	0.036099	107	5.782355	102	11.29837	50	242.6712	-4.90196	-114	107	5.782355	107.3	6.017743	107.2	6.612872	106.4	152.296	-0.0026	0.008
Z107	356	4.87	0.47	363	112.3596	6.472567	0.171	0.018622	0.024374	0.2	0.020688	0.0089	0.000513	0.67848	57.1	3.279031	184	17.18771	2530	189.006	68.96739	97.74308	57.1	3.279031	47.7	3.59041	49	8.923711	60.4	6.929981	0.158	0.028
Z108	299	1.322	0.088	190	56.7215	2.743254	0.0481	0.004496	0.40449	0.114	0.009721	0.01763	0.000853	-0.02345	112.6	5.383882	109	8.850675	120	183.1186	-3.30275	6.166667	112.6	5.383882	112.7	5.59176	112.5	6.424722	112.6	116.0041	-0.0003	0.0061
Z109	264	1.943	0.077	106	122.399	5.459484	0.071	0.010628	-0.32057	0.087	0.014826	0.00817	0.000364	0.50499	52.5	2.302849	83	13.23749	690	244.3764	36.74699	92.3913	52.5	2.302849	50	2.346852	50.1	4.278203	52.5	11.80739	0.031	0.016
Z110	50	0.464	0.012	561	5.299417	0.23756	0.0807	0.003722	0.26558	2.082	0.128189	0.1887	0.008459	0.4831	1113	45.83752	1137	42.09585	1186	94.12568	2.110818	6.155143	1113	45.83752	1104	46.74824	1070	41.20267	1006	76.05145	0.0085	0.0031
Z111	239	1.06	0.036	1223	12.7551	0.562183	0.0905	0.005108	0.45177	0.963	0.065824	0.0784	0.003455	-0.03763	486	20.5081	680	33.78956	1370	194.597	28.52941	64.52555	Discordant	Discordant	467	21.39585	469	27.56473	481	165.9201	0.0422	0.0077
Z112	91.6	1.28	0.086	89	71.63324	4.627259	0.091	0.014285	-0.12967	0.199	0.039083	0.01396	0.000902	0.65597	89.3	5.683988	175	29.57231	1130	260.3276	48.97143	92.09735	89.3	5.683988	83.4	5.429597	83.6	9.473992	88.7	16.6456	0.054	0.02
Z113	118.7	1.109	0.065	64	71.37759	3.541056	0.0535	0.008303	0.32851	0.101	0.013573	0.01401	0.000695	-0.11415	89.7	4.444572	97	12.69608	260	279.3604	7.525773	65.5	89.7	4.444572	89.2	4.662427	89.1	5.712024	88	120.6953	0.007	0.011
Z114	812	1.198	0.044	135	217.3913	9.00574	0.0481	0.004157	0.15747	0.0303	0.002422	0.0046	0.000191	0.13879	29.62	1.217188	30.3	2.347135	100	156.9779	2.244224	70.38	29.62	1.217188	29.41	1.206829	29.4	1.580923	29.64	103.4039	0.0017	0.0048
Z116	223	0.316	0.014	219	201.6129	11.16222	0.276	0.021513	0.31999	0.185	0.015002	0.00496	0.000275	0.36623	31.9	1.780487	171	12.94609	3270	102.3812	81.34503	99.02446	Discordant	Discordant	22.3	1.665333	22.4	8.013504	31.9	2.387324	0.293	0.027
Z117	111	0.67	0.082	387	11.91895	0.603927	0.058	0.004952	0.087002	0.649	0.054748	0.0839	0.004251	0.28176	519	25.28057	503	33.40618	510	193.6094	-3.18091	-1.76471	519	25.28057	516	25.82648	501	26.4449	439	94.0542	0.0026	0.0071
Z118	663	1.367	0.076	188	124.3781	5.791591	0.0483	0.004068	0.13862	0.0534	0.004563	0.00804	0.000374	0.24541	51.6	2.416139	52.7	4.379341	140	860.9275	2.087287	63.14286	51.6	2.416139	51.5	2.416139	51.4	2.976882	51.2	851.662	0.0014	0.0052
Z119	1610	2.28	0.14	499	123.9157	5.689327	0.0514	0.004323	-0.43327	0.065	0.01074	0.00807	0.000371	0.66492	51.8	2.373821	63	9.943905	300	175.778	17.77778	82.73333	51.8	2.373821	51.3	2.373821	51.3	3.407351	51.7	29.86104	0.0054	0.0065
Z120	114	0.1695	0.0074	107	136.9863	10.463	0.192	0.024308	0.52343	0.18	0.017459	0.0073	0.000558	0.026351	46.9	3.590513	166	14.78839	2550	196.9006	71.74699	98.16078	Discordant	Discordant	38.9	3.799419	39	8.452234	46.9	5.45592	0.185	0.034
Z121	401	1.004	0.037	131	108.8139	4.893371	0.0504	0.004623	-0.08643	0.0633	0.005556	0.00919	0.000413	0.40151	59	2.632561	62.1	5.345833	230	173.7285	4.991948	74.34783	59	2.632561	58.6	2.632561	58.6	3.372377	59	100.478	0.0037	0.0055
Z122	183	3.16	0.55	3550	3.968254	0.191873	0.0955	0.002885	-0.39704	3.33	0.229177	0.252	0.012185	0.85206	1448	63.51325	1474	54.34085	1521	57.34498	1.763908	4.799474	1521	57.34498	1438	64.55891	1417	54.89142	1392	50.04145	0.0069	0.0025
Z123	64.6	1.595	0.042	29.7	70.62147	3.647828	0.044	0.010138	0.11457	0.086	0.017849	0.01416	0.000731	-0.04031	90.6	4.631727	81	16.25311	170	297.1286	-11.8519	46.70588	Discordant	Discordant	91.3	4.799364	90.5	5.35897	88.2	89.15664	-0.005	0.014
Z125	2430	3.94	0.38	2160	44.36557	2.150743	0.0552	0.00187	0.40296	0.1725	0.010409	0.02254	0.001093	0.58017	143.7	6.902007	161.3	9.054528	412	88.1491	10.91135	65.12136	143.7	6.902007	142.5	6.953467	142.1	8.71397	141	59.40204	0.0079	0.0026
Z126	502	1.212	0.036	3930	6.706908	0.286945	0.0719	0.002213	0.50082	1.447	0.083132	0.1491	0.006379	0.098189	895	35.78575	911	33.90131	964	63.16181	1.756312	7.157676	895	35.78575	886	35.78575	862	33.19908	813	41.36319	0.0069	0.0025
Z127	385	0.385	0.013	157	142.4501	7.222448	0.0797	0.00665	0.26162	0.0759	0.005999	0.00702	0.000356	0.30324	45.1	2.286856	74.1	5.680724	1080	134.0303	39.1363	95.82407	45.1	2.286856	43.3	2.286856	43.3	3.912471	45.1	6.971683	0.0417	0.0079
Z128	469	1.81	0.11	178	96.5251	4.757917	0.0518	0.004596	0.20702	0.0731	0.006418	0.01036	0.000511	0.24553	66.4	3.235579	71.4	6.047184	220	142.2136	7.002801	69.81818	66.4	3.235579	66.1	3.287852	66	4.101394	65.9	66.02028	0.0056	0.006

	letkat07				Isotopic Ratios + measurement uncertainty (2s)										Ages uncorrected for common lead + measurement uncertainty (2s)									Ages corrected for common lead (Andersen routine) + measurement uncertainty (2s)							
					Data for Tera-Wasserburg plot					Data for Wetherill plot																				
Sample	U (ppm)	U/Th	U/Th uncertainty 2SE	207Pb (cps)	U238/Pb 206	U238/Pb 206 uncertainty (2s)	Pb207/Pb 206	Pb207/Pb 206 uncertainty (2s)	ρ	Pb207/U 235	Pb207/U 235 uncertainty (2s)	Pb206/U 238	Pb206/U 238 uncertainty (2s)	ρ	Age Pb206/U 238	Age Pb206/U 238 measurement uncertainty (2s)	Age Pb207/U 235	Age Pb207/U 235 measurement uncertainty (2s)	Age Pb207/Pb 206	Age Pb207/Pb 206 measurement uncertainty (2s)	Discordance Pb206/U 238 vs Pb207/U 235 (%)	Concordance Pb206/U 238 vs Pb207/Pb 206 (%)	Best age	Best age measurement uncertainty (2S)	Age Pb206/U 238	Age Pb206/U 238 measurement uncertainty (2s)	Age Pb207/U 235	Age Pb207/U 235 measurement uncertainty (2s)	Age Pb207/Pb 206	Age Pb207/Pb 206 measurement uncertainty (2s)	Common Lead fraction	Common Lead fraction uncertainty (2s)
Z001	503	1.094	0.049	143	134.4086	2.716054	0.0478	0.00413	0.28825	0.049	0.003124	0.00744	0.00015	-0.00513	47.8	0.970583	48.5	3.037306	90	819.2897	1.443299	46.88889	47.8	0.970583	47.7	1.041456	47.7	1.4432	47.8	810.732	0.0015	0.0049
Z002	935	1.145	0.055	3300	13.15789	0.192718	0.05725	0.001076	0.16885	0.603	0.016351	0.076	0.001113	0.58895	472	6.61381	478.7	10.3293	497	43.04161	1.399624	5.030181	472	6.61381	470.9	6.736414	465.9	10.3293	440	36.84019	0.00235	0.00094
Z003	3141	0.837	0.019	3959	32.15434	0.477229	0.04953	0.000965	0.11027	0.2134	0.005963	0.0311	0.000462	0.498	197.4	2.9007	196.3	4.990438	169	42.15178	-0.56037	-16.8047	197.4	2.9007	197.3	2.9007	194.4	4.661553	150	31.8266	0.0007	0.001
Z004	2250	20.17	0.6	49200	3.760812	0.063677	0.10125	0.000828	-0.05967	3.733	0.107902	0.2659	0.004502	0.90542	1519	23.2956	1577	23.24135	1650	14.84284	3.677869	7.939394	1650	14.84284	1509	23.96466	1519	28.12935	1526	22.35911	0.0077	0.0019
Z005	717	1.639	0.046	294	97.75171	1.75304	0.0488	0.003173	0.055509	0.0693	0.003742	0.01023	0.000183	0.24058	65.6	1.186794	67.9	3.565526	130	2199.545	3.387334	49.53846	65.6	1.186794	65.5	1.186794	65.4	1.827177	64.3	2197.515	0.0025	0.004
Z006	899	5.11	0.13	410	90.09009	7.078485	0.055	0.00357	0.23097	0.0809	0.006493	0.0111	0.000872	0.82374	71	5.31561	78.6	6.007913	360	105.6255	9.669211	80.27778	71	5.31561	70.3	5.31561	70.4	5.632407	69	26.7313	0.01	0.0047
Z007	797	1.413	0.029	257	121.2121	1.966409	0.0499	0.003528	-0.32441	0.0569	0.003484	0.00825	0.000134	0.51445	52.97	0.852407	56.1	3.31828	170	120.5683	5.579323	68.84118	52.97	0.852407	52.74	0.852407	52.74	1.439404	52.8	74.89836	0.0039	0.0043
Z008	469	0.974	0.026	1438	15.15152	0.370658	0.058	0.001724	0.25272	0.529	0.018679	0.066	0.001615	0.80339	412	9.407602	430	12.43241	517	76.97893	4.186047	20.30948	412	9.407602	410	10.13721	407	11.84503	382	64.49322	0.0053	0.0016
Z009	438	4.35	0.32	1700	12.2399	0.209739	0.0588	0.001672	0.36764	0.664	0.020835	0.0817	0.0014	0.3978	506.1	8.450287	516	12.72262	548	65.22411	1.918605	7.645985	506.1	8.450287	504.2	8.651494	493.2	11.85196	454	51.93616	0.0041	0.0014
Z010	242	2.394	0.035	189	53.93743	1.206343	0.0532	0.003769	0.31309	0.1353	0.006885	0.01854	0.000415	0.098483	118.4	2.597191	128.5	6.174643	310	207.3347	7.859922	61.80645	118.4	2.597191	117.7	2.741204	117.7	3.754333	118.2	180.321	0.0063	0.0042
Z012	269	1.875	0.08	111	98.71668	1.783239	0.049	0.004758	0.19043	0.0685	0.00498	0.01013	0.000183	0.046375	65	1.183864	67	4.731315	130	775.2127	2.985075	50	65	1.183864	65.2	1.322397	65.1	1.906973	64.7	763.5699	0.0023	0.0056
Z014	288	2.37	0.31	217	55.80357	1.351802	0.0532	0.004169	0.24547	0.131	0.008431	0.01792	0.000434	0.10247	114.5	2.727432	124.9	7.658929	290	190.7693	8.326661	60.51724	114.5	2.727432	113.7	2.800337	113.5	3.75084	113.6	149.8395	0.0064	0.0052
Z015	242	1.408	0.02	81	110.8647	3.168797	0.047	0.006644	0.04239	0.0582	0.006748	0.00902	0.000258	0.12809	57.9	1.661649	57	6.428824	10	251.5051	-1.57895	-479	57.9	1.661649	57.9	1.736455	57.9	2.093796	57.9	156.548	-0.0002	0.0092
Z016	48.5	2.83	0.1	65.2	34.31709	0.927071	0.0556	0.006814	0.22472	0.227	0.021128	0.02914	0.000787	0.17924	185.1	4.939854	205	17.09056	330	1024.616	9.707317	43.90909	185.1	4.939854	183.7	5.311794	183.4	6.57837	184.6	1011.196	0.0073	0.0081
Z017	621	12.5	1.3	41200	2.239642	0.038719	0.1852	0.001561	-0.18154	11.43	0.338096	0.4465	0.007719	0.9008	2378	34.40805	2556	28.0919	2699	14.07017	6.964006	11.89329	2699	14.07017	2307	39.18487	2349	40.09433	2385	33.44652	0.0362	0.0045
Z019	119.5	3.39	0.17	82.1	63.69427	1.671373	0.0528	0.006078	-0.10051	0.114	0.010567	0.0157	0.000412	0.32445	100.4	2.60741	109	9.746361	280	241.8277	7.889908	64.14286	100.4	2.60741	99.6	2.60741	99.4	3.416103	99.7	176.4795	0.0062	0.0074
Z020	267	2.19	0.13	121	90.66183	1.763081	0.0503	0.004452	-0.03182	0.0767	0.005191	0.01103	0.000214	0.24597	70.7	1.346712	74.9	4.860503	180	216.0993	5.607477	60.72222	70.7	1.346712	70.3	1.416275	70.3	2.086836	70.1	180.9742	0.0036	0.005
Z021	842	2.65	0.13	263	136.612	2.537407	0.0511	0.003207	0.12088	0.052	0.002718	0.00732	0.000136	0.25732	46.99	0.876981	51.5	2.629177	250	101.2002	8.757282	81.204	46.99	0.876981	46.7	0.897629	46.7	1.397345	46.87	36.25034	0.0052	0.0036
Z022	735	2.4	0.43	237	230.4147	12.30706	0.074	0.015372	-0.82945	0.062	0.022879	0.00434	0.000232	0.93173	27.9	1.440305	57	18.94674	640	259.8696	51.05263	95.64063	Discordant	Discordant	26.39	0.775833	26.7	1.615263	28.6	4.180847	0.034	0.024
Z023	115	2.19	0.14	70	58.20722	1.387996	0.0457	0.006456	0.054621	0.107	0.012837	0.01718	0.00041	0.055393	109.8	2.565809	102	11.25236	30	209.4363	-7.64706	-266	109.8	2.565809	109.5	2.932298	109.5	3.562374	109.8	90.31697	-0.0034	0.0087
Z024	168.9	0.872	0.04	72.3	165.0165	7.236656	0.091	0.011332	0.16689	0.0743	0.007366	0.00606	0.000266	0.21639	39	1.691691	72.5	6.96161	1290	196.9676	46.2069	96.97674	Discordant	Discordant	36.9	1.768733	36.9	2.368461	39	6.997353	0.055	0.015
Z026	929	1.76	0.12	1260	36.32401	0.915117	0.0615	0.003451	1	0.225	0.012178	0.02753	0.000694	0.28975	175	4.318686	206	9.665381	590	102.3173	15.04854	70.33898	175	4.318686	172.4	4.245568	172.4	5.822336	174.1	39.51823	0.015	0.005
Z027	552	0.566	0.028	355	88.18342	2.696626	0.074	0.009901	-0.266	0.112	0.015181	0.01134	0.000347	0.4548	72.7	2.22756	107	13.59091	950	244.2684	32.05607	92.34737	72.7	2.22756	69.8	2.077793	69.7	3.017277	71.6	9.500847	0.032	0.015
Z028	280	1.424	0.043	165	70.72136	1.777408	0.0504	0.004286	-0.01207	0.0989	0.007218	0.01414	0.000355	0.35649	90.5	2.281135	95.4	6.565962	180	506.1835	5.136268	49.72222	90.5	2.281135	90.2	2.207935	90	2.989558	87.3	492.2302	0.0032	0.0053
Z029	1158	0.255	0.017	224	202.061	3.358348	0.0476	0.003049	0.34948	0.0322	0.001461	0.004949	8.23E-05	-0.06553	31.82	0.528899	32.2	1.455322	90	282.4888	1.180124	64.64444	31.82	0.528899	31.8	0.55543	31.79	0.86831	31.78	271.2934	0.001	0.0032
Z030	316	4.93	0.57	95	159.2357	9.300159	0.0665	0.008524	-0.31171	0.059	0.008767	0.00628	0.000367	0.60231	40.4	2.313264	57.4	7.825451	730	197.132	29.61672	94.46575	40.4	2.313264	38.9	2.080431	38.9	2.425713	40.4	10.78233	0.025	0.011
Z031	505	0.991	0.019	13800	3.286231	0.050794	0.1092	0.001233	-0.06336	4.568	0.121698	0.3043	0.004703	0.79746	1712	22.79106	1742	22.10446	1785	21.19489	1.722158	4.089636	1785	21.19489	1704	24.06143	1704	25.82958	1712	22.92342	0.0052	0.0018
Z032	1165	2.553	0.077	16490	4.692633	0.098406	0.08101	0.000979	-0.05426	2.371	0.077536	0.2131	0.004469	0.9061	1245	23.67528	1231	23.30734	1219	23.76172	-1.13729	-2.1329	1245	23.67528	1243	24.38481	1220	24.44978	1185	21.92987	0.0011	0.00067
Z033	116	1.096	0.046	181	62.69592	1.478959	0.126	0.014999	-0.06414	0.28	0.031377	0.01595	0.000376	0.094537	102	2.39327	245	24.93829	1720	244.3013	58.36735	94.06977	Discordant	Discordant	91.5	2.465997	91.9	5.564087	102	10.29497	0.1	0.022
Z034	1200	17.71	0.61	7360	10.94092	0.667417	0.0769	0.001132	0.02382	0.964	0.063818	0.0914	0.005576	0.9869	562	33.44171	675	34.2581	1117	73.80694	16.74074	49.68666	562	33.44171	551	33.44171	553	35.0011	562	78.24337	0.0221	0.002
Z035	6790	1.05	0.21	2104	135.5014	2.627677	0.0517	0.001906	-0.03149	0.0522	0.002373	0.00738	0.000143	0.4979	47.4	0.899318	51.7	2.284148	252	68.09392	8.317215	81.19048	47.4	0.899318	47.12	0.892432	47.1	1.400833	46.6	12.58956	0.006	0.0029
Z036	869	3.85	0.1	9920	5.428882	0.068182	0.07568	0.000933	0.074945	1.922	0.048391	0.1842	0.002313	0.66195	1090	12.65394	1088.1	16.85187	1085	24.85665	-0.17462	-0.46083	1090	12.65394	1089	12.65394	1076	17.26189	1061	21.58595	0.00107	0.0006
Z038	286.6	1.146	0.031	210	54.85464	1.265907	0.0481	0.003494	0.14765	0.1207	0.006884	0.01823	0.000421	0.1993	116.4	2.661887	115.3	6.274243	110	148.1277	-0.95403	-5.81818	116.4	2.661887	116.4	2.734271	116.1	3.504928	115.9	107.1305	-0.0005	0.0041
Z039	464	0.98	0.037	143	114.5475	2.048271	0.0455	0.004037	0.16826	0.0543	0.003683	0.00873	0.000156	0.087551	56	1.0068	53.6	3.593122	10	130.9999	-4.47761	-460	56	1.0068	56.1	1.075289	56.1	1.529551	55.8	56.67214	-0.0023	0.0049
Z040	112	1.43	0.11	33.3	121.2121	3.207949	0.044	0.009308	0.11731	0.051	0.010303	0.00825	0.000218	0.70701	52.9	1.350073	50	9.516525	120	275.6988	-5.8	55.91667	52.9	1.350073	53.1	1.647876	53.1	1.940168	52.9	65.87418	-0.004	0.013
Z041	476	1.793	0.02	346	62.3053	1.718444	0.0568	0.003962	0.11159	0.123	0.007049	0.01605	0.000443	0.3245	102.6	2.76215	117.4	6.363493	450	132.3506	12.60647	77.2	102.6	2.76215	101.3	2.836348	101.3	3.702707	102	40.64301	0.011	0.0053
Z042	226	1.501	0.022	129	89.44544	2.951836	0.057	0.00554	-0.23642	0.09	0.008905	0.01118	0.000369	0.51905	71.7	2.375746	86.6	8.030226	460	168.8152	17.20554	84.41304	71.7	2.375746	70.5	2.224808	70.6	2.870214	71.3	34.10165	0.0119	0.0068
Z043	101.1	0.957	0.014	491	10.72961	0.198516	0.0636	0.003118	1	0.811	0.032629	0.0932	0.001724	0.12198	574	10.0292	601	18.25365	698	117.7923	4.492512	17.76504	574	10.0292	571	10.71657	558	14.09452	524	95.879	0.0074	0.0033
Z044	250	1.406	0.027	2870	5.668934	0.11612	0.0788	0.001674	0.3041	1.902	0.055804	0.1764	0.003613	0.67446	1047	19.47218	1080	19.33348	1162	44.09949	3.055556	9.89673	1047	19.47218	1041	20.88554	1032	21.96095	1027	38.19274	0.0065	0.0019
Z046	2100	2.96	0.46	682	124.2236	1.852609	0.0496	0.002167	0.22597	0.0545	0.002013	0.00805	0.00012	0.053065	51.66	0.763163	53.9	1.922252	169	85.58979	4.155844	69.43195	51.66	0.763163	51.47	0.79441	51.44	1.361489	51.58	55.27008	0.003	0.0026
Z047	112.7	0.913	0.032	443	12.10654	0.266725	0.0591	0.002858	-0.17759	0.664	0.027471	0.0826	0.00182	0.99953	512	10.47643	515	16.96246	540	112.4325	0.582524	5.185185	512	10.47643	510	11.19176	491	13.27121	407	93.91155	0.0043	0.0022
Z048	309	1.12	0.11	3060	6.169031	0.09883	0.075	0.001605	0.009615	1.677	0.052912	0.1621	0.002597	0.59076	968	14.42002	998	19.82965	1071	46.70833	3.006012	9.61718	968	14.42002	964	14.42002	958	18.31816	951	36.6105	0.0049	0.0016
Z049	107.4	1.921	0.045	67.4	67.61325	1.870298	0.0511	0.006949	-0.08992	0.103	0.010507	0.01479	0.000409	0.23774	94.6	2.589465	98	9.697214	140	445.4246	3.469388	32.42857	94.6	2.589465	93.8	2.663819	93.8	3.332382	94.6	406.9533	0.0038	0.0089
Z051	1880	7.9	1.4	660	123.4568	4.004831	0.0648	0.007965	0.1916	0.069	0.008032	0.0081	0.000263	0.016777	52	1.720836	67.6	7.399261	600	196.9565	23.07692	91.33333	52	1.720836	50.5	1.79663	50.5	2.296315	51.5	6.698253	0.019	0.01
Z052	629	3.65	0.39	164	151.0574	2.873779	0.0469	0.003809	-0.03829	0.0427	0.002778	0.00662	0.000126	0.28781	42.56	0.795143	42.4	2.695078	60	174.8576	-0.37736	29.06667	42.56	0.795143	42.57	0.802014	42.6	1.181005	42.64	135.7338	-0.0002	0.0044
Z053	834	2.07	0.28	459	75.24454	1.237158	0.0483	0.002501	0.025616	0.0878	0.00401	0.01329	0.000219	0.16688	85.1	1.414233	85.4	3.738354	118	144.1216	0.351288	27.88136	85.1	1.414233	84.8	1.480626	84.7	2.224431	84	123.2002	0.0005	0.003
Z054	740	1.71	0.13	1846	18.05054	0.305609	0.0541	0.001361	0.084413	0.4084	0.012008	0.0554	0.000938	0.57311	347.3	5.856573	349	8.933717	366	59.23739	0.487106	5.10929	347.3	5.856573	346.5	5.856573	336.6	8.038351	286	50.53977	0.00245	0.00095
Z055	349	2.91	0.52	97	148.1481	7.045794	0.0525	0.006773	0.31964	0.0474	0.005619	0.00675	0.000321	0.19122	43.4	2.008262	46.9	5.457635	260	215.5473	7.462687	83.30769	43.4	2.008262	43.1	2.162849	43.1	2.30395	43.4	35.58809	0.006	0.0091
Z056	518	6.15	0.84	603	44.84305	2.2548	0.0623	0.003201	-0.40907	0.195	0.016374	0.0223	0.001121	0.83987	142.3	6.816792	180	13.91771	680	99.83595	20.94444	79.07353	142.3	6.816792	139.4	6.43068	139.5	7.429734	140.4	32.9898	0.0169	0.0038
Z057	399	3.72	0.19	222	90.82652	4.686984	0.0668	0.005947	-0.2971	0.098	0.009714	0.01101	0.000568	0.91074	70.6	3.601685	94	8.145228	710	142.408	24.89362	90.05634	70.6	3.601685	68.3	3.292314	68.4	3.842777	69.6	14.38469	0.0245	0.0081
Z058	1280	10.1	1.1	1230	86.50519	3.10864	0.118	0.029262	-0.92641	0.211	0.066319	0.01156	0.000415	0.96334	74.1	2.609243	180	48.98814	1360	346.4707	58.83333	94.55147	Discordant	Discordant	67.3	1.361745	67.5	4.215756	74.1	4.036622	0.09	0.048
Z059	230	1.28	0.28	2570	5.503577	0.085717	0.0752	0.00184	0.2301	1.874	0.0553	0.1817	0.00283	0.3482	1076	15.55245	1074	19.27147	1065	50.00763	-0.18622	-1.03286	1076	15.55245	1073	15.55245	1045	19.27147	1006	40.21521	0.0033	0.0015
Z061	204	2.18	0.11	730	75.75758	5.019587	0.35	0.033856	-0.28747	0.611	0.069159	0.0132	0.000875	0.70244	84.5	5.487731	469	38.81923	3610	133.8942	81.98294	97.65928	Discordant	Discordant	51.7	3.242991	60	10.60206	330	133.8942	0.367	0.042
Z062	780	3.51	0.35	510	83.47245	1.866102	0.0626	0.004618	0.1705	0.1011	0.00591	0.01198	0.000268	0.30447	76.8	1.652612	97.5	5.404234	670	134.5039	21.23077	88.53731	76.8	1.652612	75.1	1.79642	75.2	2.707794	76.3	13.27829	0.0191	0.0064
Z063	570	1.411	0.084	3030	10.88139	0.279587	0.0773	0.004952	0.70477	0.938	0.043519	0.0919	0.002361	-0.4343	567	14.28622	678	25.47912	1080	158.5151	16.37168	47.5	567	14.28622	555	16.52017	555	18.75061	564	106.5656	0.0221	0.0079
Z064	159	0.721	0.064	107	93.80863	6.570351	0.071	0.009222	-0.06828	0.108	0.015165	0.01066	0.000747	0.61543	68.3	4.765638	103	13.57799	710	221.0374	33.68932	90.38028	68.3	4.765638	66.2	4.687591	66.3	5.173397	68.3	16.48789	0.03	0.013
Z065	78.2	1.86	0.025	55	84.74576	6.269159	0.0674	0.009653	-0.08294	0.11	0.014397	0.0118	0.000873	0.39869	75.4	5.320733	108	14.36093	620	222.1406	30.18519	87.83871	75.4	5.320733	73.2	5.086609	73.3	5.545392	75.4	27.68159	0.025	0.012
Z066	108.9	2.72	0.22	99	108.1081	4.977774	0.104	0.015236	-0.57776	0.133	0.021479	0.00925	0.000426	0.83742	59.4	2.731787	123	18.31654	1420	252.1023	51.70732	95.8169	Discordant	Discordant	55.4	2.19437	55.5	3.517999	59.4	8.644131	0.071	0.021
Z068	4360	1.996	0.064	3870	48.03074	1.026402	0.05116	0.000934	-0.11506	0.1464	0.004611	0.02082	0.000445	0.86036	132.8	2.794978	138.7	4.114581	243	161.8214	4.253785	45.34979	132.8	2.794978	132.4	2.794978	131.9	3.904277	124	159.695	0.00324	0.00083
Z069	1720	3.89	0.11	787	88.80995	1.384633	0.0491	0.001926	0.40854	0.0757	0.00257	0.01126	0.000176	0.038659	72.2	1.152769	74.1	2.387845	149	1311.915	2.564103	51.54362	72.2	1.152769	72	1.152769	72	1.895733	71.6	1310.757	0.0019	0.0022
Z070	488	3	0.1	257	92.08103	1.991741	0.056	0.003497	0.067851	0.0852	0.00461	0.01086	0.000235	0.41827	69.6	1.482486	82.9	4.271771	440	98.2765	16.04343	84.18182	69.6	1.482486	68.8	1.482486	68.8	2.27016	69.4	27.06935	0.0109	0.0038
Z071	386	2.37	0.28	223	66.88963	1.473408	0.0472	0.003479	0.11049	0.0969	0.006165	0.01495	0.000329	0.29804	95.7	2.081908	93.6	5.664633	60	132.6866	-2.24359	-59.5	95.7	2.081908	95.2	2.010707	95.2	2.74519	95.5	84.44711	-0.0011	0.0042
Z072	235	1.36	0.1	251	64.59948	1.502605	0.081	0.00873	0.15156	0.17	0.016991	0.01548	0.00036	0.076272	99	2.23798	158	14.57376	1040	205.1574	37.34177	90.48077	99	2.23798	95	2.529299	95.1	4.134538	99.2	13.49291	0.041	0.013
Z073	517	2.373	0.073	304	71.37759	1.441926	0.0501	0.002614	0.09267	0.0966	0.003854	0.01401	0.000283	0.44264	89.7	1.775228	93.6	3.566521	190	695.3526	4.166667	52.78947	89.7	1.775228	89.4	1.845436	89.4	2.639407	88.2	692.5681	0.003	0.0025
Z074	525	1.41	0.18	633	60.79027	2.365802	0.123	0.022375	0.77442	0.241	0.033532	0.01645	0.00064	-0.57435	105.1	4.052313	213	24.82718	1480	259.9143	50.65728	92.89865	Discordant	Discordant	96.6	5.82761	96.7	7.260128	104.4	7.234463	0.097	0.037
Z075	1303	3.312	0.059	226	238.2087	3.638276	0.0487	0.003293	0.16238	0.028	0.001415	0.004198	6.41E-05	0.080304	27.01	0.413325	28.1	1.411318	130	103.2754	3.879004	79.22308	27.01	0.413325	26.94	0.432457	26.94	0.728126	27.01	41.68838	0.0025	0.0037
Z076	1349	2.471	0.098	780	68.02721	4.056808	0.0482	0.001967	0.42794	0.097	0.006092	0.0147	0.000877	0.89161	94	5.422822	93.7	5.66534	130	100.8104	-0.32017	27.69231	94	5.422822	94	5.500581	93.9	5.81227	88.9	78.27549	0.0009	0.0025
Z077	226	1.237	0.036	130	72.51632	1.41001	0.0497	0.00464	0.060763	0.0941	0.006959	0.01379	0.000268	0.18196	88.3	1.699705	90.9	6.461828	150	8564.532	2.860286	41.13333	88.3	1.699705	88.1	1.769405	88	2.552335	87.6	8563.606	0.0024	0.0056
Z078	672	147.7	3.4	138	191.1315	3.129541	0.0469	0.004123	0.33945	0.0334	0.002187	0.005232	8.57E-05	-0.10893	33.64	0.551227	33.4	2.108254	60	232.1601	-0.71856	43.93333	33.64	0.551227	33.51	0.63173	33.53	0.930008	33.39	199.8714	0.0002	0.0049
Z079	870	7.2	1.5	310	146.8429	6.758057	0.0487	0.003198	0.13716	0.0461	0.003174	0.00681	0.000313	0.64435	43.7	2.00896	45.7	3.089819	150	146.9684	4.376368	70.86667	43.7	2.00896	43.6	2.00896	43.6	2.221302	43.6	105.4764	0.0022	0.004
Z081	1150	6.2	1.4	327	140.2525	2.932251	0.0471	0.00261	0.11391	0.0457	0.002094	0.00713	0.000149	0.39643	45.8	0.962542	45.4	2.010592	67	137.7559	-0.88106	31.64179	45.8	0.962542	45.8	0.962542	45.8	1.338611	45.8	117.6572	0	0.0028
Z082	387	1.282	0.044	333	49.45598	0.995923	0.0507	0.002977	0.29417	0.142	0.006817	0.02022	0.000407	0.040961	129.1	2.568232	134.5	6.091089	230	331.3125	4.01487	43.86957	129.1	2.568232	128.7	2.709209	128.5	3.793517	127.9	319.8037	0.0025	0.0034
Z084	211.3	1.425	0.081	135	83.61204	3.498527	0.0628	0.006333	-0.18525	0.104	0.009747	0.01196	0.0005	0.52595	76.6	3.149841	100	8.936441	610	166.981	23.4	87.44262	76.6	3.149

Z089	5650	1.643	0.067	1880	122.1001	2.188512	0.0482	0.001269	0.023741	0.054	0.001661	0.00819	0.000147	0.56964	52.6	0.923098	53.4	1.626899	108	2192.615	1.498127	51.2963	52.6	0.923098	52.5	0.923098	52.4	1.432341	52.5	2192.29	0.0013	0.0014
Z090	221	1.314	0.041	144	62.53909	1.221821	0.05	0.004271	0.089677	0.1101	0.00723	0.01599	0.000312	0.17389	102.3	2.037406	105.7	6.563974	190	901.0334	3.216651	46.15789	102.3	2.037406	102.5	2.249983	102.4	3.091303	101.9	893.2607	0.0022	0.0049
Z091	117	0.29	0.017	23.7	204.0816	10.01596	0.051	0.010324	0.083761	0.0337	0.005254	0.0049	0.00024	0.18117	31.5	1.601134	33.4	5.096555	70	274.0632	5.688623	55	31.5	1.601134	31.4	1.601134	31.4	1.749193	31.5	58.66086	0.005	0.013
Z092	3560	2.6	0.33	1200	139.8601	5.243077	0.0674	0.006571	-0.2898	0.0667	0.007559	0.00715	0.000268	0.58634	45.9	1.706303	65	7.081332	660	157.528	29.38462	93.04545	45.9	1.706303	44.3	1.554178	44.3	2.090614	45.6	4.25037	0.026	0.011
Z093	410	2.27	0.13	175	99.10803	2.783209	0.0497	0.003864	0.1597	0.0685	0.004095	0.01009	0.000283	0.30087	64.7	1.830785	67.1	3.919279	160	211.569	3.576751	59.5625	64.7	1.830785	64.5	1.905459	64.5	2.349754	64.2	185.1683	0.0029	0.0045
Z094	147	6.06	0.7	128	67.06908	2.554982	0.071	0.009039	0.049333	0.145	0.017641	0.01491	0.000568	-0.02753	95.4	3.572439	136	14.47849	740	205.9174	29.85294	87.10811	95.4	3.572439	92.7	3.87865	92.8	4.737344	98.4	22.88969	0.028	0.013
Z095	114.7	1.204	0.021	75.9	64.02049	1.217014	0.0484	0.005706	0.30255	0.106	0.009758	0.01562	0.000297	-0.10418	99.9	1.888433	102	8.945935	130	278.4558	2.058824	23.15385	99.9	1.888433	100.3	1.957748	100.2	2.830293	99.7	224.0506	0.0004	0.0069
Z097	632	1.398	0.019	328	75.75758	1.214161	0.0473	0.002948	0.2277	0.0856	0.004402	0.0132	0.000212	0.068078	84.5	1.346177	83.3	4.133614	80	117.2941	-1.44058	-5.625	84.5	1.346177	84.6	1.41138	84.5	2.187685	84	79.1099	-0.0006	0.0036
Z098	1040	2.61	0.51	575	76.04563	1.908704	0.0478	0.002152	0.2681	0.0853	0.003319	0.01315	0.00033	0.38475	84.2	2.113655	83	3.117355	97	102.2268	-1.44578	13.19588	84.2	2.113655	84.2	2.113655	83.9	2.691487	81.8	80.57758	0.0003	0.0025
Z099	3910	3.13	0.35	1300	118.0638	3.053389	0.0477	0.0016	0.17437	0.056	0.002352	0.00847	0.000219	0.55284	54.4	1.428256	55.2	2.259421	92	123.2675	1.449275	40.86957	54.4	1.428256	53.9	1.354738	53.9	1.76663	53.7	111.7852	0.0007	0.002
Z100	525	1.99	0.12	281	137.5516	6.092072	0.104	0.014903	-0.39454	0.109	0.020625	0.00727	0.000322	0.63123	46.7	2.091513	102	17.47423	1430	220.5086	54.21569	96.73427	Discordant	Discordant	42.4	1.63194	42.5	2.783653	46.7	4.498081	0.071	0.022
Z101	780	6.2	1.5	390	83.8223	3.300168	0.0565	0.005269	-0.12294	0.094	0.008927	0.01193	0.00047	0.41986	76.4	2.996109	91	8.890814	420	167.1458	16.04396	81.80952	76.4	2.996109	75.2	2.919601	75.2	3.473008	77.5	24.61959	0.0113	0.0078
Z102	990	3.24	0.56	441	100.5025	2.933214	0.078	0.011382	-0.71511	0.111	0.01985	0.00995	0.00029	0.82202	63.8	1.828167	104	17.47925	730	236.3109	38.65385	91.26027	63.8	1.828167	61.1	1.317724	61	2.651677	63.2	6.906171	0.039	0.019
Z103	188	3.8	0.37	1000	9.615385	0.176628	0.0621	0.002018	0.23549	0.887	0.028902	0.104	0.00191	0.53999	638	10.97695	643	15.55728	679	68.907	0.777605	6.038292	638	10.97695	636	11.66162	620	14.48409	576	59.89603	0.0036	0.0013
Z104	2020	2.625	0.047	638	133.8688	2.327987	0.0486	0.002065	-0.05283	0.0502	0.002017	0.00747	0.00013	0.54792	47.99	0.834008	49.7	1.93033	132	135.7259	3.440644	63.64394	47.99	0.834008	47.9	0.840709	47.88	1.326498	48	122.2091	0.0019	0.0022
Z105	347	1.59	0.16	206	105.3741	1.999365	0.0719	0.005907	-0.02019	0.0937	0.00636	0.00949	0.00018	0.22327	60.9	1.165608	90.6	5.937787	910	142.0888	32.78146	93.30769	60.9	1.165608	58.8	1.165608	58.8	2.247424	60.6	10.10493	0.0312	0.0072
Z106	138.7	1.565	0.027	101.5	72.46377	1.51859	0.0614	0.005956	0.15202	0.1159	0.008164	0.0138	0.000289	0.086999	88.4	1.840089	112.9	8.013691	590	153.6443	21.70062	85.01695	88.4	1.840089	86.7	1.911159	86.8	2.980645	88.4	35.03313	0.0172	0.0068
Z107	1065	1.033	0.045	2550	20.87683	0.581714	0.05649	0.001196	0.11211	0.37	0.012142	0.0479	0.001335	0.85825	301.7	8.178879	319.5	9.026073	467	77.88244	5.571205	35.39615	301.7	8.178879	300.2	8.253209	299.5	9.905402	300	72.94998	0.0049	0.001
Z108	325	1.459	0.024	232	60.86427	1.088482	0.0504	0.003279	-0.0972	0.1123	0.005593	0.01643	0.000294	0.41474	105.1	1.843647	107.8	5.139673	200	2697.92	2.504638	47.45	105.1	1.843647	104.8	1.843647	104.7	2.835391	104.7	2696.53	0.0027	0.0036
Z110	249	1.732	0.075	145	72.04611	1.613766	0.0509	0.004416	0.072856	0.0975	0.006538	0.01388	0.000311	0.27924	88.9	1.984692	94.1	6.036989	200	284.8792	5.526036	55.55	88.9	1.984692	88.5	2.056794	89	2.85997	88	255.5165	0.0039	0.0053
Z111	5176	8.1	1.7	2640	81.90008	2.442998	0.0477	0.001173	0.21178	0.08	0.003249	0.01221	0.000364	0.83826	78.2	2.317887	78.1	3.05637	92	57.05707	-0.12804	15	78.2	2.317887	78.2	2.317887	78	2.802391	72.8	42.21835	0.0001	0.0014
Z112	227	1.926	0.054	77	115.3403	2.442331	0.0449	0.005156	-0.26102	0.0539	0.004961	0.00867	0.000184	0.45846	55.6	1.143533	53.1	4.720527	40	154.0436	-4.7081	-39	55.6	1.143533	55.8	1.143533	55.7	1.573014	54.7	60.35909	-0.0031	0.0061
Z113	203	1.306	0.018	142	64.26735	1.168767	0.0514	0.004287	-0.02518	0.1093	0.006929	0.01556	0.000283	0.22576	99.5	1.818157	104.9	6.337973	240	314.6423	5.14776	58.54167	99.5	1.818157	99	1.886769	99	2.833567	99.8	291.6372	0.004	0.0049
Z114	607	1.616	0.072	170	150.6024	2.551974	0.0489	0.003692	-0.02234	0.0446	0.002575	0.00664	0.000113	0.26105	42.64	0.72818	44.2	2.491671	140	146.8632	3.529412	69.54286	42.64	0.72818	42.54	0.741511	42.54	1.179418	42.64	105.3147	0.0023	0.004
Z115	326	1.996	0.099	302	110.8647	4.003286	0.113	0.018748	-0.58634	0.151	0.03247	0.00902	0.000326	0.74367	57.9	2.114776	136	25.38241	1560	244.1373	57.42647	96.28846	Discordant	Discordant	51.3	1.736455	51.4	3.481526	58	5.021648	0.084	0.03
Z116	1340	1.606	0.093	642	101.9368	2.250232	0.0562	0.002993	-0.1032	0.0744	0.004006	0.00981	0.000217	0.62991	62.9	1.385333	73.7	4.038706	410	87.94614	14.654	84.65854	62.9	1.385333	62.6	1.174627	62.6	1.913935	61.7	15.32984	0.0113	0.0039
Z117	232	2.96	0.23	112	109.1703	3.704798	0.0696	0.007935	-0.07031	0.088	0.00813	0.00916	0.000311	0.38136	58.8	1.96494	84.7	7.715114	770	181.6073	30.57851	92.36364	58.8	1.96494	56.7	1.589965	56.8	2.459265	58.8	13.66733	0.029	0.011
Z118	242	1.165	0.077	152	94.87666	2.039107	0.066	0.009469	-0.3424	0.103	0.015925	0.01054	0.000227	0.46878	67.6	1.403509	97	14.34001	570	221.0546	30.30928	88.14035	67.6	1.403509	65.6	1.403509	65.6	2.518565	67.6	16.08464	0.025	0.015
Z119	1030	15.5	2.6	720	60.93845	1.192631	0.047	0.002152	0.07567	0.1044	0.004215	0.01641	0.000321	0.29475	104.9	2.048569	100.7	3.911004	63	82.33161	-4.1708	-66.5079	104.9	2.048569	104.5	1.910768	104.2	2.758252	102.6	45.74801	-0.0014	0.0027
Z120	215	3.83	0.33	1010	10.79914	0.200777	0.0614	0.002326	0.27383	0.78	0.029039	0.0926	0.001722	0.32726	571	10.01422	584	16.84958	630	86.31681	2.226027	9.365079	571	10.01422	568	10.01422	552	13.40703	496	66.40401	0.0058	0.0019
Z121	71.9	49.7	5.9	150	58.47953	3.010541	0.162	0.03591	-0.39267	0.39	0.094913	0.0171	0.00088	0.6032	109.2	5.678768	316	66.46544	1900	464.6806	65.44304	94.25263	Discordant	Discordant	92.7	5.368986	93.3	8.363167	109.2	11.71786	0.144	0.056
Z122	553	17.5	6.3	309	76.4526	2.187239	0.0493	0.002874	0.23847	0.0881	0.004219	0.01308	0.000374	0.34514	83.8	2.408428	85.6	3.946979	160	823.8861	2.102804	47.625	83.8	2.408428	83.6	2.483203	83.6	2.964733	82.8	820.1179	0.002	0.0033
Z125	207	8.1	3.3	630	91.99632	2.860338	0.256	0.037084	0.30443	0.368	0.049547	0.01087	0.000338	-0.03989	69.7	2.144273	305	36.76122	2680	322.847	77.14754	97.39925	Discordant	Discordant	52.7	3.677758	56.7	7.251665	103	52.04702	0.254	0.053
Z126	586	3.97	0.21	523	69.44444	3.66354	0.0693	0.005271	-0.28018	0.131	0.01067	0.0144	0.00076	0.65495	92.1	4.798832	124	9.073974	830	134.406	25.72581	88.90361	92.1	4.798832	89.3	4.489097	89.2	5.173026	91.7	13.04005	0.0272	0.0076
Z127	76.7	2.09	0.11	107	182.4818	11.91789	0.332	0.041946	-0.25042	0.259	0.038262	0.00548	0.000358	0.80118	35.3	2.306226	233	31.86034	3340	228.3643	84.84979	98.94311	Discordant	Discordant	23	1.684838	25.1	5.191963	310	133.8889	0.348	0.05
Z128	469	8.04	0.84	228	88.49558	6.831839	0.061	0.012176	-0.05395	0.09	0.022928	0.0113	0.000872	0.60691	72.5	5.317043	84	18.99574	600	221.3045	13.69048	87.91667	72.5	5.317043	70.1	4.848644	70.1	5.175763	70.2	20.01779	0.018	0.019
Z129	3020	1.159	0.032	2290	56.88282	0.905409	0.05	0.001352	-0.56604	0.121	0.003917	0.01758	0.00028	0.81793	112.3	1.74889	115.9	3.564156	190	137.2935	3.106126	40.89474	112.3	1.74889	112.1	1.813288	111.7	2.891921	105.3	130.3643	0.0024	0.0016
Z130	204	1.474	0.016	194	47.28132	0.997563	0.052	0.003594	0.048137	0.149	0.007589	0.02115	0.000446	0.38281	134.9	2.803155	140.7	6.706926	260	7207.411	4.122246	48.11538	134.9	2.803155	134.3	2.803155	133.8	3.889712	130.1	7206.793	0.0044	0.0039
Z131	408	4.08	0.4	296	135.8696	5.947186	0.121	0.016596	0.25434	0.12	0.015213	0.00736	0.000322	-0.0813	47.3	2.092596	114	13.61767	1960	220.5007	58.50877	97.58673	Discordant	Discordant	42.4	2.556669	42.4	3.551024	47.3	4.09052	0.094	0.025
Z132	170	4.46	0.28	83	102.3541	3.590311	0.0604	0.007653	0.12439	0.08	0.008086	0.00977	0.000343	0.11987	62.7	2.202061	80	8.061799	460	190.719	21.625	86.36957	62.7	2.202061	61.5	2.202061	61.6	2.740875	62.7	25.8117	0.017	0.01
Z134	135	1.207	0.061	74	112.8668	3.278291	0.0695	0.007859	-0.06711	0.0856	0.007583	0.00886	0.000257	0.43021	56.8	1.658698	82.9	7.017561	770	158.2575	31.48372	92.62338	56.8	1.658698	55.2	1.584134	55.2	2.372586	56.4	15.753	0.0285	0.009
Z135	671	0.752	0.038	426	68.02721	1.453436	0.0489	0.002501	0.21336	0.1	0.00456	0.0147	0.000314	0.24914	94.1	2.004494	96.6	4.198409	141	183.3688	2.587992	33.26241	94.1	2.004494	93.9	2.075908	93.7	2.842295	93.1	169.135	0.0013	0.0028
Z136	9440	1.74	0.16	3750	111.3586	3.195623	0.0499	0.000949	0.36105	0.0616	0.00206	0.00898	0.000258	0.87796	57.6	1.660907	60.7	1.960905	186	40.815	5.107084	69.03226	57.6	1.660907	57.4	1.660907	57.4	2.077582	57	28.6198	0.0035	0.0012
Z137	747	4.68	0.18	279	127.551	10.44259	0.0543	0.003604	-0.05759	0.0599	0.005834	0.00784	0.000642	0.84832	50.3	4.120394	58.8	5.591079	370	112.1198	14.45578	86.40541	50.3	4.120394	49.8	4.120394	49.8	4.301949	50.3	20.87122	0.0094	0.0044
Z138	346.8	2.112	0.046	123.3	113.3787	2.458997	0.0455	0.003994	0.26379	0.0553	0.00347	0.00882	0.000191	0.020385	56.6	1.218219	54.6	3.305732	20	125.795	-3.663	-183	56.6	1.218219	57	1.362372	56.9	1.756378	55.4	60.62717	-0.002	0.0045
Z139	2200	2.71	0.22	1240	130.5483	5.631583	0.095	0.02059	-0.82511	0.109	0.030811	0.00766	0.00033	0.91634	49.2	2.096296	105	26.86985	840	267.7271	53.14286	94.14286	Discordant	Discordant	45.2	0.97645	45.2	2.453349	48.7	3.263221	0.062	0.034
Z140	750	1.81	0.16	391	99.10803	2.278607	0.0594	0.004278	0.25264	0.082	0.0059	0.01009	0.000232	0.39303	64.7	1.463822	79.8	5.489962	570	134.6537	18.92231	88.64912	64.7	1.463822	63.6	1.392183	63.6	2.172483	64.7	14.67673	0.0155	0.0059
Z142	281	0.981	0.016	164	74.23905	1.393916	0.0489	0.004117	0.30755	0.0904	0.005671	0.01347	0.000253	-0.08211	86.3	1.621769	87.6	5.325082	130	365.0471	1.484018	33.61538	86.3	1.621769	86.2	1.691016	86.2	2.446814	86.3	345.4149	0.0016	0.005
Z143	129.3	1.269	0.014	60	111.1111	2.907502	0.0516	0.00866	-0.0038	0.067	0.009574	0.009	0.000236	0.052486	57.8	1.512826	65	9.561929	120	258.6471	11.07692	51.83333	57.8	1.512826	56.2	2.420711	56.1	2.847575	62	85.89729	0.005	0.012
Z144	130	1.954	0.054	99	65.35948	1.20369	0.0627	0.007937	-0.04327	0.133	0.0145	0.0153	0.000282	0.14663	97.9	1.81073	125	12.89324	550	200.4116	21.68	82.2	97.9	1.81073	95.7	2.01954	95.6	3.285623	97.7	37.64673	0.019	0.011
Z145	174.9	1.63	0.13	75	106.6098	2.361185	0.0504	0.005826	0.016137	0.0655	0.00579	0.00938	0.000208	0.11664	60.2	1.303359	64.1	5.543452	180	206.3882	6.084243	66.55556	60.2	1.303359	59.9	1.375116	59.9	1.910043	60.2	133.4072	0.0042	0.007
Z146	76.1	1.189	0.029	355	45.82951	1.578847	0.287	0.035749	0.53113	0.84	0.088743	0.02182	0.000752	-0.23608	139.2	4.73927	613	46.13077	3340	165.537	77.29201	95.83234	Discordant	Discordant	98.4	7.819762	100	13.16104	139.2	9.020176	0.299	0.054
Z148	465	2.96	0.1	28800	2.303086	0.042786	0.1604	0.001444	0.058048	9.61	0.262569	0.4342	0.008066	0.90463	2323	36.25442	2396	25.46206	2459	15.5515	3.046745	5.530704	2459	15.5515	2296	41.13348	2305	38.59607	2319	31.58527	0.0139	0.004
Z149	633	4.52	0.49	5670	7.861635	0.149988	0.0779	0.001758	-0.05078	1.366	0.04677	0.1272	0.002427	0.49347	771	13.57536	873	19.56214	1137	49.27489	11.68385	32.18997	771	13.57536	758	13.57536	762	17.92477	772	37.95201	0.0171	0.0025
Z150	2540	3.118	0.098	907	121.2121	1.966409	0.0493	0.001815	0.17541	0.0562	0.001977	0.00825	0.000134	0.28709	52.94	0.871931	55.5	1.884933	156	83.71805	4.612613	66.0641	52.94	0.871931	52.78	0.885058	52.73	1.438381	50.2	65.67231	0.0027	0.0019
Z151	373	2.91	0.42	228	78.36991	2.476944	0.0517	0.004027	-0.0765	0.0903	0.006186	0.01276	0.000403	0.40578	81.7	2.552752	87.4	5.767087	240	153.4964	6.521739	65.95833	81.7	2.552752	81.1	2.552752	81	3.114369	79.2	98.09222	0.0055	0.0053
Z152	129	2	0.15	94	86.95652	5.300139	0.069	0.012079	-0.10753	0.108	0.016721	0.0115	0.000701	0.2177	73.7	4.4607	102	15.13281	700	299.8528	27.7451	89.47143	73.7	4.4607	69.6	4.616432	69.7	5.102806	73.4	20.07871	0.028	0.018
Z155	920	14.7	1.9	573	69.06077	1.840629	0.0499	0.002257	0.051005	0.0995	0.004284	0.01448	0.000386	0.49962	92.7	2.435318	96.2	3.991283	180	4877.446	3.638254	48.5	92.7	2.435318	91.8	2.288313	91.8	2.997722	90.2	4876.999	0.0027	0.0027
Z156	314	1.576	0.018	137	97.18173	2.197904	0.0467	0.003845	0.21281	0.0665	0.003859	0.01029	0.000233	0.12322	66	1.468564	65.3	3.613488	40	141.0641	-1.07198	-65	66	1.468564	66	1.540675	66	2.032066	66.1	97.0855	-0.0007	0.0043
Z158	3860	10.61	0.92	1280	191.9386	20.38236	0.132	0.033207	-0.94538	0.129	0.059916	0.00521	0.000553	0.99654	33.5	3.556612	104	39.46037	1350	322.8367	67.78846	97.51852	Discordant	Discordant	28.1	0.845274	29.4	3.724546	31.7	2.732333	0.117	0.054
Z159	498	3.46	0.23	2040	13.81215	0.396458	0.0631	0.001609	0.12775	0.63	0.022584	0.0724	0.002078	0.78505	450	12.47123	495	14.24761	704	81.9444	9.090909	36.07955	450	12.47123	446	12.47123	446	14.86521	448	74.8257	0.0094	0.0017
Z160	584	8.16	0.17	5860	6.640106	0.103317	0.0748	0.001177	0.20572	1.555	0.043749	0.1506	0.002343	0.64779	904	12.8467	952	17.51571	1059	34.81063	5.042017	14.63645	904	12.8467	898	13.4825	899	17.98722	901	29.10705	0.0072	0.0015
Z161	3230	9.51	0.22	1060	132.8021	4.742756	0.0514	0.002545	0.076284	0.0527	0.003011	0.00753	0.000269	0.56692	48.3	1.711919	52.1	2.921313	240	96.36302	7.293666	79.875	48.3	1.711919	48.1	1.711919	48	2.02511	47.8	18.98857	0.005	0.0036
Z163	628	5.54	0.94	220	122.549	6.950776	0.0481	0.003292	0.068387	0.0539	0.003978	0.00816	0.000463	0.76937	52.4	2.952664	53.1	3.813892	100	1904.982	1.318267	47.6	52.4	2.952664	52.3	3.030384	52.3	3.14871	51.1	1902.64	0.0016	0.0038
Z164	2240	3.07	0.42	2370	42.95533	0.632606	0.0504	0.001163	-0.05671	0.1622	0.004934	0.02328	0.000343	0.46197	148.3	2.134173	152.6	4.268279	209	75.71845	2.817824	29.04306	148.3	2.134173	147.9	2.134173	146.9	3.654778	135.4	68.01175	0.0024	0.0011
Z165	1610	0.427	0.047	306	220.2158	4.022325	0.0527	0.004671	-0.50355	0.0325	0.002932	0.004541	8.29E-05	0.64776	29.2	0.529569	32.4	2.852259	220	126.5824	9.876543	86.72727	29.2	0.529569	29	0.496017	28.98	0.845306	28.9	12.31753	0.0083	0.007
Z168	141	1.053	0.029	103	62.22775	1.347301	0.0504	0.005987	-0.01166	0.109	0.010539	0.01607	0.000348	0.22826	102.8	2.180556	107	10.49041	170	211083.3	3.925234	39.52941	102.8	2.180556	102.5	2.251894	103.1	3.182691	102.8	211083.2	0.003	0.008
Z169	274	0.6	0.056	102	122.6994	3.393924	0.0522	0.005695	-0.40604	0.0589	0.006136	0.00815	0.000225	0.75308	52.4	1.421853	57.8	5.739483	230	164.9522	9.342561	77.21739	52.4	1.421853	51.1	1.347986	51.1	1.809605	52	49.10652	0.0067	0.0072
Z170	113.6	4.11	0.15	93	68.96552	1.730864	0.0642	0.006776	0.12916	0.128	0.009897	0.0145	0.000364	0.14481	92.8	2.288739	121	9.057754	620	160.8603	23.30579	85.03226	92.8	2.288739	90.9	2.435719	90.9	3.498158	92.8	32.8771	0.0212	0.0082
Z171	1520	2.634	0.074	509	129.5337	2.200312	0.0493	0.0022	-0.09564	0.0526	0.002113	0.00772	0.000131	0.44629	49.58	0.822013	52	2.023894	158	91.50028	4.653846	68.62025	49.58	0.822013	49.38	0.815463	49.35	1.353228	49.5	69.89579	0.003	0.0022
Z172	196	1.473	0.044	213	67.11409	2.113804	0.0757	0.007758	-0.64876	0.159	0.018476	0.0149	0.000469	0.79662	95.4	2.965353	148	15.29982	950	173.9118	35.54054	89.95789	95.4	2.965353	91.3	2.297372	91.5	3.889141	94.9	15.66385	0.036	0.011
Z173	199	2.82	0.16	148	62.93266	1.235536	0.0514	0.004303	0.22745	0.1129	0.006886	0.01589	0.000312	0.090223	101.6	1.965027	108.3	6.290004	220	341.057	6.186519	53.81818	101.6	1.965027	101.2	2.105168	100.9	2.982071	98.2	319.9753	0.0046	0.005
Z174	312	1.45	0.024	389	53.8503	1.140707	0.086	0.013024	-0.34355	0.219	0.035789	0.01857	0.000393	0.39935	118.6	2.526521	198	27.87657	1240	244.4189	40.10101	90.43548	Discordant	Discordant	111.6	3.181494	111.9	5.107954	118.6	12.79852	0.047	0.021
Z177	360	1.67	0.12	220	100.3009	2.772171	0.076	0.007739	-0.25221	0.107	0.011295	0.00997	0.000276	0.46837	64	1.754126	102	9.714706	910	173.4779	37.2549	92.96703	64	1.754126	61.5	1.680106	61.6	2.752365	64	9.450106	0.037	0.011
Z178	81	2.531	0.065	72.8	63.37136	1.421537	0.0592	0.007634	0.31924	0.131	0.012954	0.01578	0.000354	0.050217	100.9	2.245004	124	11.35064	420	198.0462	18.62903	75.97619	100.9	2.245004	99.4	2.535516	99.5	3.591239	100.9	59.28328	0.015	0.01
Z179	192	0.716	0.011	74.8	139.0821	3.586886	0.0603	0.00677	0.1881	0.0598	0.004921	0.00719	0.000185	0.093795	46.2	1.180866	58.8	4.753239	500	158.5698	21.42857

Supplementary Table 3

All apatite data from this study.

U-Pb data

AFT data

#grains	Ns	ΣpiΩi	2σΣpiΩi	eta (yr cm^2	2 sig abs	χ^2	P(χ^2)	Pooled age	2σ Ma
113	1213	4.45E-05	3.75E-07	6.92E-01	1.10E-02	145.54	0.01	18.8	1.1

Grain Number	Pb207/U 235	Pb207/U 235 error (2s)	Pb206/U 238	Pb206/U 238 error (2s)	U238/Pb 206	U238/Pb 206 error (2s)	Pb207/Pb206	Pb207/Pb206 error (2s)	Approx U (ppm)	Approx Th (ppm)	Approx Pb (ppm)	U/Th	207corrAge (Ma)	207corrAge error (2s,Ma)	Ns	Area (cm^2)	$^{238}U/^{43}Ca$	2σ	FT Age	2σ
Population 1																				
L7G2	16.08	0.67	0.162	0.013	6.165	0.494	0.822	0.036	8.78	21.84	4.61	0.37	19.7	48.7	4	4.47E-05	3.11E-03	1.92E-04	19.9	19.9
L7G4	12.1	0.53	0.128	0.012	7.819	0.734	0.802	0.054	5.93	3.09	2.34	1.78	37.4	56.7	3	3.03E-05	1.96E-03	1.25E-04	34.9	40.4
L7G6	24.57	0.85	0.253	0.021	3.953	0.328	0.816	0.037	7.42	0.20	6.13	42.10	46.4	77.7	1	2.42E-05	2.84E-03	1.59E-04	10.1	20.1
L7G9	8.89	0.51	0.096	0.008	10.471	0.910	0.786	0.031	17.41	3.61	5.26	4.51	40.5	25.0	4	5.96E-05	6.30E-03	3.94E-04	7.4	7.4
L7G10	14.91	0.65	0.152	0.013	6.562	0.560	0.835	0.045	6.32	0.40	3.10	18.20	0.8	56.9	1	4.15E-05	2.58E-03	1.68E-04	6.5	12.9
L7G14	3.04	0.15	0.032	0.003	31.348	2.752	0.751	0.035	36.43	11.99	3.83	2.87	22.3	9.5	17	3.71E-05	1.79E-02	1.20E-03	17.7	8.7
L7G16	5.62	0.24	0.059	0.005	16.949	1.465	0.764	0.044	15.60	12.56	3.12	1.18	35.4	21.6	11	4.70E-05	6.79E-03	4.02E-04	23.8	14.4
L7G23	1.508	0.058	0.015	0.001	66.845	5.809	0.709	0.042	74.00	111.80	4.48	0.68	15.6	5.4	17	1.51E-05	3.07E-02	1.84E-03	25.4	12.4
L7G24	0.407	0.017	0.006	0.000	162.602	12.426	0.466	0.020	251.90	1983.00	7.82	0.13	18.6	1.7	24	1.01E-05	1.07E-01	6.41E-03	15.4	6.3
L7G27	2.933	0.098	0.027	0.002	36.819	2.982	0.768	0.027	71.30	98.70	8.07	0.75	15.2	6.3	21	2.90E-05	2.92E-02	1.80E-03	17.1	7.5
L7G28	2.114	0.089	0.020	0.002	48.876	4.061	0.729	0.030	72.20	98.30	5.85	0.77	18.0	5.3	34	2.78E-05	3.35E-02	1.93E-03	25.2	8.8
L7G33	11.38	0.6	0.110	0.009	9.074	0.774	0.795	0.047	6.65	0.40	2.84	17.80	38.6	42.7	2	5.60E-05	2.71E-03	1.79E-04	9.1	12.9
L7G34	2.358	0.074	0.024	0.002	41.051	3.370	0.756	0.031	82.60	125.10	7.26	0.67	16.0	6.5	18	2.15E-05	3.70E-02	2.16E-03	15.7	7.4
L7G35	2.86	0.1	0.030	0.003	33.670	2.834	0.736	0.041	42.10	11.85	4.46	3.57	24.5	10.3	6	1.53E-05	1.84E-02	1.08E-03	14.7	12.1
L7G36	9.94	0.46	0.101	0.009	9.881	0.908	0.783	0.051	8.03	0.88	2.62	9.65	45.6	42.5	4	5.89E-05	4.50E-03	2.96E-04	10.4	10.5
L7G37	1.887	0.083	0.020	0.002	49.628	4.187	0.717	0.031	57.63	4.42	3.73	13.02	19.7	5.5	29	4.37E-05	1.95E-02	1.13E-03	23.6	8.9
L7G39	2.77	0.12	0.031	0.003	32.258	2.810	0.695	0.038	42.09	11.96	4.36	3.52	36.0	10.2	17	2.72E-05	2.08E-02	1.30E-03	20.8	10.2
L7G43	7.29	0.27	0.065	0.005	15.361	1.251	0.772	0.032	22.16	7.50	5.89	2.96	34.8	17.6	12	3.28E-05	1.05E-02	6.32E-04	23.9	13.9
L7G44	1.193	0.038	0.013	0.001	75.075	6.200	0.649	0.023	114.20	74.00	5.41	1.57	20.4	3.1	35	2.06E-05	5.71E-02	3.54E-03	20.5	7.1
L7G45	35.8	4.7	0.348	0.063	2.874	0.520	0.825	0.061	2.38	6.05	2.68	0.44	36.8	173.8	1	5.06E-05	6.03E-04	1.04E-04	22.6	45.4
L7G46	2.6	0.14	0.025	0.002	39.841	3.492	0.724	0.029	57.50	27.50	5.74	2.09	23.1	6.4	16	1.82E-05	3.58E-02	2.59E-03	16.9	8.5
L7G47	2.59	0.11	0.026	0.002	39.093	3.209	0.737	0.035	46.50	20.01	4.33	2.33	20.8	7.6	16	2.88E-05	2.21E-02	1.35E-03	17.3	8.7
L7G48	3.52	0.19	0.034	0.003	29.412	2.855	0.775	0.035	41.40	99.00	5.79	0.42	17.1	10.1	6	2.13E-05	1.50E-02	1.72E-03	13.0	10.7
L7G51	2.01	0.11	0.021	0.002	48.077	4.623	0.742	0.042	51.10	55.60	3.95	0.95	16.0	7.4	10	1.70E-05	2.07E-02	2.22E-03	19.6	12.6
L7G52	6.96	0.18	0.066	0.005	15.106	1.209	0.816	0.031	39.43	79.90	11.62	0.48	11.0	17.3	8	2.00E-05	1.78E-02	1.18E-03	15.6	11.1
L7G53	7.69	0.36	0.078	0.007	12.870	1.126	0.794	0.048	9.12	6.06	2.72	1.45	27.4	30.8	2	2.88E-05	4.30E-03	2.70E-04	11.2	15.8
L7G56	0.264	0.013	0.006	0.000	177.620	14.197	0.371	0.021	206.00	197.20	2.52	1.00	21.4	2.0	40	1.68E-05	8.45E-02	5.01E-03	19.5	6.3
L7G57	10.44	0.54	0.106	0.009	9.443	0.803	0.802	0.041	9.24	30.57	3.89	0.29	30.6	36.0	2	2.31E-05	3.85E-03	2.35E-04	15.5	22.0
L7G60	3.12	0.1	0.033	0.003	30.120	2.540	0.756	0.042	28.91	47.90	3.74	0.57	21.9	11.7	13	2.54E-05	1.31E-02	7.60E-04	27.0	15.1
L7G62	6.91	0.3	0.056	0.005	17.953	1.515	0.814	0.039	19.51	12.61	4.24	1.66	10.1	18.1	7	2.00E-05	8.27E-03	6.13E-04	29.3	22.2
L7G65	2.224	0.09	0.021	0.002	48.239	4.189	0.722	0.041	34.53	125.10	2.81	0.31	19.4	7.2	6	4.03E-05	1.37E-02	8.88E-04	7.5	6.2
L7G69	10.62	0.57	0.087	0.008	11.534	1.051	0.806	0.056	6.42	13.16	2.10	0.55	21.9	39.9	2	4.30E-05	2.91E-03	1.57E-04	11.1	15.7
L7G71	2.89	0.12	0.025	0.002	40.000	3.360	0.772	0.037	33.66	38.71	3.01	0.96	13.1	7.8	7	2.94E-05	1.76E-02	1.06E-03	9.3	7.1
L7G74	5.69	0.25	0.050	0.005	19.841	1.772	0.815	0.054	13.92	0.17	2.45	117.00	8.7	22.4	7	3.55E-05	6.68E-03	3.96E-04	20.4	15.5
L7G80	3.35	0.1	0.032	0.003	31.348	2.555	0.761	0.033	50.70	4.52	5.44	12.25	19.7	8.9	13	2.01E-05	2.03E-02	1.19E-03	22.0	12.3
L7G82	2.619	0.089	0.024	0.002	41.102	3.379	0.652	0.025	55.13	17.78	5.24	2.98	36.8	5.9	15	2.30E-05	2.14E-02	1.43E-03	21.0	11.0
L7G83	1.693	0.061	0.015	0.001	68.259	5.591	0.710	0.027	97.70	134.10	5.69	0.69	15.1	3.5	20	1.95E-05	3.74E-02	2.16E-03	19.0	8.6
L7G86	10.3	0.62	0.079	0.007	12.610	1.177	0.816	0.054	7.09	0.16	2.57	53.80	13.2	35.3	2	2.25E-05	3.33E-03	2.08E-04	18.4	26.1
L7G87	23.5	2.2	0.165	0.021	6.061	0.771	0.835	0.038	4.72	0.08	3.39	56.19	0.9	52.4	2	3.33E-05	1.24E-03	2.54E-04	33.3	47.6
L7G89	1.91	0.12	0.017	0.002	57.870	5.023	0.668	0.028	57.00	45.00	3.89	1.23	23.8	4.5	15	3.37E-05	2.02E-02	2.67E-03	15.2	8.1
L7G92	6.2	0.52	0.049	0.006	20.534	2.319	0.829	0.071	9.23	6.98	1.93	1.28	2.7	28.4	2	3.57E-05	5.30E-03	4.04E-04	7.3	10.3
L7G93	1.584	0.054	0.014	0.001	69.832	5.852	0.673	0.029	98.50	83.80	5.62	1.11	19.1	3.8	23	2.08E-05	4.22E-02	2.49E-03	18.1	7.6
L7G95	2.95	0.11	0.024	0.002	40.917	3.348	0.737	0.029	53.80	0.52	5.51	107.90	19.9	6.2	14	1.95E-05	2.45E-02	1.44E-03	20.2	10.9
L7G97	12.6	0.45	0.101	0.008	9.911	0.825	0.802	0.034	16.58	12.38	7.23	1.28	29.1	28.7	7	5.94E-05	6.65E-03	4.08E-04	12.2	9.3
L7G98	4.53	0.19	0.035	0.003	28.329	2.488	0.816	0.049	19.78	7.18	3.00	2.66	5.8	14.3	8	2.37E-05	7.33E-03	5.42E-04	31.8	22.6
L7G99	1.704	0.074	0.017	0.001	58.651	4.816	0.642	0.030	69.98	11.13	4.03	6.09	27.1	4.8	14	3.09E-05	2.90E-02	1.75E-03	10.8	5.8
L7G101	0.523	0.023	0.008	0.001	123.609	10.390	0.517	0.029	165.60	103.30	3.17	1.63	21.1	2.6	39	2.32E-05	6.92E-02	4.12E-03	16.8	5.5
L7G103	0.221	0.012	0.005	0.000	191.939	15.841	0.323	0.019	247.20	150.70	2.12	1.66	21.8	2.0	36	1.64E-05	1.26E-01	8.41E-03	12.0	4.1
L7G106	1.588	0.051	0.018	0.002	55.310	4.589	0.720	0.033	78.10	30.33	4.62	2.60	17.2	5.2	18	2.34E-05	3.15E-02	1.89E-03	16.9	8.0
L7G107	2.738	0.099	0.031	0.003	32.362	2.618	0.733	0.034	41.00	43.50	4.20	0.95	26.2	9.0	9	3.15E-05	1.36E-02	1.06E-03	14.5	9.7
L7G108	2.37	0.1	0.027	0.002	36.900	3.132	0.715	0.037	53.27	77.00	4.89	0.69	27.0	8.6	16	2.33E-05	2.30E-02	1.44E-03	20.6	10.4
L7G112	5.88	0.3	0.064	0.007	15.528	1.615	0.817	0.066	8.49	0.63	1.73	13.22	10.1	34.9	2	2.41E-05	3.27E-03	2.87E-04	17.5	24.8
L7G113	8.49	0.78	0.096	0.012	10.373	1.291	0.790	0.110	2.00	3.94	0.65	0.50	37.6	86.3	3	5.33E-05	8.36E-04	5.33E-05	46.4	53.7
L7G114	1.995	0.067	0.024	0.002	41.169	3.390	0.701	0.030	78.00	37.64	5.94	2.05	26.9	6.5	23	2.63E-05	3.33E-02	2.03E-03	18.1	7.6
L7G115	7.33	0.19	0.076	0.006	13.089	1.045	0.806	0.033	28.67	97.10	7.52	0.29	19.2	21.2	12	3.06E-05	1.15E-02	6.37E-04	23.6	13.7

L7G116	2.64	0.15	0.029	0.003	35.088	3.324	0.765	0.034	43.60	19.20	4.32	2.27	16.6	8.2	11	2.34E-05	2.22E-02	1.69E-03	14.6	8.9
L7G120	5.63	0.26	0.062	0.005	16.181	1.335	0.780	0.047	16.59	67.50	3.81	0.24	28.9	24.0	12	4.82E-05	6.94E-03	4.10E-04	24.7	14.4
L7G3	*16.2*	*1.1*	*0.159*	*0.015*	*6.289*	*0.593*	*0.862*	*0.047*	*4.76*	*16.21*	*2.63*	*0.27*	*-37.5*	*62.6*	*3*	*3.35E-05*	*1.95E-03*	*1.30E-04*	*31.7*	*36.6*
L7G5	*22.5*	*1.2*	*0.227*	*0.021*	*4.405*	*0.408*	*0.850*	*0.048*	*4.90*	*7.45*	*3.52*	*0.63*	*-30.3*	*90.9*	*5*	*7.72E-05*	*2.01E-03*	*1.31E-04*	*22.3*	*20.0*
L7G29	*14.63*	*0.71*	*0.129*	*0.011*	*7.764*	*0.663*	*0.848*	*0.054*	*5.98*	*23.25*	*3.13*	*0.26*	*-14.0*	*57.6*	*3*	*5.21E-05*	*2.58E-03*	*1.63E-04*	*15.4*	*17.8*
L7G30	*64.2*	*1.5*	*0.537*	*0.042*	*1.862*	*0.146*	*0.874*	*0.026*	*6.63*	*2.72*	*15.69*	*2.53*	*-239.2*	*127.3*	*4*	*5.19E-05*	*2.85E-03*	*1.83E-04*	*18.7*	*18.8*
L7G40	*11.24*	*0.55*	*0.106*	*0.010*	*9.479*	*0.854*	*0.840*	*0.061*	*7.03*	*2.88*	*2.67*	*2.50*	*-4.0*	*53.1*	*4*	*5.52E-05*	*3.45E-03*	*2.22E-04*	*14.5*	*14.5*
L7G49	*21.99*	*0.95*	*0.195*	*0.017*	*5.136*	*0.448*	*0.848*	*0.052*	*5.29*	*14.22*	*4.72*	*0.37*	*-22.0*	*84.1*	*3*	*4.74E-05*	*2.99E-03*	*1.82E-04*	*14.6*	*16.9*
L7G63	*46.9*	*1.9*	*0.358*	*0.030*	*2.793*	*0.234*	*0.852*	*0.046*	*2.05*	*1.60*	*3.11*	*1.43*	*-59.1*	*138.4*	*1*	*6.38E-05*	*7.82E-04*	*5.09E-05*	*13.8*	*27.7*
L7G68	*10.92*	*0.59*	*0.089*	*0.010*	*11.198*	*1.241*	*0.836*	*0.073*	*3.59*	*2.73*	*1.18*	*1.48*	*-0.3*	*53.6*	*4*	*2.65E-05*	*1.38E-03*	*1.32E-04*	*75.3*	*75.7*
L7G70	*182*	*7.8*	*1.464*	*0.130*	*0.683*	*0.061*	*0.856*	*0.030*	*1.62*	*0.05*	*9.99*	*31.15*	*-619.3*	*419.4*	*2*	*4.80E-05*	*5.62E-04*	*5.49E-05*	*51.1*	*72.5*
L7G73	*41.3*	*1.9*	*0.330*	*0.031*	*3.030*	*0.285*	*0.877*	*0.061*	*1.84*	*1.67*	*2.26*	*1.25*	*-137.0*	*170.9*	*0*	*5.02E-05*	*1.12E-03*	*7.41E-05*	*6.2*	*17.4*
L7G76	*22.67*	*0.83*	*0.193*	*0.016*	*5.176*	*0.429*	*0.840*	*0.041*	*5.67*	*9.85*	*4.33*	*0.63*	*-7.7*	*66.1*	*5*	*4.83E-05*	*2.44E-03*	*1.33E-04*	*29.3*	*26.2*
L7G81	*121.6*	*9.9*	*0.885*	*0.086*	*1.130*	*0.110*	*0.857*	*0.062*	*0.68*	*0.04*	*2.92*	*16.24*	*-274.8*	*476.3*	*0*	*3.85E-05*	*2.41E-04*	*2.58E-05*	*36.9*	*104.4*
L7G90	*18.37*	*0.97*	*0.134*	*0.012*	*7.485*	*0.672*	*0.837*	*0.056*	*4.71*	*0.87*	*3.18*	*5.44*	*-1.6*	*61.8*	*6*	*3.78E-05*	*2.34E-03*	*1.30E-04*	*46.8*	*38.3*
L7G100	*10.56*	*0.43*	*0.080*	*0.007*	*12.516*	*1.049*	*0.843*	*0.041*	*11.59*	*8.19*	*4.07*	*1.37*	*-5.0*	*27.3*	*2*	*3.15E-05*	*5.08E-03*	*3.01E-04*	*8.6*	*12.2*
L7G109	*133*	*12*	*1.255*	*0.130*	*0.797*	*0.083*	*0.911*	*0.081*	*0.34*	*1.00*	*1.58*	*0.35*	*-2413.0*	*1351.2*	*0*	*1.73E-05*	*1.34E-04*	*1.20E-05*	*147.1*	*416.1*
L7G111	*17.68*	*0.79*	*0.174*	*0.014*	*5.750*	*0.463*	*0.846*	*0.040*	*6.97*	*35.44*	*4.54*	*0.19*	*-16.2*	*58.2*	*3*	*3.67E-05*	*3.11E-03*	*1.89E-04*	*18.2*	*21.0*
L7G117	*41.8*	*2.1*	*0.418*	*0.037*	*2.392*	*0.212*	*0.859*	*0.054*	*1.80*	*0.40*	*2.66*	*4.63*	*-103.0*	*190.5*	*2*	*5.38E-05*	*6.97E-04*	*4.97E-05*	*36.8*	*52.1*
L7G118	*8.67*	*0.67*	*0.088*	*0.010*	*11.390*	*1.245*	*0.846*	*0.038*	*20.00*	*12.39*	*5.93*	*1.56*	*-7.8*	*28.0*	*3*	*2.56E-05*	*5.68E-03*	*1.04E-03*	*14.3*	*16.7*
Populati on 2																				
L7G1	30.3	1.8	0.312	0.029	3.205	0.298	0.814	0.056	2.07	2.98	2.17	0.66	65.2	142.5	1	6.07E-05	7.50E-04	5.22E-05	15.2	30.3
L7G11	1.14	0.046	0.019	0.002	51.546	3.986	0.476	0.022	98.50	41.08	3.78	2.23	57.1	5.6	29	1.48E-05	4.39E-02	2.56E-03	30.9	11.6
L7G12	17.28	0.69	0.178	0.015	5.618	0.473	0.802	0.044	5.60	0.61	3.54	8.86	53.5	64.5	6	4.35E-05	2.26E-03	1.57E-04	42.1	34.5
L7G19	3.27	0.16	0.041	0.003	24.691	2.012	0.628	0.036	18.53	8.12	2.22	2.15	69.5	13.2	6	4.22E-05	7.78E-03	4.47E-04	12.6	10.3
L7G21	2.073	0.096	0.027	0.002	37.313	3.063	0.544	0.025	30.48	37.07	2.70	0.87	64.2	7.6	9	2.43E-05	1.35E-02	7.79E-04	19.0	12.7
L7G25	3.42	0.19	0.038	0.003	26.247	2.342	0.648	0.043	14.24	17.44	1.90	0.84	59.1	14.4	5	2.09E-05	6.98E-03	4.26E-04	23.7	21.2
L7G26	1.049	0.066	0.017	0.001	59.559	4.966	0.454	0.026	82.90	55.40	3.02	1.56	52.4	5.6	31	2.26E-05	3.40E-02	2.65E-03	27.8	10.2
L7G31	10.2	0.53	0.103	0.009	9.728	0.861	0.777	0.049	5.69	4.49	2.18	1.62	51.6	41.5	3	3.46E-05	2.54E-03	1.75E-04	23.6	27.3
L7G32	1.189	0.058	0.019	0.002	51.760	4.287	0.464	0.024	63.70	80.60	2.94	0.83	58.7	6.2	21	2.14E-05	2.63E-02	1.84E-03	25.8	11.4
L7G50	4.99	0.38	0.053	0.005	18.762	1.760	0.676	0.039	17.84	0.27	3.29	74.90	70.8	18.2	13	3.69E-05	1.27E-02	9.88E-04	19.2	10.8
L7G58	1.459	0.07	0.021	0.002	48.544	4.242	0.578	0.035	51.80	25.77	3.13	1.89	43.5	7.0	11	2.36E-05	2.10E-02	1.24E-03	15.4	9.3
L7G64	25.6	1.2	0.209	0.018	4.776	0.411	0.804	0.046	4.19	8.80	3.70	0.53	60.2	79.1	2	2.79E-05	1.64E-03	1.12E-04	30.1	42.7
L7G66	7.1	0.27	0.063	0.006	15.773	1.368	0.732	0.037	13.87	2.42	3.04	6.40	55.1	19.9	9	4.18E-05	6.17E-03	3.57E-04	24.1	16.1
L7G67	1.768	0.076	0.022	0.002	46.490	3.890	0.544	0.029	53.74	8.90	2.98	6.74	51.4	6.7	33	4.28E-05	2.54E-02	1.38E-03	21.0	7.4
L7G75	0.835	0.038	0.015	0.001	66.313	5.277	0.403	0.020	98.10	46.94	2.53	2.29	53.3	4.9	36	2.53E-05	4.52E-02	2.65E-03	21.8	7.4
L7G78	16.79	0.81	0.151	0.014	6.609	0.612	0.799	0.054	4.44	3.90	2.48	1.23	48.8	67.0	2	2.72E-05	1.77E-03	1.08E-04	28.7	40.7
L7G84	1.048	0.065	0.015	0.001	66.800	5.355	0.430	0.025	67.80	89.60	3.00	0.72	49.6	5.0	10	1.87E-05	3.17E-02	2.43E-03	11.6	7.4
L7G85	3.6	0.2	0.036	0.003	27.778	2.315	0.613	0.037	22.59	46.85	3.26	0.46	66.1	12.2	6	2.20E-05	9.45E-03	5.57E-04	19.9	16.3
L7G88	3.58	0.17	0.034	0.003	29.412	2.682	0.647	0.034	24.20	61.60	3.33	0.38	52.9	10.7	9	3.97E-05	7.63E-03	9.21E-04	20.5	13.9
L7G96	25	1.2	0.194	0.017	5.157	0.452	0.800	0.041	3.25	0.42	2.67	9.10	62.2	65.6	4	3.58E-05	1.68E-03	1.26E-04	45.7	45.9
L7G102	2.113	0.089	0.029	0.002	34.483	2.854	0.580	0.027	38.95	25.10	3.17	1.59	60.9	8.2	9	2.81E-05	1.67E-02	1.04E-03	13.2	8.9
L7G119	0.786	0.029	0.017	0.001	58.617	4.810	0.391	0.018	122.80	82.30	3.87	1.47	62.0	5.7	17	2.07E-05	4.60E-02	3.49E-03	12.4	6.1
Populati on 3																				
L7G8	5.49	0.24	0.067	0.006	14.993	1.281	0.684	0.028	13.43	0.31	2.61	44.50	84.6	17.0	5	6.14E-05	4.80E-03	3.26E-04	11.7	10.5
L7G15	3.5	0.2	0.049	0.004	20.408	1.833	0.595	0.045	12.87	13.53	1.72	0.90	97.5	19.8	8	1.80E-05	5.16E-03	3.08E-04	59.2	42.0
L7G18	6.8	0.59	0.075	0.008	13.316	1.383	0.710	0.073	5.17	6.07	1.28	0.84	79.3	45.1	6	3.85E-05	2.37E-03	1.60E-04	45.3	37.1
L7G20	6.9	0.32	0.076	0.007	13.210	1.152	0.694	0.035	13.42	16.22	3.53	0.79	90.0	23.0	6	5.03E-05	6.02E-03	3.72E-04	13.7	11.2
L7G22	1.076	0.045	0.022	0.002	45.977	3.594	0.339	0.016	80.60	35.40	3.00	2.39	88.1	7.4	14	1.83E-05	3.23E-02	1.95E-03	16.4	8.8
L7G38	2.041	0.095	0.032	0.003	30.960	2.588	0.498	0.027	41.95	111.40	3.69	0.38	89.5	10.3	20	1.92E-05	1.99E-02	1.21E-03	36.0	16.3
L7G41	1.649	0.078	0.027	0.002	37.244	3.052	0.436	0.026	52.65	134.40	4.06	0.41	87.8	9.1	12	2.10E-05	2.42E-02	1.51E-03	16.3	9.5
L7G54	1.41	0.066	0.029	0.002	35.051	2.826	0.393	0.020	58.90	118.40	4.27	0.48	103.2	9.5	18	2.94E-05	2.41E-02	1.49E-03	17.5	8.3
L7G55	49.6	2.2	0.503	0.045	1.988	0.178	0.807	0.041	1.89	0.04	3.91	43.95	156.4	167.2	1	3.13E-05	7.51E-04	5.29E-05	29.4	58.8
L7G59	3.03	0.15	0.043	0.004	23.256	1.947	0.553	0.025	25.12	48.31	3.24	0.49	100.1	12.1	13	3.00E-05	1.12E-02	6.60E-04	26.6	14.9
L7G77	31.3	1.3	0.292	0.026	3.425	0.305	0.799	0.042	3.80	0.12	3.91	42.20	101.6	100.4	4	4.01E-05	1.28E-03	1.27E-04	53.6	53.9
L7G79	4.32	0.21	0.051	0.005	19.569	1.838	0.619	0.035	16.57	3.74	2.37	4.65	91.7	16.9	11	2.80E-05	7.57E-03	4.51E-04	35.8	21.7
L7G104	1.864	0.074	0.029	0.003	34.843	3.035	0.517	0.027	49.24	99.10	4.02	0.51	75.0	9.1	14	2.54E-05	1.88E-02	1.24E-03	20.3	10.9
L7G105	0.765	0.036	0.024	0.002	42.409	3.237	0.266	0.014	129.60	363.00	6.88	0.36	109.4	8.7	36	1.92E-05	5.94E-02	3.46E-03	21.9	7.4
L7G7	4.11	0.13	0.070	0.006	14.306	1.126	0.491	0.018	37.44	12.45	5.11	2.85	198.7	18.6	11	2.65E-05	1.33E-02	7.82E-04	21.6	13.1
L7G17	123	6.8	1.260	0.120	0.794	0.076	0.768	0.041	0.68	0.64	3.07	1.08	1550.7	367.5	1	5.23E-05	2.65E-04	2.30E-05	49.6	99.4

U-Pb data

AFT data

#grains	Ns	ΣpiΩi	2σΣpiΩi	eta (yr cm^2	2 sig abs	χ^2	P(χ^2)	Pooled age	2σ Ma
118	1049	4.11E-05	4.58E-07	6.92E-01	1.10E-02	160.23	0.00	17.6	1.1

Grain Number	Pb207/U 235	Pb207/U 235 error (2s)	Pb206/U 238	Pb206/U 238 error (2s)	U238/Pb 206	U238/Pb 206 error (2s)	Pb207/Pb206	Pb207/Pb206 error (2s)	Approx U (ppm)	Approx Th (ppm)	Approx Pb (ppm)	U/Th	207corrAge (Ma)	207corrAge error (2s,Ma)
Population 1														
L8G1	4.42	0.31	0.042	0.003	23.753	1.636	0.770	0.027	50.30	117.10	8.39	0.42	23.0	9.7
L8G2	1.499	0.11	0.016	0.001	64.226	4.537	0.708	0.031	100.90	91.30	5.41	1.12	16.3	4.2
L8G6	2.15	0.24	0.023	0.003	44.248	4.895	0.681	0.044	37.20	30.30	2.48	1.67	28.8	8.8
L8G7	3.48	0.24	0.035	0.003	28.409	2.018	0.740	0.034	39.23	26.06	5.03	1.46	27.9	10.1
L8G8	8.58	0.65	0.079	0.006	12.642	0.975	0.786	0.041	8.58	0.24	2.42	47.50	33.3	26.9
L8G9	2.84	0.22	0.032	0.003	31.447	2.472	0.670	0.031	36.50	14.39	3.54	2.50	43.5	8.8
L8G11	5.54	0.44	0.053	0.004	18.868	1.531	0.781	0.036	25.80	39.80	5.03	0.64	24.2	16.0
L8G12	1.629	0.12	0.017	0.001	59.172	4.202	0.699	0.029	116.20	174.30	6.90	0.66	19.0	4.3
L8G14	7.39	0.52	0.069	0.005	14.556	1.038	0.789	0.039	18.13	17.15	4.74	1.06	27.0	22.3
L8G15	0.693	0.069	0.010	0.001	96.525	8.199	0.504	0.056	41.00	11.41	0.94	3.51	28.1	5.3
L8G16	2.47	0.37	0.024	0.003	41.152	5.589	0.714	0.043	78.00	78.00	4.43	1.06	24.4	9.2
L8G18	10.94	0.73	0.102	0.007	9.852	0.689	0.781	0.031	26.83	0.71	10.06	40.10	47.5	26.5
L8G19	6.51	0.46	0.057	0.004	17.513	1.319	0.808	0.046	17.80	8.13	4.16	2.23	13.2	21.7
L8G21	13.11	1.2	0.114	0.010	8.795	0.774	0.821	0.038	13.80	4.28	6.35	3.62	14.4	36.0
L8G25	7.58	0.53	0.069	0.005	14.556	1.017	0.808	0.033	18.43	6.26	5.35	3.04	16.0	19.0
L8G26	1.331	0.089	0.015	0.001	66.711	4.895	0.650	0.031	123.70	33.57	6.32	3.75	22.8	4.2
L8G27	1.297	0.093	0.015	0.001	67.385	4.995	0.654	0.031	95.30	43.60	4.84	2.27	22.1	4.2
L8G29	6.34	0.44	0.058	0.004	17.271	1.163	0.794	0.039	25.42	5.84	5.72	4.50	20.2	18.8
L8G31	3.072	0.2	0.030	0.002	33.113	2.303	0.733	0.031	81.10	0.50	9.59	179.00	25.6	8.0
L8G32	9	0.6	0.085	0.006	11.834	0.854	0.800	0.036	18.34	15.77	6.51	1.21	25.6	25.4
L8G33	2.483	0.18	0.025	0.002	40.816	2.999	0.740	0.034	49.79	13.46	4.69	3.98	19.3	7.1
L8G34	6.67	0.44	0.061	0.004	16.420	1.105	0.787	0.030	19.69	41.50	5.43	0.49	24.9	15.4
L8G35	3.27	0.22	0.033	0.002	30.395	2.125	0.734	0.032	42.80	29.30	5.28	1.51	27.7	9.0
L8G36	11.72	0.75	0.109	0.007	9.217	0.620	0.791	0.031	17.03	8.21	7.73	2.17	41.7	28.3
L8G37	0.454	0.03	0.007	0.000	151.057	10.040	0.491	0.019	315.00	670.00	6.68	0.49	18.6	1.6
L8G39	2.29	0.17	0.024	0.002	41.824	2.974	0.693	0.025	76.20	30.10	7.29	2.71	28.1	5.4
L8G40	2.93	0.2	0.029	0.002	34.602	2.634	0.747	0.038	44.50	3.99	4.79	11.92	21.2	9.2
L8G42	0.862	0.057	0.010	0.001	95.785	6.331	0.602	0.019	258.60	8.52	7.88	30.20	20.0	2.1
L8G43	5.33	0.42	0.051	0.004	19.608	1.653	0.765	0.046	16.17	0.45	2.79	57.00	30.1	19.5
L8G44	6.25	0.48	0.059	0.005	17.094	1.315	0.793	0.039	27.57	69.30	6.55	0.39	20.9	19.0
L8G46	12.28	0.85	0.114	0.009	8.764	0.653	0.792	0.040	8.28	11.72	3.68	0.69	43.0	37.8
L8G48	9.22	0.69	0.087	0.007	11.455	0.918	0.805	0.058	7.06	4.88	2.19	1.41	22.8	41.6
L8G50	5.78	0.5	0.053	0.005	18.832	1.667	0.760	0.059	9.33	2.35	1.80	3.92	33.6	25.8
L8G53	0.907	0.064	0.010	0.001	95.511	6.659	0.631	0.029	144.70	249.80	4.81	0.58	17.5	2.8
L8G54	2.191	0.15	0.024	0.002	42.355	3.050	0.683	0.037	46.80	41.00	3.50	1.11	29.7	7.5
L8G55	4.4	0.3	0.040	0.003	25.063	1.759	0.816	0.040	34.60	7.07	5.15	4.92	6.5	13.3
L8G56	0.86	0.056	0.010	0.001	97.182	6.517	0.600	0.023	189.70	255.70	5.78	0.75	19.8	2.4
L8G58	4.15	0.31	0.041	0.003	24.450	1.793	0.740	0.045	23.33	2.83	3.11	8.19	32.5	15.3
L8G59	1.451	0.099	0.015	0.001	66.845	4.915	0.710	0.036	95.80	57.70	4.80	1.65	15.4	4.6
L8G62	1.293	0.088	0.014	0.001	72.516	5.259	0.711	0.037	105.60	429.80	6.42	0.23	14.1	4.4
L8G63	2.186	0.15	0.023	0.002	44.405	3.155	0.707	0.034	46.10	35.60	4.48	1.23	23.9	6.6
L8G64	4.25	0.29	0.041	0.003	24.450	1.734	0.773	0.038	40.74	3.54	7.32	10.83	21.3	13.0
L8G65	4.17	0.27	0.040	0.003	24.938	1.679	0.759	0.024	50.08	29.55	9.00	1.59	25.5	8.4
L8G66	4.77	0.38	0.047	0.004	21.368	1.644	0.763	0.051	16.60	20.93	3.41	0.75	28.3	19.7
L8G68	3.47	0.26	0.037	0.003	27.174	2.068	0.702	0.044	18.04	7.13	2.38	2.36	40.7	13.6
L8G69	3.31	0.23	0.034	0.002	29.851	2.139	0.732	0.031	45.87	18.21	6.55	2.38	28.7	8.9
L8G70	3.29	0.22	0.031	0.002	32.258	2.289	0.764	0.034	52.20	40.00	7.01	1.22	18.4	8.9
L8G71	0.212	0.022	0.005	0.000	198.413	16.141	0.317	0.032	117.20	61.60	1.25	1.77	21.3	2.2
L8G73	4.11	0.27	0.037	0.003	27.027	1.899	0.803	0.036	37.72	18.85	6.45	1.86	10.0	11.1
L8G76	1.703	0.11	0.018	0.001	55.586	3.708	0.675	0.019	179.40	57.90	13.05	2.95	23.7	3.3
L8G77	2.036	0.13	0.021	0.001	46.838	3.071	0.706	0.023	100.80	20.15	8.49	4.68	22.8	4.4
L8G78	3.33	0.22	0.031	0.002	31.949	2.246	0.774	0.031	60.90	13.63	8.34	4.29	16.0	8.2
L8G79	0.875	0.06	0.011	0.001	92.421	6.492	0.582	0.023	199.60	76.60	6.77	2.47	22.5	2.6
L8G80	3.297	0.21	0.031	0.002	32.154	2.275	0.794	0.036	56.40	16.85	8.03	3.17	10.7	9.4
L8G81	2.444	0.16	0.025	0.002	39.494	2.808	0.709	0.023	119.60	20.18	9.87	6.15	26.4	5.3

Ns	Area (cm^2)	$^{238}U/^{43}Ca$	2σ	FT Age	2σ
7	2.10E-05	1.94E-02	1.40E-03	11.9	9.0
10	2.49E-05	3.33E-02	2.74E-03	8.3	5.3
9	3.08E-05	1.01E-02	2.02E-04	20.0	13.3
11	2.78E-05	1.65E-02	1.12E-04	16.5	10.0
5	4.12E-05	3.46E-03	1.15E-04	24.2	21.7
15	2.64E-05	1.48E-02	1.99E-03	26.6	14.2
5	3.69E-05	1.15E-02	1.21E-03	8.1	7.3
17	2.01E-05	4.19E-02	2.65E-04	13.9	6.8
4	3.05E-05	6.28E-03	1.07E-03	14.4	14.6
11	2.26E-05	1.64E-02	4.90E-05	20.4	12.3
6	1.22E-05	1.34E-02	9.09E-04	25.4	20.8
15	3.57E-05	1.12E-02	3.33E-03	26.0	15.5
8	2.62E-05	7.40E-03	5.91E-05	28.5	20.2
6	2.59E-05	6.20E-03	5.07E-04	25.8	21.2
5	2.66E-05	6.43E-03	1.21E-03	20.2	18.4
22	2.38E-05	4.00E-02	5.70E-03	16.0	7.2
23	2.90E-05	3.23E-02	3.50E-04	17.0	7.1
10	2.83E-05	8.14E-03	8.00E-04	29.9	19.2
12	1.47E-05	2.84E-02	6.20E-04	19.8	11.5
3	3.99E-05	5.97E-03	1.29E-03	8.7	10.2
16	1.89E-05	2.06E-02	5.29E-04	28.4	14.2
3	1.87E-05	6.36E-03	1.52E-03	17.4	20.5
13	2.68E-05	1.31E-02	7.76E-04	25.6	14.3
3	4.59E-05	5.39E-03	5.26E-05	8.4	9.7
33	1.33E-05	1.10E-01	4.79E-04	15.6	5.4
10	1.62E-05	3.12E-02	2.83E-03	13.7	8.7
13	2.69E-05	1.42E-02	2.32E-03	23.4	13.5
25	1.45E-05	7.02E-02	1.02E-06	17.0	6.8
9	5.08E-05	5.29E-03	5.45E-04	23.1	15.6
4	1.99E-05	7.02E-03	1.57E-03	19.8	20.3
4	3.50E-05	2.47E-03	2.14E-03	31.9	42.1
1	2.50E-05	2.33E-03	4.39E-04	11.9	23.8
6	3.47E-05	3.14E-03	1.30E-03	38.0	34.8
28	3.14E-05	4.96E-02	4.27E-04	12.4	4.7
6	3.15E-05	1.59E-02	8.66E-04	8.3	6.8
7	2.51E-05	1.11E-02	4.26E-04	17.4	13.2
28	2.21E-05	5.66E-02	7.22E-03	15.5	6.2
10	3.72E-05	7.42E-03	2.16E-03	25.0	17.4
14	2.21E-05	3.08E-02	1.10E-03	14.2	7.6
14	1.85E-05	2.61E-02	1.07E-03	20.1	10.8
5	1.67E-05	1.43E-02	5.49E-03	14.4	14.0
6	1.93E-05	9.99E-03	4.10E-04	21.5	17.6
6	1.81E-05	1.22E-02	7.46E-04	18.7	15.3
2	2.02E-05	4.18E-03	1.61E-03	16.4	24.0
3	4.35E-05	4.99E-03	1.91E-04	9.6	11.0
2	2.97E-05	1.28E-02	2.17E-04	3.6	5.1
7	2.88E-05	1.48E-02	1.75E-04	11.3	8.6
16	2.45E-05	3.20E-02	6.63E-05	14.1	7.1
5	1.97E-05	9.75E-03	2.59E-04	18.0	16.1
27	1.75E-05	5.35E-02	1.22E-03	19.9	7.7
16	2.09E-05	2.87E-02	2.18E-04	18.4	9.2
12	2.51E-05	1.69E-02	3.85E-03	19.6	12.2
21	1.97E-05	5.77E-02	9.87E-04	12.8	5.6
9	2.09E-05	1.63E-02	7.82E-04	18.2	12.2
12	1.47E-05	3.78E-02	4.23E-03	14.9	8.8

L8G84	9.42	0.67	0.085	0.006	11.710	0.864	0.803	0.037	13.41	34.00	4.14	0.41	23.7	26.3	4	2.12E-05	4.54E-03	4.53E-04	28.6	28.8
L8G85	3.19	0.22	0.032	0.002	31.447	2.274	0.751	0.035	26.75	15.15	3.05	1.86	22.3	9.4	1	1.44E-05	9.05E-03	4.80E-04	5.3	10.6
L8G86	9.71	0.66	0.091	0.006	11.013	0.776	0.789	0.035	13.49	0.61	4.16	24.90	36.1	26.5	5	2.48E-05	4.55E-03	1.99E-03	30.6	30.5
L8G87	2.805	0.18	0.027	0.002	36.900	2.587	0.746	0.034	48.51	11.50	4.55	4.46	20.1	7.8	4	1.66E-05	1.64E-02	3.09E-04	10.1	10.1
L8G90	6.74	0.44	0.061	0.004	16.340	1.121	0.793	0.035	27.25	17.64	5.83	1.67	21.9	17.9	10	2.87E-05	8.72E-03	3.10E-04	27.6	17.5
L8G92	12.38	0.8	0.112	0.008	8.921	0.668	0.800	0.035	10.35	68.40	4.26	0.17	34.5	32.7	6	4.86E-05	3.48E-03	1.70E-03	24.5	23.3
L8G93	1.573	0.11	0.017	0.001	58.411	4.094	0.666	0.032	77.90	39.43	3.95	2.14	23.8	4.8	15	2.79E-05	2.57E-02	1.04E-03	14.4	7.5
L8G95	20	1.6	0.184	0.017	5.435	0.502	0.833	0.065	2.04	5.06	1.29	0.43	4.4	98.4	4	4.50E-05	6.42E-04	8.06E-04	95.1	152.6
L8G97	16.11	1	0.141	0.009	7.097	0.458	0.829	0.026	27.59	2.11	14.68	14.41	8.2	31.3	8	3.40E-05	8.91E-03	8.53E-04	18.2	13.0
L8G98	3.032	0.2	0.029	0.002	34.002	2.312	0.750	0.027	82.30	49.57	8.54	1.78	20.8	6.8	8	2.43E-05	2.58E-02	3.09E-04	8.8	6.2
L8G99	2.77	0.21	0.030	0.002	33.113	2.412	0.674	0.028	42.80	13.80	3.71	7.00	40.3	7.6	6	1.69E-05	1.45E-02	1.57E-03	16.9	13.9
L8G101	1.579	0.11	0.017	0.001	57.803	4.009	0.664	0.027	104.40	42.15	6.57	2.29	24.4	4.3	15	2.93E-05	2.87E-02	3.45E-04	12.3	6.4
L8G102	8.04	0.52	0.072	0.005	13.947	0.953	0.820	0.029	21.64	2.60	6.60	7.84	9.5	17.6	6	3.26E-05	5.46E-03	1.03E-03	23.3	19.5
L8G103	20.9	1.6	0.189	0.016	5.291	0.448	0.835	0.067	2.94	7.12	2.68	0.39	1.1	104.2	1	3.03E-05	7.88E-04	9.87E-04	28.9	68.2
L8G104	7.04	0.48	0.064	0.005	15.674	1.155	0.795	0.052	16.91	30.34	4.80	0.51	21.8	27.3	4	3.51E-05	4.35E-03	2.06E-03	18.1	20.0
L8G106	2.816	0.18	0.026	0.002	38.110	2.614	0.784	0.031	85.50	67.80	9.17	1.15	11.2	6.9	11	2.92E-05	2.23E-02	9.99E-06	11.7	7.1
L8G108	5.93	0.42	0.054	0.004	18.553	1.342	0.797	0.039	24.29	34.10	5.71	0.63	17.4	17.5	12	3.57E-05	6.33E-03	6.30E-04	36.6	21.5
L8G109	1.375	0.089	0.015	0.001	65.317	4.266	0.654	0.022	208.00	1.54	10.76	119.10	22.8	3.2	46	3.13E-05	5.27E-02	9.90E-04	19.3	5.7
L8G110	12.33	0.88	0.107	0.009	9.355	0.753	0.830	0.037	18.22	46.00	9.04	0.35	5.2	33.1	2	2.11E-05	5.21E-03	4.46E-04	12.6	17.8
L8G111	3.272	0.21	0.034	0.002	29.326	2.064	0.688	0.033	47.90	43.61	6.25	0.98	41.6	9.8	14	2.45E-05	1.21E-02	3.60E-03	32.6	19.9
L8G113	1.898	0.13	0.019	0.001	52.165	3.538	0.720	0.035	74.23	5.80	5.34	11.48	18.2	5.7	14	3.10E-05	1.88E-02	1.77E-03	16.6	9.0
L8G115	3.95	0.28	0.035	0.003	28.986	2.184	0.815	0.049	22.59	5.79	3.29	3.60	5.9	14.0	2	1.75E-05	5.31E-03	1.26E-03	14.9	21.3
L8G118	6.5	0.42	0.061	0.004	16.340	1.148	0.774	0.033	28.79	21.67	6.85	1.19	31.7	17.0	3	2.79E-05	8.41E-03	4.06E-03	8.8	11.1
L8G119	1.985	0.14	0.021	0.002	47.371	3.366	0.685	0.032	82.80	28.83	6.05	2.59	26.2	5.9	8	2.76E-05	2.33E-02	1.12E-03	8.6	6.1
L8G120	0.689	0.046	0.009	0.001	113.895	8.302	0.577	0.025	184.80	302.70	5.30	0.56	18.6	2.3	22	2.39E-05	4.56E-02	2.69E-03	13.9	6.0
L8G3	*19.98*	*1.3*	*0.169*	*0.011*	*5.921*	*0.386*	*0.850*	*0.035*	*7.85*	*22.19*	*5.37*	*0.35*	*-21.8*	*49.9*	*2*	*3.11E-05*	*3.04E-03*	*2.69E-03*	*14.6*	*24.4*
L8G4	*12.51*	*0.96*	*0.109*	*0.008*	*9.217*	*0.688*	*0.844*	*0.056*	*4.46*	*8.45*	*1.83*	*0.51*	*-7.9*	*50.2*	*1*	*1.88E-05*	*1.57E-03*	*6.14E-04*	*23.4*	*47.8*
L8G5	*13.23*	*1.1*	*0.116*	*0.011*	*8.651*	*0.823*	*0.850*	*0.065*	*3.78*	*0.21*	*1.62*	*23.90*	*-14.5*	*62.1*	*3*	*3.85E-05*	*1.48E-03*	*5.16E-05*	*36.3*	*42.0*
L8G10	*83.7*	*6.1*	*0.701*	*0.051*	*1.427*	*0.104*	*0.857*	*0.033*	*1.50*	*1.06*	*4.45*	*1.44*	*-191.4*	*202.7*	*2*	*4.31E-05*	*7.43E-04*	*3.43E-04*	*43.1*	*64.1*
L8G49	*42.2*	*3.3*	*0.365*	*0.030*	*2.740*	*0.225*	*0.838*	*0.053*	*2.29*	*4.53*	*3.37*	*0.51*	*-8.6*	*160.2*	*7*	*4.62E-05*	*6.01E-03*	*3.00E-04*	*17.4*	*13.2*
L8G75	*7.87*	*0.58*	*0.069*	*0.005*	*14.577*	*1.147*	*0.841*	*0.038*	*23.35*	*37.70*	*7.98*	*0.59*	*-3.1*	*21.8*	*1*	*6.66E-05*	*6.39E-04*	*1.17E-03*	*16.2*	*44.0*
L8G89	*78.8*	*5.1*	*0.665*	*0.045*	*1.504*	*0.102*	*0.846*	*0.021*	*9.38*	*0.81*	*24.99*	*13.06*	*-83.2*	*124.9*	*3*	*5.48E-05*	*1.15E-03*	*8.84E-05*	*33.0*	*38.1*
L8G94	*24.6*	*1.9*	*0.222*	*0.019*	*4.505*	*0.386*	*0.837*	*0.055*	*1.89*	*5.32*	*1.40*	*0.39*	*-2.8*	*100.9*	*0*	*4.88E-05*	*8.08E-04*	*2.37E-04*	*8.4*	*23.9*
L8G107	*31.8*	*2.1*	*0.272*	*0.021*	*3.676*	*0.284*	*0.848*	*0.041*	*4.54*	*18.77*	*5.83*	*0.22*	*-32.1*	*93.6*	*7*	*3.36E-05*	*3.49E-03*	*2.37E-04*	*41.1*	*31.2*
L8G112	*48.5*	*3.4*	*0.412*	*0.029*	*2.427*	*0.171*	*0.855*	*0.033*	*3.28*	*80.90*	*6.16*	*0.04*	*-83.6*	*116.6*	*1*	*3.86E-05*	*6.20E-04*	*5.98E-04*	*28.8*	*64.1*
Population 2																				
L8G17	12.65	0.85	0.118	0.008	8.467	0.581	0.775	0.036	11.74	14.01	5.15	0.84	61.8	35.3	4	4.03E-05	4.72E-03	2.43E-04	14.5	14.5
L8G20	2.78	0.19	0.033	0.002	30.581	2.151	0.625	0.027	38.54	6.69	3.65	5.88	56.8	8.3	19	2.76E-05	1.54E-02	1.83E-03	30.9	14.7
L8G23	7.7	1.2	0.076	0.010	13.106	1.718	0.733	0.047	14.40	9.95	3.56	1.41	66.0	30.5	2	3.05E-05	3.25E-03	4.42E-05	14.0	19.7
L8G38	3.38	0.23	0.039	0.003	25.381	1.804	0.634	0.029	30.10	47.00	4.31	0.67	65.6	10.5	12	3.10E-05	1.01E-02	4.91E-05	26.4	15.2
L8G41	2.18	0.15	0.026	0.002	39.032	2.742	0.607	0.033	51.50	101.50	4.34	0.50	48.2	7.7	14	2.55E-05	1.53E-02	1.24E-04	24.8	13.2
L8G45	1.92	0.18	0.026	0.002	37.879	3.013	0.536	0.030	52.10	21.31	3.40	2.42	64.9	8.3	3	1.09E-05	1.27E-02	5.73E-04	15.0	17.3
L8G47	11.78	0.79	0.113	0.008	8.873	0.630	0.765	0.033	9.54	4.63	4.14	2.05	68.4	31.1	3	2.39E-05	3.15E-03	1.75E-03	27.5	35.2
L8G57	4.09	0.31	0.044	0.004	22.883	1.833	0.684	0.039	19.60	35.70	2.68	0.56	54.9	14.6	3	3.45E-05	6.71E-03	7.46E-04	9.0	10.4
L8G60	8.81	0.66	0.086	0.007	11.641	0.894	0.750	0.043	12.91	9.39	3.72	1.40	62.3	30.6	2	1.92E-05	4.56E-03	1.02E-03	15.8	22.6
L8G82	3.55	0.24	0.041	0.003	24.450	1.734	0.649	0.035	28.33	9.55	3.30	3.09	63.1	12.6	8	2.05E-05	9.54E-03	2.42E-04	28.2	20.0
L8G96	16.97	1.2	0.158	0.011	6.333	0.441	0.793	0.041	5.83	14.91	3.19	0.42	59.4	53.4	3	3.58E-05	1.93E-03	1.84E-03	29.9	44.9
L8G100	9.54	0.7	0.091	0.007	10.989	0.821	0.761	0.039	10.68	0.81	3.30	14.70	57.7	29.5	3	4.61E-05	3.68E-03	3.79E-04	12.2	14.2
Poupulation 3																				
L8G13	319	22	2.800	0.200	0.357	0.026	0.829	0.023	2.16	0.11	24.16	20.56	150.1	550.4	2	3.24E-05	8.21E-04	5.80E-05	51.8	73.4
L8G22	2.446	0.16	0.037	0.003	27.174	1.846	0.485	0.018	54.50	31.17	4.98	1.78	105.9	9.0	19	1.87E-05	2.11E-02	2.96E-04	33.2	15.3
L8G24	42.5	3.2	0.401	0.030	2.494	0.187	0.773	0.042	1.95	0.27	3.29	9.20	250.6	134.7	1	4.08E-05	6.36E-04	1.25E-03	26.6	74.7
L8G30	3.51	0.43	0.042	0.005	23.697	2.527	0.587	0.037	32.10	76.60	4.01	0.41	86.6	15.7	6	1.14E-05	1.49E-02	1.54E-03	24.4	20.1
L8G52	7.79	0.6	0.081	0.007	12.315	1.092	0.706	0.053	7.21	2.52	1.90	2.88	88.7	35.7	1	4.33E-05	2.39E-03	8.75E-05	6.7	13.4
L8G61	8.96	0.6	0.091	0.007	11.001	0.787	0.714	0.029	17.88	21.43	6.61	0.78	93.6	22.8	6	3.61E-05	4.73E-03	4.18E-04	24.2	19.9
L8G67	1.417	0.1	0.027	0.002	36.523	2.401	0.380	0.018	96.50	190.10	7.81	0.47	101.9	7.8	10	1.24E-05	2.46E-02	3.71E-03	22.6	14.7
L8G74	1.709	0.12	0.027	0.002	36.900	2.587	0.451	0.021	57.90	98.10	5.12	0.55	85.3	7.6	7	1.90E-05	1.52E-02	3.89E-04	16.8	12.7
L8G88	27.1	1.9	0.247	0.019	4.049	0.311	0.783	0.041	3.58	6.57	3.08	0.57	119.8	82.8	3	6.17E-05	1.25E-03	8.32E-04	26.9	35.8
L8G91	3.66	0.31	0.045	0.004	22.422	1.910	0.592	0.045	12.73	9.15	1.44	1.49	89.7	17.9	7	2.06E-05	5.23E-03	5.51E-05	44.8	33.9
L8G105	1.23	0.096	0.026	0.002	38.580	2.679	0.343	0.017	82.70	129.30	5.34	0.58	104.2	8.0	16	2.15E-05	1.99E-02	1.25E-03	25.8	13.0
L8G114	4.76	0.32	0.056	0.004	17.857	1.212	0.641	0.026	31.07	25.17	5.66	1.10	90.5	13.5	14	3.74E-05	8.24E-03	5.33E-04	31.4	16.9
L8G116	4.27	0.29	0.050	0.003	20.161	1.382	0.630	0.029	35.91	44.70	6.42	0.71	84.5	13.2	13	2.82E-05	8.95E-03	3.44E-04	35.5	19.8
L8G117	1.851	0.13	0.028	0.002	35.587	2.660	0.480	0.024	39.64	23.10	2.93	1.54	81.9	8.2	8	2.60E-05	9.64E-03	5.98E-04	22.0	15.6

L8G51	5.63	0.37	0.074	0.005	13.441	0.957	0.547	0.018	39.30	8.23	7.32	4.75	178.1	16.7		2	1.22E-05	1.27E-02	6.84E-04	8.9	12.7
L8G72	276	25	2.390	0.210	0.418	0.037	0.831	0.056	0.36	2.07	4.03	0.16	2476.7	964.8		0	3.86E-05	1.08E-04	6.05E-04	5.0	15.7

U-Pb data

AFT data

#grains	Ns	ΣρiΩi	2σΣρiΩi	Zeta (yr cm²)	2 sig abs	χ^2	P(χ^2)	Pooled age	2σ Ma
114	1194	4.08E-05	5.40E-07	6.92E-01	1.10E-02	243.91	0.00	20.2	1.2

Grain Number	Pb207/U235	Pb207/U235 error (2s)	Pb206/U238	Pb206/U238 error (2s)	U238/Pb206	U238/Pb206 error (2s)	Pb207/Pb206	Pb207/Pb206 error (2s)	Approx U (ppm)	Approx Th (ppm)	Approx Pb (ppm)	U/Th	207corrAge (Ma)	207corrAge error (2s,Ma)	Ns	Area (cm^2)	$^{238}U/^{43}Ca$	2σ	FT Age	2σ
Population 1																				
L16G3	2.05	0.15	0.020	0.001	50.000	3.500	0.696	0.028	91.50	46.80	5.76	1.81	23.0	5.0	11	2.16E-05	3.03E-02	1.57E-04	11.6	7.0
L16G5	33.53	0.84	0.285	0.013	3.515	0.161	0.835	0.026	9.32	1.51	10.71	5.49	1.7	63.4	2	2.08E-05	2.64E-03	1.23E-04	25.1	35.6
L16G6	3.29	0.11	0.030	0.001	33.322	1.555	0.779	0.030	68.70	28.74	7.70	2.05	14.1	7.6	10	1.97E-05	1.93E-02	2.34E-03	18.1	11.7
L16G8	0.732	0.032	0.009	0.001	105.932	6.284	0.563	0.035	105.20	7.12	2.73	12.88	21.1	3.0	22	3.08E-05	2.97E-02	7.00E-05	16.6	7.1
L16G10	14.85	0.56	0.125	0.007	8.013	0.475	0.825	0.046	8.00	22.07	4.33	0.32	11.6	47.5	6	4.26E-05	2.36E-03	1.46E-04	41.2	33.8
L16G12	0.463	0.022	0.007	0.000	141.443	7.602	0.464	0.029	152.80	1673.00	6.74	0.08	21.5	2.0	21	2.42E-05	4.75E-02	1.19E-03	12.6	5.5
L16G13	2.694	0.087	0.026	0.001	38.595	1.788	0.712	0.026	89.50	43.95	9.21	1.82	26.4	5.8	23	3.07E-05	2.65E-02	3.57E-04	19.6	8.2
L16G14	3.21	0.14	0.028	0.002	35.714	2.296	0.797	0.056	19.14	17.99	2.32	0.96	8.9	12.9	9	3.46E-05	5.28E-03	1.85E-03	34.0	25.6
L16G16	2.087	0.071	0.021	0.001	48.473	2.350	0.695	0.030	104.30	58.90	8.54	1.63	23.9	5.3	14	1.42E-05	3.57E-02	1.06E-04	19.1	10.2
L16G17	2.922	0.098	0.028	0.002	36.232	1.969	0.739	0.034	40.15	18.44	4.70	2.04	22.0	7.9	8	4.75E-05	1.23E-02	1.35E-04	9.4	6.7
L16G18	3.76	0.14	0.036	0.002	27.624	1.374	0.728	0.034	22.36	156.80	3.73	0.14	32.3	10.3	7	3.16E-05	6.57E-03	7.43E-04	23.3	17.8
L16G19	7.64	0.41	0.072	0.005	13.850	0.940	0.760	0.051	8.53	3.82	2.46	2.10	46.0	30.3	4	2.47E-05	5.23E-03	2.39E-03	21.4	23.5
L16G21	2.239	0.051	0.021	0.001	47.281	1.967	0.730	0.022	104.30	75.40	7.08	1.35	18.4	4.1	25	3.00E-05	3.25E-02	1.41E-03	17.7	7.1
L16G22	5.63	0.22	0.051	0.003	19.685	1.201	0.777	0.041	18.47	99.10	3.45	0.18	24.9	17.3	2	2.31E-05	5.74E-03	3.40E-04	10.4	14.7
L16G23	3.68	0.15	0.038	0.002	26.247	1.447	0.706	0.035	34.36	3.63	3.70	9.39	40.9	11.2	9	2.14E-05	8.94E-03	2.47E-04	32.5	21.7
L16G24	0.831	0.028	0.010	0.000	100.705	4.766	0.594	0.021	285.10	148.90	6.78	1.82	19.6	2.0	25	1.42E-05	7.48E-02	1.95E-03	16.3	6.5
L16G28	5.62	0.25	0.049	0.003	20.492	1.218	0.827	0.042	20.78	2.83	3.24	6.88	3.5	17.0	5	3.29E-05	5.38E-03	7.30E-04	19.5	17.6
L16G29	5.43	0.17	0.047	0.002	21.231	1.037	0.795	0.024	39.34	20.33	5.91	1.76	16.0	9.7	11	2.49E-05	1.16E-02	4.03E-04	26.3	15.9
L16G34	0.878	0.046	0.010	0.001	97.466	4.940	0.584	0.016	235.00	61.10	5.40	3.38	21.1	1.8	30	2.13E-05	7.65E-02	2.99E-04	12.7	4.6
L16G39	0.837	0.032	0.010	0.001	97.847	4.883	0.560	0.027	135.60	201.10	3.72	0.59	23.0	2.6	24	2.89E-05	4.17E-02	1.07E-04	13.7	5.6
L16G42	10.94	0.2	0.097	0.004	10.363	0.440	0.792	0.024	35.63	1.30	15.42	30.00	36.0	19.8	14	3.19E-05	1.30E-02	1.70E-03	23.3	12.8
L16G43	2.295	0.081	0.023	0.001	43.497	2.081	0.702	0.031	40.04	164.10	4.00	0.27	25.3	6.1	22	3.30E-05	1.68E-02	3.05E-04	27.4	11.7
L16G45	21.81	0.81	0.185	0.010	5.420	0.285	0.829	0.041	5.22	4.52	4.51	1.29	11.0	62.9	2	2.19E-05	3.14E-03	9.02E-04	20.1	29.0
L16G46	5.9	0.25	0.053	0.003	19.048	1.052	0.780	0.034	22.99	7.78	5.60	3.32	24.4	14.9	9	4.05E-05	1.08E-02	6.65E-03	14.2	12.9
L16G47	7.44	0.34	0.066	0.004	15.175	0.875	0.795	0.049	12.12	19.21	3.75	0.71	22.6	26.6	7	3.05E-05	4.43E-03	1.81E-03	35.7	30.7
L16G50	3.41	0.28	0.033	0.003	29.940	2.331	0.751	0.034	34.20	42.80	4.53	0.91	23.4	9.6	14	2.78E-05	1.76E-02	6.42E-04	19.7	10.6
L16G52	4.96	0.19	0.045	0.002	22.222	1.086	0.781	0.037	28.14	32.55	5.51	0.95	20.5	13.9	8	2.28E-05	1.20E-02	5.36E-05	20.1	14.2
L16G54	32.5	1.1	0.278	0.014	3.597	0.181	0.820	0.031	8.61	2.14	11.42	4.49	41.3	72.2	4	3.34E-05	4.08E-03	4.78E-04	20.2	20.4
L16G55	2.84	0.13	0.027	0.002	36.765	2.027	0.731	0.033	40.97	0.98	4.65	47.80	23.5	7.6	14	1.61E-05	1.91E-02	5.95E-04	31.5	16.9
L16G57	6.27	0.32	0.057	0.004	17.483	1.161	0.776	0.041	17.46	21.70	3.91	0.87	28.6	19.5	5	3.11E-05	5.46E-03	5.75E-04	20.3	18.3
L16G58	2.356	0.09	0.024	0.001	42.052	1.945	0.693	0.034	53.62	14.94	4.84	3.86	27.9	6.8	16	2.35E-05	2.20E-02	6.38E-04	21.3	10.7
L16G60	0.984	0.034	0.012	0.001	86.881	4.152	0.604	0.031	123.00	52.70	4.46	2.51	21.8	3.1	29	2.09E-05	4.79E-02	4.31E-05	20.0	7.4
L16G66	2.631	0.093	0.026	0.001	38.580	1.786	0.695	0.026	56.60	77.10	5.50	0.79	30.0	5.8	7	1.90E-05	2.29E-02	5.44E-04	11.1	8.4
L16G67	65.4	0.98	0.551	0.022	1.815	0.072	0.834	0.015	15.93	1.60	38.40	11.06	11.5	77.0	4	2.76E-05	7.24E-03	4.83E-03	13.8	16.6
L16G68	3.91	0.14	0.038	0.002	26.110	1.227	0.729	0.033	30.56	31.07	4.70	1.07	33.9	10.6	15	2.39E-05	1.31E-02	9.53E-04	33.0	17.2
L16G69	7.97	0.23	0.070	0.003	14.306	0.675	0.806	0.030	31.73	12.62	9.02	2.76	17.5	17.7	12	2.28E-05	1.45E-02	8.51E-04	25.0	14.5
L16G70	40.6	1.9	0.342	0.019	2.924	0.162	0.831	0.041	3.17	0.92	4.96	3.82	15.8	116.5	1	2.08E-05	1.67E-03	9.32E-05	19.9	39.7
L16G72	3.61	0.12	0.032	0.002	31.250	1.563	0.786	0.039	33.31	3.92	4.29	9.36	13.2	10.4	24	3.87E-05	1.67E-02	1.09E-04	25.6	10.4
L16G74	14.61	0.78	0.129	0.009	7.728	0.537	0.795	0.055	3.27	3.30	1.69	1.10	45.7	58.3	4	4.94E-05	1.59E-03	2.14E-03	35.1	59.0
L16G76	8.87	0.28	0.075	0.004	13.280	0.670	0.831	0.039	17.86	86.60	5.76	0.23	3.0	24.5	10	4.07E-05	7.44E-03	1.70E-05	22.8	14.4
L16G78	2.574	0.098	0.025	0.001	40.016	2.082	0.736	0.036	50.21	28.94	5.00	1.97	20.5	7.5	13	1.40E-05	2.05E-02	7.18E-04	31.3	17.4
L16G80	1.161	0.032	0.013	0.001	74.850	3.025	0.621	0.017	179.80	135.20	8.09	1.53	23.5	2.2	24	1.94E-05	7.68E-02	7.02E-04	11.1	4.6
L16G83	4.53	0.29	0.044	0.003	22.831	1.720	0.731	0.029	43.00	26.00	5.94	1.38	38.1	11.0	10	3.28E-05	1.55E-02	8.80E-04	13.5	8.6
L16G84	0.539	0.025	0.008	0.000	126.263	6.217	0.481	0.024	226.80	181.50	4.35	0.98	23.0	1.9	28	2.37E-05	6.05E-02	1.29E-03	13.5	5.1
L16G87	2.334	0.071	0.024	0.001	42.123	1.952	0.714	0.027	96.60	68.50	7.05	1.06	23.8	5.5	27	3.43E-05	2.43E-02	1.94E-04	22.4	8.6
L16G89	5.06	0.18	0.046	0.002	21.834	1.049	0.793	0.038	33.32	34.64	5.04	0.70	16.3	14.5	6	2.14E-05	8.55E-03	5.99E-04	22.6	18.6
L16G91	7.8	0.24	0.070	0.004	14.286	0.776	0.813	0.043	21.45	2.19	4.85	7.16	13.4	25.0	2	6.29E-05	4.97E-03	3.19E-04	4.4	6.3
L16G92	14.9	0.59	0.132	0.007	7.576	0.390	0.826	0.042	13.94	36.42	6.76	0.27	11.1	46.0	5	2.55E-05	3.73E-03	1.27E-03	36.2	34.7
L16G94	1.617	0.06	0.017	0.001	58.140	2.704	0.685	0.028	124.50	102.60	6.30	0.86	21.3	4.1	17	2.91E-05	3.06E-02	3.95E-04	13.2	6.4
L16G96	4.96	0.15	0.047	0.002	21.186	0.988	0.786	0.038	35.97	10.32	5.33	2.52	19.6	14.9	6	4.41E-05	8.58E-03	1.43E-03	11.0	9.1
L16G104	2.027	0.091	0.021	0.001	48.077	2.774	0.724	0.034	48.20	40.20	4.04	1.39	19.1	6.0	15	2.38E-05	1.98E-02	4.45E-04	22.0	11.4
L16G106	21.62	0.86	0.194	0.011	5.165	0.293	0.812	0.032	5.47	15.51	4.30	0.43	41.3	51.8	0	4.89E-05	2.01E-03	6.40E-04	3.3	9.5
L16G108	1.758	0.052	0.019	0.001	52.632	2.438	0.670	0.025	101.20	90.90	7.01	1.31	25.9	4.2	21	2.17E-05	3.65E-02	1.79E-04	18.3	8.0
L16G109	14.98	0.51	0.130	0.007	7.692	0.402	0.816	0.038	5.83	18.75	3.29	0.36	22.3	41.1	2	6.39E-05	2.46E-03	2.39E-04	8.8	12.4
L16G111	2.178	0.075	0.023	0.001	42.863	2.205	0.693	0.029	40.34	67.70	3.28	0.69	27.4	5.8	19	3.24E-05	1.71E-02	1.13E-03	23.7	11.0
L16G112	4.96	0.15	0.048	0.002	20.921	0.963	0.740	0.031	28.98	98.90	5.55	0.33	38.1	12.5	15	5.04E-05	1.26E-02	4.65E-04	16.3	8.5
L16G117	6.14	0.18	0.059	0.003	17.036	0.755	0.748	0.027	25.84	2.53	5.78	11.23	43.1	13.4	17	4.12E-05	1.16E-02	6.23E-04	24.6	12.0
L16G119	10.84	0.41	0.099	0.005	10.070	0.517	0.792	0.035	14.60	7.92	5.72	1.95	37.1	28.9	2	2.57E-05	5.38E-03	1.17E-03	10.0	14.3
L16G120	3.92	0.12	0.037	0.002	27.248	1.411	0.774	0.029	40.60	57.00	5.46	0.75	18.8	9.0	13	3.45E-05	1.35E-02	6.47E-04	19.3	10.7
L16G15	*45.9*	*6.5*	*0.372*	*0.054*	*2.688*	*0.390*	*0.836*	*0.044*	*4.20*	*0.83*	*4.66*	*4.71*	*-1.3*	*136.0*	*6*	*2.37E-05*	*2.61E-03*	*2.68E-03*	*66.6*	*87.3*
L16G40	*133.7*	*7.1*	*1.126*	*0.076*	*0.888*	*0.060*	*0.852*	*0.046*	*0.70*	*1.19*	*2.72*	*0.54*	*-300.6*	*454.0*	*2*	*6.98E-05*	*2.01E-04*	*1.97E-03*	*97.8*	*970.1*
L16G64	*11.12*	*0.59*	*0.094*	*0.006*	*10.604*	*0.641*	*0.857*	*0.046*	*6.75*	*24.70*	*2.66*	*0.30*	*-17.4*	*36.2*	*3*	*4.27E-05*	*2.81E-03*	*6.08E-05*	*17.3*	*20.0*
L16G65	*19.9*	*1*	*0.172*	*0.011*	*5.804*	*0.371*	*0.845*	*0.048*	*4.30*	*26.76*	*3.24*	*0.17*	*-14.5*	*68.8*	*2*	*1.87E-05*	*1.70E-03*	*2.36E-04*	*43.4*	*61.7*
L16G81	*7.57*	*0.31*	*0.063*	*0.003*	*15.873*	*0.831*	*0.849*	*0.053*	*12.74*	*6.64*	*2.85*	*1.63*	*-7.1*	*27.6*	*1*	*2.99E-05*	*4.18E-03*	*1.50E-04*	*5.5*	*11.1*
L16G85	*56.1*	*1.7*	*0.477*	*0.023*	*2.096*	*0.101*	*0.838*	*0.029*	*16.80*	*0.45*	*28.83*	*32.10*	*-11.7*	*117.8*	*5*	*3.67E-05*	*4.08E-03*	*1.20E-04*	*23.0*	*20.6*
L16G107	*15.76*	*0.7*	*0.137*	*0.008*	*7.278*	*0.445*	*0.848*	*0.050*	*4.85*	*6.81*	*2.83*	*0.83*	*-15.0*	*57.1*	*5*	*4.58E-05*	*2.04E-03*	*1.15E-03*	*36.9*	*39.1*
Population 2																				
L16G7	8.4	0.24	0.079	0.005	12.626	0.749	0.744	0.040	18.86	29.10	5.41	0.57	61.3	26.3	9	2.59E-05	5.69E-03	3.97E-04	42.1	28.2
L16G26	4.01	0.14	0.043	0.002	23.364	1.201	0.650	0.027	34.77	16.17	3.72	2.02	65.8	10.2	9	2.98E-05	1.13E-02	7.13E-04	18.4	12.3
L16G31	3.05	0.13	0.034	0.002	29.586	1.488	0.623	0.033	39.48	87.20	3.71	0.41	59.3	9.6	12	2.45E-05	1.22E-02	7.50E-04	27.6	16.0
L16G36	5.59	0.26	0.053	0.003	18.727	1.017	0.712	0.026	44.80	80.40	7.15	0.49	55.0	12.0	26	4.43E-05	1.56E-02	9.36E-05	25.9	10.2
L16G37	17.51	0.64	0.153	0.008	6.553	0.335	0.797	0.038	5.96	9.06	3.07	0.59	51.9	48.0	1	3.44E-05	1.67E-03	1.91E-03	12.0	27.7
L16G38	23.56	0.95	0.209	0.010	4.794	0.230	0.794	0.040	6.46	15.52	4.26	0.36	78.7	68.5	5	4.43E-05	1.98E-03	8.71E-04	39.4	39.2
L16G41	6.44	0.16	0.065	0.003	15.337	0.659	0.697	0.022	36.27	137.00	10.36	0.29	75.6	12.5	17	4.86E-05	1.30E-02	2.04E-04	18.6	9.0

L16G53	11.74	0.52	0.109	0.006	9.217	0.527	0.772	0.041	7.12	3.21	3.32	2.44	59.3	36.7		5	2.97E-05	3.17E-03	9.49E-05	36.6	32.8
L16G56	7.52	0.53	0.074	0.005	13.532	0.934	0.734	0.040	15.73	32.70	4.49	0.54	63.2	24.6		8	2.35E-05	6.57E-03	7.24E-04	35.7	25.6
L16G59	2.72	0.1	0.034	0.002	29.499	1.566	0.577	0.032	29.90	5.91	3.21	5.43	72.2	9.7		4	1.41E-05	1.16E-02	4.07E-04	16.9	17.0
L16G62	14.73	0.88	0.138	0.009	7.257	0.474	0.785	0.062	2.50	0.96	1.39	2.76	60.9	69.6		3	4.66E-05	1.01E-03	5.80E-04	43.8	56.4
L16G63	5.36	0.23	0.058	0.003	17.182	1.004	0.675	0.037	10.45	5.99	2.09	1.87	77.9	18.2		7	1.83E-05	4.30E-03	1.37E-03	61.2	50.2
L16G73	6.02	0.32	0.059	0.005	16.949	1.293	0.734	0.050	7.75	2.53	1.71	3.54	50.2	24.4		7	3.01E-05	3.41E-03	1.55E-04	46.9	35.6
L16G77	2.52	0.1	0.030	0.002	33.223	1.656	0.624	0.036	27.25	77.40	3.04	0.40	52.5	9.3		11	3.13E-05	1.06E-02	3.95E-03	23.0	16.3
L16G79	13.85	0.54	0.128	0.007	7.813	0.415	0.778	0.040	6.22	7.56	3.27	0.94	64.0	42.2		5	4.96E-05	2.84E-03	2.21E-04	24.5	22.0
L16G82	14.61	0.9	0.136	0.008	7.337	0.452	0.771	0.037	8.88	7.87	3.95	0.95	76.6	41.7		4	4.62E-05	3.24E-03	2.14E-04	18.4	18.5
L16G88	30.2	1.1	0.272	0.015	3.676	0.203	0.806	0.035	6.77	29.64	6.60	0.17	75.9	78.7		2	4.73E-05	1.63E-03	1.02E-03	17.9	27.7
L16G90	9.66	0.42	0.095	0.005	10.560	0.558	0.739	0.036	16.61	22.17	4.81	0.54	77.8	28.3		13	3.79E-05	4.19E-03	3.32E-03	56.4	54.6
L16G95	5.77	0.26	0.060	0.003	16.722	0.867	0.689	0.029	32.74	24.44	5.76	0.95	73.2	14.8		15	4.98E-05	7.90E-03	2.72E-04	26.3	13.6
L16G97	3.66	0.24	0.040	0.003	25.063	1.822	0.674	0.030	41.40	84.20	5.12	0.36	53.4	10.6		1	5.13E-05	6.24E-03	4.47E-04	2.2	4.3
L16G98	7.5	0.27	0.073	0.004	13.699	0.788	0.742	0.037	20.01	17.63	4.50	0.83	57.6	22.5		7	3.27E-05	4.68E-03	1.22E-03	31.6	25.2
L16G101	3.09	0.11	0.034	0.002	29.412	1.471	0.637	0.025	47.30	62.00	5.58	0.89	55.7	7.6		15	3.49E-05	1.85E-02	1.13E-04	16.1	8.3
L16G102	15.2	0.68	0.138	0.009	7.262	0.475	0.786	0.053	3.61	3.07	2.11	1.38	59.6	59.7		2	4.03E-05	1.28E-03	5.14E-04	26.7	39.2
L16G103	4.62	0.31	0.048	0.004	20.833	1.693	0.694	0.025	37.40	65.60	6.24	0.65	56.5	11.0		9	2.95E-05	2.10E-02	2.18E-04	10.0	6.7
L16G115	3.61	0.14	0.040	0.002	24.876	1.238	0.669	0.036	24.50	6.65	3.40	4.05	55.4	12.2		10	2.73E-05	1.05E-02	2.80E-04	24.0	15.2
Population 3																					
L16G1	9.94	0.43	0.096	0.006	10.438	0.599	0.735	0.038	8.79	17.52	3.08	0.43	81.9	30.2		5	5.50E-05	2.62E-03	2.04E-04	23.9	21.5
L16G2	10.97	0.47	0.110	0.006	9.058	0.468	0.721	0.041	8.14	25.01	3.06	0.28	108.0	37.2		4	3.44E-05	2.22E-03	2.16E-04	36.1	36.3
L16G4	28.9	1.3	0.258	0.013	3.876	0.195	0.800	0.044	4.59	9.55	4.64	0.41	85.7	92.8		3	4.13E-05	1.18E-03	1.54E-03	42.5	74.1
L16G9	15.31	0.61	0.143	0.008	6.998	0.382	0.765	0.037	6.41	16.97	3.93	0.33	88.0	43.6		3	2.34E-05	1.91E-03	5.43E-04	46.2	54.9
L16G11	2.104	0.084	0.033	0.002	30.488	1.487	0.443	0.018	46.90	26.01	3.86	1.58	105.5	7.1		19	4.26E-05	1.36E-02	4.89E-04	22.6	10.4
L16G20	12.65	0.54	0.120	0.007	8.326	0.478	0.746	0.045	6.16	6.23	3.17	0.95	92.6	44.3		7	4.36E-05	1.98E-03	1.04E-03	56.0	51.6
L16G25	2.95	0.41	0.039	0.005	25.445	2.978	0.545	0.039	35.00	15.30	2.50	2.19	94.0	16.5		8	3.48E-05	4.44E-03	2.40E-04	35.7	25.3
L16G27	41.6	1.7	0.363	0.019	2.755	0.144	0.804	0.040	2.63	4.76	3.11	0.51	113.9	118.5		3	3.10E-05	8.73E-04	8.11E-03	76.2	713.0
L16G30	3.59	0.12	0.042	0.002	23.810	1.190	0.593	0.024	35.56	111.00	4.26	0.29	84.1	9.3		14	1.60E-05	1.09E-02	5.75E-04	55.5	29.8
L16G33	2.01	0.099	0.030	0.002	33.670	1.814	0.481	0.030	35.56	27.13	2.11	1.18	86.3	8.6		15	4.01E-05	1.04E-02	9.92E-04	24.8	13.0
L16G48	1.302	0.049	0.026	0.001	39.032	1.828	0.360	0.014	58.75	75.70	3.66	0.88	99.5	5.5		20	3.05E-05	2.37E-02	9.15E-05	19.1	8.6
L16G51	4.45	0.19	0.052	0.003	19.305	1.006	0.617	0.031	19.38	43.23	3.59	0.49	93.8	14.0		6	2.04E-05	8.61E-03	1.39E-03	23.6	19.6
L16G61	1.692	0.059	0.027	0.001	36.603	1.608	0.440	0.019	86.50	46.21	5.40	1.96	88.5	5.8		28	2.30E-05	3.71E-02	1.12E-03	22.7	8.6
L16G71	1.665	0.052	0.027	0.001	36.738	1.620	0.442	0.015	84.60	49.62	5.30	1.91	87.7	5.1		27	1.44E-05	3.66E-02	5.53E-04	35.3	13.6
L16G75	15.4	3.7	0.138	0.030	7.246	1.575	0.707	0.037	9.10	1.74	3.61	6.23	153.0	52.8		0	2.25E-05	2.67E-03	1.68E-04	5.7	16.2
L16G86	4.78	0.15	0.052	0.003	19.194	0.921	0.644	0.030	34.28	1.85	4.82	14.17	82.9	13.4		10	2.63E-05	8.31E-03	1.32E-04	31.6	20.0
L16G93	11.45	0.4	0.112	0.006	8.905	0.444	0.731	0.027	15.37	13.82	5.55	0.78	100.5	25.6		11	2.96E-05	3.87E-03	2.71E-03	66.1	61.1
L16G110	105.2	4.4	0.916	0.048	1.092	0.057	0.828	0.038	1.42	6.64	5.40	0.25	120.2	284.1		3	6.73E-05	6.00E-04	1.37E-04	51.1	60.2
L16G114	0.858	0.057	0.021	0.001	48.309	2.801	0.310	0.025	32.67	31.36	1.10	1.16	88.7	6.6		14	2.02E-05	1.39E-02	4.06E-05	34.4	18.4
L16G116	6.74	0.25	0.071	0.004	14.104	0.776	0.691	0.039	10.11	39.10	2.72	0.28	85.9	23.0		5	2.84E-05	4.16E-03	9.93E-04	29.2	27.0
L16G32	75.4	2.8	0.667	0.034	1.499	0.076	0.786	0.038	2.46	0.14	5.31	20.80	393.5	197.5		2	2.77E-05	7.79E-04	7.70E-04	63.8	110.1
L16G105	63	2.1	0.582	0.028	1.718	0.083	0.772	0.013	18.43	1.95	46.28	11.50	410.7	69.3		8	2.70E-05	9.19E-03	7.98E-04	22.2	15.9
L16G113	5.36	0.19	0.075	0.004	13.369	0.626	0.508	0.016	30.51	3.45	5.72	10.04	202.6	13.6		17	3.59E-05	1.32E-02	7.45E-04	24.8	12.1

U-Pb data

AFT dat

#grains	Ns	ΣpiΩi	2σΣpiΩi	ζeta (yr cm^2	2 sig abs	χ^2	P(χ^2)	Pooled agı	2σ Ma
82	678	1.02E-05	1.92E-07	6.92E-01	1.10E-02	103.15	0.05	45.9	3.7

Grain Number	Pb207/U235	Pb207/U235 error (2s)	Pb206/U238	Pb206/U238 error (2s)	U238/Pb206	U238/Pb206 error (2s)	Pb207/Pb206	Pb207/Pb206 error (2s)	Approx U (ppm)	Approx Th (ppm)	Approx Pb (ppm)	U/Th	207corrAge (Ma)	207corrAge error (2s,Ma)	Ns	Area (cm^2)	$^{238}U/^{43}Ca$	2σ	FT Age	2σ
Population 1																				
Y1G1	1.244	0.063	0.017	0.001	60.496	2.855	0.543	0.022	98.00	14.27	4.50	6.90	39.6	3.6	12	1.28E-05	2.69E-02	2.17E-03	24.0	14.0
Y1G3	34.08	1.7	0.300	0.017	3.333	0.189	0.823	0.030	5.98	37.50	7.66	0.16	36.5	75.7	4	2.27E-05	1.80E-03	1.54E-03	67.5	88.8
Y1G5	17.21	0.84	0.160	0.008	6.238	0.323	0.788	0.029	7.50	23.52	4.76	0.32	67.4	39.0	5	1.90E-05	2.09E-03	1.30E-04	86.6	77.6
Y1G6	23.42	1.3	0.211	0.013	4.739	0.292	0.819	0.045	5.00	18.29	4.28	0.27	32.0	78.3	0	1.86E-05	1.40E-03	7.89E-05	13.3	37.6
Y1G8	1.872	0.091	0.023	0.001	44.385	2.167	0.595	0.020	102.60	95.20	7.35	1.07	44.5	4.4	23	1.83E-05	2.80E-02	1.55E-04	31.0	12.9
Y1G10	13.02	0.78	0.117	0.007	8.584	0.530	0.821	0.055	4.68	12.08	2.19	0.39	14.8	52.8	3	1.66E-05	1.37E-03	1.07E-04	90.4	104.7
Y1G13	17.1	1.3	0.160	0.012	6.250	0.469	0.799	0.069	2.56	6.84	1.59	0.37	51.8	89.9	4	4.02E-05	7.06E-04	1.03E-04	96.8	97.8
Y1G14	1.1	0.06	0.016	0.001	63.412	3.257	0.492	0.018	152.50	71.20	5.84	2.12	44.3	3.3	29	1.33E-05	4.39E-02	2.01E-03	34.3	12.8
Y1G15	7.02	0.41	0.072	0.004	13.966	0.858	0.735	0.036	13.83	30.77	3.70	0.44	60.6	21.6	5	1.97E-05	3.64E-03	2.60E-04	48.1	43.1
Y1G16	2.707	0.13	0.029	0.002	34.722	1.808	0.672	0.026	73.90	3.57	6.71	20.34	38.9	6.6	15	1.28E-05	2.09E-02	1.05E-04	38.6	20.0
Y1G17	9.98	0.62	0.088	0.006	11.325	0.718	0.813	0.029	21.63	67.80	8.01	0.31	17.1	21.7	17	3.01E-05	6.29E-03	7.52E-05	61.8	30.0
Y1G19	2.5	0.15	0.029	0.002	34.843	2.064	0.644	0.030	39.72	2.47	3.72	16.06	45.3	7.6	14	1.51E-05	9.91E-03	3.26E-04	64.4	34.5
Y1G20	15.76	1.2	0.145	0.013	6.897	0.618	0.800	0.076	1.95	5.70	1.09	0.34	45.3	89.8	1	4.59E-05	5.32E-04	5.64E-05	28.3	56.6
Y1G21	1.67	0.081	0.021	0.001	47.483	2.255	0.577	0.018	125.70	285.80	8.58	0.43	44.7	3.8	34	2.11E-05	3.31E-02	3.24E-03	33.5	12.0
Y1G22	20.6	1.2	0.183	0.011	5.453	0.327	0.815	0.042	5.76	15.76	4.30	0.36	34.0	63.7	3	2.55E-05	1.51E-03	2.65E-04	53.6	62.6
Y1G23	2.147	0.1	0.024	0.001	41.999	1.940	0.644	0.020	107.50	186.80	8.87	0.57	37.5	4.4	38	2.20E-05	2.82E-02	1.40E-03	42.2	13.9
Y1G24	1.92	0.1	0.022	0.001	44.803	2.208	0.619	0.024	91.60	71.80	6.17	1.30	39.7	4.9	12	1.33E-05	2.04E-02	4.53E-04	30.6	17.7
Y1G25	22	1.5	0.195	0.015	5.128	0.394	0.827	0.044	4.70	14.17	3.61	0.33	15.2	71.1	5	4.77E-05	1.15E-03	1.32E-04	62.6	56.4
Y1G30	9.5	0.56	0.090	0.006	11.173	0.687	0.757	0.046	5.05	13.43	1.72	0.37	59.8	33.9	4	2.34E-05	1.47E-03	7.63E-04	79.9	90.0
Y1G31	10.47	0.52	0.096	0.006	10.373	0.635	0.803	0.036	11.16	40.80	4.27	0.27	26.9	28.9	8	3.72E-05	3.19E-03	4.28E-05	46.5	32.9
Y1G32	1.097	0.057	0.016	0.001	61.275	2.891	0.486	0.018	145.30	54.83	5.69	2.59	46.7	3.3	17	9.48E-06	3.96E-02	2.28E-03	31.3	15.3
Y1G33	10.55	0.55	0.099	0.006	10.070	0.568	0.758	0.039	8.63	23.61	3.47	0.36	65.8	32.0	4	3.62E-05	2.54E-03	1.03E-04	30.0	30.1
Y1G34	25.73	1.3	0.228	0.013	4.384	0.250	0.803	0.037	7.02	27.55	6.85	0.25	68.3	69.7	4	2.25E-05	2.20E-03	1.99E-03	55.7	75.1
Y1G35	11.85	0.97	0.107	0.009	9.355	0.805	0.795	0.047	7.67	19.43	3.27	0.38	37.4	41.4	7	4.97E-05	2.16E-03	1.97E-03	44.9	53.3
Y1G38	5.84	0.39	0.057	0.005	17.483	1.406	0.746	0.068	6.06	27.08	1.47	0.22	42.9	31.9	1	1.99E-05	1.65E-03	8.88E-05	21.0	42.0
Y1G39	59	3.8	0.517	0.033	1.934	0.123	0.831	0.041	1.36	3.02	3.04	0.45	27.5	175.6	2	2.61E-05	3.94E-04	6.97E-05	133.0	189.6
Y1G42	2.655	0.13	0.031	0.002	32.331	1.568	0.629	0.017	49.51	23.03	5.29	2.21	52.7	5.2	26	2.71E-05	1.40E-02	6.90E-05	47.3	18.6
Y1G43	1.623	0.12	0.020	0.001	49.900	2.988	0.574	0.028	64.10	23.50	3.75	2.77	43.0	5.3	9	1.22E-05	1.78E-02	5.45E-05	28.6	19.1
Y1G45	16.03	0.83	0.146	0.008	6.835	0.355	0.799	0.037	7.15	21.54	4.48	0.34	47.1	44.9	2	2.04E-05	2.19E-03	7.80E-04	30.9	45.1
Y1G46	1.996	0.11	0.023	0.001	42.918	2.579	0.625	0.033	47.30	19.80	3.47	2.41	40.3	6.8	21	2.15E-05	1.40E-02	1.11E-04	48.0	21.0
Y1G47	31.38	1.4	0.275	0.014	3.631	0.185	0.829	0.032	6.27	5.73	6.92	1.11	17.4	74.1	4	1.81E-05	1.78E-03	2.21E-04	85.4	86.1
Y1G50	2.072	0.098	0.024	0.001	40.933	2.011	0.628	0.023	73.70	10.90	5.76	6.91	41.7	5.1	15	1.47E-05	2.22E-02	2.69E-03	31.7	16.8
Y1G51	7.2	0.4	0.067	0.004	14.970	0.852	0.781	0.027	30.50	43.70	8.11	0.71	30.7	15.3	11	1.45E-05	9.87E-03	1.88E-04	53.0	32.0
Y1G53	13.37	0.82	0.123	0.009	8.157	0.572	0.809	0.058	4.15	14.40	2.04	0.29	28.4	58.3	4	2.62E-05	1.35E-03	1.56E-04	77.8	78.4
Y1G54	7.1	0.34	0.067	0.003	14.881	0.709	0.746	0.022	34.91	48.00	9.63	0.74	50.6	12.8	14	1.44E-05	1.01E-02	1.59E-04	66.0	35.3
Y1G59	20.01	1.1	0.181	0.011	5.519	0.335	0.823	0.048	4.93	14.48	3.54	0.34	20.6	71.8	6	6.19E-05	1.49E-03	9.78E-04	44.9	47.1
Y1G60	14.2	1.5	0.129	0.013	7.752	0.781	0.813	0.033	8.04	30.84	4.29	0.26	25.5	35.7	4	1.73E-05	2.38E-03	2.21E-04	66.7	67.0
Y1G61	33.8	2.1	0.298	0.019	3.356	0.214	0.833	0.035	5.35	15.01	6.63	0.35	7.6	87.4	2	1.56E-05	1.53E-03	1.22E-04	57.7	81.7
Y1G62	17.35	0.91	0.158	0.010	6.349	0.395	0.795	0.041	4.20	13.35	2.89	0.31	56.5	53.2	2	3.21E-05	1.18E-03	3.32E-05	36.5	51.6
Y1G65	10.97	0.65	0.103	0.007	9.709	0.641	0.759	0.047	4.75	12.04	1.74	0.40	67.5	39.8	1	1.94E-05	1.44E-03	1.23E-04	24.7	49.4
Y1G69	1.233	0.06	0.017	0.001	58.893	2.775	0.524	0.020	141.70	274.30	7.72	0.51	43.3	3.5	32	1.22E-05	4.09E-02	1.83E-04	44.2	15.6
Y1G71	14.7	0.82	0.130	0.007	7.716	0.411	0.831	0.043	5.64	12.10	3.04	0.46	5.2	46.3	6	3.78E-05	1.72E-03	1.00E-03	63.6	63.9
Y1G72	2.199	0.11	0.025	0.001	39.604	2.039	0.628	0.026	49.90	3.57	4.09	14.00	43.1	5.9	21	1.61E-05	1.51E-02	1.60E-03	59.5	26.7
Y1G75	7.88	0.49	0.079	0.005	12.739	0.779	0.749	0.033	11.14	29.70	3.50	0.36	57.4	21.7	9	2.48E-05	3.53E-03	1.16E-04	70.6	47.1
Y1G77	10.83	0.58	0.099	0.005	10.132	0.554	0.799	0.040	7.58	19.88	3.17	0.38	31.0	32.7	5	2.33E-05	2.25E-03	1.58E-04	65.7	59.0
Y1G78	10.29	0.59	0.097	0.005	10.267	0.569	0.768	0.040	5.24	11.21	2.03	0.46	56.2	32.2	2	3.60E-05	1.54E-03	1.13E-03	24.9	39.7
Y1G79	7.19	0.35	0.068	0.004	14.620	0.748	0.763	0.033	21.66	47.48	6.24	0.45	41.8	18.9	10	2.25E-05	6.21E-03	1.33E-04	49.3	31.2
Y1G80	13.23	0.78	0.122	0.008	8.190	0.557	0.810	0.055	3.50	12.14	1.91	0.28	27.2	55.2	1	2.58E-05	1.07E-03	1.38E-04	25.0	50.1
Y1G81	26.89	1.4	0.238	0.013	4.196	0.229	0.808	0.031	4.05	10.39	4.19	0.38	60.9	61.7	4	3.03E-05	1.18E-03	4.32E-04	76.8	81.7
Y1G83	11.62	0.62	0.108	0.006	9.294	0.492	0.789	0.027	15.55	53.30	7.17	0.29	43.1	24.6	8	1.72E-05	5.10E-03	1.60E-03	62.7	48.6
Y1G4	40.6	2.2	0.339	0.019	2.950	0.165	0.860	0.036	3.70	9.66	5.45	0.38	-82.7	104.2	2	2.18E-05	1.00E-03	7.75E-04	63.1	101.7
Y1G7	33.7	1.8	0.285	0.016	3.509	0.197	0.842	0.036	5.14	13.51	6.40	0.38	-17.4	86.3	3	1.93E-05	1.45E-03	6.62E-05	73.5	84.9
Y1G27	38.2	2.3	0.327	0.020	3.058	0.187	0.856	0.043	3.35	11.04	4.55	0.30	-66.0	118.6	5	4.57E-05	8.83E-04	1.06E-04	85.2	76.9
Y1G40	11.17	0.69	0.097	0.006	10.309	0.659	0.850	0.055	5.43	17.51	2.25	0.31	-12.0	44.2	1	4.55E-05	1.59E-03	7.45E-04	9.6	19.7
Y1G44	41.5	7.2	0.340	0.058	2.941	0.502	0.853	0.041	5.06	17.36	7.40	0.30	-59.0	118.0	3	2.06E-05	1.54E-03	6.80E-05	65.0	75.2
Y1G48	28.8	2	0.241	0.017	4.149	0.293	0.868	0.041	3.27	9.70	3.81	0.37	-73.5	83.8	1	1.24E-05	1.18E-03	2.49E-05	47.1	94.1
Y1G52	23.3	1.6	0.186	0.013	5.376	0.376	0.906	0.055	2.68	9.87	2.21	0.28	-120.3	87.0	1	1.97E-05	8.00E-04	5.37E-04	43.8	92.3
Y1G58	17.2	1.2	0.147	0.010	6.807	0.463	0.925	0.088	3.68	11.20	2.27	0.33	-117.9	108.8	5	5.38E-05	1.02E-03	8.27E-05	62.8	56.4
Y1G73	15.65	0.86	0.138	0.009	7.273	0.481	0.838	0.042	5.02	13.28	3.02	0.37	-2.9	48.1	4	3.88E-05	1.41E-03	1.02E-04	50.5	50.6
Population 2																				
Y1G2	3.649	0.17	0.045	0.002	22.371	1.051	0.585	0.016	75.50	2.78	9.77	27.10	92.5	7.5	16	1.65E-05	2.05E-02	1.92E-04	32.6	16.3
Y1G18	12.16	0.92	0.114	0.008	8.741	0.596	0.756	0.042	6.82	21.98	2.93	0.31	78.2	39.6	3	2.90E-05	1.85E-03	1.11E-04	38.6	44.6
Y1G26	79	12	0.700	0.110	1.429	0.224	0.825	0.035	3.16	8.79	9.00	0.35	97.7	202.3	2	2.68E-05	8.90E-04	9.07E-05	57.8	81.9
Y1G28	35.9	1.9	0.319	0.018	3.135	0.177	0.785	0.037	2.74	8.99	3.51	0.30	154.9	96.1	2	2.48E-05	7.49E-04	1.11E-03	74.0	151.4
Y1G29	6.2	0.47	0.071	0.005	14.184	1.006	0.645	0.023	38.18	3.73	8.56	10.26	112.2	15.6	14	1.37E-05	1.08E-02	3.78E-04	65.0	34.8
Y1G36	2.222	0.13	0.034	0.002	29.586	1.576	0.477	0.024	41.12	29.95	3.55	1.36	99.4	8.5	10	1.34E-05	1.05E-02	1.07E-04	48.8	30.9
Y1G55	58.8	2.9	0.530	0.031	1.887	0.110	0.811	0.032	3.15	7.79	6.73	0.40	145.0	139.3	1	1.41E-05	9.00E-04	1.34E-04	54.3	108.9
Y1G63	5.82	0.26	0.061	0.003	16.367	0.750	0.677	0.019	51.22	0.45	11.60	144.00	80.8	10.6	26	2.07E-05	1.47E-02	1.15E-04	58.7	23.1
Y1G64	10.35	0.65	0.099	0.006	10.132	0.616	0.748	0.029	13.22	61.50	5.63	0.21	73.7	24.2	9	1.48E-05	4.32E-03	5.84E-04	96.7	65.8

Y1G70	22.77	1.3	0.208	0.012	4.810	0.278	0.775	0.042	4.32	14.90	3.58	0.29	113.6	71.3	1	1.76E-05	1.28E-03	2.91E-03	30.7	93.3
Y1G74	10.28	0.58	0.101	0.006	9.872	0.604	0.741	0.040	7.29	19.05	3.08	0.37	81.7	33.5	4	2.78E-05	2.08E-03	1.01E-04	47.7	47.8
Population 3																				
Y1G41	58.9	3.7	0.535	0.031	1.869	0.108	0.792	0.021	6.94	16.82	14.66	0.41	255.7	94.6	4	2.00E-05	2.24E-03	1.31E-04	61.5	61.6
Y1G49	13.54	0.67	0.154	0.007	6.481	0.311	0.638	0.022	17.88	40.86	10.14	0.44	261.3	30.1	6	1.08E-05	5.27E-03	1.04E-03	72.5	60.9
Y1G56	37.6	3	0.355	0.030	2.817	0.238	0.769	0.052	1.11	3.94	1.60	0.29	229.7	147.2	1	1.87E-05	3.14E-04	1.12E-04	116.8	237.3
Y1G66	27.02	1.4	0.262	0.014	3.820	0.204	0.747	0.029	5.40	2.77	5.54	1.99	213.1	62.5	4	2.87E-05	1.68E-03	1.59E-04	57.1	57.4
Y1G68	8.73	0.43	0.111	0.006	9.009	0.511	0.594	0.020	21.97	100.80	9.34	0.22	225.4	22.1	9	1.69E-05	5.80E-03	2.69E-04	63.2	42.3
Y1G9	9.22	0.47	0.138	0.007	7.257	0.358	0.492	0.018	13.46	11.12	4.50	1.20	394.8	27.3	8	1.19E-05	3.78E-03	4.96E-04	121.7	87.6
Y1G11	42.9	2.2	0.429	0.024	2.331	0.130	0.726	0.029	3.39	10.86	5.65	0.31	464.3	99.5	1	1.78E-05	9.31E-04	1.63E-04	41.6	83.5
Y1G12	7.72	0.42	0.120	0.006	8.354	0.433	0.470	0.024	16.43	41.56	5.89	0.39	362.8	29.0	15	1.93E-05	4.35E-03	1.07E-04	122.4	63.3
Y1G37	16.53	1.1	0.204	0.011	4.902	0.264	0.576	0.027	8.29	2.06	5.15	3.94	454.9	48.6	12	3.26E-05	2.05E-03	4.80E-04	123.1	76.7
Y1G67	16.28	1.1	0.192	0.011	5.219	0.300	0.626	0.033	4.70	5.86	3.11	0.77	347.6	53.0	1	1.86E-05	1.39E-03	8.16E-05	26.7	53.5
Y1G76	8.84	0.44	0.149	0.007	6.725	0.308	0.430	0.014	22.68	30.80	9.14	0.72	498.9	27.5	7	1.69E-05	6.79E-03	9.34E-05	42.0	31.8
Y1G57	15.54	0.72	0.404	0.018	2.474	0.110	0.277	0.006	24.00	12.84	11.44	1.89	1827.5	81.5	7	1.52E-05	7.26E-03	1.01E-07	43.7	33.1

U-Pb data

AFT dat

#grains	Ns	ΣpiΩi	2σΣpiΩi	ζeta (yr cm^2	2 sig abs	χ^2	P(χ^2)	Pooled age	2σ Ma
116	1525	3.95E-05	6.44E-07	6.92E-01	1.10E-02	207.64	0.00	26.7	1.5

Grain Number	Pb207/U235	Pb207/U235 error (2s)	Pb206/U238	Pb206/U238 error (2s)	U238/Pb206	U238/Pb206 error (2s)	Pb207/Pb206	Pb207/Pb206 error (2s)	Approx U (ppm)	Approx Th (ppm)	Approx Pb (ppm)	U/Th	207corrAge (Ma)	207corrAge error (2s,Ma)	Ns	Area (cm^2)	$^{238}U/^{43}Ca$	2σ	FT Age	2σ
Population 1																				
Y2G2	2.498	0.16	0.026	0.002	37.994	2.310	0.687	0.037	39.27	6.84	3.82	5.67	32.2	8.3	19	2.56E-05	1.64E-02	5.97E-04	31.1	14.3
Y2G5	5.8	0.35	0.056	0.003	18.018	1.104	0.757	0.032	24.54	1.97	5.82	12.07	36.5	15.0	14	4.14E-05	1.07E-02	1.24E-03	21.8	11.9
Y2G6	1.002	0.063	0.012	0.001	81.301	4.891	0.591	0.029	107.30	253.00	5.05	0.41	24.6	3.3	19	1.91E-05	4.53E-02	2.22E-03	15.2	7.0
Y2G7	3.16	0.21	0.032	0.002	30.960	2.013	0.714	0.040	22.28	11.10	3.09	1.94	32.5	10.9	12	2.81E-05	9.86E-03	1.33E-03	29.9	17.7
Y2G8	2.112	0.13	0.021	0.001	46.685	2.833	0.717	0.026	82.00	42.60	6.45	1.85	20.9	4.9	27	2.19E-05	3.55E-02	8.46E-04	24.0	9.3
Y2G9	18.26	1.1	0.159	0.011	6.281	0.434	0.833	0.039	5.17	0.44	3.75	11.11	3.7	51.8	3	2.79E-05	2.86E-03	3.80E-03	25.9	45.7
Y2G13	2.14	0.16	0.023	0.002	43.478	3.025	0.656	0.036	32.50	55.60	2.88	0.55	34.0	7.2	18	2.85E-05	1.71E-02	7.71E-04	25.5	12.1
Y2G16	9.1	0.83	0.081	0.007	12.285	1.087	0.803	0.040	8.53	22.70	3.19	0.36	22.6	27.1	10	2.52E-05	5.28E-03	2.79E-03	51.8	42.7
Y2G17	3.263	0.2	0.032	0.002	30.960	1.917	0.737	0.032	41.84	80.30	5.41	0.50	26.4	8.8	22	2.72E-05	1.86E-02	2.44E-04	30.1	12.8
Y2G18	3.02	0.19	0.031	0.002	32.425	1.893	0.715	0.033	39.30	107.90	5.18	0.35	30.7	8.6	19	2.22E-05	2.06E-02	8.41E-04	28.6	13.2
Y2G23	3.86	0.23	0.038	0.003	26.525	1.829	0.761	0.040	23.01	16.59	3.12	1.39	23.4	12.6	10	2.41E-05	1.28E-02	2.40E-04	22.3	14.1
Y2G26	3.42	0.21	0.034	0.002	29.638	1.757	0.730	0.031	37.41	11.18	4.67	3.38	29.5	8.9	12	2.26E-05	1.69E-02	1.45E-04	21.7	12.5
Y2G29	0.907	0.064	0.013	0.001	79.618	5.452	0.531	0.032	64.80	86.90	2.42	0.76	31.3	3.9	27	2.37E-05	3.88E-02	1.29E-03	20.3	7.8
Y2G30	15.28	1.1	0.133	0.010	7.502	0.540	0.835	0.047	4.91	4.64	2.53	1.08	0.7	51.9	5	3.02E-05	3.25E-03	1.05E-04	35.1	31.4
Y2G31	1.523	0.096	0.017	0.001	57.274	3.608	0.634	0.033	45.64	11.04	2.57	4.10	28.9	5.1	22	2.68E-05	2.34E-02	4.54E-04	24.2	10.3
Y2G32	4.74	0.41	0.046	0.004	21.598	2.006	0.750	0.034	25.90	19.10	4.38	1.39	33.0	13.4	16	3.42E-05	1.04E-02	4.93E-04	31.0	15.6
Y2G36	1.138	0.073	0.014	0.001	71.225	4.870	0.592	0.031	79.60	25.77	3.36	3.09	28.0	4.1	26	1.66E-05	4.12E-02	1.44E-03	26.3	10.4
Y2G37	4.82	0.3	0.045	0.003	22.321	1.395	0.779	0.030	32.36	10.17	5.77	3.20	21.1	11.4	11	2.87E-05	1.71E-02	1.51E-03	15.5	9.5
Y2G38	2.43	0.16	0.026	0.002	38.168	2.477	0.691	0.037	25.98	129.60	2.69	0.20	31.2	8.3	13	2.67E-05	1.23E-02	2.74E-04	27.3	15.2
Y2G42	22.98	1.4	0.200	0.013	5.013	0.327	0.832	0.037	5.04	19.08	4.14	0.27	6.6	61.7	4	2.93E-05	2.34E-03	5.30E-05	40.2	40.2
Y2G47	1.439	0.094	0.017	0.001	59.453	3.888	0.619	0.030	52.41	23.01	2.78	2.35	29.9	4.6	14	2.23E-05	2.91E-02	1.51E-04	14.9	8.0
Y2G50	1.539	0.095	0.018	0.001	56.465	3.507	0.656	0.036	53.95	34.05	3.11	1.63	26.1	5.5	18	1.80E-05	2.78E-02	7.01E-04	24.8	11.7
Y2G57	3.54	0.22	0.033	0.002	30.769	2.083	0.771	0.042	22.30	3.72	2.81	6.25	17.4	11.4	18	2.74E-05	1.37E-02	9.90E-04	33.0	15.8
Y2G59	1.389	0.088	0.015	0.001	65.020	4.228	0.666	0.034	58.60	20.20	2.89	2.99	21.4	4.5	32	3.22E-05	3.08E-02	9.48E-04	22.3	7.9
Y2G60	5.74	0.37	0.055	0.004	18.248	1.199	0.759	0.037	17.87	30.46	3.40	0.58	35.1	16.9	4	2.13E-05	9.35E-03	2.56E-06	13.9	13.9
Y2G61	1.93	0.18	0.022	0.002	46.296	3.858	0.627	0.033	43.40	37.50	2.99	1.22	37.0	6.6	15	2.32E-05	3.18E-02	1.23E-03	14.0	7.3
Y2G63	2.351	0.15	0.025	0.002	40.650	2.809	0.704	0.041	38.64	26.10	3.30	1.48	26.7	8.5	15	2.03E-05	1.96E-02	1.48E-04	26.0	13.5
Y2G65	24	1.9	0.214	0.018	4.673	0.393	0.822	0.063	1.71	2.32	1.50	0.76	26.7	110.5	0	3.03E-05	8.79E-04	1.24E-06	13.0	36.7
Y2G67	2.208	0.13	0.024	0.001	42.499	2.529	0.685	0.028	59.20	148.70	5.14	0.40	29.2	5.8	34	2.33E-05	3.17E-02	3.08E-03	31.7	11.3
Y2G74	8.42	0.49	0.073	0.005	13.661	0.858	0.828	0.036	16.92	70.90	5.22	0.24	4.7	22.1	11	2.41E-05	9.34E-03	2.59E-04	33.7	20.3
Y2G76	4.26	0.29	0.043	0.003	23.529	1.495	0.742	0.032	28.20	110.00	4.76	0.26	33.1	11.5	5	2.07E-05	1.36E-02	1.83E-03	12.3	11.1
Y2G78	8.06	0.46	0.076	0.004	13.123	0.741	0.783	0.022	70.60	441.00	22.38	0.16	33.9	14.6	43	2.35E-05	3.90E-02	1.81E-03	32.4	10.0
Y2G81	0.275	0.02	0.006	0.000	160.772	9.822	0.323	0.020	284.90	557.00	4.32	0.52	26.0	1.9	39	8.02E-06	1.69E-01	3.01E-03	19.9	6.4
Y2G82	0.9	0.055	0.012	0.001	82.919	5.432	0.531	0.024	89.30	12.71	3.15	7.04	30.1	3.1	18	1.31E-05	5.19E-02	1.43E-03	18.3	8.6
Y2G83	6.14	0.39	0.059	0.004	17.094	1.140	0.772	0.036	17.90	36.20	4.43	0.50	31.2	17.6	9	1.37E-05	9.56E-03	9.00E-04	47.3	31.9
Y2G85	4.38	0.34	0.044	0.004	22.779	1.816	0.723	0.028	38.80	23.80	6.51	1.71	41.1	10.8	18	2.34E-05	1.60E-02	3.12E-03	33.1	16.9
Y2G86	4.13	0.33	0.043	0.004	23.474	2.094	0.746	0.069	7.10	0.70	0.95	10.41	31.7	24.2	9	2.92E-05	3.74E-03	1.29E-03	56.7	42.5
Y2G87	0.399	0.027	0.008	0.000	131.579	7.791	0.388	0.017	178.70	48.60	2.98	3.78	27.8	2.0	35	1.40E-05	8.73E-02	9.39E-04	19.8	6.7
Y2G90	2.92	0.22	0.030	0.002	33.113	2.631	0.682	0.048	14.57	5.37	1.54	2.77	38.3	12.2	4	1.83E-05	1.01E-02	1.19E-03	15.0	15.1
Y2G92	4.76	0.29	0.047	0.003	21.322	1.455	0.736	0.031	18.92	108.00	4.12	0.18	38.9	12.4	11	3.56E-05	1.17E-02	5.39E-04	18.3	11.1
Y2G97	5.88	0.36	0.058	0.004	17.241	1.130	0.759	0.034	14.99	2.49	3.31	5.96	37.2	16.6	5	1.89E-05	7.63E-03	5.05E-04	23.9	21.5
Y2G101	1.127	0.072	0.013	0.001	74.184	5.063	0.602	0.035	66.20	78.90	2.77	0.82	25.8	4.3	27	2.68E-05	2.93E-02	1.93E-04	23.7	9.1
Y2G103	2.217	0.14	0.024	0.002	41.477	2.580	0.680	0.038	32.66	17.90	2.74	1.75	30.9	7.8	10	1.56E-05	1.69E-02	9.72E-04	26.2	16.6
Y2G104	1.013	0.064	0.014	0.001	71.480	4.496	0.522	0.019	118.20	124.10	4.86	0.94	35.9	3.2	21	1.55E-05	5.56E-02	1.38E-04	16.8	7.4
Y2G106	11.66	0.79	0.109	0.008	9.166	0.639	0.806	0.053	5.78	12.60	2.54	0.45	27.9	47.5	6	1.77E-05	3.49E-03	2.35E-03	66.9	70.8
Y2G108	16.36	1.1	0.145	0.010	6.906	0.477	0.815	0.029	11.05	24.20	6.78	0.45	26.3	35.5	3	2.50E-05	8.73E-03	1.43E-04	9.5	11.0
Y2G111	0.957	0.062	0.013	0.001	79.936	5.367	0.564	0.028	88.90	21.50	3.29	4.06	27.8	3.4	34	1.62E-05	5.46E-02	2.20E-03	26.5	9.2
Y2G113	8.76	0.66	0.083	0.007	12.048	1.031	0.835	0.086	4.21	1.22	1.32	3.38	0.4	58.5	3	1.93E-05	2.72E-03	4.16E-04	39.4	45.9
Y2G114	0.786	0.051	0.011	0.001	90.744	5.764	0.516	0.024	107.50	45.62	3.19	2.33	28.8	2.9	39	2.00E-05	7.08E-02	2.21E-04	19.0	6.1
Y2G117	1.536	0.098	0.018	0.001	55.772	3.733	0.636	0.029	62.80	18.82	3.73	3.29	29.4	4.7	23	1.80E-05	3.85E-02	2.12E-03	22.9	9.6
Y2G119	2.329	0.15	0.024	0.002	42.017	3.001	0.713	0.038	23.15	3.09	1.76	7.49	24.0	7.7	13	2.17E-05	1.38E-02	1.87E-04	29.8	16.6
Y2G120	2.01	0.2	0.022	0.002	46.083	4.035	0.653	0.032	63.70	31.90	4.61	2.01	32.6	6.4	30	1.76E-05	5.14E-02	5.00E-04	22.9	8.4
Y2G11	*24*	*1.7*	*0.205*	*0.014*	*4.878*	*0.333*	*0.840*	*0.044*	*5.53*	*23.20*	*5.25*	*0.23*	*-8.2*	*75.1*	*7*	*4.08E-05*	*2.94E-03*	*7.09E-04*	*40.2*	*31.9*
Y2G15	*19.13*	*1.2*	*0.164*	*0.010*	*6.101*	*0.372*	*0.856*	*0.040*	*7.13*	*28.03*	*5.48*	*0.24*	*-29.9*	*55.1*	*2*	*2.62E-05*	*4.17E-03*	*2.05E-04*	*12.7*	*17.9*
Y2G20	*64*	*4.6*	*0.549*	*0.041*	*1.821*	*0.136*	*0.851*	*0.050*	*1.09*	*1.71*	*2.57*	*0.68*	*-96.2*	*231.5*	*2*	*2.51E-05*	*6.20E-04*	*7.73E-04*	*88.3*	*166.5*
Y2G27	*10.87*	*0.97*	*0.101*	*0.010*	*9.872*	*0.936*	*0.880*	*0.110*	*2.37*	*4.58*	*0.92*	*0.52*	*-39.0*	*92.0*	*2*	*3.20E-05*	*1.21E-03*	*5.93E-04*	*35.8*	*53.5*
Y2G46	*40*	*2.4*	*0.346*	*0.023*	*2.890*	*0.192*	*0.856*	*0.043*	*3.24*	*7.25*	*4.44*	*0.46*	*-70.7*	*125.6*	*2*	*3.39E-05*	*1.53E-03*	*4.27E-04*	*26.5*	*38.2*
Y2G52	*16.72*	*0.95*	*0.145*	*0.009*	*6.892*	*0.413*	*0.843*	*0.028*	*12.43*	*42.53*	*7.45*	*0.30*	*-9.5*	*34.7*	*7*	*2.37E-05*	*6.36E-03*	*1.60E-03*	*32.0*	*25.5*
Y2G71	*344.5*	*20*	*2.932*	*0.180*	*0.341*	*0.021*	*0.854*	*0.023*	*1.70*	*0.13*	*21.51*	*16.20*	*-376.6*	*611.3*	*1*	*3.87E-05*	*8.85E-04*	*1.13E-03*	*20.2*	*47.8*
Y2G73	*16.33*	*1*	*0.144*	*0.010*	*6.954*	*0.464*	*0.848*	*0.041*	*4.69*	*22.22*	*2.97*	*0.21*	*-15.7*	*49.3*	*2*	*3.37E-05*	*2.32E-03*	*3.18E-03*	*17.6*	*34.8*
Y2G84	*12.24*	*0.89*	*0.109*	*0.009*	*9.158*	*0.772*	*0.841*	*0.048*	*6.19*	*8.86*	*3.03*	*0.75*	*-5.1*	*43.5*	*6*	*1.40E-05*	*3.98E-03*	*1.07E-03*	*74.0*	*63.7*
Y2G88	*20.67*	*1.4*	*0.180*	*0.012*	*5.556*	*0.370*	*0.855*	*0.041*	*5.18*	*21.00*	*3.86*	*0.25*	*-31.6*	*62.0*	*7*	*3.65E-05*	*2.65E-03*	*1.23E-03*	*49.9*	*44.3*
Y2G95	*21.5*	*1.6*	*0.195*	*0.015*	*5.128*	*0.394*	*0.841*	*0.064*	*2.44*	*0.05*	*2.01*	*51.85*	*-9.5*	*103.0*	*5*	*3.26E-05*	*1.44E-03*	*1.44E-02*	*73.2*	*734.2*
Y2G107	*124.7*	*7.3*	*1.060*	*0.063*	*0.943*	*0.056*	*0.862*	*0.019*	*3.11*	*0.33*	*14.56*	*10.70*	*-471.8*	*199.0*	*2*	*1.94E-05*	*1.99E-03*	*4.08E-03*	*35.7*	*88.8*
Population 2																				
Y2G1	8.36	0.52	0.079	0.005	12.610	0.795	0.770	0.030	18.91	129.70	6.74	0.14	44.1	20.1	5	2.70E-05	7.34E-03	3.47E-03	17.4	17.6
Y2G3	3.494	0.2	0.036	0.002	27.473	1.660	0.688	0.022	64.10	244.00	9.88	0.25	44.5	7.3	37	3.22E-05	3.01E-02	1.40E-03	26.3	8.7
Y2G21	38	2.6	0.337	0.026	2.967	0.229	0.823	0.042	3.35	6.46	4.58	0.54	42.0	116.9	4	3.30E-05	1.89E-03	3.31E-03	44.1	88.9
Y2G24	3.02	0.21	0.034	0.002	29.155	1.870	0.650	0.035	26.10	53.09	3.01	0.49	52.6	10.4	15	2.30E-05	1.26E-02	1.08E-03	35.7	18.7
Y2G39	2.969	0.18	0.034	0.002	29.070	1.859	0.650	0.031	29.92	0.29	3.12	113.00	52.7	9.4	14	2.30E-05	1.35E-02	1.07E-03	31.0	16.8

Y2G43	2.64	0.17	0.030	0.002	33.333	2.111	0.653	0.037	25.94	181.00	3.23	0.15	45.2	9.6	9	2.22E-05	1.18E-02	1.32E-04	23.8	15.9
Y2G45	3.09	0.23	0.033	0.002	30.581	2.057	0.676	0.025	39.50	62.20	4.69	0.66	43.1	7.4	18	2.71E-05	1.64E-02	2.49E-03	27.9	13.8
Y2G51	29.88	1.8	0.270	0.018	3.704	0.247	0.816	0.037	4.98	10.72	5.10	0.48	50.0	82.8	4	3.37E-05	2.32E-03	7.45E-04	35.3	37.1
Y2G58	40.2	3.1	0.365	0.029	2.740	0.218	0.823	0.043	2.42	0.38	3.65	7.53	46.3	129.4	0	2.41E-05	1.15E-03	3.09E-03	2.7	8.4
Y2G64	9.26	0.65	0.086	0.006	11.669	0.844	0.764	0.049	6.36	13.35	2.12	0.49	52.1	34.6	5	2.22E-05	3.07E-03	6.36E-04	50.5	46.4
Y2G66	3.16	0.22	0.034	0.003	29.326	2.236	0.680	0.037	25.78	15.01	3.05	1.77	43.8	10.9	10	1.62E-05	1.66E-02	1.59E-03	25.7	16.5
Y2G70	6.57	0.48	0.062	0.005	16.129	1.353	0.757	0.052	5.99	31.53	1.66	0.19	40.9	26.6	3	2.21E-05	3.46E-03	2.76E-04	27.0	31.3
Y2G72	5.43	0.33	0.055	0.003	18.116	1.116	0.741	0.031	17.73	22.63	3.66	0.80	43.6	14.5	6	2.36E-05	8.56E-03	7.74E-05	20.5	16.7
Y2G77	2.68	0.17	0.030	0.002	33.898	2.183	0.648	0.032	23.21	1.68	2.23	13.98	45.6	8.3	12	1.40E-05	1.40E-02	1.33E-03	42.2	24.7
Y2G91	2.66	0.33	0.031	0.003	32.680	3.524	0.644	0.032	39.10	69.40	4.31	0.58	48.3	9.6	16	1.57E-05	2.31E-02	2.46E-03	30.4	15.5
Y2G98	26.28	1.7	0.235	0.015	4.261	0.272	0.809	0.031	5.62	13.88	5.75	0.41	57.7	60.8	6	2.61E-05	3.21E-03	5.05E-06	49.4	40.3
Y2G100	5.25	0.42	0.052	0.004	19.157	1.505	0.740	0.043	11.93	18.80	2.37	0.64	41.7	18.7	9	3.04E-05	5.53E-03	7.73E-04	36.9	25.1
Y2G112	2.82	0.18	0.031	0.002	32.680	2.243	0.667	0.037	25.90	9.50	2.70	2.68	42.6	9.8	27	2.70E-05	1.75E-02	2.75E-04	39.5	15.2
Y2G116	1.763	0.12	0.021	0.001	47.847	3.205	0.601	0.032	37.50	68.50	2.85	0.55	40.3	6.1	17	2.56E-05	2.53E-02	7.53E-05	18.1	8.8
Population 3																				
Y2G12	8.06	0.7	0.081	0.007	12.300	1.074	0.736	0.069	3.16	8.98	1.14	0.34	68.4	45.9	3	2.32E-05	1.81E-03	9.06E-04	49.3	62.0
Y2G19	9.57	0.72	0.092	0.006	10.929	0.741	0.744	0.048	5.95	15.21	2.36	0.38	71.2	36.1	5	4.07E-05	3.22E-03	3.33E-04	26.3	23.7
Y2G22	1.99	0.14	0.027	0.002	36.630	2.818	0.545	0.043	18.31	24.39	1.52	0.75	65.1	10.8	8	2.25E-05	9.39E-03	2.44E-03	26.1	19.7
Y2G34	2.041	0.13	0.028	0.002	35.373	2.127	0.534	0.028	38.18	40.04	3.05	0.96	70.0	7.7	23	2.03E-05	1.89E-02	3.02E-04	41.4	17.3
Y2G35	2.32	0.16	0.029	0.002	34.130	2.330	0.585	0.035	24.00	52.71	2.30	0.45	60.4	9.3	17	2.77E-05	1.16E-02	7.24E-03	36.4	28.8
Y2G40	4.39	0.3	0.049	0.003	20.534	1.307	0.647	0.035	15.13	25.80	2.62	0.59	76.2	14.8	17	2.99E-05	7.08E-03	2.39E-04	55.3	26.9
Y2G41	6.98	0.44	0.072	0.005	13.947	0.934	0.714	0.029	13.04	7.73	3.27	1.74	73.2	17.9	7	2.79E-05	6.30E-03	2.04E-03	27.5	22.6
Y2G56	1.342	0.095	0.021	0.002	47.170	3.560	0.469	0.029	24.49	50.60	1.43	0.50	63.6	6.9	15	2.97E-05	1.40E-02	8.56E-04	24.9	12.9
Y2G62	4.23	0.31	0.045	0.003	22.026	1.553	0.660	0.037	13.53	16.32	2.15	0.85	66.1	14.5	5	1.59E-05	6.57E-03	2.34E-03	33.0	31.8
Y2G69	6.28	0.43	0.063	0.004	15.848	0.980	0.724	0.029	15.54	33.20	3.63	0.48	59.0	15.6	14	2.98E-05	9.66E-03	9.12E-04	33.5	18.2
Y2G80	3.07	0.19	0.036	0.003	27.778	1.929	0.623	0.032	24.79	14.71	2.91	1.73	63.1	10.4	22	2.72E-05	1.33E-02	5.46E-04	41.9	17.9
Y2G93	4.5	0.34	0.050	0.004	20.161	1.545	0.675	0.053	8.86	14.82	1.74	0.60	66.2	22.0	11	1.86E-05	6.72E-03	1.32E-04	60.6	36.6
Y2G99	2.11	0.15	0.029	0.002	34.965	2.445	0.554	0.033	27.90	12.24	2.23	2.27	66.2	9.0	16	2.07E-05	1.35E-02	1.23E-04	39.4	19.7
Y2G105	6.45	0.51	0.066	0.005	15.152	1.148	0.703	0.057	6.76	9.05	1.58	0.72	73.3	31.0	9	2.46E-05	4.02E-03	7.09E-04	62.6	43.2
Y2G110	16.4	1	0.153	0.009	6.553	0.404	0.776	0.031	9.21	28.69	5.77	0.32	79.8	39.5	6	2.95E-05	5.85E-03	6.16E-04	24.0	19.8
Y2G115	14.87	0.97	0.141	0.009	7.112	0.470	0.782	0.037	5.97	14.35	3.57	0.41	65.8	43.1	12	3.09E-05	3.48E-03	2.67E-04	76.6	44.7
Y2G118	5.22	0.4	0.055	0.005	18.282	1.537	0.675	0.040	10.19	7.49	2.06	1.37	73.1	18.9	11	2.62E-05	7.00E-03	1.07E-03	41.3	25.7
Population 4																				
Y2G4	1.373	0.1	0.024	0.002	41.425	2.574	0.427	0.022	34.39	15.42	1.98	2.15	80.7	6.6	14	1.35E-05	1.70E-02	6.46E-04	42.0	22.5
Y2G14	20.4	1.5	0.194	0.014	5.152	0.372	0.779	0.054	2.72	3.39	2.21	0.76	98.5	85.2	4	2.20E-05	1.32E-03	2.39E-03	94.4	194.6
Y2G48	8.04	0.51	0.083	0.005	12.121	0.735	0.710	0.036	9.69	0.45	2.83	23.20	87.4	24.9	5	2.64E-05	5.06E-03	1.95E-03	25.8	25.1
Y2G49	8.97	0.67	0.093	0.006	10.718	0.724	0.723	0.048	5.36	23.43	2.14	0.24	89.1	36.8	1	3.22E-05	2.77E-03	1.46E-03	7.7	16.0
Y2G53	0.633	0.046	0.018	0.001	54.975	3.627	0.248	0.013	76.60	153.00	2.72	0.51	87.1	6.0	13	1.49E-05	3.58E-02	4.51E-03	16.8	9.6
Y2G54	3.04	0.19	0.040	0.003	25.000	1.625	0.559	0.026	36.47	59.13	4.39	0.63	91.1	10.4	21	2.08E-05	1.75E-02	3.64E-04	39.8	17.4
Y2G55	1.01	0.066	0.020	0.001	49.407	3.173	0.359	0.017	89.70	181.20	4.54	0.51	78.8	5.8	25	1.81E-05	4.23E-02	3.02E-04	22.5	9.0
Y2G79	3.04	0.22	0.037	0.002	26.738	1.716	0.576	0.033	21.10	8.02	2.22	2.70	80.0	11.3	25	4.23E-05	1.03E-02	1.77E-04	39.6	15.9
Y2G96	2.58	0.18	0.036	0.003	27.624	1.908	0.525	0.037	18.15	23.14	1.95	0.80	92.4	12.6	13	1.55E-05	9.39E-03	7.55E-04	61.4	34.5
Y2G102	1.535	0.1	0.026	0.002	38.640	2.538	0.433	0.025	41.70	7.82	2.27	5.14	85.3	7.7	21	1.38E-05	2.34E-02	1.00E-03	44.8	19.7
Y2G109	3.33	0.22	0.044	0.003	22.523	1.420	0.556	0.028	20.22	13.63	2.69	1.44	102.3	12.0	11	1.56E-05	1.20E-02	4.66E-04	40.6	24.5
Population 5																				
Y2G10	6.96	0.44	0.083	0.006	12.107	0.835	0.605	0.021	15.54	26.46	4.98	0.57	159.1	18.0	7	1.68E-05	1.03E-02	1.43E-03	27.8	21.4
Y2G44	8.02	0.67	0.094	0.008	10.638	0.951	0.637	0.065	3.40	12.46	1.12	0.28	156.9	50.6	2	2.73E-05	1.68E-03	2.52E-04	30.1	42.8
Y2G75	45.7	3.3	0.421	0.030	2.375	0.169	0.802	0.020	7.86	0.37	14.06	23.50	145.4	72.8	3	1.80E-05	5.04E-03	5.70E-03	22.8	36.9
Y2G89	12.6	2.9	0.118	0.025	8.475	1.795	0.705	0.057	11.00	5.36	2.02	1.64	131.7	60.7	19	3.13E-05	1.40E-02	3.06E-04	29.9	13.7
Y2G94	42.6	2.7	0.399	0.029	2.506	0.182	0.782	0.039	2.42	0.74	4.14	3.34	214.3	125.5	3	2.53E-05	1.48E-03	2.10E-03	55.3	101.5

U-Pb data

AFT dat

#grains	Ns	ΣpiΩi	2σΣpiΩi	ζeta (yr cm^2	2 sig abs	χ^2	P(χ^2)	Pooled agı	2σ Ma
115	1465	3.26E-05	4.83E-07	6.92E-01	1.10E-02	203.34	0.00	31.0	1.8

Grain Number	Pb207/U235	Pb207/U235 error (2s)	Pb206/U238	Pb206/U238 error (2s)	U238/Pb206	U238/Pb206 error (2s)	Pb207/Pb206	Pb207/Pb206 error (2s)	Approx U (ppm)	Approx Th (ppm)	Approx Pb (ppm)	U/Th	207corrAge (Ma)	207corrAge error (2s,Ma)	Ns	Area (cm^2)	$^{238}U/^{43}Ca$	2σ	FT Age	2σ
Population 1																				
Y3G1	16.18	0.62	0.145	0.006	6.916	0.306	0.822	0.037	11.16	41.79	6.86	0.27	17.3	44.6	4	2.20E-05	3.42E-03	3.30E-04	36.7	36.9
Y3G6	1.88	0.15	0.021	0.001	47.393	3.145	0.650	0.039	40.80	11.70	2.94	3.59	32.2	7.1	12	1.39E-05	1.79E-02	1.85E-03	33.3	19.5
Y3G8	5.56	0.24	0.054	0.003	18.553	0.895	0.765	0.038	21.83	32.70	4.84	0.70	31.8	17.0	10	2.08E-05	7.64E-03	1.20E-03	43.4	28.3
Y3G11	19.27	0.87	0.174	0.010	5.760	0.325	0.813	0.041	5.03	8.81	3.72	0.59	35.1	58.9	3	2.56E-05	1.69E-03	1.50E-03	47.9	69.8
Y3G13	1.746	0.11	0.021	0.001	48.567	2.595	0.614	0.027	78.00	44.30	5.08	1.79	37.5	5.0	20	1.85E-05	2.79E-02	4.74E-04	26.7	12.0
Y3G15	18.02	0.84	0.164	0.009	6.116	0.318	0.817	0.032	9.07	7.91	5.90	1.17	27.1	43.9	2	9.79E-06	3.48E-03	2.19E-03	40.5	62.7
Y3G16	1.494	0.072	0.018	0.001	55.188	2.193	0.595	0.027	86.70	137.50	5.15	0.65	35.8	4.3	22	1.82E-05	2.99E-02	9.12E-04	27.9	11.9
Y3G21	12.32	0.47	0.113	0.005	8.865	0.401	0.800	0.028	18.47	59.50	8.87	0.31	34.7	26.7	7	2.09E-05	6.06E-03	6.69E-04	38.1	29.1
Y3G22	22.81	0.75	0.200	0.007	4.993	0.162	0.820	0.026	14.36	44.00	12.01	0.32	28.4	44.4	5	2.59E-05	4.62E-03	4.59E-04	28.8	26.0
Y3G23	4.38	0.18	0.044	0.002	22.989	0.898	0.735	0.024	52.90	395.00	9.97	0.13	36.4	9.0	25	2.87E-05	1.71E-02	3.73E-03	35.0	16.0
Y3G26	2.163	0.094	0.024	0.001	41.442	1.889	0.651	0.034	71.40	24.90	5.65	2.83	36.7	7.0	12	1.95E-05	2.14E-02	1.45E-04	19.8	11.4
Y3G28	1.368	0.054	0.017	0.001	59.666	2.314	0.593	0.023	113.90	66.00	6.16	1.69	33.3	3.5	26	1.41E-05	3.36E-02	4.53E-04	37.9	14.9
Y3G31	4.58	0.15	0.043	0.002	23.095	0.907	0.760	0.029	43.82	30.20	7.53	1.41	27.2	10.6	9	1.22E-05	1.35E-02	2.41E-03	37.5	25.9
Y3G35	2.047	0.07	0.023	0.001	43.215	1.662	0.638	0.021	100.30	70.20	7.79	1.40	37.6	4.4	19	1.22E-05	3.05E-02	2.25E-03	35.3	16.4
Y3G37	1.621	0.062	0.019	0.001	51.813	1.906	0.616	0.022	142.50	82.60	8.95	1.72	34.8	3.8	26	1.26E-05	4.36E-02	3.02E-04	32.6	12.8
Y3G42	1.366	0.05	0.017	0.001	59.952	2.264	0.595	0.023	112.80	110.80	6.01	1.02	32.9	3.4	21	1.25E-05	3.20E-02	2.53E-03	36.3	16.1
Y3G46	1.288	0.052	0.016	0.001	62.305	2.290	0.581	0.020	190.00	284.90	9.92	0.66	33.5	3.0	22	1.48E-05	5.28E-02	4.19E-04	19.4	8.3
Y3G47	2.68	0.13	0.029	0.001	34.483	1.546	0.672	0.023	70.40	40.10	7.11	1.73	39.1	5.9	13	2.05E-05	1.77E-02	9.84E-04	24.8	13.8
Y3G55	5.57	0.38	0.057	0.004	17.544	1.323	0.771	0.080	6.02	12.13	1.20	0.49	30.9	37.3	2	2.71E-05	1.72E-03	2.30E-03	29.5	57.4
Y3G59	2.151	0.089	0.023	0.001	44.053	1.941	0.674	0.029	83.70	42.40	6.95	1.93	30.2	5.6	13	2.10E-05	2.44E-02	9.21E-04	17.5	9.7
Y3G60	4.95	0.19	0.047	0.002	21.097	0.935	0.752	0.031	40.80	72.40	7.68	0.55	33.0	12.4	11	2.86E-05	1.21E-02	5.00E-04	21.9	13.3
Y3G63	1.892	0.096	0.021	0.001	46.992	2.208	0.656	0.031	85.80	26.00	6.08	3.42	31.4	5.7	19	2.01E-05	2.40E-02	3.56E-04	27.2	12.5
Y3G66	5.19	0.25	0.050	0.003	20.040	1.004	0.757	0.045	22.00	35.40	4.23	0.64	32.7	18.5	7	1.40E-05	6.69E-03	1.44E-03	51.5	40.5
Y3G71	1.383	0.061	0.018	0.001	56.529	2.013	0.571	0.023	81.10	27.49	4.14	3.17	38.4	3.7	21	1.77E-05	2.64E-02	3.55E-03	31.0	14.2
Y3G72	2.3	0.16	0.024	0.002	42.017	2.825	0.709	0.028	72.00	76.90	5.81	0.99	24.8	5.8	9	1.75E-05	1.63E-02	8.99E-04	21.8	14.6
Y3G74	4.95	0.33	0.046	0.003	21.692	1.318	0.761	0.029	63.60	69.90	11.17	0.96	28.7	11.4	26	1.97E-05	2.13E-02	1.75E-03	42.8	17.2
Y3G77	11.08	0.4	0.098	0.005	10.183	0.467	0.826	0.031	25.86	19.94	10.68	1.32	8.1	25.7	6	2.03E-05	7.37E-03	2.81E-03	27.7	24.9
Y3G78	11.86	0.36	0.105	0.003	9.542	0.282	0.818	0.017	66.80	421.90	30.60	0.16	15.9	16.1	25	2.43E-05	1.89E-02	3.19E-03	37.6	16.3
Y3G80	2.18	0.086	0.024	0.001	41.000	1.647	0.641	0.031	69.80	18.61	5.63	3.86	39.0	6.4	10	1.47E-05	2.08E-02	2.97E-03	22.6	14.7
Y3G81	2.14	0.12	0.024	0.001	41.841	2.101	0.637	0.031	78.50	42.60	5.81	2.00	39.0	6.4	16	2.07E-05	1.90E-02	1.08E-03	28.0	14.1
Y3G82	1.404	0.063	0.018	0.001	56.306	2.695	0.587	0.028	70.70	54.90	3.61	1.26	36.2	4.5	17	1.87E-05	2.10E-02	1.15E-03	29.9	14.6
Y3G83	2.171	0.087	0.025	0.001	40.519	1.625	0.644	0.024	80.80	21.72	6.65	3.66	38.9	5.2	12	2.09E-05	2.35E-02	2.85E-04	16.9	9.7
Y3G84	5.55	0.25	0.054	0.002	18.657	0.835	0.763	0.037	22.29	12.47	4.49	1.80	32.5	16.5	5	2.11E-05	6.53E-03	1.43E-03	25.1	23.1
Y3G85	1.582	0.083	0.019	0.001	53.447	2.628	0.611	0.018	174.80	101.80	9.76	1.70	34.5	3.3	24	1.87E-05	4.35E-02	3.36E-04	20.3	8.3
Y3G87	5.24	0.29	0.050	0.003	20.121	1.053	0.741	0.028	50.20	102.30	9.68	0.51	39.2	11.8	9	2.13E-05	1.19E-02	2.57E-03	24.5	17.1
Y3G88	16.6	1.3	0.147	0.013	6.803	0.602	0.827	0.038	9.66	32.60	5.70	0.30	11.2	46.6	2	2.05E-05	2.20E-03	4.14E-03	30.6	72.0
Y3G90	3.67	0.16	0.036	0.002	28.090	1.262	0.749	0.026	64.60	213.60	9.08	0.29	25.6	7.9	23	1.74E-05	1.87E-02	3.53E-03	48.6	22.3
Y3G93	5.12	0.21	0.050	0.002	19.920	0.714	0.751	0.027	38.55	50.50	7.37	0.79	35.4	11.5	4	1.53E-05	1.19E-02	3.59E-04	15.1	15.1
Y3G94	4.52	0.18	0.045	0.002	22.472	1.060	0.759	0.034	28.03	29.85	4.78	0.97	28.4	12.7	7	2.73E-05	8.42E-03	2.34E-03	21.0	16.9
Y3G95	4.1	0.16	0.042	0.002	23.866	1.082	0.724	0.032	39.46	42.52	6.26	0.97	38.8	11.3	11	2.99E-05	1.04E-02	7.30E-04	24.5	14.9
Y3G97	10.33	0.34	0.095	0.004	10.560	0.390	0.808	0.028	30.29	81.70	11.32	0.38	22.4	22.4	7	2.27E-05	8.77E-03	2.21E-03	24.3	19.4
Y3G99	1.754	0.059	0.020	0.001	50.736	2.085	0.658	0.024	104.40	88.30	6.64	1.23	28.8	4.2	20	1.68E-05	3.18E-02	2.71E-03	25.8	11.8
Y3G103	1.048	0.037	0.014	0.001	72.359	2.775	0.552	0.018	214.00	283.20	8.73	0.69	32.1	2.4	24	1.26E-05	5.80E-02	1.31E-03	22.7	9.3
Y3G104	8.39	0.54	0.074	0.005	13.477	0.926	0.823	0.037	22.50	112.10	6.95	0.19	7.9	22.9	11	2.47E-05	7.55E-03	3.27E-04	40.7	24.6
Y3G109	7	0.29	0.066	0.003	15.152	0.735	0.773	0.034	20.28	10.33	5.05	1.73	34.8	18.7	6	3.25E-05	6.23E-03	2.10E-04	20.4	16.7
Y3G113	3.575	0.13	0.036	0.002	27.701	1.228	0.725	0.038	45.98	27.10	5.95	1.54	33.1	11.4	15	2.38E-05	1.31E-02	5.29E-03	33.2	21.8
Y3G114	1.97	0.15	0.023	0.002	43.860	2.886	0.624	0.027	101.40	128.00	6.95	0.70	39.7	5.7	24	2.35E-05	3.37E-02	2.17E-03	20.9	8.7
Y3G115	3.022	0.12	0.032	0.001	31.447	1.286	0.691	0.024	56.90	80.80	6.68	0.63	38.0	6.6	16	2.05E-05	1.69E-02	5.20E-04	31.9	16.0
Y3G118	0.99	0.04	0.014	0.001	73.368	2.745	0.531	0.021	158.00	43.40	5.53	3.32	34.0	2.7	16	1.07E-05	4.37E-02	1.82E-04	23.6	11.8
Y3G44	*11.63*	*0.5*	*0.104*	*0.005*	*9.634*	*0.464*	*0.837*	*0.037*	*13.24*	*31.50*	*6.24*	*0.41*	*-1.2*	*32.2*	*5*	*2.11E-05*	*3.98E-03*	*2.78E-03*	*41.1*	*46.6*
Y3G49	*445*	*16*	*3.770*	*0.150*	*0.265*	*0.011*	*0.849*	*0.012*	*6.72*	*0.23*	*109.50*	*36.00*	*-421.7*	*475.3*	*4*	*3.36E-05*	*2.03E-03*	*3.96E-04*	*40.4*	*41.2*
Y3G62	*14.9*	*1.4*	*0.134*	*0.011*	*7.463*	*0.613*	*0.850*	*0.100*	*2.05*	*8.29*	*1.15*	*0.26*	*-17.0*	*110.2*	*2*	*2.81E-05*	*7.00E-04*	*1.01E-04*	*70.0*	*99.4*
Population 2																				
Y3G3	2.61	0.14	0.029	0.002	34.247	1.877	0.642	0.036	33.90	30.30	3.26	1.20	46.6	9.0	7	2.44E-05	1.04E-02	1.24E-04	19.0	14.4
Y3G4	3.36	0.13	0.037	0.002	26.954	1.235	0.656	0.021	46.40	68.30	5.60	0.70	55.1	7.1	10	1.64E-05	1.83E-02	4.89E-04	23.0	14.6
Y3G5	11.91	0.66	0.115	0.007	8.734	0.496	0.775	0.038	14.19	17.69	6.29	0.83	59.8	36.0	6	1.43E-05	5.14E-03	1.49E-04	56.2	46.0
Y3G7	8.61	0.3	0.082	0.003	12.195	0.431	0.769	0.027	33.82	94.70	10.82	0.37	46.3	18.7	9	1.56E-05	1.14E-02	6.55E-04	35.0	23.4
Y3G9	17.77	0.84	0.160	0.009	6.250	0.340	0.803	0.027	12.14	47.80	7.94	0.28	46.2	36.6	1	2.16E-05	3.57E-03	6.71E-04	9.0	18.0
Y3G10	2.06	0.088	0.024	0.001	42.141	1.616	0.613	0.016	129.10	176.00	10.53	0.75	43.4	3.7	24	1.74E-05	4.56E-02	8.99E-04	20.9	8.5
Y3G19	3.124	0.12	0.033	0.001	30.120	1.270	0.686	0.026	73.40	85.50	8.37	0.88	41.0	7.4	12	1.58E-05	2.69E-02	2.07E-03	19.5	11.4
Y3G20	8.64	0.28	0.081	0.003	12.422	0.509	0.776	0.031	31.37	61.40	10.45	0.52	40.7	20.9	10	1.84E-05	9.42E-03	1.00E-03	39.8	25.5
Y3G24	1.753	0.071	0.022	0.001	44.464	1.621	0.573	0.017	131.60	54.80	8.62	2.38	48.5	3.7	24	1.56E-05	3.74E-02	1.90E-04	28.4	11.6
Y3G38	12.37	0.48	0.115	0.005	8.718	0.350	0.778	0.028	14.02	59.10	7.25	0.24	56.9	27.0	8	2.64E-05	4.07E-03	6.42E-05	51.3	36.3
Y3G50	0.921	0.039	0.014	0.001	69.784	2.824	0.469	0.021	109.80	40.10	3.83	2.68	43.0	3.0	23	1.88E-05	3.26E-02	2.55E-03	25.9	11.0
Y3G54	22.02	0.81	0.195	0.007	5.133	0.195	0.807	0.028	18.26	75.80	14.74	0.23	50.3	45.9	3	1.83E-05	5.41E-03	1.73E-04	20.9	24.2
Y3G64	24.8	1.2	0.214	0.010	4.679	0.208	0.811	0.034	6.70	16.66	6.09	0.42	48.0	60.5	3	2.77E-05	2.09E-03	1.73E-06	35.7	41.2
Y3G68	19.5	0.89	0.175	0.011	5.714	0.359	0.808	0.050	4.86	11.91	3.37	0.43	43.2	71.8	3	2.19E-05	1.34E-03	5.51E-04	70.5	86.5
Y3G86	8.4	0.36	0.079	0.004	12.610	0.572	0.760	0.031	21.69	78.20	7.09	0.28	50.7	20.6	8	1.89E-05	6.99E-03	8.92E-04	41.7	30.0
Y3G89	5.22	0.23	0.054	0.003	18.622	0.902	0.723	0.041	23.13	41.50	4.21	0.56	50.5	18.2	8	2.51E-05	6.87E-03	1.29E-04	32.0	22.7

Y3G96	5.13	0.42	0.052	0.004	19.268	1.485	0.711	0.025	51.10	16.70	8.38	3.00	53.9	11.7	15	1.92E-05	1.81E-02	1.08E-02	29.8	23.6
Y3G101	4.67	0.23	0.050	0.002	19.881	0.949	0.694	0.028	26.50	40.92	4.57	0.59	59.2	12.0	21	3.33E-05	8.65E-03	4.08E-04	50.2	22.1
Y3G105	4.47	0.26	0.044	0.003	22.523	1.319	0.723	0.030	32.40	11.14	5.19	2.64	41.6	11.4	8	2.60E-05	7.75E-03	2.22E-03	27.4	20.9
Y3G108	27.4	1.3	0.243	0.010	4.124	0.170	0.814	0.032	9.36	28.92	9.14	0.30	48.7	64.8	3	2.57E-05	2.83E-03	2.72E-03	28.5	42.7
Y3G112	2.163	0.088	0.025	0.001	40.388	1.501	0.633	0.024	93.60	104.60	8.09	0.80	41.3	5.2	21	2.10E-05	3.10E-02	4.87E-03	22.3	10.3
Y3G116	2.56	0.21	0.030	0.002	33.898	2.528	0.659	0.029	65.80	67.60	6.41	0.94	43.0	7.8	12	1.87E-05	2.04E-02	1.99E-03	21.8	12.7
Y3G119	3.36	0.27	0.035	0.003	28.490	2.273	0.691	0.033	48.70	63.20	6.07	0.69	42.0	10.1	9	1.58E-05	1.83E-02	3.49E-03	21.5	14.9
Population 3																				
Y3G12	19.66	0.64	0.177	0.006	5.650	0.204	0.795	0.022	15.82	96.60	11.93	0.17	64.1	33.5	3	1.55E-05	5.31E-03	1.29E-03	25.2	29.7
Y3G17	10.73	0.42	0.105	0.004	9.569	0.375	0.751	0.031	14.76	56.30	5.99	0.27	75.6	27.0	3	2.31E-05	4.74E-03	6.49E-04	18.9	22.0
Y3G18	1.8	0.11	0.025	0.002	39.526	2.343	0.522	0.036	22.55	43.00	1.83	0.54	65.1	8.4	5	9.39E-06	9.55E-03	1.71E-03	38.4	35.1
Y3G27	1.659	0.065	0.025	0.001	39.293	1.544	0.484	0.018	104.90	178.90	7.82	0.58	73.3	4.8	34	1.56E-05	3.23E-02	4.93E-03	46.5	17.5
Y3G30	2.879	0.11	0.034	0.002	29.155	1.275	0.603	0.028	39.31	113.20	5.14	0.34	65.7	8.4	15	1.61E-05	1.24E-02	1.78E-03	51.6	27.7
Y3G43	3.14	0.14	0.038	0.002	26.525	1.126	0.603	0.024	52.80	38.30	6.05	1.36	72.3	8.1	14	1.51E-05	1.61E-02	2.68E-03	39.7	22.3
Y3G51	7.19	0.36	0.074	0.004	13.532	0.641	0.729	0.041	13.88	9.79	3.70	1.41	66.3	25.0	4	1.82E-05	4.11E-03	1.75E-03	36.9	40.1
Y3G58	4.62	0.17	0.050	0.002	20.040	0.763	0.681	0.030	35.60	54.30	6.60	0.63	64.1	12.6	7	1.58E-05	1.08E-02	1.92E-03	28.4	22.1
Y3G67	3.72	0.14	0.044	0.002	22.936	0.999	0.615	0.026	36.54	79.50	5.60	0.48	79.5	10.0	7	1.63E-05	1.01E-02	6.00E-04	29.3	22.2
Y3G69	1.29	0.29	0.020	0.003	50.761	6.442	0.397	0.038	158.00	106.00	4.79	1.43	70.6	10.8	12	2.12E-05	2.19E-02	5.89E-03	17.9	11.4
Y3G70	6.32	0.29	0.066	0.003	15.152	0.781	0.694	0.039	14.49	18.96	3.48	0.81	78.2	21.4	4	1.52E-05	3.82E-03	5.71E-04	47.5	48.0
Y3G92	1.042	0.053	0.019	0.001	53.022	2.277	0.400	0.019	117.00	54.70	4.69	2.16	67.1	4.1	36	2.17E-05	4.03E-02	1.83E-03	28.4	9.6
Y3G100	1.189	0.067	0.020	0.001	50.100	2.159	0.427	0.018	130.80	58.50	5.74	2.33	66.7	4.1	27	1.79E-05	4.05E-02	4.14E-04	25.7	9.9
Y3G107	8.37	0.39	0.081	0.005	12.285	0.724	0.744	0.041	11.63	26.52	3.76	0.40	63.0	27.6	7	2.35E-05	3.69E-03	5.66E-04	55.5	42.8
Y3G110	1.76	0.071	0.025	0.001	40.437	1.799	0.521	0.026	64.10	78.10	4.27	0.73	63.8	6.0	11	2.13E-05	1.74E-02	1.62E-03	20.5	12.5
Y3G111	10.91	0.51	0.103	0.005	9.671	0.505	0.765	0.040	11.66	13.59	4.68	0.77	62.5	34.1	2	1.78E-05	3.40E-03	2.18E-03	22.8	35.4
Y3G117	2.31	0.17	0.030	0.002	33.445	2.125	0.563	0.029	36.80	15.90	2.90	2.31	67.0	8.3	7	2.50E-05	8.25E-03	3.53E-03	23.4	20.3
Y3G120	2.07	0.11	0.028	0.001	35.336	1.623	0.526	0.025	58.50	119.50	5.11	0.45	71.9	6.7	21	1.52E-05	1.98E-02	1.00E-03	48.1	21.1
Population 4																				
Y3G25	4.36	0.32	0.051	0.003	19.569	1.302	0.628	0.037	23.28	31.65	3.95	0.72	87.9	16.5	6	1.57E-05	5.73E-03	7.36E-04	45.9	38.0
Y3G32	12.17	0.82	0.118	0.007	8.503	0.535	0.747	0.038	9.05	17.90	4.03	0.49	89.6	37.0	3	1.80E-05	3.16E-03	9.89E-04	36.4	43.6
Y3G33	1.807	0.086	0.028	0.001	35.162	1.360	0.466	0.024	56.90	71.90	4.31	0.77	86.1	6.5	17	1.82E-05	1.76E-02	1.91E-03	36.6	18.2
Y3G34	6.73	0.34	0.070	0.003	14.225	0.627	0.688	0.037	12.11	16.89	3.14	0.71	86.9	21.6	6	2.09E-05	3.58E-03	7.06E-04	55.2	46.4
Y3G40	15.5	1.2	0.145	0.010	6.897	0.476	0.755	0.029	17.80	29.50	10.42	0.61	101.8	35.5	17	2.07E-05	8.03E-03	2.40E-03	70.3	40.1
Y3G45	9.33	0.49	0.094	0.006	10.650	0.658	0.733	0.046	7.81	19.03	2.70	0.41	81.8	35.5	6	2.76E-05	2.49E-03	2.45E-03	60.1	76.9
Y3G48	4.5	0.26	0.053	0.003	18.797	1.025	0.614	0.035	17.03	1.06	2.65	17.70	97.7	16.0	2	1.40E-05	5.73E-03	3.33E-03	17.2	26.3
Y3G52	15.24	0.91	0.151	0.009	6.618	0.407	0.753	0.060	3.62	9.02	1.93	0.39	109.0	73.4	2	2.01E-05	1.09E-03	7.15E-04	62.7	97.8
Y3G57	6.58	0.47	0.069	0.005	14.451	1.044	0.687	0.033	22.10	31.60	5.10	0.70	86.1	19.7	4	1.50E-05	7.28E-03	2.50E-03	25.3	26.7
Y3G61	15.7	0.64	0.151	0.007	6.636	0.321	0.767	0.034	7.50	21.88	4.81	0.35	90.5	42.4	7	2.24E-05	2.19E-03	5.62E-03	98.1	262.7
Y3G75	1.429	0.055	0.025	0.001	40.080	1.430	0.408	0.015	138.70	176.40	8.28	0.81	87.2	4.4	16	1.02E-05	4.01E-02	6.42E-04	27.0	13.5
Y3G106	2.95	0.13	0.037	0.002	26.954	1.380	0.573	0.027	29.81	43.00	3.40	0.63	80.2	9.2	11	1.89E-05	8.87E-03	1.14E-03	45.2	27.9
Population 5																				
Y3G2	1.221	0.062	0.028	0.001	36.088	1.433	0.322	0.015	60.90	90.50	3.75	0.70	116.1	5.7	20	1.13E-05	2.22E-02	7.54E-04	54.9	24.7
Y3G29	1.413	0.056	0.027	0.001	36.955	1.366	0.381	0.014	111.30	108.30	7.11	1.01	100.5	4.8	25	8.62E-06	3.48E-02	3.09E-04	57.3	23.0
Y3G41	2.323	0.08	0.036	0.001	27.701	1.074	0.473	0.017	88.80	142.80	9.21	0.61	107.4	6.6	32	1.33E-05	2.52E-02	2.63E-04	65.6	23.2
Y3G79	2.3	0.52	0.033	0.005	30.581	4.770	0.405	0.040	74.00	106.00	3.74	0.97	115.2	20.7	11	2.83E-05	7.73E-03	5.12E-04	34.7	21.0
Y3G102	1.438	0.083	0.027	0.001	36.873	1.496	0.373	0.018	93.80	165.40	6.58	0.52	102.5	5.7	32	1.97E-05	2.97E-02	1.55E-03	37.7	13.5
Population 6																				
Y3G39	1.076	0.058	0.032	0.001	31.726	1.208	0.256	0.013	80.30	40.40	3.56	1.99	148.6	6.5	37	1.38E-05	2.78E-02	3.18E-04	66.4	21.9
Y3G53	22	1.3	0.204	0.013	4.902	0.312	0.761	0.049	4.02	9.20	3.24	0.52	136.5	81.0	3	1.29E-05	1.41E-03	2.52E-03	112.9	239.8
Y3G56	15.34	0.69	0.161	0.007	6.227	0.260	0.679	0.022	20.40	65.20	13.17	0.30	217.6	30.3	10	2.46E-05	7.35E-03	1.07E-03	38.1	24.7
Y3G76	9.03	0.31	0.100	0.004	10.010	0.351	0.651	0.022	44.42	129.50	16.76	0.36	155.6	18.9	14	1.48E-05	1.25E-02	3.24E-03	52.2	31.0
Y3G98	2.61	0.13	0.046	0.002	21.930	0.818	0.408	0.016	89.40	198.80	11.07	0.46	159.6	8.4	30	1.88E-05	2.80E-02	1.43E-03	39.3	14.5

U-Pb data

AFT dat

#grains	Ns	ΣpiΩi	2σΣpiΩi	ζeta (yr cm^2	2 sig abs	χ^2	P(χ^2)	Pooled agı	2σ Ma
115	1791	2.20E-05	2.69E-07	6.92E-01	1.10E-02	267.54	0.00	55.9	2.9

Grain Number	Pb207/U235	Pb207/U235 error (2s)	Pb206/U238	Pb206/U238 error (2s)	U238/Pb206	U238/Pb206 error (2s)	Pb207/Pb206	Pb207/Pb206 error (2s)	Approx U (ppm)	Approx Th (ppm)	Approx Pb (ppm)	U/Th	207corrAge (Ma)	207corrAge error (2s,Ma)	Ns	Area (cm^2)	^{238}U/^{43}Ca	2σ	FT Age	2σ
Population 1																				
Y4G5	19.05	0.81	0.172	0.007	5.817	0.234	0.800	0.044	6.09	45.64	4.51	0.17	54.5	62.2	4	3.00E-05	2.16E-03	1.68E-04	42.5	42.6
Y4G6	11.24	0.57	0.104	0.005	9.625	0.472	0.786	0.043	9.93	20.30	4.15	0.65	44.2	36.8	7	2.78E-05	3.25E-03	5.17E-04	53.3	41.2
Y4G10	23.12	0.89	0.207	0.009	4.843	0.209	0.814	0.035	4.67	11.48	3.95	0.54	40.6	60.1	2	1.64E-05	1.84E-03	4.79E-05	45.8	64.8
Y4G28	30.1	1.3	0.269	0.014	3.717	0.193	0.819	0.056	2.35	6.50	2.76	0.34	42.2	123.3	4	3.21E-05	1.12E-03	5.02E-06	76.6	76.6
Y4G30	10.49	0.28	0.096	0.003	10.471	0.296	0.793	0.027	20.38	121.70	8.31	0.16	34.8	21.8	13	2.42E-05	9.68E-03	1.28E-04	38.3	21.2
Y4G34	9.89	0.45	0.096	0.005	10.449	0.513	0.763	0.039	9.09	21.60	3.61	0.41	59.2	30.8	5	2.12E-05	4.95E-03	2.68E-04	32.9	29.5
Y4G39	6.06	0.31	0.061	0.003	16.340	0.748	0.734	0.054	10.82	14.32	2.37	0.77	52.1	27.1	6	1.63E-05	4.62E-03	8.85E-04	54.8	46.0
Y4G44	1.298	0.052	0.022	0.001	46.339	1.739	0.448	0.025	60.43	17.97	3.08	3.13	68.4	5.1	25	1.51E-05	2.55E-02	4.18E-04	44.8	17.9
Y4G53	14.28	0.39	0.132	0.005	7.559	0.280	0.789	0.030	16.48	58.70	9.01	0.25	53.7	33.2	7	1.84E-05	6.27E-03	1.89E-04	41.8	31.6
Y4G54	2.526	0.096	0.032	0.001	31.348	1.278	0.581	0.028	30.98	37.13	3.09	0.75	66.8	7.8	7	1.24E-05	1.31E-02	1.19E-04	29.6	22.4
Y4G55	1.126	0.043	0.020	0.001	50.277	1.567	0.415	0.020	92.10	75.50	4.09	1.10	68.4	3.9	23	9.63E-06	3.65E-02	3.70E-04	45.1	18.8
Y4G57	15.41	0.91	0.143	0.010	6.993	0.479	0.808	0.042	3.96	3.67	2.13	0.99	34.7	49.7	5	1.20E-05	1.88E-03	5.79E-04	151.6	143.5
Y4G58	36.6	1.4	0.326	0.015	3.067	0.141	0.827	0.042	3.40	5.69	4.98	0.53	27.6	113.3	4	3.05E-05	1.47E-03	8.52E-04	61.3	70.8
Y4G60	16.81	0.57	0.154	0.006	6.510	0.259	0.810	0.041	6.73	19.55	4.32	0.32	34.8	52.1	10	2.39E-05	2.32E-03	5.47E-04	123.7	83.5
Y4G71	5.92	0.22	0.062	0.002	16.051	0.618	0.702	0.037	22.60	34.73	5.12	0.71	69.6	19.1	14	2.18E-05	7.75E-03	3.67E-04	57.0	30.6
Y4G72	12.62	0.56	0.113	0.005	8.881	0.418	0.830	0.047	8.89	70.50	4.54	0.14	5.5	43.8	7	1.33E-05	4.04E-03	4.06E-04	89.5	68.3
Y4G73	12.71	0.52	0.119	0.004	8.375	0.302	0.799	0.039	8.77	26.54	4.45	0.36	37.9	38.6	8	2.59E-05	4.96E-03	1.33E-03	42.9	32.5
Y4G88	6.75	0.31	0.069	0.003	14.535	0.676	0.729	0.043	14.91	41.73	3.94	0.37	61.6	24.4	11	1.76E-05	7.11E-03	3.99E-04	60.5	36.6
Y4G98	7.09	0.38	0.070	0.005	14.225	0.931	0.730	0.040	12.62	19.06	3.37	0.71	62.4	23.4	8	2.29E-05	6.68E-03	4.10E-04	36.1	25.6
Y4G99	64.5	2.8	0.571	0.028	1.751	0.086	0.831	0.042	1.55	4.30	3.48	0.40	31.9	198.4	2	5.30E-05	6.88E-04	1.31E-04	37.8	54.0
Y4G105	1.47	0.075	0.022	0.001	45.662	2.502	0.487	0.031	43.66	57.70	2.56	0.69	62.5	6.5	10	1.18E-05	1.65E-02	1.69E-03	35.3	22.6
Y4G109	27.3	1.2	0.247	0.011	4.049	0.180	0.806	0.042	4.34	11.74	4.57	0.32	67.9	85.2	2	1.57E-05	1.35E-03	1.53E-03	64.8	117.5
Y4G112	3.66	0.12	0.041	0.002	24.331	0.888	0.654	0.032	30.10	55.30	4.41	0.47	61.8	11.1	29	2.79E-05	1.32E-02	6.55E-04	54.4	20.4
Y4G113	20.09	0.67	0.185	0.009	5.408	0.257	0.802	0.045	5.87	11.37	4.14	0.44	55.7	68.3	8	2.11E-05	2.00E-03	1.22E-03	129.8	121.4
Y4G116	15.71	0.58	0.140	0.006	7.123	0.309	0.808	0.047	6.88	15.50	4.04	0.39	34.0	54.3	9	2.40E-05	3.13E-03	4.43E-04	82.3	56.1
Y4G119	4.46	0.18	0.048	0.002	20.704	0.686	0.686	0.031	20.42	69.70	3.87	0.26	60.0	12.5	9	2.11E-05	7.74E-03	3.33E-04	38.0	25.4
Y4G16	*13.11*	*0.36*	*0.113*	*0.004*	*8.842*	*0.297*	*0.841*	*0.028*	*16.22*	*129.40*	*7.99*	*0.16*	*-5.3*	*27.0*	*15*	*3.02E-05*	*6.52E-03*	*9.15E-04*	*52.5*	*28.1*
Y4G42	*1280*	*170*	*11.600*	*1.400*	*0.086*	*0.010*	*0.840*	*0.056*	*0.11*	*0.03*	*5.50*	*3.99*	*-424.8*	*5631.0*	*0*	*3.64E-05*	*3.76E-05*	*7.27E-05*	*87.5*	*266.9*
Y4G47	*814*	*33*	*7.310*	*0.290*	*0.137*	*0.005*	*0.815*	*0.016*	*0.96*	*0.08*	*29.19*	*11.37*	*0.0*	*1018.8*	*1*	*2.33E-05*	*3.94E-04*	*1.44E-04*	*75.0*	*152.5*
Y4G83	*35.8*	*1.4*	*0.302*	*0.017*	*3.311*	*0.186*	*0.841*	*0.050*	*2.82*	*7.55*	*3.57*	*0.38*	*-15.7*	*125.4*	*1*	*2.04E-05*	*9.76E-04*	*5.84E-04*	*34.6*	*72.3*
Population 2																				
Y4G8	6.92	0.22	0.070	0.003	14.286	0.571	0.712	0.034	18.17	62.60	4.91	0.39	72.6	19.8	20	3.06E-05	6.46E-03	4.96E-06	69.6	31.1
Y4G9	12.2	0.55	0.115	0.005	8.681	0.377	0.750	0.035	7.74	15.50	3.46	0.67	84.7	33.3	9	3.05E-05	2.61E-03	3.29E-05	77.8	51.9
Y4G14	3.8	0.18	0.047	0.002	21.277	0.860	0.611	0.036	19.38	77.80	3.32	0.32	87.3	14.2	13	2.57E-05	8.49E-03	5.63E-04	41.1	23.0
Y4G17	1.276	0.062	0.022	0.001	44.924	1.413	0.437	0.025	53.91	125.60	3.10	0.54	72.6	5.1	12	1.28E-05	2.02E-02	9.35E-04	32.0	18.5
Y4G19	4.59	0.22	0.052	0.002	19.268	0.854	0.644	0.042	13.15	10.35	2.23	1.51	82.5	18.1	15	1.67E-05	6.52E-03	7.60E-05	94.6	48.9
Y4G20	18.81	0.74	0.173	0.008	5.797	0.255	0.787	0.036	5.17	18.51	3.71	0.33	74.5	51.3	10	2.86E-05	2.10E-03	1.52E-03	113.9	109.4
Y4G21	1.415	0.049	0.025	0.001	39.936	1.148	0.405	0.018	66.07	46.61	3.50	1.33	88.1	4.5	23	1.46E-05	2.60E-02	9.71E-04	41.7	17.5
Y4G22	2.2	0.083	0.031	0.001	32.072	0.967	0.512	0.023	48.30	33.70	3.96	1.34	82.8	6.4	18	1.46E-05	1.86E-02	2.42E-03	45.8	22.4
Y4G23	3.83	0.12	0.045	0.002	22.472	0.858	0.630	0.031	28.04	55.39	4.37	0.47	75.7	11.7	18	1.82E-05	1.07E-02	3.40E-04	63.9	30.2
Y4G24	1.715	0.075	0.026	0.001	37.879	1.578	0.476	0.028	47.18	59.40	3.22	0.73	77.8	6.8	18	1.49E-05	2.07E-02	3.04E-05	40.3	19.0
Y4G32	2.9	0.1	0.037	0.002	26.810	1.078	0.564	0.026	33.02	78.70	4.07	0.41	83.4	8.6	29	1.92E-05	1.49E-02	3.47E-03	69.6	30.5
Y4G33	1.484	0.061	0.025	0.001	39.651	1.258	0.438	0.019	58.19	109.40	4.15	0.52	82.1	4.7	36	1.85E-05	2.48E-02	2.54E-03	54.1	18.9
Y4G36	4.5	0.2	0.052	0.002	19.268	0.891	0.641	0.040	14.87	46.20	2.76	0.32	83.8	17.3	20	1.86E-05	6.97E-03	3.73E-04	105.9	47.7
Y4G40	2.58	0.13	0.033	0.002	30.030	1.623	0.570	0.040	20.92	9.54	2.04	2.26	72.8	11.5	15	2.63E-05	8.71E-03	4.21E-04	45.1	23.4
Y4G43	0.912	0.035	0.020	0.001	49.456	1.296	0.321	0.014	118.10	81.00	4.43	1.35	84.9	3.2	39	1.22E-05	5.20E-02	8.06E-04	42.4	13.6
Y4G48	4.41	0.15	0.050	0.002	19.920	0.675	0.632	0.028	22.74	18.42	3.81	1.12	84.7	11.9	14	2.07E-05	8.91E-03	2.40E-03	52.3	31.3
Y4G59	1.03	0.11	0.022	0.001	45.872	2.735	0.357	0.036	22.10	18.17	0.98	1.12	85.2	8.1	12	1.89E-05	8.04E-03	5.84E-04	54.4	31.7
Y4G61	1.834	0.064	0.028	0.001	35.638	1.080	0.458	0.020	53.52	23.26	3.55	2.46	86.8	5.3	19	1.00E-05	1.79E-02	1.53E-03	73.1	34.1
Y4G62	10.18	0.5	0.095	0.005	10.482	0.494	0.764	0.045	6.80	16.94	2.67	0.43	58.2	35.3	6	3.04E-05	2.59E-03	1.72E-03	52.5	55.3
Y4G65	4	0.29	0.048	0.003	21.053	1.241	0.631	0.043	14.41	37.90	2.40	0.42	80.5	17.3	10	1.35E-05	5.46E-03	2.60E-04	93.1	59.1
Y4G66	6.01	0.25	0.063	0.003	15.873	0.630	0.689	0.040	14.96	30.71	3.23	0.54	77.2	20.8	16	3.21E-05	5.98E-03	1.82E-03	57.4	33.6
Y4G67	1.178	0.045	0.023	0.001	43.384	1.280	0.372	0.015	99.50	66.50	4.41	1.64	87.3	3.8	52	1.58E-05	4.10E-02	1.44E-04	55.3	15.4
Y4G69	4.47	0.13	0.052	0.002	19.380	0.601	0.626	0.022	35.06	66.90	6.36	0.57	89.7	9.9	26	2.18E-05	1.34E-02	1.05E-04	61.4	24.1
Y4G74	4.49	0.25	0.051	0.003	19.763	1.015	0.659	0.055	11.28	7.30	1.86	1.66	74.2	22.9	12	2.88E-05	5.63E-03	3.01E-04	51.0	29.6
Y4G77	2.22	0.13	0.031	0.002	32.680	1.602	0.525	0.034	29.76	45.75	2.65	0.70	78.0	9.3	20	2.58E-05	1.40E-02	5.85E-04	38.3	17.2
Y4G81	11.41	0.42	0.108	0.005	9.259	0.446	0.755	0.042	11.98	21.62	4.69	0.55	74.6	37.3	7	1.78E-05	3.90E-03	1.27E-03	69.4	57.1
Y4G87	1.342	0.049	0.023	0.001	44.072	1.399	0.430	0.018	76.90	19.66	3.68	4.04	75.3	4.1	27	1.48E-05	3.11E-02	5.43E-06	40.5	15.6
Y4G89	0.781	0.031	0.020	0.001	50.891	1.787	0.295	0.014	105.50	113.80	3.72	0.96	86.6	3.8	41	1.28E-05	4.50E-02	9.04E-04	49.1	15.4
Y4G93	7.34	0.3	0.076	0.004	13.175	0.625	0.717	0.042	13.97	21.22	3.77	0.69	75.8	26.3	7	3.66E-05	4.71E-03	3.23E-03	28.0	28.6
Y4G97	7.55	0.53	0.076	0.004	13.175	0.764	0.701	0.039	13.28	22.91	3.78	0.63	85.9	24.7	16	4.83E-05	6.60E-03	1.65E-04	34.6	17.3
Y4G115	1.459	0.062	0.024	0.001	41.824	1.504	0.444	0.023	56.04	23.89	3.09	2.06	76.6	5.3	17	9.97E-06	2.39E-02	1.61E-03	49.1	24.0
Y4G117	1.657	0.072	0.026	0.001	39.063	1.526	0.473	0.029	41.01	44.87	2.71	0.79	76.0	6.7	28	2.66E-05	1.66E-02	2.05E-04	43.7	16.5
Y4G120	0.883	0.039	0.019	0.001	53.248	1.871	0.337	0.018	93.70	95.20	3.67	0.89	76.4	3.8	25	1.22E-05	3.70E-02	1.97E-06	38.2	15.3
Population 3																				
Y4G1	18.63	0.71	0.177	0.007	5.663	0.208	0.766	0.039	7.24	27.09	5.12	0.34	108.9	56.3	2	2.64E-05	2.14E-03	1.15E-03	24.4	37.0
Y4G11	10.95	0.56	0.111	0.005	9.042	0.376	0.714	0.034	12.11	42.33	5.33	0.37	114.7	31.1	3	1.34E-05	5.05E-03	1.69E-04	30.6	35.3

Y4G12	4.76	0.18	0.056	0.002	17.986	0.485	0.627	0.025	26.24	60.40	5.03	0.57	96.3	11.8	11	1.35E-05	9.66E-03	1.04E-03	58.1	35.6
Y4G13	4.78	0.27	0.055	0.003	18.116	0.820	0.629	0.025	27.70	15.03	4.98	2.48	94.7	12.2	24	1.67E-05	1.16E-02	6.41E-04	85.2	35.1
Y4G15	5.22	0.21	0.061	0.003	16.420	0.674	0.631	0.036	14.57	35.00	3.11	0.53	103.6	18.3	10	3.75E-05	5.05E-03	4.06E-04	36.4	23.2
Y4G18	6.44	0.21	0.070	0.002	14.388	0.476	0.679	0.031	16.61	47.90	4.08	0.42	91.1	17.9	17	2.45E-05	6.35E-03	3.74E-04	75.1	36.7
Y4G25	6.4	0.26	0.071	0.003	14.164	0.542	0.679	0.039	15.19	2.11	3.49	6.81	92.6	22.7	15	1.75E-05	6.85E-03	3.88E-04	86.0	44.7
Y4G26	6.22	0.31	0.071	0.005	14.025	0.885	0.666	0.043	10.00	21.33	2.57	0.44	101.2	25.6	20	2.96E-05	4.68E-03	8.33E-04	99.2	47.8
Y4G29	17.81	0.68	0.164	0.006	6.116	0.232	0.771	0.035	5.11	12.02	3.47	0.40	93.1	47.1	6	3.11E-05	2.20E-03	1.92E-04	60.3	49.5
Y4G38	1.692	0.096	0.029	0.001	34.722	1.326	0.424	0.021	46.10	14.21	2.81	3.23	97.0	6.2	27	1.37E-05	1.91E-02	4.94E-04	70.9	27.4
Y4G41	1.981	0.084	0.031	0.001	32.154	1.137	0.456	0.020	44.70	25.43	3.22	1.67	96.7	6.1	20	1.26E-05	1.85E-02	2.60E-04	59.0	26.4
Y4G45	16.74	0.61	0.163	0.006	6.143	0.241	0.756	0.032	6.92	19.67	4.67	0.33	113.9	43.0	9	2.99E-05	2.46E-03	3.10E-04	84.0	57.0
Y4G49	34.6	1.7	0.316	0.016	3.165	0.160	0.787	0.047	2.44	6.42	3.18	0.34	147.2	119.8	3	1.86E-05	1.05E-03	3.47E-04	105.0	126.1
Y4G51	0.623	0.024	0.020	0.001	49.164	1.329	0.223	0.010	154.10	125.00	4.33	1.10	101.4	3.2	36	9.47E-06	5.47E-02	2.25E-03	47.9	16.1
Y4G52	0.434	0.026	0.018	0.001	56.306	1.744	0.178	0.011	105.90	38.26	1.70	2.52	95.0	3.3	31	1.32E-05	4.11E-02	1.01E-04	39.4	14.2
Y4G56	6.02	0.26	0.065	0.002	15.361	0.566	0.664	0.031	22.20	39.17	5.44	0.51	93.2	16.9	17	2.52E-05	9.43E-03	8.58E-04	49.3	24.3
Y4G63	1.338	0.062	0.025	0.001	39.683	1.575	0.385	0.021	47.70	104.60	3.19	0.49	92.8	5.7	25	1.74E-05	1.56E-02	2.61E-04	63.3	25.4
Y4G64	4.42	0.13	0.053	0.002	18.975	0.648	0.611	0.024	28.88	39.10	5.24	0.80	98.1	11.0	20	2.46E-05	9.53E-03	5.98E-04	58.7	26.5
Y4G68	19	2	0.180	0.018	5.556	0.556	0.767	0.047	6.11	12.16	3.68	0.53	109.6	69.4	17	3.27E-05	4.28E-03	3.27E-04	83.5	41.0
Y4G70	3.63	0.24	0.051	0.004	19.608	1.384	0.559	0.054	7.59	16.64	1.22	0.50	116.5	23.6	7	2.18E-05	3.08E-03	7.13E-05	71.7	54.3
Y4G75	6.81	0.86	0.072	0.007	13.812	1.412	0.658	0.033	26.40	34.70	5.28	0.90	107.5	22.3	31	1.14E-05	2.01E-02	1.99E-03	92.7	34.6
Y4G76	30.1	1.2	0.271	0.013	3.690	0.177	0.796	0.042	3.44	7.32	3.96	0.51	100.7	92.9	4	1.22E-05	1.61E-03	6.86E-04	139.7	152.0
Y4G78	1.859	0.071	0.029	0.001	34.118	1.164	0.460	0.021	60.50	84.10	4.56	0.76	90.2	5.9	29	1.22E-05	2.52E-02	6.80E-07	64.9	24.1
Y4G79	7.99	0.37	0.087	0.004	11.561	0.508	0.688	0.038	9.32	22.49	2.97	0.44	107.6	27.1	10	2.16E-05	4.45E-03	1.92E-03	71.5	54.8
Y4G80	9.48	0.34	0.097	0.004	10.288	0.370	0.709	0.031	22.51	26.70	7.89	0.89	104.4	25.0	18	1.76E-05	8.07E-03	5.23E-04	87.1	41.4
Y4G82	6.77	0.23	0.074	0.003	13.605	0.518	0.668	0.028	13.69	13.38	3.36	1.01	103.1	17.4	12	4.23E-05	4.69E-03	2.53E-03	41.7	33.0
Y4G85	7.28	0.39	0.077	0.004	13.004	0.643	0.691	0.035	19.54	32.60	5.42	0.60	93.4	22.5	21	2.38E-05	8.56E-03	3.63E-04	70.9	31.1
Y4G90	9.1	0.36	0.094	0.004	10.638	0.453	0.715	0.035	14.58	30.70	4.69	0.51	96.1	27.2	19	2.14E-05	5.74E-03	6.65E-04	106.0	50.2
Y4G91	7.01	0.21	0.075	0.002	13.280	0.406	0.686	0.027	29.07	31.29	7.32	0.99	94.5	17.1	27	2.62E-05	1.10E-02	1.43E-04	64.6	24.9
Y4G94	4.08	0.21	0.048	0.002	20.877	0.959	0.610	0.031	23.87	86.90	4.29	0.30	89.4	12.8	17	1.56E-05	1.23E-02	3.01E-04	61.1	29.7
Y4G95	4.28	0.16	0.053	0.002	19.011	0.759	0.588	0.029	32.16	22.53	5.00	1.53	107.8	13.2	10	1.34E-05	1.21E-02	7.93E-04	42.4	27.0
Y4G96	1.566	0.061	0.027	0.001	36.470	1.197	0.421	0.019	56.90	89.90	4.02	0.69	93.0	5.2	30	1.73E-05	2.15E-02	7.66E-04	55.7	20.4
Y4G100	5.71	0.22	0.064	0.003	15.528	0.627	0.642	0.030	18.25	50.20	3.97	0.40	103.9	16.3	14	1.56E-05	7.31E-03	1.30E-03	84.3	47.5
Y4G101	2.054	0.074	0.031	0.001	32.051	1.130	0.484	0.022	63.27	149.30	5.99	0.38	90.0	6.5	20	1.46E-05	2.45E-02	5.10E-04	38.6	17.3
Y4G102	2.057	0.067	0.032	0.001	31.546	1.095	0.459	0.020	72.80	54.50	6.03	1.21	97.8	6.2	24	1.28E-05	2.57E-02	4.68E-04	50.2	20.5
Y4G103	10.35	0.34	0.105	0.004	9.506	0.316	0.725	0.031	12.58	37.10	5.06	0.30	99.2	27.0	11	1.70E-05	4.90E-03	5.06E-05	90.7	54.7
Y4G104	2.92	0.11	0.039	0.002	25.907	1.208	0.542	0.035	28.00	8.04	2.86	3.08	93.3	11.8	11	1.38E-05	9.58E-03	4.78E-04	57.3	34.7
Y4G106	5.28	0.21	0.058	0.003	17.182	0.768	0.642	0.035	22.02	23.39	4.39	0.83	93.7	17.1	23	3.17E-05	7.51E-03	1.55E-03	66.5	30.9
Y4G107	33.1	1.1	0.303	0.013	3.300	0.142	0.794	0.036	4.01	11.92	4.87	0.29	120.3	89.3	2	3.95E-05	1.34E-03	1.63E-03	26.1	48.6
Y4G108	1.351	0.068	0.027	0.001	37.736	1.566	0.365	0.023	43.62	74.10	2.65	0.50	101.8	6.5	24	1.18E-05	2.07E-02	3.21E-04	67.4	27.6
Y4G110	2.669	0.099	0.037	0.001	26.954	0.944	0.520	0.020	46.40	32.50	4.64	1.21	96.2	7.0	26	2.52E-05	1.70E-02	6.31E-04	41.8	16.5
Y4G111	10.28	0.38	0.104	0.004	9.588	0.386	0.719	0.036	10.65	16.52	4.06	0.55	103.6	30.9	9	2.79E-05	4.17E-03	1.15E-03	53.2	38.4
Y4G118	4.43	0.19	0.054	0.002	18.692	0.699	0.604	0.036	16.15	35.24	3.11	0.40	102.6	16.1	13	1.81E-05	6.62E-03	4.33E-04	74.6	41.7
Population 4																				
Y4G3	3.77	0.49	0.065	0.007	15.291	1.683	0.530	0.100	2.12	11.57	0.47	0.24	165.2	54.9	6	6.85E-05	6.97E-04	9.23E-05	86.4	71.5
Y4G7	3.88	0.22	0.062	0.002	16.155	0.574	0.451	0.021	30.10	83.30	5.32	0.49	195.6	12.5	24	1.68E-05	1.25E-02	1.27E-03	78.6	33.1
Y4G27	2.644	0.09	0.046	0.002	21.882	0.766	0.426	0.017	35.14	153.90	6.02	0.21	153.4	8.3	22	1.60E-05	1.41E-02	9.73E-05	67.3	28.7
Y4G37	2.14	0.083	0.043	0.001	23.529	0.775	0.370	0.018	52.20	109.00	5.54	0.48	161.7	8.1	25	1.52E-05	2.36E-02	1.13E-03	48.1	19.4
Y4G84	2.84	0.3	0.047	0.003	21.231	1.217	0.422	0.027	43.20	41.30	4.24	1.12	159.6	13.6	26	1.15E-05	1.93E-02	2.84E-04	80.5	31.6
Y4G92	25.2	1.6	0.246	0.016	4.065	0.264	0.753	0.040	3.11	6.66	3.08	0.50	185.6	79.9	1	2.66E-05	1.24E-03	8.26E-04	20.9	43.9
Y4G114	13.6	1	0.154	0.009	6.494	0.392	0.647	0.021	27.60	68.10	15.96	0.37	249.3	30.2	14	1.38E-05	1.11E-02	1.44E-04	62.6	33.5
Y4G35	154.2	7.2	1.395	0.071	0.717	0.036	0.797	0.038	1.07	9.10	6.17	0.12	1232.6	367.0	1	2.41E-05	3.97E-04	9.36E-04	71.9	222.4
Y4G50	6.37	0.18	0.132	0.003	7.559	0.183	0.356	0.010	33.24	86.80	12.18	0.34	518.7	16.0	41	8.70E-06	1.40E-02	1.59E-03	228.1	75.9

Appendix 3: Supplementary Information Chapter 5 – Geochronology Methodology

1. U-Pb zircon dating methods at the University of Washington (June 2018- January 2020)

Our laser ablation system is an Analyte-G2 Excimer (ArF 193 nm) equipped with a HelEx 2-volume sample cell and controlled with the automated Chromium software, that allows us to run continuous shooting sequences longer than 10h overnight. The ablated material is carried in helium and mixed with nitrogen into the plasma source of an iCAP-RQ Q-ICP-MS, operating with a standard quartz torch, nickel cones, and a high-matrix insert on the skimmer cone. Our analytical set-up is summarized in Table 1 (following the reporting template of Horstwood et al., 2016; Tables at the end of this file). For a given laser spot diameter (25 microns), the main laser parameters (carrier gas flows, fluence, repetition rate), analyte dwell times, and work flow timing (acquisition and wash-out duration) were determined by performing line scans on NIST SRM 612 reference material glass and shooting a set of international zircon reference materials (Table 2) while monitoring the stability and sensitivity of 238U and 206Pb. We opted for 10 Hz pulse repetition rate, an energy fluence of 2.94 J cm-2 and relatively low carrier gas flows (0.5 L/min for He Mass Flow Controller 1, 0.2 L/min for He Mass Flow Controller 2, and 10 mL/min for N2 Mass Flow Controller 3); rising total gas flow above ~0.7 L/min resulted in spikes in 238U that would significantly noise isotopic ratios. Analyzed masses include 90Zr, 238U, 235U, 232Th, 207Pb, 206Pb, and 204Pb, with a total, combined dwell time of ~0.62 s.

While laser parameters remain unchanged over time, our ICP-MS instrument is tuned daily using the QTegra auto-tuning plug-in with custom in-house tuning parameters and NIST SRM 612 reference material glass to yield Th/U ratios close to unity (typically between 0.95 and 1.05) and low oxide production rates (ThO+/Th+ typically< 0.15%) while keeping 238U sensitivity high.

Workflow

Zircon crystals are extracted from 1 to 5 kg samples by traditional methods of crushing and grinding, followed by separation with a Wilfley table, heavy liquids, and a Frantz magnetic separator. A split of 100 to 1000 zircon crystals is separated (without sieving, to include all grain sizes) and incorporated into a 1" epoxy mount together with fragments of our zircon reference materials. We use the Plesovice international standard zircon (Slama et al., 2008) as our primary reference material, and commonly two secondary reference materials: GHB, our internal standard available at request, coming from the Hypersolvus granite of the Golden Horn Batholith of the North Cascades, and dated by CA-ID-TIMS at 48.205 ± 0.060 (2s) Myr (Eddy et al., 2016), and FC-1, from the Duluth gabbro complex in Minnesota, dated at 1,099.5 ± 0.33 (2s) Myr by ID-TIMS (Paces and Miller, 1993). The mounts are polished, carbon-coated, and imaged with a backscattered electron detector (BSE) with a TFS Apreo-S with Lovac Scanning Electron Microscope (SEM) to distinguish zircons from other remaining heavy minerals. Mounts are polished again prior to isotopic analysis.

Once epoxy mounts are loaded in the laser ablation cell, all zircons (standards and unknowns) are pre-ablated before the analytical session (only 2 ablations with a laser spot diameter at 50 microns, fluence of 1.47 J/cm2). Data acquisition involves (1) a single 10-s carrier gas blank with no laser firing to measure on-peak background intensities, (2) 38 s of laser ablation, and (3) 17 s of washout time with no laser firing to allow all sample material to purge through the system and to prepare for the next analysis. A session starts and ends with four Plesovice standards; additionally, we shoot a Plesovice standard every 5 unknowns, and one to two secondary standards every 20 unknowns. This yields a throughput of 40 unknown analyses per hour.

Data processing

Age calculation

U-Pb ages of individual zircons are calculated with *Iolite* using their *U_Pb_Geochron4* Data Reduction Scheme to get U-Pb ages (Paton et al., 2010). User-defined time intervals for each spot analysis are first established by using the time-stamped *QTegra* log file to automatically create the selections for the reference materials and unknowns. Each analysis is cropped by 3 s at the start because the first few seconds of acquisition have commonly rapid changes in intensity (Gehrels et al., 2008). Baseline intervals are selected as intervals with less than 600 238U cps/s. Baseline-corrected values are then calculated session-wide for each isotope. The time-dependent fractionation between U, Th, and Pb

isotopes during excavation of laser pits (downhole fractionation) is then characterized using an exponential curve downhole correction model on the signal of the primary standards. The data reduction scheme then fits this appropriate U–Th–Pb fractionation curve to the time-resolved primary and secondary standards, and the unknowns. Following this downhole fractionation correction, sample-standard bracketing is used to correct for mass bias and session drift by normalizing all isotopic ratios to those of the primary standard.

Precise measurements of the low intensity 204Pb peak would require a prohibitively long dwell time with a quadrupole, therefore we do not correct U-Pb ages for common lead using the 204Pb-based method (Mattinson, 1987). This method is also limited because of the additional complication of the isobaric mass-204 interference caused by 204Hg in the gas supply. Alternatively, one can use a 207Pb-based correction method, which has also drawbacks as it assumes that U–Pb* data (where Pb* = the radiogenic Pb component) are always concordant (Andersen, 2002; Chew et al., 2014). We thus calculate two sets of ages:

-Ages uncorrected for common lead; they are the direct result of running the *U_Pb_Geochron4* Data Reduction Scheme as explained above;

-Ages corrected for common lead using the 207Pb lead correction Andersen routine of the *VisualAge* Reduction Scheme (Chew et al., 2014); the routine is run after the calculation of ages uncorrected for common lead with the same downhole and mass-bias fractionation corrections. U-Pb ages of secondary standards acquired with this routine are yet less accurate than ages uncorrected for common lead (cf section below on accuracy). unless specified, ages we provide as “best ages” are uncorrected for common lead.

To ensure grains with a complex history (e.g., inheritance, Pb loss, overgrowths, or detectable amount of 204Pb) do not compromise data quality, the time-resolved pattern of 206Pb /238U is monitored closely during data reduction, and any analyses that show abnormal patterns (e.g., different fractionation from standards or spikes in signal intensity) are rejected (Gehrels et al., 2011). Similarly, samples with abnormally low content in 90Zr or measurable amount in 204Pb are rejected.

Calculation of random uncertainty

For each zircon, *Iolite* data reduction schemes calculate internal uncertainties by calculating the standard deviation of the mean over the duration of analysis (Paton et al., 2010). Random uncertainty (i.e., the uncertainty due to all measurement uncertainties, which takes into account the noise around the primary reference material) is then calculated by quadratically adding an excess variance to the internal uncertainty. this excess variance is calculated iteratively: for each ratio, the reference material Mean Square Weighted Deviation (MSWD) is calculated over a pool of pseudo-secondary reference materials, sub-sampled from the primary reference material, age of which is recalculated as unknown; this MSWD is commonly >1, indicating that the measurement uncertainty around the primary reference material is too low and that our reference material measurements do not represent a single population; an excess variance is thus added quadratically to the primary reference material measurement uncertainty in order to bring down the MSWD to 1 (Paton et al., 2010). A recent geochronology community-led effort has highlighted that though this approach is accurate for 206Pb /238U and 207Pb /235U ratios and ages, it is biased for 206/207Pb, for which the excess variance is significantly dependent on the intensity of the 207Pb beam (Horstwood et al., 2016). To take into account this bias, we recalculate internal and random uncertainties by adapting the approach proposed by Matthew and Guest (2017).
(1) Internal uncertainties (*s*) are corrected to take into account the number of integrations rather than the total integration time: $s = s_{io} * \mathrm{sqrt}(t_i)$ where s_{io} is the *Iolite* internal uncertainty and t_i the integration time (0.62 s here).
(2a) Excess variance in the 206Pb/238U and 207Pb /235U ratios for each session is determined on the replicate measurements of our primary reference material Plesovice. The excess variance, additional to the data point uncertainty required to give the population an MSWD of 1, is determined on all measurements. This excess variance is then quadratically added to internal uncertainty of the 206Pb/238U and 207Pb /235U ratios for all unknowns to generate the random uncertainty.
(2b) Excess variance in the 207Pb/206Pb ratio is complicated by the variable and low beam intensity for 207Pb in many zircons. To account for this, we developed a multi-session calibration curve based on 123 sessions (= 123 mounts) over two years of analysis. Excess variance was calculated for every primary and secondary standards we used per session (cf Table 2), and plotted against their average 207Pb beam intensity per session (Fig. 1). In most sessions, excess variance decreased from > 5% for 207Pb cps < 100 to < 2% for 207Pb cps > 1000, similar to what is reported by Horstwood et al. (2003) and Matthew and Guest (2017). A power curve best-fit line yields a very similar shape than the one determined by Matthew and Guest (2017), and serves as the excess variance calibration curve. To determine the excess variance calibration curve for each individual session, this power curve best-fit line is multiplied by a correction factor calculated by minimizing the misfit between the curve and the excess variance of the primary and secondary standard(s) measured during that session (Fig. 1). The excess variance is then calculated for every unknown based on the corrected power curve best-fit line, and used to calculate random uncertainties.
Note that the excess variance for all ratios is always with a 2s outlier rejection when calculating the MSWD, which is also how *Iolite* data reduction schemes proceed (Paton et al., 2010), as the presence of a single outlier is often enough to yield excessively high MSWD. In addition, the excess variance is always calculated on concordant ages only (cf next section for the definition of concordance) as discordant grains add extra variability in reference material isotopic ratios that is not an effect of measurement uncertainty.
Over our 123 sessions (n=22,103), measurement uncertainties in 206Pb/238U ages result in a 1 to 4% random uncertainty (at 2-sigma), with an average at ~3.0% for ages younger than 500 Ma and 2.2% for ages older than 2000 Ma. The random uncertainty in 207Pb/206Pb ages is substantially larger for younger grains due to low intensity of the 207Pb signal, but decrease below ~1% above 2 Ga, as found with other quadrupoles (Matthew and Guest, 2017). Our random uncertainties are on average equal or slightly better than what is proposed for other recent method development

with LA-Q-ICP-MS (Matthew and Guest, 2017) or with LA-SD-ICP-MS (Pullen et al., 2018), which yet use shorter ablation time (2-3 times shorter).

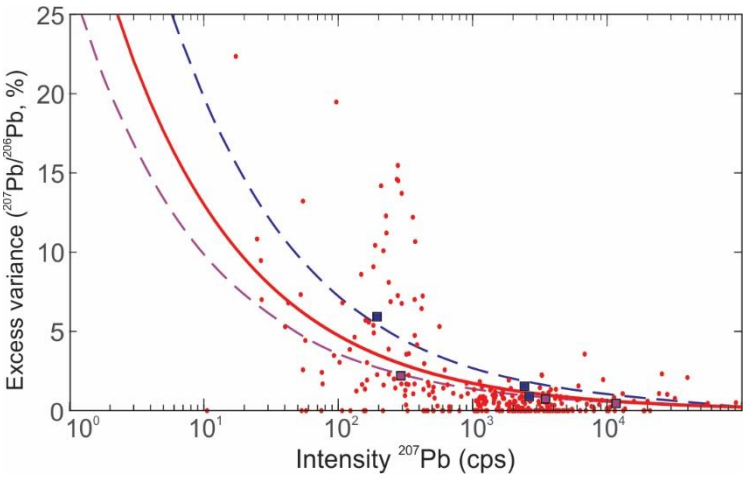

Figure 1: *Excess variance for primary and secondary reference materials across 123 sessions versus 207Pb beam intensity (red dots) and power curve best-fit line across all sessions (red curve; $y= 35.72 * x^{-0.43}$, $r^2=0.3$). Purple and blue squares are excess variance for reference materials of two different sessions (PLS, GHB, FC-1), dashed lines are the calibration curves for these two sessions, obtained by multiplying the multi-session calibration curve by a correcting factor to fit the excess variance of the two reference materials.*

Systematic uncertainty

Systematic uncertainties are calculated following recommendations of Hortswood et al. (2016) by quadratically adding (1) the uncertainty in the ratio of our primary reference material, Plesovice (Sláma et al., 2008); (2) the uncertainty in the decay constants (Jaffey et al. 1971, following modifications by Mattinson, 1987) and (3) the long-term excess variance around secondary reference materials.
The long-term excess variance in 206Pb/238U is variable between the ten secondary reference materials we used, likely reflecting matrix effects, and varying 207Pb sensitivity between sessions which differently affects young and old zircons. We use the excess variance in 206Pb/238U ratios for reference material GHB (2.66 %, 2s) as a proxy for the systematic uncertainty in 206Pb/238U, as it seems robust over a large amount of sessions (n=44); We use the excess variance in 207Pb/206Pb ratios for reference material Tanbra (1.14 %, 2s) as a proxy for the systematic uncertainty in 207Pb/206Pb, which is in the higher end of observed long-term excess variance but likely reflective of the systematic uncertainty for old ages, for which accurate 207Pb/206Pb uncertainties are critical (see below). Using these two values for the systematic uncertainty, the MSWD around the weighted age of secondary reference materials falls between 0.7 and 1.8, with an average of 1.1 . This suggests that our estimate for the systematic uncertainty is accurate on average. Total systematic uncertainties are reported in Table 3.

Determination of the best age for detrital zircon studies

determination of the cut-off for the change of age

Sedimentary provenance studies using zircon geochronology commonly look at age distributions of individual zircons. Given the relative imprecision of the 235U and 207Pb measurements in LA-ICP-MS, the 207Pb/235U age is rarely used in interpretations and is primarily used to measure the discordance of an analysis (Spencer et al., 2016); there are thus effectively two isotopic ages (206Pb/238U, and 207Pb/206Pb) from which the 'best age' of an individual zircon is chosen. It is common practice to use the 207Pb/206Pb age for zircons older than a lab-dependent age threshold (1.0 to 1.5 Gyr; Spencer et al., 2016; Pullen et al., 2018) and to use 206Pb/238U ages for those younger.

Our laboratory-dependent age cut-off is 1400 Ma, above which the random uncertainty in 207Pb/206Pb ages becomes lower than the one for 206Pb/238U ages; we use this age as the threshold to shift from 206Pb/238U to 207Pb/206Pb for the 'best age'.

determination of the cut-off for the use of discordance

As individual zircon ages can be influenced by lead loss and common lead --particularly with quadrupoles, for which 204Pb-based common lead correction is ineffective-- zircon ages are screened for concordance before use in the data set. This is generally quantified either by using the ratio of the 206Pb/238U and 207Pb/206Pb ages only, for all grains (Gehrels et al., 2011) or only old grains (Licht et al.,2018), or by using the ratio of the 206Pb/238U and 207Pb/206Pb above an age threshold and the ratio between the 206Pb/238U and 207Pb/235U ages below (Spencer et al., 2014). Discordance filters vary from 1% to 30% depending on the data processing techniques and level of interpretation desired; it is also common to have a lower tolerance on reverse discordance (Gehrels et al., 2011). There is no community-based agreement or rigorous method on how to measure the discordance for individual grains and how to rigorously establish age thresholds if a change in discordance index is needed (Nemchin and Cawood, 2005; Spencer et al., 2016).

We use here a discordance filter at >20% discordance (<80% concordance) and >5% reverse discordance (>105%

concordance) for discordant grains, in the range of what is commonly used in other geochronology studies (Spencer et al., 2016).

-For grains older than 1300 Ma, discordant grains are selected with this filter on the 206Pb/238U and 207Pb/206Pb age ratio. In the age dataset covering the 123 sessions of the years 2018-2020, the amount of discordant grains increases dramatically below 1300 Ma, likely reflecting the poor reliability of young 207Pb/206Pb ages.

-for grains younger than 1300 Ma, discordant grains are selected with the same filter on the 206Pb/238U vs 207Pb/235U age ratio.

-Below 300 Ma, the amount of discordant grains increases dramatically in our age dataset, likely due to the poor reliability of young 207Pb/235U ages. We thus do not screen for discordant grains that are younger than 300 Ma.

Validity of the approach

Accuracy

The accuracy of our method was determined by comparing ages of ten secondary reference materials with their TIMS age. Except for rare sessions during which offset around the TIMS age can reach ±6-8%, most sessions have age offsets lower than ± 3%. TIMS ages for the secondary reference materials fall within the 2s age uncertainty for 83% of session analyses. The amplitude of offset variation between sessions is similar to what is found between individual sessions of different labs (Kosler et al., 2013), and attributed to variable Pb/U elemental fractionation due to zircon matrix differences between the samples and the reference materials used for standardization (Kosler et al., 2013).

Our multi-session averages are offset by less than ± 0.5% for 207Pb/206Pb ages (standards older than 1400 Ma: Oracle, Tanbra, and OG1), and less than ± 1% for most younger reference materials (FCT, GHB, Temora2, R33, 91500, oracle, Tanbra, OG1) except for FC1 (1.3 %) and 9435 (2.2 %). The accuracy over multiple sessions is analogous to what is found with MC- and SD-ICP-MS (Gehrels et al., 2008; Pullen et al., 2018), also within the range of ± 2%, with most reference materials falling within ± 1% of their TIMS age. Multi-session average ages for all reference materials are given in Table 2; these ages are weighted means calculated using systematic uncertainty propagation on individual measurements, following Hostwood et al. (2016), with outlier rejection at 2s and concordant ages only. MSWD for reference material ages falls between 0.7 and 1.8, with an average of 1.1, which shows the accuracy of our treatment of uncertainties.

Impact of the 207-Pb correction scheme

For our secondary reference material, 206Pb/238U ages corrected for common lead using the Andersen 207Pb-correction scheme of *VisualAge* are very similar to uncorrected 206Pb/238U ages, though younger by 0.1 to 1%. This bias toward younger values does not significantly alter the accuracy of these ages. However, 207Pb/206Pb ages corrected for common lead are significantly offset toward younger ages by the 207Pb-correction scheme for our three oldest standards (up to -5% of offset for Oracle), away from their TIMS age. This bias toward younger ages suggests some degree of lead loss for these older zircons, as the 207Pb-correction scheme yields ages that are systematically too low compared to initial ages when there have experienced lead loss (Andersen 2002). We thus recommend to systematically use uncorrected ages for common lead for detrital zircon studies.

References

Andersen, T. (2002). Correction of common lead in U–Pb analyses that do not report 204Pb. *Chemical Geology*, *192*(1-2), 59-79.

Black, L. P., Kamo, S. L., Allen, C. M., Davis, D. W., Aleinikoff, J. N., Valley, J. W., ... & Foudoulis, C. (2004). Improved 206Pb/238U microprobe geochronology by the monitoring of a trace-element-related matrix effect; SHRIMP, ID–TIMS, ELA–ICP–MS and oxygen isotope documentation for a series of zircon standards. *Chemical Geology*, *205*(1-2), 115-140.

Chew, D.M., Petrus, J.A. and Kamber, B.S. (2014), U–Pb LA–ICPMS dating using accessory mineral standards with variable common Pb. *Chemical Geology*, 363: 185-199

Eddy, M. P., Bowring, S. A., Miller, R. B., & Tepper, J. H. (2016). Rapid assembly and crystallization of a fossil large-volume silicic magma chamber. *Geology*, 44(4), 331-334.

Gehrels, G. E., Valencia, V. A., & Ruiz, J. (2008). Enhanced precision, accuracy, efficiency, and spatial resolution of U-Pb ages by laser ablation–multicollector–inductively coupled plasma–mass spectrometry. *Geochemistry, Geophysics, Geosystems*, 9(3).

Gehrels, G., Kapp, P., DeCelles, P., Pullen, A., Blakey, R., Weislogel, A., ... & Yin, A. (2011). Detrital zircon geochronology of pre-Tertiary strata in the Tibetan-Himalayan orogen. *Tectonics,* 30(5).

Horstwood, M. S., Foster, G. L., Parrish, R. R., Noble, S. R., & Nowell, G. M. (2003). Common-Pb corrected in situ U–Pb accessory mineral geochronology by LA-MC-ICP-MS. *Journal of Analytical Atomic Spectrometry*, *18*(8), 837-846.

Horstwood, M. S., Košler, J., Gehrels, G., Jackson, S. E., McLean, N. M., Paton, C., ... & Bowring, J. F. (2016). Community-derived standards for LA-ICP-MS U-(Th-) Pb geochronology–Uncertainty propagation, age interpretation and data reporting. *Geostandards and Geoanalytical Research*, 40(3), 311-332.

Jaffey, A. H., Flynn, K. F., Glendenin, L. E., Bentley, W. T., & Essling, A. M. (1971). Precision measurement of half-lives

and specific activities of U 235 and U 238. *Physical review C*, *4*(5), 1889.
Klepeis, K. A., Crawford, M. L., & Gehrels, G. (1998). Structural history of the crustal-scale Coast shear zone north of Portland Canal, southeast Alaska and British Columbia. *Journal of Structural Geology*, *20*(7), 883-904.
Košler, J., Sláma, J., Belousova, E., Corfu, F., Gehrels, G. E., Gerdes, A., ... & Whitehouse, M. J. (2013). U-Pb detrital zircon analysis–Results of an inter-laboratory comparison. *Geostandards and Geoanalytical Research*, *37*(3), 243-259.
Licht, A., Dupont-Nivet, G., Win, Z., Swe, H. H., Kaythi, M., Roperch, P., ... & Jones, D. (2018). Paleogene evolution of the Burmese forearc basin and implications for the history of India-Asia convergence. *GSA Bulletin*, *131*(5-6), 730-748.
Matthews, W. A., & Guest, B. (2017). A Practical Approach for Collecting Large-n Detrital Zircon U-Pb Data sets by Quadrupole LA-ICP-MS. *Geostandards and Geoanalytical Research*, 41(2), 161-180.
Mattinson, J. M. (1987). U-Pb ages of zircons: A basic examination of error propagation. *Chemical Geology: Isotope Geoscience Section*, 66(1-2), 151-162.
Mattinson, J. M. (2010). Analysis of the relative decay constants of 235U and 238U by multi-step CA-TIMS measurements of closed-system natural zircon samples. *Chemical Geology*, *275*(3-4), 186-198.
Nemchin, A. A., & Cawood, P. A. (2005). Discordance of the U–Pb system in detrital zircons: implication for provenance studies of sedimentary rocks. *Sedimentary Geology*, *182*(1-4), 143-162.
Paces, J. B., & Miller Jr, J. D. (1993). Precise U-Pb ages of Duluth complex and related mafic intrusions, northeastern Minnesota: Geochronological insights to physical, petrogenetic, paleomagnetic, and tectonomagmatic processes associated with the 1.1 Ga midcontinent rift system. *Journal of Geophysical Research: Solid Earth*, 98(B8), 13997-14013.
Paton, C., Woodhead, J., Hellstrom, J., Hergt, J., Greig, A. and Maas, R (2010) Improved laser ablation U-Pb zircon geochronology through robust down-hole fractionation correction. *Geochemistry, Geophysics, Geosystems*, 11(3), doi:10.1029/2009GC002618
Pullen, A., Ibáñez-Mejia, M., Gehrels, G. E., Giesler, D., & Pecha, M. (2018). Optimization of a Laser Ablation-Single Collector-Inductively Coupled Plasma-Mass Spectrometer (Thermo Element 2) for Accurate, Precise, and Efficient Zircon U-Th-Pb Geochronology. Geochemistry, Geophysics, Geosystems, 19(10), 3689-3705.
Schmitz, M. D., & Bowring, S. A. (2001). U-Pb zircon and titanite systematics of the Fish Canyon Tuff: an assessment of high-precision U-Pb geochronology and its application to young volcanic rocks. *Geochimica et Cosmochimica Acta*, *65*(15), 2571-2587.
Sláma, J., Košler, J., Condon, D. J., Crowley, J. L., Gerdes, A., Hanchar, J. M., ... & Schaltegger, U. (2008). Plešovice zircon—a new natural reference material for U–Pb and Hf isotopic microanalysis. *Chemical Geology*, 249(1-2), 1-35.
Spencer, C. J., Kirkland, C. L., & Taylor, R. J. (2016). Strategies towards statistically robust interpretations of in situ U–Pb zircon geochronology. *Geoscience Frontiers*, *7*(4), 581-589.
Spencer, C. J., Prave, A. R., Cawood, P. A., & Roberts, N. M. (2014). Detrital zircon geochronology of the Grenville/Llano foreland and basal Sauk Sequence in west Texas, USA. *GSA Bulletin*, *126*(7-8), 1117-1128.
Stern, R. A., Bodorkos, S., Kamo, S. L., Hickman, A. H., & Corfu, F. (2009). Measurement of SIMS instrumental mass fractionation of Pb isotopes during zircon dating. *Geostandards and Geoanalytical Research*, *33*(2), 145-168.
Wiedenbeck, M. A. P. C., Alle, P., Corfu, F., Griffin, W. L., Meier, M., Oberli, F. V., ... & Spiegel, W. (1995). Three natural zircon standards for U-Th-Pb, Lu-Hf, trace element and REE analyses. *Geostandards newsletter*, *19*(1), 1-23.

Table 1: *Summary of analytical set-up*

Laboratory & Sample Preparation	
Laboratory name	Tracelab, University of Washington, Seattle
Sample type/mineral	Zircons
Sample preparation	Conventional mineral separation, 1 inch resin mount, 5□m polish to finish
Imaging	TFS Apreo-S with Lovac Scanning Electron Microscope and Directional-backscatter (DBS)
Laser ablation system	
Make, Model & type	Analyte-G2 Excimer
Ablation cell	HelEx 2-volume sample cell
Laser wavelength (nm)	193 nm
Pulse width (ns)	< 5 ns
Fluence (J.cm^{-2})	2.94 J.cm^{-2}
Repetition rate (Hz)	10 Hz
Ablation duration (s)	38 seconds
Ablation pit depth / ablation rate	18□m pit depth, measured using a SEM and a profilometer, equivalent to 0.05□m/pulse
Spot diameter (□m) nominal/actual	25 □m / 29 □m
Sampling mode / pattern	Static spot ablation
Carrier gas	100% He in the cell, N_2 added downstream

Cell carrier gas flow (l/min)	0.5 L/min for He (Mass Flow Controller 1), 0.2 L/min for He (Mass Flow Controller 2), and 10 mL/min for N_2 (Mass Flow Controller 3)
ICP-MS Instrument	
Make, Model & type	Icap RQ, Q-ICP-MS
Sample introduction	Ablation aerosol
RF power (W)	1550W
Make-up gas flow (l/min)	Cool flow 14 L/min, Auxilary gas flow 0.8 L/min
Detection system	Dual mode secondary electron multiplier (SEM)
Masses measured	90Zr, 204Pb, 206-208Pb, 232Th, 235U, 238U
Integration time per peak/dwell times (ms); quadrupole settling time between mass jumps	90Zr: 0.01s, 204Pb: 0.01s, 206Pb: 0.15s, 207Pb: 0.12s, 208Pb: 0.1s, 232Th: 0.1s, 235U: 0.01s, 238U: 0.12s
Total integration time per output datapoint	0.62s
'Sensitivity' as useful yield (%, element)	0.2% U
ICP-MS Dead time (ns)	40 ns
Data Processing	
Gas blank	27 second on-peak zero subtracted
Calibration strategy	Plesovice used as primary reference material, GHB and FC-1 used as secondaries/validation
Reference Material info	Plesovice (Slama et al. 2008) GHB (Eddy et al. 2016) FC-1 (Paces and Miller (1993))
Data processing package used / Correction for LIEF	*Iolite* (*U_Pb_Geochron4* and *VisualAge* DRS) and in-house Matlab algorithm (cf main text)
Mass discrimination	NIST612 used for initial mass bias correction during autotuning, then 207Pb/206Pb and 206Pb/238U normalised to reference material
Common-Pb correction, composition and uncertainty	No common-Pb correction applied to the data.
Uncertainty level & propagation	Ages are quoted at 2*s* absolute, propagation is by quadratic addition.
Quality control / Validation	Cf Table 2

Table 2: *Zircon reference material used in this study and their TIMS ages, and measured ages with our method at the University of Washington (⁺ = 206Pb/238U ages, * = 207Pb/206Pb ages; uncertainties are systematic uncertainty).*

	206Pb*/238U age (Ma, ± 2σ)	206Pb*/207Pb* age (Ma, ± 2σ)	Technique	Reference	Age measured with our method over multiple sessions (Ma, ± 2σ)
FCT (Fish Canyon Tuff)	28.478 ± 0.024	N/A	ID-TIMS	Schmitz and Bowring (2001)	28.3 ± 0.1 (n=82, MSWD=1.7)⁺
GHB	48.205 ± 0.060	N/A	CA-ID-TIMS	Eddy et al. (2016)	47.6 ± 0.1 (n=325, MSWD=0.9)⁺
9435	55.5 ± 0.08	N/A	ID-TIMS	Klepeis et al. (1998)	56.9 ± 0.3 (n=63, MSWD=0.8)⁺
Plešovice	337.1 ± 0.2	339.3 ± 0.3	ID-TIMS	Sláma et al. (2008), Horstwood et al. (2016)	N/A
Temora2	416.78 ± 0.33	420.13 ± 0.30	ID-TIMS & CA-TIMS	Black et al. (2004), Mattinson (2010)	415.5 ± 1.6 (n=78, MSWD=1.8)⁺
R33	419.3 ± 0.4	422.37 ± 0.36	ID-TIMS & CA-TIMS	Black et al. (2004), Mattinson (2010)	415.4 ± 0.9 (n=212, MSWD=1.2)⁺
91500	1,062.4 ± 1.9	1,065.4 ± 0.6	ID-TIMS	Wiedenbeck et al. (1995)	1058 ± 4 (n=92, MSWD=1.8)⁺
FC-1	1,099.5 ± 0.33	1,099.0 ± 0.16	ID-TIMS	Paces and Miller (1993)	1114 ± 2 (n=270, MSWD=0.6)⁺
Oracle	1,436.2 ± 1.3	1,437.4 ± 0.77	CA-TIMS	Bowring (Communication in Pullen et al., 2018)	1430 ± 5 (n=60, MSWD=0.9)*
TanBra	2,507.8 ± 1.5	2,512.24 ± 0.71	CA-TIMS	Pecha (Communication in Pullen et al., 2018)	2503 ± 5 (n=60, MSWD=1.3)*
OG1	3,440.7 ± 3.2	3,465.4 ± 0.6	ID-TIMS	Stern et al. (2009)	3458 ± 3 (n=61, MSWD=0.7)*

Table 3: *Total systematic uncertainties obtained with our method at the University of Washington. These uncertainties are for isotopic ratios not for ages (X% of a ratio does not equal X% of an age due to the non-linearity of the age equation).*

	Uncertainty in Plesovice Std, 2s (in %)	**Uncertainty in Decay constants, 2s (in %)**	**long-term excess variance in FC1 and OG1 reference material, 2s (in %)**	**Total systematic uncertainty, 2s (in %)**
reference	Horstwood et al., 2016	Mattinson, 1987	here	
206Pb/238U ratio	0.034	0.16	2.66	2.67
207Pb/206Pb ratio	0.027	0.26	1.14	1.17

2. Operating conditions for apatite U-Pb and AFT dating

	U-Pb apatite analyses
Laboratory & Sample Preparation	
Laboratory name	GeOHeLiS Analytical Platform, Géosciences Rennes/OSUR, Univ. Rennes
Sample type/mineral	Detritic
Sample preparation	Conventional mineral separation, 1 inch resin mount, 1μm polish to finish
Laser ablation system	
Make, Model & type	ESI NWR193UC, Excimer
Ablation cell	ESI NWR TwoVol2
Laser wavelength	193 nm
Pulse width	< 5 ns
Fluence	5 J/cm-2
Repetition rate	7 Hz
Spot size	30 µm (round spot)
Sampling mode / pattern	Single spot
Carrier gas	100% He, Ar make-up gas and N_2 (3 ml/mn) combined using in-house smoothing device
Background collection	10 seconds
Ablation duration	30 seconds
Wash-out delay	10 seconds
Cell carrier gas flow (He)	0.75 l/min
ICP-MS Instrument	
Make, Model & type	Agilent 7700x, Q-ICP-MS
Sample introduction	Via conventional tubing
RF power	1350W
Sampler, skimmer cones	Ni
Extraction lenses	X type
Make-up gas flow (Ar)	0.80 l/min
Detection system	Single collector secondary electron multiplier
Data acquisition protocol	Time-resolved analysis
Scanning mode	Peak hopping, one point per peak
Detector mode	Pulse counting, dead time correction applied, and analog mode when signal intensity > ~ 10^6 cps
Masses measured	^{35}Cl, ^{43}Ca, ^{86}Sr, ^{89}Y, ^{139}La, ^{140}Ce, ^{141}Pr, ^{146}Nd, ^{147}Sm, ^{153}Eu, ^{157}Gd, ^{159}Tb, ^{163}Dy, ^{165}Ho, ^{166}Er, ^{169}Tm, ^{172}Yb, ^{175}Lu, ^{204}(Hg + Pb), ^{206}Pb, ^{207}Pb, ^{208}Pb, ^{232}Th, ^{238}U
Integration time per peak	10-30 ms
Sensitivity / Efficiency	28000 cps/ppm Pb (50µm, 10Hz)
Dwell time per isotope	5-70 ms depending on the masses
Data Processing	
Gas blank	20 seconds on-peak
Calibration strategy	NIST 612 and Durango apatite for AFT dating (Cogné et al., 2020) Madagascar apatite used as primary reference material, Durango and McClure apatites used as secondary reference material (quality control) for U-Pb dating
Reference Material info	Madagascar (Thomson et al. 2012) Durango (McDowell et al. 2005) McClure (Schoene and Bowring 2006)
Data processing package used	Iolite (Paton et al. 2011), Trace_ElementsFTD (Woodhead et al., 2007, Cogné et al., 2020), VizualAge_UcomPbine (Chew et al. 2014)
Quality control / Validation	Durango: Weighted average ^{207}Pb corrected age = 32.08 ± 0.65 Ma (N = 135; MSWD = 0.77) McClure: Weighted average ^{207}Pb corrected age = 522.9 ± 4.5 Ma (N = 75; MSWD = 0.43)

References

Chew, D.M., Petrus, J.A., Kamber, B.S., 2014. U–Pb LA–ICPMS dating using accessory mineral standards with variable common Pb. Chem. Geol. 363, 185–199. doi:10.1016/j.chemgeo.2013.11.006

Cogné, N., Chew, D. M., Donelick, R. A., & Ansberque, C. (2020). LA-ICP-MS apatite fission track dating: A practical zeta-based approach. *Chemical Geology*, *531*, 119302.

McDowell, F.W., McIntosh, W.C., Farley, K.A., 2005. A precise 40Ar–39Ar reference age for the Durango apatite (U–Th)/He and fission-track dating standard. Chem. Geol. 214, 249–263. doi:10.1016/j.chemgeo.2004.10.002

Paton, C., Hellstrom, J., Paul, B., Woodhead, J., Hergt, J., 2011. Iolite: Freeware for the visualisation and processing of mass spectrometric data. J. Anal. At. Spectrom. 26, 2508–2518. doi:10.1039/C1JA10172B

Schoene, B., Bowring, S.A., 2006. U–Pb systematics of the McClure Mountain syenite: thermochronological constraints on the age of the 40Ar/39Ar standard MMhb. Contrib. Mineral. Petrol. 151, 615. doi:10.1007/s00410-006-0077-4

Thomson, S.N., Gehrels, G.E., Ruiz, J., Buchwaldt, R., 2012. Routine low-damage apatite U-Pb dating using laser ablation–multicollector–ICPMS. Geochem. Geophys. Geosystems 13, Q0AA21. doi:10.1029/2011GC003928

Woodhead, J., Hellstrom, J., Hergt, J., Greig, A. and Maas, R (2007) Isotopic and elemental imaging of geological materials by laser ablation Inductively Coupled Plasma mass spectrometry. *Journal of Geostandards and Geoanalytical Research*, 31, 331-343.

Appendix 4: Data tables Chapter 6

Reference: *Manuscript in preparation.*

Supplementary Table 1

All paleomagnetic data from this study and Westerweel et al. (2019). Samples are ordered per site and then per locality.

site	Coordinates (Lat/Lon)	sample	Line or Plane	anchored	Demag type	nb points	step min	step max	Dec IS	inc IS	Dec TC	inc TC	mad value	bedding (str/dip)
SW09	21.666517°/94.13420	20SW0901B	L	y	D	4	250	340	162.6	42.9	138.6	4.9	13.1	007/60
(Kabaw Fm.)		20SW0902B	L	y	F	4	300	400	181.7	30.8	157.1	11.3	14.6	007/60
		20SW0903A	L	y	D	6	250	400	194.5	17.1	175.1	15.4	12.6	007/60
		20SW0904A	L	y	D	4	340	430	193.1	41.5	150.8	24.1	4.8	007/60
		20SW0905A	L	y	D	5	250	370	182.4	37.3	151.5	14.8	6.1	007/60
		20SW0906A	L	y	D	4	250	340	196.2	43.2	149.9	26.8	8.4	007/60
		20SW0907A	L	y	D	7	250	430	189.1	56.2	134.5	26.1	9.6	007/60
		20SW0908A	L	y	D	5	250	370	184.7	68.5	120.7	27.1	9.3	007/60
		20SW0909A	L	y	D	4	340	430	160	32.7	145.3	-3.1	11.8	007/60
		20SW0911A	L	y	D	7	250	430	179.7	28.4	158.4	8.6	7	007/60
		20SW0912A	L	y	D	3	280	340	195.8	0.1	191	8.3	11.2	007/60
		20SW0913A	L	y	D	8	250	460	186.3	41.2	149.1	19.3	8.5	007/60
		20SW0914A	L	y	D	6	250	400	179.8	40.2	147.9	14.3	9.3	007/60
		20SW0915A	L	y	D	7	250	430	182.1	43	146.1	17.2	5.8	007/60
		20SW0917A	L	y	D	4	250	340	193.9	65.3	124.9	30.1	7.2	007/60
		20SW0919A	L	y	D	7	250	430	205.3	51	142.5	34.5	13.9	007/60
		20SW0920A	L	y	D	5	250	370	182.8	32.2	156.3	12.8	10.6	007/60

Wuntho data first published in: *Westerweel, J., Roperch, P., Licht, A., Dupont-Nivet, G., Win, Z., Poblete, F., … Aung, D. W. (2019). Burma Terrane part of the Trans-Tethyan arc during collision with India according to palaeomagnetic data. Nature Geoscience. https://doi.org/10.1038/s41561-019-0443-2*

site	Coordinates (Lat/Lon)	sample	Line or Plane	anchored	Demag type	nb points	step min	step max	Dec IS	inc IS	Dec TC	inc TC	mad value	bedding (str/dip)
MY03	24.030340°/95.438240	16MY0301B	L	y	F	4	18	25	62.4	2.2	62.4	2.2	8.1	000/00
		16MY0302B	L	y	F	5	13	25	88.8	-10.5	88.8	-10.5	12.5	000/00
		16MY0303B	L	y	D	5	400	560	62.1	-20.3	62.1	-20.3	7.4	000/00
MY40	24.022293°/95.434653	17MY4009A	L	y	D	8	320	590	75.4	17.4	75.4	17.4	1.6	000/00
		17MY4010A	L	y	D	7	350	590	62.3	19.2	62.3	19.2	1.5	000/00
		17MY4011A	L	y	D	7	320	560	51.7	21.5	51.7	21.5	2.5	000/00
MY04	24.024110°/95.437910	16MY0406A	L	y	F	4	18	25	57.1	9.2	57.1	9.2	6.9	000/00
		16MY0403A	L	y	F	12	15	60	62.7	-2.4	62.7	-2.4	4.1	000/00
		16MY0403B	L	y	D	8	330	590	60.6	-4.1	60.6	-4.1	2.3	000/00
		16MY0406B	f	n	D	4	380	490	48.5	2.9	48.5	2.9	19.5	000/00
		17MY0402A	L	y	F	8	35	80	68	14	68	14	2.9	000/00
		17MY0405A	L	y	F	9	35	100	71	1.9	71	1.9	2.8	000/00
		17MY0406A	L	y	D	6	400	590	71.2	8.5	71.2	8.5	2.6	000/00
		17MY0411A	L	n	D	6	450	620	79.4	10	79.4	10	6.9	000/00
		17MY0403A	P	y	D	10	130	490	327.2	-29.1	327.2	-29.1	8.2	000/00
		17MY0404A	P	y	D	6	130	320	340.5	-35.8	340.5	-35.8	12.6	000/00
MY05	24.019300°/95.437490	16MY0501B	L	y	D	4	490	600	61.2	4.1	61.2	4.1	3.6	000/00
		16MY0503A	L	y	D	5	450	590	54.2	12.7	54.2	12.7	6.6	000/00
		16MY0504B	L	y	F	7	20	45	54.8	5.7	54.8	5.7	4	000/00
		16MY0506B	L	y	F	6	10	30	70.3	-2.3	70.3	-2.3	1.3	000/00
		16MY0507A	L	y	D	5	450	590	65.3	6.4	65.3	6.4	12.9	000/00
		16MY0508B	L	y	F	5	25	45	52.3	3.3	52.3	3.3	6.7	000/00
MY39	24.019073°/95.436950	17MY3903A	L	y	D	8	320	590	34.7	4.4	34.7	4.4	2.2	000/00
		17MY3904A	L	y	F	10	30	100	62.6	7.2	62.6	7.2	2.4	000/00
		17MY3901B	f	n	F	8	18	35	61	9.5	61	9.5	5.7	000/00
		17MY3905B	f	n	F	8	18	35	40.4	-0.2	40.4	-0.2	11	000/00
		17MY3910A	f	n	F	7	18	35	71.3	15.1	71.3	15.1	8.5	000/00
		17MY3912B	f	n	F	6	15	28	52.3	6.2	52.3	6.2	16.6	000/00
MY17	24.412910°/95.759890	16MY1701B	L	y	D	10	360	660	75.3	-15.7	75.3	-15.7	2.6	000/00
		16MY1703B	L	y	D	5	450	590	73.4	-8.9	73.4	-8.9	1.9	000/00
		16MY1704B	L	y	D	5	450	600	81.3	-25.3	81.3	-25.3	4.1	000/00
		16MY1706B	L	y	D	8	360	620	66.4	-20.8	66.4	-20.8	4.9	000/00
		16MY1708B	L	y	D	5	450	600	70.9	-17.5	70.9	-17.5	5.4	000/00
		16MY1710B	L	y	F	7	18	40	71.8	-21.5	71.8	-21.5	3.3	000/00
		16MY1711A	L	y	D	5	450	590	80.6	-0.5	80.6	-0.5	3.8	000/00
		16MY1702A	L	y	F	8	30	100	66.9	-17.1	66.9	-17.1	7.6	000/00
		16MY1705A	L	y	F	10	20	100	78.6	-18.5	78.6	-18.5	2.6	000/00
		16MY1707B	L	y	F	10	20	100	71.8	-22.2	71.8	-22.2	4.3	000/00
		16MY1709A	L	y	F	10	20	100	71.1	-10.5	71.1	-10.5	5.5	000/00
MY18	24.417580°/95.761910	16MY1807A	L	y	F	9	15	60	87.9	-4.4	87.9	-4.4	10.4	000/00
		16MY1802A	L	y	D	3	400	490	77.8	-22.9	77.8	-22.9	1.1	000/00
		16MY1803B	L	y	D	5	450	590	62	-38.7	62	-38.7	3.6	000/00
		16MY1805A	L	y	F	7	40	120	86	-22.3	86	-22.3	3.1	000/00
		16MY1808B	L	y	D	5	450	590	85.5	0.5	85.5	0.5	5.4	000/00
		16MY1801A	f	n	F	8	25	60	84.6	-9.8	84.6	-9.8	17	000/00
		16MY1803A	f	n	F	5	30	50	68.5	-22.3	68.5	-22.3	7.6	000/00
		16MY1806A	f	n	F	7	20	40	85.1	-4.9	85.1	-4.9	14.2	000/00
		16MY1809A	f	n	F	7	20	45	92	-12	92	-12	11.8	000/00
		16MY1802A	P	y	D	9	170	490	134.5	52.8	134.5	52.8	5.8	000/00
MY19	24.431460°/95.736430	16MY1901A	L	y	D	5	450	590	79.2	-41.8	79.2	-41.8	6.6	000/00
		16MY1903A	L	y	D	4	450	560	69.7	-50	69.7	-50	13.6	000/00
		16MY1903B	L	y	F	10	28	90	77.4	-35.6	77.4	-35.6	6.7	000/00
		16MY1904A	L	y	D	5	450	590	78.7	-45.9	78.7	-45.9	11.2	000/00
		16MY1906A	L	y	D	5	450	600	69	-38.5	69	-38.5	4	000/00
		16MY1906B	L	y	F	4	18	25	63.4	-40.1	63.4	-40.1	2	000/00
		16MY1902B	L	y	F	9	25	65	69.5	-40.3	69.5	-40.3	3.3	000/00
		16MY1905A	L	y	F	11	23	70	69.6	-39.9	69.6	-39.9	4	000/00
MY26	24.445540°/95.814340	16MY2601A	L	y	D	6	560	680	72.6	-0.6	72.6	-0.6	5.7	000/00
		16MY2602B	f	n	F	6	13	25	66.2	8.1	66.2	8.1	11.3	000/00
MY27	24.455140°/95.815750	16MY2702B	P	y	F	9	5	25	140.3	38.7	140.3	38.7	11	000/00
		16MY2701B	L	y	F	7	40	70	52.1	13.9	52.1	13.9	6.8	000/00
		16MY2704A	L	y	D	3	360	450	44.8	5.3	44.8	5.3	14.5	000/00
		16MY2705B	P	y	F	6	8	30	136.9	16.5	136.9	16.5	10.8	000/00
		16MY2707A	P	y	D	12	130	560	332.8	-29.4	332.8	-29.4	9.9	000/00
MY46	24.440472°/95.809454	17MY4606A	L	y	D	7	350	590	54.9	-19.2	54.9	-19.2	8.6	000/00
		17MY4607A	L	y	D	6	400	590	50.9	8.7	50.9	8.7	6.3	000/00
		17MY4608A	P	y	D	9	210	490	175.5	-78.4	175.5	-78.4	18.3	000/00
		17MY4606A	P	y	D	11	130	560	97.9	64.1	97.9	64.1	13.2	000/00
		17MY4613A	P	y	D	5	130	290	149.7	-15	149.7	-15	13.4	000/00
		17MY4613B	P	y	F	8	3	20	71.4	67.5	71.4	67.5	22.5	000/00
MY48	24.424850°/95.757696	17MY4801A	L	y	D	7	350	590	115	-32.5	115	-32.5	5.8	000/00
		17MY4803A	L	y	D	7	320	560	104.8	-9.8	104.8	-9.8	5.3	000/00
		17MY4805A	L	y	D	4	350	490	120.7	-3.3	120.7	-3.3	14.1	000/00
		17MY4806A	L	y	F	10	30	100	115.7	-25.4	115.7	-25.4	3.6	000/00
		17MY4807A	L	y	D	8	320	590	112.4	-21	112.4	-21	4.3	000/00
		17MY4809A	L	y	D	8	320	590	124.6	-25.8	124.6	-25.8	8.4	000/00
		17MY4810A	P	y	D	11	130	530	22.5	-9.1	22.5	-9.1	8.4	000/00
		17MY4802A	P	y	F	11	10	40	204.4	47	204.4	47	13.5	000/00
		17MY4808A	P	y	F	15	8	60	220.4	-20.4	220.4	-20.4	13.8	000/00
MY07	23.970720°/95.761430	16MY0701A	L	y	D	5	450	600	62.3	-14.4	62.3	-14.4	2.6	000/00
		16MY0701B	L	y	F	8	20	50	61	-6.4	61	-6.4	2.5	000/00
		16MY0702A	L	y	D	5	450	590	59.8	-1.3	59.8	-1.3	3.3	000/00
		16MY0703A	L	y	D	5	450	600	67.3	1.2	67.3	1.2	3	000/00
		16MY0704A	L	y	D	5	450	590	65.7	8.7	65.7	8.7	5.8	000/00
		16MY0704B	L	y	F	8	20	55	65.1	16.2	65.1	16.2	9.5	000/00
		16MY0705A	L	y	D	5	450	600	68.7	12.2	68.7	12.2	0.9	000/00
		16MY0707A	L	y	D	5	450	590	64.7	2.3	64.7	2.3	1.4	000/00
		16MY0706A	L	y	F	9	30	70	70.1	2.3	70.1	2.3	1.1	000/00
		17MY0701A	L	y	D	7	350	590	73.5	-5.4	73.5	-5.4	1.2	000/00

		17MY0702A	L	y	D	7	350	590	74.9	7.8	74.9	7.8	2.5	000/00
		17MY0703A	P	y	D	11	130	530	343.3	-6.2	343.3	-6.2	13.9	000/00
MY08	23.927640°/95.709470	16MY0801B	L	y	D	5	450	590	123.1	35.8	123.1	35.8	0.6	000/00
		16MY0802B	L	y	D	6	410	600	93.9	40.9	93.9	40.9	2.7	000/00
		16MY0803B	L	y	D	3	530	590	95.8	28.3	95.8	28.3	1.8	000/00
		16MY0804B	L	y	F	3	18	25	106.5	30.9	106.5	30.9	0.7	000/00
		16MY0805B	L	y	D	3	530	590	88.4	28.4	88.4	28.4	1.2	000/00
		16MY0806B	L	y	F	8	20	50	100.8	24.3	100.8	24.3	5.5	000/00
		16MY0807A	L	y	F	9	20	70	117.6	40.3	117.6	40.3	0.9	000/00
MY10	23.860780°/95.603970	16MY1001B	L	y	F	7	15	45	108.8	56.7	118.2	7.3	6.6	040/51
		16MY1002B	L	y	F	13	10	70	99.8	62.5	115.8	14.2	1.3	040/51
		16MY1003B	L	y	D	4	490	590	88.7	20.1	88.9	-19.7	1.7	040/51
		16MY1004B	L	y	D	4	490	590	83.4	42.9	97.6	1.9	2.3	040/51
		16MY1005B	L	y	D	4	490	590	81	43.8	96.7	3.7	1.2	040/51
		16MY1007B	L	y	D	4	490	590	88	47.1	102.6	3.7	4.5	040/51
		16MY1008B	L	y	F	8	15	70	102.1	50.6	112.5	2.8	1.4	040/51
MY11	23.863960°/95.606060	16MY1101A	L	y	F	4	15	25	98.6	54	111.1	16.3	0.4	040/41
		16MY1102B	L	y	D	4	450	560	112.6	36.9	116.1	-2.8	1.5	040/41
		16MY1103B	L	y	D	3	530	600	103.2	38.1	109.1	0.2	0.5	040/41
		16MY1104B	L	y	F	5	15	30	101.1	38.6	107.6	1.1	0.6	040/41
		16MY1105B	L	y	D	5	450	600	108.7	44.7	114.8	5.4	1.1	040/41
		16MY1107A	L	n	F	10	13	40	82.3	40.8	95.3	9	3.8	040/41
		16MY1107B	L	y	D	5	450	590	94.3	39.7	103.1	4	2.4	040/41
		16MY1108B	L	y	D	5	450	590	95.3	40.4	104	4.4	1.5	040/41
MY12	23.840420°/95.549490	16MY1201A	L	y	D	11	360	680	64.2	50.3	64.2	50.3	1.8	000/00
		16MY1202A	L	y	F	3	40	50	53.2	47.7	53.2	47.7	1.5	000/00
		16MY1203A	L	y	D	11	360	680	73.7	40.7	73.7	40.7	1.7	000/00
		16MY1204A	L	y	F	3	80	120	70.4	47.2	70.4	47.2	0.3	000/00
		16MY1205A	L	y	D	11	360	680	59.3	41	59.3	41	1.4	000/00
		16MY1206A	L	y	F	4	60	120	52	32.7	52	32.7	0.6	000/00
MY15	23.853420°/95.586300	16MY1502B	L	y	F	9	13	45	88.4	28.8	88.4	28.8	1.8	000/00
		16MY1504B	L	y	D	5	450	590	105	28.8	105	28.8	2.4	000/00
		16MY1505B	L	y	F	11	15	55	96.6	15.3	96.6	15.3	1.3	000/00
		16MY1506A	L	y	D	10	360	490	104.8	-7.4	104.8	-7.4	1.3	000/00
		16MY1506B	L	y	F	6	13	25	108.8	-4.6	108.8	-4.6	0.2	000/00
		16MY1508B	L	y	D	13	400	590	110	-5.8	110	-5.8	0.5	000/00
		16MY1503B	P	y	D	12	170	570	355.5	-34.9	355.5	-34.9	8.8	000/00
MY34	23.878841°/95.703966	17MY3401A	L	n	D	5	320	490	98.1	-9.8	9.5	-78.7	8.8	020/82
		17MY3402A	L	n	D	5	320	490	76.4	-41.7	324.8	-45.4	8.2	020/82
		17MY3404A	L	n	D	6	290	490	80.5	-23.4	346.9	-58.3	7.2	020/82
		17MY3406A	L	n	D	3	290	350	79.3	-14.1	5	-59.9	8.7	020/82
		17MY3407A	L	n	D	6	320	530	62.1	-34.3	341.1	-39.3	10.5	020/82
		17MY3408A	L	n	D	5	320	490	109.7	-34.1	288.8	-63.9	9.6	020/82
		17MY3409A	L	n	D	5	320	490	81.3	-44	318.9	-46.5	4	020/82
		17MY3410A	L	n	D	3	290	350	79.8	-33.7	331.9	-52.5	6.2	020/82
		17MY3411A	L	n	D	3	290	350	80.1	-32.8	332.9	-53.2	2.6	020/82
		17MY3412A	L	n	D	3	290	350	73.4	-18.9	358.3	-53.4	11.6	020/82
		17MY3413A	L	n	D	3	290	350	71.9	-30.6	341.4	-48.4	1.5	020/82
MY35	23.922660°/95.712390	17MY3501A	L	y	F	8	30	80	147.2	37.7	147.2	37.7	0.7	000/00
		17MY3502A	L	y	F	10	30	100	155.1	11.4	155.1	11.4	7.6	000/00
		17MY3504A	L	y	D	8	320	590	126.2	-60.5	126.2	-60.5	2.3	000/00
		17MY3505A	L	y	F	10	30	100	249.9	61.3	249.9	61.3	2.2	000/00
		17MY3506A	L	y	D	8	320	590	50.2	12.3	50.2	12.3	5.1	000/00
		17MY3507A	L	y	D	8	320	590	257.8	-20	257.8	-20	3	000/00
		17MY3508B	L	y	F	10	30	100	118.6	26.6	118.6	26.6	1.6	000/00
		17MY3509A	L	y	D	8	320	590	67.3	33.1	67.3	33.1	5.9	000/00
		17MY3510A	L	y	F	10	30	100	342	-13.9	342	-13.9	1.5	000/00
		17MY3511A	L	y	D	8	320	590	83.2	18.3	83.2	18.3	4.6	000/00
MY37	23.851902°/95.590906	17MY3701A	P	y	D	13	130	590	26.5	-34.3	82.7	-24.5	8	000/00
		17MY3702A	P	y	D	12	130	560	24.4	-36.3	85.1	-26	12	000/00
		17MY3704A	P	y	D	12	130	560	208.7	34.5	262.7	22.6	18.4	000/00
		17MY3705A	P	y	D	12	130	560	212.5	13.3	240.2	18.6	5.2	000/00
		17MY3706A	P	y	D	12	130	560	206.1	27.5	255.2	25.2	5.2	000/00
		17MY3708A	L	y	D	6	400	590	100.2	48.1	352.7	39.7	2.8	000/00
		17MY3709A	L	y	D	6	400	590	108.7	38.9	357.8	50.2	0.8	000/00
		17MY3713A	L	y	D	6	400	590	118.1	30.2	0.8	61.7	1.3	000/00
		17MY3703A	L	y	D	5	400	560	90.4	34.6	12.5	39.1	1.6	000/00
		17MY3707A	P	y	D	12	130	560	258.9	50.5	285.1	-10.1	8.4	000/00
		17MY3710A	P	y	D	11	130	530	57	-53.3	103	-3.5	8.9	000/00
		17MY3711A	P	y	D	13	130	590	197	-6	216.2	30.4	13.4	000/00
		17MY3712A	P	y	D	12	130	560	196.5	-2	220.7	31.9	4.9	000/00
		17MY3714A	P	y	D	12	130	560	186.4	-16.2	200.5	36.6	8.3	000/00
		17MY3703B	L	y	F	10	20	50	87.4	32.3	16.2	37.2	0.6	000/00
		17MY3707B	L	y	F	7	20	40	89.7	44.9	0.7	35	5.6	000/00
		17MY3710B	P	y	F	11	3	28	46.7	-43.7	92.4	-8.8	6.3	000/00
		17MY3711B	P	y	F	10	3	25	238.7	15.2	246.1	-6.2	4.8	000/00
		17MY3712B	P	y	F	10	3	25	230.2	28.5	257.7	4	3.2	000/00
		17MY3714B	P	y	F	9	3	23	236	37.1	267	0.8	5.1	000/00
MY38	23.853420°/95.586300	17MY3801A	L	y	F	6	20	35	90.2	-0.1	90.2	-0.1	4.9	000/00
		17MY3804A	P	y	D	9	250	560	355.3	-44.8	355.3	-44.8	6	000/00
		17MY3805A	P	y	D	11	170	560	6.9	-38.8	6.9	-38.8	7	000/00
		17MY3808A	L	y	D	8	320	590	97.7	10.3	97.7	10.3	3	000/00
		17MY3809A	P	y	D	10	210	560	356	-51	356	-51	7.6	000/00
		17MY3810A	L	y	D	8	320	590	96.6	0.6	96.6	0.6	1.9	000/00
		17MY3811A	L	y	D	8	320	590	104.6	-1.3	104.6	-1.3	1.4	000/00
		17MY3802A	P	y	D	12	170	590	23.1	-42.5	23.1	-42.5	5.4	000/00
		17MY3807A	P	y	D	10	210	560	153.4	-66.1	153.4	-66.1	8.1	000/00
		17MY3802B	P	y	F	9	3	23	17.4	-42.1	17.4	-42.1	3.9	000/00
		17MY3807B	P	y	F	9	3	23	358.1	-42.8	358.1	-42.8	9.8	000/00
MY22	24.522140°/95.691800	16MY2201A	L	y	D	5	450	600	32.5	-51.7	29.5	13	2.3	115/65
		16MY2202A	L	y	D	5	450	590	41.7	-52.8	34.9	10.7	2	115/65

		16MY2203A	L	y	D	5	450	600	25.2	-33.2	25.2	31.8	5.5	115/65
		16MY2205B	L	y	D	5	450	600	39.4	-41.3	36.6	22.3	1.9	115/65
		16MY2206B	L	y	D	5	450	590	38.4	-38.4	36.5	25.2	3.6	115/65
		16MY2207B	L	y	D	4	490	590	50.1	-53	39.7	8.8	1.3	115/65
		16MY2204A	P	y	F	9	20	50	120.9	11.1	127.2	-1.2	5.9	115/65
		16MY2208A	P	y	F	13	10	50	116.6	12.4	126.5	3.2	6.8	115/65
MY23	24.514070°/95.663900	16MY2301B	L	y	D	9	290	570	50.7	-34.3	63.6	21.5	2.5	210/97
		16MY2303A	L	y	D	10	250	570	53.5	-28.1	57.1	24.5	4.9	210/97
		16MY2304A	L	y	D	9	250	560	45.7	-37.1	66.2	17.2	2.2	210/97
		16MY2305A	L	n	D	10	250	590	43	-32.9	61.7	15.2	2.8	210/97
		16MY2308A	L	y	F	13	30	120	48.6	-31.8	60.8	20	0.5	210/97
		16MY2309B	L	y	D	9	290	590	50.9	-29.5	58.4	22.2	3.5	210/97
		16MY2310B	L	y	D	9	290	570	48.6	-34.6	63.7	19.8	1.6	210/97
		16MY2302A	L	y	F	4	50	80	47.5	-27.3	55.9	19.3	2.1	210/97
		16MY2306A	L	y	F	10	30	120	49.3	-32.4	61.5	20.5	0.6	210/97
		16MY2307A	L	y	F	7	35	110	48.1	-28.5	57.3	19.7	1.4	210/97
MY24	24.510480°/95.665540	16MY2405A	L	y	F	5	15	65	22.2	-50.6	75.4	15	0.7	207/113
		16MY2408A	L	y	F	6	20	90	23.9	-45.4	70	14.5	0.9	207/113
		16MY2410A	L	y	F	7	15	80	27.1	-47.7	71.6	17.3	0.1	207/113
		16MY2401A	L	y	D	3	450	530	9.7	-39.7	68.9	2.7	7.7	207/113
		16MY2402A	L	y	D	4	360	490	18.6	-47.2	72.9	11.7	5.2	207/113
		16MY2403A	L	y	D	9	250	530	44.9	-52.5	75	29.2	2.7	207/113
		16MY2403B	L	y	F	5	20	40	42.6	-44.6	66.2	27.2	3.5	207/113
		16MY2404A	L	y	D	4	400	530	29.3	-43.5	66.9	17.6	3.9	207/113
		16MY2407A	L	y	D	5	400	560	27.8	-48.5	72.2	17.9	2.8	207/113
		16MY2409A	L	y	D	10	360	660	24.4	-45.6	70	14.9	0.7	207/113
		16MY2409B	L	y	F	12	20	140	22.5	-43.7	68.7	13	1.2	207/113
		16MY2406A	L	y	D	4	410	530	23.2	-42.9	67.7	13.2	2.3	207/113
MY25	24.539590°/95.676960	16MY2502A	L	y	D	6	400	590	49.6	-14.8	47.9	-1.3	2	098/18
		16MY2503B	L	y	D	5	400	560	56.7	-16.3	54.3	-4.2	3.6	098/18
		16MY2505A	L	y	D	5	400	560	51.4	-26.1	47.2	-12.7	4	098/18
		16MY2506A	L	y	N	8	350	650	61.8	-15.8	59.2	-4.9	2	098/18
		16MY2508A	L	y	D	6	400	590	65.5	-21.5	61	-11.4	1.2	098/18
		16MY2510A	L	y	D	6	400	590	52.3	-25.1	48.2	-11.8	2.8	098/18
		16MY2501A	L	y	F	10	15	50	46.7	-12	45.7	2.1	9.8	098/18
		16MY2504A	L	y	F	10	15	70	52.3	-10.4	51.4	2.5	5	098/18
		16MY2507A	L	y	F	9	20	80	59.6	-17	56.8	-5.6	1.7	098/18
		16MY2509B	L	y	F	5	15	30	42	-10.7	41.5	4.2	4.4	098/18
MY41	24.509810°/95.664831	17MY4101A	L	y	D	4	400	530	29.4	-53.9	84.3	17.5	5.9	213/114
		17MY4103A	L	y	D	5	320	490	28.3	-50.6	81.3	15.8	3.1	213/114
		17MY4104A	L	y	D	5	320	490	25.6	-52	83.2	14.7	5.5	213/114
		17MY4105A	L	y	D	5	320	490	25.7	-44.7	76.2	12.2	3.9	213/114
		17MY4106A	L	y	F	10	30	100	33.2	-44.9	74.6	17.2	4.7	213/114
		17MY4107A	L	y	D	4	320	450	36.9	-47.8	76.8	20.5	7	213/114
		17MY4109A	L	y	D	5	320	490	21.7	-42.9	75.7	8.8	5.7	213/114
		17MY4110A	L	y	D	4	320	450	13.9	-54.2	88.2	9.2	12.9	213/114
		17MY4111A	L	y	D	3	400	490	18.3	-48.8	82.1	9.2	8.7	213/114
		17MY4112A	L	y	D	5	320	490	34.6	-46.5	75.9	18.6	8.2	213/114
		17MY4114A	L	y	D	7	320	560	29.1	-45.6	76.1	14.7	7.4	213/114
MY42	24.513537°/95.664268	17MY4201A	L	n	D	7	290	530	36.2	-38	66.8	9.6	4.7	210/97
		17MY4202A	L	n	D	7	290	530	37.6	-39	67.8	10.7	3.3	210/97
		17MY4204A	L	n	D	6	290	490	37.7	-42.7	71.6	10.8	6.7	210/97
		17MY4205A	L	n	D	6	290	490	31.6	-42.4	71.5	6.3	2.7	210/97
		17MY4207A	L	n	D	6	290	490	31.4	-43.5	72.6	6.2	4.2	210/97
		17MY4208A	L	n	D	7	290	530	35.7	-41.9	70.8	9.4	2.6	210/97
		17MY4209A	L	n	D	6	290	490	31.8	-42.5	71.6	6.5	5	210/97
		17MY4210A	L	n	D	6	290	490	50.1	-44.9	74.7	19.6	4.6	210/97
		17MY4211A	L	n	D	6	290	490	31.8	-39	68	6.3	4	210/97
		17MY4203A	L	n	D	6	290	490	37.7	-40.4	69.3	10.8	3.2	210/97
MY43	24.546611°/95.669812	17MY4301A	L	y	D	7	350	590	54.1	-17	44.1	-24	1.1	035/27
		17MY4302A	L	y	D	7	350	590	54.6	-14.3	46	-21.8	1.5	035/27
		17MY4303A	L	y	D	7	350	590	53.8	-15.1	44.8	-22.2	1.1	035/27
		17MY4304A	L	y	D	7	350	590	58.4	-9.2	52	-18.9	0.8	035/27
		17MY4305A	L	y	D	7	350	590	51.8	-14.7	43.1	-20.9	1.2	035/27
		17MY4306A	L	y	D	7	350	590	60.5	-18.7	49.3	-28.4	1.9	035/27
		17MY4307A	L	y	F	9	35	100	48.4	-18.1	38.4	-22.5	1.1	035/27
		17MY4308A	L	y	D	7	350	590	51.4	-18.7	40.8	-24.3	1.6	035/27
		17MY4309A	L	y	F	9	35	100	56.1	-28.6	39.5	-35	1.2	035/27
		17MY4310A	L	y	D	7	350	590	59.5	-20.1	47.6	-29.1	1	035/27
		17MY4311A	L	y	D	7	350	590	52.4	-16.7	42.8	-23	2.1	035/27
		17MY4312A	L	y	D	7	350	590	54.1	-23.4	40.7	-29.6	2.5	035/27
		17MY4313A	L	y	D	7	350	590	54.4	-18.9	43.4	-25.8	1	035/27
MY44	24.547150°/95.668550	17MY4401A	L	y	F	9	35	100	24.3	-18.7	26.2	-27.7	1.4	270/10
		17MY4402A	L	n	D	6	400	590	50	-26.7	54.5	-32.8	8.2	270/10
		17MY4403B	L	y	F	12	35	120	202.9	6.8	203.7	15.9	0.9	270/10
		17MY4404A	L	n	D	7	400	620	128.7	41.6	120.7	47.4	6.3	270/10
		17MY4404B	L	n	F	7	35	80	17.5	-6.3	18.1	-15.7	7	270/10
		17MY4404C	L	n	F	7	35	80	100.5	74.1	66.2	73	7	270/10
		17MY4405A	L	n	D	5	400	560	57.8	-31.5	63.8	-36.3	7.7	270/10
		17MY4407A	L	n	D	5	400	560	50.7	-47.2	60.7	-52.8	6	270/10
		17MY4408A	L	n	D	4	400	530	40	-4.9	41	-12.4	2.1	270/10
		17MY4409A	L	n	D	5	400	560	75.4	-5	76.5	-7.3	10	270/10
		17MY4410A	L	n	D	5	400	560	62.6	-5.6	63.8	-10.1	4.2	270/10
		17MY4411A	L	n	D	6	400	590	33.8	-14.9	35.9	-23.1	3.3	270/10
MY45	24.544280°/95.667524	17MY4501A	P	y	D	10	130	490	128.9	25.8	129	-14.2	7.5	040/40
		17MY4502A	L	y	D	7	350	590	48.2	-21.3	31.7	-21.7	6.5	040/40
		17MY4504A	L	y	D	7	350	590	53.4	-22.2	34.9	-25.7	5.1	040/40
		17MY4505A	P	y	D	8	130	400	128.4	29.8	128.5	-10.2	14.9	040/40
		17MY4506A	P	y	D	10	130	490	128.5	34.2	128.6	-5.8	8.1	040/40
		17MY4508A	L	y	D	4	250	350	56.5	-11.5	45	-19.8	3.9	040/40
		17MY4509A	L	y	D	10	250	590	62.3	-30.9	34	-37.5	9.5	040/40
		17MY4510A	L	y	D	4	350	490	55.9	-24.6	34.9	-29	5.7	040/40
		17MY4511A	L	y	D	3	350	450	53.2	-26	31.8	-28.3	2.9	040/40

		17MY4512A	P	y	D	9	130	450	137	37.2	135.5	-2.5	15	040/40
		17MY4513A	P	y	D	12	130	560	320.6	8.9	326	47.8	10.8	040/40
		17MY4514A	L	y	D	4	250	350	59.6	-23.2	38.7	-30.3	5.1	040/40
		17MY4515A	P	y	D	8	130	400	294.9	-38	298	1.1	8.6	040/40
		17MY4516A	P	y	D	8	130	400	129.2	17.6	129.2	-22.4	14.9	040/40
MY51 (mafic)	24.153760°/95.54769(	19MY5101A	L	y	D	7	400	580	78.9	-3.4	78.9	-3.4	4.7	000/00
		19MY5102A	L	y	D	6	400	560	69.1	8.6	69.1	8.6	2	000/00
		19MY5104A	L	y	D	6	400	560	70.6	12.2	70.6	12.2	3.5	000/00
		19MY5105A	L	y	D	5	400	530	87.3	1.3	87.3	1.3	6.2	000/00
		19MY5111A	L	y	D	7	400	580	82.2	-0.6	82.2	-0.6	3.1	000/00
		19MY5113A	L	y	D	7	400	580	81.5	1	81.5	1	2.2	000/00
		19MY5114A	L	y	D	7	400	580	82.4	-4	82.4	-4	2	000/00
		19MY5117A	L	y	D	7	400	580	83.5	-5.6	83.5	-5.6	2.9	000/00
		19MY5107A	L	y	F	4	20	40	72.4	0.6	72.4	0.6	5.9	000/00
		19MY5109A	L	y	F	5	15	40	76.2	-4	76.2	-4	6.5	000/00
MY51 (felsic)	24.153760°/95.54769(	19MY5103A	L	y	D	7	400	580	74.7	-2.8	74.7	-2.8	2.3	000/00
		19MY5106A	L	y	D	7	400	580	74.1	-1.1	74.1	-1.1	2.6	000/00
		19MY5112A	L	y	D	7	400	580	66.9	5	66.9	5	2.1	000/00
		19MY5108A	L	y	D	7	400	580	75.7	2.9	75.7	2.9	2.2	000/00
		19MY5110A	L	y	D	7	400	580	76.8	-6	76.8	-6	2.8	000/00
		19MY5115A	L	y	D	7	400	580	75.9	-2.6	75.9	-2.6	2.8	000/00
		19MY5116A	L	y	D	7	400	580	67.6	5.6	67.6	5.6	2.4	000/00
MY53	24.173940°/95.53267(	19MY5301A	L	y	F	5	30	25	69.4	10.8	69.4	10.8	1.6	000/00
		19MY5302A	P	y	D	13	190	560	11.9	-50.4	11.9	-50.4	7.1	000/00
		19MY5304A	L	y	D	4	460	560	76.9	7.7	76.9	7.7	2.3	000/00
		19MY5305A	P	y	D	13	190	560	193.6	65.2	193.6	65.2	8.4	000/00
		19MY5308A	P	y	D	13	190	560	172.7	61.9	172.7	61.9	13.2	000/00
		19MY5310A	P	y	D	11	190	490	186.1	86.6	186.1	86.6	17.3	000/00
		19MY5313A	P	y	D	11	190	490	351.4	-65.6	351.4	-65.6	10.6	000/00
MY09	23.877040°/95.70317(	19MY0901A	L	n	D	9	250	490	40.7	-43.9	332.6	-24.4	13.3	017/80
		19MY0903A	L	n	D	3	280	370	51.3	-48.1	325.8	-30.4	3.7	017/80
		19MY0904A	L	n	D	4	250	340	63.1	-31.7	341.4	-44.6	7.3	017/80
		19MY0905A	L	n	D	5	250	370	73.2	-40.1	325.1	-47.9	9.6	017/80
		19MY0906A	L	n	D	5	250	370	85.8	-37.2	317.5	-57.1	6.9	017/80
		19MY0907A	L	n	D	4	250	340	62.2	-28	346.6	-44.9	8.6	017/80
		19MY0908A	L	n	D	5	250	370	65.1	-30.8	341.8	-46.4	4.2	017/80
		19MY0910A	L	n	D	5	250	370	61.7	-29.8	344.3	-43.9	3.2	017/80
		19MY0911A	L	n	D	3	150	370	63.3	-33.2	339.3	-44.2	0.5	017/80
		19MY0912A	L	n	D	4	280	370	58	-34.6	339.3	-39.5	4.3	017/80
		16MY0904B	L	n	D	4	250	350	50.8	-18.8	0.4	-35.6	1.9	017/80
		16MY0909B	L	n	D	6	290	450	69.6	-47.5	319	-41.4	12.4	017/80

site	Coordinates (Lat/Lon)	sample	Line or Plane	anchored	Demag type	nb points	step min	step max	Dec IS	inc IS	Dec TC	inc TC	mad value	bedding (str/dip)
ST01	20.440077°/94.27158	19ST0117A	L	y	F	5	300	600	256.4	-21.9	256.6	36.1	3.9	344/58
(Laungshe Fm.)		19ST0118A	L	y	F	6	300	700	248.5	-13.5	246.4	44.2	3.3	344/58
		19ST0119A	L	y	D	11	220	530	237.5	-27.2	237.2	28.6	6.5	344/58
		19ST0120A	L	y	F	5	200	600	259.8	-12.5	261.9	45.2	5.6	344/58
		19ST0121A	L	y	D	9	220	460	241.8	-25.9	241.2	30.9	7.6	344/58
		19ST0123A	L	y	F	7	200	800	258.7	-9.2	260.8	48.6	1.5	344/58
		19ST0124A	L	y	D	13	220	580	246.2	-24	245.4	33.4	1.8	344/58
		19ST0125A	L	y	F	9	200	900	256.7	-19.6	257.2	38.4	1.5	344/58
		19ST0126A	L	y	F	10	200	900	252.3	-16.2	251.6	41.8	2.2	344/58
		19ST0127A	L	y	F	9	200	900	241.5	-28.2	241.5	28.5	1.8	344/58
		19ST0128A	L	y	F	7	200	900	253.5	-25.1	253.4	32.9	3.2	344/58
		19ST0129A	L	y	F	8	200	800	246.1	-26.7	245.7	30.7	1.4	344/58
		19ST0130A	L	y	D	12	220	580	263.5	-18.3	265.5	39	2.2	344/58
		19ST0131A	L	y	D	15	220	580	264.6	-25.3	265.3	31.9	5.4	344/58
		19ST0132A	L	y	D	14	220	580	244.6	-25.8	244	31.4	3.3	344/58
		19ST0133A	L	y	D	13	220	580	248.8	-19.8	247.7	37.9	3.7	344/58
		19ST0134A	L	y	D	13	220	580	246	-28.1	245.9	29.3	6.7	344/58
		19ST0135A	L	y	D	13	220	580	254	-25.5	253.9	32.5	4.3	344/58
		19ST0136A	L	y	F	6	300	800	258.2	-12.1	259.7	45.8	1.8	344/58
		19ST0137B	L	y	F	13	200	1000	260.2	-20.3	261.2	37.4	1.6	344/58
		19ST0138A	L	y	D	13	220	580	268.1	-19.4	270.6	37	2.5	344/58
		19ST0139A	L	y	D	12	220	560	270.4	-30.2	269.8	26	5.7	344/58
		19ST0140A	L	y	D	13	220	580	260.5	-14	262.5	43.7	6.6	344/58
		19ST0141A	L	y	D	13	220	580	262.3	-25.3	262.8	32.2	3.6	344/58
		19ST0143A	L	y	F	6	300	800	268.5	-37.5	266.2	19.3	5.2	344/58
		19ST0148A	L	y	D	6	190	340	221.2	-37	227.6	14.3	6.4	344/58
ST02	20.485194°/94.24527	19ST0202A	L	y	D	10	250	530	129.4	-63	179.2	-7.2	6.2	295/75
(Paunggyi Fm.)		19ST0203A	L	y	D	11	250	560	296	-76.6	219.4	14.7	4.8	295/75
		19ST0203B	L	y	F	6	400	800	237.9	-57.5	222.7	12.7	3	295/75
		19ST0204A	L	y	D	6	250	400	148.4	-73.1	191.3	-5.4	2.4	295/75
		19ST0205A	L	y	D	8	340	560	184.6	-55	193.1	17.8	7.1	295/75
		19ST0206A	L	y	D	5	250	370	197.9	-70	202.9	4.8	5.2	295/75
		19ST0207A	L	y	D	9	250	490	166.5	-64.7	189.8	5	6.5	295/75
		19ST0208A	L	y	D	9	280	560	168	-53.6	183.6	14.3	7.1	295/75
		19ST0209A	L	y	D	10	250	530	172.8	-46.8	182	21.6	3.6	295/75
		19ST0210A	L	y	D	4	250	340	139.3	-54.8	173.7	0.8	5	295/75
		19ST0211A	L	y	D	5	250	370	157	-59.3	182.9	6	7.6	295/75

site	Coordinates (Lat/Lon)	sample	Line or Plane	anchored	Demag type	nb points	step min	step max	Dec IS	inc IS	Dec TC	inc TC	mad value		bedding (str/dip)
SW02	20.981750°/94.13597(	20SW0201B	L	y	D		9	220	460	44.6	39	60.8	0.7	3.1	012/55
(Laungshe Fm.)		20SW0202A	L	y	D		8	220	430	41.3	26.1	49.8	-6.6	5.4	012/55
		20SW0203A	L	y	D		9	220	460	43.7	25.6	51	-8.5	4.8	012/55
		20SW0211A	L	y	D		4	190	280	52.6	32.1	61.2	-8.8	11.6	012/55
		20SW0213A	L	y	D		9	220	460	39.8	46.3	63.5	8.3	3.6	012/55
		20SW0214B	L	y	D		9	220	460	23.8	49.8	59.5	18.9	4.1	012/55
		20SW0215A	L	y	D		7	220	400	26	42.4	54	13.5	4.1	012/55
		20SW0216A	L	y	D		9	220	460	39.9	57.5	72	15.9	4.5	012/55
		20SW0217A	L	y	D		9	220	460	35.1	48.3	62.8	12.1	3.5	012/55
		20SW0218A	L	y	D		9	220	460	3.3	3.5	9.6	8.6	4.1	012/55
		20SW0219A	L	y	D		9	220	460	12.3	11.6	21.4	5.8	3.8	012/55
		20SW0229A	L	y	D		7	220	400	49.9	25.2	54.8	-12.6	5.7	012/55
		20SW0230A	L	y	D		5	190	310	55.5	32.1	63.2	-10.3	7.5	012/55
		20SW0231A	L	y	D		9	220	460	66.8	54.2	81.9	4	13.2	012/55
		20SW0204A	L	y	D		7	220	400	150.3	14.2	153.6	-22.3	8.4	012/55
		20SW0205A	L	y	D		9	190	430	146.8	23.1	144.8	-17.6	7.3	012/55
SW03	21.116180°/94.17669(	20SW0301A	L	y	F		8	300	650	232.9	50.3	191.1	40	5.4	046/40
(Tilin Fm.)		20SW0304A	L	y	D		9	220	460	201.5	50	175.7	24.9	5.2	046/40
		20SW0305A	L	y	D		8	190	400	202.3	35.5	185.9	14	2.5	046/40
		20SW0306A	L	y	D		9	220	460	198	26.1	188.4	4.1	10.2	046/40
		20SW0307A	L	y	D		8	220	430	180.5	56.2	160.6	22.6	3.4	046/40
		20SW0303A	L	y	D		8	220	430	192.6	29.4	182.7	4.2	4.6	046/40
		20SW0308A	L	y	D		8	220	430	195.2	47.7	173.7	20.5	2.0	046/40
SW04	21.105140°/94.15290(	20SW0401A	L	y	D		7	220	400	0.6	-7.9	0.1	3.5	5.7	040/18
(Laungshe Fm.)		20SW0403A	L	y	D		8	220	430	25.2	1.1	26.2	5.4	8.4	040/18
		20SW0404A	L	y	D		6	220	370	350.6	-8.7	350.5	7.9	9.2	040/18
		20SW0405A	L	y	D		7	220	400	8.2	-11.8	6.3	0	4.1	040/18
		20SW0407A	L	y	D		6	220	370	3.2	-15.3	355.5	-0.3	4.5	040/18
		20SW0410A	L	y	D		9	220	460	334.1	-6.7	332.4	-6.4	14.9	040/18
		20SW0406A	L	y	D		7	220	400	19.3	-19.1	13.8	-10.5	8.6	040/18
		20SW0408A	L	y	D		7	220	400	7.7	-15.7	0.8	-2.5	6.9	040/18
SW07	21.225090°/94.19151(	20SW0703A	L	y	D		9	220	460	45.9	10.8	30.6	-37.9	6.3	000/71
(Tilin Fm.)		20SW0708A	L	y	D		7	220	400	27.9	16.1	25.3	-20.1	2.7	000/71
		20SW0709A	L	y	D		8	220	430	35.2	23.1	35.6	-22.5	4.7	000/71
		20SW0710A	L	y	D		9	220	460	27.3	28.5	36.3	-13.5	6.9	000/71
		20SW0711A	L	y	D		7	220	400	27.6	8.1	17.5	-23.4	4.9	000/71
		20SW0712A	L	y	D		7	220	400	17.1	4.1	9.2	-15.4	3.3	000/71
		20SW0713A	L	y	D		8	220	430	25.8	13.4	21.8	-19.6	3.5	000/71
		20SW0714A	L	y	D		7	220	400	27.5	16.2	25.3	-19.8	3.2	000/71
SW08	21.221870°/94.21148(	20SW0801A	L	y	D		9	220	460	189.7	-17.4	195	2.8	1.7	347/44
(Tabyin Fm.)		20SW0802A	L	y	D		9	220	460	191.5	-10.1	191.7	9.5	1.1	347/44
		20SW0803A	L	y	D		9	220	460	189.3	-14.8	193.1	4.5	1.8	347/44
		20SW0804A	L	y	D		9	220	460	184.5	-13.5	188.7	2.5	1.1	347/44
		20SW0805A	L	y	D		9	220	460	182.8	-14.2	187.9	0.9	0.5	347/44
		20SW0806A	L	y	D		9	220	460	185.4	-17.7	192.1	-0.1	2.5	347/44
		20SW0807A	L	y	D		9	220	460	187.1	-18.6	194	0.2	1.4	347/44
		20SW0808A	L	y	D		9	220	460	189.6	-24.7	199.6	-2.9	1.8	347/44
		20SW0809A	L	y	D		9	220	460	202	-30.7	212	-1.1	2.6	347/44
		20SW0810A	L	y	D		9	220	460	202.9	-34.5	214.8	-3.8	1.5	347/44
		20SW0811A	L	y	D		9	220	460	200	-28.8	209.5	-0.5	1.4	347/44
		20SW0812A	L	y	D		9	220	460	198.8	-31.8	210.4	-3.6	1.4	347/44
		20SW0813A	L	y	D		9	220	460	195	-29.5	206.4	-3.7	1	347/44
		20SW0814A	L	y	D		9	220	460	197.4	-19.9	202.4	5.3	1.7	347/44
		20SW0815A	L	y	D		9	220	460	207.6	-30.1	215.8	2	2.2	347/44
		20SW0816A	L	y	D		9	220	460	203.3	-31.8	213.6	-1.3	1.4	347/44

site	Coordinates (Lat/Lon)	sample	Line or Plane	anchored	Demag type	nb points	step min	step max	Dec IS	inc IS	Dec TC	inc TC	mad value	bedding (str/dip)
PD03	21.68631°/94.806340°	19PD0301A	L	y	D	9	280	530	3.7	-11.5	3.9	8.3	4.8	113/21
		19PD0302A	L	y	D	4	490	620	3.3	-13.2	3.7	6.6	5.9	113/21
		19PD0303A	L	y	D	4	500	620	3.5	-9.3	3.4	10.4	4.2	113/21
		19PD0304A	L	y	D	4	490	620	2.9	-13.9	3.4	5.8	3.7	113/21
		19PD0305A	L	y	D	8	430	640	9.4	-8.4	9.3	12	3.8	113/21
PD04	21.706944°/94.823611	19PD0401A	L	y	D	6	490	660	11	-9.8	11.7	-0.6	2.6	141/12
		19PD0402A	L	y	D	8	460	660	0.9	4	359.6	11.6	4.6	141/12
		19PD0403A	L	y	F	16	200	1500	5	4.9	3.6	13	1.4	141/12
		19PD0405A	L	y	D	8	460	660	15.9	-5.8	16	4	3.3	141/12
		19PD0406A	L	y	D	8	460	660	5.4	-19.7	7.7	-11.2	3.4	141/12
		19PD0407A	L	y	D	3	560	620	25.9	3.2	25.2	14	3.8	141/12
		19PD0408A	L	y	F	12	400	1500	9.7	-4.1	9.7	4.9	3.5	141/12
		19PD0410A	L	y	D	3	530	580	7.1	5.7	5.6	14.2	6	141/12
PD05	21.733980°/94.836820	19PD0502A	L	y	D	9	280	530	347.6	4.7	347.1	3.8	6.1	175/06
		19PD0504A	L	y	D	3	400	460	4	0.8	3.8	1.7	6.9	175/06
		19PD0508A	L	y	D	6	310	460	241.7	13.2	242.2	7.7	3.8	175/06
		19PD0510A	L	y	D	3	530	580	204.1	5.1	204.4	2.2	4.4	175/06
		19PD0511A	L	y	D	3	530	580	203.3	2.2	203.4	-0.6	14.3	175/06
PD06	21.762160°/94.842190	19PD0604A	L	y	D	10	250	540	193.5	-3.7	193.8	-3	6.5	005/05
		19PD0605A	L	y	D	12	250	580	203.9	7	203.2	8.6	4.7	005/05
		19PD0610A	L	y	D	13	340	680	215	20.8	213.2	23.2	7.4	005/05
PD07	21.761000°/94.842070	19PD0701A	L	y	D	4	250	340	174.6	7	174	6	9	005/05
		19PD0702A	L	y	D	9	370	620	211.8	4.4	211.4	6.6	6.3	005/05
PD08	21.734330°/94.723640	19PD0804A	L	y	D	3	620	660	197.2	12.8	197.3	-12.2	15	134/28
PD09	21.754110°/94.652970	19PD0903A	L	y	F	3	1300	1500	0.9	3.4	1.3	12	0.7	074/09
		19PD0904A	L	y	D	3	370	430	191.7	1.4	191.9	-6.6	5.1	074/09
		19PD0905A	L	y	D	9	400	640	162.5	-1.6	162.5	-10.6	4.9	074/09
		19PD0906A	L	y	D	6	430	640	171	1.2	171	-7.8	11.9	074/09
		19PD0909A	L	y	D	3	530	580	174.9	2.1	174.9	-6.7	4.7	074/09

Kalewa Eocene data first published in: *Westerweel, J., Roperch, P., Licht, A., Dupont-Nivet, G., Win, Z., Poblete, F., … Aung, D. W. (2019). Burma Terrane part of the Trans-Tethyan arc during collision with India according to palaeomagnetic data. Nature Geoscience. https://doi.org/10.1038/s41561-019-0443-2*

site	Coordinates (Lat/Lon)	sample	Line or Plane	anchored	Demag type	nb points	step min	step max	Dec IS	inc IS	Dec TC	inc TC	mad value	bedding (str/dip)
MA	23.245770°/94.266630	16MA0004A	L	y	D	4	260	340	159.5	17.6	155.5	-3.4	9.9	011/37
		16MA0005A	L	y	D	5	210	310	181.9	18.4	172.8	9.3	6.1	011/37
		16MA0006A	L	y	D	5	220	340	190.6	-2.7	192.4	-2.4	5.1	011/37
		16MA0009A	L	y	D	5	220	340	191.5	-12.2	198.8	-9.4	11.2	011/37
		16MA0016A	L	y	D	5	210	310	354.6	37.8	25.1	38.6	3.1	011/37
		16MA0020A	L	y	D	6	210	340	341.9	25.8	4.6	37.6	4	011/37
		16MA0021A	L	y	D	4	220	310	9.6	9	15.3	8.1	1.5	011/37
		16MA0023A	L	y	D	6	210	340	12.6	16.7	22.5	12.3	2.7	011/37
		16MA0024A	L	y	D	7	220	400	5.3	16.4	16.6	16.4	2.7	011/37
		16MA0026A	L	y	D	6	210	340	348.2	25.9	9.9	34	4.2	011/37
		16MA0027A	L	y	D	9	220	440	3.7	6	8.8	9.1	3.3	011/37
		16MA0028A	L	y	D	7	235	405	357.7	-6.2	356.6	2.9	1.9	011/37
		16MA0030A	L	y	D	8	220	425	358.4	14.7	10	19.3	2.1	011/37
		16MA0031A	L	y	D	9	210	440	2.5	9.2	9.8	12.5	2.3	011/37
		16MA0032A	L	y	D	6	235	370	14.2	5.6	16.9	2.6	4.5	011/37
		16MA0038A	L	y	D	7	210	370	27.7	14.8	33.1	2.1	6.9	011/37
		16MA0046A	L	y	D	8	235	500	14.7	5.8	17.4	2.4	3.1	011/37
		16MA0047A	L	y	D	9	210	475	24.8	31.4	40.8	17.1	3.6	011/37
		16MA0048A	L	y	D	11	220	500	18.5	26.8	33.4	16.8	5.2	011/37
		16MA0049A	L	y	D	8	210	410	8.9	25.7	25.6	21.5	3.6	011/37
		16MA0051A	L	y	D	5	220	340	10.8	20.5	23.5	16.4	7.8	011/37
		16MA0052A	L	y	D	7	210	370	2.6	24.5	20.1	24.3	4.3	011/37
		16MA0054A	L	y	D	7	250	425	3.2	-21.4	351.9	-12.4	5.4	011/37
		16MA0061A	L	y	D	9	210	440	15.4	-8.6	9.3	-9.5	6.1	011/37
		16MA0062A	L	y	D	4	235	310	6.3	-8.2	2.3	-3.8	3	011/37
		16MA0069A	L	y	F	7	24	30	20.1	8.3	23.2	1.2	4.3	011/37
		16MA0070A	L	y	F	5	24	25	2.5	8.9	9.7	12.2	3.5	011/37
		16MA0072A	L	y	D	5	250	370	338.9	-1.4	343.6	17.5	7.3	011/37
		16MA0075A	L	y	F	7	24	30	347.1	15.5	1.3	26.6	5.9	011/37
		16MA0080A	L	y	D	5	250	370	3.9	-2.6	3.7	2.2	9.6	011/37
		16MA0084A	L	y	D	8	240	440	333.9	-9.5	334.9	13.1	2.3	011/37
		16MA0086A	L	y	D	7	250	425	347.8	-36.3	331.5	-16.4	3.9	011/37
		16MA0088A	L	y	D	7	210	370	16.6	-2.1	14.2	-5.1	6.4	011/37
		16MA0094A	L	y	D	9	210	440	15.7	-19.9	2.3	-18.6	4.1	011/37
		16MA0095A	L	y	D	8	220	425	8.7	-12.8	1.4	-8.8	5.6	011/37
		16MA0096A	L	y	D	5	0	210	25	18.1	40.5	15	4.9	011/37
		16MA0111A	L	y	D	12	235	560	14.5	32.7	34.6	23.7	4.1	011/37
		16MA0112A	L	y	D	7	260	500	31.4	18.2	37.9	2.9	7.4	011/37
		16MA0114A	L	y	D	9	235	475	42.4	3.2	38.8	-15.6	4.5	011/37
		16MA0116A	L	y	D	13	250	560	21.1	22	32.3	11.6	5.1	011/37
		16MA0117A	L	y	D	9	235	475	2.6	35.2	28.2	32.2	6.3	011/37
		16MA0120A	L	y	D	12	235	560	37.8	21.2	44.6	2	3	011/37
		16MA0125A	L	y	D	9	235	475	7.5	-1.5	7.3	0.9	3	011/37
		16MA0126A	L	y	D	7	220	400	5.6	1.1	7.4	4.1	7	011/37
		16MA0127A	L	y	D	4	285	370	20.6	-14.1	9.9	-17	5.7	011/37
		16MA0130A	L	y	D	8	220	425	8.1	12.1	16	11.4	4.8	011/37
		16MA0132A	L	y	D	7	235	410	345	25.1	6.6	35.3	7.4	011/37
		16MA0134A	L	y	F	7	24	30	355.1	-1	357.6	8.6	5.1	011/37
		16MA0136A	L	y	F	8	25	30	353.2	4.9	359.5	14.6	8.1	011/37
		16MA0138A	L	y	D	12	235	560	355.4	25.6	15.3	29.4	9.1	011/37
		16MA0148A	L	y	D	12	210	530	344.6	-1.8	348.4	14	5.2	011/37
		16MA0156A	L	y	D	11	240	560	163.4	-24.7	185.1	-36	2.2	011/37
		16MA0159A	L	y	D	7	240	440	9.4	-16.7	359.6	-12.3	10.1	011/37
		16MA0169A	L	y	D	12	235	560	337.5	-0.3	343	19.2	7.2	011/37
		16MA0170A	L	y	D	13	210	560	11.9	5.8	15.2	4.1	3.8	011/37
		16MA0171A	L	y	D	12	210	560	356.5	16.9	10	22.1	3	011/37
		16MA0172A	L	y	D	11	235	560	348.9	16	3.1	26	4.4	011/37
		16MA0173A	L	y	D	13	210	560	358.1	15.6	10.4	20.2	3.1	011/37
		16MA0174A	L	y	D	12	210	560	351.8	19.2	7.8	26.7	3.3	011/37
		16MA0178A	L	y	D	12	235	560	343.3	3	350	18.8	7	011/37
		16MA0179A	L	y	D	12	235	560	0.4	6.7	6.6	11.7	3.6	011/37
		16MA0195A	L	y	D	11	240	560	198.1	3.9	194.3	7.4	4.9	011/37
		16MA0196A	L	y	D	14	235	210	183.6	-6.6	189.1	-9.7	3.5	011/37
		16MA0197A	L	y	D	13	210	560	177.4	-0.2	180.2	-8.3	1.8	011/37
		16MA0198A	L	y	D	6	265	410	190.4	3.7	188.3	2.6	2	011/37
		16MA0199A	L	y	D	12	235	560	180.4	-10.5	188.9	-14.7	3	011/37
		16MA0200A	L	y	D	13	210	560	176.7	-16.7	190.1	-21.8	3.9	011/37
		16MA0207A	L	y	D	13	240	560	157.6	-18.2	174.8	-34.4	3.1	011/37
		16MA0224A	L	y	D	8	235	490	186.4	8.3	182.3	3.9	9.9	011/37
		16MA0225M	L	y	D	9	235	475	158.4	-2.3	165.2	-20.9	5.5	011/37
		16MA0229A	L	y	D	13	210	560	355.5	14.3	7.4	20.6	3.5	011/37
		16MA0240A	L	y	D	8	235	440	2.4	10.9	10.8	13.9	4.5	011/37
		16MA0250A	L	y	D	7	235	370	5.3	-2.5	5	1.4	10.4	011/37
		16MA0251A	L	y	D	11	235	560	1.4	-15.4	354.1	-6.6	2.9	011/37
		16MA0252A	L	y	D	11	235	560	10.9	-7.1	6.7	-5.6	1.9	011/37
		16MA0254A	L	y	D	10	235	530	353.9	29.6	17.4	33.2	7.5	011/37
		16MA0257A	L	y	D	11	235	560	328.8	9.6	340.6	32.1	6.7	011/37
		16MA0275A	L	y	D	9	220	460	348.2	-10.6	346.4	4.7	2.4	011/37
MB	23.239167°/94.262500	16MB0002A	L	y	D	8	220	430	192.1	5.1	188.4	4.9	5.4	011/40
		16MB0004A	L	y	D	9	220	460	199.1	-9.6	203.3	-1.9	4	011/40
		16MB0005A	L	y	D	7	220	400	197	0.6	195.1	4.6	2.9	011/40
		16MB0009A	L	y	D	8	220	430	168.1	-4.8	176.1	-17.9	4	011/40
		16MB0010A	L	y	D	9	220	460	182.9	-4.5	187.6	-8.3	5.7	011/40
		16MB0012A	L	y	D	8	220	430	173.3	-4.9	180.3	-14.8	2.1	011/40
		16MB0016A	L	y	D	9	220	460	193.5	0.7	192.4	2.4	3.8	011/40
		16MB0018A	L	y	F	4	25	40	201.3	18.4	186.4	20.9	4.5	011/40
		16MB0019A	L	y	D	9	220	460	221.6	-29.8	232.2	-5.3	2.8	011/40
		16MB0025A	L	y	D	8	220	430	347.2	-11.1	345.5	5.8	4.9	011/40
		16MB0027A	L	y	D	8	220	430	18.5	11.1	23.7	3.4	3.9	011/40
		16MB0029A	L	y	D	8	220	430	5.6	6.1	10.7	7.8	3.4	011/40
		16MB0030A	L	y	D	9	220	460	9.3	28	28.5	21.8	3.1	011/40
		16MB0031A	L	y	D	8	220	430	28.1	8.4	29.4	-4.6	6.3	011/40
		16MB0032A	L	y	D	7	250	430	354.9	22.5	14.1	26.9	7.9	011/40
		16MB0036A	L	y	D	7	220	400	0.6	20	16.4	21.5	7.1	011/40
		16MB0037A	L	y	D	6	220	370	1.2	13.2	12	16	10.4	011/40
		16MB0038A	L	y	D	7	220	400	4.1	10.3	12.2	12	6.1	011/40
		16MB0040A	L	y	D	8	220	430	19.2	19.8	29.9	9.7	6	011/40

		16MB0041A	L	y	D	9	220	460	20	23.5	32.9	12	4.4	011/40
		16MB0042A	L	y	D	8	220	430	7.7	10.3	15.1	9.7	4.4	011/40
		16MB0044A	L	y	D	9	220	460	4	-22.8	350.8	-13.3	3.9	011/40
		16MB0045A	L	y	D	8	250	460	341.6	13.6	356.7	28.8	4	011/40
		16MB0047A	L	y	D	9	220	460	7.1	19	20.5	16.6	7.2	011/40
		16MB0050A	L	y	D	8	220	430	17.3	17.8	27.1	9.3	7.3	011/40
		16MB0058A	L	y	F	5	20	40	201.6	10.7	192	15.3	2.9	011/40
		16MB0059A	L	y	F	6	20	45	173.5	-6.1	181.3	-15.5	1.1	011/40
		16MB0060A	L	y	F	6	20	45	215.9	-7.1	214.8	10.3	7.7	011/40
		16MB0061A	L	y	F	5	20	45	213.2	6.6	204	19.5	5	011/40
		16MB0064A	L	y	F	5	20	40	171	17.3	164.7	1.3	7.1	011/40
		16MB0082A	L	y	D	10	130	400	353.4	17.1	8.9	23.9	0.9	011/40
		16MB0085A	L	y	D	7	250	430	354.1	8.1	3.1	16.8	8.5	011/40
		16MB0088A	L	y	D	7	250	430	12.3	-11.1	4.7	-9.6	5.9	011/40
		16MB0091A	L	y	D	8	220	430	1.8	6.3	7.9	10.4	4.5	011/40
		16MB0092A	L	y	D	9	220	460	345.6	0	350.9	15.7	9.1	011/40
		16MB0098A	L	y	D	8	220	430	22.1	6.4	23.5	-2.5	3.9	011/40
MC	23.241633°/94.259417	17MC0001A	L	y	D	8	220	430	204.3	-0.6	202	7	4.6	013/40
		17MC0004A	L	y	F	7	34	15	194.3	5.5	190.3	5.4	4.4	013/40
		17MC0004A	L	y	D	5	310	430	195.2	7.7	189.6	7.6	2.7	013/40
		17MC0005A	L	y	F	12	22	20	207.7	-0.3	204.4	9.5	5	013/40
		17MC0006A	L	y	F	20	22	30	189.3	-8.9	195.8	-8.9	4.9	013/40
		17MC0007A	L	y	F	9	31	15	208.7	18.6	192.3	24.5	4.7	013/40
		17MC0011A	L	y	D	7	250	430	205.2	-0.8	202.8	7.5	4.2	013/40
		17MC0012A	L	y	D	5	310	430	202.8	8.7	194.7	13.3	9.8	013/40
		17MC0013A	L	y	F	10	20	50	202.4	12.8	191.7	16.1	0.9	013/40
		17MC0015A	L	y	F	9	34	20	213.6	10.2	202.2	21.3	5.5	013/40
		17MC0018A	L	y	F	11	22	15	196.5	23.3	179.8	20.1	8.5	013/40
		17MC0020A	L	y	D	6	220	370	215.4	1.4	209.6	15.6	7	013/40
		17MC0021A	L	y	D	5	340	460	180	-10.6	189.8	-16.1	7.4	013/40
		17MC0027A	L	y	F	11	25	20	192.9	17.5	181.3	13.6	2.3	013/40
		17MC0028A	L	y	D	7	250	430	206.1	26.8	184.1	28.7	1.7	013/40
		17MC0029A	L	y	F	11	22	15	211.6	9.5	201.1	19.5	4.2	013/40
		17MC0030A	L	y	D	7	220	400	183.6	-13.9	194.8	-16.3	11.8	013/40
		17MC0031A	L	y	F	9	20	50	178	-29.1	202.3	-30.9	0.6	013/40
		17MC0032A	L	y	F	7	34	15	175.4	14.4	170.3	0.4	3.8	013/40
		17MC0034A	L	y	F	9	20	50	209.1	4.6	202.4	14.1	0.8	013/40
		17MC0036A	L	y	F	13	22	20	197.2	-6.7	200.4	-2.1	2.1	013/40
		17MC0042A	L	y	F	11	22	15	200.1	-3.9	200.9	1.9	5	013/40
		17MC0043A	L	y	D	8	220	430	198	22.1	181.8	20.3	9.5	013/40
		17MC0044A	L	y	F	19	25	30	219.1	9.9	207	24.5	1.9	013/40
		17MC0046A	L	y	D	7	220	400	197.3	-12.7	204.4	-6.7	4.3	013/40
MD	23.245600°/94.258483	17MD0001A	L	y	D	8	220	430	25.7	15.6	32.4	4.4	4.3	013/38
		17MD0003A	L	y	F	9	20	50	43.1	-10.1	31.2	-26.6	5.1	013/38
		17MD0007A	L	y	D	4	340	430	13.8	4.9	16.6	3.1	1.5	013/38
		17MD0009A	L	y	D	7	130	310	39.1	16.9	43.6	-2	3.8	013/38
		17MD0014A	L	y	D	6	160	310	211	29.9	186.3	34.2	5.2	013/38
		17MD0015A	L	y	F	12	22	15	193.4	4.8	190.3	4.4	4.4	013/38
		17MD0016A	L	y	F	9	28	15	187.4	-0.8	189	-3.7	4	013/38
		17MD0017A	L	y	D	8	220	430	198	-3.9	199.2	0.3	3.4	013/38
		17MD0019A	L	y	D	5	280	400	198.1	4	194.4	6.6	6.6	013/38
		17MD0021A	L	y	F	12	22	20	189.9	-19	202.6	-16.4	3.2	013/38
		17MD0026A	L	y	F	11	20	70	223.9	11.1	211.2	27.8	3.1	013/38
MY32	23.220730°/94.251770	16MY3206A	L	y	D	3	210	290	13.5	25.9	29.5	14.2	2.4	007/43
		16MY3210A	L	y	D	3	210	290	14.8	31.5	34.4	17.3	2.5	007/43
		16MY3212A	L	y	D	3	170	250	25.1	11.7	28	-3.7	1.2	007/43
		16MY3213A	L	y	D	3	170	250	24	11.7	27.3	-3.1	2.1	007/43
		16MY3214A	L	y	D	3	210	290	23.6	4.9	22.4	-7.9	2.8	007/43
		16MY3215A	L	y	D	3	170	250	28	10	29.1	-6.8	1.2	007/43
MY33	23.233960°/94.256950	16MY3307A	L	y	D	3	170	250	5.8	26.3	23.7	18.4	0.8	005/42
		16MY3308B	L	y	D	3	210	290	26.6	21.6	35	2.2	1.6	005/42
		16MY3309B	L	y	D	3	170	250	17.5	15.7	24.6	3.2	1.7	005/42
		16MY3310A	L	y	D	4	170	290	176	-9.1	184.4	-12.4	0.9	005/42
		16MY3315A	L	y	D	3	210	250	188.6	8.8	181.5	9.3	1.4	005/42
		16MY3316A	L	y	D	3	210	290	180	5.7	177.3	1.2	2.2	005/42
		16MY3318B	L	y	D	3	210	290	192.9	4.5	187.7	8.9	1.4	005/42
		16MY3319A	L	y	D	3	170	250	185.8	13.4	176.3	10.8	1.7	005/42
		16MY3320B	L	y	D	3	210	290	183.2	-9.5	190	-7.9	2.3	005/42
		16MY3321B	L	y	D	3	170	250	185.3	-8.2	190.6	-5.5	1.4	005/42
		16MY3322A	L	y	D	4	170	290	193.3	1.8	189.8	7.2	2.4	005/42
		16MY3323A	L	y	D	3	170	250	189.5	-3.2	190.3	0.9	2.7	005/42

site	Coordinates (Lat/Lon)	sample	Line or Plane	anchored	Demag type	nb points	step min	step max	Dec IS	inc IS	Dec TC	inc TC	mad value	bedding (str/dip)
TP01	21.234998°/94.790909	17TP0101A	L	y	F	11	100	400	350.9	10.6	349.7	5.8	1.2	199/10
		17TP0102A	L	y	D	8	220	430	356.3	12.5	354.6	8.5	1.3	199/10
		17TP0103A	L	y	D	8	220	430	353.5	12	352	7.5	2.7	199/10
		17TP0104A	L	y	D	8	220	430	345.8	14.5	344.1	8.8	1.8	199/10
		17TP0105A	L	y	D	8	220	430	350.9	10.1	349.7	5.2	1.7	199/10
		17TP0106A	L	y	D	8	220	430	358.9	17.6	356.3	13.9	3	199/10
		17TP0107A	L	y	D	8	220	430	344.5	7.4	343.9	1.6	2	199/10
		17TP0108A	L	y	D	8	220	430	356.8	19.9	353.8	15.8	2.5	199/10
		17TP0109A	L	y	D	8	220	430	2	15.1	359.7	11.9	5.4	199/10
		17TP0110A	L	y	D	8	220	430	339.5	15.4	337.9	8.9	2.2	199/10
		17TP0111A	L	y	D	8	220	430	343.1	15.2	341.4	9.1	2.9	199/10
		17TP0112A	L	y	D	8	220	430	357.3	16.5	354.9	12.5	1.5	199/10
		17TP0113A	L	y	D	8	220	430	348.4	5.6	348	0.4	2.3	199/10
TP02	21.135750°/94.794860	19TP0201A	L	y	D	9	250	490	353.6	11.4	352.2	3.6	7.3	209/13
		19TP0202A	L	y	F	8	300	800	358.3	2.8	358.4	-3.9	12.1	209/13
		19TP0203A	L	y	D	9	250	490	343.6	9.8	342.8	0.4	11.2	209/13
		19TP0204A	L	y	D	9	250	490	340.3	11.9	339.3	2	7.8	209/13
		19TP0205A	L	y	D	4	250	340	350.3	20.5	347.4	12	8.3	209/13
		19TP0207A	L	y	D	9	250	490	345.1	10	344.2	0.8	3.9	209/13
		19TP0208A	L	y	D	4	220	310	358.3	20.9	354.8	13.8	4.7	209/13
		19TP0209A	L	y	F	7	300	700	349.6	19.8	346.9	11.2	3.7	209/13
		19TP0210A	L	y	D	9	250	490	352.9	0.4	353.5	-7.3	8.2	209/13
TP03	21.133230°/94.797500	19TP0301A	L	y	D	9	250	490	11.2	17.8	23.9	2.4	4.1	005/65
		19TP0302A	L	y	D	9	280	530	13	18.5	25.3	1.2	5	005/65
		19TP0304A	L	y	D	9	250	490	21.8	31.2	40.3	0.1	4.5	005/65
		19TP0305A	L	y	D	9	250	490	12.7	8.5	16.2	-2.9	4.9	005/65
		19TP0306A	L	y	F	12	300	1200	2.4	21.7	24.1	11.6	8.4	005/65
		19TP0306B	L	y	D	10	310	580	3.4	18.5	21.5	9.5	6	005/65
		19TP0307A	L	y	D	9	250	490	6.1	19.6	23.5	7.5	5.1	005/65

site	Coordinates (Lat/Lon)	sample	Line or Plane	anchored	Demag type	nb points	step min	step max	Dec IS	inc IS	Dec TC	inc TC	mad value	bedding (str/dip)
NM01	23.272972°/94.305833	17NM0101A	L	y	D	13	190	590	359.5	38.6	29.6	37.2	4.8	012/37
		17NM0102A	L	y	D	15	190	640	4.4	37.8	32.1	33.8	4.9	012/37
		17NM0103A	L	y	D	7	460	660	356.5	32.9	22.5	35	2.7	012/37
		17NM0104A	L	y	F	21	200	1800	19	35.8	40.3	24.3	0.6	012/37
		17NM0105A	L	y	D	9	190	430	341.5	21.6	1.1	35.6	1.3	012/37
		17NM0106A	L	y	D	16	190	660	315	40.1	355.2	64.5	4.3	012/37
		17NM0107A	L	y	D	6	460	640	357.5	41	30.6	39.9	3.3	012/37
		17NM0108A	L	y	D	10	190	460	355.6	26.5	16.6	30.8	3.9	012/37
		17NM0109A	L	y	D	13	220	580	2.5	24.7	20.4	25.4	4.4	012/37
		17NM0110A	L	y	D	13	220	580	8.6	30.3	29.1	26	5.7	012/37
NM02	23.272972°/94.305833	17NM0201A	L	y	D	15	190	640	351.3	32.3	18.1	37.6	2.1	012/37
		17NM0202A	L	y	D	6	490	660	343.6	41.9	22.6	48.6	2.4	012/37
		17NM0203A	L	y	D	12	190	540	352.5	37.4	23.7	40.5	7.9	012/37
		17NM0206A	L	y	D	9	190	430	333.5	44.8	19.5	56.2	8.5	012/37
		17NM0208A	L	y	D	7	190	370	55.7	46.2	70.6	16.9	8.2	012/37
		17NM0210A	L	y	D	6	220	370	2.7	33.7	27.6	31.9	4	012/37
NM03	23.238417°/94.309722	17NM0301A	L	n	D	5	430	590	196	27.6	174.6	34.5	13.8	354/35
		17NM0306A	L	y	D	8	220	430	215.3	-17.6	218	6.3	6.4	354/35
		17NM0307A	L	y	D	11	280	620	188.4	-0.8	186.4	7.3	4.2	354/35
NM04	23.238417°/94.309722	17NM0401A	L	y	D	6	220	370	146.2	-38.7	179.1	-46.4	7.6	354/35
		17NM0403A	L	y	D	7	250	430	197	-19.4	203.7	-3.8	6.3	354/35
		17NM0406A	L	y	D	7	190	370	196.2	32.2	170.8	38	5.8	354/35
NM05	23.238417°/94.309722	17NM0501A	L	y	D	9	190	400	153.5	-1.3	157.8	-13	6.6	354/35
		17NM0502A	L	y	D	7	190	370	192.1	12	182	19.9	5.8	354/35
		17NM0503A	L	y	D	11	190	490	146.3	-19.1	162.4	-31.6	5.4	354/35
		17NM0505A	L	y	D	14	190	620	142.1	-19.9	159.2	-34.6	6.8	354/35
		17NM0508A	L	y	D	16	190	660	154.2	-8.4	162.5	-18.5	4.9	354/35
NM06	23.276806°/94.310556	17NM0601A	L	y	D	10	190	460	352.1	29.7	16.4	35.3	7.1	012/37
		17NM0603A	L	y	D	7	190	370	42.7	3.5	39.4	-14.7	13.5	012/37
		17NM0605A	L	n	D	13	190	590	42.2	52.2	65.9	26.6	6	012/37
		17NM0606A	L	y	D	11	190	490	11.9	11	18.7	9.1	3.8	012/37
		17NM0609A	L	y	D	9	190	430	326.4	19.9	345.2	42.8	8.1	012/37
NM08	23.276500°/94.311389	17NM0801A	L	y	D	9	190	430	60.7	32.9	68.4	3.3	2.8	012/37
		17NM0807A	L	n	D	10	160	430	321.2	63.4	55.3	67.6	5.7	012/37
		17NM0808A	L	y	D	16	190	660	175	-28.7	197.9	-32.8	2.9	012/37
NM09	23.276500°/94.311389	17NM0902A	L	y	D	7	190	370	189.8	-17.7	201.2	-15.6	6.4	012/37
		17NM0905A	L	y	D	8	190	430	150.1	-13	164.1	-35.1	5.6	012/37
NM10	23.277222°/94.311667	17NM1006A	L	y	D	6	190	340	157.5	-25.5	180.7	-41	9.5	012/37
		17NM1007A	L	y	D	7	190	370	151.8	-7.3	162.1	-29.4	5.6	012/37
NM12	23.283830°/94.309650	17NM1201A	L	y	D	6	190	340	156.3	-7.5	164.4	-29.8	8	023/32
		17NM1202A	L	y	D	9	190	430	207.2	4.7	204.2	6	11.8	023/32
		17NM1203A	L	y	D	7	190	370	173.8	-1.1	178.2	-16.2	9	023/32
		17NM1204A	L	y	D	8	190	400	145.1	-42.9	179.8	-65.2	6.8	023/32
		17NM1205A	L	y	D	9	190	430	178.7	-20.2	193.5	-30.1	5.4	023/32
NM13	23.285694°/94.308611	17NM1301A	L	y	D	9	190	430	347	37.7	15.7	45.4	4.1	014/32
		17NM1302A	L	y	D	9	190	430	344.4	45.7	22.2	52.4	6	014/32
		17NM1303A	L	y	D	10	190	460	0.5	20.3	14	24.5	7.2	014/32
		17NM1304A	L	y	D	13	220	580	356.2	8.3	3.2	16.7	5.1	014/32
		17NM1305A	L	y	D	8	220	430	350	19.6	4.4	29.4	5.1	014/32
		17NM1306A	L	y	D	10	190	460	349.9	22.2	6	31.6	4.6	014/32
		17NM1308A	L	y	D	9	190	430	26.4	29.3	40.2	18.6	6	014/32
		17NM1309A	L	y	D	9	190	430	355.8	21.9	10.9	28.3	6.7	014/32
NM14	23.371020°/94.325380	19NM1407A	L	y	D	9	220	460	3.4	22.8	19.8	23.4	7.4	012/37
NM15	23.215540°/94.295430	19NM1502A	L	y	D	4	190	280	29.4	30	41.1	15.2	2.5	007/31
		19NM1503A	L	y	D	7	190	370	338.6	23	354.9	34.3	7.8	007/31
		19NM1504A	L	y	D	7	190	370	1.4	13.1	9.2	14.4	8.1	007/31
		19NM1507A	L	y	D	7	190	370	120.9	-31.3	137.4	-58.1	10.3	007/31
		19NM1508A	L	y	D	7	190	370	341.2	29.8	2.1	38.6	7.5	007/31
		19NM1509A	L	y	D	13	220	580	353.9	11.3	1.7	16.7	9.8	007/31
NM16	23.231820°/94.309507	19NM1601A	L	y	D	3	280	340	190.4	25.5	179.1	17.4	7.4	020/29
		19NM1602A	L	y	D	3	400	460	151.6	24.8	147.2	2	12.6	020/29
		19NM1604A	L	y	D	6	280	430	207.7	1.6	206.1	4.9	6.5	020/29
NM17	23.231870°/94.307485	19NM1701A	L	y	D	7	310	490	181.2	-22.3	197.5	-30.1	6.1	022/33
		19NM1702A	L	y	D	6	280	430	177.1	-15.5	189.5	-26.7	3.6	022/33
		19NM1703A	L	y	D	6	250	400	166.5	-30.7	190.7	-44.7	5.6	022/33
		19NM1705A	L	y	D	14	250	640	194.8	-33	216.2	-31.2	4.4	022/33
		19NM1706A	L	y	D	12	250	580	181.7	-30.5	203.9	-36.3	4.5	022/33
		19NM1707A	L	y	D	13	250	620	193.9	-39.8	220.9	-36.8	4.2	022/33
		19NM1708A	L	y	D	14	250	640	167.6	-16.6	181.3	-32.5	5.5	022/33
		19NM1709A	L	y	D	6	250	400	160.7	-14.6	173.3	-34.2	8.6	022/33
NM18	23.231410°/94.306650	19NM1802A	L	y	D	4	160	250	8	15.9	22.7	26.2	1.8	030/38
		19NM1805A	L	y	D	7	250	430	16.1	14	28	19.8	6.2	030/38
		19NM1806A	L	y	D	8	250	460	36.1	1.5	35.8	-2.3	5.7	030/38
		19NM1808A	L	y	D	8	190	400	18.8	-12.4	13.7	-2.6	8.3	030/38
		19NM1813A	L	y	D	11	250	560	353	9.8	5.3	30.2	3.8	030/38
NM19	23.231840°/94.305160	19NM1907A	L	y	D	5	220	340	0.1	17.6	13.6	21.4	4.6	012/37
NM20	23.232680°/94.302960	19NM2008A	L	y	D	7	220	400	194.1	-0.8	194.7	-0.9	3.8	014/37
NM22	23.224444°/94.296111	19NM2202A	L	y	D	4	190	280	356	-22.7	345.9	-8.7	7.3	012/37
		19NM2204A	L	y	D	6	250	400	354.2	-1.9	356.6	9.3	7	012/37

		19NM2205A	L	y	D	5	250	370	9.2	29.3	28.8	24.9	5.9	012/37
NM23	23.258611°/95.584444	19NM2302A	L	y	D	11	250	560	345.7	21.6	4.7	33.1	3.5	012/37
		19NM2306A	L	y	D	5	220	340	155.7	-22.2	176.4	-39.4	7.1	012/37
NM24	23.340556°/94.315556	19NM2401A	L	y	D	10	250	530	348.7	-8.4	348.2	7.1	6.9	012/37
		19NM2402A	L	y	D	10	250	530	353	1.3	357.5	12.7	9.3	012/37
		19NM2403A	L	y	D	7	250	430	346.4	32.4	14.4	40.6	8.6	012/37
		19NM2404A	L	y	D	7	250	430	328.9	12.1	342.2	35	9.5	012/37
		19NM2405A	L	y	D	4	250	340	3.6	-1.4	4.6	4.2	8	012/37
		19NM2407A	L	y	D	6	250	400	345.6	22.7	5.5	34	5.4	012/37
NM25	23.371944°/94.324722	19NM2505A	L	y	D	4	400	490	180.4	5.3	178.8	1.5	10.7	007/27
		19NM2506A	L	y	D	5	310	430	214.4	-34	226	-19.1	12.5	007/27
NM26	23.261389°/94.305833	19NM2601A	L	y	D	12	250	580	10.8	27.2	28.5	22.4	3.6	012/37
		19NM2602A	L	y	D	11	250	560	3.9	13.6	14	16	6.3	012/37
		19NM2604A	L	y	D	12	250	580	358.5	14.8	10.5	20.1	5.2	012/37
		19NM2605A	L	y	D	6	340	490	6.3	19.2	19.6	18.9	7.3	012/37
		19NM2607A	L	y	D	8	250	460	6	18.7	19.1	18.7	5.3	012/37
		19NM2608A	L	y	D	12	250	580	350.9	20.7	8.4	29.4	6.1	012/37
NM27	23.210278°/94.296667	19NM2702A	L	y	D	8	250	460	162.5	1.7	166.8	-16.1	5.6	012/37
		19NM2704A	L	y	D	3	250	310	169.1	-15.6	183.3	-26.4	10	012/37

Appendix 5: Co-authored publications

1. Licht, A., Dupont-Nivet, G., Win, Z., Swe, H. H., Kaythi, M., Roperch, P., … Sein, K. (2018). Paleogene evolution of the Burmese forearc basin and implications for the history of India-Asia convergence. Geological Society of America Bulletin, 1(130), 20. https://doi.org/10.1130/B35002.1
2. Huang, H., Morley, R., Licht, A., Dupont-Nivet, G., Grímsson, F., Zetter, R., ... & Hoorn, C. (2020). Eocene palms from central Myanmar in a South-East Asian and global perspective: evidence from the palynological record. Botanical Journal of the Linnean Society. https://doi.org/10.1093/botlinnean/boaa038
3. Licht, A., Win, Z., Westerweel, J., Roperch, P., Cogné, N., Morley, C., ... & Dupont-Nivet, G. (2020). Magmatic history of central Myanmar and implications for the evolution of the Burma Terrane. https://doi.org/10.1016/j.gr.2020.06.016.
4. Roperch, P., Westerweel, J., … (In prep.). The Burma terrane related to India: Evidence from the U-Pb zircons in Late Cretaceous-Paleogene sediments from the Central Myanmar Basins. Abstract originally submitted to RST 2020 Lyon (Postponed to 2021).

THE GEOLOGICAL SOCIETY OF AMERICA®

Paleogene evolution of the Burmese forearc basin and implications for the history of India-Asia convergence

Alexis Licht[1,†], Guillaume Dupont-Nivet[2,3,4], Zaw Win[5], Hnin Hnin Swe[6], Myat Kaythi[6], Pierrick Roperch[2], Tamas Ugrai[1], Virginia Littell[1], Diana Park[1], Jan Westerweel[2], Dominic Jones[1], Fernando Poblete[2,7], Day Wa Aung[6], Huasheng Huang[8], Carina Hoorn[8], and Kyaing Sein[9]

[1]*Department of Earth and Space Sciences, University of Washington, Seattle, Washington 98195, USA*
[2]*Géosciences Rennes, UMR CNRS 6118, Université de Rennes, 35042 Rennes Cedex, France*
[3]*Potsdam University, Institute of Earth and Environmental Science, 14476 Potsdam, Germany*
[4]*Key Laboratory of Orogenic Belts and Crustal Evolution, Ministry of Education, Beijing, China*
[5]*Geology Department, Shwe Bo University, Sagaing Region, Myanmar*
[6]*Geology Department, University of Yangon, Pyay Road, Yangon, Myanmar*
[7]*Instituto de Ciencias de la Ingeniería, Universidad de O'Higgins, Rancagua, Chile*
[8]*Institute for Biodiversity and Ecosystem Dynamics, University of Amsterdam, 1098 XH Amsterdam, The Netherlands*
[9]*Myanmar Geosciences Society, Yangon, Myanmar*

ABSTRACT

The geological history of the Burmese subduction margin, where India obliquely subducts below Indochina, remains poorly documented although it is key to deciphering geodynamic models for the evolution of the broader Tibetan-Himalayan orogen. Various scenarios for the evolution of the orogen have been proposed, including a collision of India with Myanmar in the Paleogene, a significant extrusion of Myanmar and Indochina from the India-Asia collision zone, or very little change in paleogeography and subduction regime since the India-Asia collision. This article examines the history of the Burmese forearc basin, with a particular focus on Eocene–Oligocene times to reconstruct the evolution of the Burmese margin during the early stages of the India-Asia collision. We report on sedimentological, geochemical, petrographical, and geochronological data from the Chindwin Basin—the northern part of the Burmese forearc—and integrate these results with previous data from other basins in central Myanmar.

Our results show that the Burmese margin acted as a regular Andean-type subduction margin until the late middle Eocene, with a forearc basin that was open to the trench and fed by the denudation of the Andean volcanic arc to the east. We show that the modern tectonic configuration of central Myanmar formed 39–37 million years ago, when the Burmese margin shifted from an Andean-type margin to a hyper-oblique margin. The forearc basin was quickly partitioned into individual pull-apart basins, bounded to the west by a quickly emerged accretionary prism, and to the east by synchronously exhumed basement rocks, including coeval high-grade metamorphics. We interpret this shift as resulting from the onset of strike-slip deformation on the subduction margin leading to the formation of a paleo-sliver plate, with a paleo fault system in the accretionary prism, pull-apart basins in the forearc, and another paleo fault system in the backarc. This evolution implies that hyper-oblique convergence below the Burmese margin is at least twice older than previously thought. Our results reject any India-Asia convergence scenario involving an early Paleogene collision of India with Myanmar. In contrast, our results validate conservative geodynamic models arguing for a close-to-modern pre-collisional paleogeometry for the Indochina Peninsula, and indicate that any post-collisional rotation of Indochina, if it occurred at all, must have been achieved by the late middle Eocene.

1. INTRODUCTION

The Himalayan-Tibetan orogen, a result of the India-Asia collision, is commonly considered as the type orogen for continent-continent collisional systems and a natural laboratory to study the dynamics of continental convergence (Yin and Harrison, 2000). Our seemingly vast knowledge of the Himalayan-Tibetan system comes from decades of work along ~2600 km of the approximately west-east–trending arcuate strike of the orogen in NW India, Nepal, Bhutan, and Tibet (e.g., Allègre et al., 1984; Chen et al., 1993; Yin et al., 1994; Searle et al., 1997; Harrison et al., 1998; DeCelles et al., 2002, 2014; Najman et al., 2010, 2017; McQuarrie et al., 2014; Ma et al., 2016). Yet, the pre-collisional paleogeography of the Asian active margin, the chronology of the collision, and the deformation mechanisms accommodating the post-collisional convergence remain debated (e.g., Shen et al., 2001; Royden et al., 2008; van Hinsbergen et al., 2011a; Replumaz et al., 2010, 2013). Noticeably, an enormous spatial gap is left in our understanding of the convergence. With some notable exceptions (Pivnik et al., 1998; Socquet et al., 2002; Rangin et al., 2013), ~1500 km of the orogen trending north-south in Myanmar is underrepresented in our efforts to understand this complex system. The histories of the Burma Terrane, a small individual continental block located at the edge of the eastern Himalayan syntaxis, and of the active margin on the Burma Terrane, where the Indian plate subducts below the western edge of peninsular Indochina (Fig. 1A), remain virtually undocumented and are the focus of intense speculation. Reconstructing the history of the Burmese margin is, however, a prerequisite for any paleotectonic and geodynamic understanding of the broader Tibetan-Himalayan orogen.

Two end-member geodynamic models are proposed to explain how Asian lithospheric deformation has accommodated the convergence of

†licht@uw.edu

GSA Bulletin; May/June 2019; v. 131; no. 5/6; p. 730–748; https://doi.org/10.1130/B35002.1; 13 figures; 1 table; Data Repository item 2018336; published online 20 November 2018.

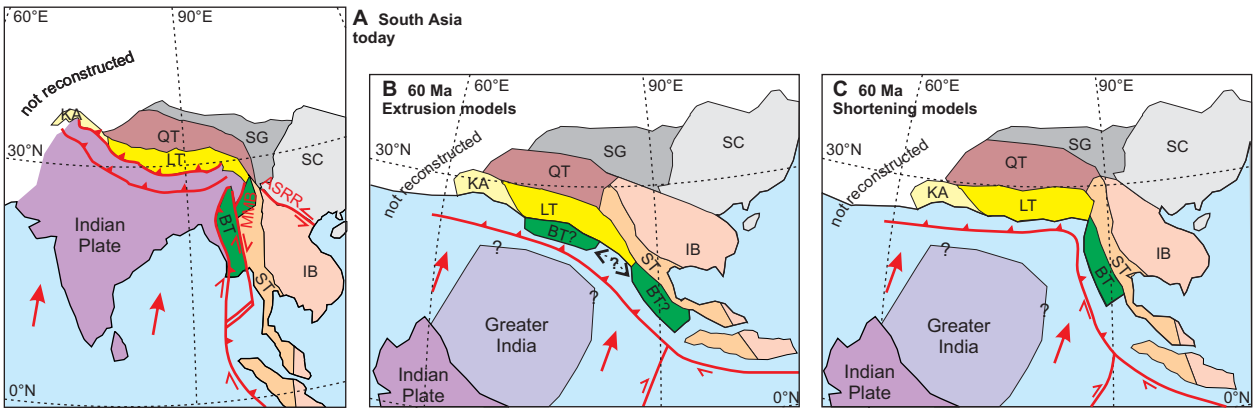

Figure 1. Structural map of South Asia today (A) and hypothetical maps 60 million years ago following deformation models dominated by extrusion (B) or shortening processes (C). Modified after Replumaz and Tapponnier (2003), Pubellier (2008), van Hinsbergen et al. (2011a), Hall (2012), and Royden et al. (2008). KA—Kohistan Arc; LT—Lhasa Terrane; QT—Qiangtang Terrane; SG—Songpan Ganzi complex; SC—South China Craton; BT—Burma terrane; ST—Sibumasu Terrane; IB—Indochina Terrane; MMB—Mogok Metamorphic Belt; ASRR—Ailao Shan–Red River shear zone. The red arrows indicate the direction of convergence (after Lee and Lawver, 1995; van Hinsbergen et al., 2011b). Note that before the India-Asia collision, extrusion models propose that the Burma Terrane was located either along the collision front (e.g., Replumaz and Tapponnier, 2003) or farther east, away from the collision zone (e.g., Royden et al., 2008).

India and Asia since the collision began: (1) lateral extrusion of Asian lithospheric blocks away from the collision zone with partial underthrusting of Asian blocks along strike-slip faults (e.g., Tapponnier et al., 1982; Replumaz and Tapponnier, 2003; Royden et al., 2008; Replumaz et al., 2010, 2013; Cogné et al., 2013), and (2) homogeneous thickening and continuous deformation of weaker Asian lithosphere (e.g., England and Houseman; 1986, Molnar et al., 1993; Hallet and Molnar, 2001; Shen et al., 2001; van Hinsbergen et al., 2011a). In most plate kinematic models dominated by extrusion, India collides with the Burmese subduction margin in the early time of the collision ca. 55 Ma (Fig. 1B; Tapponnier et al., 1982; Replumaz and Tapponnier, 2003; Replumaz et al., 2010; Cogné et al., 2013; Gibbons et al., 2015). The Burma Terrane and Indochina are later extruded from the collision zone to end up in their modern position, south of the Eastern Himalayan syntaxis. In other kinematic models dominated by extrusion, India does not collide with the Burma Terrane but with the Lhasa Terrane in Tibet (Fig. 1B); the Burma Terrane is located to the southeast of the Lhasa Terrane and is dragged northward by the Indian Plate while Indochina is extruded eastward (Royden et al., 2008). By contrast, models dominated by homogeneous thickening and continuous deformation of Asian lithosphere propose a more conservative paleogeography for the Burmese margin (Fig. 1C): pre-collisional Myanmar and peninsular Indochina already form a narrow peninsula at the southeastward extremity of East Asia very close to their modern position (Molnar et al., 1993; Hallet and Molnar, 2001; Shen et al., 2001; van Hinsbergen et al., 2011a). Most of the continuous deformation models suggest that the Burmese subduction margin lies to the east of the collision zone and is thus not particularly impacted by post-collisional deformation (van Hinsbergen et al., 2011a, 2012; Hall, 2012), but others propose that India collided first with the Burmese margin before continuing northward to its modern position (Aitchison et al., 2007; Vérard et al., 2017).

The sedimentary deposits of the forearc basin of central Myanmar provide a unique opportunity to document the paleogeography and deformation history of the Burmese subduction margin and decipher these different models. This article examines the history of the Burmese forearc basin, with a particular focus on Eocene–Oligocene times to reconstruct the evolution of the Burmese margin during the early stages of the India-Asia collision. Here, we report on sedimentological, geochemical, modal petrographical, and U-Pb detrital zircon geochronological data from the Chindwin Basin (northern part of the Burmese forearc basin), and integrate these results with previous data from other basins of central Myanmar to reconstruct the evolution of the Burmese margin through the Paleogene.

2. GEOLOGICAL CONTEXT

2.1. The Burma Terrane and the Burmese Subduction Margin

Myanmar can be divided into two roughly north-south–trending belts that lie on two basement blocks: central Myanmar on the Burma Terrane, and the Shan Plateau on the Sibumasu Terrane (Fig. 2). At the transition between both terranes, the deep basement of the Burma Terrane, consisting of Middle Jurassic ophiolites of the Burma-Sibumasu suture and metamorphics from the basement of the Sibumasu Terrane, is partially exposed and forms a succession of metamorphic belts (Jade Mine Belt, Slate Belt, Mogok Metamorphic Belt; Bertrand and Rangin 2003; Mitchell et al. 2007, 2012; Searle et al., 2012, 2017; Liu et al., 2016). It is not clear when the Burma Terrane collided with the Sibumasu Terrane; various unconstrained age estimates are proposed ranging from the Middle Jurassic to the latest Cretaceous, and the existence of a suture between both terranes is even challenged (Mitchell, 1993; Metcalfe, 2013; Sevastjanova et al., 2016; Liu et al., 2016; Searle et al., 2017); U-Pb zircon ages from intrusions and gneisses in the Mogok Metamorphic belt suggest a latest Jurassic–early Cretaceous age for the collision event (Mitchell et al., 2012).

The mid Cretaceous–early Paleogene tectonic evolution of Myanmar is marked by the subduction of the Neotethyan Ocean below western Myanmar along the Arakan Trench (Bender, 1983). The modern Burmese subduction margin formed as an Andean-type accretionary setting after rapid, forearc suprasubduction ophiolite spreading at ca. 125 Ma and the set-up of the Central Myanmar Basins developed in a forearc/backarc setting on the Burma Terrane (Bender, 1983; Pivnik et al., 1998; Liu et al., 2016; Zhang et al., 2017a). The timing of this onset mirrors the evolution of the Xigaze forearc Basin in Tibet (Maffione

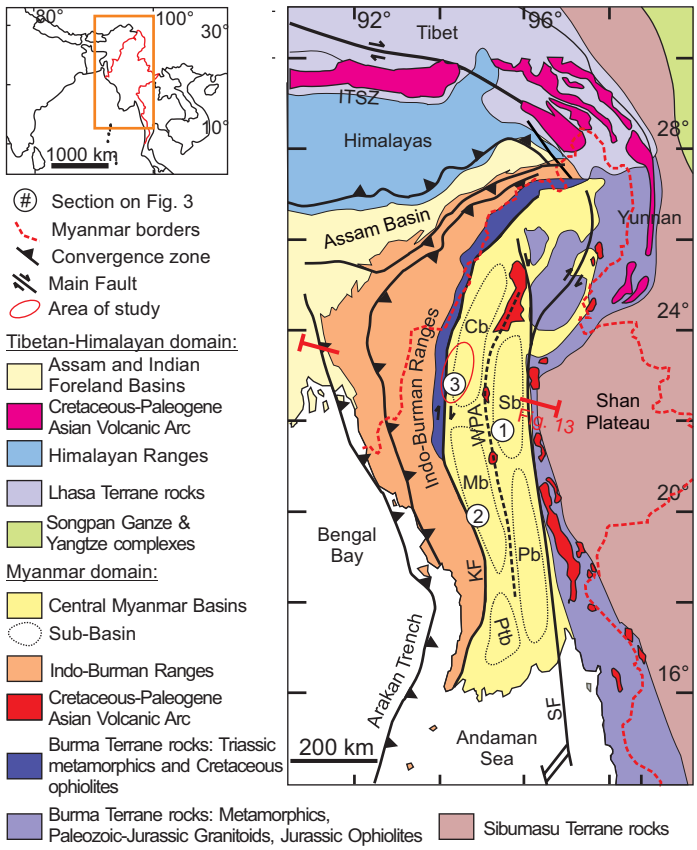

Figure 2. Schematic map of the eastern Himalayan syntaxis and central Myanmar, with the main geological units, after Licht et al. (2013); boundaries between Tibetan and SE Asian terranes are not precisely drawn because they are poorly known. The approximate axis of the Wuntho-Popa Andean arc (WPA) is shown by a thick, dashed black line. The sub-basins of central Myanmar are indicated with thin, dashed black lines: the Chindwin, Minbu, and Pathein basins (Cb, Mb, and Ptb) in the forearc, the Shwebo and Pegu basins (Sb and Pb) in the backarc. ITSZ—Indus-Tsangpo Suture Zone; SF—Sagaing Fault; KF—Kabaw Fault. Numbers in circles indicate the location of the synthetic logs in Figure 3, and the red line indicates the location of the cross section in Figure 13. Area of study is shown by a red circle. Symbol (3) sits at the location of our composite section.

et al., 2015; Liu et al., 2016; Wang et al., 2017). This period is marked by intense magmatic activity in the Andean-type Wuntho-Popa Arc, today represented by several large batholiths and related volcanic rocks that straddle the middle of the Central Myanmar Basins (Fig. 2; Zaw, 1990; Maury et al., 2004; Gardiner et al., 2015, 2017; Lee et al., 2016). The Wuntho-Popa Arc is commonly considered the eastern continuation of the Gangdese Arc of Tibet (Ma et al., 2013; Wang et al., 2014) and consists of widespread I-type batholiths and andesitic bodies punctuated with isolated S-type intrusions (Zhang et al., 2017b). Recently published U-Pb ages suggest a period of activity spanning from 110 to 30 Ma (Mitchell et al. 2012; Wang et al., 2014; Gardiner et al., 2015, 2017; Zhang et al., 2017b), with a main magmatic stage between 110 and 80 Ma and a subordinate magmatic stage at ca. 70–40 Ma. Cretaceous-Paleogene plutons are also present farther east along the Shan Scarp (Granitic Tin Belt of Gardiner et al., 2017) and may reflect temporary periods of eastward migration of the Andean-type arc (Gardiner et al., 2015), but their chronology and relationship with the Wuntho-Popa Arc remain poorly understood. The Burmese margin was then deformed by dextral strike-slip shear and other faulting, resulting in partitioning by pull-apart subsidence of the Central Myanmar Basins (Pivnik et al., 1998; Rangin et al., 1999) and in high-grade metamorphism in the Mogok Metamorphic Belt (Bertrand et al., 2001; Bertrand and Rangin, 2003; Barley et al., 2003; Searle et al., 2007). This strike-slip deformation regime is commonly explained as resulting from the hyper-oblique convergence of the Indian plate below the Burmese margin. As a result of this oblique convergence and subsequent deformation, central and western Myanmar were dragged northward (Socquet et al., 2006; Morley, 2009). The timing for the onset of strike-slip deformation and hyper-oblique regime is not clear, but oldest U-Pb zircon ages and ^{40}K-^{40}Ar cooling ages of gneisses in the Mogok Metamorphic Belt indicate that high-grade metamorphism had started by the late Eocene (ca. 37–36 Ma) along a paleo "Shan Scarp Fault" following the eastern margin of the Burma Terrane (Bertrand et al., 2001; Searle et al., 2007; Morley, 2009; 2017). Two U-Pb ages in metamorphic overgrowths of zircons suggest that it might have started even earlier, by the middle Eocene (47 and 43 Ma; Barley et al., 2003). Since the middle Miocene, following the opening of the Andaman Sea between Myanmar and Sumatra, the strike-slip motion has been partitioned and accommodated by the Sagaing Fault along the Mogok Metamorphic Belt, the Kabaw Fault in the Indo-Burman Ranges, and the Arakan Trench (Khan and Chakraborty 2005; Socquet et al., 2006). Since then, central Myanmar has formed an individual and complex sliver plate between these two faults, the total dextral displacement of which is variously estimated at 400–500 km to more than 1000 km (Maung 1987; Mitchell, 1993; Socquet et al., 2006; Morley, 2009, 2017).

2.2. The Indo-Burman Ranges

On its western margin, the Burma Terrane is separated from the Indian Foreland Basin and the Bengal Bay by the Indo-Burman Ranges, which constitute the accretionary complex produced by the Indian subduction under the Burmese active margin (Brunnschweiler, 1966; Maurin and Rangin, 2009; Bannert et al., 2011; Zhang et al., 2017a). The Indo-Burman Ranges are divided into an outer wedge made of Neogene Himalayan-sourced clastic sequences affected by folds and thrusts, and an inner wedge mainly constituted of early Cretaceous ophiolites and Triassic schists covered by Upper Cretaceous–Eocene marine turbidites (see also Figure 13C; Maurin and Rangin, 2009; Bannert et al., 2011). The origin of the Triassic schists is still unclear, but they may belong to a micro-

continent accreted and thrusted on the Burmese margin between 125 and 110 Ma (Morley, 2012), or be part of the pre-Jurassic Burma Terrane basement that was dismantled after supra-subduction spreading of the forearc (Sevastjanova et al., 2016). The oldest Cretaceous marine turbidites overlying the Triassic schists in the Indo-Burman Ranges are dated to the Campanian, but some deposits contain allochthonous blocks of Albian limestones (Bender, 1983). The outer wedge experienced uplift starting in the late Miocene as a consequence of either increased and potentially faster subduction of sediment from the Bengal Basin and Syllet Trough on the Indian Plate (Maurin and Rangin, 2009) or westward crustal flow from southeastern Tibet resulting in E-W shortening on the Burma Terrane (Rangin et al., 2013). The structure, timing of uplift, and emergence of the inner wedge remain poorly understood.

The most common view is that the inner wedge was exhumed during an early episode of accretionary building along the Burmese active margin, either during the early Cretaceous (Liu et al., 2016; Zhang et al., 2017a) or Late Cretaceous–Paleogene (Bender, 1983; Socquet et al., 2002). Acharyya (2007, 2015) and Metcalfe (2013) proposed that the early uplift of the inner wedge was caused by the accretion of individual island arc fragments that accreted along the Burmese margin during the Paleogene, but evidence for these island arc fragments in the inner wedge is lacking. Nielsen et al. (2004) and Maurin and Rangin (2009) argue that the inner wedge is more complex than a simple accretionary wedge; the core of the inner wedge follows a N-S strike-slip fault system and displays a positive flower structure, similar to retro-wedges formed along hyper-oblique convergence zones (Burbidge and Braun, 1998; McClay et al., 2004; Leever et al., 2011). Today, the inner wedge fault system is traversed by the Kabaw strike-slip fault system and accommodates a significant component (1/4–1/3) of the N-S strike slip deformation of the Burma Terrane (Nielsen et al., 2004; Socquet et al., 2006).

A combined petrographic and isotopic study of Paleogene marine turbidites from the inner wedge of the Arakan Yoma (southern edge of the Indo-Burman Ranges) identified a persistent youngest zircon-fission track population of 37 Ma in the sandstones (Allen et al. 2008). It is not clear if this fission-track age reflects a volcanic age—thus giving a maximum age for the deposition of the last flysch in the accretionary prism, suggesting that the inner wedge was emerged quickly thereafter—or if this age has been reset and reflects an episode of exhumation, indicating that the inner wedge was getting uplifted at that time. Both interpretations suggest a first, late Eocene uplift for the Indo-Burman Ranges. In addition, sedimentary provenance databased on Nd and Sr isotopes of late Paleogene units in the Central Myanmar Basin suggests that the Indo-Burman Ranges emerged in the early Oligocene (Licht et al., 2013, 2016). However, the precise timing of uplift and its mechanisms remain unknown.

2.3. The Burmese Forearc and Backarc Basins

The Central Myanmar Basins comprise two N-S–trending lateral troughs of Late Cretaceous–Cenozoic sub-basins, located both east (in a backarc position) and west (in a forearc position) of the Wuntho-Popa Arc.

The backarc basin of central Myanmar itself comprises two sub-basins, the Shwebo Basin to the north and the Pegu Basin to the south (Bender, 1983). Deposits overlie basement rocks constituted of Mesozoic marine turbidites and metamorphics and Middle Jurassic ophiolitic material (Morley, 2017; Searle et al., 2017). The sedimentary sequence starts with Upper Cretaceous–middle Eocene conglomerates, volcaniclastics, and sandstones of the Tonkyauk Chaung and Male Formations, followed by the upper Eocene–lowermost Oligocene Pondaung Formation (Fig. 3A; Thein and Maung, 2017; Zhang et al., 2017b). The Paleogene deposits of the Shwebo Basin are exclusively continental (Thein and Maung, 2017); it is not known whether the deposits in the Pegu Basin are marine or freshwater. The Paleogene sequence ends with a major Oligocene (?) unconformity observable in seismic lines (Zhang et al., 2017b). Neogene deposits consist of southward prograding tidal-influenced estuarine sequences: the Sadwingyi and Pindetaung Formations in the Shwebo Basin, and the Taungtalon, Moza, and Khabo Formations in the Pegu Basin (Khin and Myitta, 1999). These formations are unconformably overlain by the late middle Miocene–Quaternary fluviatile Irrawaddy Formation (Pivnik et al., 1998; Chavasseau et al., 2006). The Pegu Basin has been inverted and uplifted since the late Miocene and constitutes a local (and recent) topographic high (Bender, 1983).

The forearc basin of central Myanmar comprises two major sub-basins, the Chindwin Basin to the north and the Minbu (also called Salin) Basin to the south. These basins are separated today by the Pondaung Ranges, a small topographic high at ~22°N latitude where Paleogene units crop out (Bender, 1983; Pivnik et al., 1998; MGS, 2014). These two sub-basins have also been subdivided into smaller basins by previous authors (including the Pathein Sub-basin to the south; e.g., Bender, 1983) but we will keep things simple and refer only to the two main basins. On the western margin of both basins, supra-subduction ophiolites of the forearc basement crop out along a narrow window stretching along the east side of the Indo-Burman Ranges, and are presumably directly overlain by sedimentary deposits (Liu et al., 2016). On the basins' eastern edges, sediments onlap granitic rocks of the Wuntho-Popa Arc (Zhang et al., 2017b). The Cretaceous–early Cenozoic depositional history is largely similar in both sub-basins. The sequence starts with the poorly exposed Kabaw Formation, constituted of marine limestones and mudstones spanning from the Albian to the Maastrichtian (Figs. 3B and 3C; Bender, 1983). The early Cenozoic sequence includes the Paunggyi, Laungshe, Tilin, and Tabyin Formations spanning from the latest Maastrichtian (?) to the middle Eocene (Nagappa, 1959), all of which consist of shallow-marine siliciclastics with rare continental episodes (Bender, 1983). These units are only differentiated by their dominant grain-size (sandstone or mudstone); their lithostratigraphic boundaries remain vague. The late middle Eocene Pondaung Formation, present in both basins (and here older than in the backarc basin), is the only unit that has received considerable attention, because of its prolific mammalian faunal and paleobotanical remains (e.g., Jaeger et al., 1999; Chaimanee et al., 2012; Licht et al., 2014a, 2015). The Pondaung Formation reflects westward directed fluviodeltaic systems, the upper member of which is continental with carbonate-bearing paleosols, stacked channels, fossil vertebrates, and freshwater gastropods (Licht et al., 2013, 2014b, 2014c). In the Minbu Basin, the fossiliferous upper member is precisely dated at ca. 40–39 Ma via a combination of magnetostratigraphy, biostratigraphy, and geochronology (see review of dating results in Licht et al., 2015).

The late middle Eocene–upper Eocene Yaw Formation of central Myanmar represents a period of significant changes in Burmese stratigraphy, with the first pieces of evidence for differentiation between the Minbu and Chindwin Basins. In the Minbu Basin, the Yaw Formation only comprises shallow-marine, fine-grained nummulite-bearing deposits (Nagappa, 1959; Adnet et al., 2008); in the Chindwin Basin, the lithofacies of the Yaw Formation are more varied, with evidence for marine intervals, freshwater gastropods, and lignites yielding continental vertebrates (Licht et al., 2013, 2014c).

Subsequent younger geological units are significantly different in both basins (Figs. 3B and 3C). In the Minbu Basin, the Yaw Formation is followed by the Shwezetaw, Padaung,

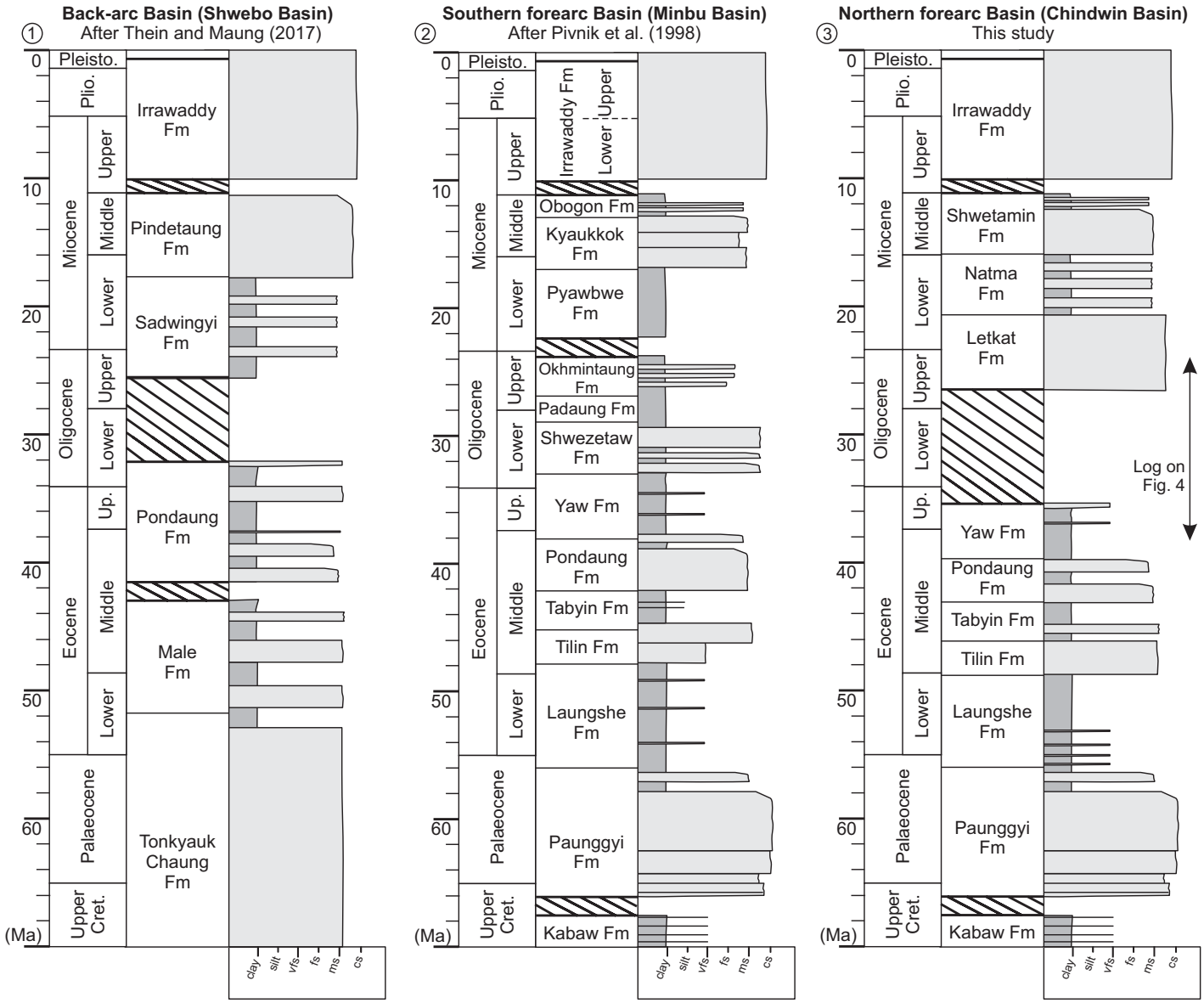

Figure 3. Synthetic logs for the three main basins of central Myanmar: (1) the Shwebo Basin in the backarc (after Thein and Maung, 2017), (2) the Minbu Basin, (southern forearc; after Pivnik et al., 1998), and (3) the Chindwin Basin (northern forearc; Bender, 1983; this study). Location of the three logs is shown on Figure 2. vfs—very fine sand; fs—fine sand; ms—medium sand; cs—coarse sand.

and Okhmintaung Formations, which all yield shallow-marine Oligocene gastropods, bivalves, and foraminifera (Bender, 1983). Gough and Hall (2017) recently interpreted these units as representing southwards-trending deltaic systems; once again, the boundaries of these units are lithologically based and often vague. They are followed by the lower to middle Miocene fluvio-deltaic Pyawbwe, Kyaukkok, and Obogon Formations (Bender, 1983) that are overlain by the fluviatile late middle Miocene–Pliocene Irrawaddy Formation (Bender, 1983; Chavasseau et al., 2006, 2010). In the Chindwin Basin, the Yaw Formation is overlain by the Letkat Formation, an ~1.5-km-thick sequence of afossiliferous fluviatile sandstones (United Nations, 1978). Some authors have proposed that the contact between the Letkat and the Yaw Formation is unconformable and that the Oligocene is missing in the Chindwin Basin (United Nations, 1978; Wang et al., 2014), whereas Bender (1983) proposes a conformable contact and indicates the presence of undescribed Oligocene sporomorphs in the Letkat Formation. The Letkat Formation is overlain by the afossiliferous fluviatile Natma and Shwetamin Formations of hypothetical Miocene age (United Nations, 1978; Bender, 1983) that are eventually unconformably overlain by the same fluviatile Irrawaddy Formation found in the Minbu Basin.

3. METHODS

3.1. Sedimentology and Stratigraphy

To determine the Paleogene evolution of the Burmese forearc basin, we explored and described deposits along a ~100 km north-south–trending portion of the Chindwin Basin in the rainshadow of the Indo-Burman Ranges. We started south of the city of Kalewa and contin-

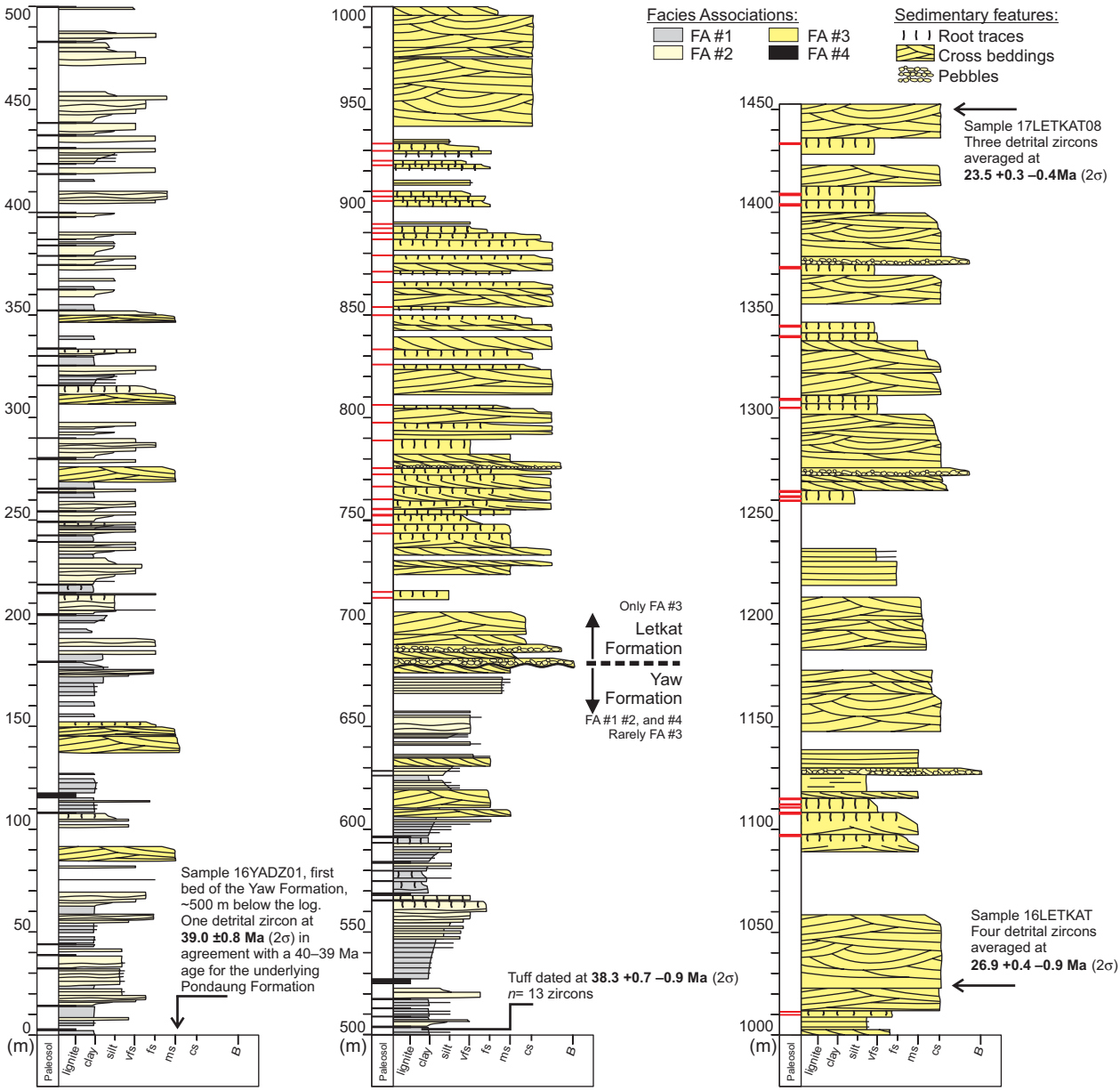

Figure 4. Composite log of the upper part of the Yaw Formation and lower part of the Letkat Formation, Chindwin Basin, with their facies associations (description in Table 1). Maximum depositional ages for our sandstone samples and age of the Tuff layer dated in this study are also shown. In the Paleosol column, black lines indicate histosols whereas red lines indicate ultisols. vfs—very fine sand; fs—fine sand; ms—medium sand; cs—coarse sand; B—Boulder.

ued up to the north of the city of Mawlaik, with a particular focus on the middle Eocene–Oligocene Pondaung, Yaw, and Letkat Formations (Fig. 2). Additionally, we measured a composite section spanning the Yaw and Letkat Formations, composed of five stratigraphic sections correlated in the field (distance between sections is ~200–2000 m). The location of the composite section is indicated on Figure 2. Detailed logs are available in Figure DR1[1], and are combined into a composite log in Figure 4. We described the sedimentary facies of these two formations, classified them into ten lithofacies adapted from the classification of Miall (2013), and grouped them into four facies associations (Table 1). Finally, we measured paleoflow directions on 3-D outcrops of sandstone trough cross-bedding (facies "St" of Table 1) according to standard field methods (Collinson et al., 2006); results are displayed on Figure 5.

3.2. Sulfur Isotope Analysis

Employing a common way to distinguish brackish from freshwater swamp deposits (Casagrande, 1987), lignite samples from the Yaw Formation were crushed and weighted for sulfur content and isotopic composition (measured as

[1]GSA Data Repository item 2018336, including supplementary figures, geochronological data, sulfur isotope and grain counting results, is available at http://www.geosociety.org/datarepository/2018 or by request to editing@geosociety.org.

TABLE 1. LITHOFACIES AND FACIES ASSOCIATIONS IDENTIFIED IN THE YAW AND LETKAT FORMATIONS, CHINDWIN BASIN

Facies	Description	Interpretation
Facies association FA1		
Fm	Massive black mudstones; sets of 10 cm to 2 m; rare preserved planar laminations with millimeter spacing.	Settling in subaqueous anoxing conditions, below depth of wave action
Fs/Fm	Grey siltstones, either showing planar laminations or small planar cross-lamination (<1 cm); occurring in small sets (<5 cm); interfingered with thicker sets of massive black mudstones.	Settling in subaqueous anoxing conditions, close to the depth of wave action
Ls/Fm	Siderite beds; nodular or continuous; 5–20 cm thick. Always interfingered with thicker sets of black mudstones, creating apparent cycling mudstone/siderite alternations.	Post-depositional mineralization in subaqueous anoxic conditions
Facies association FA2		
Sw	Heterolithic facies dominantly made of siltstones to very fine sandstones forming either climbing ripple cross-laminations, symmetrical cross-laminations with bundled and chevron upbuilding, or wavy laminations. Set thickness varies from 5 to 40 cm, with undulating bounding surfaces, and interfingered with grey mudstone beds forming flaser, lenticular, or wavy beddings. In rare places, display trace fossils *Thalassinoides* and *Skolithos*.	Tidal flats
Ssm	Dark-grey siltstones to very fine sandstones, occurring in sets of 20 cm to 4 m. commonly structureless and mixed with mud, but can sometime show either planar lanimations, small (<3 cm) trough cross-laminations, symmetrical cross-laminations with bundled and chevron upbuilding. Yield amber; fish bones; freshwater gastropods and bivalves; rich in plant debris. Show sometimes rootlets.	Coastal marsh
Cs	Sapropelic lignite, 5–50 cm thick, made of thinly laminated organic debris, interfingered with millimeter-thick layers of silt to very fine sand.	Delta front deposits of a bay-head delta
Sp	Very fine to fine sandstones occurring in 20 cm to 4 m thick beds of small (3-15 cm) sets made of horizontal laminations, planar or trough cross-laminations. Rich in plant debris; can be rich in gastropods.	Distributary mouth, bay-head delta
Facies association FA3		
St	Fine to gravelly sandstones in 50 cm to 2 m sets of trough cross-laminations. Occurs in cosets of 2 to 5 sets, arranged in wing-shaped bodies that can be 10 to 100s of meters wide. Erosive lower bounding surface, sometimes accompanied with a 5–30 cm lag of mud clast breccias, conglomerates, rounded fossil bones, and fossil wood. Commonly rich in plant debris. Uppermost sets commonly show evidence of pedogenic development.	River channel
Sm	Very fine to coarse structureless, massive sandstones, in 50 cm to 4 m thick beds commonly overlying cosets of facies St. Mud matrix, dominantly red to brown, with green to blue mottles and rare pedogenic nodules.	Pedogenised overbank
Facies association FA4		
Cv	Massive lignite, laterally extensive, 20 cm to 2 m, commonly capping cosets of facies Sw, Ssm, or St. In some locations yields lignified fossil trunks, turtle plates, and continental vertebrates.	Swamp

$\delta^{34}S$ in ‰ relative to the VCDT [Vienna Canyon Diablo Troilite] standard). Weighted samples were flash combusted at 1000 °C with excess oxygen in a Eurovector Elemental Analyzer (EA) equipped with a Costech zero-blank autosampler, and connected to a ThermoFinnigan MAT253 isotope ratio mass spectrometer for measurement of $\delta^{34}S$. Internal laboratory reference materials were interspersed with samples for a two-point calibration, allowing for conversion to the $\delta^{34}S$ VCDT scale and estimations of total sulfur content (see also Fry et al., 2002).

3.3. Sandstone Petrography and U-Pb Dating

Medium-grained sandstone samples were collected along our composite section for petrological and geochronological analyses. Thin sections of 13 sandstone samples were prepared and counted according to the Gazzi-Dickinson method to determine their quartz, feldspar and lithic grains content (Dickinson, 1985); 300–350 grains were counted per section. Detailed results and stratigraphic location of the samples are available in Table DR2 (see footnote 1).

Paleogene sedimentary rocks below and along our composite section were sampled for U-Pb dating of zircons, including one sample from the Paleocene Paunggyi Formation, two sandstones and one tuff from the Yaw Formation and four sandstones from the Letkat Formation. Detailed analytical protocols and information about the data reduction schemes are provided in the supplementary methods. Briefly, zircon crystals were extracted by traditional methods of heavy mineral separation, including concentration with a Holman-Wilfley gravity shaking table, density separation with methylene iodide and magnetic separation with a Frantz Magnetic separator. U-Pb ages were generated using laser-ablation–inductively coupled plasma–mass spectrometry (LA-ICP-MS), using an iCAP RQ Quadrupole ICP-MS coupled to an Analyte G2 excimer laser at the University of Washington, using a spot diameter of 25 microns. Data reduction was conducted with Iolite, using their Geochron Data Reduction Scheme to calculate U-Pb ages uncorrected for common lead (Paton et al., 2010), and with the Andersen Routine of the Vizualage Data Reduction Scheme (Chew et al., 2014) for U-Pb ages corrected for common lead. Both approaches yielded quasi-identical zircon ages in our data set, and ages used in this manuscript are uncorrected for common lead. Detailed location, stratigraphic level, and U-Pb data are available in Table DR3 (see footnote 1). Stratigraphic locations for the Yaw and Letkat Formation samples are also indicated on Figure 4. Maximum depositional age for detrital samples and crystallization age for volcanic samples with multiple zircon ages were calculated using Tuffzirc (Ludwig, 2003) and are also displayed on Figure 4. The final age error calculated for each sample is the quadratic sum of the uncertainty of Tuffzirc age calculation and of the systematic uncertainty during each session (~1.3%).

4. RESULTS

4.1. Sedimentology of the Eocene and Oligocene Deposits in the Chindwin Basin

Deposits and associated lithofacies of the Pondaung Formation are identical to those in the Minbu Basin farther south and have already been extensively described in Licht et al. (2014b); in the southernmost part of the Chindwin Basin, they have also been described by Oo et al. (2015). Briefly, the formation mainly consists of large, coarse-grained, sandstone bodies, 2–18 m thick, >100 m wide and are dominated by large sets (up to 1 m thick) of trough cross-bedding. The sandstone bodies are interfingered with fine-grained sequences, with pedogenised heterolithic deposits and extensive paleosol-bearing mudstone successions. Paleosols display vertic features and pedogenic nodules, as well as different stages of hydromorphic development, and were identified as hydromorphic vertisols. In the Minbu Basin, these deposits have yielded a mix of freshwater riparian and brackish water mangrove trees (Licht et al., 2014a, 2015), continental vertebrates (Jaeger et a., 1999; Chaimanee et al., 2012), freshwater gastropods (Licht et al., 2014c), and occasional seawater fishes (Adnet et al., 2008). Paleocurrent measurements indicate an unequivocal westward flow (Fig. 5).

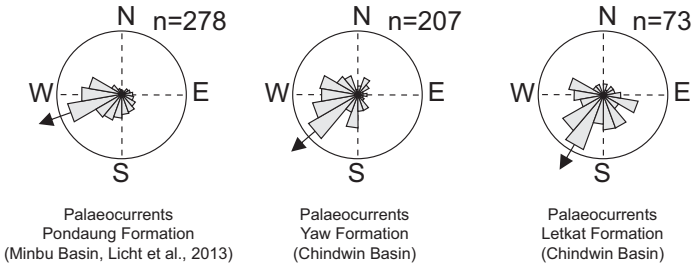

Figure 5. Paleocurrents for the Pondaung Formation in the Minbu Basin (after Licht et al., 2013), the Yaw Formation in the Chindwin Basin (including new measurements and data from Licht et al., 2013), and the Letkat Formation in the Chindwin Basin (this study). Palaeocurrent directions were measured on 3-D exposures of trough cross-beddings (facies St, Table 1).

Our 1450 m composite sedimentary log of the Yaw and Letkat Formations is displayed in Figure 4. The sedimentary log starts ~500 m above the transition from the Pondaung Formation to the Yaw Formation, which is marked by the first occurrence of lignites and black mudstones. The log ends ~700 m below the transition from the Letkat to the Natma Formation, which is marked by a significant increase in fine-grained deposits (United Nations, 1978). In total, the thickness of the Yaw Formation is estimated to be around ~1000 m, and the Letkat Formation to be around ~1500 m.

Deposits of the Yaw Formation display ten lithofacies that can be divided into four facies associations (Table 1). Facies association FA1 is mainly made of massive black mudstones (Fm) interfingered either with siderite beds (Ls/Fm; Figs. 6A and 6B) or thinly planar laminated siltstones (Fs/Fm). Facies association FA2 is more diverse and is mainly composed of beds of siltstone to very fine sandstone showing planar laminations, small planar cross-laminations, and symmetrical cross-laminations with bundled and chevron upbuilding typical of wave-formed cross-laminations (Nichols, 2009). These fine-grained beds are sometimes interfingered with gray mudstones, forming flaser, lenticular, and wavy beddings (facies Sw); these interfingered beddings can contain trace fossils of *Thalassinoides* and *Skolithos* (Figs. 6C to 6H). More commonly, these beds show evidence for partial mixing and rootlets, and yield amber, fish bones, freshwater gastropods (thiarids; Licht et al., 2013) and unionid bivalves (facies Ssm; Fig. 6G). Sapropelic lignites rich in plant debris (facies Cs) also occur in sequences of facies Sw and Ssm, together with sequences of coarser, cross-laminated sandstones that are also rich in plant debris and occur in thick (commonly >1m) tabular sets (facies Sp).

Facies association FA3 is dominated by facies St, which consists of fine to coarse sandstones organized in meter-thick sets of trough cross-stratifications. These sets commonly occur in cosets of 3–5 sets, have an erosional base, and occasionally have a basal lag full of mud-clast breccias and plant debris. These cosets occur in wide (sometimes >200 m) bodies that decrease in grain-size near their wings. In the area of Mawlaik, ~100 km north of Kalewa, sandstones are occasionally capped by structureless, pedogenised sandy beds mixed with a mudstone matrix, displaying a dominant brownish color, green mottles, sparse slickensides, and pedogenic nodules (facies Sm). This facies has, as of yet, only been observed in the uppermost layers of the Yaw Formation preceding the transition to the Letkat Formation. Finally, facies association FA4 is made of a single facies Cv, constituted of thick (up to 2 m), massive lignites that yield lignified fossil trunks and occasional vertebrate remains (Fig. 6I).

The four facies associations alternate following regular coarsening-upward cyclothems (FA1 to FA3) capped by lignites (FA4). FA3 is relatively rare and FA4 lignites can cap a smaller, FA1-FA2 sequence. The last 100 m of the Yaw Formation follows an overall coarsening upward sequence and FA3 sandstones become more common. The same facies associations can be found over the 100 km N-S area we investigated; lignite beds can be tracked over distances greater than 10 km and are currently mined for coal production. Palaeocurrents measured in FA3 trough crossbeds (facies St) cover a broad range of directions from S to WNW, with an average direction toward the southwest (Fig. 5).

There is no obvious angular unconformity at the contact between the Yaw Formation and Letkat Formation, but this contact is sharp, marked by the occurrence of several sandstones bodies with thick (>2 m) basal lags made of blocks of reworked sediment, altered siderite, and lignified fossil trunks (Fig. 6J). The Letkat Formation is only constituted of FA3. Facies St is commonly coarser than the sandstone beds observed in the Yaw Formation, and can be associated with gravels, silicified fossil trunks, and rounded vertebrate bones. We did not observe any inclined heterolithic stratification in the sandstone bodies; cosets of facies St are commonly occurring in wide (tens of meters) tabular or wing-shaped bodies. Facies Sm is also more present, usually capping 10–15 m cosets of facies St. Pedogenic features are different from what is found in the Pondaung and Yaw Formations; pedogenic nodules are rare, mottles are dominantly reddish or yellow, sometime root-shaped, and form well developed, 1–3-m-thick paleosol profiles, with increasing mottling and mixing upward resembling modern Ultisols (Fig. 6K). The first 200 m of the Formation are particularly coarse, with gravel beds made of rounded quartz being common. Gravels disappear after ~250 m, and most of the remaining deposit is made of coarse St sandstones with occasional pedogenised Sm beds. Palaeocurrents measured in FA3 trough crossbeds (facies St) cover a broad range of directions from W to E, with an average direction toward the south-southwest.

4.2. Sulfur Content and Isotopic Composition

Lignites sampled for sulfur analysis can be grouped into two families (Fig. 7). A first family, with a low amount of sulfur (~<0.8%) and a narrow range of $\delta^{34}S$ values, between –2 and +12‰ VCDT, corresponds to the values found in modern freshwater peats, where sulfur is particularly limited and mostly comes from plant sulfates (Casagrande, 1987). The second family display a much broader range of sulfur amount (up to 5%) and varying sulfur isotopic composition, from –10 to +20‰ VCDT, similar to those of peats formed under brackish water influence where regular inputs of seawater sulfate increases the availability of sulfur for bacterial reduction (Casagrande, 1987).

4.3. Sedimentary Provenance of the Paleogene Units

Sandstone grain-counting results are plotted on Q-F-L and Lm-Lv-Ls diagrams (Fig. 8) and compiled with previous data from Paleocene to middle Eocene units in the same section (Paunggyi, Tilin, and Pondaung Formations; Wang et al., 2014). Paleocene to middle Eocene sandstones are volcanic-rich, litharenitic and display similar grain-counting results to those of the Paleogene turbidite sample from the Indo-Burman Ranges of Allen et al. (2008). By contrast, the Letkat Formation is dominated by

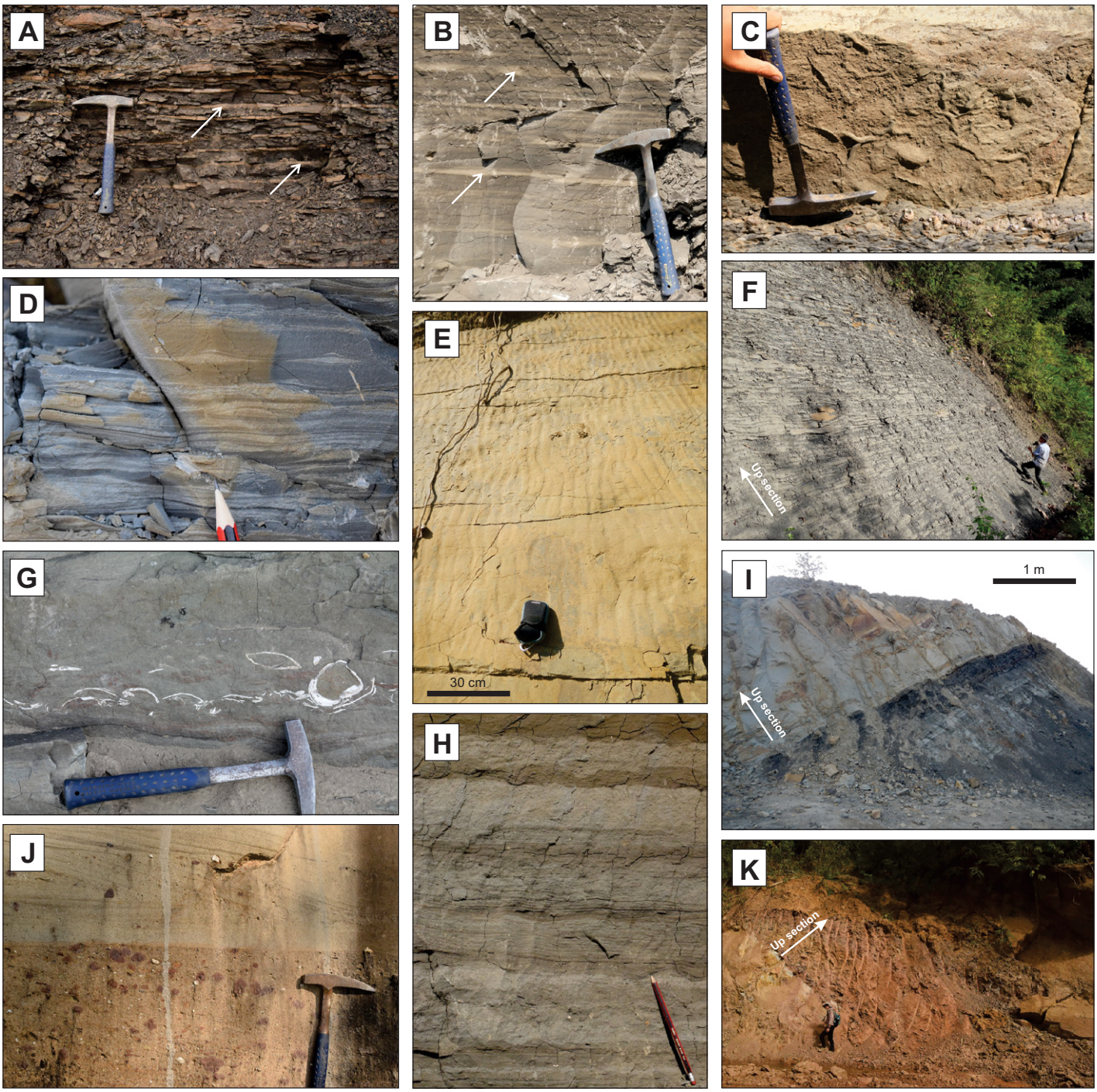

Figure 6. (A) and (B): black mudstones with cm thick siderite beds, shown by white arrows (facies Ls/Fm). (C) Trace fossil *Thalassinoides* in siltstone beds (facies Sw). (D) Wavy bedding with symmetrical cross-laminations (facies Sw). (E) Bed of symmetrical ripples in facies Sw (typical of wave-formed ripples) viewed from above. (F) Thick accumulation of wavy and flaser bedding (facies Sw). (G) Unionid fossils in massive very fine sandstone (facies Ssm). (H) Wavy and flaser bedding with planar laminations and asymmetrical cross-laminations (facies Sw). (I) Meter-thick lignite (facies Cv) overlain by a sandstone body of facies St. (J) Trough cross-bedding (facies St) rich in reworked, oxidized sedimentary clasts in the Letkat Formation. (K) Pedogenised sandstones and mudstones (facies Sm) in the Letkat Formation. When the scale is not displayed, rock hammers, pencils, and humans can be used for scale.

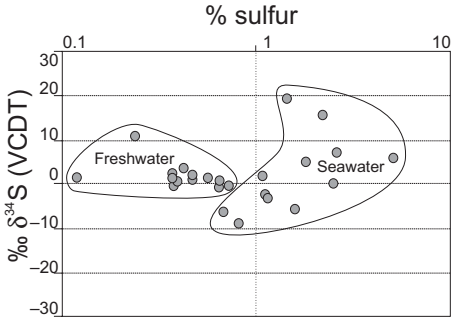

Figure 7. Percentage of sulfur and sulfur isotopic composition (expressed in ‰ of deviation from the VCDT [Vienna Canyon Diablo Troilite] international standard) in lignites of the Yaw Formation. Values form two distinct families: one with low amount of sulfur (<1%) and a homogeneous sulfur isotopic composition, around 2‰ VCDT, and one with a wide array of sulfur content (up to 5%) and isotopic compositions (–6 to +6‰ VCDT).

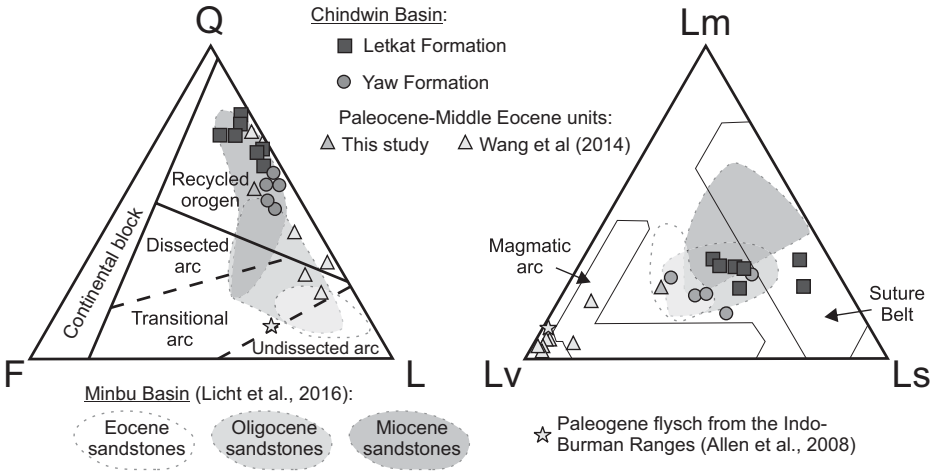

Figure 8. QFL and LvLsLm plots of the Letkat Formation, Yaw Formation, and Paleocene-middle Eocene units from the Chindwin Basin (data from Wang et al., 2014, and this study), compared with Eocene to Miocene sandstones from the Minbu Basin (Licht et al., 2016) and a Paleogene turbidite from the Indo-Burman Ranges (Allen et al., 2008). Main provenance provinces following Dickinson (1985). Q—quartz; F—feldspar; L—lithic fragments; Lm—metamorphic; Ls—sedimentary; Lv—volcanic.

volcanic-depleted quartzarenites. Sandstones from the Yaw Formation display intermediate features between both end-members. This evolution follows the same long-term pattern as sandstones in the nearby Minbu Basin (Licht et al., 2016). Eocene sandstones in the Minbu Basin are much poorer in volcanic lithics compared to the Chindwin Basin; only Miocene sandstones are purely quartzarenitic, plotting in the same area as Letkat sandstones on the QFL ternary diagram (Fig. 8). Carbonate lithic fragments were detected in insignificant proportions in all samples, as is also observed in the Minbu Basin (<1%).

Kernel density estimates (KDE) and age histograms of U-Pb age distributions of individual samples are shown in Figure DR2 (see footnote 1); individual samples are also compared with other samples from the forearc and backarc basin of central Myanmar on a multidimensional scaling map (MDS; Fig. 9). An MDS is a visual way to assess the misfit between age distributions using the Kolmogorov-Smirnov (KS) statistic as the dissimilarity measure (Vermeesch, 2013). Ages from individual samples are grouped with previous samples of the Chindwin Basin from Wang et al. (2014) into three groups on Figure 10: Paleocene to middle Eocene units (n = 601 from six samples, including five samples from the Paunggyi, Tilin, and Pondaung Formations by Wang et al., 2014), the Yaw Formation (n = 202, from two samples), and the Letkat Formation (n = 470 from five samples, including one sample from Wang et al., 2014).

Paleocene to middle Eocene sandstones from the Chindwin Basin are dominated by Late Cretaceous (ca. 90–120 Ma) zircons, with a secondary population of Paleogene (40–60 Ma) zircons. Except for a single sample (sandstone from the Tilin Formation; Wang et al., 2014), Paleocene to middle Eocene sandstones lack grains older than Late Cretaceous and are statistically distinct from younger sandstones on the MDS plot (Fig. 9). U-Pb zircon ages from a sandstone of the Pondaung Formation at the southernmost edge of the Chindwin Basin (Oo et al., 2015) corroborate the lack of older zircons in Paleocene-middle Eocene sandstones but should be interpreted with caution because of the low amount of zircon ages (n = 54). Upper Eocene to lower Oligocene sandstones from the backarc basin (Robinson et al., 2014) are similarly exempt of older zircons, but are dominated by Paleogene grains.

Samples from the Yaw Formation yield a significant proportion of older zircons, with two notable peaks at 500 and 1200 Ma, as well as a prominent population of Paleogene zircons.

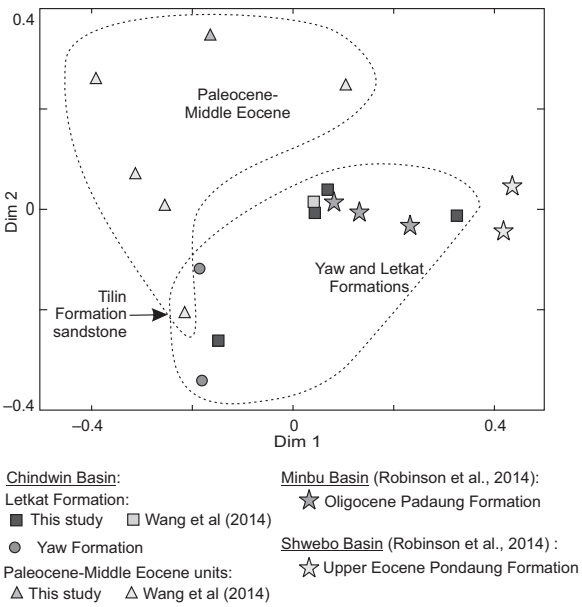

Figure 9. Multidimensional scaling map showing the dissimilarities between individual samples of this study and previously published samples (Wang et al., 2014; Robinson et al., 2014). Axes are in dimensionless "KeS units" (–1 < KS < 1) of dissimilarity between samples. Final "stress" value is 0.06, indicating a fit between "good" and "fair" (Vermeesch, 2013). Ranges of variation for individual samples of Paleocene–middle Eocene and younger deposits from the forearc basin are highlighted by dashed lines.

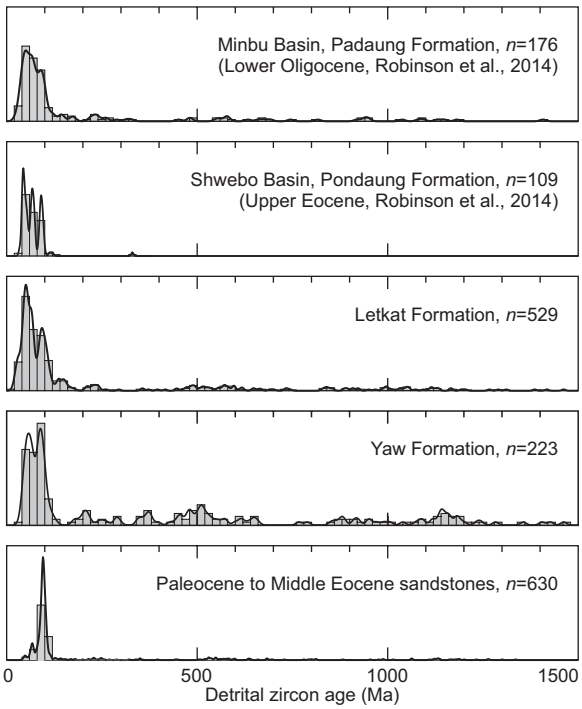

Figure 10. Kernel density estimators (KDE) and histograms (20 m.y. bins) for Paleocene to middle Eocene sandstones from the Chindwin Basin (n = 601, combining two samples from the Paunggyi Formation, one sample from the Tilin Formation, and two samples from the Pondaung Formation, all from Wang et al., 2014, and one sample from the Paunggyi Formation from this study), from the Yaw Formation (n = 202, two samples from this study), and from the Letkat Formation (n = 470, combining four samples from this study and one from Wang et al., 2014), compared to upper Eocene sandstones from the Shwebo (backarc) Basin (n = 109, two samples from Robinson et al., 2014) and lower Oligocene sandstones from the Minbu Basin (n = 176, three samples from Robinson et al., 2014). The kernel density bandwidth of each plot was determined with the plug-in bandwidth selection method of Botev et al. (2010).

This trend continues in the sandstones of the Letkat Formation, which display a dominant Paleogene peak and numerous Proterozoic zircons. Yaw and Letkat samples occupy the same space on the MDS plot. Samples from the lower Oligocene Padaung Formation (Robinson et al., 2014) in the nearby Minbu Basin display the same features. These features are also shared by Neogene samples from central Myanmar (Wang et al., 2014), as well as in most modern river samples draining the central Myanmar Basins (Garzanti et al., 2016).

4.4. Age Model for the Yaw and Letkat Formations

Youngest U-Pb ages of detrital zircons from three samples and U-Pb ages of a sampled tuff are displayed on Figure 4. The maximum age of the Yaw Formation is constrained by a maximum depositional age of 39.0 ± 0.8 Ma (2σ; n = 1 zircon) at the very most base of the formation ~500 m below the composite log. Although ages based on a single zircon must be interpreted with caution, this age is in agreement with the age estimate for the unit just below, the Pondaung Formation, the upper member of which is dated at 40–39 Ma in the Minbu Basin via a combination of biostratigraphy, geochronology, and magnetostratigraphy (see review in Licht et al., 2015). The tuff is located at level ~1000 m in the formation, ~180 m below the transition to the Letkat Formation, and yields a 38.3 +0.7/–0.9 Ma (2σ; n = 13 zircons) volcanic age. This indicates an upper Bartonian age for the Yaw Formation and extremely fast sedimentation rates (>1 m/k.y.). Assuming a similar accumulation rate, the last beds of the Yaw Formation occurred close to the Bartonian–Priabonian Boundary at 37.8 Ma (Gradstein et al., 2012).

Sandstones from the base of the Letkat Formation did not yield younger zircons, but a sample ~350 m above the base of the formation yielded a maximum depositional age of 26.9 +0.4/–0.9 Ma (2σ; n = 4 zircons). A second sample at the top of our section, ~780 m below the top of the Letkat Formation yielded a single zircon at 20.2 ± 0.5 Ma (2σ); however, a more robust maximum depositional age of 23.5 +0.3/–0.4 Ma (2σ; n = 3 zircons) was calculated using more zircons. This suggests that the upper part of the Letkat Formation is upper Oligocene or possibly lower Miocene in age. Assuming that these maximum depositional ages are close to actual depositional ages due to the proximity of an active volcanic arc, the sedimentation rate of the Letkat Formation was much lower than for the Yaw Formation (~15 cm/k.y.). This slow accumulation rate suggests that the base of the Letkat Formation would start, or be younger than, ca. 29 Ma and that most of the lower Oligocene is missing in our section.

5. DISCUSSION

5.1. Depositional Environments of the Paleogene Forearc

The depositional environments of the Pondaung Formation in the Minbu Basin have previously been interpreted as reflecting a deltaic floodplain environment created by westward-prograding fluvial systems, where avulsive channels, crevasse belts with heterolithic deposits, and pedogenic floodplain fines laterally grade into each other (Licht et al., 2014b). Our observations in the Chindwin Basin are in line with this interpretation.

The combination and alternation of facies association FA1 to FA4 in the Yaw Formation is in many ways diagnostic of barrier-bound estuaries (Dalrymple et al., 1992). FA4 and FA3 are attributed to coastal swamps (paleo-histosols) and bayhead deltaic river distributaries, respectively. Sulfur content and isotopic composition indicate that whereas some of the swamps developed in a brackish setting, most were freshwater (Casagrande, 1987). FA2 reflects near-shore environments with several variations. Facies Sp and Cs can be interpreted as representing deltaic lobes and the delta front of bayhead deltas in the estuary bay (Anthony et al., 2002; Leeder, 2009). Facies Sw, with its evidence for wave-action, heterolithic stratifications with flaser, lenticular, and wavy bedding, indicates a tidal flat environment, which are commonly found along the shores of estuaries (Tessier et al., 1995). This interpretation is corroborated by the presence of trace fossils *Thalassinoides* and *Skolithos* commonly found on firm grounds of tidal flats (Gingras et al., 2001). The prominent facies of this facies association, Ssm, contains evidence of wave-action and pedogenesis, but lacks well-marked tidal influence, and is interpreted here as reflecting either an intertidal marsh or a more vegetated shoreline (Allen, 2000). Finally, facies association FA1 reflects the sub-tidal central basin depositional environment of a barrier-bound estuary, where massive organic-rich mud is prominent (Anthony et al., 1996). The presence of marked anoxic conditions in the central basin, shown by the common occurrence of siderite beds (Mozley and Wersin, 1992), suggests poor mixing of deep water and a quasi-closed character for the estuary. Taken together, these facies associations closely resemble those of the tropical estuary of the Ouémé River in Benin, which is bounded by a large sand barrier created by longshore drift (Anthony et al., 2002). Interestingly, the relative rarity of facies Sw, the notable absence of any marine fossils, the relative abundance of freshwater gastropods and unionids, and the overall

low sulfur content in most of the coal suggests periods of intermittent estuary closure and shift to lacustrine setting, as is sometimes observed in barrier-bound estuaries (Roy et al., 1994).

Thick, wide bodies made of cosets of facies St that lack any clear inclined heterolithic stratification and are capped by pedogenised, finer grained sets of facies Sm suggest fluvial channel bodies typical of braided river systems and associated overbank deposits (Leeder, 2009). The shift to pure fluviatile deposition and the presence of a depositional hiatus at the contact between the Yaw and Letkat Formations indicate that by the end of the Yaw Formation and for most of the Oligocene, the Chindwin Basin was overfilled. Moreover, paleocurrent flow measurements from the Letkat Formation indicate a shift in drainage orientation from westward-oriented in the Eocene to southwestward-oriented in the Oligocene.

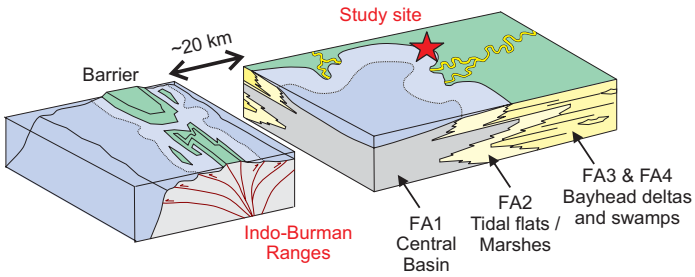

Figure 11. Depositional model for the Yaw Formation, inspired from the depositional model of tropical estuary of the Ouémé River in Benin (Anthony et al., 2002). Facies Association FA1 represents the central basin of a quasi-closed estuary; FA2 reflects the coastal/intertidal component; FA3 represents distributary channels of the bayhead delta; and FA4 deltaic swamps. We propose that the nascent Indo-Burman Ranges provided the necessary barrier to close the estuary.

5.2. Tectonic Implications for the Evolution of the Accretionary Prism

Extremely high accumulation rates (>1 km/m.y.) imply similar rates of basin subsidence to keep the bathymetry close to the tidal/shallow lacustrine domain, and indicate an active tectonic regime during the deposition of the Yaw Formation. To maintain the quasi-closed estuarine conditions over hundreds of meters of section, a permanent barrier is needed offshore to the west of our site in the area that is today occupied by the Indo-Burman Ranges. Wave-formed sandspits could have partly acted as a barrier, but the scale of the estuary (>100 km wide along the Burmese coast) is 5–10 times larger than modern wave-formed estuaries (Dalrymple et al., 1992).

Southward-directed flow measurements in the Letkat Formation indicate that by the late Oligocene, the Indo-Burman Ranges must have emerged on the western side of the Chindwin Basin in order to stop the westward progradation of fluvio-deltaic systems and instead drain fluvial systems southward. This corroborates preliminary work in the Minbu Basin farther south, where southward-prograding deltaic systems are observed starting in the early Oligocene (Gough and Hall, 2017). Incipient uplift of the accretionary prism must thus have started during or before the Oligocene. We propose that the quasi-closed estuarine conditions of the Yaw Formation in the Chindwin Basin reflect the initial emergence of the Indo-Burman Ranges offshore, which provided the necessary near-sea level topographic barrier (Fig. 11). This interpretation implies that by 39–38 Ma, the Indo-Burman Ranges were already being uplifted and were partly emerged. This timing is in agreement with geochronological data from Paleogene turbidites in the accretionary wedge farther south in the Indo-Burman Ranges, which yielded a persistent youngest zircon-fission track population at 37 Ma (Allen et al. 2008), roughly coeval to the unconformity at the top of the Yaw Formation and the complete in-filling of the estuary. A major shift from westward-oriented drainage into the proto–Bengal Bay to southward-oriented drainage systems parallel to the subduction margin would have occurred after the complete emergence of the accretionary prism and the in-filling of the Chindwin basin estuary around ca. 37 Ma.

5.3. Comparison with the Minbu Basin and Implications for the Onset of Pull-Apart Subsidence

There is a lack of sedimentological data regarding the Yaw Formation in the Minbu Basin, but the little we know contrasts with our observations in the Chindwin Basin. In the Minbu Basin, the Yaw Formation consists of gray shales with occasional limestone beds rich in shallow-marine trace fossils and fossil mollusks (Bender, 1983; Licht et al., 2013). Lignites and organic-rich black mudstones are absent. Additionally, the Minbu Basin lacks a depositional hiatus in the upper Eocene, and instead records continuous sedimentation into the lower Oligocene Padaung Formation (Nagappa, 1959). The Minbu Basin Yaw Formation is also much thinner (only ~700 m thick at the western edge of the basin; United Nations, 1978). This indicates much lower accumulation rates (<200 m/m.y.) in the late Eocene and similarly slow rates of basin subsidence to keep the bathymetry close to shallow-marine conditions. Similar shallow-marine environments, accumulation rates and associated subsidence continued through the late Oligocene, with the deposition of the Shwezetaw, Padaung, and Okhmintaung Formations (United Nations, 1978).

During the late Paleogene, the Chindwin and Minbu Basins thus appear to have followed a significantly different subsidence history. Whereas subsidence was continuous in the Minbu Basin and bathymetry kept pace with moderate accumulation rates, subsidence was extremely high around 39–38 Ma in the Chindwin Basin and significantly slowed down at 37 Ma, leading to a stop of accumulation for most of the late Eocene and early Oligocene—resulting in the observed unconformity between the Yaw and Letkat Formations. These results indicate that by 39 Ma, the forearc was already partitioned into individual sub-basins with different histories. The high subsidence rates in the Chindwin Basin are in agreement with strike-slip deformation and pull-apart subsidence as the main mechanisms for forearc basin partitioning, as proposed by Rangin et al. (1999). The ~22°N latitude topographic high, that today geomorphologically separates the two basins might have already been partly emerged or at least might have subsided more slowly, partly closing the Chindwin estuary to the south. Precise age constraints for the other Cenozoic units of the forearc basin—for a detailed backstripping analysis—and basin-wide seismic lines are as of yet still lacking, preventing us from unequivocally confirming pull-apart subsidence as the main mechanism here; however, our interpretations suggest that the onset of basin pull-apart formation and strike-slip deformation of the basin margin dates back to at least 39 Ma, if not older.

5.4. Provenance of the Paleogene Forearc Sediment and Implications for the Exhumation of the Metamorphic Belts

Our grain-counts and U-Pb ages distributions from Paleocene to middle Eocene sandstones indicate a provenance from Late Cretaceous–Paleogene rocks, likely the Wuntho-Popa magmatic arc located ~100 km to the east, which was active during the same period and displays the same age peaks (Mitchell et al. 2012; Wang et al., 2014; Gardiner et al., 2015, 2017; Zhang et al., 2017b). Robinson et al. (2014) proposed a provenance from the Gangdese Arc in Tibet via a paleo-connection between Tibet and the Central Myanmar Basins using εHf fingerprinting of detrital zircons, but Zhang et al. (2017b) showed that zircons from the Wuntho-Popa Arc hold the exact εHf fingerprint as Gangdese batholiths. Additionally, a proximal source is corroborated in the Minbu Basin by Nd and Sr isotopic values, grain-counts, and paleocurrents that all indicate a nearby volcanic source located east of the forearc (Licht et al., 2013). Interestingly, the relatively high amount of quartz in samples from both Chindwin and Minbu basins suggests that part of the arc plutonic root might have already been exhumed in the late middle Eocene, corroborating a possible early uplift of the volcanic arc (Zhang et al., 2017b). Paleocene to middle Eocene samples from the Chindwin Basin contain slightly more volcanic lithic grains compared to coeval samples from the Minbu Basin (Fig. 8), indicating small lateral changes in the lithology of the exposed rocks along the Burmese subduction margin. The higher amount of sedimentary lithics in the Minbu Basin could reflect the recycling of older sedimentary rocks upstream, or ephemeral connections to the backarc basin and areas farther east, as one sample from the Tilin Formation seems to suggest (Fig. 9).

Sandstones from the Yaw Formation are marked by an increase of petrographic maturity and a significant amount of older (>150 Ma) zircons, which are almost absent in older sandstones. This trend is even more pronounced in sandstones of the Letkat Formation and indicates an increased contribution from older, quartz-rich basement rocks. In central Myanmar, basement rocks crop out in only a few areas: (1) to the east of the backarc basins along the Mogok, Slate, and Gaolingong metamorphic belts, where Paleozoic plutons and older metamorphics are prevalent; (2) occasionally farther east on the Shan Plateau, where Paleozoic and upper Mesozoic clastics crop out; and (3) to the west of the forearc in the metamorphosed core of the inner wedge of the accretionary prism, where small pockets of Triassic metamorphics crop out (Fig. 2; Licht et al., 2016). Our paleocurrent measurements in the Yaw Formation rule out the accretionary prism as a potential source; rather, our results indicate an increased contribution from the metamorphic belts and the Shan Plateau to the east. The absence of carbonate clasts—the dominant lithology on the Shan Plateau—suggests that the metamorphic belts are the primary contributor.

Similar age distributions are found in lower Oligocene samples from the Minbu Basin (Fig. 10; Robinson et al., 2014), suggesting a similar provenance. Following the onset of southward drainage systems ca. 37 Ma, a portion of the lower Oligocene material reaching the Minbu Basin might have transited via the Chindwin Basin. We unfortunately do not have any U-Pb data from the Yaw Formation in the Minbu Basin to test if the shift to a more mature source is older or coeval to the provenance change at ca. 39–38 Ma observed in the Chindwin Basin. However, Nd isotopes, Sr isotopes, and grain-counts on sandstones in the Minbu Basin corroborate an increased contribution of the metamorphic belts in the sedimentary supply starting in the late Eocene (Licht et al., 2016).

There are unfortunately few geochronological and petrographic data from the backarc basin to compare our results with. Two upper Eocene samples from the backarc basin contain only Cretaceous-Eocene zircons (Robinson et al., 2014), unlike what we see in Yaw and Letkat Formation sandstones. Although any interpretation based on only two, low n (<60) samples is premature, we suspect that these samples might reflect local tributaries flowing down the Wuntho-Popa volcanic arc that do not reflect any contribution from the metamorphic belts that would have supplied older (>150 Ma) grains.

Our results thus show that by 39–38 Ma the Chindwin Basin had started receiving a regular supply of sediment from the metamorphic belts to the east. Interestingly, this age is roughly coeval with the 37.4 ± 1.3 Ma (2σ) onset of gneiss formation and proposed onset for high-grade metamorphism (Searle et al., 2007), as well as the 36.2 ± 1.6 Ma (2σ) age for the oldest ^{40}K-^{40}Ar exhumation age along the metamorphic belts (Bertrand et al., 2001), showing the existence of a paleo–"Shan Scarp fault" system in the backarc areas predating the modern Sagaing Fault system. Our results thus confirm that the onset of high-grade metamorphism during the late middle Eocene is associated with an early exhumation episode of the metamorphic belts, which started providing sediment to the forearc basin. Ephemeral exhumation events might have started earlier in the middle Eocene, as suggested by one sample from the middle Eocene Tilin Formation (Fig. 9) and two middle Eocene overgrowth ages in zircons of the Mogok Metamorphic Belt (Barley et al., 2003).

5.5. Evolution of the Burmese Subduction Margin during the Paleogene and Mechanisms of Uplift for the Indo-Burman Ranges

We propose a three-step scenario for the evolution of the Burmese margin during the Paleogene (Figs. 12 and 13).

(1) From the Paleocene to the middle Eocene, the Burmese subduction margin displays the regular morphology of Andean-type margins, with a nascent, underwater accretionary prism, and a forearc basin open to the trench occupied by westward-prograding deltaic systems fed by the denudation of the volcanic arc (Figs. 12A and 13A).

(2) In the late Bartonian–earliest Priabonian, around 39–38 Ma, the accretionary prism starts to emerge (Figs. 12B and 13B). The forearc basin is partitioned into two basins with varying subsidence rates likely due to pull-apart subsidence; the Minbu Basin in the south remains open to the proto–Bengal Bay to the west and the south, while in the north, quasi-closed estuarine conditions develop in the Chindwin Basin. Simultaneously, the metamorphic belts located to the east are progressively exhumed and start to feed the forearc.

(3) By 37 Ma, the Paleogene accretionary prism, that today forms the inner wedge of Indo-Burman Ranges, is completely emerged. The Chindwin Basin is temporarily overfilled and drainages in central Myanmar become southward directed (Fig. 12C). The modern geomorphology of central Myanmar is set up, with the central Myanmar low plains enclosed on the west and the east by topographic highs (Fig. 13C).

The 39–38 Ma window thus appears to be a period of significant change for the subduction margin, with the emergence of the inner wedge of the Indo-Burman Ranges, the first evidence of exhumation of the metamorphic belts, and the first indication of pull-apart partitioning of the forearc basin. Exhumation of the metamorphic belts could have sporadically started earlier in the middle Eocene, as discussed earlier, but the metamorphic belts became a prominent, continuous sediment supplier starting at 39–38 Ma. Similarly, pull-apart subsidence of the basin might have started earlier, but the forearc appears to be significantly partitioned during this time window.

Earlier onset of uplift and exhumation of the accretionary prism is also probable, as proposed by previous authors (as early as the Cretaceous; Socquet et al., 2002; Zhang et al., 2017a). However, the inner wedge lacks shallow-marine deposits and is dominated by marine turbidite sequences (Bender, 1983), indicating that depo-

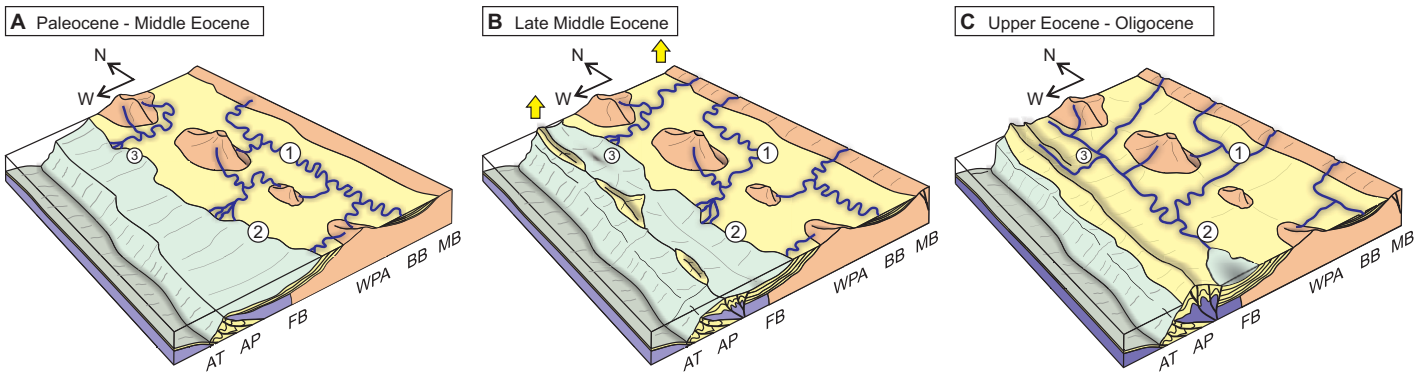

Figure 12. Evolution of the Burmese subduction margin and forearc basin from the Paleocene–middle Eocene (A), the late middle Eocene (B), and the upper Eocene–Oligocene (C). 1, 2, and 3 indicate the location of the Shwebo, Minbu, and Chindwin basins respectively (same as on Fig. 2). AT—Arakan Trench; AP—accretionary prism; FB—forearc basin; WPA—Wuntho-Popa Arc; BB—backarc basin; MB—metamorphic belts.

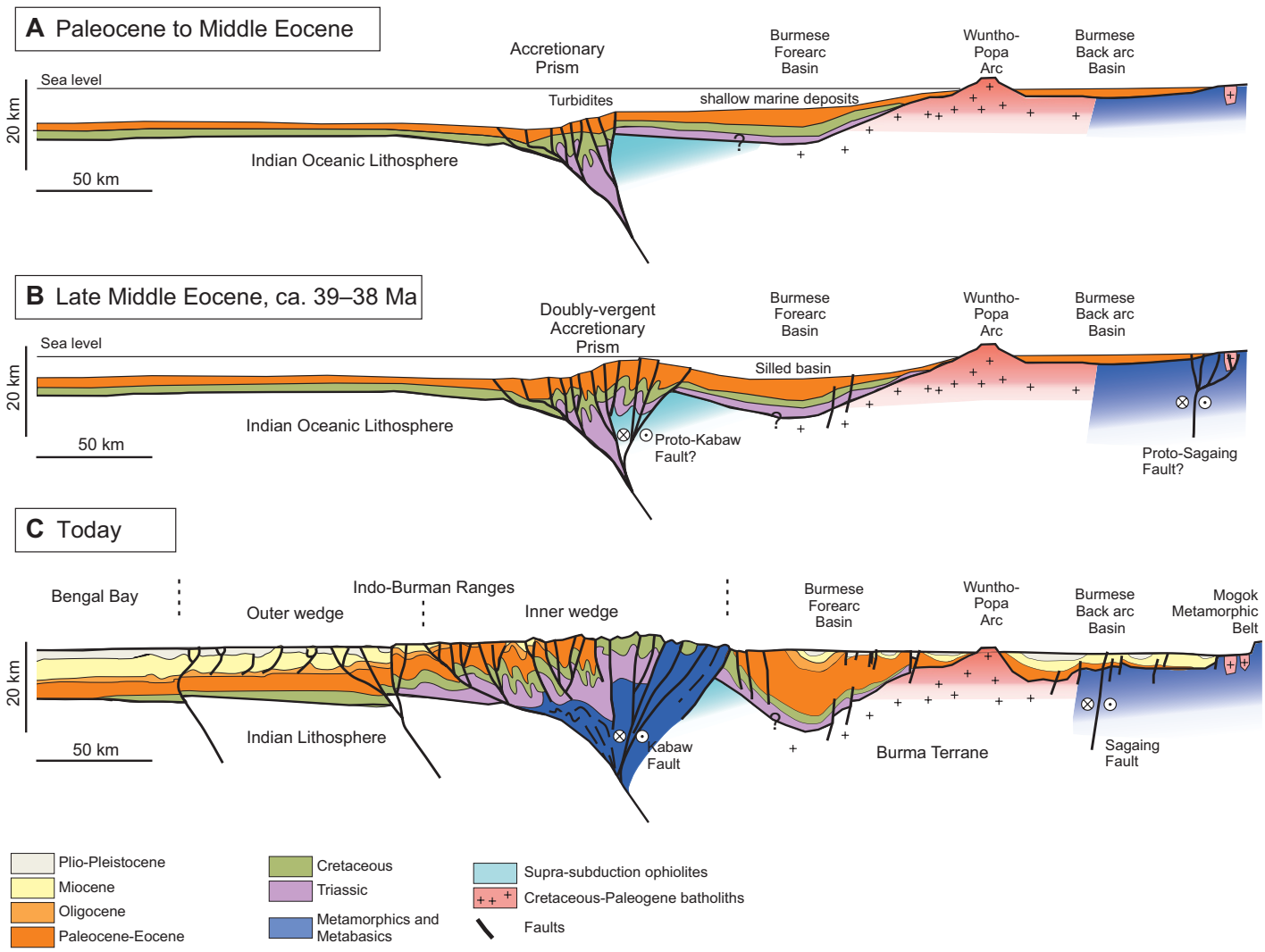

Figure 13. Schematic cross section across a W–E transect in western and central Myanmar (location on Fig. 2) during the Paleocene–middle Eocene (A), late middle Eocene (B), and today (C; after Maurin and Rangin, 2009). The question mark indicates that the presence of Triassic rocks thrusted on the ophiolitic basement of the forearc is still unclear.

sitional environments shifted very quickly from deep-sea deposition in the trench to sub-aerial deposition. It is thus likely that most of the uplift started only slightly before 39–38 Ma.

Contacts between sedimentary units exposed in the inner wedge provide a few more details about what happened after this early uplift of the accretionary prism. On the eastern side of the inner wedge of the accretionary prism, Eocene marine rocks are unconformably overlain by a conglomeratic molasse, the Maw Gravels, which yield late middle Miocene fossil mammals (Bender, 1983). In places, a 10-m-thick, ferralitic paleosol profile with a 0.5–1-m-thick petroplinthic horizon made of continuous, thick iron crust developed in the Eocene rocks at the contact between both units (Fig. DR3 [see footnote 1]; Licht, 2013). The thickness of the lateritic profile and the presence of a petroplinthic horizon indicate that the development of the paleosol likely took a significant amount of time—up to several million years (Valeton, 1994). This finding indicates that there was a long period of tectonic quiescence between the initial uplift of the inner wedge during the late Eocene and the deposition of the late middle Miocene Molasse. The deposition of the Maw Gravels was likely related to the onset of the recent, Mio-Pliocene uplift of the Indo-Burman Ranges that exposed the outer wedge of the accretionary prism (Maurin and Rangin, 2009). The uplift of the Indo-Burman Ranges thus appears to have occurred in at least two steps: first, during the late Eocene when the inner wedge was exposed, and second, during the late Miocene–Pliocene when the outer wedge was formed.

Various mechanisms are proposed to explain the late Miocene-Pliocene uplift of the Indo-Burman Ranges, including the subduction of the large amount of Neogene sediments that fill up the Bengal Basin and the Sylhet Basin (Maurin and Rangin, 2009), and increased E-W shortening of the Burmese platelet due to the arrival of mid-crustal flow from the east following the late Miocene collapse of the Tibetan Plateau (Rangin et al., 2013). However, these mechanisms are only valid for the Neogene and cannot explain the late middle Eocene uplift of the inner wedge.

A temporary shift to flat slab subduction could explain the uplift of the accretionary prism, but would not explain the extremely high subsidence rates in the foreland basin or the high-grade metamorphism throughout the backarc areas (Finzel et al., 2011). The accretion of a small allochthonous terrane or volcanic arc, as proposed by others (i.e., Acharyya, 2007, 2015), could partly explain the uplift, but would also fail to explain the coeval shift to intense strike-slip deformation and subsidence in the forearc; there is also no clear evidence for such allochthonous blocks in the accretionary prism. A change of plate kinematics driving increased E-W convergence and upper plate shortening could also explain the shift to a more compressive regime and the resulting uplift of the accretionary prism; however, in the Paleogene, the convergence of the Indian plate relative to Southeast Asia trended to lower velocities and increased obliquity, which would not favor this hypothesis (Lee and Lawver, 1995; Cande et al., 2010; van Hinsbergen et al., 2011b). Still others have proposed a collision of a northeast moving Indian plate with the Burmese margin slightly before 39–38 Ma followed by a change of convergence direction from NE to N (Morley, 2002; Aitchison et al., 2007; Vérard et al., 2017). The collision could have anchored the Burmese platelet to India and dragged it northward as the direction of convergence changed, providing an explanation for an episode of shortening in the accretionary prism followed by strike-slip deformation of the upper plate. However, it is remarkable that such a collision between a cold, thick continental plate and the weak, hot Burmese margin (Morley, 2009) did not result in more surface deformation and uplift; moreover, strike-slip deformation (and related pull-apart subsidence) seems coeval rather than posterior to accretionary wedge uplift.

Today, the obliquity ratio (ratio of the strike-slip velocity divided by the sum of strike-slip and normal velocity) of the convergence along the Burmese subduction margin is ~0.65 and so can be called "hyper-oblique" (Nielsen et al., 2004). The core of the inner wedge of the Indo-Burman Ranges displays a positive flower structure and is traversed by the Kabaw strike-slip Fault, which accommodates 1/4–1/3 of the N-S strike slip deformation of the Burma Terrane (Nielsen et al., 2004; Socquet et al., 2006; Maurin and Rangin, 2009). In this sense, the inner wedge of the Indo-Burman Ranges is very similar to retro-wedges formed along hyper-oblique convergence zones where the obliquity ratio r is > 0.5 (Burbidge and Braun, 1998; McClay et al., 2004). The Eocene uplift of the inner (retro-) wedge of the Indo-Burman Ranges can be explained in light of the known evolution of accretionary prisms formed by hyper-oblique convergence. Such systems go through a period of fast retro-wedge building and uplift via the transition from localized strain partitioning in the accretionary wedge to full strain partitioning, and all strike slip motion is eventually accommodated by one or several individual fault systems (McClay et al., 2004; Leever et al., 2011). Evidence of coeval pull-apart subsidence and partitioning in the forearc and of the onset of high-grade metamorphism associated with exhumation of the metamorphic belts corroborates intense shear and strike-slip faulting on the Burma platelet during that time. Thus, we interpret the late middle Eocene uplift of the Indo-Burman Ranges as reflecting localized strain partitioning and wedge build-up prefiguring the onset of a paleo-Kabaw Fault system ("oblique wedge stage" of Leever et al., 2011). The onset of full strain partitioning and of the paleo-Kabaw Fault system would have been coeval or have shortly followed the late middle Eocene, eventually slowing the uplift of the accretionary wedge.

5.6. Implications for the History of India Asia Convergence

Our interpretations imply that the convergence of the Indian plate along the Burmese margin has been hyper-oblique since at least the late Bartonian, ca. 39–38 Ma, and that it resulted in the coeval uplift of the inner wedge of the accretionary prism, pull-apart subsidence and partitioning of the forearc basins, and high-grade metamorphism and exhumation along the metamorphic belts (Fig. 13). While the modern Burmese sliver fault system is commonly dated to the middle Miocene and the opening of the Andaman Sea (Khan and Chakraborty 2005; Socquet et al., 2006), our results suggest that a similar paleo-sliver system, with a paleo-Kabaw Fault in the accretionary prism and a paleo–Shan Scarp Fault in the metamorphic belts, was already set up by the late middle Eocene or shortly thereafter (Fig. 13B). These observations corroborate evidence for ca. Eocene to ca. Miocene syn-kinematic deposition in the backarc basin, indicating that a proto–"Shan Scarp" Fault was already active (Morley, 2017). Strike-slip deformation of the Burmese margin could have started even earlier, sometime in the middle Eocene, but would have been less substantial.

Our results thus suggest that the northward drag of the Burmese platelet pre-dates the opening of the Andaman Sea and the set-up of the modern sliver system in the middle Miocene by at least 20 million years. Central Myanmar has thus likely moved northward by much more than 400–500 km, which is the lower-end estimate of northward motion achieved by simply closing the Andaman Sea rift system (Maung, 1987). We suspect that the actual motion of Central Myanmar over this time period to be closer to Mitchell's (1993) upper estimate of ~1100 km, with 600–700 km of the motion occurring between the late middle Eocene and the middle Miocene; this movement was accommodated to the opening of the Eocene-Miocene Mergui and North Sumatra Basins south the Andaman Rift (Hall and Morley, 2004).

There is no clear evidence for shortening and surface uplift in central Myanmar before the late middle Eocene. Leading up to the shift in sedimentation regime 39–38 Ma, accumulation in the forearc basin was continuous and dominated by the denudation of the volcanic arc from the Paleocene to the late middle Eocene, as is seen in standard Andean-type margins, and thus rules out a collision with India. A collision of the Indian Plate with the Burmese margin sometime during the early to middle Eocene, as is proposed by most of the kinematic models dominated by extrusion processes (Tapponnier et al., 1982; Replumaz and Tapponnier, 2003; Replumaz et al., 2010; Cogné et al., 2013), and more exotic scenarios (Aitchison et al., 2007; Vérard et al., 2017), seems thus unlikely. If such a collision had occurred, it would have been located in northernmost Myanmar, in the Eastern Himalayan Syntaxis—where forearc strata have not been preserved (Fig. 2), leaving most of the Burmese margin undeformed.

Our reconstruction of the history of the Burmese subduction margin validates geodynamic models that locate Myanmar east of the collision zone as early as the Paleocene, with Indochina already forming a narrow peninsula at the southeastward extremity of East Asia. This narrow peninsula must have had a similar-to-today N-S orientation since at least the late middle Eocene to explain hyper-oblique convergence along the Burmese margin. In this sense, our results are in agreement with models dominated by homogeneous thickening and continuous deformation of weaker Asian lithosphere that propose a conservative, similar-to-today pre-collisional paleogeography for SE Asia and argue that most of Myanmar and the Burma Terrane was not particularly shortened or thickened by the collision with India (Fig. 1C; e.g., England and Houseman, 1986; Molnar et al., 1993; Hallet and Molnar, 2001; Shen et al., 2001; van Hinsbergen et al., 2011a, 2012; Hall, 2012; Seton et al., 2012). However, our results do not completely exclude extrusion and rotation processes as active post-collisional processes in SE Asia; the shift to hyper-oblique convergence along the Burmese margin could be explained by an undetermined amount of post-collisional rotation of peninsular Indochina. Our reconstructions show that this rotation must have been achieved by 39–38 Ma to explain the onset of hyper-oblique convergence along the Burmese margin. The idealized extrusion-dominated reconstructions of van Hinsbergen et al. (2011a), adapted from Replumaz and Tapponnier (2003) and Royden et al. (2008) are the closest analogues to this scenario. Paleomagnetic estimates of post-collisional clockwise rotation in peninsular Indochina yield results of variable magnitude, with estimates of 20–30° for the whole of Indochina (Richter and Fuller, 1996; Charusiri et al., 2006; Li et al., 2017), and as much as >70° in some places (Sato et al., 2001; Tong et al., 2016). Yet, the lack of detailed geological data in peninsular Indochina (i.e., ages and origins of volcanism and metamorphism along shear zones) often precludes a robust age interpretation for this rotation, as evidenced by the recent synthesis of Li et al. (2017), and ultimately hinders a clear evaluation of the accuracy of this scenario.

We also see three additional mechanisms to possibly explain the shift to hyper-oblique convergence in the late middle Eocene, which are more controversial.

(1) A potential collision between the eastern tip of India and northernmost Myanmar shortly before 39 Ma could have anchored the Burmese margin to the Indian plate's northwards motion. However, this timing is at odds with many other studies along the India-Asia Suture that indicate a collision started ca. 55 Ma (see reviews in Najman, 2006; Najman et al., 2010).

(2) A late and poorly dated small rotation (~15° counterclockwise) of Indian convergence in the middle Eocene (Lee and Lawver, 1995; Cande et al., 2010) could have triggered the shift to strike-slip deformation. This late rotation would have slightly increased the convergence obliquity along the margin, but it seems too small to have alone triggered strain partitioning on the Burmese margin.

(3) A change in the properties of the subducting material may have favored the shift to strain partitioning on the Burmese margin. By the late Eocene, most of the old, Jurassic Tethyan oceanic crust had been subducted below the Asian subduction margin. The late Eocene would correspond roughly to the time when Cenozoic oceanic crust from the Indian Ocean reached the Burmese margin (Seton et al., 2012; Hall, 2012). This younger, less dense oceanic lithosphere could have acted as a giant sheet anchor increasing both the northward drag of the subduction margin and the shear on the Burmese plate.

Cretaceous–Paleogene paleomagnetic data from the Burmese platelet could potentially help us validate or reject these scenarios by reconstructing the amount and timing of paleo-rotation of the subduction margin; however, paleomagnetic data from central Myanmar are so far virtually nonexistent.

6. CONCLUSIONS

Our results show that the modern tectonic configuration of central Myanmar, today a sliver plate bounded to the west by the Indo-Burman Ranges and the Kabaw Fault, and to the east by the Burmese metamorphic belts and the Sagaing Fault, was actually first formed during a short time window in the late middle Eocene.

From the Paleocene to the middle Eocene, the Burmese margin displayed the regular morphology of an Andean-type margin, with a forearc basin developed on a nascent accretionary prism open to the trench, where westward-prograding deltaic systems were fed by the denudation of the Wuntho-Popa volcanic arc. In the late middle Eocene, around 39–38 Ma, the accretionary prism started emerging. Pull-apart subsidence partitioned the forearc basin into two basins—the Chindwin Basin to the north and the Minbu Basin to the south. Quasi-closed estuarine conditions developed in the Chindwin Basin, whereas the Minbu Basin remained more open to the ocean. Simultaneously, increased shear stress in the backarc area led to metamorphism and exhumation of the Burma terrane basement. By 37 Ma, the Paleogene accretionary prism, forming today the inner wedge of Indo-Burman Ranges, had completely emerged. The main drainages in central Myanmar became southward directed, and the modern central Myanmar low plains were formed.

This tectonic evolution can be explained in light of the known evolution of accretionary prisms formed by hyper-oblique convergence. Coeval pull-apart subsidence and partitioning in the forearc, and onset of high-grade metamorphism associated with exhumation in the metamorphic belts indicate both intense shear and strike-slip faulting on the Burmese platelet during that time, and high obliquity of the convergence at the Burmese margin. We interpret the synchronous uplift of the Indo-Burman Ranges as reflecting accretionary wedge build-up marking the onset of a paleo–Kabaw Fault system. These interpretations imply that a similar-to-today sliver system, with a paleo–Kabaw Fault in the accretionary prism and a paleo–Sagaing shear zone (the paleo–Shan Scarp Fault) creating high-grade metamorphism in the metamorphic belts to the east, was already set up by the late middle Eocene. This evolution indicates that the Burmese sliver platelet is at least twice older than previously thought and that it has experienced a significant (>500 km), but yet to be determined, amount of northward motion. Finally, our results do not support any India-Asia convergence scenario involving a Paleogene collision of India with the Burmese subduction margin. Our reconstruction for the evolution of the Burmese margin is more in agreement with conservative geodynamic models for the India-Asia convergence arguing for a close-to-modern pre-collisional paleogeometry for the Indochina Peninsula, and indicates that any post-collisional rotation of Indochina, if it existed, must have been achieved by 39 Ma.

ACKNOWLEDGMENTS

This research was primarily funded by the European Research Council Consolidator Grant MAGIC 649081, the Marie Curie fellowship ECAMMETT 656731, and the University of Washington. We thank two anonymous reviewers, Chris Morley, Kyi Kyi Thein, Chit Sein, J.-J. Jaeger, O. Chavasseau, V. Lazarri, Andrew Schauer, D. Cowan, D. van Hinsbergen, M. Mueller, M. Needle, M. Koehler, A. Gagnon, M. Pecha, G. Gehrels, D. Giesler, A. Pullen, B. Nelson, and F. Teng for prolific discussions, and assistance in the field and in the lab.

REFERENCES CITED

Acharyya, S.K., 2007, Collisional emplacement history of the Naga-Andaman ophiolites and the position of the eastern Indian suture: Journal of Asian Earth Sciences, v. 29, no. 2, p. 229–242, https://doi.org/10.1016/j.jseaes.2006.03.003.

Acharyya, S.K., 2015, Indo-Burma Range: a belt of accreted microcontinents, ophiolites and Mesozoic–Paleogene flyschoid sediments: International Journal of Earth Sciences, v. 104, no. 5, p. 1235–1251, https://doi.org/10.1007/s00531-015-1154-6.

Adnet, S., Cappetta, H., Beard, K.C., Marivaux, L., Marandat, B., Chaimanee, Y., et al., 2008, First myliobatiform teeth (Elasmobranchii, Neoselachii) from the pondaung formation (late middle Eocene) of central Myanmar: Neues Jahrbuch für Geologie und Palaontologie, Abhandlungen, v. 247, no. 3, p. 335–340, https://doi.org/10.1127/0077-7749/2008/0247-0335.

Aitchison, J.C., Ali, J.R., and Davis, A.M., 2007, When and where did India and Asia collide?: Journal of Geophysical Research. Solid Earth, v. 112, B5, https://doi.org/10.1029/2006JB004706.

Allègre, C.O., Courtillot, V., Tapponnier, P., Hirn, A., Mattauer, M., Coulon, C., et al., 1984, Structure and evolution of the Himalaya–Tibet orogenic belt: Nature, v. 307, no. 5946, p. 17–22, https://doi.org/10.1038/307017a0.

Allen, J.R., 2000, Morphodynamics of Holocene salt marshes: A review sketch from the Atlantic and Southern North Sea coasts of Europe: Quaternary Science Reviews, v. 19, no. 12, p. 1155–1231, https://doi.org/10.1016/S0277-3791(99)00034-7.

Allen, R., Najman, Y., Carter, A., Barfod, D., Bickle, M.J., Chapman, H.J., et al., 2008, Provenance of the Tertiary sedimentary rocks of the Indo-Burman Ranges, Burma (Myanmar): Burman arc or Himalayan-derived?: Journal of the Geological Society, v. 165, no. 6, p. 1045–1057, https://doi.org/10.1144/0016-76492007-143.

Anthony, E.J., Lang, J., and Oyédé, L.M., 1996, Sedimentation in a tropical, microtidal, wave-dominated coastal-plain estuary: Sedimentology, v. 43, no. 4, p. 665–675, https://doi.org/10.1111/j.1365-3091.1996.tb02019.x.

Anthony, E.J., Oyédé, L.M., and Lang, J., 2002, Sedimentation in a fluvially infilling, barrier-bound estuary on a wave-dominated, microtidal coast: The Ouémé River estuary, Benin, West Africa: Sedimentology, v. 49, no. 5, p. 1095–1112, https://doi.org/10.1046/j.1365-3091.2002.00491.x.

Bannert, D., Lyen, A.S., and Htay, T., 2011, The Geology of the Indoburman Ranges in Myanmar: Geologisches Jahrbuch, v. 101, p. 5–101.

Barley, M.E., Pickard, A.L., Zaw, K., Rak, P., and Doyle, M.G., 2003, Jurassic to Miocene magmatism and metamorphism in the Mogok metamorphic belt and the India-Eurasia collision in Myanmar: Tectonics, v. 22, no. 3, https://doi.org/10.1029/2002TC001398.

Bender, F., 1983, Geology of Burma: Berlin, Gebrüder Borntraeger, 293 p.

Bertrand, G., and Rangin, C., 2003, Tectonics of the western margin of the Shan plateau (central Myanmar): Implication for the India–Indochina oblique convergence since the Oligocene: Journal of Asian Earth Sciences, v. 21, no. 10, p. 1139–1157, https://doi.org/10.1016/S1367-9120(02)00183-9.

Bertrand, G., Rangin, C., Maluski, H., Bellon, H., and Party, G.S., 2001, Diachronous cooling along the Mogok Metamorphic Belt (Shan scarp, Myanmar): The trace of the northward migration of the Indian syntaxis: Journal of Asian Earth Sciences, v. 19, no. 5, p. 649–659, https://doi.org/10.1016/S1367-9120(00)00061-4.

Botev, Z.I., Grotowski, J.F., and Kroese, D.P., 2010, Kernel density estimation via diffusion: Annals of Statistics, v. 38, no. 5, p. 2916–2957, https://doi.org/10.1214/10-AOS799.

Brunnschweiler, R.O., 1966, On the Geology of the Indoburman Ranges: Journal of the Geological Society of Australia, v. 13, p. 137–194, https://doi.org/10.1080/00167616608728608.

Burbidge, D.R., and Braun, J., 1998, Analogue models of obliquely convergent continental plate boundaries: Journal of Geophysical Research. Solid Earth, v. 103, B7, p. 15,221–15,237, https://doi.org/10.1029/98JB00751.

Cande, S.C., Patriat, P., and Dyment, J., 2010, Motion between the Indian, Antarctic and African plates in the early Cenozoic: Geophysical Journal International, v. 183, no. 1, p. 127–149, https://doi.org/10.1111/j.1365-246X.2010.04737.x.

Charusiri, P., Imsamut, S., Zhuang, Z., Ampaiwan, T., and Xu, X., 2006, Paleomagnetism of the earliest Cretaceous to early late Cretaceous sandstones, Khorat Group, Northeast Thailand: Implications for tectonic plate movement of the Indochina block: Gondwana Research, v. 9, no. 3, p. 310–325, https://doi.org/10.1016/j.gr.2005.11.006.

Casagrande, D.J., 1987, Sulphur in peat and coal, *in* Scott, A.C., ed., Coal and coal-bearing strata: Recent advances: Geological Society of London Special Publication 32, p. 87–105, https://doi.org/10.1144/GSL.SP.1987.032.01.07.

Chaimanee, Y., Chavasseau, O., Beard, K.C., Kyaw, A.A., Soe, A.N., Sein, C., et al., 2012, Late Middle Eocene primate from Myanmar and the initial anthropoid colonization of Africa: Proceedings of the National Academy of Sciences of the United States of America, v. 109, p. 10,293–10,297, https://doi.org/10.1073/pnas.1200644109.

Chavasseau, O., Chaimanee, Y., Tun, S.T., Soe, A.N., Barry, J.C., Marandat, B., et al., 2006, Chaungtha, a new Middle Miocene mammal locality from the Irrawaddy Formation, Myanmar: Journal of Asian Earth Sciences, v. 28, no. 4, p. 354–362, https://doi.org/10.1016/j.jseaes.2005.10.012.

Chavasseau, O., Chaimanee, Y., Coster, P., Emonet, E.G., Soe, A.N., Kyaw, A.A., Maung, A., Rugbumrung, M., Shwe, H., and Jaeger, J.-J., 2010, First record of a chalicothere from the Miocene of Myanmar: Acta Palaeontologica Polonica, v. 55, p. 13–22, https://doi.org/10.4202/app.2009.0033.

Chen, Y., Courtillot, V., Cogné, J.P., Besse, J., Yang, Z., and Enkin, R., 1993, The configuration of Asia prior to the collision of India: Cretaceous paleomagnetic constraints: Journal of Geophysical Research, Solid Earth, v. 98, B12, p. 21,927–21,941.

Chew, D.M., Petrus, J.A., and Kamber, B.S., 2014, U–Pb LA–ICPMS dating using accessory mineral standards with variable common Pb: Chemical Geology, v. 363, p. 185–199, https://doi.org/10.1016/j.chemgeo.2013.11.006.

Cogné, J.P., Besse, J., Chen, Y., and Hankard, F., 2013, A new Late Cretaceous to Present APWP for Asia and its implications for paleomagnetic shallow inclinations in Central Asia and Cenozoic Eurasian plate deformation: Geophysical Journal International, v. 192, no. 3, p. 1000–1024, https://doi.org/10.1093/gji/ggs104.

Collinson, J.D., Mountney, N.P., and Thompson, D.B., 2006, Sedimentary Structures: Terra Publishing, third edition, 292 p.

Dalrymple, R.W., Zaitlin, B.A., and Boyd, R., 1992, Estuarine facies models: conceptual basis and stratigraphic implications: perspective: Journal of Sedimentary Research, v. 62, no. 6, https://doi.org/10.1306/D4267A69-2B26-11D7-8648000102C1865D.

DeCelles, P.G., Robinson, D.M., and Zandt, G., 2002, Implications of shortening in the Himalayan fold-thrust belt for uplift of the Tibetan Plateau: Tectonics, v. 21, no. 6, https://doi.org/10.1029/2001TC001322.

DeCelles, P.G., Kapp, P., Gehrels, G.E., and Ding, L., 2014, Paleocene-Eocene foreland basin evolution in the Himalaya of southern Tibet and Nepal: Implications for the age of initial India-Asia collision: Tectonics, v. 33, no. 5, p. 824–849, https://doi.org/10.1002/2014TC003522.

Dickinson, W.R., 1985, Interpreting provenance relations from detrital modes of sandstones, *in* Zuma, G.G., ed., Provenance of Arenites: Cosenza, Italy, D. Reidel Publishing Company, p. 333–361, https://doi.org/10.1007/978-94-017-2809-6_15.

England, P., and Houseman, G., 1986, Finite strain calculations of continental deformation: 2. Comparison with the India-Asia collision zone: Journal of Geophysical Research, Solid Earth, v. 91, B3, p. 3664–3676, https://doi.org/10.1029/JB091iB03p03664.

Finzel, E.S., Trop, J.M., Ridgway, K.D., and Enkelmann, E., 2011, Upper plate proxies for flat-slab subduction processes in southern Alaska: Earth and Planetary Science Letters, v. 303, no. 3-4, p. 348–360, https://doi.org/10.1016/j.epsl.2011.01.014.

Fry, B., Silva, S.R., Kendall, C., and Anderson, R.K., 2002, Oxygen isotope corrections for online $\delta^{34}S$ analysis: Rapid Communications in Mass Spectrometry, v. 16, no. 9, p. 854–858, https://doi.org/10.1002/rcm.651.

Gardiner, N.J., Searle, M.P., Robb, L.J., and Morley, C.K., 2015, Neo-Tethyan magmatism and metallogeny in Myanmar—An Andean analogue?: Journal of Asian Earth Sciences, v. 106, p. 197–215, https://doi.org/10.1016/j.jseaes.2015.03.015.

Gardiner, N.J., Hawkesworth, C.J., Robb, L.J., Whitehouse, M.J., Roberts, N.M., Kirkland, C.L., and Evans, N.J., 2017, Contrasting Granite Metallogeny through the Zircon Record: A Case Study from Myanmar: Scientific Reports, v. 7, no. 1, p. 748, https://doi.org/10.1038/s41598-017-00832-2.

Garzanti, E., Wang, J.G., Vezzoli, G., and Limonta, M., 2016, Tracing provenance and sediment fluxes in the Irrawaddy River basin (Myanmar): Chemical Geology, v. 440, p. 73–90, https://doi.org/10.1016/j.chemgeo.2016.06.010.

Gibbons, A.D., Zahirovic, S., Müller, R.D., Whittaker, J.M., and Yatheesh, V., 2015, A tectonic model reconciling evidence for the collisions between India, Eurasia and intra-oceanic arcs of the central-eastern Tethys: Gondwana Research, v. 28, no. 2, p. 451–492, https://doi.org/10.1016/j.gr.2015.01.001.

Gingras, M.K., Pemberton, S.G., and Saunders, T., 2001, Bathymetry, sediment texture, and substrate cohesiveness; their impact on modern Glossifungites trace assemblages at Willapa Bay, Washington: Palaeogeography, Palaeoclimatology, Palaeoecology, v. 169, no. 1-2, p. 1–21, https://doi.org/10.1016/S0031-0182(01)00212-7.

Gough, A., and Hall, R., 2017, Oligocene Fluvio-Deltaic Depositional Environments Salin Sub-Basin, Central Myanmar [abs.]: American Geophysical Union Fall Meeting 2017, New Orleans, abstract #EP21F-1904.

Gradstein, F.M., Ogg, J.G., Schmitz, M., and Ogg, G., eds., 2012, The Geologic Time Scale 2012: Elsevier, 1176 p.

Hall, R., 2012, Late Jurassic–Cenozoic reconstructions of the Indonesian region and the Indian Ocean: Tectonophysics, v. 570, p. 1–41, https://doi.org/10.1016/j.tecto.2012.04.021.

Hall, R., and Morley, C.K., 2004, Sundaland basins, *in* Clift, P., et al., eds., Continent-Ocean Interactions within the East Asian Marginal Seas: Washington, D.C., American Geophysical Union, Geophysical Monograph, v. 149, p. 55–85.

Hallet, B., and Molnar, P., 2001, Distorted drainage basins as markers of crustal strain east of the Himalaya: Journal of Geophysical Research, Solid Earth, v. 106, B7, p. 13,697–13,709, https://doi.org/10.1029/2000JB900335.

Harrison, T.M., Yin, A., and Ryerson, F.J., 1998, Orographic evolution of the Himalaya and Tibetan plateau: Oxford Monographs on Geology and Geophysics, v. 39, p. 39–72.

Jaeger, J.-J., Thein, T., Benammi, M., Chaimanee, Y., Soe, A.N., Lwin, T., et al., 1999, A new primate from the middle Eocene of Myanmar and the Asian early origin of anthropoids: Science, v. 286, no. 5439, p. 528–530, https://doi.org/10.1126/science.286.5439.528.

Khan, P.K., and Chakraborty, P.P., 2005, Two-phase opening of Andaman Sea: A new seismotectonic insight: Earth and Planetary Science Letters, v. 229, no. 3, p. 259–271, https://doi.org/10.1016/j.epsl.2004.11.010.

Khin, K., and Myitta, 1999, Marine transgression and regression in Miocene sequences of northern Pegu (Bago) Yoma, Central Myanmar: Journal of Asian Earth Sciences, v. 17, no. 3, p. 369–393, http:/doi.org/10.1016/S0743-9547(98)00065-8.

Lee, T.Y., and Lawver, L.A., 1995, Cenozoic plate reconstruction of Southeast Asia: Tectonophysics, v. 251, no. 1-4, p. 85–138, https://doi.org/10.1016/0040-1951(95)00023-2.

Lee, H.Y., Chung, S.L., and Yang, H.M., 2016, Late Cenozoic volcanism in central Myanmar: Geochemical characteristics and geodynamic significance: Lithos, v. 245, p. 174–190, https://doi.org/10.1016/j.lithos.2015.09.018.

Leeder, M.R., 2009, Sedimentology and Sedimentary Basins: From Turbulence to Tectonics: John Wiley & Sons, 608 p.

Leever, K.A., Gabrielsen, R.H., Sokoutis, D., and Willingshofer, E., 2011, The effect of convergence angle on the kinematic evolution of strain partitioning in transpressional brittle wedges: Insight from analog modeling and high-resolution digital image analysis: Tectonics, v. 30, no. 2, https://doi.org/10.1029/2010TC002823.

Li, S., Advokaat, E.L., van Hinsbergen, D.J., Koymans, M., Deng, C., and Zhu, R., 2017, Paleomagnetic constraints on the Mesozoic-Cenozoic paleolatitudinal and rotational history of Indochina and South China: Review and updated kinematic reconstruction: Earth-Science Reviews, v. 171, p. 58–77, https://doi.org/10.1016/j.earscirev.2017.05.007.

Licht, A., 2013, Paléodrainage, paléoenvironnements et paléoclimats de l'Eocène birman: Implications sur l'origine et l'évolution précoce des anthropoïdes asiatiques [Ph.D. thesis]: France, University of Poitiers, 264 p.

Licht, A., France-Lanord, C., Reisberg, L., Fontaine, C., Soe, A.N., and Jaeger, J.-J., 2013, A palaeo Tibet–Myanmar connection? Reconstructing the Late Eocene drainage system of central Myanmar using a multi-proxy approach: Journal of the Geological Society, v. 170, no. 6, p. 929–939, https://doi.org/10.1144/jgs2012-126.

Licht, A., Boura, A., De Franceschi, D., Ducrocq, S., Soe, A.N., and Jaeger, J.-J., 2014a, Fossil woods from the late middle Eocene Pondaung Formation, Myanmar: Review of Palaeobotany and Palynology, v. 202, p. 29–46, https://doi.org/10.1016/j.revpalbo.2013.12.002.

Licht, A., Cojan, I., Caner, L., Soe, A.N., Jaeger, J., and France-Lanord, C., 2014b, Influence of permeability barriers in alluvial hydromorphic palaeosols: The Eocene Pondaung Formation, Myanmar: Sedimentology, v. 61, p. 362–382.

Licht, A., van Cappelle, M., Abels, H. A., Ladant, J., Trabucho-Alexandre, J., France-Lanord, C., Donnadieu, Y., Vandenberghe, J., Rigaudier, T., Lecuyer, C., Terry Jr., D., Adriaens, R., Boura, A., Guo, Z., Soe, A.N., Dupont-Nivet, G., and Jaeger, J.-J., 2014c, Asian monsoons in a late Eocene greenhouse world: Nature, v. 513, p. 501–506, https://doi.org/10.1038/nature13704.

Licht, A., Boura, A., De Franceschi, D., Utescher, T., Sein, C., and Jaeger, J.-J., 2015, Late middle Eocene fossil wood of Myanmar: Implications for the landscape and the climate of the Eocene Bengal Bay: Review of Palaeobotany and Palynology, v. 216, p. 44–54, https://doi.org/10.1016/j.revpalbo.2015.01.010.

Licht, A., Reisberg, L., France-Lanord, C., Soe, A.N., and Jaeger, J.-J., 2016, Cenozoic evolution of the central Myanmar drainage system: Insights from sediment provenance in the Minbu Sub-Basin: Basin Research, v. 28, no. 2, p. 237–251, https://doi.org/10.1111/bre.12108.

Liu, C.Z., Chung, S.L., Wu, F.Y., Zhang, C., Xu, Y., Wang, J.G., et al., 2016, Tethyan suturing in Southeast Asia: Zircon U-Pb and Hf-O isotopic constraints from Myanmar ophiolites: Geology, v. 44, no. 4, p. 311–314, https://doi.org/10.1130/G37342.1.

Ludwig, K.R., 2003, User's manual for Isoplot 3.00: A Geochronological Toolkit for Microsoft Excel: Berkeley Geochronological Center Special Publication 4.

Ma, L., Wang, Y., Fan, W., Geng, H., Cai, Y., Zhong, H., et al., 2014, Petrogenesis of the early Eocene I-type granites in west Yingjiang (SW Yunnan) and its implication for the eastern extension of the Gangdese batholiths: Gondwana Research, v. 25, no. 1, p. 401–419.

Ma, Y., Yang, T., Bian, W., Jin, J., Zhang, S., Wu, H., and Li, H., 2016, Early Cretaceous paleomagnetic and geochronologic results from the Tethyan Himalaya: Insights into the Neotethyan paleogeography and the India–Asia collision: Scientific Reports, v. 6, 21605, https://doi.org/10.1038/srep21605.

Maffione, M., van Hinsbergen, D.J., Koornneef, L.M., Guilmette, C., Hodges, K., Borneman, N., et al., 2015, Forearc hyperextension dismembered the south Tibetan ophiolites: Geology, v. 43, p. 475–478, https://doi.org/10.1130/G36472.1.

Maung, H., 1987, Transcurrent movements in the Burma–Andaman Sea region: Geology, v. 15, p. 911–912, https://doi.org/10.1130/0091-7613(1987)15<911:TMITBS>2.0.CO;2.

Maurin, T., and Rangin, C., 2009, Structure and kinematics of the Indo-Burmese Wedge: Recent and fast growth of the outer wedge: Tectonics, v. 28, no. 2, https://doi.org/10.1029/2008TC002276.

Maury, R.C., Pubellier, M., Rangin, C., Wulput, L., Cotten, J., Socquet, A., et al., 2004, Quaternary calc-alkaline and alkaline volcanism in an hyper-oblique convergence setting, central Myanmar and western Yunnan: Bulletin de la Société Géologique de France, v. 175, no. 5, p. 461–472, https://doi.org/10.2113/175.5.461.

McClay, K.R., Whitehouse, P.S., Dooley, T., and Richards, M., 2004, 3D evolution of fold and thrust belts formed by oblique convergence: Marine and Petroleum Geology, v. 21, no. 7, p. 857–877, https://doi.org/10.1016/j.marpetgeo.2004.03.009.

McQuarrie, N., Tobgay, T., Long, S.P., Reiners, P.W., and Cosca, M.A., 2014, Variable exhumation rates and variable displacement rates: Documenting recent slowing of Himalayan shortening in western Bhutan: Earth and Planetary Science Letters, v. 386, p. 161–174, https://doi.org/10.1016/j.epsl.2013.10.045.

Metcalfe, I., 2013, Gondwana dispersion and Asian accretion: tectonic and palaeogeographic evolution of eastern Tethys: Journal of Asian Earth Sciences, v. 66, p. 1–33, https://doi.org/10.1016/j.jseaes.2012.12.020.

Miall, A.D., 2013, The geology of fluvial deposits: sedimentary facies, basin analysis, and petroleum geology: Springer, 582 p., https://doi.org/10.1007/978-3-662-03237-4.

Mitchell, A.H.G., 1993, Cretaceous–Cenozoic tectonic events in the western Myanmar (Burma)–Assam region: Journal of the Geological Society, v. 150, no. 6, p. 1089–1102, https://doi.org/10.1144/gsjgs.150.6.1089.

Mitchell, A.H.G., Htay, M.T., Htun, K.M., Win, M.N., Oo, T., and Hlaing, T., 2007, Rock relationships in the Mogok metamorphic belt, Tatkon to Mandalay, central Myanmar: Journal of Asian Earth Sciences, v. 29, no. 5, p. 891–910, https://doi.org/10.1016/j.jseaes.2006.05.009.

Mitchell, A., Chung, S.L., Oo, T., Lin, T.H., and Hung, C.H., 2012, Zircon U–Pb ages in Myanmar: Magmatic–metamorphic events and the closure of a neo-Tethys ocean?: Journal of Asian Earth Sciences, v. 56, p. 1–23, https://doi.org/10.1016/j.jseaes.2012.04.019.

Molnar, P., England, P., and Martinod, J., 1993, Mantle dynamics, uplift of the Tibetan Plateau, and the Indian monsoon: Reviews of Geophysics, v. 31, no. 4, p. 357–396.

Morley, C.K., 2002, A tectonic model for the Tertiary evolution of strike–slip faults and rift basins in SE Asia: Tectonophysics, v. 347, no. 4, p. 189–215, https://doi.org/10.1016/S0040-1951(02)00061-6.

Morley, C.K., 2009, Evolution from an oblique subduction back-arc mobile belt to a highly oblique collisional margin: the Cenozoic tectonic development of Thailand and eastern Myanmar, *in* Cawood, P.A., and Kröner, A., eds., Earth Accretionary Systems in Space and Time: Geological Society of London Special Publication 318, no. 1, p. 373–403, https://doi.org/10.1144/SP318.14.

Morley, C.K., 2012, Late Cretaceous–early Palaeogene tectonic development of SE Asia: Earth-Science Reviews, v. 115, no. 1-2, p. 37–75, https://doi.org/10.1016/j.earscirev.2012.08.002.

Morley, C.K., 2017, Syn-kinematic sedimentation at a releasing splay in the northern Minwun Ranges, Sagaing Fault zone, Myanmar: Significance for fault timing and displacement: Basin Research, v. 29, S1, p. 684–700, https://doi.org/10.1111/bre.12201.

Mozley, P.S., and Wersin, P., 1992, Isotopic composition of siderite as an indicator of depositional environment: Geology, v. 20, no. 9, p. 817–820, https://doi.org/10.1130/0091-7613(1992)020<0817:ICOSAA>2.3.CO;2.

Myanmar Geosciences Society (MGS), 2014, Geological map of Myanmar, revised version: Myanmar Geosciences Society, Yangon.

Najman, Y., 2006, The detrital record of orogenesis: A review of approaches and techniques used in the Himalayan sedimentary basins: Earth-Science Reviews, v. 74, no. 1–2, p. 1–72, https://doi.org/10.1016/j.earscirev.2005.04.004.

Najman, Y., Appel, E., Boudagher-Fadel, M., Bown, P., Carter, A., Garzanti, E., et al., 2010, Timing of India-Asia collision: Geological, biostratigraphic, and palaeomagnetic constraints: Journal of Geophysical Research, Solid Earth, v. 115, B12, https://doi.org/10.1029/2010JB007673.

Najman, Y., Jenks, D., Godin, L., Boudagher-Fadel, M., Millar, I., Garzanti, E., et al., 2017, The Tethyan Himalayan detrital record shows that India–Asia terminal collision occurred by 54 Ma in the Western Himalaya: Earth and Planetary Science Letters, v. 459, p. 301–310, https://doi.org/10.1016/j.epsl.2016.11.036.

Nagappa, Y., 1959, Foraminiferal biostratigraphy of the Cretaceous-Eocene succession in the India-Pakistan-Burma region: Micropaleontology, v. 5, no. 2, p. 145–177, https://doi.org/10.2307/1484208.

Nichols, G., 2009, Sedimentology and stratigraphy: Oxford, John Wiley & Sons, 355 p.

Nielsen, C., Chamot-Rooke, N., and Rangin, C., 2004, From partial to full strain partitioning along the Indo-Burmese hyper-oblique subduction: Marine Geology, v. 209, no. 1–4, p. 303–327, https://doi.org/10.1016/j.margeo.2004.05.001.

Oo, K.L., Zaw, K., Meffre, S., Aung, D.W., and Lai, C.K., 2015, Provenance of the Eocene sandstones in the southern Chindwin Basin, Myanmar: Implications for the unroofing history of the Cretaceous–Eocene magmatic arc: Journal of Asian Earth Sciences, v. 107, p. 172–194, https://doi.org/10.1016/j.jseaes.2015.04.029.

Paton, C., Woodhead, J., Hellstrom, J., Hergt, J., Greig, A., and Maas, R., 2010, Improved laser ablation U-Pb zircon geochronology through robust down-hole fractionation correction: Geochemistry Geophysics Geosystems, v. 11, no. 3, https://doi.org/10.1029/2009GC002618.

Pivnik, D.A., Nahm, J., Tucker, R.S., Smith, G.O., Nyein, K., Nyunt, M., and Maung, P.H., 1998, Polyphase deformation in a fore-arc/back-arc basin, Salin subbasin, Myanmar (Burma): AAPG Bulletin, v. 82, no. 10, p. 1837–1856.

Pubellier, M., 2008, Structural Map of Eastern Eurasia: CCGM, Commission for the Geological Map of the World, Scale at equator 1:12,500,000, 1 sheet.

Rangin, C., Maw, W., Lwin, S., Naing, W., Mouret, C., Bertrand, G., and the G.I.A.C. Scientific Party, 1999, Cenozoic Pull-Apart basins in Central Myanmar: the trace of the path of India along the Western Margin of Sundaland [abs.]: Terra Nova, v. 4, p. 59.

Rangin, C., Maurin, T., and Masson, F., 2013, Combined effects of Eurasia/Sunda oblique convergence and East-Tibetan crustal flow on the active tectonics of Burma: Journal of Asian Earth Sciences, v. 76, p. 185–194, https://doi.org/10.1016/j.jseaes.2013.05.018.

Replumaz, A., and Tapponnier, P., 2003, Reconstruction of the deformed collision zone between India and Asia by backward motion of lithospheric blocks: Journal of Geophysical Research, v. 108, https://doi.org/10.1029/2001JB000661.

Replumaz, A., Negredo, A.M., Guillot, S., and Villaseñor, A., 2010, Multiple episodes of continental subduction during India/Asia convergence: Insight from seismic

tomography and tectonic reconstruction: Tectonophysics, v. 483, no. 1, p. 125–134, https://doi.org/10.1016/j.tecto.2009.10.007.

Replumaz, A., Guillot, S., Villaseñor, A., and Negredo, A.M., 2013, Amount of Asian lithospheric mantle subducted during the India/Asia collision: Gondwana Research, v. 24, no. 3, p. 936–945, https://doi.org/10.1016/j.gr.2012.07.019.

Richter, B., and Fuller, M., 1996, Palaeomagnetism of the Sibumasu and Indochina blocks: Implications for the extrusion tectonic model, *in* Hall, R., and Blundell, D., Tectonic Evolution of Southeast Asia: Geological Society of London, Special Publication 106, no. 1, p. 203–224, https://doi.org/10.1144/GSL.SP.1996.106.01.13.

Robinson, R.A., Brezina, C.A., Parrish, R.R., Horstwood, M.S., Oo, N.W., Bird, M.I., et al., 2014, Large rivers and orogens: The evolution of the Yarlung Tsangpo–Irrawaddy system and the eastern Himalayan syntaxis: Gondwana Research, v. 26, no. 1, p. 112–121, https://doi.org/10.1016/j.gr.2013.07.002.

Roy, P.S., Cowell, P.J., Ferland, M.A., Thom, B.G., Carter, R.W.G., and Woodroffe, C.D., 1994, Wave-dominated coasts, *in* Carter, R.W.G., and Woodroffe, C.D., eds., Coastal Evolution: Late Quaternary Shoreline Morphodynamics: Cambridge University Press, p. 121–186.

Royden, L.H., Burchfiel, B.C., and van der Hilst, R.D., 2008, The geological evolution of the Tibetan Plateau: Science, v. 321, p. 1054–1058, https://doi.org/10.1126/science.1155371.

Sato, K., Liu, Y., Zhu, Z., Yang, Z., and Otofuji, Y.I., 2001, Tertiary paleomagnetic data from northwestern Yunnan, China: Further evidence for large clockwise rotation of the Indochina block and its tectonic implications: Earth and Planetary Science Letters, v. 185, no. 1, p. 185–198, https://doi.org/10.1016/S0012-821X(00)00377-0.

Searle, M., Corfield, R.I., Stephenson, B.E.N., and McCarron, J.O.E., 1997, Structure of the North Indian continental margin in the Ladakh–Zanskar Himalayas: implications for the timing of obduction of the Spontang ophiolite, India–Asia collision and deformation events in the Himalaya: Geological Magazine, v. 134, no. 3, p. 297–316, https://doi.org/10.1017/S0016756897006857.

Searle, M.P., Noble, S.R., Cottle, J.M., Waters, D.J., Mitchell, A.H.G., Hlaing, T., and Horstwood, M.S.A., 2007, Tectonic evolution of the Mogok metamorphic belt, Burma (Myanmar) constrained by U-Th-Pb dating of metamorphic and magmatic rocks: Tectonics, v. 26, no. 3, https://doi.org/10.1029/2006TC002083.

Searle, M.P., Whitehouse, M.J., Robb, L.J., Ghani, A.A., Hutchison, C.S., Sone, M., et al., 2012, Tectonic evolution of the Sibumasu–Indochina terrane collision zone in Thailand and Malaysia: Constraints from new U–Pb zircon chronology of SE Asian tin granitoids: Journal of the Geological Society, v. 169, no. 4, p. 489–500, https://doi.org/10.1144/0016-76492011-107.

Searle, M.P., Morley, C.K., Waters, D.J., Gardiner, N.J., Htun, U.K., Nu, T.T., and Robb, L.J., 2017, Tectonic and metamorphic evolution of the Mogok Metamorphic and Jade Mines belts and ophiolitic terranes of Burma (Myanmar), *in* Barber, A.J., Zaw, K., and Crow, M.J., eds., Myanmar: Geology, Resources and Tectonics: Geological Society of London Memoir 48, p. 261–293.

Seton, M., Müller, R.D., Zahirovic, S., Gaina, C., Torsvik, T., Shephard, G., et al., 2012, Global continental and ocean basin reconstructions since 200 Ma: Earth–Scientific Review (Singapore), v. 113, no. 3–4, p. 212–270.

Sevastjanova, I., Hall, R., Rittner, M., Paw, S.M.T.L., Naing, T.T., Alderton, D.H., and Comfort, G., 2016, Myanmar and Asia united, Australia left behind long ago: Gondwana Research, v. 32, p. 24–40, http://doi.org/10.1016/j.gr.2015.02.001.

Shen, F., Royden, L.H., and Burchfiel, B.C., 2001, Large-scale crustal deformation of the Tibetan Plateau: Journal of Geophysical Research, v. 106, B4, p. 6793–6816, https://doi.org/10.1029/2000JB900389.

Socquet, A., Goffé, B., Pubellier, M., and Rangin, C., 2002, Le métamorphisme Tardi-Crétacé à Éocène des zones internes de la chaîne Indo-Birmane (Myanmar occidental): implications géodynamiques: Comptes Rendus Geoscience, v. 334, no. 8, p. 573–580, https://doi.org/10.1016/S1631-0713(02)01796-0.

Socquet, A., Vigny, C., Chamot-Rooke, N., Simons, W., Rangin, C., and Ambrosius, B., 2006, India and Sunda plates motion and deformation along their boundary in Myanmar determined by GPS: Journal of Geophysical Research. Solid Earth, v. 111, B5, https://doi.org/10.1029/2005JB003877.

Tapponnier, P., Peltzer, G., Le Dain, A.Y., Armijo, R., and Cobbold, P., 1982, Propagating extrusion tectonics in Asia: New insights from simple experiments with plasticine: Geology, v. 10, no. 12, p. 611–616, https://doi.org/10.1130/0091-7613(1982)10<611:PETIAN>2.0.CO;2.

Tessier, B., Archer, A.W., Laniere, W., and Feldman, H.R., 1995, Comparison of ancient tidal rhythmites (Carboniferous of Kansas and Indiana, USA) with modern analogues (the Bay of Mont-Saint-Michel, France), *in* Flemming B.W., and Bartholomä, A., eds., Tidal Signatures in Modern and Ancient Sediments: Special Publication of the International Association of Sedimentologists 24, p. 259–271.

Thein, M., and Maung, M., 2017, The Eastern (Back-arc) Basin of Central Myanmar: Basement rocks, lithostratigraphic units, palaeocurrents, provenance and developmental history, *in* Barber, A.J., Zaw, K., and Crow, M.J., eds., Myanmar: Geology, Resources and Tectonics: Geological Society of London Memoir 48, p. 169–183.

Tong, Y., Yang, Z., Jing, X., Zhao, Y., Li, C., Huang, D., and Zhang, X., 2016, New insights into the Cenozoic lateral extrusion of crustal blocks on the southeastern edge of Tibetan Plateau: Evidence from paleomagnetic results from Paleogene sedimentary strata of the Baoshan Terrane: Tectonics, v. 35, no. 11, p. 2494–2514, https://doi.org/10.1002/2016TC004221.

United Nations, 1978, Atlas of Stratigraphy Volume V: United Nations, ESCAP, New York.

Valeton, I., 1994, Element concentration and formation of ore deposits by weathering: Catena, v. 21, no. 2–3, p. 99–129, https://doi.org/10.1016/0341-8162(94)90006-X.

van Hinsbergen, D.J., Kapp, P., Dupont-Nivet, G., Lippert, P.C., DeCelles, P.G., and Torsvik, T.H., 2011a, Restoration of Cenozoic deformation in Asia and the size of Greater India: Tectonics, v. 30, no. 5. TC5003, https://doi.org/10.1029/2011TC002908.

van Hinsbergen, D.J., Steinberger, B., Doubrovine, P.V., and Gassmöller, R., 2011b, Acceleration and deceleration of India-Asia convergence since the Cretaceous: Roles of mantle plumes and continental collision: Journal of Geophysical Research, Solid Earth, v. 116, B6, https://doi.org/10.1029/2010JB008051.

van Hinsbergen, D.J., Lippert, P.C., Dupont-Nivet, G., McQuarrie, N., Doubrovine, P.V., Spakman, W., and Torsvik, T.H., 2012, Greater India Basin hypothesis and a two-stage Cenozoic collision between India and Asia: Proceedings of the National Academy of Sciences of the United States of America, v. 109, no. 20, p. 7659–7664.

Vérard, C., Stampfli, G., Borel, G., and Hochard, C., 2017, The Indian Promontory: A Bridge between Plate Tectonics and Life Evolution Models: Universal Journal of Geoscience, v. 5, no. 2, p. 25–32, https://doi.org/10.13189/ujg.2017.050202.

Vermeesch, P., 2013, Multi-sample comparison of detrital age distributions: Chemical Geology, v. 341, p. 140–146, https://doi.org/10.1016/j.chemgeo.2013.01.010 (corrigenda at: http://dx.doi.org/10.1016/j.chemgeo.2013.12.009; http://dx.doi.org/10.1016/j.chemgeo.2016.02.005; http://dx.doi.org/10.1016/j.chemgeo.2014.07.008).

Wang, J.G., Wu, F.Y., Tan, X.C., and Liu, C.Z., 2014, Magmatic evolution of the Western Myanmar Arc documented by U–Pb and Hf isotopes in detrital zircon: Tectonophysics, v. 612, p. 97–105, https://doi.org/10.1016/j.tecto.2013.11.039.

Wang, J.G., Hu, X., Garzanti, E., An, W., and Liu, X.C., 2017, The birth of the Xigaze forearc basin in southern Tibet: Earth and Planetary Science Letters, v. 465, p. 38–47, https://doi.org/10.1016/j.epsl.2017.02.036.

Yin, A., Harrison, T.M., Ryerson, F.J., Wenji, C., Kidd, W.S.F., and Copeland, P., 1994, Tertiary structural evolution of the Gangdese thrust system, southeastern Tibet: Journal of Geophysical Research, Solid Earth, v. 99, B9, p. 18,175–18,201, https://doi.org/10.1029/94JB00504.

Yin, A., and Harrison, T.M., 2000, Geologic evolution of the Himalayan-Tibetan orogen: Annual Review of Earth and Planetary Sciences, v. 28, no. 1, p. 211–280, https://doi.org/10.1146/annurev.earth.28.1.211.

Zaw, K., 1990, Geological, petrological and geochemical characteristics of granitoid rocks in Burma: With special reference to the associated W-Sn mineralization and their tectonic setting: Journal of Southeast Asian Earth Sciences, v. 4, no. 4, p. 293–335, https://doi.org/10.1016/0743-9547(90)90004-W.

Zhang, P., Mei, L., Hu, X., Li, R., Wu, L., Zhou, Z., and Qiu, H., 2017a, Structures, uplift, and magmatism of the Western Myanmar Arc: Constraints to mid-Cretaceous-Paleogene tectonic evolution of the western Myanmar continental margin: Gondwana Research, v. 52, p. 18–38, https://doi.org/10.1016/j.gr.2017.09.002.

Zhang, J.E., Xiao, W., Windley, B.F., Cai, F., Sein, K., and Naing, S., 2017b, Early Cretaceous wedge extrusion in the Indo-Burma Range accretionary complex: Implications for the Mesozoic subduction of Neotethys in SE Asia: International Journal of Earth Sciences, v. 106, no. 4, p. 1391–1408, https://doi.org/10.1007/s00531-017-1468-7.

Science Editor: Rob Strachan
Associate Editor: Barbara Carrapa

Manuscript Received 5 April 2018
Revised Manuscript Received 18 July 2018
Manuscript Accepted 4 September 2018

Printed in the USA

Botanical Journal of the Linnean Society, 2020, **XX**, 1–30. With 14 figures.

Eocene palms from central Myanmar in a South-East Asian and global perspective: evidence from the palynological record

HUASHENG HUANG[1,*], ROBERT MORLEY[2,3], ALEXIS LICHT[4], GUILLAUME DUPONT-NIVET [5,6], FRIÐGEIR GRÍMSSON[7], REINHARD ZETTER[8], JAN WESTERWEEL[6], ZAW WIN[9], DAY WA AUNG[10] and CARINA HOORN[1]

[1]*Department of Ecosystem & Landscape Dynamics, Institute for Biodiversity and Ecosystem Dynamics (IBED), University of Amsterdam, Amsterdam 1090 GE, the Netherlands*
[2]*Palynova Ltd., 1 Mow Fen Road, Littleport, Cambridgeshire CB6 1PY, UK*
[3]*Department of Earth Sciences, Royal Holloway, University of London, Egham, Surrey TW20 0EX, UK*
[4]*Department of Earth and Space Sciences, University of Washington, Seattle, Washington 98195, USA*
[5]*Institut für Geowissenschaften, Universität Potsdam, Potsdam, Golm 14476, Germany*
[6]*Géosciences Rennes (CNRS), University of Rennes, UMR 6118, F-35000 Rennes, France*
[7]*Department of Botany and Biodiversity Research, University of Vienna, Rennweg 14, A-1030 Vienna, Austria*
[8]*Department of Palaeontology, University of Vienna, Althanstraße 14 (UZA II), A-1090 Vienna, Austria*
[9]*Geology Department, Shwe Bo University, Sagaing Region, Myanmar*
[10]*Department of Geology, University of Yangon, Pyay Road, Yangon, Myanmar*

Received 2 October 2019; revised 2 April 2020; accepted for publication 23 May 2020

In the Palaeogene, pollen assemblages at low and mid latitudes are characterized by abundant palm and palm-like (PPL) taxa. Although these taxa have been widely reported, their occurrence in the Palaeogene of Myanmar remains poorly documented. Here we report on the morphology of PPL pollen along a middle to upper Eocene sedimentary sequence in central Myanmar and discuss their nearest living relatives (NLRs). Principal components analysis (PCA) indicates that *Palmaepollenites kutchensis*, *Dicolpopollis* and *Longapertites* were dispersed from freshwater plants, whereas the parent taxon of *Proxapertites operculatus* was probably a member of the coastal vegetation in the manner of *Spinizonocolpites*. This, with sedimentological data, suggests a palaeoenvironmental change from a brackish, tidally influenced environment to a fully freshwater setting through the late Eocene. Additionally, we mapped and compared the geographical distribution of selected Eocene palm taxa and their NLRs, and found that their distributions shrank after the Eocene. Moreover, in the Palaeogene, species diversity of selected PPL taxa seems lower in Myanmar than in the Indian subcontinent and other regions in South-East Asia. We hypothesize that in the Eocene the Indo–Asian collision zone formed a 'hotspot' for palm diversity, which is reflected in species-rich palynofloras. However, the local palm diversity declined after the Eocene, whereas, at the global level, palm distribution was distinctly reduced between the Eocene and the present. We propose that the retreat of the palms may have occurred as early as the Eocene – Oligocene Transition (EOT), but this remains to be confirmed by the study of EOT pollen records in tropical regions.

ADDITIONAL KEYWORDS: Araceae – Arecaceae – biogeography – *Dicolpopollis* – *Longapertites* – palaeoenvironment – Palmae – *Palmaepollenites* – palynology – *Proxapertites* – *Spinizonocolpites*.

INTRODUCTION

The Central Myanmar Basin (CMB) has yielded an extremely rich fossil record including mammals (e.g. Jaeger *et al.*, 1999; Chavasseau *et al.*, 2010;

*Corresponding author. E-mail: buxushuang@gmail.com; H.Huang@uva.nl

De Bonis *et al.*, 2018) and wood (e.g. Gottwald, 1994; Privé-Gill *et al.*, 2004; Licht *et al.*, 2014, 2015). Palynological studies with focus on the CMB are rare (e.g. Potonié, 1960; Reimann & Aye Thaung, 1981; Engelhardt & Wrenn, 1994), but this area is of great interest, particularly for the palaeoecology of palm taxa that have implications for the palaeoenvironmental interpretation of the CMB. A > 1 km-thick middle to upper Eocene sedimentary sequence in the CMB near the Kalewa Township was recently dated at *c*. 38.3 + 0.7–0.9 Mya based on analysis of a tuff layer (Licht *et al.*, 2018). This provides an excellent opportunity to determine how the palynological record in the CMB relates to the Indo–Asian tectonic convergence and the climate change preceding the Eocene–Oligocene Transition (EOT) (as discussed by Coxall & Pearson, 2007; Dupont-Nivet, Hoorn & Konert, 2008; Abels *et al.*, 2011; Hoorn *et al.*, 2012).

In this study we address the following questions. Which PPL pollens occur in the sedimentary record at Kalewa? What are their palaeoecological implications? How do these pollen types compare with morphotaxa from Palaeogene records of adjacent regions? What is the species diversity of these taxa in the region during the Palaeogene? Are there differences in the distribution of NLRs and their fossil counterparts? Are there any environmental shifts detected by the compositional changes of these PPL taxa? What can this new record, placed in a global context, add to our understanding of palm palaeobiogeography?

To answer these questions we took the following approach: (1) we described morphological characteristics of PPL pollen along the section near Kalewa; (2) we quantified and analysed pollen types and applied principal component analysis (PCA) to determine ecological and environmental changes in the Eocene coastal systems of the CMB; (3) we correlated sedimentary changes with sporomorph composition throughout the studied section, allowing for a better understanding of the palaeoecology of the plants producing the PPL pollen for which their NLRs are uncertain (*Proxapertites*, *Longapertites* and *Palmaepollenites kutchensis*) and (4) we compiled Eocene records of palm pollen taxa and generated maps using GPlates for spatiotemporal comparisons in species distribution and diversity across the globe.

Regional setting

The studied section is situated near the Kalewa Township in the Sagaing Region, the southern part of the Chindwin sub-basin of the CMB and the north-western part of the Burma Terrane (BT; Fig. 1A, 23°14′ N, 94°15′ E). At *c*. 40 Mya, the CMB was located at the margin of Eurasia and was open towards the Indian Ocean, forming an embayment that was the locus of south-west facing deltas (Fig. 1B; Licht *et al.*, 2013; Westerweel *et al.*, 2019). During this time the inner wedge of the Indo–Burman Ranges emerged, providing a barrier that partly closed the embayment (Licht *et al.*, 2018); the BT was located in a more southerly, near-equatorial position (Westerweel *et al.*, 2019).

The *c.* 650 m-thick sedimentary sequence at Kalewa comprises the Yaw Formation and includes four facies associations deposited in an estuarine system (Licht *et al.*, 2018). Mostly, the sediments consisted of clastic sands and muds primarily provided by the unroofing of the Wuntho–Popa volcanic arc that extended onto the Burmese margin, along the flank of the modern Sino–Burman Ranges (Fig. 1A; Licht *et al.*, 2013, 2016, 2018). The studied sedimentary section starts at *c*. 500 m above the boundary of the Yaw Formation and the underlying Pondaung Formation. This boundary is marked by the first occurrence of lignite seams and black mudstones and dated at *c.* 39 Mya (Licht *et al.*, 2018). The unconformably overlying Letkat Formation consists of coarse fluviatile clastics (Bender, 1983). A dated tuffite layer, from *c*. 38.3 Mya, is positioned at *c*. 500 m above the base of the section, in the upper third of the profile. Sedimentation rates for most of the Yaw Formation are estimated at > 1 m/Kyr (Licht *et al.*, 2018) and, therefore, the studied section is dated as late Bartonian, probably extending into the early Priabonian up-section.

Palms and their palaeobiogeographical context

Palms (Arecaceae) comprise 181 genera with *c.* 2600 species (Christenhusz & Byng, 2016), most of which are currently restricted to tropical and subtropical regions (Couvreur, Forest & Baker, 2011). They are an ancient group, with a molecular age of *c.* 114 Myr (Couvreur *et al.*, 2011) and fossils dating back to the Turonian (93.5–89.0 Mya; Crié, 1892; Kvaček & Herman, 2004); the group predominated throughout the equatorial zone during the latest Cretaceous and Paleocene (Morley, 2000). In the Maastrichtian, PPL pollen of the form-genera *Spinizonocolpites* Muller, *Palmaepollenites* Potonié, *Longapertites* van Hoeken-Klinkenberg and *Proxapertites* van der Hammen are found widely across the Palaeotropics (e.g. Herngreen *et al.*, 1996; Vergara & Rodriguez, 1997; Eisawi & Schrank, 2009). The form-taxon *Dicolpopollis* Pflanzl, characteristic of subtribe Calaminae (Harley & Morley, 1995), first appeared in the Maastrichtian of Somalia (Schrank, 1994) and subsequently in the Paleocene of the Sunda region (Muller, 1968) and China (Sun *et al.*, 1981). There are questionable records from India, such as *D. kalewensis* Potonié from the Paleocene to early

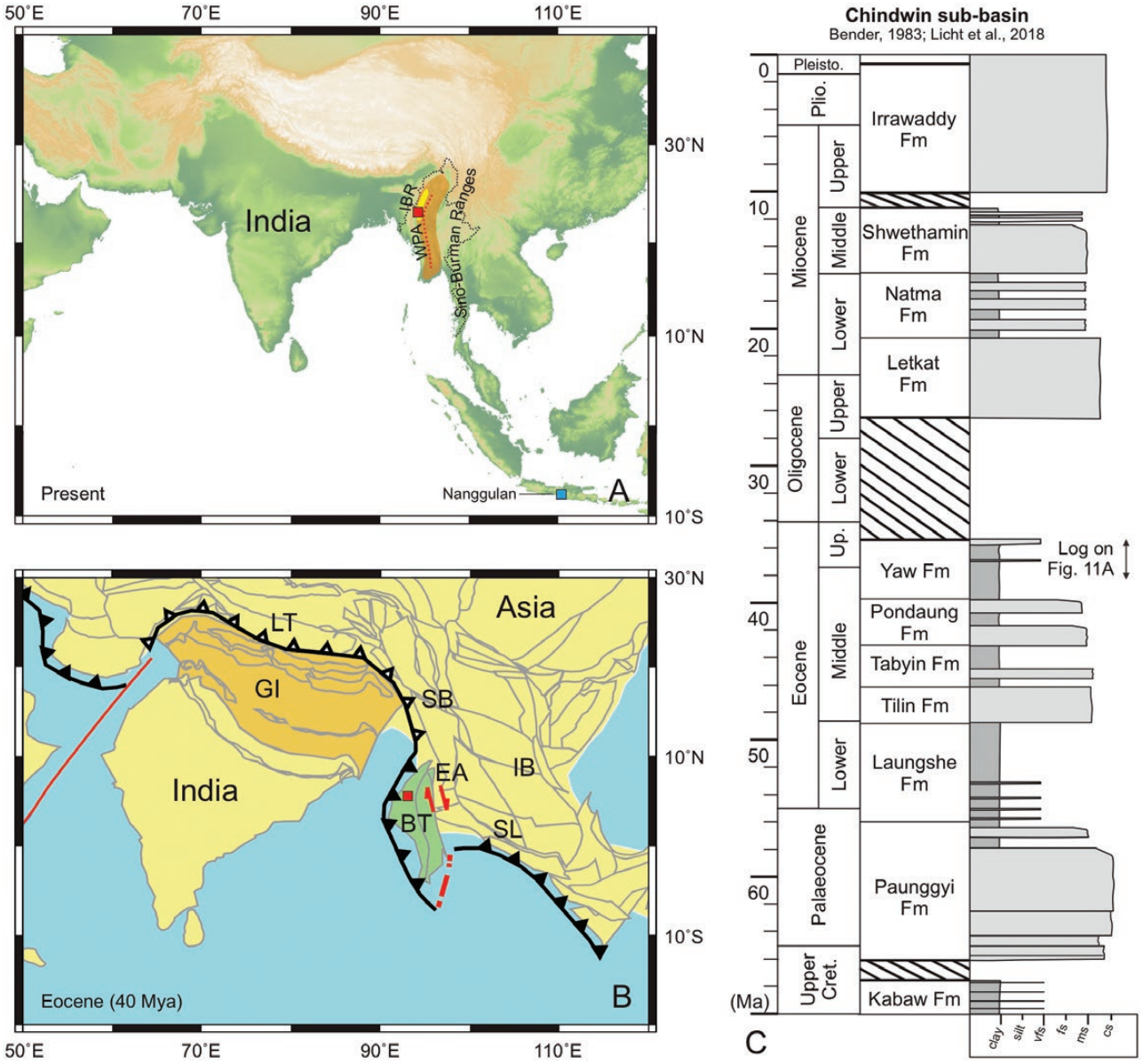

Figure 1. A, Schematic map showing the study area (red square) in the CMB, made with GeoMapApp v.3.6.10. IBR = Indo–Burman Ranges; WPA = Wuntho–Popa volcanic arc, indicated by the red dash line. Light orange shading outlines the CMB; yellow shading outlines the Chindwin sub-basin; black dash line marks the Myanmar borders. Positions of the IBR, Sino-Burman Ranges and the CMB refer to Licht *et al.* (2014), whereas the Chindwin sub-basin follows Licht *et al.* (2018). It also shows the location (blue square) of Nanggulan (Indonesia), which was used for comparison in the following several texts. B, Location of Burma Terrane at 40 Mya (modified after Westerweel *et al.*, 2019). BT = Burma Terrane, EA = Eastern Andaman, IB = Indochina Blocks, GI = Greater India, LT = Lhasa Terrane, SB = Sibumasu Block, SL = Sundaland. Red square represents the study area; C, simplified log showing the position of the studied section in the entire stratigraphy of the Chindwin sub-basin, CMB (modified after Licht *et al.*, 2018).

Eocene Nindam Formation (Mathur & Jain, 1980). *Dicolpopollis* expanded its range during the Eocene to Australia (MacPhail, Colhoun & Fitzsimons, 1995), New Zealand (Hartwich *et al.*, 2010), central Europe (Bignot *et al.*, 1985; Riegel, Wilde & Lenz, 2012) and southern North America (Harrington, 2008).

Zonasulcate taxa, such as *Spinizonocolpites* and *Proxapertites*, are characteristic of the Upper

Cretaceous and Paleocene Palmae Province (Herngreen *et al.*, 1996) and are widely reported from Palaeogene coastal records (e.g. Oman, Beialy, 1998; India, Tripathi, Kumar & Srivastava, 2009; Prasad *et al.*, 2013; Africa, Jacobs, Pan & Scotese, 2010; Australia, Macphail & Hill, 2019; Côte d'Ivoire, Guédé *et al.*, 2019). *Spinizonocolpites* and *Proxapertites* have long been considered to be derived from plants growing in humid tropical mangrove environments (Germeraad, Hopping & Muller, 1968; Schrank, 1987, 1994; Digbehi *et al.*, 1996; Herngreen, 1998), with the latter also occurring in freshwater settings (Jaramillo *et al.*, 2007). In contrast, the ecological indication of *Dicolpopollis* always points to a freshwater vegetation (Morley *et al.*, 2019).

MATERIAL AND METHODS

Samples and palynological processing

During fieldwork in 2016 and 2017, 81 samples were collected from clay, silt and fine sandstone units. The palynological processing of samples was performed at the Institute for Biodiversity and Ecosystem Dynamics (IBED), University of Amsterdam, The Netherlands. For this purpose, 1.3 g of sedimentary rock sample was boiled in 10% sodium pyrophosphate to disaggregate the matrix. Then 10% hydrochloric acid (HCl) was used to remove the calcium carbonate. Sieves with 5 and 212- μm meshes were used. The sample material was heated in acetolysis mixture (nine parts of acetic anhydride/one part of concentrated sulphuric acid) to 100 °C. Bromoform-treatment (gravity = 2.0) was applied to separate any remaining inorganic fraction. The resulting organic residue was mounted on a slide in glycerin and sealed with paraffin for the observation with a light microscope (LM). To ensure maximum recovery, an additional preparation method was conducted on samples 16MAP001, 16MAP003, 16MBP017, 16MWP001 and 17MBPA1 at the Palynological Laboratory Services (PLS) Ltd., Holyhead, United Kingdom. For this method 30 g of sedimentary rock was treated with 10% HCl to solubilize and remove the carbonate, and then washed and dried and treated with 40% hydrofluoric acid (HF) to remove the silicates. Fluoride precipitates may be present after the HF stage and these precipitates are soluble in 20% HCl, followed by a heavy liquid separation technique (a solution of zinc bromide, density = 2.0) to separate the organic and remaining inorganic fractions. Subsequently, the organic fractions were sieved at 5 μm and the filtrate was collected. This filtrate was first sieved at 10 μm, then at 150 μm to remove large organic particles, while collecting the filtrate. The final residues at 5–10 and 10–150 μm were mounted in glycerin jelly. The resulting organic residue was mounted on a slide in glycerin and sealed with paraffin for the observation with LM. Residues were further used for analysis with LM and scanning electron microscopy (SEM) at the Department of Palaeontology, University of Vienna, Austria.

Palynological analysis

The Kalewa samples have a poor sporomorph preservation and the organic material is often pyritized or corroded. To construct a reliable pollen diagram, a baseline on pollen sum of 100 grains was maintained. All samples with counts < 100 were excluded resulting in 54 positive samples. Identification of fossil PPL pollen was mainly based on Potonié (1960), Germeraad, Hopping & Muller (1968), Muller (1968), Reimann & Aye Thaung (1981) and Harley & Morley (1995). Palm pollen grains not included in *Longapertites*, *Dicolpopollis*, *Spinizonocolpites*, *Proxapertites* or *Palmaepollenites kutchensis* Venkatachala & Kar were classified as 'other palms' in the pollen diagram. The pollen diagram was constructed using the Tilia v.2.1.1 software (Grimm, 1991), with cluster analysis program CONISS (Grimm, 1987). All of the slides and pollen residues are deposited at IBED.

All pollen grains were counted and described under a LM LEICA DM LB2, and a Zeiss Universal microscope at IBED. In addition, a JEOL JSM·6400 SEM at the Department of Palaeontology, University of Vienna, was used to investigate the pollen sculpture, applying the single-grain analysis method by Zetter (1989; see also Halbritter *et al.*, 2018). LM and SEM terminologies follow Punt *et al.* (2007) and Halbritter *et al.* (2018), respectively. The morphological characters of pollen grains were measured by the software ImageJ (National Institute of Health, USA). PCA was employed in R (R Core Team, 2018) to analyse palaeoecological correlation on PPL taxa. Additionally, an analysis of variance (ANOVA) of pollen abundance among different pollen zones and a non-parametric correlation (Spearman) of taxa were performed with SPSS v.24.0 (SPSS Inc., Chicago, IL, USA).

Microphotography

The micrographs in Fig. 2 were taken at IBED using Fujifilm X-E2 and a Zeiss Universal microscope with 63× Plan Neofluar NA1, 25 oil applying Nomarski Differential Interference Contrast (DIC) following Bercovici, Hadley & Villanueva-Amadoz (2009). While making these micrographs, the varying *z*-axis was recorded, and images were later combined through manual *z*-stacking in Helicon Focus and Photoshop

Figure 2. LM micrographs for the PPL pollen under ×630 magnification from the Eocene of Kalewa, CMB. A1, A2. *Proxapertites operculatus*; B, C. *Palmaepollenites kutchensis*; D1, D2, G1, G2. *Dicolpopollis kalewensis*; E. *Longapertites retipilatus*; F. *Spinizonocolpites prominatus* and H, I, J1, J2. *Palmaepollenites* sp. 2. Scale bars = 10 μm.

CC. This stacking technique combines different layers to provide a fully focused image. LM micrographs in Figs 3–10 were taken by a ProgRes Speed XT^{core} 5 camera connected with a Nikon Eclipse 80i LM. SEM micrographs in Figs 3–10 were taken with the JEOL JSM·6400. Figs 2–10 were made with InDesign CC. The background of kerogen in the LM original micrographs was manually edited out.

Distribution maps

Mapping the global distribution of NLRs

Occurrence data (Supporting Information, Table S1) of the NLRs of the fossil form-genera *Dicolpopollis* (*Calamus* L., *Daemonorops* Blume and *Ceratolobus* Blume ex Schult. & Schult.f. in Calaminae, placed in the single genus *Calamus* by Baker (2015); GBIF.org. 2019d, https://doi.org/10.15468/dl.wvfy3m, with 10 438 locality points), *Palmaepollenites kutchensis* (Areceae subtribe Basseliniiae with details for *Basselinia* Vieill. and *Burretiokentia* Pic.Serm.; GBIF.org. 2019b, https://doi.org/10.15468/dl.bzjazl, with 1202 locality points), *Spinizonocolpites* (Nypa Steck; GBIF.org. 2019c, https://doi.org/10.15468/dl.rliz8n, with 233 locality points) and *Longapertites* (probably *Eugeissona* Griff.; GBIF.org. 2019a, https://doi.org/10.15468/dl.ag40lq, with 52 locality points) were downloaded from the Global Biodiversity Information Facility (GBIF, https://www.gbif.org) on 5 August 2019. 'Observation', 'Human observation' and 'Preserved specimen' including coordinates were included to reduce false records. The coordinates of the downloaded occurrences were then imported on the software GeoMapApp v.3.6.10 (http://www.geomapapp.org) to generate modern distribution maps of the NLRs. 'Human observation' and 'Preserved specimen' data on Calaminae (including *Calamus*, *Daemonorops* and *Ceratolobus*) and *Nypa* swere examined by R package 'CoordinateCleaner' (Zizka *et al.*, 2019) to exclude problematic points (e.g. zero coordinates, GBIF headquarters and biodiversity institutions) (Supporting Information, Figs S1–S4), as other records fall well within distribution ranges of previous studies.

Mapping the global Eocene distribution of PPL taxa with emphasis on the Palaeogene of India and South-East Asia

We compiled published global Eocene records of *Dicolpopollis*, *Longapertites*, *Spinizonocolpites* and *Palmaepollenites kutchensis* (Supporting Information, Table S2) without *Proxapertites* as it has NLRs belonging to different plant families (e.g. Annonaceae, Araceae and Nymphaeaceae). We extended this compilation with data on the distribution of *Dicolpopollis*, *Longapertites*, *Spinizonocolpites* and *Proxapertites* in the Palaeogene of the Indian subcontinent and South-East Asia for the comparison of species diversity (Supporting Information, Tables S3, S4). This compilation is based on the Palynodata database (Palynodata Inc. & White, 2008). However, we cross-checked these records where possible, and augmented the record with additional references. The global Eocene distribution data of the four taxa were plotted in the software GPlates v.2.1 (https://www.gplates.org) to generate maps of global distribution using Mercator projection, which is consistent with the modern maps produced by GeoMapApp. We used the plate model of Westerweel *et al.* (2019) in the Eocene (40 Mya), which was adjusted after Matthews *et al.* (2016). The confidence of the records was divided into three levels: level 3, records from peer-reviewed literature with pollen micrographs; level 2, records from the peer-reviewed literature without pollen micrographs and level 1, records from the inaccessible literature. Distributions were georeferenced when latitudinal and longitudinal data were not provided, and all data points were collated.

RESULTS

AGE

The age of the studied sedimentary sequence ranges from latest middle Eocene (late Bartonian) to earliest late Eocene (early Priabonian). This age is based on a dated tuff layer at 38.3 + 0.7–0.9 Mya (Licht *et al.*, 2018) and supported by the presence of age-indicative marker species such as the sporomorphs *Meyeripollis naharkotensis* Baksi & Venkatachala, *Cicatricosisporites dorogensis* Potonié & Gelletich and *Proxapertites operculatus* van der Hammen (Huang *et al.*, 2018). These sporomorphs types define the Sunda palynological Zone E8, which has an age range of *c*. 37.8–36.5 Myr (Witts *et al.*, 2012; van Gorsel, Lunt & Morley, 2014).

SYSTEMATICS

The morphology of the fossil PPL pollen is described using LM and SEM, and all measurements are available in Table S5. The pollen grains are assigned to form-genera/species. Each fossil taxon is introduced, including reference to the botanical affinity, ecology and distribution, and discussed based on the existing literature.

GENUS ***PROXAPERTITES*** VAN DER HAMMEN EMEND. SINGH

Type species: Proxapertites operculatus van der Hammen

Proxapertites was proposed by van der Hammen (1956), who considered it a Maastrichtian–Miocene marker fossil for northern South America.

PROXAPERTITES OPERCULATUS VAN DER HAMMEN (FIGS 2A1, A2, 3A–R)

Synonym: Monocolpites operculatus van der Hammen, *Proxapertites hammenii* Ventkatachala & Rawat (Thanikaimoni *et al.*, 1984).

Description (based on seven specimens): pollen, monad, heteropolar, polar/equatorial (P/E) ratio oblate, hamburger-shaped with two halves in equatorial view, outline irregularly circular to elliptic in polar view, flattened along the equatorial plane; grain size varies from 34.2–38.6 to 42.9–48.6 µm in polar view (LM); zona-aperturate, sulcus usually totally open, connecting two adhering and not quite symmetric halves, with some degrees of collapsing or folding, sometimes isolated halves occur, aperture margin straight to undulating; exine 1.1–1.6-µm thick, nexine thinner than sexine (LM), columellae distinct and robust; pollen wall tectate; sculpture psilate to scabrate in LM, perforate in SEM, fewer perforation in polar areas, appearing more or less psilate, or similar perforation in polar area as other regions of the grains, number of perforations increase towards the margin of aperture, perforation sometimes connected, diameter up to 1.6 µm (SEM; Fig. 3K); aperture margins rolled inwards, inner side of pollen wall slightly sculptured; thin and folded membrane observed in aperture area (SEM).

Botanical affinity, ecology and distribution: Proxapertites operculatus was initially compared to the South American cocosoid palm *Astrocaryum* G.Mey. by van der Hammen (1957). Muller (1968), however, envisaged it as zonocolpate and compared it to a *Spinizonocolpites* grain lacking the spines, and thus considered it as an extinct member of Nypoideae. This suggestion was supported by the fact that *Spinizonocolpites* and *Proxapertites* are often associated in the fossil record, and so both were considered to be derived from mangrove palms. This perspective has

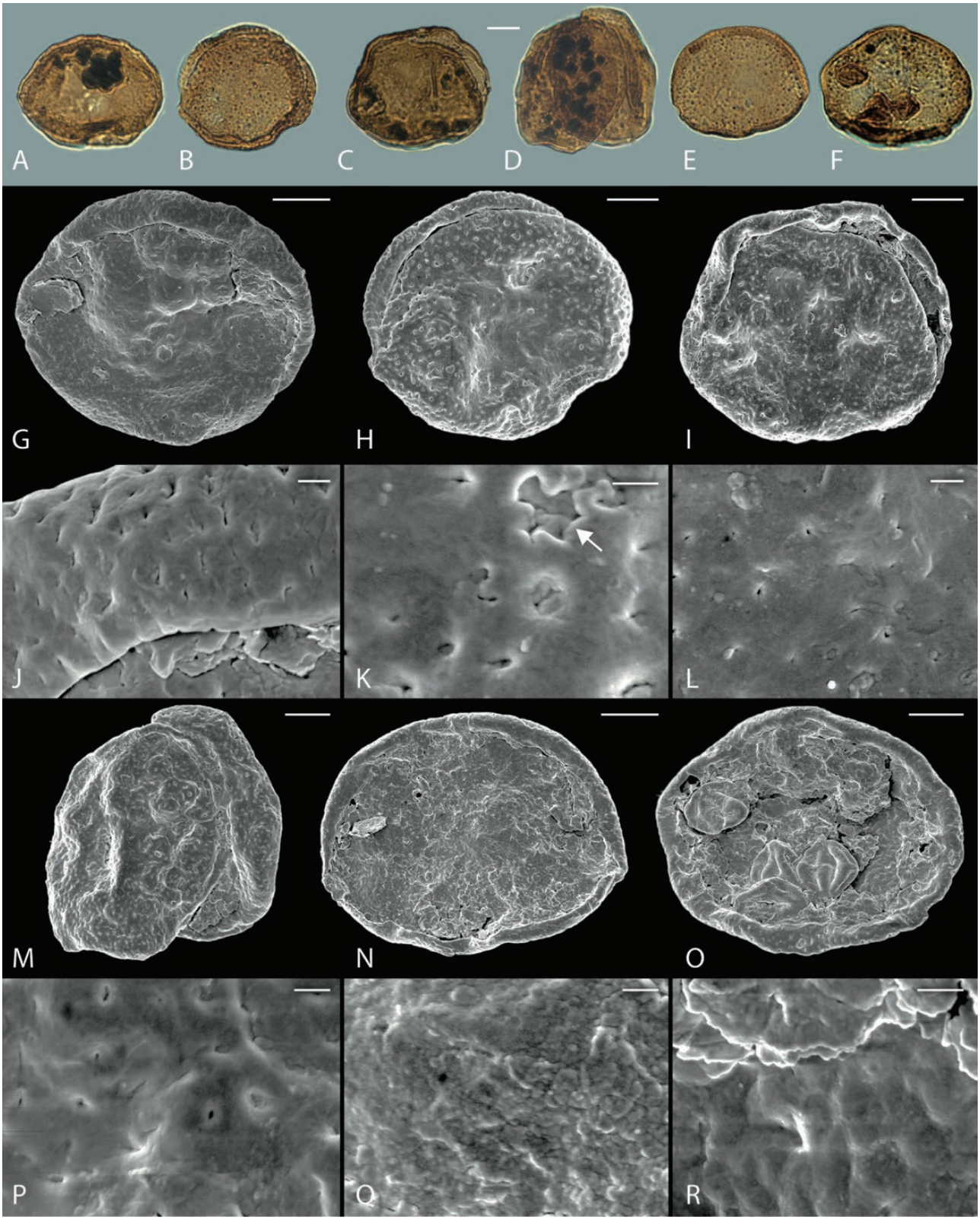

Figure 3. A–F, LM and G–R, SEM micrographs of *Proxapertites operculatus* from the Eocene of Kalewa, CMB. A, G, J, Same grain, close-up (J) of aperture region. B, H, K, Same grain, arrow in (K) pointing to infection of bacteria. C, I, L, Same grain,

been widely followed in subsequent literature (e.g. Morley, 2000). However, several authors note that *Proxapertites* is incompletely zonocolpate, and this prompted Harley & Baker (2001) to compare it with a subgroup of the arecoid palm *Areca* L., especially *A. abdulrahmanii* J.Dransf. and *A. chaiana* J.Dransf. On the other hand, Thanikaimoni *et al.* (1984) and Samant & Phadtare (1997) indicated that similar pollen occurs in Araceae (arum family). This was followed up by Zetter, Hesse & Frosch-Radivo (2001), who undertook an evaluation of the pollen wall ultrastructure and noted marked differences compared to that observed in palm pollen. They proposed a botanical affinity with the genus *Gonatopus* Engl. (Aroideae-Zamioculcadeae in Araceae).

Proxapertites operculatus has a pantropical distribution from the Late Cretaceous to early Cenozoic occurring in northern South America, south-eastern North America and Europe (Spain, Portugal, Austria and Germany), Africa, Pakistan, India and Borneo (e.g. Muller, 1968; Morley, 1978; Venkatachala *et al.*, 1998; Zetter *et al.*, 2001; Friis, Pedersen & Crane, 2004; Hesse & Zetter, 2007; Witts *et al.*, 2012; Mohammed, Awad & Eisawi, 2017; Winantris, Hamdani & Harlia, 2017; Chiadikobi *et al.*, 2018; Kingsley & Umeji, 2018; Kwetche *et al.*, 2018; Prasad *et al.*, 2018).

Remarks: Rugulate ornamentation and narrow meandering 'grooves' formed by connected perforations presented in Zetter *et al.* (2001) were not observed in the Kalewa specimens. Stratification, sometimes seen in broken exine was also not observed.

Genus *Longapertites* van Hoeken-Klinkenberg

Type species: Longapertites marginatus van Hoeken-Klinkenberg

Longapertites was first described from the Maastrichtian of Nigeria by van Hoeken-Klinkenberg (1964). Individual halves of folded *Proxapertites* are sometimes misidentified as *Longapertites* (Zetter *et al.*, 2001).

Botanical affinity, ecology and distribution: This taxon is thought to be the ancestor of the calamoid *Eugeissona* (confined to Borneo and the Malay Peninsula; Baker & Dransfield, 2000) based on its extended colpus (Morley, 2000). Nevertheless, there are some morphological differences between the two taxa, especially in configuration of the two pollen halves, with specimens of *Longapertites* showing a greater morphological differentiation than observed in *Eugeissona*. *Longapertites* apparently had a pantropical distribution during the Maastrichtian and Palaeogene, with fossil records from South America, West Africa, India and northern Australia (Barker & Dransfield, 2000; McGowran *et al.*, 2000). *Quilonipollenites* Rao & Ramanujam has been considered as a synonym of *Longapertites* (Frederiksen, 1994), and is in fact much closer to extant *Eugeissona* than *Longapertites*. Also, Venkatachala & Kar (in Frederiksen, 1994) would prefer it as a separate genus based on the coarse pollen sculpture observed with LM. *Longapertites* has been associated with back-mangrove settings in brackish water (e.g. Akkiraz, Kayseri & Akgün, 2008; Kayseri-Özer, 2013; Mathews *et al.*, 2013; Onuigbo *et al.*, 2015). This should be considered carefully as the pollen may be transported and the accumulation area needs not reflect the habitat/ecology of the parent plant.

Longapertites retipilatus Kar (Figs 2E, 4A–C, G–L)

Description (based on four specimens): pollen, monad, heteropolar, P/E ratio oblate, outline nearly circular in equatorial view (arched to obtuse distal face versus straight to slightly arched proximal face); equatorial diameter 37.5–41.9 µm, polar axis 27.1–37.6 µm (LM); monosulcate, sulcus long, extending to the proximal surface, occupying around two third of the circumference, margins of sulcus infolded; exine 0.8–1.0-µm thick, nexine thinner than sexine (LM); pollen wall tectate, columellae distinct and robust; sculpture perforate to foveolate in LM, perforate in SEM, perforations evenly distribute and become smaller towards the aperture (SEM); margin of the sulcus clearly rolled inwards (SEM).

Remarks: This pollen type is similar to *Proxapertites operculatus* with respect to the perforate sculpture observed in SEM and the inwards-rolled margin of the sulcus, but the two halves are always clearly joined and the grain does not separate into two parts.

Longapertites rugulatus Beilstein (Figs 4D–F, M–R, 5A–O)

Description (based on eight specimens): pollen, monad, heteropolar, P/E ratio oblate, outline nearly triangular or circular in equatorial view (arched to angular distal face versus straight to slightly convex proximal face); equatorial diameter 33.0–51.6 µm, polar axis 29.6–43.3 µm (LM); monosulcate, sulcus long, extending to

close-up (L) of the tectum. D, M, P, Same grain, close-up (P) of the tectum. E, N, Q, Same half of grain, showing (N, Q) inner side of pollen wall. F, O, R, Same half of grain, showing (O, R) inner side of pollen wall. LM micrographs were taken under ×1000 magnification. Scale bars: A–G, J–L = 10 µm; H–I, M–O = 1 µm.

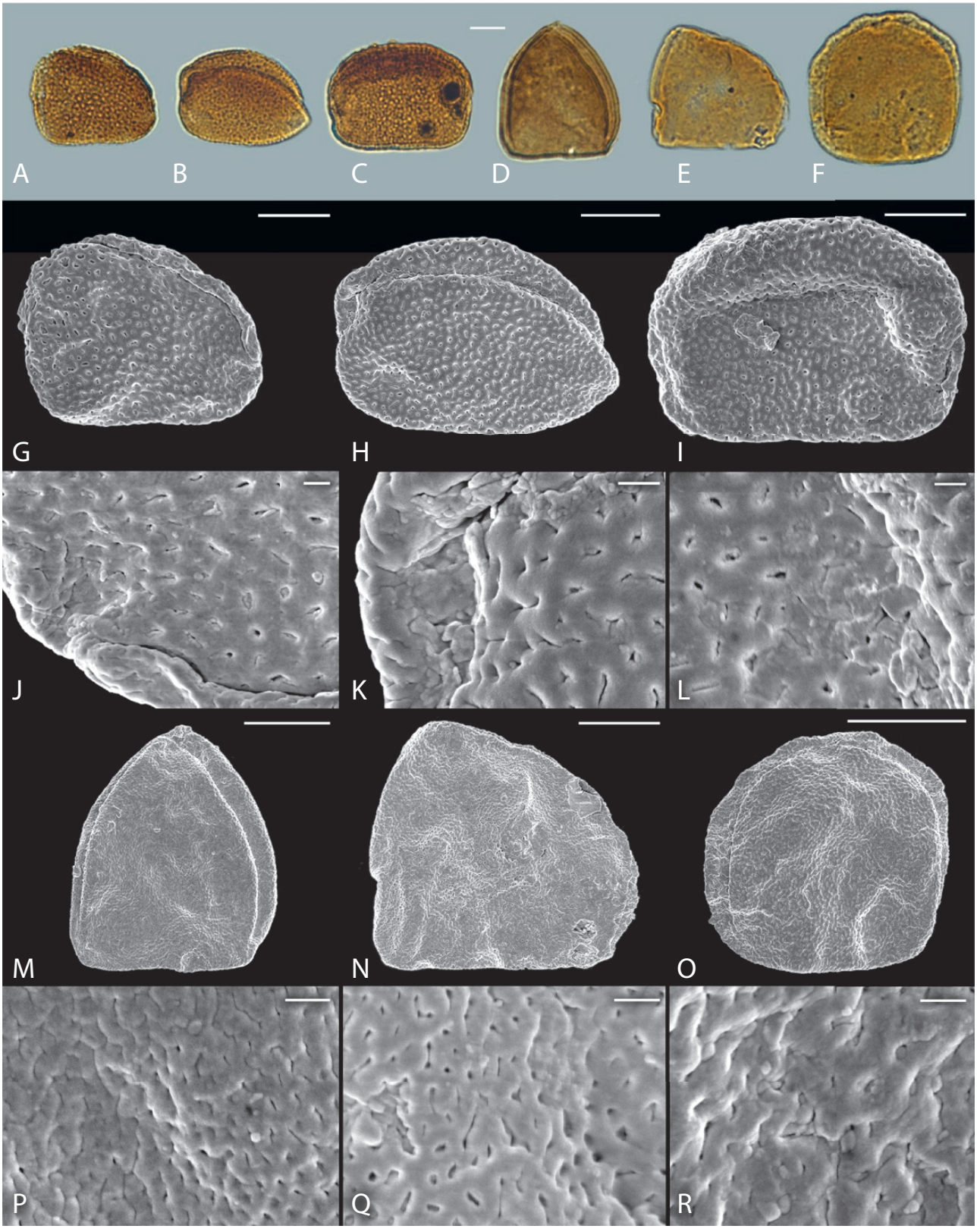

Figure 4. A–F, LM and G–R, SEM micrographs of *Longapertites* from the Eocene of Kalewa, CMB. A–C, G–L, *Longapertites retipilatus*. A, G, J, Same grain, close-up (J) of aperture region. B, H, K, Same grain, close-up (K) showing part of membrane.

the proximal surface, occupying around two third of the circumference, margins of sulcus thickened (LM), sulcus broader towards poles; exine 1.0–1.5-µm thick (LM); pollen wall tectate, columellae distinct and robust; sculpture psilate to perforate, and rugulate in LM, perforate to rugulate in SEM.

Remarks: This species is distinguished by its perforate to rugulate exine.

GENUS ***DICOLPOPOLLIS*** PFLANZL EMEND. POTONIÉ

Type species: Dicolpopollis kockelii Pflanzl

General information: The earliest reliable fossil record of *Dicolpopollis* is from the Upper Cretaceous of northern Somalia (Schrank, 1994). *Dicolpopollis* has been frequently recorded in Cenozoic sediments from low and mid latitudes (Ediger, Bati & Alişan, 1990). It is the most frequently recorded form-genus comprising disulcate pollen.

Botanical affinity, ecology and distribution: Dicolpopollis is believed to have botanical affinity to Calaminae (*Calamus*, *Daemonorops* and *Ceratolobus*) in Arecaceae (Harley & Morley, 1995; Morley, 2000). Calaminae are distributed across central Africa, and from South/southern South-East Asia into tropical Australia (Whitmore, 1973; Dransfield *et al.*, 2008). Calaminae are climbing palms (lianas) and generally termed rattans. These palms occur in all habitats, climbing within the canopy of evergreen rain forests, occurring from sea level to mountain tops. Calaminae are sometimes locally abundant in swamps and mangrove forests, and can form thickets along rivers (Dransfield, 1974).

DICOLPOPOLLIS KALEWENSIS POTONIÉ (FIGS 2D1, D2, G1, G2, 6A–R, 7A–D, F–K, M–N)

Synonym: Disulcites kalewensis Potonié, *Dicolpopollis kalewensis* (Potonié) Potonié, *Disulcipollenites kalewensis* (Potonié) Nakoman, *Dicolpopollis malesianus* Muller.

Description (based on 12 specimens): pollen, monad, heteropolar, P/E ratio oblate, outline trapezoidal in equatorial view, oval in polar view (proximal side longer than distal side, parallel and both slightly arched); grain size varies from 21.0–30.1 to 26.7–36.9 µm in polar view, and polar axis 24.3–28.5 to 22.4–31.4 µm in equatorial view, equatorial diameter 21.0–27.7 µm (LM); disulcate, sulci long and gaping; exine 0.7–1.3-µm thick, nexine around 0.5 µm thick (SEM; Fig. 7K), nexine thinner than sexine (LM and SEM); pollen wall tectate; tectum is supported by robust columellae (SEM); sculpture foveolate to perforate in SEM, foveolate in interapertual areas, becoming perforate towards apertures, lumina/perforations sometimes filled with infratectal granules and rod-like elements (SEM).

Remarks: Dicolpopollis malesianus was proposed as a new species because of its pronounced sculpture as compared to *D. kalewensis* by Muller (1968). A comparison of the material from Kalewa with the holotype and specimens of *D. malesianus* from Java by Harley & Morley (1995), suggests that the pollen grains are identical. Muller was probably misled due to the low quality of the LM micrographs of *D. kalewensis* by Potonié (1960), emphasizing the importance of displaying clear LM-SEM micrographs in publications. Therefore, it is concluded that *D. kalewensis* is the senior synonym of *D. malesianus*.

DICOLPOPOLLIS SP. (FIGS. 7E, L, O)

Description (based on one specimen): pollen, monad, heteropolar, P/E ratio oblate, outline more or less oval in polar view; grain size 28.5 × 33.1 µm (LM); disulcate, sulcus long and gaping; exine 0.6–0.8-µm thick, nexine thinner than sexine (LM); pollen wall tectate, columellae distinct and robust; sculpture foveolate to perforate in SEM, foveolate in interapertural areas, becoming perforate towards apertures, lumina variable in size, up to 2.1 µm across, oval to circular in shape (SEM).

Remarks: At Kalewa, all *Dicolpopollis* display a sculpture that ranges from foveolate in the interapertural areas towards perforate at the apertures. This pollen has similar ornamentation as *D. kalewensis*, but the lumina are much larger.

GENUS ***PALMAEPOLLENITES*** POTONIÉ

Type species: Palmaepollenites tranquillus (Potonié) Potonié (synonym: *Monocolpopollenites tranquillus* (Potonié) Thomson & Pflug)

C, I, L, Same grain, close-up (L) of tectum. D–F, M–R, *Longapertites rugulatus*. D, M, P, Same grain, close-up (P) of tectum. E, N, Q, Same grain, close-up (Q) of tectum. F, O, R, Same grain, close-up (R) of tectum. LM micrographs were taken under ×1000 magnification. Scale bars: A–I, M–O = 10 µm; J–L, P–R = 1 µm.

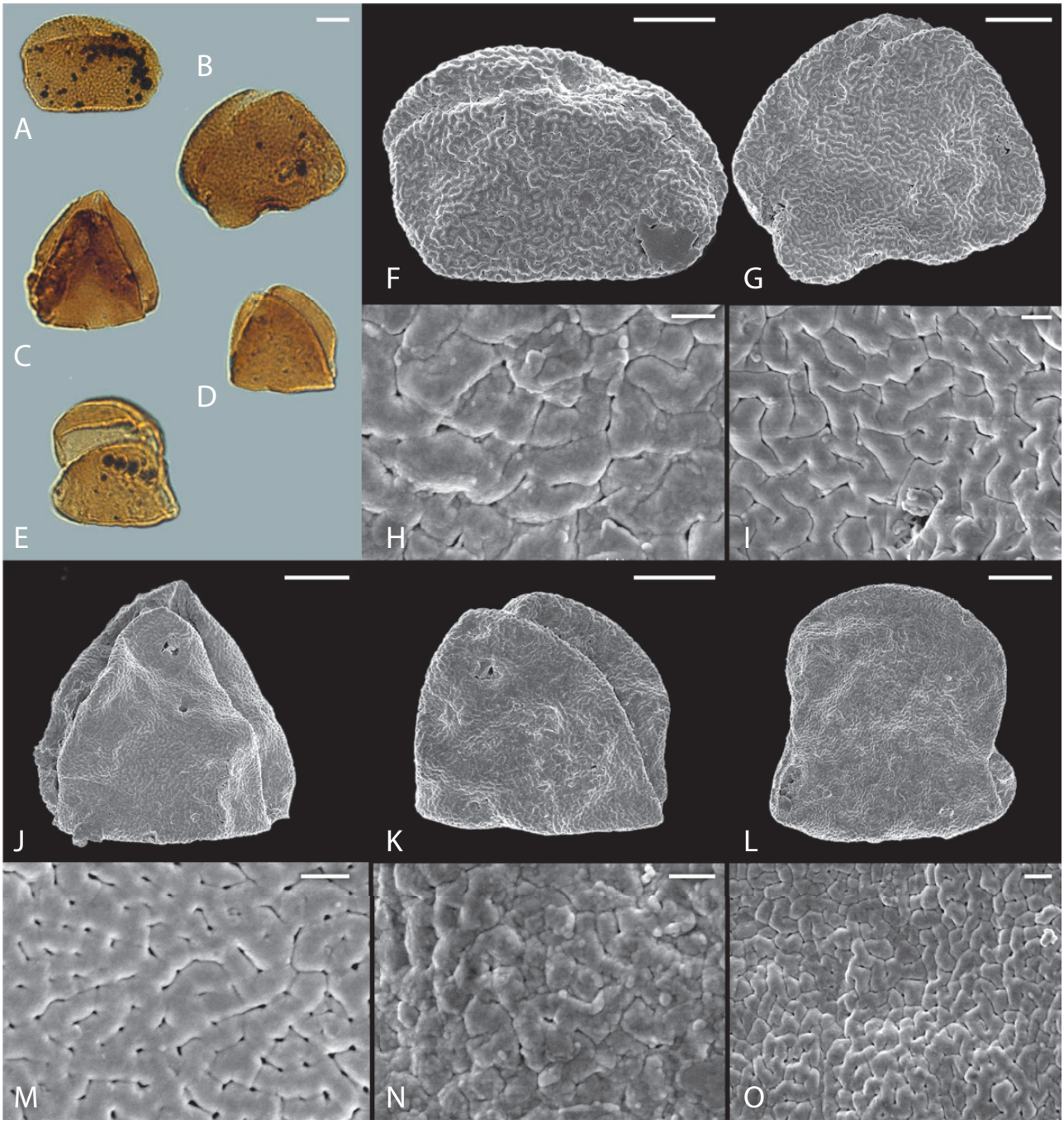

Figure 5. A–E, LM and F–O, SEM micrographs of *Longapertites rugulatus* from the Eocene of Kalewa, CMB. A, F, H, Same grain, close-up (H) of tectum. B, G, I, Same grain, close-up (I) of tectum. C, J, M, Same grain, close-up (M) of tectum. D, K, N, Same grain, close-up (N) of tectum. E, L, O, Same grain, close-up (O) of tectum. LM micrographs were taken under ×1000 magnification. Scale bars: A–G, J–L = 10 μm; H–I, M–O = 1 μm.

PALMAEPOLLENITES KUTCHENSIS VENKATACHALA & KAR (FIGS 2B, C, 8A–R)

Synonym: Monocolpites ellipticus Takahashi; *Palmaepollenites* type 1 of Harley & Morley (1995).

General information: This taxon was originally discovered in India, but its Eocene range extended into Soth-East Asia, west of Wallace's Line (Harley & Morley, 1995; Morley 1998, 2000). The source taxon, *P. kutchensis*, probably originated in India during the Late Cretaceous,

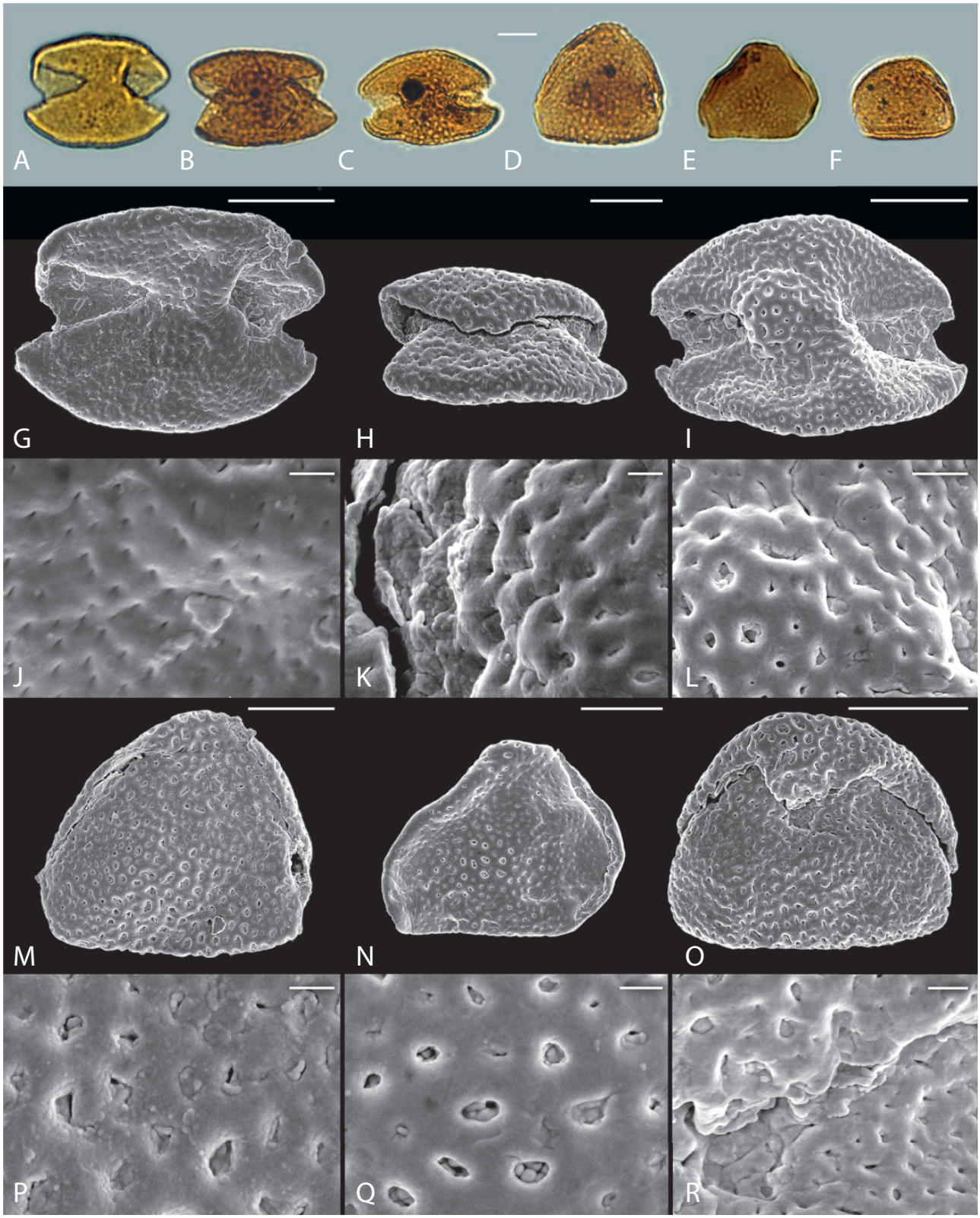

Figure 6. A–F, LM and G–R, SEM micrographs of *Dicolpopollis kalewensis* from the Eocene of Kalewa, CMB. A, G, J, Same grain, close-up (J) of tectum in polar area. B, H, K, Same grain, close-up (K) of aperture with membrane. C, I, L, Same grain,

and subsequently migrated to South-East Asia following the Indo–Asian collision in the middle Eocene (Morley, 2000, 2018). *Palmaepollenites kutchensis* gradually disappeared from the Sundanese record during the Oligocene (Harley & Morley, 1995), possibly as a result of a change to drier climatic conditions.

Description (based on seven specimens): pollen, monad, heteropolar, asymmetrical, P/E ratio oblate to suboblate, outline oval to pyriform with broadly rounded to pointed lateral ends in polar view; grain size varies from 25.8–36.2 to 37.9–42.3 µm (LM); monosulcate, sulcus distinct, broader at middle region and tapering at rounded ends, never reaching margins, sulcus length 22.1–33.5 µm, width 4.4–14.1 µm (LM); exine 1.1–2.8-µm thick, nexine thinner than sexine (LM), columellae indistinct; sculpture psilate in LM, perforate in SEM.

Botanical affinity: P. kutchensis is similar to two contrasting palm lineages. Its morphology is closest to that observed in the pollen of the Pacific coryphoid palms *Pritchardia* Seem & H.Wendl. and *Lepidorrhachis* (H.Wendl. & Drude) O.F.Cook (Harley & Morley, 1995), which have a young Neogene molecular age (Baker *et al.*, 2011) and thus the affinity is unlikely. *Palmaepollenites kutchensis* is also similar to pollen of several genera in Areceae, especially *Basselinia* and *Burretiokentia* (both Basseliniiae, confined to New Caledonia and formerly in Iguarinae; Harley & Morley, 1995), members of an older group and so a better candidate for the Eocene fossils, although no Areceae display a perfect match. The ancestors to *Basselinia* and *Burretiokentia* most likely had a wide distribution across southern Asia and Sunda in the middle Eocene and dispersed to the Pacific islands eventually finding refuge in New Caledonia prior to the formation of New Guinea (or they would still be expected to be present in the New Guinean flora), subsequently becoming extinct in India and Sunda.

Remarks: The parent plant of *P. kutchensis* was a member of the middle Eocene peat swamp vegetation in Java, as it dominates the upper part of a 1 m coal from the Nanggulan Formation (Fig. 1A) of central Java where it contributes *c.* 40% of the total pollen recovery (figs 9, 10 in Morley, 2000). It may also have been a constituent of other vegetation, but most likely was better represented in (but not confined to) areas of perhumid climate. The assumption is based on its occurrence, and then increase in abundance, in well sections from offshore South Sulawesi, following amelioration of the climate from seasonally dry to perhumid during the course of the middle Eocene (Morley, 2018).

PALMAEPOLLENITES SP. 1 (FIG. 9A–C , E–L)

Description (based on three specimens): pollen, monad, heteropolar, P/E ratio oblate to suboblate, outline oval with broadly rounded to pointed lateral ends in equatorial view; grain size varies from 22.8–34.9 to 39.1–55.1 µm (LM); monosulcate, sulcus long and narrow, tapering at ends, width 0.7–0.8 µm; exine 1.0–1.3-µm thick, nexine thinner than sexine (LM), columellae indistinct; sculpture psilate in LM, perforate in SEM.

Botanical affinity: subtribe Basseliniieae (Areceae, Arecaceae).

Remarks: The sculpture observed with SEM is similar to that of *P. kutchensis*. However, the arrangement of the sulcus in this pollen type differs from that normally observed in *P. kutchensis*.

PALMAEPOLLENITES SP. 2 (FIGS 2H, I, J1, J2, 10A–R)

Description (based on eight specimens): pollen, monad, heteropolar, P/E ratio peroblate, oblate to suboblate, outline oval to circular with broadly rounded to pointed lateral ends; grain size varies from 19.7–37.8 to 25.5–44.9 µm (LM); monosulcate, sulcus long, tapering at ends, sulcus width 0.8–5.6 µm (LM); exine 0.9–1.5-µm thick, nexine thinner than sexine (LM), columellae distinct and robust; sculpture psilate in LM, rugulate and fossulate in SEM.

Botanical affinity: Arecaceae.

Remarks: This palm pollen type is quite variable in size. As the pollen is invariably associated with *P. kutchensis*, its parent plant may have had similar ecological preferences.

GENUS *SPINIZONOCOLPITES* MULLER EMEND. MULLER *ET AL.*

Type species: Spinizonocolpites echinatus Muller

General information: Spinizonocolpites was proposed by Muller (1968). Pollen grains of this type commonly

close-up (L) of tectum in polar area. D, M, P, Same grain, close-up (P) of tectum in interapertural area. E, N, Q, Same grain, close-up (Q) of tectum in interapertural area. F, O, R, Same grain, close-up (R) of aperture with membrane. LM micrographs were taken under ×1000 magnification. Scale bars: A–I, M–O = 10 µm; J–K, P–R = 1 µm; L = 2 µm.

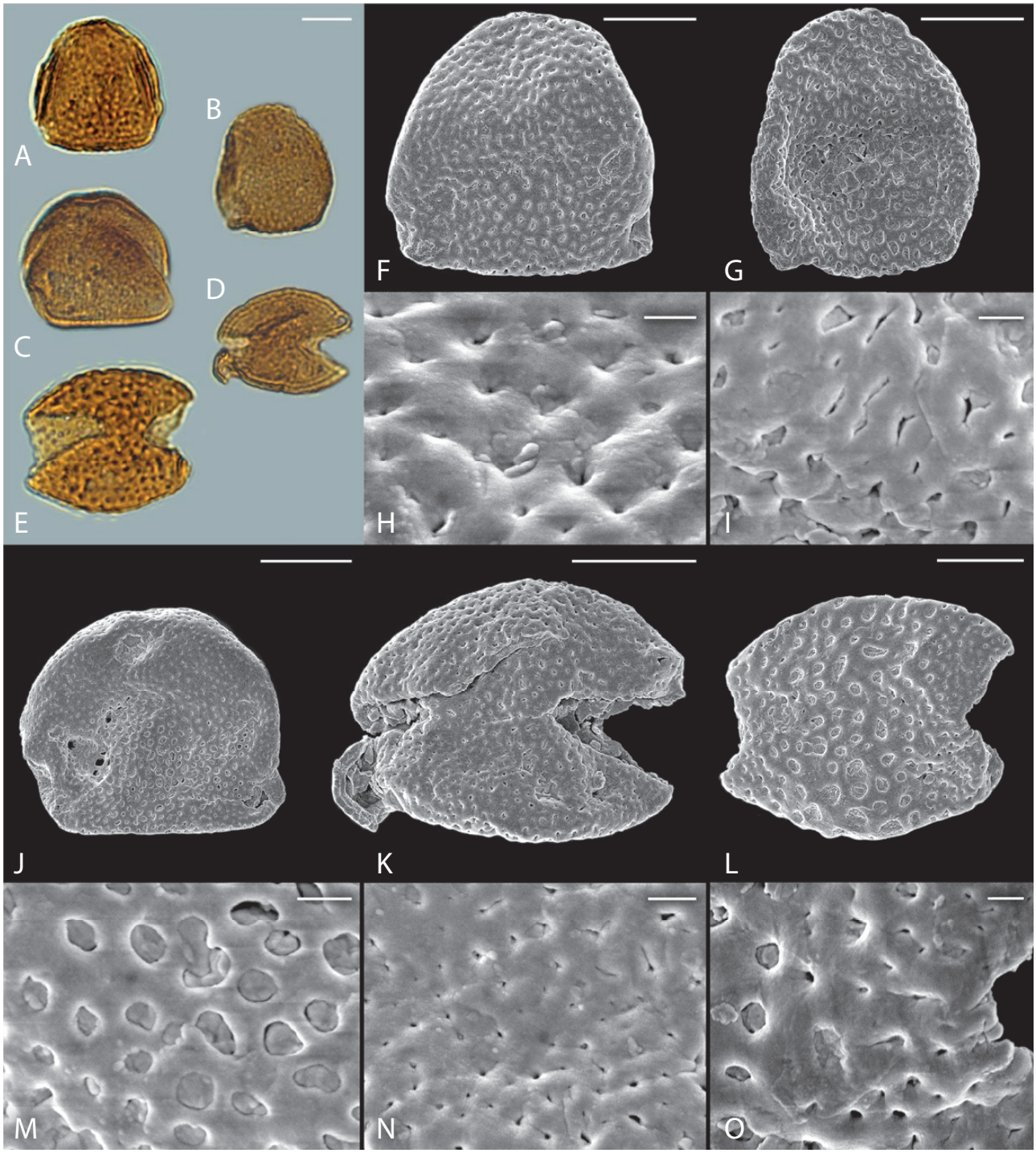

Figure 7. A–E, LM and F–O, SEM micrographs of *Dicolpopollis* from the Eocene of Kalewa, CMB. A–D, F–K, M–N, *Dicolpopollis kalewensis*. A, F, H, Same grain, close-up (H) of tectum. B, G, I, Same grain, close-up (I) of tectum. C, J, M, Same grain, close-up (M) of tectum. D, K, N, Same grain, close-up (N) of tectum. E, L, O, *Dicolpopollis* sp., same grain, close-up (O) of tectum in interapertural area. LM micrographs were taken under ×1000 magnification. Scale bars: A–G, J–L = 10 μm; H–I, M–O = 1 μm.

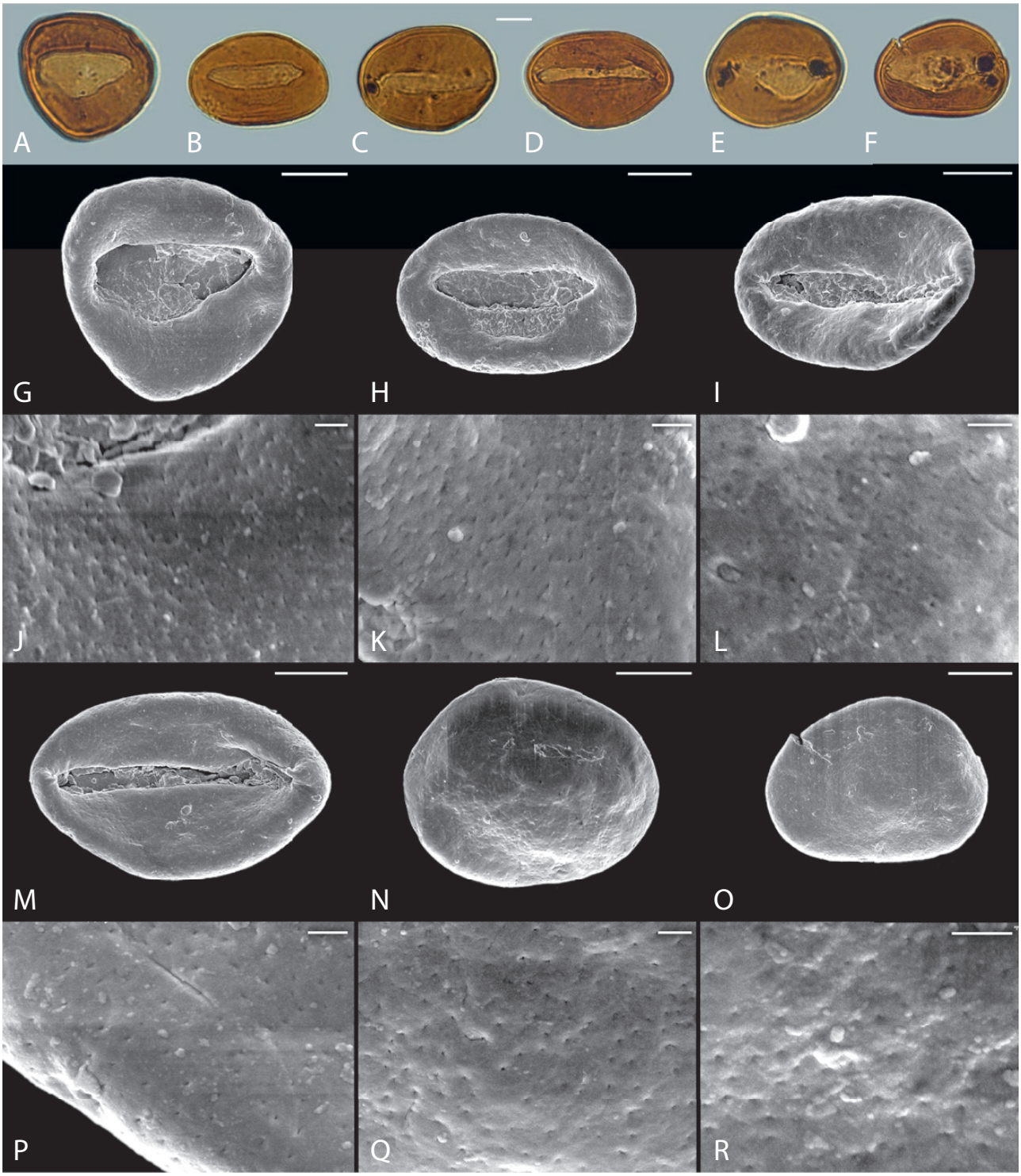

Figure 8. A–F, LM and G–R, SEM micrographs of *Palmaepollenites kutchensis* from the Eocene of Kalewa, CMB. A, G, J, Same grain, close-up (J) of tectum. B, H, K, Same grain, close-up (K) of tectum. C, I, L, Same grain, close-up (L) of tectum. D, M, P, Same grain, close-up (P) of marginal area. E, N, Q, Same grain, close-up (Q) of tectum. F, O, R, Same grain, close-up (R) of tectum. LM micrographs were taken under ×1000 magnification. Scale bars: A–I, M–O = 10 μm; J–L, P–R = 1 μm.

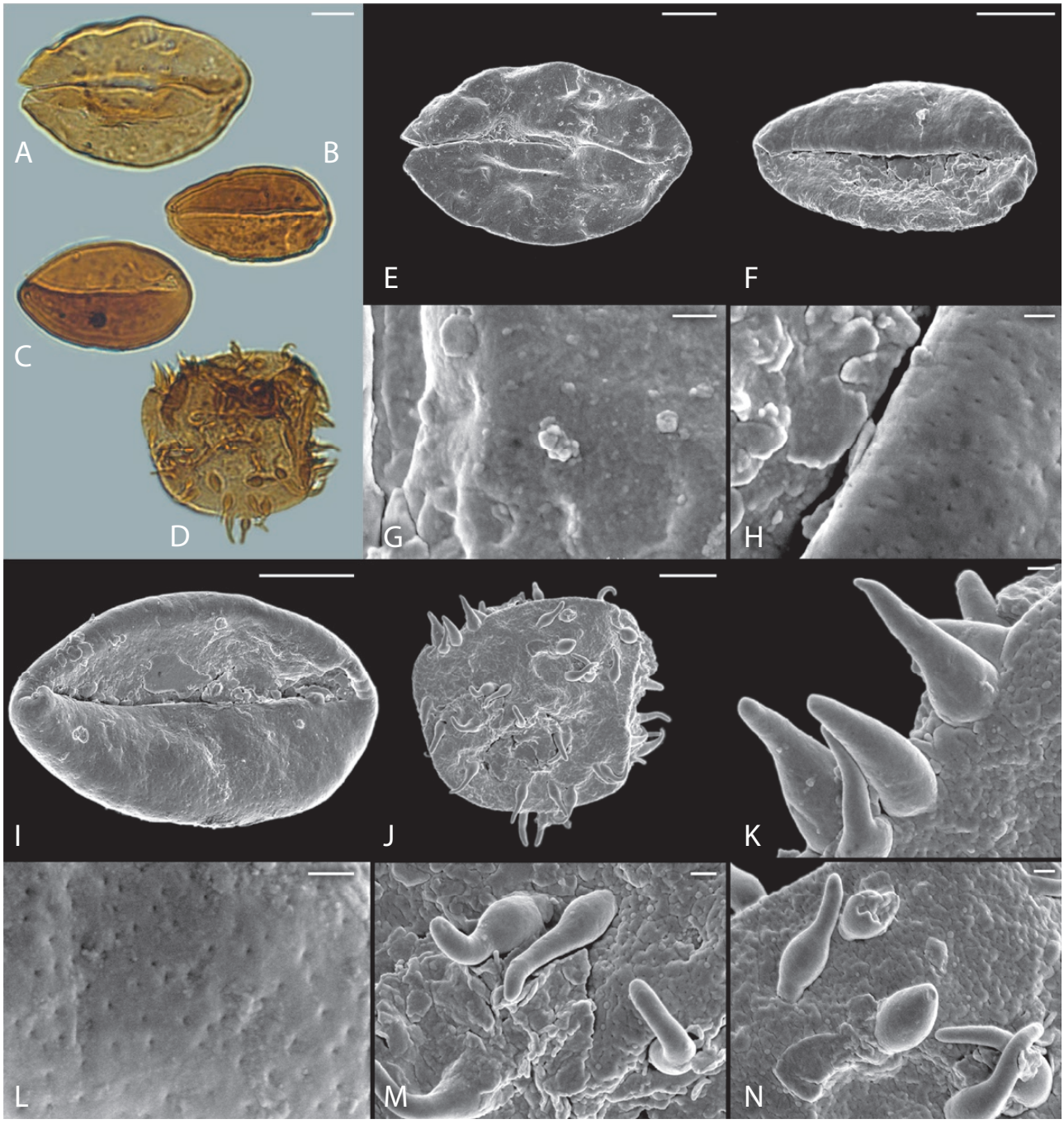

Figure 9. A–D, LM and E–N, SEM micrographs of *Palmaepollenites* sp. 1 and *Spinizonocolpites prominatus* from the Eocene of Kalewa, CMB. A–C, E–I, L. *Palmaepollenites* sp. 1. A, E, G, Same grain, showing (G) inner side of pollen wall. B, F, H, Same grain, close-up (H) of aperture area. C, I, L, Same grain, close-up (L) of tectum. D, J–K, M–N, *Spinizonocolpites prominatus*, same grain, close-up (K, M, N) of tectum and spines. LM micrographs were taken under ×1000 magnification. Scale bars: A–F, I–K = 10 μm; G–H, L–N = 1 μm.

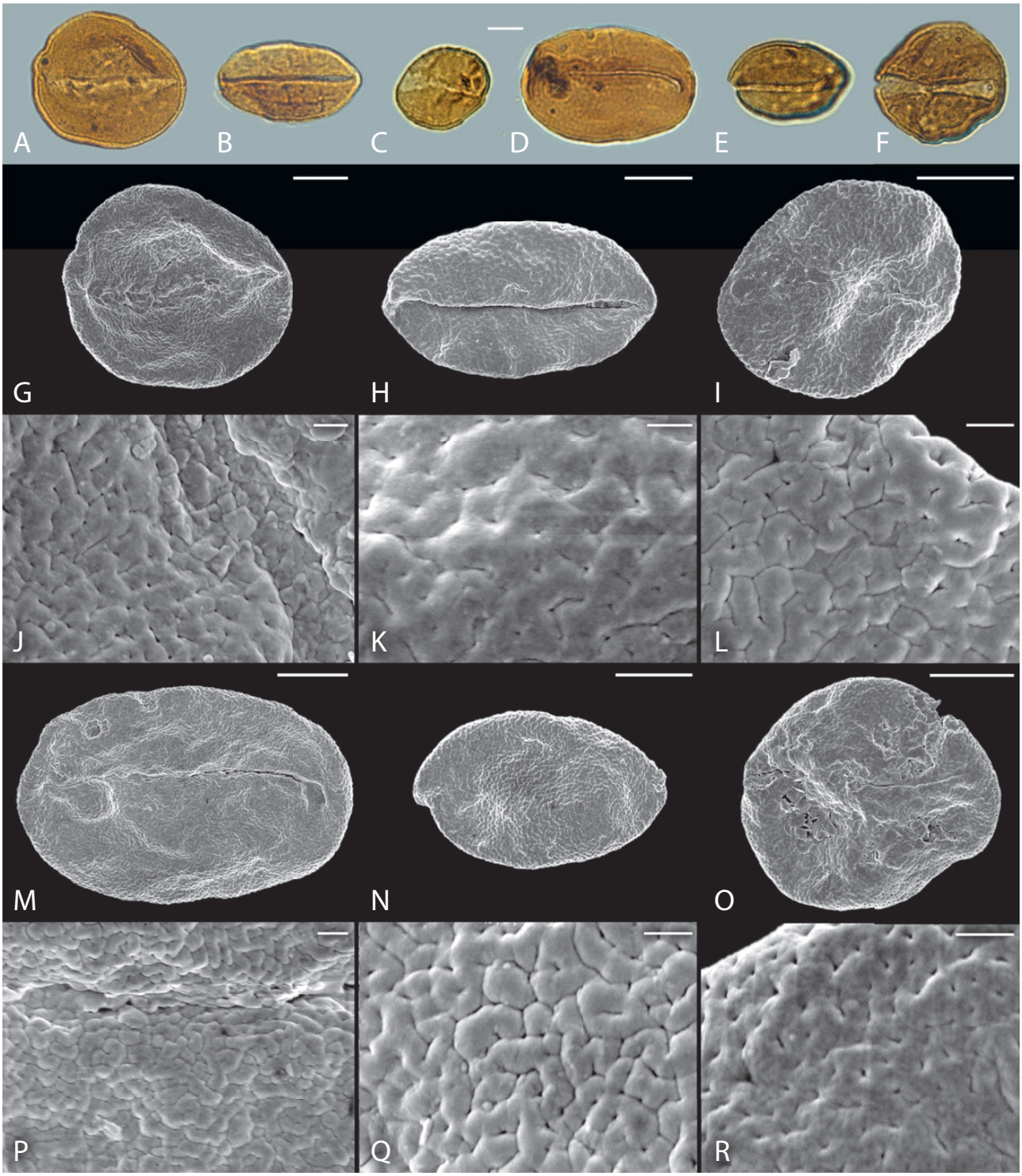

Figure 10. A–F, LM and G–R, SEM micrographs of *Palmaepollenites* sp. 2 from the Eocene of Kalewa, CMB. A, G, J, Same grain, close-up (L) of aperture area. B, H, K, Same grain, close-up (K) of tectum. C, I, L, Same grain, close-up (L) of marginal area. D, M, P, Same grain, close-up (P) of aperture area. E, N, Q, Same grain, close-up (Q) of tectum. F, O, R, Same grain, close-up (R) of marginal area. LM micrographs were taken under ×1000 magnification. Scale bars: A–I, M–O = 10 μm; J–L, P–R = 1 μm.

occur as whole grains or split into two halves when found dispersed. This pollen is widely distributed from the Maastrichtian onwards (Gee, 1990; Morley, 2000).

Botanical affinity, ecology and distribution: The NLR of *Spinizonocolpites* is *Nypa fruticans* Wurmb from the monotypic subfamily Nypoideae (Baker & Couvreur, 2013), a mangrove palm that often grows in vast natural stands in a range of estuarine conditions (Baker *et al.*, 1998). It is found in the mangrove habitats in the Indo–Malaysian region (Tomlinson, 1986). Morley *et al.* (2019) emphasized that *Nypa* is a back-mangrove palm, growing in slightly brackish or freshwater, but mostly within the reach of tidal influence. Today, *Nypa* is restricted to the Indo–Malaysian region, but during the Palaeogene it had a pantropical distribution. *Spinizonocolpites* can be used as a marker fossil for the poleward extension of moist tropics during early Eocene, at which time it was widely distributed in both the northern and southern hemispheres (Vinken, 1988; Pole & MacPhail, 1996; Morley, 2000).

Spinizonocolpites prominatus (Mcintyre) Stover & Evans (Figs 2F, 10D, J, K, M, N)

Description (based on two specimens): pollen, monad, heteropolar, P/E ratio oblate, outline oval to circular in equatorial and polar view; polar axis (excluding spines) 44.7–51.0 µm (LM & SEM); zonasulcate; exine 1.0–1.7-µm thick (LM & SEM); pollen wall tectate, columellae indistinct; sculpture echinate in LM, perforate and echinate in SEM; echini conical, bulbous above the base, irregularly distributed, echini diameter 1.7–2.8 µm, 5.3–7.3-µm long (LM & SEM).

Botanical affinity: This taxon is comparable to pollen of *Nypa* (Muller, 1968; Frederiksen, 1980). *Nypa* is also represented by fruits, widely recorded from the Eocene of Europe. Statistical analysis of fossil *Nypa* fruits from Belgium (Collinson, 1993) showed that their variation (in size and shape) is very similar to that observed in modern *Nypa*. Therefore, it is likely that the Eocene species producing the pollen shown herein may have been closely related to modern *Nypa*. However, it is possible that *Nypa* was more diverse during the early Palaeogene, as there are other morphotypes, such as *S. baculatus* from Malaysia (Muller, 1968) and several additional taxa from India (such as *S. echinatus*, *S. brevispinosus* and *S. bulbospinosus* in Khanolkar & Sharma, 2019). In the earliest Eocene of Krappfeld. Austria, *Nypa* pollen grains also show variation in the configuration of echini and other morphological details (Zetter & Hofmann, 2001).

Remarks: Spinizonocolpites is not well preserved in the studied samples. This may be due to up-river transport by tides from the coastal regions. The *Spinizonocolpites* specimens from Kalewa have sparse echini, on the basis of which it was assigned to *S. prominatus* and not *S. echinatus*.

DISCUSSION

Palynological zones, palaeovegetation and palaeoenvironment

The Eocene Kalewa pollen assemblage is diverse, reflecting a rich and diverse palaeovegetation, with a predominance of dicotyledons and pteridophytes and a good representation of monocots, particularly palms, but with few gymnosperms. The palynological assemblage represents a seasonally wet flora that mainly includes pollen from tropical plants. There are numerous megathermal tropical forest elements, including *Anacolosidites* Krutzsch (Olacaceae), *Lanagiopollis nanggulanensis* Morley (*Alangium* Lam., Cornaceae), *Cupanieidites flaccidiformis* Venkatachala & Rawat (Sapindaceae) and *Margocolporites* Ramanajuan (*Caesalpinia* L., Fabaceae), some mesothermal and microthermal angiosperms, such as *Alnipollenites* Potonié (*Alnus* Mill., Betulaceae), *Betulapollenites* Potonié (*Betula* L., Betulaceae), *Celtispollenites* (*Celtis* L., Cannabaceae) and *Gothanipollis* Krutzsch (Loranthaceae), Fagaceae and some rare montane gymnosperms [e.g. *Podocarpidites* Cookson (*Podocarpus* L'Hér. ex Pers., Podocarpaceae)] and abundant pteridophytes [e.g. *Acrostichum* L. (Pteridaceae) and *Verrucatosporites* Pflug & Thomson (Polypodiaceae)) (Huang *et al.*, 2018). The pollen diagram (Fig. 11; for raw pollen counts see Table S6) is subdivided into three main zones (Zones A–C) reflecting environmental shifts and ecological changes. The ANOVA result (P value > 0.05; Table S7) indicates that there are no significant differences in pollen abundances among the three pollen zones, which means that the establishment of the pollen zones is feasible. The summary diagram showing palm taxa versus other palaeofloral elements (Fig. 11B) indicates three main palaeoecological stages in the development of the vegetation in the estuary.

In Zone A, the percentage of palms in relation to the total sporomorph sum is low (up to 16.4%). However, there are peaks of *Longapertites*, *Proxapertites*, *Spinizonocolpites* and 'other palms', at *c.* 50 m, of which the former three achieved the highest abundance in the entire section. *Palmaepollenites kutchensis* and *Dicolpopollis* percentages are relatively low and discontinuous. Other mangrove pollen is rare, but *Acrostichum* (ferns typical of disturbed/open areas in

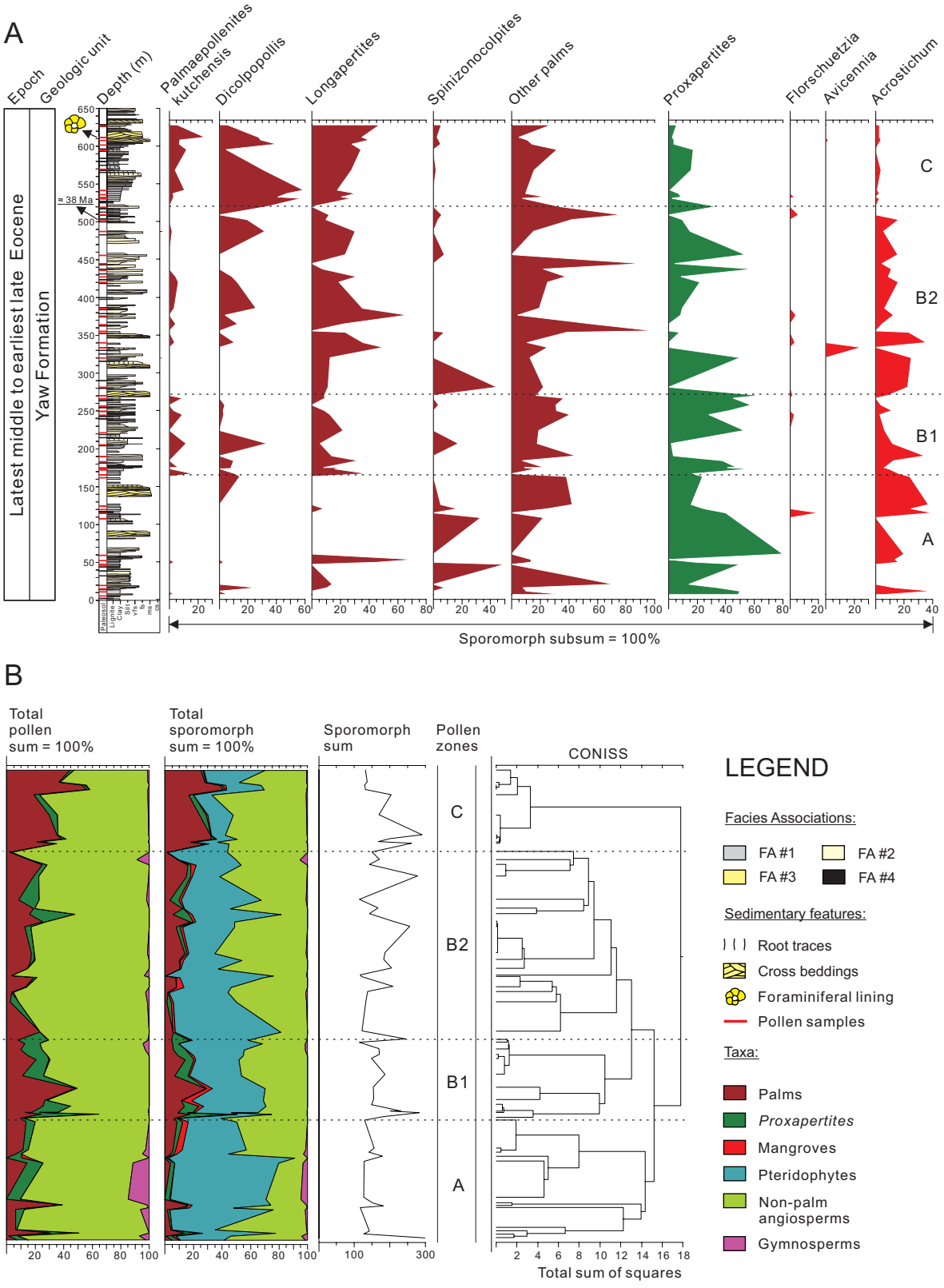

Figure 11. A, B, Pollen diagram, showing the shift of different environmental indicators. In the palaeosol column, black lines indicate histosols. Vfs = very fine sand; fs = fine sand; ms = medium sand; cs = coarse sand; B = Boulder.

mangrove/back-mangrove swamps) reaches its highest peak. This implies an association with a coastal environment subjected to regular disturbance.

In Zone B, there is a gradual increase of palm percentages (up to 28.6%). *Longapertites*, *Proxapertites* and other palms have several peaks, whereas *Spinizonocolpites* has a solitary peak at *c*. 280 m. *Palmaepollenites kutchensis* and *Dicolpopollis* increase gradually and their general trends are similar, not only in this zone, but throughout the entire succession (Fig. 11A). This is consistent with the indication from the middle Eocene Nanggulan coal (Fig. 1A) that *P. kutchensis* is a swamp taxon (Morley, 2000), and its association with the commonly occurring *D. kalewensis* suggests extensive freshwater swamps. This zone is divided into two subzones, subzone B1 and subzone B2. In subzone B1, *Longapertites* has low percentages, whereas the percentages of *Spinizonocolpites* and *Proxapertites* are relatively high. This indicates closer proximity to the palaeo-shoreline. At the transition into subzone B2, *Spinizonocolpites* is absent, *Proxapertites* is reduced and *Longapertites* increases in abundance. Other mangrove pollen is rare in this subzone, whereas *Acrostichum* spores are still common. This could be explained by that *Acrostichum* may also occur in disturbed floodplain settings, as emphasized by Moreno-Domínguez *et al.* (2016). The compositional changes in the palynoflora suggest an environmental shift from the coastal plain to more freshwater conditions, upstream the estuary.

In Zone C, *Dicolpopollis* is the dominant palm pollen type, but *P. kutchensis* and *Longapertites* are also common. The increase in palm pollen (up to 40.9%) coincides with a decrease in pteridophyte spores, suggesting that ferns no longer were a major part of the regional vegetation. Also, *Proxapertites* and *Acrostichum* spores decrease and *Spinizonocolpites* and other mangrove pollen become rare. This suggests deposition in a fluvial setting.

Palaeoecological correlation of selected PPL taxa

The PCA (Fig. 12) of PPL pollen (*Spinizonocolpites*, *Proxapertites*, *Longapertites*, *Dicolpopollis* and *Palmaepollenites kutchensis*) and *Acrostichum* from Kalewa shows that *P. kutchensis* correlates well with *Dicolpopollis*, both of which display an inverse correlation with *Spinizonocolpites* and *Acrostichum* that are mangrove/back-mangrove taxa. The closeness of *P. kutchensis* and *Dicolpopollis* in the PCA indicates they are likely to originate from a similar swamp environment, a theory also supported by analysis of the Nanggulan coal (Figs 9.10, in Morley, 2000).

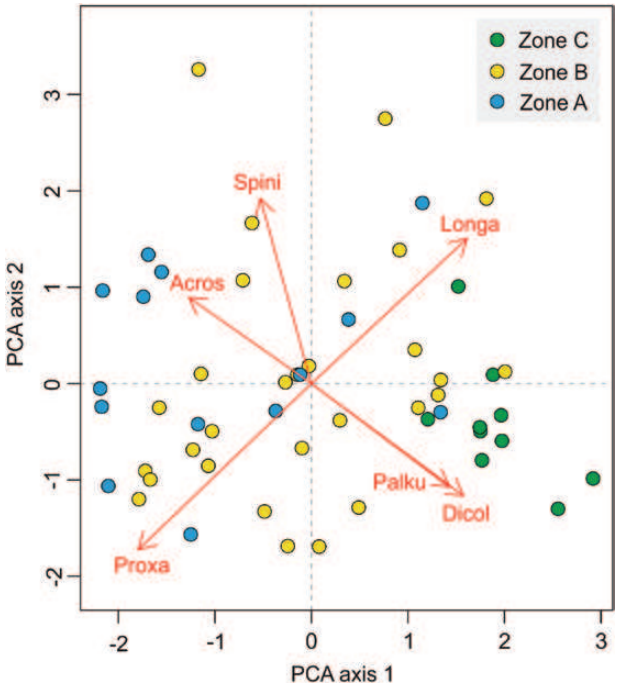

Figure 12. PCA biplot showing correlation between the PPL pollen (*Spinizonocolpites*, *Proxapertites*, *Longapertites*, *Dicolpopollis* and *Palmaepollenites kutchensis*) and *Acrostichum* from the Eocene of Kalewa, CMB. Variance explained: axis 1: 35.1%; axis 2: 19.4%. Dicol = *Dicolpopollis*, Palku = *Palmaepollenites kutchensis*, Longa = *Longapertites*, Spini = *Spinizonocolpites*, Proxa = *Proxapertites* and Acros = *Acrostichum*.

Longapertites has a positive correlation with both *P. kutchensis* and *Dicolpopollis*, and possibly also belongs to a freshwater taxon. *Longapertites* is well represented at Kalewa, but rare at Nanggulan (Morley, 2000), which might relate to the higher Eocene latitude and increased seasonality in Kalewa compared to Nanggulan (Huang *et al.*, unpubl. data). *Proxapertites* shows an inverse correlation with *P. kutchensis*, *Dicolpopollis*, *Longapertites* and *Spinizonocolpites* and a positive correlation with *Acrostichum*. A non-parametric correlation (Spearman, Table S7) between *Proxapertites* vs. *Acrostichum* and *Proxapertites* vs. *Spinizonocolpites* shows that the levels of significance 96.5 and 84.8%, respectively, illustrating that the result of the correlation with *Acrostichum* is reliable. Thus, its parent plant is more likely to have been a member of coastal vegetation. Accordingly, axis 1 of the PCA (Fig. 12) reflects proximity to the coast/salinity. Arrows towards positive values indicate freshwater settings, while arrows towards negative values suggest brackish environment.

Eocene and modern geographical distribution of selected palms

At present, Calaminae (including *Calamus*, *Daemonorops* and *Ceratolobus*) occur in South-East Asia, central Africa, southern China, India, Sri Lanka, the Pacific islands and Australia (Fig. 13B), whereas *Basselinia* and *Burretiokentia* have a relict New Caledonian distribution (Fig. 13D). Areceae occur in South-East Asia, southern China, southern India, northern Australia, North Island of New Zealand and Madagascar (Fig. 13D). *Nypa* occurs naturally in South-East Asia, the Ganges Delta, the western Pacific, Sri Lanka and northern Australia (Fig. 13F), and *Eugeissona* is distributed in the Malay Peninsula and Borneo (Fig. 13H). GBIF data on Basseliniiae (including *Basselinia* and *Burretiokentia*; one unlikely record in Italy was excluded; see Fig. 13B), *Eugeissona* (see Fig. 13H), Calaminae (including *Daemonorops* and *Ceratolobus*) and 'Observation' data on *Calamus* and *Nypa* falls well within the ranges from previous studies (Ruddle, 1979; Baker *et al.*, 1998; Mehrotra, Tiwari & Mazumder, 2003; Dransfield *et al.*, 2008). The Eocene maps show that *Dicolpopollis*, *Spinizonocolpites* and *Longapertites* had a pantropical distribution, whereas *P. kutchensis* was restricted to the Indian subcontinent and South-East Asia. Also, *Dicolpopollis* was absent from Africa and South America and present in southern North America and Europe, whereas *Longapertites* was absent from Europe. The presence of *Calamus deeratus* G.Mann & H.Wendl. in equatorial Africa may therefore reflect a Neogene dispersal (Fig. 13A, B). Basseliniiae, producing *P. kutchensis* Pollen type, were widespread across the Indian Plate and South-East Asia. This pollen type is now restricted to the relict *Basselinia* and *Burretiokentia* that occur in New Caledonia (Fig. 13C, D). *Nypa* became extinct across the Americas, Africa and Europe after the Eocene (Fig. 13E, F), possibly as a result of changing climate and/or sea level (Morley, 2000). *Eugeissona* became restricted to the Malay Peninsula and Borneo from a possible global distribution due to climatic change and competition from other plants (Fig. 13G, H). Based on the comparison between the Eocene and modern distribution maps, we suggest that their distributional ranges shrank due to changing climatic and tectonically forced factors, as well as sea level change and competition from other plants.

A comparison of PPL pollen diversity in the Palaeogene of the Indian subcontinent, Myanmar and South-East Asia

The composition at genus level of PPL pollen at Kalewa is similar to that of adjacent areas during the Palaeogene, whereas the species diversity of these palm taxa is quite different. This becomes clear when the fossil records and diversity of *Dicolpopollis*, *Longapertites*, *Spinizonocolpites* and *Proxapertites* from the Indian subcontinent, Myanmar and other areas in South-East Asia are compared (Supporting Information, Tables S3, S4; Fig. 14).

The oldest reliable Asian records of *Dicolpopollis* (*D. malesianus* = *D. kalewensis* and *D. elegans* Muller) are from the Paleocene of Sarawak, tropical Asia (Muller 1968; Morley, 1998). *Dicolpopollis* is also recorded from the Paleocene of India (e.g. Mathur & Jain, 1980), but the age of this deposit is still under debate. *Dicolpopollis* is also a frequent component in middle Eocene samples from the southern Sunda margin, from central Java (Takahashi, 1982; Harley & Morley, 1995; Lelono, 2000; Morley, 2000), and from southern Sulawesi (Morley, 1998). Lelono (2000) noted various morphotypes from the middle and late Eocene Nanggulan Formation (Fig. 1A), supported by data from the late Eocene of west Java (Morley & Morley, unpubl. data). *Dicolpopollis* is common in the Oligocene of Sunda, but is of reduced diversity compared to the middle and late Eocene (Jais, 1997; Morley, Morley & Restrepo-Pace, 2003; Morley *et al.*, 2019).

In the Eocene and Oligocene of the Indian subcontinent, *Dicolpopollis* shows a different pattern, with just a couple of morphotypes, such as *D. kalewensis* and *D. elegans*, known from the Eocene. The diversity increased during the Oligocene, adding *D. proprius* Salujha, Kindra & Rehman, *D. kalewensis*, *D. fragilis* Salujha, Kindra & Rehman, *D. cuddalorense* Krutzsch and *D. psilatus* A.Kumar & K.Takah. to the types extending from the Eocene. Several studies (e.g. Kumar & Takahashi, 1991; Saxena & Trivedi, 2009) suggest that different species occur at different localities in India, but with no more than two species at one locality. It is possible that some of these might be synonyms. In Myanmar *Dicolpopollis* is not diverse and only represented by two species (*D. kalewensis* and *D.* sp.). Thus, the diversity of Eocene *Dicolpopollis* is high in Java, intermediate in India and low in Myanmar.

Longapertites, *Spinizonocolpites* and *Proxapertites* are more diverse in the Palaeogene of the Indian subcontinent than in contemporaneous Myanmar and other areas in South-East Asia. Two *Longapertites* spp. (*L. retipilatus* and *L. rugulatus*) occur in Myanmar, and one (*L. vaneendenburgi* Geermerad *et al.*) in the late Eocene of South-East Asia (Lelono, 2000; Morley *et al.*, 2003; Winantris *et al.*, 2017). In the Indian subcontinent, *Longapertites* seems to be diverse, especially in the Paleocene and early Eocene. Samant & Phadtare (1997) reported 12 different *Longapertites* pollen types from an Eocene assemblage in India, and Frederiksen (1994) identified seven *Longapertites* spp. in a Paleocene assemblage from

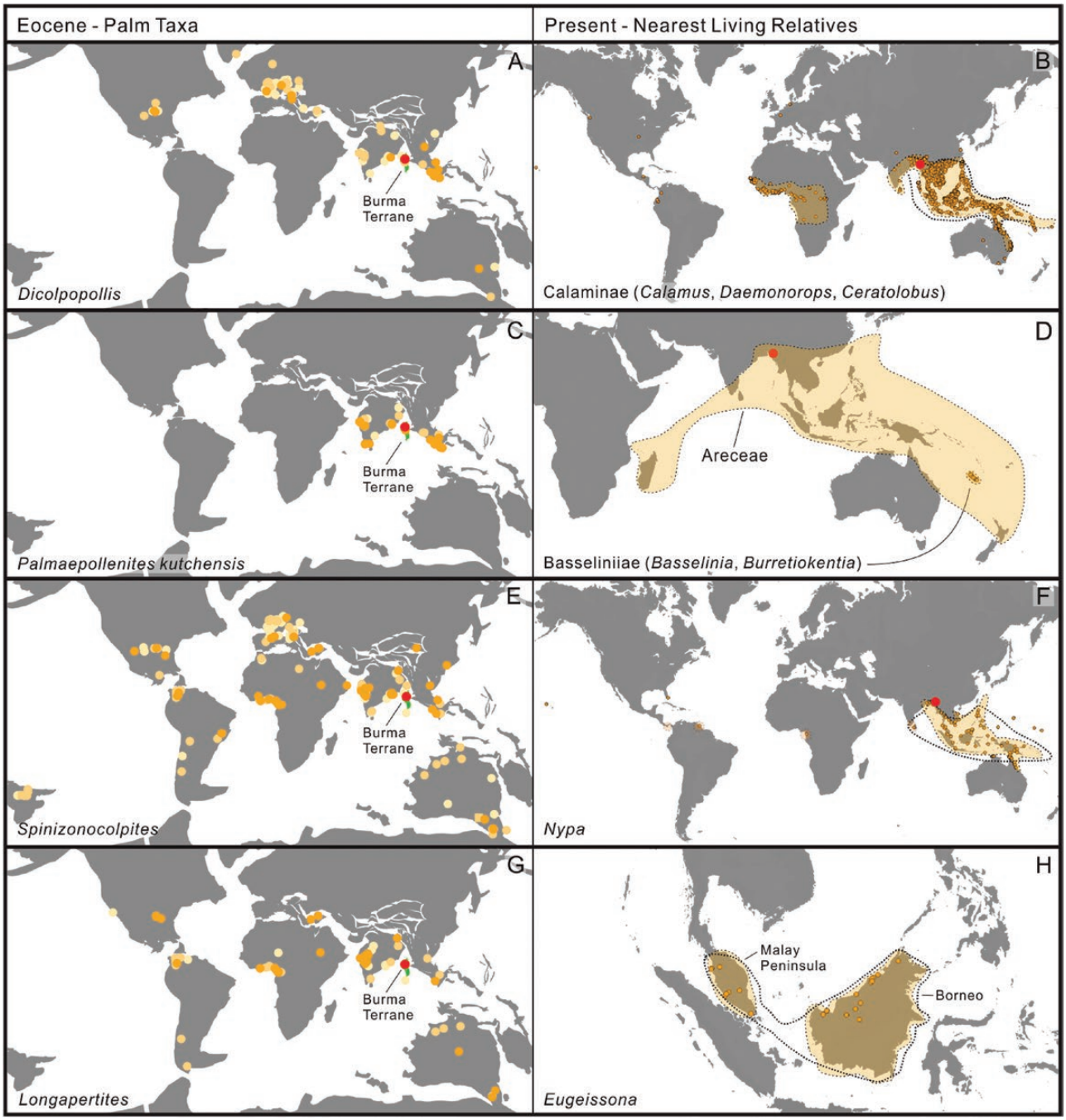

Figure 13. Global distribution maps of selected palm pollen records (Supporting Information, Table S2) in the Eocene and their NLRs. The red circle indicates the Kalewa site. In A, C, E and G, dark, intermediate and light colours indicate level 3, 2, 1 on the confidence of the records. Noting that there are three Eocene level-2 records (square) with the name of *Nypa* (E). Range between the dashed line in B is from Baker *et al.* (1998), indicating the distribution of *Calamus* in SE Asia. Range of dash line in F is from Mehrotra *et al.* (2003), showing the global distribution of *Nypa*. Range of dash line in H is from Ruddle (1979) and Baker *et al.* (1998), illustrating the global distribution of *Eugeissona*. Ranges of light orange areas in B, D, F and H are from Dransfield *et al.* (2008), demonstrating the global distribution of Calaminae (including *Calamus*, *Daemonorops* and *Ceratolobus*), Basseliniiae (including *Basselinia* and *Burretiokentia*), *Nypa* and *Eugeissona*, respectively.

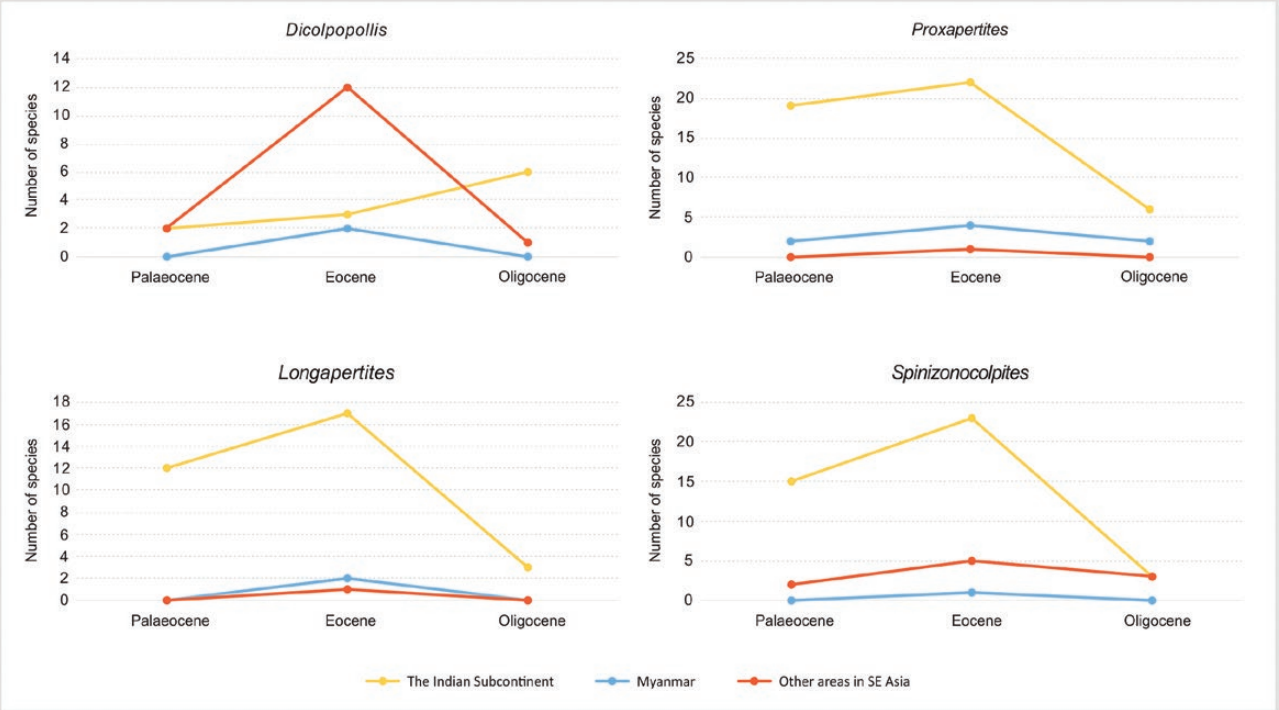

Figure 14. Species diversity of selected PPL pollen from the Palaeogene of the Indian subcontinent, Myanmar and other areas in South-East Asia.

Pakistan. *Spinizonocolpites prominatus* is the only representative of that genus in Myanmar, but seven different *Spinizonocolpites* were described from a single palynoflora from the Paleocene of India (Singh, 1990), and four distinct species were found in a Paleocene palynoflora from Pakistan (Frederiksen, 1994). Three *Spinizonocolpites* pollen types occur in the early Eocene of Irian Jaya (Indonesia), which would have formed part of the northern Australian margin at the time (Morley, 1998, 2000). Two species were reported by Muller (1968) from the Paleocene and Eocene of Malaysia. All these records suggest that the diversity of *Spinizonocolpites* was high in the Paleocene of northern India, intermediate in the Paleocene and early Eocene of South-East Asia and the northern Australian margin (but reduced to a single species during the middle Eocene to Oligocene), and low in Myanmar. *Proxapertites operculatus* is the only representative of that genus from Myanmar. *Proxapertites* is exceptionally diverse in the Paleocene of the Indian subcontinent, represented by 19 species in the Paleocene and 22 species in the Eocene (e.g. Frederiksen, 1994; Samant & Phadtare, 1997; Table S4). However, only three *Proxapertites* spp. were recorded in Indonesia (e.g. Muller, 1968; Morley, 1998; Lelono, 2000, 2007), showing greatest diversity in the late Eocene. This suggests that *Proxapertites* was more diverse in the Indian subcontinent and other areas of South-East Asia than in Myanmar during the Palaeogene.

Palaeoenvironmental, palaeoclimatic and tectonic implications

The palynological record at Kalewa is divided into two general stages, with the boundary lying at *c*. 520 m and dividing pollen zones B and C. The first stage is characterized by a low proportion of palms. *Dicolpopollis* is rare, but pteridophyte *Spinizonocolpites*, *Proxapertites* and *Acrostichum* spores are more frequent. Few additional mangrove pollen also occur. This suggests a freshwater setting that is just within reach of tidal influence. During the second stage, *Dicolpopollis* increases, but *Spinizonocolpites*, *Proxapertites* and *Acrostichum* spores are reduced. This composition suggests a lower energy environment than during the previous stage. Therefore, based on the shift in pollen composition (palms and mangrove elements), an environmental change from a tidally influenced setting to a setting without tidal influence is suggested.

The above scenario fits well within the geological context. The CMB was placed on the southern margin of Eurasia and open towards the Indian Ocean at *c*. 40 Mya (Fig. 1B, Licht *et al.*, 2013, 2014, 2018; Westerweel *et al.*, 2019). The sedimentological study

of the Yaw Formation has shown that through the studied interval, the depositional environment of the Chindwin sub-basin shifted from barrier-bound estuary to fluviatile setting (Licht *et al.*, 2018). This was the result of basin overfilling due to the incipient uplift of the Indo–Burman Ranges, blocking the direct connection between central Myanmar and the Indian Ocean (Licht *et al.*, 2018; Westerweel *et al.*, 2019). This tectonically controlled shift in depositional environment is now corroborated by the palynological data presented herein, supporting the concept that late Eocene was a period of environmental change in the broader geographic setting of the Burma Terrane.

Spatiotemporal changes in palm pollen diversity during the Palaeogene of the Indian subcontinent and South-East Asia

The Paleocene and Eocene represent a time of high palm (pollen) diversity across the region (Fig. 14). This is noticeable in *Longapertites*, *Spinizonocolpites* and *Proxapertites* from the Indian subcontinent, which were particularly diverse in the early Eocene, and in *Dicolpopollis*, which was diverse in the middle and late Eocene of South-East Asia. There is a decline in the diversity of *Longapertites*, *Spinizonocolpites* and *Proxapertites* across the whole region, and in *Dicolpopollis* of South-East Asia in the late Palaeogene. This poses the question if climatic events such as the Early Eocene Climatic Optimum and the global cooling at the EOT influenced the species diversity of these lineages. For example, the diversity of *Dicolpopollis* is high in the middle and late Eocene of South-East Asia, but declines during the Oligocene, which is probably due to the change from a perhumid to a more monsoonal climate following the EOT (Morley, 2018). Still, climate change does not explain the patterns observed in *Longapertites*, *Spinizonocolpites* and *Proxapertites*.

Here, we propose that tectonic activity played a critical role, with the Indo–Asian collision situated in a tropical location generating a northern Indian 'hotspot'. During the late Paleocene and early Eocene, the collision of the Indian Plate with the Kohistan-Ladakh Arc (Chatterjee & Scotese, 1999), and their subsequent collision with Asia, would have resulted in an archipelagic area comparable with Western Tethys during the Eocene, the Arabian Sea during the early Miocene and the present-day Indonesian Archipelago. Such a high-relief archipelago in a wet tropical region would have provided an ideal setting for species differentiation in the sense of 'hopping hotspots' of Renema *et al.* (2008). Diversification of coastal taxa in such a setting would be expected and could explain the greatly increased numbers of taxa in *Spinizonocolpites*, *Longapertites* and *Proxapertites* compared to other tropical regions of the Paleocene and Eocene. Such a 'hotspot' would have been in place with respect to coastal taxa until the late Eocene establishment of a land connection between the Indian Plate and Asia (Klaus *et al.*, 2016). A diversity hotspot, in an archipelagic area with a perhumid climate could have facilitated the early diversification of rainforest taxa, such as Dipterocarpaceae preserved as wood fossils in the underlying Pondaung Formation (Licht *et al.*, 2014). The rainforest taxa may subsequently have dispersed to the Sunda region following the Indo–Asian collision (Morley, 2018).

Sunda was a diversity hotspot for *Dicolpopollis* during the Eocene, possibly, but not exclusively, due to the warm climate. Although there are some putative Paleocene *Dicolpopollis* records from India (e.g. Mathur & Jain, 1980), the ages of these deposits are still under debate. There are firm records of *Dicolpopollis* from the Eocene of India, whereas South-East Asia has Paleocene records (such as in Sarawak, Muller, 1968), indicating a dispersal from South-East Asia to India. This is consistent with the point stated in Morley (2018) and supported by molecular data that Indian Calamoidae are deeply nested in Sunda clades (Baker *et al.*, 2009; Barrett *et al.*, 2016). Additionally, caution should be taken concerning the increase of *Dicolpopollis* species during EOT in the Indian subcontinent, as this might be due to problems of synonymy in the Paleocene, and insufficient localities in Eocene, or other reasons. These problems could also exist in other taxa, but they have been well resolved in the Sunda Shelf.

Since only few sites with Palaeogene fossil pollen have been discovered in Myanmar, it is not reasonable to take them as conclusive evidence for the palaeogeographic distribution and diversity of palms in this area. However, first indications are that in terms of the diversity of *Dicolpopollis*, *Longapertites*, *Spinizonocolpites* and *Proxapertites*, Myanmar is less diverse than the Indian subcontinent and other areas in South-East Asia (Fig. 14). As portrayed in Figure 1B, during the Eocene Kalewa was farther north than most of the Indian subcontinent and South-East Asia, while the latter two were closer to the equator. This might explain a northwards decline due to the latitudinal gradient, which affects the distribution of modern palms including Calamoideae (Eiserhardt *et al.*, 2011), showing that species diversity increased closer to the equator. Nevertheless, it will take further work in Myanmar and elsewhere to fully explain the perceived changes noted in the species richness of the fossil palm pollen.

CONCLUSIONS

In this study we investigate fossil PPL pollen of *Dicolpopollis*, *Longapertites*, *Spinizonocolpites*, *Palmaepollenites* and *Proxapertites* from the Eocene of Kalewa, CMB. We revise all *Dicolpopollis*, *Longapertites*, *Spinizonocolpites* and *Proxapertites* taxa using both light and SEM, and classify them at species level where possible. Based on the pollen morphology we conclude that *D. kalewensis* is the senior synonym of *D. malesianus*. Following a quantitative analysis of the PPL pollen, and additional mangrove elements throughout the Kalewa section, we conclude that: (1) the lower part of the Kalewa section is characterized by abundant *Acrostichum* spores but low mangrove elements, indicating a fluvial environment within the uppermost reaches of tidal influence; (2) in the middle part of the section, mangrove elements increase, suggesting a closer proximity to a palaeo-shoreline and (3) towards the top, the increase in *Dicolpopollis* coupled with the reduction of *Acrostichum* spores indicates a fluvial setting without tidal influence. Our PCA further confirms that the parent plants of *Proxapertites* and *Spinizonocolpites* co-occurred in tidal-influenced settings. Whereas parent plants of *Palmaepollenites kutchensis*, *Dicolpopollis* and *Longapertites* probably derived from freshwater settings without tidal influence, as they are closely associated and the former two show inverse correlation with *Spinizonocolpites* and *Acrostichum*. Together, the change in pollen composition and the PCA suggest an environmental change, from a tidally influenced estuary to a fluvial setting without tidal influence.

When comparing the global distribution of the Eocene palm taxa with the distribution of their NLRs, a compelling reduction in the distribution ranges is visible. We propose that this shrinking is related to the changing global climate and geography at the EOT, but this will need to be tested further. A comparison of the species diversity of *Dicolpopollis*, *Longapertites*, *Spinizonocolpites* and *Proxapertites* in the Palaeogene of the Indian subcontinent and South-East Asia, further suggests that their increased diversity reflects a diversity hotspot prior to, and during the time of collision of the Indian Plate with the Kohistan-Ladakh Arc and their subsequent collision with Asia. We hypothesize that these collisions in tropical locations with island settings and significant topographic gradients influenced the species diversity of coastal palms and resulted in a northern Indian diversity 'hotspot' with respect to palms that may have extended to other rainforest taxa.

Our study forms a basis for further palynological work in Myanmar, particularly in other CMB sub-basins. Most importantly, the study of selected PPL pollen taxa on morphology, palaeoecology and palaeoenvironment extends the general understanding on the species evolution of Arecaceae and its relation with palaeoclimate. Moreover, we anticipate that these data may prove useful for palaeobiogeographic modelling of the history of Arecaceae, particularly in India and South-East Asia.

ACKNOWLEDGEMENTS

We are indebted to all the members of the Myanmar Paleoclimate and Geodynamics Research Group (MyaPGR) for sample collection. We thank Henry Hooghiemstra for pollen identification and orientation at the start of the PhD project of H. Huang; Annemarie Philip and Jan van Arkel for processing pollen samples and microphotography, respectively (University of Amsterdam); Eko Budi Lelono (LEMIGAS, Indonesia) for permission to use data from his unpublished PhD thesis; Malcolm Jones (PLS Ltd., UK) for processing pollen samples; Christopher Scotese (Northwestern University, US) and Thijs de Boer (University of Amsterdam) for guidance on GPlates software and mapping, respectively. We are grateful to Carlos Jaramillo and an anonymous reviewer for the constructive comments. This work was supported by the China Scholarship Council (CSC) PhD grant (No. 201604910677) to H. Huang, the University of Amsterdam (UvA), and the European Research Council (ERC) grant (MAGIC (No. 649081).

REFERENCES

Abels HA, **Dupont-Nivet G**, **Xiao G**, **Bosboom RE**, **Krijgsman W. 2011.** Step-wise change of Asian interior climate preceding the Eocene–Oligocene transition (EOT). *Palaeogeography, Palaeoclimatology, Palaeoecology* **299:** 399–412.

Akkiraz MS, **Kayseri MS**, **Akgün F. 2008.** Palaeoecology of coal-bearing Eocene sediments in central Anatolia (Turkey) based on quantitative palynological data. *Turkish Journal of Earth Sciences* **17:** 317–360.

Baker WJ. 2015. A revised delimitation of the rattan genus *Calamus* (Arecaceae). *Phytotaxa* **197:** 139–152.

Baker WJ, **Coode MJE**, **Dransfield J**, **Dransfield S**, **Harley MM**, **Johns RJ. 1998.** Patterns of distribution of Malesian vascular plants. In: Hall R, Holloway JD, eds. *Biogeography and geological evolution of SE Asia*. Leiden: Backhuys, 243–258.

Baker WJ, **Couvreur TLP. 2013.** Global biogeography and diversification of palms sheds light on the evolution of tropical lineages. I. Historical biogeography. *Journal of Biogeography* **40:** 274–285.

Baker WJ, **Dransfield J. 2000.** Towards a biogeographic explanation of the calamoid palms. In: Wilson KL,

Morrison DA, eds. *Monocots: systematics and evolution*. Melbourne: CSIRO, 545–553.

Baker WJ, **Norup MV**, **Clarkson JJ**, **Couvreur TLP**, **Dowe JL**, **Lewis CE**, **Pintaud J-C**, **Savolainen V**, **Wilmot T**, **Chase MW. 2011.** Phylogenetic relationships among arecoid palms (Arecaceae: Arecoideae). *Annals of Botany* **108:** 1417–1432.

Baker WJ, **Savolainen V**, **Asmussen-Lange CB**, **Chase MW**, **Dransfield J**, **Forest F**, **Harley MM**, **Uhl MW**, **Wilkinson M. 2009.** Complete generic-level phylogenetic analyses of palms (Arecaceae) with comparisons of supertree and supermatrix approaches. *Systematic Biology* **58:** 240–256.

Barrett CF, **Bacon CD**, **Antonelli A**, **Cano A**, **Hofmann T. 2016.** An introduction to plant phylogenomics with a focus on palms. *Botanical Journal of the Linnean Society* **182:** 234–255.

Beialy EI. 1998. Stratigraphic and palaeoenvironmental significance of Eocene palynomorphs from the Rusayl Shale Formation, Al Khawd, northern Oman. *Review of Palaeobotany and Palynology* **102:** 249–258.

Bender F. 1983. *Geology of Burma.* Berlin: Borntraeger.

Bercovici A, **Hadley A**, **Villanueva-Amadoz U. 2009.** Improving depth of field resolution for palynological photomicrography. *Palaeontologia Electronica* **12:** 12.

Bignot G, **Blondeau A**, **Guernet C**, **Perreau M**, **Poignant A**, **Renard M**, **Riveline J. 1985.** Age and characteristics of the Eocene transgression at Gant (Vertes Mountains, Transdanubia, Hungary). *Acta Geologica Hungarica* **28:** 29–48.

Chatterjee S, **Scotese CR. 1999.** The breakup of Gondwana and the evolution and biogeography of the Indian plate. *Proceedings of the Indian National Science Academy* **65:** 397–425.

Chavasseau O, **Chaimanee Y**, **Coster P**, **Emonet E-G**, **Soe Aung Naing**, **Aung Aung Kyaw**, **Aye Maung**, **Rugbumrung M**, **Hla Shwe**, **Jaeger J-J. 2010.** First record of a chalicothere from the Miocene of Myanmar. *Acta Palaeontologica Polonica* **55:** 13–22.

Chiadikobi KC, **Chiaghanam OI**, **Onyemesili OC**, **Omoboriowo AO. 2018.** Palynological study of the Campano-Maastrichtian Nkporo Group of Anambra Basin, southeastern Nigeria. *World News of Natural Sciences* **20:** 31–53.

Christenhusz MJM, **Byng JW. 2016.** The number of known plants species in the world and its annual increase. *Phytotaxa* **261:** 201–217.

Collinson ME. 1993. Taphonomy and fruiting ecology of recent and fossil *Nypa*. *Special Papers in Palaeontology* **49:** 165–180.

Couvreur TLP, **Forest F**, **Baker WJ. 2011.** Origin and global diversification patterns of tropical rain forests: inferences from a complete genus-level phylogeny of palms. *BMC Biology* **9:** 44.

Coxall HK, **Pearson PN. 2007.** The Eocene–Oligocene transition. In: Williams M, Haywood AM, Gregory FJ, Schmidt DN, eds. *Deep-time perspectives on climate change: marrying the signal from computer models and biological proxies*. London: The Geological Society, 351–387.

Crié L. 1892. Recherches sur les palmiers silicifiés des terrains Crétacés de l'Anjou. *Bulletin de la Société des Études Scientifiques d'Angers* **21:** 97–103.

De Bonis L, **Solé F**, **Chaimanee Y**, **Aung Naing Soe**, **Chit Sein**, **Lazzari V**, **Chavasseau O**, **Jaeger J-J. 2018.** New hyaenodonta (Mammalia) from the middle Eocene of Myanmar. *Comptes Rendus Palévol* **17:** 357–365.

Digbehi ZB, **Yao KR**, **Tea YJ**, **Boblai G. 1996.** Contribution á l'étude palynologique et paléoenvironmentale du Campanien et du Maastrichtien du Bassin offshore de Côte d'Ivoire. *Géologie Méditerranéenne* **23:** 155–171.

Dransfield J. 1974. *A short guide to rattans*. Bogor: Regional Center for Tropical Biology (BIOTROP).

Dransfield J, **Uhl NW**, **Asmussen CB**, **Baker WJ**, **Harley MM**, **Lewis CE. 2008.** *Genera palmarum–the evolution and classification of palms*. Richmond: Royal Botanic Gardens, Kew.

Dupont-Nivet G, **Hoorn C**, **Konert M. 2008.** Tibetan uplift prior to the Eocene–Oligocene climate transition: evidence from pollen analysis of the Xining Basin. *Geology* **36:** 987–990.

Ediger VŞ, **Bati Z**, **Alişan C. 1990.** Paleopalynology and paleoecology of *Calamus*-like disulcate pollen grains. *Review of Palaeobotany and Palynology* **62:** 97–105.

Eisawi A, **Schrank E. 2009.** Terrestrial palynology and age assessment of the Gedaref Formation (eastern Sudan). *Journal of African Earth Sciences* **54:** 22–30.

Eiserhardt WL, **Svenning J-C**, **Kissling WD**, **Balslev H. 2011.** Geographical ecology of the palms (Arecaceae): determinants of diversity and distributions across spatial scales. *Annals of Botany* **108:** 1391–1416.

Engelhardt DW, **Wrenn JH. 1994.** Palynology and paleoenvironments of Eocene sediments, Saw area, Salin Basin, Myanmar (Burma). *Palynology* **18:** 243–244.

Frederiksen NO. 1980. Sporomorphs from the Jackson Group (Upper Eocene) and adjacent strata of Mississippi and western Alabama. *U.S. Geological Survey Professional Paper* **1084:** 1–75.

Frederiksen NO. 1994. Middle and late Palaeocene angiosperm pollen from Pakistan. *Palynology* **18:** 91–137.

Friis EM, **Pedersen KR**, **Crane PR. 2004.** Araceae from the Early Cretaceous of Portugal: evidence on the emergence of monocotyledons. *Proceedings of the National Academy of Sciences of the United States of America* **101:** 16565–16570.

GBIF.org. 2019a. GBIF Occurrence Download. Available at: https://doi.org/10.15468/dl.ag40lq.

GBIF.org. 2019b. GBIF Occurrence Download. Available at: https://doi.org/10.15468/dl.bzjazl.

GBIF.org. 2019c. GBIF Occurrence Download. Available at: https://doi.org/10.15468/dl.rliz8n.

GBIF.org. 2019d. GBIF Occurrence Download. Available at: https://doi.org/10.15468/dl.wvfy3m.

Gee CT. 1990. On the fossil occurrences of the mangrove palm *Nypa*. In: Knobloch E, Kvaček Z, eds. *Paleofloristic and paleoclimatic changes in the Cretaceous and Tertiary*. Prague: Geological Survey of Czechoslovakia, 315–319.

Germeraad JH, **Hopping CA**, **Muller J. 1968.** Palynology of Tertiary sediments from tropical areas. *Review of Palaeobotany and Palynology* **6:** 189–348.

Gottwald, HPJ. 1994. Tertiäre Kieselhölzer aus dem Chindwinn-Bassin im nordwestlichen Myanmar (Birma). *Documenta Naturae (Munich)* **86:** 1–90.

Grimm EC. 1987. CONISS: a FORTRAN 77 program for stratigraphically constrained cluster analyses by the method of incremental sum of squares. *Computers & Geosciences* **13:** 13–35.

Grimm EC. 1991. *Tilia and tiliagraph*. Springfield: Illinois State Museum.

Guédé KÉ, **Slimani H**, **Jean-Paul Yao N**, **Chekar M**, **Jean-Claude Koffi N**, **M'Hamdi A**, **Mouah R**, **Digbehi BZ. 2019.** Late Cretaceous to Early Eocene dinoflagellate cysts from the "12 frères" borehole, Fresco, southwestern Côte d'Ivoire: biostratigraphy and paleobiogeographic implication. *Journal of African Earth Sciences* **150:** 744–756.

Halbritter H, **Ulrich S**, **Grímsson F**, **Weber M**, **Zetter R**, **Hesse M**, **Buchner R**, **Svojtka M**, **Frosch-Radivo A. 2018.** *Illustrated pollen terminology*, *2nd edn*. Vienna: Springer.

Harley MM, **Baker WJ. 2001.** Pollen aperture morphology in Arecaceae: application within phylogenetic analyses, and a summary of the fossil record of palm-like pollen. *Grana* **40:** 45–77.

Harley MM, **Morley RJ. 1995.** Ultrastructural studies of some fossil and extant palm pollen, and the reconstruction of the biogeographical history of subtribes Iguanurinae and Calaminae. *Review of Palaeobotany and Palynology* **85:** 153–182.

Harrington GJ. 2008. Comparisons between Palaeocene–Eocene paratropical swamp and marginal marine pollen floras from Alabama and Mississippi, USA. *Palaeontology* **51:** 611–622.

Hartwich SJ, **Conran JG**, **Bannister JM**, **Lindqvist JK. 2010.** Calamoid fossil palm leaves and fruits (Arecaceae: Calamoideae) from late Eocene Southland, New Zealand. *Australian Systematic Botany* **23:** 131–140.

Herngreen GFW. 1998. Cretaceous sporomorph provinces and events in the equatorial region. *Zentralblatt für Geologie und Paläontolgie* **1996:** 1313–1323.

Herngreen GFW, **Kedves M**, **Rovnina LV**, **Smirnova SB. 1996.** Cretaceous palynofloral provinces: a review. In: Jansonius J, McGregor DC, eds. *Palynology: principles and applications 3*. Dallas: American Association of Stratigraphic Palynologists Foundation, 1157–1188.

Hesse M, **Zetter R. 2007.** The fossil pollen record of Araceae. *Plant Systematics and Evolution* **263:** 93–115.

Hoorn C, **Straathof J**, **Abels HA**, **Xu YD**, **Utescher T**, **Dupont-Nivet G. 2012.** A late Eocene palynological record of climate change and Tibetan Plateau uplift (Xining Basin, China). *Palaeogeography, Palaeoclimatology, Palaeoecology* **344:** 16–38.

Huang H, **Licht A**, **Morley R**, **Dupont-Nivet G**, **Win Z**, **Westerweel J**, **Littell V**, **Swe HH**, **Kaythi M**, **Wa Aung D**, **Roperch P**, **Poblete F**, **Sein K**, **Jardine P**, **Philip A**, **Hoorn C. 2018.** Palynology of the central Myanmar basin corroborates Eocene–Oligocene monsoonal conditions in south-east Asia. In: Abstract volume of the European Palaeobotany and Palynology Conference, 12–17 August 2018, Dublin, Ireland.

Jacobs BF, **Pan AD**, **Scotese CR. 2010.** Chapter 5: a review of the Cenozoic vegetation history of Africa. In: Werdelin L, Sanders WJ, eds. *Cenozoic mammals of Africa*. Berkeley: University of California Press, 57–72.

Jaeger J-J, **Tin Thein**, **Benammi M**, **Chaimanee Y**, **Naing SA**, **Thit L**, **Tun T**, **Wai S**, **Ducrocq S. 1999.** A new primate from the middle Eocene of Myanmar and the Asian early origin of anthropoids. *Science* **286:** 528–530.

Jais JHM. 1997. *Oligocene to Pliocene quantitative stratigraphic palynology of the southern Malay Basin, offshore Malaysia*. Unpublished D. Phil. Thesis, Sheffield University.

Jaramillo CA, **Bayona G**, **Pardo-Trujillo A**, **Rueda M**, **Torres V**, **Harrington GJ**, **Mora G. 2007.** The palynology of the Cerrejón Formation (Upper Paleocene) of northern Colombia. *Palynology* **31:** 153–189.

Kayseri-Özer MS. 2013. Spatial distribution of climatic conditions from the Middle Eocene to Late Miocene based on palynoflora in Central, Eastern and Western Anatolia. *Geodinamica Acta* **26:** 122–157.

Khanolkar S, **Sharma J. 2019.** Record of early to middle Eocene paleoenvironmental changes from lignite mines, western India. *Journal of Micropalaeontology* **38:** 1–24.

Kingsley OK, **Umeji OP. 2018.** Oil shale prospects of Imo Formation Niger Delta Basin, southeastern Nigeria: palynofacies, organic thermal maturation and source rock perspective. *Journal of Geology Society of India* **92:** 498–506.

Klaus S, **Morley RJ**, **Plath M**, **Zhang YP**, **Li JT. 2016.** Biotic interchange between the Indian subcontinent and mainland Asia through time. *Nature Communications* **7:** 12132.

Kumar A, **Takahashi K. 1991.** Palynology of the Tertiary sediments of southern Assam, India. *Bulletin of the Faculty of Liberal Arts, Nagasaki University, (Natural Science)* **31:** 515–659.

Kvaček J, **Herman AB. 2004.** Monocotyledons from the Early Campanian (Cretaceous) of Grünbach, Lower Austria. *Review of Palaeobotany and Palynology* **128:** 323–353.

Kwetche P, **Ntamak-Nida MJ**, **Nitcheu ALD**, **Etame J**, **Owono FM**, **Mbesse CO**, **Kissaaka JBI**, **Ngon GN**, **Bourquin S**, **Bilong P. 2018.** Facies analysis and sequence stratigraphy of Missole Outcrops: N'Kapa Formation of the south-eastern edge of Douala Sub-Basin (Cameroon). *Earth Science Research, Canadian Center of Science and Education* **7:** 35–54.

Lelono EB. 2000. *Palynological study of the Eocene Nanggulan Formation, Central Java, Indonesia*. Unpublished D. Phil. Thesis, Royal Holloway University of London.

Lelono EB. 2007. Palinomorf Eosen dari Selat Makasar. *Lembaran Publikasi Lemigas* **41:** 1–10.

Licht A, **Boura A**, **De Franceschi D**, **Ducrocq S**, **Naing SA**, **Jaeger J-J. 2014.** Fossil woods from the late middle Eocene Pondaung Formation, Myanmar. *Review of Palaeobotany and Palynology* **202:** 29–46.

Licht A, **Boura A**, **De Franceschi D**, **Utescher T**, **Sein C**, **Jaeger J-J. 2015.** Late middle Eocene fossil wood of Myanmar: implications for the landscape and the climate of

the Eocene Bengal Bay. *Review of Palaeobotany Palynology* **216:** 44–54.

Licht A, **Dupont-Nivet G**, **Win Z**, **Swe HH**, **Kaythi M**, **Roperch P**, **Ugrai T**, **Littell V**, **Park D**, **Westerweel J**, **Jones D**, **Poblete F**, **Wa Aung D**, **Huang H**, **Hoorn C**, **Sein K. 2018.** Paleogene evolution of the Burmese forearc basin and implications for the history of India-Asia convergence. *Geological Society of America Bulletin* **131:** 730–748.

Licht A, **France-Lanord C**, **Reisberg L**, **Fontaine C**, **Naing SA**, **Jaeger J-J. 2013.** A palaeo Tibet-Myanmar connection? Reconstructing the Late Eocene drainage system of central Myanmar using a multi-proxy approach. *Journal of the Geology Society* **170:** 929–939.

Licht A, **Reisberg L**, **France-Lanord C**, **Naing SA**, **Jaeger J-J. 2016.** Cenozoic evolution of the central Myanmar drainage system: insights from sediment provenance in the Minbu Sub-Basin. *Basin Research* **28:** 237–251.

Macphail MK, **Colhoun EA**, **Fitzsimons SJ. 1995.** Key periods in the evolution of the Cenozoic vegetation and flora in western Tasmania: the Late Pliocene. *Australian Journal of Botany* **43:** 505–526.

Macphail MK, **Hill RS. 2019.** What was the vegetation in northwest Australia during the Paleogene, 66–23 million years ago? *Australian Journal of Botany* **66:** 556–574.

Mathews RP, **Tripathi SM**, **Banerjee S**, **Dutta S. 2013.** Palynology, palaeoecology and palaeodepositional environment of Eocene lignites and associated sediments from Matanomadh mine, Kutch Basin, western India. *Journal of the Geological Society of India* **82:** 236–248.

Mathur YK, **Jain AK. 1980.** Palynology and age of the Dras Volcanics near Shergol, Ladakh, Jammu and Kashmir, India. *Geoscience Journal* **1:** 55–74.

Matthews KJ, **Maloney KT**, **Zahirovic S**, **Williams SE**, **Seton M**, **Müller RD. 2016.** Global plate boundary evolution and kinematics since the late Paleozoic. *Global and Planetary Change* **146**, 226–250.

McGowran B, **Archer M**, **Bock P**, **Darragh TA**, **Godthelp H**, **Hageman S**, **Hand SJ**, **Hill R**, **Li Q**, **Maxwell PA**, **McNamara KJ**, **MacPhail M**, **Mildenhall D**, **Partridge AD**, **Richardson J**, **Shafik S**, **Truswell EM**, **Warne M. 2000.** Australasian palaeobiogeography: the Paleogene and Neogene record. In: Wright AJ, Young GC, Talent JA, Laurie JR, eds. *Palaeobiogeography of Australasian faunas and floras*. Canberra: Memoir 23 of the Association of Australasian Palaeontologists, 405–470.

Mehrotra RC, **Tiwari RP**, **Mazumder BI. 2003.** *Nypa* megafossils from the Tertiary sediments of northeast India. *Geobios* **36:** 83–92.

Mohammed Z, **Awad Z**, **Eisawi A. 2017.** Upper Cretaceous to Neogene palynology of the Rawat Basin, White Nile State, Sudan. *Journal of Earth Science & Climatic Change* **8:** 397.

Moreno-Domínguez R, **Cascales-Miñana B**, **Ferrer J**, **Diez JB. 2016.** *Acrostitium*, a pioneering fern of floodplain areas from the Late Oligocene Sariñena Formation of the Iberian Peninsula. *PLoS One* **11:** e0162334.

Morley RJ. 1978. Palynology of Tertiary and Quaternary sediments in Southeast Asia. In: Proceeding of Indonesian Petroleum Association 6th Annual Convention, 255–276.

Morley RJ. 1998. Palynological evidence for Tertiary plant dispersal in the SE Asian region in relation to plate tectonics and climate. In: Hall R, Halloway JD, eds. *Biogeography and geological evolution of SE Asia*. Leiden: Backhuys, 211–234.

Morley RJ. 2000. *Origin and evolution of tropical rain forests*. Chichester: John Wiley and Sons, Ltd.

Morley RJ. 2018. Assembly and division of the South and South-East Asian flora in relation to tectonics and climate change. *Journal of Tropical Ecology* **34:** 209–234.

Morley RJ, **Dung BV**, **Tung NT**, **Kullman AJ**, **Bird RT**, **van Kieu N**, **Chung NH. 2019.** High resolution Palaeogene sequence stratigraphic framework for the Cuu Long Basin, offshore Vietnam, driven by climate change and tectonics, established from sequence biostratigraphy. *Palaeogeography, Palaeoclimatology, Palaeoecology* **530:** 113–135.

Morley RJ, **Morley HP**, **Restrepo-Pace P. 2003.** Unravelling the tectonically controlled stratigraphy of the West Natuna Basin by means of palaeo-derived mid-Tertiary climate changes. In: Proceedings of the Indonesian Petroleum Association 29th Annual Convention & Exhibition. Jakarta: Indonesian Petroleum Association, 264–288.

Muller J. 1968. Palynology of the Pedawan and Plateau Sandstone Formations (Cretaceous–Eocene) in Sarawak, Malaysia. *Micropaleontology* **14:** 1–37.

Onuigbo EN, **Okoro AU**, **Etu-Efeotor JO**, **Akpunonu EO**, **Okeke HC. 2015.** Paleoecology of Enugu and Mamu Formations in Anambra Basin, Southeastern Nigeria. *Advances in Applied Science Research* **6:** 23–39.

Palynodata Inc., White JM. 2008. *Palynodata Datafile: 2006 version, with introduction by White JM.* Geological Survey of Canada Open File 5793, 1 CD-ROM.

Pole MS, **Macphail MK. 1996.** Eocene *Nypa* from Regatta Point, Tasmania. *Review of Palaeobotany and Palynology* **92:** 55–67.

Potonié R. 1960. Sporologie der eozänen Kohle von Kalewa in Burma. *Senckenbergiana Lethaea* **41:** 451–481.

Prasad V, **Singh IB**, **Bajpai S**, **Garg R**, **Thakur B**, **Singh A**, **Saravanan N**, **Kapur VV. 2013.** Palynofacies and sedimentology-based high-resolution sequence stratigraphy of the lignite-bearing muddy coastal deposits (early Eocene) in the Vastan Lignite Mine, Gulf of Cambay, India. *Facies* **59:** 737–761.

Prasad V, **Utescher T**, **Sharma A**, **Singh IB**, **Garg R**, **Gogoi B**, **Srivastava J**, **Uddandam PR**, **Joachimski MM. 2018.** Low-latitude vegetation and climate dynamics at the Paleocene Eocene transition–a study based on multiple proxies from the Jathang section in northeastern India. *Palaeogeography, Palaeoclimatology, Palaeoecology* **497:** 139–156.

Privé-Gill C, **Vozenin-Serra C**, **Ducrocq S**, **Soe Aung Naing**, **Jaeger J-J. 2004.** Bois de la Formation Pondaung, Eocène moyen du Myanmar. Implications paléoenvironnementales. *Palaeontographica Abteilung B* **267:** 57–65.

Punt W, **Hoen PP**, **Blackmore S**, **Nilsson S**, **Le Thomas A. 2007.** Glossary of pollen and spore terminology. *Review of Palaeobotany and Palynology* **143:** 1–81.

R Core Team. 2018. *R: A language and environment for statistical computing*. Vienna: R Foundation for Statistical Computing.

Reimann KU, **Thaung A. 1981.** Results of palynostratigraphical investigations of the Tertiary sequence in the Chindwin Basin/Northwestern Burma. In: Bharadwaj DC, ed. *Proceedings of IV International Palynological Conference*. Lucknow: Birbal Sahni Institute of Palaeobotany, 380–395.

Renema W, **Bellwood DR**, **Braga JC**, **Bromfield K**, **Hall R**, **Johnson KG**, **Lunt P**, **Meyer CP**, **McMonagle LB**, **Morley RJ**, **O'Dea A**, **Todd JA**, **Wesselingh FP**, **Wilson MEJ**, **Pandolfi JM. 2008.** Hopping hotspots: global shifts in marine biodiversity. *Science* **321:** 654–657.

Riegel W, **Wilde V**, **Lenz OK. 2012.** The early Eocene of Schöningen (N-Germany)–an interim report. *Australian Journal of Earth Sciences* **105:** 88–109.

Ruddle K. 1979. The distribution of sago-producing palms. *Bulletin of the National Museum Ethnology* **3:** 572–594.

Samant B, **Phadtre NR. 1997.** Stratigraphic palynoflora of the early Eocene Rajpardi lignite, Gujarat and the lower age limit of the Tarkeshwar Formation of South Cambay Basin, India. *Palaeontographica Abteilung B* **245:** 1–108.

Saxena RK, **Trivedi GK. 2009.** Palynological investigation of the Kopili Formation (Late Eocene) in North Cachar Hills, Assam, India. *Acta Palaeobotanica* **49:** 253–277.

Schrank E. 1987. Biostratigraphic importance of microfloras from the Late Cretaceous Clastic Series of northwestern Sudan. *Cretaceous Research* **8:** 29–42.

Schrank E. 1994. Palynology of the Yesomma Formation in the northern Somalia: a study of pollen, spores and associated phytoplankton from the Late Cretaceous Palmae Province. *Palaeontographica Abteilung B* **231:** 63–112.

Singh RS. 1990. Palynology of Langrin Coalfield, South Shillong Plateau, Meghalaya. *Palaeobotanist* **38:** 217–228.

Sun XJ, **Li M**, **Zhang Y**, **Lei Z**, **Kong Z**, **Li P**, **Ou Q**, **Liu Q. 1981.** Pollen and spores. In: Hou Y, ed. *Tertiary Paleontology of North Continental Shelf of South China Sea*. Guangzhou: Guangdong Science and Technology Press.

Takahashi K. 1982. Miospores from the Eocene Nanggulan Formation in the Yogyakarta Region, Central Java. *Transactions and Proceedings of the Palaeontological Society of Japan, New Series* **126:** 303–326.

Thanikaimoni G, Caratini C, Venkatachala BS, Ramanujam CGK, Kar RK, eds. 1984. Selected Tertiary angiosperm pollens from India and their relationship with African Tertiary pollens. *Travaux de la Section Scientifique et Technique, Institut Français de Pondichéry* **19:** 1–93.

Tomlinson PB. 1986. *The botany of mangroves*. Cambridge: Cambridge University Press.

Tripathi SKM, **Kumar M**, **Srivastava D. 2009.** Palynology of Lower Palaeogene (Thanetian-Ypresian) coastal deposits from the Barmer Basin (Akli Formation, Western Rajasthan, India): palaeoenvironmental and palaeoclimatic implications. *Geologica Acta* **7:** 147–160.

van der Hammen T. 1956. Description of some genera and species of fossil pollen and spores. *Boletín Geológico (Bogotá)* **4:** 111–117.

van der Hammen T. 1957. Climatic periodicity and evolution of South American Maastrichtian and Tertiary floras. *Boletín Geológico (Bogotá)* **5:** 49–91.

van Hoeken-Klinkenberg PMJ. 1964. A palynological investigation of some Upper Cretaceous sediments in Nigeria. *Pollen et Spores* **6:** 209–231.

van Gorsel JT, **Lunt P**, **Morley RJ. 2014.** Introduction to Cenozoic biostratigraphy of Indonesia-SE Asia. *Berita Sedimentologi* **29:** 6–40.

Venkatachala BS, **Kar RK**, **Rajanikanth A**, **Ly A. 1998.** Palynology of the Cretaceous Tertiary transition in an Atlantic bore core, off Senegal Coast, West Africa. *Palaeobotanist* **47:** 60–67.

Vergara SLE, **Rodriguez CHG. 1997.** The Upper Cretaceous and lower Paleocene of the Eastern Bogota Plateau and Llanos Thrustbelt, Colombia: alternative appraisal to the nomenclature and sequence stratigraphy. *Geología Colombiana* **22:** 51–79.

Vinken R. 1988. The Northwest European Tertiary Basin. *Geologisches Jahrbuch Reihe A* **100:** 1–508.

Westerweel J, **Roperch P**, **Licht A**, **Dupont-Nivet G**, **Win Z**, **Poblete F**, **Ruffet G**, **Swe HH**, **Kai Thi M**, **Wa Aung D. 2019.** Burma Terrane part of the Trans-Tethyan arc during collision with India according to palaeomagnetic data. *Nature Geoscience* **12:** 863–868.

Whitmore TC. 1973. *Palms of Malaysia*. London: Oxford University Press.

Winantris W, **Hamdani H**, **Harlia E. 2017.** Paleoenvironment of Tanjung Formation Barito Basin Central Kalimantan Based on palynological data. *Journal of Geoscience, Engineering, Environment, and Technology* **2:** 110–116.

Witts D, **Hall R**, **Nichols G**, **Morley RJ. 2012.** A new depositional and provenance model for the Tanjung Formation, Barito Basin, SE Kalimantan, Indonesia. *Journal of Asian Earth Sciences* **56:** 77–104.

Zetter R. 1989. Methodik und Bedeutung einer routinemäßig kombinierten lichtmikroskopischen und rasterelektronischen Untersuchung fossiler Mikrofloren. *Courier Forschungsinstitut Senckenberg* **109:** 41–50.

Zetter R, **Hesse M**, **Frosch-Radivo A. 2001.** Early Eocene zona-aperturate pollen grains of the *Proxapertites* type with affinity to Araceae. *Review of Palaeobotany and Palynology* **117:** 267–279.

Zetter R, **Hofmann C-C. 2001.** New aspects of the palynoflora of the lowermost Eocene (Krappfeld Area, Carinthia). In: Piller, WE, Rasser MW, eds. *Paleogene of the Eastern Alps*. Vienna: Verlag der Österreichischen Akademie der Wissenschaften, 473–507.

Zizka A, **Silvestro D**, **Andermann T**, **Azevedo J**, **Ritter CD**, **Edler D**, **Farooq H**, **Herdean A**, **Ariza M**, **Scharn R**, **Svantesson S**, **Wengström N**, **Zizka V**, **Antonelli A. 2019.** CoordinateCleaner: standardized cleaning of occurrence records from biological collection databases. *Methods in Ecology and Evolution* **10:** 744–751.

SUPPORTING INFORMATION

Additional Supporting Information may be found in the online version of this article at the publisher's web-site.

Figure S1. Flagged result of global GBIF data on basis of record 'Human observation' of *Calamus* using the R package 'CoordinateCleaner'.
Figure S2. Flagged result of global GBIF data on basis of record 'Preserved specimen' of *Calamus* using the R package 'CoordinateCleaner'. Some records in northern America and Europe are problematic likely because of misidentification, cultivation or planting.
Figure S3. Flagged result of global GBIF data on basis of record 'human observation' of *Nypa* using the R package 'CoordinateCleaner'.
Figure S4. Flagged result of global GBIF data on basis of record 'preserved specimen' of *Nypa* using the R package 'CoordinateCleaner'.
Table S1. Coordinates of global occurrences of Calaminae (including *Calamus*, *Daemonorops* and *Ceratolobus*), Basseliniiae (including *Basselinia* and *Burretiokentia*), *Nypa* and *Eugeissona* accessed from GBIF.
Table S2. Global Eocene pollen records of *Dicolpopollis*, *Longapertites*, *Spinizonocolpites* and *Palmaepollenites kutchensis*.
Table S3. Palaeogene pollen records of *Dicolpopollis*, *Longapertites*, *Spinizonocolpites* and *Proxapertites* in the Indian subcontinent, Myanmar and other areas in South-East Asia.
Table S4. Species diversity of *Dicolpopollis*, *Longapertites*, *Spinizonocolpites* and *Proxapertites* in the Indian subcontinent, Myanmar and other areas in South-East Asia.
Table S5. Measurements on some palm pollen grains from the Eocene of Kalewa, CMB.
Table S6. Pollen raw counts on the sporomorphs from the Eocene of Kalewa, CMB that generated the pollen diagrams (Fig. 11).
Table S7. The results of analysis of variance (ANOVA) among three pollen zones, and a non-parametric correlation (Spearman) between *Proxapertites* vs. *Acrostichum* and *Proxapertites* vs. *Spinizonocolpites*.

Gondwana Research 87 (2020) 303–319

Contents lists available at ScienceDirect

Gondwana Research

journal homepage: www.elsevier.com/locate/gr

Magmatic history of central Myanmar and implications for the evolution of the Burma Terrane

Alexis Licht [a,*], Zaw Win [b], Jan Westerweel [c], Nathan Cogné [c], Chris K. Morley [d], Sarawute Chantraprasert [d], Fernando Poblete [c,e], Tamas Ugrai [a], Bruce Nelson [a], Day Wa Aung [f], Guillaume Dupont-Nivet [c,g,h]

[a] Department of Earth and Space Sciences, University of Washington, Seattle, WA 98195, USA
[b] Geology Department, Shwe Bo University, Sagaing Region, Myanmar
[c] Géosciences Rennes, UMR CNRS 6118, Univ. Rennes, 35042 Rennes Cedex, France
[d] PTTEP, Enco, 555 Vibhavadi-Rangsit Road, Chatuchak, Bangkok, 10900, Thailand
[e] Departamento de Geología, Universidad de Chile, Santiago, Chile
[f] Geology Department, University of Yangon, Pyay Rd, Yangon, Myanmar
[g] Potsdam University, Institute of Earth and Environmental Science, 14476 Potsdam, Germany
[h] Key Laboratory of Orogenic Belts and Crustal Evolution, Ministry of Education, Beijing, China

ARTICLE INFO

Article history:
Received 24 April 2020
Received in revised form 15 June 2020
Accepted 16 June 2020
Available online 12 August 2020

Handling Editor: S. Kwon

Keywords:
Myanmar
Magmatism
Tibet
India-Asia collision
Transthetyan arc

ABSTRACT

The Burma Terrane is a microplate at the eastern edge of the Tibetan-Himalayan orogen, the origin of which remains poorly understood. Its basement comprises metamorphic and igneous rocks forming the Wuntho-Popa Arc (WPA) and has been correlated with Tibetan, Gondwana or Transtethyan rocks. Yet, little is known about the magmatic history of the WPA. We report elemental and Sr-Nd isotopic compositions of magmatic rocks, crystallization (zircon and apatite U-Pb) and exhumation (apatite fission-track) ages from rocks and river sands, and structural measurements from the Wuntho Ranges, central Myanmar, where the WPA is best exposed. We show that the WPA in the Wuntho Ranges is characterized by two magmatic events at 108–90 Ma and 46–32 Ma. Magmatism is subduction-related for both events, characterized by depleted Nd and Sr isotopic compositions, with more enriched values with time. Apatite fission-track data suggest arc exhumation during the 39–22 Ma time interval, partly overlapping with the last magmatic event. Structural data indicate NW-SE-striking tilting, folding, and thrusting that we associate with at least two phases of deformation, in the Cretaceous and the late Paleogene. Correlating the WPA with Tibetan, Gondwana or Transtethyan rocks based on its magmatic history remains ambiguous; however, models arguing for a Transtethyan origin for the WPA are most compatible with our results combined with available Burmese geological data.

1. Introduction

The Tibetan-Himalayan orogen is a puzzling assemblage of individual terranes that have been shortened, extruded, and sometimes subducted to accommodate the convergence between India and Asia (Fig. 1; Ding et al., 2001). Documenting the affinity and history of these terranes is particularly critical to reconstruct how the convergence has been accommodated along the Asian margin, a topic that is still controversial (e.g., Shen et al., 2001; Royden et al., 2008; van Hinsbergen et al., 2011; Replumaz et al., 2010, 2013; Kapp and DeCelles, 2019).

Located at the southern edge of the eastern Himalayan Syntaxis, Myanmar hosts less deformed remnants of these terranes that have only recently been the focus of geological investigations. In particular, recent paleomagnetic results showing late Cretaceous to Eocene equatorial paleolatitudes for parts of Myanmar imply a complete revision of the number, location, and evolution of subduction zones and associated magmatic arcs that accommodated India-Asia convergence (Westerweel et al., 2019). Myanmar is divided into four provinces, from west to east (Fig. 2): (1) the Indo-Burman Ranges, corresponding to the accretionary prism formed in the zone of Indian Plate subduction below western Myanmar; (2) the Burma Terrane, forming the bulk of central Myanmar and occupied by late Mesozoic – Cenozoic basins and magmatic rocks; (3) the Mogok-Mandalay-Mergui Belt (MMMB), a roughly N-S trending belt of low- and high-grade metamorphic, ultramafic, and Jurassic to Miocene S-type intrusive rocks; and (4) the Shan-Thai Plateau, consisting of Paleozoic and Mesozoic meta-sedimentary rocks attributed to the Sibumasu Terrane of Sundaland (Bender, 1983; Metcalfe, 2013). The origin of the Burma Terrane, its relationship to Tibetan terranes, Sundaland, and the MMMB are uncertain. Four types of

* Corresponding author at: Department of Earth and Space Sciences, University of Washington, Johnson Hall Rm-070, Box 351310, Seattle, WA 98195-1310, USA.
E-mail address: licht@uw.edu (A. Licht).

https://doi.org/10.1016/j.gr.2020.06.016
1342-937X/

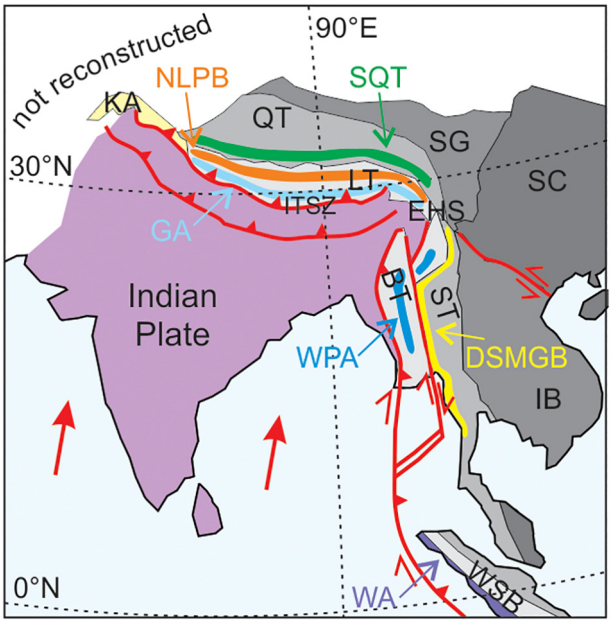

Fig. 1. Schematic map of South and East Asia with major blocks (LT: Lhasa Terrane, QT: Qiangtang Terrane; BT: Burma Terrane; ST: Sibumasu Terrane; IB: Indochina Block; SC: South China Block; SG: Songpan Ganzi Complex; WSB: West Sumatra Block) and magmatic arcs addressed in this paper (KA: Kohistan Arc; GA: Gangdese Arc; NLPB: North Lhasa Plutonic Belt; SQT: Southern Qiangtang; WPA: Wuntho-Popa Arc; DSMGB: Dianxi-Shan Scarp-Mergui Granite Belt; WA: Woyla Arc). Red lines indicate major faults; red arrows indicate the modern convergence of the Indian Plate. EHS: Eastern Himalayan Syntaxis; ITSZ = Indus-Tsangspo Suture Zone.

models have been proposed for the origin of the Burma Terrane (Table 1):

Model A. The first family of models proposes that the Burma Terrane belongs to Sundaland since at least the early Mesozoic, either as part of Sibumasu, Cathaysia (remnants of which are found in West Sumatra), or a combination of both. Since the late Triassic, the Burma Terrane built-up as a consequence of the long-term outboard growth of the accretionary prism of Tethyan subduction along the western edge of Sundaland. These models are based on the correlation of Burmese magmatic rocks with their counterparts along the Asian subduction margin (Zhang et al., 2018, 2019; Li et al., 2020). They are supported by the Cathaysian affinity of some fossil invertebrates found in Burma Terrane Paleozoic limestones (Thein et al., 1982, 1987; Ueno et al., 2016; Metcalfe, 2013). In addition, Sevastjanova et al. (2016) argued that U-Pb age distributions of detrital zircons in basement units of the Indo-Burman Ranges —namely the Pane Chaung Formation and Kanpetlet schists— support an overall Sibumasu affinity (Sevastjanova et al., 2016); however, this provenance interpretation has been recently challenged by Yao et al. (2017).

Model B. The Burma Terrane is the lateral continuation of the Lhasa Terrane of Tibet (e.g. Mitchell, 1993). This model implies a distinct origin for the Burma Terrane and Sundaland, based on the uncertain existence of a suture between the Burma Terrane and the Shan Plateau, that closed sometime between Jurassic and late Eocene (Mitchell, 1993; Mitchell et al., 2007, 2012; Mitchell et al., 2015; Ridd, 2016; Curray, 2005). This suture runs between the Burma Terrane and the MMMB and is represented today by the Myitkyina Ophiolite Belt (MOB, Fig. 2) in north Myanmar (Liu et al., 2016), and/or the cryptic Median Myanmar Suture zone, whose location remains uncertain (Mitchell et al., 2015; Ridd, 2016). The MOB represents the closure of the Mesotethys that separated the Lhasa Terrane from Sibumasu and the Qiangtang Terrane, its western continuation in Tibet (Fig. 1; Liu et al., 2016). A Lhasa affinity for the Burma Terrane is also supported by the presence of an additional ophiolite belt in Myanmar: the Western Ophiolite Belt (WOB; Fig. 2), which separates the Burma Terrane from the Indo-Burman Ranges. The nature of the WOB (accretionary or obducted) is not clear (Morley et al., 2020), but the WOB is typically correlated to the Indus-Tsangpo Suture Zone in Tibet (ITSZ; Mitchell, 1993; Mitchell et al., 2012; Liu et al., 2016). The ITSZ ophiolites are interpreted as originated and emplaced in a supra-subduction setting along the southern Lhasa margin (Maffione et al., 2015; Wang et al., 2017); the correlation between the WOB and the ITSZ thus supports a Lhasa affinity for the Burma Terrane. Correlations between Burmese and Lhasa magmatic rocks have also been used to argue for this scenario (Mitchell et al., 2012), a correlation that we will address in this study.

Model C. A third family of models proposes that the Burma Terrane and the core of the Indo-Burman Ranges originated along the northern margin of Gondwana and drifted across the Tethys as part of a wide "Greater Argoland" archipelago (Argoland referring to Gondwana-derived rocks in East Java and Sulawesi; Hall et al., 2009), before becoming an intra-oceanic arc (Morley et al., 2020). This Gondwanan origin is supported by an alternate interpretation of U-Pb age distributions of detrital zircons from basement units in the Indo-Burman Ranges, interpreted as similar to several Gondwanan units found in the Himalayas (Yao et al., 2017). This model is also supported by paleomagnetic data that locate the Burma Terrane far from the Asian margin at 100 Ma, as part of an intra-oceanic Transtethyan Arc possibly correlative with the Kohistan Arc in Tibet or the Woyla arc of Sumatra (Westerweel et al., 2019). This model is, however, contradicted by the Cathaysian affinity of Burma Terrane Paleozoic limestones (Table 1).

Model D. The final family of models hypothesizes that western Myanmar is an assembly of at least two terranes: a western block composed of the core of the Indo-Burman Ranges, including its basement units, named the Mount Victoria Block (Mitchell, 1986, 1993; Mitchell et al., 2010; Acharyya, 2007, 2015; Maurin and Rangin, 2009; Rangin, 2018), and the Burma Terrane itself, separated by the WOB. In these models, the Mount Victoria Block is either part of the Greater Argoland archipelago or a small fragment of India (Mitchell, 1981; Rangin, 2018). The Burma Terrane originated either as an intra-oceanic arc, or along the southern margin of Sundaland, as a correlative to West Sumatra, where Cathaysian fragments are present (Barber and Crow, 2009; Metcalfe, 2013) and later separated from the Asian margin by back-arc spreading, during the episode of WOB and ITSZ ophiolite formation (Gibbons et al., 2015). The Mount Victoria Block and the Burma Terrane collided at low latitudes during the Cretaceous (Morley et al., 2020). More complex variations of this model with multiple blocks for the Burma Terrane basement have also been suggested (Ridd et al., 2019; Aitchison et al., 2019). There is, as yet, no clear evidence of thickened crust reflecting accreted continental lithosphere around the Mount Victoria Block (Morley et al., 2020).

These models imply significantly different scenarios for the evolution of magmatism in Myanmar (Table 1). Two parallel magmatic belts extend N-S in Myanmar, following the Burmese subduction margin, with different history and chronology: To the east, the Dianxi-

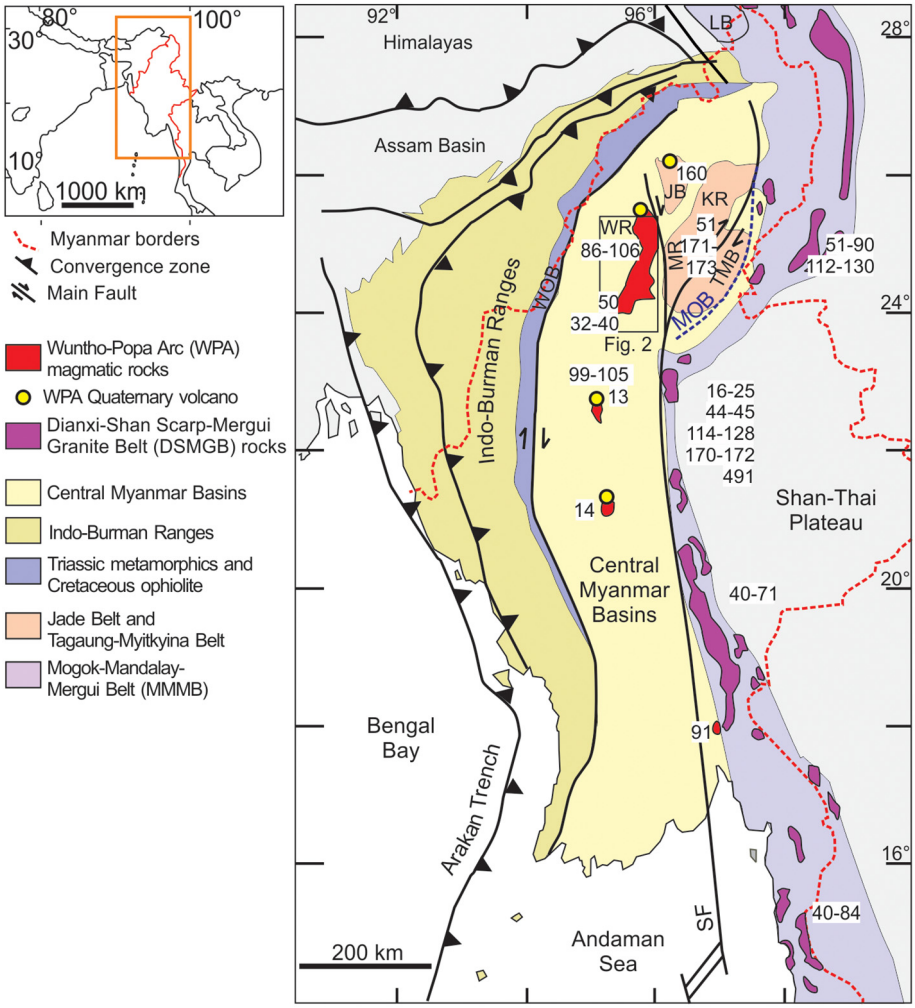

Fig. 2. Schematic map of western Myanmar, with the main geological units, after Licht et al. (2019), with published crystallization ages of Mesozoic and Cenozoic magmatic rocks of the WPA and DSMGB (ages in millions of years). Data compilation available in Supplementary Table 1. WR: Wuntho Ranges; JB: Jade Belt; TMB: Tagaung-Myitkyina Belt; WOB: Western Ophiolite Belt; MOB: Myitkyina Ophiolite Belt (dashed blue line); LB: Lohit Batholith; MR: Minwun Range; KR: Kumon and Katha-Gangaw Ranges.

Table 1
The four families of models proposed for the origin of the Burma Terrane. For abbreviations see main text.

Paleographic models for the Burma Terrane	Key reference	Pros	Cons	Implications for the WPA/correlation with Tibetan arcs
A- Conservative models: Burma Terrane is part of Sundaland	Zhang et al. (2019)	-Correlation between the WPA and the Gangdese arc of Tibet -Cathaysian affinity of Burma Terrane Paleozoic limestones -Zircon age distribution of Indo-Burman Ranges basement showing Sibumasu affinity	-In disagreement with paleomagnetic data -reject the existence of Meso-Cenozoic suture zones in Myanmar	-Same magmatic history as the one of the southern Qiangtang Arc since the early Triassic until ~130–120 Ma and the collision of Lhasa and Qiangtang. -Similar magmatic history as the one of the Gangdese Arc after 120 Ma.
B- Burma Terrane is the easternmost part of the Lhasa Terrane	Mitchell (1993)	-Correlation between the WPA and the Gangdese arc of Tibet -Correlation between the WOB and ITSZ	-In disagreement with paleomagnetic data -In disagreement with the Cathaysian affinity of Paleozoic limestones	-Same magmatic history as the one of the Gangdese Arc since its creation.
C- Burma Terrane is a Gondwana-derived fragment (part of Greater Argoland)	Morley et al. (2020)	-Zircon age distribution of Indo-Burman Ranges basement showing Gondwana affinity -Equatorial paleolatitude of the terrane in the Cretaceous shown by paleomagnetism	-Incompatible with suture and arc correlations -In disagreement with the Cathaysian affinity of Paleozoic limestones	-No direct correlation with Tibet, but potentially same magmatic history as the one of the Kohistan Arc.
D- Composite models: Burma Terrane is a mosaic of collided fragments	Rangin (2018)	-Potentially compatible with all the above	-No evidence for thickened crust at the location of potential microcontinents	-No direct correlation with Tibet.

Shan Scarp-Mergui Granite Belt, part of the "Tin Belt" of Southeast Asia, spanning across the MMMB and mostly comprised of S-type granites, and to the west, the Wuntho-Popa Arc (WPA), part of the Southeast Asian "Copper Belt", extending across the Burma Terrane (Gardiner et al., 2016, 2017). The history of magmatism along the DSMGB has been thoroughly documented (Zaw, 1990; Barley et al., 2003; Searle et al., 2007, 2020; Mitchell et al., 2012; Zhang et al., 2018; Lin et al., 2019); data from the WPA are rarer, but suggest periods of coeval magmatism in both belts (Zhang et al., 2017a; Gardiner et al., 2017; Li et al., 2019, 2020).

Isotopic and geochronological correlations have been used to propose that both the WPA and DSMGB represent the southeastward continuation of Tibetan arcs across the eastern Himalayan Syntaxis (Fig. 1; Zhang et al., 2017a, 2019; Lin et al., 2019; Li et al., 2020). The WPA shares a similar depleted isotopic signature in Nd, Sr, and Hf isotopes with the Gangdese Arc of the Lhasa Terrane and the easternmost Gangdese plutons in the eastern Himalayan syntaxis, the Lohit Batholith (Wang et al., 2014; Zhang et al., 2017a; Lin et al., 2019). By contrast, the DMSGB shares a similar enriched isotopic signature with the Northern Lhasa Plutonic Belt and its continuation in the eastern Himalayan syntaxis, the Bomi-Chayu batholith (Mitchell et al., 2012; Lin et al., 2019). It has also been argued that these arcs share the same episodes of magmatic flare-ups and lulls (e.g. Zhang et al., 2019; Li et al., 2020).

Some studies have proposed that the DSMGB and WPA reflect different coeval melts (Gardiner et al., 2015, 2017) and periods of advance and retreat of the same Andean-type Arc (Zhang et al., 2018), similar to the Gangdese Arc and Northern Lhasa Plutonic Belt (Chapman et al., 2017; Alexander et al., 2019). Other studies have proposed that the belts correspond to two different arcs accreted during the late Cretaceous-Paleogene (Jagoutz et al., 2015; Westerweel et al., 2019). Understanding the age and geochemical relationship between these arcs and their relationship with Tibetan arcs would help us decipher the origin of the Burma Terrane. However, this is hampered by the lack of geochronological and isotopic data from both areas, particularly from the WPA which is poorly exposed and hard to access.

This paper investigates the magmatic history of the WPA in the Wuntho Ranges, where it is most exposed. We provide new zircon and apatite U-Pb ages, apatite fission-track ages, Nd-Sr isotopic ratios and elemental composition of rocks from the WPA. We then compare the WPA with the DSMGB and the Tibetan arcs, discuss the potential correlation between Tibetan and Burmese magmatic rocks, and apply our new data to test the viability of the four models proposed for the origin of the Burma Terrane.

2. Geological context

2.1. Western Myanmar and the Burma Terrane

The Burma Terrane forms the bulk of western Myanmar and is almost entirely covered by the Central Myanmar Basins, a N-S trending belt of Late Cretaceous - Cenozoic sedimentary basins comprising two lateral troughs of sub-basins located both east (in a backarc position) and west (in a forearc position) of the WPA (Bender, 1983). The basement of the Burma Terrane crops out in several areas (Fig. 1): the Wuntho Ranges, where it comprises magmatic rocks of the WPA and Mesozoic metamorphic rocks; the Jade Belt and Minwun Ranges, where it is predominantly serpentinite and locally jade-bearing metamorphic rocks; and the Tagaung-Myitkyina Belt, Kumon and Katha-Gangaw Ranges, where it is composed of Triassic to Jurassic metasedimentary rocks and Jurassic to Cretaceous mafic plutons (Mitchell, 2017).

On its western margin, the Burma Terrane is separated from the Indian Foreland Basin and the Bengal Bay by the Indo-Burman Ranges, which are interpreted as the accretionary complex produced by subduction of the Indian Plate beneath the Burmese active margin (Maurin and Rangin, 2009; Bannert et al., 2011; Zhang et al., 2017b). This accretionary complex started forming after forearc spreading at 120–130 Ma and the subsequent development of the Central Myanmar Basins (Bender, 1983; Pivnik et al., 1998; Liu et al., 2016; Zhang et al., 2017b), but subduction could have started earlier (Zhang et al., 2018). Most of the Indo-Burman Ranges consist of Neogene Himalayan-sourced clastic sequences, but the inner wedge of the range comprises early Cretaceous ophiolites of the WOB, Triassic metasediments that are covered by the *Orbitolina*-bearing Paung Chaung Limestone, and Upper Cretaceous – Eocene marine turbidites (Maurin and Rangin, 2009; Bannert et al., 2011). The Paung Chaung Limestone is widespread on the Burma Terrane, and dated as Upper Albian-Cenomanian (Mitchell, 1993; Bannert et al., 2011). The origin of the Triassic metasediments is uncertain (Sevastjanova et al., 2016; Yao et al., 2017); they may have formed an independent continental fragment that accreted to the Burmese accretionary complex before the Upper Albian (see review in Morley et al., 2020).

The eastern margin of the Burma Terrane and its transition to the MMMB is marked by MOB ultramafics in northern Myanmar. In the south, this transition is hidden by Neogene fluvial deposits and is marked by the trace of the Sagaing Fault (Fig. 2). The MMMB is a ~2000-km long belt of high-grade metamorphic rocks; metamorphism is thought to start in the Cretaceous and reached its peak between 45 and 25 Ma (Searle et al., 2007, 2020); MMMB rocks were later exhumed during the Oligo-Miocene (Bertrand et al., 2001; Bertrand and Rangin, 2003). The MMMB has been interpreted as the western margin of Sibumasu but it is not clear when and if the Burma Terrane collided with the MMMB. Various unconstrained age estimates for collision have been proposed, ranging from Triassic to Miocene, and the existence of a suture represented by the MOB between both blocks has even been challenged (Mitchell, 1993; Metcalfe, 2013; Sevastjanova et al., 2016; Zhang et al., 2018; Westerweel et al., 2019; Morley et al., 2020). The MMMB includes the Jurassic to Miocene plutons of the DSMGB (Bertrand and Rangin, 2003; Mitchell et al., 2007, 2012; Searle et al., 2012; Liu et al., 2016). The DSMGB includes plutons of the Dianxi Batholith in northern Myanmar and Yunnan, Shan Scarp plutons in central Myanmar and the Mergui intrusives in southern Myanmar (Fig. 2). Zircon U-Pb dating of the DSMGB yielded igneous ages at ~170 Ma in central Myanmar (Barley et al., 2003; Searle et al., 2020), 130–110 Ma in central Myanmar and the Dianxi Batholith, forming the Cretaceous Mondaung-Lawa Arc of Mitchell et al. (2020), 85–40 Ma for the most widespread plutons all along the DSMGB, and a final 25–17 Ma magmatic event in central Myanmar (Fig. 2; Mitchell et al., 2012; Gardiner et al., 2017, 2018; Zhang et al., 2018). All of them show geochemical evidence for some crustal contamination, with low εNd (<0), zircon εHf, (<0) and high $^{87}Sr/^{86}Sr$ isotopic ratios (>0.7065; Zaw, 1990; Mitchell et al., 2012; Gardiner et al., 2017; Lin et al., 2019). Jurassic and Cretaceous plutons are almost all foliated, whereas Cenozoic plutons are not systematically metamorphosed (Mitchell, 2017).

The Cenozoic deformation regime of Myanmar is a result of the hyper-oblique convergence of the Indian Plate below the Burmese margin that drags western Myanmar northwards (Socquet et al., 2006; Rangin et al., 1999; Morley, 2009). Since at least the Oligocene, the Sagaing Fault along the MMMB and the later opening of the Andaman Sea, between Myanmar and Sumatra, have accommodated the strike-slip motion (Morley and Arboit, 2019; Westerweel et al., 2019). The total dextral displacement of central Myanmar, today a forearc sliver since the establishment of the Sagaing Fault along its modern trace, has been variously estimated at 300–400 km to >2000 km (Mitchell, 1993; Curray, 2005; Zhang et al., 2018; Westerweel et al., 2019).

2.2. The Wuntho-Popa Arc

The WPA consists of isolated Quaternary volcanoes and crater lakes spread over a ~1000 km N-S trend in western Myanmar (Mounts Popa, Taungtalon, Loimye, and Monywa crater lakes) and Pre-Quaternary igneous rocks. The youngest magmatic event is dated to the early

Holocene and early to middle Pleistocene (Maury et al., 2004; Lee et al., 2016; Belousov et al., 2018). Quaternary and pre-Quaternary rocks of the WPA display low Sr isotopic ratios ($^{87}Sr/^{86}Sr < 0.708$), high εNd and zircon εHf values (>0; Mitchell et al., 2012; Zhang et al., 2017a; Gardiner et al., 2017; Lin et al., 2019), which barely overlap with the more enriched isotopic values of the DSMGB rocks.

In central Myanmar, Pre-quaternary WPA rocks are barely exposed and consist of isolated intrusives (Fig. 2), and poorly exposed schists and gneiss near Monywa (Mitchell, 2017). In northern Myanmar, where deeply buried rocks have been exhumed along splays of the Sagaing Fault, pre-Quaternary rocks attributed to the WPA and the basement of the Burma Terrane are exposed in the Tagaung-Myitkyina Belt and surrounding ranges (Kumon and Katha-Gangaw), the Jade Belt, and Minwun Range (Fig. 2; Mitchell, 2017). We cannot yet exclude that these areas are individual blocks of different origin subsequently accreted together (Ridd et al., 2019). The geology of these areas is described below.

In the Tagaung-Myitkyina Belt, WPA and Burma Terrane basement rocks include the Jurassic to lower Cretaceous Ngapyawdaw Chaung Formation, consisting of basalts, andesitic flows, rhyolitic tuffs and volcaniclastics, as well as isolated Jurassic (?) gabbros, diorites, and dacites (Mitchell, 2017), including one dacite dated at 171 Ma (Gardiner et al., 2018). North of the Tagaung-Myitkyina Belt, exposure of basement rocks continues in the less studied Katha-Gangaw and Kumon Ranges (Mitchell, 2017). To the south, the Tagaung-Myitkyina Belt grades into the MOB, and the relationship between both belts is not clear. Zhang et al. (2018) reject the ophiolitic nature of the MOB and consider all MOB rocks as belonging to the Tagaung-Myitkyina Belt, whereas Liu et al. (2016) make a clear distinction between these rocks. Diorites near Myitkyina at 171–173 Ma (Liu et al., 2016) are the oldest dated rocks attributed to the WPA (Mitchell, 2017). The nearby Sodon Batholith, at the transition between the Tagaung-Myitkyina Belt and MMMB, has been assigned to the WPA due to its relatively depleted Hf isotope signature (zircon εHf values between −5 and + 10) and has been dated at 51 Ma (Lin et al., 2019). In the Jade Belt, WPA rocks include mafic volcaniclastics in the Jurassic to lower Cretaceous (?) Mawlin Formation and undated diorites (Mitchell, 2017). Jade-bearing metamorphic rocks in the Jade Belt are serpentinites in which jadeite occurs as dykes or veins, and are attributed to the WPA; they have yielded ages of 160–163 Ma (Shi et al., 2008; Yui et al., 2013); metamorphic overgrowth in the same zircons was dated at 77 Ma (Yui et al., 2013).

The Minwun Range, located between the Wuntho Ranges and the Sagaing Fault, exposes patches of Paleozoic and Mesozoic rocks attributed to the Burma Terrane basement and unconformably covered by Cenozoic clastic rocks (Thein et al., 1982, 1987; Thein, 2015). They include undated serpentinites, crystalline rocks called the Mayathein Metamorphics which comprise gneisses, schists, migmatites, calc-silicates, marbles and rare amphibolites, overlain to the west by discontinuous outcrops of Permian and Carboniferous limestones, which in turn are overlain by the Kywethe Chaung Limestones, highly silicified volcanic rocks, and Jurassic-Cretaceous metasedimentary rocks tentatively correlated to the Ngapyawdaw Chaung Formation of the Tagaung-Myitkyina Belt (United Nations, 1979; Thein et al., 1987). These limestones are typically highly sheared and folded, suggesting their incorporation in a paleo-shear zone predating the Sagaing Fault (Thein, 2015). In some places the Permian limestone has yielded fossils that include bryozoan, brachiopods, crinoid stems, and fusulinids (Thein et al., 1987; Ueno et al., 2016). Significantly for paleogeographic reconstructions, the fauna in the Carboniferous sequence has warm water affinity (Thein et al., 1987); recent investigations of the Permian limestones indicate they too formed in a warm water environment and display biogeographic affinities with Cathaysia and West Sumatra limestones (Barber and Crow, 2009; Ueno et al., 2016).

In central western Myanmar, the WPA straddles the middle of the Central Myanmar Basins (Fig. 2); pre-Quaternary rocks are covered by Neogene fluvial sediment in most places. Granites and andesites sampled by oil and gas exploration wells have been dated at 64–69 Ma (Zhang et al., 2017a, 2017b) and 102–106 Ma (Li et al., 2013; Zhang et al., 2017a, 2017b). When exposed, pre-Quaternary rocks comprise I-type batholiths and andesitic bodies punctuated with rarer S-type intrusions. Small intrusives are exposed around Mount Popa, Monywa, and Salingyi and consist of felsic intrusives dated at 13–15 Ma (Mitchell et al., 2012; Lee et al., 2016; Lin et al., 2019) and 98–105 Ma (Mitchell et al., 2012; Gardiner et al., 2017). Directly west of the Shan Scarp, the Mokpalin granite, dated at 91 Ma (Mitchell et al., 2012), has also been attributed to the WPA as it exhibits a characteristic depleted isotopic signature (Lin et al., 2019). The largest exposure of WPA rocks is found in the Wuntho Ranges, the target area of this study.

The Wuntho Ranges are a 150-km long N-S trending belt of rugged terrain, with elevations up to 1300 m, covered by dense forests. Igneous rocks are exposed along river beds and in isolated quarries. A simplified geological map is provided in Fig. 3, and the regional stratigraphy in Fig. 4. The oldest units of the Wuntho Ranges are the Shwedaung Formation, made of chlorite schists, tremolite schists, silicic tuffs, and the Hpyu Taung Metamorphics, consisting of gneisses, mica schists, and amphibolites (Mitchell, 2017). The age of these units is unknown; Mitchell (2017) correlates these units to Triassic (?) metamorphic rocks found as basement in the Jade Belt and Tagaung-Myitkyina Belt. They form the exposed metamorphic root of the Burma Terrane and have been proposed as a source and/or a lateral extension of the Upper Triassic metasediment in the Indo-Burman Ranges (United Nations, 1978; Sevastjanova et al., 2016).

The Mawgyi Volcanics, Maingthon Dacite, and Mawlin Formation are the oldest volcanogenic units of the Wuntho Ranges. The Mawgyi Volcanics comprise augite basalts and basaltic andesites, with rare pillow lavas, sills and dykes. The Mawlin Formation is composed of volcaniclastics and less common andesite flows that are affected in places by low-grade metamorphism and hydrothermal alteration (Westerweel et al., 2019). They are intruded by the Maingthon Dacite. The age of these three units is uncertain, but they are regionally correlated with the Jurassic to middle Cretaceous Ngapyawdaw Chaung Formation in the Tagaung-Myitkyina Belt and the igneous protolith of the Jade Belt which dates back to middle Jurassic (Mitchell, 2017). The only two published ages from the Mawgyi Volcanics are one whole rock Ar-Ar age of 101 Ma (Westerweel et al., 2019) and one uncertain K-Ar age of 71 Ma (United Nations, 1978). These ages are partly younger than overlying and intruding units, and it is possible they were reset by the low-grade metamorphism and hydrothermal alteration (Westerweel et al., 2019).

The Mawlin Formation is overlain by the Namakauk Limestone and Nankholon Formation, also grouped under the Kondan Chaung Group (United Nations, 1978). The Namakauk Limestone is correlated with the *Orbitolina*-bearing Paung Chaung Limestone found throughout the Burma Terrane, including in the Jade and Tagaung-Myitkyina Belts, and dated to the Upper Albian – Cenomanian (Mitchell, 2017). The Nankholon Formation includes mudstone, shales, and tuff, and has yielded two whole rock Ar-Ar ages of 91 and 85 Ma (Turonian to Santonian; Westerweel et al., 2019). Similar to the Mawgyi Volcanics, there is evidence for low-grade metamorphism and hydrothermal alteration in this formation which may have reset these Ar-Ar ages (Westerweel et al., 2019).

The Kanza Chaung Batholith is the best exposed pluton in the Wuntho Ranges and includes gabbros, I-type diorites and granodiorites, as well as 2-mica granites in the northern part of the ranges. This batholith is particularly well dated, with more than thirty U-Pb and Ar-Ar ages spanning 107 to 87 Ma (United Nations, 1978; Barley et al., 2003; Gardiner et al., 2017; Lin et al., 2019; Westerweel et al., 2019; Li et al., 2020). The oldest age is from a gabbro dated at 106.7 ± 0.5 Ma by zircon U-Pb dating near Shangalon (Li et al., 2020).

The Mansi Gale Group is only exposed at the margins of the Wuntho Ranges and encompasses all younger volcaniclastic units. It is made of tuffs, volcanic conglomerates and volcanogenic sandstones. At the

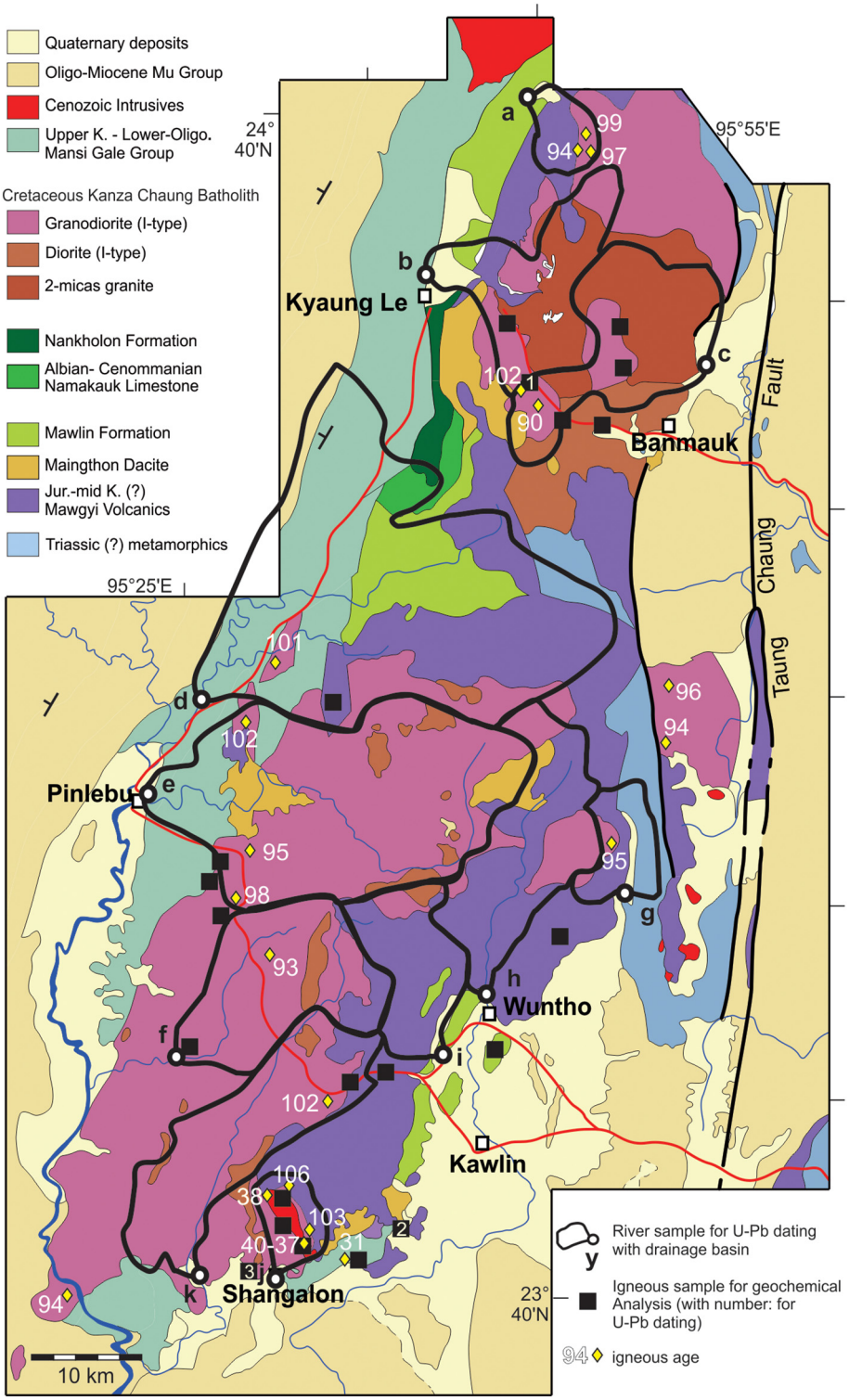

Fig. 3. Schematic map of the Wuntho Ranges with the main geological units, after United Nations (1978), Mitchell (2017) and Westerweel et al. (2019). Locations of published U-Pb ages of Barley et al. (2003), Gardiner et al. (2016, 2017), and Li et al. (2019, 2020) are indicated with yellow diamonds (ages in white, in million years). K-Ar ages of United Nations (1978) and U-Pb ages of Lin et al. (2019) are not displayed because they were not published with exact coordinates. Location of river sands samples in this study are indicated by white dots (black lines: river drainages; letters refer to rivers of Fig. 7); igneous samples for geochemical analysis are indicated by black squares; black squares with numbers are igneous samples dated by zircon U-Pb analyses.

southern margin of the Wuntho Ranges, in the Shangalon area, the Mansi Gale Group is intruded by Eocene-Oligocene diorites and porphyries associated with copper mineralization and dated by U-Pb and K-Ar between 40 and 31 Ma, with one older K-Ar age at 50 Ma (Barley et al., 2003; Gardiner et al., 2016; Li et al., 2019). The Mansi Gale Group is covered by the Neogene fluvial deposits of the Mu Group, that laterally grades into thicker Neogene fluvial units (Pegu Group and Irrawaddy Formation) in the Central Myanmar Basins.

The deformation history of the Cenozoic sediments is described in the study of Zhang et al. (2017a), which provides seismic data south

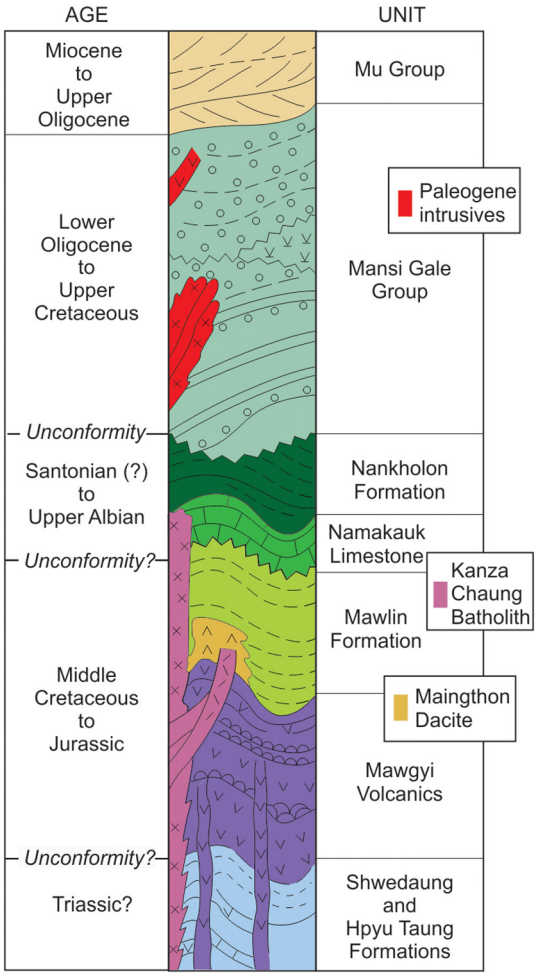

Fig. 4. Stratigraphy in the Wuntho Ranges, after Mitchell (2017). Color coding is the same as in Fig. 3.

of the Wuntho Ranges where magmatic rocks are buried by Cenozoic sediment. The Cenozoic history of deformation inferred from the seismic data includes 1) Normal faulting predominantly affecting the back-arc during the Late Cretaceous-Oligocene; fault-related section expansion is greatest during the Eocene and Oligocene (T8 to T6 seismic horizons); 2) a first unconformity sometime between the middle Eocene and early Oligocene (between the T6 and T7 horizons) associated with uplift of the arc, which could be related to footwall uplift of the extensional faults at the western boundary of the back-arc, coupled with magmatic activity; 3) An unconformity during the late Oligocene (above T6 horizon), associated with *E*-W shortening and uplift of the arc; the uplift is concomitant with denudation of the arc and is expressed by a 22 Ma apatite fission-track age in a diorite of the Kanza Chaung Batholith, sampled at the bottom of an oil and gas exploration well (Li et al., 2013); 4) thrusting that post-dates the Miocene-Pliocene boundary (T3 horizon). Some reactivation of normal faults during the Miocene is also inferred.

The only available map of the Wuntho Ranges is low resolution (1:250,000; United Nations, 1978; refined in Mitchell, 2017); most of the ranges are covered by vegetation.

3. Methods

We combined two approaches to document the history of the WPA in the Wuntho Ranges. First, we observed freshly exposed igneous rocks in isolated quarries and river beds, where we measured bedding, deformation and sampled for U-Pb dating of zircons, Sr and Nd isotopic composition and trace element composition. Exposure was poor and fresh rock samples were often hard to get for some units (Paleogene intrusives; 2-mica granite of the Kanza Chaung Batholith). Some of our samples have experienced some degree of weathering; the location and nature of every sample is described in Supplementary Table 2. We particularly focused on units that have not been dated in previous studies, including all the units predating the emplacement of the Kanza Chaung Batholith. Unfortunately, these units are poorly exposed and we were unsuccessful at dating the few sites with decent exposure: many of our samples from these units, including the Mawlin Formation (two samples), Maingthon Dacite (one sample), Mawgyi Volcanics (two samples), Nankholon Formation (one sample) and Shwedaung Formation (one sample) did not yield any zircon. In addition, we sampled individual rivers draining the ranges for zircon U-Pb dating, apatite fission-track and U-Pb dating. This approach allows us to document the range of igneous and exhumation ages where rocks are covered, in the hope of capturing zircons and apatites from the units that we did not succeed in dating.

3.1. Bulk elemental composition

Twenty-three samples were analyzed for major and trace elements. Seven of them were powdered and analyzed using an inductively-coupled-plasma mass-spectrometer (ICP-MS) iCapQ and an ICP-optical emission spectrometer iCap6500 at the SARM (CRPG, Vandoeuvre les Nancy, France). The remaining sixteen samples were powdered and analyzed both by X-ray fluorescence analysis using a ThermoARL Advant XP+ automated sequential wavelength and by inductively coupled plasma-mass spectrometry using an Agilent 7700 at the GeoAnalytical Lab of Washington State University (USA). Detailed data are available in Supplementary Table 2.

3.2. Zircon U-Pb dating

Among all the units we sampled for U-Pb dating, we succeeded in extracting zircons from one granodiorite of the Kanza Chaung Batholith (sample 1 in Fig. 3), one tuff layer from the Maingthon Dacite (sample 2 in Fig. 3) and one volcanic conglomerate of the Mansi Gale Group (sample 3 in Fig. 3). We also sampled sands from eleven rivers draining the Wuntho Ranges. The sampling locations and river drainage basins are shown on Fig. 3; with detailed results and GPS coordinates provided in Supplementary Table 3. Detailed analytical protocols and information about the data reduction schemes are provided in Supplementary File 1. Briefly, zircons were extracted by traditional methods of heavy mineral separation, including concentration with a Holman-Wilfley gravity table, density separation with methylene iodide, and magnetic separation with a Frantz Magnetic separator. U-Pb dates were generated via laser-ablation inductively-coupled-plasma mass-spectrometry (LA-ICP-MS), using an iCAP-RQ Quadrupole ICP-MS coupled to an Analyte G2 excimer laser at the University of Washington TraceLab facility, with a spot diameter of 25 μm. Data reduction was conducted with *Iolite*, using their *U_Pb_Geochron4* data reduction scheme to calculate U-Pb dates uncorrected for common lead (Paton et al., 2010). Dating uncertainties for all samples were calculated using a modified version of the method of Matthews and Guest (2017) that takes into account the impact of ^{207}Pb beam intensity on date uncertainties (Horstwood et al., 2016). The ten secondary zircon reference materials during these sessions yielded deviations from TIMS ages of <1% in most cases, and <2% otherwise.

Ages for the Kanza Chaung Batholith and Maingthon Dacite samples are weighted means using *Tuffzirc* (Ludwig, 2003). The final age error calculated for each sample is the quadratic sum of the uncertainty of *Tuffzirc* age calculation and of the systematic uncertainty (~2.67% for

the $^{238}U/^{206}Pb$ ratios). Concordia plots for these two samples are also available in Supplementary Table 3.

3.3. Apatite U-Pb and fission-track dating

Detrital apatites were extracted from river sands for apatite U-Pb and fission-track (AFT) dating. Only four samples yielded apatites for dating. Both types of dates were acquired simultaneously in the GeOHeLiS analytical platform (Univ. Rennes, France), using an ESI NWR193UC Excimer laser coupled to a quadrupole Agilent 7700× ICP-MS that is equipped with a dual pumping system to enhance sensitivity (Paquette et al., 2014). A 30 μm spot diameter was used with a repetition rate of 7 Hz during 30 s. Detailed analytical conditions are found in Cogné et al. (2020). Results are synthesized in Table 2, detailed data are available in Supplementary Table 4, Tera-Wasserburg diagrams for U-Pb ages and radial plots for AFT ages in Supplementary File 2.

Data reduction for U-Pb dates was conducted with *Iolite* (Paton et al., 2011), using the *VisualAgeUcomPbine* data reduction scheme of Chew et al. (2014). Ages were calculated using *IsoplotR* (Vermeesch, 2018) and correspond to the lower intercept of discordia in Tera-Wasserburg (TW) plots. Initial common lead values ($^{207}Pb/^{206}Pbi$) were then calculated from the terrestrial Pb isotope evolution model of Stacey and Kramers (1975) for the TW age. A second discordia is anchored on the y-axis of the TW plot to this value. Both anchored and unanchored discordia yielded similar results. The same $^{207}Pb/^{206}Pbi$ value is used in Iolite to calculate a single grain date corrected for common lead (207CorrAge in Supplementary Table 4, Chew et al., 2014).

For fission-track dating, spontaneous tracks were revealed by acid etching with 5.5 M HNO_3 at 21 °C for 20 s. The Grain mounting and etching procedures used are similar to the protocol described by Donelick et al. (2005). Fission-track counting was performed using a Zeiss AxioImager Z1m microscope equipped with an Autoscan automated stage system. AFT data were obtained on the same spot as the U-Pb measurements using the protocol of Cogné et al. (2020). Data reduction was conducted using *Iolite* with a modified version of the *Trace_Elements* data reduction scheme (Woodhead et al., 2007; Cogné et al., 2020) and an in-house spreadsheet. AFT data were plotted in a radial plot to obtain the AFT ages using *IsoplotR* (Vermeesch, 2018).

3.4. Nd and Sr isotopic composition

Isotopic ratios for Sr and Nd were measured for 16 samples at the University of Washington Isotope Geochemistry Lab using a Nu Instruments multiple-collector inductively-coupled-plasma mass spectrometer (MC-ICP-MS). Sr and Nd column separation are described in Nelson (1995), and MC-ICP-MS analytical procedures follow those in Gaffney et al. (2007) for Nd and Brach-Papa et al. (2009) for Sr. Results are summarized Supplementary Table 2, together with raw data. Errors shown in the table are within-run statistics and represent errors in the last significant digits. The external reproducibility at 2σ is Nd = ±40 ppm; Sr = ±40 ppm. Sr and Nd compositions are normalized to $^{86}Sr/^{88}Sr = 0.1194$ and $^{146}Nd/^{144}Nd = 0.7219$. ε_{Nd} (0) is a deviation from chondritic $^{144}Nd/^{143}Nd = 0.512638$ in units of parts per 10^4.

4. Results

4.1. Structural analysis

We synthesize our bedding and foliation measurements and field observations with previous structural data from United Nations (1978) maps. Regionally, the Shwedaung Formation (Fig. 4) is dominated by approximately N-S striking, sub-vertically dipping bedding and foliations (Fig. 5a). In the unconformably overlying Cretaceous volcanic and sedimentary units, the United Nations (1978) maps report regional dips that are mostly between 45° and 25°, with a regional NE-SW direction which is also the dominant trend of stratigraphic boundaries in the area (Fig. 3) compatible with our observations (Fig. 5b–d).

Typically, bedding is difficult to identify in the Mawgyi Volcanics, but we observed bedding-cleavage relationships within andesitic pyroclastic rocks in some quarries. The cleavage strikes in approximately the same direction as bedding, and dips with respect to bedding can be slightly (c. 10°) steeper, shallower, or similar, suggesting that the cleavage is axial planar, and that much of the bedding orientations were acquired during deformation in a predominantly contractional setting (Fig. 5b). The presence of cleavage suggests significant burial, probably to between 150 and 200 °C (e.g. Engelder and Marshak, 1985). Remagnetizations recognized in the Mawgyi Volcanics also support burial and metamorphism related to the emplacement of the Kanza Chaung batholith (Westerweel et al., 2019). Sub-vertical conjugate strike-slip faults (strike 044° dextral, and 280° sinistral) were observed in one quarry in Mawgyi Volcanics; however, their structural context and timing is uncertain. The Mawlin Formation is affected by a broad NE-SW trending syncline, where dips typically range between 50 and 20°, but can be as high as 70° (United Nations, 1978).

Further detail on deformation affecting the Cretaceous units was observed locally around Shangalon, where we recorded structures in roadcuts that revealed extensive thrust and fold structures in the Maingthon Dacite. The unit shows regular, thin (10–30 cm) layering, but is highly weathered, and the layering is laterally discontinuous. Open to tight folds and disharmonic folds, with parallel to similar geometries, and wavelengths in the order of meters to tens of meters characterize the section. Numerous small thrusts are also present. Some NE-SW trending bedding was observed, but dominant bedding orientations are NNW-SSE (Fig. 5c). Most thrusts in the section strike NW-SE, although a few are oriented NNE-SSW (Fig. 5e–f). Fold axes and hinges are oriented between N-S and NW-SE trends. The deformation is complex, and in one area, a N-S striking thrust was observed to cross-cut NW-SE trending thrust structures. We were not able to make observations over a large enough area to determine whether such complexities are local features, or part of a more regional pattern. However, we suspect that there are two structural trends present in the Shangalon section, and that the NW-SE trend is older than the N-S to NE-SW trend. Since the Maingthon Dacite is an extrusive sequence, it is possible that the earlier NW-SE trend represents gravity-driven deformation on the slope of a volcanic edifice. However, testing this hypothesis was not possible.

The Late Cretaceous-Eocene Mansi Gale Group lies unconformably over the earlier sequences, and is broadly folded on NE-SW trending structures (United Nations, 1978). Dips in the Oligocene sedimentary section are variable, particularly close to major N-S trending dextral Cenozoic strike-slip faults. But overall the Oligocene bedding exhibits NNE-SSW to N-S strikes and low (<40°) dips (Fig. 5d). More recent deposits related to the fluvial Mu Group are affected by the same type of deformation found in the Neogene deposits of the Central Myanmar Basins (Pivnik et al., 1998) which comprises intense folding, thrusting and strike-slip faulting close to major fault zones; with increasing distance a range of structures of various orientations have developed, including normal faults, folds and thrusts. Often faults may be related to classic strike-slip R, R′, P and Y shear orientations, while folds have en-echelon buckle fold trends (e.g. Sylvester, 1988). These structures have been related to the regional dextral strike-slip deformation (Pivnik et al., 1998).

4.2. Major and trace elements

Samples from the Mawgyi Volcanics and Mawlin Formation are tephrite to rhyolite in composition (Fig. 6a) and belong to the tholeiite and calc-alkaline series (Fig. 6b). Samples from the Kanza Chaung batholith show gabbro to granite composition, and belong mostly to the tholeiite series with a few samples belonging to the calc-alkaline series. Samples from Paleogene intrusives include basaltic-andesite to trachyte

Table 2
Synthesis of the U-Pb ages of the zircon main population, apatite U-Pb and fission-track ages for the river sands yielding both apatites and zircons.

	Weighted mean of main zircon age population, age + 2 s (Ma)	Apatites	
		U-Pb ages + 2 s (unanchored; Ma)	Fission track ages + 2 s (pooled; Ma)
River b	98.9 ± 2.7 (n = 60, MSWD = 21)	93.0 ± 1.6 (n = 107, MSWD = 0.96)	38.8 ± 3.0 (p(χ2) = 0.47, n = 107)
River c	99.4 ± 2.6 (n = 89, MSWD = 4.2)	94.4 ± 1.4 (n = 117, MSWD = 2.2)	26.6 ± 1.5 (p(χ2) = 0.16, n = 117)
River f	96.6 ± 2.6 (n = 114, MSWD = 3.4)	96.7 ± 7.5 (n = 28, MSWD = 2.4)	31.0 ± 4.9 (p(χ2) = 0.08, n = 28)
River j	38.2 ± 1.0 (n = 98, MSWD = 6.3)	38.0 ± 1.2 (n = 114, MSWD = 1.8)	35.3 ± 2.3 (p(χ2) = 0.99, n = 114)

compositions and display K_2O content that varies from calc-alkaline to tholeiitic, as previously observed by Li et al. (2019); one sample taken from a mining pit near Shangalon displays unusually low K_2O and high SiO_2 content likely reflecting weathering (sample "w" on Fig. 6a and b).

The Mawgyi and Mawlin volcanic samples show no or only slight light rare earth element (LREE) enrichment (Fig. 6c) and no negative Eu anomaly. On extended trace element diagrams (Fig. 6d), they display weak positive Pb anomalies and negative Ti anomalies, and depletion of Nb and Ta compared to La and K. These rocks have however been affected by some degree of hydrothermal alteration (Westerweel et al., 2019), likely affecting mobile elements on REE diagrams. Enrichment in LREE is stronger in the Kanza Chaung batholith samples (Fig. 6e), which display more well-marked positive Pb and negative Ti anomalies, and depletion of Nb and Ta (Fig. 6f). Enrichment in LREE, anomalies in Pb, Ti, and depletion in Nb and Ta are even more marked in Paleogene intrusives. Only one sample, from a 2-mica granite of the Cretaceous Kanza Chaung Batholith has a strong Eu anomaly (Fig. 6e). A second sample from the 2-mica granite displays an unusually low REE concentration compared to other Kanza Chaung Batholith samples; this sample is a river clast and its mineralogy is predominantly quartz.

4.3. U-Pb zircon ages

Zircon age distributions of river sands are displayed in Fig. 7. Sands from rivers a, b, and c from the Banmauk area (northern part of the ranges, Fig. 3), drain the Mawgyi Volcanics, granodiorites and 2-micas granites of the Kanza Chaung Batholith. River drainages a, b and c have similar age populations that cover the 90 to 110 Ma time interval, with a weighted mean at ~100 Ma. The mean square weighted deviation (MSWD) around the weighted mean for the 90 to 110 Ma zircon population, in these and the following samples, is always >3 and often >10, indicating that this population likely includes a mixture of crystals with several crystallization ages (e.g. Table 2). Sands from river d (Pinlebu area, western part of the ranges) display a much broader age population, including some young (~30 Ma) and old (>1000 Ma, not shown) zircons; the drainage basin of river d includes a broad range of units, and its western boundary includes the Oligo-Miocene deposits of the Mu Group; it is thus likely that some of these grains are reworked from more recent fluvial deposits and do not reflect direct input from the Wuntho Ranges. Sands from rivers e and f of the same area, draining the Mansi Gale Group, Maingthon Dacite and Kanza Chaung Batholith, display the same 90–110 Ma population, centered at 101 and 97 Ma.

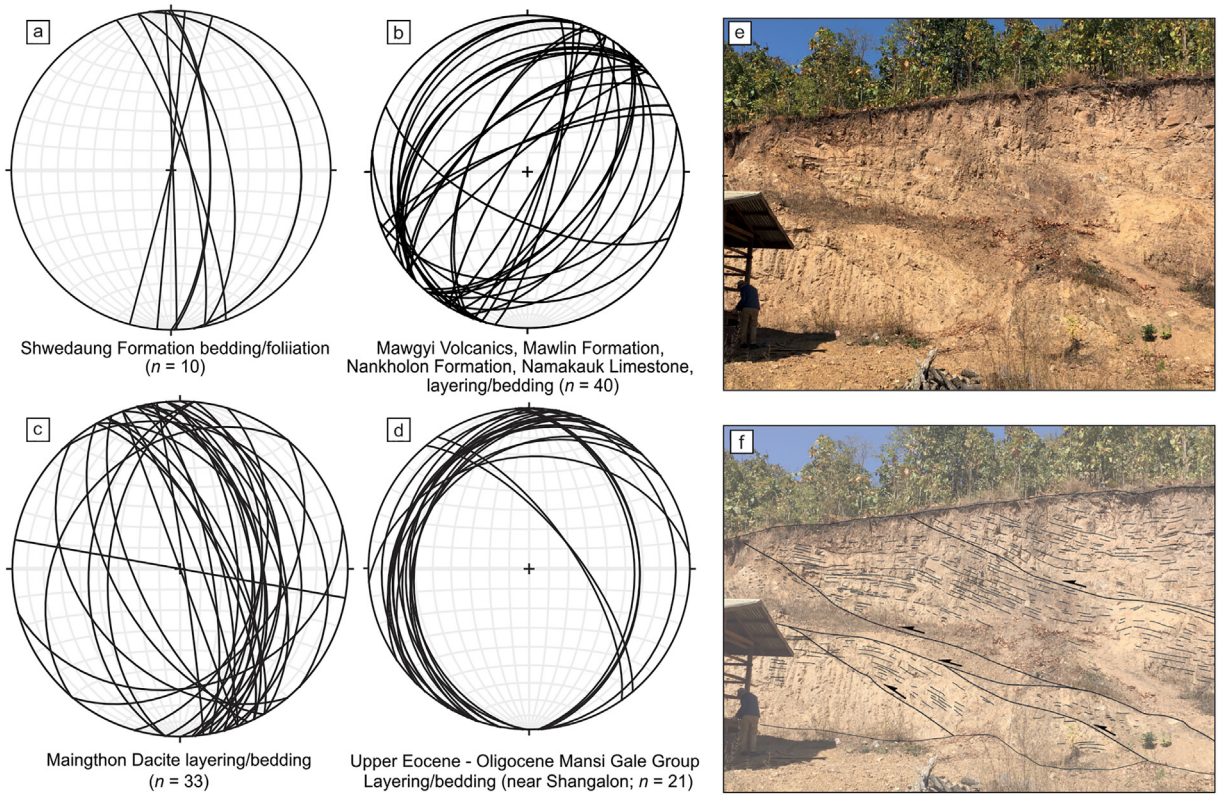

Fig. 5. Stereonets displaying strikes and dips for bedding, layering and foliation in (a) the Shwedaung Formation, (b) Mawgyi Volcanics, Mawlin Formation, Nankholon Formation and Mamakauk Limestone (c) Maingthon Dacite, (d) Upper Eocene - Oligocene outcrops of the Mansi Gale Group near Shangalon (after United Nations, 1978 and our own field measurements). (e) and (f): structures in the Maingthon Dacite near Shangalon (location 2 in Fig. 3).

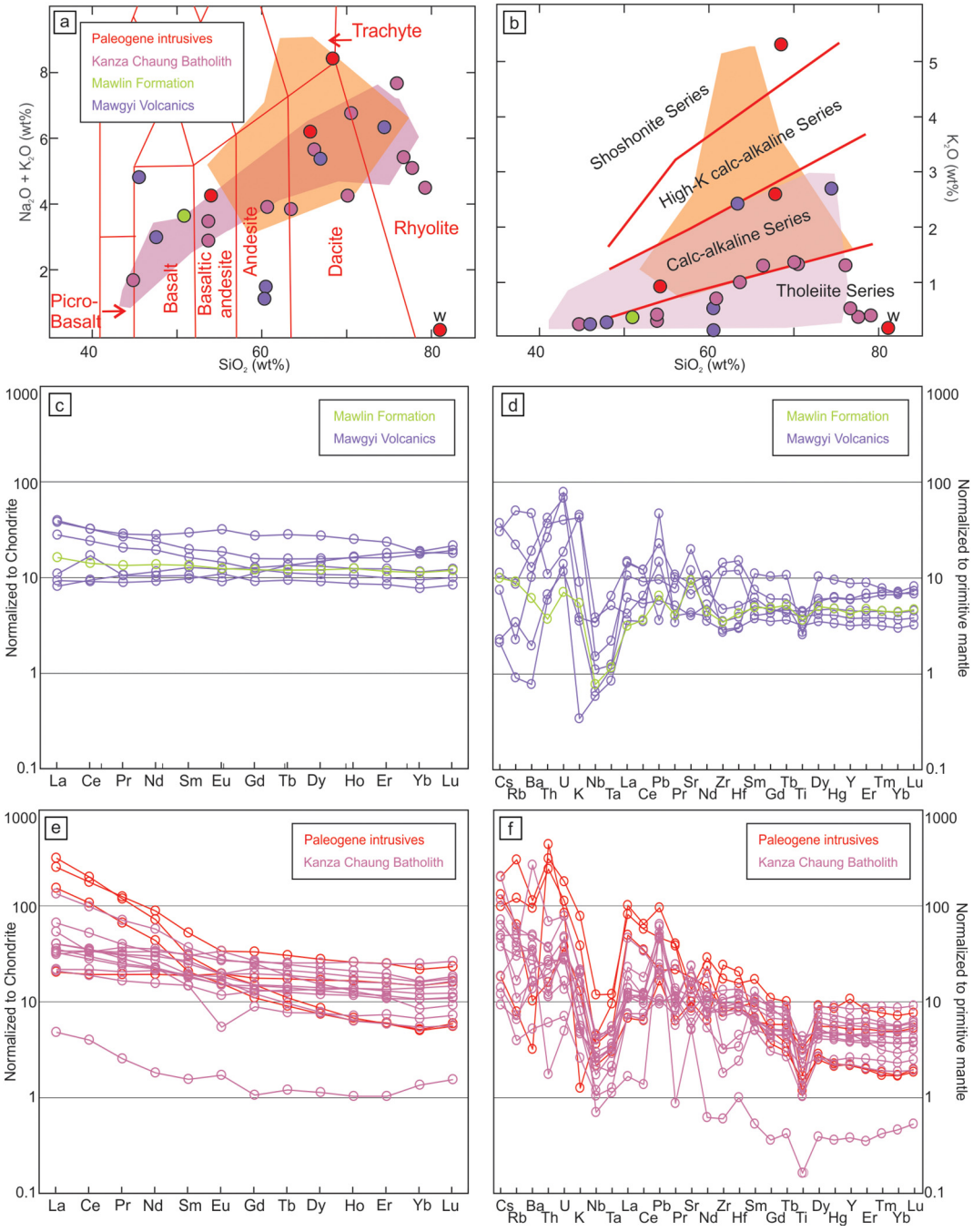

Fig. 6. Composition of samples from the Wuntho Ranges: (a) K2O + Na2O versus SiO2 diagram (field for volcanic rocks from Le Maitre et al., 2005; plutonic rocks composition is also plotted for comparison) and (b) K2O versus SiO2 diagram (field for magmatic series from Peccerillo and Taylor, 1976); colored areas indicate published data from the Kanza Chaung Batholith (purple; Li et al., 2020) and Paleogene intrusives (orange; Li et al., 2019); sample tagged with letter "w" has been affected by weathering. Chondrite- and primitive mantle-normalized element patterns for (c, d) Mawlin and Mawgyi Volcanics, and (e, f) Kanza Chaung batholith and Paleogene intrusives; normalized to elemental concentrations from Sun and McDonough (1989).

Sands from rivers g, h, and i from the Wuntho area (eastern part of the ranges), draining the Mawgyi Volcanics, Triassic metamorphic rocks and Kanza Chaung Batholith, have the same age population, centered at 94, 99, and 101 Ma. In addition, rivers g and i yielded Pleistocene zircons (three zircons between 64 ka to 192 ka; not shown). River i mainly drains Triassic metamorphic rocks and yielded two Paleogene zircon grains (23 and 57 Ma) and only one pre-Cretaceous zircon (not shown). River j drains the Eocene intrusives near the Shangalon area and yielded a population of late Paleogene grains dated between 32 and 47 Ma, centered around 38 Ma, with a minor older population of 90–110 Ma grains. Finally, sands of river k, draining the Kanza Chaung batholith near Shangalon, have the same 90–110 Ma population, with one late Eocene grain (37 Ma) and two pre-Cretaceous zircons (not shown).

One sample from the Kanza Chaung Batholith has a U-Pb age of 97.1 ± 2.6 Ma (MSWD = 1.9, n = 33; location 1 on Fig. 3). A U-Pb age of 105.8 ± 2.8 Ma (MSWD = 2.6, n = 34; location 2 on Fig. 3) was obtained for a tuff sample from the Maingthon Dacite. Finally, the U-Pb age distribution of the zircons sampled from a volcanic conglomerate layer of the Mansi Gale Group (location 3 on Fig. 3) is displayed on

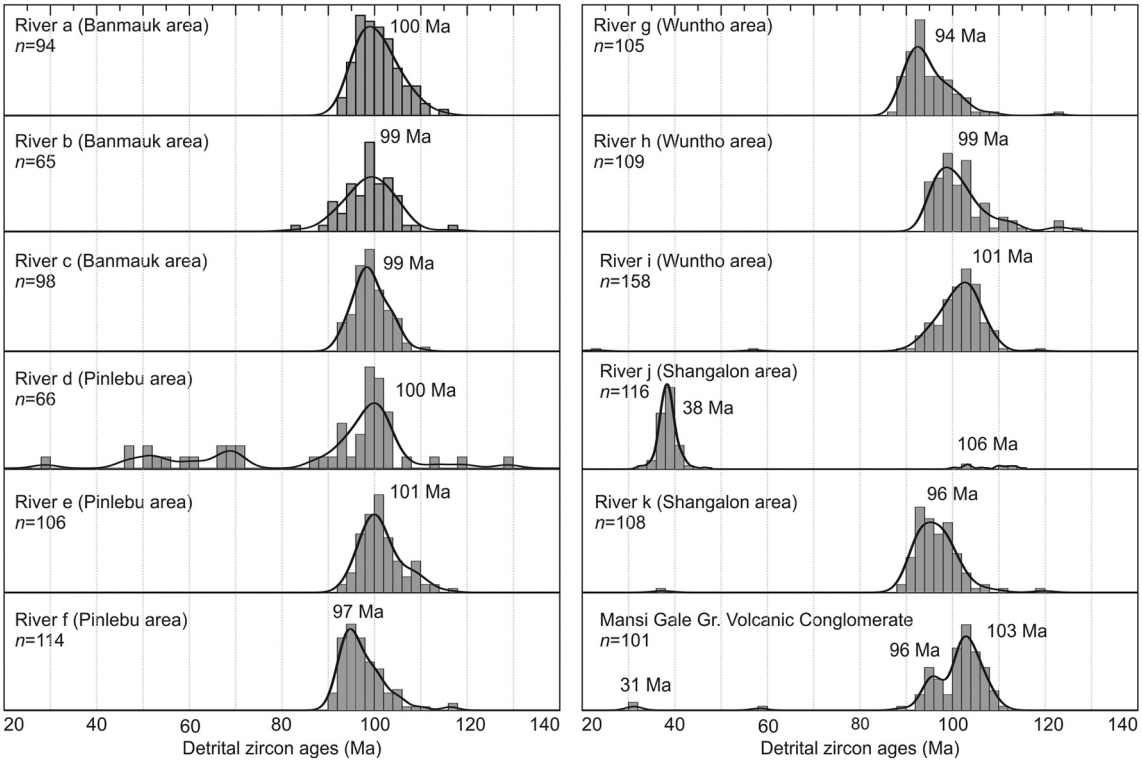

Fig. 7. Age distribution for the eleven modern river sands and a volcanic conglomerate sample from the Mansi Gale Group. See Fig. 3 for location. Ages are weighted means over age populations.

Fig. 7. The sample yielded two early Oligocene zircons U-Pb dated at 31 Ma, one at 58 Ma, and a broad 90–110 Ma population with two age peaks, at 96 and 103 Ma.

4.4. Apatite U-Pb and fission-track ages

Apatite U-Pb and fission-track ages of the four river sands that yielded apatites are displayed on Tera-Wasserburg and radial plots in Supplementary File 2 and synthesized in Table 2, where they are compared with weighted mean of the main population of zircon ages.

Rivers b and c from the Banmauk area have consistent unanchored apatite U-Pb mean ages at ~93 and 94 Ma, five million years younger than the weighted mean of the zircon age population. The MSWD around U-Pb ages is much smaller than for zircon ages, suggesting they represent a single event. The younger apatite ages and much lower MSWD compared to zircon ages suggest that they represent a homogeneous late cooling age rather than emplacement ages. Apatite and zircon U-Pb mean ages of sands from river f and j are statistically indistinguishable at 97 Ma and 38 Ma.

Apatite fission-track ages range between 39 and 27 Ma. All samples passed the $\chi 2$ test suggesting that for each sample there is only one age population of apatite, potentially derived from a limited area within the drainage system of each river. The distribution of AFT ages does not display any clear geographical pattern; for example, neighboring rivers b and c have mean AFT ages that are 12 Myr apart.

4.5. Nd and Sr isotopes

Strontium and Nd isotope data are summarized in Supplementary Table 2 and compared with previously published data from the WPA and from the DMSGB (Fig. 8). The long-term trend for Nd-Sr isotopic values in the Wuntho Ranges is toward more enriched values (higher $^{87}Sr/^{86}Sr_{(i)}$ and lower $eNd_{(t)}$) becoming more distinct from typical Neotethyan ophiolite isotopic compositions with time (Fig. 8a). Mawlin Formation and Mawgyi Volcanics samples have whole-rock $^{87}Sr/^{86}Sr_{(i)}$ ratios between 0.704 and 0.705, and $\varepsilon Nd_{(t)}$ between +3.4 and +7; Kanza Chaung Batholith samples have $^{87}Sr/^{86}Sr_{(i)}$ ratios between 0.745 and 0.7056, and $\varepsilon Nd_{(t)}$ between +0.7 and +4.7; Paleogene intrusives have $^{87}Sr/^{86}Sr_{(i)}$ ratios between 0.753 and 0.7063, and $\varepsilon Nd_{(t)}$ between −1.7 and +3.1. The trend toward more enriched values is even better expressed when data from Li et al. (2019, 2020; Fig. 8a) is included. Neogene and Quaternary volcanic rocks have less enriched isotopic values than Paleogene intrusives and fall within the range of Sr-Nd composition of the ca. 100 Ma Kanza Chaung Batholith.

Regardless of their crystallization ages, WPA rocks are always less isotopically enriched than DSMGB rocks (Fig. 8b; Zaw, 1990; Mitchell et al., 2012; Gardiner et al., 2017; Lin et al., 2019). DSMGB rocks display $^{87}Sr/^{86}Sr_{(i)}$ ratios commonly higher than 0.707 and εNd lower than −5; they also display a trend toward more enriched values, with many late Cretaceous-Paleogene plutons (90–40 Ma) displaying higher $^{87}Sr/^{86}Sr_{(i)}$ ratios and lower εNd than earlier plutons.

5. Discussion

5.1. Magmatic and deformation history recorded in the Wuntho Ranges

Though weathering (for Paleogene intrusives), and potentially hydrothermal activity (for the Mawgyi Volcanics and Mawlin Formation), had likely an impact on the composition of some of our samples, trace element characteristics (enrichment in LREE, positive Pb and negative Ti anomalies, depletion of Nb and Ta) for all samples analyzed here point to a subduction-related origin for the Wuntho igneous rocks (Hawkesworth et al., 1993). This feature was recognized for the Kanza Chaung plutons by Li et al. (2020) and Shangalon Paleogene intrusives by Li et al. (2019); we extended these observations to the earlier Mawlin Formation and Mawgyi Volcanics. All zircon grains from rivers draining the Mawlin Formation, Maingthon Dacite, and Mawgyi Volcanics yield U-Pb ages between 90 and 110 Ma, with no evidence for

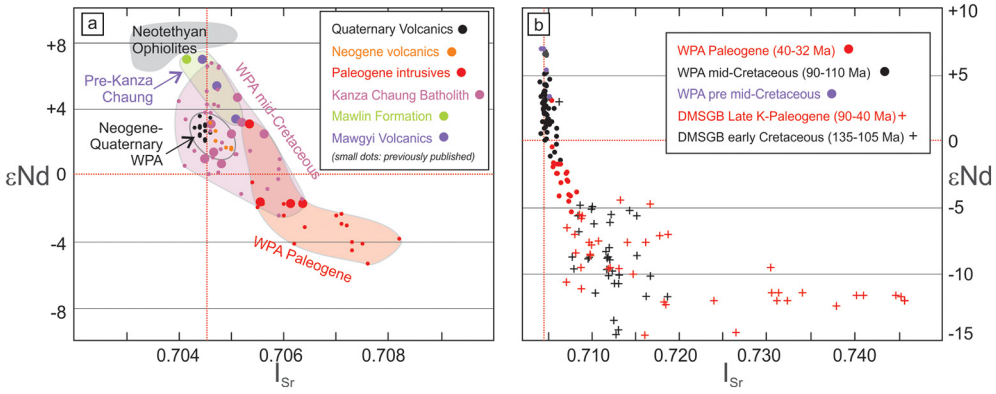

Fig. 8. Whole rock initial Sr-Nd isotopic composition from the WPA (a), including previously published data from Quaternary and Neogene volcanics (Mitchell et al., 2012; Lee et al., 2016), Paleogene intrusives (Li et al., 2019) and Kanza Chaung batholith (Li et al., 2020), compared with isotopic composition range of Neotethyan ophiolites from Li et al. (2020); Pre-Kanza Chaung data refer to Mawlin Formation and Mawgyi Volcanics; (b) comparison of WPA Sr-Nd isotopic data with published data from the DSMGB (Nd-Sr data compilation available in Supplementary Table 1).

older age populations. These zircon ages overlap with the age range of the Kanza Chaung batholith, as does our new age of 106 Ma for the Maingthon Dacite near Shangalon. Rocks from the Malwin and Mawgyi Volcanics have slightly more depleted Nd and Sr isotopic signatures than those of the Kanza Chaung Pluton (Fig. 8a). We thus propose that the Mawlin Formation, Maingthon Dacite, and Mawgyi Volcanics are contemporaneous with the early phase Kanza Chaung magmatism (~105 Ma) and represent the associated volcanic rocks of the oldest Kanza Chaung plutons. We cannot exclude the possibility that the Mawgyi Volcanics extends deeper in time, as proposed for its correlative units in the Jade and Tagaung-Myitkyina Belts (Mitchell, 2017). However, the exposed units of the Mawgyi Volcanics include rocks of andesitic to rhyolitic composition that commonly yield zircons; therefore, the near-absence of pre-110 Ma zircons in the Wuntho river sediments make older ages for these lithologies less likely.

The absence of pre-Cretaceous zircons in river sediments raises questions regarding the nature, age, and thickness of the arc metamorphic basement in the Wuntho Ranges. A detailed study of the metamorphic units of the WPA was beyond the scope of our sampling; however, our results show that the correlation between Wuntho basement units and metamorphosed units of the Jade and Tagaung-Myitkyina Belts (which yield Phanerozoic zircons; Zhang et al., 2018) is not straightforward. These data also eliminate the Wuntho Ranges as a potential source for the pre-Cretaceous zircons found in the Pane Chaung Formation of the Indo-Burman Ranges (Sevastjanova et al., 2016) or in the Central Myanmar Basins (Licht et al., 2019).

Neodymium and Sr isotopic compositions show a long-term younging trend toward more enriched values (higher $^{87}Sr/^{86}Sr_{(i)}$ and lower $\varepsilon Nd_{(t)}$) from the Mawgyi Volcanics to Paleogene intrusives, in parallel with increased LREE enrichment. Neodymium and Sr isotopic compositions of the Mawgyi Volcanics and Mawlin Formation are particularly depleted but still differ from the range of values found in Neotethyan ophiolites (Fig. 8), indicating some degree of slab-material addition (slab-derived and/or sediment melts). The increased range and more enriched Nd and Sr isotopic compositions found in ca. 100 Ma Kanza Chaung plutons and in later Paleogene intrusives indicate a higher degree of a subducted component, and/or some assimilation and crustal contamination of the older metamorphic basement in the arc lower crust (Chapman et al., 2017). Li et al. (2019) interpret the enriched Nd-Sr isotopic values found in Paleogene intrusives to reflect the onset of underthrusting of Indian continental crust below western Myanmar. Yet, the nature of the crust currently subducted below northern Myanmar (oceanic or thinned continental) is unclear (Steckler et al., 2016). The trend toward more enriched Nd-Sr isotopic compositions may reflect two other non-exclusive processes:

(1) increased incorporation of Indian-derived sediment on the Neotethyan slab into the subduction zone and subsequent incorporation into the slab-component in arc volcanism;
(2) increased crustal assimilation of the arc metamorphic basement due to the thickening of the Burma Terrane.

Miocene and Quaternary volcanic rocks from Mount Popa and Monywa areas have much more depleted Nd and Sr isotope compositions (Fig. 8; Lee et al., 2016). These two volcanic areas are located south of the Wuntho Ranges, where the Burma Terrane crust (Morley et al., 2020) and the offshore sedimentary cover (Curray, 2014) are much thinner. Less crustal assimilation and/or contribution of a slab component can explain the difference between Sr and Nd isotope compositions at these southern sites and in the Wuntho Ranges.

Finally, our apatite fission-track data highlight a phase of Paleogene cooling in the WPA. River j, which drains Paleogene intrusives near Shangalon, yielded overlapping AFT, zircon, and apatite U-Pb ages at 35–38 Ma. This indicates that Paleogene intrusives were likely emplaced at much shallower levels than exposed Cretaceous plutons. By contrast, AFT ages are much younger than zircon and apatite U-Pb ages for river b (39 Ma), c (27 Ma) and f (31 Ma). It is possible that the 39 Ma and 31 Ma AFT ages recorded in river b and f resulted from regional thermal resetting following the Paleogene intrusive episode also recorded in river j, though no Paleogene intrusives are recorded in these drainage basins. However, the large difference in AFT ages (ca. 12 ± 5 Ma) between the two northern samples (river b and c), despite their geographical proximity, is not consistent with regional thermal resetting. We thus interpret these AFT ages as representing exhumation ages rather than thermal resetting. This phase of exhumation would have started at least at 39 Ma and can be extended to 22 Ma after including the fission-track age of Li et al. (2013) for the Kanza Chaung south of the Wuntho Ranges. This time interval overlaps with the two phases of uplift of the WPA identified in seismic lines: between the Middle Eocene and early Oligocene, and in the late Oligocene (Zhang et al., 2017a). This suggests that our apatite fission-track ages and the phase of *E*-W deformation found in seismic lines all reflect the same middle Eocene to earliest Miocene deformation events. Comparison of AFT ages between river b and c suggests that this deformation was diachronous between both sides of the range, though this remains to be confirmed with further sampling.

The difference in intensity and orientation of the bedding measurements between Cretaceous and Cenozoic units, indicate there has to be deformation prior to the Cenozoic, and that deformation has an overall NE-SW to NNE-SSW trend before correction of the ~60° clockwise

rotation indicated by paleomagnetism (Westerweel et al., 2019). The observed NW-SE-striking tilting, folding, and thrusting of Cenozoic beds in the WPA is likely associated with the two Paleogene phases of uplift of the WPA coeval to our apatite fission-track ages, with fold and thrust development likely belonging to the later event, associated with E-W shortening (Zhang et al., 2017a).

5.2. The WPA: continuation of the Gangdese Arc? Comparison with the DSMGB and the Lhasa Terrane

The age population of zircons from river sediment derived from the Wuntho Ranges have the same two age peaks of ~90–108 Ma and 32–46 Ma identified in the crystallization age compilation (Fig. 9a, b), as well as river apatites showing ~95 Ma and ~38 Ma U-Pb populations. The oldest measured crystallization ages of the WPA are 170–173 Ma in the Tagaung-Myitkyina and Jade Belts; they are coeval with the oldest Mesozoic igneous rocks of the DSMGB (Fig. 9c; Barley et al., 2003; Searle et al., 2020). These early Jurassic igneous ages are not observed in the Wuntho Ranges (oldest age: 107 Ma), which is noteworthy as it remains unclear if the Tagaung-Myitkyina and Jade Belts are parts of the Burma Terrane (Ridd et al., 2019). WPA crystallization ages at ~50 Ma and ~70 Ma in the Sodon Batholith and below the Eocene sedimentary cover in the central Myanmar (Zhang et al., 2017a; Lin et al., 2019) indicate continuous yet more sporadic magmatic activity between the two high-flux events recorded in the Wuntho Ranges, which is not uncommon within subduction-related arcs (Paterson and Ducea, 2015). The compilation of igneous ages of the WPA and DSMGB show a clear distinction between both arcs: Magmatic lulls in the WPA were associated with magmatic flare-ups in the DSMGB, and vice versa. There is no evidence for coeval activity of both arcs based on crystallization ages, unlike claimed by others (Wang et al., 2014; Gardiner et al., 2015). Wang et al. (2014) and Gardiner et al. (2015) attribute Late Cretaceous – early Paleogene zircons with depleted Hf isotopic signature found in central Myanmar Paleogene sediments to WPA igneous activity, but the source of these zircons remains unclear as they are not found in the Wuntho Ranges. They could be sourced from WPA rocks now buried below Neogene sediments (Licht et al., 2013; Zhang et al., 2017a), or from the eastern Himalayan Syntaxis (Robinson et al., 2014).

When compared with Tibetan igneous age compilations, the chronology of magmatism onset, later high-flux events and lulls in the WPA does not mirror the evolution of the Gangdese Arc, despite claims to the contrary (Zhang et al., 2019; Li et al., 2020). First, none of the oldest igneous ages found in the Wuntho Ranges or in the Tagaung-Myitkyina and Jade Belts are as old as the earliest record of magmatic activity along the Gangdese Arc, where subduction-related magmatism is recorded as early as ~210 Ma and was continuous for most of the late Triassic, Jurassic and early Cretaceous (Fig. 9d; Zhu et al., 2019; Kapp and DeCelles, 2019). Later magmatic high-flux events in the WPA seem unrelated to the timing of Gangdese flare-ups; Gangdese flare-ups are either ten million years younger (95–85 Ma) or older (60–52 Ma; Zhu et al., 2019).

The oldest igneous ages in the DSMGB are roughly coeval with the onset of magmatism along the North Lhasa Plutonic Belt, dated at 180–170 Ma. However, it is hard to draw a firm chronological correlation between both arcs beyond the age of onset. Kapp and DeCelles (2019) identify flare-up events at ~115 Ma, 90 Ma and 15 Ma in the North Lhasa Plutonic Belt; the latter two events are obscured by the over-representation of 125 Ma igneous ages in our compilation (Fig. 9e). The DSMGB age compilation shows a first peak of igneous ages at ~125 Ma, and continuous activity from 90 to 40 Ma, without clearly-defined high-flux events during this time window, likely due to an undersampling of the arc.

There is thus no firm ground for a chronological correlation between Tibetan and Burmese arcs. Moreover, the similar isotopic signature in Nd, Sr, and Hf shared by arcs of both these areas is not particularly

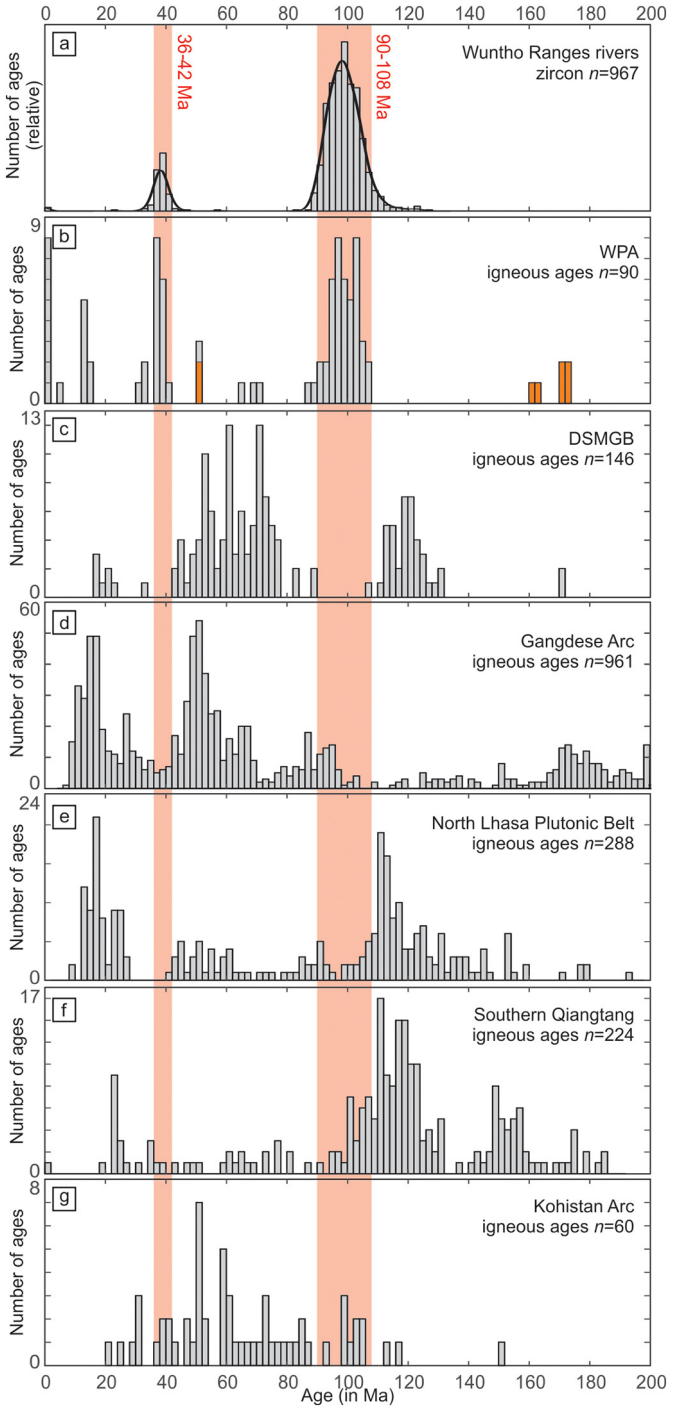

Fig. 9. Comparison of (a) Wuntho river zircon U-Pb ages (this study), crystallization ages from (b) the WPA and (c) DSMGB (igneous ages include Ar-Ar and K-Ar ages, zircon U-Pb ages of individual plutons and intrusives, including data from this study). For the WPA, ages coming from the Tagaung-Myitkyina and Jade Belts are displayed in orange. These compilations are compared with those of the (d) Gangdese Arc, (e) North Lhasa Plutonic Belt, (f) Southern Qiangtang Arc, and (g) Kohistan Arc. Data for the Gangdese Arc, North Lhasa Plutonic Belt, and Southern Qiangtang Arc are from the Tibetan Magmatism Database (Chapman and Kapp, 2017) purged of redundancies; data from the Kohistan Arc are from Jagoutz et al. (2019). Age compilations are available in Supplementary Table 1. Red shades correspond to the two main age populations identified in the Wuntho Ranges.

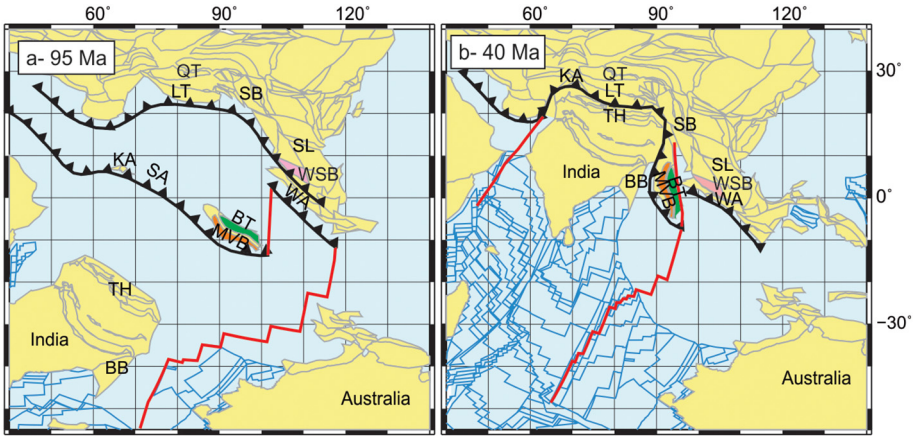

Fig. 10. Proposed scenario for the evolution of western Myanmar at 95 Ma (a) and 40 Ma (b) for Greater Argoland and composite models (models C and D, Table 1). Reconstruction made with GPlates software adapted from Westerweel et al. (2019). BT: Burma Terrane (in green), WSB: West Sumatra Block (in pink) MVB: Mount Victoria Block (in orange), TH: Tethyan Himalayas, BB: Bengal Bay, KA: Kohistan Arc, QT: Qiangtang Terrane, LT: Lhasa Terrane, KA: Kohistan Arc, SA: Spong Arc; SB: Sibumasu, WA: Woyla Arc, SL: Sundaland. Red lines are transform boundaries.

diagnostic, as near-trench arcs share similar depleted signatures worldwide (Chapman et al., 2017).

5.3. Testing the validity of the scenarios for the origin of the Burma Terrane

Our comparison shows that the correlation of magmatic rocks between Myanmar and Tibet proposed to support a Sundaland or a Lhasa origin for the Burma Terrane are unfounded (Models A and B, Table 1). However, we do not reject the possibility that these arcs have been parts of the same subduction systems in the past. The lack of correlation between Myanmar and Tibet could reflect along-strike variations of convergence angle, magma addition rates, and other processes that control arc magmatic tempos along the same subduction margins (Paterson and Ducea, 2015). In particular, the contrasting magmatic histories of the WPA and DSMGB is compatible with the model proposing a Sundaland origin for the Burma Terrane (Model A, Table 1), in which the two arcs are actually part of a single, complex arc developed along the southwestern margin of Sundaland, with periods of advance and retreat (Zhang et al., 2018; Li et al., 2020). Yet, these two models are mainly based on weak magmatic correlations and are therefore less persuasive, particularly since they are contradicted by paleomagnetic data that require the Burma Terrane to be in the southern hemisphere during the Late Cretaceous (Westerweel et al., 2019).

The Greater Argoland and composite models (models C and D), which are compatible with paleomagnetic data, propose different origins for the Burma Terrane but the same Transtethyan nature for the WPA (Fig. 10). Multiple models and arcs have been proposed to explain Transtethyan arc rocks (Jagoutz et al., 2015; Kapp and DeCelles, 2019). Catlos et al. (2019) propose onset of intra-oceanic subduction and suprasubduction spreading that started arc activity at around 130 Ma, compatible with the oldest crystallization ages and the absence of older basement in the Wuntho Ranges and the age of WOB ophiolites. Few crystallization ages are available for comparison with potential candidates for Transtethyan arc rocks, such as the Woyla Arc in Sumatra (Barber et al., 2005; Advokaat et al., 2018) or the Spong Arc in western Tibet (Corfield et al., 2001). The biggest dataset is from the Kohistan Arc (60 ages; Fig. 9g), interpreted to have initially formed as an intra-oceanic arc between around 136 and 120 Ma with continuous magmatic activity from ~120 Ma to 20 Ma (see review in Petterson, 2019, Searle, 2019), though the oldest pluton of the arc is dated at 154 Ma (Jagoutz et al., 2019). Mid-Cretaceous arc building in Kohistan rocks is locally important (Jijal complex: 118–91 Ma, Sapat Complex: 105–99 Ma, Chilas Complex: 86–81 Ma; Petterson, 2019), with some early Palaeogene volcanism recorded (Bouilhol et al., 2013; Jagoutz et al., 2019). Collision with India is generally proposed between around 64 and 42 Ma (e.g. Catlos et al., 2019; Petterson, 2019). The Kohistan Arc displays the same long-term isotopic trend from depleted toward more enriched values as the WPA, with a more dramatic decrease of εNd values and increase of $^{87}Sr/^{86}Sr_{(i)}$ values after 50 Ma, interpreted as reflecting Kohistan-India collision and onset of Indian crust underthrusting (Bouilhol et al., 2013).

The comparison between Transtethyan and WPA magmatic features and chronology, though based on little data, is thus compatible with the Greater Argoland and composite models (models C and D). They are not yet fully satisfactory. The Greater Argoland model remains inconsistent with the presence of Paleozoic limestones of Cathaysian affinity on the Burma Terrane and a potential correlation with West Sumatra (Barber and Crow, 2009). The composite model could reconcile the Cathaysian affinity on the Burma Terrane with the Gondwanan affinity of the Pane Chaung Formation and Kanpetlet Schist in the Indo-Burman Ranges as part of the postulated Mount Victoria Block (Yao et al., 2017; Morley et al., 2020). The two crustal fragments may have amalgamated during the mid-Cretaceous following the development of the Burma Terrane as an intra-oceanic arc. However, the composite model requires multiple sutures and collision episodes between individual continental fragments for which evidence is elusive. Both models also require a collision and reunification of the Burma Terrane with Sibumasu/Sundaland sometime after 100 Ma, the timing of which remains unconstrained. Late Cretaceous to Eocene (90–40 Ma) plutons of the DSMGB have been interpreted as subduction-related (Zhang et al., 2018; Gardiner et al., 2017), and metamorphism and deformation along the DSMGB and Sibumasu margin have been proposed to reflect collision and underthrusting of continental crust below Sibumasu since at least 45 Ma (Sautter et al., 2019; Searle et al., 2020). Paleomagnetic constraints (Westerweel et al., 2019) show low latitudes during the Eocene, such that a possible BT-Sibumasu collision at 45 Ma may have occurred along the eastern Andaman Sea. It could have reactivated subduction below the WPA, resulting in the magmatic flare-up at 42–36 Ma, with the more recent magmatic events becoming rarer due to the oblique nature of subduction. Yet, this explanation raises issues about the evolution of the Sibumasu margin in the eastern Andaman Sea area, which experienced extension rather than shortening during that time interval (Morley and Alvey, 2015). Our apatite fission-track data show WPA exhumation starting at ~39 Ma, but the seismic data of Zhang et al. (2017a) instead indicate shortening in the late Oligocene (Zhang et al., 2017a), which could alternatively represent the collision of the northern part of the Burma Terrane with Sibumasu. However,

most of the shortening in the neighboring Central Myanmar Basins is associated with Late Miocene-Plio-Pleistocene deformation (Pivnik et al., 1998; Ridd and Racey, 2015).

6. Conclusion

We show that the WPA in the Wuntho Ranges is characterized by only two magmatic events at 46–32 Ma and ~108–90 Ma, possibly extending to a few million years before 108 Ma due to our inability to precisely date the most mafic parts of the Mawgyi Volcanics. We find no evidence for earlier magmatism or earlier zircon ages in basement units, though Jurassic igneous ages have been reported in other parts of the Burma Terrane. Consistent with previous work (Gardiner et al., 2018; Li et al., 2019, 2020), we show that magmatism is subduction-related for both these events, and is characterized by a depleted Nd and Sr isotopic signature that tends toward more enriched values through time. We explain this isotopic trend either by increased incorporation of Indian-derived sediment of the Bengal Basin into the subduction zone or by increased crustal assimilation due to the long-term thickening of the Burma Terrane crust. Apatite fission-track data and field measurements, together with previous seismic imaging of the WPA (Zhang et al., 2017b) indicate arc exhumation during 39 to 22 Ma, overlapping with the last magmatic event and a subsequent phase of *E*-W shortening.

By comparing Tibetan and Burmese igneous rock ages, we find no support for a correlation between the Gangdese Arc and the WPA, as argued by models associating the Burma Terrane with Sundaland or the Lhasa Terrane. We show that models proposing an intra-oceanic origin for the WPA are both compatible with the magmatic history of the Wuntho Ranges and supported by paleomagnetic data, though not completely satisfactory. The lack of available structural data to constrain the relationships between the different regions of Myanmar, leaves considerable room for further interpretation regarding the origin of the terrane.

Supplementary data to this article can be found online at https://doi.org/10.1016/j.gr.2020.06.016.

CRediT authorship contribution statement

Alexis Licht: Conceptualization, Methodology, Investigation, Data curation, Writing - original draft, Supervision. **Zaw Win:** Investigation, Data curation, Writing - review & editing. **Jan Westerweel:** Investigation, Data curation, Writing - review & editing. **Nathan Cogné:** Investigation, Data curation, Writing - review & editing. **Chris Morley:** Investigation, Data curation, Writing - review & editing. **Sarawute Chantraprasert:** Investigation, Data curation, Writing - review & editing. **Fernando Poblete:** Investigation, Data curation, Writing - review & editing. **Tamas Ugrai:** Investigation, Data curation, Writing - review & editing. **Bruce Nelson:** Investigation, Data curation, Writing - review & editing. **Day Wa Aung:** Supervision, Project administration. **Guillaume Dupont-Nivet:** Writing - review & editing, Supervision, Funding acquisition.

Declaration of competing interest

The authors declare that they have no known competing financial interests or personal relationships that could have appeared to influence the work reported in this paper.

Acknowledgments

This research was primarily funded by the ERC consolidator grant MAGIC 649081 and the University of Washington. We thank Kyi Kyi Thein, Kyaing Sein, D. Cowan, D. van Hinsbergen, M. Mueller, A. Gagnon, M. Pecha, G. Gehrels, and F. Teng for prolific discussions, and assistance in the field and in the lab. This paper benefited from careful reviews by A.J. Barber and A. Mitchell.

References

Acharyya, S.K., 2007. Collisional emplacement history of the Naga-Andaman ophiolites and the position of the eastern Indian suture. J. Asian Earth Sci. 29 (2), 229–242.
Acharyya, S.K., 2015. Indo-Burma Range: a belt of accreted microcontinents, ophiolites and Mesozoic–Paleogene flyschoid sediments. Int. J. Earth Sci. 104 (5), 1235–1251.
Advokaat, E.L., Bongers, M.L., Rudyawan, A., BouDagher-Fadel, M.K., Langereis, C.G., van Hinsbergen, D.J., 2018. Early Cretaceous origin of the Woyla arc (Sumatra, Indonesia) on the Australian plate. Earth Planet. Sci. Lett. 498, 348–361.
Aitchison, J.C., Ao, A., Bhowmik, S., Clarke, G.L., Ireland, T.R., Kachovich, S., ... Zhen, Y., 2019. Tectonic evolution of the western margin of the Burma microplate based on new fossil and radiometric age constraints. Tectonics 38 (5), 1718–1741.
Alexander, E.W., Wielicki, M.M., Harrison, T.M., DePaolo, D.J., Zhao, Z.D., Zhu, D.C., 2019. Hf and Nd isotopic constraints on pre-and syn-collisional crustal thickness of Southern Tibet. J. Geophys. Res. Solid Earth 124 (11), 11038–11054.
Bannert, D., Lyen, A.S., Htay, T., 2011. The geology of the Indoburman Ranges in Myanmar. Geol. Jahrb. 101, 5–101.
Barber, A.J., Crow, M.J., 2009. Structure of Sumatra and its implications for the tectonic assembly of Southeast Asia and the destruction of Paleotethys. Island Arc 18 (1), 3–20.
Barber, A.J., Crow, M.J., Milsom, J. (Eds.)., 2005. Sumatra: Geology, Resources and Tectonic Evolution. Geological Society of London.
Barley, M.E., Pickard, A.L., Zaw, K., Rak, P., Doyle, M.G., 2003. Jurassic to Miocene magmatism and metamorphism in the Mogok Metamorphic Belt and the India-Eurasia collision in Myanmar. Tectonics 22. https://doi.org/10.1029/2002TC001398.
Belousov, A., Belousova, M., Zaw, K., Streck, M.J., Bindeman, I., Meffre, S., Vasconcelos, P., 2018. Holocene eruptions of Mt. Popa, Myanmar: volcanological evidence of the ongoing subduction of Indian Plate along Arakan Trench. J. Volcanol. Geotherm. Res. 360, 126–138.
Bender, F., 1983. Geology of Burma. Gebrüder Borntraeger edition. Stuttgart, Berlin.
Bertrand, G., Rangin, C., 2003. Tectonics of the western margin of the Shan plateau (central Myanmar): implication for the India–Indochina oblique convergence since the Oligocene. J. Asian Earth Sci. 21 (10), 1139–1157.
Bertrand, G., Rangin, C., Maluski, H., Bellon, H., Scientific-Party, G.I.A.C., 2001. Diachronous cooling along the Mogok Metamorphic Belt (Shan Scarp, Myanmar): the trace of the northward migration of the Indian syntaxis. J. Asian Earth Sci. 19, 649–659.
Bouilhol, P., Jagoutz, O., Hanchar, J.M., Dudas, F.O., 2013. Dating the India–Eurasia collision through arc magmatic records. Earth Planet. Sci. Lett. 366, 163–175.
Brach-Papa, C., Van Bocxstaele, M., Ponzevera, E., Quétel, C.R., 2009. Fit for purpose validated method for the determination of the strontium isotopic signature in mineral water samples by multi-collector inductively coupled plasma mass spectrometry. Spectrochim. Acta Part B 64, 229–234.
Catlos, E.J., Pease, E.C., Dygert, N., Brookfield, M., Schwarz, W.H., Bhutani, R., ... Schmitt, A.K., 2019. Nature, age and emplacement of the Spongtang ophiolite, Ladakh, NW India. Journal of the Geological Society 176 (2), 284–305.
Chapman, J.B., Kapp, P., 2017. Tibetan magmatism database. Geochem. Geophys. Geosyst. 18 (11), 4229–4234.
Chapman, J.B., Ducea, M.N., Kapp, P., Gehrels, G.E., DeCelles, P.G., 2017. Spatial and temporal radiogenic isotopic trends of magmatism in Cordilleran orogens. Gondwana Res. 48, 189–204.
Chew, D.M., Petrus, J.A., Kamber, B.S., 2014. U-Pb LA-ICPMS dating using accessory mineral standards with variable common Pb. Chem. Geol. 363, 185–199. https://doi.org/10.1016/j.chemgeo.2013.11.006.
Cogné, N., Chew, D.M., Donelick, R.A., Ansberque, C., 2020. LA-ICP-MS apatite fission track dating: a practical zeta-based approach. Chem. Geol. 531, 119302.
Corfield, R.I., Searle, M.P., Pedersen, R.B., 2001. Tectonic setting, origin, and obduction history of the Spontang Ophiolite, Ladakh Himalaya, NW India. The Journal of Geology 109 (6), 715–736.
Curray, J.R., 2005. Tectonics and history of the Andaman Sea region. J. Asian Earth Sci. 25 (1), 187–232.
Curray, J.R., 2014. The Bengal depositional system: from rift to orogeny. Mar. Geol. 352, 59–69.
Ding, L., Zhong, D., Yin, A., Kapp, P., Harrison, T.M., 2001. Cenozoic structural and metamorphic evolution of the eastern Himalayan syntaxis (Namche Barwa). Earth Planet. Sci. Lett. 192 (3), 423–438.
Donelick, R.A., O'Sullivan, P.B., Ketcham, R.A., 2005. Apatite fission-track analysis. Rev. Mineral. Geochem. 58 (1), 49–94.
Engelder, T., Marshak, S., 1985. Disjunctive cleavage formed at shallow depths in sedimentary rocks. J. Struct. Geol. 7, 327–343.
Gaffney, A.M., Blichert-Toft, J., Nelson, B.K., Albarède, F., 2007. Constraints on source-forming processes of West Greenland kimberlites inferred from Hf–Nd isotope systematics. Geochim. Cosmochim. Acta 71, 2820–2836.
Gardiner, N.J., Searle, M.P., Robb, L.J., Morley, C.K., 2015. Neo-Tethyan magmatism and metallogeny in Myanmar–an Andean analogue? J. Asian Earth Sci. 106, 197–215.
Gardiner, N.J., Robb, L.J., Morley, C.K., Searle, M.P., Cawood, P.A., Whitehouse, M.J., ... Myint, T.A., 2016. The tectonic and metallogenic framework of Myanmar: A Tethyan mineral system. Ore Geology Reviews 79, 26–45.
Gardiner, N.J., Hawkesworth, C.J., Robb, L.J., Whitehouse, M.J., Roberts, N.M., Kirkland, C.L., Evans, N.J., 2017. Contrasting granite metallogeny through the zircon record: a case study from Myanmar. Sci. Rep. 7 (1), 748.
Gardiner, N.J., Searle, M.P., Morley, C.K., Robb, L.J., Whitehouse, M.J., Roberts, N.M., ... Spencer, C.J., 2018. The crustal architecture of Myanmar imaged through zircon U-Pb, Lu-Hf and O isotopes: tectonic and metallogenic implications. Gondwana Research 62, 27–60.
Gibbons, A.D., Zahirovic, S., Müller, R.D., Whittaker, J.M., Yatheesh, V., 2015. A tectonic model reconciling evidence for the collisions between India, Eurasia and intra-oceanic arcs of the central-eastern Tethys. Gondwana Res. 28 (2), 451–492.

Hall, R., Clements, B., Smyth, H.R., 2009. Sundaland: Basement Character, Structure and Plate Tectonic Development.

Hawkesworth, C.J., Gallagher, K., Hergt, J.M., McDermott, F., 1993. Mantle and slab contributions in arc magmas. Annu. Rev. Earth Planet. Sci. 21 (1), 175–204.

Horstwood, M.S., Košler, J., Gehrels, G., Jackson, S.E., McLean, N.M., Paton, C., ... Bowring, J.F., 2016. Community-derived standards for LA-ICP-MS U-(Th-) Pb geochronology–Uncertainty propagation, age interpretation and data reporting. Geostandards and Geoanalytical Research 40 (3), 311–332.

Jagoutz, O., Royden, L., Holt, A.F., Becker, T.W., 2015. Anomalously fast convergence of India and Eurasia caused by double subduction. Nat. Geosci. 8 (6), 475–478.

Jagoutz, O., Bouilhol, P., Schaltegger, U., Müntener, O., 2019. The isotopic evolution of the Kohistan Ladakh arc from subduction initiation to continent arc collision. Geol. Soc. Lond., Spec. Publ. 483 (1), 165–182.

Kapp, P., DeCelles, P.G., 2019. Mesozoic–Cenozoic geological evolution of the Himalayan-Tibetan orogen and working tectonic hypotheses. Am. J. Sci. 319 (3), 159–254.

Le Maitre, R.W., Streckeisen, A., Zanettin, B., Le Bas, M.J., Bonin, B., Bateman, P. (Eds.)., 2005. Igneous Rocks: A Classification and Glossary of Terms: Recommendations of the International Union of Geological Sciences Subcommission on the Systematics of Igneous Rocks. Cambridge University Press.

Lee, H.Y., Chung, S.L., Yang, H.M., 2016. Late Cenozoic volcanism in central Myanmar: geochemical characteristics and geodynamic significance. Lithos 245, 174–190.

Li, R., Mei, L., Zhu, G., Zhao, R., Xu, X., Zhao, H., ... Ma, Y., 2013. Late Mesozoic to Cenozoic tectonic events in volcanic arc, West Burma Block: evidences from U-Pb zircon dating and apatite fission track data of granitoids. Journal of Earth Science 24 (4), 553–568.

Li, J.X., Fan, W.M., Zhang, L.Y., Evans, N.J., Sun, Y.L., Ding, L., ... Sein, K., 2019. Geochronology, geochemistry and Sr–Nd–Hf isotopic compositions of Late Cretaceous–Eocene granites in southern Myanmar: petrogenetic, tectonic and metallogenic implications. Ore Geology Reviews 112, 103031.

Li, J.X., Fan, W.M., Zhang, L.Y., Peng, T.P., Sun, Y.L., Ding, L., ... Sein, K., 2020. Prolonged Neo-Tethyan magmatic arc in Myanmar: evidence from geochemistry and Sr–Nd–Hf isotopes of Cretaceous mafic–felsic intrusions in the Banmauk–Kawlin area. International Journal of Earth Sciences 109 (2), 649–668.

Licht, A., France-Lanord, C., Reisberg, L., Fontaine, C., Soe, A.N., Jaeger, J.J., 2013. A palaeo Tibet–Myanmar connection? Reconstructing the Late Eocene drainage system of central Myanmar using a multi-proxy approach. J. Geol. Soc. 170 (6), 929–939.

Licht, A., Dupont-Nivet, G., Win, Z., Swe, H.H., Kaythi, M., Roperch, P., ... Jones, D., 2019. Paleogene evolution of the Burmese forearc basin and implications for the history of India-Asia convergence. Bulletin 131 (5-6), 730–748.

Lin, T.H., Mitchell, A.H., Chung, S.L., Tan, X.B., Tang, J.T., Oo, T., Wu, F.Y., 2019. Two parallel magmatic belts with contrasting isotopic characteristics from southern Tibet to Myanmar: zircon U–Pb and Hf isotopic constraints. J. Geol. Soc. 176 (3), 574–587.

Liu, C.Z., Chung, S.L., Wu, F.Y., Zhang, C., Xu, Y., Wang, J.G., ... Guo, S., 2016. Tethyan suturing in Southeast Asia: Zircon U-Pb and Hf-O isotopic constraints from Myanmar ophiolites. Geology 44 (4), 311–314.

Ludwig, K.R., 2003. Isoplot 3.00: a geochronological toolkit for Microsoft Excel. Berkeley Geochronology Center Special Publication. 4, p. 70.

Maffione, M., Van Hinsbergen, D.J., Koornneef, L.M., Guilmette, C., Hodges, K., Borneman, N., ... Kapp, P., 2015. Forearc hyperextension dismembered the south Tibetan ophiolites. Geology 43 (6), 475–478.

Matthews, W.A., Guest, B., 2017. A practical approach for collecting large-n detrital zircon U-Pb data sets by quadrupole LA-ICP-MS. Geostand. Geoanal. Res. 41 (2), 161–180.

Maurin, T., Rangin, C., 2009. Structure and kinematics of the Indo-Burmese Wedge: recent and fast growth of the outer wedge. Tectonics 28. https://doi.org/10.1029/2008TC002276.

Maury, R.C., Pubellier, M., Rangin, C., Wulput, L., Cotten, J., Socquet, A., ... Htun, H.M., 2004. Quaternary calc-alkaline and alkaline volcanism in an hyper-oblique convergence setting, central Myanmar and western Yunnan. Bulletin de la Société Géologique de France 175 (5), 461–472.

Metcalfe, I., 2013. Gondwana dispersion and Asian accretion: tectonic and palaeogeographic evolution of eastern Tethys. J. Asian Earth Sci. 66, 1–33.

Mitchell, A.H.G., 1981. Phanerozoic plate boundaries in mainland SE Asia, the Himalayas and Tibet. J. Geol. Soc. 138 (2), 109–122.

Mitchell, A.H.G., 1986. Mesozoic and Cenozoic Regional Tectonics and Metallogenesis in Mainland SE Asia.

Mitchell, A.H.G., 1993. Cretaceous–Cenozoic tectonic events in the western Myanmar (Burma)–Assam region. J. Geol. Soc. 150 (6), 1089–1102.

Mitchell, A., 2017. Geological Belts, Plate Boundaries, and Mineral Deposits in Myanmar. Elsevier.

Mitchell, A.H.G., Htay, M.T., Htun, K.M., Win, M.N., Oo, T., Hlaing, T., 2007. Rock relationships in the Mogok metamorphic belt, Tatkon to Mandalay, central Myanmar. J. Asian Earth Sci. 29 (5), 891–910.

Mitchell, A.H.G., Hlaing, T., Htay, N., 2010. Indo-Myanmar Ranges in the tectonic framework of the Himalaya and Southeast Asia. Indo-Burman Ranges in the Tectonic Framework of the Himalaya and Southeast Asia. Geological Society of India, Memoir 75, pp. 3–24.

Mitchell, A., Chung, S.L., Oo, T., Lin, T.H., Hung, C.H., 2012. Zircon U–Pb ages in Myanmar: magmatic–metamorphic events and the closure of a neo-Tethys ocean? J. Asian Earth Sci. 56, 1–23.

Mitchell, A.H.G., Htay, M.T., Htun, K.M., 2015. The medial Myanmar suture zone and the Western Myanmar–Mogok foreland. Journal of the Myanmar Geosciences Society 6 (1), 73–88.

Mitchell, A., Htun, Kyaw Min, Htay, Myint Thein, Lin, T.H., 2020. Post-Triassic Myanmar west of the Salween: three crustal blocks, two arcs and the Mogok Metamorphics nappe. Journal of the Myanmar Geosciences Society 9, 71–84.

Morley, C.K., 2009. Evolution from an oblique subduction back-arc mobile belt to a highly oblique collisional margin: the Cenozoic tectonic development of Thailand and eastern Myanmar. Geol. Soc. Lond., Spec. Publ. 318 (1), 373–403.

Morley, C.K., Alvey, A., 2015. Is spreading prolonged, episodic or incipient in the Andaman Sea? Evidence from deepwater sedimentation. J. Asian Earth Sci. 98, 446–456.

Morley, C.K., Arboit, F., 2019. Dating the Onset of Motion on the Sagaing Fault: Evidence From Detrital Zircon and Titanite U-Pb Geochronology.

Morley, C.K., Naing, T.T., Searle, M., Robinson, S.A., 2020. Structural and tectonic development of the Indo-Burma Ranges. Earth Sci. Rev. 102992.

Nelson, B.K., 1995. Fluid flow in subduction zones: evidence from Nd- and Sr-isotope variations in metabasalts of the Franciscan Complex, California. Contrib. Mineral. Petrol. 119, 247–262.

Paquette, J., Piro, J., Devidal, J., Bosse, V., Didier, A., Sanac, S., Abdelnour, Y., 2014. Sensitivity enhancement in LA-ICP-MS by N2 addition to carrier gas: application to radiometric dating of U-Th-bearing minerals. Agil. ICP-MS J. 58, 1–5.

Paterson, S.R., Ducea, M.N., 2015. Arc magmatic tempos: gathering the evidence. Elements 11 (2), 91–98.

Paton, C., Woodhead, J.D., Hellstrom, J.C., Hergt, J.M., Greig, A., Maas, R., 2010. Improved laser ablation U-Pb zircon geochronology through robust downhole fractionation correction. Geochem. Geophys. Geosyst. 11 (3).

Paton, C., Hellstrom, J., Paul, B., Woodhead, J., Hergt, J., 2011. Iolite: freeware for the visualisation and processing of mass spectrometric data. J. Anal. At. Spectrom. 26, 2508–2518.

Peccerillo, A., Taylor, S.R., 1976. Geochemistry of Eocene calc-alkaline volcanic rocks from the Kastamonu area, northern Turkey. Contrib. Mineral. Petrol. 58 (1), 63–81.

Petterson, M.G., 2019. The plutonic crust of Kohistan and volcanic crust of Kohistan–Ladakh, north Pakistan/India: lessons learned for deep and shallow arc processes. Geol. Soc. Lond., Spec. Publ. 483 (1), 123–164.

Pivnik, D., Nahm, J., Tucker, R., Smith, G., NNyein, K., Nyunt, M., Maung, P., 1998. Polyphase deformation in a fore-arc/back-arc basin, Salin Subbasin, Myanmar (Burma). AAPG Bull. 82, 1837–1856.

Rangin, C., 2018. The Western Sunda Basins and the India/Asia Collision: An Atlas. Geotecto consulting.

Rangin, C., Maw, Win, Lwin, S., Naing, W., Mouret, C., Bertrand, G., the G.I.A.C, 1999. Scientific party. Cenozoic pull-apart basins in central Myanmar: the trace of the path of India along the western margin of Sundaland. Terra Abstracts (Journal of Conference Abstracts of the EGU) 4, 59.

Replumaz, A., Negredo, A.M., Guillot, S., Villaseñor, A., 2010. Multiple episodes of continental subduction during India/Asia convergence: insight from seismic tomography and tectonic reconstruction. Tectonophysics 483 (1), 125–134.

Replumaz, A., Guillot, S., Villaseñor, A., Negredo, A.M., 2013. Amount of Asian lithospheric mantle subducted during the India/Asia collision. Gondwana Res. 24 (3), 936–945.

Ridd, M.F., 2016. Should Sibumasu be renamed Sibuma? The case for a discrete Gondwana-derived block embracing western Myanmar, upper Peninsular Thailand and NE Sumatra. J. Geol. Soc. 173 (2), 249–264.

Ridd, M.F., Racey, A., 2015. Onshore petroleum geology of Myanmar: Central Burma depression. Geol. Soc. Lond. Mem. 45 (1), 21–50.

Ridd, M.F., Crow, M.J., Morley, C.K., 2019. The role of strike-slip faulting in the history of the Hukawng Block and the Jade Mines Uplift, Myanmar. Proceedings of the Geologists' Association.

Robinson, R.A., Brezina, C.A., Parrish, R.R., Horstwood, M.S., Oo, N.W., Bird, M.I., ... Zaw, K., 2014. Large rivers and orogens: The evolution of the Yarlung Tsangpo–Irrawaddy system and the eastern Himalayan syntaxis. Gondwana Research 26 (1), 112–121.

Royden, L.H., Burchfiel, B.C., van der Hilst, R.D., 2008. The geological evolution of the Tibetan Plateau. science 321 (5892), 1054–1058.

Sautter, B., Pubellier, M., Schlögl, S.K., Matenco, L., Andriessen, P., Mathew, M., 2019. Exhumation of west Sundaland: a record of the path of India? Earth Sci. Rev. 102933.

Searle, M., 2019. Ophiolites and regional tectonics. Geology of the Oman Mountains, Eastern Arabia. Springer, Cham, pp. 85–115.

Searle, M.P., Noble, S.R., Cottle, J.M., Waters, D.J., Mitchell, A.H.G., Hlaing, T., Horstwood, M.S.A., 2007. Tectonic evolution of the Mogok Metamorphic Belt, Burma (Myanmar) constrained by U-Th-Pb dating of metamorphic and magmatic rocks. Tectonics, 26 https://doi.org/10.1029/2006TC002083.

Searle, M.P., Whitehouse, M.J., Robb, L.J., Ghani, A.A., Hutchison, C.S., Sone, M., ... Oliver, G.J.H., 2012. Tectonic evolution of the Sibumasu–Indochina terrane collision zone in Thailand and Malaysia: constraints from new U–Pb zircon chronology of SE Asian tin granitoids. Journal of the Geological Society 169 (4), 489–500.

Searle, M.P., Garber, J.M., Hacker, B.R., Htun, K., Gardiner, N.J., Waters, D.J., Robb, L.J., 2020. Timing of syenite-charnockite magmatism and ruby- and sapphire metamorphism in the Mogok valley region, Myanmar. Tectonics 39, e2019TC005998. https://doi.org/10.1029/2019TC005998.

Sevastjanova, I., Hall, R., Rittner, M., Paw, S.M.T.L., Naing, T.T., Alderton, D.H., Comfort, G., 2016. Myanmar and Asia united, Australia left behind long ago. Gondwana Res. 32, 24–40.

Shen, F., Royden, L.H., Burchfiel, B.C., 2001. Large-scale crustal deformation of the Tibetan Plateau. J. Geophys. Res. 106 (B4), 6793–6816.

Shi, G., Cui, W., Cao, S., Jiang, N., Jian, P., Liu, D., ... Chu, B., 2008. Ion microprobe zircon U–Pb age and geochemistry of the Myanmar jadeitite. Journal of the Geological Society 165 (1), 221–234.

Socquet, A., Vigny, C., Chamot-Rooke, N., Simons, W., Rangin, C., Ambrosius, B., 2006. India and Sunda plates motion and deformation along their boundary in Myanmar determined by GPS. J. Geophys. Res. Solid Earth 111 (B5).

Stacey, J.S., Kramers, J.D., 1975. Approximation of terrestrial lead isotope evolution by a 2-stage model. Earth Planet. Sci. Lett. 26, 207–221.

Steckler, M.S., Mondal, D.R., Akhter, S.H., Seeber, L., Feng, L., Gale, J., ... Howe, M., 2016. Locked and loading megathrust linked to active subduction beneath the Indo-Burman Ranges. Nature Geoscience 9 (8), 615–618.
Sun, S.S., McDonough, W.F., 1989. Chemical and isotopic systematics of oceanic basalts: implications for mantle composition and processes. Geol. Soc. Lond., Spec. Publ. 42 (1), 313–345.
Sylvester, A.G., 1988. Strike-slip faults. Geol. Soc. Am. Bull. 100, 1666–1703.
Thein, Myint, 2015. The Pre-Tertiary carbonate rocks exposed at the NE margin of the Central Myanmar Basin and their developmental history. Journal of the Myanmar Geosciences Society 6, 1–16.
Thein, Myint, Maung, Maung, Myint, Khin Maung, Aung, Aye Ko, Than, Khin Aung, 1982. Geology of the area between Tigyaing and Katha. Research Titles. Natural Science Research Group, Policy Directing Committee on Research Projects, Science and Technology Committee, Burma.
Thein, Myint, Saw, Kan, Aung, Aye Ko, Tint, Kyaw, 1987. Geology of the area between Tigyaing and Katha. Research Titles. Natural Research Group, Burma, pp. 135–219.
Ueno, K., Thein, M., Barber, A.J., 2016, October. Permian fusuline fauna from the Minwun Range, Central Myanmar. 5th Symposium of the International Geosciences Programme (IGCP). vol. 589, pp. 27–28.
United Nations, 1978. Geology and Exploration Geochemistry of the Pinlebu-Banmauk Area, Sagaing Division, Northern Burma. Technical Report No.2, United Nations Development Programme, UN/BUR-72 002/6. United Nations, New York (69 p).
United Nations, 1979. Mineral exploration in selected areas. Technical Report No. 6, United Nations Development Programme, DP/UN/BUR-72-002/15. United Nations, New York (86 p).
Van Hinsbergen, D.J., Kapp, P., Dupont-Nivet, G., Lippert, P.C., DeCelles, P.G., Torsvik, T.H., 2011. Restoration of Cenozoic deformation in Asia and the size of Greater India. Tectonics 30 (5).
Vermeesch, P., 2018. IsoplotR: a free and open toolbox for geochronology. Geosci. Front. (5), 1479–1493.
Wang, J., Wu, F., Tan, X., Liu, C., 2014. Magmatic evolution of the Western Myanmar Arc documented by U-Pb and Hf isotopes in detrital zircon. Tectonophysics 612-613, 97–105.
Wang, J.G., Hu, X., Garzanti, E., An, W., Liu, X.C., 2017. The birth of the Xigaze forearc basin in southern Tibet. Earth Planet. Sci. Lett. 465, 38–47.
Westerweel, J., Roperch, P., Licht, A., Dupont-Nivet, G., Win, Z., Poblete, F., ... Aung, D.W., 2019. Burma Terrane part of the Trans-Tethyan arc during collision with India according to palaeomagnetic data. Nature Geoscience 12 (10), 863–868.
Woodhead, J., Hellstrom, J., Hergt, J., Greig, A., Maas, R., 2007. Isotopic and elemental imaging of geological materials by laser ablation inductively coupled plasma mass spectrometry. Journal of Geostandards and Geoanalytical Research 31, 331–343.
Yao, W., Ding, L., Cai, F., Wang, H., Xu, Q., Zaw, T., 2017. Origin and tectonic evolution of upper Triassic Turbidites in the Indo-Burman ranges, West Myanmar. Tectonophysics 721, 90–105.
Yui, T.F., Fukoyama, M., Iizuka, Y., Wu, C.M., Wu, T.W., Liou, J.G., Grove, M., 2013. Is Myanmar jadeitite of Jurassic age? A result from incompletely recrystallized inherited zircon. Lithos 160, 268–282.
Zaw, K., 1990. Geological, petrological and geochemical characteristics of granitoid rocks in Burma: with special reference to the associated W-Sn mineralization and their tectonic setting. J. SE Asian Earth Sci. 4 (4), 293–335.
Zhang, P., Mei, L., Hu, X., Li, R., Wu, L., Zhou, Z., Qiu, H., 2017a. Structures, uplift, and magmatism of the Western Myanmar Arc: constraints to mid-Cretaceous-Paleogene tectonic evolution of the western Myanmar continental margin. Gondwana Res. 52, 18–38.
Zhang, J.E., Xiao, W., Windley, B.F., Cai, F., Sein, K., Naing, S., 2017b. Early Cretaceous wedge extrusion in the Indo-Burma Range accretionary complex: implications for the Mesozoic subduction of Neotethys in SE Asia. Int. J. Earth Sci. 1–18.
Zhang, J.E., Xiao, W., Windley, B.F., Wakabayashi, J., Cai, F., Sein, K., ... Naing, S., 2018. Multiple alternating forearc-and backarc-ward migration of magmatism in the Indo-Myanmar Orogenic Belt since the Jurassic: documentation of the orogenic architecture of eastern Neotethys in SE Asia. Earth Sci. Rev. 185, 704–731.
Zhang, X., Chung, S.L., Lai, Y.M., Ghani, A.A., Murtadha, S., Lee, H.Y., Hsu, C.C., 2019. A 6000-km-long Neo-Tethyan arc system with coherent magmatic flare-ups and lulls in South Asia. Geology 47 (6), 573–576.
Zhu, D.C., Wang, Q., Chung, S.L., Cawood, P.A., Zhao, Z.D., 2019. Gangdese magmatism in southern Tibet and India–Asia convergence since 120 Ma. Geol. Soc. Lond., Spec. Publ. 483 (1), 583–604.

Article in preparation

The Burma Terrane related to India: Evidence from the U-Pb zircons in Late Cretaceous-Paleogene sediments from the Central Myanmar Basins

Pierrick Roperch[1], Jan Westerweel[1], et al.

[1]*Géosciences Rennes, CNRS-INSU, Université de Rennes1, Campus de Beaulieu, 35042 Rennes, France*

ABSTRACT

Recent paleomagnetic data from Myanmar demonstrate that the Burma Terrane (BT) underwent an impressive northward translation alongside India in the Cenozoic. Near-equatorial paleolatitudes during the Eocene imply that the Central Myanmar Basins (CMB) were far away from a potential source in Sibumasu. A review of the numerous studies on detrital zircons from the CMB highlights a clear correlation in the distribution of the ages of the pre-Cretaceous zircons from the Late Cretaceous - Paleogene sediments with the one from the Triassic turbidites (Pane Chaung Formation) of the Indo-Burman Ranges and the Triassic sediments from the Tethyan Himalaya. This result demonstrates that the nearby early Late Cretaceous and Cenozoic magmatic arc cannot be the unique source of Paleogene sediments. The large northward motion of the BT likely impeded active subduction below Myanmar during the Paleogene. This is confirmed by the lack of evidence for detrital magnetite in the sediments in agreement with few record of magmatic activity along the WPA. These observations support a paleogeography where the BT is isolated from the Sibumasu block during the Paleogene. Filling of the BT sedimentary basins is clearly controlled by Cenozoic tectonics north of the BT due to the collision of India with the Trans-

Tethyan Arc and then with Asia. We argue that the distribution of the ages of Cenozoic zircons and the little evidence for a tectonically active Cenozoic magmatic arc in Myanmar imply the Gangdese volcanics as the main sources of sediments filling the CMB. There is no conflict between a rapid northward moving BT with such a new paleogeographic model of basin fill in Myanmar.

1. Introduction

Paleomagnetic results have shown that the Burma terrane (BT) has been moving northward alongside India for the last ~40 Ma (Westerweel et al., 2019). However, paleomagnetism cannot bring direct constraints on the longitudinal position of the BT, impeding the definition of the time and conditions of the BT collision with the western margin of Sundaland. Thick sedimentary basins, filled during the Cenozoic, characterize the geology of the BT. These Central Myanmar Basins (CMB) were first considered as the receptacle for the erosion products of the India-Asia collision (Métivier et al., 1999).

In an attempt to reconstruct the drainage system over time, a link was proposed between the river traversing the Yarlung Tsangpo Suture Zone and the Irrawaddy River prior to its capture by the Brahmaputra River during the Miocene (Robinson et al., 2014; Zhang et al., 2019a). By contrast, more local sources have also been proposed for the filling of the CMB, which are often presented in this context as forearc and back-arc basins of an Andean-type magmatic arc source alongside uplifted parts of eastern Myanmar such as the Mogok Metamorphics and the Shan Plateau as additional sources (Fig. 1; Allen et al., 2008; Licht et al., 2013; Wang et al., 2014; Licht et al., 2016, 2018; Cai et al., 2019; Najman et al., 2020).

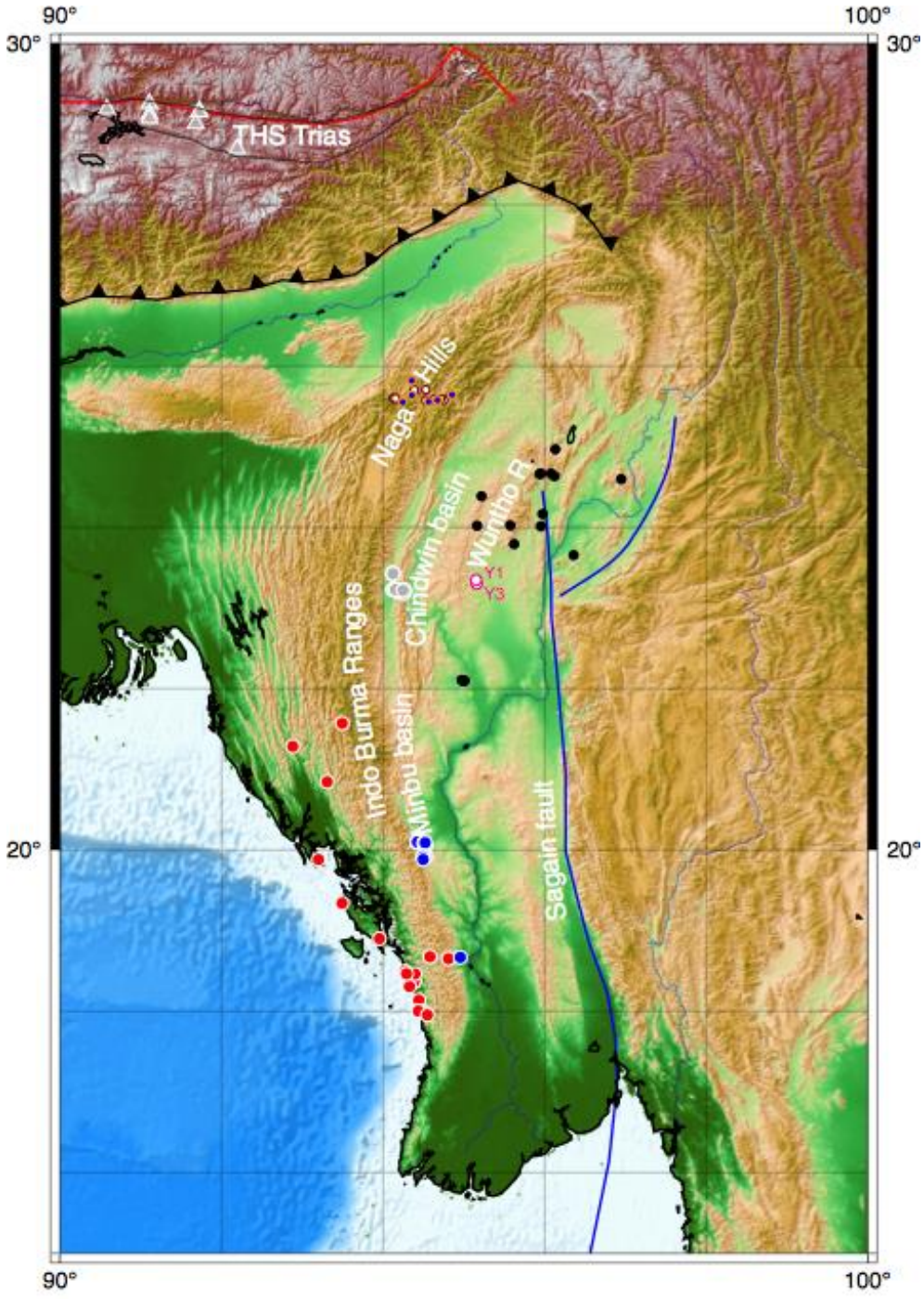

Figure 1. Map showing the location of the samples with U-Pb ages from detrital zircons in Late Cretaceous to Paleogene sediments from the Chindwin Basin (grey circles), the Minbu Basin (blue circles), the IBR (red circles) and the "arc area" with sample closer to the Wunth-Popa Arc. Y1 and Y3 are the position of the wells with sample studied by Zhang et al. (2017). The triangles in the Tethyan Himalaya correspond to the locations of some of the samples studied in the Triassic Langjiexue Formation. Sampling in the Naga Hills correspond to the Phokphur Formation and Naga Hills metamorphics.

However, the late Eocene equatorial position of the BT challenges all previous interpretations made with a BT closer to Sibumasu and the Eastern Himalaya Syntaxis at that time.

Our main objective is to propose a challenging discussion with respect to previous interpretations and a new source to sink model for the thick CMB that is compatible with a northward moving BT. The regional sedimentary record can be used to test the validity of the large northward motion and proposed new paleogeography.

The location of the source is indeed the main constraint on the longitudinal position of the BT, as well as the timing and location of its collision with Sundaland. A western position of the BT closer to India would imply an almost inactive subduction below the BT during the Paleogene as it seems difficult to move a plunging slab in the asthenosphere over large distances. Hence, the Myanmar arc (Wuntho-Popa Arc, WPA) as a main source of sediments during the Paleogene is also questionable. If the BT accreted to Sumatra in the Eocene, it would imply almost full partitioning (Beck, 1991) of the motion between India and Sundaland with the sedimentary basins of the BT recording extreme margin-parallel displacement of arc and forearc slivers. An improved knowledge of the paleogeography will also help understand the early displacements of the Sagaing Fault, which is the most active fault in Asia (Fig. 1; Socquet et al., 2006; Morley and Arboit, 2019).

During the last decade, the CMB have been intensively studied (Allen et al., 2008; Licht et al., 2013; Wang et al., 2014; Robinson et al., 2014; Kyaw Linn Oo et al., 2015; Licht et al., 2016, 2018; Zhang et al., 2019a; Cai et al., 2019; Najman et al., 2020; Arboit et al., 2020), providing a large number of ages from the detrital zircons within the sediments filling the CMB. We have compiled all the published data on the CMB and Indo-Burman Ranges (IBR). Most of the data come from the Chindwin and Minbu Basins forming the western trough of the CMB. Despite a possible bias in the sampling, for example due to spatial or temporal

distribution and oversampling of the same zircons family such sedimentary layers rich in tuff, the large total number of studied zircons may still provide some clues on the source of the sediments.

The number of studied zircons per individual sample is usually low (~100), and most studies have focused their attention on the largest peaks corresponding to the early Late Cretaceous and Cenozoic period.

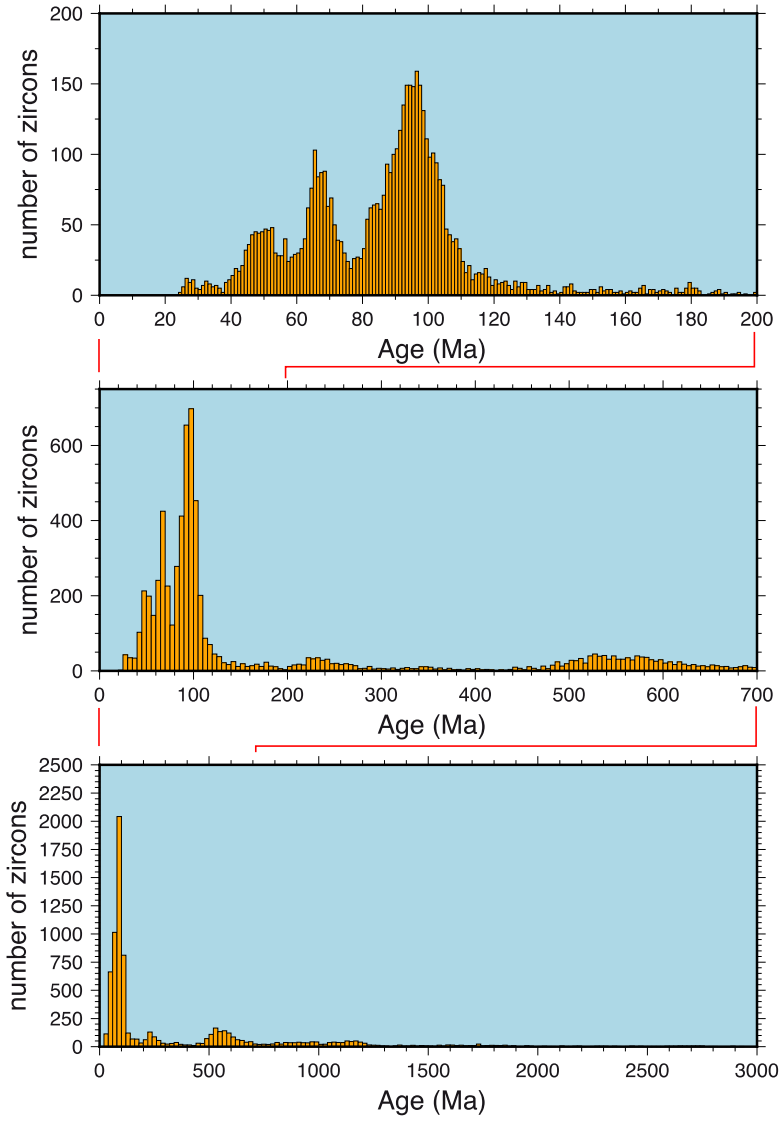

Figure 2. Bottom) distribution of all zircons in the Late Cretaceous to Paleogene sediments. A prominent peak is observed for the late Mesozoic and Cenozoic period. This peak is usually the one attracting most of the attention and the data are presented either on an intermediate time scale (middle plot) or only focused on the main peak (upper plot).

However, there are a large number of pre-Cretaceous zircons in several samples and their distribution has not been studied. On average 40% of the zircons have pre-Cretaceous ages (Fig. 2). To this end, we will discuss the information contained in these old zircons after stacking multiple samples from several studies. We also reinterpret the source of the youngest zircons and indicate that a Gangdese Arc source in the Himalayan collision zone is more likely than a local source related to the WPA.

2. Geology of Myanmar

The geology of Myanmar is usually defined by several longitudinal belts. The present-day active Sagaing Fault is a ~N-S trending dextral strike-slip fault separating the BT to its west and Sibumasu to its east. The metamorphic Mogok-Mandalay-Mergui Belt (MMMB) and the Shan scarp form the western border of Sibumasu. Zircons from both the MMMB and the Tin Belt to the south have Cenozoic magmatism with well-defined negative εHf(t) values (Gardiner et al., 2017). The IBR mark the western border of the BT. The basement of the IBR is made of the Triassic Kanpetlet schists and the Pane Chaung Triassic turbidites, which possibly constitute the Mount Victoria Block accreted to the BT. A longitudinal belt of ophiolitic material called the Western Belt Ophiolite limits the IBR and the CMB. Several sub-basins comprise the CMB, divided into forearc and back-arc basins separated by a central longitudinal magmatic arc (WPA). The Chindwin and Minbu/Salin Basins are respectively the northern and southern sub-basins of the forearc, while the Shwebo basin is the north-eastern basin within the back-arc.

The WPA is the magmatic arc of the BT delineating these basins, and is believed to have formed as part of a Trans-Tethyan subduction system (Westerweel et al., 2019). Magmatic activity along the WPA is usually defined by a main phase during a short period around 100 Ma that is well-established by I-type intrusive rocks in the Wuntho Ranges (northern WPA) and in the Monywa area (central WPA), followed by subordinate phases during the Cenozoic

(Crow and Khin Zaw, 2017; Mitchell, 2018; Westerweel et al., 2019; Li et al., 2020). However, Cenozoic ages of the detrital zircons in the Paleogene sediments are often used as evidence for the subordinate stage of magmatic activity (Fig. 2), while direct evidence for volcanic activity is scarce. Drill cores close to the arc (Zhang et al., 2017) recovered mid and late Cretaceous granites as bedrocks below a thick Paleogene sedimentary cover. Paleocene tuffs near Ngape on the western side of the Minbu Basin (Cai et al., 2019) and one trachy-basalt near Salingy (Zhang et al., 2017) confirm some volcanic activity at ~69-65 Ma. The late Eocene Shangalon small-size porphyry copper deposit of ~42-36 Ma and associated volcanics within the Wuntho Ranges are the only evidence for magmatic activity during the Eocene with two dated late Eocene tuff layers within the basins (Khin Zaw et al., 2014; Licht et al., 2018) possibly related to the Shangalon magmatic event. Finally, an Oligocene rhyolite is described near Monywa, while middle Miocene (~16-13 Ma) and Quaternary volcanics are found near Monywa and Mount Popa (central WPA). A recent study on detrital zircons in sands from streams draining the Wuntho Ranges confirm the lack of a Paleogene source of volcanism, with the exception of the Shangalon magmatic suite of limited volume and age (Licht et al., 2020).

There is almost no information about the basement underlying the CMB and the WPA. The Sagaing Fault and the Shan scarp border of Sibumasu to the east separate two very different crusts supporting the hypothesis that the BT is a terrane with no common features with Sibumasu. Sibumasu has a hot and weak crust with high modern geothermal gradient (Morley, 2009), while the BT is a low relief cold terrane with thick subsiding sedimentary basins.

As a result, The pieces of evidence indicating either Gondwanan, Sibumasu or Cathaysian origins (Barber and Crow, 2009; Metcalfe, 2013; Ueno et al., 2016; Sevastjanova et al., 2016a; Yao et al., 2017) for the BT are contradictory. The Triassic Kanpetlet schist at the

core of the IBR and its associated Triassic turbidites of the Pane Chaung Formation constituting the Mount Victoria Block provide the best piece of evidence for a Gondwanan origin. The Pane Chaung Formation is now clearly correlated to the Langjiexue Formation of the NE Tethyan Himalaya (Cai et al., 2016; Yao et al., 2017; Liu et al., 2020) contradicting preliminary evidence for a correlation to Sibumasu (Sevastjanova et al., 2016b). The Mount Victoria Block can instead be seen as a Gondwanan crustal fragment that was incorporated along the Trans-Tethyan subduction system. Such Gondwanan crustal fragments have been referred to as the 'Greater Argoland' archipelago (Argoland specifically referring to rocks of Gondwanan affinity in East Java and Sulawesi; Hall et al., 2009; Sikumbang, 1990; Wakita et al., 1998), which would have rifted at ~155 Ma from NW Australia (Seton et al., 2012; Hall, 2012; I'Anson et al., 2019; Morley et al., 2020). The Greater Argoland origin would mean that sporadic Cathaysian fragments along the Sagaing Fault were not part of the BT at first, but are displaced slices of Sundaland (Metcalfe, 2017).

Both the Greater Argoland and composite origins for the BT can explain the potential collision of the Gondwana-derived Mount Victoria Block with the BT. This collision should have occurred by the mid-Cretaceous (Mitchell, 2017; Morley et al., 2020), as it has been shown that the basal conglomerates of the uppermost Cretaceous Kabaw Formation are mainly derived from the Pane Chaung Formation (Cai et al. 2019).

3. The zircon record

A number of studies are now providing zircons ages from a large amount of samples of various ages within the Myanmar sedimentary deposits. We have analysed the zircon record according to the estimated stratigraphic age and its geographical location (Chindwin Basin, Minbu Basin, WPA, and Paleogene deposits of the IBR).

The number of zircons with ages younger than 100Ma is so large that the pre-Cretaceous zircons record was almost not taken into account in most previous studies, who focussed more trying to determine the Maximum depositional age (MDA) of the sediments instead of determination of the source. At the sample level with usually only ~100 ages available, the prominent peak in the time range 0-100 Ma completely blurred out the distribution of the old zircons.

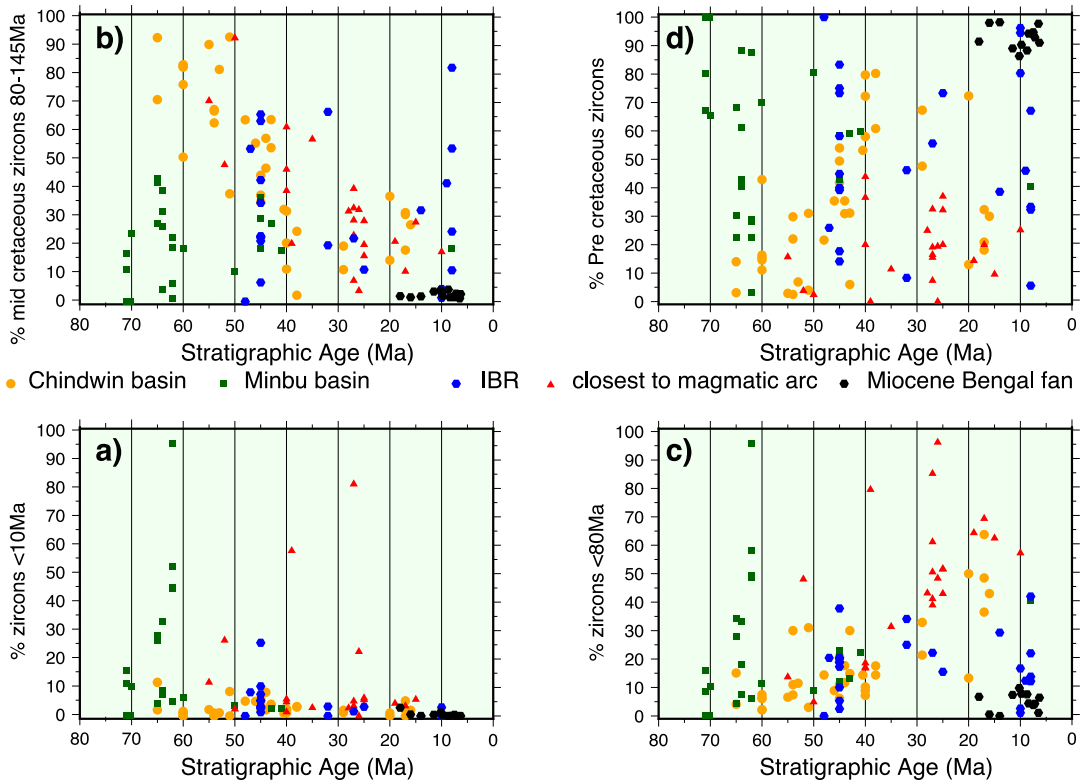

Figure 3. Plot of the percentage of zircon ages in different window where each point represents a sample with 80 to 100 dated zircons. a) % of zircons with ages within a 10Myr window below the estimated age stratigraphic age with respect to all detrital zircon ages within a sample. b) % of zircons with late K to Cenozoic ages; % of zircons corresponding to the main Cretaceous magmatic peak; d) % of pre-Cretaceous zircon ages per studied samples. Data from the Miocene Bengal sediments are shown for comparison.

There are almost no Late Jurassic or Early Cretaceous zircons in the sediments from the CMB and there is a clear minimum in the distribution of ages around 80 Ma (Fig. 2). We thus

decided to separate the distribution into three main groups, one for the pre-Cretaceous record, the second one for the mid-Cretaceous (145-80 Ma), and the third one for zircons younger than 80 Ma. The stratigraphic age is in most cases quite well-defined for the CMB by combining the stratigraphy in the field and the MDA. For the Eocene deposits of the IBR, the stratigraphy is less well-constrained and it is therefore often difficult to assess a precise age for the Paleogene sediments (e.g. Mitchell, 2017; Morley et al., 2020). Therefore, an age of 50 Ma was arbitrarily set for these samples.

The relative percentages of the three age populations are shown in figure 3 for each sample. It is obvious that the content in old zircons is far from negligible and often larger than the mid-Cretaceous percentage. The percentage of zircons ages in a 10 Ma window below the depositional age is also very low, except for the Late Cretaceous – Paleocene sediments of the Minbu Basin where there is evidence for a more active volcanic activity at the time of deposition of the sediments. Based on the large percentage of old zircons, the data overall indicates that the filling of the CMB is not related to the erosion of an active volcanic arc but rather to the erosion of a volcanic/plutonic basement.

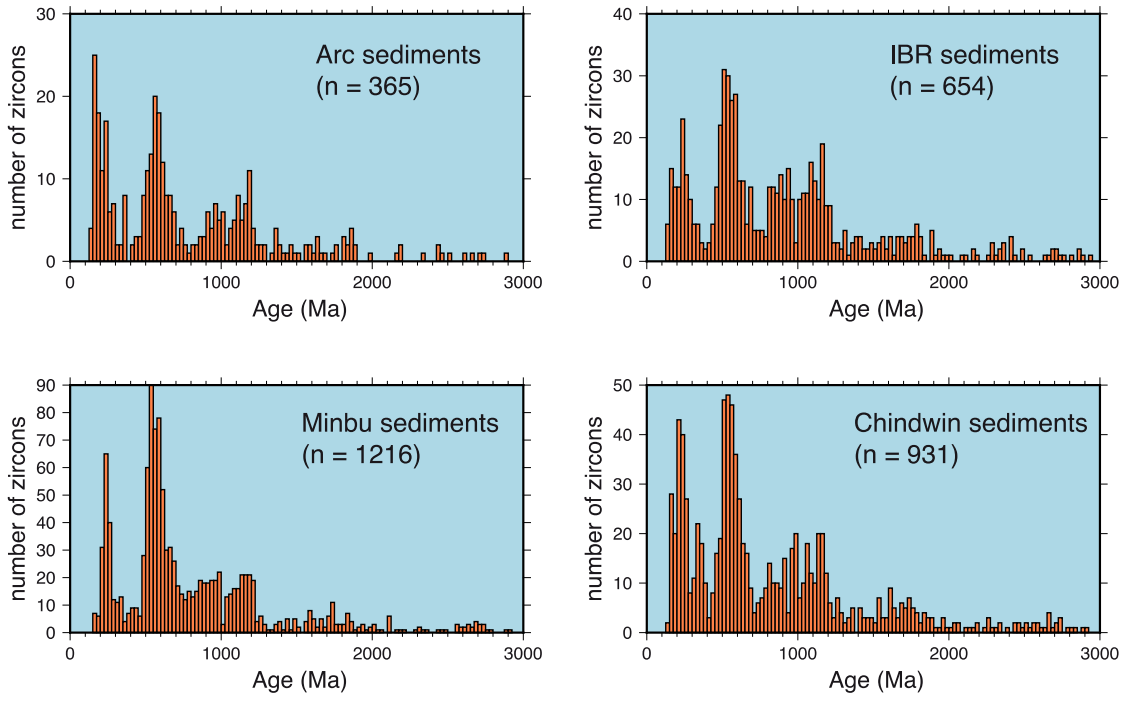

Figure 4. Distribution of pre-Cretaceous zircon ages in Late Cretaceous to Paleogene samples for the four geographic areas.

3.1. The pre-Cretaceous zircon record

The presence of Cenozoic zircons with negative εHf(t) values isotopic values clearly indicates a source of sediments from the India-Asia collision zone and the MMMB in Neogene sediments. Apatite U-Pb ages and apatite fission track data in the lower Miocene Letkat Formation clearly demonstrate high exhumation in the Eastern Himalayan Syntaxis in the early Miocene (Westerweel et al. 2020). For this reason, we will only consider samples in Late Cretaceous to Paleogene sediments, and only the location of these samples are shown in figure 1.

Despite some variations, likely due to insufficient sampling in certain areas such as along the WPA, the pre-Cretaceous distributions of ages share a similar pattern in the four studied areas (Fig. 4).

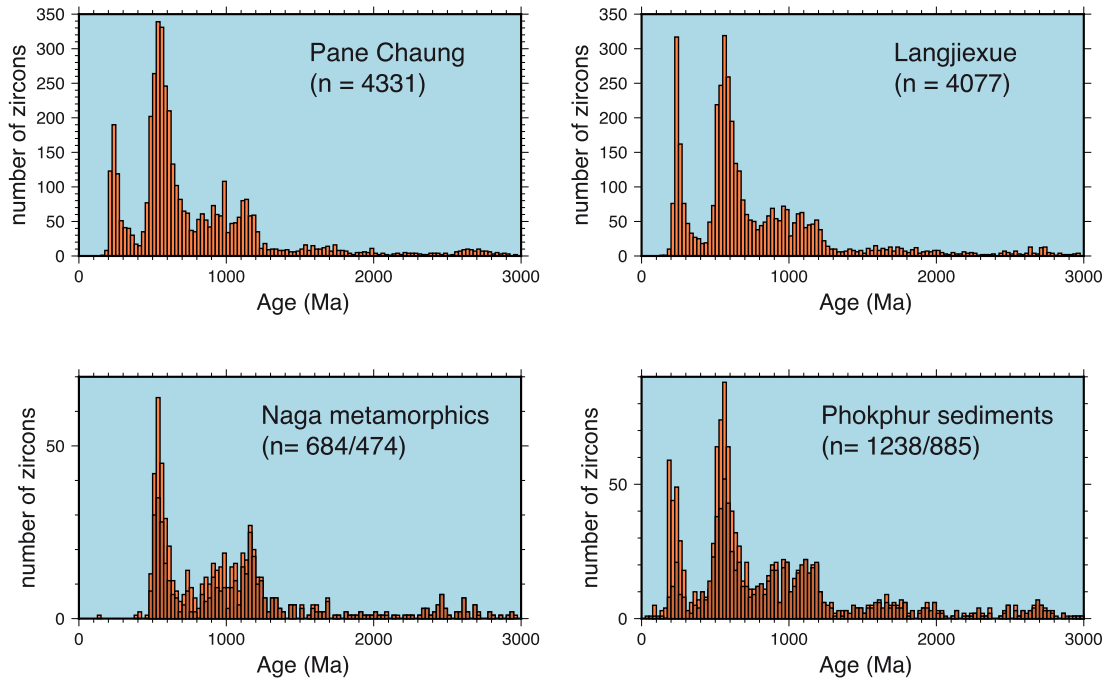

Figure 5. Distribution of zircon ages from Triassic Formation Pane Chaung and Langjiexue, the Naga metamorphics as well as the Eocene Phokphur sediments from the Naga Hills. The discordant ages are also shown for the Naga Hills data.

As already pointed out by Cai et al. (2019) in the Minbu Basin, the distribution of the old zircons is similar to the one found in the nearby Triassic rocks of the IBR. The four samples in the Kabaw formation indeed only contain pre-Cretaceous zircons. In addition, we compared the age distributions of the Pane Chaung Triassic turbidites, the Langjiexue Triassic rocks from the NE Tethyan Himalaya, as well as the Phokphur Eocene rocks and the Naga Hills metamorphics from the Naga Hills in the northern IBR (Aitchison et al., 2019) (Fig. 5). The Naga Hills metamorphics do not have Triassic zircons but sediments from the Eocene Phokphur Formation contain Triassic zircons. There is a large number of discordant ages in the Phokphur Formation, and these ages do not have a random distribution. The whole dataset including discordant ages has an even more striking similar distribution to the Pane Chaung Formation (Fig. 5).

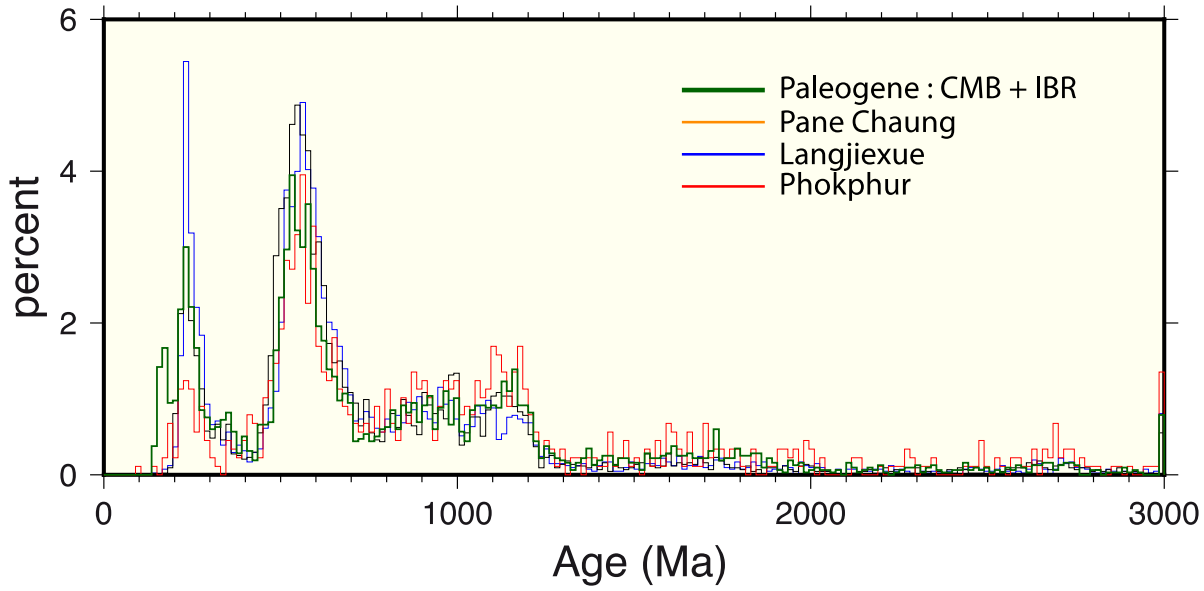

Figure 6. Normalized distribution of ages. The Phokphur is in the Naga Hills area.

The data from the four geographic groups (Minbu, Chindwin, Arc, IBR) shown in figure 5 were then stacked and compared after normalization by the number of zircon ages with the three other groups in figure 6 (Pane Chaung Formation, Langjiexue Formation and Naga hills Phokphur Eocene sediments). We do not need a sophisticated statistical analysis to recognize an obvious correlation between these units.

This correlation implies that most of the pre-Cretaceous zircons within the basin likely come from recycling of the Triassic rocks found in the IBR and Naga Hills as well as possibly from the NE Tethyan Himalaya. Moreover, it is important to note that rutile ages in the range 500-600 Ma are also a common feature of these units (Zhang et al., 2019a; Bracciali, 2019; Najman et al., 2020; Arboit et al., 2020). In Myanmar, the IBR is supposed to be covered by deep-marine sediments (Gough et al., 2019; Najman et al., 2020) and thus local sources from the western IBR are not expected. The Greater Burma region north of the Naga Hills could be the main location for such Triassic sources (Westerweel et al., 2020).

3.2. The mid-Cretaceous and Cenozoic record

The evidence from a sediment source located to the west or the north-west of the CMB questions the source of the Cretaceous to Cenozoic zircons coming from the nearby WPA located to the east, especially since samples from the Paleogene basins close to the arc also received sediments from the same old source. Indeed some of these samples close to the arc may not have many pre-Cretaceous zircons but contain the typical old rutiles (Zhang et al., 2017).

The εHf(t) isotopic signatures from the Paleogene sediments show zircons coming from juvenile rock sources, obviously contradicting that magmatic rocks from the Tin Belt and Sibumasu with negative εHf(t) values (Gardiner, 2018) were sedimentary sources at that time.

The prominent peak in Cretaceous ages led most authors (Wang et al., 2014; Licht et al., 2018, Cai et al., 2019) to suggest that the proximal WPA at the eastern edge of the Chindwin Basin (Zhang et al., 2017) was a dominant source for sediments in the Chindwin Basin until at least the late Eocene. However, no one has really tried to evaluate whether this arc, whose currently exposed surface area is very small (~5,000 km^2), could really be a significant source in volume. We also know that active volcanism is rather sporadic as seen by the number of dated Cenozoic magmatic bodies (Crow and Khin Zaw, 2017) or the low percentage of zircons with ages in a 10 Ma window below the stratigraphic age (Fig. 3).

We have analysed the record of the detrital zircons according to three main time intervals of sedimentary deposition (Fig. 7).

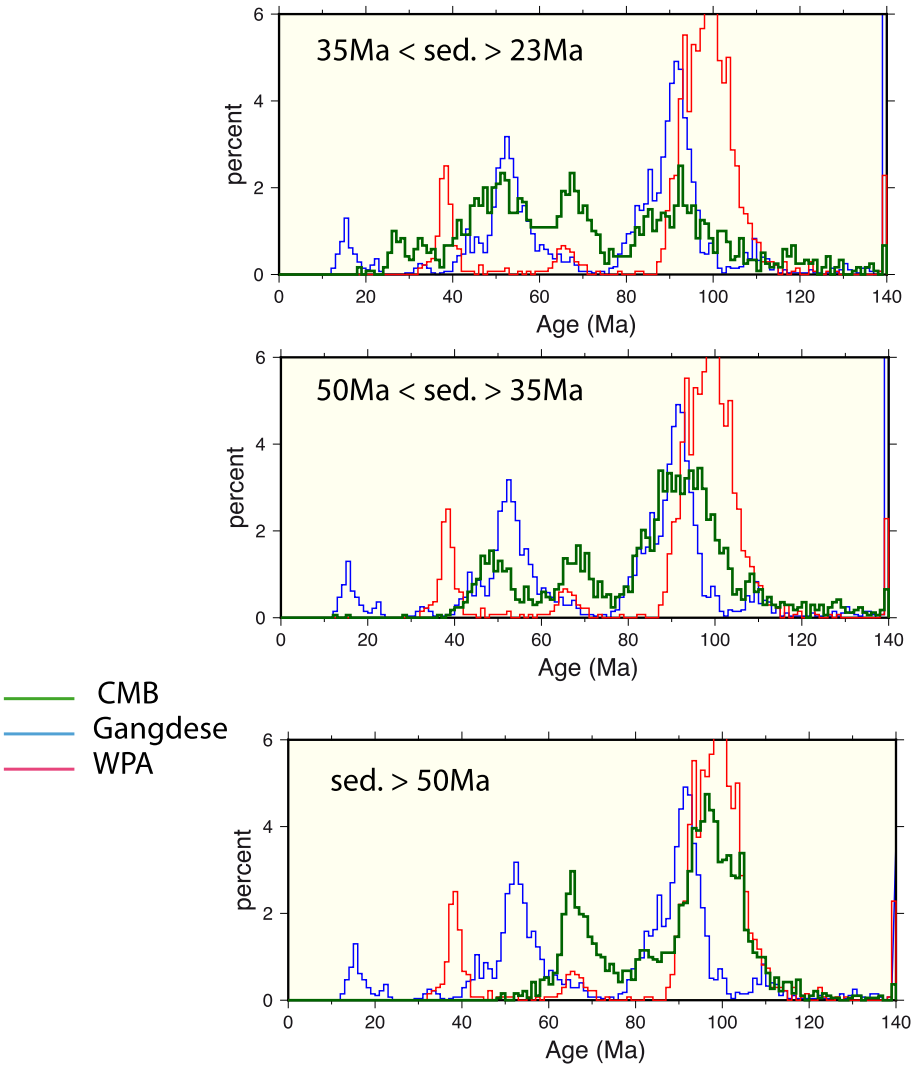

Figure 7. Comparison of the distribution of ages from the detrital zircons according to the stratigraphic ages of three groups of samples. The WPA are data from detrital zircons in sands from the Wuntho Ranges with additional data from tuffs in Late Cretaceous sediments from Minbu. The Gangdese contain a compilation of ages from Zhang et al. as well as a detrital record from the Xigaze basin .

The first group correspond to samples with stratigraphic ages older than 50 Ma; the second group corresponds mainly to sediments deposited during the Eocene, and the third group to sediments deposited mainly during the Oligocene. Samples from the first group correspond to a time period when the BT is located far from the southern Asia margin (Westerweel et al., 2019). In the Eocene group, we will try to recognize a connection to the India-Asia collision zone, while during the Oligocene it is even more likely that the BT was receiving detritus from the northern collision zone.

We compare the detrital record in sediments to a newly established record in sands from streams draining the Wuntho Ranges, which is the main massif representative of the plutonic activity in the WPA (Licht et al., 2020). To compare our dataset with the Gangdese Arc in the collision zone, we used a compilation of ages made by Zhang et al. (2019) completed by a record of detrital zircons in the Upper Cretaceous sediments of the Xigaze basin (Orme et al., 2015).

The Upper Cretaceous to Paleocene sediments of both the Chindwin and Minbu Basin have Cretaceous zircons with ages in the same time interval found in the Wuntho Ranges (Fig. 7). Samples of the Upper Cretaceous to Paleocene sediments of the Minbu Basin also contain a significant fraction of zircons with ages in the ~60-70 Ma range, while sedimentary samples from the same age range in the Chindwin Basin have mainly a mid-Cretaceous signature. The presence of tuff layers in the Paunggyi Formation near Ngape (Cai et al., 2019) provide additional evidence for magmatic activity in the Minbu Basin at that time. Finally, samples

291 from the Minbu Basin have a larger fraction of pre-Cretaceous zircons in contrast to those of
292 the Chindwin Basin (Figs. 3 and 7).

293 In Eocene samples, the mid-Cretaceous population represents younger zircons than observed
294 in Wuntho Ranges (Fig. 7). Furthermore, there is an input of Eocene zircons not directly
295 identified in the Wuntho Ranges. During the Oligocene, the trend as previously observed in
296 Eocene sediments is further enhanced with an increase in the relative content of Cenozoic
297 zircons compared to Cretaceous zircons. The distribution of ages of detrital zircons in
298 Oligocene sediments clearly supports evidence for a significant contribution from the
299 Gangdese Arc area (Fig. 7). As a similar trend is already observed in Eocene sediments, it is
300 possible to assert that a Gangdese source is also very likely for sediments deposited during
301 the Eocene. It should be noted that positive εHf(t) values observed in the Paleogene
302 sediments permit to reject eastern sources (e.g. Sibumasu), but that both the Gangdese Arc
303 and the WPA have juvenile magmas.

304

305 **3.3. Geology of the WPA.**

306 From the distribution of the Cenozoic zircons (Fig. 7), it appears that a source in the
307 Gangdese Arc cannot be discarded. The fundamental question then becomes: Is the
308 hypothesis of the WPA as a potential source for sediments filling the CMB supported by
309 available geological data in Myanmar?

310 The WPA is currently largely covered by Neogene sediments and this situation has been used
311 to speculate a large contribution of that arc to sediments filling the basins during the
312 Paleogene. However, the geology of the WPA is now better known, especially since the
313 publication of seismic lines across the arc south of the Wuntho Ranges (Zhang et al., 2017).
314 Seismic sections across and along the axis of the WPA indicate that large parts of the WPA

315 were buried by Eocene sediments (Li et al., 2013; Zhang et al., 2017). Shallow marine
316 sediments were recovered in the drill cores and plutonic rocks form the basement of the
317 sedimentary sequence. The recovery of the mid-Cretaceous plutonic rocks in these wells
318 suggests that the Cretaceous magmatic arc was already significantly eroded by the end of the
319 Cretaceous to permit the observation of these plutonic rocks immediately below the shallow
320 marine sediments covering it. The Cretaceous WPA batholith was likely emplaced in the
321 upper crust as suggested by $^{40}Ar/^{39}Ar$ ages on biotites and paleomagnetic data showing no
322 remagnetization (Westerweel et al., 2019). The 30 Ma period following batholith
323 emplacement was likely sufficiently long to allow a significant erosion of the arc, akin to
324 observations from the Andes where the mid-Cretaceous arc (coastal batholith) was
325 significantly eroded during the Late Cretaceous (Parada et al., 2005).

326 Paleocene and Eocene sediments are recognized in the wells defined by MDA from detrital
327 zircons. The seismic reflectors corresponding to these Paleogene sequences are roughly
328 parallel, suggesting that sediments were deposited on flat areas with very little tectonic
329 disturbance at that time. Within the Wuntho Ranges, the early Eocene Ketpanda formation
330 was also deposited at sea level (Arboit et al., 2020). The low relief of the WPA and large
331 subsidence of significant parts of the WPA demonstrate that there was no active erosion
332 during the Eocene in the central part of the WPA. The main unconformity in the seismic
333 sections is of late Oligocene age (Zhang et al., 2017). This is also supported by the apatite
334 fission track data in the plutonic rock below the sediment sequence in one of the drill cores
335 (Li et al., 2013), which show late Oligocene cooling associated to the tectonic event seen in
336 the seismic lines. This late Oligocene tectonic uplift event marks the end of significant
337 subsidence during the Eocene, as the apatite fission track data suggest significant burial to
338 reach the reset temperature of apatite (i.e. the plutonic rock was obviously cold before the
339 deposition of the overlying sediments). The present-day geothermal gradient is very low

(20°/km, (Li et al., 2013), but the uncertainty in the past geothermal gradient in the area precludes further estimation of the thickness of the Paleogene sedimentary sequence covering the arc and the amount of late Eocene eroded material. Yet, the late Oligocene unconformity on the seismic lines suggests erosion of several hundreds of meters of late Eocene sediments. This sequence of events is also reported in the western part of the Chindwin Basin, alongside evidence for reworking of sediments (Westerweel et al., 2020)

In the Chindwin Basin, high sedimentation rate has been suggested from MDA on zircons (Licht et al., 2018) and magnetostratigraphy in the upper Eocene Yaw formation (Westerweel et al., 2020). The available published MDA on samples in the underlying middle Eocene (~45-39 Ma) Poundang Formation show that this formation is possibly up to ~5 km thick with even higher sedimentation rates than the Yaw Formation. The magnetic properties of the sediments are also in contradiction with an active erosion of a nearby magmatic arc. With the exception of the lower Miocene Letkat Formation that contains large detrital magnetite grains, most of the studied samples have their magnetic susceptibility controlled by paramagnetic phases such as clay minerals (Westerweel et al., 2020).

For these reasons, a sediment source with active tectonism and erosion during the middle to late Eocene is required, and such a source is not observed along the WPA. Moreover, the only documented Eocene volcanism in the WPA is from the ~40 Ma U-Pb ages from Shangalon magmatic suite in the Wuntho Ranges directly east of the Chindwin Basin (Barley & Zaw, 2009; Gardiner et al., 2015), and this volcanism is almost not represented in the basins except possibly by a few thin volcanic tuffs (Khin Zaw et al., 2014; Licht et al., 2018).

4. Discussion

We concur with Guo et al. (2020) that the use of single-mineral data in the calculation of sediment budgets and inferences on erosion patterns is a complex and possibly impossible

task, unless the composition of the bulk sediment together with a spectrum of different mineral groups are taken into account. We also know that most terranes from southern Asia originally drifted from Gondwana, and these terranes share many features with the detrital zircons from the CMB (Zhang et al., 2019b). However, the striking similarities in the relative proportions of the various characteristic zircon sources from Gondwana in the different records shown in figure 6 is best explained by a simple recycling of the Triassic sediments either from the northern IBR or the Langjiexue Formation. Even the Naga Hills metamorphics have a similar distribution except the lack of Permo-Triassic ages. Therefore, the available data strongly reinforces a link between the BT and potential sources to the north-west, and permit to discard a source in Sundaland. Most of the previous geodynamic models did place the BT in the active Sundaland margin and often in the collision zone between India and Asia. However, sedimentary basins show marine depositional environments, and do not record strong collisional tectonics within the basins during the Paleogene. In our most recent plate reconstructions (Westerweel et al. 2020; in preparation), the BT is located on the eastern side of India and is effectively protected from collision until the end of the Oligocene. These observations clearly strengthen the link between the BT and the Indian Plate.

The exact location of the main source for the old pre-Cretaceous zircons is uncertain, as the northern IBR may have contributed to the source of zircons with the same signature than the Triassic rocks of the Pane Chaung and Langjiexue Formations. In Myanmar, the IBR directly west of the CMB is supposed to be only sporadically uplifted during the Paleogene, as evidenced by deep sea turbidites with similar provenance as the CMB covering large parts of the IBR (Mitchell, 2017; Najman et al., 2019). Hence, it is unlikely that the oldest pre-Cretaceous grains were sourced only locally from the IBR west of the CMB. There is plenty of evidence that uplift was more consequent in the northernmost part of the BT in the Naga

Hills area and possibly in the region of the Jade belt, where poorly understood basement rocks crop out extensively (e.g. Aitchison et al., 2019; Mitchell, 2017; Morley et al., 2020). As discussed in Westerweel et al., (2020), the Greater Burma region, the northern extension of the BT now underthrusted below Asia, may also be a major area with potential sources. The Eocene Phokphur sediments have mainly pre-Cretaceous zircons, which Aitchison et al. (2019) contribute to the Naga Hills metamorphics, but these authors do not explain the origin of the Triassic zircons in the Phokphur Formation that are not found in the Naga Hills metamorphics. We suggest a possible mixed source between the Triassic Pane Chaung Formation and the Naga Hills metamorphics, but so far the Triassic Pane Chaung Formation is not described in northern Myanmar or the Naga Hills.

Moreover, the present surface of the Wuntho Ranges is about 5% of the surface of the sedimentary basins west of the WPA, comprised mainly of the Chindwin and Minbu Basins. As discussed before, evidence for active erosion and active volcanism is low, ruling out the WPA as a main sedimentary source for these basins. It is difficult to estimate the volume of the Paleogene sediments deposited above and west of the IBR. If the reset of the Zircon helium thermochronometer in the Paleogene sediments from the IBR (Najman et al., 2020) is due to burial, that would add an additional large volume of sediments with the same sediment sources than those of the Central basin.

In Late Cretaceous to Paleocene sedimentary samples, the mid-Cretaceous zircons may come from direct erosion from the WPA, but a possible recycling of Cretaceous sediments deposited during the erosion of the WPA following its emplacement should be further investigated. Indeed, the bedrock of Paleocene sediments covering the arc is mainly intrusive rocks as discussed before, suggesting previous erosion of the volcanic rocks of the WPA.

From the early Eocene to Oligocene, sediments must have a source from the Gangdese Arc area in the collision zone to the north to provide the Cenozoic detritus. Paleocene zircons may come from the Trans-Tethyan Arc entering the collision zone, but a Gangdese contribution could also be possible.

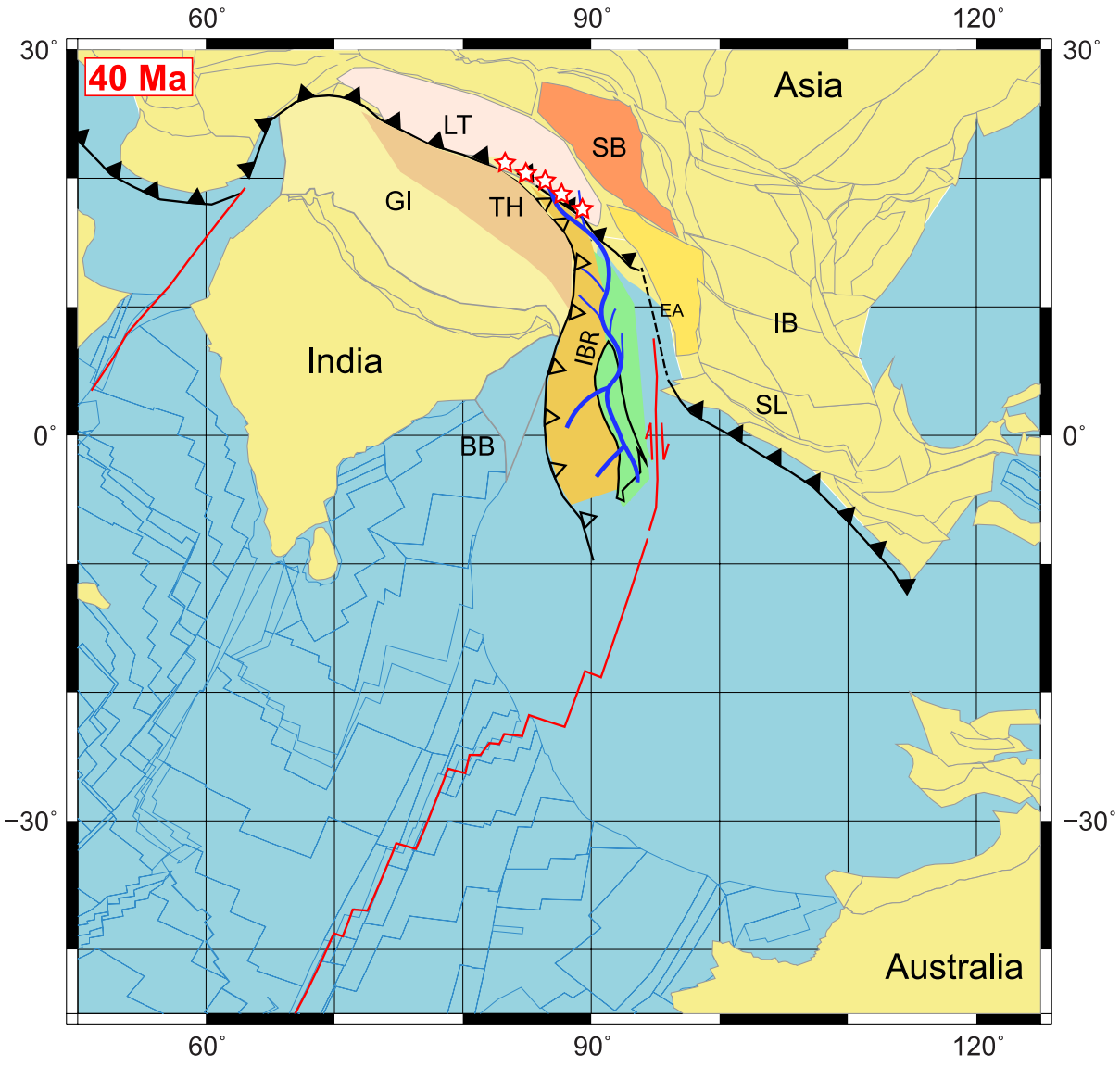

Figure 8. Reconstruction at 40 Ma modified from Westerweel et al. (2020). Abbreviations: GI: Greater India; TH= Tethyan Himalaya Triassic rocks, notably the Langjiexue block in the north-east; LT: Lhasa terrane; SB: Sibumasu block (presently eastern Myanmar).

Our paleogeographic model (Fig. 8) shows a completely different sedimentary sourcing at 40 Ma for the BT and eastern Myanmar (Sibumasu) region than proposed before, although our

423 model is not free of uncertainties with several unresolved questions. In this paleogeography,
424 the BT is a low land terrane being the sink of erosion coming from the collision zone. By
425 contrast, Sibumasu is extruded southward towards its present-day position at a later point in
426 time, and is therefore separated from the BT. The main uncertainty in our model is the
427 unresolved nature of the plate boundary between India and Sibumasu/Sundaland east of the
428 BT (Fig. 7).
429 In addition, the Langjiexue block to the north-west of the BT, which is located in the NE
430 Tethyan Himalaya at present, may be an allochthonous block with the same paleogeographic
431 evolution as the IBR before the India-Asia collision. The Upper Triassic Langjiexue
432 Formation is exposed south of the Yarlung Tsangpo Suture Zone in the central-eastern
433 Himalayas, where it is in fault contact with other Tethyan Himalayan series. Despite evidence
434 that provenance signatures of the Qulonggongba sandstones, located within the centre of the
435 Tethyan Himalaya, and Langjiexue sandstones are similar (Meng et al., 2019) indicating a
436 common source of detritus, the similarities with the Pane Chaung Formation of the IBR
437 support the possibility that the Langjiexue Group represents an exotic block related to the
438 IBR. Yet, there are several contradictory findings for the origin of the sediments and the
439 tectonic evolution of the Langjiexue block (Ao et al., 2016).
440 The IBR could be part of a Greater Argoland crustal fragment (see Section 2) that drifted
441 away from India before entering in collision with the Trans-Tethyan Arc. The basement of
442 the BT is likely made of a thin continental crust (Mitchell, 2018), but it is unknown if this
443 basement similarly constitutes a Greater Argoland crustal fragment. By contrast, several
444 models suggest that the Trans-Tethyan Arc was formed on southward drifting blocks rifted
445 from the Asian margin (Gibbons et al., 2012; Zahirovic et al., 2014).

446 A final uncertainty is the age of metamorphism in the IBR. Aitchison et al. (2019) consider
447 that the Naga Hills metamorphics are an integral part of India, although the complex tectonic

relation with the ophiolite slices impedes a good understanding of the shape of the plate prior to Cenozoic deformation. While the Pane Chaung turbidites could be the protolith of the Kanpetlet schists, the Naga Hills metamorphics do not have the Permo-Triassic zircons present there, and their metamorphic grade is higher than the Kanpetlet schists. Metamorphism of the Kanpetlet schists was considered to be Late Cretaceous by (Socquet et al., 2002). Since clasts of these schist are found in the Kabaw Formation (Cai et al., 2019), the metamorphism should have occurred earlier (Morley et al., 2020). Brunnschweiler (1966) even suggested that the Kanpetlet schists are pre-Cretaceous basement rocks in sharp contact with the Cenozoic units. Despite the high temperature (~400°C) reached during metamorphism of the schists (Socquet et al., 2002), zircon fission track data in one sample from the Kanpetlet schists indicates Permo-Triassic ages (Najman et al., 2020). It is also interesting to note that one sample from the Pane Chaung turbidites does not show Cretaceous or Cenozoic reset of the zircon/helium thermochronometer, while most of the samples in Cenozoic sediments from the IBR do show young ZHe ages.

5. Conclusions

Paleomagnetic data demonstrate a northward motion of the BT alongside the Indian Plate. Contrary to previous claims, Paleogene filling of the BT may be better explained by sediment sources located to the north and north-west of the BT, constituting a source to sink model similar to the one proposed for the Oligocene (Gough et al., 2019). Erosion of Triassic turbidites and Cretaceous to Eocene volcanics in a Greater Burma block as well as from the Gangdese Arc may provide a sediment signature in better agreement with the distribution of ages found in the detrital zircons from Paleogene sediments of the CMB.

ACKNOWLEDGEMENTS

We thank Francesco Arboit, Nathan Cogné, François Guillocheau, Amy Gough, Chris Morley, Yani Najman, Jean-Noël Proust, Ed Sobel and Douwe van Hinsbergen for prolific discussions during this study.

REFERENCES CITED

Aitchison, J.C. et al., 2019, Tectonic Evolution of the Western Margin of the Burma Microplate Based on New Fossil and Radiometric Age Constraints: Tectonics, v. 38, p. 1718–1741, doi:10.1029/2018TC005049.

Allen, R., Najman, Y., Carter, A., Barfod, D., Bickle, M.J., Chapman, H.J., Garzanti, E., Vezzoli, G., Ando, S., and Parrish, R.R., 2008, Provenance of the Tertiary sedimentary rocks of the IBR, Burma (Myanmar): Burman arc or Himalayan-derived? Journal of the Geological Society, v. 165, p. 1045–1057, doi:10.1144/0016-76492007-143.

Ao, H., Roberts, A.P., Dekkers, M.J., Liu, X., Rohling, E.J., Shi, Z., An, Z., and Zhao, X., 2016, Late Miocene–Pliocene Asian monsoon intensification linked to Antarctic ice-sheet growth: Earth and Planetary Science Letters, v. 444, p. 75–87, doi:10.1016/j.epsl.2016.03.028.

Arboit, F., Min, M., Chew, D., Mitchell, A., Drost, K., Badenszki, E., and Daly, J.S., 2020, Constraining the links between the Himalayan belt and the Central Myanmar Basins during the Cenozoic: An integrated multi-proxy detrital geochronology and trace-element geochemistry study: Geoscience Frontiers, p. S1674987120301705, doi:10.1016/j.gsf.2020.05.024.

Barber, A.J., and Crow, M.J., 2009, Structure of Sumatra and its implications for the tectonic assembly of Southeast Asia and the destruction of Paleotethys: Island Arc, v. 18, p. 3–20, doi:10.1111/j.1440-1738.2008.00631.x.

Beck, M.E., 1991, Coastwise transport reconsidered: lateral displacements in oblique subduction zones, and tectonic consequences: Physics of the Earth and Planetary Interiors, v. 68, p. 1–8, doi:10.1016/0031-9201(91)90002-Y.

Bracciali, L., 2019, Coupled Zircon-Rutile U-Pb Chronology: LA ICP-MS Dating, Geological Significance and Applications to Sediment Provenance in the Eastern Himalayan-Indo-Burman Region: Geosciences, v. 9, p. 467, doi:10.3390/geosciences9110467.

Brunnschweiler, R.O., 1966, On the geology of the Indoburman ranges: (Arakan Coast and Yoma, Chin Hills, Naga Hills): Journal of the Geological Society of Australia, v. 13, p. 137–194, doi:10.1080/00167616608728608.

Cai, F., Ding, L., Laskowski, A.K., Kapp, P., Wang, H., Xu, Q., and Zhang, L., 2016, Late Triassic paleogeographic reconstruction along the Neo–Tethyan Ocean margins, southern Tibet: Earth and Planetary Science Letters, v. 435, p. 105–114, doi:10.1016/j.epsl.2015.12.027.

Cai, F., Ding, L., Zhang, Q., Orme, D.A., Wei, H., Li, J., Zhang, J., Zaw, T., and Sein, K., 2019, Initiation and evolution of forearc basins in the Central Myanmar Depression: GSA Bulletin, doi:10.1130/B35301.1.

Crow, M.J., and Khin Zaw, 2017, Appendix Geochronology in Myanmar (1964–2017): Geological Society, London, Memoirs, v. 48, p. 713–759, doi:10.1144/M48.32.

Gardiner, N.J., Hawkesworth, C.J., Robb, L.J., Whitehouse, M.J., Roberts, N.M.W., Kirkland, C.L., and Evans, N.J., 2017, Contrasting Granite Metallogeny through the Zircon Record: A Case Study from Myanmar: Scientific Reports, v. 7, doi:10.1038/s41598-017-00832-2.

Gibbons, A.D., Barckhausen, U., van den Bogaard, P., Hoernle, K., Werner, R., Whittaker, J.M., and Muller, R.D., 2012, Constraining the Jurassic extent of Greater India: Tectonic evolution of the West Australian margin: GEOCHEMISTRY GEOPHYSICS GEOSYSTEMS, v. 13, p. Q05W13.

Gough, A., Hall, R., and BouDagher-Fadel, M.K., 2019, Mid-Cenozoic fluvio-deltaic to marine environments of the Salin Sub-basin, Central Myanmar: Journal of Asian Earth Sciences, p. 104143, doi:10.1016/j.jseaes.2019.104143.

Hall, R., 2012, Late Jurassic–Cenozoic reconstructions of the Indonesian region and the Indian Ocean: Tectonophysics, v. 570–571, p. 1–41, doi:10.1016/j.tecto.2012.04.021.

I'Anson, A., Elders, C., and McHarg, S., 2019, Marginal fault systems of the Northern Carnarvon Basin: Evidence for multiple Palaeozoic extension events, North-West Shelf, Australia: Marine and Petroleum Geology, v. 101, p. 211–229, doi:10.1016/j.marpetgeo.2018.11.040.

Khin Zaw, Meffre, S., Takai, M., Suzuki, H., Burrett, C., Thaung Htike, Zin Maung Maung Thein, Tsubamoto, T., Egi, N., and Maung Maung, 2014, The oldest anthropoid primates in SE Asia: Evidence from LA-ICP-MS U–Pb zircon age in the Late Middle Eocene Pondaung Formation, Myanmar: Gondwana Research, v. 26, p. 122–131, doi:10.1016/j.gr.2013.04.007.

Kyaw Linn Oo, Khin Zaw, Meffre, S., Myitta, Day Wa Aung, and Lai, C.-K., 2015, Provenance of the Eocene sandstones in the southern Chindwin Basin, Myanmar: Implications for the unroofing history of the Cretaceous–Eocene magmatic arc: Journal of Asian Earth Sciences, v. 107, p. 172–194, doi:10.1016/j.jseaes.2015.04.029.

Li, J.-X., Fan, W.-M., Zhang, L.-Y., Peng, T.-P., Sun, Y.-L., Ding, L., Cai, F.-L., and Sein, K., 2020, Prolonged Neo-Tethyan magmatic arc in Myanmar: evidence from geochemistry and Sr–Nd–Hf isotopes of Cretaceous mafic–felsic intrusions

in the Banmauk–Kawlin area: International Journal of Earth Sciences, doi:10.1007/s00531-020-01824-w.

Li, R., Mei, L., Zhu, G., Zhao, R., Xu, X., Zhao, H., Zhang, P., Yin, Y., and Ma, Y., 2013, Late mesozoic to cenozoic tectonic events in volcanic arc, West Burma Block: Evidences from U-Pb zircon dating and apatite fission track data of granitoids: Journal of Earth Science, v. 24, p. 553–568, doi:10.1007/s12583-013-0349-7.

Licht, A. et al., 2020, Magmatic history of central Myanmar and implications for the evolution of the Burma Terrane.: Gondwana Research, doi:10.1016/j.gr.2020.06.016.

Licht, A. et al., 2018, Paleogene evolution of the Burmese forearc basin and implications for the history of India-Asia convergence: Geological Society of America Bulletin, v. 130, p. 20.

Licht, A., France-Lanord, C., Reisberg, L., Fontaine, C., Soe, A.N., and Jaeger, J.-J., 2013, A palaeo Tibet–Myanmar connection? Reconstructing the Late Eocene drainage system of central Myanmar using a multi-proxy approach: Journal of the Geological Society, v. 170, p. 929–939.

Licht, A., Reisberg, L., France-Lanord, C., Naing Soe, A., and Jaeger, J.-J., 2016, Cenozoic evolution of the central Myanmar drainage system: insights from sediment provenance in the Minbu Sub-Basin: Basin Research, v. 28, p. 237–251, doi:10.1111/bre.12108.

Liu, Y.M., Dai, J.G., Wang, C.S., Li, H.A., Wang, Q., and Zhang, L.L., 2020, Provenance and tectonic setting of Upper Triassic turbidites in the eastern Tethyan Himalaya: Implications for early-stage evolution of the Neo–Tethys: Earth-Science Reviews, v. 200, p. 103030, doi:10.1016/j.earscirev.2019.103030.

Meng, Z., Wang, J., Ji, W., Zhang, H., Wu, F., and Garzanti, E., 2019, The Langjiexue Group is an in situ sedimentary sequence rather than an exotic block: Constraints from coeval Upper Triassic strata of the Tethys Himalaya (Qulonggongba Formation): Science China Earth Sciences, doi:10.1007/s11430-018-9314-9.

Metcalfe, I., 2013, Gondwana dispersion and Asian accretion: Tectonic and palaeogeographic evolution of eastern Tethys: Journal of Asian Earth Sciences, v. 66, p. 1–33, doi:10.1016/j.jseaes.2012.12.020.

Metcalfe, I., 2017, Tectonic evolution of Sundaland: v. 63, p. 35.

Métivier, F., Gaudemer, Y., Tapponnier, P., and Klein, M., 1999, Mass accumulation rates in Asia during the Cenozoic: Geophysical Journal International, v. 137, p. 280–318, doi:10.1046/j.1365-246X.1999.00802.x.

Mitchell, A., 2017, Geological Belts, Plate Boundaries, and Mineral Deposits in Myanmar: Elsevier.

Mitchell, A., 2018, Popa–Loimye Magmatic Arc, *in* Geological Belts, Plate Boundaries, and Mineral Deposits in Myanmar, Elsevier, p. 277–323, doi:10.1016/B978-0-12-803382-1.00009-2.

Morley, C.K., 2009, Evolution from an oblique subduction back-arc mobile belt to a highly oblique collisional margin: the Cenozoic tectonic development of Thailand and eastern Myanmar: Geological Society, London, Special Publications, v. 318, p. 373–403, doi:10.1144/SP318.14.

Morley, C.K., and Arboit, F., 2019, Dating the onset of motion on the Sagaing Fault: Evidence from detrital zircon and titanite U-Pb geochronology from the North Minwun Basin, Myanmar: Geology, v. 47, p. 581–585, doi:10.1130/G46321.1.

Morley, C.K., Tin Tin Naing, Searle, M., and Robinson, S.A., 2020, Structural and tectonic development of the Indo-Burma ranges: Earth-Science Reviews, v. 200, p. 102992, doi:10.1016/j.earscirev.2019.102992.

Najman, Y. et al., 2020, The exhumation of the IBR, Myanmar: Earth and Planetary Science Letters, v. 530, p. 115948, doi:10.1016/j.epsl.2019.115948.

Orme, D.A., Carrapa, B., and Kapp, P., 2015, Sedimentology, provenance and geochronology of the upper Cretaceous-lower Eocene western Xigaze forearc basin, southern Tibet: Basin Research, v. 27, p. 387–411, doi:10.1111/bre.12080.

Parada, M.A., Feraud, G., Fuentes, F., Aguirre, L., Morata, D., and Larrondo, P., 2005, Ages and cooling history of the Early Cretaceous Caleu pluton: testimony of a switch from a rifted to a compressional continental margin in central Chile: Journal of the Geological Society, v. 162, p. 273–287, doi:10.1144/0016-764903-173.

Robinson, R.A.J., Brezina, C.A., Parrish, R.R., Horstwood, M.S.A., Nay Win Oo, Bird, M.I., Myint Thein, Walters, A.S., Oliver, G.J.H., and Khin Zaw, 2014, Large rivers and orogens: The evolution of the Yarlung Tsangpo–Irrawaddy system and the eastern Himalayan syntaxis: Gondwana Research, v. 26, p. 112–121, doi:10.1016/j.gr.2013.07.002.

Seton, M., Müller, R.D., Zahirovic, S., Gaina, C., Torsvik, T., Shephard, G., Talsma, A., Gurnis, M., Turner, M., and Maus, S., 2012, Global continental and ocean basin reconstructions since 200 Ma: Earth-Science Reviews, v. 113, p. 212–270.

Sevastjanova, I., Hall, R., Rittner, M., Paw, S.M.T.L., Naing, T.T., Alderton, D.H., and Comfort, G., 2016a, Myanmar and Asia united, Australia left behind long ago: Gondwana Research, v. 32, p. 24–40, doi:10.1016/j.gr.2015.02.001.

Sevastjanova, I., Hall, R., Rittner, M., Paw, S.M.T.L., Naing, T.T., Alderton, D.H., and Comfort, G., 2016b, Myanmar and Asia united, Australia left behind long ago: Gondwana Research, v. 32, p. 24–40, doi:10.1016/j.gr.2015.02.001.

Socquet, A., Goffé, B., Pubellier, M., and Rangin, C., 2002, Le métamorphisme Tardi-Crétacé à Éocène des zones internes de la chaîne Indo-Birmane (Myanmar occidental) : implications géodynamiques: , p. 8.

626 **Socquet, A., Vigny, C., Chamot-Rooke, N., Simons, W., Rangin, C., and Ambrosius, B.,**
627 **2006, India and Sunda plates motion and deformation along their boundary in**
628 **Myanmar determined by GPS: Journal of Geophysical Research: Solid Earth, v.**
629 **111, p. B05406, doi:10.1029/2005JB003877.**

630 **Ueno, K., Thein, M., and Barber, A.J., 2016, Permian fusuline fauna from the Minwun**
631 **Range, Central Myanmar, *in* 5th Symposium of the International Geosciences**
632 **Programme (IGCP), v. 589, p. 27–28.**

633 **Wang, J.-G., Wu, F.-Y., Tan, X.-C., and Liu, C.-Z., 2014, Magmatic evolution of the**
634 **Western Myanmar Arc documented by U–Pb and Hf isotopes in detrital zircon:**
635 **Tectonophysics, v. 612–613, p. 97–105, doi:10.1016/j.tecto.2013.11.039.**

636 **Westerweel, J., Roperch, P., Licht, A., Dupont-Nivet, G., Win, Z., Poblete, F., Ruffet, G.,**
637 **Swe, H.H., Thi, M.K., and Aung, D.W., 2019, Burma Terrane part of the Trans-**
638 **Tethyan arc during collision with India according to palaeomagnetic data:**
639 **Nature Geoscience, v. 12, p. 863–868, doi:10.1038/s41561-019-0443-2.**

640 **Westerweel, J., Licht, A., Cogné, N., Roperch, P., Dupont-Nivet, G., Thi, M. K., …**
641 **Aung, D. W. (2020). Burma Terrane collision and northward indentation in the**
642 **Eastern Himalayas recorded in the Eocene - Miocene Chindwin Basin**
643 **(Myanmar). Tectonics. https://doi.org/10.1029/2020TC006413**
644
645 **Yao, W., Ding, L., Cai, F., Wang, H., Xu, Q., and Zaw, T., 2017, Origin and tectonic**
646 **evolution of upper Triassic Turbidites in the IBR, West Myanmar: Tectonophysics, v.**
647 **721, p. 90–105, doi:10.1016/j.tecto.2017.09.016.**

648 **Zahirovic, S., Seton, M., and Müller, R.D., 2014, The Cretaceous and Cenozoic tectonic**
649 **evolution of Southeast Asia: Solid Earth, v. 5, p. 227–273, doi:10.5194/se-5-227-**
650 **2014.**

651 **Zhang, P. et al., 2019a, Palaeodrainage evolution of the large rivers of East Asia, and**
652 **Himalayan-Tibet tectonics: Earth-Science Reviews, v. 192, p. 601–630,**
653 **doi:10.1016/j.earscirev.2019.02.003.**

654 **Zhang, X., Chung, S.-L., Lai, Y.-M., Ghani, A.A., Murtadha, S., Lee, H.-Y., and Hsu,**
655 **C., 2019b, A 6000-km-long Neo-Tethyan arc system with coherent magmatic**
656 **flare-ups and lulls in South Asia: Geology, v. 47, p. 4.**

657 **Zhang, P., Mei, L., Hu, X., Li, R., Wu, L., Zhou, Z., and Qiu, H., 2017, Structures,**
658 **uplift, and magmatism of the Western Myanmar Arc: Constraints to mid-**
659 **Cretaceous-Paleogene tectonic evolution of the western Myanmar continental**
660 **margin: Gondwana Research, v. 52, p. 18–38, doi:10.1016/j.gr.2017.09.002.**

661

662

Abstract

The Himalayan-Tibetan orogen, formed primarily due to the India-Asia collision, represents a complex interplay of collisional tectonics, climate and environmental processes. However, its paleogeographic evolution, as well as the timing of the collision itself, remain the subject of intense debate. This controversy is partly the result of understudying major components of the Himalayan orogen. At the eastern edge of the orogen, the paleogeography of the Burma Terrane (Myanmar) is particularly uncertain but key for solving the India-Asia collision puzzle. Therefore, this thesis presents a complete set of Late Cretaceous to Miocene paleomagnetic data from the Burma Terrane. With sedimentology and geochronology data, these results were incorporated into plate tectonic reconstructions to elucidate the paleogeographic history of the India-Asia collision from the perspective of the Burma Terrane. The three key implications are: (1) the Burma Terrane was in an equatorial position distant from Asia from the Cretaceous until the Paleogene, (2) it was incorporated onto the Indian Plate in the latest Paleocene – middle Eocene, and (3) it subsequently moved northward with India. This latitudinal displacement explains why the Burma Terrane does not record major compressional deformation before the late Oligocene – early Miocene. Yet, the sedimentary basins of Myanmar received erosional products from the collision zone already in the Eocene. By the Miocene, they record rapid exhumation of the Eastern Himalayan Syntaxis. The complete dataset is used to infer an India-Asia collision model with a Trans-Tethyan Arc, which comprises the Burma Terrane formed from Gondwanan crustal fragments. This model invites a critical re-evaluation of many aspects of the regional tectonic history, and has additional implications for Asian biotic and climatic evolution.

Keywords

Paleomagnetism, plate tectonics, paleogeography, Burma Terrane, India-Asia collision, Myanmar

UNIVERSITÉ DE RENNES 1

Titre : La collision Inde-Asie vue de la Birmanie : Aperçus du paléomagnétisme et des reconstructions paléogéographiques

Mots clés : Paléomagnétisme, tectonique des plaques, paléogéographie, Birmanie, collision Inde-Asie

Résumé : L'orogène Himalayen-Tibétain, formé principalement par la collision Inde-Asie, représente une interaction complexe de la tectonique, du climat et des processus environnementaux. Cependant, l'évolution paléogéographique et la chronologie de la collision, restent l'objet d'un débat intense. Cette controverse est en partie le résultat d'une sous-étude de la partie orientale de l'orogène Himalayen. L'histoire paléogéographique du Terrane de Birmanie (Myanmar) est particulièrement incertaine mais importante pour une meilleure compréhension de la collision Inde-Asie. C'est pourquoi cette thèse présente des données uniques de paléomagnétisme sur des roches du Crétacé au Miocène de la région du Myanmar. Avec les données sédimentologiques et géochronologiques, ces résultats ont été incorporés dans des reconstructions de la tectonique des plaques pour élucider l'histoire paléogéographique du Terrane de Birmanie lors de la collision Inde-Asie. Les trois principaux résultats sont: (1) le Terrane de Birmanie était situé dans une position équatoriale très éloignée de l'Asie du Crétacé au Paléocène, (2) il a été incorporé à la plaque Indienne au cours du Paléocène, et (3) il s'est ensuite déplacé vers le nord avec la plaque Indienne. Ce déplacement latitudinal explique pourquoi le Myanmar n'enregistre pas de déformation compressive majeure avant la fin de l'Oligocène - début du Miocène. Par contre les bassins sédimentaires du Myanmar reçoivent les produits de l'érosion de la zone de collision. Une exhumation très rapide au niveau de la Syntaxe Est-Himalayenne est mise en évidence dans les sédiments du Miocène inférieur. L'ensemble des données permet de proposer un modèle de collision Inde-Asie avec un Arc Trans-Téthysien, qui comprend le Terrane de Birmanie formé à partir de fragments crustaux du Gondwana. Ce modèle invite à une réévaluation critique de nombreux aspects de l'histoire tectonique régionale et des paléoenvironnements.

Title : The India-Asia collision from the perspective of Myanmar: Insights from paleomagnetism and paleogeographic reconstructions

Keywords : Paleomagnetism, plate tectonics, paleogeography, Myanmar, India-Asia collision

Abstract : The Himalayan-Tibetan orogen, formed primarily due to the India-Asia collision, represents a complex interplay of collisional tectonics, climate and environmental processes. However, its paleogeographic evolution, as well as the timing of the collision itself, remain the subject of intense debate. This controversy is partly the result of understudying major components of the Himalayan orogen. At the eastern edge of the orogen, the paleogeography of the Burma Terrane (Myanmar) is particularly uncertain but key for solving the India-Asia collision puzzle. Therefore, this thesis presents a complete set of Late Cretaceous to Miocene paleomagnetic data from the Burma Terrane. With sedimentology and geochronology data, these results were incorporated into plate tectonic reconstructions to elucidate the paleogeographic history of the India-Asia collision from the perspective of the Burma Terrane. The three key implications are: (1) the Burma Terrane was in an equatorial position distant from Asia from the Cretaceous until the Paleogene, (2) it was incorporated onto the Indian Plate in the latest Paleocene – middle Eocene, and (3) it subsequently moved northward with India. This latitudinal displacement explains why the Burma Terrane does not record major compressional deformation before the late Oligocene – early Miocene. Yet, the sedimentary basins of Myanmar received erosional products from the collision zone already in the Eocene. By the Miocene, they record rapid exhumation of the Eastern Himalayan Syntaxis. The complete dataset is used to infer an India-Asia collision model with a Trans-Tethyan Arc, which comprises the Burma Terrane formed from Gondwanan crustal fragments. This model invites a critical re-evaluation of many aspects of the regional tectonic history, and has additional implications for Asian biotic and climatic evolution.